NanoScience and Technology

Vladimir M. Fomin *Editor*

Physics of Quantum Rings

Second Edition

Springer

NanoScience and Technology

The series NanoScience and Technology is focused on the fascinating nano-world, mesoscopic physics, analysis with atomic resolution, nano and quantum-effect devices, nanomechanics and atomic-scale processes. All the basic aspects and technology-oriented developments in this emerging discipline are covered by comprehensive and timely books. The series constitutes a survey of the relevant special topics, which are presented by leading experts in the field. These books will appeal to researchers, engineers, and advanced students.

More information about this series at http://www.springer.com/series/3705

Vladimir M. Fomin
Editor

Physics of Quantum Rings

Second Edition

Springer

Editor
Vladimir M. Fomin
Institute for Integrative Nanosciences
Leibniz Institute for Solid State and
Materials Research (IFW) Dresden
Dresden, Germany

ISSN 1434-4904 ISSN 2197-7127 (electronic)
NanoScience and Technology
ISBN 978-3-319-95158-4 ISBN 978-3-319-95159-1 (eBook)
https://doi.org/10.1007/978-3-319-95159-1

Library of Congress Control Number: 2018947471

This Springer imprint is published by the registered company Springer Nature Switzerland AG
The registered company address is: Gewerbestrasse 11, 6330 Cham, Switzerland

Foreword

Physics of Solids developed into an independent discipline at the end of the 30s of last century with the formulation of the theory of electronic band structure. Boundary condition for the validity of this theory is the assumption of an infinitely extended crystal showing no defects, interfaces, or surfaces. Almost at the same time, the quantum mechanical problem of a particle in a one-dimensional potential well was solved for the first time.

Semiconductors were recognized as an important class of solids only a decade later, although the first roots go back to the nineteenth century when Ferdinand Braun, well known as the inventor of the cathode ray tube, wrote in 1874 his thesis on "Current Conduction through Sulfur-Metals". The subject of this thesis got much later the name "Schottky Diode". The development of the transistor by William Shockley and his coworkers starting 1947 and of III–V compounds by Heinrich Welker already in 1951 present landmarks decisive for the development of modern multi-targeted technologies enabling today solar cells, microprocessors, or semiconductor lasers, to mention a few device groups having diffused into our daily life. Indeed, it is unthinkable to live without such devices enabling, in particular, modern communication technologies.

Heterostructures, layered semiconductor/semiconductor or semiconductor/insulator structures like Si/SiO_2, were essential parts of devices like transistors from the very beginning. With the advent of III–V-based heterostructures, presenting the basis for light emitting, but also highly efficient light-harvesting devices, the material basis for a wealth of devices and systems broadened enormously and the scientific community embarked to explore "chemical engineering" in a very systematic way. Twice Nobel prizes were awarded for the physics of Si- and III–V-based heterostructures in 1985 and 2000. The limits of combining materials of varying chemical composition on top of each other were discovered to be controlled by the variation of lattice constants between different materials. If this difference is too large, defects like dislocations develop and the device properties degrade. Thus, the original enthusiasm on "chemical engineering" was fast decaying at the end of the 80s of last century and almost entirely "lattice-matched heterostructures"

were thought to be useful, restricting enormously the range of structures being available for III–V-based applications or fundamental physics investigations.

At the end of the 60s the first nanostructures caught very rapidly increasing interest of the community. Dingle and coauthors fabricated the first "particle-in-a-box" structure, which is called today a "quantum well" or a "two-dimensional structure". The fundamental band gap of a thin layer of a narrow-band-gap material, with a thickness below the de Broglie wavelength of a charge carrier, inserted between two barriers of larger gap materials, was discovered to be thickness dependent, thus confirming the theoretical prediction. The emission wavelength of a laser based on quantum wells is consequently tunable via the thickness of the active layer. This discovery marks the advent of modern nanostructure physics. Soon later in the 70s and 80s, research moved to structures of still lower dimensionality, like one-dimensional and zero-dimensional structures, quantum wires, and quantum dots (QDs). Efficient technologies for easy fabrication of defect-free nanostructures were missing, however, and the interest faded away until the beginning of the 90s. Then, the Stranski–Krastanow mode of self-organized growth of strained zero-dimensional nanostructures was discovered [1], theoretically founded by modern theory of surface physics and demonstrated to present the basis of active layers, e.g., lasers with lower threshold current density than ever thought of [2]. Surprisingly, two paradigms of modern semiconductor physics had to be given up at the same time by these discoveries: The "lattice match paradigm for heterostructures" and the "fabrication paradigm" that lithography-based method must be employed to create quantum wires and QDs. A minimum amount of strain induced by lattice mismatch of the heterostructures is the driving source for QD formation. Zero-dimensional structures, from the point of view of their electronic properties, do not resemble any more classical semiconductors with their continuous dispersion of energy as a function of momentum. They behave like giant hydrogen atoms in a dielectric cage and show a very simple twofold degenerate energy level system [2], thus presenting a potential source of qubits and entangled photons.

In the twenty-first century, the hallmarks of modern solid-state physics, far beyond just semiconductors, are design, fabrication, study, and applications of the now existing great variety of nanostructures. Among them, quantum rings, which are the subject of the present book, take an outstanding place, because they are not simply zero-dimensional coherent clusters of atoms or molecules on a surface. Quantum rings combine sizes at the nanoscale with a nontrivial topology: doubly connectedness of a ring or even more complicated topological properties like one-sidedness of a Möbius strip. This combination leads again to the occurrence of unique physical properties, in particular, persistent currents. Quantum rings present a unique playground for quantum mechanical paradigms. Their physical properties are designed by controlling the geometry of a ring and the magnetic flux threading it, as well as by creating assemblies of quantum rings.

The present book gives an exhaustive and clear overview of this vigorously developing field, starting with a comprehensive pedagogical introduction of the fundamentals, via a profound presentation of the key technologies for their fabrication, characterization tools, discoveries, and findings, to a discussion of the most

recent advancements and current research activities. The style of the book is highly motivating for both experienced and young scientists: it finally leads a reader straightforward toward still open problems in this fascinating field.

The book is written by a group of the world's leading scientists of this field, who have provided fundamental contributions to the fabrication, characterization, and theoretical analysis of quantum rings. Hence, a reader receives a unique access to their "scientific laboratory", in particular, about state-of-the-art methods of growth (MBE, droplet epitaxy, lithographic patterning, etc.), characterization (Scanning probe imaging like STM, SEM, XSTM, etc.), and theoretical analysis of nanostructures and metamaterials.

Based on their unprecedented tunability, quantum rings are highly prospective as elemental base for various applications: photonic detectors and sources, including single-photon emitters, nanoflash memories, qubits for spintronic quantum computing, magnetic random access memory, recording medium, and other spintronic devices. The book contains roadmaps for the implementation of quantum rings into such real-world devices.

This book will be the required reading for all those who are active in nanoscience, nanotechnology, and the applications of quantum rings.

Berlin, Germany Dieter Bimberg

References

1. V. Shchukin, D. Bimberg, Rev. Mod. Phys. **71**, 1125 (1999)
2. D. Bimberg, M. Grundmann, N. N. Ledentsov, *Quantum Dot Heterostructures* (Wiley, Chichester, 1999)

Preface

The first edition of this book for the first time in monographic literature provided a broad panorama of the physics of quantum rings. The present second edition comprises 10 new chapters and 8 extended chapters from the first edition, with emphasis on *modern advancements* in theoretical and experimental investigations of quantum rings.

It is written in a style which makes these issues accessible to theoretical physicists, experimental researchers, and technologists with different levels of experience: from graduate and Ph.D. students to experts. The book is also intended to convey the fascination of quantum rings to specialists in other disciplines: mathematics, chemistry, electronic and optical engineering, and information technologies. Our goal is that this book will succeed in invigorating research interests toward the further development of fundamental insight in and applications of quantum rings.

It starts with an introduction into the fundamental physics of quantum rings as a heuristically unique playground for the quantum–mechanical paradigm and a concise overview of the state-of-the-art in the field, with a particular emphasis on the quantum interference phenomena like the Aharonov–Bohm effect in quantum rings (Chap. 1). The book consists of four main parts, though the borders between them are conventional: Part I. Topology-driven effects, Part II. Fabrication and characterization, Part III. Optical Aharonov–Bohm effect, and Part IV. Theory.

The *first part* introduces quantum rings in a general context of topologically nontrivial nanostructures. Chapter 2 by L. Ma, O.G. Schmidt, and me analyzes the optical Berry phase in micro/nanoring resonators. In metallic/dielectric Möbius rings, plasmon/photon modes with non-integer numbers of wavelengths along the circumference are revealed, while in cone-shaped anisotropic microtube resonators, the optical spin–orbit coupling is enabled for generation of the Berry phase acquired in a non-cyclic and non-Abelian evolution. A tunable exciton topology—from quantum dot to quantum ring—on type II InAs/GaAsSb quantum nanostructures is represented by J.M. Llorens, V. Lopes-Oliveira, V. López-Richard, J.M. Ulloa, and B. Alén in Chap. 3. Due to the large spin–orbit coupling of III-Sb nanostructures, the

modulation of the orbital confinement geometry and topology allows control of the spin dynamics by external voltages.

The *second part* represents advanced methods of fabrication of quantum rings: self-organized growth, droplet epitaxy, and lithographic patterning, as well as their characterization based on scanning probe microscopy. In Chap. 4 by V.N. Gladilin, M. Flatté, J. van Bree, J.T. Devreese, P.M. Koenraad, and me, we discuss how the modern characterization of self-assembled InGaAs/GaAs quantum rings using XSTM has allowed for a development of an adequate model of their shape, which quantitatively explains the Aharonov–Bohm effect observed in the magnetization. Large magnetic moments of quantum rings are shown to originate from the presence of spin-correlated orbital currents, induced by the spin–orbit interaction. Scanning probe electronic imaging (scanning gate microscopy) of lithographically patterned quantum rings, which is discussed in Chap. 5 by F.R. Martins, D. Cabosart, H. Sellier, M.G. Pala, B. Hackens, V. Bayot, and S. Huant, can access the intimate properties of buried electronic systems. This technique unravels a new counterintuitive behavior of branched-out rectangular quantum rings, which turns out to be a mesoscopic analog of the Braess paradox, and allows detecting recurrence of the radial pattern of scarred wave functions in graphene quantum rings. Another promising technique of controllable self-assembled fabrication of quantum rings—droplet epitaxy—is overviewed in Chap. 6 by C. Heyn, M. Zocher, and W. Hansen, who represent the functionalization of droplet etching of quantum rings (through GaAs recrystallization during the local droplet etching with Ga droplets on AlGaAs, the wave-function tuning of V-shaped GaAs quantum dots by a gate voltage, and the partial depletion of a near-surface GaAs quantum well due to tunneling), in Chap. 7 by J. Wu and Z.M. Wang with emphasis on vertically and laterally ordered arrays of quantum rings, and in Chap. 8 by S. Sanguinetti, T. Mano, and T. Kuroda, where the focus is on semiconductor quantum-ring complexes: multiple concentric quantum rings and coupled ring–disk, dot–ring, and dot–disk structures.

The *third part* deals with the optical Aharonov–Bohm effect in quantum rings, for excitons and plasmons. In Chap. 9, K. Kyhm, H.D. Kim, R. Okuyama, M. Eto, K.C. Je, R.A. Taylor, G. Nogues, L.S. Dang, A.A.L. Nicholet, M. Potemski, J.S. Kim, and J.D. Song review recent experimental and theoretical investigations on optical Aharonov–Bohm oscillations of an exciton and a biexciton in a quantum ring in the presence of structure anisotropy, localization, internal electric field, and impurity scattering. Occurrence of a strongly correlated exciton pair in a quantum ring is detected by new oscillations of photoluminescence at increased magnetic fields. Theory meets experiment on the Aharonov–Bohm effect for neutral excitons in quantum rings in Chap. 10 by M.D. Teodoro, V.L. Campo, Jr., V. López-Richard, E. Marega, Jr., G.E. Marques, and G.J. Salamo. Magneto-photoluminescence spectra reveal effects associated to built-in electric fields and to the temperature on the Aharonov–Bohm oscillations in a topmaster single layer of InAs quantum rings grown on a vertically stacked and laterally aligned InGaAs quantum dot superlattice.

The *fourth part* represents advancements in theory of quantum rings. Electronic, magnetic, and optical properties of a few electron quantum rings of novel materials are overviewed in Chap. 11 by T. Chakraborty, A.Kh. Manaselyan, and M.G. Barseghyan. In particular, a few electron ZnO quantum rings are shown to be appropriate for locating the Majorana fermions. The effects of spin interference in Rashba quantum rings are analyzed in Chap. 12 by C. Ortix, who shows the connection between the conductance modulations and the geometric phase acquired by the spin during transport. The basic approaches to theoretical modeling of electronic and optical properties of semiconductor quantum rings and quantum-ring molecules in electromagnetic fields are overviewed by A.M. Alexeev and M.E. Portnoi in Chap. 13 and by H.M. Baghramyan, M.G. Barseghyan, A.A. Kirakosyan, and D. Laroze in Chap. 14 ; both chapters can be also used as tutorials for students. A survey on the electron–phonon interaction in topologically nontrivial nanostructures, in particular, semiconductor core–shell nanowires, is provided in Chap. 15 by C. Trallero-Giner, D.G. Santiago-Pérez, L. Chico, and R. Pérez-Álvarez.

In Chap. 16, B. Lassen, M. Willatzen, and J. Gravesen represent applications of differential geometry methods to quantum rings and nanostructures with complicated topology, like Möbius rings, in particular, for derivation of the elastic energy for a thin shell. In Chap. 17, C. Segarra, J. Planelles, and J.I. Climente discuss effects of hole mixing in semiconductor quantum rings and show that the strong strain potential may compete against the band-offset potential in quantum rings. Due to the coupling between conduction and valence bands, mid-gap topological states occur, which localize near the dot edge and are analogous to those of one-dimensional quantum rings. Quantum interference in circular n–p nanojunctions in graphene nanoribbons is described in Chap. 18 A. Mreńca-Kolasińska and B. Szafran. The Aharonov–Bohm oscillations in conductance occur provided that the persistent currents localized at the junction currents are coupled to the quantum Hall edge currents.

The *main message* of the present book is that the frontline methods of fabrication and characterization of quantum rings together with the sophisticated cutting-edge theoretical research have allowed for accumulation of a significant thesaurus of fundamental information on their behavior. This highly diversified knowledge underpins numerous suggestions for prospective applications of nanostructures with nontrivial topology, like quantum rings, as a highly tunable elemental base for future device design and optimization, in particular, in optoelectronics, spintronics, information storage and processing, as magnetic memory elements as well as photonic sources and detectors.

I am indebted to my teacher and friend Evghenii Petrovich Pokatilov of blessed memory, who introduced me into the fascinating world of theoretical physics. My special thanks are due to Lutz Wendler: we started together with the investigations in the field of physics of quantum rings. This was made possible by awarding me a Humboldt Fellowship, for which I am deeply grateful to the Alexander von Humboldt Foundation.

I want to thank very warmly my colleagues and friends for fruitful and motivating collaborations related to various problems related to physics of quantum rings: Janneke H. Blokland, Iris M. A. Bominaar-Silkens, Jörg B. Götte, Murat Bozkurt, Alexander V. Chaplik, Liviu F. Chibotaru, Peter C. M. Christianen, Jozef T. Devreese, Jorge M. García, Vladimir N. Gladilin, Alexander O. Govorov, Daniel Granados, Martina Hentschel, Suwit Kiravittaya, Niek A. J. M. Kleemans, Serghei N. Klimin, Paul M. Koenraad, Arkady A. Krokhin, Matthew R. Jorgensen, Shilong Li, Libo Ma, Jan Kees Maan, Vyacheslav R. Misko, Victor V. Moshchalkov, Peter Offermans, Oliver G. Schmidt, Alfonso G. Taboada, Jacques Tempere, Eric C. M. van Genuchten, Joachim H. Wolter, Yin Yin, Uli Zeitler, and Hu Zhao.

I am extremely grateful to many colleagues for insightful discussions: Benito Alén, Dieter Bimberg, Stefan Böttner, Mario Capizzi, Peter Cendula, Venkat Chandrasekhar, Valeri G. Grigoryan, Yoseph Imry, John C. Inkson, Khaled Karrai, Peter Kratzer, Jörg P. Kotthaus, Jean-Pierre Leburton, Axel Lorke, Dominiqe Mailly, Algirdas, Matulis, Carmine Ortix, Vladimir A. Osipov, Pierre M. Petroff, James A. Sauls, Vitaly A. Tkachenko, Jeroen van den Brink, Felix von Oppen, Jiming Wang, Achim Wixforth, Roger Wördenweber, and Vladimir I. Yudson. I thankfully recall stimulating interactions with the blessed memory Markus Büttiker, Manuel Cardona, and Rolf Landauer.

I am very thankful to the State University of Moldova, my *alma mater*, where my research career was launched. Various stages of my research activities were performed in a number of institutions, to which I am very grateful: Martin-Luther University of Halle-Wittenberg, University of Antwerp, Eindhoven University of Technology, Catholic University of Leuven, Research Center Jülich, University of Duisburg–Essen, and, most recently, Institute for Integrative Nanosciences (IIN)—Leibniz Institute for Solid State and Materials Research (IFW) Dresden.

I highly appreciate great enthusiasm, time, and effort of all contributors to this book. I would like to express my deep gratitude to Claus E. Ascheron, Senior Editor, Adelheid Duhm and Ravi Vengadachalam, Project Coordinators, and Sindhu Sundararajan, Project Manager, for a vigorous support of the publication of the second edition of the book, and to Alexander A. Balandin, Kwangseuk Kyhm, Ian R. Sellers, and Jiming Wang for their valuable support while I was preparing this book for publication.

With profound gratitude I keep the memory of my parents, who nurtured my aspiration to comprehend the world. Special thanks are due to my wife and children for their understanding and patience in the course of my work on this book.

Dresden, Germany Vladimir M. Fomin

Contents

Contributors

A.M. Alexeev School of Physics, University of Exeter, Exeter, UK

Benito Alén IMN, Instituto de Micro y Nanotecnología (CNM, CSIC), Madrid, Tres Cantos, Spain

H.M. Baghramyan Instituto de Alta Investigación, CEDENNA, Universidad de Tarapacá, Arica, Chile; Armenian State Pedagogical University after Khachatur Abovyan, Yerevan, Armenia

Manuk G. Barseghyan Department of Solid State Physics, Yerevan State University, Yerevan, Armenia; National University of Architecture and Construction of Armenia, Yerevan, Armenia

V. Bayot Université Catholique de Louvain, IMCN/NAPS, Louvain-La-Neuve, Belgium

D. Cabosart Université Catholique de Louvain, IMCN/NAPS, Louvain-La-Neuve, Belgium

V.L. Campo Jr. Departamento de Física, Universidade Federal de São Carlos, São Carlos, São Paulo, Brazil

Tapash Chakraborty Department of Physics and Astronomy, University of Manitoba, Winnipeg, Canada

Leonor Chico Materials Science Factory, Instituto de Ciencia de Materiales de Madrid (ICMM), Consejo Superior de Investigaciones Científicas (CSIC), Madrid, Spain

Juan I. Climente Departament de Química Física i Analítica, Universitat Jaume I, Castelló, Spain

L.S. Dang Department of NANO Science, Institute Néel CNRS, Grenoble, France

J.T. Devreese Theory of Quantum and Complex Systems, University of Antwerp, Antwerpen, Belgium

M. Eto Faculty of Science and Technology, Keio University, Yokohama, Japan

M.E. Flatté Department of Physics and Astronomy, University of Iowa, Iowa, USA

Vladimir M. Fomin Institute for Integrative Nanosciences, IFW Dresden, Dresden, Germany

V.N. Gladilin Theory of Quantum and Complex Systems, University of Antwerp, Antwerpen, Belgium

Jens Gravesen Department of Applied Mathematics and Computer Science, Technical University of Denmark, Kongens Lyngby, Denmark

B. Hackens Université Catholique de Louvain, IMCN/NAPS, Louvain-La-Neuve, Belgium

Wolfgang Hansen Center for Hybrid Nanostructures (CHyN), University of Hamburg, Hamburg, Germany

Christian Heyn Center for Hybrid Nanostructures (CHyN), University of Hamburg, Hamburg, Germany

S. Huant Université Grenoble Alpes, CNRS, Institut Néel, Grenoble, France

K.C. Je Department of Physics, Saints Cyril and Methodius University, Skopje, Republic of Macedonia

H.D. Kim Department of Opto-mechatronics, Pusan National University, Busan, South Korea; Department of Physics Education, Pusan National University, Busan, South Korea

J. S. Kim Department of Physics, Yeungnam University, Gyeongsan, South Korea

A.A. Kirakosyan Department of Solid State Physics, Yerevan State University, Yerevan, Armenia

P.M. Koenraad Photonics and Semiconductor Nanophysics, Eindhoven University of Technology, Eindhoven, The Netherlands

Takashi Kuroda National Institute for Materials Science, Tsukuba, Japan

K. Kyhm Department of Opto-mechatronics, Pusan National University, Busan, South Korea; Department of Physics Education, Pusan National University, Busan, South Korea

D. Laroze Instituto de Alta Investigación, CEDENNA, Universidad de Tarapacá, Arica, Chile; Yachay Tech University, School of Physical Sciences and Nanotechnology, Urcuquí, Ecuador

Benny Lassen Mads Clausen Institute, University of Southern Denmark, Sønderborg, Denmark

José M. Llorens IMN, Instituto de Micro y Nanotecnología (CNM, CSIC), Madrid, Tres Cantos, Spain

Vivaldo Lopes-Oliveira Departamento de Física, Universidad Federal de São Carlos, São Paulo, Brazil

Victor López-Richard Departamento de Física, Universidad Federal de São Carlos, São Paulo, Brazil

Libo Ma Institute for Integrative Nanosciences, IFW Dresden, Dresden, Germany

Aram Kh. Manaselyan Department of Solid State Physics, Yerevan State University, Yerevan, Armenia

Takaaki Mano National Institute for Materials Science, Tsukuba, Japan

E. Marega Jr. Instituto de Física de São Carlos, Universidade de São Paulo, São Carlos, São Paulo, Brazil

G.E. Marques Departamento de Física, Universidade Federal de São Carlos, São Carlos, São Paulo, Brazil

F. Martins Université Catholique de Louvain, IMCN/NAPS, Louvain-La-Neuve, Belgium

Alina Mreńca-Kolasińska AGH University of Science and Technology, Kraków, Poland

A.A.L. Nicholet Laboratoire Natioal des Champs Magnetiques Intenses, Magnetiques Intenses, CNRS-UJF-UPS-INSA, Grenoble, France

G. Nogues Department of NANO Science, Institute Néel CNRS, Grenoble, France

R. Okuyama Faculty of Science and Technology, Keio University, Yokohama, Japan

Carmine Ortix Institute for Theoretical Physics, Center for Extreme Matter and Emergent Phenomena, Utrecht University, CC Utrecht, The Netherlands; Dipartimento di Fisica “E. R. Caianiello”, Universitá di Salerno, Fisciano, Italy

M.G. Pala C2N, CNRS, Univ Paris-Sud, Université Paris-Saclay, Orsay, France

Josep Planelles Departament de Química Física i Analítica, Universitat Jaume I, Castelló, Spain

M.E. Portnoi School of Physics, University of Exeter, Exeter, UK

M. Potemski Laboratoire Natioal des Champs Magnetiques Intenses, Magnetiques Intenses, CNRS-UJF-UPS-INSA, Grenoble, France

R. Pérez-Álvarez Centro de Investigación en Ciencias, Instituto de Investigación en Ciencias Básicas y Aplicadas, Universidad Autónoma del Estado de Morelos, Cuernavaca, Morelos, Mexico

G. J. Salamo Arkansas Institute for Nanoscale Materials Science and Engineering, University of Arkansas, Fayetteville, AR, USA

Stefano Sanguinetti LNESS and Dipartimento di Scienza dei Materiali, Universitá di Milano Bicocca, Milan, Italy

Darío G. Santiago-Pérez Universidad de Sancti Spiritus José Martí Pérez, Sancti Spiritus, Cuba

Oliver G. Schmidt Institute for Integrative Nanosciences, IFW Dresden, Dresden, Germany

Carlos Segarra Departament de Química Física i Analítica, Universitat Jaume I, Castelló, Spain

H. Sellier Université Grenoble Alpes, CNRS, Institut Néel, Grenoble, France

J.D. Song Center for Optoelectronic Convergence System, KIST, Seoul, South Korea

Bartłomiej Szafran AGH University of Science and Technology, Kraków, Poland

R.A. Taylor Clarendon Laboratory, Department of Physics, University of Oxford, Oxford, UK

M.D. Teodoro Departamento de Física, Universidade Federal de São Carlos, São Carlos, São Paulo, Brazil

C. Trallero-Giner Department of Theoretical Physics, University of Havana, Havana, Cuba

José M. Ulloa Institute for Systems based on Optoelectronics and Microtechnology (ISOM), Universidad Politécnica de Madrid, Madrid, Spain

J. van Bree Institute for Molecular Engineering, University of Chicago, Chicago, USA

Zhiming M. Wang Institute of Fundamental and Frontier Sciences, University of Electronic Science and Technology of China, Chengdu, China

Morten Willatzen Department of Photonics Engineering, Technical University of Denmark, Kongens Lyngby, Denmark; Beijing Institute of Nanoenergy and Nanosciences, Chinese Academy of Sciences, Beijing, China

Jiang Wu Institute of Fundamental and Frontier Sciences, University of Electronic Science and Technology of China, Chengdu, China

Michael Zocher Center for Hybrid Nanostructures (CHyN), University of Hamburg, Hamburg, Germany

Part I
Topology-driven Effects

Chapter 1
Quantum Ring: A Unique Playground for the Quantum-Mechanical Paradigm

Vladimir M. Fomin

У кольца нет конца.
Русская пословица[a]

Man kan mit Recht und Fug den Jahr-Bezirck vergleichen
Mit einem runden Ring/ der keinen Anfang hat/
Und auch kein Ende kennt;[b]

Abstract The physics of quantum rings is reviewed from basic concepts rooted in the quantum-mechanical paradigm—via unprecedented challenges brilliantly overcome by both theory and experiment—to promising application perspectives.

1.1 Prologue

Doubly-connected (ring-like) structures at the scale of nanometers (nanoscale) are generally termed *Quantum Rings* (QRs). They exhibit a unique density of states for charge carriers and quantum fields and hence a vast variety of physical properties, which are cardinally different from those of singly-connected structures (like quantum dots). Moreover, the topologically-determined properties have been revealed

[a]В.И. Даль, Пословицы русского народа, Москва, Художественная литература 1989. "A ring has no end." (Translation by V.M. F.)
[b]Christliche Betrachtungen Und Sitten-Lehren…, Wolffgang Wickhart, Prag, (1714), S. 172; the original orthography is kept. "One can rightly compare a year/ With a round ring that has no beginning/ And knows no end…" (Translation by V.M. F.)

V.M. Fomin (✉)
Institute for Integrative Nanosciences, IFW Dresden, Dresden, Germany
e-mail: v.fomin@ifw-dresden.de

V.M. Fomin (ed.), *Physics of Quantum Rings*, NanoScience and Technology,
https://doi.org/10.1007/978-3-319-95159-1_1

for various quantum fields in confined geometries, varying from excitons and electrons in graphene to plasmons and electromagnetic waves in topologically nontrivial structures.

Circular electric currents prophetically introduced by Ampère [1] to explain the origin of magnetism: "…un aimant doit être considéré comme un assemblage de courans électriques qui ont lieu dans des plans perpendiculaires à son axe…"[1] were an essential precursor of persistent currents in the modern physics of QRs. A magnetic field was related to the currents circulating along concentric paths: "…à chacun des pôles d'un aimant, les courants électriques dont il se compose sont dirigés suivant des courbes fermées concentriques…"[2] Quantum mechanics predicts that small enough ring-like structures threaded by a magnetic flux, in the equilibrium state, carry *persistent* (dissipationless) circulating electron currents that do not require an external power source. A prerequisite is that the electron state keeps quantum coherence over the whole doubly-connected system.

There have been a number of reviews representing various aspects of physics of QRs, for example, effects of a finite width of the QRs [2], mesoscopic phenomena in QRs with strongly coupled polarons [3], possible types of III-V semiconductor QRs [4], equilibrium properties of mesoscopic metal rings [5], ring-like nanostructures as a leitmotif in plasmonics and nanophotonics [6], theoretical modeling of the self-organized QRs on the basis of the modern characterization of those nanostructures [7], theoretical analysis and experimental observations of persistent currents by virtue of the magnetic flux quantization phenomenon [8], and advancements in experimental and theoretical physics of QRs [9]. In the present Chapter, we discuss a number of contributions to the physics of QRs, essential for the topics of the present book—(i) fundamentals of physics of QRs and (ii) semiconductor QRs—without any claim for an exhaustive presentation of the extensive literature in this vigorously developing field.

1.2 At Dawn

The following studies, commenced already at the very early stage of the quantum physics, unraveled the key properties of persistent currents in ring-like quantum structures.

For calculating the magnetically induced current densities of aromatic hydrocarbon ring molecules, Pauling [10] advanced a hypothesis that the external electrons in the benzene molecule can *circulate freely* and provide a very large contribution to the diamagnetic susceptibility with the magnetic field normal to the plane of the carbon hexagon: "We may well expect that in these regions the potential function

[1] "…a magnet should be considered as an assembly of electric currents that occur in planes perpendicular to its axis…" (Translation by V.M. F.).

[2] "…at each of the poles of a magnet, the electrical currents, of which it consists, are directed along concentric closed curves…" (Translation by V.M. F.).

representing the interaction of an electron with the nuclei and other electrons in the molecule would be approximately cylindrically symmetrical with respect to the hexagonal axis of the molecule, the electron, some distance above or below the plane of the nuclei, passing almost imperceptibly from the field of one carbon atom to that of the next."

Within the framework of a quantum-mechanical derivation, London [11] demonstrated that the diamagnetic susceptibility of aromatic ring molecules was related to a *current circulating around the opening* induced by the magnetic field: "La susceptibilité… correspond à des courants induits qui circulent d'un atome à l'autre autour de la chaîne cyclique."[3] This current belonged to the *ground state*, in analogue with superconducting currents: "Nous pouvons… disant que les combinaisons aromatiques se comportent comme des supraconducteurs."[4]

Calculating the magnetic response of ultrasmall magnetic ring-shaped particles on the basis of the Schrödinger equation, Hund [12] showed that both at zero temperature and in thermodynamic equilibrium at temperature $T>0$, there existed a *total current circulating around the annulus*, which was *dissipationless*: "…ein wesentlicher Teil des der diamagnetischen Magnetisierung entsprechenden Stromes um das Loch herumfließt; dieser Strom hat keine Joulesche Warme, da die Besetzung der Zustande dem Temperaturgleichgewicht entspricht."[5] Further, it was demonstrated that a set of eigenstates found for an electron in a ring in a magnetic field B led to jumps in the magnetization from negative (diamagnetic) to positive (paramagnetic) at certain values of the applied magnetic field: "…es tritt zu der negativen (diamagnetischen) Magnetisierung plötzlich eine konstante positive Magnetisierung hinzu, und dies wiederholt sich nach einem gewissen Zuwachs von B."[6] As a result, the current circulating around the opening of the ring acquires *a zigzag form* as a function of the applied magnetic field (shown in Fig. 4 of [12]).

Systematically developing the earlier ideas, Dingle found [13] that the equilibrium properties calculated for small *free-electron systems* in a perfect ring and in a perfect infinite cylinder were sensitive to the *magnetic flux* Φ threading the system, the magnetic permittivity consisting of a steady part and periodic in the magnetic flux terms. The fundamental dimensionless quantity, which determined the *periodic* dependence, was (in the modern notation) the ratio Φ/Φ_0, where the magnetic flux quantum $\Phi_0 = h/e$ was determined by universal constants: the Planck constant h and the elementary charge e. Dingle already noticed the challenges in observing those periodic terms: "…a single cylinder would possess only a very small magnetic moment, whilst it would be difficult to ensure a uniform radius for a bundle

[3] "The susceptibility… corresponds to the induced currents that flow from one atom to another around the cyclic chain." (Translation by V.M. F.)

[4] "We can… say that the aromatic combinations behave as superconductors." (Translation by V.M. F.)

[5] "…an essential part of the current corresponding to the diamagnetic magnetization flows around the annulus; this current produces no Joule heat, as the population of states corresponds to the thermal equilibrium." (Translation by V.M. F.)

[6] "…a constant positive magnetization occurs to be suddenly added to the negative (diamagnetic) magnetization, and this is repeated after a certain increase in B." (Translation by V.M. F.)

of cylinders"—a conclusion that has remained very urgent for experimentalists ever since then. The key challenges in detecting persistent currents experimentally are twofold: they produce exceptionally small signals and they are very sensitive to the environment [14].

1.3 Fundamentals of Topological Effects

A fundamental role of the ring-topology for the quantum-mechanical paradigm was unraveled within the theory of a geometric phase [15–18]. Berry [15] provided a simple but intuitively appealing derivation of the geometric (Berry) phase, which will be recalled below. A system is considered whose Hamiltonian H depends on a set of varying parameters $\mathbf{R}\equiv\mathbf{R}(t)$ forming a closed path C between the instant $T=0$ and the instant $t=T$ such that $\mathbf{R}(0)=\mathbf{R}(T)$.

The evolution of the state of the system is governed by the Schrödinger equation:

$$i\hbar\left|\dot{\psi}(t)\right\rangle = H(\mathbf{R}(t))|\psi(t)\rangle. \tag{1.1}$$

At any instant t, the eigenstates satisfy the stationary Schrödinger equation

$$H(\mathbf{R})|n(\mathbf{R})\rangle = E_n(\mathbf{R})|n(\mathbf{R})\rangle, \tag{1.2}$$

where $|n(\mathbf{R})\rangle$ is single-valued in the region that includes C. Within the *adiabatic* approximation [19], the system prepared in one of these states $|n(\mathbf{R}(0))\rangle$ will evolve with the Hamiltonian $H(\mathbf{R}(t))$ and be in the state $|n(\mathbf{R}(t))\rangle$ at the instant t. A gauge-invariant generalization to the phase-coherence phenomena in *nonadiabatically* evolving quantum systems was proposed by Aharonov and Anandan [20]. The solution to the Schrödinger equation (1.1) is sought in the form

$$|\psi(t)\rangle = \exp\left[-\frac{i}{\hbar}\int_0^t d\tau\, E_n(\mathbf{R}(\tau))\right]\exp\left[i\,\gamma_n(t)\right]|n(\mathbf{R}(t))\rangle. \tag{1.3}$$

Substituting (1.3) into the Schrödinger equation (1.1) and taking into account (1.2), we find the equation for the *geometric phase* $\gamma_n(t)$:

$$\dot{\gamma}_n(t) = i\,\langle n(\mathbf{R}(t)) \mid \nabla_{\mathbf{R}} n(\mathbf{R}(t))\rangle \cdot \dot{\mathbf{R}}(t).$$

(A gauge can be chosen so that the Aharonov–Bohm phase is included in the dynamical phase instead of the geometric phase, see, e.g., [21, 22].) The total phase change of the state of (1.3) on the path C

$$|\psi(T)\rangle = \exp\left[-\frac{i}{\hbar}\int_0^T d\tau\, E_n(\mathbf{R}(\tau))\right]\exp\left[i\gamma_n(C)\right]|\psi(0)\rangle \tag{1.4}$$

is then determined by the *geometric phase change*

$$\gamma_n(C) = i\oint_C \langle n(\mathbf{R}) \mid \nabla_{\mathbf{R}} n(\mathbf{R})\rangle \cdot d\mathbf{R}. \tag{1.5}$$

A generalization of the phase factor $i\gamma_n(C)$ in (1.4) (which was initially derived for a non-degenerate Hamiltonian) to the Hamiltonian with degenerate energy levels, was provided in terms of the path-ordered integrals involving non-Abelian gauge fields [23].

Magnetic field is an important tool revealing physical effects due to the doubly-connected topology. Consider a magnetic flux line [24] (or tube) carrying a flux Φ. For positions $\mathbf{R}$ outside of the flux line (tube), the magnetic field is zero, but there exists a set of gauge-equivalent vector potentials $\mathbf{A}(\mathbf{R})$ such that for any closed path C threaded by the magnetic flux line (tube)

$$\oint_C \mathbf{A}(\mathbf{R}) \cdot d\mathbf{R} = \Phi.$$

Further, let a particle carrying a charge q be confined to a box at $\mathbf{R}$, which is not penetrated by the flux line (tube). Without a flux, the Hamiltonian of the particle $\mathrm{H}(\mathbf{p}, \mathbf{r}–\mathbf{R})$ depends on the momentum $\mathbf{p}$ and the relative position $\mathbf{r}–\mathbf{R}$ and possesses the eigenfunctions $\psi_n(\mathbf{r}-\mathbf{R})$ that satisfy (1.2) with eigenenergies independent of $\mathbf{R}$. With non-zero flux, the states $|n(\mathbf{R})\rangle$ satisfy

$$H(\mathbf{p} - q\mathbf{A}(\mathbf{r}), \mathbf{r} - \mathbf{R})|n(\mathbf{R})\rangle = E_n|n(\mathbf{R})\rangle \tag{1.6}$$

with the eigenenergies unaffected by the vector potential. Solutions of (1.6) are obtained in terms of the Dirac phase factor [25]

$$\langle \mathbf{r} \mid n(\mathbf{R})\rangle = \exp\left[i\frac{q}{\hbar}\int_{\mathbf{R}}^{\mathbf{r}} d\boldsymbol{\rho}\cdot\mathbf{A}(\boldsymbol{\rho})\right]\psi_n(\mathbf{r}-\mathbf{R}). \tag{1.7}$$

Within a thought experiment, the box is transported round a closed doubly-connected path C threaded by the flux line (tube). Any such path is topologically equivalent to a *ring*. The integrand in the geometric phase change of (1.5) is then

$$\begin{aligned}\langle n(\mathbf{R}) \mid \nabla_{\mathbf{R}} n(\mathbf{R})\rangle &= \int d^3r\,\psi_n^*(\mathbf{r}-\mathbf{R})\left[-i\frac{q}{\hbar}\mathbf{A}(\mathbf{R})\psi(\mathbf{r}-\mathbf{R}) + \nabla_{\mathbf{R}}\psi_n(\mathbf{r}-\mathbf{R})\right] \\ &= -i\frac{q}{\hbar}\mathbf{A}(\mathbf{R}).\end{aligned}$$

The integral of the second term in the integrand vanishes because of the wave function normalization. Consequently, the geometric phase change

$$\gamma_n(C) = \frac{q}{\hbar} \oint\limits_C \mathbf{A}(\mathbf{R}) \cdot d\mathbf{R} = \frac{q\Phi}{\hbar} \tag{1.8}$$

is independent of n. With $q = \text{sign}(q)e$, $\frac{q\Phi}{\hbar} = \text{sign}(q)\ \frac{\Phi}{\Phi_0}$. Thus, a charged particle *gains a phase* as it moves over a closed path about the flux line (tube):

$$|\psi(\Phi)\rangle = \exp\left[i\frac{q\Phi}{\hbar}\right]|\psi(\Phi = 0)\rangle = \exp\left[i\,\text{sign(q)}\frac{\Phi}{\Phi_0}\right]|\psi(\Phi = 0)\rangle. \tag{1.9}$$

The geometric phase occurring in (1.9) leads to a *quantum interference* between the states of the particles in the transported box and those in a box that was not moved about the flux line (tube). There are numerous manifestations of this quantum interference, which is known as the Aharonov–Bohm effect [24, 26]. They are revealed in the electronic spectra, magnetization, optical and transport properties of QRs and, in particular, represented in the present book. Observation of the Aharonov–Bohm effect was significantly facilitated by nano-scale fabrication and low-temperature detection techniques, which minimize dephasing, as demonstrated in the beautiful experiment on dephasing in electron interference by a 'which-path' detector [27]. The phase acquired by a particle with nonzero spin can also follow from spin-orbit-coupling instead of a magnetic field (Aharonov–Casher effect) [28].

Oscillating persistent currents were extensively investigated in superconductor QRs, which are beyond the scope of the present book; see [29–31] for references.

1.4 Renaissance

In their works dealing with the flux quantization in *superconducting* rings, Byers and Yang [21] and Bloch [32] showed that "the magnetic flux through any surface whose boundary loop lies entirely in superconductors is quantized in units" $\Phi_0^{\text{sup}} = h/(2e)$, where $2e$ is the charge of a Cooper pair [21]. As a result, a general theorem follows: all physical properties of a doubly-connected system are periodic in the magnetic flux through the opening Φ with the period Φ_0^{sup}. The experimental detection of the periodicity of the magnetization as a function of magnetic flux ("magnetic flux quantization") in superconducting rings [33] and cylinders [34] was used to demonstrate that charge in superconductors was carried in units of $2e$ [34].

Gunther and Imry [35] analyzed persistent currents in a hollow, cylindrically shaped superconductor taking into account that the magnetic flux consists of two parts: that due to the external magnetic field and that due to the current. The flux quantization was shown to be exhibited when the cylinder was thick enough as compared to the penetration depth of the superconductor and thin enough as compared

to the temperature-dependent coherence length as to exclude the off-diagonal long-range order.

Kulik [36] discussed the persistent currents and the flux quantization in a hollow thin-walled normal metallic cylinder and ring threaded by a tube of magnetic flux-lines that were confined within an inner cylinder (a magnetic coil) with a radius smaller than the radius of the outer cylinder, in which no electric or magnetic field was present.

In cylindrical bismuth single-crystal whiskers 200–800 nm thick, oscillations in the longitudinal magnetoresistance with the period $\Phi_0/\cos\theta$ (θ was the angle of the tilt of the magnetic field with respect to the cylinder axis) observed by Brandt et al. [37, 38] were interpreted as a possible manifestation of the Aharonov–Bohm effect.

Büttiker et al. [39] were the first to consider persistent currents in a strictly one-dimensional *normal-metal* ring with disorder. It was concluded that "Small and strictly one-dimensional rings of normal metal, driven by an external magnetic flux, act like superconducting rings with a Josephson junction, except that $2e$ is replaced by e." These authors noticed a fundamental analogy between the energy spectrum of an electron traversing the ring and that of an electron in a periodic potential: it consisted of bands of width V with band gaps Δ. Such band states carried persistent currents. The heuristic value of the possibility to conduct a persistent-current calculation using the widely developed solid-state band-structure theory could be hardly overestimated. It was pointed out, that the band energy in a ring oscillated periodically as a function of the enclosed flux: $E_n(\Phi) = E_n(\Phi+\Phi_0)$ and carried the (*single-band*) *persistent current* $I_n = -\mathrm{d}E_n(\Phi)/\mathrm{d}\Phi$. For a geometrically perfect ring, the persistent currents carried by consecutive bands had opposite signs.

The key criteria for a possible observation of the persistent current are represented in Chap. 4 of [40]. Firstly, the electron level width (determined as $\hbar/\tau_\phi$ through the inelastic scattering time τ_ϕ) must be much smaller than the typical values of the band gap Δ and the bandwidth V. The latter condition is equivalent to the requirement that *phase coherence be maintained along the whole ring*, i.e., the phase-coherence length l is larger than the mean circumference L of the ring (ballistic regime). With increasing disorder, when the electron free path is smaller than the ring circumference (diffusive regime), the period of the Aharonov–Bohm effect becomes $\Phi_0/2$ [41]. Secondly, the *temperature must be low* enough: $k_\mathrm{B}T \leq \Delta$. Otherwise, the sum of the persistent currents (with alternating signs) carried by the occupied levels would lead to a strong reduction of the overall persistent current.

The seminal work by Büttiker et al. [39] initiated a tremendous interest in the persistent current problem, starting with the papers on the resistance of small one-dimensional rings of normal metal driven by an external time-dependent magnetic flux [42] and the persistent currents and the absorption of power in the ring that was coupled via a single current lead to a dissipative electron reservoir [43].

The first evidence for persistent currents in mesoscopic rings was provided in the following three pioneering experiments. The persistent current in the *diffusive regime,* where the *elastic* (non-dephasing) *mean free path* l was much smaller than the mean circumference L of the ring, was measured in an ensemble of 10^7 copper rings [44] with a SQUID magnetometer and for a single (isolated) gold ring

[45] using a highly sensitive thin-film miniature dc-SQUID magnetometer. At the turn of 1980s and 1990s, first semiconductor quantum rings were fabricated with decreasing average diameter: 2 μm [46], 1.7 μm [47], and 600–700 nm [48], which manifested the Aharonov–Bohm effect. For a lithographically prepared single GaAs ring of the average diameter 2.7 μm [49], in the *ballistic regime* (i.e., for $L<l$), the Aharonov–Bohm effect in the magnetic response was first detected using a special technique, where the sample and the SQUID were made on the same chip. Further measurements of persistent currents were made on arrays of gold QRs [50, 51] and an ensemble of 10^5 disconnected silver rings [52].

The problem of matching theoretical predictions with the emerging experimental evidence stimulated the further intensive research aimed at a development of more realistic models of QRs, taking into account effects due to the finite size, disorder of different nature, and the electron-electron interaction.

For the metallic QRs (in the diffusive regime), the magnitudes of the persistent currents occurred much larger (by two orders of magnitude) than those predicted using the model of non-interacting electrons [53, 54], while for the semiconductor QRs in the ballistic regime this simple theory seemed to agree with experiment. This stimulated investigations (see [2, 40] for details) of the following issues: (i) the role of the choice of the statistical ensemble (canonical versus grand canonical) to calculate average values of persistent currents [55–57], (ii) the role of spin in producing the fractional Aharonov–Bohm effect [58–60], (iii) the role of the electron-electron interaction [61–63], (iv) the role of correlations due to the electron-electron interaction beyond the first-order perturbation approach [64–67].

Important conceptual ingredients to resolve the discrepancy between the measured and observed values of the magnitude of persistent currents in metallic QRs were (i) the argument of local charge neutrality in volume elements larger than the screening length [63, 68] and (ii) the fact that the effect of disorder may be strongly reduced by the electron-electron interaction [69–71]. Another interesting way to get agreement was based on the diamagnetic sign of the persistent currents observed in metal QRs, e.g., by [44], which suggested that the materials were weak superconductors [66] with a very low critical temperature [64]. The attractive electron-electron interaction may enhance the magnetic response of a QR due to the contribution of high energy levels [66]. Resolving the contradiction between experiment and theory in what concerns the magnitude of persistent currents in metallic QRs was recognized as a major open challenge in mesoscopic physics [50, 65, 67, 72].

A rigorous quantum-mechanical theory of persistent currents developed for QRs in the ballistic regime revealed that the coupling between the different channels of the electron motion caused the occurrence of higher harmonics of Φ_0 in the persistent current. Three fundamental findings were achieved in the middle of 90s. (i) The halving of the fundamental period of the persistent current may occur in a single finite-width [73] or finite-height [74] QR due to the coupling of the azimuthal or, correspondingly, radial or paraxial electron motions by virtue of the impurity scattering. Later it was shown that for the magnetic field penetrating the conducting region of the finite-width QR, the Aharonov–Bohm-type oscillations due to the magnetic flux threading the opening coexisted with the diamagnetic shift of energy levels due

to the magnetic field in the QR and were aperiodic [75, 76]. The density of states in a finite-width QR was evaluated by measuring the temperature dependence of the radiative recombination of excitons, where the photoluminescence decay time as a function of temperature was calibrated through the low-temperature integrated intensity and linewidth [77]. The quasi-continuous finely-spaced levels arising from the rotation energy were shown to give rise to a quasi-one-dimensional density of states, as long as the confined exciton was allowed to rotate around the opening of the anisotropic QR structure possessing a finite rim width.

(i) The role of the electron-electron interaction in a finite-width QR for a sufficiently low density, at which the correlation energy was much larger than the Fermi energy, consisted in formation of an N-electron Wigner molecule with relative angular motions of the electrons in the form of harmonic oscillations and radial motions depending on the shape of the confining potential [78], further developed and specified in [73, 79, 80]. The results for highly correlated electrons were, generally speaking, distinct from those for free electrons, except for the case of low temperatures, when a high-symmetry equilibrium configuration of electrons occurred by virtue of the strong repulsion between them.

(ii) A Wigner molecule determined the ring-specific rich spectra of absorption, PL, and Raman scattering [81], which were significantly distinct from those of free electrons in a QR (see also [82]). A later study of electronic transitions in QRs caused by a high-frequency inhomogeneous piezoelectric field accompanying a surface acoustic wave (SAW) unveiled another possibility to distinguish the Wigner-molecule-regime from that of the free electrons by virtue of a different mechanism of the electronic absorption: for free electrons, the dipole matrix element was other than zero, while in the Wigner molecule the absorption occurred due to quadruple and higher multipolar transitions [83].

Effect of the spin-orbit interaction was shown to dramatically change persistent currents in QRs as a function of the magnetic flux as compared to the case without the spin-orbit coupling; in particular, it may suppress the first Fourier harmonic in the persistent current and thus simulate the $\Phi_0/2$-periodicity [84]. The presence of magnetic impurities in a QR may induce bistability of the persistent current of two interacting electrons and a hysteresis in its dependence on the magnetic flux [85].

Interesting effects were unveiled in systems, where quantum rings were coupled to quantum dots. For a mesoscopic ring with a quantum dot inserted in one of its arms, it was shown that the phase of the Aharonov–Bohm oscillations was not related to the dot charge alone but instead to the total charge of the system [86]. In the presence of the Aharonov–Bohm flux, a charge response of a mesoscopic ring coupled to a side-branch quantum dot revealed a sequence of plateaus of diamagnetic and paramagnetic states, while a mesoscopic ring containing an embedded quantum dot with leads exhibited a number of sharp peaks in the persistent current depending on the parity of the total number of electrons in the system [87].

Emergence of novel materials, e.g., carbon nanotubes, provided a new playground for observation and investigation of the Aharonov–Bohm effect [88].

1.5 Florescence

As the cornerstone of high-tech industry of the twenty-first century, nanostructures [89] are known as the cradle of new fabrication technologies [90], new characterization instruments [91, 92], and new theoretical insights [40].

A remarkable breakthrough in the physics of QRs was related to the discovery of the self-organized formation of QRs of a few tens of nm in diameter in 1997 by García, Medeiros-Ribeiro, Schmidt, Ngo, Feng, Lorke, Kotthaus and Petroff for the InAs/GaAs system [93]. It opened unprecedented perspectives to fabricate, characterize and investigate large arrays of semiconductor QRs as well as to control their size and shape.

1.5.1 Self-assembly Through Partial Overgrowth

It was demonstrated that by using a partial capping process the shape and size of InAs self-assembled quantum dots grown by Molecular Beam Epitaxy (MBE) may be modified in a way that led to the fabrication of self-assembled QRs [93]. The fabrication process was monitored using the in situ Reflection High-Energy Electron Diffraction (RHEED) technique [94], cross-section Transmission Electron Microscopy (TEM) [93, 95] and Atomic Force Microscopy (AFM) [93, 96, 97] measurements.

Two mechanisms were revealed, which mainly contributed to the self-assembled formation of QRs via partial overgrowth technique. One of them was *kinetic diffusion*: the In atoms, due to their higher diffusion mobility at the interface as compared to the diffusion mobility of the Ga atoms, could diffuse out of the partially capped quantum dots outwards onto the surface of the surrounding GaAs forming a ring-shaped InGaAs island [98]. Another mechanism was based on the thermodynamically driven *dewetting*: the imbalance of surface and interface forces acting upon the partially capped islands InAs/GaP [97]. Formation of liquid In droplets on the top of the InAs quantum dots under partial capping due to the *stress-induced melting* effect was established experimentally [94] and theoretically [99].

Unlike mesoscopic QRs defined lithographically, the self-assembled QRs, embedded in a GaAs matrix, could function in the quantum limit, *free of decoherence*, owing to scattering processes [100, 101]. The energy spectra of self-assembled QRs were thoroughly studied through their peculiar optical properties using photoluminescence (PL) [96, 102], Time-Resolved PL and PL Excitation [103], as well as Photoemission Microscopy [104] both in single QRs and QR-arrays.

Being embedded in a heterostructure, the QRs could be electrically tuned by an electric field, and carriers could be injected with single-electron/single-hole precision. The detailed energy structure of electrons (holes) in QRs was obtained using the following three spectroscopic techniques. The PL (optical emission) of a single QR changed as electrons were added one-by-one. The emission energy changed

abruptly whenever an electron was added, the sizes of the jumps revealing a shell structure [101]. Capacitance-voltage measurements allowed for probing the single-particle and many-particle ground states as a function of the applied electric field. Far-infrared absorption spectra demonstrated the effect of flux quantization on the intraband transitions.

1.5.2 Characterization

Cross-Sectional Scanning Tunneling Microscopy (X-STM), Atom Probe Tomography and Scanning-Gate Microscopy (SGM) belong to the advanced characterization methods that can access the intimate behavior of buried electronic systems and have been successfully exploited to get insight into the geometric structure of QRs.

X-STM of self-assembled InGaAs/GaAs QRs revealed the remaining quantum dot material, whereas the AFM represented the erupted QD material [105]. Based on this structural information from the X-STM measurements, a model of a self-assembled QR as a *singly-connected* "quantum volcano" (with a strong dip rather than opening in the center) was substantiated [105–107]. The electron magnetization was calculated as a function of the applied magnetic field for single-electron [75, 106] and two-electron [108] QRs. Quite surprizingly, even though those nanostructures were *singly-connected* and *anisotropic*, they exhibited the Aharonov–Bohm behavior, which was generally considered to be restricted to *doubly-connected* topologies. This was due to the fact that the electron wave functions in a "quantum volcano" were decaying towards the center so rapidly (exponentially) that they were *topologically identical* to the electron wave functions in doubly-connected QRs. The theory allowed for a quantitative explanation of the Aharonov–Bohm oscillations in the magnetization observed using the torsion magnetometry on those ring-like structures [109]. For measurements of the persistent currents in metal QRs, a micromechanical detector based on cantilever torsion magnetometry was proved to provide orders of magnitude greater sensitivity than SQUID-based detectors [14]. X-STM in combination with powerful Atom Probe Tomography [110] revealed how GaSb/GaAs quantum dots disintegrate into ring-like clusters of islands upon capping, ensuring a 3D structural and compositional characterization of semiconductor QRs at the atomic scale.

The Aharonov–Bohm oscillations of conductance in a mesoscopic ring defined by dry etching in a two-dimensional electron gas below the surface of an $Al_xGa_{1-x}As$/GaAs heterostructure and interrupted by two tunnel barriers were modified by a perpendicular magnetic field and a bias voltage [111]. As a result, the nonequilibrium electron dephasing time was found to be significantly shortened at high voltages and magnetic fields.

Studies of the lithographically patterned InGaAs-based QRs by means of Scanning Gate Microscopy (SGM) provided unique imaging of Aharonov–Bohm interferences in real space and the electronic local density-of-states at low magnetic fields [112] and Coulomb islands in the quantum Hall regime at high magnetic fields and very

low temperatures [113]. This allowed for unveiling the spatial structure of transport inside a quantum Hall interferometer and, subsequently, for deciphering the high-magnetic field magnetoresistance oscillations. Scanning-probe technique unraveled, also, a counter-intuitive behavior of a two-path network patterned from a GaInAs heterojunction in the form of a rectangular QR-structure connected to a source and a drain via two openings [114]. The antidot in the initial rectangular QR-structure could then be bypassed by a third path for the electrons. Partially blocking the electron transport through this additional branch by using SGM resulted in an *increased* current through the whole device. This counterintuitive effect was interpreted as a mesoscopic analog of the Braess paradox known for classical networks.

A theoretical justification was proposed for an Aharonov–Bohm interferometer at the n-p junction in graphene nanoribbons induced by the potential of the AFM tip, as in SGM [115, 116]. The conductance of the system was shown to exhibit Aharonov–Bohm oscillations in case if the persistent currents localized at the junction were coupled to the quantum Hall edge currents, the coupling being controlled by the Fermi energy and the tip potential.

1.5.3 Various Materials Systems

The self-assembly was proved to be an efficient method of QR formation also in diverse materials systems, for instance, InAs/InP [117], Ge/Si [118] and GaSb/GaAs [119]. Capping the InAs or InGaAs quantum dots by a GaAs/AlAs layer before annealing allowed for impeding the inward diffusion of the Ga and Al atoms and resulted in nicely shaped self-assembled QR-structures [120].

In contrast to the InGaAs/GaAs materials system, where capping of quantum dots followed by a growth interruption was necessary to initiate the quantum-dot to QR transformation, GaSb QRs occurred just after the deposition of GaSb on GaAs(001). Ring-shaped GaSb/GaAs quantum dots, grown by MBE, were characterized using X-STM [121]. These QRs, as distinct from the self-assembled InGaAs/GaAs QRs, possessed *a clear central opening* extending over about 40% of the outer base length and were therefore truly doubly-connected objects.

A distinct series of quantized modes in the vortex state observed in the spin excitations of ferromagnetic rings at the micrometer scale, fabricated using electron beam lithography, was attributed to spin waves that circulated around the ring and interfered constructively [122]. This is a representative example of the vigorously developing spin-wave physics in devices with topologically nontrivial magnetization profile.

1.5.4 Droplet Epitaxy and Lithography

Besides the above-described partial overgrowth technique within the Stranski–Krastanov growth mode, another technique of the QRs fabrication was developed, which allowed for preparation of strain free GaAs/AlGaAs QRs and QR-complexes—droplet epitaxy [123–125]. This method started with formation of group-III liquid-metal droplets within a Volmer–Weber growth mode on the substrate surface. The nanostructures were subsequently formed by being exposed to a group-V element (As, Sb, P). The temporal evolution of these nanometer-scale objects was tracked in situ during the growth process using the RHEED technique [126]. It was found that nanodroplets tended to nucleate at the location of existing nanocrystals formed by droplet epitaxy [127, 128]. Hence, the already existing nanostructures served as nucleation sites for both homo- and heteroepitaxy. In thus way, vertically aligned quantum rings could be produced by sequential deposition using droplet epitaxy [128].

Local droplet etching (LDE) allowed for the self-assembled drilling of nanoholes into semiconductor surfaces where the openings were surrounded by a mostly circular wall of recrystallized material [129, 130]. Two different approaches were developed for QR fabrication by LDE. (i) QRs inside the GaAs walls which were recrystallized during LDE with Ga droplets [131]. GaAs recrystallization was assumed to take place also inside the nanoholes and to contribute to the QR confinement. (ii) LDE with Al droplets formed AlAs walls that were optically inactive. The nanoholes were filled with GaAs to form V-shaped GaAs QDs. By applying a vertical electric field, the wave functions of electron and holes were spatially separated. For one type of charge carriers, the wave functions in V-shaped QDs were tuned to form QRs, thereby implementing an effective transformation of singly connected QDs to doubly connected QRs by a gate voltage [132]. As distinct from QRs out of the recrystallized GaAs, which were formed without an electric field, a V-shaped QD required a vertical electric field for switching into a QR. For both types (i) and (ii), the charge carriers were localized by the confinement potential due to embedding of GaAs into the barrier material AlGaAs.

Droplet epitaxy demonstrated a unique ability to assemble QR nanostructures of complex morphologies ranging from single QRs [133], concentric double QRs [125, 134] and double-QR complexes [135] to concentric higher-order multiple QRs [136] and coupled QR/disks [137]. In GaAs double QRs formed by the droplet epitaxy, the size and height of the QRs were shown to depend on the supplied As flux. At a low As flux, larger and flatter rings were obtained. The formation of outer and inner rings was attributed to crystallization of out-diffused Ga and nanodrilling of Ga on the GaAs surface, correspondingly [125].

In semiconductor nanostructures, the use of twisted light/matter allowed one to populate precisely one desired electronic level using an appropriate combination of the light-beam parameters. For instance, the coupled QD-QR systems fabricated by the droplet epitaxy [138], provided a prototypical example of the class of nanostructures, where the use of twisted light/matter displayed a wealth of opportunities

for the optical control of electronic states by tuning the position, waist and orbital angular momentum of the light beam.

Optical properties of GaAs/$Al_xGa_{1-x}As$ QRs grown on GaAs (100) by droplet epitaxy were explored as a function of the Al-content in the barrier. A transition from type-I (at $x \leq 0.45$) to type-II (at $x \geq 0.60$) band alignment was detected for the QRs via photoluminescence and time-resolved photoluminescence measurements [139]. Owing to the height fluctuation of QR structures grown by droplet epitaxy, the long lifetime became the key feature to identify the type-II band alignment, rather than the large blue shift of emission energy. At $x \geq 0.60$, both the measured carrier relaxation time ~200 ps and the carrier recombination time ~6 ns for the type-II GaAs/AlGaAs QRs were much longer than their counterparts for the type-I GaAs/AlGaAs QRs.

There has been a continuing insightful analysis of lithographically determined QRs. Magnetotransport experiments in the Coulomb blockade regime [140] and magnetoresistance measurements [141] on closed rings, fabricated with AFM oxidation lithography, confirmed that a microscopic understanding of energy levels of band charge carriers in QRs with the SO-interaction could be extended to a many-electron system.

1.5.5 Novel Manifestations of the Aharonov–Bohm Effect

New conditions for manifestation of the Aharonov–Bohm effect through *neutral composite entities* consisting of charged particles in QRs were actively sought for starting with the seminal paper [84]. For an exciton in a one-dimensional QR placed in a perpendicular magnetic field, a Φ_0-periodic dependence of the exciton binding energy on the magnetic flux was found. In [142] the same result for the exciton ground-state energy was obtained within another analytical approach.

Extending the Berry's analysis of the phase evolution for a charge carrier, given in (1.9), consider the case when a particle (exciton) composed of an electron ($q=-e$) and a hole ($q=e$) is confined to a box that is transported around an opening of a doubly-connected system threaded by a magnetic flux line (tube). The wave function of the exciton

$$|\Psi(\Phi_h, \Phi_e)\rangle = \exp\left[i\frac{(\Phi_h - \Phi_e)}{\Phi_0}\right]|\Psi(\Phi_h = 0, \Phi_e = 0)\rangle \tag{1.10}$$

gains a phase, which is determined by a difference between the magnetic fluxes through the paths C_h and C_e encircled by the hole and the electron, respectively:

$$\Phi_h = \oint\limits_{C_h} \mathbf{A}(\mathbf{R}) \cdot d\mathbf{R},\ \Phi_e = \oint\limits_{C_e} \mathbf{A}(\mathbf{R}) \cdot d\mathbf{R}. \tag{1.11}$$

If the exciton is *polarized*, the paths C_h and C_e are different from each other (cp. [143]), the quantum interference, according to (1.10), is caused by the magnetic flux ($\Phi_h - \Phi_e$) through the area between the two paths. Being manifested mainly through optical response of QRs, it is called *excitonic (or optical) Aharonov–Bohm effect* [143–146].

An example of the occurrence of the excitonic Aharonov–Bohm effect in transport phenomena was provided by the following feature of the vertical transport through a QR, which was immersed in a dielectric matrix: the tunnel current, as a function of magnetic flux for a given voltage across the structure, had the form of modulated oscillations with a characteristic period Φ_0 [147]. The optical Aharonov–Bohm effect became more prominent if the dc electric field was applied in the plane containing a QR [148] or in the vertical direction [149], because of the enhanced polarization of the exciton. Control over the Aharonov–Bohm oscillations in the energy spectrum of a QR could be realized also using low-frequency electromagnetic radiation [150].

The first experimental verification of the excitonic Aharonov–Bohm effect in self-assembled QRs was obtained by tracing patterns of the PL intensity under increasing magnetic field at different temperatures [151]. The role of the built-in piezoelectric fields in strained QR-systems consisted in changing the sequence of maxima and minima of the Aharonov–Bohm oscillations. For those observations, a correlation between the electron and hole due to the Coulomb interaction was shown to be a necessary condition. The integrated σ^--polarized intensities of laterally ordered InGaAs/GaAs QD and InAs/GaAs QR stacks demonstrated different behavior below and above 6 T [152]. The QR σ^-intensity was almost constant below 6 T and decreased gradually with increasing field, while the σ^- intensity for QD superlattice increased quadratically below 6T and slightly oscillated around a constant value above 6T. The change in the magneto-photoluminescence (MPL) spectrum detected at about 6 T was attributed to the type-I to type-II transition in the valence band [152].

The existence of the optical Aharonov–Bohm effect was first demonstrated through PL for type-II InP/GaAs quantum dots [153] and Zn(SeTe) quantum dots in ZnTe/ZnSe superlattice [154]. Large and persistent oscillations in both the energy and the intensity of the PL unveiled the presence of coherently rotating exciton states. These remarkably robust Aharonov–Bohm oscillations were shown to persist until 180 K. The magnitude of the observed effects was attributed to the geometry of the columnar type-II structures investigated, which created a ring-like topology of the electron state. The advantage of this geometry to favor the optical Aharonov–Bohm effect was demonstrated in magnetic (ZnMn)Te quantum dot structures, where the strength of the Aharonov–Bohm interference effect could be controlled by the spin disorder in the system [155].

The first MPL study of single neutral excitons was performed in single self-assembled InGaAs/GaAs QRs, which were fabricated by MBE combined with $AsBr_3$ in situ etching [149]. Oscillations in the neutral exciton radiative recombination energy and in the emission intensity were detected as a function of the applied magnetic field. Effective control over the period of the oscillations was achieved through a gate potential that modified the exciton confinement [149, 156]. Strain

was shown to play a crucial role to govern the localization of electrons and holes in type-I semiconductor QRs, eventually leading to spatially separated charge carriers [157].

Singly charged excitons (trions) and multiply charged excitons in QRs were extensively studied, both theoretically and experimentally. The period of oscillations of the binding energy of charged complexes in a magnetic flux was shown to differ from Φ_0, being determined by the number of electrons and the ratio of effective masses of the electron and the hole [158]. The diamagnetic shift of the exciton PL line was found to be positive for a neutral exciton and negative for a trion and other negatively charged complexes [159]. Circularly polarized MPL spectra of a single QR, fabricated with the modulated-barrier approach, were dominated by two features: a high-energy line due to neutral exciton recombination and a low-energy line owing to emission from charged excitons [160]. The photon energy from charged exciton recombination measured as a function of the magnetic field clearly revealed the oscillatory behavior, which was in antiphase with the calculated electron's energy [161].

The excitonic Aharonov–Bohm effect, originally considered for a one-dimensional model, was shown to remain essentially unchanged in QRs of finite width [162]. Though the Aharonov–Bohm oscillations of the oscillator strength as a function of the magnetic flux for the ground state of the exciton decreased with increasing the QR width, their amplitude remained finite down to radius-to-width ratios less than unity due to the non-simple-connectedness of the confinement potential. That implied that the key condition needed for the observation of the excitonic Aharonov–Bohm effect was the avoidance of the QR center.

The exciton energy spectra and optical transitions spectra calculated for excitons with the realistic confinement potential of self-assembled QRs [105] taking into account the strain revealed a very high sensitivity to the size, anisotropic shape, and composition of a QR [163]. Photoluminescence spectroscopy of a large ensemble of InAs/GaAs QRs in magnetic fields up to 30 T for different excitation densities unveiled that the confinement of an electron and a hole along with the Coulomb interaction suppressed the excitonic Aharonov–Bohm effect in these QRs [102, 164]. This suppression was confirmed also by MPL studies of type-II self-assembled GaSb/GaAs QRs [165].

Optical Aharonov–Bohm oscillations of an exciton and a biexciton in a QR in the presence of structure anisotropy, localization, internal electric field, and impurity scattering revealed modulations. Occurrence of a strongly correlated exciton pair (excitonic Wigner molecule) in a QR was experimentally detected by new oscillations in MPL at increased magnetic fields [166]. The biexciton emission energy changed abruptly at transition magnetic fields with a fractional oscillation period compared to that of the exciton, resulting in fractional optical Aharonov–Bohm oscillations.

Another manifestation of the Aharonov–Bohm effect in neutral formations was related to magnetoplasmon oscillations in QRs [167]. The plasmon frequency in a finite-width QR constituted of a monotonous part superposed with Aharonov–Bohm oscillations. Their period and amplitude were found to vary with the magnetic field.

Polaron shift in QRs revealed the non-monochromaticity of the Aharonov–Bohm oscillations, which was attributed to the difference in the magnetic fluxes that were encircled by different electron trajectories [168]. When an exciton was generated, the contributions of the electron and the hole to the polarization of the medium had opposite signs, and it was therefore important to take the finiteness of the ring into account when calculating the net effect determined by the wave functions of the particles.

1.5.6 Advancements of Theory

Embedding QRs in various multilayer structures is an important tool to control their physical properties. The non-trivial role of strain in QR multilayer systems was theoretically revealed in [169]. In GaAs-capped InAs/$In_{0.53}Ga_{0.47}As$ QRs, there occurred an anomalous strain relaxation: GaAs embedded in the $In_{0.53}Ga_{0.47}As$ matrix considerably weakened each strain component and biaxial strain by providing enough room for the atomic relaxation of InAs. GaAs embedded in $In_{0.53}Ga_{0.47}As$ acted as a potential barrier for both electrons and heavy holes and as a potential well for light holes. The weak positive biaxial strain of InAs along with the strong negative biaxial strain of GaAs in a QR led to an enhancement of the light-hole character of the states in the valence band of a QR as compared to those in a quantum dot.

Calculating the strain profile as well as the charge carriers energy and other properties (shell filling, spin polarization, exciton fine structure, magnetization…) in QRs requires the extensive use of a great variety of the advanced tools of the modern theoretical physics, of which we name below only a few.

Exact diagonalization method revealed the fractional Aharonov–Bohm effect of a few-electron system in a one-dimensional QR taking into account spin, disorder and the Coulomb interaction [170]. A great challenge for the theory—to find analytical solutions for quantum states in QRs—was addressed for two electrons on a one-dimensional QR for particular values of the radius [171]. Many-electron QRs were studied using a number of versions of the Density Functional Theory [172, 173].

After calculating the strain with the atomistic Valence Force Field method, the electronic properties were derived in the framework of the Empirical Pseudopotential method [174] or the Empirical Tight-Binding method [84, 175, 176, 177]. A continuum description of the QR system was assumed within the single-band Effective-Mass approximation [178, 179] and its diversified generalizations onto multiband k·p approaches [180]. Of importance for modeling the self-assembled QRs was the finding [181], that the 14-band k·p model can accommodate for the correct symmetry of the underlying GaAs zincblende lattice, which was not reflected in the standard 8-band model. The ground-state energy of the few-particle systems in QRs was calculated within the Configuration Interaction method [149, 174].

Transfer-Matrix method was employed to account for the mutual influence of the radial and azimuthal motions in the presence of impurities in the finite-width QR [182]. The Landauer–Büttiker formalism was used to analyze transport properties of

QRs [183, 184]. Using the Keldysh Green's function formalism enabled unveiling two contributions, thermodynamic and kinetic, to the disorder-averaged magnetization of QRs [185].

Path-Integral Quantum-Monte-Carlo method was applied for investigation of the energy spectra of few-electron systems in QRs as a function of their geometry [58]. The interplay between the confinement geometry and the Coulomb interaction was pronouncedly manifested through the electronic properties of a QR. The ground state of a perfect QR containing a small number of interacting electrons was analyzed as a function of its geometric parameters: ring radius, radial confinement, and eccentricity. A Path-Integral Quantum-Monte-Carlo calculation demonstrated a strong dependence of the total spin of the ground state on the structure geometry. For instance, for a three-electron QR, changing the radius produced a spin polarization of the ground state, while an elliptical deformation resulted in a spin-depolarized ground state [186].

A finite mixing of the heavy-hole subband with the light-hole subband in self-assembled QRs affected hole spin properties. The large light-hole component in QRs underpinned their perspectives for applications requiring enhanced tunneling rates [187] and spin-orbit mediated control [188].

The Hamiltonian of the electron-phonon interaction, which was systematically derived within the continuum approach for semiconductor core-shell Si/Ge nanowires and using the symmetry analysis due to Bir and Pikus [189], provided a basis for treatment of acoustical and optical phonons as well as other vibrational excitations in topologically nontrivial nanostructures. A 3D continuum phonon model for group-IV 2D materials [190] was applied to compute phonon dispersion for 2D single-layer graphene and reveal significant differences between the planar and cylinder-shaped graphene layers [191].

Research on control of the quantum-interference effects in semiconductor quantum rings via the external applied fields attracted significand interest. THz transitions in infinitesimally thin quantum rings in an external electric field were shown to produce magneto-oscillations of the electric dipole moment of a ring accompanied by periodic changes of the selection rules for inter-level optical transitions. Electromagnetic radiation associated with these transitions in quantum rings with the radial size of 10–20 nm occurred at THz frequencies [192]. For QRs pierced by a magnetic flux and subjected to a lateral electric field in high-Q single-mode microcavities, the magnetic and electric fields were shown to be efficient means to tune the QR-microcavity coupling strength, and hence, to control the emission spectrum of the system [193], what suggested quantum rings to be promising candidates for photonic devices operating at THz spectral range. An additional control parameter was shown to be the angle between the lateral electric field and the polarization plane of the optical pumping field. Influence of the intense THz laser radiation and the applied electric field on electronic states and the related intraband optical properties of laterally coupled GaAs/GaAlAs quantum rings ("QR molecules") [194] implied novel potentialities of QRs for optoelectronic applications.

1.6 Multi-faceted Horizons

In view of the emerging high-tech realizations, finding and exploiting novel phenomena in QR-structures will be the key issues for the future development in the theoretical and experimental physics of QRs. At the time of writing this Chapter, the perspective research directions in the field range from non-trivial topologies, new materials, alignment and assembly of QRs arrays—through engineering topology- and geometry-driven QR-based metamaterials—to device design, validation, manufacturing, and application.

1.6.1 Novel Topology-Driven Properties of Quantum-Ring Structures

Nanostructure fabrication techniques have allowed for generating topologically nontrivial manifolds at the micro- and nanoscale with manmade space metrics, which determine the energy spectrum and other physical properties of electrons confined in such objects. For instance, when spooling a single crystalline $NbSe_3$ ribbon on a selenium droplet, surface tension produced a twist in the ribbon, leading to the formation of a one-sided Möbius ring [195]. Analytical and computational differential geometry methods have been developed to examine particle quantum eigenstates and eigenenergies in curved and strained nanostructures [196, 197]. Significant changes in eigenstate symmetry and eigenenergy were revealed due to the interplay between curvature and strain effects for bending radii of a few nanometers. Curvature effects became negligible at bending radii above ~50 nm. The elastic energy for a thin shell was obtained using a differential-geometric formulation [191].

Symbiosis of the geometric potential and an inhomogeneous twist renders an observation of the topology effect on the electron ground-state energy in microscale Möbius rings into the realm of experimental verification. A "*delocalization-to-localization*" transition for the electron ground state was unveiled in inhomogeneous Möbius rings. This transition could be quantified through the Aharonov–Bohm effect on the ground-state persistent current as a function of the magnetic flux threading the Möbius ring [198]. The theoretical analysis of such topologically nontrivial manifolds at the nanoscale will have practical relevance, as any pertinent fabrication techniques are likely to generate geometric and structural inhomogeneities.

Theory of the energy spectra of the few-electron ZnO QRs revealed the Aharonov–Bohm oscillations to be strongly dependent on the electron number in the ring, and therefore highly sensitive to changes in the confinement potential, sizes of the QR and the magnetic field [199]. In particular, unlike in conventional QRs topology, the Aharonov–Bohm effect in ZnO QRs could be efficiently controlled by varying the electron number: for two interacting electrons in a ZnO QR, the Aharonov–Bohm oscillations became aperiodic, while for three interacting electrons the Aharonov–Bohm oscillations disappeared.

InAs QRs with a strong Spin-Orbit Interaction (SOI), proximity-coupled to an s-wave superconductor, were shown to reveal both the topological superconducting phase and confined Majorana fermions [200]. Spin-induced modulations of unpolarized currents were revealed in quantum rings subject to the Rashba SOI [201]. The conductance modulations due to the Aharonov–Anandan geometric phase [20] acquired by the spin during transport around a ring made quantum rings a perspective spintronic element to control spins at the mesoscopic scale.

In a spin interferometer with an external planar magnetic field assuming rings tangentially coupled to leads, the dynamical Zeeman phases could provide both constructive and destructive interference, and consequently, the conductance was modulated by both the magnetic-field dependent dynamical phase and the magnetic-field dependent geometric phase [202]. Distinct phase dislocations surprisingly occurred along the critical line, on which the effective magnetic field textures changed topology.

Edge states occurring in the gap of finite MoS_2 systems [203] were revealed as mid-gap topological states, which localized near the edge of monolayer MoS_2 quantum dots subject to a magnetic field in analogy to those of 1D quantum rings. When anticrossing with delocalized states of the quantum dots, they were shown to give rise to Aharonov–Bohm-like oscillations of the low-lying states in conduction and valence bands [204]. External potentials, modifying energy of the edge states, could be used to tune the range of magnetic fields, where these quantum-ring like features emerged.

1.6.2 Graphene QRs

Electronic quantum interference in QR-structures based on graphene was investigated with a focus on the interplay between the Aharonov–Bohm effect and the peculiar electronic and transport properties of this material [184]. The first experimental realization of a graphene ring structure was provided [205]. In this work, the authors investigated the Aharonov–Bohm oscillations in diffusive single-layer graphene as a function of the magnetic field which was applied perpendicularly to the graphene plane in a two-terminal setup. The clear magnetoconductance oscillations were found with the expected period of Φ_0 on the top of a low-frequency background signal due to universal conductance fluctuations. A significant increase in the oscillation amplitude at strong magnetic fields close to the onset of the quantum Hall regime was strong enough to make the second harmonic (oscillations of period $\Phi_0/2$) visible in the frequency spectrum. Such a behavior, observed in smaller rings using a two-terminal as well as four-terminal geometry was attributed to scattering on magnetic impurities [206].

The interplay between the valley polarization and the Coulomb interaction in graphene QRs was addressed in [207]. The change of the interacting ground state between singlet, triplet and degenerate singlet-triplet ones resulted in the fractional

Aharonov–Bohm oscillations in the persistent current, and in the steps and intensity changes in the absorption spectrum as a function of the magnetic flux.

Additional tunability was introduced into the graphene ring device by applying a side gate potential to one of the ring arms. Investigation of the influence of such side gates on a four-terminal geometry in the diffusive regime revealed phase shifts of the Aharonov–Bohm oscillations as a function of the gate voltage as well as phase jumps of π at zero magnetic field—direct consequences of the electrostatic Aharonov–Bohm effect as well as the generalized Onsager relations [208]. The electrostatic Aharonov–Bohm effect appeared to be more feasible in graphene QRs than in metal QRs due to the low screening of this material [209, 210]. Voltage-driven charge-carrier states ranging from metallic to semiconductor ones were theoretically revealed for QRs determined by a set of concentric circular gates over a graphene sheet placed on a substrate [211].

The inner radial fringes observed in the arms of QRs [212, 213] were interpreted as semiclassical privileged paths, along which the electron/hole wave functions were concentrated ("scarred wave functions"). Scar patterns (associated with semiclassical periodic orbits) were predicted to reappear periodically with the Fermi energy E_F in systems with the Dirac dispersion law, in contraposition to the square root of E_F dependence in conventional semiconductor systems [214]. This prediction was confirmed through SGM-experiments realized on graphene QRs. In QRs with modest low-temperature charge carrier mobility (~1000 cm^2/Vs), at low charge carrier densities in the vicinity of the Dirac point, SGM revealed Coulomb blockade oscillations due to the disorder-induced localized states similar to those in isolated QDs, tunnel-coupled with the transmitting channels, and in constrictions [215–217]. At higher charge carrier densities, as long as disorder was screened, SGM imaging on the graphene QR revealed scars similar to those known in heterostructure-based QRs [218]. The recurrence of the radial pattern of scars with energy was detected using SGM in graphene QRs with higher charge carrier mobility (~10,000 cm^2/Vs), deposited on top of a hexagonal boron nitride flake [219]. The energy difference between the successive maxima in the radial pattern allowed for an association of the sequence of maxima in SGM image correlation parameters with radial scars [219].

1.6.3 Ordering of QRs. Metamaterials

Great efforts have been devoted to achieve vertical and lateral alignment of QRs. Stacking of three InGaAs/GaAs QRs is demonstrated to provide a broad-area laser [220]. In QR complexes and stacks, novel correlations show up, which allow for control over their electronic and magnetic properties.

One-dimensional ordered QR-chains have been fabricated on a quantum-dot superlattice template by MBE. The quantum-dot superlattice template is prepared by stacking multiple quantum-dot layers. The lateral ordering is introduced by engineering the strain field of a multi-layer InGaAs quantum-dot superlattice. QR chains

are then formed by partially capping InAs quantum dots with a thin layer of GaAs which introduces a morphological change from quantum dots to QRs [221]. It is shown that two-dimensional periodically aligned QR-arrays can be fabricated on GaAs high-index [(311)B and (511)B] surfaces [222].

An alternative approach to self-assembly of aligned QRs is to create an artificially ordered template by pre-patterning. Nanosphere lithography is used to create ordered GeSi quantum dots, and ordered GeSi QRs are subsequently formed by capping the quantum dots with a thin Si capping layer [223]. When the Si capping layer is more than 3 nm thick, most quantum dots are converted into QRs. Additional fabrication techniques, such as Ar^+ sputter redeposition using porous alumina templates [224] and laser-interference lithography in conjunction with electrochemical deposition [225] are promising, low-cost, and scalable tools for producing ordered QR-arrays.

QRs are a very promising building block for metamaterials. High-density assemblies of QRs may contain clusters of close or even partially overlapping QRs [120]. A moderate coupling between adjacent QRs in a cluster is shown to significantly influence the energy spectrum: while its lowest part may preserve the single-QR behavior, the high-energy part is strongly modified [226]. Metamaterials consisting of split nanosize gold QRs are found to possess unusual electromagnetic response properties like a negative index of refraction for wavelengths in the micrometer region [227, 228], where the resonance wavelength scales linearly with the size of the circuit. A possible control over the electromagnetic response in QR composite metamaterials made from metals and semiconductors is an attractive goal for further investigations.

1.6.4 Photonic Sources, Detectors and Waveguides

Using QRs as photon sources and detectors is based on their unique optical properties associated with the excitonic Aharonov–Bohm effect [229]. Using QRs, a technique is theoretically devised to completely freeze and release individual photons at will by tuning magnetic and electric fields that enable QRs *to trap and store light* [229]. Application of these QRs as light capacitors or buffers is expected in the fields of photonic computing and communications technologies [229, 230]. The shallow bound-state energy levels of the InGaAs QRs are shown to be feasible for detecting photons in the THz regime [231].

Single InAs/GaAs QRs embedded in a photonic crystal lattice are demonstrated to allow for single-photon emission and photon antibunching between the exciton and biexciton emissions [232]. This extends the realm of the QRs investigations towards quantum electrodynamics. The antibunching of photons observed in a double QR [233] is a clear signature of a single photon emitter.

Advancements in fabrication of geometrically and topologically nontrivial cavities at micro- and nanoscale have provided novel instruments to control properties of optical waveguides. When optical electric field is forced to be twisted around when propagating in Möbius-band-like microring and cone-shaped anisotropic microtube

cavities, there occurs twist-determined geometric phase in Abelian and non-Abelian evolutions of light, correspondingly. In dielectric Möbius-band-like microring cavities, optical modes with non-integer number of wavelengths along the circumference are manifested due to the occurrence of the twist-determined geometric phase, which goes beyond the paradigm for untwisted topologies [234]. Geometric phase acquired in non-cyclic non-Abelian evolution is found experimentally and interpreted theoretically in cone-shaped anisotropic microtube cavities by enabling optical spin-orbit coupling [235]. In metallic Möbius-band-like nanorings, higher-order plasmon modes are shown to possess a net dipole moment due to symmetry breaking and hence to be bright, as distinct from dark plasmon modes in conventional metallic nanorings [236]. Topology-induced phenomena in photonic/plasmonic Möbius band-like microstructures will pave the way for on-chip integration of topological photonic devices.

1.6.5 Spintronics. Magnetic Memory

An effective confinement-governed wave function engineering is explored theoretically in systems with QRs: two-dimensional complex nanostructures in the form of double concentric QRs and dot-QR nanostructures that consist of a QR with a quantum dot inside. The higher spin stability in a QR than in a quantum dot makes QRs attractive for the realization of spin qubits, because the relaxation and decoherence processes take place at the time scale that is sufficiently long for spin manipulations and readout [237]. The dot-QR nanostructure allows, by changing the potential barrier separating the dot from the QR and the potential well offset between the dot and the QR, for a significant alteration of coherent, optical and transport properties of the structure. In particular, the spin relaxation time of dot-QR nanostructures, used as spin qubits or spin memory devices, can be modified by orders of magnitude [238]. A crossover from the ballistic to the resonant tunneling transport, unveiled for an ideal one-dimensional QR with spin-orbit interaction, underpins the suggestion to use QRs for fabricating one-qubit spintronic quantum gate and thus, for quantum information processing [183]. An Aharonov-Bohm interferometer consisting of a QR with two quantum dots embedded in its arms reveals sensitive spin-polarized electron transmission that might be useful for spintronics applications [239]. QR arrays offer superior prospects in high density magnetic memory applications as magnetic random access memory, recording medium, and other spintronic devices [240].

A deep understanding of the gyromagnetic (g) tensor is a pre-requisite for spin-based technologies. The g-tensor is shown to be strongly affected by the presence of spin-correlated orbital currents, driven by the topological nature of the wave functions, and thus directly related to the shape of the nanostructure [241, 242]. Large magnetic moments of QRs originate from spin-correlated circulating currents in the ground state of an electron or hole in a QR [243]. The largest g-factor and spin-orbit coupling constants of all semiconductors are known in III-Sb compounds.

They reveal topological properties, which can be controlled by electric and magnetic fields. For instance, topology of the valence band ground-state wave function changes from single- to double-connectedness by applying an electric field to a type II InAs/GaAsSb QD (a QD to QR transition) [244]. Owing to the large spin-orbit coupling of III-Sb compounds, a change of this kind in the hole orbital confinement opens an efficient way for the control of the hole g-factor, as demonstrated by ensemble MPL experiments at 4.2 K [245]. This is an example of novel, topology-driven resources for functionalization in quantum electronics.

In conclusion, a great variety of semiconductor QR-systems, in particular, single and multiple QRs, ordered arrays of QRs, complexes of QRs in combination with other nanostructures, and Möbius QRs, have been fabricated with advanced high-tech methods, characterized with cutting-edge technologies, and analyzed with innovative theoretical tools. Their unique *doubly-connected topology* and the *ring-like density of states* for charge carriers, spins, plasmon and photon fields provide a veritable cornucopia of fascinating properties and possibilities to boost development of the strategic domains of technology: quantum computing based on photon and spin manipulations, photonic sources and detectors, magnetic memory, and functionalization of nanostructured metamaterials.

References

1. A.-M. Ampère, Ann. de Chim. et Phys. **15**, 59 (1820); ibid., **15**, 170 (1820)
2. L. Wendler, V.M. Fomin, Phys. Stat. Sol. (b) **191**, 409 (1995)
3. M. Bayindir, I.O. Kulik, in *Quantum Mesoscopic Phenomena and Mesoscopic Devices in Microelectronics*, ed. by I.O. Kulik, R. Ellialtıoğlu. NATO Science Series, Series C: Mathematical and Physical Sciences, vol. 559 (Kluwer, Dordrecht, 2000), pp. 283–292
4. B.C. Lee, O. Voskoboynikov, C.P. Lee, Phys. E **24**, 87 (2004)
5. L. Saminadayar, C. Bäuerle, D. Mailly, in *Encyclopedia of Nanoscience and Nanotechnology*, vol. 3, ed. by H.S. Nalwa (American Scientific Publishers, Valencia, CA 2004), pp. 267–285
6. P. Nordlander, ACS Nano **3**, 488 (2009)
7. V.M. Fomin, L.F. Chibotaru, J. Nanoelectron. Optoelectron. **4**, 3 (2009)
8. I.O. Kulik, Low Temp. Phys. **36**, 1063 (2010)
9. V.M. Fomin (ed.), A special issue on modern advancements in experimental and theoretical physics of quantum rings. J. Nanoelectron. Optoelectron. **6**, 1–86 (2011)
10. L. Pauing, J. Chem. Phys. **4**, 673 (1936)
11. F.J. London, J. Phys. Radium **8**, 397 (1937)
12. F. Hund, Ann. Phys. (Leipzig), 5. Folge **32**, 102 (1938)
13. R.B. Dingle, Proc. R. Soc. Lond. A **212**, 47 (1952)
14. A.C. Bleszynski-Jayich, W.E. Shanks, B. Peaudecerf, E. Ginossar, F. von Oppen, L. Glazman, J.G.E. Harris, Science **326**, 272 (2009)
15. M.V. Berry, Proc. R. Soc. Lond. A **392**, 45 (1984)
16. S. Pancharatnam, Proc. Ind. Acad. Sci. A **44**, 247 (1956)
17. S.M. Rytov, Dokl. Akad. Nauk SSSR **18**, 263 (1938) (English translation in B. Markovsky and S. I. Vinitsky (eds.), *Topological Phases in Quantum Theory*, World Scientific, Singapore, 1989, pp. 6–10)
18. V.V. Vladimirskii, Dokl. Akad. Nauk SSSR **21**, 222 (1941) (English translation in B. Markovsky, S.I. Vinitsky (eds.), *Topological Phases in Quantum Theory*, World Scientific, Singapore, 1989, pp. 11–16)

19. M. Born, V. Fock, Z. Phys. **51**, 165 (1928)
20. Y. Aharonov, J. Anandan, Phys. Rev. Lett. **58**, 1593 (1987)
21. N. Byers, C.N. Yang, Phys. Rev. Lett. **7**, 46 (1961)
22. F. Bloch, Phys. Rev. **137**, A787 (1965).
23. F. Wilczek, A. Zee, Phys. Rev. Lett. **52**, 2111 (1984)
24. Y. Aharonov, D. Bohm, Phys. Rev. **115**, 485 (1959)
25. P.A.M. Dirac, Proc. R. Soc. Lond. A **133**, 60 (1931)
26. W. Ehrenbug, R.E. Siday, Proc. R. Soc. Lond. B **62**, 8 (1949)
27. E. Buks, R. Schuster, M. Heiblum, D. Mahalu, V. Umansky, Nature **391**, 871 (1998)
28. Y. Aharonov, A. Casher, Phys. Rev. Lett. **53**, 319 (1984)
29. J.T. Devreese, V.M. Fomin, V.N. Gladilin, J. Tempere, Phys. C **470**, 848 (2010)
30. V.M. Fomin, V.R. Misko, J.T. Devreese, V.V. Moshchalkov, Phys. Rev. B **58**, 11703 (1998)
31. H. Zhao, V.M. Fomin, J. T. Devreese, V.V. Moshchalkov, Solid State Commun. **125**, 59 (2003)
32. F. Bloch, Phys. Rev. **137**, A787 (1965)
33. R. Doll, M. Näbauer, Phys. Rev. Lett. **7**, 51 (1961)
34. B.S. Deaver Jr., W.M. Fairbank, Phys. Rev. Lett. **7**, 43 (1961)
35. L. Gunther, Y. Imry, Solid State Commun. **7**, 1391 (1969)
36. I.O. Kulik, JETP Lett. **11**, 275 (1970); Sov. Phys. JETP **31**, 1172 (1970)
37. N.B. Brandt, D.V. Gitsu, A.A. Nikolaeva, Ya.G. Ponomarev, JETP Lett. **24**, 272 (1976)
38. N.B. Brandt, E.N. Bogachek, D.V. Gitsu, G.A. Gogadze, I.O. Kulik, A.A. Nikolaeva, Ya.G. Ponomarev, Sov. J. Low Temp. Phys. **8**, 358 (1982)
39. M. Büttiker, Y. Imry, R. Landauer, Phys. Lett. A **96**, 365 (1983)
40. Y. Imry, *Introduction to Mesoscopic Physics* (Oxford University Press, Oxford, 1997), p. 234
41. J.P. Carini, K.A. Muttalib, S.R. Nagel, Phys. Rev. Lett. **53**, 102 (1984)
42. R. Landauer, M. Büttiker, Phys. Rev. Lett. **54**, 2049 (1985)
43. M. Büttiker, Phys. Rev. B **32**, 1846 (1985)
44. L.P. Lévy, G. Dolan, J. Dunsmuir, H. Bouchiat, Phys. Rev. Lett. **64**, 2074 (1990)
45. V. Chandreasekhar, R.A. Webb, M.J. Brandy, M.B. Ketchen, W.J. Gallagher, A. Kleinsasser, Phys. Rev. Lett. **67**, 3578 (1991)
46. G. Timp, A.M. Chang, J.E. Cunningham, T.Y. Chang, P. Mankiewich, R. Behringer, R.E. Howard, Phys. Rev. Lett. **58**, 2814 (1987)
47. C.J.B. Ford, T.J. Thornton, R. Newbury, M. Pepper, H. Ahmed, D.C. Peacock, D.A. Ritchie, J.E.F. Frost, G.A.C. Jonesless, Appl. Phys. Lett. **54**, 21 (1989)
48. A.A. Bykov, Z.D. Kvon, E.B. Olshanetskii, L.V. Litvin, YuV Nastaushev, V.G. Mansurov, V.P. Migal', S.P. Moshchenko, V.G. Plyukhin, JETP Lett. **57**, 613 (1993)
49. D. Mailly, C. Chapelier, A. Benoit, Phys. Rev. Lett. **70**, 2020 (1993)
50. H. Bluhm, N.C. Koshnick, J.A. Bert, M.E. Huber, K.A. Moler, Phys. Rev. Lett. **102**, 136802 (2009)
51. E.M.Q. Jariwala, P. Mohanty, M.B. Ketchen, R.A. Webb, Phys. Rev. Lett. **86**, 1594 (2001)
52. R. Deblock, R. Bel, B. Reulet, H. Bouchiat, D. Mailly, Phys. Rev. Lett. **89**, 206803 (2002)
53. H.-F. Cheung, Y. Gefen, E.K. Riedel, W.-H. Shih, Phys. Rev. B **37**, 6050 (1988)
54. F. von Oppen, E.K. Riedel, Phys. Rev. Lett. **66**, 84 (1991)
55. B.L. Altshuler, Y. Gefen, Y. Imry, Phys. Rev. Lett. **66**, 88 (1991)
56. H. Bouchiat, G. Montambaux, J. Phys. (Paris) **50**, 2695 (1989)
57. H.-F. Cheung, E.K. Riedel, Y. Gefen, Phys. Rev. Lett. **62**, 587 (1989)
58. A. Emperador, F. Pederiva, E. Lipparini, Phys. Rev. B **68**, 115312 (2003)
59. D. Loss, P. Goldbart, Phys. Rev. B **43**, 13762 (1991)
60. J.F. Weisz, R. Kishore, F.V. Kusmartsev, Phys. Rev. B **49**, 8126 (1994)
61. V. Ambegaokar, U. Eckern, Phys. Rev. Lett. **65**, 381 (1990)
62. U. Eckern, A. Schmid, Europhys. Lett. **18**, 457 (1992)
63. A. Schmid, Phys. Rev. Lett. **66**, 80 (1991)
64. H. Bary-Soroker, O. Entin-Wohlman, Y. Imry, Phys. Rev. Lett. **101**, 057001 (2008)
65. U. Eckern, P. Schwab, V. Ambegaokar, Phys. Rev. Lett. **93**, 209701 (2004)
66. M. Schechter, Y. Oreg, Y. Imry, Y. Levinson, Phys. Rev. Lett. **90**, 026805 (2003)

67. M. Schechter, Y. Oreg, Y. Imry, Y. Levinson, Phys. Rev. Lett. **93**, 209702 (2004)
68. N. Argaman, Y. Imry, Phys. Scr. T. **49**, 333 (1993)
69. A. Altland, S. Iida, A. Müller-Groeling, H.A. Weidenmüller, Ann. Phys. **219**, 148 (1992)
70. A. Müller-Groeling, A. Weidenmüller, C.H. Lewenkopf, Europhys. Lett. **22**, 193 (1993)
71. A. Miiller-Groeling, H.A. Weidenmuller, Phys. Rev. B **49**, 4752 (1994)
72. Y. Imry, *Introduction to Mesoscopic Physics*, 2nd edn. (Oxford University Press, Oxford, 2005), p. 236
73. L. Wendler, V.M. Fomin, A.V. Chaplik, A.O. Govorov, Z. Phys. B **100**, 211 (1996)
74. L. Wendler, V.M. Fomin, Z. Phys. B **96**, 373 (1995)
75. V.M. Fomin, V.N. Gladilin, S.N. Klimin, J.T. Devreese, N.A.J.M. Kleemans, P.M. Koenraad, Phys. Rev. B **76**, 235320 (2007)
76. W.C. Tan, J.C. Inkson, Phys. Rev. B **53**, 6947 (1996)
77. H.D. Kim, W.J. Lee, S.H. Park, K. Kyhm, K. Je, R.A. Taylor, G. Nogues, L.S. Dang, J.D. Song, Sci. Rep. **7**, 40026 (2017)
78. L. Wendler, V.M. Fomin, A.V. Chaplik, Superlattices Microstruct **16**, 311 (1994)
79. A.O. Govorov, A.V. Chaplik, L. Wendler, V.M. Fomin, JETP Lett. **60**, 643 (1994)
80. L. Wendler, V.M. Fomin, A.V. Chaplik, Solid State Commun. **96**, 809 (1995)
81. L. Wendler, V.M. Fomin, A.V. Chaplik, A.O. Govorov, Phys. Rev. B **54**, 4794 (1996)
82. L. Wendler, V.M. Fomin, A.V. Chaplik, A.O. Govorov, Phys. B **227**, 397 (1996)
83. V.M. Kovalev, A.V. Chaplik, Semiconductors **37**, 1195 (2003)
84. A.V. Chaplik, JETP Lett. **62**, 900 (1995)
85. L. Wendler, V.M. Fomin, Phys. Rev. B **51**, 17814 (1995)
86. A. Levy Yeyati, M. Büttiker, Phys. Rev. B **52**, R14360 (1995)
87. M. Büttiker, C.A. Stafford, Phys. Rev. Lett. **76**, 495 (1996)
88. C. Schönenberger, A. Bachtold, Ch. Strunk, J.-P. Salvetat, J.-M. Bonard, L. Forró, T. Nussbaumer, Nature **397**, 673 (1999)
89. D. Bimberg (ed.), *Semiconductor Nanostructures* (Springer, Berlin, 2008), 357 pp
90. D. Bimberg, M. Grundmann, N.N. Ledentsov, *Quantum Dot Heterostructures* (Wiley, Chichester, 1999), p. 338
91. G. Binnig, H. Rohrer, IBM J. Res. Dev. **30**(4) (1986)
92. R. Wiesendanger, *Scanning Probe Microscopy: Analytical Methods* (Springer, Berlin, 1998), p. 216
93. J.M. García, G. Medeiros-Ribeiro, K. Schmidt, T. Ngo, J.L. Feng, A. Lorke, J. Kotthaus, P.M. Petroff, Appl. Phys. Lett. **71**, 2014 (1997)
94. J.M. García, J. Silveira, F. Briones, Appl. Phys. Lett. **77**, 409 (2000)
95. D. Granados, J.M. García, Appl. Phys. Lett. **82**, 2401 (2003)
96. D. Granados, J.M. García, T. Ben, S.I. Molina, Appl. Phys. Lett. **86**, 071918 (2005)
97. R. Blossey, A. Lorke, Phys. Rev. E **65**, 021603 (2002)
98. A. Lorke, R.J. Luyken, J.M. García, P.M. Petroff, Jpn. J. Appl. Phys. **40**, 1857 (2001)
99. D.J. Bottomley, Appl. Phys. Lett. **80**, 4747 (2002)
100. A. Lorke, R.J. Luyken, A.O. Govorov, J. Kotthaus, J.M. García, P.M. Petroff, Phys. Rev. Lett. **84**, 2223 (2000)
101. R.J. Warburton, C. Schaflein, D. Haft, F. Bickel, A. Lorke, K. Karrai, J. Garcia, W. Schoenfeld, P. Petroff, Nature **405**, 926 (2000)
102. N.A.J.M. Kleemans, J.H. Blokland, A.G. Taboada, H.C.M. van Genuchten, M. Bozkurt, V.M. Fomin, V.N. Gladilin, D. Granados, J.M. García, P.C.M. Christianen, J.C. Maan, J.T. Devreese, P.M. Koenraad, Phys. Rev. B **80**, 155318 (2009)
103. B. Alén, J. Martínez-Pastor, D. Granados, J.M. García, Phys. Rev. B **72**, 155331 (2005)
104. G. Biasiol, S. Heun, L. Sorba, J. Nanoelectron. Optoelectron. **6**, 20 (2011)
105. P. Offermans, P.M. Koenraad, J.H. Wolter, D. Granados, J.M. García, V.M. Fomin, V.N. Gladilin, J.T. Devreese, Appl. Phys. Lett. **87**, 131902 (2005)
106. V.M. Fomin, V.N. Gladilin, J.T. Devreese, P. Offermans, P.M. Koenraad, J.H. Wolter, J.M. García, D. Granados, AIP Conf. Proc. **772**, 803 (2005)

107. P. Offermans, P.M. Koenraad, J.H. Wolter, D. Granados, J.M. García, V.M. Fomin, V.N. Gladilin, J.T. Devreese, Phys. E **32**, 41 (2006)
108. V.M. Fomin, V.N. Gladilin, J.T. Devreese, N.A.J.M. Kleemans, P.M. Koenraad, Phys. Rev. B **77**, 205326 (2008)
109. N.A.J.M. Kleemans, I.M.A. Bominaar-Silkens, V.M. Fomin, V.N. Gladilin, D. Granados, A.G. Taboada, J.M. García, P. Offermans, U. Zeitler, P.C.M. Christianen, J.C. Maan, J.T. Devreese, P.M. Koenraad, Phys. Rev. Lett. **99**, 146808 (2007)
110. A.J. Martin, J. Hwang, E.A. Marquis, E. Smakman, T.W. Saucer, G.V. Rodriguez, A.H. Hunter, V. Sih, P.M. Koenraad, J.D. Phillips, J. Millunchick, Appl. Phys. Lett. **102**, 113103 (2013)
111. W.G. van der Wiel, YuV Nazarov, S. De Franceschi, T. Fujisawa, J.M. Elzerman, E.W.G.M. Huizeling, S. Tarucha, L.P. Kouwenhoven, Phys. Rev. B **67**, 033307 (2003)
112. B. Hackens, F. Martins, T. Ouisse, H. Sellier, S. Bollaert, X. Wallart, A. Cappy, J. Chevrier, V. Bayot, S. Huant, Nat. Phys. **2**, 826 (2006)
113. B. Hackens, F. Martins, S. Faniel, C.A. Dutu, H. Sellier, S. Huant, M. Pala, L. Desplanque, X. Wallart, V. Bayot, Nat. Commun. **1**, 39 (2010)
114. M.G. Pala, S. Baltazar, P. Liu, H. Sellier, B. Hackens, F. Martins, V. Bayot, X. Wallart, L. Desplanque, S. Huant, Phys. Rev. Lett. **108**, 076802 (2012)
115. A. Mreńca-Kolasińska, S. Heun, B. Szafran, Phys. Rev. B **93**, 125411 (2016)
116. A. Mreńca-Kolasińska, B. Szafran, Phys. Rev. B **94**, 195315 (2016)
117. T. Raz, D. Ritter, G. Bahir, Appl. Phys. Lett. **82**, 1706 (2003)
118. J. Cui, Q. He, X.M. Jiang, Y.L. Fan, X.J. Yang, F. Xue, Z.M. Jiang, Appl. Phys. Lett. **83**, 2907 (2003)
119. S. Kobayashi, C. Jiang, T. Kawazu, H. Sakaki, Jpn. J. Appl. Phys. **43**, L662 (2004)
120. B.C. Lee, C.P. Lee, Nanotechnology **15**, 848 (2004)
121. R. Timm, H. Eisele, A. Lenz, L. Ivanova, G. Balakrishnan, D. Huffaker, M. Dähne, Phys. Rev. Lett. **101**, 256101 (2008)
122. J. Podbielski, F. Giesen, D. Grundler, Phys. Rev. Lett. **96**, 167207 (2006)
123. Ch. Heyn, A. Stemmann, Ch. Strelow, T. Köppen, D. Sonnenberg, A. Graf, S. Mendach, W. Hansen, J. Nanoelectron. Optoelectron. **6**, 62 (2011)
124. S. Sanguinetti, N. Koguchi, T. Mano, T. Kuroda, J. Nanoelectron. Optoelectron. **6**, 34 (2011)
125. J. Wu, Z.M. Wang, A.Z. Li, Z. Zeng, S. Li, G. Chen, G.J. Salamo, J. Nanoelectron. Optoelectron. **6**, 58 (2011)
126. Á. Nemcsics, Ch. Heyn, A. Stemmann, A. Schramm, H. Welsch, W. Hansen, Mater. Sci. Eng., B **165**, 118 (2009)
127. M. Elborg, T. Noda, T. Mano, T. Kuroda, Y. Yao, Y. Sakuma, K. Sakoda, J. Cryst. Growth (2017)
128. J. Wu, Y. Hirono, X. Li, Z.M. Wang, J. Lee, M. Benamara, S. Luo, Y.I. Mazur, E.S. Kim, G.J. Salamo, Adv. Func. Mater. **24**, 530 (2014)
129. Ch. Heyn, A. Stemmann, W. Hansen, Appl. Phys. Lett. **95**, 173110 (2009)
130. Ch. Heyn, Th Bartsch, S. Sanguinetti, D.E. Jesson, W. Hansen, Nanoscale Res. Lett. **10**, 67 (2015)
131. A. Graf, D. Sonnenberg, V. Paulava, A. Schliwa, Ch. Heyn, W. Hansen, Phys. Rev. B **89**, 115314 (2014)
132. A. Küster, C. Heyn, A. Ungeheuer, G. Juska, S. Tommaso Moroni, E. Pelucchi, W. Hansen, Nanoscale Res. Lett. **11**, 282 (2016)
133. T. Kuroda, T. Mano, T. Ochiai, S. Sanguinetti, K. Sakoda, G. Kido, N. Koguchi, Phys. Rev. B **72**, 205301 (2005)
134. T. Mano, T. Kuroda, S. Sanguinetti, T. Ochiai, T. Tateno, J. Kim, T. Noda, M. Kawabe, K. Sakoda, G. Kido, N. Koguchi, Nano Lett. **5**, 425 (2005)
135. S. Huang, Z. Niu, Z. Fang, H. Ni, Z. Gong, J. Xia, Appl. Phys. Lett. **89**, 031921 (2006)
136. C. Somaschini, S. Bietti, N. Koguchi, S. Sanguinetti, Nano Lett. **9**, 3419 (2009)
137. C. Somaschini, S. Bietti, S. Sanguinetti, N. Koguchi, A. Fedorov, Nanotechnology **21**, 125601 (2010)

138. F. Biccari, S. Bietti, L. Cavigli, A. Vinattieri, R. N¨otzel, M. Gurioli, S. Sanguinetti, J. Appl. Phys. **120**, 134312 (2016)
139. L. Su, Y. Wang, Q. Guo, X. Li, S. Wang, G. Fu, Y.I. Mazur, M.E. Ware, G.J. Salamo, B. Liang, J. Phys. D: Appl. Phys. **50**, 32LT01 (2017)
140. A. Fuhrer, S. Lüscher, T. Ihn, T. Heinzel, K. Ensslin, W. Wegscheider, M. Bichler, Nature **413**, 822 (2001)
141. B. Grbić, R. Leturcq, T. Ihn, K. Ensslin, D. Reuter, A.D. Wieck, Phys. E **40**, 1273 (2008)
142. R.A. Römer, M.E. Raikh, Phys. Rev. B **62**, 7045 (2000)
143. A.O. Govorov, S.E. Ulloa, K. Karrai, R.J. Warburton, Phys. Rev. B **66**, 081309 (2002)
144. A.V. Chaplik, JETP Lett. **75**, 292 (2002)
145. M. Grochol, F. Grosse, R. Zimmermann, Phys. Rev. B **74**, 115416 (2006)
146. A.V. Kalameitsev, A.O. Govorov, V.M. Kovalev, JETP Lett. **68**, 669 (1998)
147. V.M. Kovalev, A.V. Chaplik, JETP **95**, 912 (2002)
148. A.V. Maslov, D.S. Citrin, Phys. Rev. B **67**, 121304(R) (2003)
149. F. Ding, N. Akopian, B. Li, U. Perinetti, A. Govorov, F.M. Peeters, C.C. Bof Bufon, C. Deneke, Y.H. Chen, A. Rastelli, O.G. Schmidt, V. Zwiller, Phys. Rev. B **82**, 075309 (2010)
150. V.M. Kovalev, A.V. Chaplik, Europhys. Lett. **77**, 47003 (2007)
151. M.D. Teodoro, V.L. Campo Jr., V. Lopez-Richard, E. Marega Jr., G.E. Marques, Y. Galvao Gobato, F. Iikawa, M.J.S.P. Brasil, Z.Y. AbuWaar, V.G. Dorogan, Yu.I. Mazur, M. Benamara, G.J. Salamo, Phys. Rev. Lett. **104**, 086401 (2010)
152. V. Lopes-Oliveira, Y.I. Mazur, L.D. de Souza, L.A.B. Marcal, J. Wu, M.D. Teodoro, A. Malachias, V.G. Dorogan, M. Benamara, G. Tarasov, E. Marega Jr., G.E. Marques, Z.M. Wang, M. Orlita, G.J. Salamo, V. Lopez-Richard, Phys. Rev. B **90**, 125315 (2014)
153. E. Ribeiro, A.O. Govorov, W. Carvalho, Jr., G. Medeiros-Ribeiro Phys. Rev. Lett. **92**, 126402 (2004)
154. I.R. Sellers, V.R. Whiteside, I.L. Kuskovsky, A.O. Govorov, B.D. McCombe, Phys. Rev. Lett. **100**, 136405 (2008)
155. I.R. Sellers, V.R. Whiteside, A.O. Govorov, W.C. Fan, W.-C. Chou, I. Khan, A. Petrou, B.D. McCombe, Phys. Rev. B **77**, 241302 (2008)
156. F. Ding, B. Li, N. Akopian, U. Perinetti, Y.H. Chen, F.M. Peeters, A. Rastelli, V. Zwiller, O.G. Schmidt, J. Nanoelectron. Optoelectron. **6**, 51 (2011)
157. M. Tadić, N. Čukarić, V. Arsoski, F.M. Peeters, Phys. Rev. B **84**, 125307 (2011)
158. A.O. Govorov, A.V. Chaplik, JETP Lett. **66**, 454 (1997)
159. A.V. Chaplik, JETP **92**, 169 (2001)
160. M. Bayer, M. Korkusinski, P. Hawrylak, T. Gutbrod, M. Michel, A. Forchel, Phys. Rev. Lett. **90**, 186801 (2003)
161. M. Korkusiński, P. Hawrylak, M. Bayer, Phys. Status Solidi (b) **234**, 273 (2002)
162. C. González-Santander, F. Domínguez-Adame, R.A. Römer, Phys. Rev. B **84**, 235103 (2011)
163. V.M. Fomin, V.N. Gladilin, J.T. Devreese, N.A.J.M. Kleemans, M. Bozkurt, P.M. Koenraad, Phys. Status Solidi (b) **245**, 2657 (2008)
164. V.M. Fomin, V.N. Gladilin, J.T. Devreese, J.H. Blokland, P.C.M. Christianen, J.C. Maan, A.G. Taboada, D. Granados, J.M. García, N.A.J.M. Kleemans, H.C.M. van Genuchten, M. Bozkurt, P.M. Koenraad, Proc. SPIE **7364**, 736402 (2009)
165. M. Ahmad Kamarudin, M. Hayne, R.J. Young, Q.D. Zhuang, T. Ben, S.I. Molina, Phys. Rev. B **83**, 115311 (2011)
166. H.D. Kim, R. Okuyama, K. Kyhm, M. Eto, R.A. Taylor, A.L. Nicolet, M. Potemski, G. Nogues, L.S. Dang, K.C. Je, J.S. Kim, J.H. Kyhm, K.H. Yoen, E.H. Lee, J.Y. Kim, I.K. Han, W.J. Choi, J.D. Song, Nano Lett. **16**, 27 (2016)
167. V.M. Kovalev, A.V. Chaplik, JETP Lett. **90**, 679 (2009)
168. V.M. Kovalev, A.V. Chaplik, JETP **101**, 686 (2005)
169. P. Moon, K. Park, E. Yoon, J.P. Leburton, Phys. Status Solidi – Rapid Res. Lett. **3**, 76 (2009)
170. K. Niemela, P. Pietilainen, P. Hyvonen, T. Chakraborty, Europhys. Lett. **36**, 533 (1996)
171. P.-F. Loos, P.M.W. Gill, Phys. Rev. Lett. **108**, 083002 (2012)
172. E. Räsänen, S. Pittalis, C.R. Proetto, E.K.U. Gross, Phys. Rev. B **79**, 121305 (2009)

173. S. Viefers, P. Singha Deo, S.M. Reimann, M. Manninen, M. Koskinen, Phys. Rev. B **62**, 106683 (2000)
174. W. Zhang, Z. Su, M. Gong, C.-F. Li, G.-C. Guo, L. He, Europhys. Lett. **83**, 67004 (2008)
175. T. Meier, P. Thomas, S.W. Koch, K. Maschke, Phys. Stat. Sol. (b) **234**, 283 (2002)
176. Y. Meir, Y. Gefen, O. Entin-Wohlman, Phys. Rev. Lett. **63**, 798 (1989)
177. P. Potasz, A.D. Güçlü, P. Hawrylak, Phys. Rev. B **82**, 075425 (2010)
178. J.A. Barker, R.J. Warburton, E.P. O'Reilly, Phys. Rev. B **69**, 035327 (2004)
179. T. Chakraborty, P. Pietilainen, Phys. Rev. B **50**, 8460 (1994)
180. J.I. Climente, J. Planelles, J. Nanoelectron. Optoelectron. **6**, 81 (2011)
181. O. Marquardt, S. Schulz, Ch. Freysoldt, S. Boeck, T. Hickel, E.P. O'Reilly, J. Neugebauer, Opt. Quant. Elec. **44**, 183 (2012)
182. L. Wendler, V.M. Fomin, A.A. Krokhin, Phys. Rev. B **50**, 4642 (1994)
183. S. Bellucci, P. Onorato, Phys. Rev. B **78**, 235312 (2008)
184. J. Schelter, P. Recher, B. Trauzettel, Solid State Commun. **52**, 1411 (2012)
185. O.L. Chalaev, V.E. Kravtsov, Phys. Rev. Lett. **89**, 176601 (2002)
186. B. Baxevanis, D. Pfannkuche, J. Nanoelectron. Optoelectron. **6**, 76 (2011)
187. M.F. Doty, J.I. Climente, M. Korkusinski, M. Scheibner, A.S. Bracker, P. Hawrylak, D. Gammon, Phys. Rev. Lett. **102**, 047401 (2009)
188. S.E. Economou, J.I. Climente, A. Badolato, A.S. Bracker, D. Gammon, M.F. Doty, Phys. Rev. B **86**, 085319 (2012)
189. D.G. Santiago-Pérez, C. Trallero-Giner, G.E. Marques, Phys. Rev. B **95**, 155317 (2017)
190. M. Willatzen, L.C. Lew Yan Voon, A.N. Gandi, U. Schwingenschl¨ogl, Beilstein J. Nanotechnol. **8**, 1345 (2017)
191. B. Lassen, M. Willatzen, J. Gravesen, Chapter16 in the present book
192. A.M. Alexeev, M.E. Portnoi, Phys. Stat. Sol. C **9**, 1309 (2012)
193. A.M. Alexeev, I.A. Shelykh, M.E. Portnoi, Phys. Rev. B **88**, 085429 (2013)
194. H.M. Baghramyan, M.G. Barseghyan, D. Laroze, Sci. Rep. **7**, 10485 (2017)
195. S. Tanda, T. Tsuneta, Y. Okajima, K. Inagaki, K. Yamaya, N. Hatakenaka, Nature **417**, 397 (2002)
196. J. Gravesen, M. Willatzen, Phys. Rev. A **72**, 032108 (2005)
197. B. Lassen, M. Willatzen, J. Gravesen, J. Nanoelectron. Optoelectron. **6**, 68 (2011)
198. V.M. Fomin, S. Kiravittaya, O.G. Schmidt, Phys. Rev. B **86**, 195421 (2012)
199. T. Chakraborty, A. Manaselyan, M. Barseghyan, J. Phys.: Condens. Matter **29**, 075605 (2017)
200. A. Ghazaryan, A. Manaselyan, T. Chakraborty, Phys. Rev. B **93**, 245108 (2016)
201. Z.-J. Ying, P. Gentile, C. Ortix, M. Cuoco, Phys. Rev. B **94**, 081406 (2016)
202. H. Saarikoski, J.E. Vázquez-Lozano, J.P. Baltanás, F. Nagasawa, J. Nitta, D. Frustaglia, Phys. Rev. B **91**, 241406 (2015)
203. C. Segarra, J. Planelles, S.E. Ulloa, Phys. Rev. B **93**, 085312 (2016)
204. C. Segarra, J. Planelles, J.I. Climente, Chapter 17 in the present book
205. S. Russo, J.B. Oostinga, D. Wehenkel, H.B. Heersche, S.S. Sobhani, L.M.K. Vandersypen, A.F. Morpurgo, Phys. Rev. B **77**, 085413 (2008)
206. M. Huefner, F. Molitor, A. Jacobsen, A. Pioda, C. Stampfer, K. Ensslin, T. Ihn, Phys. Status Solidi (b) **246**, 2756 (2009)
207. D.S.L. Abergel, V.M. Apalkov, T. Chakraborty, Phys. Rev. B **78**, 193405 (2008)
208. M. Huefner, F. Molitor, A. Jacobsen, A. Pioda, C. Stampfer, K. Ensslin, T. Ihn, New J. Phys. **12**, 043054 (2010)
209. B. Szafran, Phys. Rev. B **77**, 205313 (2008)
210. B. Szafran, Phys. Rev. B **77**, 235314 (2008)
211. L. Villegas-Lelovsky, C. Trallero-Giner, V. Lopez-Richard, G.E. Marques, C.E.P. Villegas, M.R.S. Tavares, Nanotechnology **23**, 385201 (2012)
212. F. Martins, B. Hackens, H. Sellier, P. Liu, M.G. Pala, S. Baltazar, L. Desplanque, X. Wallart, V. Bayot, S. Huant, Acta Phys. Polon. A **119**, 569 (2011)
213. M.G. Pala, S. Baltazar, F. Martins, B. Hackens, H. Sellier, T. Ouisse, V. Bayot, S. Huant, Nanotechnology **20**, 264021 (2009)

214. L. Huang, Y.C. Lai, D.K. Ferry, S.M. Goodnick, R. Akis, Phys. Rev. Lett. **103**, 054101 (2009)
215. M.R. Connolly, K.L. Chiu, A. Lombardo, A. Fasoli, A.C. Ferrari, D. Anderson, G.A.C. Jones, C.G. Smith, Phys. Rev. B **83**, 115441 (2011)
216. N. Pascher, D. Bischoff, T. Ihn, K. Ensslin, Appl. Phys. Lett. **101**, 063101 (2012)
217. S. Schnez, J. Guttinger, M. Huefner, C. Stampfer, K. Ensslin, T. Ihn, Phys. Rev. B **82**, 165445 (2010)
218. D. Cabosart, S. Faniel, F. Martins, B. Brun, A. Felten, V. Bayot, B. Hackens, Phys. Rev. B **90**, 205433 (2014)
219. D. Cabosart, A. Felten, N. Reckinger, A. Iordanescu, S. Toussaint, S. Faniel, B. Hackens, Nano Lett. **17**, 1344 (2017)
220. F. Suárez, D. Granados, M.L. Dotor, J.M. García, Nanotechnology **15**, S126 (2004)
221. J. Wu, Z. Wang, K. Holmes, E. Marega, Y. Mazur, G. Salamo, J. Nanopart. Res. **14**, 919 (2012)
222. J. Wu, Z.M. Wang, K. Holmes, E. Marega Jr., Z. Zhou, H. Li, Y.I. Mazur, G.J. Salamo, Appl. Phys. Lett. **100**, 203117 (2012)
223. Y. Ma, J. Cui, Y. Fan, Z. Zhong, Z. Jiang, Nanoscale Res. Lett. **6**, 205 (2011)
224. K.L. Hobbs, P.R. Larson, G.D. Lian, J.C. Keay, M.B. Johnson, Nano Lett. **4**, 167 (2004)
225. R. Ji, W. Lee, R. Scholz, U. Gösele, K. Nielsch, Adv. Mater. **18**, 2593 (2006)
226. J. Planelles, J.I. Climente, F. Rajadell, Phys. E **33**, 370 (2006)
227. S. Linden, C. Enkrich, M. Wegener, J. Zhou, T. Koschny, C.M. Soukoulis, Science **306**, 1351 (2004)
228. R.A. Shelby, D.R. Smith, S. Schultz, Science **292**, 77 (2001)
229. A.M. Fischer, V.L. Campo Jr., M.E. Portnoi, R.A. Römer, Phys. Rev. Lett. **102**, 096405 (2009)
230. M.F. Borunda, X. Liu, A.A. Kovalev, X.-J. Liu, T. Jungwirth, J. Sinova, Phys. Rev. B **78**, 245315 (2008)
231. H. Ling, S. Wang, C. Lee, M. Lo, J. Appl. Phys. **105**, 034504 (2009)
232. E. Gallardo, L.J. Martínez, A.K. Nowak, D. Sarkar, D. Sanvitto, H.P. van der Meulen, J.M. Calleja, I. Prieto, D. Granados, A.G. Taboada, J.M. García, P.A. Postigo, J. Opt. Soc. Am. B **27**, A21 (2010)
233. M. Abbarchi, C. Mastrandrea, A. Vinattieri, S. Sanguinetti, T. Mano, T. Kuroda, N. Koguchi, K. Sakoda, M. Gurioli, Phys. Rev. B **79**, 085308 (2009)
234. S.L. Li, L.B. Ma, V.M. Fomin, S. Böttner, M.R. Jorgensen, O.G. Schmidt, arXiv:1311.7158 [physics.optics], 1–9 (2013)
235. L.B. Ma, S.L. Li, V.M. Fomin, M. Hentschel, J.B. Götte, Y. Yin, M.R. Jorgensen, O.G. Schmidt, Nat. Comms. **7**, 10983 (2016)
236. Y. Yin, S. Li, V. Engemaier, E.S. G. Naz, S. Giudicatti, L. Ma, O.G. Schmidt, Laser Photonics Rev. 1600219 (2017)
237. E. Zipper, M. Kurpas, J. Sadowski, M.M. Maska, J. Phys. Condes. Matter **23**, 115302 (2011)
238. E. Zipper, M. Kurpas, M. Maska, New J. Phys. **14**, 093029 (2012)
239. E.R. Hedin, Y.S. Joe, J. Appl. Phys. **110**, 026107 (2011)
240. Z.C. Wen, H.X. Wei, X.F. Han, Appl. Phys. Lett. **91**, 122511 (2007)
241. J. van Bree, AYu. Silov, P.M. Koenraad, M.E. Flatté, Phys. Rev. Lett. **112**, 187201 (2014)
242. J. van Bree, AYu. Silov, M.L. van Maasakkers, C.E. Pryor, M.E. Flatté, P.M. Koenraad, Phys. Rev. B **93**, 035311 (2016)
243. V.M. Fomin, V.N. Gladilin, M. Flatté, J. van Bree, J.T. Devreese, P.M. Koenraad, Chapter 4 in the present book
244. J.M. Llorens, L. Wewior, E.R. Cardozo de Oliveira, J.M. Ulloa, A.D. Utrilla, A. Guzmán, A. Hierro, B. Alén, Appl. Phys. Lett. **107**, 183101 (2015)
245. J.M. Llorens, E.R. Cardozo de Oliveira, L. Wevior, V. Lopes-Oliveira, V. López-Richard, J.M. Ulloa, M.D. Teodoro, G.E. Marques, A. García-Cristóbal, G. Quiang-Hai, B. Alén, arXiv:1710.08828 (2017)
246. I.R. Sellers, A.O. Govorov, B.D. McCombe, J. Nanoelectron. Optoelectron. **6**, 4 (2011)

Chapter 2
Optical Berry Phase in Micro/Nano-rings

Libo Ma, Vladimir M. Fomin and Oliver G. Schmidt

Abstract Theoretical and experimental results are presented, which introduce topology into the field of optical and plasmonic resonances in ring resonators. Due to occurrence of the Berry phase in non-trivial evolution, plasmon/photon modes with non-integer numbers of wavelengths along the circumference are revealed in metallic/dielectric Möbius rings, which do not exist in conventional ring resonators. In cone-shaped anisotropic microtube resonators, the optical spin-orbit coupling is enabled for generation of the Berry phase acquired in a non-cyclic and non-Abelian evolution. These topology-induced effects imply promising applications related to manipulating photons in on-chip integrable quantum devices.

2.1 Introduction

The phase factor is a common quantity for all physical wave systems ranging from classical to quantum case. The conventionally known phase factor is dependent on the system energy and evolves over time. This kind of phase factor is called *dynamical phase*. Next to it, in topologically non-trivial systems another phase factor—*Berry phase* (also called *geometrical phase*) was discovered, which plays an important role in a startling variety of physical contexts such as in condensed matter, photonics, high-energy and space physics [1, 2]. The dynamical phase reflects the system's evolution in time and is universal, while the Berry phase keeps the "memory" of its evolution path in a parameter space and only occurs in non-trivial topological evolution. Berry phase was first discussed for cyclic evolution within adiabatic approximation and

L. Ma (✉) · V.M. Fomin · O.G. Schmidt
Institute for Integrative Nanosciences, IFW Dresden,
Helmholtzstr. 20, 01069 Dresden, Germany
e-mail: l.ma@ifw-dresden.de

V.M. Fomin
e-mail: v.fomin@ifw-dresden.de

O.G. Schmidt
e-mail: o.schmidt@ifw-dresden.de

V.M. Fomin (ed.), *Physics of Quantum Rings*, NanoScience and Technology,
https://doi.org/10.1007/978-3-319-95159-1_2

later was generalized to the notion of non-cyclic and non-Abelian evolution [3–9]. For the adiabatic transport of light in a cyclic evolution, the optical Berry phase can be quantified by the corresponding solid angle in the parameter space determined by either the wave vector on a momentum sphere, or the wave polarization state vector on a Poincaré sphere [4]. The acquired Berry phase is equal to the solid angle subtended by the trace of the wave vector at the origin of the momentum space, or a half of the solid angle subtended by the loop of the polarization vector at the origin of a Poincaré sphere.

The first experiment to verify the existence of the Berry phase was carried out by propagating light along a helically wound fiber and later on by the interferences in a nonplanar Mach-Zehnder interferometer [10–12]. A photon, as a typical boson, is a spinning particle with a polarization state comprised of right and left circular polarization states. These two circular basis components can acquire a Berry phase with opposite signs when the light undergoes a spin-orbit coupling. In the helical system, optical spin-orbit coupling was realized by a non-trivial evolution of the wave vector **k** occurring in an adiabatic process. The acquired Berry phase for each circular basis (right and left circular polarization components) of resonant light is directly related to the solid angle Ω subtended to a loop traced out by the wave vector **k** on a sphere in momentum space. As a result, the Berry phase of light depends only on topology of the evolution of a physical system in the parameter space, and thus it is independent of the device material and photon energy. While Berry phase of light has been revealed in open light paths, a closed planar light path, such as in whispering-gallery mode (WGM) cavities [13], is supposed to preclude the Berry phase because of the topologically trivial evolution of wave vector (see Fig. 2.1) [14]. In this context, the polarization state vector has to experience a topologically non-trivial evolution in order to enable the occurrence of the optical Berry phase in WGM micro-ring cavities. To address this issue, Möbius strip and cone-shaped microtube cavities are used to discuss the generation of Berry phase [14–16]. As shown in Fig. 2.1, unlike a conventional ring cavity, optical electric field gets twisted around when propagating in the Möbius strip and cone-shaped microtube cavities, which lead to the occurrence of the optical Berry phase. In this chapter, we show the occurrence of the Berry phase in both metallic Möbius nanorings and dielectric Möbius microrings. In metallic Möbius nanoring, the higher order plasmon modes possess a net dipole moment due to symmetry breaking. As a result, the higher-order plasmon modes turn into bright ones induced by Berry phase, which are supposed to be dark in conventional metallic nanorings. In dielectric Möbius microring cavities, non-integer mode number is formed due to the occurrence of the Berry phase, which breaks the paradigm of topologically trivial behavior that an integer mode number is required for constructive interference. In the end of the chapter, a non-cyclic Berry phase acquired in non-Abelian evolution is discussed in cone-shaped microtube ring cavities.

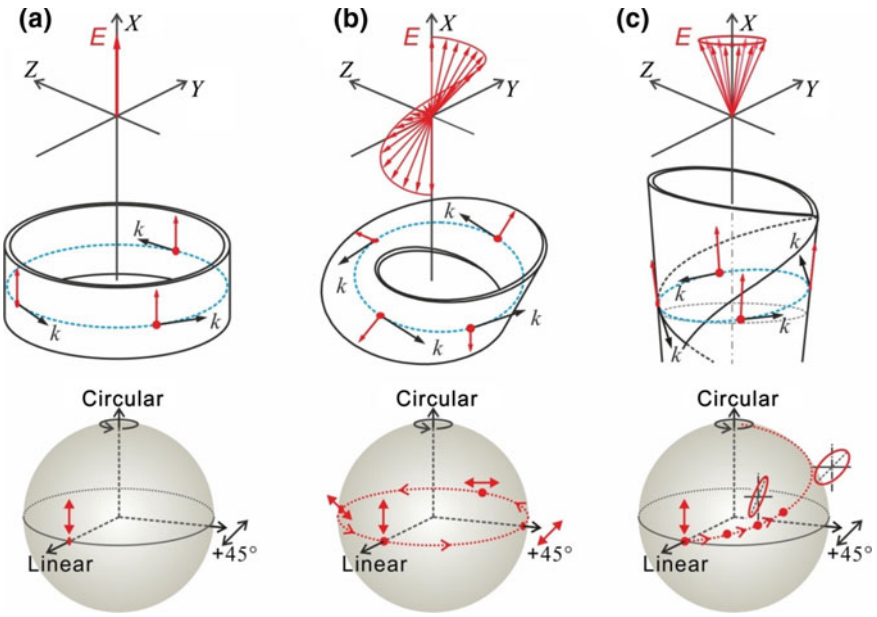

Fig. 2.1 **a** Trivial evolution of light in cylindrical ring microcavity, and non-trivial evolutions in **b** a Möbius ring and **c** cone-shaped microtube ring. The bottom panels show the corresponding polarization evolutions on the Poincaré sphere. The variations of the major polarization axis of the optical field ***E*** (red arrows) are shown with respect to the laboratory coordinate frame (XYZ). The blue dashed lines represent light trajectories, while the red dotted lines represent the polarization evolution trace on the Poincaré sphere. (After [14]. This work is licensed under a Creative Commons Attribution 4.0 International License, http://creativecommons.org/licenses/by/4.0/.)

2.2 Berry Phase in Möbius Rings

The Möbius strip is a well-known one-sided three-dimensional ring structure. While it has been investigated in other systems for years [17–20], it is of high interest to study the effect of Möbius topology on optical wave resonances. A Möbius ring is a WGM-type resonator, where a Berry phase accompanying adiabatic changes can be generated due to a parallel transport of the in-plane polarized optical waves along the twisted strip. The occurrence of the Berry phase leads to unusual optical interference and manifests itself in a non-integer number of optical modes. The Berry phase in Möbius-ring resonators is topologically robust against shape deformation of ring structure. These investigations introduce topology to the field of optical microcavities, and may lead to many promising applications in nanophotonics and quantum information technologies.

2.2.1 Plasmonic Möbius Nanorings

Plasmonic nanoring resonators are known to support surface plasmon resonant modes, which are expected to be essential elements of future subwavelength-scale photonic systems [21–23]. Surface plasmons, which originate from collective oscillations of electrons on metal surfaces, are able to couple with light, leading to the formation of surface plasmon polaritons (SPPs). The SPPs wave can propagate along the metal surface and form resonant modes in metallic nanostructures. In addition to a dipole-like mode, which exists in all metallic nanostructures, metallic nanoring resonators can support plasmonic WGM-like multiple modes, formed by self-interference of SPP waves along the ring-like structures. Owing to the constraint of resonance condition, only integer numbers of plasmon mode pairs (waveforms) exist in nanoring resonators [24]. In conventional metallic rings, the integer numbers of plasmon mode pairs show antisymmetric charge distributions, which do not provide any net dipole moment. Thus the WGM-like plasmon modes exhibit inhibited radiative losses (so-called dark plasmon modes) in conventional metallic nanoring resonators.

Traditionally, the plasmonic resonances in metallic nanostructures mainly concern the structure size, geometry and symmetry, where the topology has attracted less attention. In the following, we discuss the demonstration of topology induced anomalous plasmon modes in metallic Möbius nanorings [15]. Due to the occurrence of a Berry phase in the Möbius configuration, half-integer plasmon modes were observed, which cannot exist in conventional plasmonic rings. Owing to symmetry breaking, the higher-order plasmon modes turn into bright ones in the Möbius nanorings, which are supposed to be dark in conventional cylindrical rings. The feature of half-integer numbers of plasmon modes as well as the corresponding resonant frequencies is robust to the variation of the surface-charge distribution on the Möbius nanoring due to the non-trivial topology. Owing to the ultra-small mode volume, an extremely high sensitivity as well as a remarkable figure of merit was obtained in sensing performance. These works present a topological metallic nanostructure for the investigation of localized plasmon modes exhibiting unique phenomena in plasmonic applications such as enhanced light-matter interactions and plasmonic nanolasers.

As an example, here a silver Möbius nanoring is prepared by rolling up a half-twisted silver nanostrip, as schematically illustrated in Fig. 2.2. The dimension of the nanostrip is set as $w = 80$ nm in width, $t = 10$ nm in thickness, and $L = 300\pi$ nm in length. For comparison, a silver cylindrical ring is also constructed by rolling up the same nanostrip without twist. The Drude model is adopted to describe the dispersive permittivity of silver as $\varepsilon(\omega) = \varepsilon_\infty - \omega_p^2/(\omega^2 + i\omega\gamma)$. The high-frequency bulk permittivity is $\varepsilon_\infty = 6$, the plasma frequency is $\omega_p = 1.5 \times 10^{16}$ rad/s and the collision frequency is $\gamma = 7.73 \times 10^{13}$ rad/s [25]. The surrounding medium is air with a refractive index of $n = 1$. Linearly polarized light is employed to excite the plasmon modes in the nanoring structures. Finite-element method (FEM) is used to calculate the plasmonic modes using the commercial software COMSOL.

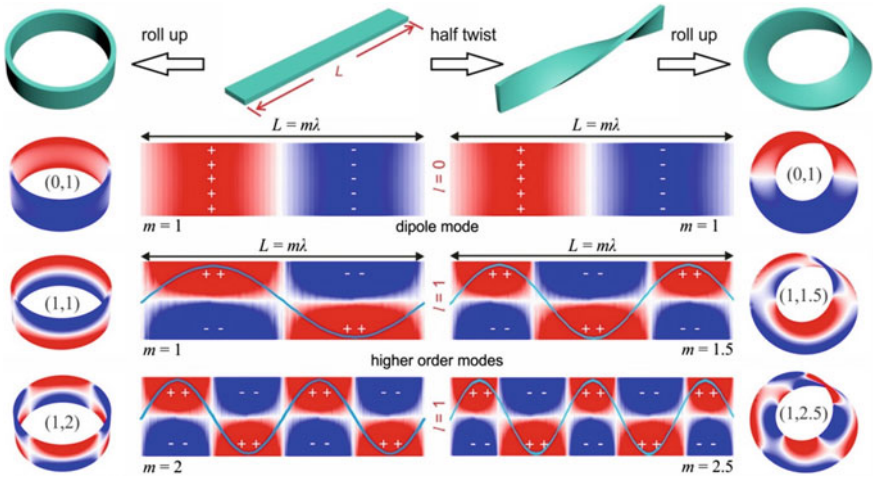

Fig. 2.2 Plasmon modes excited in a cylindrical nanoring (left panel), and a Möbius nanoring (right panel) both made of silver. Similar dipole-like plasmonic resonant modes (0, 1) are identified in both cylindrical and Möbius nanorings, in which the plasmon resonances ignore the ring structure. Distinct antisymmetric higher order plasmon modes are revealed in the cylindrical and Möbius ring, formed by interferences of integer [(1, 1) and (1, 2)] and half-integer number [(1, 1.5) and (1, 2.5)] of transverse-like waves, respectively, as indicated by the solid sinusoids. The charge distributions of the plasmon modes are represented by false color (red and blue represent positive and negative charges, respectively), shown in both the rings and the corresponding planar strip forms. (Reprinted from [15], Copyright Wiley-VCH Verlag GmbH & Co. KGaA. Reproduced with permission.)

Wave resonances can be formed when SPP waves propagate along the ring trajectory in the cylindrical and Möbius nanorings. These resonances are established when resonant waves satisfying the resonant condition, i.e. an integer number (m) of effective wavelength λ fits into the perimeter (L) of the trajectory. In contrast to dipole mode, for higher-order resonance SPPs can oscillate along the lateral direction of the strip with an integer number (l) of the plasmon mode. In this sense, each plasmon mode in the nanoring can be identified by a (l, m) index. As the basic plasmonic resonance, the dipole plasmon-mode (0, 1) has no lateral oscillation along the strip and can be found in both cylindrical and Möbius nanorings, as shown in Fig. 2.2. Similar to previous reports, the dipole plasmon-mode is formed by charge oscillations as a longitudinal wave in the metallic ring structure [24]. Such a charge oscillation can be formed in all metallic structures.

For the higher-order plasmon resonances, the SPPs wave would oscillate along the lateral direction of the nanostrip in addition to oscillating in the azimuthal plane of the ring cavities. The lateral oscillation can be viewed as a transverse-like wave with respect to the ring centerlines, where the waveforms are represented by the periodic oscillation of plasmon modes (see Fig. 2.2). For the formation of constructive interference, the resonant waves are required to be in-phase, or equivalently a phase difference of an integer number of 2π, after one-round trip along the center-

line trajectory to satisfy the resonant condition. In the cylindrical nanoring, integer numbers (e.g. $m = 1, 2$) of waves are present, and each waveform carries a phase change of 2π, satisfying the resonant condition. This phenomenon can also be found in optical WGM resonances in ring cavities [13, 16]. In contrast to the cylindrical nanorings, half-integer numbers (i.e. $m = 1.5, 2.5$) of resonant waves are supported in the metallic Möbius nanorings. The formation of half-integer waves, i.e. half-integer plasmon mode pairs, is induced by the occurrence of the Berry phase π in the Möbius nanoring, which has been reported in Möbius-ring resonators for both radio and visible frequency resonances [16, 18], as well as in the half-twisted band structure of topological insulators for spin transport [19].

The occurrence of Berry phase leads to anomalous surface charge distributions on the non-orientable surface of a metallic Möbius nanoring. The anomalous surface charge distribution breaks the symmetry that exists in conventional cylindrical rings, consequently providing a net dipole moment, which is active in far-field excitation and emission. Plasmon modes possessing a net dipole moment, such as the dipole-like plasmon modes, are referred to as "bright modes", which can be directly excited and readily characterized by far-field means. On the contrary, higher order plasmon modes without net dipole moment are called "dark modes", which cannot be excited nor detected in the far field due to efficient inhibition of radiative losses [26]. To investigate the far-field properties, transmission (T) and reflectance (R) spectra of a cylindrical ring and a Möbius ring are calculated, as shown in Fig. 2.3a, b, respectively. Only one resonant peak located at 1408 nm is recognized in the cylindrical ring, which is induced by the charge oscillation of the dipole mode (0, 1), as shown in the right inset of Fig. 2.3a. The charge distribution in the dipole mode possesses C_{1v} symmetry, manifesting a net dipole moment. In contrast, for the higher order plasmon modes the charge oscillations exhibit antisymmetric distributions of D_{1h} and D_{2h} symmetries for modes (1, 1) and (1, 2), respectively. Hence, these modes cannot be probed in either transmission or reflectance spectra due to the absence of net dipole moment. The near-field calculation results of (1, 1) and (1, 2) plasmon modes show that their optical resonant wavelengths are located at 565 and 539 nm, respectively, as indicated in Fig. 2.3a.

In the Möbius nanoring, the resonant peak of the dipole mode (0, 1) is located at 1416 nm, as shown in Fig. 2.3b. Although the length of the centerline in the Möbius ring is the same as that of the cylindrical ring, a slight mode shift of 8 nm is observed due to the difference of dipole moment formed in the cylindrical and Möbius nanoring. In contrast to the cylindrical nanoring where the higher order plasmon modes exhibit dark feature, efficient far-field transmission/scattering peaks are observed at 550 and 522 nm for (1, 1.5) and (1, 2.5) plasmon modes, respectively, as shown in Fig. 2.3b. The intrinsic resonances with half-integer mode numbers violate the resonant condition valid in conventional rings. However, they are supported by the Möbius ring due to the occurrence of Berry phase. The half-integer modes located at the non-orientable plane of the Möbius ring allow for the presence of net dipole moment and enable the feature of bright modes.

The quality (Q) factor of the dipole plasmon modes is relatively low owing to significant radiative losses [24]. However, the Q-factors of higher-order modes (1,

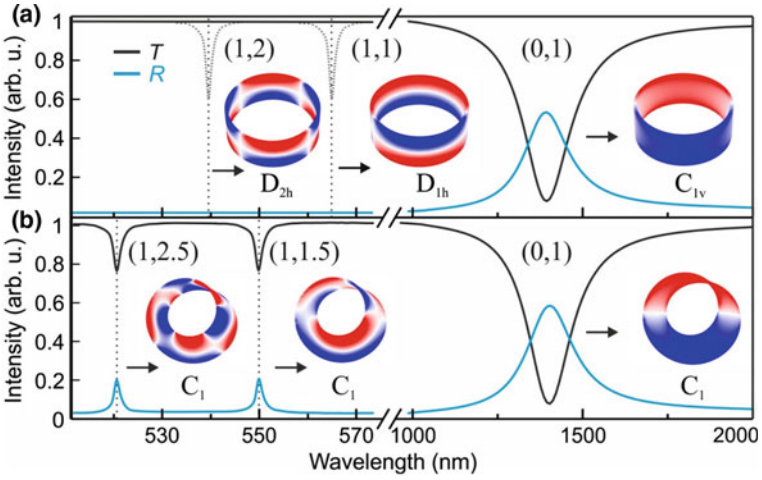

Fig. 2.3 Transmission (T) and reflectance (R) spectra of a cylindrical ring (**a**) and Möbius ring (**b**). Bright modes (0, 1) caused by dipole-like surface charge oscillation are revealed in both cylindrical and Möbius rings. The higher order plasmon modes exhibit dark feature in the cylindrical ring due to the antisymmetric surface charge distribution, while they turn to be bright in the Möbius ring due to the broken symmetry of charge distribution. The dark modes are indicated by dashed curves. The insets display the near-field charge distributions (red and blue colors indicate positive and negative charges, respectively) of the corresponding modes in the ring cavities. (Reprinted from [15], Copyright Wiley-VCH Verlag GmbH & Co. KGaA. Reproduced with permission.)

1.5) and (1, 2.5) are around six times higher than that of the dipole mode. The Q-factor enhancement indicates a smaller mode volume for the higher-order plasmon modes in the Möbius nanoring. In the Möbius nanoring, the mode volume is as small as $0.003\lambda_0^3$ calculated by the formula $V_{\text{eff}} = \int \varepsilon(r)E(r)^2 d^3r/(\varepsilon E_{\text{max}}^2)$, where λ_0 is the resonant wavelength, $\varepsilon(r)$ the permittivity and $E(r)$ is the electric field strength, ε is the permittivity at the E_{max} position. The small mode volume indicates a strongly localized electric field with an enhancement factor of $(E_{\text{max}}/E_0)^2 \approx 1000$ (E_{max} is the local field at the plasmon mode and E_0 is the electric field of the excitation wave), which is promising for the investigation of the light-matter interactions.

Cylindrical rings possess rotational symmetry with respect to the ring axis. Therefore, the resonant wavelength and surface charge distribution of both dipole and high order plasmon modes are constant with respect to the excitation-polarization orientation. As a result, the transmission peak of dipole modes is a constant resonant peak, when excited under different polarization angles with respect to the ring axis. On the contrary, the Möbius ring has no rotational symmetry C_1. Therefore, the surface-charge distribution (or net dipole moment) varies when the polarization orientation of the excitation light changes. As a consequence, the resonant peaks of the dipole mode vary when excited at different polarization orientations. Interestingly, for the topology induced half-integer modes such as (1, 1.5), the resonant wavelength is constant despite the changes of the charge distribution along the Möbius ring, as

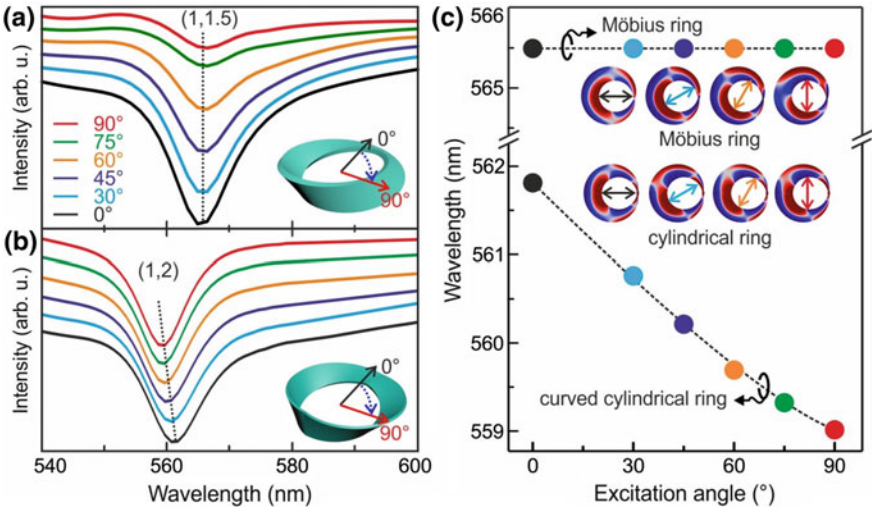

Fig. 2.4 Transmission spectra of the high order mode (1, 1.5) in the Möbius ring (**a**) and the mode (1, 2) in the curved cylindrical ring (**b**) excited with different polarization angles. **c** Upon varying the excitation polarization, the resonant wavelength is constant in Möbius nanoring due to the topological structure, while shifts significantly in curved cylindrical nanoring. The insets show the representative surface charge distributions in the two nanoring structures. (Reprinted from [15], Copyright Wiley-VCH Verlag GmbH & Co. KGaA. Reproduced with permission.)

shown in Fig. 2.4. Compared with the dipole mode, which occurs independently of topology, the half-integer mode is induced by the topology of the Möbius nanoring. The constancy of the resonant plasmon mode indicates that the net dipole moment in total is constant, no matter how the charge distribution of the half-integer plasmon mode changes on the Möbius ring. This topology origin can be further verified by a similar examination in a cylindrical-like nanoring made of a curved but not twisted nanostrip, i.e. having the same topology of the cylindrical ring. The higher order plasmon mode (1, 2) shows the integer number of waves, and the corresponding resonant wavelength varies when excited at different polarization orientations, as shown in Fig. 2.4b, c. This difference implies that the resonant peak constancy is induced by the topology of the Möbius ring, rather than the curvature of the nanostrip. Moreover, the mode intensity in the transmission spectrum varies when excited with different polarization orientations. This transmission variation is caused by the change of extinction cross section when exciting the Möbius ring with different polarization orientations.

As the higher order plasmon modes in the Möbius ring possess small mode volumes, a high sensitivity is expected due to the enhanced local field. Based on the analysis of the mode (1, 1.5), a sensitivity of 1000 nm per refractive index unit (RIU) is obtained, exhibiting an excellent bright-mode-based sensing performance. The figure of merit (FOM) is calculated to further demonstrate the sensing performance of the Möbius nanoring, where the FOM is defined as $FOM = S/w_{\lambda}$ (S is

the sensitivity and w_λ is the resonance line width). A FOM of 100 is calculated for the mode (1, 1.5), which is remarkable for a plasmonic resonator. In addition, the intrinsic absorption loss of metallic structures can be compensated by introducing active/optical gain media, which can efficiently improve the Q-factor of plasmonic nanosystems. Therefore, an even higher FOM can be expected, which is not only attractive for sensing applications, but also interesting for nonlinear optics, such as plasmonic nanolasers.

2.2.2 Dielectric Möbius Microrings

In this section we discuss the topological effects on constructive optical interference in a Möbius ring made of a twisted dielectric strip [16]. As a reference, a cylindrical ring structure was also considered in the calculations. For comparison, all the ring structures are formed from strips equal in size and with the same refractive index n. The strip thickness d is assumed smaller than the wavelength λ of the considered light, i.e. $d < \lambda/n$, so that the electric field is stringently confined within the strip during propagation. The strip width is taken larger than the wavelength, and the strip length is chosen to be in the micrometer range to support optical resonances in the visible spectral range.

Linearly polarized light is first considered for the discussion of WGM resonances in Möbius ring resonators. Calculations for a cylindrical ring cavity confirm the expected optical resonant modes with wavelength $\lambda = L/m$, where L is the optical length and m is an integer mode number. In contrast to this, optical resonant modes supported by a Möbius ring accommodate half-integer number of wavelengths interfering in the ring resonator, and which is correspondingly indexed by a *half-integer* mode number. Figure 2.5 shows examples of antinode patterns for optical resonances in a cylindrical ring and a Möbius ring with mode numbers $m = 8$ and 7.5, respectively. Although the length of the optical path in the cylindrical ring and the Möbius-ring is the same, the resonant wavelengths are different (see Fig. 2.5b). This unusual phenomenon is explained in the following by the presence of an optical Berry phase.

When a linearly polarized light is confined in the Möbius-ring structure, the optical electric field locally remains parallel to the plane of the Möbius strip, and consequently the polarization orientation is forced to continuously vary along the twisted strip during propagation in the Möbius-ring cavity (see Fig. 2.6a). This motion exhibits an adiabatic parallel transport of the linearly polarized light in the smoothly curved strip. In the adiabatic transport of a degenerate physical system, the Berry phase can be quantified by the corresponding solid angle in the parameter space determined by either the wave vector k, which forms a sphere in the momentum space, or the wave polarization, which forms a Poincaré sphere.

For the parallel transport of in-plane polarized light [described by $\boldsymbol{a} = \boldsymbol{a}_+ + \boldsymbol{a}_-$ where $\boldsymbol{a}_+$ and $\boldsymbol{a}_-$ are right and left circular basis components] in a Möbius ring, the continuous variation of the polarization orientation can be visualized by a closed loop along the equator of the Poincaré sphere (see Fig. 2.6b) [4]. One full round trip

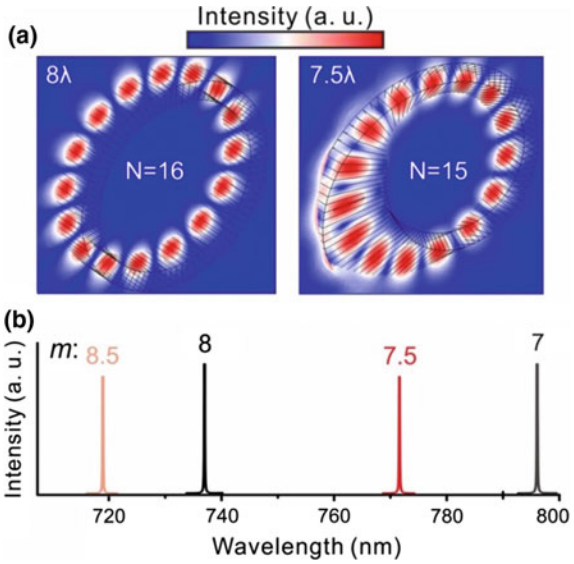

Fig. 2.5 Constructive self-interference of light with integer and non-integer number of wavelengths for a cylindrical ring and a Möbius ring (with air as surrounding medium). **a** Cross-sectional resonant antinode amplitude profiles calculated in cylindrical-ring (left) and Möbius-ring (right) resonators with numbers of antinodes N = 16 and N = 15, respectively. The odd numbers of antinodes are a result of constructive self-interference of light with a half-integer number of wavelengths. **b** Calculated resonant spectra including two resonant modes for the cylindrical ring and the Möbius ring. The modes labelled with half-integer azimuthal mode numbers correspond to the Möbius ring. Both ring structures are formed from strips of the same size (320 nm wide, 2510 nm long, 80 nm thick) with a refractive index n = 3.5. (Reprinted from [16])

generates a geometric phase equal to half of the solid angle $\Omega/2 = \pi$ for the right and left circular polarization basis components as $\boldsymbol{a}' = \frac{1}{\sqrt{2}}\left(e^{i\pi}\boldsymbol{a}_+ + e^{-i\pi}\boldsymbol{a}_-\right)$. Figure 2.6c shows the optical self-interference for half-integer mode numbers in a Möbius ring. Apparently, the dynamical phase, which changes by 2π for one wavelength, cannot accomplish constructive interference in the Möbius-ring because it is exactly off-phase in the case of half-integer numbers of wavelengths. However, the presence of the geometric phase π leads to an effective wave-flip, which precisely compensates for the unmatched dynamical phase. It is therefore the geometric phase π that allows for constructive interference in the Möbius ring with non-integer numbers of wavelengths. In this sense, the occurrence of the geometric phase changes the conventional requirement that a difference equal to an integer number of wavelengths is needed for constructive interference. Remarkably, the geometric phase is wavelength independent, since it is only related to the intrinsic topological property of the physical evolution. In the model shown in Fig. 2.6, a single light wave is assumed to be self-interfering after one round-trip. An alternative way to describe the resonances in a ring cavity considers two light waves starting from the same point and propagating in the opposite directions. In this model, the two beams meet after a half round-trip

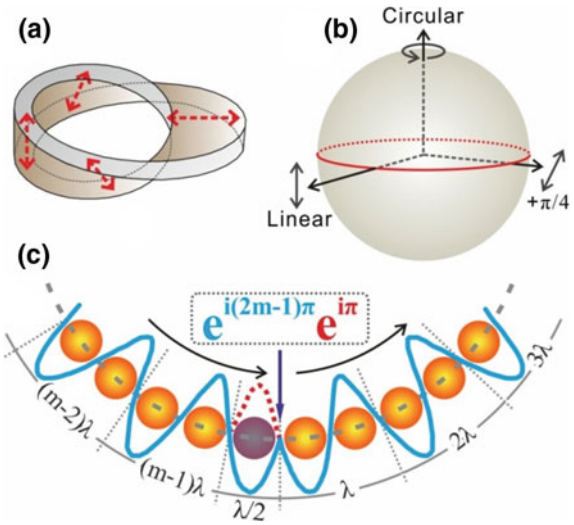

Fig. 2.6 Constructive interference of light with a half-integer number of wavelengths caused by the presence of a geometric phase π after parallel transport of polarization along a Möbius ring. **a** Sketch of parallel transport of a linear polarization along the Möbius ring in real space. **b** In polarization vector space, the linear polarization state evolves along the equator of a Poincaré sphere. **c** Generation of a twist-induced geometric phase of π in addition to the dynamical phase of (2m−1)π leads to constructive interference with a half-integer number of wavelengths. The solid circles represent optical resonant antinodes. Solid blue curve represents the light wave carrying the dynamical phase. Dashed red curve represents the effective wave-flip caused by the geometric phase. The green arrow points at the starting point, while the black arrows indicate the propagation direction in the Möbius ring. (Reprinted from [16])

and interfere with each other. Both considerations result in an equivalent loop on the Poincaré sphere, and therefore lead to the same result.

A geometric phase represents the global topological feature of a physical evolution, which is therefore invariant to local distortions. In particular, the geometric phase in a Möbius ring is topologically robust, since all topologically-equivalent paths will project to the same loop on the Poincaré sphere. These topologically-equivalent paths exist, for instance, when the Möbius ring is deformed by stretching and bending the ring structure, or produced from a strip with an odd number of half-twists. As shown in Fig. 2.7, in the case of the linearly polarized light, the geometric phase π is invariant in both cases and causes waves to interfere with a non-integer number of wavelengths.

The topological robustness of the geometric phase is a result of the gauge invariance in the adiabatic evolution [3]. The gauge invariance, in turn, indicates that the geometric phase is an important property of a physical system. A topologically-protected geometric phase implies an intrinsic fault-tolerance towards environmental perturbance, which is of profound importance for practical applications. In particular,

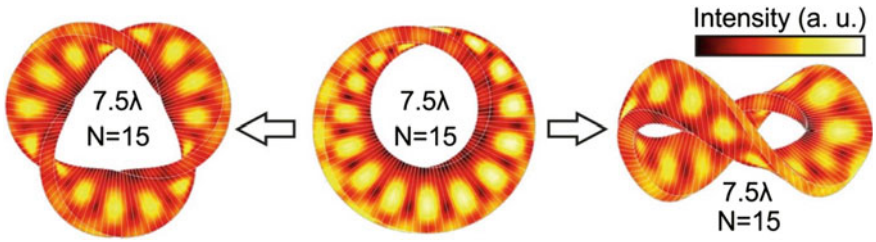

Fig. 2.7 Topological protection of the geometric phase in transformed Möbius-ring structures. From left to right: Optical resonant profiles in a three-half-twisted Möbius-ring, a Möbius-ring, a stretched and twisted Möbius-ring. The number of antinodes $N = 15$, which corresponds to 7.5λ over the centerline, is shown as an example. (Reprinted from [16])

it has been shown that geometric phases can act as quantum logic gates in quantum computation.

Following the analysis above, consider the introduction of light with different ellipticities e ($0 \leq e \leq 1$) propagating in the Möbius ring. In this case, the major axis orientation of the polarization ellipse is confined locally to stay in-plane in the twisted strip, performing a cyclic evolution. The propagation of differently polarized light rays in the Möbius ring projects a series of loops on a Poincaré sphere, varying from the equator (linear polarization, $e = 1$) to the two poles (circular polarization, $e = 0$), as shown in Fig. 2.8. The left (right) handed chirality is defined as that of the Möbius ring along the propagation direction, which is found the southern (northern) hemisphere of the Poincaré sphere. The solid angle (Ω) subtended by the corresponding loop varies from 0 to 2π (in the northern hemisphere) and $2–4\pi$ (in the southern hemisphere). Consequently, the Berry phase ($\varphi = \Omega/2$) varies from 0 to π and π to 2π, respectively. The optical mode number can be defined as $m = M_i - \varphi/2\pi$, where M_i is an integer number. By correlating the solid angle Ω, and therefore the geometric phase φ, with the polarization ellipticity e spread over the Poincaré sphere, the optical mode number behaves as shown in Fig. 2.8. When changing the ellipticity from linear ($e = 1$) to circular ($e = 0$), the optical mode symmetrically approaches the neighbouring integer numbers owing to the opposite light chirality. The mode number rapidly changes from a half integer towards a whole integer when e changes from 0.5 to 1. At $e = 0$, the right and left handed circular polarization states are degenerated at integer mode numbers due to the trivial topology. This trivial topological effect is due to the rotational symmetry of the circle depicted by the electric field vector in the circular polarization. In this way, the optical mode number is continuously tuned into an arbitrary fractional number other than only a half integer. Alternatively, an arbitrary fractional number can also be realized, for example, in a Möbius ring made of an anisotropic inhomogeneous medium, where the geometric phase might be no longer restricted to π due to a non-Abelian evolution. These findings introduce a non-trivial topology to the field of optical microcavities, and may lead to many promising applications in nanophotonics and quantum information technologies.

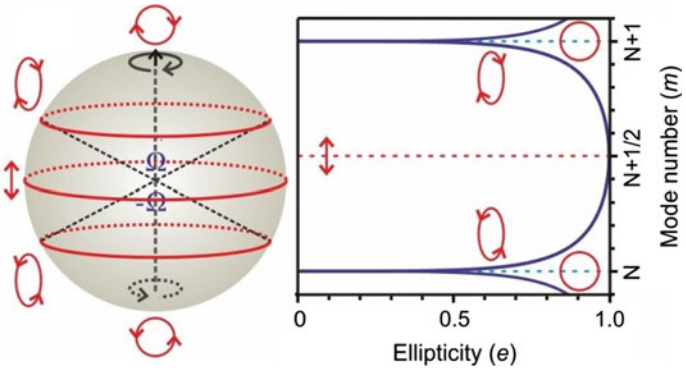

Fig. 2.8 L.h.s. panel: a schematic of the optical Berry phases depending on the light polarization state; r.h.s. panel: the resultant non-integer number modes as a function of the light polarization state

2.3 Berry Phase in Asymmetric Microtube Rings

2.3.1 Optical Spin-Orbit Coupling in Anisotropic Medium

When spinning particles, such as electrons and photons, undergo spin-orbit coupling, they can acquire a Berry phase in addition to the dynamical phase [1, 4, 9, 27–29]. The Berry phase was originally discussed for a cyclically evolving physical system with an Abelian evolution, and was later generalized to non-cyclic and non-Abelian cases, which are important fundamental subjects in this area and indicate promising applications in various fields [6, 7, 9, 30]. In the present section, we discuss the realization of the optical spin-orbit coupling in asymmetric microcavities and the experimental observation of a non-cyclic optical geometric phase acquired in a non-Abelian evolution [14]. This work is relevant to fundamental studies and implies promising applications by manipulating photons in on-chip quantum devices.

Microtube cavities are fabricated by releasing differentially strained SiO/SiO_2 bilayer nanomembranes (in circular pattern) which curl into microtube structures on a silicon substrate [31]. To support the optical spin-orbit coupling, cone-like asymmetric microtubes are prepared by releasing and rolling up tubes in an uneven fashion as discussed previously. The resonators are subsequently coated with a layer of HfO_2 by atomic layer deposition (ALD) to modify their effective refractive indices. As shown in Fig. 2.9, the tube has less than two windings in the end of the tube, where the measurements were performed. The layered thin tube wall (~100 nm) is examined using cross-sectional scanning electron microscopy (SEM). The white traces in outer sides of the tube wall correspond to the HfO_2 layer, while the middle dark layer corresponds to the SiO/SiO_2 nanomembrane. The refractive index of the tube wall is calculated by averaging the refractive indices of each layer in the tube

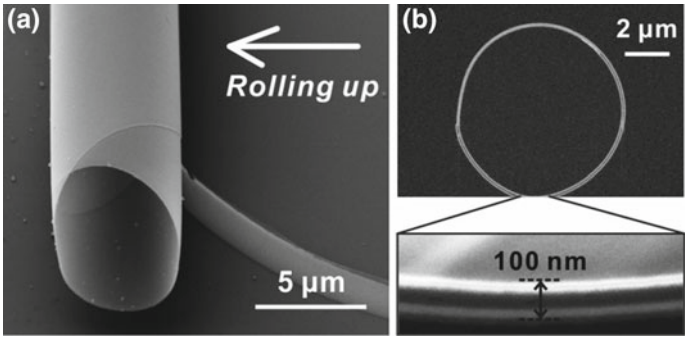

Fig. 2.9 **a** SEM image of a microtube prepared by rolling up a nanomembrane. **b** Cross-sectional SEM image of a rolled-up microtube revealing multi-layered thin-wall tube structure, where the HfO_2 layers appear bright and the middle SiO/SiO_2 nanomembrane appears dark

wall. Therefore, the averaged refractive index of the tube wall varies along the tube axis due to the variation of the number of windings.

Optical microcavities, which confine light to small volumes by a resonant circulation in a dielectric medium, play an indispensable role in both fundamental studies and a wide range of applications. In a general theory, describing the evolution of light in a dielectric medium, a quantum-mechanical diagonalization procedure is applied to Maxwell equations and Berry's phase theory [9], giving the effective Hamiltonian

$$\hat{h} = \frac{1}{2}\left[\mathbf{p}^2 - \varepsilon_0(\mathbf{r})\right]\hat{\mathrm{I}} - \frac{\lambda}{2\pi}\widehat{\mathrm{A}}\cdot\dot{\mathbf{p}} - \frac{1}{2}\widehat{\Delta}, \tag{2.1}$$

where $\mathbf{p}$ is a momentum operator, $\varepsilon_0(\mathbf{r})$ represents the scalar isotropic component of the medium, $\hat{\mathrm{I}}$ stands for a unit matrix, the matrix $\widehat{\Delta}$ denotes the anisotropic component of the dielectric permittivity, λ is the wavelength, $\widehat{\mathrm{A}}$ represents the gauge potential, and $\dot{\mathbf{p}}$ is the derivative of $\mathbf{p}$. The Hamiltonian can be divided into three parts $\hat{h} = \hat{h}_0 + \hat{h}_{SOI} + \hat{h}_A$. The first part $\hat{h}_0 = \frac{1}{2}\left[\mathbf{p}^2 - \varepsilon_0(\boldsymbol{r})\right]\hat{\mathrm{I}}$ characterizes the ordinary light propagation and the interference. The second part $\hat{h}_{SOI} = -\frac{\lambda}{2\pi}\widehat{\mathrm{A}}\cdot\dot{\mathbf{p}}$ denotes the spin-orbit coupling of photons, and the third part $\hat{h}_A = -\frac{1}{2}\widehat{\Delta}$ describes the medium anisotropy.

In the conventional optical WGM microcavities, such as a cylindrical ring resonator (see Fig. 2.1a), the electric field vector does not change with respect to the wave vector $\mathbf{k}$ in the process of the propagation. In addition, the resonant light propagates along a closed-loop trajectory, which is distinct from the open helical trajectories, which have been used to enable the optical spin-orbit interactions [4, 10, 28]. Unlike the propagation via helical trajectories, the wave vector $\mathbf{k}$ experiences a trivial evolution, when propagating along a closed loop. As such, the optical spin-orbit interaction is irrelevant, and the corresponding Hamiltonian contains only the $\hat{h}_0$ part, which results in ordinary discrete eigenmodes in the optical WGM resonators. Experimentally, the eigenmodes manifest themselves by discrete peaks in the reso-

nant spectra. Each peak in the resonant spectrum is formed by self-interference with an integer number of waves along the closed-loop trajectory. In these systems, the optical polarization states are conserved at each resonance.

However, the optical spin-orbit coupling can be induced in specially designed cavity structures. For example, one can introduce topology into a WGM cavity by employing a Möbius ring as an optical microring cavity. Although the wave vector **k** experiences a trivial evolution in this geometry, the transverse electric field twists around during the propagation along the centerline (see Fig. 2.1b). In this way, an effective orbital angular momentum (OAM), similar to that of an optical vortex or a transformed light beam, is generated for the spin-orbit coupling. Thus, the effective Hamiltonian takes the form $\hat{h} = \hat{h}_0 + \hat{h}_{SOI}$, where the spin-orbit coupling leads to the occurrence of a geometric phase. This extra phase leads to a non-integer number of waves for constructive interferences along a closed-loop trajectory, which has been discussed in previous sections. Similar to the previously reported helical waveguides, this behavior represents an Abelian evolution, where the polarization orientation varies, while the polarization eccentricity does not.

In the microtube cavity, optical WGM-type resonances are established via optical self-interference along a closed-loop trajectory guided by the cylindrical tube wall. To pump the resonances, a laser line (at 532 nm) is focused on the larger tube edge, where resonant modes of higher Q-factor exist. The laser excites luminescent defects in the amorphous silicon oxide microtube, which emit light in the visible spectral range at room temperature. Due to the subwavelength-thin tube wall, photons linearly polarized along the tube wall are allowed to circulate around a closed trajectory within the microtubes, which ensures that the initial state of the resonant light is linearly polarized with the polarization orientation parallel to the tube axis. Finally, the photons circulating along the closed trajectory escape from the microtube cavity and are then measured and analyzed by a laser confocal configuration.

When the light propagates in the thin-walled microtube, the electric field vector rotates around the tube axis being forced by the cone-shape of the microtube (see Fig. 2.10b). This rotation generates an effective OAM $\boldsymbol{L}$ along the tube axis. In the conventional WGM cylindrical cavities, the wave vector **k** [indicating the direction of the spin angular momentum (SAM)] of the resonant light is orthogonal to the tube axis; thus, there is no possibility to generate the spin-orbit interactions, even if there is an OAM along the axis. However, at the larger end part of a cone-shaped tube, the average refractive index varies along the tube axis owing to the variation in the number of windings. In this particular geometry, the resonant trajectory slightly tilts out of plane in order to reduce the optical path according to Fermat's principle. This tilt effect is illustrated in Fig. 2.10a, where the resonant trajectory has to tilt away to reach a minimum optical length in a cone-shaped microtube cavity. It is this tilted trajectory that causes the SAM to be not orthogonal to the OAM, which, in turn, enables the coupling between the spin and the orbital degree of freedom $\left(\hat{h}_{SOI}\right)$.

In addition, the resonant light experiences an anisotropic refractive index in the asymmetric tube when it propagates along a tilted trajectory, which contributes to the $\hat{h}_A$ term. To discuss this effect, the effective refractive index is calculated by

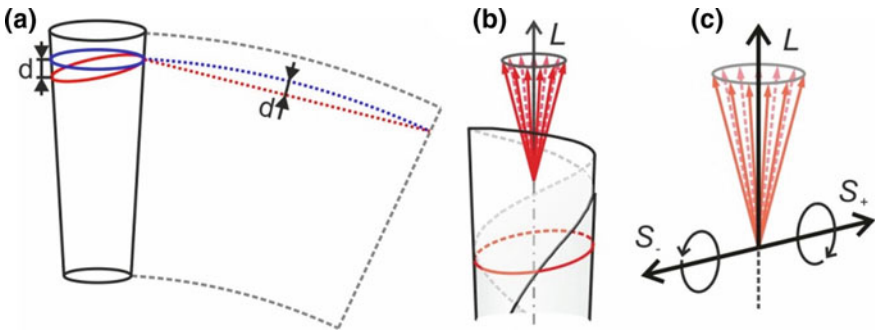

Fig. 2.10 **a** The resonant trajectory (red curve) has to tilt to provide a minimum optical length in a cone-shaped microtube cavity. **b** An effective orbital angular momentum L is generated by the rotation of the optical electric field around the tube axis. **c** Schematic shows the optical spin-orbit coupling enabled in a cone-shaped microtube cavity

solving the Maxwell's equations in the curved microtubular structure. In a planar slab waveguide, the first-order approximation is sufficient for the calculation of the effective refractive index. In the microtubular structure, the curvature plays a role for the effective refractive index and therefore the second-order correction needs to be considered [32].

For the case of light propagating paraxially, the effective refractive index n_{ax} is calculated from:

$$\left[\frac{\partial^2}{\partial\rho^2}+\frac{1}{\rho}\frac{\partial}{\partial\rho}-\frac{1}{\rho^2}+\varepsilon(\rho)\left(\frac{\omega}{c}\right)^2\right]F=\varepsilon_{\text{avg}}^{(x)}\left(\frac{\omega}{c}\right)^2F \tag{2.2}$$

For the case of light propagating in the azimuthal direction, the effective refractive index n_{az} is calculated from:

$$\left[\rho^2\frac{\partial^2}{\partial\rho^2}+\rho\frac{\partial}{\partial\rho}+\varepsilon(\rho)\left(\frac{\omega}{c}\right)^2\rho^2\right]F=R^2\varepsilon_{\text{avg}}^{(\theta)}\left(\frac{\omega}{c}\right)^2F, \tag{2.3}$$

where R is a squared average radius of the microtube. In Fig. 2.11, the effective refractive indices of n_{ax} and n_{az} are plotted as a function of the wavelength. It is shown the microtube cavity exhibits an anisotropic effective refractive index. In a tilted trajectory in the tubular cavity, the light travels in a weakly anisotropic inhomogeneous medium, which would lead to a non-Abelian evolution as theoretically predicted in [9].

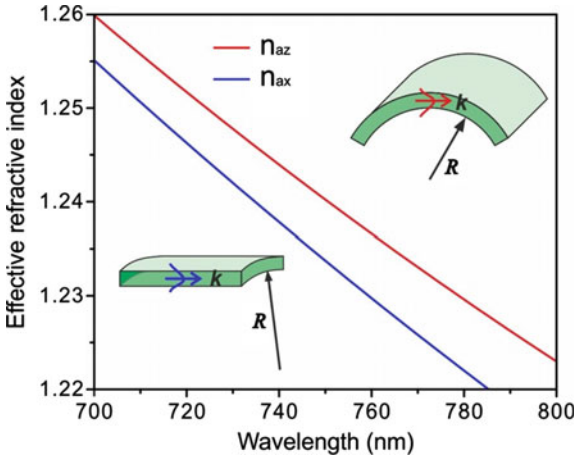

Fig. 2.11 Effective refractive indices of n_{ax} and n_{az} are plotted as a function of the wavelength, showing anisotropy of the microtubular structure

2.3.2 *Non-cyclic Berry Phase Acquired in Non-Abelian Evolution*

The terms $\hat{h}_{SOI}$ and $\hat{h}_A$ determine the polarization evolution of the optical wave. By expanding the two terms in (2.1) in the basis of Pauli matrices $\hat{\boldsymbol{\sigma}}$, the expression $-\left[\frac{\lambda}{2\pi}\widehat{\mathrm{A}}\cdot\dot{\mathbf{p}}-\frac{1}{2}\widehat{\Delta}\right]=\frac{\lambda}{2\pi}\boldsymbol{\alpha}\cdot\hat{\boldsymbol{\sigma}}$ exhibits a similar form to that of electrons under the interaction between the spin and orbital magnetic moments, where the vector $\boldsymbol{\alpha}$ plays the role of an "effective magnetic field" [9]. Based on the Schrödinger equation, the polarization evolution equation reads [9, 30]

$$\dot{\boldsymbol{a}}=i\left[\widehat{\mathrm{A}}\cdot\dot{\mathbf{p}}-\frac{\pi}{\lambda}\widehat{\Delta}\right]\boldsymbol{a}, \tag{2.4}$$

where the polarization state $\boldsymbol{a}=\begin{pmatrix}a_+\\a_-\end{pmatrix}$ is comprised of right $\boldsymbol{a}_+=\begin{pmatrix}a_+\\0\end{pmatrix}$ and left $\boldsymbol{a}_-=\begin{pmatrix}0\\a_-\end{pmatrix}$ components in the circular polarization basis. A well-known solution of (2.4) takes the form

$$\boldsymbol{a}=P\,exp\left[i\int_0^t\left(\mathbf{A}\cdot\dot{\mathbf{p}}\hat{\sigma}_3-\frac{\pi}{\lambda}\hat{\sigma}_1\right)d\tau\right]\boldsymbol{a}(0), \tag{2.5}$$

where P represents the path-ordering operator, and $\boldsymbol{a}(0)=\frac{1}{\sqrt{2}}\begin{pmatrix}1\\1\end{pmatrix}$ is the linear polarization state parallel to the tube axis, which is supposed to be the initial state. The first term in the integral accounts for the Berry phase

$$\varphi_{SOI} = \int_0^t \mathbf{A} \cdot \dot{\mathbf{p}} \hat{\sigma}_3 d\tau. \tag{2.6}$$

The second term in the integral in (2.5) results in a factor C_A that originates from the anisotropy of the system. C_A enables the interplay between the two polarization states that gives rise to the mutual conversion of the right and left circular polarization components $\boldsymbol{a}_+$ and $\boldsymbol{a}_-$. One should note that the tensor $\widehat{\Delta} = \hat{\sigma}_1$ is non-diagonal due to the anisotropy of the medium. In the present system the Berry phase is non-cyclic; in general it takes the form [7]

$$\varphi_{SOI} = arg\boldsymbol{a}(0)|\boldsymbol{a} + i \int_0^t d\tau \dot{\mathbf{p}} \cdot \boldsymbol{a}(\mathbf{p}(\tau))|\nabla_\mathbf{p}|\boldsymbol{a}(\mathbf{p}(\tau)), \tag{2.7}$$

where $\boldsymbol{a}$ is the final state on an open path in the parameter space. Unlike for the cyclic case, a non-cyclic geometric phase usually cannot easily be derived from (2.7), and practical measurements could be more complicated [33, 34]. A different convenient strategy is elaborated to measure this noncyclic geometric phase [14].

Starting from (2.5), one can present the polarization evolution in terms of the Jones vector

$$\boldsymbol{a} = \begin{pmatrix} a_+ \\ a_- \end{pmatrix} = \exp\begin{pmatrix} -i\varphi & iC_A \\ iC_A & i\varphi \end{pmatrix} \frac{1}{\sqrt{2}} \begin{pmatrix} 1 \\ 1 \end{pmatrix} = \frac{1}{\sqrt{2}} \begin{pmatrix} \cos\sqrt{\varphi^2 + C_A^2} + i(\varphi - C_A) \frac{\sin\sqrt{\varphi^2+C_A^2}}{\sqrt{\varphi^2+C_A^2}} \\ \cos\sqrt{\varphi^2 + C_A^2} + i(\varphi + C_A) \frac{\sin\sqrt{\varphi^2+C_A^2}}{\sqrt{\varphi^2+C_A^2}} \end{pmatrix}. \tag{2.8}$$

The $\mp i\varphi$ terms denote the geometric phase acquired for each circular basis state. $|a_+|^2$ and $|a_-|^2$ represent the redistributed circular components after the mode conversion, where

$$|a_+|^2 = \frac{1}{2}\left(1 - 2\varphi C_A \frac{\sin^2\sqrt{\varphi^2 + C_A^2}}{\varphi^2 + C_A^2}\right); \quad |a_-|^2 = \frac{1}{2}\left(1 + 2\varphi C_A \frac{\sin^2\sqrt{\varphi^2 + C_A^2}}{\varphi^2 + C_A^2}\right). \tag{2.9}$$

It is the non-diagonal element iC_A in the matrix in (2.8) that leads to the coupling and, consequently, to a mutual conversion between the two circular polarization components $\boldsymbol{a}_+$ and $\boldsymbol{a}_-$.

For optical characterizations, a 50× objective lens was used to focus the excitation laser beam on the tube wall, while the emitted photons were collected by the same objective and sent to the spectrometer. The polarization states of the resonant light were examined by a fixed polarizer in front of the detector of the spectrometer and a rotatable λ/2 plate. By rotating the λ/2 plate, the polarization orientation of the measured light can be rotated step-by-step and subsequently filtered by the polarizer

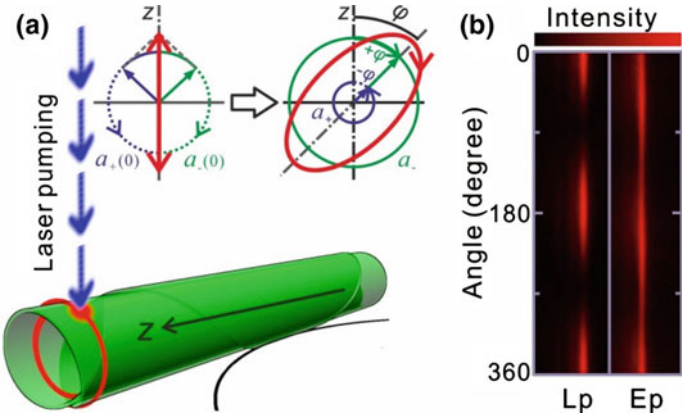

Fig. 2.12 **a** In a rolled-up asymmetric microtube being pumped by a laser beam (532 nm), the linearly polarized light evolves into elliptically polarized one with the major axis tilted out of (with an angle φ) the tube axis. **b** Resonant mode intensity maps of a linear polarization (Lp) state measured from a symmetric tube without a spin-orbit interaction and an elliptical polarization (Ep) state measured in the presence of the spin-orbit coupling of light in an asymmetric tube. (After [14]. This work is licensed under a Creative Commons Attribution 4.0 International License, http://creativecommons.org/licenses/by/4.0/.)

and recorded by the detector. In this way, both the polarization orientation (with respect to the tube axis) and the polarization eccentricity can be resolved.

It is well known that the resonant light in WGM microcavities is either transverse magnetic (TM) or transverse electric (TE) linearly polarized. For symmetric microtubes, the measured optical electric field is linearly polarized and oriented parallelly to the tube axis for the TM modes. However, in cone-shaped microtube cavities the resonant light is no longer linearly polarized. Figure 2.12b shows the intensity maps for the linearly (Lp) and elliptically polarized (Ep) modes as a function of the orientation angle (0°–360°), which are measured from a symmetric and an asymmetric tube, respectively. In the intensity map measured from the symmetric tube, the polarization state is clearly shown to be linearly polarized along the tube axis. In the asymmetric tube case, the varying but unbroken polarization trace is characteristic of elliptical polarization. Moreover, the major axis of the ellipse (or, in other words, the polarization orientation) is found to tilt away from the tube axis. These unusual phenomena go beyond the conventional knowledge of optical WGM resonances in microcavities and can be attributed to the occurrence of a geometric phase in a non-Abelian evolution of light [14].

As mentioned above, the initial state of the resonant light in the microtube cavity is linearly polarized. A linear polarization state is comprised of the in-phase components of the right and left circular polarization components as $\boldsymbol{a}(0) = \boldsymbol{a}_+(0) + \boldsymbol{a}_-(0)$, with the same probability amplitude $\left(|a_+(0)|^2 = |a_-(0)|^2 = 1/2\right)$, as schematically shown in Fig. 2.12a. Due to the spin-orbit coupling, the right and left circular components acquire a geometric phase with opposite signs: $\boldsymbol{a} = \boldsymbol{a}_+ e^{-i\varphi} + \boldsymbol{a}_- e^{i\varphi}$, where

φ is a geometric phase, $|a_+|^2$ and $|a_-|^2$ are redistributed vector amplitudes for each component due to the mode conversion, as described in (2.9). As shown in Fig. 2.12a, the conversion of amplitudes between the two circular components leads to a change from a linear to an elliptical polarization, while the geometric phase causes the orientation of the major axis of the polarization to tilt by an angle (equal to φ) with respect to the initial orientation. Since the outgoing state differs from the incoming one as stated above, the evolution generates a non-cyclic geometric phase. Here we show that the non-cyclic geometric phase can be readily measured by simply recording the tilt angle of the light polarization ellipse. The change of the circular basis states is evidence for the lack of independent modes, which is a consequence of the intricate non-Abelian evolution as described above. Since the photons are guided in the tube wall and their polarization states vary smoothly, the evolution can be described as an adiabatic process [4, 28].

The resonant light experiences the spin-orbit coupling in an anisotropic medium, when resonating in an asymmetric microtube cavity, hence the polarization state (described by the eccentricity and the tilt angle) continuously changes during the resonances, as schematically shown in Fig. 2.13a. However, the polarization state can only be measured when the light escapes from the microtube cavity, at which point the final state of the evolution has been reached. In order to depict the evolution trace, a series of final polarization states were measured from different asymmetric tubes, in which the resonant light experiences different extents of the polarization evolution. Figure 2.13b shows these series of polarization states plotted on a Poincaré sphere. In our measurements, tilt angles (the Berry phases) up to ~44.5° and an eccentricity of 0.7 is recorded. It is found that a larger eccentricity is accompanied by a larger tilt angle (φ) due to their co-evolution in (2.5). This kind of the evolution trace can be well reproduced by (2.8), indicating a good agreement between the theoretical model and measurements. In addition, we have performed polarization measurements for different mode frequencies in the same tube cavity and found that the tilt angle as well as the eccentricity is independent of the wavelength. This is a clear evidence that the effect is of purely geometric, rather than dynamical origin.

In contrast to previous reports on optical spin-orbit coupling, where the right- and left-handed circular polarization basis states are often spatially separated [28, 35], here we do not observe such a spatial separation of the spin components, but rather an amplitude conversion between basis vectors during the evolution, as discussed above. This process is systematically shown in Fig. 2.14 by comparing the variation of the squared moduli of the coefficients $|a_+|^2$ and $|a_-|^2$ accompanied by the tilt angle φ. In the measured elliptical polarization curves, the maximum intensity represents the sum of the two moduli squared $|a_+|^2 + |a_-|^2$, while the minimum represents the difference $|a_+|^2 - |a_-|^2$. Based on the measured results, the respective squared amplitudes for the right $|a_+|^2$ and left $|a_-|^2$ circular components are extracted. The two squared vector amplitudes vary in an opposite way and therefore result in the vector splitting of the spinning photons in a Hilbert space. The evolution traces of the two vector amplitudes agree well with the theoretical model of (2.9), as shown in Fig. 2.14.

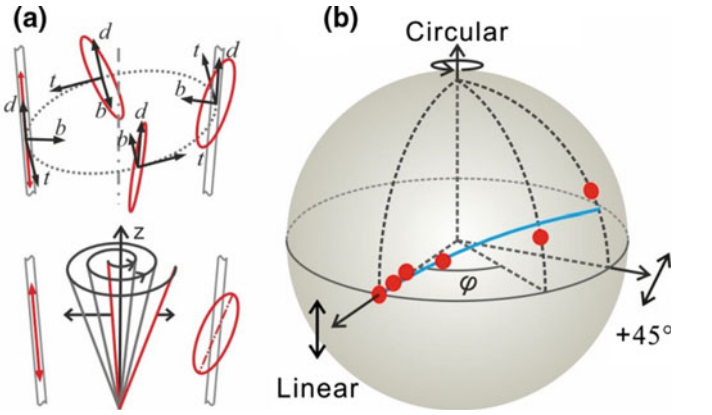

Fig. 2.13 **a** The polarization state of light circulating in an asymmetric tube changes from linear to elliptical one, which is recorded by defining a wave-accompanying coordinate frame (bottom panel). In this process, the major axis of the evolving polarization states ascribes a spiral around the tube axis, which is shown with respect to the laboratory coordinate frame (top panel). **b** A series of polarization states (red dots) measured after different extents of evolutions in different asymmetric tubes are plotted on a Poincaré sphere. The blue line plotted according to (2.9) traces the non-cyclic evolution from the linear to elliptical polarization states. (After [14]. This work is licensed under a Creative Commons Attribution 4.0 International License, http://creativecommons.org/licenses/by/4.0/.)

Light propagating around a dielectric microsphere cavity has been used to mimic the effect of gravitational lensing. Furthermore, the analogy between a static gravitational field and an anisotropic medium has been utilized to realize a Spin-Hall effect triggered by a gravitational field. In this sense, our asymmetric microtube cavity could provide an effective analogue for the laboratory study of the light evolution in a gravitational field. Moreover, in WGM microcavities light is confined in a small volume. This avoids a large space required in the previously reported open light-path systems, and is therefore attractive for integrating photonic applications on a chip. This finding may motivate the search for many novel applications, such as those for on-chip quantum information technologies, or exploiting interactions of light with chiral molecules.

The cone-like asymmetric optical microcavities establish an ideal platform to realize the spin-orbit coupling for the examination of non-trivial topological effects in the context of a non-Abelian evolution. The non-cyclic geometric phase and the mode conversion for degenerate photon systems can be readily demonstrated in a compact optical microtube cavity. The geometric phase can be directly measured by simply monitoring the polarization tilt angles, while the eccentricities indicate the mode conversion between the right and left circular basis components. This issue, which is interesting from both fundamental and experimental points of view, implies promising applications related to manipulating photons in on-chip integrable quantum devices.

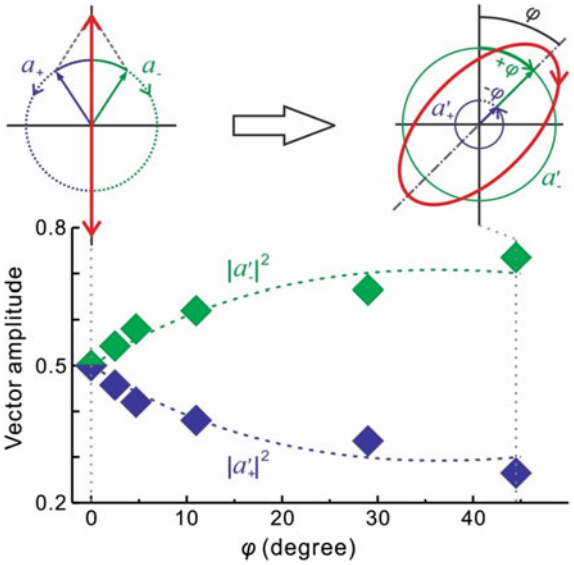

Fig. 2.14 Measured vector amplitudes of the right ($\boldsymbol{a}_+$) and left ($\boldsymbol{a}_-$) components with the concurrent geometric phase φ. The evolution traces agree well with the theoretical model in (2.9) (dashed curves). Top panel shows (l.h.s.) a linear polarization comprised of in-phase rotating right and left circular polarization components, and (r.h.s.) geometric phase $+\varphi$ (shown with the bold green arc) acquired for $\boldsymbol{a}_-$ and $-\varphi$ (shown with the dotted blue arc) acquired for $\boldsymbol{a}_-$. (After [14]. This work is licensed under a Creative Commons Attribution 4.0 International License, http://creativecommons.org/licenses/by/4.0/.)

References

1. M.V. Berry, Proc. R. Soc. Lond. Ser. A **392**, 45 (1984)
2. A. Shapere, F. Wilczek, (eds.) *Geometric Phase in Physics*, Advanced Series in Mathematical Physics: Volume 5 (World Scientific, Singapore, 1989)
3. Y. Aharonov, J. Anandan, Phys. Rev. Lett. **58**, 1593 (1987)
4. M.V. Berry, Nature **326**, 277 (1987)
5. Y.-S. Wu, H.-Z. Li, Phys. Rev. B **38**, 11907 (1988)
6. J. Zak, Europhys. Lett. **9**, 615 (1989)
7. G. Garcia de Polavieja, Phys. Rev. Lett. **81**, 1 (1998)
8. S. Filipp, Y. Hasegawa, R. Loidl, H. Rauch, Phys. Rev. A **72**, 021602 (2005)
9. K.Y. Bliokh, D.Y. Frolov, Y.A. Kravtsov, Phys. Rev. A **75**, 053821 (2007)
10. R.Y. Chiao, Y.-S. Wu, Phys. Rev. Lett. **57**, 933 (1986)
11. A. Tomita, R.Y. Chiao, Phys. Rev. Lett. **57**, 937 (1986)
12. R.Y. Chiao, A. Antaramian, K.M. Ganga, H. Jiao, S.R. Wilkinson, H. Nathel, Phys. Rev. Lett. **60**, 1214 (1988)
13. K.J. Vahala, Nature **424**, 839 (2003)
14. L.B. Ma, S.L. Li, V.M. Fomin, M. Hentschel, J.B. Gotte, Y. Yin, M.R. Jorgensen, O.G. Schmidt, Nat. Commun. **7** (2016)
15. Y. Yin, S. Li, V. Engemaier, E.S.G. Naz, S. Giudicatti, L. Ma, O. G. Schmidt, Laser Photonics Rev. **11**, https://doi.org/10.1002/lpor.201600219 (2017)

16. S.L. Li, L.B. Ma, V.M. Fomin, S. Böttner, M. Jorgensen, O.G. Schmidt, arXiv:1311.7158 (2013)
17. V.M. Fomin, S. Kiravittaya, O.G. Schmidt, Phys. Rev. B **86**, 195421 (2012)
18. D.J. Ballon, H.U. Voss, Phys. Rev. Lett. **101**, 247701 (2008)
19. H.C. Manoharan, Nat. Nanotechnol. **5**, 477 (2010)
20. S.O. Demokritov, A.A. Serga, V.E. Demidov, B. Hillebrands, M.P. Kostylev, B.A. Kalinikos, Nature **426**, 159 (2003)
21. E.M. Larsson, J. Alegret, M. Käll, D.S. Sutherland, Nano Lett. **7**, 1256 (2007)
22. A.W. Clark, J.M. Cooper, Small **7**, 119 (2011)
23. C.-Y. Tsai, J.-W. Lin, C.-Y. Wu, P.-T. Lin, T.-W. Lu, P.-T. Lee, Nano Lett. **12**, 1648 (2012)
24. J. Aizpurua, P. Hanarp, D.S. Sutherland, M. Käll, G.W. Bryant, F.J. García de Abajo, Phys. Rev. Lett. **90**, 057401 (2003)
25. Y. Liu, T. Zentgraf, G. Bartal, X. Zhang, Nano Lett. **10**, 1991 (2010)
26. V. Giannini, G. Vecchi, J. Gómez, Rivas. Phys. Rev. Lett. **105**, 266801 (2010)
27. K.Y. Bliokh, V.D. Freilikher, Phys. Rev. B **72**, 035108 (2005)
28. K.Y. Bliokh, A. Niv, V. Kleiner, E. Hasman, Nat. Photon. **2**, 748 (2008)
29. K.Y. Bliokh, F.J. Rodriguez-Fortuno, F. Nori, A.V. Zayats, Nat. Photon. **9**, 796 (2015)
30. F. Wilczek, A. Zee, Phys. Rev. Lett. **52**, 2111 (1984)
31. V.A. Bolaños Quiñones, L. Ma, S. Li, M. Jorgensen, S. Kiravittaya, O.G. Schmidt, Opt. Lett. **37**, 4284 (2012)
32. P. Yeh, *Optical Waves in Layered Media*, Wiley Series in Pure & Applied Optics, vol. 61 (Wiley, New York, 1988)
33. E. Sjöqvist, A.K. Pati, A. Ekert, J.S. Anandan, M. Ericsson, D.K.L. Oi, V. Vedral, Phys. Rev. Lett. **85**, 2845 (2000)
34. H. Weinfurter, G. Badurek, Phys. Rev. Lett. **64**, 1318 (1990)
35. O. Hosten, P. Kwiat, Science **319**, 787 (2008)

Chapter 3
From Dot to Ring: Tunable Exciton Topology in Type-II InAs/GaAsSb Quantum Dots

José M. Llorens, Vivaldo Lopes-Oliveira, Victor López-Richard, José M. Ulloa and Benito Alén

Abstract We present an experimental and theoretical study about the carrier confinement geometry and topology in InAs/GaAsSb quantum dots. The investigated sample consists of a field-effect device embedding a single layer of dot-in-a-well InAs/GaAsSb nanostructures. These nanostructures exhibit large electron-hole dipole moments and radiative lifetimes under externally applied electric fields. Both phenomena are related to the type-II band alignment existing between the two materials which, in principle, could also result in a change of the hole orbital confinement topology from simply to doubly connected. The latter aspect will be confirmed by ensemble magnetophotoluminescence experiments at 4.2 K. The oscillations observed in the photoluminescence intensity and degree of circular polarization will be described by an axially symmetric $\mathbf{k} \cdot \mathbf{p}$ model combining vertical electric and magnetic fields. Due to the large spin-orbit coupling of III-Sb nanostructures, the modulation of the orbital confinement geometry and topology reported here shall open a venue to control the spin dynamics by external voltages. This exciting idea will be theoretically discussed through band-effective models including spin-orbit coupling and anisotropic confinement effects.

J.M. Llorens · B. Alén (✉)
IMN, Instituto de Micro y Nanotecnología (CNM, CSIC),
Isaac Newton 8, 28760 Madrid, Tres Cantos, Spain
e-mail: benito.alen@csic.es

J.M. Llorens
e-mail: jose.llorens@csic.es

V. Lopes-Oliveira · V. López-Richard
Departamento de Física, Universidad Federal de São Carlos,
Rodovía Washington Luis, s/n., São Paulo, Brazil
e-mail: lopes@df.ufscar.br

V. López-Richard
e-mail: vlopez@df.ufscar.br

J.M. Ulloa
Institute for Systems based on Optoelectronics and Microtechnology (ISOM),
Universidad Politécnica de Madrid, Ciudad Universitaria s/n, 28040 Madrid, Spain
e-mail: jmulloa@isom.upm.es

V.M. Fomin (ed.), *Physics of Quantum Rings*, NanoScience and Technology,
https://doi.org/10.1007/978-3-319-95159-1_3

3.1 Introduction

InAs and AlSb form together with GaSb the so-called "6.1 Ångstrom" family. With a very similar lattice constant, these semiconductor compounds can be stacked and/or alloyed to fabricate unstrained heterostructures whose fundamental band-gap cover a spectral (energy) range from 12.4 μm (0.1 eV) for InAsSb to 0.77 μm (1.615 eV) for AlSb: the largest energy span of all III-V lattice-matched families. They also have, together with InSb, the largest electron mobilities, the highest electronic g-factors and the biggest spin-orbit coupling of all III-V semiconductors. All these characteristics are of fundamental character and give antimony-based semiconductors major potential for the future of electronics, optoelectronics, and quantum information technologies.

Quantum information technologies rely on our ability to manipulate the quantum properties of matter. With III-V quantum semiconductors, the state of the art is currently defined by experiments done using InGaAs QDs in a GaAs matrix. To name a few examples, bright single-photon sources have been developed using QDs either stand alone or embedded in optical resonators like microcavities and micropillars [1–3]. By increasing the Q-factor of the optical resonator, the rate of emission of single photons can be increased by several orders until the strong coupling regime between light and matter is eventually reached. Such entanglement between carrier spins and photons is necessary to create essential quantum information technologies like quantum memories and repeaters. Quantum dots are also at the heart of quantum light emitting diodes [4–7]. Direct electrical operation is one of the advantages of solid-state technologies over single atom or crystal defect approaches. These integrated sources have been used in a proof-of-principle demonstration for quantum key distribution, [8] but have yet to make commercial impact.

Experimental demonstrations of quantum technologies using Sb-containing nanostructures are significantly less mature. Optical isolation of individual nanostructures has been demonstrated a few times revealing nanostructures with sharp excitonic emission [9–11]. III-Sb nanostructures grown on GaAs emit in the telecoms band and could provide quantum light sources for 1310 and 1550 nm wavelengths [12–14]. GaSb/GaAs and InAs/GaAsSb quantum dots and rings grown on GaAs are especially appealing for quantum memories and gates since they can confine single hole spins more efficiently than InGaAs/GaAs QDs [15–20]. The dephasing rate of the hole spin due to hyperfine coupling with the nuclei is orders of magnitude smaller than for electrons. In addition, the large g-factor and spin-orbit coupling of III-Sb might boost the manipulation of the hole spin state in quantum information processing operations [21].

An emergent application of III-Sb nanostructures for quantum information science and technology relies in the realization of topological insulators and Majorana fermions with these materials [22]. The high-mobility, strong spin-orbit coupling and small fundamental energy gap are among the most wanted material characteristics to build topologically protected quantum states in highly correlated electron systems. These quantum states form the spanning basis of topological quantum bits,

which thanks to their non-local character (spatially delocalized) become largely protected from the environment and are thus highly coherent. These systems however are meant for electrical readout of their quantum states and do not interact with visible and infrared light as required for quantum communication technologies.

Such requirements might be fulfilled instead by other III-Sb quantum nanostructures with type-II confinement, including InAs/GaAsSb quantum dots, where voltage tuneable geometry and topology could open new paths for single spin manipulation as discussed below.

The chapter is organized as follows: Sect. 3.2 describes the growth process, device layout and experimental techniques. It also summarizes the structural and morphological parameters that define the InAs/GaAsSb quantum dots studied here. Their response to an externally applied vertical electric field is investigated in Sect. 3.3. Large electron-hole dipole moments (vertical and lateral) and radiative lifetimes are found and a theory is presented which suggests a hole orbital confinement topology changing from simply to doubly connected as a function of the electric field. This latter possibility is throughly discussed in Sect. 3.4 where experiments and theories combining external electric and magnetic fields are explained in the framework of the Aharonov-Bohm effect. Finally, the voltage modulation of the exciton g-factor found in our system is analyzed through effective models including spin-orbit coupling and anisotropic confinement effects in Sect. 3.5.

3.2 Samples and Experiments

To study voltage tunable effects on type-II InAs/GaAsSb nanostructures, a p-i-n diode structure was grown by molecular beam epitaxy (MBE) on an n-type GaAs (001) substrate. InAs QDs were grown by depositing 2.7 monolayers (ML) of InAs at 450 °C and 0.04 ML/s. After 20 s of growth interruption, the QD layer was capped with a 6 nm thick GaAsSb layer grown at 470 °C and was subsequently covered with intrinsic GaAs grown at 580 °C. The nominal Sb content was 28% and the intrinsic region of the p-i-n diode spans 400 nm embedding the QDs and GaAsSb in its centre as shown in Fig. 3.1a.

We have proven in the past that a rapid thermal annealing treatment (RTA) is beneficial for these nanostructures, not only blueshifting their fundamental energy and narrowing and boosting their emission as shown in Fig. 3.1b, but also maintaining the type-II band alignment [23]. The same RTA treatment was applied in this case. Regarding the QD structural properties, transmission electron microscopy reveals that the QDs become flatter (more quantum disk-like) after annealing. The average QD height is reduced by 1 nm (from 3.5 to 2.5 nm) while the QD height distribution becomes narrower (the standard deviation decreases from 0.57 to 0.39 nm).The base diameter increases by 6 nm (from 16 to 22 nm) and the thickness of the capping layer decreases ∼1 nm, from 6.5 to 5.5 nm. Regarding the Sb content actually incorporated in the capping layer, far from the QDs we find that x_{Sb} remains uniform and equal to 20 ± 1% (slightly lower than the nominal value). All this information can be

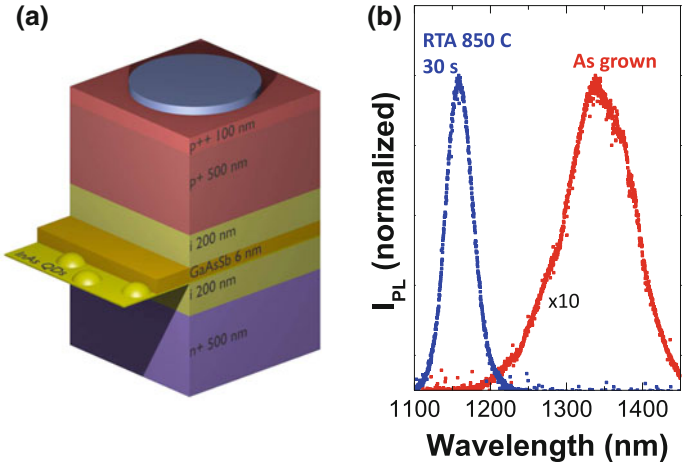

Fig. 3.1 **a** Schematics of the device structure with doping concentrations, layer thicknesses and active layer composition indicated. Reprinted from [20], with the permission of AIP Publishing. **b** Photoluminescence spectrum obtained at 15 K in a similar sample before and after applying a rapid thermal annealing treatment [23]

incorporated in a realistic theoretical model to calculate the electronic structure in different situations as described below.

Several devices were defined on the wafer by conventional optical lithography techniques and investigated by photoluminescence (PL) and time resolved PL (TRPL) as a function of external electric and magnetic fields applied in the growth direction. At 5 K, the sample was mounted in a cryostat equipped with piezo motors while a 785 nm laser diode, either continuous wave (CW) or pulsed in the ps range, was focused down to a 50 μm diameter spot. For CW measurements, the emitted light was detected with a peltier cooled InGaAs photodiode array attached to a 0.3 m focal length spectrometer. For time resolved measurements we used a fast InGaAs photomultiplier (transit time spread 400 ps) attached to a 0.3 m focal length spectrometer and connected to time correlation electronics.

Ambipolar electric fields were supplied by biasing the device in the rectifying region while magnetic fields were applied in the Faraday configuration using a 9 T superconducting magnet. In the latter case, light polarization was also analyzed in the σ^+ and σ^- basis.

3.3 Voltage Tunable Exciton Geometry

For many years, self-assembled In(Ga)As/GaAs QDs have been the preferred system to debug new quantum optical information technologies concepts in the solid state. Owing to its type-I band alignment, electrons and holes in this system are

strongly confined within the In(Ga)As material, being the response of their ground state wavefunctions to the external bias correspondingly small and similar for both carriers [24–26]. Typical values are ∼0.08 meV/kV cm^{-1} for quantum rings of 3.6 nm of maximum height [25, 27, 28]. As a function of the QD height the shift might range from 0.014 meV/kV cm^{-1} at 5.4 nm to 0.29 meV/kV cm^{-1} at 7.8 nm [29]. A possible way to extend the energy tunability is to confine separately electrons and holes in the two different QDs of a vertical QD molecule. A shift of 0.97 meV/kV cm^{-1} has been reported for such an indirect transition, in clear contrast with the intradot shift in the same system 0.113 meV/kV cm^{-1} [30].

For the type-II band alignment, in which either the holes or electrons are confined within the QD whereas the complementary particle remains weakly localized outside, the electro-optical response is comparatively unexplored. It is expected that the weakly confined particle would be more sensitive to external *stimuli*, resulting in a larger electrical polarizability along with other characteristics associated to the very different confinement regime for electrons and holes [16, 17, 31]. The confinement potential for electrons and holes together with their mutual Coulomb interaction define the size and the symmetries of the density of probability of the neutral exciton wavefunction, named hereafter, exciton geometry. At low excitation power, only one electron and one hole are confined at a given time. Multicharged exciton states are not populated and thus high order Coulomb terms are not relevant for the exciton geometry formation. Furthermore, being spatially separated, the leading terms of the neutral exciton Coulomb interaction: electron-hole attraction and exchange are smaller than in type-I systems [32]. In the following, the exciton geometry in type-II InAs/GaAsSb nanostructures and its evolution under an electric field applied in the growth direction will be investigated. Firstly, we will study the permanent dipole moment and polarizability, then, to get further insight over the in-plane exciton confinement, we will show measurements of the exciton radiative lifetime. These experiments will be discussed in the framework of a realistic theoretical model of the energy band structure described in Sect. 3.3.3.

3.3.1 Exciton Dipole Moment and Polarizability

For an Sb amount exceeding ≈16%, the valence band alignment across the InAs/GaAsSb interfaces turns from type-I to type-II, as revealed by the excitation power and temperature dependence of the photoluminescence (PL) studied by several authors [17, 18, 33, 34]. Thus, for the particular amount used here of ≈20%, the holes have been fully expelled from the QDs to the capping layer already at zero field, leaving the electrons confined within the InAs QD.

When a vertical electric field F is applied, electrons and holes are brought together or apart changing the exciton energy E through the quantum confined Stark-effect (QCSE) [35]. The second order perturbation theory equation $E(F) = E_0 - pF + \beta F^2$ can thus be used to extract the permanent electron-hole dipole moment p and polarizability β analyzing the voltage dependence of the PL spectrum. The results are

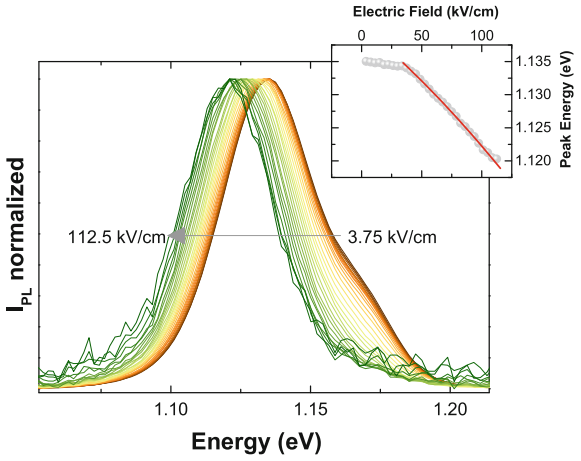

Fig. 3.2 Evolution of the photoluminescence in a vertical electric field at 5 K. Each spectrum has been normalized to its maximum for clarity. Inset: the ground state peak energies (circles) follow $E(F) = E_0 - pF + \beta F^2$ (solid line) in the rectifying region

displayed in Fig. 3.2. At 38 kV cm^{-1}, the spectrum is dominated by the ground state emission centered at 1.134 eV with full with at half maximum $FWHM \approx 36$ meV. The shoulder at higher energies corresponds to an excited state whose integrated intensity after gaussian deconvolution varies with field (21% of the total emission at 38 kV cm^{-1} and 6% at 112.5 kV cm^{-1}). Therefore, in the following we focus only on the fundamental transition.

Figure 3.2 shows how in the rectifying region (40–113 kV cm^{-1}) the ground state peak energy shifts by 13 meV, nearly 40% of its inhomogeneous bandwidth, while the $FWHM$ remains constant in the same range of electric fields (variation < 1 meV). A fit to the perturbation theory equation is shown in the inset of the same figure. The permanent dipole positive value $p/e = 1.48$ nm indicates that the hole average vertical position is above the electron one at zero bias as expected. We find a polarizability $\beta = -0.32$ μeV kV^{-2} cm^2 and an average shifting rate of ≈0.118 meV/kV cm^{-1} which are large but comparable to the values found for InAs/GaAs quantum dots mentioned above. It should be noted that the polarizability of a particle of mass m^* in an infinitely deep quantum well of width L scales like $\beta \propto m^* L^4$ [36]. Thus one would expect a greater change in the polarizability by expelling the heavier particle (hole) from the QD to the 6 nm thick GaAsSb capping layer. To explain this result, the hole shall be strongly localized in practice. According to results shown in Sect. 3.3.3, such localization comes from the strain and piezoelectric fields surrounding the InAs QD even in the absence of Coulomb interaction.

3.3.2 *Exciton Lifetime*

The analysis of the QCSE shown above does not provide much insight about the exciton wavefunction spread in the growth plane. This information can be accessed

more directly through the evolution of the PL spectrum in a magnetic field applied in the Faraday configuration as shown in Sect. 3.4. The exciton radiative lifetime on the other hand strongly depends on the electron-hole overlap in all three spatial directions and its value can be straightforwardly related to changes in the vertical and lateral confinement geometry as explained below.

To analyze the carrier dynamics in our device we have performed time resolved photoluminescence experiments also at 15 K. Fig. 3.3a contains decay curves recorded for two values of the electric field. The solid lines represent the convolution of the system response with single exponential decay fits for each dataset. We obtain long decay times, in excess of 6 ns, confirming that carriers exhibit type-II confinement after the RTA [23]. The full evolution of the decay time with the external electric field is represented in Fig. 3.3b. For each point, the decay time and its statistical error were estimated at the maximum of the emission following the Stark shift of the ground state.

The decay time increases up to a maximum of 7.5 ns at 42 kV cm^{-1} before decreasing abruptly as shown in Fig. 3.3b. This dome shape arises from two competing processes. The region of lifetime increase up to 50 kV cm^{-1} corresponds to the vertical separation of the electron and hole wavefunctions dictated by the QCSE. The region of lifetime decrease will be associated to the reduction of the

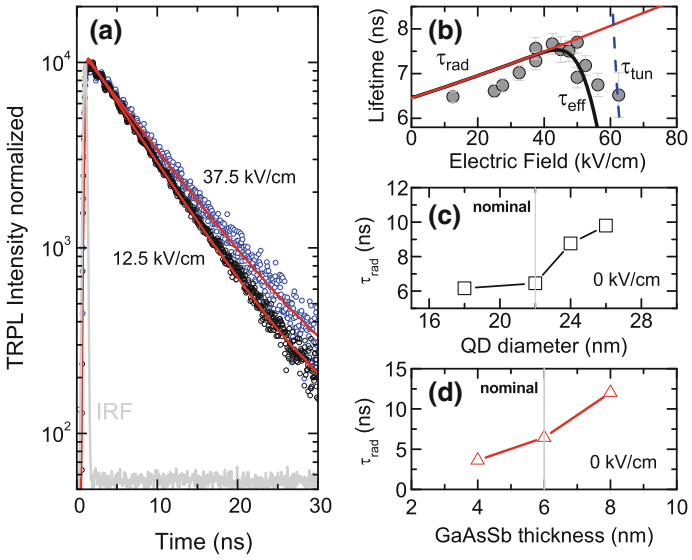

Fig. 3.3 **a** TRPL experimental data obtained at 5 K and corresponding decay curve fits are plotted with symbols and lines, respectively. The system response is plotted with gray line. **b** Best fit of the theoretical radiative lifetime (solid line), tunneling time (dotted line), and effective lifetime (thick solid line) to the experimental decay times (circles). **c** Evolution of the radiative lifetime for varying QD diameter and $t_{SRL} = 6$ nm. **d** Evolution of the radiative lifetime for varying SRL thickness and $D_{QD} = 22$ nm (**a** and **b** adapted from [20])

electron tunnelling time through the InAs/GaAs interface. It can be calculated using the Wentzel-Kramers-Brillouin approximation for a triangular well [37]:

$$\frac{1}{\tau_{\text{tun}}} = \frac{\hbar}{8m_e^* H^2} \exp\left\{-\frac{4}{3}\frac{\sqrt{2m_e^*}}{e\hbar F}[E_c - E_e(F)]^{3/2}\right\} \tag{3.1}$$

where we introduce the electron effective mass of compressed InAs, $m_e^* = 0.1$, the GaAs band edge at the QD base, $E_c = 0.765$ eV, $H = 2.3$ nm, for the QD height determined independently, [23] and $E_e(F)$ for the electron ground state energy.

Both contributions can be calculated independently from the electron and hole wavefunctions and energies obtained in Sect. 3.3.3. The black solid curve in Fig. 3.3b has been obtained using the nominal parameters for the grown nanostructures. It slightly overestimates the experimental lifetimes in the region of lifetime increase, but otherwise the nominal parameters nicely reproduce the experimental evolution.

A better fit could be obtained varying the diameter of the QD, D_{QD} and/or the thickness of the GaAsSb SRL, t_{SRL}. At zero bias, increasing any of them leads to longer radiative lifetimes as shown in Fig. 3.3c, d, respectively. To analyze such evolution, color maps of the density of probability of the ground state electron and hole states have been depicted in Figs. 3.4 and 3.5. The color map for each carrier has been averaged in the [110] and [1$\bar{1}$0] crystal directions and its scale has been normalized to the maximum obtained for the nominal values: $t_{\text{SRL}} = 6$ nm and $D_{\text{QD}} = 22$ nm. Coulomb interactions are not considered in the model, thus, band offsets at the material interfaces together with strain and piezoelectric fields fully determine the electron and hole overlap.

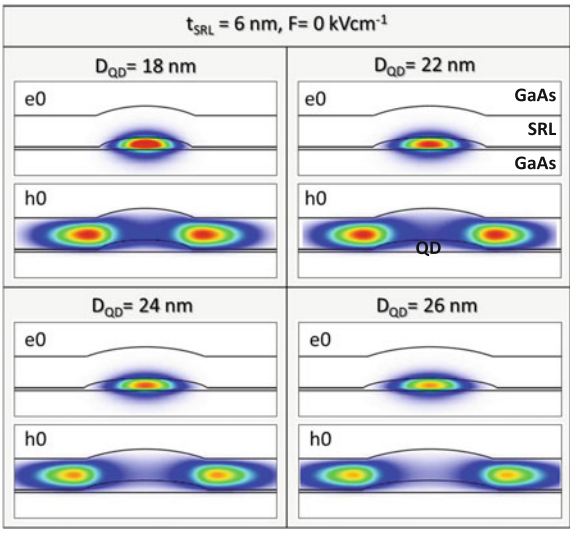

Fig. 3.4 Color maps of the density of probability of the ground state electron and hole states calculated varying the QD diameter for $t_{\text{SRL}} = 6$ nm and $F = F_z = 0$ kV cm^{-1}

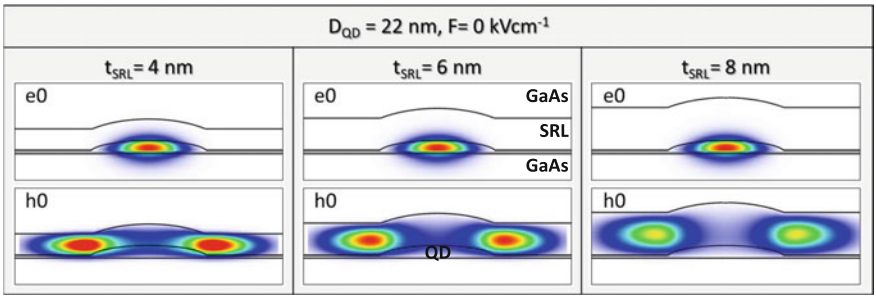

Fig. 3.5 Color maps of the density of probability of the ground state electron and hole states calculated varying SRL thickness for $D_{\mathrm{QD}} = 22$ nm and $F = F_z = 0$ kV cm^{-1}

At zero bias, the ground state electron wavefunction is well localized and centered within the QD volume. Although the density of probability spreads in the growth plane as the QD diameter increases, the leakage in the surrounding GaAs and GaAsSb barriers diminishes as shown in Fig. 3.4. For the same bias, the heavy hole ground state is bound to regions within the GaAsSb SRL where the strain deformation is large. This creates a characteristic annular pattern which for a round symmetric QD is only modulated by the different piezoelectric field in the [110] and [1$\bar{1}$0] directions [17, 18]. The large valence band offset between $GaAs_{0.81}Sb_{0.20}$ and GaAs prevents any significant leakage of the hole wavefunction out of the SRL. The hole penetration in the QD volume is however more pronounced and, as expected, decreases in the central regions of the QD as the diameter increases. These qualitative effects lead to an overall reduction of the electron-hole overlap with increasing QD diameter and, numerically, to the non monotonic increase of the radiative lifetime observed in Fig. 3.3c.

Changing the thickness of the SRL also causes a major impact in τ_{rad} but leaves the electron wavefunction mostly unaffected as depicted in Fig. 3.5. This is a purely valence band effect. Type II InAs/GaAsSb QD systems have been reported whose lifetimes are as long as 65 ns [38] and get reduced for thinner SRL thicknesses [39]. A large SRL thickness is very effective in diminishing the strain field around the QD and the quantum confinement in the barrier [12]. The net result is a rather delocalized hole only bound to the electron by Coulomb effects. The type-II QD system investigated here presents much faster radiative recombination and, as discussed above, has a polarizability, β, not very different from the one found for large InAs/GaAs QDs. The contour maps in Fig. 3.5 show the transition from one regime to the other. For $t_{\mathrm{SRL}} \leq 6$ nm the heavy hole is strongly bound to the InAs/GaAsSb interface and has a substantial penetration within the QD volume. Under these conditions, the indirect exciton might be a very effective probe to map the hole spin and the topological changes of the hole wavefunction in an external field as discussed in the following sections.

3.3.3 *Energy Levels Versus Electric Field*

We have developed an eight-band $\mathbf{k} \cdot \mathbf{p}$ theoretical model for the QD based on the geometrical characterization of the capped nanostructure reported in [23]. The same model was employed previously for the study of the influence of Sb in the QD [40] and in the cap layer [18]. We have considered a lens shaped $Ga_{0.27}In_{0.73}As$ QD of 11 nm radius and 2.3 nm height embedded in a conformal $GaAs_{0.81}Sb_{0.20}$ strain reducing capping layer of 6 nm thickness unless stated otherwise. The structure was surrounded by a GaAs matrix. The applied electric field was introduced in the model through charge neutral contacts, meaning that complications derived from the dopants distribution were not taken into account. We considered a linear dependence of the electric potential across the intrinsic region of the device described in Sect. 3.2. We obtain the energy levels of the electron and hole states solving the eight-band $\mathbf{k} \cdot \mathbf{p}$ Hamiltonian including the effects of the strain and linear piezoelectric field [41]. From the electron and hole wavefunctions we also computed the radiative lifetimes, τ_{rad}, and the expected value of the vertical (in-plane) electron and hole separation, $\langle z_{\text{e-h}} \rangle = \langle z_{\text{h}} \rangle - \langle z_{\text{e}} \rangle$ ($\langle \rho_{\text{e-h}} \rangle = \langle \rho_{\text{h}} \rangle - \langle \rho_{\text{e}} \rangle$), and density of probability distribution for each type of carrier.

The permanent dipole moment is related to the expectation value of the electron and hole z coordinate at $F = 0$ kV cm^{-1} through $p/e = \langle z_{\text{e-h}} \rangle = \langle z_{\text{h}} \rangle - \langle z_{\text{e}} \rangle$. Our model predicts that the strain and piezoelectric potentials are enough to stabilize the hole wavefunction above the electron one at zero bias with $p/e = 2.3$ nm very close to the experimental value $p/e = 1.48$ nm quoted in Sect. 3.3.1. In addition, we find that the polarizability $\beta_{\text{kp}} = -0.39$ μeV kV^{-2} cm^2 also agrees well with the experimental value $\beta_{\text{exp}} = -0.32$ μeV kV^{-2} cm^2, concluding that the key parameters of the electrical response of these QDs are well reproduced by the $\mathbf{k} \cdot \mathbf{p}$ model using the nominal parameters.

In the application sphere, a large p and β are desirable to fabricate electro-absorption modulators with small modulation voltages and low insertion losses. From the discussion in the previous sections, it became clear that we need to increase the thickness of the SRL to increase the polarizability at the expense of larger radiative lifetimes. Figure 3.6 summarizes the results. We find p/e (nm) = 1.4, 2.2 and 3.2 and β (μeV kV^{-2} cm^2) = −0.21, −0.39 and −0.78 for t_{SRL} (nm) = 4, 6 and 8, respectively. As shown in Fig. 3.6b, the larger p/e value translates in slower radiative dynamics of the system at zero bias while, as expected, the larger β value brings much wider modulation of the radiative lifetime when applying vertical electric fields [37].

An additional feature arises from the large asymmetry between electron and hole confinement geometry. As shown in Fig. 3.6a, in the investigated bias range, the energy of the strongly confined ground state electron changes by less than 1 meV and almost independently of t_{SRL}. Therefore, the large energy shifts and β values of the InAs/GaAsSb QD system are entirely due to the electrical modulation of the hole wavefunction. For the tunnelling dynamics the situation is reversed. We have found that the hole ground state cannot tunnel through the GaAs interface due to its deeper

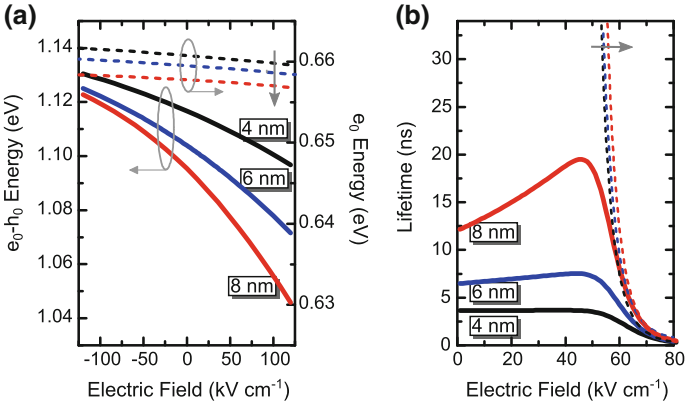

Fig. 3.6 **a** Theoretical evolution of different parameters calculated varying the vertical electric field and SRL thickness: **a** fundamental transition energy (solid lines) and electron ground state energy (dashed lines), **b** effective lifetime (solid lines) and tunneling lifetime (dashed lines). Adapted from [20]

confinement potential in the GaAsSb layer and its large effective mass. Meanwhile, at $\approx$60 kV cm^{-1}, the electron tunnelling through the standard InAs/GaAs interface becomes very effective quite independently of the GaAsSb layer thickness (dashed lines in Fig. 3.6b).

A system where electron and hole confinement geometry can be tuned independently can be exploited in optoelectronic devices such as QD lasers [42–44] and photovoltaic solar cells [45–50]. Yet, our calculations suggest that the external electric field also induces a change in the hole wavefunction topology opening a venue for new applications. The idea is better explained looking at the contour maps shown in Fig. 3.7a. The density of probability for each carrier has been depicted for varying F. In contrast to typical type-I systems, here the hole can move easily within the GaAsSb SRL pushed by the external electric field, not only changing the vertical dipole moment $\langle z_{\text{e-h}} \rangle$, but also winding around the QD and inducing a large modulation of the in-plane dipole moment $\langle \rho_{\text{e-h}} \rangle$. The calculated dipole moments are depicted in Fig. 3.7b. At $F = 0$, $\langle \rho_{\text{e-h}} \rangle$ is already 9 nm with $\langle z_{\text{e-h}} \rangle = 2.3$ nm. A reverse bias ($F \geq 0$), causes an upward shift of the hole wavefunction increasing the vertical dipole moment and decreasing the in-plane one, which might achieve $\langle z_{\text{e-h}} \rangle = 10$ nm and $\langle \rho_{\text{e-h}} \rangle = 0$ nm at $F = 200$ kV cm^{-1}. In this reverse bias region is where the radiative lifetime increase is more apparent as described above. On the other hand, for $F \leq 0$, the hole will move downwards towards the underlying GaAs barrier. Since there is no significant penetration through this interface, the in-plane dipole moment remains large and mostly unchanged by the field, making this bias region the most favorable for the observation of optical Aharonov-Bohm effects as explained in the following section.

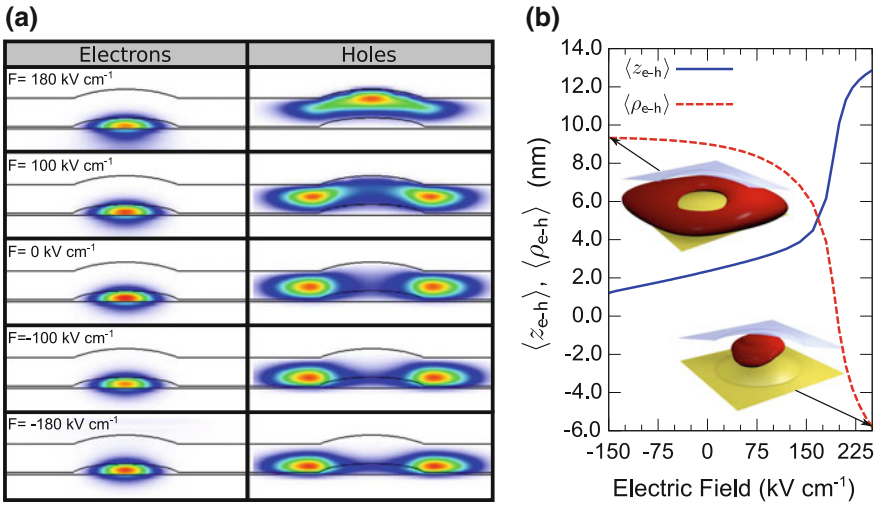

Fig. 3.7 **a** Color maps of the density of probability of the ground state electron and hole calculated for varying electric field. **b** Expected value of vertical (blue solid line) and radial (red dashed line) separation between electron and hole. The insets show three dimensional color plots of the ground state hole wavefunction probability density calculated at the indicated electric fields. Reprinted from [20], with permission of AIP publishing

3.4 Voltage Tunable Exciton Topology

In the previous section, the probability density calculated by the eight-band $\mathbf{k} \cdot \mathbf{p}$ model provided a set of intuitive pictures to understand the electrical modulation of the hole wavefunction in the InAs/GaAsSb QD system. We have found that for $F = F_z \leq 0$, the combination of type-II confinement, strain and piezoelectric fields results in a hole wavefunction that adopts a non-singly connected topology (ring-like) and the formation of a large in-plane permanent dipole. The effect of a magnetic field applied along the growth direction in a type-I nanostructure is a well studied problem [51]. In contrast, in a type-II nanostructure, the non-singly connected topology and the in-plane dipole shall result in the appearance of a relative Berry phase between the electron and hole wavefunctions. An excellent introduction to the topic can be found in Chap. 1 [52] and, in particular for type-II QDs, Chap. 11 [53] of the current book. The key signature to identify the optical Aharonov-Bohm effect is the change in orbital angular momentum of the electron with respect to the hole. From an optical point of view, this means that the exciton ground state evolves with the applied magnetic field from a bright state into a dark state, hence producing a fade-out of the emitted intensity. In actual samples such a reduction on the emitted light is not observed because of the reduced symmetry of the system, i.e. the total angular momentum is not a good quantum number. As a consequence, oscillations in intensity are observed instead of a quench [54–56]. Quantum nanostructures with ring-like

topology for electrons, holes or both are known as quantum rings (QR) and have been the object of intense theoretical and experimental research in the last years [57]. In this endeavour, it was soon revealed that the charge separation between electron and hole in the radial direction is crucial for the observation of optical or exciton AB oscillatory effects [55, 58]. Generally speaking $\langle \rho_{\text{e-h}} \rangle$ is relatively small in type-I QR systems making the detection of optical AB effects a challenging task [59, 60]. In this context, a vertical electric field was proven useful to modulate $\langle \rho_{\text{e-h}} \rangle$ without destroying the ring potential and thus identify voltage tunable AB oscillations in GaAs/AlGaAs QR [61, 62]. The spatial separation occurring in semiconductor nanostructures with type-II confinement shall make the observation of optical AB effects more amenable even if the ring-like topology emerges for only one type of carrier [53, 63–65]. In the following, we will show how thanks to the polarizability of the hole wavefunction characteristic of the InAs/GaAsSb QD system, voltage tunable topological effects might be also more pronounced.

3.4.1 Magneto-Photoluminescence

To investigate optical AB effects in our sample, magneto-photoluminescence (MPL) spectra were recorded at 5 K in the Faraday configuration. For every magnetic field, B: 0–9 T, a PL spectrum was recorded for $V(\text{V}) = -1$, 0 and 1 ($F = 63$, 38 and 13 kV cm^{-1}, respectively). Each spectrum was normalized by its corresponding excitation power. To do so, the laser power was registered simultaneously being its value constant within ±4% during the whole experiment and within ±2 parts per thousand while recording the three spectra at each B.

Figure 3.8 shows the evolution of the MPL obtained this way for σ^+ detection. The electric field not only changes the peak emission energy and intensity as already discussed, but it also changes the magnetic response of the sample. To maintain a unified description, the CW excitation power was kept approximately the same in the experiments of Sect. 3.3.1 and here. Thus, the PL emission comprises two bands which at 0 V and 0 T are split by ≈36 meV. These bands arise from ground state and excited state recombination whose integrated intensity ratio was >7 throughout the experiment. To discuss the magnetic properties of the InAs/GaAsSb QD system, the inhomogeneously broadened ground state emission will be analyzed separately. To do so, a conventional gaussian deconvolution procedure has been performed as depicted in Fig. 3.8d–f. From the deconvoluted MPL peak energy, E^{σ}, and integrated intensity, I^{σ}_{PL}, we obtain the average energy shift, $E_{\text{av}}(B) = (E^{\sigma^+} + E^{\sigma^-})/2$, unpolarized intensity, $I_u(B) = (I^{\sigma^+}_{PL} + I^{\sigma^-}_{PL})/2$, Zeeman splitting, $\Delta E_z(B) = E^{\sigma^+} - E^{\sigma^-}$, and degree of circular polarization, $DCP(B) = (I^{\sigma^+}_{PL} - I^{\sigma^-}_{PL})/(I^{\sigma^+}_{PL} + I^{\sigma^-}_{PL})$ for the ground state alone.

Figure 3.9 gathers $\Delta E_{\text{av}}(B) = E_{\text{av}}(B) - E(0)$ and $\Delta E_z(B)$ for the three investigated voltages. Solid lines are conventional fittings to the perturbation theory expected evolution: $\Delta E_{\text{av}}(B) = \alpha_D B^2$ and $\Delta E_z(B) = \mu_0 g B$, where μ_0 is the Bohr magneton, and α_D and g represent the quadratic diamagnetic shift coefficient and

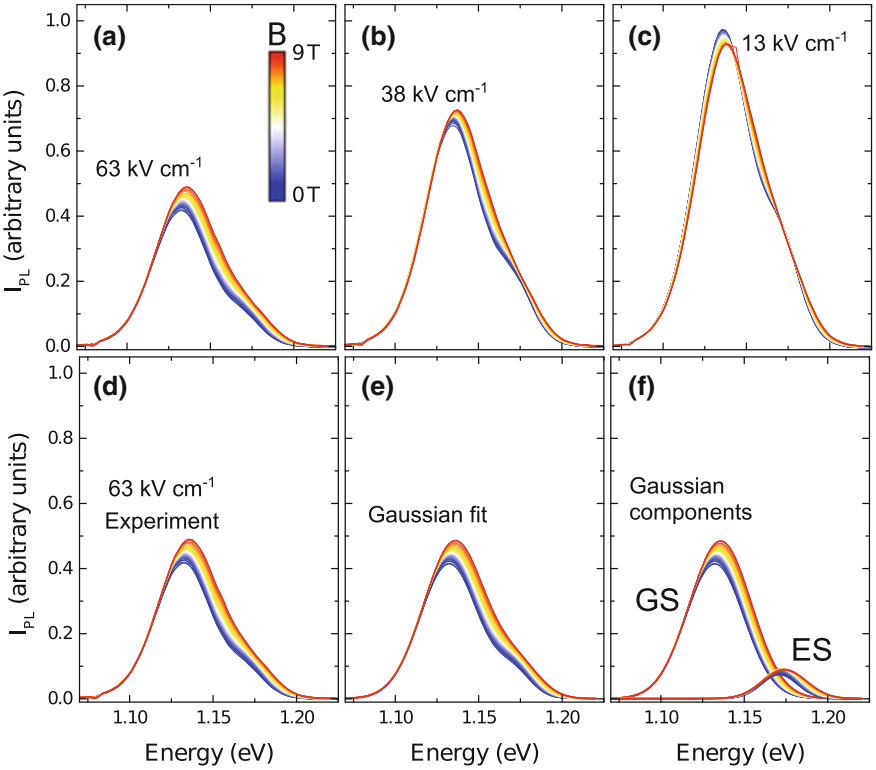

Fig. 3.8 Evolution in magnetic field of the σ^+ polarized PL spectrum for three different device bias (**a**–**c**). Measurements done at 5 K in the Faraday configuration. Gaussian deconvolution of MPL spectra measured at 63 kV cm^{-1}: **d** original data curves, **e** curves resulting from gaussian deconvolution, **f** individual gaussian components for ground state (GS) and excited state (ES). Adapted from [66]

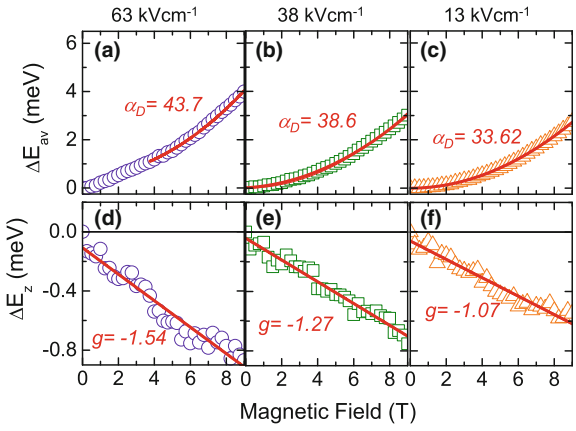

Fig. 3.9 **a**–**c** Average energy shift in magnetic field of the fundamental transition at different electric fields (open symbols). Solid lines stand for the corresponding parabolic fits with diamagnetic shift coefficient, α_D (μeV/T^2), indicated. **d**–**f** Experimental Zeeman splitting (open symbols) and g-factors extracted from the corresponding linear fits (solid lines). Adapted from [66]

g-factor for the type-II exciton, respectively. Both functions describe accurately the data, except for an initial linear deviation for $\Delta E_{\mathrm{av}}(B)$ at small magnetic fields. We observe that both α_D and g are affected by the external electric field and also that oscillations in magnetic field are absent for the ground state peak energy. The relative g-factor change is almost 50% and shall be attributed to the voltage modulation of the spin-orbit coupling that will be discussed in detail in Sect. 3.5.

The α_D variation is smaller but exhibits a clear diminishing trend reducing the reverse bias. For a magnetic field applied in the growth direction, the diamagnetic shift coefficient is directly proportional to the exciton wavefunction extension in the growth plane [67]. This simple relation works better for low magnetic fields, where Landau level formation and changes of the exciton binding energy can be safely ignored. For high magnetic fields, strong deviations from a quadratic shift are expected [51]. In the investigated range, our data follow a quadratic evolution but the diamagnetic shift increases with the electric field while the in-plane exciton dipole moment (and thus the exciton size) decreases as discussed in Sect. 3.3.3. We believe that this discrepancy is related to the crossing of electronic levels with different angular momentum in the fundamental state. These level crossings are the signature of AB effects in quantum rings and might reveal themselves as a flattening of $\Delta E_{\mathrm{av}}(B)$ and the observed evolution of α_D *versus* F. In addition, the fact that the tunnelling becomes more important as the positive field increases might also affect the value α_D. Next section will cover these issues in more detail.

The relative evolution of the MPL unpolarized intensity, $\Delta I_u(B)$, and *DCP* are depicted in Fig. 3.10. The DCP is positive, as expected from the negative g-factor, and evolves with magnetic field from a rather monotonic dependence at 63 kV cm^{-1} to a clearly oscillatory one at 13 kV cm^{-1}. In the same bias range, $\Delta I_u(B)$ show even more abrupt changes. At large positive electric fields, the unpolarized intensity increases with B exhibiting a strong magnetic brightening. The dependence follows a fixed linear slope with small oscillations which are only apparent plotting the first derivative of the data. Reducing the bias, the magnetic brightening effect diminishes and, for 13 kV cm^{-1}, an oscillatory dependence can be clearly seen on the data.

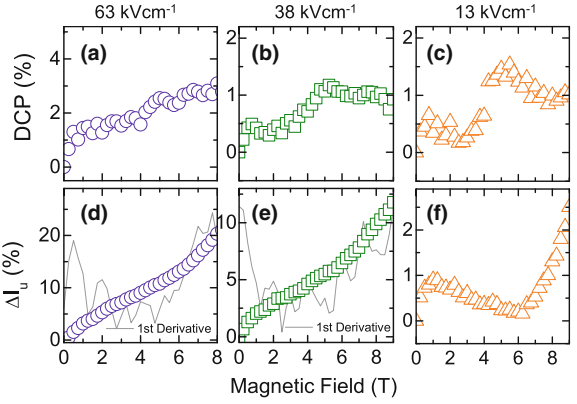

Fig. 3.10 **a–c** Evolution in magnetic field of the degree of circular polarization of the fundamental transition at different electric fields (open symbols). **d–f** Same for the relative change of the unpolarized PL intensity. The first derivative of the data is shown with a gray line where relevant. Adapted from [66]

In the quantum ring literature, MPL intensity oscillations are related to the changes in the ground state angular momentum arising from the AB effect. Voltage modulation of such oscillations have been reported for type-I InAs/GaAs single quantum rings by Ding et al. [61, 68]. The modulation being associated to changes in the effective quantum ring confinement potential. Such oscillations must diminish with the positive electric field as the hole wavefunction moves upwards changing from ring-like to QD-like topology (see Fig. 3.7). Our experiments in magnetic field, while done on QD ensembles, look compatible with this picture. In the following, a theoretical analysis will be performed which shall give a more quantitative description of these effects.

3.4.2 *Energy Levels Versus Magnetic Field*

The model used to explain the results in Sect. 3.3 was constructed on top of the NextNano numerical tool. The symmetry group of the Hamiltonian, including the piezoelectric field, is C_{2v}. For such a system there is no good quantum number to label the electronic states. The topological changes to be described here arise from complex state crossings and anticrossings in the valence band which would be difficult to describe without a proper labeling scheme. Thus, we have opted for a custom model forcing the whole Hamiltonian to be axially symmetric which results in a $C_{\infty v}$ description. Hence, even in the multiband case, the states can be labeled according to the z-component of the total angular momentum (M). The introduction of a magnetic field (B) along the [100] direction results in a system with C_{∞} symmetry and the states with positive and negative M become non-degenerate. Under these approximations, each electronic state is expressed as:

$$\Psi^{(M)}(\mathbf{r}) = \sum_{k=1}^{8} F_{m,k}^{(M)}(\mathbf{r}) u_k = \sum_{k=1}^{8} \frac{1}{\sqrt{2\pi}} e^{im\phi} \mathcal{F}_{m,k}^{(M)}(\rho, z) u_k, \tag{3.2}$$

where u_k is the Bloch amplitude of the k band at the origin of the Brilloin zone, $F_{m,k}^{(M)}(\mathbf{r})$ is the envelope function associated to the k Bloch component and is defined by the z-projection of the orbital momentum (m). We have expressed the envelope function in cylindrical coordinates defined by a phase factor characterized by m and a two dimensional component $\mathcal{F}_{m,k}^{(M)}(\rho, z)$. The $\mathbf{k} \cdot \mathbf{p}$ Hamiltonian together with the confinement potential is solved by expanding the envelope function in a complete basis of functions. This basis is defined by the eigenfunctions of a hard-wall cylinder. Strain plays a critical role in our system, given that it is responsible of the hole confinement in the SRL. The zincblenda crystal structure has lower symmetry than our Hamiltonian, therefore we are forced again to describe the strain distribution as that of an isotropic material, i.e. the elastic constant C_{11} is approximated by the value $C_{12} + 2C_{44}$. The impact of the strain on the QD electronic structure is described by the Bir-Pikus Hamiltonian. An additional consequence is the absence

of a piezoelectric field, since no polarization charges are induced by an isotropic strain in these semiconductors. Further details are moved to the appendix Sect. 3.6.

3.4.2.1 Exciton Level Crossings

We will rely on the excitonic picture in the presentation of the numerical results. Each electron (hole) state is defined by the quantum number $M_{e(h)}$ introduced in (3.2). Hence, the exciton states are defined by the addition of the total angular momentum of the constitutive particles $M = M_e + M_h$. The only optically active exciton states are those characterized by $M = 0, \pm 1$. The emitted photons are polarized along the z direction for $M = 0$ and circularly polarized $\sigma_\pm$ for $M = \pm 1$. As a reference QD, we consider one of equal geometrical parameters as those of Sect. 3.3: $R_{QD} = 11$ nm, $H_{QD} = 3$ nm, $t_{SRL} = 6$ nm and $d_{WL} = 0.5$ nm and composition $Ga_{0.25}In_{0.75}As$ (QD) and $GaAs_{0.80}Sb_{0.20}$ (SRL). In Fig. 3.11 we show the exciton energy levels close to the ground state. The sign and value of M can be inferred from the color lines as well as the radiative rate. We have selected three values of electric field coincidental with the experimental values shown in Fig. 3.8, i.e. 10, 40 and 60 kV cm^{-1} together with two extreme values (-30 and 115 kV cm^{-1}) to stress the role of the hole wavefunction localization. To understand the effect of the magnetic field in our system, we start by focussing at the dispersion for $F = 115$ kV cm^{-1} (large reverse bias). At $B = 0$ T, the ground state is composed of the fourth-fold degenerated quadruplet with $M = \pm 1, \pm 2$. The magnetic field splits this level into two almost two-fold degenerated branches. In particular, the $M = \pm 1$ can be distinguished by the non-zero radiative rate (dots over the line) and the intense color used in the representation. This four exciton states result of the combination of two electron and two hole states whose dominant Bloch amplitudes are $|1/2, \pm 1/2\rangle$ and $|3/2, \pm 3/2\rangle$.

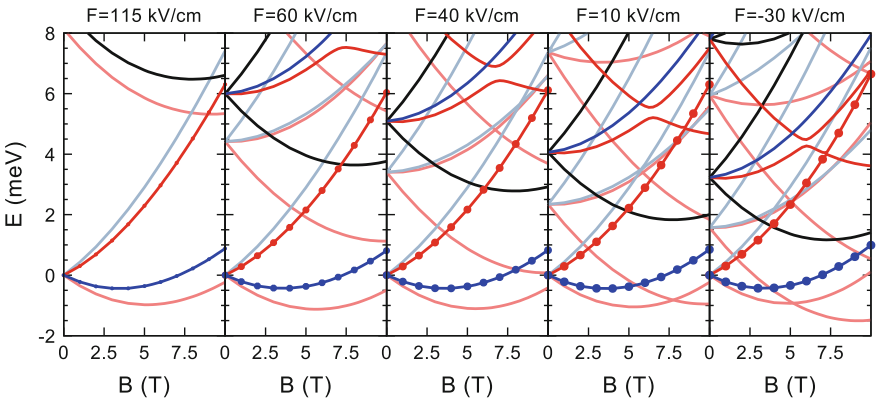

Fig. 3.11 Exciton energy levels refereed to the ground state energy at $B = 0$ T. Blue lines are states with $M = -1$, red $M = 1$, light-red $M > 1$, light-blue $M < -1$ and black $M = 0$. The spot size is proportional to the radiative rate

From the addition of angular momentum, it is direct to infer that the envelope function multiplying the Bloch amplitudes are defined by $m = 0$. This explains the weak dependence of the internal structure of the quadruplet to the electric field and hence to the topology of the hole wavefunction. Irrespective of whether the hole is located above the apex of the QD ($F = 115$ kV cm^{-1}) or close to its bottom ($F = -30$ kV cm^{-1}) the energy levels are weakly perturbed. In contrast, the excited states get strongly modified with the electric field. These states are characterized by $|m| > 0$ an are more sensitive to the effective radial confinement as the hole drifts downhill within the SRL.

The increase on the number of exciton states in the region close to the ground state as a function of the applied electric field is a remarkable property of our system. Fig. 3.11 clearly shows the ability of the system to evolve from the trivial electronic structure of a QD ($F > 60$ kV cm^{-1}) to an enriched mixture of states of different total angular momentum ($F < 60$ kV cm^{-1}). Our model predicts two crossings between the $M = 3$ excited state and the $M = -1$ (bright) and $M = 2$ (dark) ground states. Explicitly, these crossings take place at $B = 5.4$ and 7.8 T for $F = 10$ kV cm^{-1}, respectively. These crossings occur at fields within the range of the experimental values presented before. This would result in, at least, one optical Aharonov-Bohm (AB) oscillation. Its observation would depend on the thermalization of the excited carriers and the eventual relaxation of the selection rules in the actual system as explained below. The positions of the crossings in the magnetic field axis as a function of the applied electric field are shown in Fig. 3.12a. As expected for AB related effects, the number of crossings and their actual position depends on the exciton in-plane

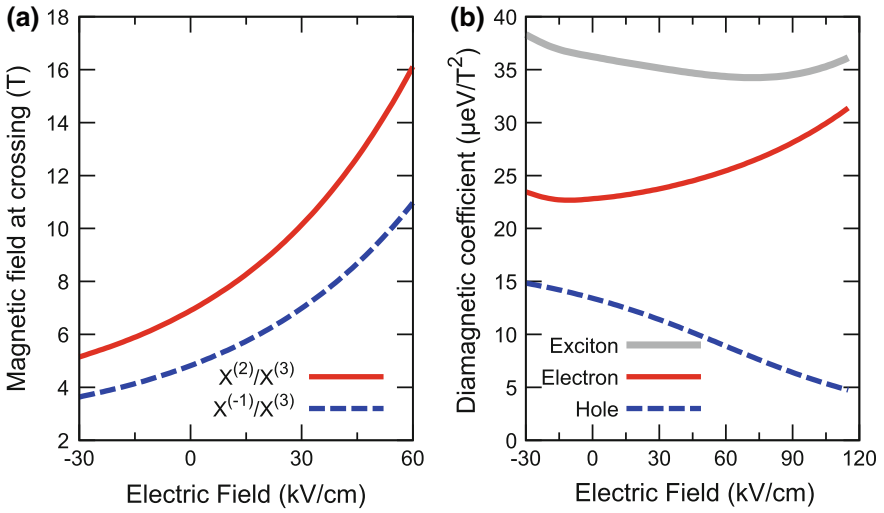

Fig. 3.12 **a** Value of the magnetic field at the crossing between the energy levels of the excitons $M = 2$ and $M = 3$ (solid line) and $M = -1$ and $M = 3$ (dashed line). **b** Diamagnetic coefficient for the electron state (solid line), hole (dashed line) and the exciton (thick-solid line)

dipole moment which, in our case, decreases with the electric field, as discussed in Sect. 3.4. This result strongly supports that the oscillatory dependence observed for the *DCP* and unpolarized integrated intensity in Fig. 3.10 is a consequence of a change in the total angular momentum of the ground state and hence a signature of the AB.

Our ensemble experiment prevents the observation of energy resolved features in the inhomogeneously broadened PL spectrum. Yet, our results clearly show that larger emission energy shifts *versus B* and diamagnetic shift coefficients take place for larger electric fields (reverse bias) (Fig. 3.9a–c). Figure 3.12b shows the theoretical evolution obtained for α_D for the electron, hole and bright exciton ($|M| = 1$). The first thing to observe is the drop of the hole diamagnetic shift with the increasing electric field. This is expected since, as the hole drifts from the apex towards the base, its wavefunction spreads in the SRL plane (see Fig. 3.7) increasing the diamagnetic shift from ∼5 to ∼15 μeV/T^2, accordingly. [67] In the same bias range, the electron diamagnetic shift goes from from ∼23 to ∼32 μeV/T^2, increasing with the reverse bias. This is a consequence of the spill-over of the electron wavefunction in the GaAs barrier underneath. As discussed in Sect. 3.3, for $F > 60\,\mathrm{kV\,cm^{-1}}$, electron tunneling out of the InAs QD becomes noticeable, increasing the value of $\langle \rho_e \rangle$ and hence of α_D. Both contributions must be added to compare with the experimental diamagnetic shift evolution. Experimentally, α_D finds a minimum value of 33.6 μeV/T^2 at $F =$ 13 kV cm^{-1} and increases to 43.7 μeV/T^2 at $F = 63$ kV cm^{-1}. Meanwhile, the calculated exciton values find a maximum value of 38.3 μeV/T^2 at $F = -30$ kV cm^{-1} and decreases to 34.3 μeV/T^2 at 70 kV before increasing again due to the electron tunneling. Thus, without any fitting parameter, our axially symmetric theory correctly predicts the magnitude of the diamagnetic shift and the relevance of electron tunneling for large reverse bias, but it cannot reproduce the experimentally observed decreasing trend as we approach $F = 0$. As shown in Fig. 3.11, in this bias range, the ground state of the electron-hole system is composed mostly of states with angular momentum $|M| > 1$. These states are purely dark in our theory but might achieve oscillator strength if the symmetry of the actual confinement potential is lowered. This would explain the lower experimental value found for α_D near $F = 0$ and will be discussed in detail in the next section.

3.4.2.2 In-Plane Asymmetry Effects

Both the tuning of the spin splitting and the diamagnetic shift can arise from the symmetry reduction in the confinement potential or the competition between the external magnetic field and the intrinsic field arising from spin orbit coupling effects. As such, this section addresses the link between spatial symmetry and spin properties. It has been profusely reported that quantum dot elongation can take place after capping. The strain fields that build up during this process provoke the anisotropic segregation of In atoms leading to an eccentricity increase of previously cylindrical

systems [69, 70]. Analogous process is also triggered during the synthesis of type-II InAs/GaAsSb quantum dots which also might lead to anisotropic piezoelectric fields [17, 71]. Thus, it is a goal of our following discussion to assess the effects of in-plane confinement anisotropy in the electronic properties. To this end, we introduce an effective mass description of both the conduction and valence band, and incorporate the effects of confinement asymmetry for electrons and holes in a model that can emulate quantum dots and rings within the same framework, as well as the resulting Rashba spin orbit coupling fields arising from confinement and external fields.

As one would expect, there are pronounced spatial asymmetry effects in the angular momentum quantization and the spin character of different states. Degeneracies are broken and these asymmetries, introduced or enhanced by shape anisotropies and by the confinement potential itself, are found to play an important role in determining the magneto-optical response.

The eigen-value problem for the conduction band will be solved by expanding the corresponding wave functions in the basis of the eigen-solutions of the following effective mass Hamiltonian,

$$H = \frac{\hbar^2}{2\mu^*}k^2 + V_0(z) + V_0(\rho) + \frac{g^*\mu_B}{2}\mathbf{B}\cdot\boldsymbol{\sigma}\,, \tag{3.3}$$

with $\mathbf{k} = -i\nabla + e/\hbar\mathbf{A}$ and the magnetic field pointing along the growth z-direction, where $\boldsymbol{\sigma}$ is the Pauli matrix vector, and $\mathbf{A} = B/2\rho\hat{\varphi}$. For the unperturbed basis, $V_0(z)$ will be assumed as a rigid wall potential profile while the in-plane confinement in polar coordinates takes the form reported in [72]

$$V_0(\rho) = \frac{a_1}{\rho^2} + a_2\rho^2 - 2\sqrt{a_1 a_2}, \tag{3.4}$$

which allows obtaining an exact solution that covers both the quantum ring confinement and the quantum dot. The parameters a_1 and a_2 define the structure shape and for $a_1 \neq 0$, a ring with radius $R_{\mathrm{QR}} = (a_1/a_2)^{1/4}$ is obtained. In turn, by setting $a_1 = 0$, a parabolic quantum dot with effective radius $R^2_{\mathrm{QD}} = \hbar/(2\pi\sqrt{2a_2\mu^*})$ can be emulated. For the valence band basis, used to expand the Luttinger Hamiltonian eigen-solutions, we use an analogous separable problem yet assuming anisotropic effective masses in (3.3), and replacing $g^*/2$ and σ_z, by -2κ and the angular momentum matrix for $j = 3/2$, J_z, respectively.

The solution for the 3D Schrödinger equation, $\Phi(\rho, \varphi, z)$, corresponding to the potential profile in (3.4) is given by

$$\psi^{(e/h)}_{n,m,l}(\rho, \varphi, z) = \phi^{(e/h)}_{n,m}(\rho, \varphi)\chi^{(e/h)}_{l}(z)u_{e/h}, \tag{3.5}$$

where $\chi^{(e/h)}_{l}(z)$ is the wave function for a rigid square well and $u_{e/h} = |j, m_j\rangle$ are the basis functions at the Brillouin zone center in the Kane model: $|1/2, \pm 1/2\rangle$,

$|3/2, \pm 3/2\rangle$ and $|3/2, \pm 1/2\rangle$, for the electron, heavy hole, and light hole states, respectively. The planar wave function has the form

$$\phi_{n,m}^{(e/h)}(\rho,\varphi) = \frac{1}{\lambda_{(e/h)}}\left(\frac{\Gamma[n+\mathcal{M}_{(e/h)}+1]}{2^{\mathcal{M}_{(e/h)}} n!(\Gamma[\mathcal{M}_{(e/h)}+1])^2}\right)^{1/2} \times \left(\frac{\rho}{\lambda_{(e/h)}}\right)^{\mathcal{M}_{(e/h)}} \frac{e^{-im\varphi}}{\sqrt{2\pi}} e^{-\frac{1}{4}\left(\frac{\rho}{\lambda_{(e/h)}}\right)^2} \times {}_1F_1\left(-n, \mathcal{M}_{(e/h)}+1, \frac{1}{2}\left(\rho/\lambda_{(e/h)}\right)^2\right), \tag{3.6}$$

where ${}_1F_1$ is the confluent hypergeometric function, $n = 0, 1, 2, \ldots$ is the radial quantum number, and $m = 0, \pm 1, \pm 2, \ldots$ labels the angular momentum. The corresponding eigen-energies for the 3D problem are

$$E_{n,m,l,s_z}^{(e/h)} = \left(n + \frac{1}{2} + \frac{\mathcal{M}_{(e/h)}}{2}\right)\hbar\omega_{(e/h)} - \frac{m}{2}\hbar\omega_{c(e/h)}^* - \frac{\mu_{(e/h)}^*}{4}\omega_{0(e/h)}{}^2 R_{\mathrm{QR}}{}^2 + \left(\frac{l^2\pi^2\hbar^2}{2\mu_{(e/h)}^* L^2}\right) + g_{(e/h)}^*\mu_B B \cdot s_z, \tag{3.7}$$

with $\mathcal{M}_{(e/h)} = \sqrt{m^2 + \frac{2a_1\mu_{(e/h)}^*}{\hbar^2}}$, $\omega_{c(e/h)}^* = eB/\mu_{(e/h)}^*$, $\omega_{0(e/h)} = \sqrt{8a_2/\mu_{(e/h)}^*}$, $\omega_{(e/h)} = \sqrt{\omega_{c(e/h)}^2 + \omega_{0(e/h)}^2}$ and $\lambda_{(e/h)} = \sqrt{\frac{\hbar}{\mu_{(e/h)}^*\omega_{(e/h)}}}$.

The symmetry constrains can be subsequently relaxed by reshaping the in-plane confinement in the following way, $V(\rho,\varphi) = V_0(\rho,\varphi) + \delta\cdot\rho^2\cos^2\varphi$. This is an extension of the profile proposed in [73, 74], where the term controlled by the parameter δ determines the quantum ring eccentricity of the outer rim of the confinement. The values of the eccentricity are given by $e = \sqrt{1 - a_2/(a_2+\delta)}$, for $\delta > 0$, that corresponds to an elliptical shrinking, or $e = \sqrt{1-(a_2+\delta)/a_2}$ for $\delta < 0$, that leads to an elliptical stretching. Additionally, an electric field along the growth direction can be considered by inserting the term eFz into $V(z)$ that will couple the wave function components, $\chi_l^{(e/h)}(z)$, with different parities and finally, the spin orbit interaction can be introduced through the Rashba contribution to the total Hamiltonian $H_R = \alpha_c\boldsymbol{\sigma}\cdot(\nabla V \times \mathbf{k})$ for the conduction band or $H_R = \alpha_v\mathbf{J}\cdot(\nabla V\times\mathbf{k})$, for the valence band.

Increasing the eccentricity provokes the mixing of angular momentum components, or enhances it, if some degree of hybridization is already present in the valence band. This plays a crucial role in the character of the ground state of both conduction and valence bands and affects the diamagnetic shift when compared to the cylindrical symmetric case.

The eccentricity breaks the cylindrical symmetry and so the angular momentum stops being a good quantum number. The impact on the valence band energy levels for the first few states confined in a quantum ring have been displayed in Fig. 3.13a. For

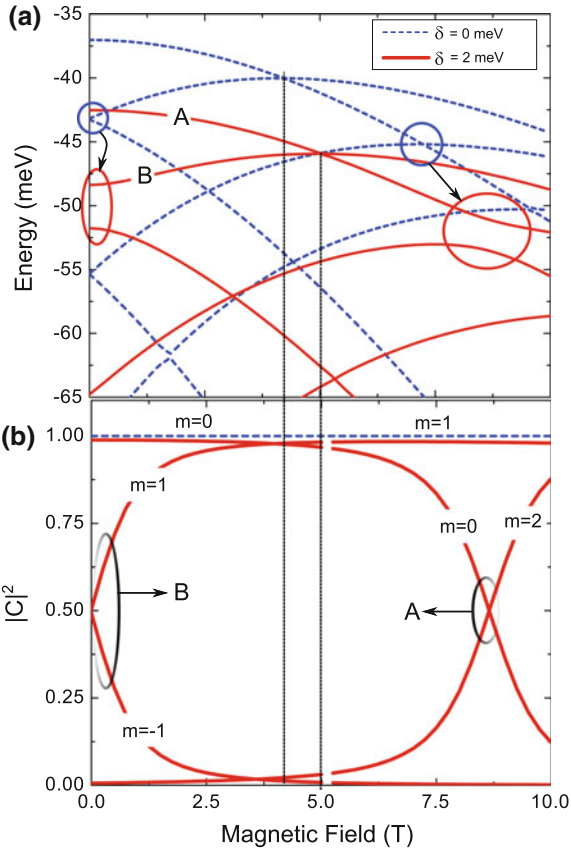

Fig. 3.13 **a** Calculated energy levels in a quantum ring for the top valence subband: solid curves correspond to an eccentric ring while the dashed curves are calculated for a cylindrical geometry. **b** Calculated weight coefficients for the ground state as function of magnetic field strength for the symmetric and asymmetric cases

this calculation we have omitted the spin splitting. Note the degeneracy lifting highlighted in the picture that reduces the effective diamagnetic shift of the valence band ground state. This can also be traced down to the character modulation with magnetic field as the symmetry is reduced. In Fig. 3.13b the weight coefficients resulting from the diagonalization of the valence band Hamiltonian have been depicted. The symmetric case shows the expected angular momentum crossings for the quantum ring states with sharp transitions of the character. In constrast, the eccentricity softens the character evolution with field.

3.5 Spin Manipulation Through SO Coupling

Additionally to the angular momentum hybridization, the modification of the wavefunction shape also translates into the spin tuning as reported in Sect. 3.4.1. According to the results presented in Fig. 3.9, the spin splitting energy is also affected by the

modifications induced in the effective confinement and this appears as a monotonic tuning of the g-factor. Such effects can be unveiled once the spin-orbit coupling is introduced into the electronic structure description as reported by several authors [75–81].

The expression for the spin orbit Hamiltonian assuming the confinement profile that includes all the asymmetry terms is given by

$$\begin{aligned} H_R = 2\alpha_c\sigma_z \Bigg[& \left(-\frac{a_1}{\rho^2} + a_2\rho^2 + \delta\rho^2\cos^2(\varphi)\right)\frac{eB}{2c\hbar} - i\delta\sin(\varphi)\cos(\varphi) \\ & - i\delta\rho\sin(\varphi)\cos(\varphi)\frac{\partial}{\partial\rho} - \frac{i}{\rho^2}\left(-\frac{a_1}{\rho^2} + a_2\rho^2 + \delta\rho^2\cos^2(\varphi)\right)\frac{\partial}{\partial\varphi}\Bigg] \\ & - \alpha_c\frac{\partial V}{\partial z}\left\{\sigma_+\left[e^{-i\varphi}\left(\frac{\partial}{\partial\rho} - \frac{i}{\rho}\frac{\partial}{\partial\varphi} + \frac{eB}{2c\hbar}\rho + \frac{1}{\rho}\right)\right]\right. \\ & \left. - \sigma_-\left[e^{i\varphi}\left(\frac{\partial}{\partial\rho} + \frac{i}{\rho}\frac{\partial}{\partial\varphi} - \frac{eB}{2c\hbar}\rho + \frac{1}{\rho}\right)\right]\right\}, \end{aligned} \tag{3.8}$$

with $\sigma_\pm = 1/2(\sigma_x \pm \sigma_y)$, being σ_i the components of the Pauli matrices.

In turn, we can separate the spin orbit effects induced by confinement and asymmetry into first or higher order contributions. The latter ones are produced by the coupling of previously unperturbed levels and appear strongly when these levels cross inducing (or enhancing) anticrossings, mostly at higher fields. The first order terms appear already at vanishing fields and may provoke, for instance, the tuning of the effective Landé factor. We shall focus the discussion on these ones.

We can extract from (3.8) the diagonal terms that contribute to the first order renormalization of the spin-splitting of the ground state with $m = 0$ for $B \to 0$, $\Delta E_{spin} = \Delta E^{(0)} + \Delta E^{(1)}$, in the basis of unperturbed states introduced by (3.5). The zero order value is essentially the Zeeman splitting given by

$$\Delta E^{(0)} = g^*\mu_B B, \tag{3.9}$$

and, in the case of the conduction band spin orbit Hamiltonian, the first order contribution will be reduced to

$$\Delta E^{(1)} = \frac{4m_0\alpha_c}{\hbar^2}\left[a_2\left\{1 + \text{sign}(\delta)\frac{e^2}{2 - \left[1 + \text{sign}(\delta)\right]e^2}\right\}\langle\rho^2\rangle - a_1\left\langle\frac{1}{\rho^2}\right\rangle\right]\mu_B B. \tag{3.10}$$

For the valence band, the expression is analogous. This allows introducing the first order correction to the Landé factor defined as $g^{(1)} \equiv \Delta E^{(1)}/(\mu_B B)$ and one may now assess the relative effect of the confinement shape on the spin splitting. Note in Fig. 3.14a that by fixing a_2 and increasing a_1 the quantum ring radius increases as a result of widening the inner rim. Such a modulation of the confinement profile can either increase or decrease the Landé factor correction according to the value of the

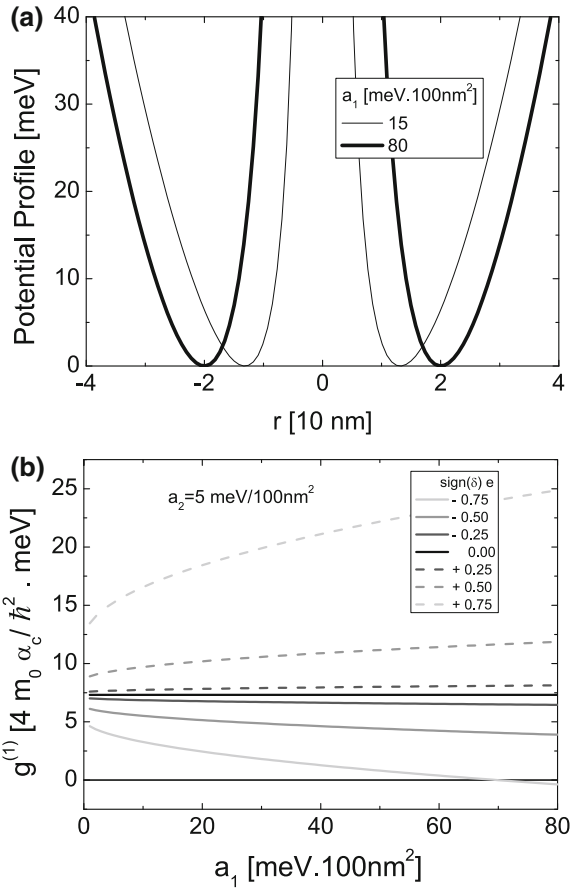

Fig. 3.14 **a** In-plane confinement profiles for fixed a_2 and varying a_1. **b** Calculated first order correction of the Landé factor for fixed a_2 and varying eccentricity as function of a_1

eccecntricity and the sign of δ as has been displayed in Fig. 3.14b. For large enough rings, the eccentricity may even lead to an absolute reduction of the Landé factor.

If in contrast, the parameter a_1 is fixed while increasing a_2, the confinement potential shrinks as a result of the reduction of the external radius. This condition is plotted in Fig. 3.15a while the corresponding first order correction to the g-factor appears in panel(b). Such a reduction of the quantum ring radius provokes a monotonic increase of this factor regardless the value of the eccentricity.

To assess the absolute values of the g-factor correction, and the relevance of antimonides in that respect, we may contrast two systems with relatively small and large spin orbit coupling: GaAs, GaSb and InSb, respectively. For electrons in the conduction band of these materials, the Rashba coefficient is $\alpha_c^{\mathrm{GaAs}} = 5.206$ e Å^2, $\alpha_c^{\mathrm{GaSb}} = 33.1$ e Å^2 and $\alpha_c^{\mathrm{InSb}} = 523.0$ e Å^2 [83], respectively. According to these values the units used in Figs. 3.14 and 3.15 for the Landé factor corrections are 0.0028 for GaAs, 0.0168 for GaSb and 0.28 for InSb.

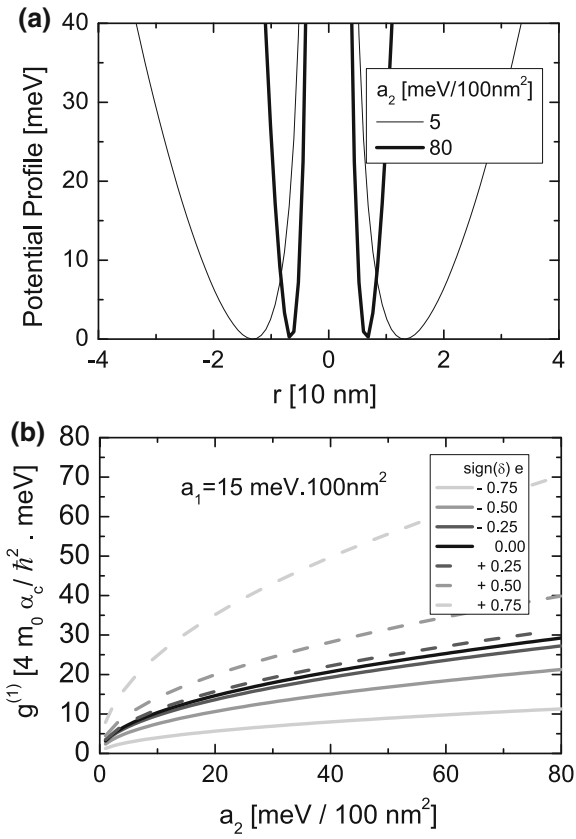

Fig. 3.15 **a** In-plane confinement profiles for fixed a_1 and varying a_2. **b** Calculated first order correction of the Landé factor for fixed a_1 and varying eccentricity as function of a_2

For $a_1 = 0$, the first order correction to the Zeeman splitting induced by the spin orbit coupling can be calculated exactly for the ground state of a quantum dot [82]

$$g^{(1)} = \frac{2m_0\alpha_c}{\mu^* R_{\mathrm{QD}}^2}\left[1 + \mathrm{sign}(\delta)\frac{e^2}{2 - \left[1 + \mathrm{sign}(\delta)\right]e^2}\right]. \tag{3.11}$$

This result is depicted in Fig. 3.16 and illustrates how the Landé factor correction grows as the quantum dot volume is reduced be it by shortening R_{QD} or by shrinking the lateral confinement into an ellipse. Thus, the symmetry reduction induced by a finite eccentricity reduces the effective diamagnetic shift of the ground state in a quantum ring as the angular momentum states become intermixed. In turn, the spin states are also modified by both asymmetries and lateral confinement. For a quantum ring, such a modulation is not trivial and depends on the way the confinement shape is modified. Overall, reducing the volume leads to an absolute increase of the Landé factor as discussed for the quantum dot case. The monotonic increase of the

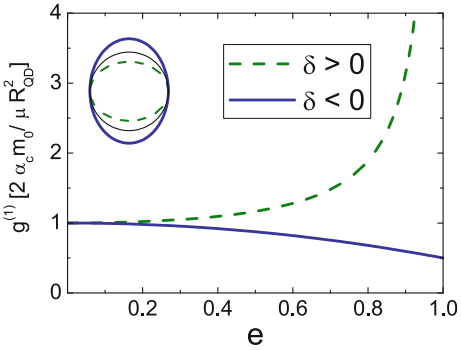

Fig. 3.16 Calculated first order correction of the Landé factor as function of the eccentricity for a quantum dot according to [82]

experimental effective g-factor displayed in Fig. 3.9 can be unambiguously ascribed to the effective confinement shrinkage and symmetry reduction caused by the vertical drift of the hole wavefunction in the SRL.

3.6 Conclusions

In summary, we have presented experimental evidence on the tuning of the electronic structure of type-II InAs/GaAsSb quantum dots under vertical electric and magnetic fields. Induced by the external bias, the drift of the hole wavefunction in the soft confinement of the GaAsSb layer encompasses a wide range of geometrical and also topological changes in the effective potential. These changes cannot be easily induced in type-I systems and provide a rich variety of insights on the way geometry affects the electronic structure and thus the optical response. The observed effects have been emulated with theoretical approaches that include electronic confinement, strain fields and spin effects on the same foot. In particular, we report how the application of an external bias tunes independently the electron and hole confinement geometry. Under certain bias conditions, the hole confinement topology changes and magnetic field oscillations are observed. The oscillations follow the orbital quantization of the hole state and are thus susceptible to the confinement size and eccentricity. Overall, thanks to the large spin-orbit coupling of III-Sb compounds, the modulation of hole orbital quantization is also accompanied by the tuning of the exciton g-factor and might pave the way for the voltage control of spin degrees of freedom as required by nanotechnologies.

Acknowledgements The authors gratefully acknowledge financial support from EURAMET European agency through grant EMPIR-17FUN06/f02, from Spanish MINEICO grants TEC2015-72009-EXP, TEC2015-64189-C3-2-R, MAT2016-77491-C2-1-R, EUIN2017-88844, from Comunidad de Madrid grant S2013/MAE-2780, and from CSIC grant I-COOP-2017-COOPB20320. Support from Brazilian agencies is also acknowledged through FAPESP grant 2014/02112-3 and CNPq grant 306414/2015-5.

Appendix: Axially-Symmetric Model Details

For the sake of simplicity, the SRL model presented in the Sect. 3.3 has been slightly modified to discuss magnetic field induced effects within the $\mathbf{k} \cdot \mathbf{p}$ formalism. Instead of a continuous layer conformal to the QD, we have consider an overlayer of finite extension. The number of geometrical parameters hence reduces to six as can be seen in Fig. 3.17. This approximation simplifies the strain calculation, as border effects on the overlayer are avoided. There is no impact on the results from a qualitative point of view, since, as we will show below, the hole wavefunction localizes either in the surroundings of the QD or in its interior. The material band parameters are extracted from [84]. The parameters used to describe the spin Zeeman effect are shown in Table 3.1. The values of the compounds GaInAs and GaAsSb are obtained through linear interpolation when no bowing parameters is reported.

In the implementation of the model we have adopted a further approximation, only the band edges are consider to the be discontinuous across the nanostructure interfaces. The motivation is two-fold. In first place we preserve the Hermiticity of the Hamiltonian avoiding the problem of the operator symmetrization. In second place, we simplify the calculation of the Hamiltonian matrix elements, which can be computed just once significantly speeding up the construction of the Hamiltonian. Such an approximation is justified for QDs exhibiting a type-I alignment, as the wavefunction is strongly localized in a homogeneous domain, inside of the nanostructure. However, our system could exhibit either type-I or type-II band alignment, meaning that in the latter case either the conduction and valence band states will be

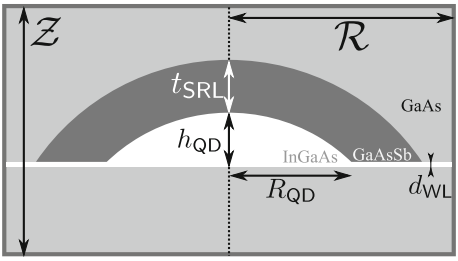

Fig. 3.17 Depiction of the geometrical model to describe a QD of radius R_{QD} and height h_{QD}, a SRL of thickness t_{SRL} and a wetting-layer of thickness d_{WL} embedded in hard-wall cylinder of radius $\mathcal{R}$ and height $\mathcal{Z}$

Table 3.1 Parameters related with the spin Zeeman effect. The values of GaAs and InAs are taken from [83] (p. 221) and those of GaSb from [85] (pp. 486 and 491)

	g	k	q
GaAs	−0.44	1.20	0.01
InAs	−14.90	7.60	0.39
GaSb	−9.25	4.60	0.00

hosted by different materials. To solve that issue, we decided to decouple both bands which implies to nullify the Kane parameter. Hence the holes states will be described by a 6×6 Hamiltonian and the electron states by a 2×2 Hamiltonian. As most of the phenomenology observed in the experiments is associated to the properties of the hole states, we consider this approximation as safe in the context of the current study.

The strain field is calculated as if the semiconductor material were elastically isotropic. The procedure is based on the Eshelby's inclusions method [86]. The lattice mismatch between the quantum dot and overlayer with respect to the GaAs matrix can be computed independently because of the linearity of elasticity equations. Analytical and compact expressions are obtained for the Fourier transform of the strain tensor [87]. In the past, we successfully used this method to explain Raman [88, 89] and middle energy ion scattering [90] experiments.

The basic equations of the $\mathbf{k} \cdot \mathbf{p}$ method are very compact. However, when many bands are considered to be in interaction a broad set of choices in terms of notation and basis expansion appears. To maintain the consistency in the development of the model, we follow the derivation of Trebin et al. [91, 92]. The final Hamiltonian results of adding the $\mathbf{k} \cdot \mathbf{p}$, the strain interactions (Bir-Pikus Hamiltonian) and the magnetic interactions:

$$H = H_{\mathbf{k}\cdot\mathbf{p}} + H_{\varepsilon} + H_B. \tag{3.12}$$

We have neglected the linear k_i terms in the valence-valence interaction, the quadratic $k_i k_j$ and ε_{ij} terms in the conduction-valence interaction and the $k_i \varepsilon_{jk}$ in the strain-induced interactions. The solution of the Schrödinger-like equation is obtained by expanding the envelope: wavefunction of (3.2) in the eigenfunctions of a hard-wall cylinder:

$$\mathcal{F}^{(M)}_{m,k} = \sum_{\alpha,\mu} \mathcal{N}^{(m)}_{\alpha} J_m\left(k^{(m)}_{\alpha} \rho/\mathcal{R}\right) \sqrt{2/\mathcal{Z}} \sin\left[\mu\pi\left(z/\mathcal{Z} - 1/2\right)\right], \tag{3.13}$$

where $J_m(x)$ is the Bessel function of order m, $k^{(m)}_{\alpha}$ is its zero number $\alpha = 1, 2, \ldots$, $\mu = 1, 2, \ldots, \mathcal{R}$ and $\mathcal{Z}$ are the radius and height of the expansion cylinder and

$$N^{(m)}_{\alpha} = \frac{\sqrt{2}}{\mathcal{R}\left|J_{m+1}\left(k^{(m)}_{\alpha}\right)\right|} \tag{3.14}$$

is the normalization of the radial part. This definitions ensure the orthonormality of the expansion basis. By writing the Hamiltonian (3.12) in the associated representation, the electron and hole states are obtained after solving the eigenvalue problem. A similar procedure was followed in [93, 94]. Further details can be found in [95].

References

1. P. Michler, A. Kiraz, C. Becher, W.V. Schoenfeld, P.M. Petroff, L. Zhang, E. Hu, A. Imamoglu, Science **290**(5500), 2282 (2000)
2. D. Englund, D. Fattal, E. Waks, G. Solomon, B. Zhang, T. Nakaoka, Y. Arakawa, Y. Yamamoto, J. Vuckovic, Phys. Rev. Lett. **95**(1), 013904 (2005)
3. C. Santori, D. Fattal, J. Vuckovic, G.S. Solomon, Y. Yamamoto, Nature **419**(6907), 594 (2002)
4. Z. Yuan, B.E. Kardynal, R.M. Stevenson, A.J. Shields, C.J. Lobo, K. Cooper, N.S. Beattie, D.A. Ritchie, M. Pepper, Science **295**, 102 (2002)
5. C.L. Salter, R.M. Stevenson, I. Farrer, C.A. Nicoll, D.A. Ritchie, A.J. Shields, Nature **465**(7298), 594 (2010)
6. J.P. Lee, E. Murray, A.J. Bennett, D.J.P. Ellis, C. Dangel, I. Farrer, P. Spencer, D.A. Ritchie, A.J. Shields, Appl. Phys. Lett. **110**(7), 071102 (2017)
7. P. Munnelly, T. Heindel, A. Thoma, M. Kamp, S. Höfling, C. Schneider, S. Reitzenstein, ACS Photonics **4**(4), 790 (2017)
8. B. Dzurnak, R.M. Stevenson, J. Nilsson, J.F. Dynes, Z.L. Yuan, J. Skiba-Szymanska, I. Farrer, D.A. Ritchie, A.J. Shields, Appl. Phys. Lett. **107**(26), 261101 (2015)
9. K. Matsuda, S.V. Nair, H.E. Ruda, Y. Sugimoto, T. Saiki, K. Yamaguchi, Appl. Phys. Lett. **90**(1), 013101 (2007)
10. M.P. Young, C.S. Woodhead, J. Roberts, Y.J. Noori, M.T. Noble, A. Krier, E.P. Smakman, P.M. Koenraad, M. Hayne, R.J. Young, AIP Adv. **4**(11), 117127 (2014)
11. J.R. Orchard, C. Woodhead, J. Wu, M. Tang, R. Beanland, Y. Noori, H. Liu, R.J. Young, D.J. Mowbray, ACS Photonics **4**(7), 1740 (2017)
12. K. Akahane, N. Yamamoto, N. Ohtani, Phys. E **21**(2–4), 295 (2004)
13. H.Y. Liu, M.J. Steer, T.J. Badcock, D.J. Mowbray, M.S. Skolnick, P. Navaretti, K.M. Groom, M. Hopkinson, R.A. Hogg, Appl. Phys. Lett. **86**(14), 143108 (2005)
14. J.M. Ripalda, D. Granados, Y. González, A.M. Sánchez, S.I. Molina, J.M. García, Appl. Phys. Lett. **87**(20), 202108 (2005)
15. M. Geller, C. Kapteyn, L. Müller-Kirsch, R. Heitz, D. Bimberg, Appl. Phys. Lett. **82**(16), 2706 (2003)
16. D. Alonso-Álvarez, B. Alén, J.M. García, J.M. Ripalda, Appl. Phys. Lett. **91**, 263103 (2007)
17. P. Klenovský, V. Křápek, D. Munzar, J. Humlíček, Appl. Phys. Lett. **97**(20), 203107 (2010)
18. J.M. Ulloa, J.M. Llorens, M. del Moral, M. Bozkurt, P.M. Koenraad, A. Hierro, J. Appl. Phys. **112**(7), 074311 (2012)
19. M. Hayne, R.J. Young, E.P. Smakman, T. Nowozin, P. Hodgson, J.K. Garleff, P. Rambabu, P.M. Koenraad, A. Marent, L. Bonato, A. Schliwa, D. Bimberg, J. Phys. D: Appl. Phys. **46**(26), 264001 (2013)
20. J.M. Llorens, L. Wewior, E.R.C.d. Oliveira, J.M. Ulloa, A.D. Utrilla, A. Guzmán, A. Hierro, B. Alén. Appl. Phys. Lett. **107**(18), 183101 (2015)
21. S. Nadj-Perge, V.S. Pribiag, J.W.G. van den Berg, K. Zuo, S.R. Plissard, E.P.A.M. Bakkers, S.M. Frolov, L.P. Kouwenhoven, Phys. Rev. Lett. **108**(16), 166801 (2012)
22. V. Mourik, K. Zuo, S.M. Frolov, S.R. Plissard, E.P.A.M. Bakkers, L.P. Kouwenhoven, Science **336**(6084), 1003 (2012)
23. J.M. Ulloa, J.M. Llorens, B. Alén, D.F. Reyes, D.L. Sales, D. González, A. Hierro, Appl. Phys. Lett. **101**(25), 253112 (2012)
24. P.W. Fry, I.E. Itskevich, D.J. Mowbray, M.S. Skolnick, J.J. Finley, J.A. Barker, E.P. O'Reilly, L.R. Wilson, I.A. Larkin, P.A. Maksym, M. Hopkinson, M. Al-Khafaji, J.P.R. David, A.G. Cullis, G. Hill, J.C. Clark, Phys. Rev. Lett. **84**(4), 733 (2000)
25. R.J. Warburton, C. Schulhauser, D. Haft, C. Schaflein, K. Karrai, J.M. Garcia, W. Schoenfeld, P.M. Petroff, Phys. Rev. B **65**(11), 113303 (2002)
26. J.J. Finley, M. Sabathil, P. Vogl, G. Abstreiter, R. Oulton, A.I. Tartakovskii, D.J. Mowbray, M.S. Skolnick, S.L. Liew, A.G. Cullis, M. Hopkinson, Phys. Rev. B **70**(20), 201308 (2004)
27. P. Offermans, P.M. Koenraad, J.H. Wolter, D. Granados, J.M. García, V.M. Fomin, V.N. Gladilin, J.T. Devreese, Appl. Phys. Lett. **87**(13), 131902 (2005)

28. J.M. García, B. Alén, J.P. Silveira, D. Granados, in *Physics of Quantum Rings*, ed. by V.M. Fomin, 1st edn. (Springer, Berlin, Heidelberg, 2014), Chap. 3
29. W. Sheng, J.P. Leburton, Phys. Rev. B **67**(12), 125308 (2003)
30. S. Ramanathan, G. Petersen, K. Wijesundara, R. Thota, E.A. Stinaff, M.L. Kerfoot, M. Scheibner, A.S. Bracker, D. Gammon, Appl. Phys. Lett. **102**(21), 213101 (2013)
31. K.L. Janssens, B. Partoens, F.M. Peeters, Phys. Rev. B **67**, 235325 (2003)
32. P. Klenovský, P. Steindl, D. Geffroy, Sci. Rep. **7**, srep45568 (2017)
33. N. Pavarelli, T.J. Ochalski, H.Y. Liu, K. Gradkowski, M. Schmidt, D.P. Williams, D.J. Mowbray, G. Huyet, Appl. Phys. Lett. **101**(23), 231109 (2012)
34. A. Hospodková, M. Zíková, J. Pangrác, J. Oswald, J. Kubištová, K. Kuldová, P. Hazdra, E. Hulicius, J. Phys. D: Appl. Phys. **46**(9), 095103 (2013)
35. D.A.B. Miller, D.S. Chemla, T.C. Damer, A.C. Gossard, W. Weigmann, T.H. Wood, C.A. Burrus, Phys. Rev. Lett. **53**, 2173 (1984)
36. J.A. Barker, E.P. O'Reilly, Phys. Rev. B **61**(20), 13840 (2000)
37. B. Alén, J. Bosch, D. Granados, J. Martínez-Pastor, J.M. García, L. González, Phys. Rev. B **75**(4), 045319 (2007)
38. Y.D. Jang, T.J. Badcock, D.J. Mowbray, M.S. Skolnick, J. Park, D. Lee, H.Y. Liu, M.J. Steer, M. Hopkinson, Appl. Phys. Lett. **92**(25), 251905 (2008)
39. W.T. Hsu, Y.A. Liao, F.C. Hsu, P.C. Chiu, J.I. Chyi, W.H. Chang, Appl. Phys. Lett. **99**(7), 073108 (2011)
40. A.G. Taboada, J.M. Llorens, D. Alonso-Álvarez, B. Alén, A. Rivera, Y. González, J.M. Ripalda, Phys. Rev. B **88**(8), 085308 (2013)
41. S. Birner, T. Zibold, T. Andlauer, T. Kubis, M. Sabathil, A. Trellakis, P. Vogl, I.E.E.E. Trans. Electron Devices **54**(9), 2137 (2007). https://doi.org/10.1109/TED.2007.902871
42. J. Tatebayashi, A. Khoshakhlagh, S.H. Huang, G. Balakrishnan, L.R. Dawson, D.L. Huffaker, D.A. Bussian, H. Htoon, V. Klimov, Appl. Phys. Lett. **90**(26), 261115 (2007)
43. K.S. Hsu, T.T. Chiu, W.H. Lin, K.L. Chen, M.H. Shih, S.Y. Lin, Y.C. Chang, Appl. Phys. Lett. **98**(5), 051105 (2011)
44. A.D. Utrilla, J.M. Ulloa, A. Guzman, A. Hierro, Appl. Phys. Lett. **103**(11), 111114 (2013)
45. A. Gonzalo, A.D. Utrilla, D.F. Reyes, V. Braza, J.M. Llorens, D.F. Marrón, B. Alén, T. Ben, D. González, A. Guzman, A. Hierro, J.M. Ulloa, Sci. Rep. **7**(1), 4012 (2017)
46. I. Ramiro, J. Villa, C. Tablero, E. Antolín, A. Luque, A. Martí, J. Hwang, J. Phillips, A.J. Martin, J. Millunchick, Phys. Rev. B **96**(12), 125422 (2017)
47. W.S. Liu, H.M. Wu, F.H. Tsao, T.L. Hsu, J.I. Chyi, Solar Energy Mater. Solar Cells **105**, 237 (2012)
48. Y. Cheng, M. Fukuda, V.R. Whiteside, M.C. Debnath, P.J. Vallely, T.D. Mishima, M.B. Santos, K. Hossain, S. Hatch, H.Y. Liu, I.R. Sellers, Solar Energy Mater. Solar Cells **147**, 94 (2016)
49. S. Hatch, J. Wu, K. Sablon, P. Lam, M. Tang, Q. Jiang, H. Liu, Optics Express **22**(103), A679 (2014)
50. A.D. Utrilla, D.F. Reyes, J.M. Llorens, I. Artacho, T. Ben, D. González, Z. Gačević, A. Kurtz, A. Guzmán, A. Hierro, J.M. Ulloa. Solar Energy Mater. and Solar Cells **159**, 282 (2017)
51. M. Hayne, B. Bansal, Luminescence **27**(3), 179 (2012)
52. V.M. Fomin, in *Physics of Quantum Rings*, 2nd edn., ed. by V.M. Fomin (Springer, Cham, 2018), Chap. 1
53. I.R. Sellers, I.L. Kuskovsky, A.O. Govorov, B.D. McCombe, in *Physics of Quantum Rings*, 1st edn., ed. by V.M. Fomin (Springer, Berlin, Heidelberg, 2014), Chap. 11
54. Y. Aharonov, D. Bohm, Phys. Rev. **115**(3), 485 (1959)
55. A.O. Govorov, S.E. Ulloa, K. Karrai, R.J. Warburton, Phys. Rev. B Rapid Comm. **66**, 081309R (2002)
56. M.D. Teodoro, V.L. Campo Jr., V. López-Richard, E. Marega Jr., G.E. Marques, G.J. Salamo, in *Physics of Quantum Rings*, 2nd edn., ed. by V.M. Fomin (Springer, Cham, 2018), Chap. 10
57. V.M. Fomin (ed.), *Physics of Quantum Rings* (Springer, Berlin, Heidelberg, 2014)
58. L.G.G.V. Dias da Silva, S.E. Ulloa, T.V. Shahbazyan, Phys. Rev. B **72**(12), 125327 (2005)

59. M.D. Teodoro, V.L. Campo Jr., V. Lopez-Richard, E. Marega Jr., G.E. Marques, Y. Galvão Gobato, F. Iikawa, M.J.S.P. Brasil, Z.Y. AbuWaar, V.G. Dorogan, Y.I. Mazur, M. Benamara, G.J. Salamo, Phys. Rev. Lett. **104**, 086401 (2010)
60. H.D. Kim, R. Okuyama, K. Kyhm, M. Eto, R.A. Taylor, A.L. Nicolet, M. Potemski, G. Nogues, L.S. Dang, K.C. Je, J. Kim, J.H. Kyhm, K.H. Yoen, E.H. Lee, J.Y. Kim, I.K. Han, W. Choi, J. Song, Nano Lett. **16**(1), 27 (2016)
61. F. Ding, N. Akopian, B. Li, U. Perinetti, A. Govorov, F.M. Peeters, C.C. Bof Bufon, C. Deneke, Y.H. Chen, A. Rastelli, O.G. Schmidt, V. Zwiller, Phys. Rev. B **82**(7), 075309 (2010)
62. B. Li, F.M. Peeters, Phys. Rev. B **83**(11), 115448 (2011)
63. E. Ribeiro, A.O. Govorov, W. Carvalho, G. Medeiros-Ribeiro, Phys. Rev. Lett. **92**(12), 126402 (2004)
64. I.L. Kuskovsky, W. MacDonald, A.O. Govorov, L. Mourokh, X. Wei, M.C. Tamargo, M. Tadic, F.M. Peeters, Phys. Rev. B **76**, 035342 (2007)
65. M. Royo, C. Segarra, A. Bertoni, G. Goldoni, J. Planelles, Phys. Rev. B **91**(11), 115440 (2015)
66. J.M. Llorens, E.R. Cardozo de Oliveira, L. Wevior, V. Lopes-Oliveira, V. López-Richard, J.M. Ulloa, M.D. Teodoro, G.E. Marques, A. García-Cristóbal, G.Q. Hai, B. Alén, ArXiv: 1710.08828 (2017)
67. K.J. Nash, M.S. Skolnick, P.A. Claxton, J.S. Roberts, Phys. Rev. B **39**(15), 10943 (1989)
68. F. Ding, B. Li, F.M. Peeters, A. Rastelli, V. Zwiller, O.G. Schmidt, in *Physics of Quantum Rings*, 1st edn., ed. by V.M. Fomin (Springer, Berlin, Heidelberg, 2014), Chap. 12
69. D. Alonso-Álvarez, B. Alén, J.M. Ripalda, A. Rivera, A.G. Taboada, J.M. Llorens, Y. González, L. González, F. Briones, APL Mater. **1**(2), 022112 (2013)
70. M.D. Teodoro, A. Malachias, V. Lopes-Oliveira, D.F. Cesar, V. Lopez-Richard, G.E. Marques, E. Marega, M. Benamara, Y.I. Mazur, G.J. Salamo, J. Appl. Phys. **112**(1), 014319 (2012)
71. V. Krapek, P. Klenovsky, T. Sikola, Phys. Rev. B **92**(19), 195430 (2015)
72. W.C. Tan, J.C. Inkson, Semicond. Sci. Technol. **11**(11), 1635 (1996)
73. V. Lopes-Oliveira, Y.I. Mazur, L.D. de Souza, L.A.B. Marçal, J. Wu, M.D. Teodoro, A. Malachias, V.G. Dorogan, M. Benamara, G.G. Tarasov, E. Marega, G.E. Marques, Z.M. Wang, M. Orlita, G.J. Salamo, V. Lopez-Richard, Phys. Rev. B **90**(12), 125315 (2014)
74. V. Lopes-Oliveira, L.K. Castelano, G.E. Marques, S.E. Ulloa, V. Lopez-Richard, Phys. Rev. B **92**(3), 035441 (2015)
75. N. Ares, V.N. Golovach, G. Katsaros, M. Stoffel, F. Fournel, L.I. Glazman, O.G. Schmidt, S. De Franceschi, Phys. Rev. Lett. **110**(4), 046602 (2013)
76. A.J. Bennett, M.A. Pooley, Y. Cao, N. Sköld, I. Farrer, D.A. Ritchie, A.J. Shields, Nat. Commun. **4**, 1522 (2013)
77. P. Corfdir, Y. Fontana, B. Van Hattem, E. Russo-Averchi, M. Heiss, A. Fontcuberta i Morral, R.T. Phillips. Appl. Phys. Lett. **105**(22), 223111 (2014)
78. V. Jovanov, T. Eissfeller, S. Kapfinger, E.C. Clark, F. Klotz, M. Bichler, J.G. Keizer, P.M. Koenraad, G. Abstreiter, J.J. Finley, Phys. Rev. B **83**(16), 161303 (2011)
79. F. Klotz, V. Jovanov, J. Kierig, E.C. Clark, D. Rudolph, D. Heiss, M. Bichler, G. Abstreiter, M.S. Brandt, J.J. Finley, Appl. Phys. Lett. **96**(5), 053113 (2010)
80. J.H. Prechtel, F. Maier, J. Houel, A.V. Kuhlmann, A. Ludwig, A.D. Wieck, D. Loss, R.J. Warburton, Phys. Rev. B **91**(16), 165304 (2015)
81. H.M.G.A. Tholen, J.S. Wildmann, A. Rastelli, R. Trotta, C.E. Pryor, E. Zallo, O.G. Schmidt, P.M. Koenraad, A.Y. Silov, Phys. Rev. B **94**(24), 245301 (2016)
82. L. Cabral, F.P. Sabino, V. Lopes-Oliveira, J.L.F. Da Silva, M.P. Lima, G.E. Marques, V. Lopez-Richard, Phys. Rev. B **95**(20), 205409 (2017)
83. R. Winkler, *Spin-Orbit Coupling Effects in Two-dimensional Electron and Hole Systems* (Springer, Berlin, 2003)
84. I. Vurgaftman, J. Meyer, L. Ram-Mohan, J. Appl. Phys. **89**, 5815 (2001)
85. F. Meier, B.P. Zakharchenya, *Optical Orientation (Modern Problems in Condensed Matter Sciences)* (Elsevier, Amsterdam, 1984)
86. J.D. Eshelby, Proc. R. Soc. Lond. A **241**(1226), 376 (1957)
87. A.D. Andreev, J.R. Downes, D.A. Faux, E.P. O'Reilly, J. Appl. Phys. **86**(1), 297 (1999)

88. A. Cros, N. Garro, J.M. Llorens, A. García-Cristóbal, A. Cantarero, N. Gogneau, E. Monroy, B. Daudin, Phys. Rev. B **73**(11), 115313 (2006)
89. N. Garro, A. Cros, J.M. Llorens, A. García-Cristóbal, A. Cantarero, N. Gogneau, E. Sarigiannidou, E. Monroy, B. Daudin, Phys. Rev. B **74**(7), 075305 (2006)
90. D. Jalabert, J. Coraux, H. Renevier, B. Daudin, M.H. Cho, K.B. Chung, D.W. Moon, J.M. Llorens, N. Garro, A. Cros, A. García-Cristóbal, Phys. Rev. B **72**(11), 115301 (2005)
91. H.R. Trebin, U. Rössler, R. Ranvaud, Phys. Rev. B **20**(2), 686 (1979)
92. R. Winkler, *Spin-Orbit Coupling Effects in Two-Dimensional Electron and Hole Systems* (Springer, Berlin, Heidelberg, 2003)
93. M. Tadić, F.M. Peeters, K.L. Janssens, Phys. Rev. B **65**(16), 165333 (2002)
94. M. Tadić, F.M. Peeters, Phys. Rev. B **71**(12), 125342 (2005)
95. J.M. Llorens Montolio, Estructura electrónica y propiedades ópticas de puntos cuánticos autoorganizados. Ph.D. thesis, Institut de Ciéncia dels Materials, Universitat de Valéncia, 2007

Part II
Fabrication and Characterization

Chapter 4
Self-organized Quantum Rings: Physical Characterization and Theoretical Modeling

V.M. Fomin, V.N. Gladilin, J. van Bree, M.E. Flatté, J.T. Devreese and P.M. Koenraad

Abstract An adequate modeling of self-organized quantum rings is possible only on the basis of the modern characterization of those nanostructures. We discuss an atomic-scale analysis of the indium distribution in self-organized InGaAs quantum rings (QRs). The analysis of the shape, size and composition of self-organized InGaAs QRs at the atomic scale reveals that AFM only shows the material coming out of the QDs during the QR formation. The remaining QD material, as observed by Cross-Sectional Scanning Tunneling Microscopy (X-STM), shows an asymmetric indium-rich crater-like shape with a depression rather than an opening at the center and determines the observed ring-like electronic properties of QR structures. A theoretical model of the geometry and materials properties of the self-organized QRs is developed on that basis and the magnetization is calculated as a function of the applied magnetic field. Although the real QR shape differs strongly from an idealized circular-symmetric open-ring structure, Aharonov-Bohm-type oscillations in the magnetization have been predicted to survive. They have been observed using the torsion magnetometry on InGaAs QRs. Large magnetic moments of QRs are shown

V.M. Fomin (✉)
Institute for Integrative Nanosciences, IFW Dresden, Dresden, Germany
e-mail: v.fomin@ifw-dresden.de

V.N. Gladilin · J.T. Devreese
Theory of Quantum and Complex Systems, University of Antwerp, Antwerpen, Belgium
e-mail: vladimir.gladilin@uantwerpen.be

J.T. Devreese
e-mail: jozef.devreese@gmail.com

J. van Bree
Institute for Molecular Engineering, University of Chicago, Chicago, USA
e-mail: jvanbree@uchicago.edu

M.E. Flatté
Department of Physics and Astronomy, University of Iowa, Iowa, USA
e-mail: michael_flatte@mailaps.org

P.M. Koenraad
Photonics and Semiconductor Nanophysics, Eindhoven University of Technology, Eindhoven, The Netherlands
e-mail: P.M.Koenraad@tue.nl

V.M. Fomin (ed.), *Physics of Quantum Rings*, NanoScience and Technology,
https://doi.org/10.1007/978-3-319-95159-1_4

to originate from dissipationless circulating currents in the ground state of an electron or hole in the QR. Examples of prospective applications of QRs are presented that do and do not utilize the topological properties of QRs.

4.1 Introduction

Remarkable advancements in the field of self-assembled quantum rings (QRs) are a result of mutually stimulating developments of novel fabrication technologies, powerful characterization instruments and adequate theoretical approaches. A striking example is the rapidly progressing production and investigation of $In_xGa_{1-x}As$ self-assembled QRs, which are represented in detail in Chaps. 7 and 8 and [1–4]. A deep insight into the structure of QRs and quantum dots is obtained on the base of the Cross-Sectional Scanning Tunneling Microscopy (X-STM), see, for instance, Chap. 5 and reviews [5, 6]. In the present Chapter, we demonstrate that a high level of complexity is needed for a dedicated theoretical model to adequately represent the specific features of QRs as determined by X-STM. The model of a self-assembled QR, which is *singly connected* and *anisotropic,* suggested in [7, 8] has found a vast number of applications and developments. In particular, it was used to demonstrated that Aharonov–Bohm oscillations in the magnetization and the magnetic susceptibility peak persist even though self-assembled QRs are singly connected and show a pronounced shape anisotropy, to interpret the magnetization behavior of a self-assembled QR in a nice quantitative agreement with the experiment [9], to demonstrate that inherent structural asymmetry combined with the interparticle Coulomb interactions, plays a crucial role in the diamagnetic shift of excitons and biexcitons in self-assembled QRs [10], to analyze effects due to a tensile-strained insertion layer on strain and electronic structure of self-assembled QRs [11, 12]. Using significantly simplified models of the QR shape, only qualitative conclusions could be drawn, e.g., on the energy spectra [13] and magnetic response [14].

$In_xGa_{1-x}As$ QRs are formed by capping self-organized quantum dots (QDs) grown by Stranski-Krastanov (SK) mode with a layer thinner than the dot height and subsequent annealing [1]. During this process, the QD material suffers an anisotropic redistribution, resulting in elongated ring-shaped islands on the surface, with crater-like holes in their centers as was shown with AFM measurements [1]. The dot-to-ring transition has been attributed to a dewetting process which expels indium from the QD [15] and a simultaneous temperature dependent Ga–In alloying process [16]. Capacitance and far-infrared spectroscopy measurements on buried QR structures have provided evidence of the Aharonov-Bohm oscillation [2]. Although no direct measurements were available, an electronic radius of about 14 nm was deduced. This led to the conclusion that the QR shape as determined from AFM topography is preserved when buried [2]. Until [17], however, no structural measurements of buried QRs have been available. Evolution of InAs/GaAs QDs partially capped with GaAs has been experimentally studied as an annealing process transforms them first into QRs and later into holes penetrating the whole cap layer, [18], shape, compo-

sition, and optical emission being monitored by using AFM, X-ray photoemission microscopy, and photoluminescence, respectively. The sizes of self-assembled QRs determined by Cross-Sectional Transmission Electron Microscopy (X-TEM) [19] matched the AFM results. In-plane mapping by grazing-incidence X-ray diffraction [20] has revealed the lateral extent of strained regions in the buried buried In_xGa_{1-x} As QRs; a comparison between strain and composition maps of QDs and QRs allows for inferring on how the QR configuration affects its optical characteristics. Development of conductive scanning microscopy-based characterization tools, allows for the investigation of the electrical properties of individual self-assembled GeSi QRs at the nanoscale by combining the scanning Kelvin microscopy, conductive AFM and scanning capacitance microscopy [21]. On this base, the electrical properties of a QR have been explained by the fact that the QR rim has a lower barrier height with respect to the tip and a higher carrier density, giving rise to a higher conductivity at the rim compared to the QR opening and the wetting layer.

Although detailed measurements of the QR structure and composition are required for quantitative descriptions of the QR magnetization, the fundamental origin of the large magnetic moments can be identified even in simplified models of the QR shape. As the magnetic moment of a semiconductor heterostructure describes the linear response of an electronic state to an applied magnetic field, the origin of the magnetic moment should lie in the eigenstates of the heterostructure in the absence of any magnetic field. For bulk semiconductors the very large magnetic moments originate from the presence of Spin-correlated orbital currents, induced by the spin-orbit interaction [22, 23]. The spatial structure of these spin-correlated orbital currents has been calculated, both analytically and numerically, for a variety of spherically or cylindrically symmetric III-V heterostructures [22, 24]. These dissipationless ground-state currents are fundamentally orbital currents, but they are forced to track the spin of the electronic state through the role of the spin-orbit interaction. Implications of this current picture for other settings [25–29], including topological insulators, have been identified.

For a simply connected topology, the peak spin-correlated orbital currents are located midway between the center of the structure and the edge, along the axes perpendicular to the orientation of the spin. For QRs, however, there are two locations exhibiting peak currents, with counter-propagating directions. Calculations of the spin-correlated orbital currents show that their contribution to the magnetic moment of the spin depends almost entirely on the difference between the outer and inner radius of the QR.

4.2 X-STM Characterization

Measurements of the vertical Stark effect of excitons confined to individual QRs [4] showed rather large dipole moments with opposite sign as compared to QDs [30]. Theoretical calculations indicated that both the observed electronic radius and dipole moment of the QRs were inconsistent with the geometry as determined by

AFM. In order to unambiguously resolve this discrepancy, twenty layers of QRs separated from each other by 18 nm were grown by using solid source molecular-beam epitaxy (MBE) on a Si-doped n-type GaAs (001) substrate and the shape, size, and composition of buried QRs were analyzed at the atomic scale by cross-sectional scanning tunneling microscopy (X-STM) [7, 8]. The X-STM measurements were performed in an ultra-high-vacuum chamber on the orthogonal (110) and $(1\bar{1}0)$ cross-sectional surfaces.

Figure 4.1 shows an AFM image of the surface layer of the structure. The ring-shaped islands (density $10^{10}\,\mathrm{cm}^{-2}$) are elongated along the $[1\bar{1}0]$ direction, with an outer size of about 100 by 70 nm and an average height of about 1 nm. The holes in the center of the islands are asymmetric as well and have a size of 30 by 20 nm and a depth of about 0.5–1.5 nm. Figure 4.2a shows a large scale X-STM image of three of the QR layers. The bright spots correspond to In atoms in the top layer of the cleaved surface. In the image the cross-sections of two flat indium-rich nanostructures can be seen. The averaged height profiles, taken across the middle QR layer in the growth direction between the points A and B, are displayed in Fig. 4.2b. The profiles clearly indicate two peaks in the indium concentration. The highest peak can be attributed to the wetting layer on which the QDs are formed during growth. The presence of the second indium layer is attributed to the accumulation of segregated indium from the wetting layer at the surface of the partial capping layer and to surface migration of indium atoms that have been expelled from the quantum dots during QR formation [31–34]. The separation between the wetting layer and the second indium layer increases with about 2 bilayers towards the nanostructure. This change in separation is in agreement with the height and diameter of the uncapped QRs as measured by

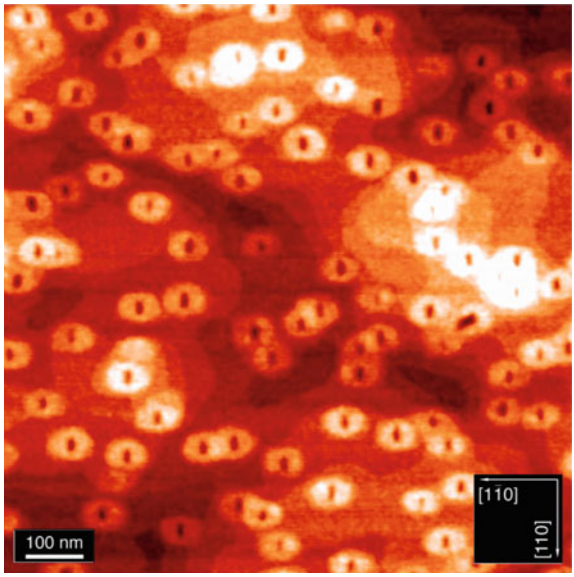

Fig. 4.1 $1 \times 1\ \mu\mathrm{m}^2$ atomic force microscopy image showing the anisotropic distribution of InAs/GaAs dot material after 2 nm GaAs capping and 1 min annealing at growth temperature under As_2 flux. The height scale is 0 (dark) to 2.5 nm (bright). The height of the ring-shaped islands is about 1 nm. Atomic steps can be seen in the image. After [7]

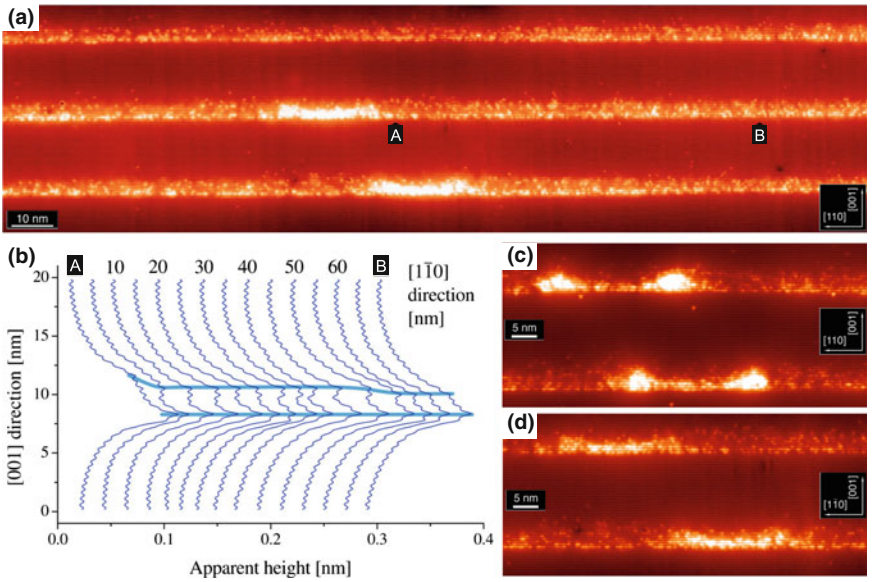

Fig. 4.2 **a** Empty states X-STM image showing two buried QRs, $V_{\text{sample}} = 1.45\,\text{V}$. **b** Averaged apparent height profiles taken in the growth ([001]) direction across the InAs layer between points A and B of panel (**a**). The height profiles are averaged over a distance of 10 nm and show two peaks in the indium concentration. Panels **c** and **d** show the filled states topography images of a cleaved QR in the $(1\bar{1}0)$ plane and (110) plane, respectively, $V_{\text{sample}} = -3\,\text{V}$. The height scale is 0 (dark) to 0.25 nm (bright). After [7]

AFM. Thus at least to some extent the shape of the ring-shaped islands as observed by AFM is preserved after capping.

Enlarged views of the nanostructures can be seen in Fig. 4.2c and d where we show filled states topography images of the orthogonal $(1\bar{1}0)$ and (110) cleavage planes, which correspond with the short and long axis of the ring-shaped islands observed by AFM, respectively. The nanostructures have a crater-like shape which can be attributed to the remainder of the quantum dots after the QR formation process. It is clearly seen that these quantum craters do not have an opening at the center. Furthermore, in the [110] direction, the rim of the quantum crater appears brighter and higher (8 BLs) compared to the $[1\bar{1}0]$ direction where the rim is less pronounced. This asymmetry is attributed to the preferential diffusion of the dot material in the $[1\bar{1}0]$ direction [35] as can be seen from the elongation of the ring-shaped islands in Fig. 4.1. The indium-rich asymmetric crater-like shapes, observed in the X-STM measurements, differ substantially from the ring-shaped islands on the surface of uncapped QR structures. The observation that buried QRs have a smaller size and a larger height than the ring-shaped islands as revealed by AFM, offers an explanation for the observed discrepancies between the measured and theoretical values for the electronic radius and dipole moment of the QRs [36].

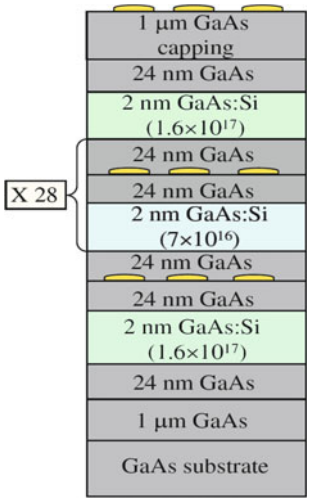

Fig. 4.3 Layer structure of the InAs/GaAs sample for magnetization, consisting of 29 layers of self-assembled InAs nanostructures. The nanostructures are located between two 24 nm GaAs layers. The repeated sequence contains a modulation doping layer, which provides electrons to the nanostructured layers. Two additional doping layers are inserted to accommodate for the depletion toward the capping layer and the undoped substrate. After [9]

Figure 4.3 schematically shows a QR sample used to study persistent currents in QRs. The sample was grown by molecular beam epitaxy and contains 29 mutually decoupled periods [17]. Each period consists of a nanostructured InAs layer, between two 24 nm GaAs layers, and a 2 nm doped ($7 \times 10^{16}\,\mathrm{cm}^{-3}$ Si) GaAs layer, that provides electrons to the InAs nanostructures. Using a one-dimensional Poisson solver, the average number of electrons per nanostructure was estimated to be less than 1.5. The sample is capped by a final nanostructured layer. By performing Atomic Force Microscopy (AFM) on this layer, the nanostructure density was determined to be $9 \times 10^{9}\,\mathrm{cm}^{-2}$ per layer. Photoluminescence (PL) experiments showed a single peak, indicating a unimodal size distribution, at 1.3 eV which is typical for these nanostructures [16]. The FWHM of the PL peak is 40 meV, from which the estimated size dispersion is about 5%.

4.3 Modeling of Shape and Materials Properties

By imaging QRs at a high voltage [$V_{\mathrm{sample}} = -3\,\mathrm{V}$; see Fig. 4.2c and d], electronic contributions to the contrast in the image are minimized and only the true outward surface relaxation due to the lattice mismatch (7%) between the InAs and surrounding GaAs is imaged. The outward relaxation of the cleaved surface is used to determine the indium composition of the quantum craters [37, 38]. The quantum craters are modeled with a varying-thickness InGaAs layer embedded in an infinite GaAs medium. The bottom of the InGaAs layer is assumed to be perfectly flat and parallel to the xy-plane. The height of the $\mathrm{In}_x\mathrm{Ga}_{1-x}\mathrm{As}$ layer as a function of the radial coordinate ρ and the angular coordinate φ is modeled by the expression

$$h(\rho,\varphi) = h_0 + \frac{\left[\tilde{h}_M(\varphi) - h_0\right]\left\{1 - [\rho/\tilde{R}(\varphi) - 1]^2\right\}}{\left\{[\rho - \tilde{R}(\varphi)]/\tilde{\gamma}_0(\varphi)\right\}^2 + 1}, \qquad \rho \le \tilde{R}(\varphi),$$

$$h(\rho,\varphi) = h_\infty + \frac{\tilde{h}_M(\varphi) - h_\infty}{\left\{[\rho - \tilde{R}(\varphi)]/\tilde{\gamma}_\infty(\varphi)\right\}^2 + 1}, \qquad \rho > \tilde{R}(\varphi) \tag{4.1}$$

with

$$\tilde{h}_M(\varphi) = h_M\,(1 + \xi_h \cos 2\varphi)\,, \qquad \tilde{\gamma}_0(\varphi) = \gamma_0\left(1 + \xi_\gamma \cos 2\varphi\right),$$
$$\tilde{\gamma}_\infty(\varphi) = \gamma_\infty\left(1 + \xi_\gamma \cos 2\varphi\right), \qquad \tilde{R}(\varphi) = R\,(1 + \xi_R \cos 2\varphi)\,. \tag{4.2}$$

Here, h_0 corresponds to the thickness at the center of the crater, h_M to the rim height and h_∞ to the thickness of the $In_xGa_{1-x}As$ layer far away from the ring-like structure. The γ_0 and γ_∞ parameters define the inner and outer slopes of the rim, respectively. The parameters ξ_h, ξ_γ, ξ_R describe the ring-shape anisotropy. An example of the QR shape, described by (4.1), is shown in Fig. 4.4a.

A three-dimensional finite element calculation based on elasticity theory has been applied to determine the relaxation of the cleaved surface of the modeled QR. With $R = 10.75\,\text{nm}$, $h_0 = 1.6\,\text{nm}$, $h_M = 3.6\,\text{nm}$, $h_\infty = 0.4\,\text{nm}$, $\gamma_0 = \gamma_\infty = 3\,\text{nm}$, $\xi_h = 0.2$, $\xi_\gamma = -0.25$ and $\xi_R = 0.07$, an indium concentration of 55% (see Fig. 4.5) results in a calculated surface relaxation that matches the measured relaxation of the cleaved surface, as shown in [8]. This set of geometric parameters of a QR is selected as standard for the calculations discussed below, unless stated otherwise.

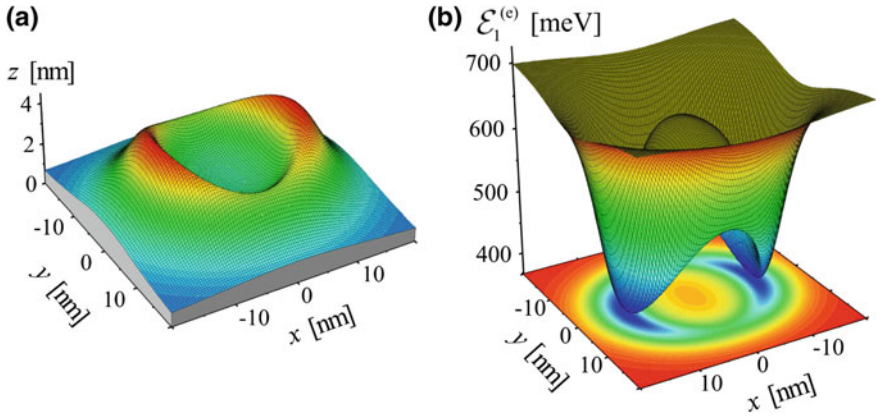

Fig. 4.4 **a** Height of a QR as a function of the radial and the azimuthal coordinates as modeled by (4.1) with $R = 11.5\,\text{nm}$, $h_0 = 1.6\,\text{nm}$, $h_M = 3.6\,\text{nm}$, $h_\infty = 0.4\,\text{nm}$, $\gamma_0 = 3\,\text{nm}$, $\gamma_\infty = 5\,\text{nm}$, $\xi_h = 0.2$, $\xi_\gamma = \xi_R = 0$. **b** The adiabatic potential governing the electron motion in an unstrained $In_{0.6}Ga_{0.4}As$ QR shown in panel (**a**). After [39]

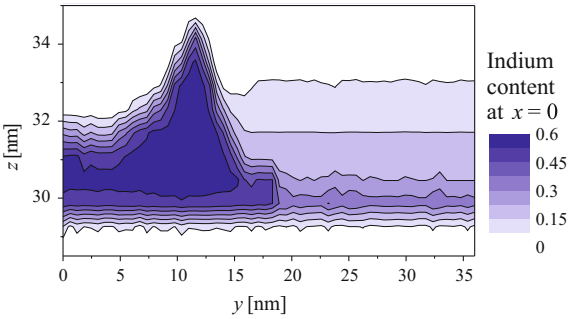

Fig. 4.5 Indium distribution in the yz plane in the QR. After [39]

4.4 Theory of Electronic Properties of One-Electron Rings, Including Magnetization

The single-particle Hamiltonians in a strained ring have the form [40, 41]

$$H_e = -\frac{\hbar^2}{2}\left(\nabla + \frac{ie}{\hbar}\mathbf{A}\right)\frac{1}{m_e(\mathbf{r}_e)}\left(\nabla + \frac{ie}{\hbar}\mathbf{A}\right) + V_e(\mathbf{r}_e) + \delta E_e(\mathbf{r}_e) - eV_P(\mathbf{r}_e), \tag{4.3}$$

$$H_h = -\frac{\hbar^2}{2}\left(\nabla - \frac{ie}{\hbar}\mathbf{A}\right)\frac{1}{m_h(\mathbf{r}_h)}\left(\nabla - \frac{ie}{\hbar}\mathbf{A}\right) - V_h(\mathbf{r}_h) - \delta E_h(\mathbf{r}_h) + eV_P(\mathbf{r}_h), \tag{4.4}$$

where $m_e(\mathbf{r}_e)$ $[m_h(\mathbf{r}_h)]$ is the conduction-electron [heavy-hole] mass and $\mathbf{A} = \mathbf{e}_\varphi H\rho/2$ is the vector potential of the uniform magnetic field $\mathbf{B} = \mathbf{e}_z B$. $V_e(\mathbf{r}_e)$ $[V_h(\mathbf{r}_h)]$ is the bottom of the conduction band [top of the valence band], determined by the In content x, in the absence of strain. The strain-induced shift of the conduction band

$$\delta E_\beta = a_\beta\left(\varepsilon_{xx} + \varepsilon_{yy} + \varepsilon_{zz}\right) \tag{4.5}$$

depends on the hydrostatic component of the strain tensor ε_{jk}. Here, $\beta = e, h$.

The shear strains give rise to the piezoelectric potential

$$V_P(\mathbf{r}) = -\frac{1}{4\pi\varepsilon_0\varepsilon_r}\int\frac{\mathrm{div}\mathbf{P}}{|\mathbf{r}-\mathbf{r}'|}d^3\mathbf{r}' \tag{4.6}$$

determined by the piezoelectric polarization $P_i = e_{ijk}\varepsilon_{jk}$, where for InAs and GaAs only the piezoelectric moduli $e_{123} = e_{213} = e_{312}$ are other than zero; ε_r is the relative dielectric constant. The relevant material parameters are: $e_{123}^{\mathrm{InAs}} = 0.045\,\mathrm{C/m^2}$, $e_{123}^{\mathrm{GaAs}} = 0.16\,\mathrm{C/m^2}$, $a_e^{\mathrm{InAs}} = -5.08\,\mathrm{eV}$, $a_e^{\mathrm{GaAs}} = -7.17\,\mathrm{eV}$, $a_h^{\mathrm{InAs}} = 1.00$ eV, $a_h^{\mathrm{GaAs}} = 1.16\,\mathrm{eV}$ [42]. The band gap and the effective masses as well as the parameters e_{123}

and a_β for $In_xGa_{1-x}As$ are taken from a linear interpolation between the corresponding values for InAs and GaAs. We further assume that for the conduction and valence bands in $In_xGa_{1-x}As$ the band edge variations with x in the absence of strain are to each other as 7:3.

The single-particle Schrödinger equations are solved within the adiabatic approximation, using the Ansatz:

$$\Psi^{(\beta)}(\mathbf{r}) = \psi_k^{(\beta)}(z;\rho,\varphi)\Phi_{kj}^{(\beta)}(\rho,\varphi), \tag{4.7}$$

where the index k numbers subbands due to the size quantization along the z-axis:

$$\left[-\frac{\hbar^2}{2}\frac{\partial}{\partial z}\frac{1}{m_\beta(\rho,\varphi,z)}\frac{\partial}{\partial z} \pm V_\beta(\rho,\varphi,z) \pm \delta E_\beta(\rho,\varphi,z) \mp eV_P(\rho,\varphi,z)\right]\psi_k^{(\beta)}(z;\rho,\varphi)$$
$$= \mathscr{E}_k^{(\beta)}(\rho,\varphi)\psi_k^{(\beta)}(z;\rho,\varphi). \tag{4.8}$$

In (4.8), the upper (lower) sign stands for conduction electrons (heavy holes), i.e. for $\beta = e$ ($\beta = h$). The Schrödinger (4.8) for the "fast" degree of freedom (along the z-axis) is solved numerically, obtaining, in particular, the adiabatic potentials $\mathscr{E}_k^{(\beta)}(\rho,\varphi)$.

An example of the calculated adiabatic potential $\mathscr{E}_1^{(e)}(\rho,\varphi)$, which corresponds to the lowest state of the size quantization along the z-axis, is shown in Fig. 4.4b. A QR – though it reveals a potential hill near its axis – is a singly connected structure. So, it is not evident whether or not electronic states in it resemble those in a doubly connected (ideal ring-like) geometry. Moreover, the adiabatic potential possesses two pronounced minima, which can be regarded as the potential profile of two quantum dots. If the potential minima are deep enough, then the electron is localized in one of those quantum dots, and no persistent current occurs at all.

Figure 4.6 shows the adiabatic potentials $\mathscr{E}_1^{(e)}(\rho,\varphi)$ corresponding to the indium distribution (see Fig. 4.5) and strain data for a realistic QR as found using the finite-element numerical calculation package ABAQUS [43], which is based on the elasticity theory. Due to strain the depth of a potential well for an electron significantly decreases (cp. panels *b* and *a* in Fig. 4.6). The influence of the piezoelectric potential on the shape of the adiabatic potential $\mathscr{E}_1^{(e)}$ along the x- and y-axes is almost negligible. For the direction $x = y$, the effect of the piezoelectric potential on $\mathscr{E}_1^{(e)}$ is more pronounced but still does not seem to be crucial in governing the electron in-plane motion.

The Schrödinger equations for the "slow" degrees of freedom,

$$\left[-\frac{\hbar^2}{2}\left(\nabla_{\rho,\varphi} \mp \frac{e}{\hbar}\mathbf{A}\right)\frac{1}{m_k^{(\beta)}(\rho,\varphi)}\left(\nabla_{\rho,\varphi} \mp \frac{e}{\hbar}\mathbf{A}\right) + \mathscr{E}_k^{(\beta)}(\rho,\varphi)\right]\Phi_{kj}^{(\beta)}(\rho,\varphi)$$
$$= E_{kj}^{(\beta)}\Phi_{kj}^{(\beta)}(\rho,\varphi), \tag{4.9}$$

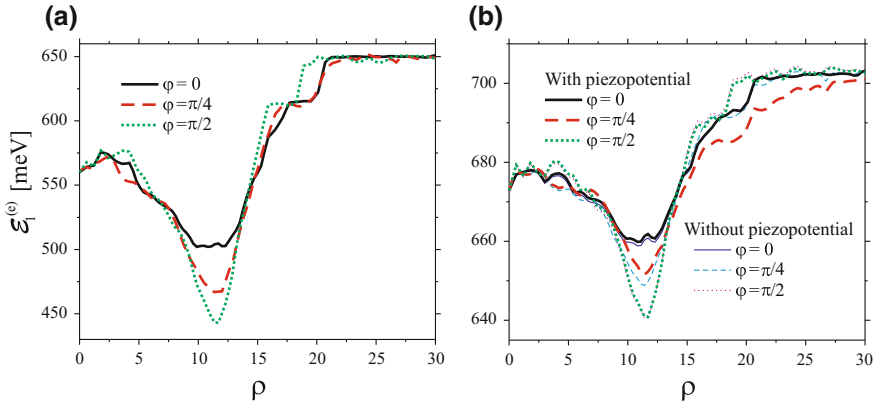

Fig. 4.6 Adiabatic potential, calculated in the absence (**a**) and in the presence (**b**) of strain, as a function of the radial coordinate ρ for three different in-plane directions, determined by the angular coordinate φ. In panel (**b**), heavy (thin) curves are obtained with (without) the piezoelectric potential. After [39]

with the upper (lower) sign for $\beta = e$ ($\beta = h$) and the effective masses

$$m_k^{(\beta)}(\rho, \varphi) = \int dz \left| \psi_k^{(\beta)}(z; \rho, \varphi) \right|^2 m_\beta(\rho, \varphi, z) \tag{4.10}$$

determine the eigenstates of the in-plane motion, which are labeled by the index j. We are interested in the lowest states of an electron and a hole in the quantum ring. Therefore, we restrict our calculations to the states in the lowest subband of the (strong) size-quantization along the z -axis (i.e., we consider states with $k = 1$). For each value of the applied magnetic field, the electron and hole eigenstates in the quantum ring are found by numerical diagonalization of the adiabatic Hamiltonian, which enters the lhs of (4.9).

The effect of the ring-height anisotropy on the oscillations of the calculated zero-temperature electron magnetic moment μ as a function of magnetic field B [44] is illustrated in Fig. 4.7, where we compare the magnetic moment for QRs with nonzero ξ_h and ξ_γ with the results for a perfectly symmetric ring. The magnetic moment of an electron in the applied magnetic field H is calculated as

$$\mu = -\frac{\mu_B}{Z} \sum_j \exp\left(-\frac{E_{1j}^{(e)}}{k_B T}\right) \frac{\partial E_{1j}^{(e)}}{\partial B}, \tag{4.11}$$

where μ_B is the Bohr magneton, T is the temperature and $Z = \sum_j \exp\left(-E_{1j}^{(e)}/(k_B T)\right)$. Shape anisotropy of the QR results in a mixing of electron states with different magnetic quantum numbers. Variations of the height of the rim $\tilde{h}_M(\varphi)$ with φ tend to suppress oscillations of μ versus B. However, well-pronounced oscillations of $\mu(B)$

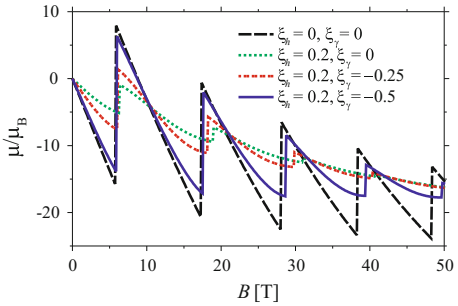

Fig. 4.7 Magnetic moment induced by the ground-state persistent current as a function of the applied magnetic field for unstrained $In_{0.6}Ga_{0.4}As$ QRs with $R = 10.75\,\text{nm}$, $h_0 = 1.6\,\text{nm}$, $h_M = 3.6\,\text{nm}$, $\gamma_0 = \gamma_\infty = 3\,\text{nm}$, $\xi_R = 0$ at different values of the anisotropy parameters ξ_h and ξ_γ. After [39]

can be expected even for QRs with a strong shape anisotropy, provided that the width of the rim changes as a function of φ in antiphase with the rim height. Remarkably, this condition is satisfied for realistic SAQRs as characterized by X-STM [7] (see also Fig. 4.6).

In Fig. 4.8, the lowest electron energy levels, calculated with and without effects due to strain, are shown as a function of the applied magnetic field B. Since the potential well for an electron in the strained QR is relatively shallow (see Fig. 4.6b), there are only few discrete energy levels below the continuum of states in the GaAs barrier. Due to a reduced potential barrier at the center of a strained ring, the effective electron radius decreases when taking into account strain. Correspondingly, the transition magnetic fields, where the ground and first excited electron states interchange, are higher in a strained ring than in an unstrained one. Strain-induced effects

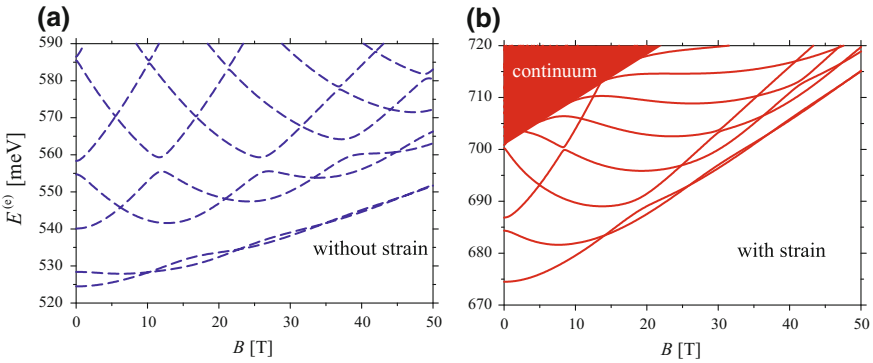

Fig. 4.8 Electron energy spectra in a QR, calculated without **a** and with **b** taking into account effects due to strain. Energies are counted from the bottom of the conduction band in unstrained InAs. The region of continuum as assessed by our numerical simulation is shadowed. After [39]

reduce the magnitude of variations of the adiabatic potential as a function of the azimuthal angle. As a result, the mixing of electron states with different magnetic quantum numbers, which occurs due to shape anisotropy of a QR, is weakened. Consequently, at relatively weak fields B the energy spacing between the lowest electron state (which arises from the state with $L = 0$ in a circularly symmetric ring) and the first excited state (which arises from the state with $L = 1$ in a circularly symmetric ring) is strongly enhanced due to strain, while the zero-field splitting between the first and second excited states (which correspond to $L = 1$ and $L = -1$ in a circularly symmetric ring) is significantly reduced.

As shown in Fig. 4.9, the main effect of strain on the behavior of the electron magnetic moment $\mu(B)$ is a shift of transition fields towards higher B. This shift, already noticed when discussing the electron energy spectra, appears because strain makes shallower the potential well in the rim. When decreasing the depth of this potential well, the electron states tend to those in a flat disk. This leads to an overall shift of the curve $\mu(B)$ (at nonzero B) towards larger negative values. The oscillation amplitudes for $\mu(B)$ are not significantly influenced by strain. There are two competitive effects of strain on these amplitudes. On the one hand, due to strain-induced reduction of the potential-well depth, there is an increasing penetration of the electron wave function into barriers, so that the effective width of the ring increases. Such an increase of the ring width tends to decrease the oscillation amplitude. On the other hand, the strain-induced reduction of the potential-well depth weakens the influence of shape anisotropy on electron states. Correspondingly, the suppression effect of shape anisotropy on the oscillations of $\mu(B)$ is weakened, too. As further illustrated in Fig. 4.9, an increase of the temperature tends to smooth out the Aharonov-Bohm oscillations of $\mu(B)$. Importantly, suppression of the first Aharonov-Bohm oscillations (at relatively low B) is not dramatic for liquid He temperatures.

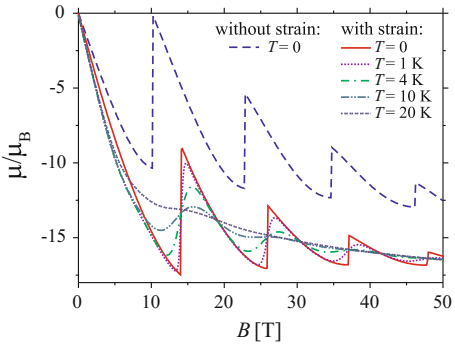

Fig. 4.9 Magnetic moment of an electron, calculated without strain with and without taking into account effects due to strain. In the case of a strained QR, the results for different temperatures are shown. After [39]

4.5 Observation of the AB Effect Through Magnetization

In [9], the AB oscillations of persistent currents were detected via the magnetic moment of electrons in a highly homogeneous ensemble of InAs self-assembled QRs. The magnetic moment of the nanostructures was obtained from magnetization experiments using a torque magnetometer [45]. These measurements were performed at temperatures of $T = 1.2$ K and $T = 4.2$ K in magnetic fields up to 15 T. The sensitivity of the magnetometer was 2.8×10^{-12} J/T, i. e. $3 \times 10^{11} \mu_B$ at $B = 14$ T, and it was limited by mechanical noise, which was about 8% of the experimentally observed oscillation magnitude. The total magnetization of the sample was due to about 1.5×10^{11} nanostructures with a total number of electrons $N \sim 2.2 \times 10^{11}$. Over the entire magnetic field range a relatively large background signal was observed due to the substrate and to dia- and paramagnetic materials close to the sample. To enhance the visibility of the AB oscillations, this linear background was subtracted and the signal was normalized to the total number of electrons N in the sample, resulting in the magnetic moment per electron $\mu = M/N$ [Fig. 4.10a]. To prove that the observed oscillation is not an artefact due to the background subtraction, we also plot the first derivative of the signal [inset to Fig. 4.10a], which is much less sensitive to the monotonous background. This procedure reveals an oscillation around 14 T as a fingerprint of the AB effect.

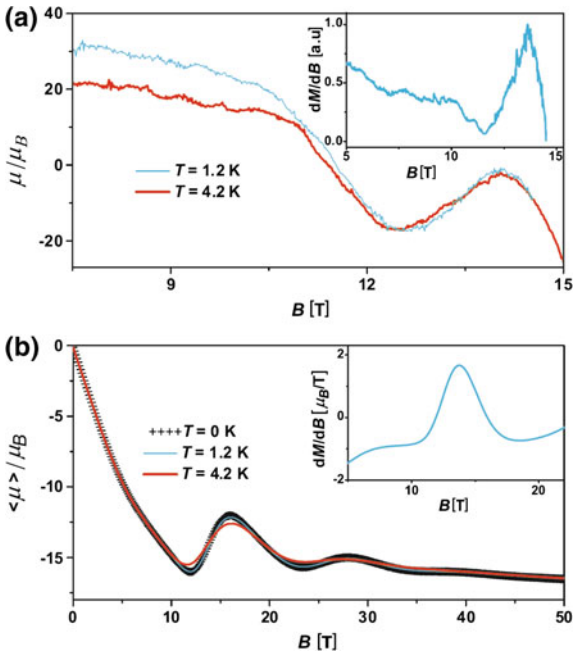

Fig. 4.10 **a** Oscillation in the magnetic moment per electron, obtained at 1.2 K and at 4.2 K, after subtracting the linear background from the measured signal, dividing by the total number of electrons, and averaging over several measurements. The inset shows the first derivative of the experimental magnetic moment with respect to B at $T = 1.2$ K. **b** Calculated magnetic moment, and its derivative (inset), of a single electron in a nanostructure at different temperatures. After [9]

Figure 4.10b shows the calculated magnetization curve, which results from averaging over a QR ensemble with a size dispersion of 5%, consistent with the measured width of the PL peak. As seen from a comparison between Fig. 4.10a, b, the model described in the previous section accurately explains the position of the observed AB oscillation around 14 T, rather than at 5 T expected for an ideal 1D ring of the same radius. This difference in the position of the AB oscillations is due to the influence of strain in the self-assembled "volcano-like" QRs as well as to the singly-connectedness of these QRs. Figure 4.10b also shows the calculated magnetic moment for higher magnetic fields that are not yet accessible by magnetization experiments. The higher order AB oscillations are strongly damped. This is a consequence of the presence of the magnetic field in the rim of the QRs, which enhances the electron localization close to the minima of the adiabatic potential. In Fig. 4.10b the calculated results are plotted for three temperatures. Without including size variations of the QRs, the calculated amplitude of the AB oscillations decreases with increasing temperature (see Fig. 4.9). A negligible temperature effect on the electron magnetic moment in Fig. 4.10b is due to the QR ensemble averaging.

The shown results confirm the existence of an oscillatory persistent current in self-assembled QRs containing only a single electron. Even though the investigated nanostructures are singly connected and anisotropic, they show the AB behavior that is generally considered to be restricted to ideal (doubly connected) topologies.

4.6 Theory of Two-Electron Systems and Excitons in Quantum Rings

The purpose of the first part of this section is to consider the contribution from QRs with two electrons to the magnetization. The Hamiltonian of the two electrons in a QR is represented as

$$H_{ee}(\mathbf{r}_1, \mathbf{r}_2) = H_e(\mathbf{r}_1) + H_e(\mathbf{r}_2) + V_{\text{Coul}}(\mathbf{r}_1, \mathbf{r}_2), \tag{4.12}$$

where $H_e(\mathbf{r}_1)$ is the single-electron Hamiltonian [see (4.3)], $V_{\text{Coul}}(\mathbf{r}_1, \mathbf{r}_2)$ describes the Coulomb interaction between the electrons with radius-vectors $\mathbf{r}_1$ and $\mathbf{r}_2$. In order to obey the Pauli exclusion principle, the spin-singlet (spin-triplet) states in the two-electron rings must possess orbital wave functions which are symmetric (antisymmetric) with respect to the permutation of the coordinates of electrons. Aimed at finding two-electron eigenstates, we start with constructing the basis functions, which describe the orbital wave functions of spin-singlet and spin-triplet states in the absence of the electron-electron interaction:

$$\Psi^{(ee,0)}_{j_1 j_2}(\mathbf{r}_1, \mathbf{r}_2) = c_{j_1 j_2}\left[\Psi^{(e)}_{1j_1}(\mathbf{r}_1)\Psi^{(e)}_{1j_2}(\mathbf{r}_2) + \Psi^{(e)}_{1j_1}(\mathbf{r}_2)\Psi^{(e)}_{1j_2}(\mathbf{r}_1)\right], \tag{4.13}$$

$$\Psi^{(ee,1)}_{j_1 j_2}(\mathbf{r}_1, \mathbf{r}_2) = c_{j_1 j_2}\left[\Psi^{(e)}_{1j_1}(\mathbf{r}_1)\Psi^{(e)}_{1j_2}(\mathbf{r}_2) - \Psi^{(e)}_{1j_1}(\mathbf{r}_2)\Psi^{(e)}_{1j_2}(\mathbf{r}_1)\right], j_1 \neq j_2, \tag{4.14}$$

where $c_{j_1 j_2} = 1/\sqrt{2}$ for $j_1 \neq j_2$ and $c_{j_1 j_1} = 1/2$. We numerically diagonalize the Hamiltonian (4.12) in the above basis, looking for the wave functions of the two interacting electrons in the form

$$\tilde{\Psi}_J^{(ee,S)}(\mathbf{r}_1, \mathbf{r}_2) = \sum_{j_1=1}^{j_{max}} \sum_{j_2=1}^{j_1-S} A_{J j_1 j_2} \Psi_{j_1 j_2}^{(ee,S)}(\mathbf{r}_1, \mathbf{r}_2), \tag{4.15}$$

where $S = 0$ ($S = 1$) in the case of spin-singlet (spin-triplet) states (see [46] for more details).

For short, the states $\Psi_{j_1 j_2}^{(ee,S)}$ for $S = 0, 1$ are labeled below as $(j1, j2)^S$, where the numbers j_1 and j_2 correspond to the order of the single-electron energy levels at $B = 0$. The states $\tilde{\Psi}_J^{(ee,S)}$ are labeled as $(J)^S$ for $S = 0, 1$. In Fig. 4.11 the calculated two-electron energy spectra are plotted for the cases of no electron-electron interaction and with the Coulomb interaction taken into account. It is worth recalling here that the index j, rather than the electron angular momentum L, is specific for single-electron eigenstates in an anisotropic quantum ring. Approximately, the correspondence between the states of two electrons in a quantum ring with account for the Coulomb interaction and the states of two non-interacting electrons in a quantum ring is as follows: $(1, 1)^0 \rightarrow (1)^0$; $(2, 1)^0 \rightarrow (2)^0$; $(2, 2)^0 \rightarrow (3)^0$; $(2, 1)^1 \rightarrow (1)^1$; $(3, 1)^1 \rightarrow (2)^1$. Due to the Coulomb interaction, the degeneracy between the spin-singlet and spin-triplet states is lifted. For example, there is a significant splitting between the spin-singlet $(2)^0$ and the spin-triplet $(1)^1$ states, although the corresponding states of two non-interacting electrons $(2, 1)^0$ and $(2, 1)^1$ are degenerate. This fact indicates a strong exchange interaction in the quantum ring under consideration.

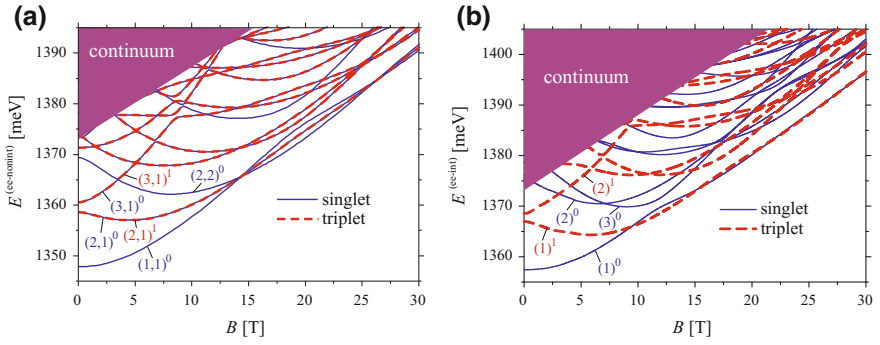

Fig. 4.11 Energy spectrum of two noninteracting **a** and interacting **b** electrons in a strained QR as a function of the applied magnetic field. For $S = 0, 1$ the states $\Psi_{j_1,j_2}^{ee,S}$ of noninteracting electrons are labeled as $(j_1, j_2)^S$, where the numbers j_1 and j_2 correspond to the order of the single-electron energy levels at $B = 0$. All triplet energy levels $(j_1, j_2)^1$ for $j_1 \neq j_2$ overlap with singlet energy levels $(j_1, j_2)^0$. The states $\tilde{\Psi}_J^{ee,S}$ of interacting electrons are labeled as $(J)^S$ for $S = 0, 1$. The region of the energy continuum as obtained from our numerical simulation is shadowed. After [46]

While at relatively low magnetic fields the ground state in Fig. 4.11b corresponds to the lowest spin-singlet energy level, at $B \approx 10\,\mathrm{T}$ the ground state becomes spin-triplet. With further increasing magnetic field, the lowest spin-singlet and spin-triplet states sequentially replace each other as the ground state. This behavior is reminiscent of the Aharonov-Bohm effect in a single-electron quantum ring. At $B \approx 12\,\mathrm{T}$ the state originating from $(1, 1)^0$ reveals anticrossing from those states which originate from $(2, 1)^0$ and $(2, 2)^0$.

In Fig. 4.12, the calculated magnetic moment μ of the two non-interacting and interacting electrons is plotted as a function of the applied magnetic field. The Coulomb interaction leads to a more complicated oscillating structure of μ versus B as compared to the case when the electron-electron interaction is absent. In particular, the first oscillation of the magnetic moment shifts due to the Coulomb interaction towards weaker magnetic fields. One of the reasons for this shift is an increase of the effective electronic radius of the ring due to the mutual Coulomb repulsion of the two electrons. At $B > 15$ T, the Aharonov-Bohm oscillations of the magnetic moment are still present, but substantially smoothed out.

As implied by Fig. 4.12, for two-electron anisotropic QRs with radial sizes $\sim$10 nm, the Aharonov-Bohm-effect-related phenomena appear at magnetic fields $\sim$10 T. In the experiment on magnetization [9], no appreciable oscillations are detected in the above region. Therefore one may assume assumed that the observed Aharonov-Bohm effect [9] is mainly due to the single-electron quantum rings in the ensemble of rings under investigation.

In [47, 48], the method presented in [46] for two-electron QRs, has been extended to excitons in QRs and applied to calculate the exciton energy spectra and the optical transition probabilities in QRs with a realistic anisotropic singly connected shape. The Hamiltonian of an exciton in a strained quantum ring is

$$H_{ex} = H_e + H_h + V_{\mathrm{Coul}}(\mathbf{r}_e, \mathbf{r}_h), \tag{4.16}$$

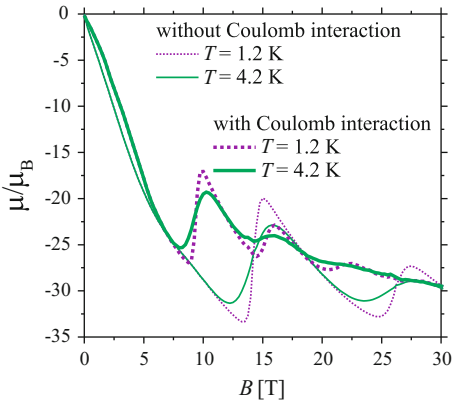

Fig. 4.12 The calculated magnetic moment of two noninteracting (interacting) electrons in a strained quantum ring is shown by the thin (heavy) lines for two different temperatures. After [46]

where H_e [H_h] is the single-particle Hamiltonian of an electron [a hole] determined by (4.3) [(4.4)], $V_{\text{Coul}}(\mathbf{r}_e, \mathbf{r}_h)$ describes the Coulomb interaction between an electron and a hole with radius-vectors $\mathbf{r}_e$ and $\mathbf{r}_h$, respectively. We consider hear only heavy holes and treat them within the one-band model.

In order to find exciton eigenstates, we start with constructing the basis functions, which describe a non-interacting *eh*-pair:

$$\Psi^{(eh)}_{j_e j_h}(\mathbf{r}_e, \mathbf{r}_h) = \Psi^{(e)}_{1j_e}(\mathbf{r}_e)\Psi^{(h)}_{1j_h}(\mathbf{r}_h). \tag{4.17}$$

Then we diagonalize the Hamiltonian (4.16) in the above basis, looking for the exciton wavefunctions in the form

$$\Psi^{(ex)}_{J}(\mathbf{r}_e, \mathbf{r}_h) = \sum_{j_e, j_h=1}^{j_{max}} A_{J j_e j_h} \Psi^{(eh)}_{j_e j_h}(\mathbf{r}_e, \mathbf{r}_h). \tag{4.18}$$

Then for each value of the applied magnetic field B the lowest exciton states are found by numerical diagonalization of the Hamiltonian (4.16) in the basis (4.17).

The effect of the electron-hole Coulomb interaction on the energy spectrum and transition probabilities is illustrated in Fig. 4.13 for an unstrained azimuthally isotropic $In_{0.55}Ga_{0.45}As/GaAs$ ring-like structure with the shape shown in the inset to Fig. 4.13a. Due to strong selection rules, applicable for the highly symmetric structure under consideration, only a small fraction of the states of the non-interacting *eh*-pair, namely the states with zero envelope angular momentum $L_e + L_h = 0$, are dipole active. As seen from Fig. 4.13a, the electron-hole Coulomb interaction, which mixes *eh*-states with the same $L_e + L_h$ and different $L_e(= -L_h)$, n_e, n_h, leads to anticrossing for the lowest two dipole-active energy levels (for a non-interacting *eh*-pair, the corresponding levels cross each other). This mixing of states due to the electron-hole Coulomb interaction is accompanied by a redistribution of oscillator strengths (usually, in favor of lower-lying states). This is illustrated in Fig. 4.13b, where we plot the spectral distributions of the calculated probabilities P for optical transitions to different states of an exciton. In order to enhance visualization, a small Gaussian broadening ($\sim$1 meV) is introduced for all the energy levels. In the energy range, which corresponds to anticrossing of the lowest two dipole active energy levels, the upper of these two levels becomes "dark", while the transition probability P for the lower level increases.

The electron energy spectrum, the magnetization, and the optical-transition probabilities were analyzed for excitons in strained axially symmetric ring-like structures (see the inset in Fig. 4.14a) with different In concentration in the In-rich region. The strain-induced flattening of the adiabatic potential makes the structure under consideration "disk-like" rather than"ring-like". However, when increasing the In content x, the depth of the adiabatic potential well in the In-rich region significantly increases both for an electron and for a hole. This results, in particular, in a decrease of the electron ground-state energy (see Fig. 4.14a). In Fig. 4.14b, we show spectral distributions of the calculated probabilities P for optical transitions to different states

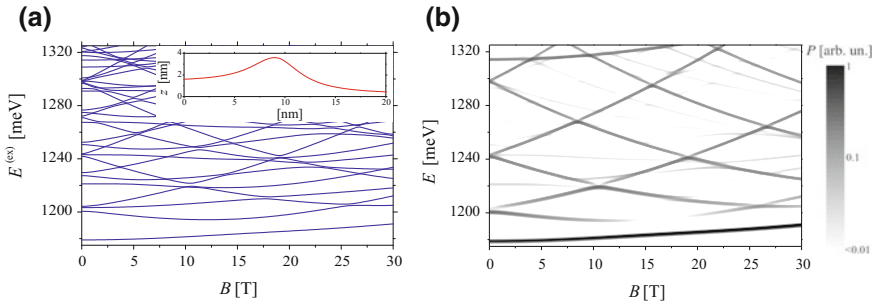

Fig. 4.13 **a** Energies of the lowest dipole active exciton states in an unstrained axially symmetric $In_{0.55}Ga_{0.45}As/GaAs$ ring-like structure as a function of the applied magnetic field. Inset: Shape of the structure. **b** Spectral distribution of the optical transition probabilities P for an exciton as a function of the applied magnetic field ($\Gamma = 1$ meV). After [48]

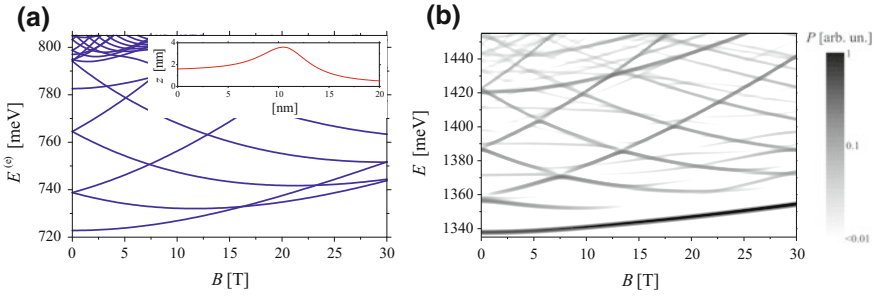

Fig. 4.14 **a** Energies of the lowest electron states in a strained axially symmetric $In_{0.65}Ga_{0.35}As/GaAs$ ring-like structure as a function of the applied magnetic field. Inset: Shape of the structure. **b** Spectral distribution of the optical transition probabilities P for an exciton as a function of the applied magnetic field ($\Gamma = 1$ meV). After [48]

of an exciton in a strained $In_{0.65}Ga_{0.35}As/GaAs$ ring-like structure. At relatively low magnetic fields B, a complicated pattern of P starts for energies $\sim$100 meV above the lowest exciton state. This energy region actually corresponds to continuum states.

In Figs. 4.15 and 4.16 we show the calculated probabilities P of optical transitions for ring-like structures with $x = 0.7$ and with realistic shape anisotropy. As seen from Fig. 4.15a, for a noninteracting electron-hole pair there is a crossover in the ground-state energy around $B = 15$ T, in agreement with magnetization experiments [9]. The Coulomb interaction results into a smooth behavior of the ground-state energy as function of B, as shown in Fig. 4.15b. Due to the Coulomb interaction the oscillator strengths of the two lowest "bright" *eh*-states are significantly redistributed in favor of the lowest level. Therefore, despite a relatively large splitting between these two exciton energy levels, the upper one is practically unresolvable in the case of an appreciable energy-level broadening, $\Gamma = 10$ meV (see Fig. 4.16).

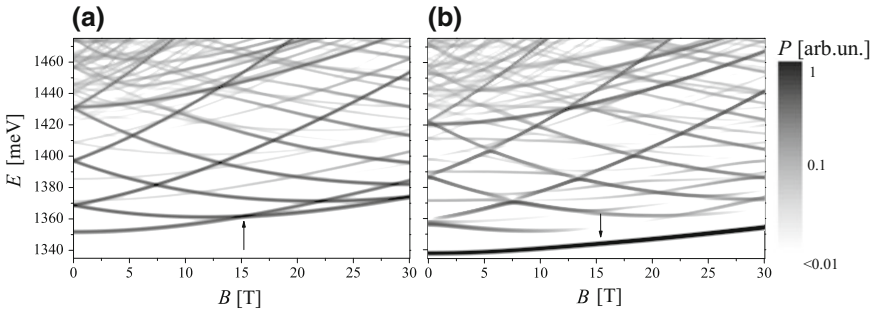

Fig. 4.15 Calculated optical transition probabilities for an anisotropic strained $In_{0.7}Ga_{0.3}As/GaAs$ QR with $R = 9\,nm$, $h_0 = 1.6\,nm$, $h_M = 3.6\,nm$, $h_\infty = 0.4\,nm$, $\gamma_0 = \gamma_\infty = 3\,nm$, $\xi_R = \xi_\gamma = 0$, $\xi_h = 0.2$, $\Gamma = 1\,meV$, in the case of **a** a noninteracting electron-hole pair and **b** an interacting electron-hole pair. The arrows correspond to the first excitonic AB resonance in the ground state. After [49]

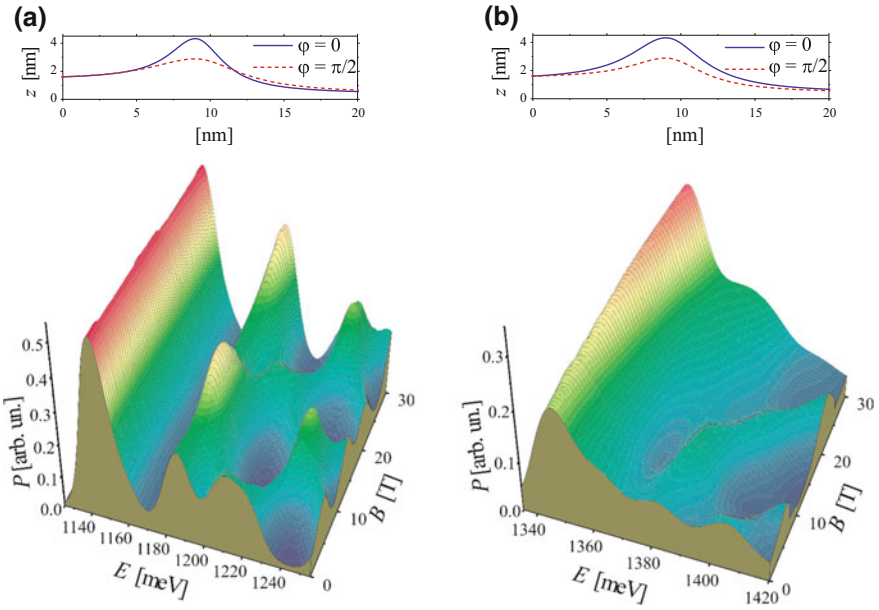

Fig. 4.16 **a** Shape of the structure (top) and broadened spectral distributions of P for an exciton in the anisotropic unstrained $In_{0.7}Ga_{0.3}As/GaAs$ QR with $R = 9\,nm$, $h_0 = 1.6\,nm$, $h_M = 3.6\,nm$, $h_\infty = 0.4\,nm$, $\gamma_0 = \gamma_\infty = 3\,nm$, $\xi_R = 0$, $\xi_h = 0.2$, $\xi_\gamma = -0.25$, and with $\Gamma = 10\,meV$. **b** Same as in panel (**a**) but for a strained ring with $\xi_\gamma = 0$. After [47]

4.7 Experiments on Excitonic Properties of Quantum Rings

In [49], the exciton energy level structure of a large ensemble of InAs/GaAs quantum rings was experimentally investigated by photoluminescence spectroscopy in magnetic fields up to 30 T for different excitation densities. For the PL studies, a sample containing a single layer of QRs [16] was mounted in a liquid-helium bath cryostat at T = 4.2 K. Static magnetic fields up to 30 T were applied parallel to the growth direction and the PL was detected in the Faraday configuration. The dependence of the QR emission energy on the excitation density is shown in Fig. 4.17**a**. The ground-state emission energy of the QRs is centered around 1.308 eV, typical for these nanostructures [16]. The ground-state emission has an inhomogeneous broadening with a full width at half maximum of 20 meV. With increasing excitation density two additional peaks can be resolved. These peaks have an energy of 39 and 63 meV above the ground-state energy.

To investigate the influence of the ringlike geometry on the excitonic behavior in the excited states of the QRs, the magneto-PL of these structures for higher excitation intensities was measured. With increasing B, both resolvable excited states split up in two separate peaks. Each of the PL peaks splits further with a smaller energy separation into two peaks of opposite circular polarization [see Fig. 4.17b]. Figure 4.18a shows the higher excitation data in σ^--polarization as function of B in intervals of 1 T. The calculated transition probabilities are plotted in Fig. 4.18b. The calculated and measured spectra show a qualitative resemblance. Within the theoretical model, which was successfully applied to explain the magnetization behavior of QRs on similar samples [9, 39], one finds that for all realistic ring parameters the PL of the first-excited state is concealed by the ground-state luminescence if an inhomogeneous broadening of about 20 meV is included. The ring character of the

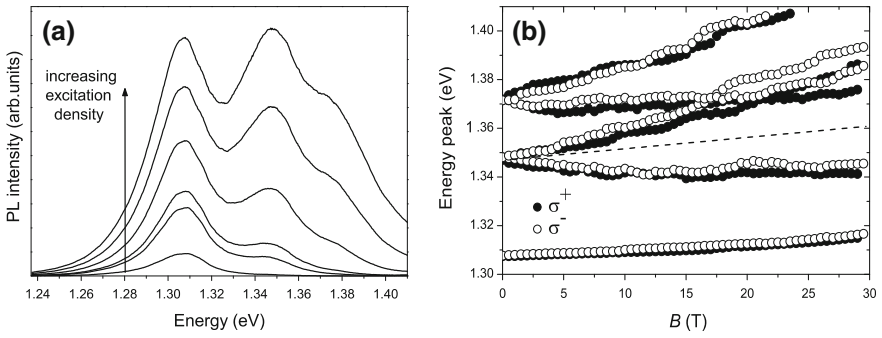

Fig. 4.17 **a** PL as a function of excitation density, for which the lowest (highest) excitation density is 102 W cm^{-2} (105 W cm^{-2}). Two excited states can be distinguished for higher excitation density located 38 and 63 meV above the ground-state emission energy. **b** The energy diagram showing the peak position in B in both σ^- (empty circles) and σ^+ (filled circles) polarization. The QRs exhibit splittings into two states of the different excited states, in contrast to QDs where a third peak (indicated by the dashed line) is observed. After [49]

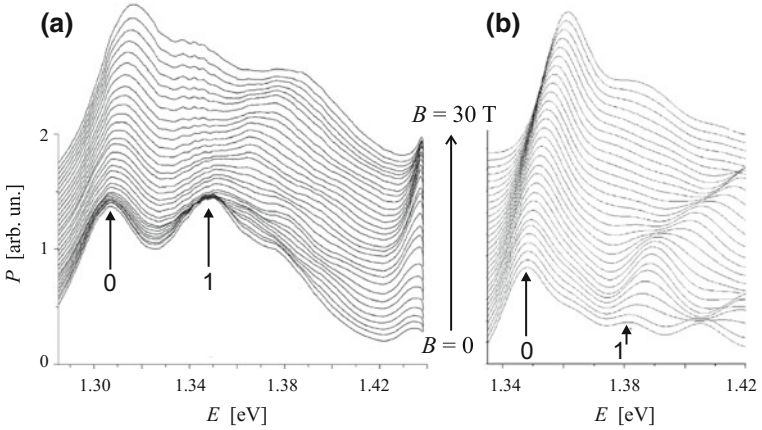

Fig. 4.18 **a** Experimental σ^+ photoluminescence spectra of self-assembled InGaAs/GaAs quantum rings in magnetic fields from 0 T (the lowest curve) to 30 T (the highest curve) with the step 1 T. The two lowest peaks at $B = 0$ are indicated with labels "0" (at 1.30735 eV) and"1" (at 1.34945 eV), corresponding to the peaks "0" and"1" in panel (**b**), where the theoretical spectra of the optical transition probabilities are shown (cf. Fig. 4.16b). After [48]

nanostructures under consideration results in non-equidistant energy level splittings in the exciton diagram and in a magnetic field induced splitting of each excited state into two states. This is in contrast to what has been observed in the measurements on quantum dots [50–52], which show a magnetic induced splitting of the d-state into three states and equidistant energy levels.

In contrast to the AB effect of single electrons in QRs under consideration, an excitonic AB effect in an ensemble of those QRs was not observed nor expected based on the theoretical model [48, 49]. The absence of prominent oscillations in the ground-state energy of the calculated exciton spectra as compared to the case of a noninteracting electron-hole pair is a consequence of the Coulomb interaction. As implied by the results of magnetophotoluminescence measurements on single InGaAs/GaAs QRs [53], the amplitude of the AB oscillations in the ground-state energy of a QR is as small as about few μeV, so that in a PL spectrum of an ensemble of QRs these oscillations are fully hidden due to the size and shape dispersion of QRs.

4.8 Spin-Correlated Orbital Currents in QRs

Carriers in III–V semiconductors[1] can have magnetic moments much larger than expected on basis of their bare orbital **L** and spin **J** angular momenta, due to the presence of spin-correlated orbital currents [23]. The spatial distribution of these

[1]This section is based on [24], certain parts of which are reproduced here with permission.

currents has recently been studied in the context of semiconductor nanostructures [22]. In this section we will explore how these spin-correlated currents affect the magnetic moment of electrons in idealized QRs [24]. The orbital magnetic moment $\boldsymbol{\mu}_{\text{orb}}$ can be found [54] from the orbital current density $\mathbf{j}(\mathbf{r})$, as described in [24], by

$$\boldsymbol{\mu}_{\text{orb}} = \frac{1}{2}\int_V \mathbf{r} \times \mathbf{j}(\mathbf{r})\ d^3r = \frac{1}{2}\sum_s \int_{V_s} \mathbf{r} \times \mathbf{j}(\mathbf{r})\ d^3r, \tag{4.19}$$

where the moment is a summation of moments from each of s unit cells having volume V_s. The average current density $\langle \mathbf{j} \rangle_s$ in a unit cell is:

$$\langle \mathbf{j} \rangle_s = \frac{1}{V_s}\int_{V_s} \mathbf{j}(\mathbf{r})\ d^3r. \tag{4.20}$$

Using $\langle \mathbf{j} \rangle_s$ we split the orbital current into an itinerant current (IC) that flows into and out of a unit cell, and a localized current (LC) whose average over the unit cell vanishes, given by $\mathbf{j}(\mathbf{r}) - \langle \mathbf{j} \rangle_s$. The magnetic moment can then be expressed as [55]:

$$\boldsymbol{\mu}_{\text{orb}} = \frac{1}{2}\sum_s \Bigg\{ \underbrace{V_s \mathbf{r}_s \times \langle \mathbf{j} \rangle_s}_{\text{Itinerant current (IC)}} + \underbrace{\int_{V_s} (\mathbf{r} - \mathbf{r}_s) \times \{\mathbf{j}(\mathbf{r}) - \langle \mathbf{j} \rangle_s\}\ d^3r}_{\text{Localized (circulating) current (LC)}} \Bigg\} \tag{4.21}$$

where $\mathbf{r}_s$ is the vector pointing to unit cell s. The first term is the orbital moment due to itinerant currents, while the second term is the sum of orbital moments due to a (circulating) current localized within each unit cell. These orbital currents follow from [56]:

$$\mathbf{j}(\mathbf{r}) = \frac{e\hbar}{m_0}\text{Im}\left\{\Psi^*(\mathbf{r})\,\nabla\Psi(\mathbf{r})\right\}. \tag{4.22}$$

The LC contributions are small compared to the IC contributions, and will be neglected here.

For nanostructures the envelope function approximation (EFA) is an accurate way to describe the state $\Psi(\mathbf{r})$ in more detail [57, 58]:

$$\Psi(\mathbf{r}) = \sum_i F_i(\mathbf{r}) u_i(\mathbf{r}), \tag{4.23}$$

where the wave function is written as the product of a Bloch state $u_i(\mathbf{r})$ of band i with its corresponding spatially slowly varying envelope function $F_i(\mathbf{r})$, assumed to be constant in a unit cell. This results in currents which are related to the Bloch velocity (BV) and envelope velocity (EV):

$$\mathbf{j}(\mathbf{r}) = \frac{e\hbar}{m_0}\sum_{i,j}\mathrm{Im}\Big\{\underbrace{u_i^*(\mathbf{r})u_j(\mathbf{r})\left[F_i^*(\mathbf{r})\nabla F_j(\mathbf{r})\right]}_{\text{Envelope velocity related (EV)}} + \underbrace{F_i^*(\mathbf{r})F_j(\mathbf{r})\left[u_i^*(\mathbf{r})\nabla u_j(\mathbf{r})\right]}_{\text{Bloch velocity related (BV)}}\Big\} \tag{4.24}$$

The BV related current dominates over the EV related current by $\sim d/a_0$, where d is the typical size of the envelope wave function and a_0 the size of the unit cell [22]. This coincides with the condition for the validity of the envelope function approximation. For realistically sized nanostructures, the BV related current is $\geq$5 times the EV related current. Thus we shall ignore the EV related current here; for more details about these subdominant currents consult [24].

The unit cell averaged current density for the BV related current $\langle\mathbf{j}\rangle^{\mathrm{BV}}$ becomes:

$$\langle\mathbf{j}\rangle^{\mathrm{BV}}(\mathbf{r}_s) = \frac{1}{V_s}\frac{e\hbar}{m_0}\sum_{i,j}\mathrm{Im}\left\{F_i^*(\mathbf{r}_s)F_j(\mathbf{r}_s)\langle u_i|\nabla|u_j\rangle\right\} \tag{4.25}$$

where $\langle u_i|\nabla|u_j\rangle$ are momentum matrix elements. These are only non-zero when i labels a conduction band state and j a valence band state. Since we are examining a stationary state, the divergence of the current is zero. The current must therefore circulate within the nanostructure along a closed surface. This resembles a current loop extended throughout the nanostructure and arising completely from the intermixing of valence band states in the ground state of the nanostructure. This BV related itinerant current leads to a magnetic moment

$$\boldsymbol{\mu}_{\text{IC-BV}}(\mathbf{r}_s) = \mu_B\sum_{i,j}\mathrm{Im}\{F_i^*(\mathbf{r}_s)F_j(\mathbf{r}_s)(\mathbf{r}_s\times\langle u_i|\nabla|u_j\rangle)\}. \tag{4.26}$$

Generally speaking, the $\mathbf{k}\cdot\mathbf{p}$ Hamiltonian $\mathscr{H}$ can formally be decomposed in terms having respectively cylindrical, cubic and tetragonal symmetry:

$$\mathscr{H} = \mathscr{H}_{\text{cyl}} + \mathscr{H}_{\text{cub}} + \mathscr{H}_{\text{tet}} \tag{4.27}$$

using a procedure reported in [59]. Since we will be investigating cylindrically symmetric nanostructures, we will use only the cylindrically symmetric part $\mathscr{H}_{\text{cyl}}$. Moreover, it has been shown [59] that $\mathscr{H}_{\text{cub}}$ is proportional to a difference of Luttinger parameters, $\gamma_3 - \gamma_2$, which is for most semiconductors a small quantity compared to γ_1 and γ_2. This Hamiltonian will now be block diagonal in a basis of eigenstates of F_z (where $\mathbf{F} = \mathbf{L} + \mathbf{J}$ is the total angular momentum) [60]:

$$\mathscr{H} = \sum_{F_z}\mathscr{H}_{F_z} \tag{4.28}$$

since only $F_z = L_{\mathrm{E},z} + J_z$, the projection of the total angular momentum on the symmetry axis, remains quantized for nanostructures with cylindrical symmetry. A convenient basis are the product states:

$$|F_z; J, J_z; k, k_z\rangle = |J, J_z\rangle |k, k_z, L_{\mathrm{E},z} = F_z - J_z\rangle \tag{4.29}$$

where $|J, J_z\rangle$ are Bloch functions, $|k, k_z, L_{\mathrm{E},z} = F_z - J_z\rangle$ the envelope wave functions, k is the radial wave number, and k_z the wave number along the symmetry axis (which we choose to be the z-axis). The envelope wave function has the coordinate representation:

$$\begin{aligned}\langle r, \theta, z|k, k_z, L_{\mathrm{E},z} = F_z - J_z\rangle = \\ \frac{i^{L_{\mathrm{E},z}}}{2\pi}\left\{J_{L_{\mathrm{E},z}}(kr) + \xi N_{L_{\mathrm{E},z}}(kr)\right\} e^{iL_{\mathrm{E},z}\theta} e^{ik_z z}\end{aligned} \tag{4.30}$$

where $J_l(r)$ is the lth-order Bessel function of the first kind, $N_l(r)$ is the lth-order Neumann function of the first kind, and ξ a dimensionless parameter determined by the boundary conditions. Using the transformation as outlined in [60], we can represent $\mathscr{H}_{\mathrm{cyl}}$ in the cylindrical envelope basis. Although the transformation of [60] is correct, the cylindrical symmetry is not correctly introduced in their Hamiltonian. We have therefore used the correctly derived Hamiltonian of [59]. The Hamiltonian of [60] and our Hamiltonian are identical in the spherical approximation ($\gamma_2 = \gamma_3 = \gamma_{23}$, where $\gamma_{23} = \frac{2}{5}\gamma_2 + \frac{3}{5}\gamma_3$). We will show that only in the cylindrical approximation it will be possible to independently tune the confinement energy and magnetic moment.

We now consider a ring, with inner radius R_{in}, outer radius R_{out}, and height H, of which the confining potential is given by:

$$V(r, z) = \begin{cases} 0 & R_{\mathrm{in}} \le r \le R_{\mathrm{out}} \quad \text{and} \quad |z| \le H/2 \\ \infty & \text{elsewhere} \end{cases} \tag{4.31}$$

In contrast to the case of cylindrical disks [24], the Neumann functions $N_{L_{\mathrm{E},z}}(r)$ do play a role, since the origin is not involved in the wave function. The parameter ξ is therefore non-zero and should follow from the boundary conditions. Since the electron ground state predominantly originates from conduction band states, we choose the approximate boundary condition:

$$\langle r, \theta, z|k, k_z, 0\rangle_{r=R_{\mathrm{in}}, r=R_{\mathrm{out}}, z=\pm\frac{H}{2}} = 0 \tag{4.32}$$

This condition leads to the system of equations:

$$\begin{cases} J_0(kR_{\mathrm{in}}) + \xi N_0(kR_{\mathrm{in}}) = 0 \\ J_0(kR_{\mathrm{out}}) + \xi N_0(kR_{\mathrm{out}}) = 0 \end{cases} \tag{4.33}$$

which determine (ξ, k) for a given $(R_{\text{in}}, R_{\text{out}})$. Although this system of equations is not generally analytically solvable, it can be inferred that both ξ and kR_{out} depend only on the ratio $R_{\text{in}}/R_{\text{out}}$. This can also be seen when analyzing the asymptotic limit of the equations, which results in approximate solutions:

$$k \approx \frac{\pi}{R_{\text{out}} - R_{\text{in}}} \tag{4.34}$$

$$\xi \approx \tan\left(kR_{\text{out}} + \tfrac{\pi}{4}\right) \tag{4.35}$$

These approximate relations resemble the ones found for spherical shells [24]. In Fig. 4.19a we plot the current distribution of a ring with $R_{\text{in}}/R_{\text{out}} = \frac{1}{3}$. The presence of an inner and outer surface of the nanostructure leads to two oppositely circulating current loops. Thus the topology of the nanostructure has a profound influence on the orbital current distribution. These two current loops carry an equal amount of current, so that, irrespective of the size, the integrated current is zero. The orbital moments generated by each of the currents will partially cancel, the degree of cancellation depending on the ring thickness. This result was to be expected, since the radial wave number is determined by the ring thickness $R_{\text{out}} - R_{\text{in}}$, and the orbital moment of a disk depends on $R/\rho_{0,1} = 1/k$. The orbital moment can therefore only be tuned either via the thickness or the height of the ring.

To be complete, the above reasoning only holds as long as the approximate solution is valid: in general, k might not depend only on the ring thickness. We have therefore computed numerically the solution of the boundary conditions, and used them to numerically calculate the radius dependence of the most important integrated orbital moment $\boldsymbol{\mu}_{\text{IC-BV}}$, see Fig. 4.19b. It can readily be seen that this orbital moment depends only on the ring thickness. Only when R_{in} approaches zero, R_{out} starts to have an

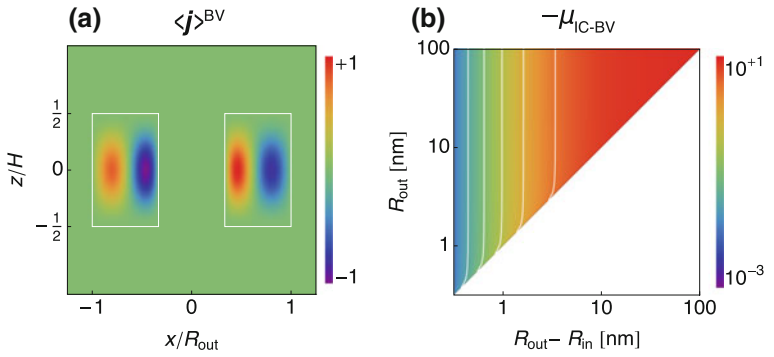

Fig. 4.19 **a** The xz-cross-section of the spatial distribution of the normalized magnitude of the $\mathbf{e}_y$-component of $\langle \mathbf{j} \rangle^{\text{BV}}$ of a ring. Similar to the spherical shells, there are two oppositely circulating current loops. For the plot we choose $R_{\text{in}}/R_{\text{out}} = \frac{1}{3}$. **b** The dependence of $\boldsymbol{\mu}_{\text{IC-BV}}$ (in μ_B) on the ring thickness $R_{\text{out}} - R_{\text{in}}$ and outer radius R_{out}, for an InAs ring with $H = 100\,\text{nm}$. Similar to the spherical shells, the orbital moment depends only on the ring thickness, as can be seen from the white contour lines. After [24]

influence too. These small values of R_{in} correspond to an inner region comparable to the unit cell of the crystal, and the validity of the envelope function approximation is questionable. Finally we note that having a finite barrier will also lead to substantial changes at small R_{in}: tunneling through the inner region reduces the strength of the inner current loop and decreases the radius of the outer current loop, both leading to a reduction of the degree of cancellation of the orbital moments.

4.9 Applications of QRs

From a fundamental point of view, semiconductor QRs are fascinating topological structures, whose unique features are represented in the present book. From an applied point of view it is less obvious, where the applications of QRs can be found, if one wants to utilize the unique topological properties of QRs. The suggested applications of QRs that make use of the topological properties are, not surprisingly, primarily found in the field of spintronics and involve spin manipulation of carriers captured in or passing through the ring structure. In order to exploit the topological properties of QRs, it is crucial that the phase scattering and spin scattering rates of carriers in the QR, which lead to decoherence of QR states, are small. This unfortunately limits any by now suggested application to low temperatures and makes the chance of real applications in the near future very dim. However, additional applications have been suggested that do not depend on the topological properties of QRs, but use, for instance, the special charge distribution or the frequently observed anisotropy in the shape of self-assembled rings. Below, we will first discuss some examples of applications that do not utilize the topological properties of QRs and then a number of examples that are based on topologically induced features.

In 2003, Granados and Garcia [16] reported a strong dependence of the PL spectrum on the actual shape of InAs/GaAs self-assembled quantum structures. Depending on the growth conditions during capping and annealing of InAs self-assembled dots they observe quantum dots, QRs and more complicated structures. The luminescence for these structures varied from 1.1 eV (quantum dots) to 1.35 eV (QRs) depending on the shape of the nanostructure. This shift is of course due to the shallower confinement of the carriers in a QR compared to those captured in a quantum dot. This feature does not, however, make them attractive, because typically more effort is put in getting the emission of semiconductor nanostructures at longer (rather than shorter) wavelengths that are accessible by standard InAs/GaAs quantum dots. Nevertheless, InAs/GaAs QR structures have been analyzed for their use in THz detectors, because they give rise to a very low dark current [61] and GaAs/AlGaAs QRs have been proposed in solar cells because these strain-free QRs might give rise to a better quantum efficiency [62], see also Chap. 14. In these applications, neither the topology, nor the ring-shaped charge distribution is essential for the operation of the device.

The following applications make use of the special geometry of the ring without exploiting the topological aspects. Due to the fact, discussed in detail in the present Chapter, that InAs/GaAs QRs are often asymmetric [7], they can give rise to a strong optical anisotropy [63, 64]. This property can be useful in situations, where optical polarization detection or manipulation is needed. The ring-shaped potential, independent of any in-plane anisotropy, is important in type-II QRs that have been shown to work as memory devices with a long storage time because of the spatial separation of the electron and hole, which prevents carrier recombination [65]. In these devices the hole is confined in a dot potential, whereas the electron is confined in a ring potential that runs around the dot. Wavefunction engineering in a similar quantum dot-ring nanostructure was proposed in [66]. They proposed electrical gating to control exciton relaxation and absorption by manipulating the confinement parameters. The envisioned device can be actively tuned from being highly absorbing to almost transparent in a specific part of the infrared or microwave spectrum.

More sophisticated is the idea to control the transition probability of an electron-hole pair captured in a ring by transforming a bright exciton state into a dark exciton state and vice versa [67]. In this device, the combination of a perpendicular magnetic and in-plane electric field is used to control the exciton state and this should make it possible to store and to release an optically excited exciton in a QR, which can be also be read out by an additional approach. Interestingly, GaAs/AlGaAs double QRs obtained by droplet epitaxy [68] have been proven to show photon antibunching, which is essential for single photon devices. Only the inner ring showed a strong photon antibunching, whereas this is relaxed in the outer ring probably due to a stronger inhomogeneity in the potential of the outer ring. Without being specific the authors suggest that these single photon emitting ring structures can be of relevance for quantum computational devices.

The most exciting applications are of course those that are based on the topological properties of the ring geometry. Not without surprise, these applications lie in the field of quantum computing, where spin manipulation is of essence. For instance, sequential spin flips were observed in lithographic GaAs/AlGaAs QRs [69]. In these QRs, operating in the Coulomb blockade regime, experimental results were obtained that showed the ability to probe individual spin flips, which is an important step towards accurate spin control. The detection of spin flips was possible due to the characteristic electronic spectrum of the QR structure. Spin relaxation in QRs and dots was explored [70]. The authors report higher spin stability in a QR than in a quantum dot, supporting the use of QRs as a spin qubit. They also present a discussion on quantum state manipulation in a QR in relation to its use as a spin qubit [70].

In summary, the ongoing studies revealed great potentialities of QRs as basis elements for a broad spectrum of applications, starting from THz detectors, efficient solar cells and memory devices, through electrically tunable optical valves and single photon emitters, and further to spin qubits for quantum computing.

References

1. J.M. García, G. Medeiros-Ribeiro, K. Schmidt, T. Ngo, J.L. Feng, A. Lorke, J. Kotthaus, P.M. Petroff, Appl. Phys. Lett. **71**, 2014 (1997)
2. A. Lorke, R.J. Luyken, A.O. Govorov, J.P. Kotthaus, J.M. García, P.M. Petroff, Phys. Rev. Lett. **84**, 2223 (2000)
3. R.J. Warburton, C. Schäflein, D. Haft, F. Bickel, A. Lorke, K. Karrai, J.M. García, W. Schoenfeld, P.M. Petroff, Nature **405**, 926 (2000)
4. R.J. Warburton, C. Schulhauser, D. Haft, C. Schäflein, K. Karrai, J.M. García, W. Schoenfeld, P.M. Petroff, Phys. Rev. B **65**, 113303 (2002)
5. V.M. Fomin, J. Nanoelectronics Optoelectronics **6**, 1 (2011)
6. G. Biasiol, S. Heun, Phy. Rep. **500**, 117 (2011)
7. P. Offermans, P.M. Koenraad, J.H. Wolter, D. Granados, J.M. García, V.M. Fomin, V.N. Gladilin, J.T. Devreese, Appl. Phys. Lett. **87**, 131902 (2005)
8. P. Offermans, P.M. Koenraad, J.H. Wolter, D. Granados, J.M. García, V.M. Fomin, V.N. Gladilin, J.T. Devreese, Phys. E **32**, 41 (2006)
9. N.A.J.M. Kleemans, I.M.A. Bominaar-Silkens, V.M. Fomin, V.N. Gladilin, D. Granados, A.G. Taboada, J.M. García, P. Offermans, U. Zeitler, P.C.M. Christianen, J.C. Maan, J.T. Devreese, P.M. Koenraad, Phys. Rev. Lett. **99**, 146808 (2007)
10. T.-C. Lin, C.-H. Lin, H.-S. Ling, Y.-J. Fu, W.-H. Chang, S.-D. Lin, C.-P. Lee, Phys. Rev. B **80**, 081304(R) (2009)
11. P. Moon, K. Park, E. Yoon, J.-P. Leburton, Phys. Status Solidi RRL **3**, 76 (2009)
12. P. Moon, W.J. Choi, K. Park, E. Yoon, J.D. Lee, J. Appl. Phys. **109**, 103701 (2011)
13. V. Arsoski, N. Čukarić, M. Tadić, F.M. Peeters, Phys. Scr. T **149**, 014054 (2012)
14. L.M. Thu, W.T. Chiu, O. Voskoboynikov, Phys. Rev. B **85**, 205419 (2012)
15. R. Blossey, A. Lorke, Phys. Rev. E **65**, 021603 (2002)
16. D. Granados, J.M. García, Appl. Phys. Lett. **82**, 2401 (2003)
17. D. Granados, J.M. García, T. Ben, S.I. Molina, Appl. Phys. Lett. **86**, 071918 (2005)
18. V. Baranwal, G. Biassol, S. Heun, A. Locatelli, T.O. Mentes, M.N. Orti, L. Sorba, Phys. Rev. B **80**, 155328 (2009)
19. C.H. Lin, H.S. Lin, C.C. Huang, S.K. Su, S.D. Lin, K.W. Sun, C.P. Lee, Y.K. Liu, M.D. Yang, J.L. Shen, Appl. Phys. Lett. **94**, 183101 (2009)
20. M.D. Teodoro, A. Malachias, V. Lopes-Oliveira, D.F. Cesar, V. Lopez-Richard, G.E. Marques, E. Marega Jr., M. Benamara, YuI Mazur, G.J. Salamo, J. Appl. Phys. **112**, 014319 (2012)
21. Y. Lv, J. Cui, Z.M. Jiang, X. Yang, Nanoscale Res. Lett. **7**, 659 (2012)
22. J. van Bree, A.Y. Silov, P.M. Koenraad, M.E. Flatté, Phys. Rev. Lett. **112**, 187201 (2014)
23. Y. Yafet, Solid State Phys. **14**, 1 (1963)
24. J. van Bree, A.Y. Silov, P.M. Koenraad, M.E. Flatté, Phys. Rev. B **90**, 165306 (2014)
25. J. van Bree, AYu. Silov, M.L. van Maasakkers, C.E. Pryor, M.E. Flatté, P.M. Koenraad, Phys. Rev. B **93**, 035311 (2016)
26. V.V. Belykh, D.R. Yakovlev, J.J. Schindler, J. van Bree, P.M. Koenraad, N.S. Averkiev, M. Bayer, AYu. Silov, J. Appl. Phys. **120**, 084301 (2016)
27. H.M.G.A. Tholen, J.S. Wildmann, A. Rastelli, R. Trotta, C.E. Pryor, E. Zallo, O.G. Schmidt, P.M. Koenraad, AYu. Silov, Phys. Rev. B **94**, 245301 (2016)
28. Athmane Tadjine, Christophe Delerue, Phys. Rev. B **95**, 235426 (2017)
29. Athmane Tadjine, Yann-Michel Niquet, Christophe Delerue, Phys. Rev. B **95**, 235437 (2017)
30. P.W. Fry, I.E. Itskevich, D.J. Mowbray, M.S. Skolnick, J.J. Finley, J.A. Barker, E.P. O'Reilly, L.R. Wilson, I.A. Larkin, P.A. Maksym, M. Hopkinson, M. Al-Khafaji, J.P.R. David, A.G. Cullis, G. Hill, J.C. Clark, Phys. Rev. Lett. **84**, 733 (2000)
31. L.G. Wang, P. Kratzer, M. Scheffler, Q.K.K. Liu, Appl. Phys. A: Mater. Sci. Process. **73**, 161 (2001)
32. Z.R. Wasilewski, S. Fafard, J.P. McCaffrey, J. Cryst. Growth **201/202**, 1131 (1999)
33. E. Steimetz, T. Wehnert, H. Kirmse, F. Poser, J.-T. Zettler, W. Neumann, W. Richter, J. Cryst. Growth **221**, 592 (2000)

34. A. Lenz, H. Eisele, R. Timm, S.K. Becker, R.L. Sellin, U.W. Pohl, D. Bimberg, M. Dähne, Appl. Phys. Lett. **85**, 3848 (2004)
35. K. Shiraishi, Appl. Phys. Lett. **60**, 1363 (1992)
36. J.A. Barker, R.J. Warburton, E.P. O'Reilly, Phys. Rev. B **69**, 035327 (2004)
37. P. Offermans, P. Koenraad, J. Wolter, K. Pierz, M. Roy, P. Maksym, Phys. E **26**, 236 (2005)
38. D.M. Bruls, J.W.A.M. Vugs, P.M. Koenraad, H.W.M. Salemink, J.H. Wolter, M. Hopkinson, M.S. Skolnick, F. Long, S.P.A. Gill, Appl. Phys. Lett. **81**, 1708 (2002)
39. V.M. Fomin, V.N. Gladilin, S.N. Klimin, J.T. Devreese, N.A.J.M. Kleemans, P.M. Koenraad, Phys. Rev. B **76**, 235320 (2007)
40. M. Grundmann, O. Stier, D. Bimberg, Phys. Rev. B **52**, 11969 (1995)
41. J.A. Barker, E.P. O'Reilly, Phys. Rev. B **61**, 13840 (2000)
42. C.G. Van de Walle, Phys. Rev. B **39**, 1871 (1989)
43. http://www.simulia.com/products/abaqus_fea.html
44. V.M. Fomin, V.N. Gladilin, J.T. Devreese, P. Offermans, P.M. Koenraad, J.H. Wolter, J.M. García, D. Granados, AIP Conf. Proc. **772**, 803 (2005)
45. M.R. Schaapman, P.C.M. Christianen, J.C. Maan, D. Reuter, A.D. Wieck, Appl. Phys. Lett. **81**, 1041 (2002)
46. V.M. Fomin, V.N. Gladilin, J.T. Devreese, N.A.J.M. Kleemans, P.M. Koenraad, Phys. Rev. B **77**, 205326 (2008)
47. V.M. Fomin, V.N. Gladilin, J.T. Devreese, N.A.J.M. Kleemans, M. Bozkurt, P.M. Koenraad, Phys. Stat. Sol. (b) **245**, 2657 (2008)
48. V.M. Fomin, V.N. Gladilin, J.T. Devreese, J.H. Blokland, P.C.M. Christianen, J.C. Maan, A.G. Taboada, D. Granados, J.M. García, N.A.J.M. Kleemans, H.C.M. van Genuchten, M. Bozkurt, P.M. Koenraad, Proc. SPIE **7364**, 736402 (2009)
49. N.A.J.M. Kleemans, J.H. Blokland, A.G. Taboada, H.C.M. van Genuchten, M. Bozkurt, V.M. Fomin, V.N. Gladilin, D. Granados, J.M. García, P.C.M. Christianen, J.C. Maan, J.T. Devreese, P.M. Koenraad, Phys. Rev. B **80**, 155318 (2009)
50. S. Raymond, S. Studenikin, A. Sachrajda, Z. Wasilewski, S.J. Cheng, W. Sheng, P. Hawrylak, A. Babinski, M. Potemski, G. Ortner, M. Bayer, Phys. Rev. Lett. **92**, 187402 (2004)
51. A. Babinski, M. Potemski, S. Raymond, J. Lapointe, Z.R. Wasilewski, Phys. Rev. B **74**, 155301 (2006)
52. S. Awirothananon, S. Raymond, S. Studenikin, M. Vachon, W. Render, A. Sachrajda, X. Wu, A. Babinski, M. Potemski, S. Fafard, S.J. Cheng, M. Korkusinski, P. Hawrylak, Phys. Rev. B **78**, 235313 (2008)
53. F. Ding, N. Akopian, B. Li, U. Perinetti, A. Govorov, F.M. Peeters, C.C. Bof Bufon, C. Deneke, Y.H. Chen, A. Rastelli, O.G. Schmidt, V. Zwiller, Phys. Rev B **82**, 075309 (2010)
54. J.D. Jackson, *Classical Electrodynamics*, 3rd edn. (Wiley, New York, 1998), p. 259 and 443
55. T. Thonhauser, D. Ceresoli, D. Vanderbilt, R. Resta, Phys. Rev. Lett. **95**, 137205 (2005)
56. A. Messiah, *Quantum Mechanics* (Wiley, New York, 1961)
57. J.M. Luttinger, W. Kohn, Phys. Rev. **97**, 869 (1955)
58. J.M. Luttinger, Phys. Rev. **102**, 1030 (1956)
59. H.R. Trebin, U. Rössler, R. Ranvaud, Phys. Rev. B **20**, 686 (1979)
60. P.C. Sercel, K.J. Vahala, Phys. Rev. B **42**, 3690 (1990)
61. G. Huang, W. Guo, P. Bhattacharya, G. Ariyawansa, A.G.U. Perera, Appl. Phys. Lett. **94**, 101115 (2009)
62. J. Wu, Z.M. Wang, V.G. Dorogan, S. Li, Z. Zhou, H. Li, J. Lee, E.S. Kim, G.J. Salamo, Appl. Phys. Lett. **101**, 043904 (2012)
63. D. Granados, J.M. Garcia, J. Crystal Growth **251**, 213 (2007)
64. W. Zhang, Z. Su, M. Gong, C.-F. Li, G.-C. Guo, L. He, Europ. Phys. Lett. **83**, 67004 (2008)
65. R.J. Young, E.P. Smakman, A.M. Sanchez, P. Hodgson, P.M. Koenraad, M. Hayne, Appl. Phys. Lett. **100**, 082104 (2012)
66. E. Zipper, M. Kurpas, M.M. Maska, New J. Phys. **14**, 093029 (2012)
67. A.M. Fisher, V.L. Campo, M.E. Portnoi, R. Rudolf, Phys. Rev. Lett. **102**, 096405 (2009)

68. M. Abbarchi, C.A. Mastrandrea, A. Vinattieri, S. Sanguinetti, T. Mano, T. Kuroda, N. Koguchi, K. Sakoda, M. Gurioli, Phys. Rev. B **79**, 085308 (2009)
69. E. Rasanen, A. Muhle, M. Aichinger, R.J. Haug, Phys. Rev. B **84**, 165320 (2011)
70. E. Zipper, M. Kurpas, J. Sadowski, M.M. Maska, J. Phys. Condes. Matter **23**, 115302 (2011)

Chapter 5
Scanning-Probe Electronic Imaging of Lithographically Patterned Quantum Rings

F. Martins, D. Cabosart, H. Sellier, M.G. Pala, B. Hackens, V. Bayot and S. Huant

Abstract Quantum rings patterned from two-dimensional semiconductor heterostructures exhibit a wealth of quantum transport phenomena at low temperature and in a magnetic field that can be mapped in real space thanks to dedicated scanning probe techniques. Here, we summarize our studies of GaInAs- and graphene-based quantum rings by means of scanning-gate microscopy both at low magnetic field, where Aharonov-Bohm interferences and the electronic local density-of-states are imaged, and at high magnetic field and very low temperatures, where the scanning probe can image Coulomb islands in the quantum Hall regime. This allows decrypting the apparent complexity of the magneto-resistance of a mesoscopic system in this regime. Beyond imaging and beyond a strict annular shape of the nanostructure, we show that this scanning-probe technique can also be used to unravel a new counter-intuitive behavior of branched-out rectangular quantum rings, which turns out to be a mesoscopic analog of the Braess paradox, previously known for road or other classical networks only.

F. Martins (✉) · D. Cabosart · B. Hackens · V. Bayot
Université Catholique de Louvain, IMCN/NAPS, Louvain-La-Neuve, Belgium
e-mail: fredmarte@hotmail.com

B. Hackens
e-mail: benoit.hackens@uclouvain.be

V. Bayot
e-mail: vincent.bayot@uclouvain.be

H. Sellier · S. Huant
Université Grenoble Alpes, CNRS, Institut Néel, 38000 Grenoble, France
e-mail: hermann.sellier@neel.cnrs.fr

S. Huant
e-mail: serge.huant@neel.cnrs.fr

M.G. Pala
C2N, CNRS, Univ Paris-Sud, Université Paris-Saclay, 91405 Orsay, France
e-mail: marco.pala@c2n.upsaclay.fr

V.M. Fomin (ed.), *Physics of Quantum Rings*, NanoScience and Technology,
https://doi.org/10.1007/978-3-319-95159-1_5

5.1 Introduction

Electron systems confined in mesoscopic quantum rings (QRs) patterned from two-dimensional charge carrier systems exhibit a wealth of quantum transport phenomena at low temperature and in a magnetic field such as the Aharonov-Bohm effect (AB) or the quantum Hall effect (QH). These effects have usually been observed thanks to measurements of the device electrical resistance vs the magnetic field. Such data yield "global" information on the phenomenon, i.e. on the scale of the device. During the last fifteen years, numerous attempts have been made to obtain real-space information on these mesoscopic phenomena down to the nanometer scale (i.e. on a smaller scale than the device size), thanks to dedicated scanning probe techniques. Mapping locally these phenomena give new insights, which allow for a more in-depth comparison with simulations. This chapter focuses on GaInAs- and graphene-based open QRs that are imaged by scanning-gate microscopy (SGM), a variant of electric atomic-force microscopy (AFM), which can access to the intimate behavior of buried electronic systems, not accessible to the tip of scanning tunneling microscopy (STM).

After a brief introduction to SGM in Sects. 5.2 and 5.3 focuses on the low-magnetic field range where the conductance modulations of a ring device induced by the scanning probe provide rich patterns that are either concentric or radial with the ring geometry. The concentric patterns, primarily seen when the tip scans outside the ring area [1], image in real space the AB interferences taking birth in the ring device as a consequence of its ability to capture a magnetic flux or to differentially probe in its two arms a remote electrostatic potential. Radial patterns, that are seen when the probe scans directly over the ring, indirectly map the electronic local density of states (LDOS) at the Fermi energy [2, 3], as does STM in a direct way for surface electron systems [4]. Quantum simulations give a limit to the range of validity for the correspondence between conductance and LDOS maps and show how robust this correspondence can be against, for example, the introduction of impurities in the ring materials [5].

Beside conventional semiconductor systems, the last decade has witnessed the advent of new types of materials with unusual charge carrier dynamics. The most striking example is graphene, a two-dimensional crystal of carbon atoms arranged on a honeycomb lattice [6]. Charge carriers in graphene behave as massless relativistic particles and novel properties emerge in particular close to the Dirac point, where valence and conduction bands touch. Section 5.4 focuses on QRs carved out of graphene, and examine the consequences of the peculiar band structure and charge carrier dynamics on scanning gate imaging of coherent transport in such devices. In particular, radial patterns were also imaged in disordered graphene rings [7], and they were found to be recurrent when varying the charge carrier energy [8]. The observation is consistent with an earlier theoretical prediction of "relativistic quantum scars" [9] , i.e. semiclassical orbits scarring the LDOS.

At high magnetic field, which is the focus of Sect. 5.5, the charge carrier system enters into the QH regime, where electrons should only be transmitted through spatially separated edge states (ESs) near integer filling of the Landau levels. In contrast

to extended 2D systems that exhibit vanishing longitudinal resistance concomitant to Hall plateaus in the QH regime, mesoscopic devices lead to surprising observations [10], such as pseudo-AB oscillations with "sub-periods" and "super-periods" compared to the orthodox AB oscillations seen at low field. To explain these observations, recent models [11] put forward the theory that, when counter-propagating ES come close to each other, electrons can hop between ES, or tunnel through quantum Hall insulating islands. Such islands, also called localized states, are made of ES rotating around hills or dips in the potential landscape, or around the central antidot in a ring geometry. SGM reveals to be very powerful in locating QH islands in GaInAs QRs, and in revealing the spatial structure of transport inside the QH interferometer that they form [12]. Locations of QH islands are found by modulating, with the scanning tip, the tunneling between ESs and confined electron orbits. Tuning the magnetic field, SGM unveils a continuous evolution of active QH islands [12]. This allows decrypting the complexity of high-magnetic field magnetoresistance oscillations, and opens the way to further local-scale manipulations of QH localized states.

In Sect. 5.6 we consider the possibility to control the electron transport through the buried semiconductor nanostructure by means of the SGM tip. In doing so, we find evidence for a counterintuitive behavior of mesoscopic networks [13] that presents a striking similarity with the Braess paradox encountered in traffic or classical networks [14]. A simulation of quantum transport in a two-branch mesoscopic network of rectangular shape reveals that adding a third branch can paradoxically reduce transport efficiency. This manifests itself in a sizable conductance drop of the network. A SGM experiment using the tip to modulate the transmission of one branch in the network reveals the occurrence of this paradox by mapping the conductance variation as a function of the tip voltage and position [13].

5.2 A Brief Introduction to the Technique of Scanning-Gate Microscopy

Unlike common AFM-based imaging techniques, scanning gate microscopy does not rely on a measurement of the cantilever property (i.e. its deflection angle, or resonance frequency shift), but rather of the device electrical characteristics. The principle of SGM [15–17] is sketched in Fig. 5.1. A voltage-biased (V_{tip}) metal-coated AFM tip is laterally scanned at an altitude of a few tens of nm over the device surface to perturb locally its electrical conductance G (or resistance). The changes in the device conductance ΔG are mapped as a function of the relative tip-sample position (x,y) to draw a $\Delta G(x,y)$ SGM map. Depending on the device impedance, a current-biased device (I) or voltage-biased (V) configuration can be used. The whole setup is immersed into a cryostat to operate down to below 100 mK for the coldest SGM setups [12, 18]. Optionally, an external magnetic field can be applied. The combined low-temperature and magnetic field environment requires the use of cryogenic magnetic-free displacement units, such as for example titanium-made

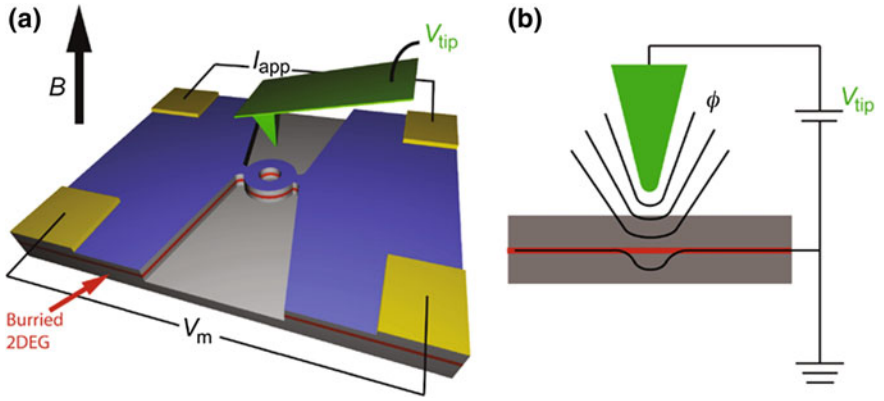

Fig. 5.1 Principle of scanning-gate microscopy. Frame **a** depicts a sketch of a SGM experiment on a ring-shaped device that hosts a buried 2DEG. A current I_{app} is applied to the device and the voltage drop V_m across it is measured, while the biased tip (V_{tip}) is raster scanned over the device. A perpendicular magnetic field $\boldsymbol{B}$ is applied. In frame **b**, curved lines sketch the tip-induced isopotential lines ϕ felt by the buried electron system. For a sufficiently negative tip voltage, a depleted region is formed below the tip in the case of semiconductor 2DEGs (not for graphene)

inertial step motors [19, 20] for the in situ coarse positioning of the tip relative to the nanostructure over a few millimeters. In our setup, fine positioning over a few micrometers for image acquisition is ensured by commercially available piezoelectric scanner elements.

Using an AFM environment allows for locating the active device by measuring the sample topography, e.g. by using the dynamic mode of the AFM. Instead of using an optical method to measure the AFM cantilever deflection, as commonly done in AFM, it is advantageous to use a light-free setup [21], so that photosensitive devices remain under dark conditions during the entire experiment. One solution consists in gluing the AFM cantilever on a piezoelectric tuning fork, and monitoring the shift Δf of its resonance frequency observed when the tip approaches the surface. Sample topography is performed by using a feedback loop on Δf while scanning the tip over the device surface. Once the device topography has been mapped, SGM is performed by lifting the tip at some tens of nanometers (typically 20–50 nm) above the surface and scanning it along a plane parallel to the 2D electron gas (2DEG), with a voltage applied to the tip. SGM measurements are carried out without contact between tip and sample, so that there is no electrical current through the tip, which acts indeed as a flying nanogate.

SGM has been used to image a broad range of transport-related phenomena in various nanostructures, such as for example the branching of conductance channels transmitted through quantum-point contacts (QPCs) [16, 17, 22], magnetic steering in a series of connected QPCs [23], Coulomb blockade in quantum dots [24–26], scarred wavefunctions in quantum billiards [27], and various graphene-based nanodevices [28–35], including in the quantum Hall regime [34]. We refer the reader to [36] for a

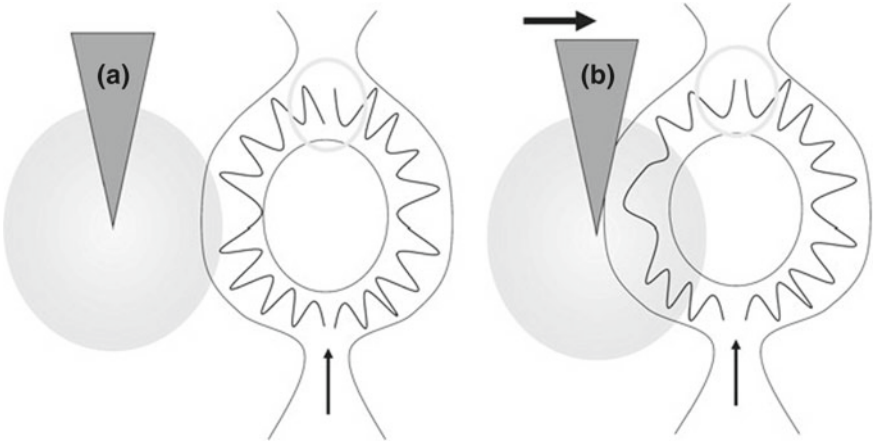

Fig. 5.2 Sketch of the electrostatic AB effect in a QR due to the tip bias. The cone and disk stand for the tip and potential range, respectively. Approaching the tip to the QR from the left modifies the electrostatic potential felt by the electrons in the left arm, tuning the wavefunction interference at the output of the device from destructive (**a**) to constructive (**b**)

more extensive review. In the rest of this chapter, we focus on our own work devoted to GaInAs- and graphene-based QRs.

5.3 Imaging of Quantum Rings in the Low-Field Aharonov-Bohm Regime

If electrons maintain their phase coherence over sufficiently long distances, an open QR sees its conductance peaking when electron waves interfere constructively at the output contact, and decreasing to a minimum for destructive interference. Varying either the electrostatic potential in one arm, e.g., by approaching the SGM biased tip as shown schematically in Fig. 5.2, or the magnetic flux captured by the QR allows the interference to be tuned. This gives rise to the electrostatic [37] and magnetic [38] AB oscillations in the ring conductance.

These interference phenomena can be imaged in real space by SGM [1]. An example of such imaging is shown in Fig. 5.3. Here, the QR is patterned from a $Ga_{0.3}In_{0.7}As$-based heterojunction with carrier concentration and mobility at 4.2 K of 2.0×10^{16} cm^{-2} and 100.000 cm^2 V^{-1} s^{-1}, respectively. The QR is connected to the 2D electron reservoir, which is buried 25 nm below the free surface, by two upper and lower narrow constrictions. The mean-free path and coherence length in $Ga_{0.3}In_{0.7}As$ at 4.2 K are 2 and 1 μm, respectively, so that the electron transport is in the ballistic and (partly) coherent regimes. The coherent nature is confirmed

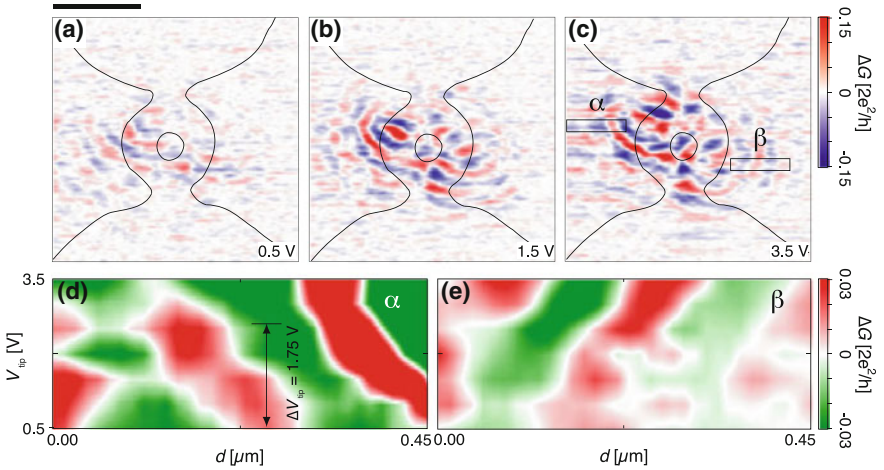

Fig. 5.3 SGM images (**a**–**c**) of a GaInAs QR whose geometry is shown schematically by full lines (image size: 2 μm × 2 μm; T = 4.2 K; zero magnetic field). The inner and outer ring diameters are 210 and 610 nm, respectively. The images are acquired for different tip voltages V_{tip} indicated on the figures and are all filtered [1] to compensate for a slowly varying strong background, which masks part of the interference pattern. Frames d and e are two sequences of profile plots as function of the tip bias. Each horizontal line corresponds to a vertical average of the conductance map in regions (α) and (β) shown in Fig. 5.3c, respectively. Adapted from [39]

by the observation of AB oscillations in the magneto-conductance when the QR is subjected to a perpendicular magnetic field [1].

One also observes an electrostatic AB effect which gives rise, at low magnetic field, to a well-developed fringe pattern in the SGM conductance image of the QR when the tip scans outside the QR. This outer pattern is mainly concentric with the ring geometry, as can be seen in the sequence of images shown in Fig. 5.3a–c obtained at different voltages applied to the tip. The interference pattern is here best seen on the left part of the ring, possibly due to a ring asymmetry. The qualitative interpretation in terms of a scanning-gate-induced electrostatic AB effect is that as the tip approaches the QR, either from the left or right, the electrical potential mainly increases on the corresponding side of the QR (see Fig. 5.2). This induces a phase difference between electron wavefunctions traveling through the two arms of the ring, and/or bends the electron trajectories, tuning the interference alternatively from constructive to destructive, thereby producing the observed pattern. Figure 5.3d, e shows how the interference pattern evolves for increasing tip voltages when the tip scans over the left hand-side and right hand-side regions of the QR, respectively [39]. It is clear from this figure that for increasing tip voltages the interference fringes shift away from the QR to the left in d and to the right in e, respectively. This is a direct manifestation of the tip-induced electrostatic AB effect. From Fig. 5.3d, we find that a phase shift of π is obtained for a tip bias variation $\Delta_{tip} = 1.75$ V [39].

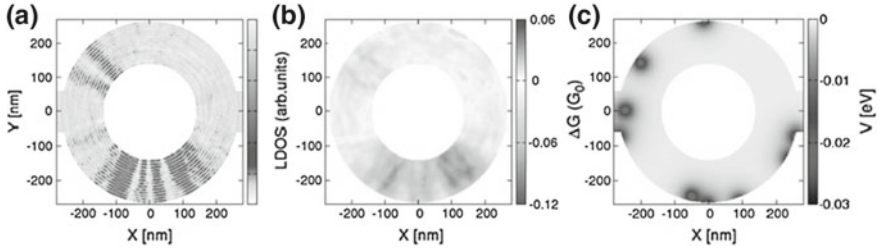

Fig. 5.4 Quantum simulation of a SGM experiment on a QR in the presence of positively charged impurities. The outer diameter, inner diameter and opening width are 530, 280, and 120 nm, respectively. The effective mass is 0.04 m_0 as in GaInAs (m_0 is the free electron mass). The Fermi energy is $E_F = 107.4$ meV. Frames **a** and **b** are simulated images of the LDOS and conductance changes (in units of G_0, the quantum of resistance), respectively, calculated for the random distribution of positively-charged impurities shown in frame (**c**). In the simulation, the tip potential has a Lorentzian shape with 10 nm range and amplitude $E_F/50$. Adapted from [5]

Now, modifying the magnetic field strength, another phase term contributes through the magnetic AB effect, i.e. the capture of the magnetic flux threading the QR area. The flux periodicity of such oscillations correspond to the flux quantum $\phi_0 = h/e$. This displaces the whole fringe pattern with respect to the QR. This displacement is periodic in magnetic field strength with the same periodicity (here 13 mT, in nice agreement with the average area of the QR) than the AB oscillations seen in the magneto-conductance [1, 39], which gives further support to the interpretation in terms of AB effects. This interpretation was confirmed by density functional theory [40].

In Fig. 5.3a–c, it is clear that the conductance images also exhibit a complex pattern when the tip scans directly over the QR region. These inner fringes are linked to the local electron-probability density in the QR [2, 3, 5], provided that the tip potential is weak enough not to distort the QR electron density (see also [40]). A detailed analysis based on quantum mechanical simulations of the electron probability density, including a model tip potential, the magnetic field, and randomly distributed impurities, reproduces the main experimental features and demonstrates the relationship between SGM conductance maps and electron probability density, i.e. LDOS, at the Fermi energy. An example of such a relationship is shown in Fig. 5.4 in the case of a realistic QR perturbed by positively charged impurities (in the experiments on $Ga_{0.3}In_{0.7}As$ heterojunction devices, the electrostatic potential experienced by electrons is influenced by ionized dopants located a few nm above the conducting 2D electron system). Although impurities distort the LDOS, this distortion is reflected back in the conductance image in such a way that the conductance map can still be seen as a mirror of the electronic LDOS. As shown in Fig. 5.4, both the LDOS and conductance images tend to develop radial fringes, which are mostly, but not entirely, anchored to the impurity locations.

The discussion above suggests that SGM can be viewed as the analog of STM [4] for imaging the electronic LDOS in open mesoscopic systems buried under an

insulating layer. It can also be seen as the counterpart of the near-field scanning optical microscope that can image photonic [41, 42] LDOS in confined nanostructures, provided that the excitation light source can be considered as point-like such as in active tips based on fluorescent nano-objects [43].

5.4 Recurrent Quantum Scars in Graphene Quantum Rings

In a semiclassical framework, the inner radial fringes observed in the arms of QRs (discussed in previous section) can be viewed as "privileged paths" along which charge carrier wavefunctions are concentrating, also named "scarred wavefunctions", or "scars". Such scars have been introduced in the framework of quantum chaos theories [44]; in the latter case, they were associated with unstable semiclassical periodic orbits in quantum billiards. A specific aspect of semiclassical periodic orbits, useful for probing their existence in the experiment, is their recurrence originating from their finite orbit length: scar patterns associated with such semiclassical periodic orbits were predicted to reappear periodically with the Fermi energy E_F in relativistic systems like graphene while the recurrence should occur with the square root of E_F in the case of a conventional semiconductor system [9].

This prediction was investigated using SGM, through experiments realized on two different graphene QRs, fabricated from exfoliated graphene, transferred either directly on top of a degenerately doped oxidized silicon substrate acting as a back-gate [7], or on hexagonal boron nitride (h-BN) deposited on top of a similar silicon substrate [8]. In the first case, the measured low temperature mobility of charge carriers was relatively modest (around 1000 cm^2/Vs). In the low density regime (close to the Dirac point), SGM reveals Coulomb blockade oscillations, associated with disorder-induced localized states. Such localized states are ubiquitous in low-mobility graphene devices at low charge carrier density since the disorder landscape induces randomly located electron and hole puddles which can constitute and act like isolated quantum dots, tunnel-coupled with the transmitted channels. They have already been imaged indirectly using tip-induced tuning of Coulomb blockade in various SGM experiments, in particular in small constrictions [31–33]. In contrast, at higher charge carrier densities, disorder is at least partially screened and electron/hole puddles disappear. In these conditions, SGM imaging on the graphene QR revealed radial fringes (scars) [7] very similar to those found in heterostructure-based QRs [2]. Simulations realized on graphene QR with similar degree of disorder confirmed that radial patterns naturally emerge at various locations along QR's arms in the LDOS.

The recurrence of the radial pattern of scars with energy was studied using SGM in another graphene QR with higher charge carrier mobility (~10000 cm^2/Vs), deposited on top of an h-BN flake [8]. A large number of radial scars was observed in this case, and sequences of SGM images obtained at various back-gate voltage were thoroughly examined, in order to find evidence of recurring patterns. Cross-correlations

between successive images were calculated, both for full SGM images and for specific areas on SGM images where radial patterns were observed. Local maxima in the correlation parameters were found when varying the Fermi energy, clearly indicating the energy recurrence, with an average distance between maxima varying slightly depending on the examined portion of the SGM image. This distance in energy can be directly converted in semiclassical orbit lengths corresponding to twice the QR arm width, which allowed to associate the sequence of maxima in SGM image correlation parameters with radial scars. Note that similar energy recurrence was also found for patterns of radial scars obtained in simulated QR LDOS.

5.5 Imaging Quantum Rings in the Quantum Hall Regime

In the two previous sections we focused on transport at zero or low-magnetic field (B) through a QR. The wave-like nature of electrons could be revealed by periodic AB oscillations in the magneto-resistance of the device. They originate from the different phases that electrons acquire along both arms of a QR when B is applied perpendicular to the 2D electron system. In this section, we will discuss another type of periodic magneto-resistance oscillations, which show up at high B in QRs.

At high magnetic field the electron transport picture changes drastically as the cyclotron radius shrinks, highly degenerate Landau levels (LLs) form and the 2DEG enters in the "QH regime". When the Fermi energy lies between two Landau levels (i.e. around integer LL filling factor ν), the bulk of the 2DEG becomes insulating and current flows through counter-propagating one-dimensional channels, the so-called ESs, confined along the borders of the device, where the Fermi energy crosses LLs. In macroscopic devices, scattering between opposite ESs vanishes and the electron mean free path becomes of the order of several millimeters. Moreover, QH islands (QHIs), i.e. electrons trapped in closed ESs pinned around potential inhomogeneities, remain electrically isolated and do not contribute to electron transport. This gives rise, as shown in Fig. 5.5a, to plateaus in the transverse resistance R_{xy}, and to a vanishing longitudinal resistance R_{xx} measured in a macroscopic Hall bar (for review see e.g. [45]).

However, when the size of the device is reduced and becomes comparable with the size of QHIs, this picture is no longer valid. In such conditions, several experiments have reported "sub-periodic" and "super-periodic" magnetoresistance oscillations, i.e. with a flux period corresponding to a fraction, or a multiple of the usual AB period observed at low-magnetic field (see sections above) [10, 46–51]. Driven by these intriguing results, theoretical efforts have explained these oscillations within a model where Coulomb interactions dominate [11]. In small devices, the counter-propagating ESs are indeed brought close to each other so that electrons may tunnel between them, either directly, and/or through a QHI that mediates electron transmission [52, 53]. Rather than coherent effects, the discrete nature of electrons has naturally been put forward.

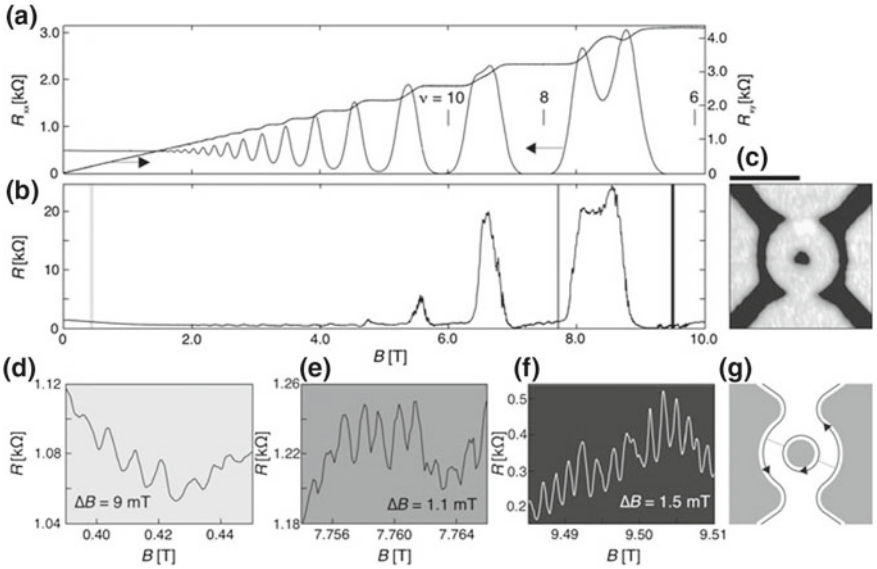

Fig. 5.5 Quantum Hall effect on a mesoscopic QR. In **a** the black and red curves are the longitudinal (*Rxx*) and the transverse (*Rxy*) resistances of a Hall bar, respectively, as function of the magnetic field (*B*). At high *B*, *Rxy* is quantized in $e^2/(N.h)$, where *N* is the number of fully occupied Landau levels, while *Rxx* becomes zero. The AFM micrograph of the QR is shown in **c** where the black bar represents 1 μm. In **b** we display the magnetoresistance measured across the QR in the same range of *B* and at a temperature $T = 100$ mK. Close-ups of **b** are shown in (**d**–**f**). At low-*B* (**d**), the periodicity of the oscillations is $\Delta B_{AB} = 9$ mT which, given the geometry presented in (**c**), is consistent with AB interferences. At high magnetic field, for $N = 8$, shown in (**e**) the periodicity is $\Delta B = 1.1$ mT while, for $N = 6$, displayed in (**f**), we find $\Delta B = 1.5$ mT. The latter oscillations are explained, as sketched in (**g**), as tunneling between edge states through a Coulomb island located around the central anti-dot of the QR. This gives rise to periodic oscillations with $\Delta B.N = \Delta B_{AB}$

The experiments discussed in this section [12] are performed at a temperature $T = 100$ mK, inside a ^{3}He/^{4}He dilution refrigerator, equipped with a superconducting coil that can provide a magnetic field up to 15/17 T. The 2DEG in which the QR is patterned is located 25 nm below the surface and, at low-*T*, the electron density and mobility are 1.4×10^{16} m^{-2} and 4 m^2/Vs, respectively. Figure 5.5c shows the device topography. The QR has an average outer diameter of 1 μm, two apertures and a central antidot diameter of approx. 300 nm. The magneto-resistance of the quantum ring (*R* versus *B*), measured simultaneously with R_{xx} and R_{xy} in the bulk, is shown in Fig. 5.5b, d–f. Figure 5.5b shows *R* versus *B* over the full magnetic field range, from 0 to 10 T. At low magnetic field, Fig. 5.5d, periodic AB oscillations with $\Delta B_{AB} = 9$ mT are observed. This is consistent with an average radius of 380 nm for the QR. In Fig. 5.5e, f, two *B*-ranges are zoomed, around $\nu = 8$ and 6, respectively. In these ranges the magnetoresistance of the device displays oscillations with two different "sub-periods": $\Delta B = 1.1$ mT around $\nu = 8$ and, around $\nu = 6$, $\Delta B = 1.5$ mT. As sketched in Fig. 5.5g, one can understand these oscillations within a Coulomb-

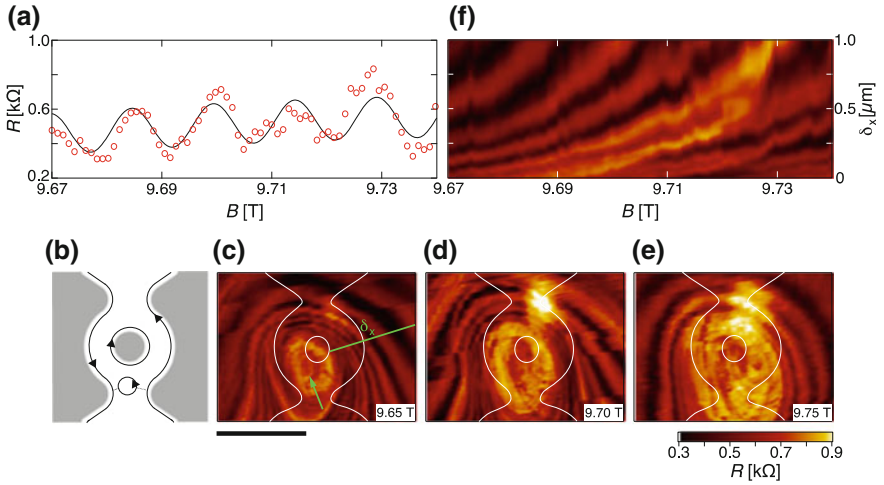

Fig. 5.6 Identification of the centre of a Coulomb island inside a QR using SGM. Frame **a** shows R versus B in the range $B = [9.67\ \text{T}, 9.74\ \text{T}]$. The periodicity of the fringes is $\Delta B = 17$ mT, which corresponds to a QHI with a surface equivalent to a disc of radius ~65 nm located, as sketched in (**b**), somewhere in the arms of the 300-nm-wide QR. **c**–**e** are SGM resistance maps obtained at $B = 9.65$, 9.70 and 9.75 T, respectively, with $V_{tip} = -1$ V. The white lines correspond to the position of the QR and the scale bar represents 1 μm. This sequence of images reveals the position of the center of the QHI [marked with a green arrow in (**c**)], inside the QR. **f** depicts B-dependence of the $R(x, y)$ profile measured along the green line in **c**, $V_{tip} = -1$ V. The fringes share the same periodicity $\Delta B = 17$ mT as in (**a**)

dominated model where electrons tunnel between propagating ESs through a QHI with discrete energy levels, located around the central anti-dot of the QR [11]. The basis of this model is that a change in magnetic field induces a periodic change in the QHI energy with respect to the ES energy. For each flux quantum added to the QHI, one electron has to be added to each populated ES in the QHI, which means that, in this case, Coulomb blockade oscillations are observed, with a period:

$$\Delta B = (\varphi_0/A)/N;$$

where N is the number of filled ESs around the QHI of area A. Indeed, the periods measured in Fig. 5.5e, f are consistent with this relation. Nevertheless, shifting the magnetic field range to $B = [9.67\ \text{T}, 9.74\ \text{T}]$ (still around $\nu = 6$), the magnetoresistance, as displayed in Fig. 5.6a, reveals "super-period" oscillations with $\Delta B = 17$ mT. Using the previous model, we conclude that they correspond to ES loops with a radius of ~65 nm, which would not fit around the QR antidot. However, it could well be located, as drawn in Fig. 5.6b, somewhere in the 300-nm-wide arms of the QR, or near its openings, and be connected to the propagating ES through tunnel junctions.

In order to precisely locate such a QHI, we now use SGM since this technique is particularly well adapted to image electronic transport through buried 2DEG in

the quantum Hall regime [12, 18, 36, 39, 54–59]. Here, we measure the resistance of the device as the electrically polarized AFM tip scans over the surface. Within the Coulomb-dominated model, as the negatively biased tip approaches a QHI, it progressively changes the electrostatic potential experienced by electrons trapped in the QHI and modify the QHI surface which, in turn, induces an energy imbalance between the QHI and the ESs [11, 12]. As with the magnetic field, this imbalance then allows electrons to tunnel between ESs and the QHI in the Coulomb blockade regime, whenever a QHI energy level lies in the energy window defined by the propagating ES potential. In a SGM map, one therefore expects to observe sets of concentric resistance fringes, each one corresponding to a Coulomb blockade peak, encircling each active QHI.

Three consecutive SGM maps for $B = 9.65$, 9.70 and 9.75 T are shown in Fig. 5.6c–e, respectively, where the position of the QR is drawn, superimposed on the SGM data. Concentric fringes are observed, centered close to one of the openings of the QR. As B increases the position of resistance fringes evolves. This is clearly illustrated in Fig. 5.6f, where B is swept while scanning with a negatively polarized tip ($V_{tip} = -1$ V) along the same line, highlighted in green and denoted δx in Fig. 5.6c. As B increases the concentric fringes shift away from their center, indicated by the green arrow in Fig. 5.6c. Importantly, we also note that the periodicity ΔB = 17 mT found in Fig. 5.6f is the same as the one extracted from the magnetoresistance curve in Fig. 5.6a. This allows concluding that the QHI, which is at the origin of these "super-period" oscillations, has its center indicated by the green arrow in Fig. 5.6c.

Remarkably, the slope direction in the plane B versus δx can be used to discriminate between ESs surrounding a potential hill or looping around a potential well. If we assume that a QHI is created around a potential hill, approaching a negatively biased tip will raise the potential and increase the QHI area. On the other hand, in the case of a QHI formed around a potential well, the effect of a negatively biased tip would be to reduce the QHI surface. In Fig. 5.6f, isoresistance lines, that correspond to isoflux states through the QHI, move away from their center as B is raised, which unambiguously indicates that the QHI surrounds a potential hill. Such a potential hill could be caused by the presence of one or several ionized dopants located a few nm above the 2D electron system.

In addition to pinpointing the location of QHIs and understanding their contribution in the high-B magnetoresistance oscillations, SGM can also yield spectroscopic information on QHIs. This is achieved by positioning the tip close to a QHI, and varying the microscope tip bias as well as current bias across the device. This way, we uncovered the QHI discrete energy spectrum arising from electronic confinement and extracted estimates of the gradient of the confining potential, as well as the edge state velocity [58]. Moreover, we also used the SGM tip to modify the configuration of QH edge states in the vicinity of a constriction in order to form a QH interferometer, i.e. a small quantum ring formed by tunnel-coupled QH edge states [59].

5.6 Revealing an Analog of the Braess Paradox in Branched-Out Rectangular Rings

In the above sections, SGM has been used to image the electron transport in annular shaped QRs. In this section, we demonstrate that SGM can also be used to tune the electron transport by depleting, by gate effect, a conduction channel in a branched-out mesoscopic network, whose primary shape is a rectangular ring. This leads to the discovery of a mesoscopic analog [13] of the Braess paradox [14].

Adding a new road to a congested network can paradoxically lead to a deterioration of the overall traffic situation, i.e. longer trip times for road users. Or, in reverse, blocking certain streets in a complex road network can surprisingly reduce average trip time [60]. This counter-intuitive behavior has been known as the Braess paradox [14]. Later extended to other networks in classical physics, such as mechanical or electrical networks [61, 62], this paradox lies in the fact that adding extra capacity to a congested network can counter-intuitively degrade its overall performance. Initially known for classical networks only, we have extended the concept of the Braess paradox to the quantum world [13]. By combining quantum simulations of a model network and SGM, we have discovered that an analog of the Braess paradox can occur in mesoscopic semiconductor networks, where electron transport is ballistic and coherent.

We consider a simple two-path network in the form of a rectangular ring connected to source and drain via two openings (see Fig. 5.7a for the network geometry). In practice, this ring is patterned from a GaInAs heterojunction as for the QRs discussed in the previous sections. The dimensions are chosen to ensure that the embedded 2DEG is in the ballistic and coherent regimes of transport at 4.2 K. The short wires in the ring are chosen to be narrower than the source/drain openings to behave as congested constrictions for propagating electrons. Branching out this ring by patterning a central wire (see Fig. 5.7a) opens a third path to the electrons that bypasses the antidot in the initial rectangular ring. Then, we use SGM to partially block by gate effects the transport through the additional branch. Doing so should intuitively result in a decreased current transmitted through the device, but this is just the opposite behavior that is found in certain conditions, both experimentally and in quantum simulations [13]. Therefore, in a naive picture, electrons in such networks turn out to behave like drivers in congested cities: blocking one path favors "traffic" efficiency.

The above finding is summarized in the simulations of Fig. 5.7a, d, which show the network geometry and a calculated conductance crosscut as a function of tip position, respectively. Here, the outer width and length of the initial corral are 0.75 and 1.6 μm, respectively, whereas the widths of the lateral, upper/lower, and central (additional) arms are $W = 140$ nm, $L = 180$ nm, and $W3 = 160$ nm, respectively. The width of the source and drain openings are $W0 = 320$ nm. This ensures that electron flow in the lateral arms (in the absence of the central arm) is congested because $2\,W < W0$. In other words, all injected conduction channels (about 10) into the network cannot be admitted in these arms [13].

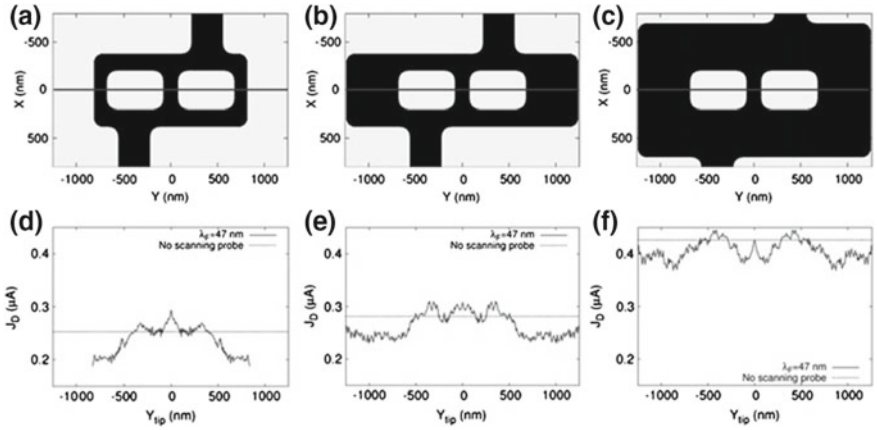

Fig. 5.7 Evidence for a Braess-like paradox in a mesoscopic rectangular network. Frames **a–c** depict the network geometries with parameters given in the text. Frames **d–f** are the corresponding calculated conductance crosscuts in the presence of a depleting SGM tip scanning along the median lines of (**a–c**), respectively. The horizontal dotted lines give the unperturbed conductance without tip. The Fermi wavelength is 47 nm. Fluctuations in the conductance profiles are UCFs due to the tip-induced change in the potential felt by electrons propagating through the device

The crosscut in Fig. 5.7d is obtained by computing the network conductance (source-drain voltage = 1 mV) as function of the tip position scanned along the median line of Fig. 5.7a. This line crosses the lateral and central arms. The tip potential is mimicked by a point-like potential of −1 V placed at 100 nm above the 2DEG [13], which corresponds to a lateral extension of ≈400 nm for the tip-induced potential perturbation at the 2DEG level. This model potential entirely depletes the 2DEG in one arm when the tip passes above it.

It is clear from Fig. 5.7d that depleting the central arm produces a distinctive conductance peak that goes well beyond the unperturbed value. This peak has a much larger amplitude as the universal conductance fluctuations (UCFs) that are seen as small oscillations for any tip position along the median lines, as a consequence of the tip-induced change in the potential felt by electrons propagating through the device [63]. This strong central peak is the signature of the counter-intuitive Braess-like behavior mentioned above. Noteworthy, closing one of the lateral arms reduces the conductance, in agreement with the intuitive expectation: the paradox is seen only when the central branch is closed, not the lateral ones, which stresses the particular role played by this central branch.

Congestion plays a key role in the occurrence of the classical Braess paradox [14, 60, 61]. In order to probe a similar role in the mesoscopic counterpart paradox, we have simulated two additional networks with enlarged lateral arms (Fig. 5.7b, e: W = 560 nm, L unchanged) and with both enlarged lateral and upper-lower arms (Fig. 5.7c, f: W = 560 nm, L = 500 nm) [63]. This releases congestion in the lateral arms. It is clear from Fig. 5.7e, f that releasing congestion smoothens the counter-

intuitive conductance peak seen in the congested network when the central arm is blocked. Nevertheless, there is still a slight conductance (current) increase when the tip scans just above the central arms in networks e and f, but it no longer goes beyond the unperturbed conductance for the largest network f. This finding entails the particular roles played by the additional branch and by network congestion in the occurrence of a distinctive Braess-like paradox. Yet, more experimental and theoretical work is needed to put forward a conclusive explanation at the microscopic level for the paradoxical behavior reported here.

5.7 Conclusion

The few examples presented in this chapter show how powerful is SGM in imaging, and possibly tuning, the electronic transport in ring-shaped semiconductor and graphene devices and to reveal how electrons behave down there. It gives valuable complementary view on phenomena that are usually considered within a macroscopic experimental scheme. The imaging of AB interferences and quantum scars, the ability of locating precisely compressible Coulomb islands in a quantum Hall interferometer, and the closing of a selected branch in a mesoscopic rectangular ring to induce a Braess-like phenomenon, all are illustrative of this claim.

Acknowledgements B. H. and F. M. are associate and postdoctoral researchers respectively with the Belgian FRS-FNRS. This work has been supported by FRFC grant no. 2.4.546.08.F and FNRS grant no 1.5.044.07.F and J.0067.13, by the Belgian Science Policy (Interuniversity Attraction Pole Program IAP-6/42) as well as by the PNANO 2007 program of the Agence Nationale de la Recherche, France ("MICATEC" project). VB acknowledges the award of a "Chaire d'excellence" by the Nanoscience Foundation in Grenoble.

References

1. B. Hackens, F. Martins, T. Ouisse, H. Sellier, S. Bollaert, X. Wallart, A. Cappy, J. Chevrier, V. Bayot, S. Huant, Nat. Phys. **2**, 826 (2006)
2. F. Martins, B. Hackens, M.G. Pala, T. Ouisse, H. Sellier, X. Wallart, S. Bollaert, A. Cappy, J. Chevrier, V. Bayot, S. Huant, Phys. Rev. Lett. **99**, 136807 (2007)
3. M.G. Pala, B. Hackens, F. Martins, H. Sellier, V. Bayot, S. Huant, T. Ouisse, Phys. Rev. B **77**, 125310 (2008)
4. M.F. Crommie, C.P. Lutz, D.M. Eigler, Science **262**, 218 (1993)
5. M.G. Pala, S. Baltazar, F. Martins, B. Hackens, H. Sellier, T. Ouisse, V. Bayot, S. Huant, Nanotechnology **20**, 264021 (2009)
6. K.S. Novoselov, A.K. Geim, S.V. Morozov, D. Jiang, Y. Zhang, S.V. Dubonos, I.V. Grigorieva, A.A. Firsov, Science **306**, 666 (2004)
7. D. Cabosart, S. Faniel, F. Martins, B. Brun, A. Felten, V. Bayot, B. Hackens, Phys. Rev. B **90**, 205433 (2014)
8. D. Cabosart, A. Felten, N. Reckinger, A. Iordanescu, S. Toussaint, S. Faniel, B. Hackens, Nano Lett. **17**, 1344 (2017)
9. L. Huang, Y.C. Lai, D.K. Ferry, S.M. Goodnick, R. Akis, Phys. Rev. Lett. **103**, 054101 (2009)

10. B.J. van Wees, L.P. Kouwenhoven, C.J.P.M. Harmans, J.G. Williamson, C.E. Timmering, M.E.I. Broekaart, C.T. Foxon, J.J. Harris, Phys. Rev. Lett. **62**, 2523 (1989)
11. B. Rosenow, B.I. Halperin, Phys. Rev. Lett. **98**, 106801 (2007)
12. B. Hackens, F. Martins, S. Faniel, C.A. Dutu, H. Sellier, S. Huant, M. Pala, L. Desplanque, X. Wallart, V. Bayot, Nat. Commun. **1**, 39 (2010)
13. M.G. Pala, S. Baltazar, P. Liu, H. Sellier, B. Hackens, F. Martins, V. Bayot, X. Wallart, L. Desplanque, S. Huant, Phys. Rev. Lett. **108**, 076802 (2012)
14. D. Braess, A. Nagurney, T. Wakolbinger, Transp. Sci. **39**, 446 (2005)
15. M.A. Eriksson, R.G. Beck, M. Topinka, J.A. Katine, R.M. Westervelt, K.L. Campman, A.C. Gossard, Appl. Phys. Lett. **69**, 671 (1996)
16. M.A. Topinka, B.J. LeRoy, S.E.J. Shaw, E.J. Heller, R.M. Westervelt, K.D. Maranowski, A.C. Gossard, Science **289**, 2323 (2000)
17. M.A. Topinka, B.J. LeRoy, R.M. Westervelt, S.E.J. Shaw, R. Fleischmann, E.J. Heller, K.D. Maranowski, A.C. Gossard, Nature **410**, 183 (2001)
18. N. Paradiso, S. Heun, S. Roddaro, G. Biasiol, L. Sorba, V. Venturelli, F. Taddei, F. Giovannetti, F. Beltram, Phys. Rev. B **86**, 085326 (2012)
19. C. Obermüller, A. Deisenrieder, G. Abstreiter, K. Karrai, S. Grosse, S. Manus, J. Feldmann, H. Lipsanen, M. Sopanen, J. Ahopelto, Appl. Phys. Lett. **75**, 358 (1999)
20. M. Brun, S. Huant, J.C. Woehl, J.F. Motte, L. Marsal, H. Mariette, J. Microsc. **202**, 202 (2001)
21. K. Karrai, R.D. Grober, Appl. Phys. Lett. **66**, 1842 (1995)
22. B. Brun, F. Martins, S. Faniel, B. Hackens, G. Bachelier, A. Cavanna, C. Ulysse, A. Ouerghi, U. Gennser, D. Mailly, S. Huant, V. Bayot, M. Sanquer, H. Sellier, Nat. Commun. **5**, 4290 (2014)
23. K.E. Aidala, R.E. Parrott, T. Kramer, E.J. Heller, R.M. Westervelt, M.P. Hanson, A.C. Gossard, Nat. Phys. **3**, 464 (2007)
24. A. Pioda, S. Kicin, T. Ihn, M. Sigrist, A. Fuhrer, K. Ensslin, A. Weichselbaum, S.E. Ulloa, M. Reinwald, W. Wegscheider, Phys. Rev. Lett. **93**, 216801 (2004)
25. P. Fallahi, A.C. Bleszynski, R.M. Westervelt, J. Huang, J.D. Walls, E.J. Heller, M. Hanson, A.C. Gossard, Nano Lett. **5**, 223 (2005)
26. A.C. Bleszynski, F.A. Zwanenburg, R.M. Westervelt, A.L. Roest, E.P.A.M. Bakkers, L.P. Kouwenhoven, Nano Lett. **7**, 2559 (2007)
27. R. Crook, C.G. Smith, A.C. Graham, I. Farrer, H.E. Beere, D.A. Ritchie, Phys. Rev. Lett. **91**, 246803 (2003)
28. M.R. Connolly, K.L. Chiou, C.G. Smith, D. Anderson, G.A.C. Jones, A. Lombardo, A. Fasoli, A.C. Ferrari, Appl. Phys. Lett. **96**, 113501 (2010)
29. J. Berezovsky, M.F. Borunda, E.J. Heller, R.M. Westervelt, Nanotechnology **21**, 274013 (2010)
30. J. Berezovsky, R.M. Westervelt, Nanotechnology **21**, 274014 (2010)
31. S. Schnez, J. Guttinger, M. Huefner, C. Stampfer, K. Ensslin, T. Ihn, Phys. Rev. B **82**, 165445 (2010)
32. M.R. Connolly, K.L. Chiu, A. Lombardo, A. Fasoli, A.C. Ferrari, D. Anderson, G.A.C. Jones, C.G. Smith, Phys. Rev. B **83**, 115441 (2011)
33. N. Pascher, D. Bischoff, T. Ihn, K. Ensslin, Appl. Phys. Lett. **101**, 063101 (2012)
34. M.R. Connolly, R.K. Puddy, D. Logoteta, P. Marconcini, M. Roy, J.P. Griffiths, G.A.C. Jones, P.A. Maksym, M. Macucci, C.G. Smith, Nano Lett. **12**, 5448 (2012)
35. S. Bhandari, G.-H. Lee, A. Klales, K. Watanabe, T. Taniguchi, E. Heller, P. Kim, R.M. Westervelt, Nano Lett. **16**, 1690 (2016)
36. H. Sellier, B. Hackens, M.G. Pala, F. Martins, S. Baltazar, X. Wallart, L. Desplanque, V. Bayot, S. Huant, Semicond. Sci. Technol. **26**, 064008 (2011)
37. S. Washburn, H. Schmid, D. Kern, R.A. Webb, Phys. Rev. Lett. **59**, 1791 (1987)
38. R.A. Webb, S. Washburn, C.P. Umbach, R.B. Laibowitz, Phys. Rev. Lett. **54**, 2696 (1985)
39. F. Martins, B. Hackens, H. Sellier, P. Liu, M.G. Pala, S. Baltazar, L. Desplanque, X. Wallart, V. Bayot, S. Huant, Acta Phys. Polon. A **119**, 569 (2011)
40. B. Szafran, Phys. Rev. B **84**, 075336 (2011)

41. G.C. des Francs, C. Girard, J.C. Weeber, C. Chicane, T. David, A. Dereux, D. Peyrade, *Phys. Rev. Lett.* **86**, 4950 (2001)
42. C. Chicanne, T. David, R. Quidant, J.C. Weeber, Y. Lacroute, E. Bourillot, A. Dereux, G. Colas des Francs, C. Girard, Phys. Rev. Lett. **88**, 097402 (2002)
43. A. Cuche, O. Mollet, A. Drezet, S. Huant, Nano Lett. **10**, 4566 (2010)
44. E.J. Heller, Phys. Rev. Lett. **53**, 1515 (1984)
45. R.E. Prange, S.M. Girvin, *The Quantum Hall Effect*, 2nd edn. (Springer, New York, 1990)
46. V.J. Goldman, B. Su, Science **267**, 1010 (1995)
47. R.P. Taylor, A.S. Sachrajda, P. Zawadzki, P.T. Coleridge, J.A. Adams, Phys. Rev. Lett. **69**, 1989 (1992)
48. M. Kataoka, C.J.B. Ford, G. Faini, D. Mailly, M.Y. Simmons, D.R. Mace, C.-T. Liang, D.A. Ritchie, Phys. Rev. Lett. **83**, 160 (1999)
49. F.E. Camino, W. Zhou, V.J. Goldman, Phys. Rev. B **72**, 075342 (2005)
50. Y. Zhang, D.T. McClure, E.M. Levenson-Falk, C.M. Marcus, L.N. Pfeiffer, K.W. West, Phys. Rev. B **79**, 241304 (2009)
51. A.J.M. Giesbers, U. Zeitler, M.I. Katsnelson, D. Reuter, A.D. Wieck, G. Biasiol, L. Sorba, J.C. Maan, Nat. Phys. **6**, 173 (2010)
52. C. Zhou, M. Berciu, Phys. Rev. B **72**, 085306 (2005)
53. E. Peled, D. Shahar, Y. Chen, E. Diez, D.L. Sivco, A.Y. Cho, Phys. Rev. Lett. **93**, 236802 (2003)
54. N. Aoki, C.R. da Cunha, R. Akis, D.K. Ferry, Y. Ochiai, Phys. Rev. B **72**, 155327 (2005)
55. A. Baumgartner, T. Ihn, K. Ensslin, K.D. Maranowski, A.C. Gossard, Phys. Rev. B **76**, 085316 (2007)
56. A. Baumgartner, T. Ihn, K. Ensslin, G. Papp, F. Peeters, K.D. Maranowski, A.C. Gossard, Phys. Rev. B **74**, 165426 (2006)
57. N. Paradiso, S. Heun, S. Roddaro, D. Venturelli, F. Taddei, V. Giovannetti, R. Fazio, G. Biasiol, L. Sorba, F. Beltram, Phys. Rev. B **83**, 155305 (2011)
58. F. Martins, S. Faniel, B. Rosenow, M.G. Pala, H. Sellier, S. Huant, L. Desplanque, X. Wallart, V. Bayot, B. Hackens, New J. Phys. **15**, 013049 (2013)
59. F. Martins, S. Faniel, B. Rosenow, M.G. Pala, H. Sellier, S. Huant, L. Desplanque, X. Wallart, V. Bayot, B. Hackens, Sci. Rep. **3**, 1416 (2013)
60. H. Youn, M.T. Gastner, H. Jeong, Phys. Rev. Lett. **101**, 128701 (2008)
61. C.M. Penchina, L.J. Penchina, Am. J. Phys. **71**, 479 (2003)
62. D. Witthaut, M. Timme, New J. Phys. **14**, 083036 (2012)
63. M. Pala, H. Sellier, B. Hackens, F. Martins, V. Bayot, S. Huant, Nanoscale Res. Lett. **7**, 472 (2012)

Chapter 6
Functionalization of Droplet Etching for Quantum Rings

Christian Heyn, Michael Zocher and Wolfgang Hansen

Abstract We give an overview on various types of strain-free semiconductor quantum ring (QR) structures created in a self-assembled fashion with the local droplet etching (LDE) method. LDE is fully compatible with conventional molecular beam epitaxy (MBE) and utilizes liquid Ga or Al droplets which drill nanoholes into semiconductor surfaces. The nanohole openings are surrounded by walls composed of Arsenides of the droplet material. Here the nanohole and wall formation mechanisms and the tunability of their structural properties are discussed. Three different concepts for QR generation by LDE are addressed. In the first concept, GaAs recrystallized during LDE with Ga droplets on AlGaAs substrates forms directly GaAs quantum rings. The second concept is based on the wave-function tuning of V-shaped GaAs QDs by an applied gate-voltage. Here, either the electron or the hole wave function can be transformed into a ring-shape, whereas the respective other charge carrier type remains in a zero-dimensional QD state. The third concept considers the partial depletion of a near surface GaAs quantum well (QW) due to tunneling. The LDE-related wall increases locally the distance to the surface which reduces tunneling and generates a ring-shaped charge-carrier concentration in the QW below the wall. The fabrication and structural properties of these three types of QRs, simulations of the quantized electronic levels and wave functions, and first optical data are discussed.

6.1 Introduction

Semiconductor quantum rings (QRs) represent a fascinating class of quantum structures with intriguing properties highlighted, e.g., in the introduction part of this book. As a prominent example, quantum-interference phenomena in the rings, the so-called

C. Heyn (✉) · M. Zocher · W. Hansen
Center for Hybrid Nanostructures (CHyN), University of Hamburg,
Luruper Chaussee 149, 22761 Hamburg, Germany
e-mail: heyn@physnet.uni-hamburg.de

M. Zocher
e-mail: mzocher@physnet.uni-hamburg.de

W. Hansen
e-mail: hansen@physnet.uni-hamburg.de

V.M. Fomin (ed.), *Physics of Quantum Rings*, NanoScience and Technology,
https://doi.org/10.1007/978-3-319-95159-1_6

Aharonov-Bohm effect [1], have attracted a lot of interest. Recently, the oscillatory persistent current carried by a single electron in self-assembled InAs/GaAs QRs was directly measured by means of ultrasensitive magnetization experiments [2].

The fabrication of large ensembles of QRs is possible by utilizing self-assembly schemes during epitaxial growth. A prominent mechanism for QR self-assembly has been established by Garcia et al. [3, 4]. Here, strain-induced InAs quantum dots (QDs) formed in Stranski-Krastanov mode were overgrown with a thin GaAs layer. This causes the transformation of the initial QDs into InAs QRs. Spectroscopic investigations reveal the quantum ring nature of these systems [5]. However, due to unintentional intermixing with GaAs from the substrate [6], the composition of the QRs is hardly controlled. Furthermore, such InAs QRs in GaAs matrix are substantially strained and, thus, the electronic states are modified by piezoelectric fields.

Strain-free GaAs QRs have been fabricated in a self-assembled fashion by utilizing liquid metal droplets during semiconductor epitaxy, i.e., with droplet epitaxy [7–10] or local droplet etching (LDE) [11, 12]. A droplet epitaxy process [13–20] starts with the deposition of metallic droplets in Volmer-Weber growth mode [21]. During this step, the arsenic flux to the substrate surface is switched-off. After droplet generation, the liquid droplets are crystallized under an arsenic atmosphere. Dependent on the arsenic pressure during crystallization, the self-assembled generation of semiconductor quantum dots (QDs) [15–19], lateral QD pairs [20], and quantum ring complexes [7–10] has been demonstrated.

Droplet epitaxy with crystallization of the liquid droplets is performed at an As flux of $F \simeq 10^{-5}$ Torr. In contrast to that, at a minimized As flux of $F < 10^{-6}$ Torr, the droplets can act as an etchant performing a self-organized local drilling of deep and spatially well separated nanoholes into semiconductor surfaces. Examples of nanoholes drilled into an AlGaAs surface are shown in Fig. 6.1. This local droplet etching method was introduced by Wang et al. [22] for etching of nanholes into GaAs surfaces with Ga droplets. Later, we have demonstrated the high flexibility of droplet etching and used Ga [23], Al [24–26], In [12], InGa, GaAl, and InGaAl droplets for etching of GaAs, AlGaAs, and AlAs substrates.

First functionalizations of the droplet etched nanoholes include the controlled nucleation of strain-induced InAs QDs in such holes [27], the creation of strain-free GaAs QDs of adjustable size [24–26, 28] by hole filling in a post-LDE deposition step, and self-aligned quantum dot molecules with strong coupling [29]. Furthermore, ultra-short nanopillars in so-called air-gap heterostructures [30] were realized, which are interesting, e.g., for thermoelectric applications [31].

The nanohole openings are surrounded by ring-like walls (Fig. 6.1) consisting of a crystallized As compound of the droplet material [32]. That means, LDE with Ga or Al droplets results in formation of GaAs [12] or AlAs [24] walls, respectively. If the structures are embedded in AlGaAs, the GaAs wall will form a quantum-ring like structure while the AlAs wall remains optically inactive. Thus, nanoholes with GaAs walls represent a first example for self-assembled QRs fabricated using LDE.

In this chapter, we start with an overview of the general mechanism and structural properties of nanoholes created with the self-assembled local droplet etching method.

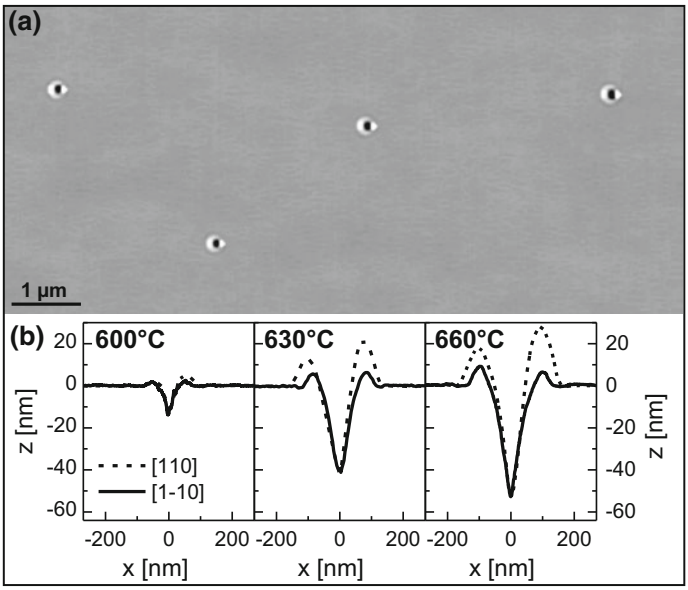

Fig. 6.1 **a** AlGaAs surface with low-density nanoholes after local droplet etching (LDE) with Al droplets at $T = 660$ °C. **b** AFM depth profiles of nanoholes etched at varied temperatures T as indicated

This is followed by a description of three different concepts for GaAs quantum ring generation by LDE. First, recrystallized GaAs forms QRs around LDE nanoholes. Second, an applied electric field induces QRs in wave-function tunable V-shaped GaAs QDs. Third, QRs are localized in partially depleted near surface GaAs quantum wells (QW). In addition to the structural properties, simulations of the quantized electronic states in the QRs and first optical data are discussed.

6.2 Local Droplet Etching of Nanoholes

The samples discussed here are fabricated using a conventional solid-source molecular beam epitaxy (MBE) system equipped with a valved cracker source for As_4 evaporation. After MBE growth of an AlGaAs buffer layer, the As cell shutter and valve are closed yielding a reduction of the As_4 flux by a factor of at least 100 in comparison to typical MBE growth of GaAs. Now, droplet etching is performed in two steps. In the first step, step, the droplet material e.g. Ga or Al is deposited and droplets are nucleated in Volmer-Weber mode (Fig. 6.2a) [17, 21]. The coverage with droplet material is usually in the range of 1–3 monolayers (ML). During a subsequent post-growth annealing step of 180 s, the initial droplets are transformed into nanoholes surrounded by walls (Fig. 6.2b, c, d) [23, 33].

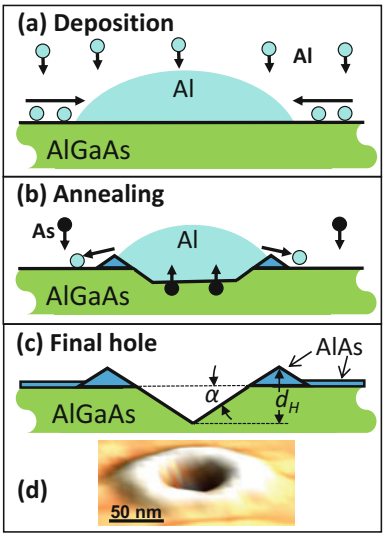

Fig. 6.2 Cross-sectional schematics of the processes during the self-assembled formation of nanoholes in AlGaAs surfaces by local droplet etching (LDE) with Al droplets. **a** Droplet material deposition and droplet formation in Volmer-Weber growth mode. **b** Post-growth thermal annealing with droplet to hole transformation. **c** Final nanohole with opening surrounded by a crystalline wall. The central structural properties are the hole depth d_H between the top of the wall and the hole bottom and the angle α between the hole side-facet and the plane surface. **d** Perspective AFM image of a nanohole

The central process for nanohole formation is diffusion of As from the crystalline AlGaAs substrate into the liquid droplet driven by the concentration gradient. As a consequence, the substrate liquefies at the interface to the droplet. As a further consequence, the As concentration in the liquid droplet material increases. This As concentration crystallizes together with droplet material the wall around the nanohole opening [33]. The next important process is the removal of the liquid material from the initial droplet position. Previous studies indicated that a small arsenic background of $F \gtrsim 1 \times 10^{-7}$ Torr is essential for this [33, 34]. Without As background, the initial droplets are conserved and no holes are formed. We assume that droplet material detaches from the droplets during annealing and spread over the substrate surface. Without As background, the droplet material re-attaches and conserves the droplets. On the other hand, a small As background crystallizes the detached droplet material on the planar surface, thus, the liquid material is permanently removed, and the nanoholes are open [33]. Interestingly, the As background can be supplied by both a small As flux to the surface as well as by the topmost As layer in an As-terminated surface reconstruction acting as a reservoir [35].

The density, shape, and size of LDE nanoholes can be tuned over a wide range by the process conditions. Central parameters are the coverage θ of deposited droplet material, the process temperature T, the arsenic flux F_{As}, as well as the droplet

and substrate materials. The influence of θ and T is systematically investigated and modeled in terms of scaling laws [36]. Examples for etching with Al droplets, the hole density can be varied from 10^6 to 10^8 cm^{-2} by the process temperature resulting in hole depths of up to 125 nm. Typical AFM profiles of nanoholes etched at different temperatures are plotted in Fig. 6.1b. A simple model of the droplet etching process including recrystallization of the droplet material is discussed in Sect. 6.4.2.

6.3 Simulation of Electronic States

LDE nanoholes are used as a template for the creation of versatile nanostructures like quantum dots or quantum rings. A simple single-particle simulation model based on effective mass approximation in cylindrical symmetry [37] is used for the calculation of the electron and hole wave functions Ψ and the quantized energy levels of such nanostructures. Starting point is the one-band Schrödinger equation in the effective mass approximation:

$$-\frac{\hbar^2}{2}\nabla\cdot\left(\frac{1}{m^*}\nabla\Psi\right)+V\Psi=E\Psi \tag{6.1}$$

where $\hbar$ is Planck's constant divided by 2π, m^* is the charge carrier effective mass, V is the band-edge potential energy, E is the energy of the quantized charge carrier, and Ψ is the envelope of the charge carrier wave function. In cylindrical symmetry we have the coordinates (z, r, φ), where z is the axial coordinate, r is the radial coordinate, and φ is the azimuthal angle.

As an extension to the basic model in [37], a vertical electrical field F along z-direction is considered in the potential via $V = V_0 + F(z - z_0)$ for electrons and $V = V_0 - F(z - z_0)$ for holes, with the potential V_0 at zero field and the neutral point z_0 of the field. The model distinguishes two regions, the GaAs QR (or QD) and the $Al_xGa_{1-x}As$ barrier (x = 0.35). The respective potentials and effective masses are for the GaAs QRs: $V_0 = 0$ (electrons and holes), $m^*/m_0 = 0.067$ (electrons), $m^*/m_0 = 0.51$ (holes) and for the AlGaAs barrier: $V_0 = 0.3$ eV (electrons), $V_0 = 0.177$ eV (holes), $m^*/m_0 = 0.092$ (electrons), $m^*/m_0 = 0.6$ (holes), with the free electron mass m_0.

According to [37], (6.1) rewritten in cylindrical coordinates and supplemented by corresponding boundary conditions becomes a partial differential equation (PDE) eigenvalue problem. The computation is performed with the finite element method (FEM) using the software package COMSOL Multiphysics. First, the QD shape is defined and discretized and, second, the PDE is solved site-specific for the calculation of the energies of the first 20 eigenstates as well as of the corresponding wave functions. For the discretization, we use a triangular mesh with irregular element size ranging from 0.0016 to 0.8 nm. Independent model calculations for electrons and holes yield the nth state single-particle energies $E_{e,n}$, $E_{h,n}$ and the corresponding wave functions $\Psi_{e,n}$, $\Psi_{h,n}$, respectively.

From the simulated wave functions, we calculate the Coulomb interaction energy between the electron and hole with the Coulomb integral:

$$C_{eh,n} = -\frac{e^2}{4\pi\epsilon_s} \iint \frac{\left|\Psi_{e,n}(\vec{r_e})\right|^2 \left|\Psi_{h,n}(\vec{r_h})\right|^2}{\left|\vec{r_e} - \vec{r_h}\right|} d\vec{r_e}\, d\vec{r_h} \tag{6.2}$$

where e is the elementary charge and ϵ_s the semiconductor dielectric constant.

Now, the energy of an optical transition between an electron and hole of the nth state is given by:

$$E_n = E_g + E_{e,n} + E_{h,n} + C_{eh,n} \tag{6.3}$$

with the GaAs band-gap energy E_g. An additional influence of correlation effects [38] is not considered.

6.4 Quantum Rings by Local Droplet Etching

The common feature of the different types of QRs discussed here is the LDE-based fabrication method and, thus, the nanohole related geometry. We will start with GaAs QDs (Fig. 6.3a) filled into nanoholes as a reference system. In the first type of QR structures, a ring-like confinement is located in recrystallized GaAs formed around the nanohole openings during LDE with Ga droplets on AlGaAs substrates (Fig. 6.3b). The second type is based on the wave-function tuning of V-shaped GaAs QDs by a vertical electric field (Fig. 6.3c) and the third type uses the partial depletion of a near surface GaAs quantum well (Fig. 6.3d).

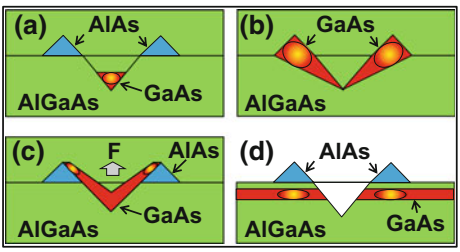

Fig. 6.3 Schematics of the various types of LDE nanostructures that are discussed in this chapter. **a** Reference cone-shaped GaAs QDs fabricated by filling of Al-etched nanoholes with GaAs. **b** Recrystallized GaAs forms QRs during LDE with Ga droplets. **c** Field-induced QRs in wave-function tunable V-shaped GaAs QDs filled into Al-etched nanoholes. **d** Non-confined QRs in a partially tunnel-depleted GaAs QW. The respective localized electron wave-functions are illustrated by red/yellow ellipsoids

6.4.1 QDs as a Reference System

This section addresses LDE GaAs quantum dots as a reference system. For QD fabrication, nanoholes drilled with Al droplets into AlGaAs or AlAs/AlGaAs surfaces are filled by deposition of a planar GaAs layer with a thickness d_F [23, 39]. Subsequently, a 80 nm thick AlGaAs cap layer is grown.

Two types of nanoholes are used for QD creation where the hole shape is mainly determined by the temperature T during droplet etching and the choice of the substrate material. The central structural properties are the hole depth d_H defined as the distance between the average top of the wall and the hole bottom and the angle α between the hole side-facet and the plane surface (Fig. 6.4a). Here we discuss QDs where the nanoholes are prepared by etching at $T = 650\,^{\circ}\mathrm{C}$ on an AlAs layer. AFM measurements of such holes under air are not reliable due to the very fast oxidation of open AlAs surfaces. Therefore, we analyze the hole shape using cross sectional transmission electron microscopy (TEM) [40]. An example for a TEM image of a GaAs QD formed in an AlAs/AlGaAs hole is shown in Fig. 6.4b. From the TEM

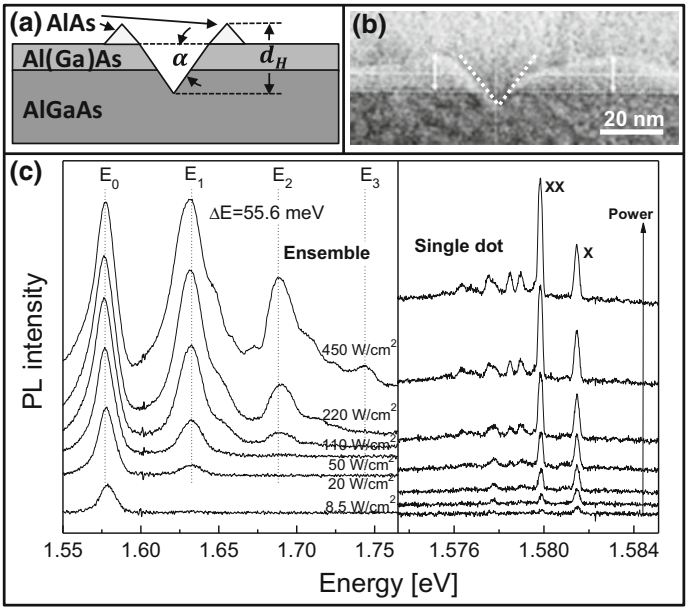

Fig. 6.4 **a** Schematic of an Al droplet etched nanohole with AlAs wall drilled either into an AlAs/AlGaAs substrate or into AlGaAs. The relevant structural features are the hole depth d and the hole side-facet angle α. **b** Cross-sectional TEM image of a GaAs QD fabricated by filling of a hole in AlAs/AlGaAs [40]. The dashed lines indicate the assumed hole side-facets with $\alpha \simeq 50°$ and $d_H \simeq 17$ nm. **c** Left: ensemble PL spectra from GaAs QDs in AlAs/AlGaAs with filling layer thickness $d_F = 0.57$ nm at varied excitation power P_E as indicated. Right: single-dot PL measurement of the sample with P_E varied from 0.06 to 0.26 μW in equidistant steps. Exciton (X) and biexciton (XX) peaks are indicated. The PL spectra are vertically shifted for clarity

data we extract an average $d = 17$ nm and $\alpha = 50°$. GaAs QDs filled into holes in AlGaAs surfaces are discussed in Sect. 4.3. There, oxidation does not alter the hole shape and the structural properties are obtained from AFM images.

GaAs QDs in AlAs/AlGaAs (Fig. 6.4b) have a density of about 4×10^8 cm^{-2}. The optical properties of the QD samples are studied using photoluminescence (PL) spectroscopy at $T = 8$ K. Ensemble and single-dot PL measurements are performed, where for single-dot PL individual QDs are selected using a focused laser for excitation. A typical ensemble PL measurement at varied excitation power P_E is shown in Fig. 6.4c. The data establish a clear shell structure with four quantized states $E_0, \ldots, E_3$. At low P_E, a narrow ensemble PL linewidth of about 10 meV indicates a highly uniform QD ensemble. The peaks are nearly equidistant with $\Delta E = E_{i+1} - E_i = 55.6$ meV as indicated by the dotted vertical lines in Fig. 6.4c. A single-dot measurement of a GaAs QD is shown in Fig. 6.4c. The spectra show clear excitonic peaks with exciton labeled as X and red-shifted biexciton as XX, respectively. The X and XX peaks are identified by their excitation power dependence [41].

Measurements of the excitonic ground-state energy yield a systematic decrease with increasing d_F in the range from $E_x = 1.69$ down to 1.55 eV (Fig. 6.5a). Values of the level separation $\Delta E = E_1 - E_0$ show a decrease from 90 meV down to 40 meV with increasing hole filling level d_F and, thus, increasing QD size (Fig. 6.5b).

We interpret the PL data of GaAs QDs in AlAs/AlGaAs substrate using simulations where an inverted cone shape is assumed for the dots (Fig. 6.5c). Since the

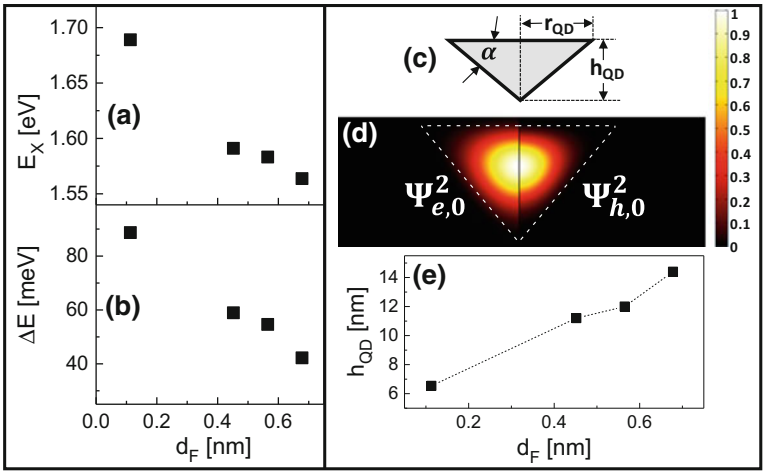

Fig. 6.5 **a** Measured exciton ground-state energies E_X of GaAs QDs in AlAs/AlGaAs at varied hole filling level d_F. **b** Measured quantization energies $\Delta E = E_1 - E_0$. **c** Schematics of the rotational-symmetric cone-shape used for the QD simulations. **d** Cross-sectional simulated probability densities $\Psi^2_{e,0}$, $\Psi^2_{h,0}$ of the electron and hole ground-states in a cone-shaped QD with $\alpha = 50°$ and $h_{QD} = 11.2$ nm. The color code used for the probability densities is valid also for the following figures. **e** Height h_{QD} of cone-shaped quantum dots with best agreement between simulated ground-state emission energy and measured E_x at varied hole filling level d_F

side angle of the cone is given by the side-facet angle α of the initial nanoholes, the quantum dot height h_{QD} is the only free parameter. Figure 6.5d shows as an example the simulated electron and hole probability densities $\Psi^2_{e,0}$ and $\Psi^2_{h,0}$ inside the cone-shaped QD.

Operationally, h_{QD} is adjusted for best agreement between the simulated ground-state emission energy E_0 and the measured exciton peak energy E_x (Fig. 6.5a). In the next step, the simulated quantization energy $\Delta E = E_1 - E_0$ is compared to the experimental value. We find that the simulated ΔE overestimates the experimental data by a factor of about 1.5. Despite this deviation, we consider a cone shape as a reasonable approximation for dots in AlAs/AlGaAs. A better approximation basing on a polynomial shape is discussed in [41]. Figure 6.5e shows for dots in cone-shape approximation the values of h_{QD} that yield best agreement with the experimental E_x as function of the hole filling level d_F.

Droplet etched GaAs QDs in AlAs/AlGaAs or in AlGaAs are suggested for applications in quantum information technology since they demonstrate an optical emission wavelength tunable by the hole filling-level from 700 to 800 nm, small exciton peak linewidths down to 25 μeV, low neutral exciton fine-structure splittings down to 4 μeV, and clear single-photon emission [39].

6.4.2 QRs in Recrystallized GaAs

As is discussed in Sect. 6.2, the openings of droplet etched nanoholes are surrounded by recrystallized walls that are composed of Arsenides of the droplet material. To form GaAs QRs, GaAs walls formed after LDE with Ga droplets on AlGaAs surfaces are overgrown with 80 nm AlGaAs as barrier material (Fig. 6.3b). The structural properties of the QRs before overgrowth are studied with AFM. Figure 6.6a, b show examples of AlGaAs surfaces with GaAs QRs. The QRs are spatially well separated and the AlGaAs surface between the individual rings is nearly atomically flat.

The density N of the QRs is plotted in Fig. 6.6c as function of the temperature T during LDE for two sample series. The data shows the expected decrease of N with increasing T which is related to the droplet nucleation kinetics [17]. In addition, there is a very strong difference between the two sample series which is attributed to an unintentional variation of the background As pressure during the LDE process. In detail, the main shutter in front of the sample surface is closed during LDE of sample series 1, whereas series 2 is processed with open main shutter. The reason is a maintenance of the MBE chamber after fabrication of sample series 1, during which the distance between main shutter and sample surface was reduced. Now, due to heat reflection at the shorter distance, with closed main shutter the sample temperature is only poorly controlled. Therefore, the series 2 samples are grown with open main shutter. An open main shutter causes a higher As background flux F_{As} which substantially reduces the nanohole density for series 2 samples [35].

In addition, Fig. 6.6d shows the inner r_I and outer r_O radius of the GaAs walls around the nanohole as function of LDE temperature. The inner wall radius r_I is

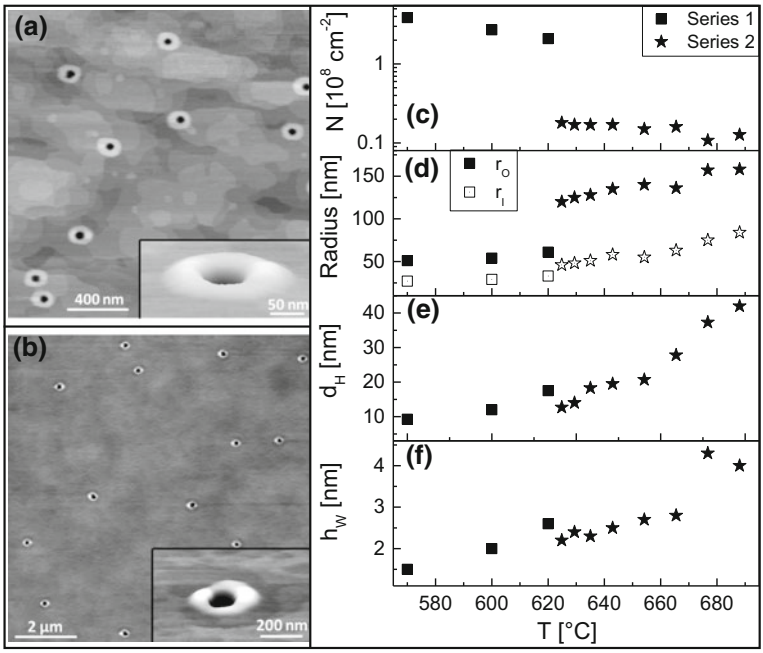

Fig. 6.6 **a** AFM image of an AlGaAs surface with sample series 1 GaAs quantum rings created using droplet etching at $T = 600$ °C. The inset shows a perspective view of a single ring. **b** AFM image of an AlGaAs surface with sample series 2 GaAs QRs fabricated at $T = 655$ °C. The inset shows a perspective view of a ring. **c** Density N of GaAs QRs as function of process temperature T for two sample series. **d** Average inner r_I and outer r_O radius of the GaAs walls around the hole opening. **e** Average depth d_H of LDE nanoholes in the center of the QRs. **f** Average wall height h_W

equal to the radius of the nanohole opening. We observe an increase of the radii with T in agreement with earlier results [36] and larger walls for series 2 samples. The temperature dependent depth d_H of the nanoholes is depicted in Fig. 6.6e and the average height of the walls h_W in Fig. 6.6f.

The optical properties of samples with Ga-LDE QRs are studied using PL at $T =$ 8 K. An ensemble PL measurement of a series 1 QR sample etched at $T = 540$ °C is plotted in Fig. 6.7a together with a measurement from a reference sample with the same layer sequence but without LDE step. Obviously, the reference sample shows no PL signals which clearly proves that the peaks in the QR sample are related to the LDE step. The ensemble QR optical emission is rather broad with several peaks in the range between 1.69 eV up to 1.87 eV. Figure 6.7b shows an example for a single-ring measurement from a QR sample etched at $T = 580$ °C in sample series 1. The higher process temperature yields a reduced QR density (Fig. 6.6c) which is advantageous for an easy selection of a single ring by a focused laser. The single-ring spectra show a peak at about 1.625 eV and a bunch of peaks in the range from 1.66 up to 1.7 eV. Excitation power dependent measurements show that the peak at 1.625 eV arises first at low excitation power and the higher energy peaks become

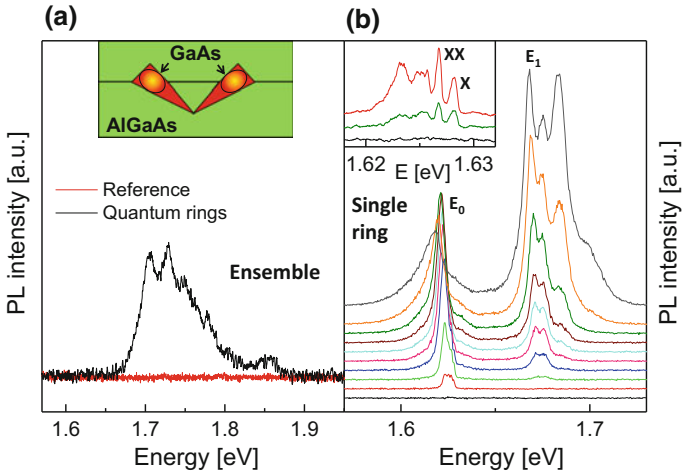

Fig. 6.7 **a** Low temperature PL spectra of a sample containing an ensemble of GaAs quantum rings in AlGaAs. In addition, a reference sample without LDE step is shown. The samples are fabricated at $T = 540$ °C and part of sample series 1. **b** PL measurements of a single GaAs QR fabricated in sample series 1 at $T = 580$ °C. The excitation power is varied from 0.7 up to 210 nW. The inset shows high-resolution spectra of the peaks around 1.625 eV at an excitation power varied from 0.7 up to 22 nW with labeled exciton (X) and biexciton (XX) peaks. The spectra are vertically shifted for clarity

visible with increasing excitation. This behavior is in agreement with the typical excitation power dependence of the shell-structure of the electronic states in QD samples (Fig. 6.4c). Assuming a shell structure, we attribute the peak at 1.625 eV to the ground state E_0 (s-shell) and the peak at 1.668 eV to the first excited state E_1 (p-shell). This yields a quantization energy of $E_1 - E_0 = 43$ meV. The substructure of the p-shell emission might be related to a slightly asymmetric shape of the QRs.

The inset of Fig. 6.7b shows high-resolution spectra from the QR ground-state emission at very low excitation powers. There are several peaks that we identify according to the PL emission of single GaAs LDE QDs [41] (Fig. 6.4c), i.e., the peak with highest energy is an exciton (X) and the red-shifted peak a biexciton (XX). The excitation-power dependence supports this identification, with a stronger increase of the XX peak intensity at increasing excitation power. The exciton-biexciton splitting is 1.42 meV, which is in agreement with typical values of GaAs LDE QDs [41]. The additional further red-shifted peaks are attributed to multi-excitonic complexes.

We have performed simulations of the electronic states (see Sect. 6.3) for the further interpretation of the PL data. In a first approach, we consider the crystallized GaAs wall around the nanohole opening as QR and approximate the circular ring shape using a isosceles triangle as cross-section (Fig. 6.4b). The sizes $r_O = 52$ nm, $r_I = r_O/2$, and $h_W = 2$ nm are taken from the AFM data (Fig. 6.6b, d) with respect to the fabrication conditions of the PL sample in Fig. 6.7b. Figure 6.8a shows for illustration a corresponding QR cross-section together with the simulated electron

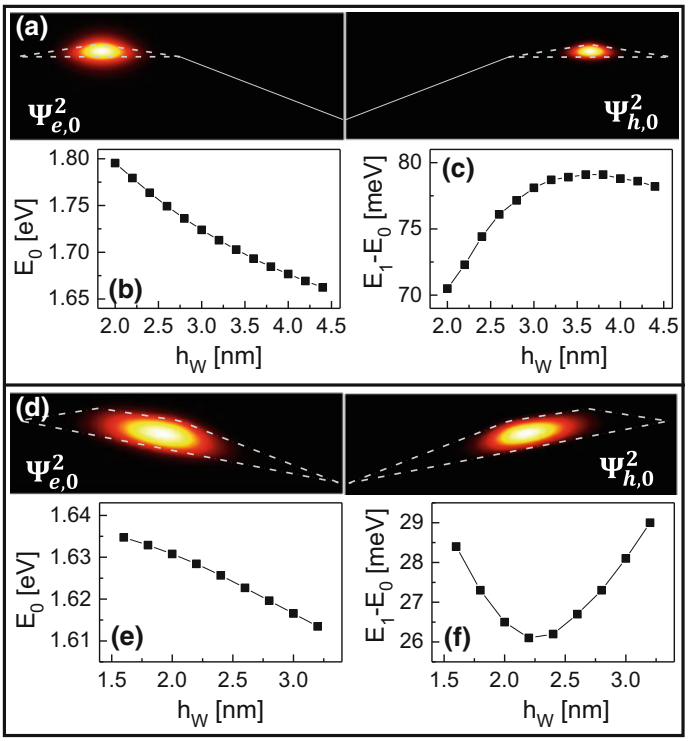

Fig. 6.8 **a** Cross-sectional simulated probability densities $\Psi^2_{e,0}$, $\Psi^2_{h,0}$ of the electron and hole ground-states in a crystallized GaAs wall with r_O = 52 nm, $r_I = r_O/2$, and h_W = 2 nm. The dashed lines indicate the shape of the QR with cylindrical symmetry. **b** Simulated PL ground-state emission energy E_0 of a GaAs QR with r_O = 52 nm, $r_I = r_O/2$, and varied h_W. **c** Simulated PL quantization energy $E_1 - E_0$ at varied h_W. **d** Cross-sectional simulated electron and hole probability densities in a crystallized GaAs wall with recrystallization also inside the nanohole with r_O = 52 nm, $r_I = r_O/2$, h_W = 2 nm, and d_H = 11 nm. **e** Simulated PL ground-state emission energy of a GaAs QR with recrystallization inside the hole, where r_O = 52 nm, $r_I = r_O/2$, h_W is varied, and $d_H = h_W + 9$ nm. **f** Simulated PL quantization energy at varied h_W

and hole probability densities $\Psi^2_{e,0}$, $\Psi^2_{h,0}$. The simulated PL ground state emission energy E_0 at varied wall height h_W is plotted in Fig. 6.8b and the quantization energy $E_1 - E_0$ in Fig. 6.8c. For the measured h_W = 2.0 nm the simulation yields a value of E_0 = 1.795 eV which is substantially higher than the experimental value of 1.625 eV. Furthermore, the simulated quantization energy $E_1 - E_0$ = 70 meV is also higher than the measured one of 43 meV. We assume that this discrepancy between PL results and simulations is caused by a QR shape that differs from a simple triangular cross-section. Or, in other words, the quantum ring morphology is not identical with the shape of the wall as imaged via AFM on the surface. A possible explanation is recrystallization of GaAs not only on the planar surface in form of the wall but also inside the nanohole.

Since no further structural data are available, we discuss now possible QR geometries on basis of a simple model of the droplet etching process. The model is a simplification of a previous model [32] without consideration of the As concentration in the droplets and the temperature dependence. Stating point is a liquid Ga droplet with volume $V = \theta/N$, with the deposited droplet material coverage θ and the droplet density N. The droplet volume shrinks during post growth annealing due to detachment of Ga atoms with a rate R_d. The detached Ga atoms spread over the substrate surface and form a planar GaAs film with the background As flux [33]. Two approximations are applied to describe the detachment process. First, the detachment takes place locally at the border line between the droplet surface and the substrate surface. In this case, the time evolution of the droplet volume would be $dV/dt = -R_d V^{1/3}$, where the details of the droplet geometry are neglected for simplicity. Alternatively, the Ga atom detachment can take place from the whole droplet surface which yields $dV/dt = -R_d V^{2/3}$. Figure 6.9a shows the time evolution of the droplet volume V and Fig. 6.9b that of the droplet radius r_D for both approximations.

For the calculation of the evolution of the crystalline surface morphology we use a one-dimensional finite element approach with a cell size of 1 nm. We start with a flat surface at $z = 0$. Etching removes crystalline material at the interface to the

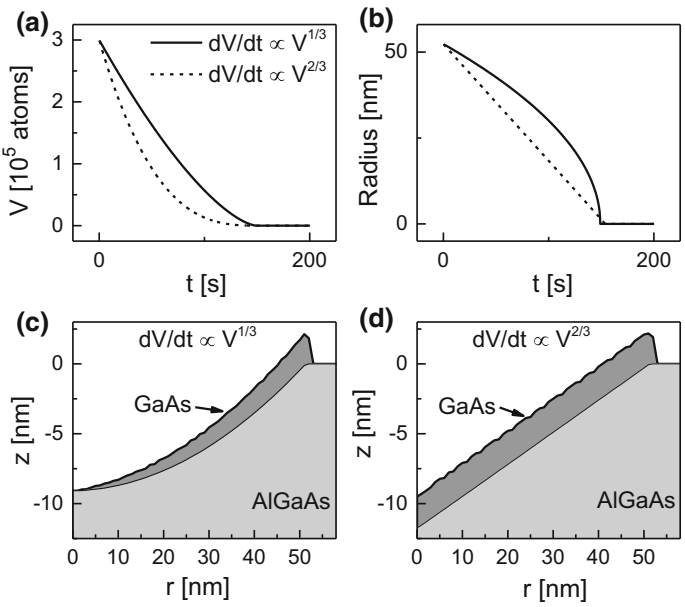

Fig. 6.9 **a** Calculated time evolution of the droplet volume V during post growth annealing. Two approximations for the Ga atom detachment are considered with $dV/dt \propto V^{1/3}$ and $dV/dt \propto V^{2/3}$ as indicated. **b** Calculated time evolution of the droplet radius r_D. **c** Calculated profile of the GaAs quantum ring (red) in the approximation $dV/dt \propto V^{1/3}$. The AlGaAs substrate is in green color. **d** Calculated profile of the QR for $dV/dt \propto V^{2/3}$

liquid droplet for surface cells at radii $<r_D$. Here, the surface level is decreased by $dz/dt = -R_e$, with the etching rate R_e. Recrystallization of GaAs is assumed at the borderline between the droplet surface and the surface of the crystalline substrate. This is modeled by an increase of the surface level for the cell at radius r_D by $dz/dt = R_r$, with the recrystallized rate R_r. Operationally, the value of R_d is adjusted for a time up to droplet removal of 150 s according to [32], the value of R_e for a hole depth of 9 nm according to the AFM data, and the value of R_r for a wall height of 2 nm. Figure 6.9c shows calculated profiles of the etched AlGaAs substrate surface and the surface of the recrystallized GaAs in the approximation $dV/dt \propto V^{1/3}$. The recrystallized GaAs in the approximation $dV/dt \propto V^{2/3}$ is shown in Fig. 6.9d. Interestingly, the thickness of the recrystallized GaAs decreases with decreasing r in Fig. 6.9c, whereas Fig. 6.9d shows a constant thickness. This is related to the time evolution of the droplet radius (Fig. 6.9b) with a constant time interval per radius and, thus, a constant recrystallization rate for Fig. 6.9d and a reduced recrystallization for small radii in Fig. 6.9c. A comparison with AFM linescans (Fig. 6.1b) indicates a better agreements with the approximation $dV/dt \propto V^{2/3}$ and, thus, suggests Ga atom detachment from the whole droplet surface. A more elaborated model assuming a core-shell geometry for the droplets [32] provides also agreements with AFM profiles of the wall around the hole opening. In summary, the model calculations illustrate that recrystallization of GaAs inside the nanohole is a possible process and that the shape of an LDE GaAs QR can substantially deviate from that of the surface wall. Nevertheless, additional structural investigations are required to obtain a more realistic shape of the QRs.

We consider now the recrystallization of GaAs also inside the nanoholes and simulate the QR optical properties using an approximated ring shape which combines Fig. 6.9c, d. Figure 6.8d illustrates this QR shape together with examples of simulated electron and hole probability densities. The simulated PL ground-state emission energy E_0 for a crystallized GaAs wall with recrystallization inside the nanohole at varied h_W is plotted in Fig. 6.8e and the quantization energy $E_1 - E_0$ in Fig. 6.8f. The value of E_0 = 1.630 eV simulated for h_W = 2.0 nm is now close to the PL result, whereas the simulated quantization energy of 26.5 meV underestimates the experimental value. Nevertheless, due to the missing structural data, the aim of the simulations at this stage is not a quantitative reproduction of the PL results. As a more general outcome, we have clarified that the shape of the quantum rings is not identical with the walls crystallized on the surface. Redeposited GaAs inside the holes must be considered as an additional contribution.

6.4.3 Field-Induced QRs in V-Shaped Nanostructures

The next concept for QR creation by using droplet etching is fundamentally different from the previous approach. Here, we use Al droplets for drilling of about 30 nm deep nanoholes surrounded by an optically inactive AlAs wall [39]. The holes are filled with GaAs similar to the procedure described in Sect. 6.4.1 for QD fab-

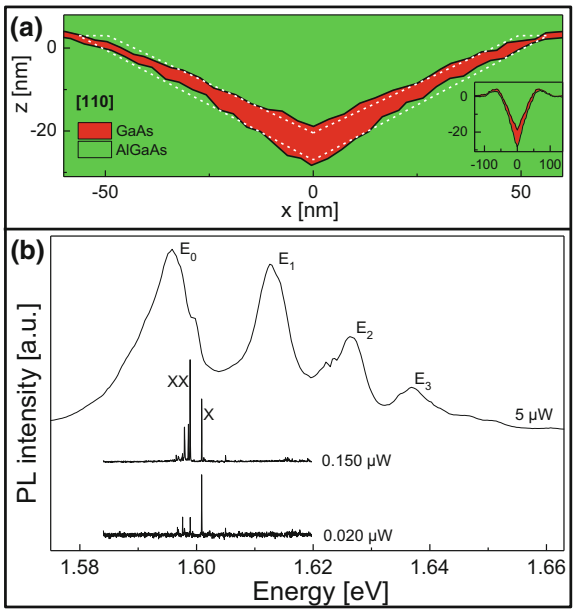

Fig. 6.10 **a** AFM linescans equally scaled in x- and z-axis of the center part of a nanohole in AlGaAs and a hole filled with a V-shaped GaAs QD ($d_F = 0.45$ nm). The baselines of the individual AFM scans are offset by the respective deposited layer thickness. The dashed white lines indicate the approximated dot shape used for the simulations. The inset shows an overview of the dot. **b** Single-dot PL measurements of a V-shaped QD with filling level $d_F = 0.45$ nm at varied excitation power and without applied electric field. The spectra are vertically shifted for clarity

rication. In contrast to the QDs of Sect. 6.4.1, here an AlGaAs substrate is used for etching. This results in a strongly different shape of the nanoholes and, thus, also of the GaAs nanostructures inside the hole template. Figure 6.10a shows AFM linescans of a sample series where the fabrication process has been stopped at the different interfaces. The data indicate for the hole morphology a depth of $d_H = 32$ nm and a side-facet angle $\alpha = 30°$. GaAs is filled into the nanohole template by deposition of a planar GaAs layer with thickness d_F. In contrast to the approximately cone-shaped QDs in AlAs/AlGaAs surfaces (Sect. 6.4.1) the QDs in AlGaAs have a V-shape (Fig. 6.10a). We note that, without electric field, the ground-state probability densities are disk-like (see below).

Due to their low density of about 2×10^7 cm^{-2}, single V-shaped QDs are selected for PL measurements using a focused laser for excitation. An example of a single-dot measurements at varied excitation power P_E is shown in Fig. 6.10b. At low $P_E = 0.02$ μW, a sharp exciton peak (X) is visible. At increased $P_E = 0.15$ μW, a biexciton (XX) and additional red-shifted peaks indicate the formation of multi-excitonic complexes. The situation changes qualitatively at high $P_E = 5$ μW. Now the single-dot peaks are very broad, which we attribute to strong spectral diffusion caused by charge carriers generated by the intense laser irradiation. Furthermore, the maximum of the peak E_0 with lowest energy is red-shifted by about 5 meV in comparison to the exciton peak (X). This red-shift is caused by the contribution of multi-excitonic complexes to the line shape. Furthermore, the PL data at high P_E establish a clear shell structure with four visible quantized states $E_0, \ldots, E_3$.

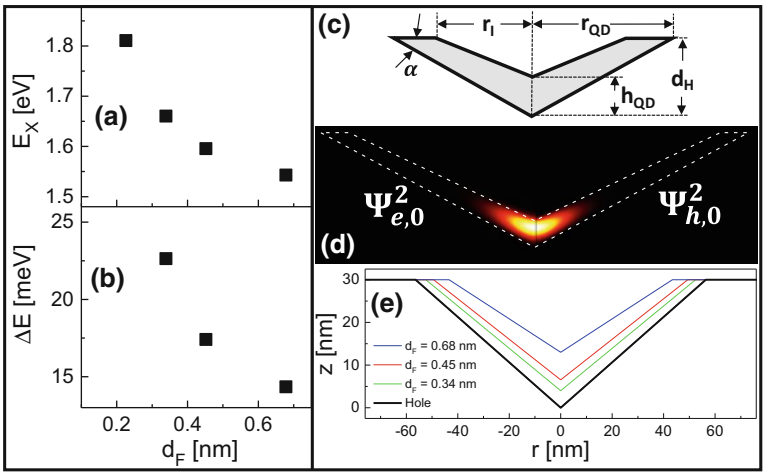

Fig. 6.11 **a** Measured exciton ground-state energies E_X of V-shaped GaAs QDs at varied hole filling level d_F. **b** Measured quantization energies $\Delta E = E_1 - E_0$. **c** Schematics of the approximated rotational-symmetric QD V-shape used in the simulations. **d** Cross-sectional simulated probability densities $\Psi^2_{e,0}$, $\Psi^2_{h,0}$ of the electron and hole ground-states in a V-shaped QD in AlGaAs. The dashed lines indicate the QD cross-section. Without electric field, the ground-state probability densities are disk-like. **e** Approximated QD shapes with best agreement between simulations and PL data for varied d_F

The excitonic ground-state energy decreases with increasing d_F and demonstrates a very wide range of tunability from E_x = 1.81 down to 1.55 eV (Fig. 6.11a). The higher E_x of the V-shaped dots compared to cone-like QDs is caused by their smaller height (Fig. 6.5a). The level separation $\Delta E = E_1 - E_0$ shows a decrease from 23 meV down to 14 meV with increasing d_F (Fig. 6.11b). In comparison to cone-like dots (Fig. 6.5b), the V-shaped QDs have a smaller quantization energy which is related to their larger lateral extension.

As is described before for the cone-like QDs (Sect. 6.4.1), the PL data are interpreted with the help of simulations. We start with an inverted cone-shape also for the dots in AlGaAs. After adjusting the QD height for agreement with the ground-state emission, the simulated ΔE overestimates the experimental values by a factor of at least 5. This very strong disagreement indicates that a cone shape is not a reasonable approximation for the dots in AlGaAs. For a better agreement with the experiments we model the dots on AlGaAs now by a V-shape. Figure 6.10a shows a comparison between AFM linescans of a dot and the corresponding V-shape approximation used for the simulation. The approximated V-shape geometry is characterized by 4 parameters as is sketched in Fig. 6.11c. We assume in addition that the side angle of the QD equals the hole side-facet angle $\alpha = 28°$ and that the wall of the nanohole is completely covered with QD material which yields d_H = 30 nm (Fig. 6.10a). Now, two parameter remain for fitting: h_{QD} and r_I (Fig. 6.11c). An example of the simulated electron and hole ground-state probability densities is shown in Fig. 6.11d.

Adjustment of the two dot-shape related fitting parameters (h_{QD}, r_I) allows an exact reproduction of both the experimental E_x and ΔE. A summary of the approximated dot geometries with best agreement between simulations and measured optical data is shown in Fig. 6.11e for a varied hole filling level d_F.

In the next step, the influence of a vertical electric field F on the exciton recombination energy is discussed, the so-called Stark shift [42] in analogy to spectroscopy on atoms. Simulation results for a cone-shaped QD (not shown here) show a parabola-like dependence of the exciton peak energy on F which is also observed for many other QD systems [43–45].

For field-dependent PL measurements the QDs are embedded in a Schottky-diode with an 18 nm thick evaporated Ti-layer as top gate. A gate-voltage V_g is applied between top and back gate (distance $d_g = 200$ nm) to adjust a vertical electric field F. An example for the measured field-dependent optical emission from a V-shaped QD is show in Fig. 6.12a. The data show a complex behavior with several lines and prominent intensity variations. Additional measurements (not shown here) identify a zero photo-current between top and back-gate at a gate-voltage $V_g = V_0 \simeq 0.8$ V. We assume that this gate voltage compensates the Schottky barrier and yields flat-band conditions with $F(V_0) = 0$. This corresponds to the situation without metalization. The gate-voltage controlled field is $F(V_g) = (V_g - V_0)/d_g$. We identify the exciton (X) and biexciton (XX) transitions from excitation-power dependent measurements [41] at $F = 0$. The additional lines occurring at higher $|F|$ are attributed to charged excitons. Most importantly here, the exciton line deviates from the usual parabolic behavior and shows an only weak field dependence in the regime $-0.4 < V_g < 1.1$ V corresponding to fields of $-20 < F < 15$ keV.

Simulations of the PL emission from V-shaped QDs are performed for an understanding of their unexpected field-dependence. In detail, in Fig. 6.12b the single-particle energies of the electron $E_{e,0}$ and hole $E_{h,0}$ ground-states as function of F are plotted. The variation of $E_{e,0}$ and $E_{h,0}$ is controlled by the influence of the electric field on the band-edge potential $V \propto zF$ and the shift of the z-positions of the wave-function centers. The z-positions z_e, z_h of the center of mass of the electron and hole wave functions are plotted in Fig. 6.12c with respect to the center of the positions at $F = 0$. The very strong and highly asymmetric shift of z_e and z_h is caused by the V-shape of the QD. Dependent on the sign of the electric field, either the electron or the hole is pushed into the wing of the V. Figure 6.13 illustrates the corresponding probability densities. The shift is stronger for holes compared to electrons due to their smaller size. In addition to the shift along z-direction there is also a strong radial shift of the wave-function center of mass. This huge displacement of the electron and hole at high $|F|$ yields a strong variation of the Coulomb energy (Fig. 6.12d) with $C_{eh} \simeq 15$ meV at $F = 0$ and $C_{eh} < 2$ meV for $F < -20$ kV/cm or $F > 10$ kV/cm. The simulated exciton recombination energy E_x is shown in Fig. 6.12e together with the single-particle recombination energy $E_{single} = E_g + E_{e,0} + E_{h,0}$ without consideration of C_{eh}. In the field range of -20 kV/cm $< F < 10$ kV/cm the simulations predict an approximately constant E_x. A comparison with E_{single} indicates that this non-parabolic Stark shift is caused by the strong variation of C_{eh}. The simulated field range with approximately constant E_x agrees quantitatively with the experimental

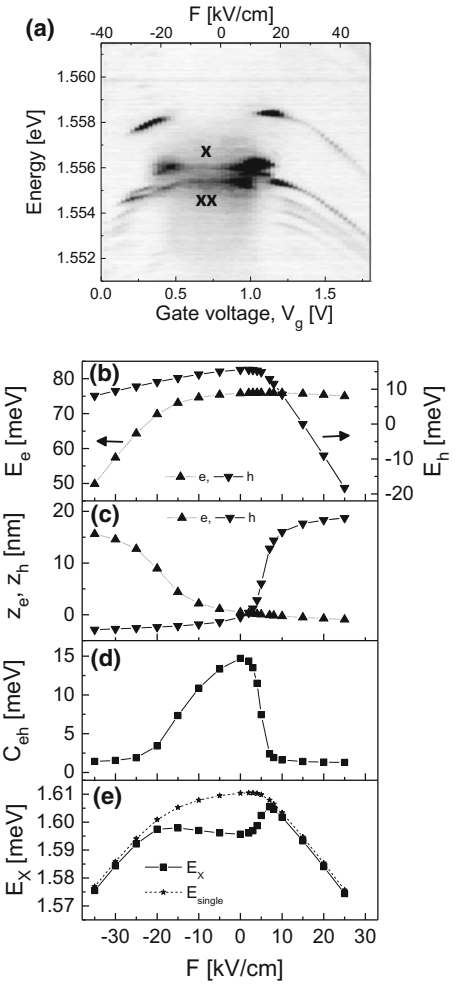

Fig. 6.12 Vertical electric field F dependent results of a GaAs QD with V-shape. **a** Grey-scale plot of the PL emission intensity at $T = 8$ K from a V-shaped QD with $d_F = 0.45$ nm as function of F varied by a gate-voltage V_g. Exciton (X) and biexciton (XX) lines are marked. **b** Simulated single-particle energies of electron (e) and hole (h) ground-states. **c** Simulated z-positions z_e, z_h of the center of mass of the electron and hole wave functions. **d** Simulated Coulomb energy C_{eh}. **e** Simulated exciton energy E_x together with the single-particle recombination energy E_{single}

finding (Fig. 6.12a). This good agreement supports the interpretation of a huge electron or hole displacement and a corresponding very strong variation of the Coulomb energy, which compensates the single particle Stark shift.

As the key outcome here, the simulations demonstrate that the shape of the electron or hole wave-function can be substantially transformed by an electric field. This wave-function tuning is visualized in Fig. 6.13, where a disk-like wave function at $F = 0$ is transformed with increasing absolute field into a wave function on a conical surface (electron at $F = -20$ kV/cm) and finally into a ring-like wave function. Importantly, either the electron or the hole wave-function is transformed whereas the respective other charge carrier type is pushed into the QD apex with only minor changes of its wave function. These simulation results suggest the V-shaped GaAs QDs as promising candidates for the realization of field-tunable quantum rings.

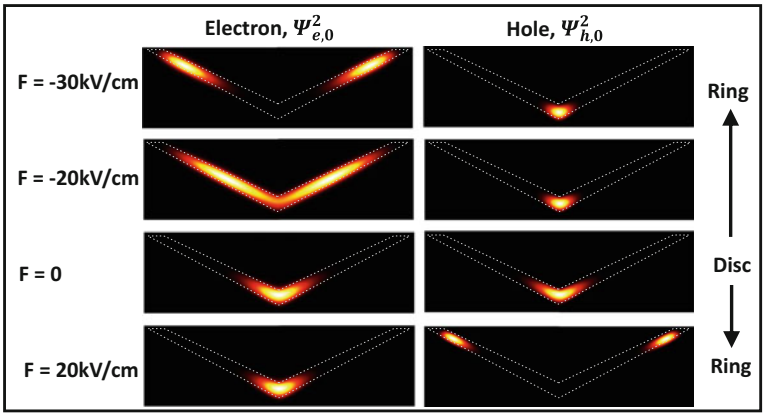

Fig. 6.13 Wave-function tuning in V-shaped GaAs QDs probability densities $\Psi^2_{e,0}$, $\Psi^2_{h,0}$ of the electron and hole ground-states in a V-shaped GaAs QD at varied vertical electric field F. The dashed lines indicate the QD shape

6.4.4 QRs in Partially Depleted QWs

The third concept for LDE based QR creation starts with a shallow GaAs quantum well embedded in AlGaAs barrier material. The cap layer is very thin allowing a fast tunneling of charge carriers from the well into the closely neighbored surface [46]. Thus, the QW is mostly depleted. Nanoholes drilled with Al droplets into the QW are surrounded by AlAs walls which locally increase the tunnel barrier thickness. Below the wall, tunneling is reduced due to the thicker tunnel barrier and a ring-shaped charge carrier concentration can be formed (Fig. 6.3d).

Figure 6.14a shows a room temperature PL measurement from a 6 nm wide GaAs QW with 100 nm thick AlGaAs cap layer. The QW emission around 1.525 eV is clearly visible. The additional weaker peak at 1.426 eV is attributed to the GaAs substrate. PL data from another QW sample now with only 5 nm cap layer thickness are plotted in Fig. 6.14b. Now, the QW emission is about 100 weaker compared to the QW with thicker cap and even weaker than the GaAs substrate peak. Figure 6.14c shows a summary of the normalized QW intensity from several samples with varied d_{cap}. The data indicate no significant intensity reduction for $d_{cap} \geq 20$ nm, followed by a very strong decrease of the QW emission with thinner cap layer.

The influence of the cap layer thickness on the QW emission is interpreted using a simple rate model. The PL intensity I_{QW} from a QW in units of the number of radiatively emitted photons per time can be estimated from $I_{QW} = N/\tau_r$, with the exciton population N and the recombination lifetime τ_r. The exciton population follows $dN/dt = R_e - N/\tau_r - N/\tau_t$, with the excitation rate R_e and the tunneling lifetime τ_t. In equilibrium ($t \to \infty$) $dN/dt = 0$ and, thus, $R_e = N/\tau_r + N/\tau_t = N(1/\tau_r + 1/\tau_t)$, $N = R_e/(1/\tau_r + 1/\tau_t)$. The intensity becomes

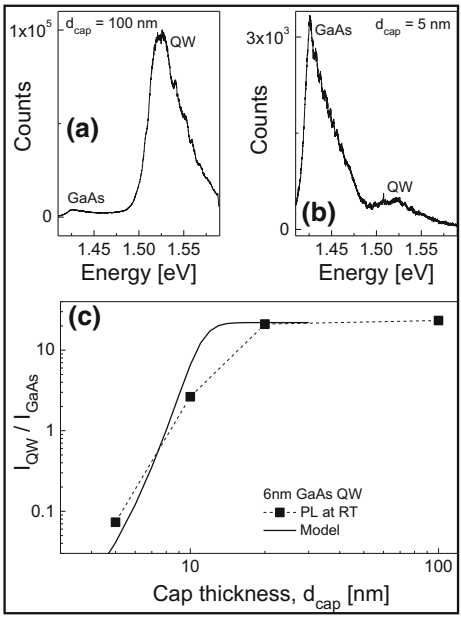

Fig. 6.14 Room temperature photoluminescence (PL) measurements of a 6 nm GaAs quantum well embedded in AlGaAs. **a** PL spectrum of a GaAs QW with cap layer thickness d_{cap} = 100 nm. The QW emission and the emission from the GaAs substrate is indicated. **b** PL spectrum of a GaAs QW with $d_{cap} = 5$ nm. **c** Symbols: intensity I_{QW} of the measured QW emission normalized with respect to the GaAs substrate emission I_{GaAs} at varied d_{cap}. Line: calculated QW emission

$$I_{QW} = N/\tau_r = R_e/(1 + \tau_r/\tau_t) \tag{6.4}$$

To estimate the tunneling lifetime τ_t we assume for the QW a rectangular potential of width w confined by a rectangular barrier of height V_b and width b. For areas between nanoholes without wall we use $b = d_{cap}$. A particle moving inside the dot with average velocity v performs collisions with the barrier with frequency $v/(2w)$. The tunneling rate $(1/\tau_t)$ is given by the frequency of wall collisions multiplied with the transmission coefficient [44]. For tunneling through a rectangular barrier the well known transmission coefficient is $T \simeq e^{-2\gamma b}$, with $\gamma = \sqrt{2m^*(V_b - E)/\hbar^2}$, the effective mass m^*, and the energy E of the particle. The average velocity of the particle is estimated via the uncertainty principle as $v \simeq \hbar/(2m^* w)$ [44]. This yields for the tunneling lifetime

$$\tau_t \simeq \frac{4m^* w^2}{\hbar} \exp\left[2b\sqrt{2m^*(V_b - E)/\hbar^2}\right] \tag{6.5}$$

For the calculations of the PL intensity of QWs with planar cap layers of varied thickness $b = d_{cap}$ we assume a QW width of $w = 6$ nm, a radiative lifetime of $\tau_r \simeq 10$ ns [47], tunneling of electrons due to their lower effective mass, a barrier height of $V_b = 220$ meV, and a particle energy of $E = 5$ meV (ground-state energy). Figure 6.14c demonstrates that the calculated I_{QW} reproduces the experimental behavior with a significant PL intensity reduction for $d_{cap} < 10$ nm. This result is in agreement with the literature [46].

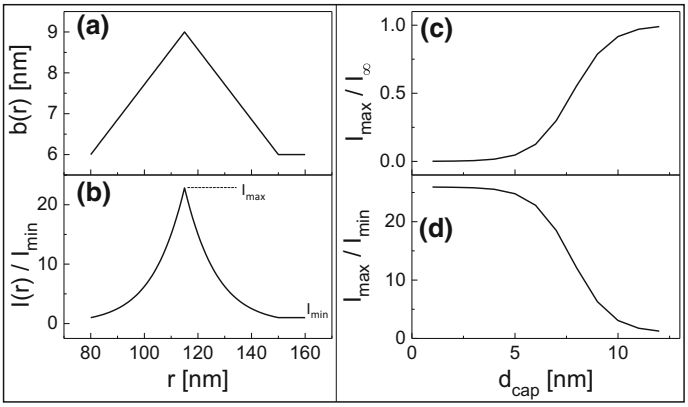

Fig. 6.15 **a** Example of an approximated profile of a tunnel barrier composed of cap layer plus wall. **b** Calculated local variation of the PL intensity $I(r)$ normalized to the minimum intensity I_{min} from a region beside the wall. The maximum intensity I_{max} is expected at the center of the wall. **c** Calculated maximum PL intensity I_{max} in the center of the wall normalized to the PL intensity I_∞ from a QW with infinitely thick cab layer. **d** Calculated intensity ratio I_{max}/I_{min}

In the next step we have calculated the local PL intensity from a QW below an AlAs wall, where the cap layer thickness $b > d_{cap}$ depends on the position. The example in Fig. 6.15a, b reflects etching with Al droplets at $T = 620\,^{\circ}\mathrm{C}$ with a wall inner radius $r_I = 80$ nm, outer radius $r_O = 150$ nm, and maximum height of $h_W = 3$ nm. Figure 6.15a illustrates an approximated surface morphology with wall. The PL intensity $I(r)$ for a cap layer with thickness $b(r) = d_{cap} + h_W(r)$ locally varied by the wall is calculated using (6.4) and (6.5) (Fig. 6.15b). The exponential dependence of I on the local $b(r)$ (6.5) yields a localization of the PL emission at the center of the wall. This is accompanied by a localization also of the charge carrier density $N \propto I$ (6.4).

The design of such a QR sample and in particular the choice of the planar cap-layer thickness d_{cap} requires a compromise between a high absolute PL intensity and a high signal ratio induced by the wall. This is illustrated in Fig. 6.15c, d. Up to d_{cap} of 5 nm the ratio between the maximum PL intensity I_{max} at the center of the wall and the minimum intensity I_{min} from areas beside the wall is high. On the other hand, the absolute intensity I_{max} is only very weak and probably hard to measure. In the range 5 nm $< d_{cap} <$ 10 nm, I_{max} increases and the ratio I_{max}/I_{min} becomes smaller. And for $d_{cap} > 10$ nm, the ratio I_{max}/I_{min} is negligible small. This suggests a choice of $d_{cap} = 7\ldots8$ nm as a reasonable regime with absolute intensities I_{max} of 30…55% of the intensity from a QW with infinitely thick cap and and a signal ratio I_{max}/I_{min} of 11…18.

We note that these simple calculations are only a starting point for modeling and do neither consider surface effects nor a possible lateral diffusion of the charge carriers. Furthermore, no optical measurements on such QRs in partially depleted QWs are have been performed, so far. Nevertheless, we feel that this concept for QR generation

should be discussed here, since it is based on a fundamentally different approach in comparison to other types of self-assembled QRs. Usually, the charge carriers in QRs are localized by a confining potential that allows an energy minimization. This is usually realized by combining semiconductor materials with different band-gap energies. In contrast to that, the present concept does not apply a lateral confining potential. The localization of the charge carriers is achieved by adding a loss channel for charge carriers around the rings via tunneling through a thin cap-layer.

As a further important point, the QRs in partially depleted QWs are not overgrown after the droplet etching step and the etched nanoholes are still open. This allows an interesting functionalization which is not possible with refilled nanoholes. In detail, an MBE heterostructure with AlAs sacrificial layer, an AlGaAs bottom barrier, a GaAs quantum Well, and an AlGaAs top barrier can be grown. A subsequent Al LDE step at $T = 630\,^{\circ}\mathrm{C}$ drills about 30 nm deep nanoholes. After selective removal of the AlAs sacrificial layer by wet chemical etching, a thin membrane with embedded GaAs QW remains. Importantly, the depth of the LDE holes must exceed the thickness of the membrane. Then, the LDE holes represent nanopores surrounded by quantum rings in a thin membrane and might be used, e.g., for the detection of charged molecules [48].

6.5 Summary and Conclusions

Local droplet etching allows the self-assembled drilling of nanoholes into semiconductor surfaces where the hole openings are surrounded by a mostly circular wall of recrystallized material. Thus, it is intuitive to utilize the LDE method for the fabrication of semiconductor quantum rings. We describe here three different concepts for QR fabrication by LDE. The first concept considers QRs inside the GaAs walls which are recrystallized during LDE with Ga droplets. Simulations of the optical properties and a simple growth model indicate that the shape of these QRs deviates from the surface-visible wall as imaged with AFM. We assume that GaAs recrystallization takes place also inside the nanoholes and contributes the QR confinement. In a second concept, LDE with Al droplets forms AlAs walls that are optically inactive. Here, the nanoholes are filled with GaAs to form V-shaped GaAs QDs'. By applying a vertical electric field, wave functions in V-shaped dots can be tunned to form quantum rings. This wave-function tuning provides the unique possibility to switch from zero-dimensional quantum dots to one-dimensional quantum rings by a gate voltage. We note that here the electrons and holes are separated and only one charge-carrier type forms the ring. Both types of QRs, recrystallized GaAs during Ga LDE and filled holes after Al LDE, show a somewhat similar shape. However, as a central difference, recrystallized GaAs forms a QR already at zero field, whereas a V-shaped QD requires a vertical electric field for the transformation into a QR. For both types, the charge carriers are localized using a confinement which is achieved by the embedding of GaAs into AlGaAs as a barrier material. In the third concept, non-confined QRs are proposed. Here, the rings are located in a GaAs QW with thin

cap layer. On the planar surface beside the rings, the QW is depleted due to charge carrier tunneling into surface states. Below the AlAs wall, the thicker local tunnel barrier is expected to yield a ring like charge-carrier localization.

In summary, the various discussed concepts demonstrate the flexibility of the LDE method for QR generation. First optical measurements of single LDE QRs show already excitonic features similar to those of QDs. The quantum-ring nature of these structures can be proved and studied e.g. using capacitance-voltage (CV) spectroscopy under a magnetic field [5].

Acknowledgements The authors thank S. Schnüll and A. Küster for MBE growth as well as A. Küster, A. Graf, A. Ungeheuer, and A. Gräfenstein for PL measurements. Finanzial support is acknowledged from the Deutsche Forschungsgemeinschaft via GrK 1286, HA 2042/6-1, and HA 2042/8-1. Furthermore, this project has received funding from the European Unions Horizon 2020 research and innovation programme under the Marie Skodowska-Curie grant agreement No 721394.

References

1. Y. Aharonov, D. Bohm, Phys. Rev. **115**, 485 (1959)
2. N.A.J.M. Kleemans, I.M.A. Bominaar-Silkens, V.M. Fomin, V.N. Gladilin, D. Granados, A.G. Taboada, J.M. García, P. Offermans, U. Zeitler, P.C.M. Christianen, J.C. Maan, J.T. Devreese, P.M. Koenraad, Phys. Rev. Lett. **99**, 146808 (2007)
3. J.M. Garcia, G. Medeiros-Ribeiro, K. Schmidt, T. Ngo, J.L. Feng, A. Lorke, J.P. Kotthaus, P.M. Petroff, Appl. Phys. Lett. **71**, 2014 (1997)
4. D. Granados, J.M. Garcia, Appl. Phys. Lett. **82**, 2401 (2003)
5. A. Lorke, R.J. Luyken, A.O. Govorov, J.P. Kotthaus, J.M. Garcia, P.M. Petroff, Phys. Rev. Lett. **10**, 2223 (2000)
6. Ch. Heyn, Phys. Rev. B **64**, 165306 (2001)
7. T. Kuroda, T. Mano, T. Ochiai, S. Sanguinetti, K. Sakoda, G. Kido, N. Koguchi, Phys. Rev B **72**, 205301 (2005)
8. S. Huang, Z. Niu, Z. Fang, H. Ni, Z. Gong, J. Xia, Appl. Phys. Lett. **89**, 031921 (2006)
9. J. Wu, Z.M. Wang, V.G. Dorogan, S. Li, Z. Zhou, H. Li, J. Lee, E.S. Kim, Y.I. Mazur, G.J. Salamo, Appl. Phys. Lett. **101**, 043904 (2012)
10. S. Sanguinetti, T. Mano, T. Kuroda, J. Nanoelectron. Optoelectron. **6**, 34 (2011)
11. A. Stemmann, Ch. Heyn, T. Köppen, T. Kipp, W. Hansen, Appl. Phys. Lett. **93**, 123108 (2008)
12. A. Stemmann, Ch. Heyn, W. Hansen, J. Appl. Phys. **106**, 064315 (2009)
13. T. Chikyow, N. Koguchi, Jpn. J. Appl. Phys. **29**, L2093 (1990)
14. J.H. Lee, ZhM Wang, E.S. Kim, N.Y. Kim, S.H. Park, G.J. Salamo, Nanoscale Res. Lett. **5**, 308 (2010)
15. T. Mano, K. Watanabe, S. Tsukamoto, N. Koguchi, H. Fujioka, M. Oshima, C.D. Lee, J.Y. Leem, H.J. Lee, S.K. Noh, Appl. Phys. Lett. **76**, 3543 (2000)
16. J.S. Kim, N. Koguchi, Appl. Phys. Lett. **85**, 5893 (2004)
17. Ch. Heyn, A. Stemmann, A. Schramm, H. Welsch, W. Hansen, A. Nemcsics, Phys. Rev. B **76**, 075317 (2007)
18. M. Abbarchi, C.A. Mastrandrea, T. Kuroda, T. Mano, K. Sakoda, N. Koguchi, S. Sanguinetti, A. Vinattieri, M. Gurioli, Phys. Rev. B **78**, 125321 (2008)
19. E. Stock, T. Warming, I. Ostapenko, S. Rodt, A. Schliwa, J.A. Tfflinger, A. Lochmann, A.I. Toropov, S.A. Moshchenko, D.V. Dmitriev, V.A. Haisler, D. Bimberg, Appl. Phys. Lett. **96**, 093112 (2010)
20. M. Yamagiwa, T. Mano, T. Kuroda, T. Tateno, K. Sakoda, G. Kido, N. Koguchi, Appl. Phys. Lett. **89**, 113115 (2006)

21. M. Volmer, A. Weber, Z. Phys. Chem. **119**, 277 (1926)
22. ZhM Wang, B.L. Liang, K.A. Sablon, G.J. Salamo, Appl. Phys. Lett. **90**, 113120 (2007)
23. Ch. Heyn, A. Stemmann, W. Hansen, Appl. Phys. Lett. **95**, 173110 (2009)
24. Ch. Heyn, A. Stemmann, T. Köppen, Ch. Strelow, T. Kipp, S. Mendach, W. Hansen, Appl. Phys. Lett. **94**, 183113 (2009)
25. Ch. Heyn, M. Klingbeil, Ch. Strelow, A. Stemmann, S. Mendach, W. Hansen, Nanoscale Res. Lett. **5**, 1633 (2010)
26. D. Sonnenberg, A. Graf, V. Paulava, W. Hansen, Ch. Heyn, Appl. Phys. Lett. **101**, 143106 (2012)
27. P. Alonso-González, D. Fuster, L. González, J. Martín-Sánchez, Y. González, Appl. Phys. Lett. **93**, 183106 (2008)
28. Y.H. Huo, A. Rastelli, O.G. Schmidt, Appl. Phys. Lett. **102**, 152105 (2013)
29. Ch. Heyn, A. Küster, A. Ungeheuer, A. Gräfenstein, W. Hansen, Phys. Rev. B **96**, 085408 (2017)
30. Ch. Heyn, M. Schmidt, S. Schwaiger, A. Stemmann, S. Mendach, W. Hansen, Appl. Phys. Lett. **98**, 033105 (2011)
31. Th Bartsch, M. Schmidt, Ch. Heyn, W. Hansen, Phys. Rev. Lett. **108**, 075901 (2012)
32. Ch. Heyn, Phys. Rev. B **83**, 165302 (2011)
33. Ch. Heyn, Th Bartsch, S. Sanguinetti, D.E. Jesson, W. Hansen, Nanoscale Res. Lett. **10**, 67 (2015)
34. D. Fuster, Y. González, L. González, Nanoscale Res. Lett. **9**, 309 (2014)
35. Ch. Heyn, M. Zocher, S. Schnüll, W. Hansen, Nanoscale Res. Lett. **11**, 428 (2016)
36. Ch. Heyn, S. Schnüll, W. Hansen, J. Appl. Phys. **115**, 024309 (2014)
37. R.V.N. Melnik, M. Willatzen, Nanotechnology **15**, 1 (2004)
38. P.-O. Löwdin, Phys. Rev. **97**, 1474 (1955)
39. A. Küster, C. Heyn, A. Ungeheuer, G. Juska, S. Tommaso Moroni, E. Pelucchi, W. Hansen, Nanoscale Res. Lett. **11**, 282 (2016)
40. Á. Nemcsics, Ch. Heyn, L. Toth, L. Dobos, A. Stemmann, W. Hansen, J. Cryst. Growth **335**, 58 (2011)
41. A. Graf, D. Sonnenberg, V. Paulava, A. Schliwa, Ch. Heyn, W. Hansen, Phys. Rev. B **89**, 115314 (2014)
42. D.A.B. Miller, D.S. Chemla, T.C. Damen, A.C. Gossard, W. Wiegmann, T.H. Wood, C.A. Burrus, Phys. Rev. Lett. **53**, 2173 (1984)
43. S.A. Empedocles, M.G. Bawendi, Science **278**, 2114 (1997)
44. W. Heller, U. Bockelmann, G. Abstreiter, Phys. Rev. B **57**, 6270 (1998)
45. J.J. Finley, M. Sabathil, P. Vogl, G. Abstreiter, R. Oulton, A.I. Tartakovskii, D.J. Mowbray, M.S. Skolnick, S.L. Liew, A.G. Cullis, M. Hopkinson, Phys. Rev. B **70**, 201308 (2004)
46. Y.-L. Chang, I.-H. Tan, Y.-H. Zhang, D. Bimberg, J. Merz, E. Hu, J. Appl. Phys. **74**, 5144 (1993)
47. Y. Arakawa, H. Sakaki, M. Nishioka, J. Yoshino, T. Kamiya, Appl. Phys. Lett. **46**, 519 (1985)
48. P.V. Gwozdz, S. Ramachandran, A. Dorn, A. Drews, A. Bhat, R.H. Blick, Appl. Phys. Lett. **109**, 223103 (2016)

Chapter 7
Fabrication of Ordered Quantum Rings by Molecular Beam Epitaxy

Jiang Wu and Zhiming M. Wang

Abstract Quantum rings have attracted a lot of attention due to their unique properties and have been under extensive theoretical and experimental investigations. For example, Aharonov-Bohm effect has been observed in quantum rings which shows potential to realize quantum computational devices. In addition, quantum rings have found application in optoelectronics. Due to the ring-shaped morphology altered from dots, the vertical confinement in nanorings is stronger than in quantum dots. Laser and infrared photodetectors have recently been demonstrated by using quantum rings. To meet the urgent demands for quantum rings, various effects have been devoted to quantum ring fabrication techniques. There are two of the most used bottom-up fabrication methods of self-assembled rings using molecular beam epitaxy (MBE). Semiconductor quantum rings can be created by conventional molecular beam epitaxy and Droplet Epitaxy technique. Despite great efforts devoted to quantum ring fabrication using these techniques, alignment of quantum rings is not well documented. Fabrication of ordered quantum rings is of high priority for theoretical as well as practical investigations, such as persistent current and photodetectors. Recently, both vertically and laterally ordered quantum rings have been demonstrated. In this chapter, the growth mechanisms and fabrication techniques for aligned quantum rings grown are reviewed.

J. Wu (✉) · Z.M. Wang (✉)
Institute of Fundamental and Frontier Sciences, University of Electronic Science and Technology of China, Chengdu, China
e-mail: jiangwu@uestc.edu.cn

Z.M. Wang
e-mail: zhmwang@uestc.edu.cn

V.M. Fomin (ed.), *Physics of Quantum Rings*, NanoScience and Technology,
https://doi.org/10.1007/978-3-319-95159-1_7

7.1 Introduction

Unique properties of nanomaterials have attracted considerable interest over the last two decades in various fields in physics, engineering, chemistry, and biology, which present the promise of realizing next generation electronic and optoelectronic devices.

Among various nanomaterials, quantum rings show interesting electronic, magnetic and optical properties and attracted considerable attention [1–8]. For example, quantum phase coherence effects, such as the Aharonov-Bohm and Aharonov-Casher effects, have been observed in quantum rings [4]. The optical Aharonov-Bohm effect has also been predicted and demonstrated, which can be potentially used for applications in quantum information processing systems [9–11]. In addition, research efforts on quantum rings have also led to various practical applications in the last few years. Quantum ring infrared photodetectors have been reported in the mid-infrared and THz spectral range [12, 13]. Nanorings have shown promise in high density magnetic memory applications [14]. Quantum ring lasers have also been reported [15].

The increasing interest in quantum rings gives rise to a variety of fabrication techniques [16–19]. Currently, quantum rings are mainly fabricated by two major fabrication methods, conventional molecular beam epitaxy and Droplet Epitaxy technique. Generally, nanostructures fabricated by these two methods are randomly distributed. However, for many applications, it is advantageous to achieve ordered nanostructures in order to provide optimum performance. For example, ordered quantum dot arrays can result in a higher absorption and higher responsivity for quantum dot infrared photodetectors [20]. Three-dimensionally aligned quantum dot array can provide a strong electron wave function overlap, which is considered to be beneficial for intermediate band solar cells [21]. A lot of ordered nanostructures, such as nanowires, quantum dots and nanoparticles are fabricated by different methods, [22–27] including template growth and drying mediated self-assembly [28–30]. However, there are only a few reports on ordered quantum rings.

In this chapter, we present different growth techniques to fabricate ordered quantum rings. We first review fabrication of quantum ring chains on GaAs (100) surface. After that, in Sect. 7.2.2, fabrication of two-dimensionally aligned quantum rings grown on a high index surface is presented. In Sect. 7.3, fabrication of vertically aligned quantum rings by Droplet Epitaxy is introduced. In Sect. 7.4, fabrication of GeSi quantum rings on pre-patterned substrate is overviewed. Finally, future prospects of the ordered quantum rings are presented in Sect. 7.5.

7.2 Fabrication of Laterally Ordered Quantum Rings on Quantum Dot Superlattice Template

7.2.1 Fabrication of Ordered Quantum Ring Chains on GaAs (100) Surface

Generally, quantum rings can be fabricated from S-K quantum dots and by Droplet Epitaxy technique. By using S-K growth mode, strained quantum dots, which are partially capped by a thin layer of a substrate material, undergo a morphological transformation from quantum dots to ring-shaped nanostructures. Alternatively, ring-shaped nanostructure can be formed by Droplet Epitaxy through control over the crystallization process of nano-droplets. The morphology of crystallized nanostructures can be well controlled from quantum dots to quantum rings. However, both processes in general result in randomly distributed quantum rings.

Nevertheless, growth of ordered quantum dots has been demonstrated [31]. One approach to obtain ordered quantum dots is based on multiple quantum dot stacking. The strain field introduced into the system by quantum dots results in increasing size and spacing uniformity in successive quantum dot layers because the nucleation rate is strongly dependent on the strain field. For example, Wang et al. have produced laterally ordered quantum dot chains on GaAs(100) by stacking multiple quantum dot layers. Similarly, multiple quantum dot layers can be adopted for quantum ring growth and used to form a template for laterally ordered quantum rings. Currently, the formation of laterally ordered quantum dots by strain field engineering has been well studied [32]. In this section, lateral ordering of self-assembled quantum rings is presented.

A molecular Beam Epitaxy (MBE) system has been used for fabricating ordered quantum ring chain samples on semi-insulating GaAs (100) substrates. First, the native oxide is removed at 610 °C under an As_4 flux for ten minutes. The deoxidized GaAs substrate temperature is then changed to 590 °C. A GaAs buffer layer (200 nm) is grown, after which the substrate temperature is changed again to 540 °C. The formation of ordered quantum ring chains is divided into two major steps, (i) formation of ordered quantum dot chain template and (ii) quantum ring conversion. Formation of quantum dot chains has been investigated by growth of multilayers of InGaAs/GaAs quantum dots. Quantum dot chains with length over five microns have been demonstrated. The growth procedure for quantum ring chains consists of formation of quantum dot chains as a template. For the quantum ring chain template growth, $In_{0.4}Ga_{0.6}As$ (8.4 ML) is deposited first and then growth interruption (10 s) is introduced. The $In_{0.4}Ga_{0.6}As$ quantum dots are sequentially capped by 20 ML GaAs. Another 60 ML thick GaAs spacer is deposited after raising the substrate temperature back to 580 °C. The $In_{0.4}Ga_{0.6}As$ (8.4 ML)/GaAs (80 ML) quantum dot structure is repeated eight times in order to improve the vertical correlation and to obtain uniform quantum dot chains. Deposition of multi-layer InGaAs quantum dots creates a uniform strain field. The quantum dot superlattice strain field in turn,

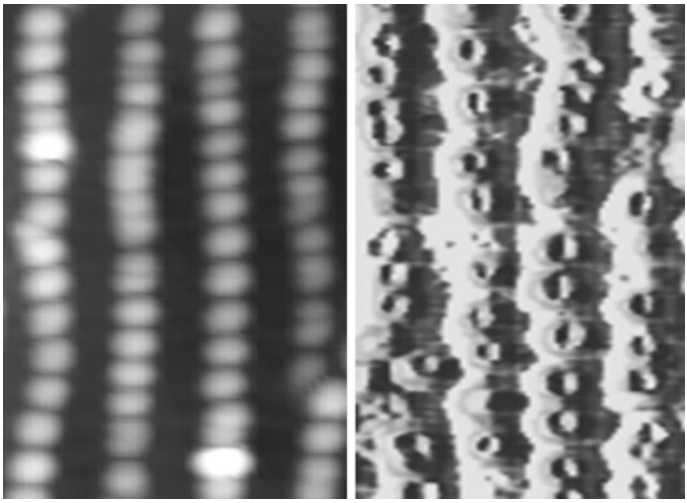

Fig. 7.1 AFM images of quantum dot chains and quantum ring chains. After [36]

can lead to the ordered arrangement of the last layer of quantum rings [33]. After completion of the eight periods of multiple $In_{0.4}Ga_{0.6}As/GaAs$ quantum dots, the substrate temperature is reduced to 540 °C again. At the same time, the As cracker is operated at a temperature about 900 °C to produce As_2. When the growth conditions are ready, the RHEED screen shows the c(4 × 4) surface reconstruction [34] In order to create quantum rings, InAs quantum dots are grown using the S-K mode by depositing 2.1 ML InAs. After formation of InAs quantum dots, the growth is interrupted and the sample is annealed for a few tens of seconds. The growth interruption has been found to be helpful in alignment of quantum dots along the [01-1] direction. In addition, the interruption also promotes nucleation of quantum dots more uniformly. After formation of well-aligned quantum dot chains, those chains are immediately covered by 4 nm GaAs. The as-grown InAs quantum dots are about 6–8 nm in height. The deposition of 4 nm GaAs only partially covers the quantum dots, which results in unbalanced surface forces. These forces convert nanodots into ring-shaped nanostructures [35].

Figure 7.1a shows an example of the Atomic Force Microscopy (AFM) image of InAs quantum dot and quantum rings chains. The growth of multiple quantum dot layers increases the uniformity of the quantum dot arrangement. Stacking of multiple quantum dot layers promotes the vertical correlation of quantum dots due to the nucleation of quantum dots at the strain minima [31]. The resulted ordering pattern is related to the morphology of the quantum dots and the elastic medium in which the quantum dots are included. The anisotropy of GaAs matrix and InAs quantum dots introduces a strain field along the [01-1] direction. Therefore, the multiple stacking of the quantum dots led to formation of quantum dot chains along the [01-1] direction.

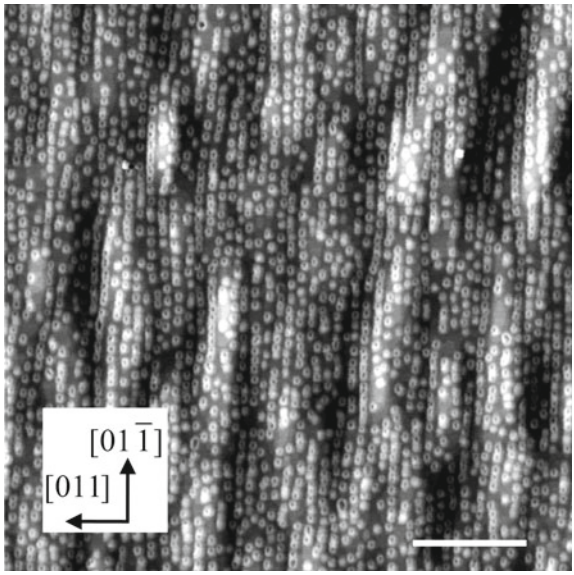

Fig. 7.2 Tapping mode 5.0×5.0 μm AFM image of quantum ring chains grown on an $In_{0.4}Ga_{0.6}As/GaAs(100)$ multi-layered quantum-dot superlattice. The scale bar is 1 μm. After [36]

According to the "dewetting model" proposed by Blossey and Lorke [35], it is the instability of quantum dots introduced by the unbalanced surface forces that causes the conversion of quantum dots into quantum rings during capping. The process of quantum ring formation based on the "dewetting model" is briefly reviewed in Chaps. 2 and 3. An AFM image of the ordered quantum rings converted from partially capped quantum dots is shown in Fig. 7.2. The lateral ordering of quantum rings is well preserved. Figure 7.2 shows that the quantum ring chain is formed along the [01-1] direction and the average chain length is about 1.0 μm. The quantum ring chains share similar surface morphology to the quantum dot chains because the rings are directly converted from the quantum dots. The length and regularity of the quantum ring chain may be further improved by improving the regularity of the quantum dot chain template. In addition, the process of dot-to-ring transformation can be also improved by using different growth conditions, such as thickness of the GaAs capping layer.

To obtain a better characterization of the quantum ring chains, Fig. 7.3 compares two typical AFM images of quantum ring chains and quantum dot chains as well as AFM line profiles of a typical quantum ring and quantum dot. The partial capping truncates the quantum dots and, thus, quantum rings become lower than quantum dots. However, the outward reconfiguration of the nanostructure makes rings slightly larger than the quantum dots. Quantum rings also show an oval morphology along the [01-1] direction, which is likely because of an isotropic redistribution of materials during the ring-to-dot transformation process [37]. The insets in Fig. 7.3a, b show corresponding Fourier transforms of quantum ring and quantum dot chains. The

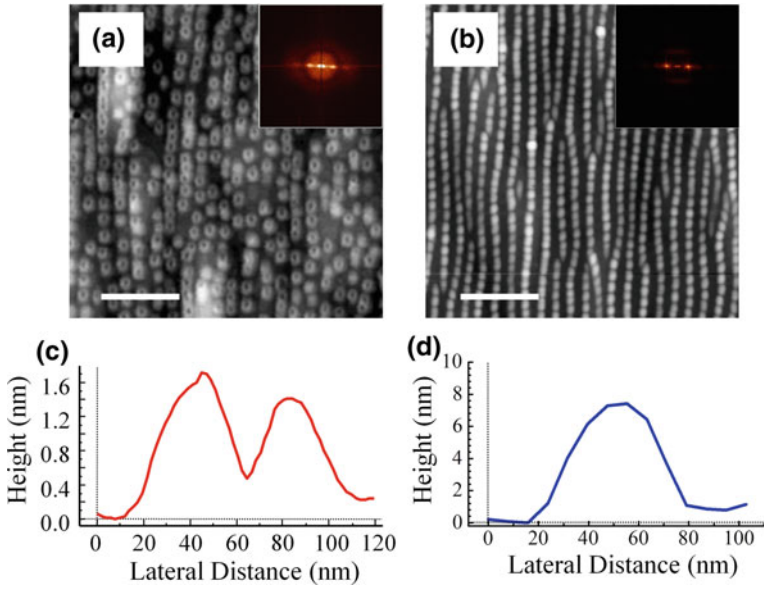

Fig. 7.3 **a** Tapping mode AFM image of quantum ring chains. **b** Tapping mode AFM image of quantum dot chains. The insets are Fourier transforms from the AFM image of quantum-ring chains and quantum-dot chains. **c** Cross-sectional line profile of a quantum ring. **d** Cross-sectional line profile of a quantum dot. The scale bar is 500 nm. After [36]

Fourier transforms confirm the long-range one-dimensional ordering of quantum rings and quantum dots.

The photoluminescence measurement of a capped quantum ring sample (50 nm GaAs cap layer) suggests a strong emission from ordered quantum ring chains, as shown in Fig. 7.4. Two photoluminescence peaks, at 1060 and 1163 nm, of Gaussian profiles are observed. The photoluminescence peak at 1060 nm is due to the multiple $In_{0.4}Ga_{0.6}As$ quantum dot layers. The peak at 1163 nm is assigned to the quantum rings based on a narrower bandgap of the InAs. The difference in the strain and quantum confinement between the multiple quantum dots and quantum rings are also accounted for the shift of photoluminescence emission peak. The emission from the quantum rings also shows a broader line-width than the emission spectrum from $In_{0.4}Ga_{0.6}As$ quantum dots. This can be explained by the reduced quantum ring uniformity. As shown in the AFM images, after the partial capping process, there are imperfect rings formed which broadens the photoluminescence spectrum. In order to improve the quantum ring chain quality, a number of factors require a further improvement. First, improvement of ordering and uniformity of the initial quantum dot chains would be helpful to obtain better quantum ring chains.

Second, optimization the capping layer thickness and post-growth annealing also plays a critical role in improving quantum ring chain quality.

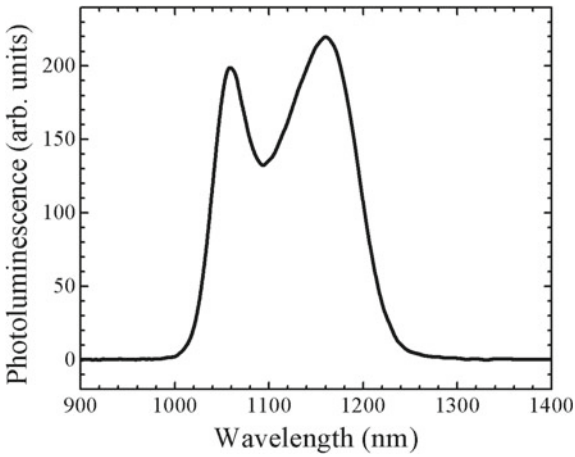

Fig. 7.4 PL spectrum of the ordered quantum ring chains on the quantum dot superlattice template measured at 77 K. After [36]

7.2.2 Fabrication of Laterally Ordered Quantum Ring Arrays on GaAs High Index Surfaces

To investigate control over the lateral quantum ring ordering by the "self-organized anisotropic strain engineering" technique [38], fabrication of quantum rings on high index surfaces is performed. Compared with one-dimensional quantum ring chains observed on GaAs (100) surface, a periodic two dimensional quantum ring array has been demonstrated on high index surfaces. Likewise, the semi-insulating GaAs substrates are used for sample preparation by molecular beam epitaxy [39]. The growth conditions are the same as those for quantum ring chain growth. In this study, GaAs (311)B and (511)B high index surfaces are used in addition to GaAs (100) surface. Figure 7.5 shows the AFM images of the laterally alignment of quantum rings formed on different GaAs surfaces. Interestingly, quantum ring chains are formed on the (100) surface while different patterns are formed on the high index surfaces, (311)B and (511)B.

Even though the quantum rings are grown under the same conditions, the multiple quantum dots and then, the over-grown quantum rings show quite different surface morphology on different surfaces. The distinct morphological differences embrace the shape of quantum rings and lateral alignment pattern of quantum rings. Typical AFM images and cross-sectional pro files of quantum rings grown on different surfaces are shown in Fig. 7.6. The quantum rings grown on (100), (311)B and (511)B surfaces show similarity in size and density as listed in Table 7.1. However, slightly elongated quantum rings are observed on GaAs (100) surfaces. On the other hand, quantum rings formed on high index surfaces appear more spherical but with a more asymmetrical height distribution. This difference results mainly from two factors. First, the surface diffusion of In adatoms, surface energy, and step bunches vary on surfaces with different Miller indices, which results in different shape and size of InAs quantum dots [41–44]. On high index surfaces, the diffusion along the [01-1]

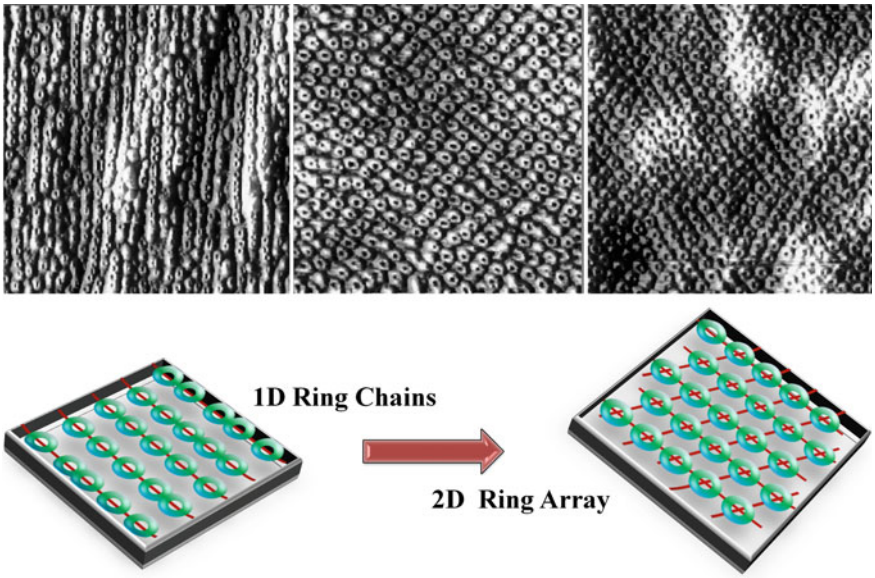

Fig. 7.5 AFM images of quantum rings grown on GaAs (100), (311)B, and (511)B surfaces. The bottom illustration shows a transition from a one-dimensional ordering on the (100) surface to a two-dimensional array on high index surfaces. After [40]

Table 7.1 Average radii and density of quantum rings on GaAs (100), (311)B, and (511)B surfaces

Surface	(100)	(311)B	(511)B
Average radius (nm)	26.3 ± 8.2	37.6 ± 10.7	35.2 ± 7.5
Density (cm^{-2})	7.9×10^9	5.0×10^9	5.6×10^9

direction can be tuned to match with diffusion along the [011] direction [45]. Second, as mentioned in the previous section, the surface energy is orientation-dependent and facet-dependent. The net force acting upon the quantum dot during the ring transformation differs on different surfaces [35]. As shown in Fig. 7.6b, c, the AFM line profiles of quantum rings show different heights along the [23-3] and [25-5] directions. The height distribution of quantum rings on high index surface is attributed to the process of dot-to-ring conversion because the initial shape of quantum dots on high index surfaces is rather spherical. Since the initial quantum dots are expected to be a round dome shape, the anisotropic rings may be attributable to the process of dot-to-ring transformation. As mentioned earlier, the anisotropic ring morphology can be affected by different facets, orientation-dependent free energy, and strain effects, which may be the main factors leading to direction-dependent forces and thus, uneven material distribution of quantum rings on high index surfaces.

More importantly, quantum rings formed on the (100) surface align in a chain-shaped pattern, while a two-dimensional periodical alignment of rings is observed

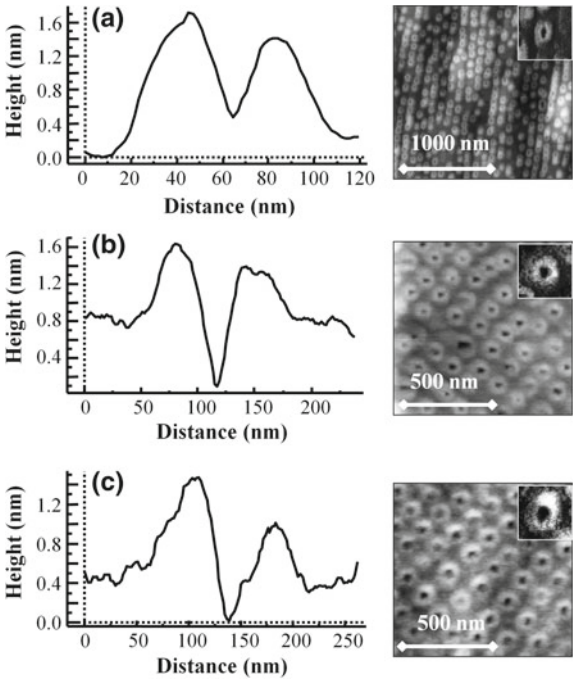

Fig. 7.6 Cross-sectional line-profiles of quantum rings grown on **a** GaAs (100) surface; **b** GaAs (311)B surface; **c** GaAs (511)B surface. The line-profiles are taken along the [01-1], [23-3], and [25-5] for the (100), (311)B, and (511)B, respectively. The right side of the line-profiles are the AFM images of quantum rings grown on the (100), (311)B, and (511)B surfaces. The insets are AFM images of a single quantum ring grown on each surface. After [40]

on high index surfaces when a strain quantum dot superlattice template is present. Generally, it is considered that the elastic interactions of multiple layers of quantum dots result in the lateral ordering of quantum dots or quantum rings [31, 46]. On GaAs (100) surface, the adatoms mainly diffuse along the [01-1] direction and quantum dots are more relaxed along the [01-1] direction. Therefore, the strain field transferred to the subsequent quantum dot layer is elliptical. The elliptical field tends to align the subsequent quantum dots along the [01-1] direction. Similarly, there are surface steps with variable separations perpendicular to the [2n–n] directions on high index (n11)B surfaces. The nominal step separation for a GaAs (n11) surface consisting of the (001) terraces, denoted as S, is equal to $0.2 \times$ n nm, Therefore, the nominal step separation can be adjusted from 0.6 nm [(311)B surface] to 1.8 nm [(911)B surface]. The change in surface steps affects the adatom surface diffusion as well as strain field correlation between adjacent quantum dot layers. On high index surfaces, the diffusion along the [01-1] and [011] directions can be adjusted to closely match [45]. Consequently, control over S creates the opportunity to manipulate the surface adatom migration pattern, which, therefore, is promising for tuning the nanostructure ordering pattern.

Figure 7.7 shows AFM images ($2.5\ \mu m \times 2.5\ \mu m$) and the corresponding fast Fourier transforms of quantum ring arrays grown on the (100), (311)B, and (511)B surfaces. The Fourier transform from quantum rings on the (100) surface confirms long range one-dimensional ordering while the Fourier transforms from quantum

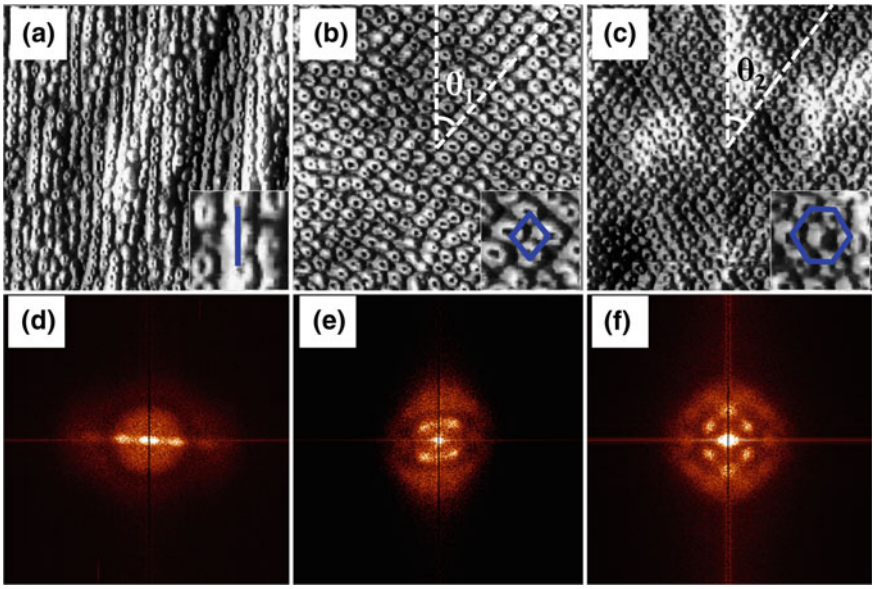

Fig. 7.7 AFM images of ordered quantum rings on the top of multilayered $In_{0.4}Ga_{0.6}As$ quantum dot templates grown on **a** GaAs (100), **b** (311)B, and **c** (511)B surfaces. The second row images are fast Fourier transforms taken from the corresponding AFM images: **d** GaAs (100), **e** (311)B, and **f** (511)B surfaces. The insets are magnified AFM images showing different quantum ring lattice structures. After [40]

rings on the (311)B and (511)B surfaces confirm two-dimensional ordering due to more isotropic strain field of quantum dot superlattices. The Fourier transforms of AFM images show quantum ring array patterns with two symmetry axes for (311)B surface and with four symmetry axes for (511)B surface. These Fourier transform patterns and the magnified AFM images indicate that the quantum rings on the (311)B and (511)B surfaces align in rhombic and hexagonal symmetry, respectively. By adjusting the nominal surface step separation, the strain is most relaxed along an in-plane direction which is deflected by about 40 degrees to the [23-3] (or [25-5]) direction. From the AFM images, the measured angles between the strain relaxation direction and the [2n-n] direction are 41.6 [(311)B surface] and 36.2 [(511)B surface] degrees. To sum up, lateral alignment of quantum ring arrays can be achieved by strain engineering and quantum ring conversion through partial capping. The order pattern can also be tuned by choosing substrates with different Miller Indices.

7.3 Fabrication of Vertically Aligned Quantum Rings by Droplet Epitaxy

Although spatial alignment has been well achieved, the growth aligned quantum rings in the vertical direction is less explored. As shown in previous section, the strain field of the S-K quantum dots can lead to vertical correlation of quantum dot self-assembly. Fabrication of vertically aligned quantum rings is feasible via such an approach along with conversion of dots into rings by partial capping, but it has not been reported, probably due to the complexity in growth and/or lack of applications. On the other hand, Droplet Epitaxy has emerged as a facile and versatile method to fabricate quantum rings and many other quantum structures, that are not easily obtainable by S-K growth mode [17, 47, 48]. Droplet Epitaxy that is based crystallization of metal lacks a mechanism to couple neighboring layers like the S-K method, even though a vertical growth protocol of Droplet Epitaxy can add another dimension of control in fabricating nanostructures. It has been found that nanodroplets tend to nucleate at the location of existing nanocrystals formed by Droplet Epitaxy [49, 50]. The existing nanostructures serve as preferred nucleation sites for both homo- and hetero-epitaxy and thus, vertically aligned nanostructures can be fabricated to sequential deposition using Droplet Epitaxy. In this section, a method to fabricate vertically aligned quantum rings using Droplet Epitaxy is presented.

Samples were grown by Droplet Epitaxy using a Molecular Beam Epitaxy (MBE) system. Droplets were deposited without any As flux at a low substrate temperature of 280 °C. Both a single element, e.g. Ga, or alloy, e.g. AlGa, can be deposited for form nanodroplets. Instead of one crystallization step, sequential multiple deposition can be carried out to form vertically aligned structures, as summarized in Table 7.2. The RHEED patterns were recorded during each deposition. Prior droplet deposition, the surface reconstruction was (2×4) according to RHEED. The surface reconstruction changed from (2×4) to (2×1) immediately after metal droplet deposition, indicating transformation of As-rich surface to Ga-rich surface. At the same time, the RHEED intensity decreased and changed to spotty features after supplying As flux. The crystallization was carried out at the same substrate temperature for 60 s with As beam equivalent pressure (BEP) of 1.2×10^{-5} Torr. The evolutions of RHEED patterns were similar for subsequent droplet deposition and crystallization steps, suggesting same growth dynamics.

Figure 7.8 illustrates the fabrication of vertically aligned nanostructures by sequential Droplet Epitaxy and AFM measurements of samples A, B, and C. Although conventional growth of nanostructures by single step Droplet Epitaxy has been well documented, it is interesting to observe that the sequential deposition of group III elements or alloys tend to nucleate nanodroplets right over the existing nanostructures, as shown in Fig. 7.8. Droplet localization in holes has also been realized by groups [51, 52]. The direct nucleation of nanodroplets on the pre-existing nanostructures provides a way to fabricate vertically aligned nanostructures by Droplet Epitaxy.

Table 7.2 Summary of the growth procedures of all samples

Sample #	Growth procedures
A	Ga 3 ML deposition
B	Ga 3 ML deposition → As crystallization 60 s
C	Ga 3 ML deposition → As crystallization 60 s → Ga 3 ML deposition
D	(Ga 3 ML deposition → As crystallization 60 s) × 2 cycles
E	(Ga 3 ML deposition → As crystallization 60 s) × 3 cycles
F	(Ga 3 ML deposition → As crystallization 60 s) × 4 cycles
G	(Ga 3 ML deposition → As crystallization 60 s) × 5 cycles
H	(Ga 3 ML deposition → As crystallization 60 s → $Al_{0.3}Ga_{0.7}$ 3 ML → As crystallization 60 s) × 10 cycles

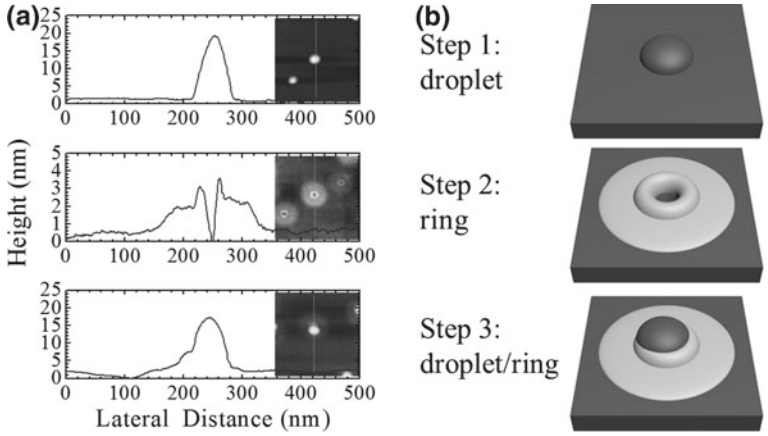

Fig. 7.8 **a** Schematics of forming nanodroplets, nanorings, and nanodroplet/nanoring hybrids by sequential Droplet Epitaxy. **b** AFM line profiles of samples A, B, and C: a single Ga nanodroplet, GaAs nanoring, and nanodroplet/nanoring hybrid. The profiles taken along the lines indicated in insets. After [49]

The nucleation of nanodroplets on existing nanorings can be understood by the nucleation thermodynamics of droplets. Based the nucleation thermodynamics, the dependence of ΔG^*, the energy barrier for the formation of a critical nucleus, on θ, the angle between the nanostructure and substrate surface, can be expressed as

$$\Delta G^* = -\frac{32\gamma_{lv}^3 f_1^3(\theta,\alpha)}{27 g_v^2 f_2^2(\theta,\alpha)} \quad (1)$$

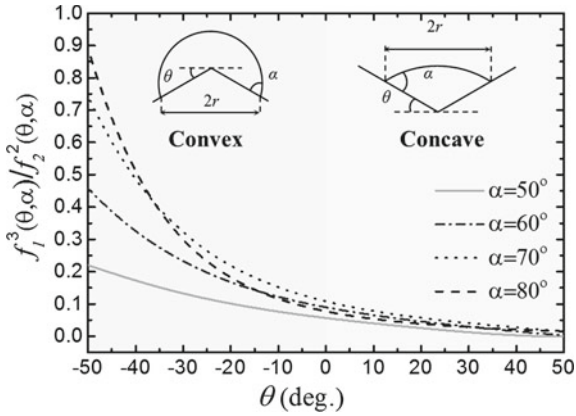

Fig. 7.9 Geometric factor ratio $f_1^3(\theta, \alpha)/f_2^2(\theta, \alpha)$ as a function of angle θ. The contact angle α is set at different values: 50°, 60°, 70°, and 80°, respectively. The insets illustrate that nanodroplets form on convex and concave surfaces [49]

where γ_{lv} is the surface energy density of a droplet, α is the contact angle of droplet with substrate surface, g_v is the Gibbs free energy per unit volume, and $f_1(\theta, \alpha)$ and $f_2(\theta, \alpha)$ are geometric factors. As shown in the inset of Fig. 7.9, the surface represents a concave surface when $\theta > 0$ or convex when $\theta < 0$. ΔG^* is only determined by the geometric factor ratio $f_1^3(\theta, \alpha)/f_2^2(\theta, \alpha)$, because γ_{lv} and g_v are constants determined by material properties. Therefore, the geometric factor ratio represents the droplet nucleation energy barrier. Figure 7.9 shows the geometric factor ratio for different droplet contact angles as a function of angle θ.

Regardless of the droplet contact angle, the geometric factor ratio and hence the nucleation energy barrier decreases with increasing θ. As a results, the critical nucleus on a concave surface has a smaller energy barrier than that on the convex or flat surfaces. Therefore, sequential deposition of Ga nanodroplets favors nucleation of droplets in the center of nanorings where angle θ is the largest. In experiment, nanoholes are not symmetric and are elongated in the [01-1] direction due to anisotropic diffusion. As shown in Fig. 7.8, The asymmetry of the nanoholes caused the nanodroplets slightly off-center on the rings along the [01-1] direction.

Figure 7.10a shows the AFM images of samples B, D, E, F, and G. With increasing of deposition cycles, the surface morphology of the stacked rings doesn't change significantly, which confirms the vertical correlation in nanoring growth by Droplet Epitaxy. In order to provide further insight into the formation of vertically stacked nanorings, the final shapes of GaAs after different deposition cycles are simulated based on a kinetic growth mode [53]. Figure 7.10a, b shows the simulation and experimental AFM results of final shapes of GaAs rings after one to five deposition cycles. Figure 7.10c, d also shows the simulated and measured of cross-sectional height profiles. In the simulation, the anisotropic surface diffusion is ignored. Both the experimental results and simulation show that the height of nanorings increases with deposition cycles while the radius of rings remain nearly unchanged for all five samples. However, there are some distinct differences in surface morphologies between the simulations and AFM measurements. For example, in experiment, the

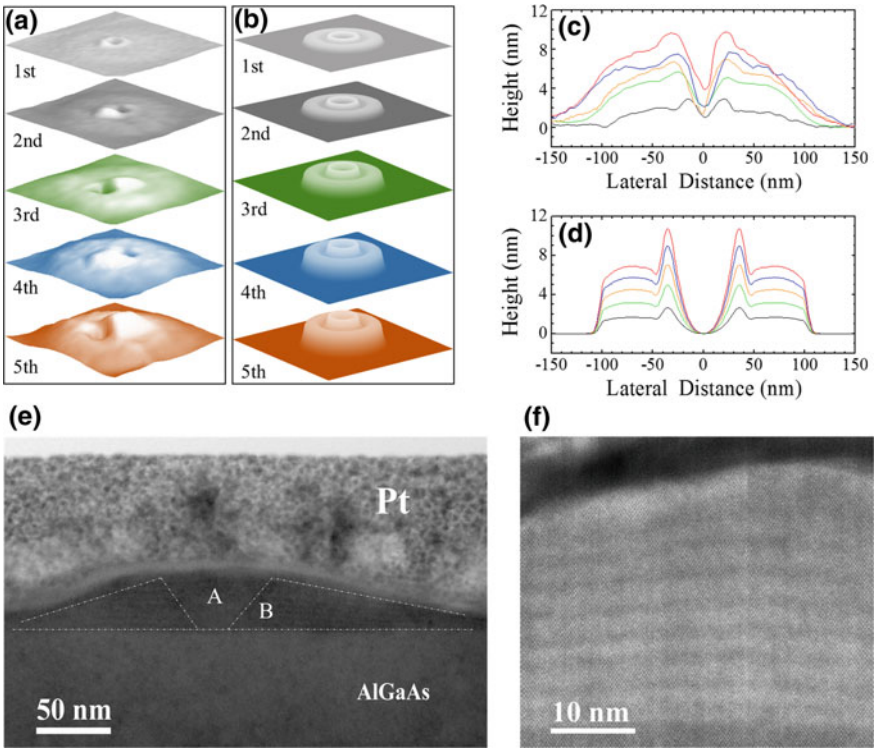

Fig. 7.10 **a** and **b** are AFM images and the simulated three dimension surface morphologies of GaAs nanorings after multiple deposition cycles. **c** and **d** are the cross-sectional height profiles obtained from simulated results and AFM images. The initial radius of Ga droplet 40 nm. The AFM line profiles are taken along the [011] direction [49]. **e** and **f** are the cross sectional transmission electron microscopy images of stacked quantum rings

nanoring edge becomes beveled with increasing deposition cycles. This deviation from simulation is caused by the out-diffusion of the ring material during the growth pauses which was not taken into account in the simulation [10]. Nonetheless, from the simulated and measured cross-sectional line profiles of the nanorings, the proposed kinetic growth simulation agrees well with the experiment. The simulated and measured nanorings match well in terms of lateral dimension as well as heights of both inner and outer rings.

The vertical stacking of quantum rings also applies to metal alloys. The alloyed metal droplets also nucleate at the exact location of existing nanorings, similar to single element droplets. In addition, alternating epitaxy of different materials by Droplet Epitaxy also follows the same growth mechanism. Figure 7.10e, f shows cross-sectional transmission electron microscopy (TEM) images of sample H, stacked nanorings fabricated by ten sequential cycles of GaAs/$Al_{0.3}Ga_{0.7}As$ droplet heteroepitaxy. Figure 7.10e clearly shows a nanoring with two regions, A and B. Multiple

layers are present in the B region while absent in the A region. The A region is the hole observed from the AFM images located at the center of the rings and the layered structures in the B region are the stacked GaAs/$Al_{0.3}Ga_{0.7}As$ multiple quantum rings. The high resolution TEM image of the layered structures in B region is shown in Fig. 7.10f. The bright and gray layers are the GaAs and $Al_{0.3}Ga_{0.7}As$ rings, respectively. It should be noted that only eight periods of GaAs and $Al_{0.3}Ga_{0.7}As$ layers can be identified although 10 cycles of deposited were carried out. This may be due to missing stacking of nanodroplets during growth. Similar to droplet homo-epitaxy of GaAs nanorings, the vertically stacked GaAs/$Al_{0.3}Ga_{0.7}As$ quantum rings also have beveled edges due to diffusion. It is also expected that the vertical correlation of Droplet Epitaxy may also apply to other material systems, e.g. strained InAs/GaAs, because the vertical correlation is originated from the nucleation thermodynamics of the droplets.

7.4 Fabrication of Quantum Rings on Pre-patterned Substrates

7.4.1 Simulations of Formation of Ordered Quantum Dots and Quantum Rings Through Pre-patterning

Alternative approach to self-assembly of aligned nanostructures is to create ordered artificial template by pre-patterning. A few methods have been proposed to fabricate ordered nanostructures on pre-patterned substrates, which consist of ordered pits, or ordered humps, or regularly distributed strain energy profiles [54, 55]. The idea is to form nanostructures on the patterned pit or hump with one-to-one correlation in the subsequent growth. However, it faces great challenges to achieve well-aligned nanostructure arrays through surface pre-patterning. For example, it is challenging to obtain one-to-one correlation between pattern and nanostructures, Phase diagrams for heteroepitaxy of quantum structures on patterns are theoretically simulated by a model [56]. The phase diagrams for fabrication of ordered quantum dots and rings provide insight in obtaining the one-to-one correlation between patterns and the subsequently grown quantum structures. The model assumes a fixed pre-patterned substrate surface and a thin transition layer with a linearly varied mismatch strain atop. The surface morphology evolves with deposition and the surface diffusion, which is governed by surface chemical potential. A small random noise to the deposition is added to the simulation of growth with random fluctuation. Cosine-shaped pits or humps are considered on the pre-patterned substrate. The simulation also assumes that the radius of the pits (or humps) is comparable with the surface roughness wavelength.

The simulated phase diagrams for pit and hump pre-patterning with the variation of the normalized deposition rate R^* and diagonal edge-to-edge distance P^* are shown in Fig. 7.11. The phase diagrams for pit and hump pre-patterning show three

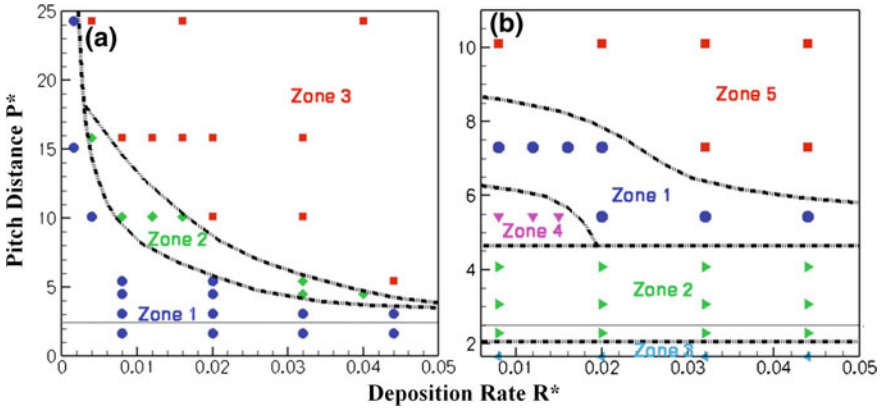

Fig. 7.11 Calculated phase diagram for **a** pit and **b** hump pre-patterning. Points on the diagrams denote the calculated cases. After [56]

and five phase zones, respectively. On the phase diagram for pit pre-patterning, as shown in Fig. 7.11a, the one-to-one relation between the pits and quantum dots is maintained in zone 1. The formed dots are stable against growth noise during the growth process. However, no one-to-one correlation is observed between pits and formed dots. In zone 2, additional dots or structures with different morphologies are formed between the patterned pits. However, one-to-one correlation can be still obtained because the additional dots disappear with further growth. In the zone 1 of the phase diagram for hump pre-patterning, one-to-one correlation is also achieved but with shape transition during the growth process. First, quantum rings are formed on the humps. Sequentially, the rings gradually shrink and eventually change into dots when the growth proceeds. In zones 2 and 3, only dots form between humps during growth. However, the nucleation positions vary for zones 2 and 3. Incomplete rings form at the early stage and further break up into dots without order arrangements for zone 4. Both dots and rings form in zone 5. There is no one-to-one correlation for zones 4 and 5.

Two examples of nanostructures formed on pits and humps are shown in Fig. 7.12. Figure 7.12a1, a2 show the cases in zone 1 and zone 3 of the phase diagram for pit pre-patterning, respectively. Quantum dot arrays are formed with one-to-one correlation in zone 1. However, surface morphology conversion between dots to ripples is observed for zone 3 without one-to-one correlation. Figure 7.12b shows an example of nanostructures formed on humps. Clearly, shape transitions have occurred during the growth. The surface chemical potential profiles play an important role in the formation of the one-to-one correlation between patterns and nanostructures. The simulated phase diagrams can serve as guideline for optimized fabrication of ordered quantum dot or quantum ring arrays.

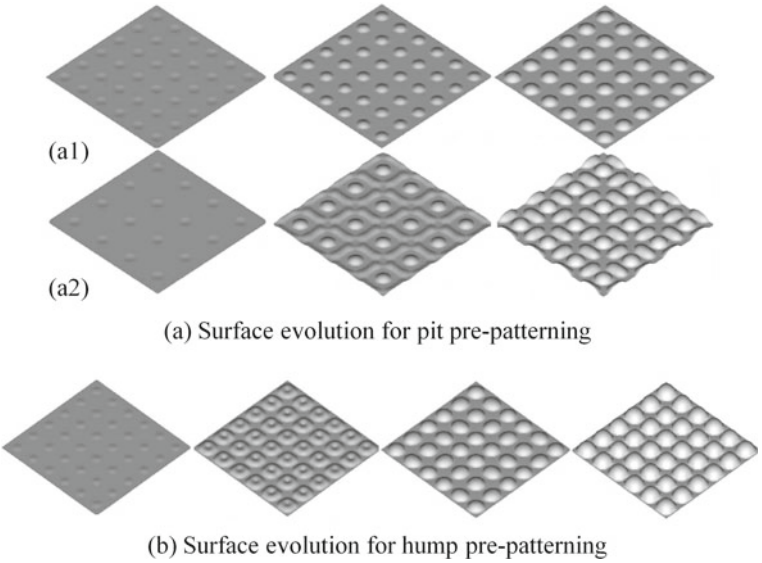

Fig. 7.12 **a** Snapshots of surface evolution for pit pre-patterning: (a1) a case in zone 1 and (a2) a case in zone 3. **b** Snapshots of surface evolution for hump pre-patterning: a case in zone 1. From [56]. Reprinted with the permission of the American Institute of Physics

7.4.2 Fabrication of GeSi Nanorings on Patterned Si (100) Substrate

Laterally aligned nanostructures can be obtained on a pre-patterned substrate with ordered nanopatterns. A number of methods have been developed to create nanopatterns, including nanoimprint lithography, holographic lithography, anodic oxidation nanolithography, and nanosphere lithography. Nanosphere lithography is a cost-effective and high throughput nanofabrication technique. Nanosphere lithography has been used to create ordered GeSi QDs. The GeSi nanorings are formed by capping the GeSi QDs with a thin Si capping layer [57].

Figure 7.13 shows a schematic illustration for nanopatterning using nanosphere lithography. Nanopatterning consists of four major steps.

1. The polystyrene sphere (diameter of 430 nm) suspension is mixed with methanol (1:1). Weekes' method is used to assemble polystyrene nanospheres on the surface of deionized water in a close-packed monolayer, which is then transferred onto a clean p-type Si (001) substrate with hydrogen-terminated surface by draining the de-ionized water.
2. The diameter of polystyrene spheres is shrunk down to about 80 nm by the reactive ion etching.
3. Au–Si alloy and SiO_2 mask are formed via Au-catalyzed oxidation after deposition of a thin Au film (1 nm) on a surface covered with polystyrene spheres. The

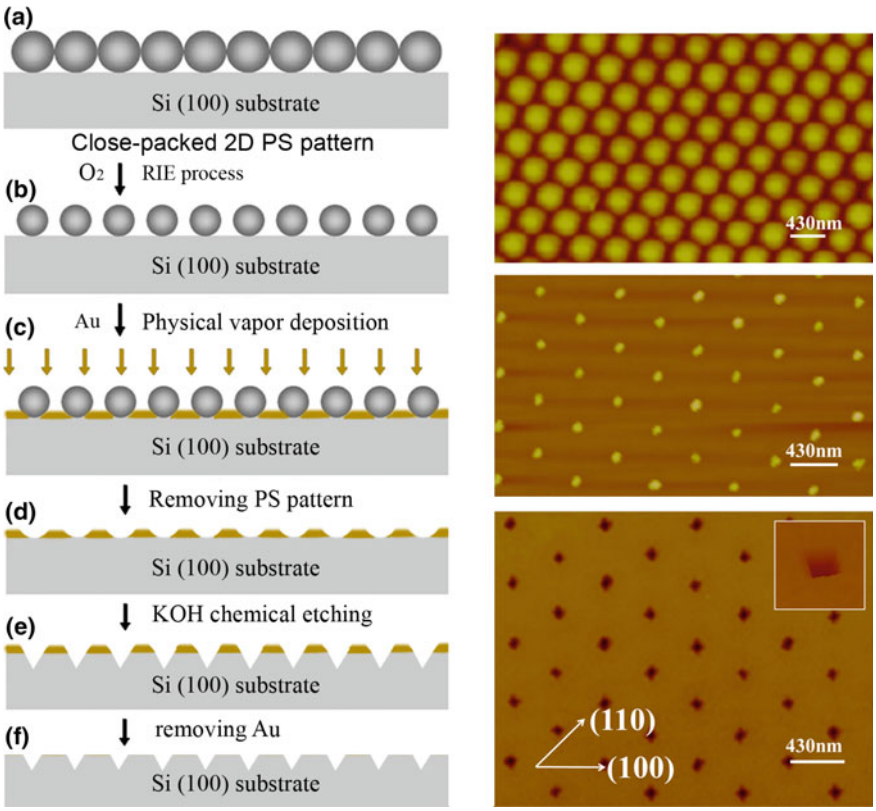

Fig. 7.13 Schematic illustration for the fabrication of ordered pit-pattern. **a** Closed-packed PS single ML pattern. **b** PS pattern after O_2 RIE. **c** Au film deposition. **d** Removing PS pattern in THF. **e** KOH selective etching. **f** Inverted pyramid-like pits pattern with {111} facets after Au has been removed. The panels at the right side show the AFM images at corresponding stages [57]

polystyrene spheres are removed from the substrate by immersing in tetrahydrofuran under ultrasonic treatment.

4. After formation of the mask, ordered inverted pyramid-like pits with {111} facets are created by etching the substrate in KOH solution. The substrate is immersed in KI: I_2: H_2O (4:1:40) solution for 10 h to remove the Au and Au–Si alloy mask and then cleaned and passivated.

The sample structure of ordered quantum rings is illustrated in Fig. 7.14. The growth recipe for GeSi quantum rings is as follows. First, the substrate is thermally treated at 860 °C for 3 min. Buffer layer of 130 nm thick Si is deposited while the substrate temperature is increasing from 400 to 500 °C. A quantum dot layer is grown by a two-step deposition of Ge; the first 5 ML Ge are deposited when growth temperature increases from 500 to 640 °C while the subsequent 7 ML Ge are deposited at 640 °C. After the formation of the first quantum dot layer, the substrate

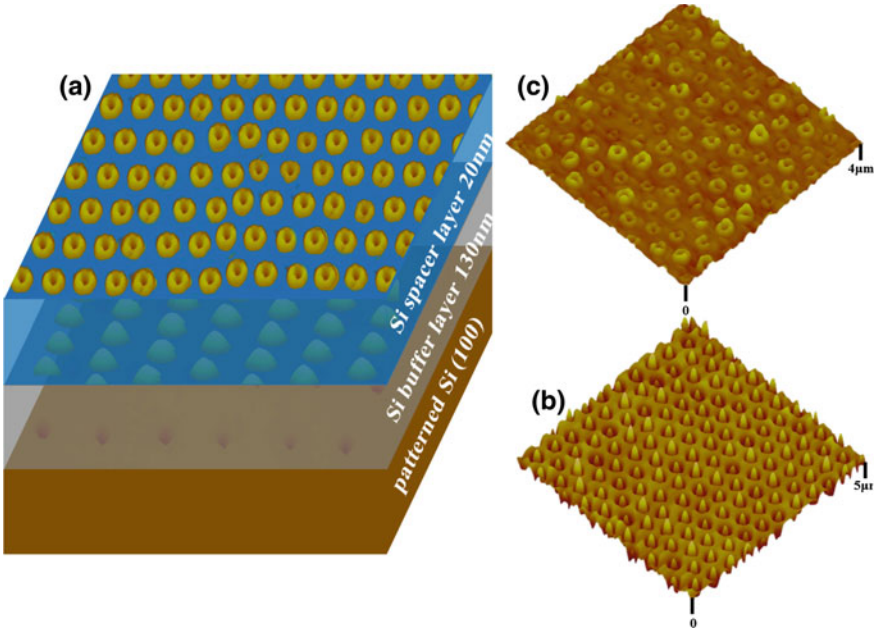

Fig. 7.14 **a** Schematic sample structure. AFM images of **b** ordered GeSi QDs and **c** ordered GeSi nanorings. After [57]

temperature is ramped down to 500 °C again and then the substrate temperature is immediately ramped back to 640 °C while a 20 nm thick Si spacer is grown. A second layer of GeSi quantum dots is formed by depositing 8 ML Ge at 640 °C. Sequentially, a thin Si capping layer is deposited over the GeSi quantum dots to transform the ordered GeSi quantum dots into ordered GeSi nanorings. Figure 7.14 also shows the quantum dots formed in the first layer and quantum rings formed in the second layer.

As discussed in the previous section, the distance between adjacent nanopatterns plays a critical role in fabrication of an ordered nanostructure array.

When the distance is small, e.g. 200 nm, the Ge adatoms also accumulate between adjacent pits in addition to assembling in the pits. In such a case, dot-to-ring transformation is hardly attainable. Using polystyrene spheres as large as 430 nm, the quantum dots are mainly formed in the pits. However, reactive ion etching is required to shrink the size of the nanospheres in order to reduce the size of the nanopits. If the size of the pits is much larger than that of the quantum dots, multiple quantum dots tend to nucleate in a single pit.

The AFM images of the GeSi nanostructure samples capped with Si thin films of different thickness are shown in Fig. 7.14. A thin Si capping layer (<2 nm) only results in dots with shallow dips in the center or a small portion of converted rings. When

the Si capping layer thickness is over 3 nm, most quantum dots can be converted into quantum rings.

The surface morphology of nanostructures after the capping process also varies at different capping temperature. When a thin Si capping layer is deposited at 610 °C, the mean lateral size of transformed nanorings is 175 nm. The value decreases to 165 nm when the capping layer is deposited at 640 °C. The standard deviation of lateral size also decreases from 24.3 (capping at 610 °C) to 21.8 nm (capping at 640 °C). After annealing the sample with 2 nm Si capping layer at 610 °C for 30 min, it has been shown that a part of the quantum dots is converted into quantum rings. However, other quantum dots disappear due to mass migration at long-term annealing. Under a further increase of the annealing time to 60 min, the effects involving mass migration and intermixing cause formation of superdomes and no quantum rings remain visible anymore. High growth temperature and long-term annealing can significantly modify the surface morphology.

7.5 Perspectives and Future Work

For optoelectronic and electronic devices, both the well control in the quantum ring shape and uniformity and the precise positing of quantum rings play a critical role in optimizing the device performance. In addition, investigation of the physical properties has been focused on a single quantum ring. New collective behavior may be revealed from coupled quantum ring arrays. Therefore, fabrication of laterally and vertically ordered quantum ring arrays opens the opportunities for investigations of new physics and device applications. The major research efforts on quantum rings can be directed towards developing large scale well-ordered quantum ring arrays and their applications.

First, additional fabrication techniques, such as “interference lithography”, can be explored for fabricating of ordered quantum ring arrays in addition to self-assembly and pre-patterning overgrowth. For example, wafer-scale metallic nanoring array has been obtained by using “interference lithography” [58, 59]. Ordered arrays of Au, Ni, and Si nanorings have also demonstrated by using a porous alumina mask. Improvements in the array periodicity, the control over quantum ring size and shape, and the control over array pattern will be the key factors in future efforts for fabrication of ordered arrays of quantum rings.

Second, it is interesting to study the collective effects of ordered quantum ring arrays. The ordered nanostructure array is considered to show an interesting “atomic states” analogy to atoms in a periodic lattice. Moreover, quantum rings show distinct properties, such as persistent currents, which cannot be found in other systems. The experimental investigation in ordered quantum ring arrays may reveal further new phenomena.

Finally, ordered quantum ring arrays also open wide possibilities for functional devices, such as quantum computing and optoelectronic devices. Quantum rings possess unique optical properties which can be employed for novel photodetectors

and lasers. For example, the shallow bound-state energy levels of the quantum rings can be employed to detect photons in the terahertz regime [60]. Polarization sensitive photoconductivity could be realized in quantum ring based photodetectors as a result of the unique morphology of quantum rings. Moreover, Aharonov-Bohm and unique magnetic-optical effects have been found in nano-rings [61, 62]. Quantum rings also have high stability of spin states and spin-dependent transport properties [63, 64]. One-qubit spintronic quantum gates has been fabricated using quantum rings, and thus, being assisted by resonant tunneling transport and spin-orbit interaction, quantum information processing can be achieved [65]. The development of ordered quantum ring arrays may assist in realizing semiconductor-based quantum computing devices.

References

1. R. Leturcq, L. Schmid, K. Ensslin, Y. Meir, D.C. Driscoll, A.C. Gossard, Phys. Rev. Lett. **95**, 126603 (2005)
2. A. Fuhrer, S. Luscher, T. Ihn, T. Heinzel, K. Ensslin, W. Wegscheider, M. Bichler, Nature **413**, 822 (2001)
3. V.M. Fomin, V.N. Gladilin, J.T. Devreese, N.A.J.M. Kleemans, P.M. Koenraad, Phys. Rev. B **77**, 205326 (2008)
4. M. Zarenia, J.M. Pereira, F.M. Peeters, G.A. Farias, Nano Lett. **9**, 4088 (2009)
5. A.J.M. Giesbers, U. Zeitler, M.I. Katsnelson, D. Reuter, A.D. Wieck, G. Biasiol, L. Sorba, J.C. Maan, Nat. Phys. **6**, 173 (2010)
6. W. Chang, C. Lin, Y. Fu, T. Lin, H. Lin, S. Cheng, S. Lin, C. Lee, Nanoscale Res. Lett. **5**, 680 (2010)
7. A. Lorke, R. Johannes Luyken, A.O. Govorov, J.P. Kotthaus, J.M. Garcia, P.M. Petroff, Phys. Rev. Lett. **84**, 2223 (2000)
8. N.A.J.M. Kleemans, I. Bominaar-Silkens, V.M. Fomin et al., Phys. Rev. Lett. **99**, 146808 (2007)
9. A.O. Govorov, S.E. Ulloa, K. Karrai, R.J. Warburton, Phys. Rev. B **66**, 081309 (2002)
10. I.R. Sellers, V.R. Whiteside, I.L. Kuskovsky, A.O. Govorov, B.D. McCombe, Phys. Rev. Lett. **100**, 136405 (2008)
11. M.D. Teodoro, V.L. Campo, V. Lopez-Richard et al., Phys. Rev. Lett. **104**, 086401 (2010)
12. S. Bhowmick, G. Huang, W. Guo, C.S. Lee, P. Bhattacharya, G. Ariyawansa, A.G.U. Perera, Appl. Phys. Lett. **96**, 231103 (2010)
13. J. Wu, Z. Li, D. Shao, M.O. Manasreh, V.P. Kunets, Z.M. Wang, G.J. Salamo, B.D. Weaver, Appl. Phys. Lett. **94**, 171102 (2009)
14. Z.C. Wen, H.X. Wei, X.F. Han, Appl. Phys. Lett. **91**, 122511 (2007)
15. T. Mano, T. Kuroda, K. Mitsuishi, M. Yamagiwa, X. Guo, K. Furuya, K. Sakoda, N. Koguchi, J. Cryst. Growth **301–302**, 740 (2007)
16. Y.S. Jung, W. Jung, C.A. Ross, Nano Lett. **8**, 2975 (2008)
17. C. Somaschini, S. Bietti, N. Koguchi, S. Sanguinetti, Nano Lett. **9**, 3419 (2009)
18. D. Granados, J.M. Garcia, Appl. Phys. Lett. **82**, 2401 (2003)
19. A.Z. Li, Z.M. Wang, J. Wu, G.J. Salamo, Nano Res. **3**, 490 (2010)
20. P. Martyniuk, A. Rogalski, in *Proceedings of SPIE*, (2008), p. 694004
21. Q. Shao, A.A. Balandin, A.I. Fedoseyev, M. Turowski, Appl. Phys. Lett. **91**, 163503 (2007)
22. Y. Chang, S. Jian, J. Juang, Nanoscale Res. Lett. **5**, 1456 (2010)
23. Z.M. Wang, S. Seydmohamadi, J.H. Lee, G.J. Salamo, Appl. Phys. Lett. **85**, 5031 (2004)
24. Q. Wei, J. Lian, W. Lu, L. Wang, Phys. Rev. Lett. **100**, 076103 (2008)
25. C.M. Müller, F.C.F. Mornaghini, R. Spolenak, Nanotechnology **19**, 485306 (2008)

26. J.L. Baker, A. Widmer-Cooper, M.F. Toney, P.L. Geissler, A.P. Alivisatos, Nano Lett. **10**, 195 (2010)
27. Z. Huang, T. Shimizu, S. Senz, Z. Zhang, X. Zhang, W. Lee, N. Geyer, U. GoÌˆsele, Nano Lett. **9**, 2519 (2009)
28. S. Lee, C. Mao, C.E. Flynn, A.M. Belcher, Science **296**, 892 (2002)
29. Z. Fan, J.C. Ho, Z.A. Jacobson, R. Yerushalmi, R.L. Alley, H. Razavi, A. Javey, Nano Lett. **8**, 20 (2008)
30. M. Junkin, J. Watson, J.P.V. Geest, P.K. Wong, Adv. Mater. **21**, 1247 (2009)
31. J. Tersoff, C. Teichert, M.G. Lagally, Phys. Rev. Lett. **76**, 1675 (1996)
32. H. Wen, Z.M. Wang, G.J. Salamo, Appl. Phys. Lett. **84**, 1756 (2004)
33. Z.M. Wang, K. Holmes, Y.I. Mazur, G.J. Salamo, Appl. Phys. Lett. **84**, 1931 (2004)
34. Z.M. Wang, G.J. Salamo, Phys. Rev. B **67**, 125324 (2003)
35. R. Blossey, A. Lorke, Phys. Rev. E **65**, 021603 (2002)
36. J. Wu, Z. Wang, K. Holmes, E. Marega, Y. Mazur, G. Salamo, in *Ordered Quantum-Ring Chains Grown on a Quantum-Dot Superlattice Template*, vol 14 (Springer, Netherlands, 2012), p. 1
37. Z.M. Wang, H. Churchill, C.E. George, G.J. Salamo, J. Appl. Phys. **96**, 6908 (2004)
38. H. Lan, Y. Ding, Nano Today (2012)
39. L. Hrivnák, Czech J. Phys. **34**, 436 (1984)
40. J. Wu, Z.M. Wang, K. Holmes, E.M. Jr., Z. Zhou, H. Li, Y.I. Mazur, G.J. Salamo, Appl. Phys. Lett. **100**, 203117 (2012)
41. B.L. Liang, Z.M. Wang, K.A. Sablon, Y.I. Mazur, G.J. Salamo, Nanoscale Res. Lett. **2**, 609–613 (2007)
42. Z.M. Wang, V.R. Yazdanpanah, C.L. Workman, W.Q. Ma, J.L. Shultz, G.J. Salamo, Phys. Rev. B **66**, 193313 (2002)
43. Z. Li, J. Wu, Z. Wang, D. Fan, A. Guo, S. Li, S. Yu, O. Manasreh, G. Salamo, Nanoscale Res. Lett. **5**, 1079 (2010)
44. M. Henini, S. Sanguinetti, L. Brusaferri, E. Grilli, M. Guzzi, M.D. Upward, P. Moriarty, P.H. Beton, Microelectron. J. **28**, 933–938 (1997)
45. M. Schmidbauer, S. Seydmohamadi, D. Grigoriev, Z.M. Wang, Y.I. Mazur, P. Schäfer, M. Hanke, R. Köhler, G.J. Salamo, Phys. Rev. Lett. **96**, 066108 (2006)
46. G. Springholz, M. Pinczolits, V. Holy, S. Zerlauth, I. Vavra, G. Bauer, Physica E **9**, 149 (2001)
47. R. Stockill, C. Le Gall, C. Matthiesen, L. Huthmacher, E. Clarke, M. Hugues, M. Atatüre, Nat. Commun. **7** (2016)
48. X. Li, J. Wu, Z.M. Wang, B. Liang, J. Lee, E. Kim, G.J. Salamo, Nanoscale **6**, 2675 (2014)
49. J. Wu, Y. Hirono, X. Li, Z.M. Wang, J. Lee, M. Benamara, S. Luo, Y.I. Mazur, E.S. Kim, G.J. Salamo, Adv. Func. Mater. **24**, 530 (2014)
50. M. Elborg, T. Noda, T. Mano, T. Kuroda, Y. Yao, Y. Sakuma, K. Sakoda, J. Cryst. Growth (2017)
51. E.M. Sala, M. Bollani, S. Bietti, A. Fedorov, L. Esposito, S. Sanguinetti, J. Vac. Sci. Technol. B Nanotechnol. Microelectron. Mater. Process. Meas. Phenom. **32**, 061206 (2014)
52. M. Bollani, S. Bietti, C. Frigeri, D. Chrastina, K. Reyes, P. Smereka, J. Millunchick, G. Vanacore, M. Burghammer, A. Tagliaferri, Nanotechnology **25**, 205301 (2014)
53. X.L. Li, G.W. Yang, J. Appl. Phys. **105**, 103507 (2009)
54. H. Brune, M. Giovannini, K. Bromann, K. Kern, Nature **394**, 451 (1998)
55. R. Li, P. Dapkus, M.E. Thompson, W. Jeong, C. Harrison, P. Chaikin, R. Register, D. Adamson, Appl. Phys. Lett. **76**, 1689 (2000)
56. P. Liu, Y.W. Zhang, C. Lu, Appl. Phys. Lett. **90**, 071905 (2007)
57. Y. Ma, J. Cui, Y. Fan, Z. Zhong, Z. Jiang, in *Ordered GeSi Nanorings Grown on Patterned Si (001) Substrates*, vol 6 (Springer, New York, 2011), p. 1
58. R. Ji, W. Lee, R. Scholz, U. Gösele, K. Nielsch, Adv. Mater. **18**, 2593 (2006)
59. K.L. Hobbs, P.R. Larson, G.D. Lian, J.C. Keay, M.B. Johnson, Nano Lett. **4**, 167 (2004)
60. H. Ling, S. Wang, C. Lee, M. Lo, J. Appl. Phys. **105**, 034504 (2009)
61. I.R. Sellers, A.O. Govorov, B.D. McCombe, J Nanoelectron Optoe (2011)

62. A.O. Govorov, A.V. Kalameitsev, R. Warburton, K. Karrai, S.E. Ulloa, Physica E **13**, 297 (2002)
63. E. Zipper, M. Kurpas, J. Sadowski, M.M. Maska, J. Phys.: Condens. Matter **23**, 115302 (2011)
64. R. Citro, F. Romeo, Phys. Revi. B **75**, 073306 (2007)
65. S. Bellucci, P. Onorato, Phys. Revi. B **78**, 235312 (2008)

Chapter 8
Self-assembled Semiconductor Quantum Ring Complexes by Droplet Epitaxy: Growth and Physical Properties

Stefano Sanguinetti, Takaaki Mano and Takashi Kuroda

Abstract Extremely complex semiconductor quantum ring based structures, as single ring, multiple concentric quantum rings and coupled ring-disk, dot-ring and dot-disk structures, can be easily designed and grown by Droplet Epitaxy. In this paper, the fabrication and the characterization of such complex quantum nanostructures are reviewed. Electronic structure, single photon emission, carrier dynamics and magnetic properties in ring structures will be discussed.

8.1 Introduction

Ring geometries have fascinated the physics community, as electron confinement in nanometric rings induces a topological quantum mechanical coherence, the Ahronov-Bohm effect [1]. Since the exciton has a non zero orbital magnetic moment, exciton Ahronov-Bohm effect has been predicted as well [2]. It is also possible to fabricate semiconductor quantum ring molecules, made by concentric quantum ring structures: these structures could permit to explore the magneto-optical excitations due to the Rashba spin orbit interaction [3]. Magnetic field level dispersion in quantum ring is different from quantum dots and useful: the ground state total angular momentum changes from zero to non zero by applying a magnetic field [4, 5]. This also produces a different energy dispersion of the excitons depending on ring radius. Moreover, charge tunneling between states of different angular momentum is strongly suppressed in concentric quantum ring by selection rules. Therefore,

S. Sanguinetti (✉)
LNESS and Dipartimento di Scienza dei Materiali,
Universitá di Milano Bicocca, Via Cozzi 53, 20125 Milan, Italy
e-mail: stefano.sanguinetti@unimib.it

T. Mano · T. Kuroda
National Institute for Materials Science, 1-2-1 Sengen,
Tsukuba 305-0047, Japan
e-mail: Mano.Takaaki@nims.go.jp

T. Kuroda
e-mail: Kuroda.Takashi@nims.go.jp

V.M. Fomin (ed.), *Physics of Quantum Rings*, NanoScience and Technology,
https://doi.org/10.1007/978-3-319-95159-1_8

concentric quantum ring are very relevant in the research on semiconductor-based quantum computational devices because they offer the control of effective coupling of direct–indirect excitons [6]: this could be a promising way to fabricate multiple two level states devices with switchable interaction. The possibility to fill the ring with few electrons allowed to detect the Ahronov-Bohm effect through the magnetic oscillation in the persistent current carried by the single electron states [7].

Recently, the possibility to investigate nanostructures with cylindrical symmetry (quantum disks or quantum ring) by twisted light has opened novel scenarios. Twisted light is light carrying orbital angular momentum and it has attracted a lot of attention from researchers in the last two decades because of its interesting fundamental properties and applications. Since the pioneering work of Allen et al. in 1992 on twisted light [8], the proposed applications of twisted light covered different areas such as the interaction with mesoscopic particles (optical tweezers) [9], the interaction with atoms and molecules [10], the interaction with Bose-Einstein condensates [11], observational astronomy [12] and finally, since the discrete nature of the orbital angular momentum, encoding of information for quantum communications [13, 14]. In semiconductor nanostructures the use of twisted light would allow to select precisely the electronic level one wishes to populate using the appropriate combination of light-beam parameters.

Two different Molecular Beam Epitaxy (MBE) growth methods can be used to self-assemble compound semiconductor quantum rings. The first one is based on the Stranki-Krastanov (SK) growth of InAs/GaAs, InAs/InP or GaSb/GaAs(001) nano-islands; a partial GaAs capping and a subsequent high temperature annealing produce a significant mass transfer between the center and the edge of the island [15–18] thus producing a ring shaped nanostructure. Due to the high complexity of the phenomena, this method offers only a limited degree of freedom for the design of the nanostructure. This rules out a precise on demand control of size and shape of the quantum ring, and thus of their electronic properties. Moreover, strain in the ring structures possibly brake the rotational symmetry of the electronic structures in these lattice-mismatched systems.

An alternative fabrication method is based on Droplet Epitaxy (DE) [19]. DE is a flexible growth technique which allows for the fabrication of quantum dots with governable size and density in strain free materials [20–22]. Furthermore, a designable wetting layer [23] avoids well know issues in SK dots [24–29], and the method has been demonstrated on many growth surface, including (311)A [30] and (111)A [31]. In addition, DE allows to obtain a large variety of three dimensional nanostructures with different geometries, ranging from rings to complex dot configurations [32–38]. This intrinsic design flexibility is due mainly to the splitting, in time, of the III-column and V-column element supply, with an independent choice, for each of the two elements, of the best growth conditions. DE allows the fabrication of rings from strained [39–45] or unstrained heterostructure, with single and multiple concentric quantum ring geometries [32, 33, 46] as well as more exotic dot/ring structures [47].

In this review we will summarize the main results about growth design of DE ring shaped nanostructures, theoretical study of their electronic properties and experimental characterization of DE-quantum rings.

The review is organized as follows. Section 8.2 describes the fabrication of quantum rings with different shapes by DE, Sect. 8.3 is dedicated to the electronic structure of the DE-quantum rings. The photoluminescence properties of the DE rings are shown in Sect. 8.4 while in Sect. 8.5 carrier dynamics experimental results in DE-quantum rings are reported.

8.2 The Droplet Epitaxy

Droplet Epitaxy (DE), an MBE based growth technique for the fabrication of three-dimensional quantum nanostructures [19], has demonstrated an unmatched ability to assemble quantum ring semiconductor nanostructures with complex geometries. Nanostructures morphologies range from single rings (single ring) [33], concentric double (double ring) [32], concentric triple rings [46], ring-disks [48] dot-rings [47] and dot-disks [49]. DE exploits the sequential supply of group-III and group-V elements, unlike standard MBE growth, where the elements are simultaneously supplied to the substrate. In DE growth of GaAs, first Ga irradiation in absence of As leads to the formation of nanometric droplets with homogeneous size then an As flux is supplied for the crystallization of the metallic Ga droplets into GaAs quantum nanostructures. A proper choice of the growth conditions allows to obtain different morphologies of the GaAs quantum nanostructures. Figure 8.1 clarifies, in a qualitative way, the effect of the growth conditions on the obtained nanostructures and shows how DE gives a large freedom in the shape design.

The authors present a systematic study on the formation of GaAs/AlGaAs quantum nanostructures: starting from an identical set of Ga droplets, crystallization is performed at different substrate temperatures and As fluxes. As clearly shown, the conditions for the crystallization are crucial for the shape control of the GaAs quantum nanostructures. Indeed, in the case of lower As flux or higher temperatures, it was not possible to obtain 3D island growth, because of the annihilation of droplets. The position occupied by the droplets before As crystallization is marked by a shallow holes surrounded by a tiny ring. The presence of avoided growth below the Ga droplet has been attributed to the preferential As crystallization in the droplet at the triple point [46]. Additional effects related to Ga etching may be possible [50], although strongly quenched by the low growth temperature. By irradiation with a higher As flux, 3D dimensional growth occurs, as a result of incorporation of arsenic atoms inside the Ga droplet, thus giving rise to GaAs nanocrystals with dome (Fig. 8.1d) and ring (Fig. 8.1c) shapes.

DE therefore enables the fabrication of 3D nanostructures with shapes ranging from dots to rings. Mano et al. [32] reported a wide sampling of the growth conditions space and demonstrated, for the first time, the self-assembly of GaAs/AlGaAs double rings. No other techniques are available for the fabrication of such complex semiconductor ring structures. Recent advances in DE permit an even larger degree

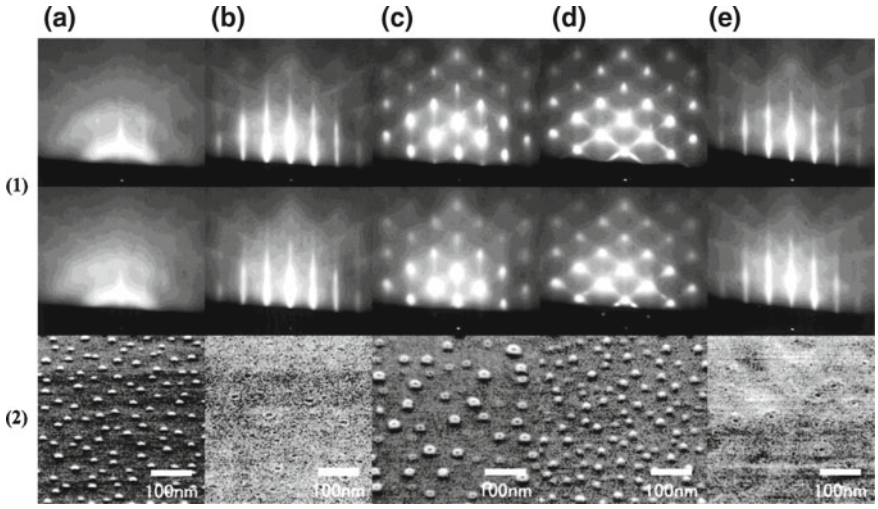

Fig. 8.1 (1) and (2) are the RHEED patterns and surface morphologies (Scanning Electron Microscopy) of the samples at each stage of the growth process, respectively. In (1), upper column: the electron beam along [110]; lower column: the electron beam along [1$\bar{1}$0]. **a** is after the Ga deposition at 200 °C. **b**–**e** are after subsequent As_4 molecular-beam irradiation with 4×10^{-7} Torr at 200 °C, 4×10^{-5} Torr at 200 °C, 4×10^{-5} Torr at 150 °C and 4×10^{-7} Torr at 150 °C, respectively. Reprinted from [20], Copyright (2000), with permission from Japanese Applied Physical Society)

of freedom in the design of the nanostructures, allowing the assembly of multi-ring and ring structures coupled with dot and disks [46–49].

A conventional MBE apparatus is used for the fabrication by DE of all the GaAs/AlGaAs ring structures. For the precise and abrupt control of As flux intensities, a valved cell is highly required for the supply of As flux. After the growth an $Al_{0.3}Ga_{0.7}As$ barrier layer, the substrate temperature is reduced to a range between 200 and 350 °C, depending on requirements of the size and density of the nanostructures [20, 22], the As valve is closed and the As pressure in the growth chamber depleted. When pressure is low enough, only cation (Ga) atoms are supplied. In the experiment here reported, As_4 was used. In absence of As, Ga atoms are incorporated into the As terminated surface, resulting in the transition to a Ga stabilized reconstruction [51]. Subsequent Ga deposition gives rise to the formation of tiny Ga droplets on the surface. Density and size of the Ga droplets depends on substrate temperature and total amount of Ga supplied. Since Ga diffusion on the Ga terminate substrate is a temperature activated process, the higher the temperature the smaller droplets density. Note that the size and density of the droplets can be controlled within wide range independently, which is highly advantageous. This step sets the initial condition from which the DE-rings will be fabricated. During As supply, metallic Ga droplets act as nanometer scale local reservoirs of group III material.

8.2.1 Fabrication of Ring Structures

In order to get single ring and double ring structures, after the deposition of the droplets, the substrate temperature was set around 200 °C. Rings formation can be obtain by the irradiation of an As_4 molecular beam with a fluxes of $\approx 0.8-1 \times 10^{-5}$ Torr beam equivalent pressure (BEP) for single ring [52] and $\approx 0.5-2 \times 10^{-6}$ Torr BEP for double ring [32]. In this growth step, Ga contained in the droplets fully crystallizes in form of GaAs rings. Real-time process observation is possible through reflection high-energy electron diffraction (RHEED): the complete change of the pattern from halo to spots corresponds to the crystallization of the Ga contained in the droplets. After crystallization, an annealing of 10 min at 350 °C at constant As flux was performed. While the annealing step does not cause significant morphological change of the ring structures, this last step ensured the complete crystallization of the metallic Ga reservoirs on the surface and enable to grow capping layer at more than 300 °C, which is essentially important to obtain optically active quantum rings. [53, 54]

Figure 8.2 shows AFM images of a single nanostructure of the uncapped single ring and double ring samples. Well defined, not topologically connected, rings are clearly visible. The latter characteristic is peculiar only of DE-quantum rings.

Coupled structures, as a nanometer-high holed flat disk with a diameter of hundreds of nanometers on which a ring structure lays down, can also be grown by DE. These coupled ring/disk nanostructures show how it is possible to obtain localized states with different dimensionality and tunable coupling in a designable structure [48, 55].

Ring/disks growth was performed in close resemblance of the single ring and double ring procedure. After supplying 10 MLs of Ga on the substrate, the formation of nearly hemispherical Ga droplets occurred. Straight afterward, an As flux in the range 8×10^{-7} to 8×10^{-6} Torr was irradiated on the substrate at the constant temperature of 350 °C for 20 min.

An AFM image of an uncapped sample is shown in Fig. 8.3. A well defined ring/disk is visible, made up of a disk with height of ≈6 nm and diameter of around 300 nm and an inner ring marked by a 10 nm high ridge and a diameter of around 80

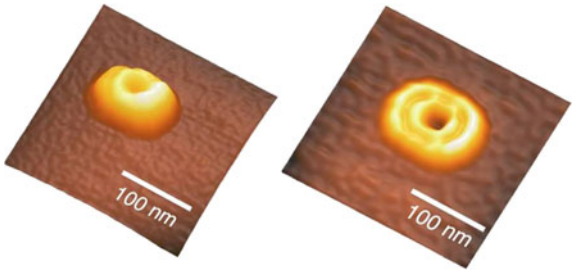

Fig. 8.2 Left panel: AFM image of a single ring. Right panel: AFM image of a single concentric ring (From Kuroda et al. [33])

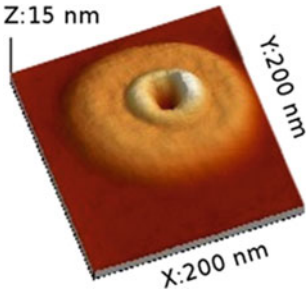

Fig. 8.3 AFM image of GaAs ring/disk crystallized under an As flux of 8×10^{-6} Torr (Reprinted from [48], Copyright (2010), with permission from Institute of Physics)

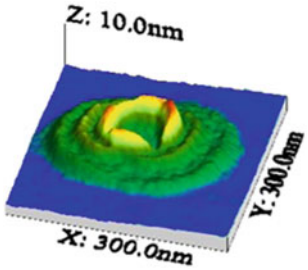

Fig. 8.4 AFM images of a typical triple ring. The crystallographic axis are parallel to the image border: $[1\bar{1}0]$ (horizontal on image) and [110] (vertical on image) (Reprinted from [46], Copyright (2009), with permission from American Chemical Society)

nm. A decrease of the As flux leads to the expansion of the disk and to its thinning, whereas the central hole diameter remains unaltered [48].

DE method can be extended to produce triple rings and multiple quantum rings. The key process for realize these complex nanostructures is the use of multiple short time As pulses at different substrate temperatures in order to partially crystallize the metallic Ga in the droplet [46]. The process to obtain GaAs/AlGaAs triple ring is as follows. After the growth of the AlGaAs barrier, substrate temperature was lowered to 350 °C and As valve was closed. At this temperature, the surface had an As-rich $c(4 \times 4)\beta$ surface reconstruction [56]. A subsequent three-step growth procedure was performed. Step 1 requires the supply of 10 MLs of Gallium at 350 °C in absence of As, step 2 corresponds to an As flux supply equal to 8×10^{-7} Torr at 250 °C for 20 s and step 3 consists of the supply of an As flux of the same intensity at 300 °C for 20 min (thus on until complete crystallization of the deposited Ga).

Figure 8.4 is the AFM image of the nanostructure fabricated by such three-steps growth DE procedure. Ga droplets evolved in well-defined GaAs triple rings structures with good rotational symmetry. Inner, middle and outer ring have diameters of around 80, 140 and 210 nm respectively and heights around 7 nm for the inner rings, 4 nm for middle rings and 3 nm for the outer rings. A slight elongation of $\approx$11% along the $[0\bar{1}1]$ direction can be observed, probably due to the anisotropic surface migration of Ga on the (100) GaAs surface [57]. As in the ring/disks, the inner ring diameter is nearly equal to that of the original Ga droplet. triple rings density matches that of the original droplets, confirming that also in this case all Ga droplets transforms into GaAs triple rings. More complex ring structures, obtained through a four step DE procedure, are reported in Fig. 8.5 [46].

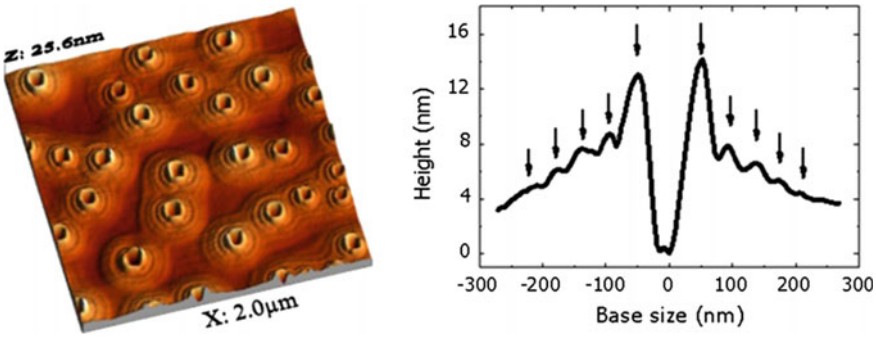

Fig. 8.5 Left panel: AFM images of a typical five-ring structures. Right panel: Line profile along the [0$\bar{1}$1] direction of a GaAs five-ring structure. Starting from the inner and moving to the outermost ring, the ring radii of the structures are around 50, 90, 130, 170, and 210 nm, while the heights are around 13, 8, 7, 5.5, and 4.5 nm, respectively (Reprinted from [46], Copyright (2009), with permission from American Chemical Society)

8.2.2 Growth Model

Growth dynamics of triple rings was investigated by stopping the process at different steps and morphological characterizing the samples via ex-situ AFM measurements. The quenching was just after: (i) droplet formation, (ii) the short time As supply; iii) the full crystallization of the droplet. Selective wet etching was used to remove metallic Ga on the surface [46]. AFM images and typical line profiles of the six samples are reported in Fig. 8.6. 10 MLs Ga were supplied at 350 °C (sample S1, Fig. 8.6a) and numerous nearly hemispherical Gallium droplets were formed. Average diameter was around 80 nm, height around 35 nm and density around 8×10^8 cm^{-2}.

At first step, Ga etching allows to observe the presence of a GaAs ring structure just under the original droplet, due to the crystallization at the droplet's edge (Fig. 8.6b). The partial crystallization step, when the initial Ga droplets are irradiated with an Arsenic flux of 250 °C for 20 s, led to a structure formed by a central dome of unreacted Ga, with the same radius of the initial Ga droplet, surrounded by a shallow ring of ≈140 nm diameter (Fig. 8.6c). Ga etching shows the formation of a GaAs double ring structure, whose inner ring is lying just under the edge of the metallic Ga droplet (Fig. 8.6d). The third step, the final As supply at 300 °C for 20 min, completely crystallizes Ga atoms, forming the outermost third ring structure with a diameter of around 210 nm. Therefore, a complete GaAs triple ring structure was obtained (Fig. 8.6e–f).

A discussion of the phenomenology is now presented. The semiconductor quantum ring which were characterized exhibit three concentric rings. However, the rings do not share the same origin. The two crystallization steps in presence of an As flux form the two external rings, whereas the inner ring is formed during the Ga droplet formation, when no intentional As flux is supplied to the sample. The ring

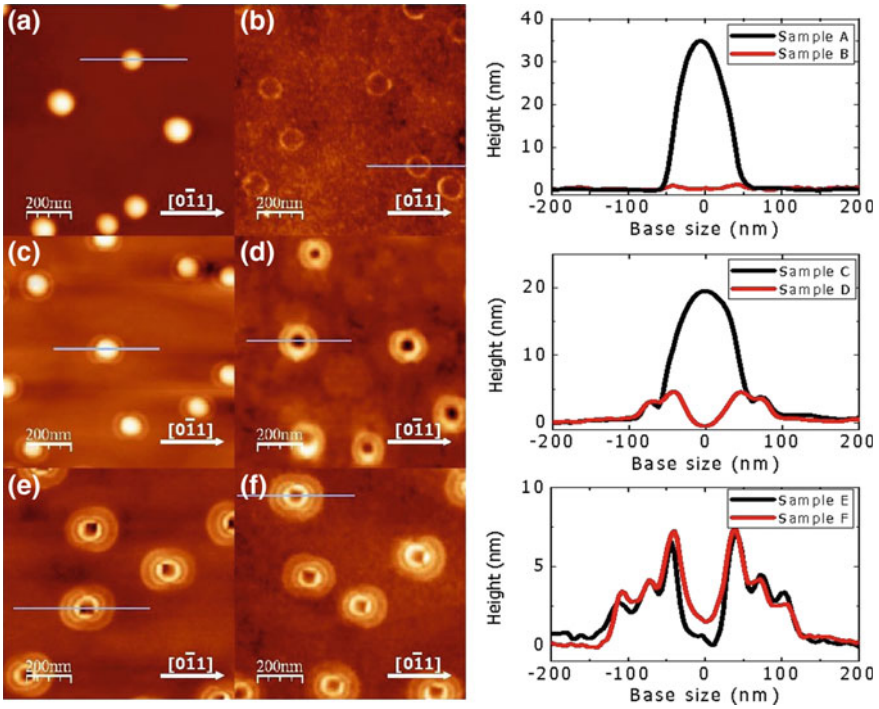

Fig. 8.6 AFM images of As-grown samples S1, S2, and S3 (left panels), etched samples S1–E, S2–E and S3–E (center panels) and corresponding line profiles taken along [0-11] direction (right panels), after 10 MLs Ga supply at 350 °C (top panels), after 8×10^{-7} Torr As supply at 250 °C for 20 s (middle panels) and after 8×10^{-7} Torr As supply at 300 °C for 20 min (bottom panels) (Reprinted from [46], Copyright (2009), with permission from American Chemical Society)

lies underneath the Ga droplet, at its edge, and is not altered by the subsequent steps of the fabrication process. The formation of the inner ring can be accounted for by an internal transport of As atoms incorporated at the droplet edge. Therefore, the inner ring might be due to the low solubility of As in the metallic Ga and of its accumulation on the GaAs tiny ring, found just after the droplet deposition, because of internal convection flux. The same diameter is thus preserved for all the growth conditions. It is worth noting that the inner ring shares the same origin of the inner ring in double rings, because its formation does not depend on the specific conditions used during the arsenization step [32]. Mano et al. [32] already showed clearly this behavior and pointed out that radius of single ring, inner ring in double ring and Ga metallic droplet are identical (see Fig. 8.7).

To the outer rings, which are formed during the arsenization steps, can be associated a different formation mechanism. In DE a reservoir of the III-column species (the droplet) resides permanently on the surface and the V-column species is supplied in form of distributed flux. Therefore the balance between the Ga migration from the droplet and As flux determines the growth of the GaAs nanostructure. Then,

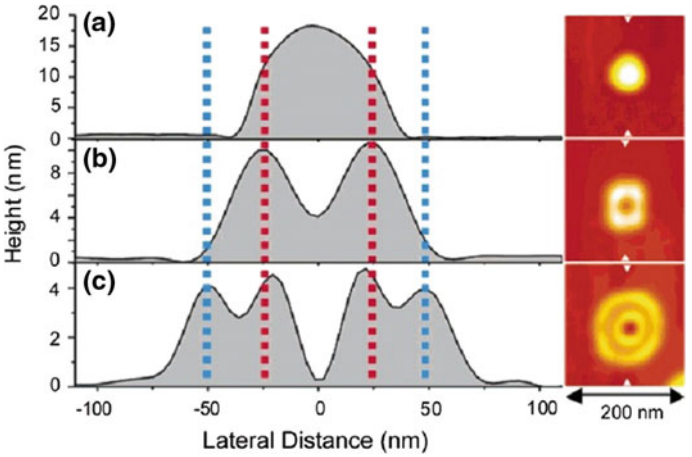

Fig. 8.7 AFM images of the As-grown droplet (upper panel), single ring (center panel) and double ring (bottom panel) nanostructures obtained from the same initial droplet configuration (Reprinted from [32], Copyright (2005), with permission from American Chemical Society)

following the changes in average surface reconstruction during the growth process is the utmost importance in order to understand such mechanism. These changes have been determined by [46], through the analysis of the RHEED pattern and of the RHEED specular beam intensity. During the deposition step, after 1.7 MLs supply of Ga molecular-beam Ga-rich (4× 6) surface reconstruction [58] appeared, while during As supply the surface changed from the Ga-rich limit (4 × 6) to As-stabilized (2 × 4) and finally to As-rich c(4 × 4).

The interplay between the As adsorption on the Ga-rich (4 × 6) surface and the Ga migration on the As-stabilized (2 × 4) is supposed to be the key point for the formation of quantum ring structures. Figure 8.8 shows a schematic diagram of the proposed mechanism. 10 MLs Ga are supplied: just after 1.7 MLs the c(4×4) reconstruction changes to a Ga-rich (4 × 6) surface and subsequently droplets are formed (Fig. 8.8a). As soon as Arsenic molecular beam is supplied, the substrate starts to change to an As-stabilized (2 × 4) surface reconstruction and nearly simultaneously some Ga atoms migrate and form a monolayer of GaAs around the droplet [59] (Fig. 8.8b). Because of the cylindrical symmetry of the diffusion dynamics, Ga atoms can cover a mean displacement area $\approx D\tau$ where D is the surface diffusion coefficient of Ga atoms and τ the average time interval between arrival and adsorption of As atoms at a specific site [60]. At the same time, far from the Ga droplets, the Arsenic adsorption on the surface not affected by Ga diffusion makes the reconstruction to change to c(4 × 4). The detailed model of ring formation by droplet epitaxy can be found in [61] where the role of As diffusion in the formation of the outer ring is highlighted.

It's worth noting that step 2 and step 3 starts from similar configurations, characterized by a reservoir of metallic Ga in the position of the droplet and a Ga-rich (4 × 6) surface reconstruction. The change in surface reconstruction from As-rich

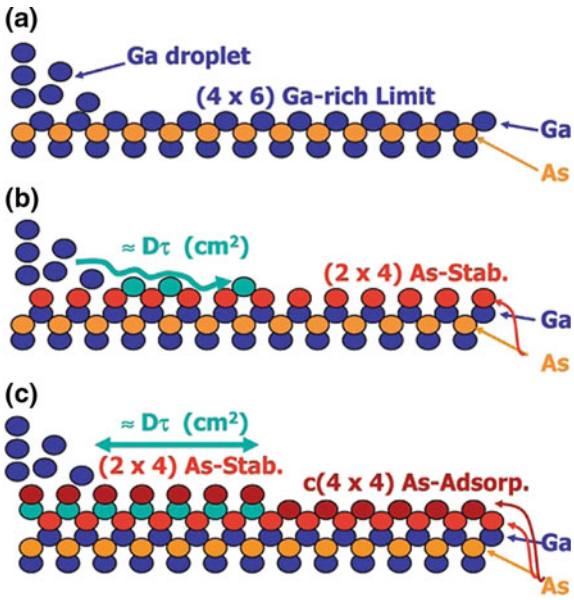

Fig. 8.8 Schematic explanation of the proposed growth mechanism for the formation of outer rings structures. Ga droplets are formed on a Ga-rich (4 × 6) surface reconstruction (**a**). During As supply a (2 × 4) surface reconstruction appears all over the substrate on the top of which the Ga atoms, coming from the droplets, can migrate covering a mean displacement area of $\approx D\tau$ (**b**). Far away from the droplet the surface turns to the As-rich c(4×4). The border of this area act as a pinning site for the migration of the Ga atoms (**c**). The detailed atomic arrangements for the different surface reconstructions are ignored for simplicity (Reprinted from [46], Copyright (2009), with permission from American Chemical Society)

to Ga-rich between step 2 and 3 might be due to a diffusion of Ga from the droplets on the As-rich surface, forming a 2D GaAs thin layer, in absence of an intentional As flux.

Also the formation dynamics of the double rings and ring/disks can be easily explained [32, 48] by this model. The double ring and ring/disk are realized via a two-step growth process: first a deposition of Ga into droplets in absence of As flux and then a step where As with moderate flux ($\approx 1 \times 10^{-7}$ Torr BEP) is irradiated on the sample at 250 °C until full crystallization is achieved. The inner ring has, like in our triple ring structure, the same radius of the initial droplet and therefore should be formed just after the droplet deposition [32]. The subsequent arsenization step is responsible of the formation of the outer ring.

It is important to point out that there is a significant difference, in the case of multi-step growth, between the amount of Ga atoms initially supplied (typically 10 ML in the case of triple rings) and the corresponding to the equivalent amount of Ga contained inside the final structure. This difference suggests that only a fraction of the initially supplied Ga atoms effectively concur to the formation of the 3D nanostructure, while the other part, estimated to be around 6–7 MLs, might be consumed

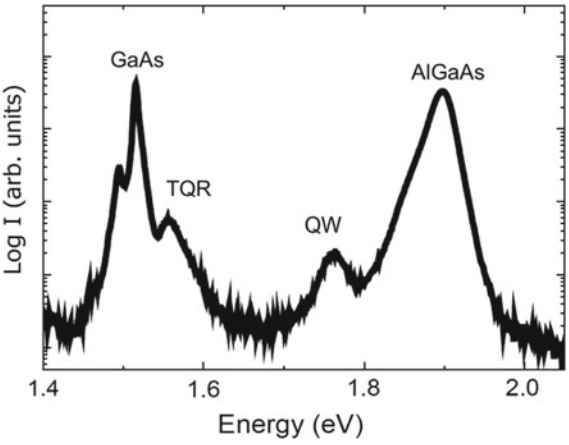

Fig. 8.9 Pholuminescence spectra of triple rings (TQR) recorded at 15 K. GaAs and $Al_{0.3}Ga_{0.7}As$ peaks appeared at 1.52 and 1.90 eV, respectively. Between them additional two features, attributed to triple rings (1.55 eV) and to a 7MLs QW (1.76 eV). Data from [62]

in another process. The reason of this discrepancy might be found considering the fabrication procedure for the formation of triple rings. As mentioned before, the three main steps of the growth are performed at different temperatures: 350 °C for the droplets formation, 250 °C for the first As supply and 300 °C for the second As supply. The change in substrate temperature requires growth interruption times of about one hour for each change. During this waiting time a portion of the Ga atoms stored in the droplets might be consumed to form a 2D GaAs thin layer all over the substrate. We believe this phenomenon to be caused by a slow 2D crystallization of Ga atoms diffusing from the droplets, even in absence of an intentional As supply. Indeed, an As background pressure of around 1×10^{-9} Torr is present during the whole procedure, thus providing an unintentional As pressure which promotes the partial crystallization of Ga atoms contained in the droplet during the growth interruptions. A slow GaAs crystallization all over the substrate might take place also in case of very low As pressure [48]. In these conditions of very low As flux, the surface mobility of Ga atoms is so large that an uniform layer of GaAs might be formed all over the substrate surface. In a capped sample, embedded in an $Al_{0.3}Ga_{0.7}As$ barrier, this layer can act as a quantum well, confining carriers and eventually being optically active. Photoluminescence investigation on capped triple ring substrates confirm this assumption (see Fig. 8.9) showing that in the region where the emission from quantum confined GaAs structures is expected, two peaks, corresponding to emission from the triple ring ensemble ($E_{\text{triplering}} = 1.55$ eV) and from the expected 6–7 MLs-thick GaAs QW ($E_{\text{QW}} = 1.76$ eV), originating from the GaAs layer formed during growth interruptions, are present.

8.2.3 Coupled Topologically Distinct Nanostructures

It possible to extend the concept of pulsed deposition of III and V column elements at controlled temperatures and fluxes, used in multiple rings fabrication, in order to combine rings with structures showing different topologies. In particular it is possible to combine quantum dots, rings and disks in a single nanostructure. Some examples of complex GaAs nanostructures grown on $Al_{0.3}Ga_{0.7}As$ buffer layers are reported in Fig. 8.10. The nanostructures are made by a dot or a ring at the center and an outer region made by a ring or a disk. The fabrication procedure is detailed in [32, 46–48]. When droplets with the required density and size are formed, the fabrication of nanostructures proceeds via the pulsed supply of predetermined As quantities at controlled fluxes and substrate temperatures. This allows for the fine control of the three phenomena, described in Sect. 8.2.2, that are occurring during the As supply: (i) the thermodynamically driven diffusion of Ga atoms from the droplets to form a two dimensional (2D) layer on the substrate; (ii) The incorporation of As in the liquid Ga at the droplet original position, thus developing a 3D nanocrystal; and (iii) the kinetic of the change in the surface reconstruction around the droplets from Ga-rich to As-rich, caused by the adsorption of As on the flat surface. The interplay between these phenomena sets the final configuration of the GaAs nanostructure, between the limit cases of a total lateral growth of GaAs around the droplet edges (strong Ga diffusion) and of a complete crystallization of Ga within the original droplets (very efficient As incorporation).

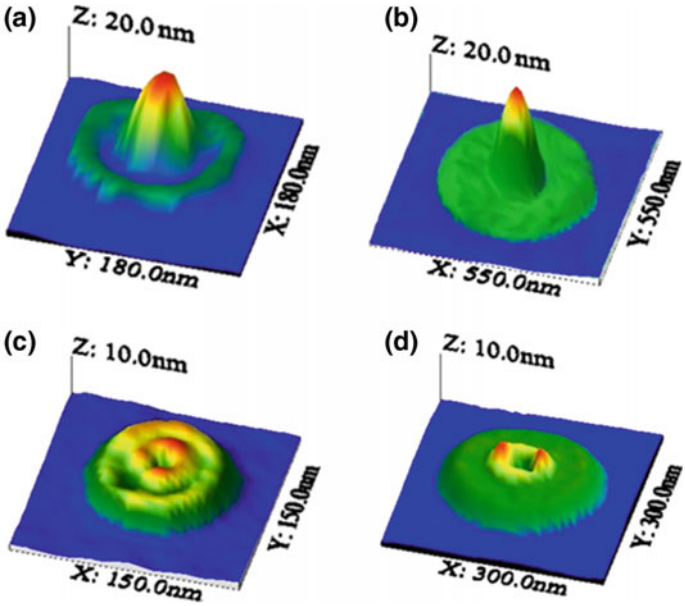

Fig. 8.10 Atomic force microscope (AFM) images of dot-ring (**a**), dot-disk (**b**), double ring (**c**) and ring-disk (**d**) GaAs/AlGaAs nanostructures. Data from [63]

Dots are indeed formed, from metallic Ga droplets, at low substrate temperature and high As flux, due to the incorporation of As in the liquid Ga, thus developing a three-dimensional crystal at the droplets original position [64, 65]. This is caused by the very low mobility of Ga in these conditions which freezes the atoms close to their initial positions. On the contrary GaAs rings could be fabricated outside of the original droplet exploiting the Ga diffusion during As supply at intermediate temperatures, around 300 °C [32]. Both the As flux intensity and the substrate temperature can be used to finely tune the diameter of outer portion of the structure [46, 48] due to the effects of Ga diffusion on the final morphology [66, 67]. In particular, higher substrate temperatures during the As irradiation, as well as lower As flux were found to increase the diameter of the nanostructure outer portion [46]. The quantum dot dimensions are instead determined by the original droplets ones, thus being fully controllable over a wide range. Therefore the shape and the size of the single nanostructures, which constitute the final complex nanostructure, are completely designable by governing the transformation kinetics of the Ga contained in the single droplet. With the large design flexibility intrinsic in the DE process, we can thus fabricate, by the pure self-assembly, nanostructures where is possible to couple, within a single structure, systems with different dimensionality (dot and rings), brought together in close spatial proximity.

The typical growth procedure for the fabrication of the dot-ring sample was followed step-by-step via ex-situ AFM characterization by Somaschini et al. [47] (see

Fig. 8.11). Just after the Ga deposition, nearly hemispherical droplets were formed (Fig. 8.11a). After the first pulse of As at 275 °C, a ring with a radius of 60 nm was clearly developed around the droplet (Fig. 8.11b) by transforming part of the Ga stored in the droplet. This step not only resulted in the formation of a well defined GaAs ring, but also left a certain amount of Ga in the original droplet, which still resided in its initial position, as shown by selective chemical etching [46]. Finally, the second, high intensity As supply at 150 °C formed the central quantum dot (Fig. 8.2c). Similarly, in the case of the dot-ring-ring sample the first and the second As pulses caused the formation of the two concentric rings, while the final As irradiation promoted the crystallization of the remaining Ga atoms into the central dot. Large area AFM scan of the samples (Fig. 8.12) clearly shows the stability of such growth procedure based on the control of the growth kinetics. In general, less than 10% of the fabricated structures showed morphological defects.

8.2.4 Ring Anisotropy

At high growth temperatures, where a (2×4) As rich surface reconstruction is expected to dominate [51], the well known anisotropy in the diffusion coefficient of Ga between the two [110] and [1$\bar{1}$0] directions [57] leads to GaAs nanostructures

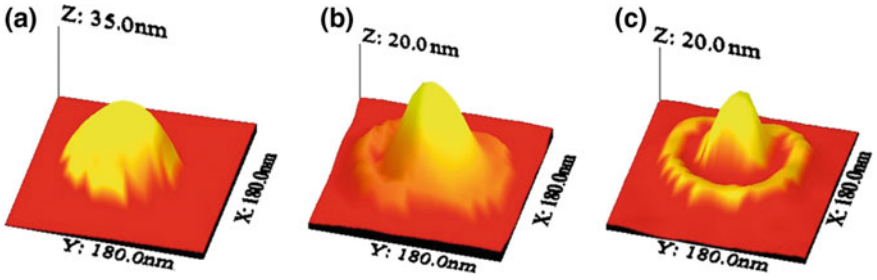

Fig. 8.11 Evolution of the dot-ring formation, followed step-by-step by AFM analysis of dedicated samples. Ga droplets just after the Ga deposition (**a**), formation of the GaAs outer ring after the first As supply, with unreacted Ga at the center (**b**), dot-ring formed after the second irradiation with As, Data from [47]

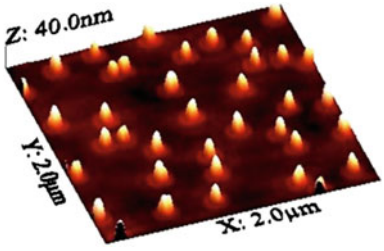

Fig. 8.12 Large area (2 μm × 2 μm) AFM image of a dot-ring sample. Data from [47]

with a shape anisotropy. In order to quantify this effect on the droplet ring shape, Somaschini et al. [68] realized a five-ring sample with As crystallization temperatures between 380 and 320 °C. The AFM image of the five-ring is shown in Fig. 8.13. As expected the anisotropy is clearly visible in the image. The Ga atoms migration from the original droplet perimeter during As adsorption as a function of temperature was characterized via the diffusion equivalent area $D\tau$. The results are shown in Fig. 8.13 for both [110] and [1$\bar{1}$0] directions. The exponential dependence of $D\tau$ on the temperature is confirmed in both cases. By the Arrhenius plot the values of 1.28 and 0.85 eV for the activation energy for the Ga migration along [110] and [1$\bar{1}$0] respectively were obtained. These values should not be considered as universal values since the Ga migration happens on a non perfectly flat GaAs (001) surface. In fact the surface of the outer ring shows a sub-nanometer surface roughness. Although the detailed mechanism is not yet clear, the roughness of the actual surface over which gallium atoms can migrate might in general affect their diffusion length.

8.3 Electronic Properties

8.3.1 Theoretical Predictions

The energy levels of the ring can be evaluated in the framework of a single-band effective-mass envelope model approximation (EMA) [69, 70]. Although being a simple method, compared to more complex pseudopotential and multiband k·p meth-

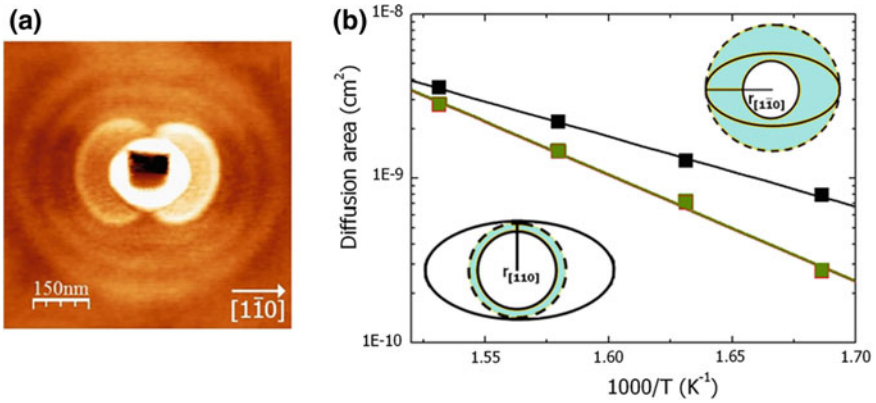

Fig. 8.13 **a** AFM image of a single GaAs five-ring structure fabricated in [62]. **b** Arrhenius plot of the diffusion area covered by Ga atoms during their migration from the Ga droplets as a function of the reverse temperature. In the insets: scheme of the procedure to calculate the diffusion area (blue zone delimited by the dashed line) for both [1$\bar{1}$0] (top panel) and [110] (bottom panel). Solid lines represent the inner ring and an outer ring with a marked anisotropy. Data from [68]

ods [71, 72], the model catches the relevant electronic characteristics of the droplet epitaxy quantum nanostructures. The actual shape measured by AFM is adopted as the potential of quantum confinement; for simplicity, the ring is assumed to hold a cylindrical symmetry, although, in most of the cases, a slight (within 15%) asymmetry is present. In DE *lattice-matched* GaAs/AlGaAs rings, strain effects are negligible. Thus the simple EMA is expected to provide accurate energy levels. In the case of SK grown dots, instead, the electronic structure is strongly modified by complex strain effects [73]. The reliability of the present method is seen in [22, 74], where good agreement is shown between the asymmetric photoluminescence (PL) lineshape in a GaAs/AlGaAs quantum dot ensemble and the calculation, which takes into account the morphological distribution of dots. Since DE rings are sufficiently small, confinement effects are dominant and Coulomb interaction can be treated as a constant shift in the transition energies, independent of the choice of an electron state and the hole state.

The expected eigenfunctions, taking into account the rotational symmetry of the Hamiltonian, are of form Φ_L, where $L(= 0, \pm 1, \ldots)$ is the azimuthal quantum number, is expanded in terms of a complete set of the base functions, $\xi^L_{i,j}$, formed by products of Bessel functions of integer order L and sine functions of z,

$$\Phi_L(z, r, \theta) = \sum_{i,j>0} A^L_{i,j} \xi^L_{i,j}(z, r, \theta), \tag{8.1}$$

$$\xi^L_{i,j}(z, r, \theta) = \beta^L_i J_L(k^L_i r) e^{iL\theta} \sin(K_j z), \tag{8.2}$$

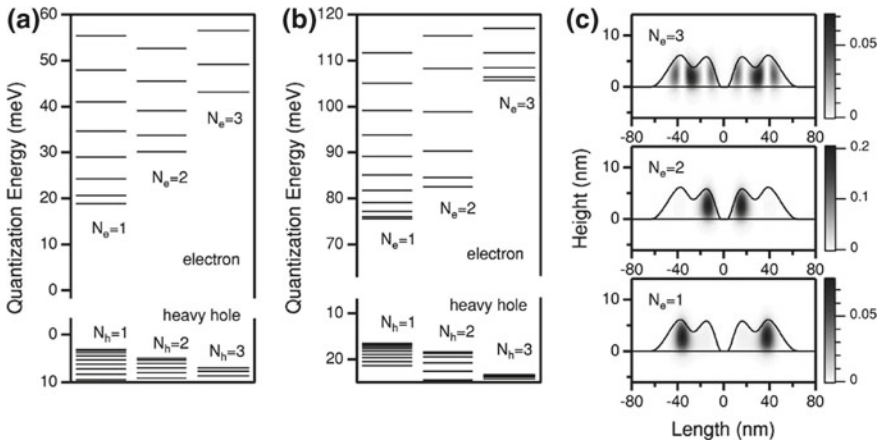

Fig. 8.14 Single-carrier energy levels in **a** quantum ring and **b** double ring. Quantization energies for an electron (a heavy hole) with the three lowest z-radial quantum numbers, $N_{e(h)}$ and various angular momenta (up to 10) are presented. **c** Cross-sectional imaging of electronic probability density in double ring for $N_e = 1, 2$, and 3 with $L = 0$. The line represents the potential of confinement used for calculation (Reprinted from [33])

where $k_i^L R_c$ is the i the zero of the Bessel function of integer order $J_L(x)$, $K_j = \pi j / Z_c$, and β_i^L is appropriate normalization factors [69].

Figure 8.14a shows a series of single carrier levels of single ring. Because the system has cylindrical symmetry, each carrier level is specified by the z-radial quantum number, $N(= 1, 2, \ldots)$, and an azimuthal quantum number L, corresponding to the angular momentum. The L-dependent sequence of quantized levels shows a typical signature of ring-type confinement. For an ideal ring with infinitesimal width, being treated as a one-dimensional system with translational periodicity, the level series is expressed as

$$E_L = \frac{\hbar^2}{2m^* R^2} L^2, \tag{8.3}$$

where R and m^* respectively represent the radius of the ring and the carrier mass. The line sequence in Fig. 8.14a reflects clearly the bilinear dependence of the level series, shown in (8.3). In addition, the L-dependent sequence is less crowded for larger N. According to (8.3), the situation corresponds to an increase in the effective value of R, implying a stretched orbital trajectory caused by in-plane centrifugal force.

Figure 8.14b shows the energy levels in double ring. Due to the smaller height, the quantization energies are larger than those of quantum ring. The level sequence of $N = 1$ is more densely populated than that of $N = 2$, suggesting a large difference in carrier trajectories between the two levels. This difference is confirmed by the wavefunctions shown in Fig. 8.14c, which illustrates the envelope wavefunction of an electron with various values of N. They are of zero angular momentum. The electron of $N = 1$ is confined mainly in the outer ring. That of $N = 2$ is in the inner ring, and that of $N = 3$ is situated in both rings. That differential confinement engenders remarkable changes in their trajectory. The amount of penetration for the electron of $N = 1$ to the inner ring is found to be $\sim$0.1, whereas that of $N = 2$ to the outer ring is $\sim$0.05.

In the case of triple ring, predicted ground state wavefunction is completely localized within the inner ring, while for more excited states wavefunctions localized within the two external rings can be found [46]. The expected electronic properties of a ring/disk are more complex. These structures constitute the good example of nanostructures with coupled localized-extended states with cylindrical symmetry (the protrusion at the inner ring edge acts, in fact, as three-dimensional electronic carrier confinement potential, thus being like a ring laid down on top of quantum disk). Ring/disks thus offer additional degrees of freedom for the control of effective coupling between excitons entrapped in quantum nanostructures [6]. The calculated ring/disk ground electronic and hole states appear to be confined in the ring structure at the edge of the inner ring/disk hole. The ring/disk excited state is, on the other side, a quantum well like state extended along the disk [75].

8.3.2 Beyond Effective Mass Approximation

Electronic properties of complex quantum nanostructured systems were also studied at the atomistic level using the empirical tight-binding method [76], confirming the EMA results.

In the EMA approach mentioned above, Coulomb interactions between carriers has been ignored. Coulomb effects can be included using the configuration mixing (CM) method, where the interaction Hamiltonian is expanded by the single-carrier wavefunction configurations, then diagonalized [73]. With the CM method it is possible to correctly describe the binding energies of excitons in strongly-confined quantum dots, such as the (In,Ga)As/GaAs systems, where the Coulomb terms is treated as weak perturbation on the single-carrier states. For weakly-confined quantum dot systems, on the other hand, the CM method often fails, thus it is hard to reach sufficient convergence even with large CM matrices available by practical computational capacity. The quantum ring systems would belong to the latter category, since the single-particle levels are densely packed in spectra compared to the typical energy range of Coulomb binding (a few tens of meV).

An alternative method to overcome this conversion problem is the quantum Monte-Carlo (QMC) method, which enables to determine the exact many-body ground-state energies under the condition of EMA. The details of this method are given by [77]. In this approach single-particle energies were calculated as well as multi-particle energies on an equal footing, including all correlation effects. The multiple exciton spectra of DE grown GaAs quantum dots calculated by means of QMC show a size dependence which quantitatively agrees with the experimental results. [78]

8.4 Photoluminescence Emission

8.4.1 Broad Area Photoluminescence

In Fig. 8.15 typical broad area PL spectra of the ring samples capped with an $Al_{0.3}Ga_{0.7}As$ barrier are reported. It is worth mentioning that the capping procedure does not induce strong changes in the droplet epitaxy made nanostructure shape, as demonstrated in [79]. Thermal annealing processes, required to recover the crystalline quality of the barrier, induces some limited intermixing at the barrier with less than 0.5 nm diffusion length even at the higher annealing temperatures [80].

In all samples PL is characterized by a broad emission band located between the GaAs and the $Al_{0.3}Ga_{0.3}As$ energy gaps.

The experiment reported by [81] shows samples ranging from quantum dots to double ring obtained from an identical droplet configuration. In this way it is possible to observe the effect of structure evolution at constant volume, determined by the Ga content of the initial droplets.

The nanostructure emission blue-shifts as the structure evolves from quantum dot to double ring. The structural evolution [81] is accompanied both by an increase of the nanostructure radius, by a strong reduction of the nanostructure height and by the presence of an additional lateral confinement in ring structures. The anti-correlation of E_{emi} and height in the DE-nanostructures (see Fig. 8.16) shows that height reduction is the main factor affecting the emission energy, whereas additional lateral confinement given by the ring width in quantum ring structures plays a minor role. A correlation between the nanostructure shape and its PL full width at half maximum (FWHM) can be observed. Being the initial droplet configuration the same, such PL broadening cannot be related to shape dependent nanostructure volume fluctuations. Bietti et al. [81] thus attributes such dependence of PL FWHM to shape fluctuation. In single ring and double ring fabrication, the presence of a slower crystallization step reduces shape disorder.

Figure 8.17a shows the ensemble optical emission of triple ring structures embedded. A clear emission peak is visible at E_A = 1.56 eV (band A) with a full width at half maximum 30 meV, above the excitonic GaAs signature at 1.519 eV. As excitation power density (P_{exc}) is increased (Fig. 8.17a) a second band (band B) appears on the high energy side of the fundamental band (E_B = 1.58 eV). The intensity of

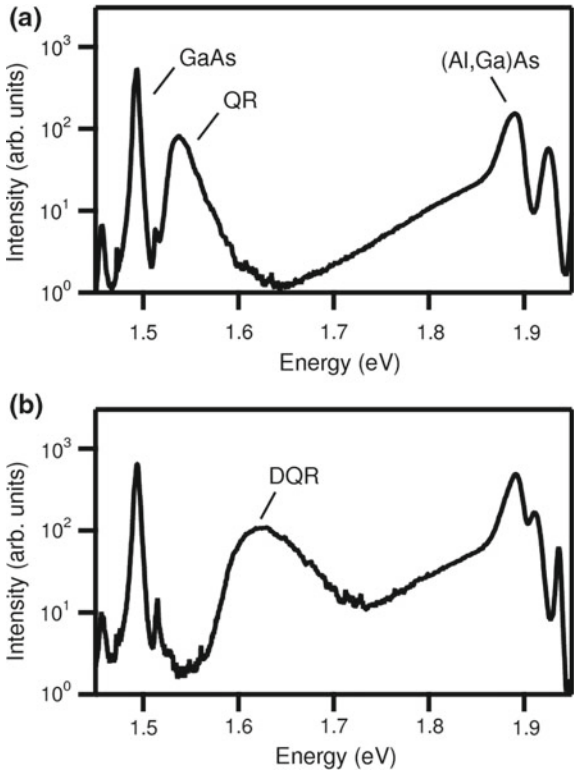

Fig. 8.15 Far-field emission spectra of the sample with **a** single rings and **b** double rings at 5 K plotted on a logarithmic scale. The excitation density is 50 mW/cm^2 (Reprinted from [33])

this band increases super-linearly with the laser excitation power. The theoretically predicted triple ring ground state transition energy is $E_{GS} = 1.58$ eV. The ground state wavefunction is completely localized in the inner ring. The first radial excited state is located 20 meV above the ground state ($E_{ES} = 1.60$). Also in this case, the wavefunction is localized within the inner ring volume. The predicted transition energy E_{GS} lies well within the A line bandwidth. Band A thus belongs to the ensemble emission from the triple ring ground states. Moreover, the energy difference between A and B bands matches the energy difference $E_{ES} - E_{GS} = 20$ meV. In addition, the P_{exc} behavior of band A and B is very similar to that shown by quantum dot ensembles where the additional band appearing at high P_{exc} is attributed to excited states emission. The excited state population in quantum dots is linked to the ground state by a waterfall-like chain, thus being visible only when the ground state of the quantum dot is occupied. On this basis, we attribute band B to first excited transition. It is worth noting that the linked dynamics between the ground state and the first excited state arises from the fact that the two are localized within the same ring, therefore showing an agreement with what has been found in single ring structures [33].

Ring/disks constitute a good example of nanostructures with coupled localized-extended states with cylindrical symmetry (the protrusion at the inner ring edge acts,

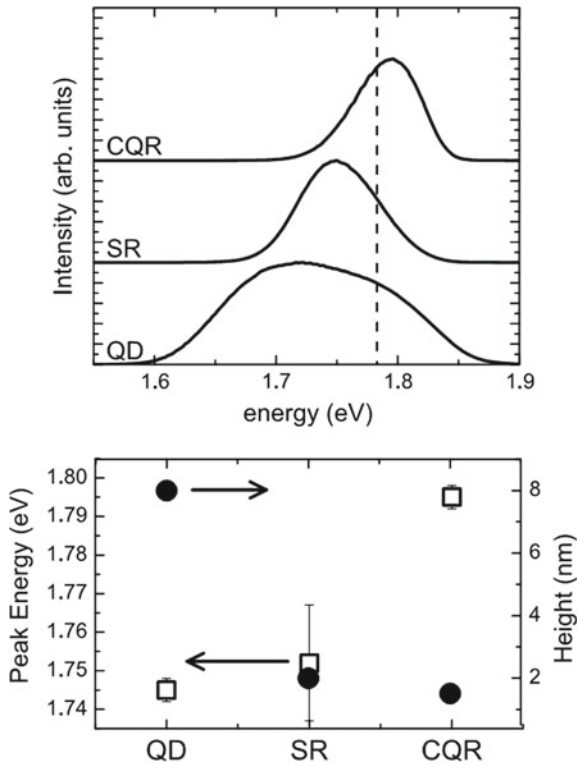

Fig. 8.16 Top panel: PL of quantum dot, single ring and double ring samples. The vertical line indicates the laser excitation energy for RPL measurements. Bottom panels: PL peak energy (open squares) and height (black circles) of the three nanostructure (Reprinted from [81], Copyright Wiley-VCH Verlag GmbH and Co. KGaA (2009), reproduced with permission)

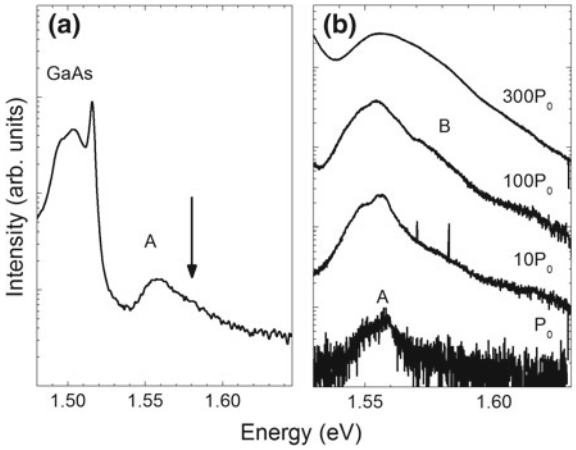

Fig. 8.17 **a** PL spectra of the triple ring sample measured at T = 15 K and P_{exc}= 10 W/cm^2. The arrow indicates the theoretical prediction based on a typical triple ring AFM image. **b** PL spectra of the triple ring sample measured at T = 15 K as a function of P_{exc} in the range 5–1500 W/cm^2. Here $P_0 = 5$W/cm^2. A and B labels indicate triple ring ground state and excited state emission, respectively (Reprinted from [82], Copyright (2009), with permission from Institute of Physics)

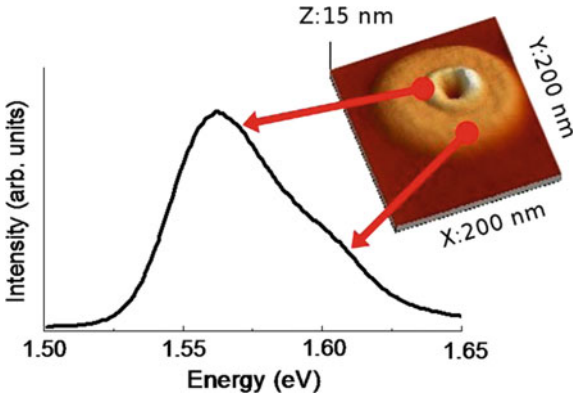

Fig. 8.18 PL spectrum of the ring/disk sample at low temperature (T = 14 K). Upper right corner: AFM image of a single ring/disk. The emission at 1.55 eV is attributed to carriers confined in the ring protrusion of the ring/disk, while the shoulder at 160 eV to states belonging to the disk (Reprinted from [75])

in fact, as three-dimensional electronic carrier confinement potential, thus being like a ring laid down on top of quantum disk). In Fig. 8.18 the PL spectra at T = 14 K of the sample is reported. An intense and broad band is clearly visible at 1.55 eV, with a full width at half maximum of ≈30 meV. The band shows a shoulder at 1.60 eV. The observed PL peak value is in good agreement with the calculated emission energy ($E^{th}_{GS} = 1.56$ eV). The theoretically calculated ring/disk ground electronic and hole states appear to be confined in the ring structure which is formed at the edge of the inner ring/disk hole. The ring/disk excited state is, on the other side, a quantum well like state extended along the disk ($E^{th}_{EX} = 1.59$ eV).

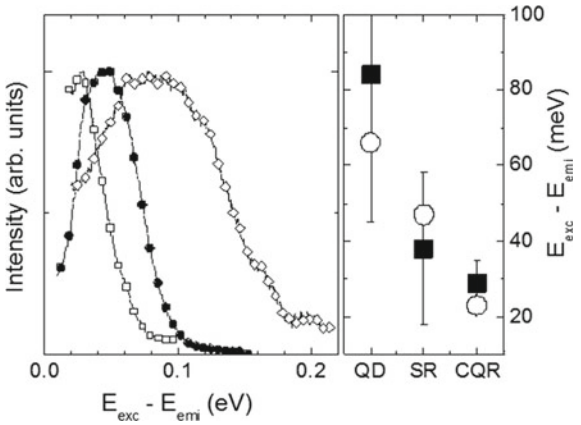

Fig. 8.19 Left panel: RPL spectra of quantum dot (open diamonds), single ring (full circles) and double ring(open squares) samples. Experimental conditions were: $E_{\mathrm{exc}} = 1.78\,\mathrm{eV}$ and $T = 10\,\mathrm{K}$. All the spectra are normalized to their maximum. Right panel: Experimental RPL peak energy (full squares) and theoretical calculations of the energy difference between the ground and the excited state of the DE-nanostructure (circles). The error bars indicate the experimental band FWHM (Reprinted from [81], Copyright Wiley-VCH Verlag GmbH and Co. KGaA (2009), reproduced with permission)

8.4.2 Resonant Photoluminescence

From the RPL spectra some information on the carrier dynamics in the DE-nanostructure can be deduced. In Fig. 8.19 the resonant PL spectra (RPL) of the single ring and double ring samples are illustrated in comparison with that of a quantum dot. All the spectra are characterized by large, unstructured bands located at decreasing $\Delta E \equiv E_{\mathrm{exc}} - E_{\mathrm{emi}}$ energies. The PL emission from the samples shows its maximum intensity at $\Delta E = 84$ meV, $\Delta E = 38$ meV and $\Delta E = 29$ meV for quantum dot, single ring and double ring, respectively. The ΔE values strongly depends on the actual DE-nanostructure. Such dependence allows us to safely attribute the RPL peak, according to [83], to the emission of the ground state of DE-nanostructure, whose excited state energy corresponds to the laser excitation energy E_{exc}. Moreover, the absence, in the spectra, of any modulation with a spacing corresponding the GaAs LO-phonon energy (36 meV) implies that carrier relaxation in DE-nanostructure is not affected by polaronic [84, 85] or phonon-bottleneck effects [86, 87]. The reduction of the FWHM of the RPL spectra as the shape evolves from quantum dot to double ring should be related to the narrower density of states, owing to the smaller size dispersion, of the latter DE-nanostructure, as shown by the PL spectra.

In Fig. 8.19 the calculated energy separation between the DE-nanostructure ground and excited states is reported, together with the experimental ΔE values. There is a rather good agreement between the theoretical predictions and the experimental results. The maxima of the RPL spectra always correspond to the ΔE values

determined by absorption of photons on the first excited state. The energy separation between the ground and the excited state decreases as the nanostructure evolves from quantum dot to double ring (see Fig. 8.19). Theoretical calculations state that ΔE is determined by the radius of the DE-nanostructure. In fact, in all the three DE-nanostructure, the first excited state corresponds to a change in the radial quantum number. In quantum dot the ground and excited state corresponds to a *s*- and *p*-type modulations of both electronic and hole radial wavefunction 3D confined in the dot. In single ring structures, the wavefunction is naturally confined in the ring. The first excited state shows a *p*-type modulation of the radial part of the wavefunction [33]. In the double ring the ground state is localized in the outer ring, while the first excited state lies in the inner ring, around 4 meV above the outer ring state [32]. However, the RPL resonance is located at 29 ± 6 meV, thus much higher than the inner ring resonance. Such energy corresponds, for both rings, to the energy difference between the ground state and the first excited state whose wavefunction lies in the same ring. In double ring, this excited state corresponds, in analogy to the single ring case, to a *p*-type modulation of the radial part of the ring wavefunction. This means a suppression, in double ring, of the two ring coupling.

8.4.3 Single Nanostructure Photoluminescence

Spectroscopy of a single quantum ring

In Fig. 8.20a, typical single ring PL spectra (and their dependence on excitation intensity) are reported. Quantum ring density is of the order of $6 \times 10^8/\text{cm}^2$ (DE allows to control density on four order of magnitude) and is thus possible to measure single nanostructure emission with standard micro-PL apparatus [33]. In single ring at low excitation, we find a single emission line appearing at 1.569 eV, due to recombination of an electron and a hole both occupying the ground state of the ring. Increasing excitation intensity, a new emission line, indicated by an arrow, emerges at 1.582 eV. Further increase in excitation density causes saturation in the intensity of the original line along with a nonlinear increase in the new line. Superlinear dependence of the emission intensity suggests that the satellite line comes from the electron-hole recombination from an excited level of the ring. Thus, the energy difference between the the ground and the excited state in the single ring is 13 meV.

In addition to the state-filling feature associated with photo-injection, the ground-state emission is shifted to lower energies. This is a signature of multi-carrier effects. If multiple carriers are present inside a ring, their energy levels are modified by the Coulomb interaction among them. Because the energies are renormalized according to exchange corrections for *parallel-spin* carriers, this results in spectral red shift of the emission, depending on the number of carriers. Similar features have been reported in GaAs quantum dots [21] and InAs quantum rings [88]. At high excitation, we also find spectral broadening, which is attributed to carrier collision processes.

Single ring emission is considerably large compared with those observed in quantum dots [21]. Line broadening can be ascribed to spectral diffusion, i.e., an effect of

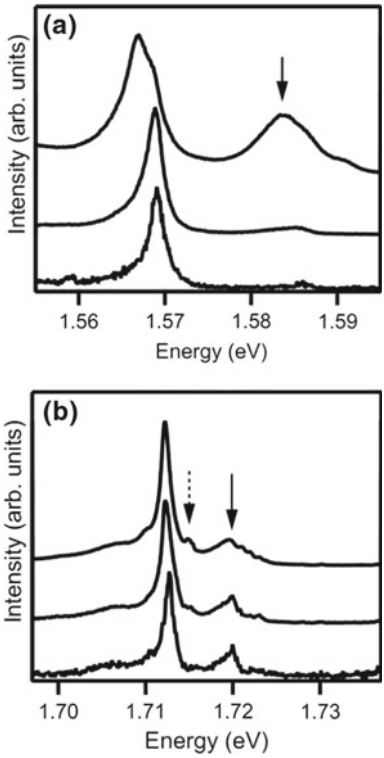

Fig. 8.20 Emission spectra for a single GaAs single ring (**a**) and double ring (**b**). Their respective excitation densities were, from bottom to top, 1, 10, and 30 W/cm^2. Spectra are normalized to their maxima and offset for clarity (From [33])

the local environment that surrounds each quantum ring. Our samples are expected to contain a relatively large density of imperfections and excess dopants, associated with low-temperature growth. This causes local-field fluctuation, leading to efficient broadening of the PL spectra. Detailed discussion on the origin of line broadening in quantum nanostructure is presented in [89]

Figure 8.20b shows PL spectrum of a single double ring. As in the case of single ring, the spectra consist of discrete lines, i.e., a main peak and a satellite one, which is on the high energy side of the main peak. The former is associated with recombination of carriers in the ground state, whereas the latter comes from the excited states. The energy difference between ground-state and excited-state lines is 7.2 meV. In contrast to the single ring case, we observe the satellite peak even at the lowest excitation, where the estimated carrier population inside a ring should be less than 0.1, according to [33]. Observation of the excited state emission suggests a reduction of carrier relaxation from the excited level to the ground level. This feature will be discussed later. At high excitation, we find several additional lines superimposed on the spectra, as shown by the broken arrows. These contributions imply the presence of fine energy structures in double ring.

Figure 8.21a shows a series of transition energies for single ring. For comparison, the emission spectra of quantum ring are plotted. The main peak and the high-energy

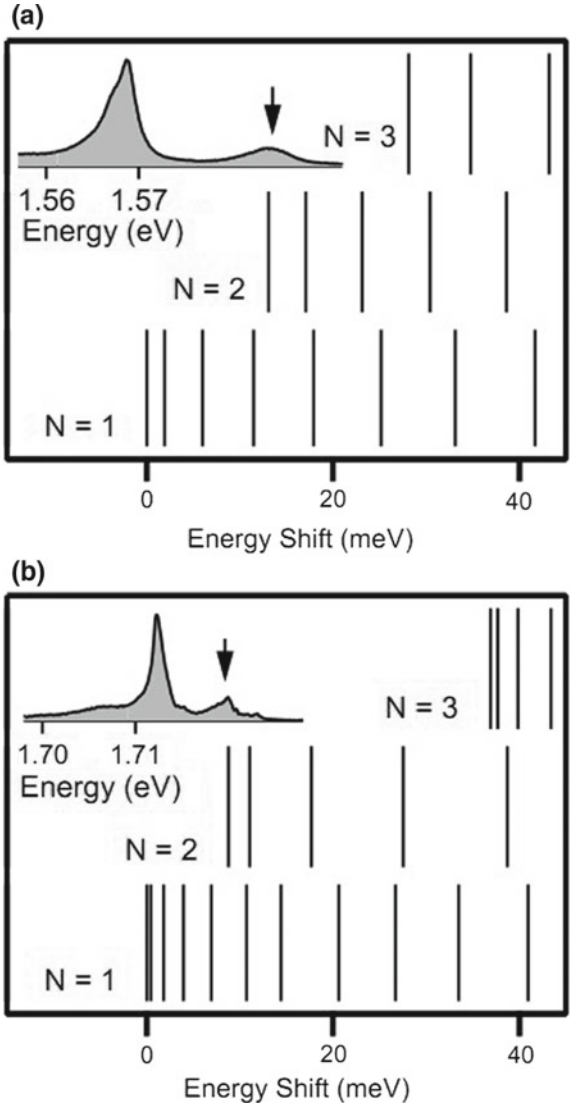

Fig. 8.21 **a** A series of optical transition energies in quantum ring, obtained by the calculation. The PL spectrum of a quantum ring at 15 W/cm^2 is shown in the inset. **b** The energies of optical transitions in double ring, together with the PL spectrum of a double ring at 10 W/cm^2 for comparison (Reprinted from [33])

satellite in the observed spectra are assigned respectively to the recombination of the *e-h* pair in the lowest state, $(N, L) = (1, 0)$, and to that of the first excited *z-radial* state, $(2, 0)$. The split between the two transitions is estimated in 13.1 meV, in agreement with the energy shift obtained by experiments. The emissions associated with high angular momenta are not present, which suggests rapid relaxation of angular momentum, whose process is quite faster than transition between z-radial quantization levels or recombination between an electron and a hole. A possible origin for fast angular momentum relaxation is structural asymmetry of the ring, due to

elongation, impurity and surface roughness. In this case, angular momentum is not a good quantum number, and scattering between different L levels efficiently occurs.

Comparison between the experimental spectra of double ring and calculation is reported in Fig. 8.21b. As in the case of quantum ring, the main PL peak and the satellite one are attributed respectively to the transition of $(N, L) = (1, 0)$ and that of $(2, 0)$. The energy split deduced from calculation is 8.8 meV, which agrees with the experimental value. It is worth noting that, in double ring, the wavefunction of $N = 1$ is localized mainly in the outer ring, while that of $N = 2$ is localized in the inner ring. Thus, the two peaks in the observed spectra come from the two rings, which consist of a double ring. In this connection, the excited-state emission in our experiment appears even when the carrier population is less than one. This constitutes direct evidence for the carrier confinement into the two rings. Tunneling probability between inner and outer ring is not very large, engendering the observation of the excited-state emission.

8.5 Carrier Dynamics in Ring Structures

Double ring emission consists of a doublet emission, attributed to the inner ring (IR), the higher energy line, and to the outer ring (OR), the lower energy line. The relative intensity, at low temperature, of the two lines does not depend on laser excitation power density P_{exc}. This behavior is the fingerprint of a decoupled dynamics of the two rings, although a strong phonon bottleneck effect between the ground and excited state of the double ring could give rise to similar CW spectra. Fundamental insights on possible coupling mechanisms between double ring excited states may be obtained by time resolved state filling experiments on single double rings. Sanguinetti et al. [90] reports the time resolved emission, at low P_{exc}, of the two lines of different double ring doublets. The rise-time of the IR and OR lines is $\tau_R = 120 \pm 40$ ps, thus being about four times larger than the commonly measured τ_R for quantum dot structures, even in the case of GaAs/AlGaAs quantum dots [28]. Despite small differences (within 30%) between IR and OR decay times (τ_D), the two lifetimes are quite similar for each pairs of rings, although the overall lifetime varies by more than a factor four in different double rings (200 ps $< \tau_D <$ 900 ps), possibly due to different defectivity of the environment [89]. Time resolved PL measurements as a function of P_{exc}, reported in Fig. 8.22, can give more information on the nature of the mutiplets origin. Increasing power density, strong increases of the rise PL times of the fundamental optical transition are found, as due to state filling condition. At high P_{exc}, correlated dynamics between two lines is observed, which originates from the multiexcitonic states in the OR (lines L1 and L2 in Fig. 8.22), in close resemblance to the quantum dot case [21, 91, 92]. Risetime of the line L1 corresponds to decaytime of line L2, thus demonstrating a link between the carrier population in the two states. Such correlation between decay and rise times arises from states which are bound in a cascade-like behavior. As far as the carrier dynamics is concerned, IR fundamental line shows a similar behavior, indicating an independent state filling mechanism

with respect to the OR case, although the cascade-like dynamics in the IR multiplet is partially hidden by OR recombination present on the low energy side of the IR line.

The overall phenomenology clearly excludes a carrier transfer between IR and OR. Recombination kinetics of carriers in the inner and outer rings are then decoupled. In fact, if the carrier dynamics in the two structures were in some way correlated, a hierarchical order in the PL decay, with the shorter decay time belonging to the higher state, should be observed, denoting a cascade mechanism associated to the carrier relaxation paths. On the contrary, the IR recombination lifetimes is always larger than the risetime of the OR time resolved emission. Moreover, almost the same decay-times are observed in IR and OR recombination for each double ring, even if large variations are observed for different double rings. The analysis of carrier dynamics under large optical injection suggests similar conclusions. For both IR and OR emission we observe the increase of rise times when increasing P_{exc}, a clear evidence of saturation effects associated to state filling conditions. This dynamics is illustrated by the lines L1 and L2 present at high P_{exc} in the emission of the OR of double ring. In this case, the τ_D of L2 corresponds to the rise time of L1 implying that the two emissions come from energy states connected in a cascade type dynamics, where the higher states in the ladder act as feeders of the ground state. As reported before, the L1 and L2 lines of the OR multiplet are ascribed to single and multi exciton recombination and the difference in their emission energy stems from a different occupation of the ring, which changes the number of spectator excitons from several (line L2) to zero (line L1), thus making the dynamics of two lines strictly correlated. At the same time, comparing the time dependence of the IR and OR at P_{exc}= 70 W/cm^2 lines, we cannot find any correlation between rise and

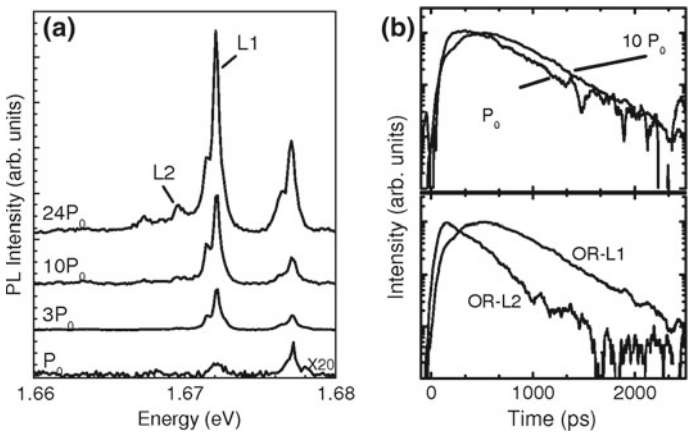

Fig. 8.22 **a** Time integrated spectra of a double ring at different excitation power densities. T = 10 K and $P_0 = 3$ W/cm^2. **b** Top panel: time resolved PL of the OR line of a double ring at T=10K and at different P_{exc} (From [90])

decay times of the emission, thus demonstrating that the carrier dynamics in the two rings is decoupled.

The decoupling of the carrier kinetics happens despite the proximity of the two rings in a double ring structure. Supposing that the exciton are free to move over the whole ring, the lack of coupling could be traced back to the lack of resonance conditions between states having the same angular momentum value inside the IR and OR.

8.5.1 Ring Shape Disorder Effects

As far as the energy relaxation efficiency of the electron-hole pairs photogenerated in the quantum rings is concerned, it is worth noting that the low P_{exc} measurements show relative large values of τ_R, compared to the quantum dot case. This can be explained as a less effective relaxation channel in the double ring, compared to the quantum dot case, despite the much closer spacing of the ring states which should prevent a phonon-bottleneck effect. These are quite controversial considerations, linked with the puzzling large broadening of 1 meV of the PL lines. It should be noted that quantum rings possess an electronic structure which is a crossover between the dot and the wire cases due to their rather peculiar annular shape [33], since the linear extension of a ring of 80 nm diameter is already quite large (250 nm). Therefore quantum rings can be considered as a warped analogous of quantum wires (QWi). Confinement energy fluctuations, whose magnitude is significantly lower than the exciton binding energy [93], can be observed in QWi, due to their size disorder. Such disorder principally affects the exciton center of mass (COM) part of the exciton wavefunction, giving rise to states with a spatially localized COM motion. The presence of such states has strong effects on the optical properties of QWi: the more evident is, naturally, the inhomogeneous broadening of the emission lines, which is related to the exciton energy disorder. Moreover, the exciton COM localization in QWi induces a serious reduction of the phonon scattering rates [93]. At the same time, as far as the kinetics of excitons in localized states induced by disorder is concerned, it is well known that an increase of the emission risetime associated to the exciton motion toward the state of minimum energy is observed. There are two main effects of the exciton COM localization on the coupling of OR and IR. On one side, excitonic COM localization makes possible the coupling between states with different angular momentum of the two rings because it partially relaxes the angular momentum conservation in exciton transitions. But, on the other side, it increases the average spatial separation between the exciton states, which are now localized in small regions of the rings, thus making the coupling between states belonging to OR and IR even more difficult.

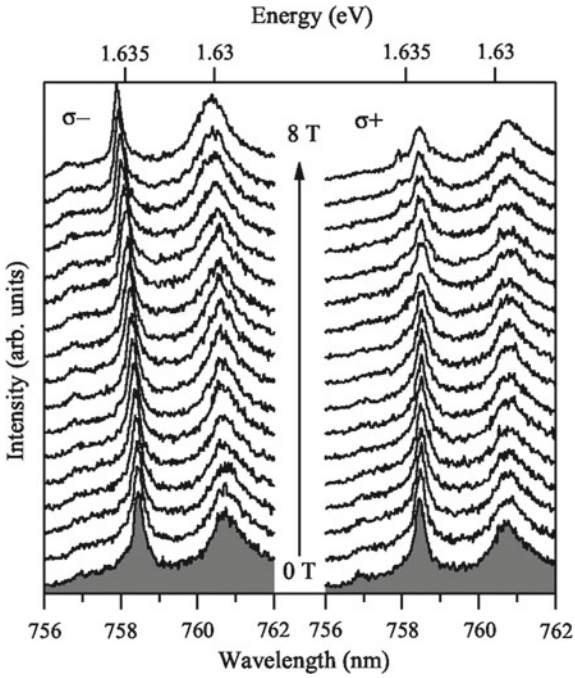

Fig. 8.23 Circularly polarized PL spectra of a double ring as a function of magnetic field from 0 T to 8 T (from bottom to top) with 0.5 T step. A left panel shows the magnetic dependence for the σ_- component, and a right panel shows that for the σ_+ component (Reprinted from [94], Copyright Wiley-VCH Verlag GmbH and Co. KGaA (2009), reproduced with permission)

8.5.2 Magneto-Photoluminescence

Magneto PL measurement were performed on single double rings [94]. A series of polarized PL spectra with varying magnetic field in Faraday geometry is shown in Fig. 8.23. The left and right series corresponds to σ_- and σ_+ polarized signals, respectively. Both polarizations have identical spectra at 0 T. They consist of a sharp line at 758.6 nm and a broad line at 760.8 nm, which are assigned to the recombination of carriers inside the inner ring and the outer ring of a double ring.

Increasing the magnetic field, the σ_- spectra shift to shorter wavelengths, while the σ_+ spectra slightly move to longer wavelengths, as expected for the Zeeman effect of quantum ring excitons. According to a fit to a quadratic dependence on magnetic field, we estimated an exciton g factor $g_X = 2.4\,(\pm 0.3)$, and a diamagnetic coefficient 9.5 (± 1) μeV/T^2. The value of g_X is almost the same reported by previous studies on GaAs lens-shaped dots, while the diamagnetic coefficient is around two times larger for the present quantum ring than the dots [95]. Difference in the diamagnetic shift is probably due to lateral expansion of carrier confinement in quantum rings.

A striking feature is that the intensity of the σ_+ signals is significantly quenched by around 20 %, compared to that of the σ_- signals, at fields more than 6 T. Note that the σ_+ signal, which shows the PL quench, arises from the lower Zeeman level. We can therefore rule out the possibility of carrier relaxation between the Zeeman levels.

Two processes can be accountable for the PL quench at high magnetic field were proposed. The first is the exciton AB effect, which comes from level crossing between different orbital states in quantum ring. According to the theoretical proposal of [96], the transition strength decreases to zero when relative orbital angular momentum is changed from 0 to 1, being realized at a particular field. The field of level crossing is given by a equation, $\Delta\Phi/\Phi_0 = 1/2$, where $\Delta\Phi$ is the number of magnetic flux which inserts relative trajectory for electron and hole motion, and Φ_0 is a flux quantum. As a rough estimation which ignores Coulomb interaction sand assuming a ring shape studied in [33], the transition field is expected to be ~10 T, in reasonable agreement with the present result.

The second process is related to the level crossing between bright and dark trions. Because of unintentional doping, our sample can possibly be *p* type, leading to the formation of positive trions. In this case, the ground-state trion is bright at zero field, and a dark trion with triplet holes should be present at a higher energy. The g factor for the relevant emission is given by $|g_c|$ for the bright cold trion, and $|g_c - 2g_v|$ for the dark hot trion, the latter becoming larger than the former. Thus, the bright-to-dark transition can appear at sufficiently high field, in contrast to the case of neutral excitons. The value of the field of this transition is related to the energy split from a cold trion to a hot trion, which is essentially given by the *s*-*p* orbital splitting for a hole. This splitting is on the order of 10 meV for conventional quantum dots, requiring an extremely high field for the transition. In the double rings, on the other hand, the orbital split is as small as ≤1 meV, because of their expanded shape. Therefore, the magnetically-induced transition can be realized at a field available in this experiment.

8.5.3 Single Photon Emission

In order to investigate the peculiar phenomena typical of quantum rings [1, 3–5], they are usually considered as an ideal quantum system. However, in real semiconductor quantum devices disorder cannot be neglected. Effects related to disorder are largely discussed in quantum wells and quantum wire literature, leading to the concept of exciton localization [97]. On the other hand, carrier confinement in quantum dots occurs over a spatial region much smaller that the exciton Bohr radius. For this reason disorder does not play a role and the single quantum dot electronic properties are well described as a two level system. This is clearly demonstrated by antibunching measurements [98]. In quantum rings, the length of the circumference is usually larger than the exciton Bohr radius. This means that quantum rings electronic structure is a crossover between the dot and the wire cases, due to quantum rings rather peculiar annular shape which. Intensity time correlation experiments based on Hanbury, Brown and Twiss interferometer can address this issue. The second order correlation function $g^{(2)}$ well characterizes the quantum nature of the emitter by the presence or not of photon antibunching [98–100].

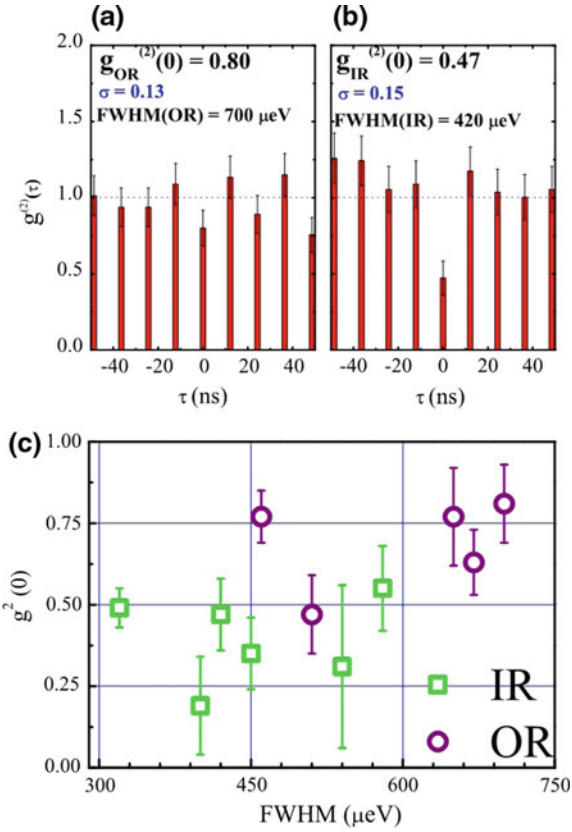

Fig. 8.24 Panel **a** and **b** are pulsed excitation measurement of $g^{(2)}(\tau)$ for OR and IR, respectively. The error bar associated to each peak is the coincidence count square root normalized to the average value of the peaks intensity. σ is the standard deviation of the average value of the peak intensity (except for the zero-delay one). Panel **c** Summary of all the measured $g^{(2)}(0)$ for IR (squares) and OR (circles); the error bars are the measured standard deviation σ (Reprinted from [101])

The second-order autocorrelation function for both the OR and IR emissions of a single double ring is reported in [101] (see Fig. 8.24a, b). The reduced intensity of the peak at zero time delay indicates that there is a small probability of finding two or more photons inside each emitted pulse. This is the signature of a single-photon emitter under pulsed excitation. While $g^{(2)}(0) = 0$ is expected for a ideal two levels system, the condition of $g^{(2)}(0) < 0.5$ is required for a single photon emitter and the condition $g^{(2)}(0) < 1$ still denotes the quantum nature of the emitter [98, 102]. In our case, the correlation function at zero time delay, $g^{(2)}(0)$, is estimated to be 0.47 ($\pm$0.15) for the IR recombination and 0.80 ($\pm$0.13) for the OR recombination.

The same analysis was performed on several double rings (Fig. 8.24c), showing an increase of $g^{(2)}(0)$ with the increasing linewidth. The condition $g^{(2)}(0) < 0.5$is usually fulfilled by the IR but not by the OR. Finally, cross correlation intensity measurements between IR and OR give $g^{(2)}_{IR-OR}(0) = 1$ within the experimental error. These results are not unexpected because of the independent dynamic already reported on these nanostructures [90].

On the basis of the previous results, [101] concluded that IR is usually small enough to contain well-separated quantum states and gives rise to an optical transition with antibunching features. On the contrary the OR is sufficiently large to be influenced by structural disorder, resulting in an inhomogeneously broadening of the emission band. Therefore, even if disorder turns out to be an important issue for large quantum rings, for sufficiently small ring diameter, DE quantum rings can be considered as an almost ideal quantum system.

8.5.4 Fast Exciton Dynamics in Complex Nanostructures

As reported in [103] (see Fig. 8.25), triple rings show an extremely fast decay time τ_D = 40 ps, to be compared with the usual DE quantum dot and quantum ring values, which range between 300 and 500 ps [21, 90, 104]. The short decay time is a general feature of all the triple ring structures measured in the sample. The fast optical response cannot be likely attributed to non radiative processed arising from the defected triple ring barrier, because of the much longer decay times of the GaAs (τ_{GaAs} = 300 ps) and of the $Al_{0.3}Ga_{0.7}As$ barrier (τ_{AlGaAs} = 200 ps), measured in the same sample at the same conditions.

Similar results are observed in the time resolved PL of ring/disk materials grown on Si/Ge substrates [105] (see Fig. 8.25). As in the case of triple ring, ring/disk show an extremely fast decay time of τ_D = 60 ps and, also here, the observed fast optical response cannot be attributed to non radiative processed arising from the defected ring/disk barrier (τ_{AlGaAs} = 200 ps, (τ_{GaAs} = 300 ps)).

The puzzling short τ_D was attributed in both structures to the outcome of an intrinsic decay mechanism in the triple ring and ring/disk such as the strong electron-hole overlap and large transition dipole matrix element in such extended, complex nanostructures. Ring based nanostructures are then promising self-assembled materials for ultrafast optical switches for high-bit-rate operations.

8.5.5 Carrier Dynamics in Ring-Dot Complex Structures

The possibility to employ of twisted light/matter (TL) interaction should make possible to populate selectively the electronic level of a semiconductor nanostructure by the appropriate combination of light-beam parameters. The coupled dot-ring nanostructures [106] introduced in Sect. 8.2.3, can be considered a prototypical example of the class of nanostructures where the use of TL could allow for optical control of electronic states by simply changing the position, waist and orbital angular momentum of the light beam.

These nanostructures belong to type II configuration, with a spatial separation between the electrons, localized in the external ring, and the holes, which lie in the dot. The reduced electron hole overlap guarantees a long storage time, thus with direct

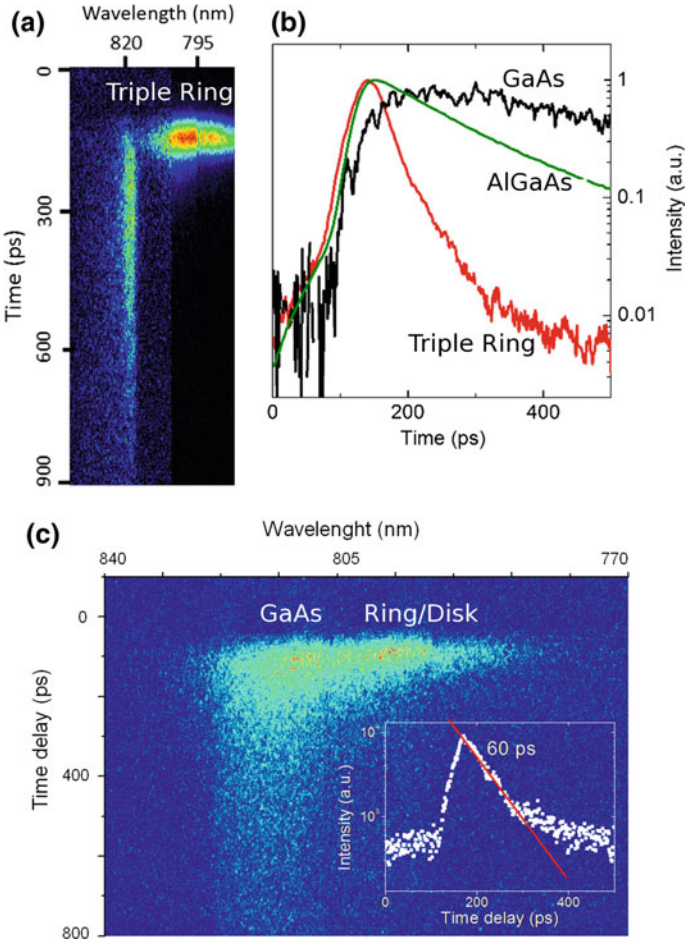

Fig. 8.25 **a** Temporally and spectrally resolved images of the triple ring sample. GaAs and triple ring emissions are labeled. Data from [103] (**b**): Time resolved PL traces of the GaAs, AlGaAs and triple ring emissions. **c** Temporally and spectrally resolved image of the ring/disk emission. GaAs and ring/disk emissions are labeled. Inset: Time resolved PL traces of the ring/disk emission. The exponential fit, with a $\tau_D = 60$ ps is also shown (red line). Data from [105]

implications in optical memory devices. However, the physical implementations of quantum information processing requires, among others, long decoherence time, much longer than the gate operation times. In spin qubits or in spin memory devices, operation time must be shorther than spin relaxation time. The peculiar confining potential hybrid nanostructures made by coupled QRs and QDs leads to a large decrease of the wave function overlap factor, thus increasing the relaxation time as required by quantum information implementations.

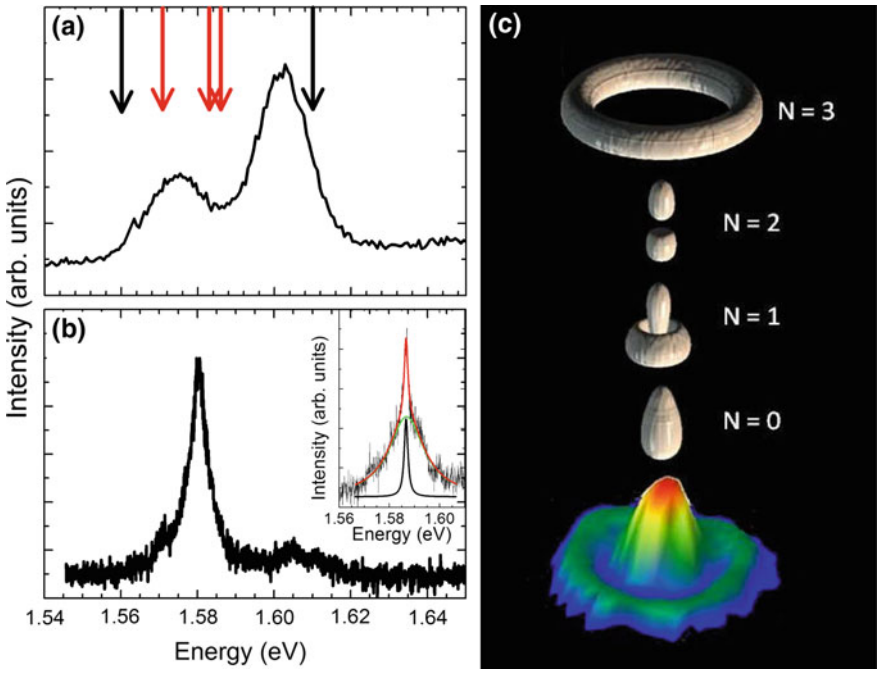

Fig. 8.26 **a** Dot-ring ensemble photoluminescence at $T = 15\,\mathrm{K}$, using $P_{\mathrm{exc}} = 60\,\mathrm{mWcm}^{-2}$. Black arrows: calculated dot ($E_{\mathrm{dot}} = 1.56\,\mathrm{eV}$) and ring ($E_{\mathrm{ring}} = 1.61\,\mathrm{eV}$) transition energies. Red Arrows: Dot excited states. **b** Photoluminescence spectrum taken at 10 K of a single Dot-ring. Inset: magnification of the dot spectral region; the red curve is the fit of the dot emission band; it is a sum of two Lorentzian functions (green and black), one describing the background due to the nearest dots, while the other describes the peak. The FWHM of the latter is 1.8 meV. **c** Isosurface plots of the electronic probability density at 50% of the wave functions in Dot-ring and, at the bottom, the AFM profile used for calculation. $N = 0$ indicates the ground state while $N = 1, 2, 3$ indicate the first excited radial states with $J = 0$. Reprinted from [106]

Figure 8.26a reports PL at $T = 14\,\mathrm{K}$ of the dot-ring ensemble. It displays a clear double peak structure, with emission bands are centered at 1.578 eV (band A) and 1.603 eV (band B). The two bands are relatively narrow, compared to the usual Droplet Epitaxy nanostructure emission [20], due to the low size fluctuation observed in the dot-ring structures.

The micro-PL emission from a single dot-ring shows as well two spatially correlated bands which lie at the same wavelength of those observed in broad area PL. This demonstrates that the two emission bands belongs to the same nanostructure.

By means of effective-mass envelope model calculations [47], band A was attributed to the emission from the dot ground-state ($E_{\mathrm{dot}}^{\mathrm{TH}} = 1.565\,\mathrm{eV}$) and band B to the emission from the ring ground-state ($E_{\mathrm{ring}}^{\mathrm{TH}} = 1.610\,\mathrm{eV}$).

The two bands in the emission of the dot-ring ensemble show a slightly superlinear dependence, with a constant integrated intensity ratio, from the laser excitation power

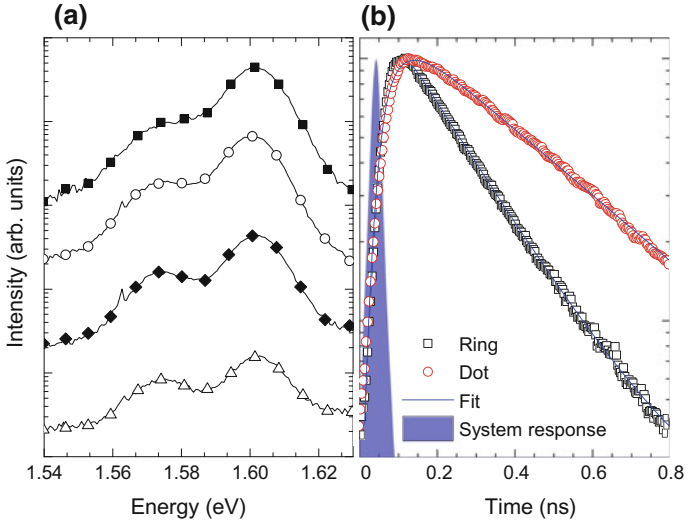

Fig. 8.27 **a** Dependence of the ensemble PL at $T = 15\,\mathrm{K}$ on power excitation density (P_{exc}): P_0 (triangles), $10P_0$ (diamonds), $100P_0$ (circles) and $1000P_0$ (squares). Here P_0 is $0.1\,\mathrm{Wcm}^{-2}$. **b** Time resolved PL of dot (red circles) and ring (black squares), using $P_{\mathrm{exc}} = 100\,\mathrm{Wcm}^{-2}$. The system response to laser pulse is also reported. The blue continuous lines represent the fit of the data as explained in the text. Reprinted from [106]

density (see Fig. 8.27a). This implies a decoupled carrier dynamics in the dot and the ring, since a charge transfer, dependent on the excitation power, would be expected from band B to band A in the case of a coupled structure. The broadening of the band A observed at high excitation power density is due to the population of dot excited states.

Time resolved PL (TR-PL) measurements (see Fig. 8.27) give access to carrier dynamics. The rise times of the dot and ring are $\tau^{\mathrm{R}}_{\mathrm{dot}} = (50 \pm 10)\,\mathrm{ps}$ and $\tau^{\mathrm{R}}_{\mathrm{ring}} = (33 \pm 10)\,\mathrm{ps}$, respectively. The dot value is larger expected in GaAs/AlGaAs dots [107]. The PL lifetimes are $\tau^{\mathrm{D}}_{\mathrm{dot}} = (335 \pm 5)\,\mathrm{ps}$ and $\tau^{\mathrm{D}}_{\mathrm{ring}} = (195 \pm 5)\,\mathrm{ps}$ for dot and ring emissions, respectively. The PL time trace of the two bands show a clear decoupled dynamics. As a matter of fact, the rise time of the dot band is uncorrelated with decay time of the ring, despite the fact that band A lies at lower energy respect to band B. This excludes carrier transfer between the dot and the ring, at least at low temperature.

In addition, in the case of correlated carrier dynamics a hierarchical order in the PL decay of the two bands is expected, with the shorter time belonging to the emission higher in energy. In the experiments reported by [106] the ring recombination lifetime is always larger than the rise time of the dot emission (Fig. 8.27b) while, at the same time, τ^{D} of the same order of magnitude are observed in dot and ring emission decay (335 vs. 195 ps). State filling experiments, performed exciting the nanostructures at

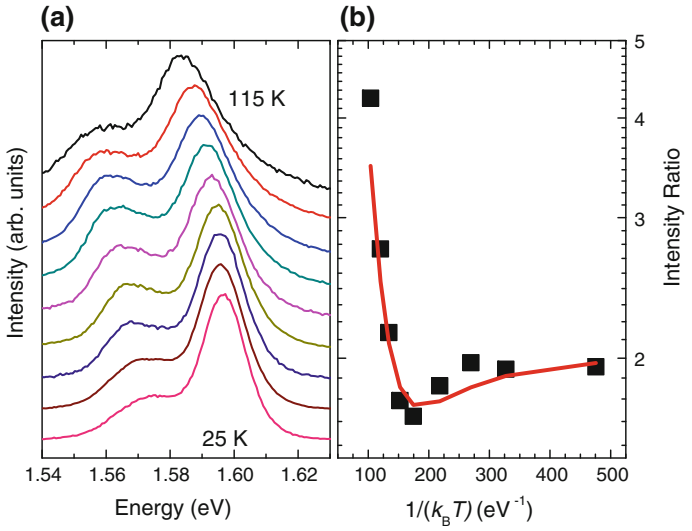

Fig. 8.28 **a** Temperature dependence of the ensemble PL between 25 and 115 K. **b** Experimental integrated intensity ratio (R_{PL}) between ring and dot emissions (black squares). The red line shows the prediction of 8.5. Here $\mu_D = 170$ and $\mu_R = 2$. Reprinted from [106]

increasing power densities, confirm the independence of the carrier dynamics in the dot and the ring despite the proximity of the two nanostructures.

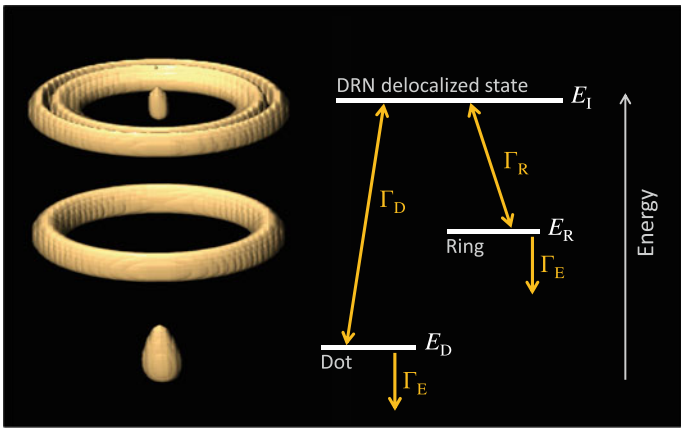

Fig. 8.29 Left, from bottom: isosurface plots of the electronic probability density at 50% of dot and ring ground states and of the first delocalized state between the dot and the ring in a dot-ring. Right: schematics of the energy levels of the states reported on the left. The excitation and de-excitation processes, together with the symbols indicating their probabilities, are also reported. Reprinted from [106]

Rising the temperature (see Fig. 8.28a), while the dot emission increases in intensity, reaching its maximum around 70 K, the ring to dot intensity ratio R_{PL} (see Fig. 8.28b) displays a minimum. The integrated PL intensity of the dot-ring above 70 K decreases and R_{PL} increases. This behaviour is the outcome of a transfer of excitation, activated by the temperature, between the two nanostructures. The same phenomenology was observed in QD ensembles [108, 109] and attributed to a delocalized high energy state connecting the QDs. The same explanation could also be valid for the dot-ring structure, where an excited state, common to the dot and the ring lies at $\Delta E_D = E_I - E_D = 41$ meV above the dot and $\Delta E_R = E_I - E_R = 12$ meV above the ring ground states, respectively. The wave function of such delocalized excited state is reported in Fig. 8.29. At higher energies, additional mixed dot-ring states are present. Hole states, due to the relatively large radius of both nanostructures, are closely spaced in energy, replicating the electron state structure on a narrower energy scale.

The carrier dynamics can be modeled via the simple set of rate equations:

$$\begin{aligned}
\frac{dn_D}{dt} &= n_I\Gamma_D - n_D\Gamma_E^D - n_D\Gamma_D\rho_D \exp[-\Delta E_D/k_BT] \\
\frac{dn_R}{dt} &= n_I\Gamma_R - n_R\Gamma_E^R - n_R\Gamma_R\rho_R \exp[-\Delta E_R/k_BT] \\
\frac{dn_I}{dt} &= G - n_I(\Gamma_D + \Gamma_R) + n_D\Gamma_D\rho_D \exp[-\Delta E_D/k_BT] \\
&\quad + n_R\Gamma_R\rho_R \exp[-\Delta E_R/k_BT]
\end{aligned} \tag{8.4}$$

where n_D, n_R and n_I are the populations of the dot, ring and intermediate state, respectively. Γ_E^D and Γ_E^R are the radiative recombination probabilities of dot and ring, respectively. Γ_D and Γ_R are the thermalization probabilities from the intermediate state to dot and ring, and ρ_D and ρ_R are the effective degeneracy ratios between intermediate state and dot and ring states, respectively (see the schematic energy diagram in Fig. 8.29). In steady state conditions and after simple algebraic manipulation:

$$R_{PL}(T) = \frac{n_R\Gamma_E^R}{n_D\Gamma_E^D} = \frac{\Gamma_R}{\Gamma_D}\frac{1 + \mu_D \exp[-\Delta E_D/k_BT]}{1 + \mu_R \exp[-\Delta E_R/k_BT]} \tag{8.5}$$

where $\mu_D = \Gamma_D\rho_D/\Gamma_E^D$ and $\mu_R = \Gamma_R\rho_R/\Gamma_E^R$

The relative thermalization probabilities of the ring and the dot at low temperature are given by (8.5): $R_{PL}(T = 0) = \Gamma_R/\Gamma_D$. The ring thermalization probability is larger than the dot one and related to the smaller number of intermediate states involved in the thermalization process. By fixing ΔE_D and ΔE_R to the calculated electron values and using $\mu_D = 170$ and $\mu_R = 2$ as fitting parameters, it is possible to reproduce the observed $R_{PL}(T)$ dependence on the temperature (red curve in Fig. 8.28b). In [106] the authors observe nearly two orders of magnitude difference between the dot and ring prefactors in (8.5) only partially due to the longer decay

time and lower thermalization probability of the dot respect to the ring. In this case a fundamental role is played in the dot-ring system carrier dynamics by the effective degeneracy ratios between intermediate state and dot and ring states.

8.6 Conclusions

The DE-quantum ring, disk and dot complexes are intriguing examples of designable, complex, topology controlled nanostructures and they can be devised and fabricated using the highly flexible DE process. Some examples of this large design flexibility in semiconductor nanostructure fabrication by DE are concentric multiple ring structures and coupled dot-rings. The growth mechanism is based on the control of Ga surface diffusion and As incorporation in tiny (nanometer size) Ga droplets formed in the first step of the DE process. Partial crystallization of the Ga contained in the droplets by pulsed As deposition at different conditions permits to obtain the different nanostructures which constitute the complex structures from the same droplet. Due to this multi-step kinetic controlled fabrication, DE-quantum rings are designable in size, shape and density.

Electronic structures of the DE-quantum nanostructures have been identified using an optical, non-contact approach. In the quantum rings, carriers are quantized along two orthogonal degrees of freedom: radial motion and rotational motion. Optical transition takes place on recombination of an electron and a heavy hole, being in the ground state of the ring and in the excited radial state. In concentric double quantum rings, emission originating from the outer and from the inner ring are observed distinctly. Results of effective-mass calculations well reproduce the emission spectra.

Since well separated quantum states are present in DE-quantum rings, optical transitions exhibiting antibunching features has been observed. Thus DE-quantum rings can be considered as an almost ideal quantum system. Circular nanostructures show a large variety of fascinating phenomena based on the quantum carrier confinement, of the utmost relevance for the possibility of their exploitation in the research of quantum computational devices.

As far as carrier dynamics is concerned, despite the small spatial separation between the different nanostructures constituting dot-ring or the double ring complexes, the carrier relaxation dynamics and the exciton kinetics in the different structures is decoupled at low temperature. The presence of the a temperature activated coupling channel has been demonstrated in the dot-rings. This thermally activated coupling can open up more possibilities in the application of dot-ring in the field of quantum information processing.

DE technique therefore enables to produce singly-addressable, self-assembled, topologically controlled, complex structures, including rings, dots and disks, that could pave the way to multiple two level states devices with switchable interaction.

Acknowledgements The authors gratefully acknowledge collaboration with K. Sakoda, M. Abbarchi, F. Biccari, S. Bietti, M. Gurioli, M. Guzzi, E. Grilli, G. Kido, X. Marie, F. Minami, C. Somaschini, B. Urbaszek, A. Vinattieri and K. Watanabe.

References

1. Y. Aharonov, D. Bohm, Phys. Rev. **115**(3), 485 (1959)
2. M. Grochol, F. Grosse, R. Zimmermann, Phys. Rev. B **74**(11), 115416 (2006)
3. W.H. Kuan, C.S. Tang, C.H. Chang, Phys. Rev. B **75**(15), 155326 (2007)
4. A. Lorke, R.J. Luyken, A.O. Govorov, J.P. Kotthaus, J.M. Garcia, P.M. Petroff, Phys. Rev. Lett. **84**(10), 2223 (2000)
5. A. Fuhrer, S. Lüscher, T. Ihn, T. Heinzel, K. Ensslin, W. Wegscheider, M. Bichler, Nature **413**(6858), 822 (2001)
6. L. Dias da Silva, J. Villas-Bôas, S. Ulloa, Phys. Rev. B **76**(15), 155306 (2007)
7. N. Kleemans, I. Bominaar-Silkens, V. Fomin, V. Gladilin, D. Granados, A. Taboada, J. García, P. Offermans, U. Zeitler, P. Christianen, J. Maan, J. Devreese, P. Koenraad, Phys. Rev. Lett. **99**(14), 146808 (2007)
8. L. Allen, M.W. Beijersbergen, R.J.C. Spreeuw, J.P. Woerdman, Phys. Rev. A **45**(11), 8185 (1992)
9. M. Padgett, R. Bowman, Nat. Photonics **5**(6), 343 (2011)
10. F. Araoka, T. Verbiest, K. Clays, A. Persoons, Phys. Rev. A **71**(5), 055401 (2005)
11. M.F. Andersen, C. Ryu, P. Cladé, V. Natarajan, A. Vaziri, K. Helmerson, W.D. Phillips, Phys. Rev. Lett. **97**(17), 170406 (2006)
12. N. Uribe-Patarroyo, A. Alvarez-Herrero, A.L. Ariste, A.A. Ramos, T. Belenguer, R.M. Sainz, C. LeMen, B. Gelly, Astron. Astrophys. **526**, A56 (2011)
13. A. Mair, A. Vaziri, G. Weihs, A. Zeilinger, Nature **412**(6844), 313 (2001)
14. M. Mirhosseini, O.S. Magaña-Loaiza, M.N. O'Sullivan, B. Rodenburg, M. Malik, M.P.J. Lavery, M.J. Padgett, D.J. Gauthier, R.W. Boyd, New J. Phys. **17**(3), 033033 (2015)
15. J.M. Garcia, G. Medeiros-Ribeiro, K. Schmidt, T. Ngo, J.L. Feng, A. Lorke, J. Kotthaus, P.M. Petroff, Appl. Phys. Lett. **71**(14), 2014 (1997)
16. D. Granados, J.M. Garcia, Appl. Phys. Lett. **82**(15), 2401 (2003)
17. S. Kobayashi, C. Jiang, T. Kawazu, H. Sakaki, Jpn. J. Appl. Phys. **43**(No. 5B), L662 (2004)
18. R. Timm, H. Eisele, a. Lenz, L. Ivanova, G. Balakrishnan, D. Huffaker, M. Dähne, Phys. Rev. Lett. **101**(25), 256101 (2008)
19. N. Koguchi, T. Satoshi, T. Chikyow, J. Cryst. Growth **111**, 688 (1991)
20. K. Watanabe, N. Koguchi, Y. Gotoh, Jpn. J. Appl. Phys. **39**(2), L79 (2000)
21. T. Kuroda, S. Sanguinetti, M. Gurioli, K. Watanabe, F. Minami, N. Koguchi, Phys. Rev. B **66**(12), 121302(R) (2002)
22. V. Mantovani, S. Sanguinetti, M. Guzzi, E. Grilli, M. Gurioli, K. Watanabe, N. Koguchi, J. Appl. Phys. **96**(8), 4416 (2004)
23. S. Sanguinetti, K. Watanabe, T. Tateno, M. Gurioli, P. Werner, M. Wakaki, N. Koguchi, J. Cryst. Growth **253**(1–4), 71 (2003)
24. S. Sanguinetti, M. Padovani, M. Gurioli, E. Grilli, M. Guzzi, a. Vinattieri, M. Colocci, P. Frigeri, S. Franchi, Appl. Phys. Lett. **77**(9), 1307 (2000)
25. D. Colombo, S. Sanguinetti, E. Grilli, M. Guzzi, L. Martinelli, M. Gurioli, P. Frigeri, G. Trevisi, S. Franchi, J. Appl. Phys. **94**(10), 6513 (2003)
26. S. Sanguinetti, M. Gurioli, E. Grilli, M. Guzzi, M. Henini, Appl. Phys. Lett. **77**(13), 1982 (2000)
27. S. Sanguinetti, T. Mano, M. Oshima, T. Tateno, M. Wakaki, N. Koguchi, Appl. Phys. Lett. **81**(16), 3067 (2002)

28. S. Sanguinetti, K. Watanabe, T. Tateno, M. Wakaki, N. Koguchi, T. Kuroda, F. Minami, M. Gurioli, Appl. Phys. Lett. **81**(4), 613 (2002)
29. M. Gurioli, S. Sanguinetti, M. Henini, Appl. Phys. Lett. **78**(7), 931 (2001)
30. T. Mano, T. Kuroda, K. Mitsuishi, Y. Nakayama, T. Noda, K. Sakoda, Appl. Phys. Lett. **93**, 203110 (2008)
31. T. Mano, M. Abbarchi, T. Kuroda, B. McSkimming, A. Ohtake, K. Mitsuishi, Y. Nakayama, T. Noda, K. Sakoda, Appl. Phys. Express **3**, 065203 (2010)
32. T. Mano, T. Kuroda, S. Sanguinetti, T. Ochiai, T. Tateno, J. Kim, T. Noda, M. Kawabe, K. Sakoda, G. Kido, N. Koguchi, Nano Lett. **5**(3), 425 (2005)
33. T. Kuroda, T. Mano, T. Ochiai, S. Sanguinetti, K. Sakoda, G. Kido, N. Koguchi, Phys. Rev. B **72**(20), 205301 (2005)
34. M. Yamagiwa, T. Mano, T. Kuroda, T. Tateno, K. Sakoda, G. Kido, N. Koguchi, F. Minami, Appl. Phys. Lett. **89**(11), 113115 (2006)
35. K.a. Sablon, J.H. Lee, Z.M. Wang, J.H. Shultz, G.J. Salamo, Appl. Phys. Lett. **92**(20), 203106 (2008)
36. Z.M. Wang, B. Liang, K.A. Sablon, J. Lee, Y.I. Mazur, N.W. Strom, G.J. Salamo, Small **3**(2), 235 (2007)
37. T. Mano, T. Kuroda, K. Mitsuishi, M. Yamagiwa, X.J. Guo, K. Furuya, K. Sakoda, N. Koguch, J. Cryst. Growth **301–302**, 740 (2007)
38. T. Mano, T. Kuroda, K. Kuroda, K. Sakoda, J. Nanophoton. **3**, 031605 (2009)
39. N. Pankaow, S. Thainoi, S. Panyakeow, S. Ratanathammaphan, J. Cryst. Growth **323**(1), 282 (2011)
40. W. Jevasuwan, P. Boonpeng, S. Panyakeow, S. Ratanathammaphan, Microelectron. Eng. **87**(5–8), 1416 (2010)
41. N. Pankaow, S. Panyakeow, S. Ratanathammaphan, J. Cryst. Growth **311**(7), 1832 (2009)
42. C. Zhao, Y.H. Chen, B. Xu, C.G. Tang, Z.G. Wang, F. Ding, Appl. Phys. Lett. **92**(6), 063122 (2008)
43. T. Noda, T. Mano, M. Jo, T. Kawazu, H. Sakaki, J. Appl. Phys. **112**(6), 063510 (2012)
44. P. Alonso-Gonzalez, L. Gonzalez, D. Fuster, Y. Gonzalez, A.G. Taboada, J.M. Ripalda, A.M. Beltran, D.L. Sales, T. Ben, S.I. Molina, Cryst. Growth Des. **9**, 1216 (2009)
45. T. Noda, T. Mano, Appl. Surf. Sci. **254**(23), 7777 (2008)
46. C. Somaschini, S. Bietti, N. Koguchi, S. Sanguinetti, Nano Lett. **9**(10), 3419 (2009)
47. C. Somaschini, S. Bietti, N. Koguchi, S. Sanguinetti, Nanotechnology **22**(18), 185602 (2011)
48. C. Somaschini, S. Bietti, S. Sanguinetti, N. Koguchi, A. Fedorov, Nanotechnology **21**(12), 125601 (2010)
49. C. Somaschini, S. Bietti, A. Scaccabarozzi, E. Grilli, S. Sanguinetti, Cryst. Growth Des. **12**(3), 1180 (2012)
50. Z.M. Wang, B.L. Liang, K.a. Sablon, G.J. Salamo. Appl. Phys. Lett. **90**(11), 113120 (2007)
51. A. Ohtake, Surf. Sci. Rep. **63**(7), 295 (2008)
52. T. Mano, N. Koguchi, J. Cryst. Growth **278**(1–4), 108 (2005)
53. T. Mano, M. Abbarchi, T. Kuroda, C.A. Mastrandrea, A. Vinattieri, S. Sanguinetti, K. Sakoda, M. Gurioli, Nanotechnology **20**(39), 395601 (2009)
54. M. Jo, G. Duan, T. Mano, K. Sakoda, Nanoscale Res. Lett. **6**(1), 76 (2011)
55. S. Bietti, C. Somaschini, S. Sanguinetti, N. Koguchi, G. Isella, D. Chrastina, Appl. Phys. Lett. **95**(24), 241102 (2009)
56. A. Ohtake, N. Koguchi, Appl. Phys. Lett. **83**(25), 5193 (2003)
57. K. Ohta, T. Kojima, T. Nakagawa, J. Cryst. Growth **95**, 71 (1989)
58. A. Ohtake, P. Kocán, K. Seino, W. Schmidt, N. Koguchi, Phys. Rev. Lett. **93**(26), 266101 (2004)
59. K. Kanisawa, J. Osaka, S. Hirono, N. Inoue, Appl. Phys. Lett. **58**(May), 2363 (1991)
60. S. Bietti, C. Somaschini, L. Esposito, A. Fedorov, S. Sanguinetti, J. Appl. Phys. **116**(11) (2014)
61. Z.Y. Zhou, C.X. Zheng, W.X. Tang, J. Tersoff, D.E. Jesson, Phys. Rev. Lett. **111**(3), 036102 (2013)

62. C. Somaschini, S. Bietti, A. Fedorov, N. Koguchi, S. Sanguinetti, Nano. Res. Lett. **5**(12), 1897 (2010)
63. S. Sanguinetti, C. Somaschini, S. Bietti, N. Koguchi, Nanomater. Nanotechnol. **1**(1), 14 (2011)
64. N. Koguchi, K. Ishige, J. Vac. Sci. Technol. B **11**(3), 787 (1993)
65. S. Bietti, C. Somaschini, S. Sanguinetti, Nanotechnology **24**, 205603 (2013)
66. S. Bietti, C. Somaschini, L. Esposito, A. Fedorov, S. Sanguinetti, J. Appl. Phys. **116**(11), 114311 (2014)
67. S. Bietti, J. Bocquel, S. Adorno, T. Mano, J.G. Keizer, P.M. Koenraad, S. Sanguinetti, Phys. Rev. B **92**(7), 075425 (2015)
68. C. Somaschini, S. Bietti, A. Fedorov, N. Koguchi, S. Sanguinetti, Nanoscale Res. Lett. **5**(12), 1865 (2010)
69. J.Y. Marzin, G. Bastard, Solid State Commun. **92**(5), 437 (1994)
70. M. Califano, P. Harrison, Phys. Rev. B **61**(16), 10959 (2000)
71. J.W. Luo, G. Bester, A. Zunger, Phys. Rev. B **79**(12), 125329 (2009)
72. R. Heitz, H. Born, F. Guffarth, O. Stier, A. Schliwa, A. Hoffmann, D. Bimberg, Phys. Status Solidi **190**(2), 499 (2002)
73. O. Stier, M. Grundmann, D. Bimberg, Phys. Rev. B **59**(8), 5688 (1999)
74. S. Sanguinetti, K. Watanabe, T. Kuroda, F. Minami, Y. Gotoh, N. Koguchi, J. Cryst. Growth **242**(3–4), 321 (2002)
75. S. Bietti, C. Somaschini, E. Sarti, N. Koguchi, S. Sanguinetti, G. Isella, D. Chrastina, A. Fedorov, Nano. Res. Lett. **5**, 1650–1653 (2010)
76. W. Rodrigues, M. Auf Der Maur, A. Di Carlo, D. Barettin, A. Pecchia, S. Sanguinetti, in *15th IEEE International Conference on Nanotechnology* (2015), p. 809. https://doi.org/10.1109/NANO.2015.7388735
77. T. Tsuchiya, S. Katayama, Solid State Electron. **42**, 1523 (1998)
78. M. Abbarchi, T. Kuroda, T. Mano, K. Sakoda, C.A. Mastrandrea, A. Vinattieri, M. Gurioli, T. Tsuchiya, Phys. Rev. B **82**(20), 201301(R) (2010)
79. J.G. Keizer, J. Bocquel, P.M. Koenraad, T. Mano, T. Noda, K. Sakoda, Appl. Phys. Lett. **96**(6), 062101 (2010)
80. S. Sanguinetti, T. Mano, A. Gerosa, C. Somaschini, S. Bietti, N. Koguchi, E. Grilli, M. Guzzi, M. Gurioli, M. Abbarchi, J. Appl. Phys. **104**(11), 113519 (2008)
81. S. Bietti, C. Somaschini, M. Abbarchi, N. Koguchi, S. Sanguinetti, E. Poliani, M. Bonfanti, M. Gurioli, A. Vinattieri, T. Kuroda, T. Mano, K. Sakoda, Phys. Status Solidi (C) **6**(4), 928 (2009)
82. C. Somaschini, S. Bietti, S. Sanguinetti, N. Koguchi, A. Fedorov, M. Abbarchi, M. Gurioli, in *IOP Conference Series: Materials Science and Engineering*, vol. 6 (2009), p. 012008
83. M. Bissiri, G. Baldassarri, Höger Von Högersthal, M. Capizzi, P. Frigeri, S. Franchi. Phys. Rev. B **64**(24), 245337 (2001)
84. A.S. Bhatti, M. Capizzi, A. Frova, M. Bissiri, G. Baldassarri, Höger Von Högersthal, P. Frigeri, S. Franchi. Phys. Rev. B **62**(7), 4642 (2000)
85. R. Heitz, I. Mukhametzhanov, O. Stier, A. Madhukar, D. Bimberg, Phys. Rev. Lett. **83**, 4654 (1999)
86. R. Heitz, M. Grundmann, N.N. Ledentsov, L. Eckey, M. Veit, D. Bimberg, Appl. Phys. Lett. **68**(3), 361 (1996)
87. S. Sanguinetti, D. Colombo, M. Guzzi, E. Grilli, M. Gurioli, L. Seravalli, P. Frigeri, S. Franchi, Phys. Rev. B **74**(20), 1 (2006)
88. R.J. Warburton, C. Schaflein, D. Haft, F. Bickel, A. Lorke, K. Karrai, J. Garcia, W. Schoenfeld, P. Petroff, Nature **405**(6789), 926 (2000)
89. M. Abbarchi, F. Troiani, C. Mastrandrea, G. Goldoni, T. Kuroda, T. Mano, K. Sakoda, N. Koguchi, S. Sanguinetti, A. Vinattieri, M. Gurioli, Appl. Phys. Lett. **93**(16), 162101 (2008)
90. S. Sanguinetti, M. Abbarchi, A. Vinattieri, M. Zamfirescu, M. Gurioli, T. Mano, T. Kuroda, N. Koguchi, Phys. Rev. B **77**(12), 125404 (2008)
91. E. Dekel, D. Gershoni, E. Ehrenfreund, J.M. Garcia, P.M. Petroff, Phys. Rev. B **61**(16), 11009 (2000)

92. E. Dekel, D.V. Regelman, D. Gershoni, E. Ehrenfreund, Phys. Rev. B **62**(16), 11038 (2000)
93. A. Feltrin, J.L. Staehli, B. Deveaud, V. Savona, Phys. Rev. B **233309**, 233309 (2004)
94. T. Kuroda, T. Mano, T. Belhadj, B. Urbaszek, T. Amand, X. Marie, S. Sanguinetti, K. Sakoda, N. Koguchi, Phys. Status Solidi (B) **246**(4), 861 (2009)
95. M. Abbarchi, T. Kuroda, T. Mano, K. Sakoda, M. Gurioli, Phys. Rev. B **81**(3), 035334 (2010)
96. A.O. Govorov, S.E. Ulloa, K. Karrai, R.J. Warburton, Phys. Rev. B **66**(8), 081309 (2002)
97. V. Savona, J. Phys.: Condens. Matter **19**(29), 295208 (2007)
98. C. Becher, a. Kiraz, P. Michler, a. Imamolu, W. Schoenfeld, P. Petroff, L. Zhang, E. Hu, Phys. Rev. B **63**(12), 1 (2001)
99. T. Kuroda, M. Abbarchi, T. Mano, K. Watanabe, M. Yamagiwa, K. Kuroda, K. Sakoda, G. Kido, N. Koguchi, C. Mastrandrea, L. Cavigli, M. Gurioli, Y. Ogawa, F. Minami, Appl. Phys. Express **1**, 042001 (2008)
100. T. Kuroda, T. Belhadj, M. Abbarchi, C. Mastrandrea, M. Gurioli, T. Mano, N. Ikeda, Y. Sugimoto, K. Asakawa, N. Koguchi, K. Sakoda, B. Urbaszek, T. Amand, X. Marie, Phys. Rev. B **79**(3), 035330 (2009)
101. M. Abbarchi, C. Mastrandrea, A. Vinattieri, S. Sanguinetti, T. Mano, T. Kuroda, N. Koguchi, K. Sakoda, M. Gurioli, Phys. Rev. B **79**(8), 085308 (2009)
102. R. Loudon, *The Quantum Theory of Light* (Oxford University Press, New York, 1983)
103. M. Abbarchi, L. Cavigli, C. Somaschini, S. Bietti, M. Gurioli, A. Vinattieri, S. Sanguinetti, Nano. Res. Lett. **6**(1), 569 (2011)
104. M. Abbarchi, M. Gurioli, S. Sanguinetti, M. Zamfirescu, A. Vinattieri, N. Koguchi, Phys. Status Solidi (C) **3**(11), 3860 (2006)
105. L. Cavigli, S. Bietti, M. Abbarchi, C. Somaschini, A. Vinattieri, M. Gurioli, A. Fedorov, G. Isella, E. Grilli, S. Sanguinetti, J. Phys.: Condens. Matter **24**(10), 104017 (2012)
106. F. Biccari, S. Bietti, L. Cavigli, A. Vinattieri, R. Nötzel, M. Gurioli, S. Sanguinetti, J. Appl. Phys. **120**(13), 134312 (2016)
107. S. Sanguinetti, T. Kuroda, M. Gurioli, K. Watanabe, Y. Gotoh, F. Minami, N. Koguchi, Phys. Status Solidi (a) **190**(2), 589 (2002)
108. L. Brusaferri, S. Sanguinetti, E. Grilli, M. Guzzi, A. Bignazzi, F. Bogani, L. Carraresi, M. Colocci, A. Bosacchi, P. Frigeri, S. Franchi, Appl. Phys. Lett. **69**(22), 3354 (1996)
109. S. Sanguinetti, M. Henini, M. Grassi Alessi, M. Capizzi, P. Frigeri, S. Franchi, Phys. Rev. B **60**(11), 8276 (1999)

Part III
Optical Aharonov-Bohm Effect

Chapter 9
Optical Aharonov-Bohm Oscillations with Disorder Effects and Wigner Molecule in a Single GaAs/AlGaAs Quantum Ring

K. Kyhm, H.D. Kim, R. Okuyama, M. Eto, K.C. Je, R.A. Taylor, G. Nogues, L.S. Dang, A.A.L. Nicholet, M. Potemski, J.S. Kim and J.D. Song

Abstract The optical Aharonov-Bohm effect in a single quantum ring is associated with disorder effects. In the presence of structure anisotropy, localisation, internal electric field, and impurity scattering, optical Aharonov-Bohm oscillations of an electron-hole pair become modulated. Additionally, provided that a strongly correlated exciton pair is formed in a single quantum ring similar to the Wigner molecule, novel oscillations can be observed for increasing magnetic field. In this case, the biexciton emission energy changes abruptly at transition magnetic fields with a fractional oscillation period compared to that of the exciton, the so-called fractional optical Aharonov-Bohm oscillations.

9.1 Introduction

The Aharonov-Bohm (AB) effect in quantum rings (QRs) is observed mostly by electrical measurements at extremely low temperatures ($\sim$100 mK) through oscillations of the conductance and persistent current with external magnetic field [1–6]. Very recently, the AB effect became accessible to optical experiments at tens of Kelvin by using type-II quantum dots (QDs) and nanoscale quantum rings. While either individual electron or hole rotation in the shell results in the optical AB effect in type-II QDs, both electrons and holes are involved for a QR. Since most of the optical AB effects were measured in ensembles of QRs and type-II QDs, inhomogeneities arising from the size distribution and the morphology lead to the energy variation of $\sim 10^2$ meV, which is far larger than the energy variation of excitonic AB oscillations ($\sim 10^{-1}$ meV). Since this limits the ability to uncover the underlying physics of a single electron-hole pair, optical AB oscillations need to be measured in a single QR. However, the exciton Aharonov-Bohm oscillations in a single quantum ring are rarely observed. This difficulty is associated with localisation due to

K. Kyhm (✉) · H.D. Kim
Department of Opto-mechatronics,
Pusan National University, Busan 462-41, South Korea
e-mail: kskyhm@pusan.ac.kr

V.M. Fomin (ed.), *Physics of Quantum Rings*, NanoScience and Technology,
https://doi.org/10.1007/978-3-319-95159-1_9

the volcano-like anisotropic structure. Regarding large lateral diameters of droplet structures, the spectral inhomogeneity is dominated by morphology. Additionally, an internal electric field and an impurity scattering are also involved to the AB oscillations. From a general perspective, this is of importance for understanding the AB effect in disordered systems.

H.D. Kim
e-mail: Heedaekim3@googlemail.com

K. Kyhm · H.D. Kim
Department of Physics Education,
Pusan National University, Busan 462-41, South Korea

R. Okuyama · M. Eto
Faculty of Science and Technology,
Keio University, Yokohama 223-8522, Japan
e-mail: rokuyama@rk.phys.keio.ac.jp

M. Eto
e-mail: eto@rk.keio.ac.jp

K.C. Je
Department of Physics, Saints Cyril and Methodius University,
Skopje 1000, Republic of Macedonia
e-mail: jekoochul@gmail.com

R.A. Taylor
Clarendon Laboratory, Department of Physics,
University of Oxford, Oxford OX1 3PU, UK
e-mail: robert.taylor@physics.ox.ac.uk

G. Nogues · L.S. Dang
Department of NANO Science,
Institute Néel CNRS, Grenoble 38045, France
e-mail: gilles.nogues@neel.cnrs.fr

L.S. Dang
e-mail: lesidang@neel.cnrs.fr

A.A.L. Nicholet · M. Potemski
Laboratoire Natioal des Champs
Magnetiques Intenses, Magnetiques Intenses, CNRS-UJF-UPS-INSA,
Grenoble 38042, France
e-mail: aurelien.nicolet@lncmi.cnrs.fr

M. Potemski
e-mail: potemski@lncmi.cnrs.fr

J.S. Kim
Department of Physics, Yeungnam University,
Gyeongsan 712-749, South Korea
e-mail: jongsukim@ynu.ac.kr

J.D. Song
Center for Optoelectronic Convergence System, KIST,
Seoul 136-791, South Korea
e-mail: Jdsong72@gmail.com

Three important disorder effects associated with the optical AB effect in a single QR will be introduced. First, the anisotropy of a QR gives rise to a characteristic magnetic field, where the onset of circumferential phase coherence overcomes wavefunction localisation. Secondly, when internal fields are present in a QR, the AB oscillations become modulated. This may open a new way of quantum state control in a QR by using both electric and magnetic fields [7–9]. Thirdly, an anti-splitting of the photoluminescence spectrum at the transition magnetic field was also observed as a consequence of a break-down in the rotational symmetry due to anisotropy and localised impurities.

Additionally, an optical analogy of the correlation effect in a QR has been investigated in terms of the biexcitonic fractional AB effect. As the electronic correlation becomes enhanced in a one-dimensional structure, a pair of electrons can behave as a single composite particle under certain conditions, giving rise to the so-called Wigner molecule (WM). In this case, the AB oscillation period becomes fractional compared to that of a single electron, termed the fractional AB effect [10–16]. For the optical analogy, a pair of the interacting excitons (biexcitons) located at opposite positions in a QR forms a WM. In this case, novel saw-like oscillations can be observed [17, 18], where the emission energy changes abruptly at a transition magnetic field with a fractional oscillation period compared to that of the exciton, giving rise to fractional optical AB oscillations. In particular, it is of great importance, as the Wigner localisation provides the novel fundamental many-body physics associated with the correlation effect.

9.2 Experiment

The nanoscale quantum rings were grown in Riber Compact21 MBE system. After thermal removal of any surface oxide on the GaAs under an As tetramer ambience of 620 °C, a ∼100 nm-thick GaAs buffer layer was grown at 580 °C. 20 pairs of (61.35 nm-thick AlAs and 53.2 nm-thick $Al_{0.31}GaAs$) and 53.2 nm-thick $Al_{0.31}GaAs$ were grown successively. The substrate temperature was then cooled to 310 °C and the supply of As tetramer was disconnected until the partial pressure of As and the pressure of the main chamber became less than 1×10^{-11} Torr and 1.5×10^{-9} Torr, respectively. Ga metal was introduced on the substrate in this clean state of the chamber, equivalent to 1 monolayer of GaAs. In this state, the density of Ga droplets was $\sim 7 \times 10^8\,cm^{-2}$. After As tetramer introduction at a beam equivalent pressure of 1.25×10^{-7} Torr at 200 °C, the Ga droplets changed into GaAs quantum ring structures. A 53.2 nm-thick layer of $Al_{0.31}GaAs$ was then grown on the rings. Finally, the whole structure was annealed in the chamber under an As tetramer ambient of beam equivalent pressure of 3.00×10^{-6} Torr at 600 °C for 1 h.

The micro-photoluminescence (PL) spectrum of a single NQR was measured at 4.2 K using a confocal arrangement, where the PL spectrum was measured by charge coupled device under the excitation of frequency-doubled (400 nm) Ti:sapphire laser pulse (120 fs pulse duration at a 80 MHz repetition rate). Magneto-PL from a single

NQR was also performed in a resistive DC magnet (52 mm-bore diameter), where a miniaturised optical alignment system was installed and the sample position was controlled by a piezoelectric stage. Excitation by a continuous-wave Ar^{+}-ion laser (488 nm) was introduced to the sample through a multi-mode fiber, and the PL was detected through another single-mode optical fiber.

9.3 Theoretical Model for Optical Aharonov-Bohm Oscillations

For the theoretical model of a quasi one-dimensional QR, the radial confinement needs to be considered by regarding the finite rim width. This model enables to obtain the eigenenergy levels and the two-body density for the exciton and biexciton by using the exact diagonalisation method, where a Coulomb interaction between the electron and the hole was also considered in the presence of an external magnetic field ($B = B\hat{z}$) applied perpendicular to the lateral xy plane of a QR. When the isotropic confinement potential is assumed as an ideal theoretical reference, this will be compared with experimental results, where the anisotropy effect of a volcano-like QR is present. While experimental AB oscillations of our QR emerge beyond a characteristic magnetic field (B_c), theoretical AB oscillations begin from $B = 0$. Therefore, the theoretical results can be used as a reference to measure a magnetic field difference (δB) for the AB oscillation extremum between theory and experiment, whereby the modulated AB oscillations in a real NQR is defined in this context.

Different orbital radii of the electron (R_e) and the hole (R_h) can be used in order to consider charge separation effects for the electron and hole, which are known to be crucial for optical AB oscillations to emerge [19–21]. Suppose the electron and hole of a QR are confined in an anharmonic potential along the radial direction, tunneling towards the direction away from the ring center should be different for an electron and a hole due to the mass difference. Also, any asymmetry of the confinement potential likely gives rise to a so-called radially polarised electron-hole pair, whereby the electron and hole rotate along the different orbits. There are various other effects which possibly result in a radially-polarised electron-hole pair in a QR such as the deformation potential with a large difference in the conduction and valence bands, the built-in electric field, and the local electric field arising from the charge-trapped interface defects. Therefore, it is plausible to assume different orbital radii for the electrons and holes ($R_e \neq R_h$) to describe the charge separation effect. When indium ingredients are present, strain effects are known to localise the hole toward the ring center [22], whereas the electron resides within the rim width. However, in the case of GaAs, the local electric field arising from the charge-trapped defects is a possible origin for the charge separation. As the charge separation is inevitable, we assume the orbital radius of the electron is larger than that of the hole ($R_e > R_h$). Nevertheless, this model is still incomplete as experimental clarification has yet to be accomplished for the separation between the electron and hole.

Suppose N_e electrons and N_h holes are given in a single QR, the effective mass Hamiltonian can be given by $H = H_e + H_h + V_C$,

$$H_{\mathrm{e}} = \sum_{j=1}^{N_{\mathrm{e}}} \left\{ \frac{[p_{\mathrm{e},j} + eA(r_{\mathrm{e},j})]^2}{2m_{\mathrm{e}}} + V_{\mathrm{e}}(r_{\mathrm{e},j}) + \frac{1}{2}E_{\mathrm{g}} + g_{\mathrm{e}}\mu_{\mathrm{B}} S^z_{\mathrm{e},j} B \right\}, \tag{9.1}$$

$$H_{\mathrm{h}} = \sum_{j=1}^{N_{\mathrm{h}}} \left\{ \frac{[p_{\mathrm{h},j} - eA(r_{\mathrm{h},j})]^2}{2m_{\mathrm{h}}} + V_{\mathrm{h}}(r_{\mathrm{h},j}) + \frac{1}{2}E_{\mathrm{g}} + g_{\mathrm{h}}\mu_{\mathrm{B}} S^z_{\mathrm{h},j} B \right\}, \tag{9.2}$$

$$V_{\mathrm{C}} = \sum_{1\le j<k\le N_{\mathrm{e}}} \frac{e^2}{4\pi\epsilon|r_{\mathrm{e},j} - r_{\mathrm{e},k}|} + \sum_{1\le j<k\le N_{\mathrm{h}}} \frac{e^2}{4\pi\epsilon|r_{\mathrm{h},j} - r_{\mathrm{h},k}|} - \sum_{j=1}^{N_{\mathrm{e}}}\sum_{k=1}^{N_h} \frac{e^2}{4\pi\epsilon|r_{\mathrm{e},j} - r_{\mathrm{h},k}|}, \tag{9.3}$$

with $A(r) = (1/2)B \times r$. H_{e} (H_{h}) is the Hamiltonian for non-interacting electrons (holes), whereas V_{C} describes the Coulomb interaction. m_α and g_α are the effective mass and g-factor for electrons ($\alpha = \mathrm{e}$) and holes ($\alpha = \mathrm{h}$), respectively. E_{g}, ϵ, and μ_{B} are the band gap, the dielectric constant, and the Bohr magneton, respectively. One can use $m_{\mathrm{e}} = 0.067m_0$, $m_{\mathrm{h}} = 0.51m_0$, and the effective Bohr radius $a_{\mathrm{B}} = 4\pi\epsilon\hbar^2/(\mu e^2) = 12$ nm with $\mu^{-1} = m_{\mathrm{e}}^{-1} + m_{\mathrm{h}}^{-1}$ for GaAs. The g-factors for electrons (g_{e}) and holes (g_{h}) are associated with the observable excitonic g-factor ($g_{\mathrm{X}} = g_{\mathrm{e}} - g_{\mathrm{h}} = -1.3$). The anharmonic confinement potential energy $V_\alpha(r)$ is given by [23]

$$V_\alpha(r) = \frac{\hbar^2\lambda_\alpha^2}{2m_\alpha r^2} + \frac{1}{2}m_\alpha\omega_\alpha^2 r^2. \tag{9.4}$$

Using $\lambda_\alpha = (1/2)(R_\alpha/W_\alpha)^2$ and $\omega_\alpha = \hbar/(2m_\alpha W_\alpha^2)$, this can be approximated as

$$V_\alpha(r) = \frac{\hbar^2}{2m_\alpha W_\alpha^2}\left[\frac{1}{4}\left(\frac{R_\alpha}{W_\alpha}\right)^2 + \left(\frac{r - R_\alpha}{W_\alpha}\right)^2 + \mathscr{O}\left(\frac{r - R_\alpha}{W_\alpha}\right)^3\right]. \tag{9.5}$$

Therefore, $V_{\alpha=\mathrm{e,h}}(r)$ describes a quasi one-dimensional isotropic confinement potential energy with orbital radius R_α and confinement width W_α. Since R_{e} and R_{h} are much larger than the atomic scale, the effective mass approximation is still valid. For simplicity, this model considers only the heavy-hole state, which means the mixing between the heavy-hole and light-hole states is ignored.

Note that $V_{\alpha=\mathrm{e,h}}(r)$ is a lateral confinement potential energy. In order to explain the energy of the X PL spectrum near $\sim$1.732 eV, the vertical confinement energy of a QR structure also needs to be considered by regarding the AFM height profile. Because the lateral size of our QR is larger than the vertical size, similar to the case of a pancake, the vertical confinement energy can be separated according to the adiabatic approximation [24, 25]. The so-called adiabatic potential obtained through this approximation corresponds to $V_{\alpha=\mathrm{e,h}}(r)$, which also represents the morphology of a QR. Therefore, the vertical confinement energy gives an energy offset of

$V_{\alpha=\mathrm{e,h}}(r)$ with respect to the conduction and valence band edge of bulk GaAs, respectively. For ∼10, nm height of our QR, the total vertical confinement energy for an electron-hole pair is ∼194.1 meV. With rough estimation of the Coulomb interaction by $\frac{e^2}{4\pi\epsilon|R_\mathrm{e}-R_\mathrm{h}|} \sim 6\,\mathrm{meV}$, the energy of the observed X PL spectrum near ∼1.732 eV can be explained. Therefore, this is the case that both lateral and vertical confinement energy are larger than the Coulomb interaction. However, our calculation is not the case of single-particle states with Coulomb corrections. The many-body correlation is fully taken into account. The many-body states can be expanded by the single-particle states. In this case, a large number of the single-particle states are required for calculation to converge. It has confirmed that the truncation error becomes negligibly small with few thousands of the single-particle states.

For the single-particle states ($H_{\alpha=\mathrm{e,h}}$) of a QR in the presence of an external magnetic field, the eigenenergy and eigenfunction can be obtained analytically as [26]

$$E_{\alpha,n,m} = \frac{\hbar^2}{2m_\alpha W_\alpha^2}\left\{\frac{1}{2}\left[\left(\frac{R_\alpha}{W_\alpha}\right)^4 + m^2\right]^{1/2} + 2n + 1\right\}\left[1 + 4\left(\frac{W_\alpha}{R_\alpha}\right)^4\phi_\alpha^2\right]^{1/2} - \frac{\hbar^2\phi_\alpha m}{m_\alpha R_\alpha^2} + \frac{1}{2}E_\mathrm{g}, \tag{9.6}$$

$$\psi_{\alpha,n,m}(r) = \left[\frac{n!}{\pi\Gamma(\mu_{\alpha,m}+n+1)}\right]^{1/2}\frac{1}{\Omega_\alpha}\left(\frac{r}{\Omega_\alpha}\right)^{\mu_{\alpha,m}} \mathrm{e}^{-r^2/(2\Omega_\alpha^2)} P_n^{\mu_{\alpha,m}}\left(\frac{r^2}{\Omega_\alpha^2}\right)\mathrm{e}^{\mathrm{i}m\theta}, \tag{9.7}$$

for angular momentum $m = 0, \pm1, \pm2, \ldots$ and radial quantum number $n = 0, 1, 2, \ldots$ with $P_j^k(x)$ being the associated Laguerre polynomials and

$$\phi_\alpha = \mp\frac{\pi R_\alpha^2 B}{h/e}, \quad \mu_{\alpha,m} = \frac{1}{2}\left[\left(\frac{R_\alpha}{W_\alpha}\right)^4 + 4m^2\right]^{1/2}, \tag{9.8}$$

$$\Omega_\alpha = \sqrt{2}W_\alpha\left[1 + 4\left(\frac{W_\alpha}{R_\alpha}\right)^4\phi_\alpha^2\right]^{-1/4}. \tag{9.9}$$

Using these states, the Hamiltonian H can be diagonalised numerically, and the matrix elements of the Coulomb interaction were evaluated analytically by the use of the multipole expansion. As $(R_\alpha/W_\alpha)^2 \gg 1$, only the states with $n = 0$ is considered. The states with $n > 0$ hardly modify the calculated results.

Finally, the exciton eigenenergies ($E_\mathrm{X}^L(B)$) for total exciton orbital angular momenta (L) were obtained as a function of the external magnetic field (B). When the excitonic Zeeman effect is considered with the exciton g-factor (g_X), the two exciton PL peak energy of spin-parallel ($E_\mathrm{X}^{\sigma^+}$) and anti-parallel ($E_\mathrm{X}^{\sigma^-}$) can be given as

$$E_{\mathrm{X-PL}}^{\sigma^\pm}(B) = E_\mathrm{X}^L(B) \mp \frac{1}{2}g_\mathrm{X}\mu_\mathrm{B}B, \tag{9.10}$$

where $E_\mathrm{X}^L(B)$ is the lowest energy among various L at a certain B to minimise $E_{\mathrm{X-PL}}^{\sigma^\pm}(B)$. Also, the theoretical $E_\mathrm{X}^L(B)$ can be compared with the measured

$E^{\sigma^{\pm}}_{\mathrm{X-PL}}(B)$ as

$$E^{L}_{\mathrm{X}}(B) = [E^{\sigma^{+}}_{\mathrm{X-PL}} + E^{\sigma^{-}}_{\mathrm{X-PL}}]/2. \tag{9.11}$$

Likewise, the XX eigenenergy ($E^{L}_{\mathrm{XX}}(B)$) of total exciton orbital angular momenta (L) were obtained as a function of the external magnetic field (B) through an exact diagonalisation method by taking into account the Coulomb interaction amongst the two electrons and two holes. For a XX, our model conserves the electron and hole spins, separately as $\mathbf{S}_{\mathrm{e}} = \mathbf{S}_{\mathrm{e1}} + \mathbf{S}_{\mathrm{e2}}$ and $\mathbf{S}_{\mathrm{h}} = \mathbf{S}_{\mathrm{h1}} + \mathbf{S}_{\mathrm{h2}}$. Thus, the 4-particle Hilbert space can be split into 4 sectors, i.e., (electron singlet) × (hole singlet), (electron singlet) × (hole triplet), (electron triplet) × (hole singlet), and (electron triplet) × (hole triplet). This method drastically reduces calculation costs. For each sector, we used 500 low-lying states to diagonalize the Hamiltonian with the Coulomb interaction. For comparison, we also diagonalized it with 1,000 states, and confirmed that the truncation error in the total energy is less than 0.1%.

When considering the biexciton emission between $E^{L}_{\mathrm{XX}}(B)$ and $E^{L}_{\mathrm{X}}(B)$, the oscillation period for the minimum $E^{L}_{\mathrm{XX}}(B)$ with B is shorter than that for the minimum $E^{L}_{\mathrm{X}}(B)$. The selection rule adds a restriction such that the emission only occurs when $E^{L}_{\mathrm{XX}}(B)$ and $E^{L}_{\mathrm{X}}(B)$ have the same L. For example, when the biexciton energy changes from $E^{L=0}_{\mathrm{XX}}$ to $E^{L=1}_{\mathrm{XX}}$ with increasing B, $E^{L=0}_{\mathrm{X}}$ is still less than $E^{L=1}_{\mathrm{X}}$. Therefore, an emission between $E^{L=1}_{\mathrm{XX}}$ and $E^{L=0}_{\mathrm{X}}$ gives the minimum biexciton PL energy. However, this is not the case. The emission occurs between $E^{L=1}_{\mathrm{XX}}$ and $E^{L=1}_{\mathrm{X}}$ due to the selection rules. Consequently, an abrupt decrease of the XX PL energy can be measured at the transition magnetic field, where the biexciton changes its L from 0 to 1 (Fig. 9.7c, d).

Given the observed AB oscillation period of excitons ($\Delta B_{\mathrm{X}} \sim 1.8\,\mathrm{T}$) in a GaAs QR, we found the optimum parameters of $R_{\mathrm{e}} = 32\,\mathrm{nm}$, $R_{\mathrm{h}} = 15\,\mathrm{nm}$, and $W_{\mathrm{e}} = W_{\mathrm{h}} = 5\,\mathrm{nm}$ to reproduce the same AB oscillation period of excitons theoretically. On the other hand, for a biexciton, we found the confinement parameters (R'_{e}, R'_{h}, W'_{e}, W'_{h}) should be 1.4 times those for exciton. When a single particle is confined, $V_{\alpha}(r)$ is determined by geometric structure. However, interaction among the N_{e} electrons and N_{h} holes can also modify $V_{\alpha}(r)$ as well as the band gap E_{g} through the electron-electron and hole-hole repulsion with re-distribution of the surrounding electrons and holes. Therefore, the relatively large values in the parameters (R'_{e}, R'_{h}, W'_{e}, W'_{h}) effectively describe the modified $V'_{\mathrm{e,h}}(r, N_{\mathrm{e,h}})$.

We also calculate the two-body densities,

$$\rho_{\mathrm{ee}}(x_{\mathrm{e}}|X_{\mathrm{e}}) = \tfrac{1}{2}\sum_{\sigma,\sigma'}\left\langle \hat{\psi}^{\dagger}_{\mathrm{e},\sigma}(x_e)\hat{\psi}^{\dagger}_{\mathrm{e},\sigma'}(X_e)\hat{\psi}_{\mathrm{e},\sigma'}(X_e)\hat{\psi}_{\mathrm{e},\sigma}(x_e)\right\rangle, \tag{9.12}$$

$$\rho_{\mathrm{he}}(x_{\mathrm{h}}|X_{\mathrm{e}}) = \sum_{\sigma,\sigma'}\left\langle \hat{\psi}^{\dagger}_{\mathrm{h},\sigma}(x_h)\hat{\psi}_{\mathrm{h},\sigma}(x_h)\hat{\psi}^{\dagger}_{\mathrm{e},\sigma'}(X_e)\hat{\psi}_{\mathrm{e},\sigma'}(X_e)\right\rangle, \tag{9.13}$$

that are the probabilities to find an electron at x_{e} and a hole at x_{h}, respectively, with an electron fixed at X_{e}. Here, $\hat{\psi}_{\mathrm{e},\sigma}(x)$ $\left[\hat{\psi}_{\mathrm{h},\sigma}(x)\right]$ is the field operator of the electron

[hole] with spin σ and position x. We choose X_e at which the electron density has a maximum.

Since excitons are charge neutral, the exciton AB effect requires a difference between the phases acquired by the electron and the hole when the magnetic flux threads the ring. Suppose the electron and the hole in a widthless one-dimensional (1D) loop are independent or weakly bound through a short-range interaction, optical AB oscillations can be seen in the ground states of the bright exciton, where the total angular momentum of the exciton is kept null as the individual orbital angular momentum of the electron and the hole are canceled ($L = \ell_e + \ell_h = 0$). When a finite width of the ring structure is considered, a quasi one-dimensional geometric confining potential $V_\alpha(r)$ is obtained, which depends on only ring radius (r) under the assumption of rotational symmetry. In this case, it was known that the ratio of exciton orbit-to-width ($\gamma = R_x/W \geq 1$) is crucial in determining the amplitude of the excitonic AB oscillations. With increasing W, up to R_x in a QR, the excitonic AB oscillations become suppressed. However, when the e-h pair confined in a finite ring width is strongly bound through a long-range Coulomb interaction, the recent model [23] proposed that the emergence of excitonic AB oscillations is determined by the ring width and the strain, i.e., the excitonic AB oscillations occur in a limited range of the widths for an isotropic $V_\alpha(r)$. Additionally, the presence of the ring core layer (otherwise the core area is open), plays an important role in enhancing the excitonic AB oscillations via strain effects [27].

In the case of a strongly bound e-h pair, the one-dimensional model claims that the initial bright exciton ($L = 0$) becomes dark states ($L \neq 0$) with increasing magnetic field, resulting in no excitonic AB oscillation with an emission quenching [20]. However, exciton AB oscillations were still observed from QRs with non-zero total orbital angular momentum ($L \neq 0$). The exact reason is not clear at the moment. However, regarding the anisotropy of the volcano-like structure, the ideal selection rule for bright and dark exciton states may break down. Therefore, the fine states of the PL spectrum could be described by the mixed states of the spin and orbital angular momentum of bright and dark exciton states. Similar results were also observed in type-II QDs [28, 29]. While orbital angular momentum is also added to the charged single particle rotating in the shell of a type-II QD for increasing an external magnetic field, clear AB oscillations were confirmed in terms of both the peak energy and the integrated PL intensity. Regarding the elongated structure of QDs, the selection rules may be relaxed allowing observation of the dark states ($L \neq 0$).

Although the finite rim width can be considered in the quasi one-dimensional model, the strongly correlated states of excitons and the Wigner molecularisation between two excitons in a biexciton can be approximated into a simplified one-dimensional model. When the ring width is ignored, the effective mass Hamiltonian in (9.1)–(9.3) for an electron and a hole can be simplified as [20]

$$\begin{aligned} H &= \frac{\hbar^2}{2m_e R_e^2}\left(\hat{\ell}_e + \frac{\pi R_e^2 B}{h/e}\right)^2 + \frac{\hbar^2}{2m_h R_h^2}\left(\hat{\ell}_h - \frac{\pi R_h^2 B}{h/e}\right)^2 \\ &\quad - \frac{e^2}{4\pi\epsilon}\left[(R_e - R_h)^2 + 4R_e R_h \sin^2\left(\frac{\theta_e - \theta_h}{2}\right)\right]^{-1/2}, \end{aligned} \tag{9.14}$$

where, θ_e (θ_h) and $\hat{\ell}_e = -i\partial/\partial\theta_e$ ($\hat{\ell}_h = -i\partial/\partial\theta_h$) are the azimuth angle and angular momentum of the electron (hole) respectively, and the Zeeman effect is not included. The center-of-mass and relative coordinates of the exciton are given by

$$\Theta = \frac{m_e R_e^2 \theta_e + m_h R_h^2 \theta_h}{m_e R_e^2 + m_h R_h^2}, \quad \theta = \theta_e - \theta_h. \tag{9.15}$$

Then, the Hamiltonian in (9.14) becomes decoupled as $H = H_{CM} + H_{rel}$,

$$H_{CM} = \frac{\hbar^2}{2m_X R_X^2}\left[\hat{L} + \frac{\pi(R_e^2 - R_h^2)B}{h/e}\right]^2, \tag{9.16}$$

$$H_{rel} = \frac{\hbar^2}{2\mu R_{rel}^2}\left(\hat{\ell} + \frac{\pi R_{rel}^2 B}{h/e}\right) - \frac{e^2}{4\pi\epsilon}\left[(R_e - R_h)^2 + 4R_e R_h \sin^2\frac{\theta}{2}\right]^{-1/2}, \tag{9.17}$$

with $R_X^2 = (m_e R_e^2 + m_h R_h^2)/(m_e + m_h)$, $R_{rel} = R_e R_h / R_X$, and $m_X = m_e + m_h$. We have introduced the total angular momentum $\hat{L} = \hat{\ell}_e + \hat{\ell}_h = -i\partial/\partial\Theta$ and relative angular momentum $\hat{\ell} = \frac{m_h R_h^2 \hat{\ell}_e - m_e R_e^2 \hat{\ell}_h}{m_e R_e^2 + m_h R_h^2} = -i\partial/\partial\theta$. The energy eigenstates can be given as $\Psi_{X,L}(\theta_e, \theta_h) = e^{iL\Theta}\psi_{X,L}(\theta)$ with L $(= 0, \pm 1, \pm 2, \ldots)$. We see that the center-of-mass and relative motion are not completely decoupled; $\Psi_L(\theta_e, \theta_h) = \Psi_L(\theta_e \pm 2\pi, \theta_h) = \Psi_L(\theta_e, \theta_h \pm 2\pi)$, and an unusual boundary condition for $\psi_L(\theta)$ is given by

$$\psi_L(\theta \pm 2\pi) = \exp\left[\pm i 2\pi L \frac{m_e R_e^2}{m_e R_e^2 + m_h R_h^2}\right]\psi_L(\theta). \tag{9.18}$$

The low-lying states of an exciton can be estimated by using the harmonic approximation. By expanding the Coulomb interaction up to θ^2, we obtain $\psi_{X,L}(\theta) \propto \exp\{-\theta^2/(2\xi_X^2)\}$ with the "localisation length" defined by

$$\xi_X = \left[\frac{a_B R_X^2 |R_e - R_h|^3}{(R_e R_h)^3}\right]^{1/4}. \tag{9.19}$$

As $\xi_X \sim 0.64$ in our system is sufficiently small compared to π, the harmonic approximation can be justified. This indicates that the electron and the hole are strongly correlated to each other, and move together with $\theta_e \simeq \theta_h$, as schematically shown in Fig. 9.1a. The low-lying energies can also be approximated as

$$E_X(L) = \frac{\hbar^2}{2m_X R_X^2}\left[L + \frac{\pi(R_e^2 - R_h^2)B}{h/e}\right]^2 + \text{const.}, \tag{9.20}$$

which is in agreement with the recent one-dimensional model [20]. On the other hand, for a biexciton, instead of two electrons and two holes, we consider two excitons as point particles that move in the ring, as shown in Fig. 9.1b. Suppose a ring orbit radius $R'_{\rm X}$ is given for the exciton, the effective Hamiltonian for two excitons with the dipole-dipole interaction can be given by

$$H = \sum_{j=1}^{2} \frac{\hbar^2}{2m_{\rm X} R_{\rm X}^{'2}} \left[\hat{\ell}_j + \frac{\pi (R_{\rm e}^{'2} - R_{\rm h}^{'2}) B}{h/e} \right]^2 + \frac{e^2 (R'_{\rm e} - R'_{\rm h})^2}{4\pi\epsilon R_{\rm X}^{'3}} \frac{1 + \sin^2 \frac{\theta_1 - \theta_2}{2}}{8 \left| \sin^3 \frac{\theta_1 - \theta_2}{2} \right|}. \tag{9.21}$$

The dipole-dipole interaction becomes minimised when $|\theta_1 - \theta_2| = \pi$, i.e., the two excitons are located at opposite sides of the ring. In a similar case to that used for the exciton, the harmonic approximation enables us to estimate the wavefunction of the biexciton (or interacting two exciton dipoles) in relative coordinates as $\psi_{{\rm XX},L}(\theta_1 - \theta_2) \propto \exp[-(|\theta_1 - \theta_2| - \pi)^2/(2\xi_{\rm XX}^2)]$ $(|\theta_1 - \theta_2| < 2\pi)$. Since the "localization length" of the biexciton,

$$\xi_{\rm XX} = \left[\frac{64}{5} \frac{\mu}{m_{\rm X}} \frac{a_{\rm B} R'_{\rm X}}{(R'_{\rm e} - R'_{\rm h})^2} \right]^{1/4} \sim 0.91, \tag{9.22}$$

is smaller than π, the harmonic approximation is still valid again. Likewise, the low-lying energy of the biexciton can be approximated as

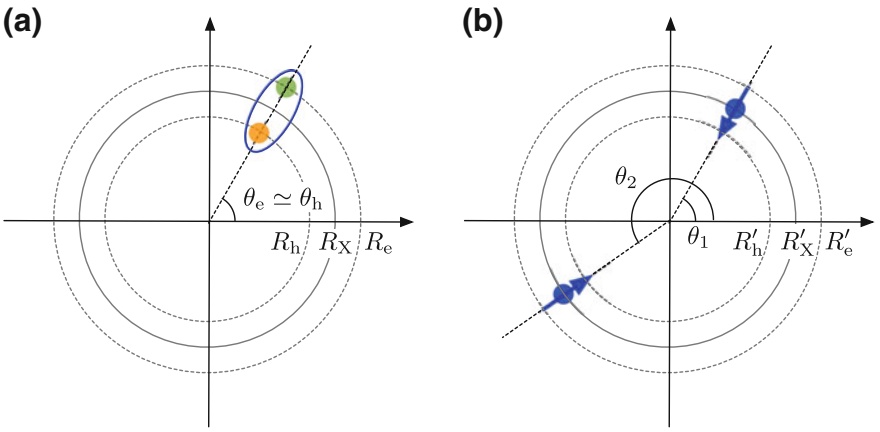

Fig. 9.1 **a** Schematic view of the low-lying states of an exciton in a quantum ring. An electron and a hole are strongly coupled to each other, and they move together with $\theta_e \simeq \theta_h$. **b** Simplified model of a biexciton in the ring, where each exciton is treated as a point particle with a radial electric dipole moment (Reprinted with permission from [18]. Copyright (2016) American Chemical Society.)

$$E_{\mathrm{XX}}(L) = \frac{\hbar^2}{2(2m_{\mathrm{X}})R_{\mathrm{X}}^{\prime 2}}\left[L + 2\frac{\pi(R_{\mathrm{e}}^{\prime 2} - R_{\mathrm{h}}^{\prime 2})B}{h/e}\right]^2 + \text{const.} \tag{9.23}$$

This equation suggests the biexciton can be treated as a single particle with twice the exciton mass (m_{X}). Indeed, when the dipole-dipole interaction becomes minimised with $|\theta_1 - \theta_2| = \pi$, the distance between the two excitons becomes maximised. This condition indicates the formation of a Wigner molecule from the two excitons [17].

9.4 Optical Aharonov-Bohm Oscillations of an Exciton in a Single Quantum Ring and Disorder Effects

As excitons are charge neutral, the exciton AB effect in a ring structure requires a difference between the phases ($\Delta\phi$) acquired by the electron and the hole when a magnetic field threads the ring. This means that their orbits should be unequal, whereby a difference between the magnetic fluxes ($\Delta\Phi$) penetrating their paths results in the phase of a radially polarised exciton ($\Delta\phi = e\Delta\Phi/\hbar$). Therefore, $\Delta\phi$ is proportional to the radial dipole moment, and can be measured through the photon emitted by the electron-hole pair, i.e., the center-of-mass exciton energy is given by $E_{\mathrm{X}} = \hbar^2(L + \Delta\phi)^2/(2MR_{\mathrm{X}}^2)$, where L, M, and R_{X} are the angular momentum, the effective mass, and the orbit radius, respectively. Therefore, when an exciton is confined to a ring structure, an oscillation in the emission energy of the exciton as a function of magnetic flux can be observed. Therefore, a delocalised wavefunction around the rim is a prerequisite for the AB effect.

However, the presence of localised states has been reported in a volcano-like QR arising from height anisotropy [25, 30–33], whereby the phase coherence around the rim can be inhibited. The degree of localisation seems to depend upon the anisotropy; when this is negligible, excitonic AB oscillations begin at low magnetic fields [8, 34]. In the intermediate range of localisation, excitons are localised separately near the two highest rims in a QR, but the two excitons can be paired in a biexciton with sub-meV binding energy [30]. In the case of strong localisation in a QR [25], no persistent current emerges unless a large magnetic field is applied. Therefore, optical AB oscillations in a QR need to be considered in the context of the exciton localisation induced by rim height-anisotropy. This may explain why some experiments failed to observe excitonic AB oscillations in a QR. We confirm the presence of a strongly localised state in a volcano-like QR with an absence of excitonic AB oscillations up to 14 T, a small diamagnetic coefficient, and a large polarisation asymmetry. These arise as a consequence of the small lateral extension and asymmetry of the strongly localised crescent-like structure in the QR.

Although ring structures were observed in a field emission scanning electron microscope (FESEM) image of the uncapped sample (Fig. 9.2b), it is known that a volcano-like anisotropic morphology is significant in the QR [25]. The height anisotropy gives rise to a crescent-shaped adiabatic potential and localisation of the

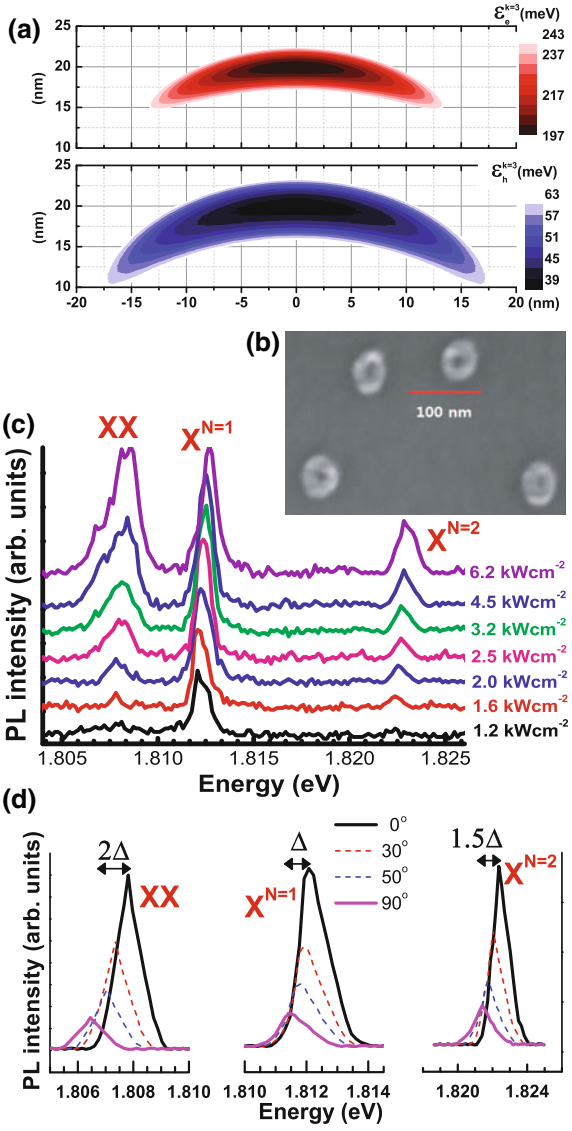

Fig. 9.2 **a** Electrons and holes are localised in crescent-like adiabatic potentials for a vertical quantum number $k = 3(\varepsilon_{e,h}^{k=3})$. **b** A single ring structure observed by FESEM. Biexciton (XX) and excited state exciton ($X^{N=2}$) emission appear near ground exciton ($X^{N=1}$) for increasing excitation power (**c**), among which analyzer angle dependence of the PL spectrum are compared under an excitation power of $2\,kWcm^{-2}$ (**d**) (Reproduced from [32], with the permission of AIP Publishing.)

potential becomes significant as the vertical quantum number (k) is increased [31, 32]. For a QR with ~20 nm-radius and ~10 nm-height, localised states for a vertical quantum number of $k = 3$ can be seen at an energy close to the barrier ($Al_{0.3}Ga_{0.7}As$) bandgap. As shown in Fig. 9.2a, localised adiabatic potentials ($\varepsilon_{e,h}^{k=3}$) of the electron and the hole for a vertical quantum number of $k = 3$ have a crescent-like shape. An estimated ground state confinement energy for the electron (241 meV) and the hole (60 meV) predicts a PL energy for the ground state exciton $X^{N=1}$ of ~1.812 eV in

excellent agreement with the PL spectrum in Fig. 9.1c, where the radial quantum number N denotes the states defined in the adiabatic potential ($\varepsilon_{e,h}^{k=3}$). It should be noted that the wavefunction contour areas should be larger than the localised potentials due to tunnelling effects.

The blueshift in the PL from $X^{N=1}$ with increasing excitation power (Fig. 9.2c) suggests the presence of fine structure states, where a sequential state-filling gives rise to the observed blueshift. As a consequence of asymmetry of the crescent-like adiabatic potential in Fig. 9.2a, the fine structure states of $X^{N=1}$ within the ~1.5 meV PL linewidth can be resolved by measuring the PL at different linear polariser angles (Fig. 9.2d). As the excitation power (I_{ex}) is increased, two additional PL peaks emerge at low (1.808 eV) and high energy (1.822 eV) with respect to $X^{N=1}$ (1.812 eV). The superlinear increase of the PL intensity ($\sim I_{ex}^{\alpha}$) was characterized in terms of the power factor (α) by integrating the PL spectrum. $\alpha \sim 2.3 \pm 0.1$ and $\sim 1.5 \pm 0.1$ were obtained for the low and the high energy peaks compared with $\alpha \sim 0.9 \pm 0.1$ measured for $X^{N=1}$ before saturation of the PL intensity. Therefore, the two additional peaks can be attributed to biexciton states (XX) and excited exciton states ($X^{N=2}$) of the localised $X^{N=1}$, respectively, Both wavefunctions for XX and $X^{N=2}$ are possibly more extended and asymmetric than that of $X^{N=1}$. However, as $X^{N=2}$ is located ~10 meV above $X^{N=1}$, the range of $X^{N=2}$ is not extended significantly (~few nm) in the contour areas of $\varepsilon_e^{k=3}$ and $\varepsilon_h^{k=3}$, but a node of the wavefunction must exist in the middle of the crescent structure similar to p-orbitals. This possibly results in a large polarisation asymmetry and polarity. Since XX consists of two $X^{N=1}$s, the area could be nearly doubled, but shrinks due to bonding. As the observed binding energy of the XX is large (~4 meV), this is the case of a strongly localised XX in a crescent-like structure rather than a pair of two different excitons, which are located separately at different rims [30]. Again, the asymmetry of the local structure gives rise to a strong polarisation dependence, where the emission energy difference of XX for perpendicular polarisations is twice (2Δ) that of $X^{N=1}$ ($\Delta \sim 0.8$ mev) due to selection rule breaking [31]. On the other hand, the emission energy difference of $X^{N=2}$ for perpendicular polarisations is 1.5Δ. Although $X^{N=2}$ possibly has a relatively smaller wavefuction area than XX, the wavefunction shape should be very asymmetric, i.e., a node is present as in p-orbitals and is confined in the crescent-like structure. Therefore, the emission energy difference in the level spacing between the fine structure states of $X^{N=2}$ is relatively large compared to that of $X^{N=1}$.

As $X^{N=1}$, $X^{N=2}$, and XX are all localised, delocalisation around the whole rim in a QR is unlikely. However, provided that an external magnetic field (B) is strong enough to overcome the energy barrier between the two separate localised states in an anisotropic QR, a phase coherent delocalisation can be induced; as persistent current [25] was induced in an anisotropic QR beyond ~14 T, it is challenging to observe an induced excitonic AB oscillation in an anisotropic QR beyond a characteristic magnetic field (B_c). We measured magneto-PL of localised excitons at a slightly lower energy ($E(0) = 1.7809$ eV) (Fig. 9.3a) in the absence of B, which possibly gives rise to more extended localised structure and a reduced B_c. Spectral splitting of the localised excitons in an anisotropic QR becomes significant when $B \geq 4$ T, where the Zeeman splitting becomes comparable to the energy difference

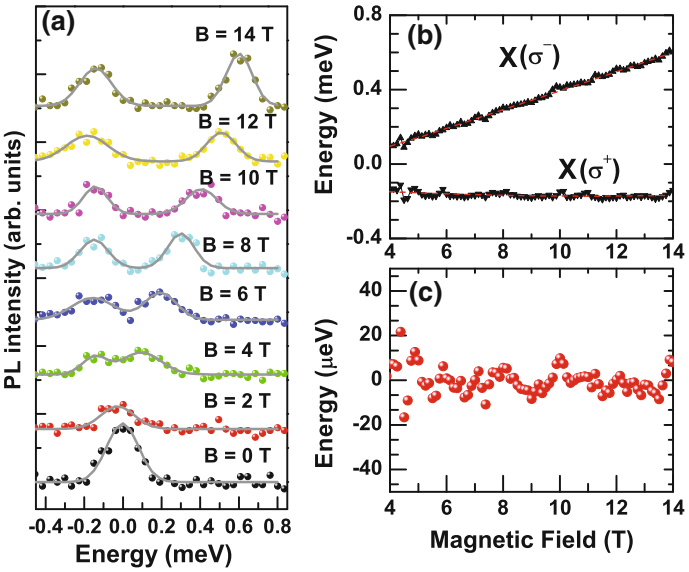

Fig. 9.3 The PL spectrum (**a**) and fitted peak energy (**b**) of localised exciton Zeeman doublet with increasing an external magnetic field, where the energy oscillation is not significant with an error range of 20 μeV after removing Zeeman splitting and diamagnetic shift (**c**) (Reproduced from [32], with the permission of AIP Publishing.)

for perpendicular linear polarisations (∼2 meV), similar to the case of asymmetric quantum dots. The high ($E(\sigma^-)$) and low energy ($E(\sigma^+)$) states of the exciton as a function of B (Fig. 9.3b) were obtained by Lorentzian fitting, whereby the excitonic g-factor ($g_X = [E(\sigma^+) - E(\sigma^-)]/\mu_B B \sim -0.2$) and diamagnetic coefficient ($\gamma = \frac{[E(\sigma^+)+E(\sigma^-)]/2 - E(B=0)}{B^2} \sim 1.3\,\mu\text{eV}T^{-2}$) were also obtained. These small values can be attributed to the small lateral area of the local structure. After removing the Zeeman splitting and diamagnetic shift (Fig. 9.3c), an energy drift of ∼20 μeV is seen with a Gaussian fitting accuracy of ∼ 2.5 μeV. However, it is still difficult to define a significant single period. We found several QRs grown under the same conditions all show such a noisy or aperiodic oscillations. It is therefore possible that 14 T is an insufficient field to produce a phase coherent delocalisation around the whole QR. Therefore, it would be important to try to induce delocalisation by either applying a larger magnetic field or by suppressing the anisotropy in the QR.

Figure 9.4a shows an atomic force microscope (AFM) image taken from an uncapped GaAs QR. As both anisotropy and asymmetry are present in the QR structure, the volcano-like ring structure can be modelled in cylindrical coordinates ($z = z(r, \phi)$), where the rim height ($z(r, \phi)$) is described by radius r and azimuthal angle (ϕ). The rim height is maximum at the azimuthal angles of 0° and 180° along the [1$\bar{1}$0] direction, and a minimum at the perpendicular angles of 90° and 270° along the [110] direction, respectively. Also, the in-plane shape is elliptical with the long axis along [1$\bar{1}$0]. While the lateral size distribution of QRs is not signifi-

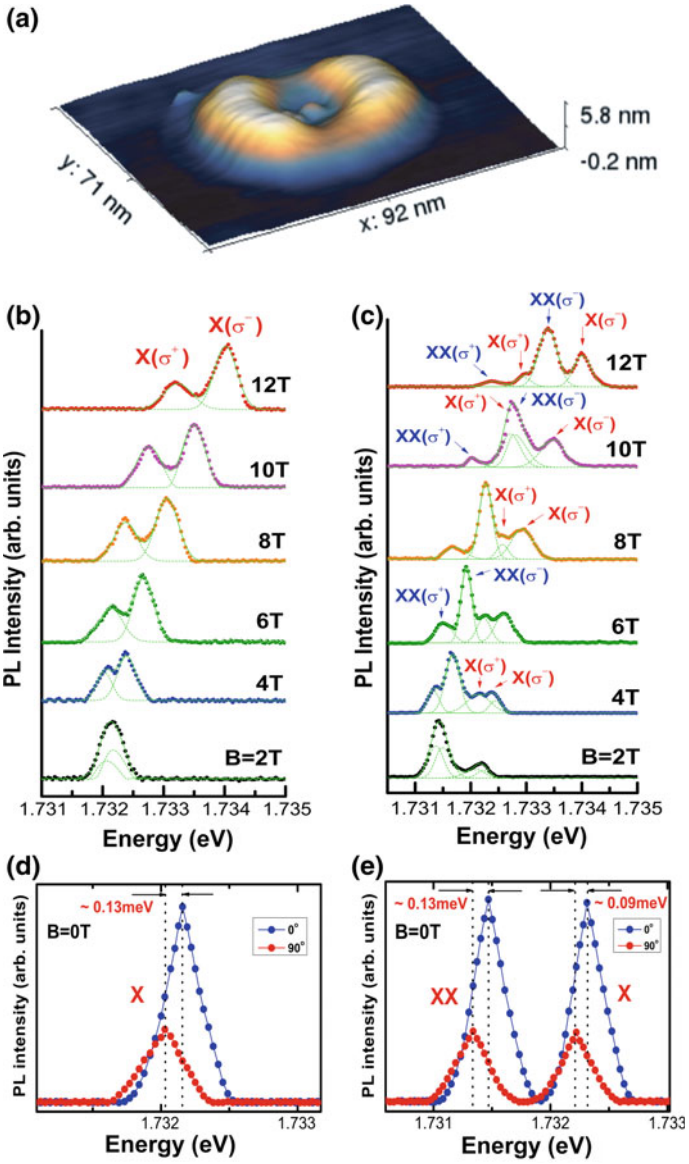

Fig. 9.4 **a** AFM image of a quantum ring. Magneto-PL spectrum with an excitation intensity of $P_{ex} = 0.7\,\mathrm{kWcm}^{-2}$ (**b**) and $10P_{ex}$ (**c**), where the energy difference for perpendicular polarisations was also measured separately without B for both Xs (Δ_X) and XXs (Δ_{XX}), respectively(d,e) (Reprinted with permission from [18]. Copyright (2016) American Chemical Society.)

cant (Fig. 9.2b), the spectral inhomogeneity of ensemble QRs is quite broad [35, 36] due to the anisotropic volcano-like morphology, ranging from the bandgap of bulk GaAs up to that of AlGaAs. Although the micro-PL emission of high spectral energy ranges close to the AlGaAs barrier are mostly strongly localised states in a crescent-like shape, the localised wavefunctions at low spectral energy ranges can extend over the whole rim of a QR with the assistance of tunneling. For example, we concluded that the exciton micro-PL spectrum near ∼1.7 eV possibly results from a couple of two crescent-shape adiabatic potentials, where the distance between two crescent-shape adiabatic potentials is short enough for the wavefunction tunneling. Because of a subtle difference between the model and a real QR, it is not sure whether tunneling effect between the two crescent-like localised wavefunctions is strong enough to give rise to a single wavefunction over the whole rim. If it is the case of localised states, exciton AB oscillations can emerge in the anisotropic QR beyond a characteristic magnetic field (B_c). Because the potential barrier between the two separate localised states in a QR is overcome due to the diamagnetic effect, B_c can be a measure of the degree of localisation.

As the volcano-model suggests, we selected a single QR near ∼1.732 eV. In Fig. 9.4b, magneto-PL spectra of the Xs for an excitation intensity of $P_{ex} = 0.7\,\mathrm{kWcm^{-2}}$ is plotted from $B_c \sim 2$ T, below which the Zeeman splitting is not significant enough to be resolved. When the excitation becomes stronger by an order of magnitude ($10P_{ex}$), we found XXs also emerge (Fig. 9.4c), which has been identified by excitation dependence and time-resolved PL. All magneto-PL spectra were carefully fitted by using Gaussian functions (dotted lines in Fig. 9.5a) in order to obtain the central emission energy of X and XX as a function of B. In the absence of B, we also measured an energy difference ($\Delta_X \sim 0.13$ meV) in the X PL for perpendicular polarisations to evaluate the anisotropy of the localised states in a QR (Fig. 9.4d) [32]. With an excitation of $10P_{ex}$, a blueshift is observed as well as a decrease in Δ_X (from ∼0.13 to ∼ 0.09 meV) (Fig. 9.4e). These results are possibly associated with screening of the lateral electric field (E_{lat}) [37]. Because a GaAs/AlGaAs QR is a lattice matched system, E_{lat} is possibly generated by defects at the interface between the GaAs and AlGaAs such as Ga-antisite and As-vacancies, where trapped carriers may cause E_{lat}, and a large number of optically injected carriers in the AlGaAs can suppress E_{lat} by screening.

In addition, the energy difference of the XX emission energy for perpendicular polarisations ($\Delta_{XX} \sim 0.13$ meV) is different from that of the excitons ($\Delta_X \sim 0.09$ meV) (Fig. 9.4e). In the case of an elliptical quantum dot (QD), an asymmetric electron-hole exchange interaction causes a splitting (Δ_X) of the spin-degenerate exciton states into two singlet states, where two linearly orthogonally polarized dipoles are defined along the symmetric axes of the QD. The selective transition from the polarized XX and X states in an elliptical QD also gives rise to an identical splitting in the XX PL spectrum ($\Delta_{XX} = \Delta_X$). Therefore, the differences seen in a QR ($\Delta_{XX} \neq \Delta_X$) can be attributed to a selection rule change in the anisotropic structure [31, 32].

Given the inherent structural anisotropy and E_{lat} in a QR, the AB oscillations can be modulated by morphological control, excitation intensity, and an external electric

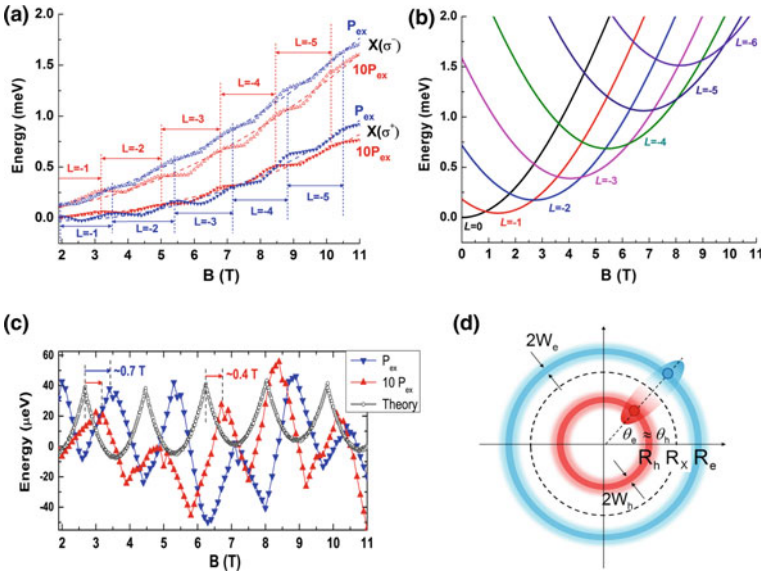

Fig. 9.5 Optical AB oscillations of the exciton in a single QR. **a** Central energy of the X emission for weak ($P_{ex} = 0.7\,\mathrm{kWcm^{-2}}$) and strong ($10P_{ex}$) excitation intensity is plotted from 2 T to 11 T. When $B \leq 2\,\mathrm{T}$, the spectral splitting is too small to distinguish between the peaks X (σ^+) and X(σ^-). **b** Theoretical X energy change ($E_X^L(B) - E_X^{L=0}(B=0)$) for the various orbital angular momenta ($L = 0, -1, -2, -3, \ldots$) with B for a quasi one-dimensional isotropic quantum ring model, where the many-body correlation is fully taken into account for the Coulomb interaction. **c** Theory and experiment are compared after removing the quadratic fitting term, where the period of exciton AB oscillations ($\Delta B_X \sim 1.8\,\mathrm{T}$) is the same, but a magnetic field difference in the oscillation extremum ($\delta B_X \sim 0.7\,\mathrm{T}$ for P_{ex} and $\delta B_X \sim 0.4\,\mathrm{T}$ for $10P_{ex}$) is observed. **d** When the strong Coulomb interaction between the electron and hole is considered, the X can also be approximated as a single particle ($\theta_e \approx \theta_h$) with its orbit at R_X.(Reprinted with permission from [18]. Copyright (2016) American Chemical Society.)

field. In this case, disorder effects in QRs are of great potential for quantum coherence control. As shown in Fig. 9.5a, optical AB oscillations of the X energy with B are significant for both weak (P_{ex}) and strong ($10P_{ex}$) excitation intensity, and both these cases have the same period ($\Delta B_X \sim 1.8\,\mathrm{T}$). The period of X AB oscillations was also calculated theoretically by using our quasi one-dimensional potential $V_{e,h}(r, R_{e,h})$ for the electron and hole of a QR, which is anharmonic and axially symmetric with a centrifugal core. Here the quasi-1 dimensional model implies the width ($W_{e,h}$) of $V_{e,h}(r)$ is still smaller than the orbit size ($R_{e,h}$). It is also known that the electron and hole are likely to rotate along different orbits ($R_e \neq R_h$) due to their different effective masses, deformation potential, and strain [20, 22, 37–41], whereby the phase difference ($\Delta\phi$) between the electron and hole as a function of B controls the X AB oscillations [20, 21, 42].

When the Coulomb interaction between the confined electron and hole was considered in $V_{e,h}(r, R_{e,h}, W_{e,h})$, we obtained the X eigenstates of different orbital

angular momentum (L) as a function of B by using an exact diagonalisation method, where the many-body states are expanded by a large number of the single-particle states. We also found that the exciton can be approximated as a single composite particle ($\theta_e \approx \theta_h$) (Fig. 9.1a) with its orbit at R_X and angular momentum $L = \ell_e + \ell_h$, where ℓ_e and ℓ_h are constituent orbital angular momenta for the electron and the hole. Recently, it was found that the ratio of exciton orbit-to-confinement width ($R_X/W_{e,h}$) is crucial in determining the amplitude of the excitonic AB oscillations [27, 43], whereby the emergence of the X AB oscillations occurs under limited conditions ($1 \leq R_X/W_{e,h} \leq 10$). We found optimum values for the different orbits ($R_e = 32\,\text{nm}$, $R_h = 15\,\text{nm}$) and the rim width ($W_e = 5\,\text{nm}$, $W_h = 5\,\text{nm}$) for the electron and the hole empirically to obtain the measured AB oscillation period ($\Delta B_X \sim 1.8\,\text{T}$), which is also the case for the limiting condition ($R_X/W_{e,h} \sim 4.7$) of the AB oscillation. Figure 9.5b shows theoretical X energy for the various orbital angular momenta ($L = 0, -1, -2, -3, \ldots$) for increasing B, where the average exciton energy of L ($E_X^L(B)$) between the two X states for spins parallel ($X(\sigma^+)$) and anti-parallel ($X(\sigma^-)$) to B were subtracted by that of $L = 0$ ($E_X^{L=0}(B = 0)$), and we used the same diamagnetic coefficient for $X(\sigma^+)$ and $X(\sigma^-)$. Therefore, the level spacing among L-states can be seen in terms of $E_X^L(B) - E_X^{L=0}(B = 0)$ for increasing B.

After removing the fitted quadratic functions in Fig. 9.5a, b, which are determined by the exciton g-factor ($g_X \sim -1.3$) and the diamagnetic coefficient ($\gamma_X \sim 10\,\mu\text{eV/T}^2$) of the exciton, the experimental data are compared with theory (Fig. 9.5c). The oscillation maxima and minima for weak (P_{ex}) and strong ($10P_{ex}$) excitation occur at different magnetic fields despite the fact that all show the same $\Delta B_X \sim 1.8\,\text{T}$. This result can be associated with B_c, i.e., as the AB effect emerges at finite B_c, the first transition from $L = 0$ to $L = 1$ also occurs at a relatively large magnetic field compared to the case of ideal theory. For a weak excitation P_{ex}, a magnetic field difference for the oscillation extremum between theory and experiment ($\delta B_X \sim 0.7\,\text{T}$) is obtained (Fig. 9.5c). On the other hand, when the excitation is $10P_{ex}$, a small $\delta B_X \sim 0.4\,\text{T}$ is obtained. Recently, changes in the sequence of maxima and minima of the X PL intensity oscillations with B were claimed to be due to E_{lat} and thermal effects [37, 38]. Also, the presence of B_c was shown experimentally in a volcano-like anisotropic QR [25]. Therefore, the so-called modulated X AB oscillations in Fig. 9.5c possibly result from a combined effect of B_c, E_{lat}, and thermal phonons in an anisotropic QR.

Even though the wavefunction is delocalised around the anisotropic rim, the rotational symmetry of a QR most likely breaks down due to the scattering potential arising from anisotropy and localised impurities. In this case, the orbital angular momentum L is not a good quantum number, and the coupling between different L states are involved. As a result, an anti-crossing splitting of the PL spectrum appears at the transition B-field of the AB oscillations, where the exciton changes L to minimize its energy [21, 42]. As evidence of the anti-crossing splitting, a dip in the middle of the Gaussian PL peak was observed up to the transition from $L = -2$ to $L = -3$ for both weak and strong excitation (Fig. 9.6a, b). For the case of impurity

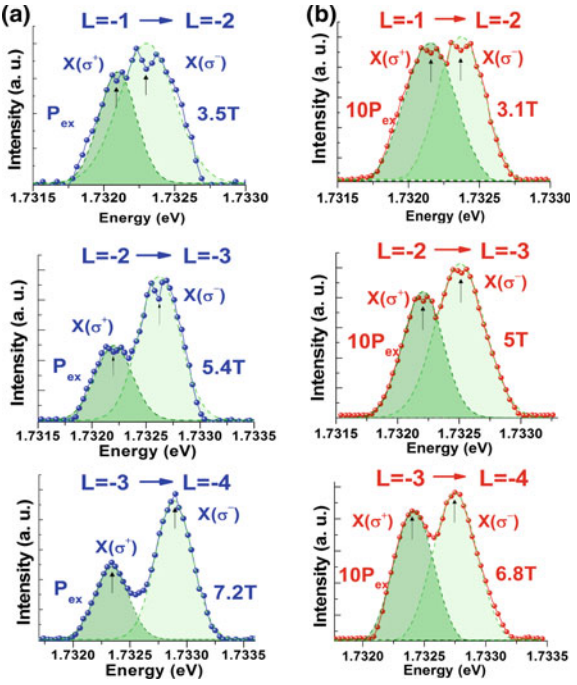

Fig. 9.6 The anti-crossing splitting in the presence of disorder. Provided that the rotational symmetry of a QR breaks down due to disorder, the anti-crossing splitting, i.e. the dip in the middle of the PL peak, is significant when L changes, but eventually disappears when B is strong enough to overcome the disorder effect for weak ($P_{\mathrm{ex}} = 0.7\,\mathrm{kWcm}^{-2}$) (**a**) and strong ($10P_{\mathrm{ex}}$) (**b**) excitation intensity (Reprinted with permission from [18]. Copyright (2016) American Chemical Society.)

disorder, a δ-function scattering potential ($U_{\mathrm{e,h}}^{\mathrm{imp}}\delta(\theta_{\mathrm{e,h}} - \theta_i^0)$) can be used, where θ_i^0 is a fixed angle of the impurity localised at the electron/hole orbit [42]. In comparison to the measured anti-crossing ($60 \sim 120\,\mu\mathrm{eV}$), we estimate $\sim 110\,\mu\mathrm{eV}$ for the splitting with $U_{\mathrm{e,h}}^{\mathrm{imp}} \sim 50\,\mu\mathrm{eV}$ by using recent theory [42]. However, a dip is not seen at the transition from $L = -3$ to $L = -4$ for both weak and strong excitation. This result suggests that the rotational symmetry recovers, with a good quantum number L, when a strong magnetic field overcomes disorder effects.

9.5 Fractional Optical Aharonov-Bohm Oscillations of a Biexciton Wigner Molecule in a Single Quantum Ring

As the electronic correlation effect is enhanced in a quasi one-dimensional QR, an electronic Wigner molecule (WM) can be formed. For optical experiments, a XX in a NQR is a good candidate for an excitonic WM. In Fig. 9.7a, the central emission energies of the X and XX with B are compared, where both the X and XX show an oscillatory behaviour, although the AB period of the XX ($\Delta B_{\mathrm{XX}} \sim 0.5\,\mathrm{T}$) is shorter than that of the X ($\Delta B_{\mathrm{X}} \sim 1.8\,\mathrm{T}$). We claim that the fractional AB oscillation arises from the XX WM in a QR. In order to explain the fractional period, we have calculated the theoretical eigenenergy levels of the XXs (E_{XX}^L) and Xs (E_{X}^L) for

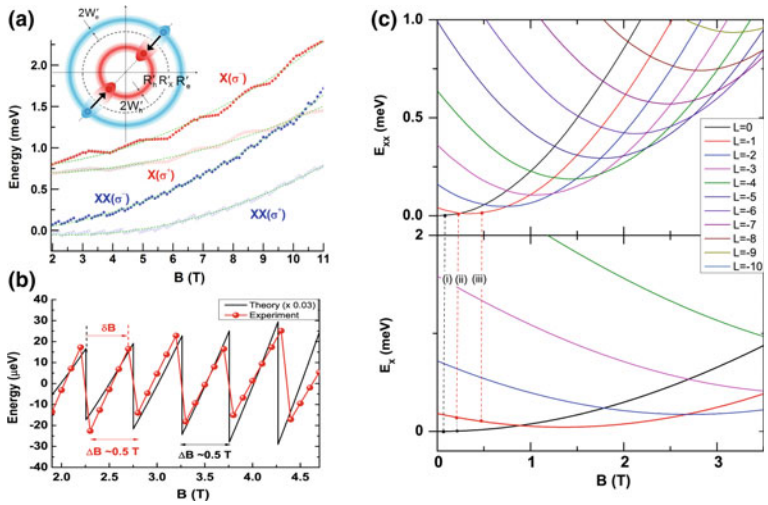

Fig. 9.7 The AB oscillation period of XXs in a single QR is fractional compared to that of Xs. **a** Central emission energy of the X and XX for strong ($10P_{ex} = 7.0\,\mathrm{kWcm^{-2}}$) excitation intensity is plotted from 2 T to 11 T. XX in a QR can be considered as a pair of the interacting X dipoles, where the dipole-dipole interaction becomes minimised when the both are located at opposite positions as shown schematically. **b** Saw-like AB oscillations arising from the emission between $E^L_{XX}(B)$ and $E^L_X(B)$ in experiment and theory are compared after removing the quadratic fitted functions. **c**, **d** Theoretical energy change of the XX ($E^L_{XX}(B) - E^{L=0}_{XX}(B=0)$) and X ($E^L_X(B) - E^{L=0}_X(B=0)$) for the various orbital angular momenta ($L = 0, -1, -2, -3, \ldots$) with increasing B (Reprinted with permission from [18]. Copyright (2016) American Chemical Society.)

various Ls in a quasi one-dimensional QR as a function of B (Fig. 9.7c, d), where the Coulomb interactions between the two electrons and two holes are fully taken into account. Note that the XX PL results from a transition from E^L_{XX} and E^L_X, but the energy oscillation periods of E^L_{XX} and E^L_X are different. For example, at the (i)-transition marked in Fig. 9.7c, d, both the XX and X have the same orbital angular momentum $L = 0$. On the other hand, at the (iii)-transition, the XX has already changed its orbital angular momentum from $L = 0$ to $L = -1$ to minimize its energy. However, emission occurs between $E^{L=-1}_{XX}$ and $E^{L=-1}_X$ due to a selection rule. In other words, emission between $E^{L=-1}_{XX}$ and $E^{L=0}_X$ is not allowed although $E^{L=0}_X < E^{L=-1}_X$. Consequently, while B increases, an abrupt change of the PL energy can be seen near the (ii)-transition. More specifically, two PL peaks are expected at the (ii) transition, i.e, $E^{L=0}_{XX} - E^{L=0}_X$ and $E^{L=-1}_{XX} - E^{L=-1}_X$, and the energy separation between the two peaks is also expected to increase with B. Additionally, when considering disorder, an anti-crossing splitting is also expected for the XX. Interestingly, no splitting was found in the XX PL spectrum at any B. If a splitting of the XX PL spectrum were present, a fast intra-relaxation between the two states could be one explanation, whereby only the low emission energy would be dominant at the (ii)-transition. Alternatively, the XX WM is possibly less susceptible to anisotropic disorder when

it consists of interacting Xs located at opposite positions in the NQR (Fig. 9.7a). Nevertheless, the exact reason is not clear at the moment. Ultrafast spectroscopy at the transition magnetic field could be employed to clarify this issue. In Fig. 9.7b, $\Delta B_{XX} \sim 0.5\,\mathrm{T}$ was reproduced using the quasi one-dimensional QR model and compared to the experimental data after removing the fitted quadratic terms from Fig. 9.7a, c and d, whereby the diamagnetic coefficient of the XX ($\gamma_{XX} \sim 12.4\,\mu\mathrm{eV/T^2}$) was also obtained. Because of the abrupt change of the XX PL energy near the transition magnetic field, saw-like AB oscillations are seen. Also, the magnetic field difference of the XX oscillation extremum between theory and experiment is the same as that of the modulated X AB oscillations ($\delta B_{XX} \approx \delta B_X \sim 0.4\,\mathrm{T}$) due to structural anisotropy.

When a XX becomes a WM in a QR, two cases are possible; either two Xs form a WM or electrons and holes form a WM independently. In order to better understand this issue, correlation effects associated with the formation of a WM can be visualised in terms of a two-body charge density, which is the probability to find either an electron (ρ_{ee}) or a hole (ρ_{he}) at the position of a fixed electron. Figure 9.8a shows that ρ_{he} for X is localised due to the strong Coulomb interaction. This result verifies that the exciton can be approximated as a single particle. On the other hand, the localised distribution of ρ_{ee} and ρ_{he} for XX (Fig. 9.8b, c) suggests that a XX WM in a QR is the former case, where the pair of Xs are strongly localised opposite each other. Therefore, the description of a XX in a QR can be simplified as a pair of the interacting X dipoles as shown schematically in Fig. 9.8a, where the two Xs should be maximally separated to minimize the dipole-dipole interaction.

Note also that $\Delta B_{XX} \sim 0.5\,\mathrm{T}$ in Fig. 9.7b is not half of $\Delta B_X \sim 1.8\,\mathrm{T}$. In order to obtain $\Delta B_{XX} \sim 0.5\,\mathrm{T}$, we found $R_{e,h}$ and $W_{e,h}$ of the quasi one-dimensional potential $V_{e,h}(r)$ for a XX, and these should be 1.4 times those for an X as empirical optimum parameters, i.e. both the orbit and width of the confinement potential for XX increase. The larger orbit for XX is due to the electron-electron and hole-hole repulsion in a QR with re-distribution of the surrounding electrons and holes, whereby the confinement potential of XX becomes different from $V_{e,h}(r)$ determined by the geometric

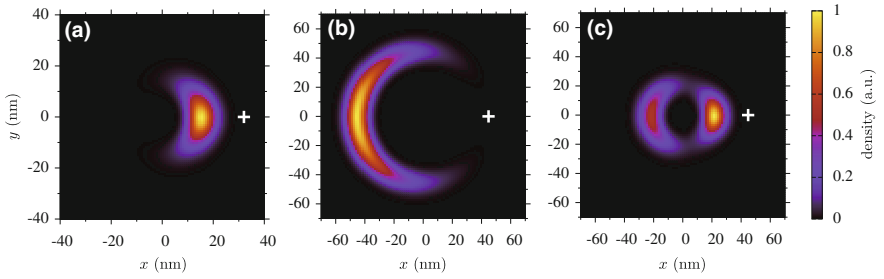

Fig. 9.8 Two-body charge density of an isotropic QR model at $B = 0$. The probability distribution of a hole with respect to the electron fixed at the marked position for an X (**a**) and the probability distribution of another electron (**b**) and two holes (**c**) to a fixed electron for XXs localised with Wigner molecule character (Reprinted with permission from [18]. Copyright (2016) American Chemical Society.)

structure. Therefore, a modified $V_{e,h}(r)$ for XX can be an effective correction, and partial Wigner localisation can also be a candidate [12], but the exact reason remains an open question. As a possible origin, the presence of a local electric field (E_{Loc}) is quite likely at the interface between a QR and the capping barrier material. Suppose that carriers excited in a capping barrier affect E_{Loc} at the interface, the wavefunction modification of a QR might be susceptible to optical excitation intensity changes.

9.6 Summary and Outlook

Ring structures remind topologically doubly connected structures such as a donut or a loop, but epitaxially grown quantum ring structures are singly connected, where the central part of a QR structure is not open. Additionally, the rim height of QRs grown by the droplet method shows a volcano-like morphology, where the anisotropic height likely results in two separate potential valleys at opposite positions of a QR. Consequently, a pair of localised states are formed in a QR, where two different potential valleys are of a crescent-like shape. Although the two energy levels are likely non-resonant, the energy difference can be decreased by controlling the rim height anisotropy or applying an external magnetic field. Suppose the tunneling effect between the two localised potential valleys is enhanced, the two different energy levels of localised excitons can be spectrally overlapped within the emission linewidth similar to a laterally coupled quantum-dot-dimer. Also, a biexciton can be formed through the dipole-dipole interaction between the two non-resonant exciton. Therefore, provided that a fine energy difference is given between the two localised exciton levels, the biexciton transition toward the nearly degenerate emission spectrum of two localised exciton states in a QR can be utilized in the context of an entangled photon pair.

On the other hand, for increasing an external magnetic field, the two crescent-like localised wavefunctions can be merged gradually into a single wavefunction, which extends over the whole circumference of a QR. This conjecture has already been manifested by the presence of characteristic magnetic field, where optical AB oscillations become significant. Nevertheless, the critical transition from a pair of localised states to a single delocalised state needs to be investigated further in terms of the onset of circumferential phase coherence against the anisotropic potential structure. Because the exciton AB oscillations are governed by the orbit radii of an electron and a hole as well as the Coulomb interaction in a finite rim width, the transition condition may contain a lot of novel physics. This topic can also be extended to the fractional AB oscillations, whereby the biexciton Wigner molecule condition can be refined. Additionally, the disorder effects in a QR are of great importance not only for fundamental knowledge but also for prospective applications. In particular, the modulation of AB oscillations can be further developed by applying an external electric field, an external excitation light, and an external strain.

Acknowledgements This work was supported by Korea Grant (NRF-2017R1A2B4011594, Pioneer Research 2013M3C1A3065522), French-Korean LIA, JSPS KAKENHI Grant (JP15H05870, JP26220711), and the European Commission from the seventh framework programme "Transnational Access", contract no. 228043-EuroMagNet II-Integrated Activities.

References

1. F. Martins, H. Sellier, M.G. Pala, B. Hackens, V. Bayot, S. Huant, in *Physics of Quantum Rings*, 1st edn., ed. by V.M. Fomin (Springer, Berlin, Heidelberg, 2014), pp. 107–121
2. A. Lorke, R.J. Luyken, A.O. Govorov, J.P. Kotthaus, J.M. Garcia, P.M. Petroff, Phys. Rev. Lett. **84**, 2223 (2000)
3. A.V. Oudenaarden, M.H. Devoret, Y.V. Nazarov, J.E. Mooij, Nature **391**, 768 (1998)
4. A.C. Bleszynski-Jayich, W.E. Shanks, B. Peaudecerf, E. Ginossar, F. von Oppen, L. Glazman, J.G.E. Harris, Science **326**, 272 (2009)
5. A.J.M. Giesbers, U. Zeitler, M.I. Katsnelson, D. Reuter, A.D. Wieck, G. Biasiol, L. Sorba, J.C. Maan, Nat. Phys. **6**, 173 (2010)
6. H. Bary-Soroker, O. Entin-Wohlman, Y. Imry, Phys. Rev. Lett. **101**, 057001 (2008)
7. A.M. Alexeev, M.E. Portnoi, Phys. Rev. B **85**, 245419 (2012)
8. F. Ding, N. Akopian, B. Li, U. Perinetti, A. Govorov, F.M. Peeters, C.C. Bof Bufon, C. Deneke, Y.H. Chen, A. Rastelli, O.G. Schmidt, V. Zwiller, Phys. Rev. B **82**, 075309 (2010)
9. A. Ghazaryan, A. Manaselyan, T. Chakraborty, Phys. E **66**, 157 (2015)
10. A. Singha, V. Pellegrini, A. Pinczuk, L.N. Pfeiffer, K.W. West, M. Rontani, Phys. Rev. Lett. **104**, 246802 (2010)
11. R. Egger, W. Hausler, C.H. Mak, H. Grabert, Phys. Rev. Lett. **82**, 3320 (1999)
12. C. Ellenberger, T. Ihn, C. Yannouleas, U. Landman, K. Ensslin, D. Driscoll, A.C. Gossard, Phys. Rev. Lett. **96**, 126806 (2006)
13. S. Pecker, F. Kuemmeth, A. Secchi, M. Rontani, D.C. Ralph, P.L. McEuen, S. Ilani. Nat. Phys. **9**, 576 (2013)
14. T. Chakraborty, P. Pietilainen, Phys. Rev. B **50**, 8460 (1994)
15. T. Chwiej, B. Szafran, Phys. Rev. B **79**, 085305 (2009)
16. K. Niemela, P. Pietilainen, P. Hyvonen, T. Chakraborty, Europhys. Lett. **36**, 533 (1996)
17. R. Okuyama, M. Eto, H. Hyuga, Phys. Rev. B **83**, 195311 (2011)
18. H.D. Kim, R. Okuyama, K. Kyhm, M. Eto, R.A. Taylor, A.L. Nicolet, M. Potemski, G. Nogues, L.S. Dang, K.C. Je, J.S. Kim, J.H. Kyhm, K.H. Yoen, E.H. Lee, J.Y. Kim, I.K. Han, W.J. Choi, J.D. Song, Nano Lett. **16**, 27 (2016)
19. A.V. Chaplik, V.M. Kovalev, in *Physics of Quantum Rings*, 1st edn., ed. by V.M. Fomin (Springer, Berlin, Heidelberg, 2014), pp. 199–246
20. A.O. Govorov, S.E. Ulloa, K. Karrai, R.J. Warburton, Phys. Rev. B **66**, 081309 (2002)
21. L.G.G.V. Dias da Silva, S.E. Ulloa, T.V. Shahbazyan, Phys. Rev. B **72**, 125327 (2005)
22. V.V. Arsoski, M.Z. Tadic, F.M. Peeters, Phys. Rev. B **87**, 085314 (2013)
23. G. Gonzalez-Santander, F. Dominguez-Adame, R.A. Romer, Phys. Rev. B **84**, 235103 (2011)
24. V.M. Fomin, V.N. Gladilin, J.T. Devreese, P.M. Koenraad, in *Physics of Quantum Rings*, 1st edn., ed. by V.M. Fomin (Springer, Berlin, 2014), pp. 83–104
25. N.A.J.M. Kleemans, I.M.A. Bominaar-Silkens, V.M. Fomin, V.N. Gladilin, D. Granados, A.G. Taboada, J.M. Garcia, P. Offermans, U. Zeitler, P.C.M. Christianen, J.C. Maan, J.T. Devreese, P.M. Koenraad, Phys. Rev. Lett. **99**, 146808 (2007)
26. W.C. Tan, J.C. Inkson, Semicond. Sci. Technol. **11**, 1653 (1996)
27. M. Tadic, N. Cukaric, V. Arsoski, F.M. Peeters, Phys. Rev. B **84**, 125307 (2011)
28. I.R. Sellers, V.R. Whiteside, I.L. Kuskovsky, A.O. Govorov, B.D. McCombe, Phys. Rev. Lett. **100**, 136405 (2008)

29. E. Ribeiro, A.O. Govorov, W. Carvalho Jr., G. Medeiros-Ribeiro, Phys. Rev. Lett. **92**, 126402 (2004)
30. T. Lin, C. Lin, H. Ling, Y. Fu, W. Chang, S. Lin, C. Lee, Phys. Rev. B **80**, 081304 (2009)
31. H.D. Kim, K. Kyhm, R.A. Taylor, G. Nogues, K.C. Je, E.H. Lee Lee, J.D. Song, Appl. Phys. Lett. **102**, 033112 (2013)
32. H.D. Kim, K. Kyhm, R.A. Taylor, A.A. Nicolet, M. Potemski, G. Nogues, K.C. Je, E.H. Lee, J.D. Song, Appl. Phys. Lett. **103**, 173106 (2013)
33. H.D. Kim, W.J. Lee, S.H. Park, K. Kyhm, K. Je, R.A. Taylor, G. Nogues, L.S. Dang, J.D. Song, Sci. Rep. (2017). https://doi.org/10.1038/srep40026
34. F. Ding, B. Li, F.M. Peeters, A. Rastelli, V. Zwiller, O. G. Schmidt, in *Physics of Quantum Rings*, 1st edn., ed. by V.M. Fomin (Springer, Berlin, Heidelberg, 2014), pp. 299–328
35. S. Sanguinetti, T. Mano, T. Kuroda, in *Physics of Quantum Rings*, 1st edn., ed. by V.M. Fomin (Springer, Berlin, 2014), pp. 161–193
36. T. Kuroda, T. Mano, S. Sanguinetti, K. Sakoda, G. Kido, N. Koguchi, Phys. Rev. B **72**, 205301 (2005)
37. M.D. Teodoro, V.L. Campo Jr., V. Lopez-Richard, E. Marega Jr., G.E. Marques, Y. Galvao Govato, F. Iikawa, M.J.S.P. Brasil, Z.Y. AbuWaar, V.G. Dorogan, Y.I. Mazur, M. Benamara, G.J. Salamo. Phys. Rev. Lett. **104**, 086401 (2010)
38. M.D. Teodoro, V.L. Campo Jr., V. Lopez-Richard, E. Marega Jr., G.E. Marques, G.J. Salamo, in *Physics of Quantum Rings*, 1st edn., ed. by V.M. Fomin (Springer, Berlin, Heidelberg, 2014), pp. 247–265
39. A.V. Maslov, D.S. Citrin, Phys. Rev. B **67**, 121304 (2003)
40. J.A. Barker, R.J. Warburton, E.P. O'Reilly, Phys. Rev. B **69**, 035327 (2004)
41. R.J. Warburton, C. Schulhauser, D. Haft, C. Schaflein, K. Karrai, J.M. Garcia, W. Schoenfeld, P.M. Petroff, Phys. Rev. B **65**, 113303 (2002)
42. L.G.G. Dias da Silva, S.E. Ulloa, A.O. Govorov, Phys. Rev. B **70**, 155318 (2004)
43. B. Alen, J. Martinez-Pastor, D. Granados, J.M. Garcia, Phys. Rev. B **72**, 155331 (2005)

Chapter 10
Aharonov-Bohm Effect for Neutral Excitons in Quantum Rings

M.D. Teodoro, V.L. Campo Jr., V. López-Richard, E. Marega Jr., G.E. Marques and G.J. Salamo

Abstract Quantum interference patterns predicted by theory due to the finite structure of neutral excitons in a single layer of InAs quantum rings are corroborated experimentally in the magneto-photoluminescence spectra of these nanostructures. The effects associated to built in electric fields and to the temperature on these Aharonov-Bohm-like oscillations are described and confirmed by complementary experimental procedures. Also a similar behavior was observed in a hybrid structure composed by a topmaster single layer of InAs quantum rings grown on a vertically stacked and laterally aligned InGaAs quantum dot superlattice.

10.1 Introduction

Attempts to verify fundamental quantum mechanical phenomena experimentally are some times hampered by serious scale limitations of a system. Nonetheless, the astonishing progress observed in the synthesis and growth of nanoscopic systems has opened opportunities for raising anew old questions while developing the technical ways for finding answers to them. This has certainly been the case of the search for optical implications associated to [1, 2] effect in nanoscale ring structures, or quantum rings (QRs), that gained a significant impetus in the last decades [3–6]. Their peculiar rotational symmetry has encouraged the search for a myriad of effects related to the quantization of the and to the unique spatial distribution of the wave function [7–10].

M.D. Teodoro · V.L. Campo Jr. · V. López-Richard · G.E. Marques
Departamento de Física, Universidade Federal de São Carlos,
São Carlos, São Paulo 13565-905, Brazil

E. Marega Jr. (✉)
Instituto de Física de São Carlos, Universidade de São Paulo, São Carlos,
São Paulo 13.566-590, Brazil
e-mail: euclydes@ifsc.usp.br

G.J. Salamo
Arkansas Institute for Nanoscale Materials Science and Engineering,
University of Arkansas, Fayetteville, AR 72701, USA

V.M. Fomin (ed.), *Physics of Quantum Rings*, NanoScience and Technology,
https://doi.org/10.1007/978-3-319-95159-1_10

There is however, at this moment, an important shortcoming in the experimental emulation of the original conditions for AB-effect in nanoscopic QRs. Unlike the famous picture of an AB scattering situation, for the available experimental configurations, the carriers are confined within QR regions with finite values of magnetic field. Although experimentally we shall renounce, for now, to test the seeming "paradox" of carriers being affected by a static in a region with zero field, we still consider an observed effect as of the AB-type if it can be explained assuming that the magnetic field is ideally concentrated in the middle of the QRs. Thus, we shall demonstrate that the experimental effects described bellow arise essentially from potential vector-mediated quantum interference.

As highlighted in previous chapters, in stationary systems, the "interference" patterns that will be assigned to an AB-nature are beyond the angular momentum quantization that affects the modulation with the external magnetic field of a single carrier selfenergy and we will focus on the excitonic states that can be characterized as proposed theoretically [11–13]. Instead of looking only at the dependence on the magnetic flux of the electron-hole recombination energy during photo-luminescence (PL), [14] we also consider the excitonic oscillator strength whose oscillatory behavior reflects directly the changes in the exciton wave function as the magnetic flux increases [15]. A similar experimental work was reported [4] for type-II QRs, however, here we are considering both electron and hole moving inside the ring so that the correlation between them becomes crucial to the oscillatory behavior found in the PL integrated intensity.

We will report the observation of a very unusual and difficult to be detected effect, since display a weak sensitivity to magnetic fields due to their neutrality [16]. Their coupling to the vector potential (or magnetic field) will be revealed when their finite structure is considered. Thus, interesting properties of coupled electrons and holes will rise during light absorption or emission of these QRs that can, in turn, be affected by structural factors such as piezoelectricity [17] and strain fields, [18] valence mass anisotropy, [18, 19] or temperature. We will contrast the experimental observations with the theoretical predictions. We were able to detect, analyze, and discuss systematically the different patterns observed in the oscillation of the integrated PL as function of the magnetic flux (not just the magnetic field) given that the ring size turns into a critical scaling factor for the experimental observation of this phenomenon, as reported [20]).

10.2 Experiment

The samples were grown by molecular beam epitaxy on a semi-insulating GaAs (100) substrate. After the growth of 0.5 μm GaAs buffer layer at 580 °C, cycles of 0.14 ML of InAs plus 2 s interruption under As_2 flux were deposited until the total formation of 2.2 ML of InAs QDs at 520 °C. Then, QDs were annealed during 30 s to improve the size distribution. In order to obtain the QRs structures, the dots were partially capped with 4 nm of GaAs cap layer grown at 520 °C. The growth rate was

measured by RHEED at 1 and 0.065 ML/s for GaAs and InAs respectively. Two different samples were grown with the same conditions. The first one contain uncapped quantum rings for morphological studies and the second one, a 50 nm GaAs cap layer was deposited to investigate the optical emission. Structural and morphological analysis of both samples were carried out by atomic force microscopy (AFM) and transmission electron microscopy (TEM). The magneto-photoluminescence experiments were performed at 2 K, with magnetic field up to 15 T, using a laser (532 nm) with 10 mW as excitation source. The luminescence was detected by a liquid-nitrogen-cooled InGaAs charged coupled device camera.

10.3 Results and Discussion

Figure 10.1a shows an atomic force microscopy image of the uncapped InAs ring sample. A 3D image of a single quantum ring is also displayed in Fig. 10.1b, which represents the statistical average of ring sizes in the sample: 0.9 nm in height, 15 nm inner and 60 nm outer diameters. In Fig. 10.1c is shown a plan-view TEM image from the sample with 50 nm GaAs cap layer that shows clearly the ring-like shape. A reduction in the quantum ring dimensions, if compared with the sample without cap layer, can be clearly observed but the origin for causing this change is not yet well understood. As will be discussed later, the ring radius of the capped samples is compatible with the optical experimental results. A cross-section TEM image, taken closer to $\langle 110 \rangle$ direction, is shown in Fig. 10.1d, where a 30 nm distance between the rims of the torus-like structure can be measured [21].

The PL spectra of the QRs, taken at 2 K and for B = 15 T (gray line), is shown in Fig. 10.2a. Only two radiative recombination channels due to a of ring distributions are observed: a shoulder at the low energy side and a main peak at higher energy side, labeled QR1 and QR2, respectively. The typical qualitative aspects for the shapes of these rings are shown on the left side of the figure. Both spectra were fit with two Gaussian lines to evaluate the evolution of the peaks energy and the area below the curves (integrated intensities) as a function of the applied magnetic field.

Under an external magnetic field, applied along the growth direction, we observed the expected blue shift of both emission bands, shown in Fig. 10.2b. The experimental points for the magnetic shift were obtained from the peak position at given B-value and subtracted the energy value at zero field. As the magnetic field increases, the changes from angular momentum from $l = 0$ to $l = 1$, from $l = 1$ to $l = 2$, and etc., and the energy being an slightly function of magnetic field [10]. The small oscillations of the peak position with increasing magnetic field were detected clearly for both ring emissions. However, being the amplitude of the oscillations of the QR1 structure $\sim$0.5 meV, or too small when compared to the linewidth of the PL band, $\sim$60 meV, the uncertainty of the energy oscillation becomes large for high fields. Yet, unambiguous oscillations of the integrated intensities are much easier to be detected.

The oscillations of the integrated intensity, as the magnetic field increases, are depicted in Fig. 10.3 [22]. One must note that the period and the sequences of minima

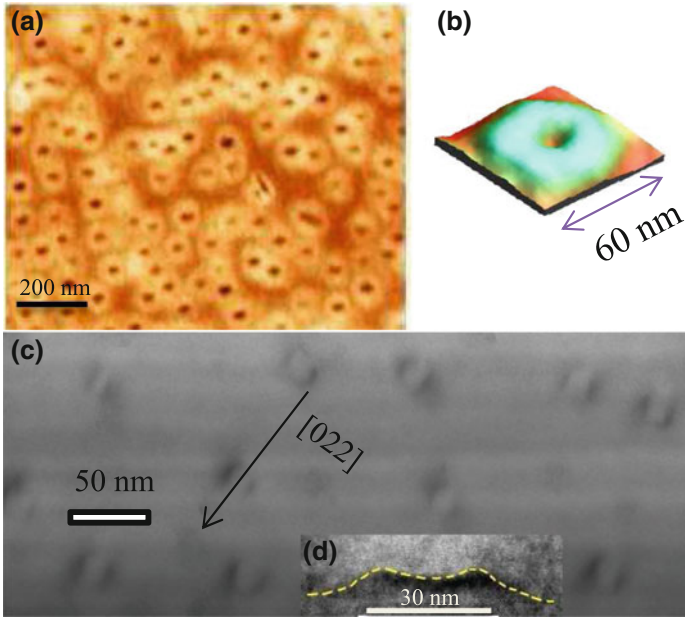

Fig. 10.1 **a** Atomic force microscope image from the InAs uncapped quantum rings sample. **b** 3D AFM image from a single quantum ring. **c** TEM plan-view image, taken slightly off the ⟨110⟩ direction. **d** A cross-section TEM image from the buried quantum ring samples. Yellow dashed-line is just a guide to the eyes

and maxima differ in these PL intensities (the same behavior was observed for the peak intensity plot). To understand their nature we will adapt the theoretical model of Römmer and Raikh [12, 13] to the structural conditions and parameters of our samples. According to this model, the electron and the hole move in a ring of radius R and zero cross-section width threaded by a magnetic flux $\Phi = B\pi R^2$ and they interact by means of a contact potential. The corresponding is given by

$$\widehat{H}_0 = \frac{(\widehat{P}_n + \frac{e\Phi}{2\pi Rc})^2}{2m_n} + \frac{(\widehat{P}_p - \frac{e\Phi}{2\pi Rc})^2}{2m_p} - 2\pi V \delta_P(\varphi_n - \varphi_p), \qquad (10.1)$$

where $\varphi_{n(p)}$ is the angular position of electron (hole) with orbital angular momentum $\widehat{P}_{n(p)} = \frac{\hbar}{iR}\frac{\partial}{\partial \varphi_{n(p)}}$.

The last term, representing an attractive short-range interaction, the function $\delta_P(\varphi_n - \varphi_p)$ is a 2π-periodic Dirac's δ-function. The strength of the interaction parameter V was chosen so that the exciton ground-state energy obtained by this expression fits the reported value of the exciton binding energy, and we have used for the exciton binding energy, the value 4.35 meV as reported [23]. As the strength of V increases, a more tightly bound exciton is produced, becoming thus less sensitive to magnetic and electric fields. The theoretical study of the model above will

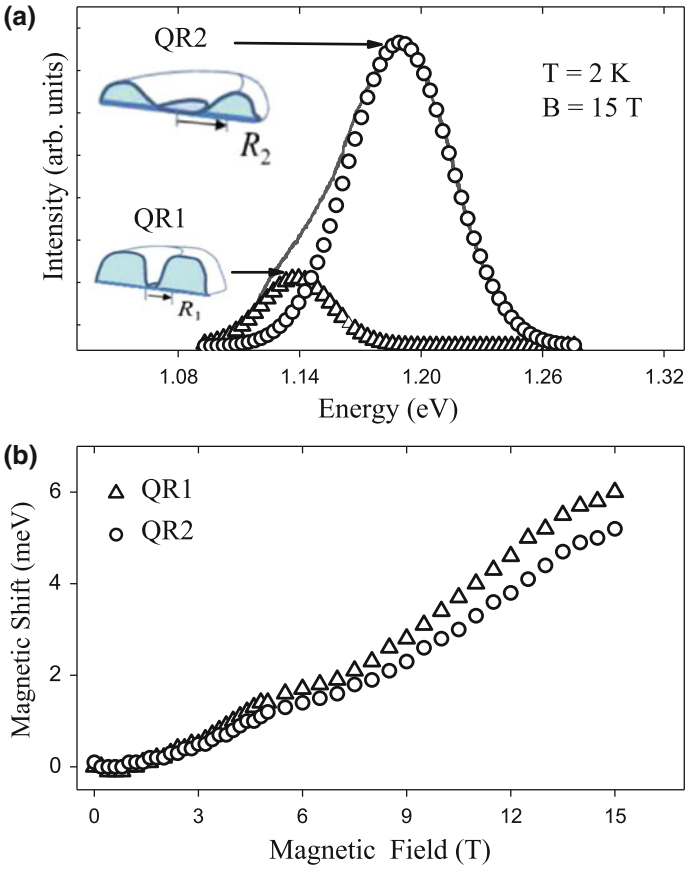

Fig. 10.2 **a** Photoluminescence spectra of InAs quantum ring sample, taken at 2 K and for B = 15 T (gray line). There are two radiative channels (triangles - peak 1 - and circles - peak 2) identified as the recombination from two different size of quantum rings, and with morphologies represented by the pictures on the left side. **b** The magnetic shift taken from the PL spectra at increasing magnetic field. One angular momentum transition is clearly observed at B = 5.5 T. Anther occurs near B = 13 T but only becomes clear in the integrated intensity

follow the work [11], which Chaplik and Kovalev, in Chap. 9 of the present book, extend in several ways. While we consider a contact interaction between electron and hole, Chaplik and Kovalev treat the more realistic, providing analytical results for the strong-coupling regime.

If we change to center-of-mass and relative coordinates,

$$\varphi_c = \left(m_n\varphi_n + m_p\varphi_p\right)/M, \tag{10.2}$$

$$\theta = \varphi_n - \varphi_p, \tag{10.3}$$

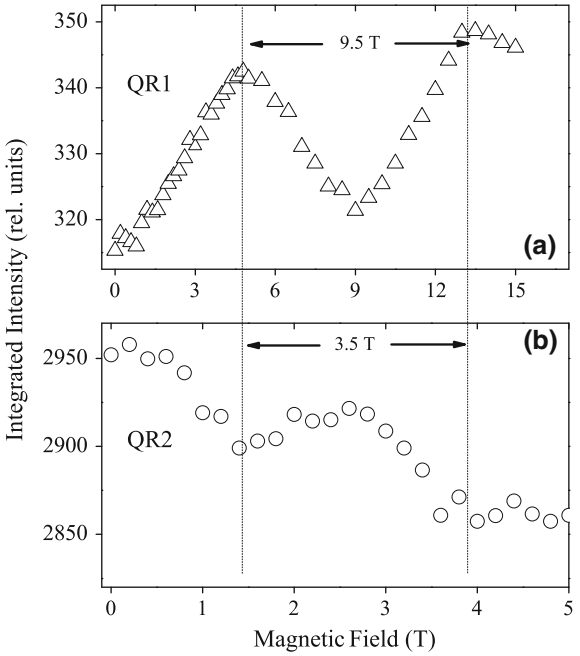

Fig. 10.3 Integrated intensities of the two emission lines as a function of the magnetic field. **a** In-phase AB-oscillations of the lower energy emission line of QR1 rings show a period corresponding to an effective radius $R = 11.6\,\text{nm}$. **b** Counterphase oscillations of the higher energy emission line of QR2 rings show a period corresponding to an effective radius $R = 19$ nm

with $M = m_n + m_p$ being the total mass, and θ being the angular separation between electron and hole positions on the ring. The Hamiltonian becomes,

$$\widehat{H}_0 = \widehat{H}_0^{\varphi_c} + \widehat{H}_0^{\theta}, \tag{10.4}$$

where

$$\widehat{H}_0^{\varphi_c} = -\frac{\hbar^2}{2MR^2}\frac{\partial^2}{\partial\varphi_c^2}, \tag{10.5}$$

$$\widehat{H}_0^{\theta} = \frac{\hbar^2}{2\mu R^2}\left(\frac{1}{i}\frac{\partial}{\partial\theta} + \frac{\Phi}{\Phi_0}\right)^2 - 2\pi V\delta_P(\theta), \tag{10.6}$$

and μ is the exciton reduced mass defined by $1/\mu = 1/m_n + 1/m_p$.

The solution for the center-of-mass motion equation is given by

$$\psi_c(\varphi_c) = \frac{e^{iJ\varphi_c}}{\sqrt{2\pi}} \tag{10.7}$$

with the corresponding eigenenergies

$$E_c(J) = \frac{\hbar^2 J^2}{2MR^2}. \tag{10.8}$$

As already stated, the main effects will be connected to the relative motion, i.e., to the internal structure of the exciton. Firstly, we can make a gauge transformation from an eigenfunction $\phi_{int}(\theta)$ of the Hamiltonian $\widehat{H}_0^{\theta}$ to a new function $\chi(\theta)$, as

$$\phi_{int}(\theta) = e^{-i\frac{\Phi}{\Phi_0}\theta}\chi(\theta). \tag{10.9}$$

One should note that both $|\phi_{int}(\theta)|^2$ or $|\chi(\theta)|^2$ give the probability density of finding electron and hole angular positions differing by θ. In terms of χ, the eigenequation for the relative motion reads

$$-\frac{\hbar^2}{2\mu R^2}\chi''(\theta) - 2\pi V\delta_P(\theta)\chi(\theta) = w\chi(\theta) \tag{10.10}$$

which is an eigenequation for a particle moving in a 2π-periodic potential. So, following Chaplik [11] the function χ satisfies Bloch's theorem and can be written as

$$\chi(\theta) = e^{ip\theta}\nu(\theta), \tag{10.11}$$

where ν is a 2π-periodic function. The Bloch function $\chi(\theta)$ satisfies the relation

$$\chi(\theta + 2\pi) = e^{i2p\pi}\chi(\theta) \tag{10.12}$$

and p can be restricted to the first Brillouin zone $(-1/2, 1/2]$. The total exciton wave function will be

$$\Psi_J(\Lambda, \theta) = \frac{e^{iJ\Lambda}}{\sqrt{2\pi}}\, e^{i(-\frac{\Phi}{\Phi_0}+p)(\theta)}\nu(\theta). \tag{10.13}$$

Given (10.12), we just need to determine the function $\chi(\theta)$ in the interval $[-\pi, \pi]$ using the torsional boundary conditions

$$\chi(\pi) = e^{i2p\pi}\chi(-\pi), \tag{10.14}$$

$$\chi'(\pi) = e^{i2p\pi}\chi'(-\pi). \tag{10.15}$$

One could understand the torsional boundary condition in terms of the AB effect: imagine the hole being at the origin. When the electron leaves the origin, it can arrive at the diametrically opposite point in the ring moving clockwise in one half or counterclockwise in the other half of the ring. Due to the magnetic field, its wave function will acquire according to these paths, so at the opposite point, there will be interferences. For zero or for $p = 1/2$ phase shifts along the half cycle paths, the interference will be constructive or destructive, a situation similar to the original AB effect detected in transport.

In order to determine the values for angular momentum J in the center of mass eigenfunction and p parameter phase value in the function χ, we need to go back to the coordinates φ_n and φ_p and impose that the total wave function be periodic if the

angular positions φ_n or φ_p change by 2π. The periodicity of $\Psi(\varphi_c, \theta)$ in φ_n and φ_p yields

$$Jm_n/M + \left(p - \frac{\Phi}{\Phi_0}\right) = N_n \in \mathbf{Z}, \tag{10.16}$$

$$Jm_p/M - (p - \frac{\Phi}{\Phi_0}) = N_p \in \mathbf{Z}. \tag{10.17}$$

The addition of these last equations yields

$$J = N_n + N_p \in \mathbf{Z}, \tag{10.18}$$

which means that the center-of-mass angular momentum, measured in units of $\hbar$, assumes integer values $J = 0, \pm 1, \pm 2, \ldots$, what is totally reasonable because it is exactly what would happen for a single particle of mass M moving in the ring.

By subtracting (10.16) from (10.17) we are lead to

$$\gamma J + 2\left(\frac{\Phi}{\Phi_0} - p\right) = N_p - N_n \in \mathbf{Z}, \tag{10.19}$$

where we have introduced the constant

$$\gamma = \frac{m_p - m_n}{M}. \tag{10.20}$$

Given an integer value for J, the parameter p can be determined uniquely in the interval $(-1/2, 1/2]$ because the integer $\gamma J + 2(\frac{\Phi}{\Phi_0} - p) = N_p - N_n$ has the same parity as J. Once we have determined p, we can solve the eigenequation (10.10) for χ under the boundary conditions (10.14) and (10.15) to find several internal eigenfunctions. Analogously to band structure calculations, for each Bloch wavevector p we have several eigenfunctions, one for each band. The fact that the parameter p depends on the becomes a relevant feature when dealing with excitons that involve either heavy or light holes. We will demonstrate that the hole in-plane effective mass can affect the way the AB oscillations are affected by external factors such as.

At this point it is easy to understand that several physical properties of this system will be invariant when the magnetic flux through the ring changes by a multiple of the quantum flux. The ratio $\frac{\Phi}{\Phi_0}$ enters in the equation (10.19) and determines p. If $\frac{\Phi}{\Phi_0}$ changes by an integer n, we can consider (10.18) and (10.19) with N_h increased by n and N_e decreased by n, so that the eigenvalues for J and the value for p remain unchanged. Therefore, the function χ and the internal energy w will be unchanged, while the total wave function will change by a local phase factor $e^{-in\theta}$. Any property which is not affected by this local phase factor will oscillate periodically as a function of the magnetic field.

To study the function χ giving the internal structure of the exciton in more detail, it is convenient to rewrite (10.10) in terms of dimensionless quantities,

$$-\chi'' - V_0\delta(\theta)\chi = \epsilon_{int}\chi, \tag{10.21}$$

where $\epsilon_{int} = w/\epsilon_0$ and $V_0 = 2\pi V/\epsilon_0$, with $\epsilon_0 = \hbar^2/2\mu R^2$. If we write negative energies as $\epsilon_{int} = -\kappa^2$ and positive energies as $\epsilon_{int} = k^2$, we get the following transcendental equations to determine the energies

$$\cosh(2\pi\kappa) - \cos(2\pi p) = \pi V_0 \frac{\sinh(2\pi\kappa)}{2\pi\kappa}, \tag{10.22}$$

for negative energies and

$$\cos(2\pi k) - \cos(2\pi p) = \pi V_0 \frac{\sin(2\pi k)}{2\pi k}, \tag{10.23}$$

for positive energies.

The corresponding eigenfunctions are

$$\chi_\kappa(\theta) = \begin{cases} N_{\kappa,p}[\sinh(\kappa\theta) - e^{-i2p\pi}\sinh(\kappa(\theta - 2\pi))], 0 \le \theta \le \pi \\ N_{\kappa,p}e^{-i2p\pi}[\sinh(\kappa(\theta + 2\pi)) - e^{-i2p\pi}\sinh(\kappa\theta)] - \pi \le \theta \le 0, \end{cases} \tag{10.24}$$

and

$$\chi_k(\theta) = \begin{cases} N_{k,p}[\sin(k\theta) - e^{-i2p\pi}\sin(k(\theta - 2\pi))], 0 \le \theta \le \pi \\ N_{k,p}e^{-i2p\pi}[\sin(k(\theta + 2\pi)) - e^{-i2p\pi}\sin(k\theta)], -\pi \le \theta \le 0 \end{cases} \tag{10.25}$$

where $N_{\kappa,p}$ and $N_{k,p}$ are normalization factors.

One needs to be careful when considering the cases $p = 0$ and $p = 1/2$. From (10.24) and (10.25), the corresponding functions χ will display even parity, i.e, $\chi(-\theta) = \chi(\theta)$. However, there are also special odd functions. When $p = 0$, we have special solutions of (10.23) which correspond to $k = 1, 2, 3, 4, \ldots$. Substituting these values of k in (10.24), one apparently gets functions identically equal to zero. However, a careful account of the dependence of the normalization factor on k implies that at these special values of k, the wave functions are, in fact, given by $\chi(\theta) = \sin(k\theta)/\sqrt{2\pi}$, which display odd parity. Analogously, when $p = 1/2$, we have special solutions of (10.23) corresponding to $k = 1/2, 3/2, 5/2, \ldots$, whose wave functions are also given by $\chi(\theta) = \sin(k\theta)/\sqrt{2\pi}$. It is easy to understand these odd solutions directly from (10.21). Being equal to zero at the origin, implies that the solutions will not feel the delta potential. Therefore, the equation is simply $-\chi'' = \epsilon_{exc}\chi$, which allows solutions of form $\sin(k\theta)$. To satisfy the boundary conditions, in (10.14) and (10.15), k must be integer when $p = 0$ and half-integer when $p = 1/2$.

The of the ground-state with wave function $\Psi_0(\Lambda, \theta)$ (see 10.13), will be given by

$$\mathscr{O}_0 = |\int_{-\pi}^{\pi} \Psi_0(\varphi_c, 0)\, d\varphi_c|^2, \tag{10.26}$$

and, therefore, is a on the magnetic flux through the ring since upon increasing the magnetic flux by Φ_0 the excitonic wave function changes by the phase-factor $e^{i\theta}$, which is equal to one for $\theta = 0$. This periodic behavior is displayed in Fig. 10.4a. In Chap. 9, Chaplik and Kovalev found oscillations of the intensity of the exciton line along with those of the biding energy in the strong-coupling case.

According to the contact interaction model just presented, the oscillations in Fig. 10.4a can be understood as follows. The ground-state has a center-of-mass angular momentum $J = 0$ and it is an even function. When the magnetic flux is zero, the χ function is 2π-periodic, on the other hand, for magnetic flux equal to $\frac{\Phi}{\Phi_0} = 1/2$, the χ function is anti-periodic. This fact combined with the fact that the ground-state wave function should not have any node, implies that $\chi(-\pi) = \chi(\pi) = 0$ and therefore the function χ for $\Phi = \Phi_0/2$ must be more concentrated around $\theta = 0$ than the χ function corresponding to the ground-state in the absence of magnetic flux. See this effect depicted in Fig. 10.4b. So, the oscillator strength should have a maximum at $\frac{\Phi}{\Phi_0} = 1/2$ according to the model presented above. It worths noticing

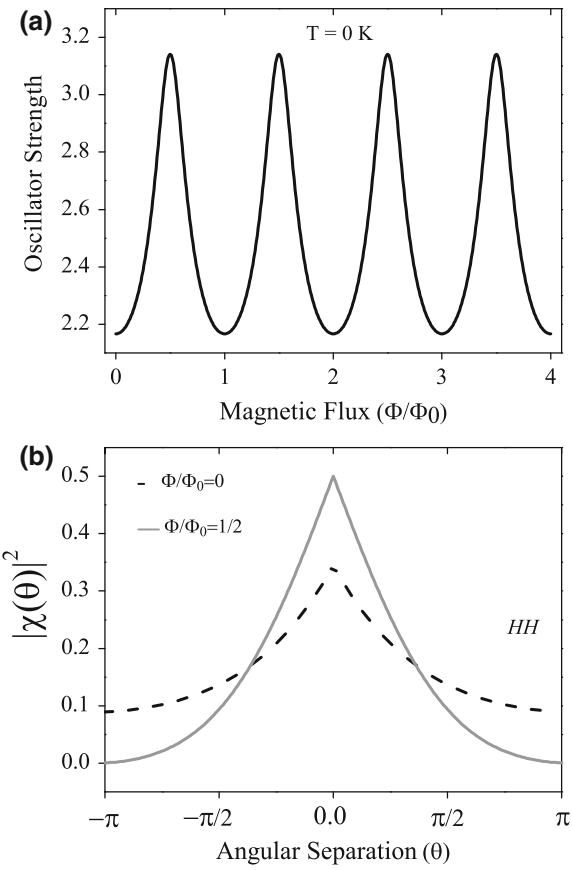

Fig. 10.4 **a** Oscillator strength as a function of magnetic flux for an heavy-hole exciton binding energy, $E_b = 4.35$ meV. **b** Probability density of finding the electron and the hole angular positions differing by θ for heavy-hole. Dotted black line correspond to magnetic flux equal to zero and gray curve corresponds to magnetic flux equal to $\Phi_0/2$. In this case, the value of the magnetic flux requires that the ground-state wave function be equal to zero at $\theta = \pm\pi$, and to keep the normalization, a more pronounced peak appears at $\theta = 0$ with direct impact on the oscillator strength

that the oscillation pattern just described is qualitatively similar for both heavy and light-hole excitons. However, quantitatively, the way the pattern is affected by external factors may depend drastically on the character of the valence band state involved. The oscillations of the oscillator strength of the excitonic recombination are a direct consequence of the of electrons and holes due to the Coulomb attraction, leading to the peculiar AB interference obtained experimentally. In the absence of, electron and hole would be independent particles and the corresponding oscillator strength would be independent of the magnetic flux through the ring. Yet, the sequence of minima and maxima obtained after this brief theoretical discussion would correspond only to the picture displayed in Fig. 10.3a of QR1 with an effective radius $R = 11.6$ nm. The oscillations corresponding to the QR2 emission appear in counterphase. Thus, additional ingredients must be added to the model as well as complementary experimental facts must be sought to understand such an anomalous behavior. If their period was also to be defined by the flux quantum, their effective QR radius would be $R = 19$ nm. The fact that the emission band QR2 has higher transition energy and larger average radius than QR1 suggests that QR2 may present smaller ring width and height than those for QR1. Also, note in Fig. 10.3b, that a monotonic decrease of the center of the oscillations takes place. Such an effect cannot be understood within our one-dimensional ring model, where the rings have zero width. The combination of finite ring width and certainly potential localization effects cannot be discarded as causes for the background shifts of the PL oscillations.

10.4 Inquiring for Reasons of AB-Oscillations in Counterphase

We turn next to a discussion of an effect which may potentially invert the sequence of minima and maxima of the oscillator-strength oscillations: the heating. In order to take into account the, one should generalize (10.26) including all excitonic states,

$$\mathscr{O}(T) = \frac{\sum_n \mathscr{O}_n e^{-E_n/k_B T}}{\sum_n e^{-E_n/k_B T}}, \tag{10.27}$$

where $\mathscr{O}_n$ is the oscillator strength for the $n-$th state (whose wave function is Ψ_n),

$$\mathscr{O}_n = |\int_{-\pi}^{\pi} \Psi_n(\varphi_c, 0)\, d\varphi_c|^2. \tag{10.28}$$

The electronic structure engineering in 0-dimensional structures appears as an effective tool for tuning the magnetic properties of these systems [24–26]. In particular, and configurations can be adjusted so that the character of the valence band ground-state can be changed from heavy- to light-hole character. As demonstrated below, this will have implications in the way the exciton recombination responds to

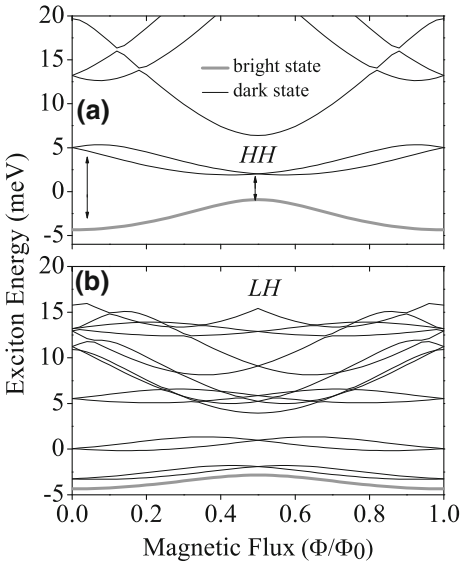

Fig. 10.5 Magnetic flux dependence of the first states of the exciton in the case of **a** heavy hole and **b** light hole. Exciton binding energy is $E_b = 4.35$ meV. The gray curves denotes the bright excitons (which have center-of-mass angular momentum $J = 0$), while black curves correspond to dark ones

the magnetic field and temperature. In Fig. 10.5, the exciton energy levels are displayed for HH and LH excitons, where the only parameter changed has been the in-plane hole mass. We must note that their in-plane effective masses (in the parabolic approximation) are related to the in the following way: $m_{HH} = 1/(\gamma_1 + \gamma_2)$ and $m_{LH} = 1/(\gamma_1 - \gamma_2)$ [24]. The character of the involved in the exciton recombination will, thus, affect the picture of the exciton energy dispersion and modify the shape of these levels as the magnetic field is varied. In the calculations, the InAs band parameters used are $m_e = 0.026$, $\gamma_1 = 20.4$, and $\gamma_2 = 8.3$ [23].

As the temperature rises, the occupation of excited levels of the exciton becomes more probable. Note that the first excited levels correspond all to dark excitons. As the dark exciton levels approach the bright one the net occupation of the ground-state changes and reduces the thermalized oscillator strength. At relatively high temperatures, this effect transforms the of the at $\frac{\Phi}{\Phi_0} = 1/2$ into a for the HH exciton as displayed in Fig. 10.6a. As the temperatures rises, the net occupation of the ground-state decreases as these levels become closer, what takes place at $\frac{\Phi}{\Phi_0} = 1/2$ for the HH-exciton. This, in turn, reduces the thermalized oscillator strength and its amplitude. Yet, for the LH exciton, such a reversion of the maximum is not observed for temperatures up to 34 K (see Fig. 10.6b). This is due to the peculiar electronic structure of the first LH-exciton levels displayed in Fig. 10.5b. According to our model, the temperature inversion of the maximum appears practically undetectable since the oscillator strength becomes essentially flat before inversion. Therefore the heating may invert the sequence of maxima and minima of the AB-oscillations, at least in the case of the heavy-hole excitons. However, this would take place at temperatures well above the 2 K and most of our magneto-optical measurements were performed below these temperatures. Hence, an alternative hypothesis must be

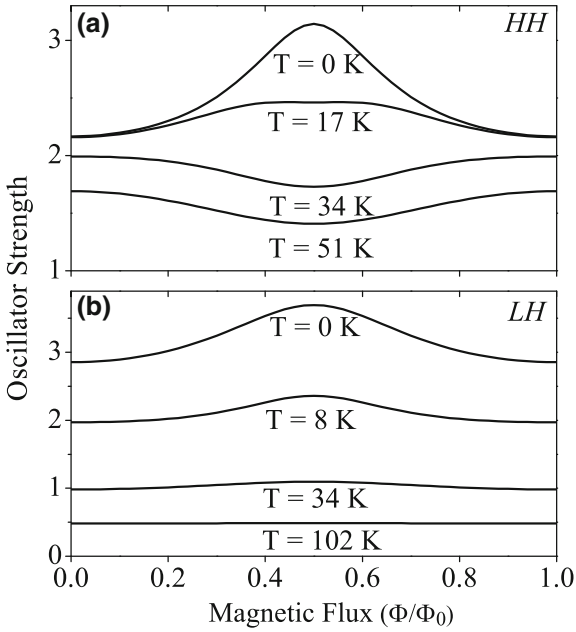

Fig. 10.6 Average oscillator strength as a function of magnetic flux for an exciton binding energy equal to $E_b = 4.35$ meV and for various temperatures. Panel **a** corresponds to the heavy-hole case and panel **b** corresponds to the light hole case. In case **a**, for magnetic flux equal to $\Phi_0/2$, the maximum oscillator strength gets converted into a minimum. In case **b**, since the total mass $(m_h + m_e)$ is large, the center-of-mass states are almost degenerated and the thermal average mix so many states that the oscillator strength decreases and becomes flat

searched in order to explain the experimental observation. Before considering another mechanism for the inversion in the sequences of maxima and minima, we should point out that [4] reports measurements of oscillatory behavior with the magnetic field at temperatures as high as 180 K for type II QDs. It is interesting that the data in [4] in fact show the inversion in the sequence of maxima and minima when the temperature is raised from 4 to 60 K (and, apparently, another inversion when the temperature is raised to 180 K) despite the difference between the system there and our system.

Another effect that can lead to the reversion of the maximum of the oscillator strength of the exciton ground-state, even at low temperatures, is the appearance of an in-plane electric field. Such an electric field can be caused by uniaxial strains and by eccentricity of the QR. We can explain this straightforwardly. The effect of an in-plane electric field F along x-axis can be added to the Hamiltonian used in the previous explanations as

$$\widehat{H} = \widehat{H}_0 + eFR(\cos(\varphi_n) - \cos(\varphi_p)). \tag{10.29}$$

In order to compute the eigenfunctions in the presence of the in-plane electric field, we write down the Hamiltonian matrix in the basis of the eigenfunctions of $\widehat{H}_0$ and proceed with a numerical diagonalization. Since we are interested in low temperatures, we can truncate the matrix dimension after including all basis states whose energies are lower than some high enough cut-off value. It is easy to show that the electric field can only couple states whose center-of-mass angular momenta

differ by one, an this simplifies significantly the task of building the Hamiltonian matrix.

With respect to the dependence of the matrix elements on the magnetic flux, we see immediately that the diagonal elements are periodic, since they correspond to the energies in the absence of the electric field, which remain unchanged when the magnetic flux changes by a multiple of the flux quantum Φ_0, as discussed in the previous section. The off-diagonal elements $\langle \Psi_m | eFR(\cos(\varphi_n) - \cos(\varphi_p)) | \Psi_{m'} \rangle$ are also periodic. This is due to the fact that the eigenfunctions Ψ_m and $\Psi_{m'}$, in the absence of electric field, change by the same phase factor $e^{in(\varphi_n - \varphi_p)}$ when the magnetic flux is changed by $n\Phi_0$ (n integer). This common phase-factor is canceled out when computing the off-diagonal matrix element above. Therefore the exciton energies and the oscillator strength in the presence of an in-plane electric field will be periodic functions of the magnetic flux with period equal to Φ_0. In general, we expect that the oscillator strength will decrease when we increase the electric field, since the angular separation between the electron and the hole becomes larger.

For the particular cases of magnetic flux equal to zero or equal to $\Phi_0/2$, we can get a more detailed understanding exploiting a symmetry of the Hamiltonian. The Hamiltonian in (10.29) is invariant under a reflection relative to the x-axis combined with an inversion of the magnetic field. For zero magnetic flux, this implies that the eigenfunctions will be even or odd. For magnetic flux equal to $\Phi_0/2$, the symmetry under simultaneous reflexion and inversion of the magnetic field leads to a relation between the eigenfunctions for $\Phi = \Phi_0/2$ and for $\Phi = -\Phi_0/2$,

$$\Psi(-\varphi_c, -\theta, \Phi = -\Phi_0/2) = \pm \Psi(\varphi_c, \theta, \Phi = \Phi_0/2). \tag{10.30}$$

On the other hand we know, from the previous discussions, that increasing the magnetic flux by Φ_0 adds a phase-factor to the eigenfunction,

$$\Psi(\varphi_c, \theta, \Phi = \Phi_0/2) = e^{-i\theta}\, \Psi(\varphi_c, \theta, \Phi = -\Phi_0/2). \tag{10.31}$$

With (10.30) and (10.31), we get

$$\Psi(\varphi_c, \theta, \Phi = \Phi_0/2) = \pm e^{-i\theta}\, \Psi(-\varphi_c, -\theta, \Phi = \Phi_0/2), \tag{10.32}$$

and after making the same gauge transformation as before, defining

$$\tilde{\Psi}(\varphi_c, \theta, \Phi = \Phi_0/2) = e^{i\frac{\Phi}{\Phi_0}\theta}\, \Psi(\varphi_c, \theta, \Phi = \Phi_0/2), \tag{10.33}$$

we find that these functions $\tilde{\Psi}$ will have defined parity when $\Phi = \Phi_0/2$,

$$\tilde{\Psi}(\varphi_c, \theta, \Phi = \Phi_0/2) = \pm \tilde{\Psi}(-\varphi_c, -\theta, \Phi = \Phi_0/2). \tag{10.34}$$

Naturally, the same is true for any half-integer value of Φ/Φ_0. For such special values of magnetic flux, an even ground-state will exist as we increase the electric field until

some , F_C, is achieved. It is natural that at low electric fields the ground-state be even, since at zero electric field the ground-state has center-of-mass angular momentum $J = 0$ and an even function χ. At F_C, there is a level-crossing between an even and an odd state and, above F_C, the ground-state becomes odd, and where electron and hole becoming more separated allows leads to lower energy. Here it is also natural that, at high electric fields, the ground-state wave function be odd, since it will have significant projection on zero electric field states whose corresponding χ functions are odd, since only these functions can give rise to electron and hole well separated as we must have at high electric field.

At $\Phi = \Phi_0/2$, by (10.33) and (10.34), the odd ground-state wave functions satisfies $\Psi(\varphi_c, 0) = -\Psi(-\varphi_c, 0)$, which implies zero oscillator strength when we consider (10.26). Therefore, if for zero electric field, we had a maximum in the oscillator strength at $\Phi = \Phi_0/2$, for electric field above the critical value, we have a minimum in the oscillator strength at $\Phi = \Phi/2$ as illustrated in Fig. 10.7. The inversion of the maximum in the curves of OS against magnetic flux at $T = 0$ K occurs as the result of increasing the in-plane electric field above certain critical value. This effect was first discussed in [13], where the electric field was supposed applied in a controllable fashion. Here, however, the electric field is supposed to be present in the sample due to uniaxial strains and eccentricity of the QR.

According to the description above, the stronger the electric field becomes the higher is the projection of the ground-state over states with electron and hole more separated, decreasing the oscillator strength as well as its sensitivity to the magnetic field. This is particularly relevant at $\Phi/\Phi_0 = 1/2$ beyond the critical field, when the ground-state becomes a pure odd function with null oscilator strength [13]. For QR with finite width this reduction to zero is not expected.

Since the AB-oscillations in counterphase appear only for the QR2 emission, a set of complementary measurements can be put in place to elucidate whether or not in-plane electric fields are present in one quantum ring set and not in the other.

Throughout the course of the synthesis of self-assembled quantum dots and rings, strain fields are formed in the (001) plane. This has been used to control the alignment and elongation of these 0-dimensional structures along certain crystallographic directions. Given the spatial differences of In migration velocities, [27] the $[1\bar{1}0]$ appears as the preferential direction for QR elongation and a built-in electric field may appear due to the piezoelectric effect [28]. The potential appearance of built-in electric fields in such structures has been a topic discussed previously [17]. Since the piezoelectric polarization leads to the red-shift of the PL emission line (Stark effect), increasing the free-carrier density one may screen the built-in electric field provoking a subsequent blue-shift of the transition energy. This can be achieved by varying the excitation intensity. In Fig. 10.8 we have displayed the PL spectra versus excitation intensity. Since exciton excited states decay non-radiatively much faster than by photon emission, the hypothesis of bimodal subsets of QRs prevails. In the PL spectra displayed in Fig. 10.8, we see that only for very high power excitation it is possible to see emission from excited states. In Fig. 10.2, the power excitation was very low, reinforcing the interpretation of bimodal QRs. The excitation power

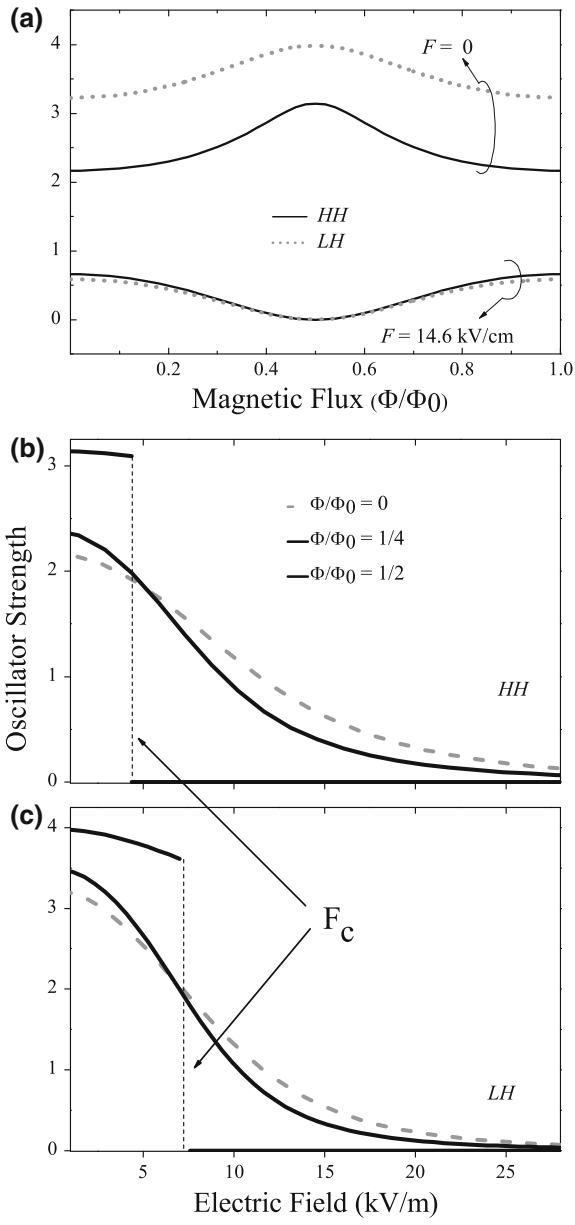

Fig. 10.7 **a** Average oscillator strength for the ground-state excitons as a function of the magnetic flux. Top curves calculated for $F = 0$ and bottom curves for $F = 14.6\,\text{kV/cm}$. For electric fields above some critical value, F_c, the oscillator strengths become equal to zero at the magnetic flux equal to $\Phi_0/2$. Panels **b** and **c**: Oscillator strength for heavy- and light-hole exciton ground-states as a function of the electric field for some values of magnetic flux. For $\frac{\Phi}{\Phi_0} = 1/2$, there is an abrupt change of the oscillator strength due to level crossing happening at $F \simeq 4.8\,\text{kV/cm}$: for lower electric fields, the ground-state displays even parity, for higher electric fields, the ground-state changes to odd parity. Since the symmetry is exact at this particular magnetic flux, even and odd states do not couple and, thus, the occurrence of level crossing with consequent abrupt changes in the oscillator strengths. In this figure, we considered a ring of radius 10 nm for both heavy and light holes

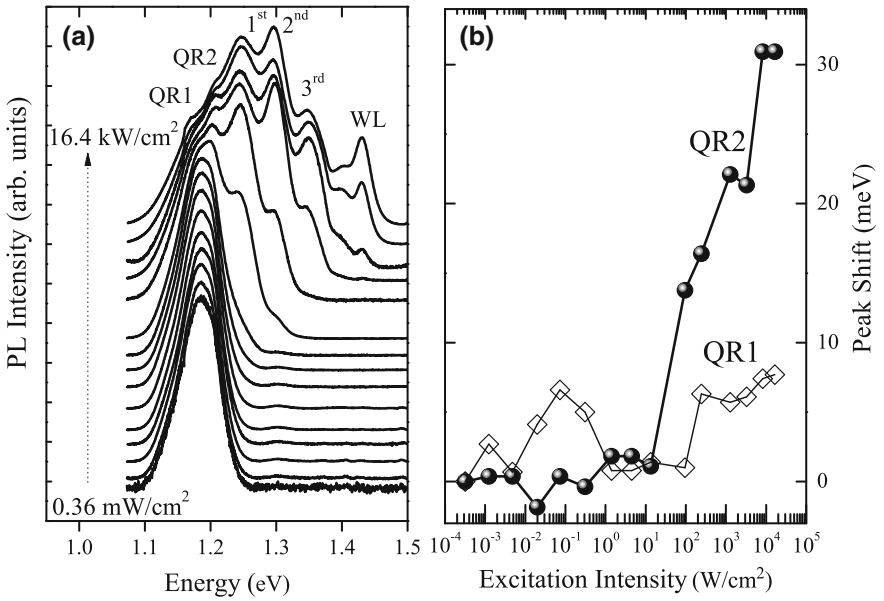

Fig. 10.8 **a** Series of the PL emission for increasing excitation powers from 0.36 mW/cm^2 (bottom) to 16.4 kW/cm^2 (top). **b** Position of emission peaks versus excitation power

increase has provoked the appearance of additional emission bands corresponding to the the excited states of QR2 band.

In Fig. 10.8b, we plotted the energy shift of the QR1 and QR2 versus excitation intensity. Note the blue shift of the emission band QR2 at the high excitation regime while the emission band QR1 remains practically constant. This would accord with the idea that a has been in QR2 set and not in QR1 which is consistent with the contrasting AB-interference patterns. We are however faced with the question: why the built-in electric fields related to the band QR1 are negligible if the effect of the elongation should affect all rings? The potential answer to that question may reside in different ring widths corresponding to each emission band: for QR1 it is larger than that for QR2, as mentioned above, leading to a more significant strain field relief for the former than for the latter. This would ultimately result in a much lower piezoelectric field in the QR2 set. Yet, one may still argue that this cannot be considered a definitive proof.

To construct a more convincing argument for the presence of the built-in electric field in QR2 while expecting negligible values in QR1, additional optical experiments were performed: PL measurements experiments versus temperature are displayed in Fig. 10.9a. The variation of the integrated intensity for each emission band, as a function of temperature, is plotted in Fig. 10.9b. It is reasonable to assume that a decrease of the PL intensity with temperature should take place when dark excitonic states become thermally occupied. The QR1 emission follows this expected pattern. Yet,

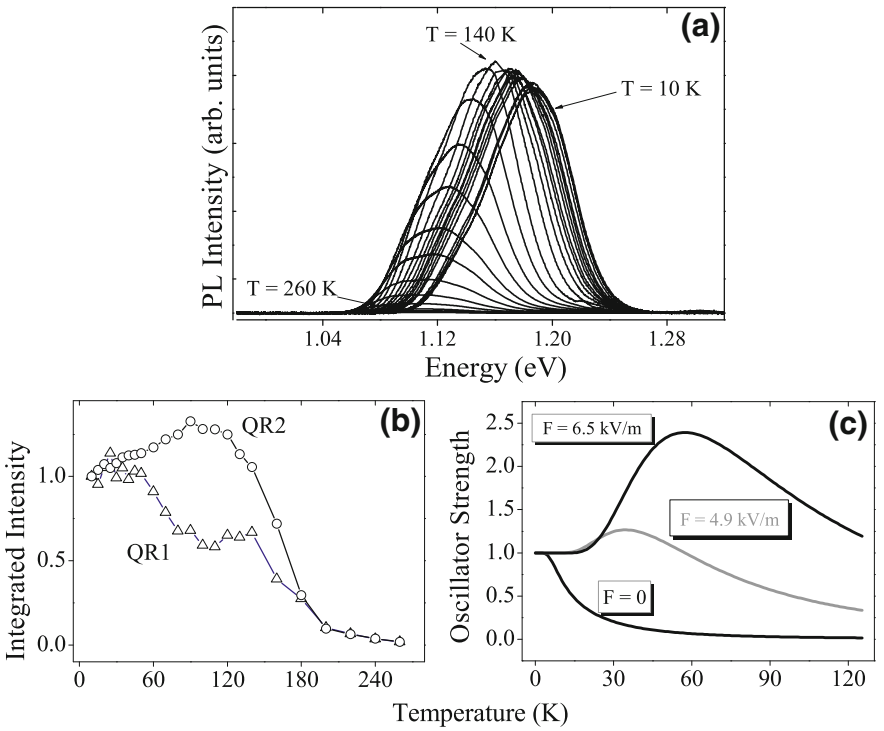

Fig. 10.9 **a** PL spectra obtained for several temperatures. At low temperature, the PL spectra are dominated by the emission band QR2, whereas above 160 K, it becomes dominated by QR1, which is attributed to the transference of carriers between QRs, via wetting layer (WL), favoring the lower energy states, as also observed in QD systems. **b** and **c** PL integrated intensity normalized to the value at T = 10 K, for the emission bands QR1 and QR2, respectively. **c** Calculated OS (normalized to the value at T = 0) for three values of the in-plane electric field F considering a ring of radius 19 nm. The increase of PL intensity at low temperatures can be understood as an electric field effect

an intensity increase takes place for QR2 at $T < 100$ K and we may prove that this is another signature of the presence of an in-plane electric field in this set of ring samples. By using our previously described model we are able to calculate the oscillator strength as a function of temperature for finite values of the in-plane field and the results are shown in Fig. 10.9c. According to this model, the oscillation strength increases by the activation of more efficient channels for optical recombination at excited states, where the electron-hole angular separation is smaller if compared to the ground-state. It is interesting that this complementary experiment confirms that the for the band QR2 (Fig. 10.3b) cannot be ascribed to occupation effects induced by temperature for HH-excitons, since only for $T > 150$ K an effective reduction of the ground-state population takes place, which is far above the temperature of 2 K where the AB-oscillations were detected. It is common, in systems that display bimodality, to ascribe the increase in intensity of the lower energy emission with respect to the

one at higher temperature to thermal redistribution of carriers to the lower energy ensemble with increasing temperature. However, in the results displayed in Fig. 10.9, it is the QR2 emission, with higher energy, that suffers the relative increase for temperatures between 10 and 140 K. This reinforces the conviction of the presence of an in plane electric field in the QR2 set that opposes the mechanism of thermal activation transference of carriers from QR2 to QR1.

Finally, other attempts were made to find such oscillations in neutral excitons using similar samples like the one described here [29]. According to [20], the main condition for observation AB effect in in quantum rings, is the presence of an effective confinement region close to 7 nm, given by the difference between the outer and inner radii. This is approximately the value reported in Fig. 10.1d.

10.5 Magneto-Optical Properties of Laterally Ordered Quantum Rings

In this section[1] we investigate a hybrid type of structure, similar to the one described in Chap. 7, where one layer of InAs/GaAs QRs was grown on a of InGaAs/GaAs QDs laterally ordered. This hybrid nanostructure reveals strong anisotropy in polarized PL spectrum and unusually strong oscillations of PL intensities as a function of magnetic field in both QDs and QRs spectral emission range. These oscillations are observed simultaneously and related to the AB interference. Such behavior of the magneto-PL can be understood in terms of joint effects associated to strain, spatial and magnetic confinements affecting the valence band states forming the ground state of the hybrid structure.

The sample used in this section was grown as described in Chap. 7 (Sect. 7.2). In order to obtain realistic strain profiles inside the QDs and QR layers of our hybrid structures, we used a commercial software package to simulated nanostructures with finite-element method (FEM). The QDs and QR dimensions as well as morphologies were matched to the TEM observations and inserted into a GaAs matrix [30, 31]. The In composition inside the QDs was fixed to 40% while at the QR it was set to 25%, according to previous results [21]. A lateral cut from the FEM results is shown in Fig. 10.10b superimposed to a TEM image of the QD/QR stack. The color code with green/yellow/red areas represent regions of the dots and rings subjected to tensile (positive) out-of-plane strain, due to pseudomorphic relaxation under in-plane compressive strain, while blue regions show areas subjected to compressive (negative) strain due to an in-plane lattice expansion associated to GaAs capping regions between QDs. Strain profiles along selected directions are extracted from the FEM data and used for valence band deformation potential calculations and displayed in Fig. 10.10c for the lowest QD. Note the difference between the heavy

[1]This section is based on the publication [33], certain parts of which are reproduced here with permission.

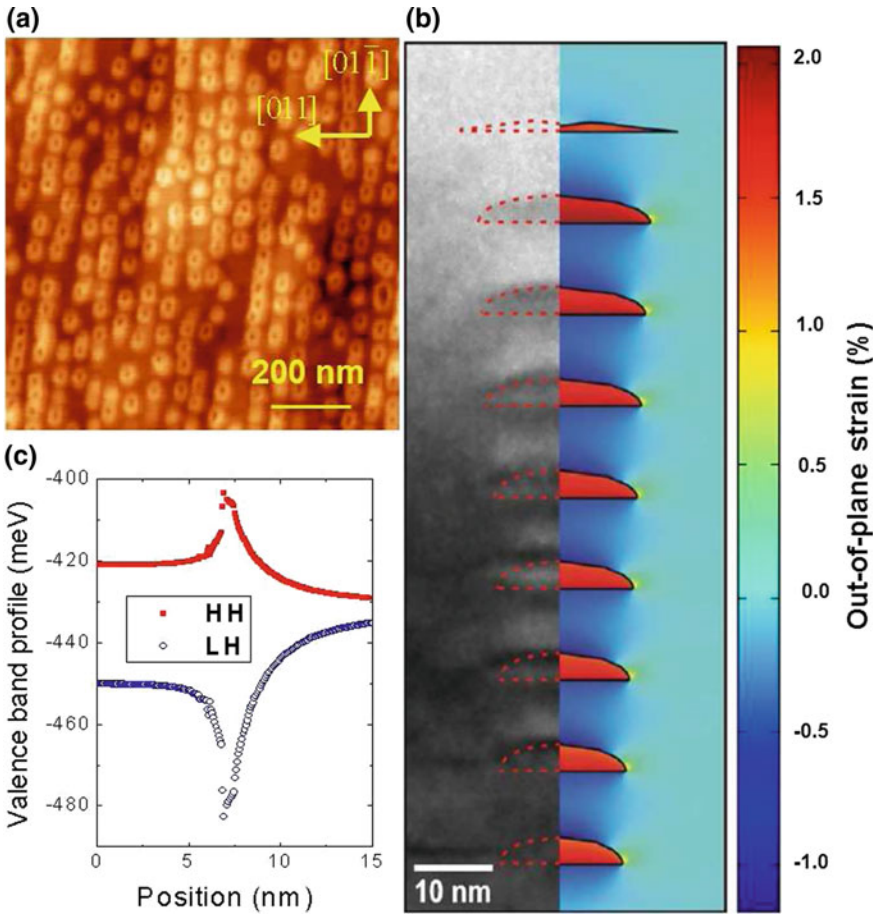

Fig. 10.10 Panel **a**: AFM image of the topmost layer containing QR chains grown on an $In_{0.4}Ga_{0.6}As/GaAs(100)$ vertical. Panel **b**: Left side: Multi-beam bright field TEM images of the hybrid multilayered sample used in this work. Right side: The FEM model of the QD/QR stack. For the out-of-plane strain in color code shown on the right, the blue colors are related to compressive (negative) out-of plane strain while green/yellow/red colors denote tensile (positive) out-of-plane strain. Panel **c**: Calculated valence band deformation potential profiles for repulsive heavy-hole (HH) and attractive light-hole (LH) carriers in the QD region (adapted from [33])

(HH) and light-hole (LH) energy shifts that would ultimately lead to difference on the character of the hole confinement according to the subband.

The photoluminescence (PL) measurements were performed in a variable temperature, closed-cycle, helium cryostat using various laser sources for the PL excitation. The laser spot diameter was $\sim$20 μm and the optical excitation power was kept in the range of $10^{-7} - 10^{2}$ mW. The PL signal from the sample was dispersed by a monochromator and detected by a liquid nitrogen-cooled InGaAs photodiode de-

tector array. Magneto-photoluminescence (MPL) measurements were performed at 4.2 K and with magnetic fields up to 21 T. A monomode optical fiber with 5 μm core was used to bring the 640 nm excitation from a diode laser to the sample, with a focus of 1 μm spot and an excitation power of 1 mW. The luminescence from the sample was then collected by a multimode 200 μm optical fiber before being dispersed by a 0.5 m spectrometer and analyzed with a diffraction grating and a nitrogen-cooled CCD. A set of quarter wave plates and linear polarizers, placed close to the sample were then used to circularly polarize the emissions. Both σ^+ and σ^- polarizations were analyzed by changing from $+45°$ to $-45°$ the direction of the magnetic field with respect to light propagation direction.

Figure 10.11a shows continuous wave PL spectra measured at different excitation wavelengths and normalized to the PL peak values in each spectrum and the lines were intentioned displaced vertically for clarity and easier comparison. The relative contribution from the low energy PL band to the total low temperature spectrum increases if the excitation wavelength λ_{ex} is shortened. The band at E = 1.079 eV, is ascribed to the ground state excitonic transition in the QR layer. On the contrary, the contribution from the high energy PL band, at E = 1.179 eV, increases if the λ_{ex} value is increased. This high energy band corresponds to excitonic transitions from the buried layers of dots. While the absorption coefficient of our multilayered structure depends substantially on the radiation wavelength [34], a short wavelength radiation will be absorbed predominantly by the top QR layer. Therefore, short excitation wavelengths increase the QR contribution to the whole PL spectrum, as can be seen in Fig. 10.11a, and reaches only a few buried top dot layers. The deeper the excitation

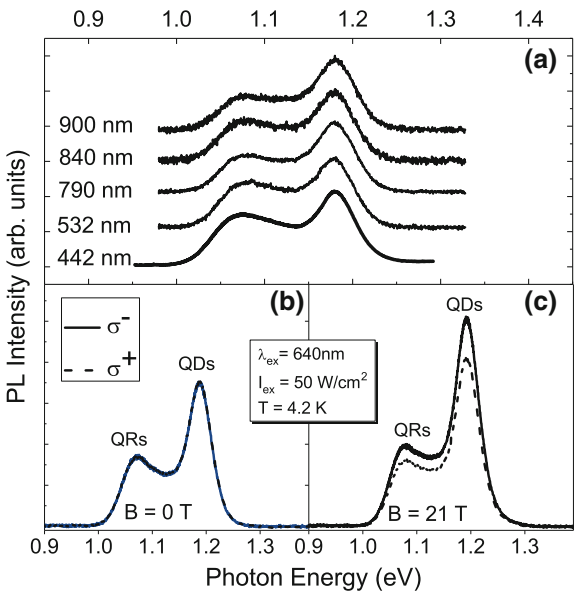

Fig. 10.11 Panel **a**: PL spectra measured at different excitation wavelengths. Panels **b**, **c**: Spectra excited with $\lambda_{ex} = 640$ nm, excitation power $I_{ex} = 50\,W/cm^2$ and measured for the circular polarizations, σ^+ and σ^-, in Faraday geometry for: **b** B = 0 T and **c** B = 21 T (adapted from [33])

reaches, the larger is the relative intensity difference between QR and QD emission signals.

For magneto-PL measurements, the emission signals were collected after using an excitation intensity I_{ex} = 50 W/cm^2, and the low temperature spectra for circular polarizations are shown in panel (b) for B = 0 T and in panel (c) for B = 21 T of Fig. 10.11. Both lower and higher energy PL bands are blueshifted for increasing magnetic field, regardless the type of polarized emission, although the PL intensities for QR (lower) and QD (higher) bands behave rather differently as the field is increased. The circular polarized anisotropy that arises, for finite magnetic fields, can be seen in the panels of Fig. 10.12. The diamagnetic shift, defined as $\Delta E_{Diam} = [E^{\sigma+}(B) + E^{\sigma-}(B)]/2 - E(0)$, is shown in Fig. 10.12a. The positive curvature is characteristic of a diamagnetic behavior and reveals a smooth dependence on the magnetic field up to ∼6 T. Furthermore, significant changes in the diamagnetic curvature for field strengths above 6 T can be noted. It is known, that the PL emission split into lower and upper branches due to Zeeman effect for excitons under magnetic field. As reported in [35] for very similar system, the value of Zeeman splitting shows linear dependence on B and with a slope of ≃120 μ eV/T. By applying this rate to our QD/QR hybrid structure, we estimated the value for the Zeeman splitting on the order of 2.5 meV for B = 21 T in the sample. Taking into account the width ≃50 meV of the PL bands for both QD and QR ensembles we see that it is not possible to resolve such a small splitting, in our case. The total shift to higher energies of the PL peak positions with applied field, behaves distinctly as seen in our experiments. For the QR emission line, no sudden changes can be identified in the peak position at the critical field $B_c = 6$ T, beside the subtle oscillations above B_c

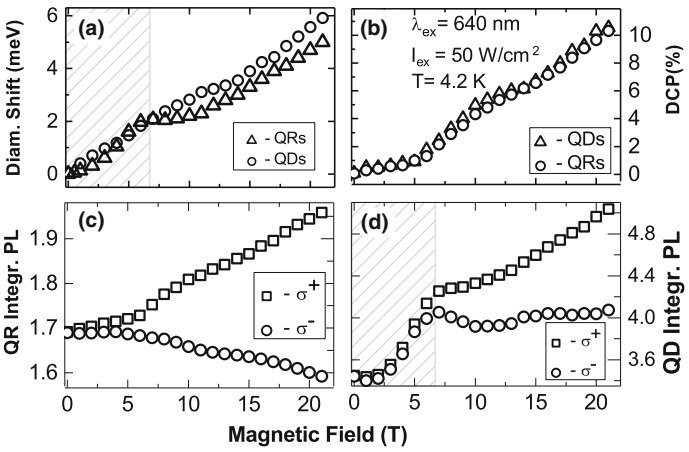

Fig. 10.12 **a** Diamagnetic shift of the exciton ground state transitions versus magnetic field. **b** Degree of Circular Polarization measured at the peak energies, for QDs and QRs σ^+ and σ^- emissions. The integrated PL intensities for the hybrid sample, with σ^+ and σ^- polarizations measured in Faraday geometry, are shown for: QRs (panel **c**) and QDs(panel **d**) as a function of magnetic field (adapted from [33])

that can be ascribed to the changes in the angular momentum of the ground state with increasing magnetic field [22]. The superlattice of QDs shows a discontinuity on the rate of change at 6 T and then, an almost quadratic increase above B_c. However, the degree of circular polarization (DCP), although increasing for increasing B, displays equal rates for the QR and QD emission bands up to 21 T, as depicted in Fig. 10.12b. The QR integrated σ^+ intensities, displayed in Fig. 10.12c, d, also oscillates slightly displaying changes very similar to the diamagnetic shift behavior; although the integrated σ^- intensities of QD and QR show rather different behavior below and above 6 T. The QR σ^- intensity is almost constant below 6 T and then decreases gradually with increasing field whereas the σ^- intensity for QD superlattice increases almost quadratically below 6 T and oscillates slightly around a constant value above 6 T. The most drastic changes in PL occurring at about 6 T is reflected in the energy position and PL intensity of the QD emission band. This peculiarity can only be expected when analyzing the potential differences between the HH and LH potential profiles and the tuning of the ground state character of the valence band with the magnetic field. As reported previously, the valence ground state can be transformed from type I to type II in strained QDs, with profiles shown in Fig. 10.10c.

The details of the transformation of valence band due to the combination of strain profiles, confinement, magnetic field, and interdot coupling are given in a number of studies [36–38]. The magnetic tuning of the valance band character (HH or LH) in QDs has been already reported experimentally and confirmed theoretically [24, 26] and physical explanation for the origin of the type-I to type-II transition in the valence band can be given as in [36]. Accordingly, the LH in type I QD is localized inside the central area while HH ground state appears at the boundary in type-II systems, as expected from the results displayed in Fig. 10.10c. The transition from type I to type II occurs when the eigenstates of the carriers change localization and angular momentum, with the probability for excitonic recombination decreasing drastically. Thus, a quenching of the PL spectrum is expected after a certain value of the magnetic field. If the QD structure occurs in type II state the conditions for optical AB can be fulfilled. Therefore, we consider that the kink in frequency observed together with PL oscillations are related to the character transition accompanied with the subsequent AB interference.

To understand the reason for the subtle oscillations of the QR emission line while the corresponding QD peak suffers abrupt changes, we have included the results of an electronic structure calculation in Fig. 10.13. In this case, we applied the model reported in [32] for a hybrid QD-QR system, without inter-subband coupling. For QR with wide rims, the oscillations of the ground state due to angular momentum transitions are attenuated by the effective dielectric shift related to the lateral wave function confinement with the magnetic field. Note, that for a QR profile as depicted in Fig. 10.13a, the overlap of various angular momentum valence band levels (with pure HH-character) describes almost a parabola with B. For narrower QR, as shown in Fig. 10.13c, the angular momentum transitions for the ground state are more clearly defined. It is the case for the predicted type I - type II transition in the valence band for a strained QD. The HH-wave function is confined in a narrow rim near the QD interfaces [37]. This transition is apparent in the ground state if the proper combination

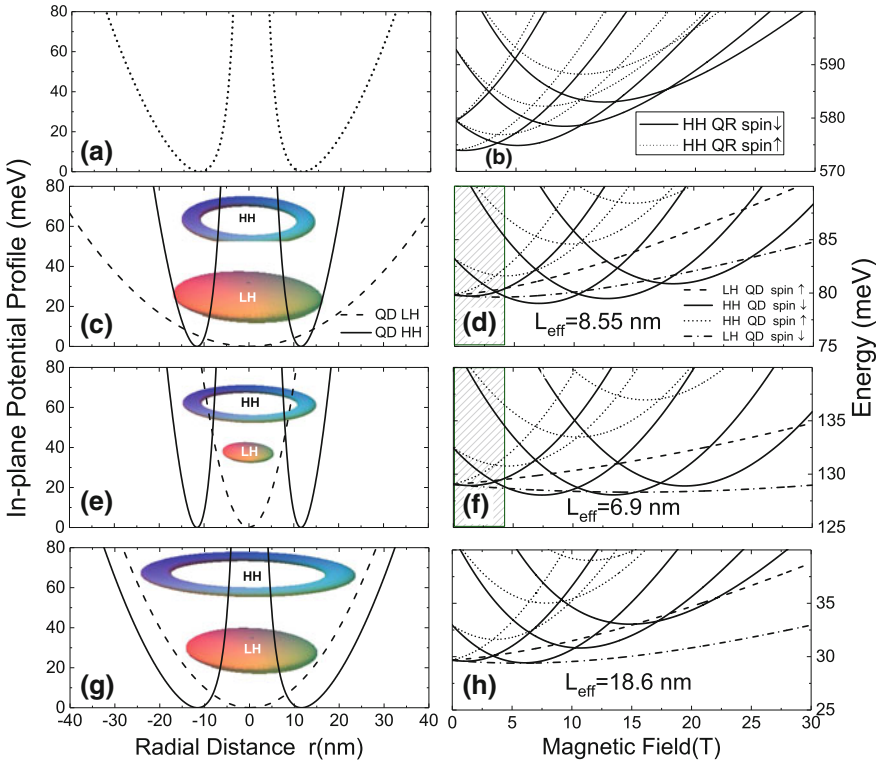

Fig. 10.13 **a** Lateral QR profile and **b** the corresponding lower valence band levels with HH character. Various combinations of QD profiles for the HH and LH subbands (**c**, **e**, **g**) with a HH in the outer rim and a LH confined inside and **d**, **f**, **g** the corresponding lower valence band states in a QD with HH in the outer rim and a LH confined inside (adapted from [33])

of strain fields and QD sizes is tuned, as illustrated in Fig. 10.13c–h. Here, the HH QD state corresponds to the type II transition while the LH optical recombination remains type-I in the QD. Another interesting fact detected experimentally is that the type I - type II transition with magnetic field is strongly spin-dependent, as shown in Fig. 10.12d, where the kink of the peak oscillation is almost imperceptible for the σ^+ polarization. In this case, the valence band g-factor plays a role. In Fig. 10.13d, f, the ground state character changes at the boundary of the shadowed region, yet this transition is only available for the spin-down polarization. The spin-up ground state may remain type-I for the whole magnetic field range.

References

1. Y. Aharonov, D. Bohm, Phys. Rev. **115**, 485 (1959)
2. Y. Aharonov, D. Bohm, Phys. Rev. **123**, 1511 (1961)

3. M. Grochol, F. Grosse, R. Zimmermann, Phys. Rev. B **74**, 115416 (2006)
4. I.R. Sellers, V.R. Whiteside, I.L. Kuskovsky, A.O. Govorov, B.D. McCombe, Phys. Rev. Lett. **100**, 136405 (2008)
5. I.R. Sellers, A.O. Govorov, B.D. McCombe, J. Nanoelectron. Optoelectron. **6**, 4 (2011)
6. P.A. Orellana, M. Pacheco, Phys. Rev. B **71**, 235330 (2005)
7. J.M. García, G. Medeiros-Ribeiro, K. Schmidt, T. Ngo, J.L. Feng, A. Lorke, J. Kotthaus, P.M. Petroff, Appl. Phys. Lett. **71**, 2014 (1997)
8. A. Lorke, R.J. Luyken, A.O. Govorov, J.P. Kotthaus, J.M. García, P.M. Petroff, Phys. Rev. Lett. **84**, 2223 (2008)
9. F.M. Alves, C. Trallero-Giner, V. Lopez-Richard, G.E. Marques, Phys. Rev. B **77**, 035434 (2008)
10. A. Lorke, R.J. Luyken, A.O. Govorov, J.P. Kotthaus, J.M. García, P.M. Petroff, Phys. Rev. Lett. **84**, 2223 (2000)
11. A. Chaplik, Zh Pis'ma, Éksp, Teor. Fiz. **62**, 885 (1995). [JETP Lett. **62**, 900(1995)]
12. R.A. Römer, M.E. Raikh, Phys. Rev. B **62**, 7045 (2000), Phys. Stat. Sol. (b) **221**, 535 (2000)
13. A.M. Fischer, V.L. Campo Jr., M.E. Portnoi, R.A. Röomer, Phys. Rev. Lett. **102**, 096405 (2009)
14. E. Ribeiro, A.O. Govorov, W. Carvalho Jr., G. Medeiros-Ribeiro, Phys. Rev. Lett. **92**, 126402 (2004)
15. C. Gonzalez-Santander, F. Dominguez-Adame, R.A. Romer, Phys. Rev. B **84**, 235103 (2011)
16. A.O. Govorov, S.E. Ulloa, K. Karrai, R.J. Warburton, Phys. Rev. B **66**, 081309(R) (2002)
17. J.A. Barker, R.J. Warburton, E.P. O'Reilly, Phys. Rev. B **69**, 035327 (2004)
18. J.I. Climente, J. Planelles, F. Rajadell, J. Phys.: Condens. Matter **17**, 1573 (2005)
19. J.I. Climente, J. Planelles, W. Jaskólski, Phys. Rev. B **68**, 075307 (2003)
20. M. Tadić, N. Cukarić, V. Arsoski, F.M. Peeters, Phys. Rev. B **84**, 125307 (2011)
21. M.D. Teodoro, A. Malachias, V. Lopes-Oliveria, D.F. Cesar, V. Lopez-Richard, G.E. Marques, E. Marega Jr., M. Benamara, YuI Mazur, G.J. Salamo, J. Appl. Phys. **112**, 014319 (2012)
22. M.D. Teodoro, V.L. Campo Jr., V. Lopez-Richard, E. Marega Jr., G.E. Marques, Y. Galvao Gobato, F. Iikawa, M.J.S.P. Brasil, Z.Y. AbuWaar, V.G. Dorogan, YuI Mazur, M. Benamara, G.J. Salamo, Phys. Rev. Lett. **104**, 086401 (2010)
23. Landölt-Börnstein Comprehensive Index. edited by O. Madelung and W. Martienssen (Springer, Berlin, 1996)
24. E. Margapoti, F.M. Alves, S. Mahapatra, T. Schmidt, V. Lopez-Richard, C. Destefani, E. Menendez-Proupin, Qu Fanyao, C. Bougerol, K. Brunner, A. Forchel, G.E. Marques, L. Worschech, Phys. Rev. B **82**, 2053181 (2010)
25. E. Margapoti, L. Worschech, S. Mahapatra, K. Brunner, A. Forchel, F.M. Alves, V. Lopez-Richard, G.E. Marques, C. Bougerol, Phys. Rev. B **77**, 073308 (2008)
26. E. Margapoti, F.M. Alves, S. Mahapatra, V. Lopez-Richard, L. Worschech, K. Brunner, F. Qu, C. Destefani, E. Menendez-Proupin, C. Bougerol, A. Forchel, G.E. Marques, New J. Phys. **14**, 043038 (2012)
27. V. Baranwal, G. Biasiol, S. Heun, A. Locatelli, T.O. Mentes, M.N. Orti, Phys. Rev. B **80**, 155328 (2009)
28. M. Hanke, E. YuI Mazur, Z.Y. Marega Jr., G.J. AbuWaar, P.Schäfer Salamo, M. Schmidbauer, Appl. Phys. Lett. **91**, 043103 (2007)
29. N.A.J.M. Kleemans, J.H. Blokland, A.G. Taboada, H.C.M. van Genuchten, M. Bozkurt, V.M. Fomin, V.N. Gladilin, D. Granados, J.M. García, P.C.M. Christianen, J.C. Maan, J.T. Devreese, P.M. Koenraad, Phys. Rev. B **80**, 155318 (2009)
30. T. Benabbas, Y. Androussi, A. Lefebvre, J. Appl. Phys. **86**, 1945 (1999)
31. J. Stangl, V. Holy, G. Bauer, Rev. Mod. Phys. **76**, 725 (2004)
32. M.D. Teodoro, A. Malachias, V. Lopes-Oliveira, D.F. Cesar, V. Lopez-Richard, G.E. Marques, E. Marega Jr., M. Benamara, YuI Mazur, G.J. Salamo, J. Appl. Phys. **112**, 014319 (2012)
33. V. Lopes-Oliveira, Y.I. Mazur, L.D. de Souza, L.A.B. Marcal, J. Wu, M.D. Teodoro, A. Malachias, V.G. Dorogan, M. Benamara, G. Tarasov, E. Marega Jr., G.E. Marques, Z.M. Wang, M. Orlita, G.J. Salamo, V. Lopez-Richard, Phys. Rev. B **90**, 125315 (2014)

34. ZhM Wang, Y.I. Mazur, Sh Seydmohamadi, G.J. Salamo, H. Kissel, Appl. Phys. Lett. **87**, 213105 (2005)
35. D. Haft, C. Schulhauser, A.O. Govorov, R.J. Warburton, K. Karrai, J.M. Garcia, W. Schoenfeld, P.M. Petroff, Phys. E **13**, 165 (2002)
36. M. Tadić, F.M. Peeters, K.L. Janssens, Phys. Rev. B **65**, 165333 (2002)
37. K.L. Janssens, B. Partoens, F.M. Peeters, Phys. Rev. B **67**, 235325 (2003)
38. L. Villegas-Lelovsky, M.D. Teodoro, V. Lopez-Richard, C. Calseverino, A. Malachias, E. Marega, B.L. Liang, YuI Mazur, G.E. Marques, C. Trallero-Giner, G.J. Salamo, Nanoscale Res. Lett. **6**, 56 (2011)

Part IV
Theory

Chapter 11
Electronic, Magnetic and Optical Properties of Quantum Rings in Novel Systems

Tapash Chakraborty, Aram Kh. Manaselyan and Manuk G. Barseghyan

Abstract In the past few decades, major advances in nanofabrication techniques have resulted in the creation of tunable few-electron nanoscale quantum rings with unique topology and the energy spectrum. These rings display many remarkable effects in magnetotransport and optical spectroscopy that were predicted earlier in theoretical studies. Having external control over the size and the number of electrons in such a ring offers intriguing possibilities to study the interplay between the confinement and the electron-electron interaction. Here we review the physics of quantum rings in a few novel situations and unravel some new physical phenomena involving these rings that go beyond our current understandings of physics derived from conventional nanoscale quantum rings.

11.1 Introduction

Research on the electronic and optical properties of quantum confined nanoscale structures, such as quantum dots and quantum rings has made great strides in recent years in unraveling new phenomena. Their enormous potentials in device applications have also contributed significantly in the pursuit of those activities. In this context, quantum rings with its doubly-connected geometry deserves special attention. Its unique topological structure provides a rich variety of fascinating physical phenomena in this system. Observation of the Aharonov-Bohm (AB) oscillations [1] and the persistent current [2] in small semiconductor quantum rings (QR), and recent experimental realization of QRs containing only a few electrons [3–5] have

T. Chakraborty (✉)
Department of Physics and Astronomy,
University of Manitoba, Winnipeg R3T 2N2, Canada
e-mail: Tapash.Chakraborty@umanitoba.ca

A.Kh. Manaselyan · M.G. Barseghyan
Department of Solid State Physics, Yerevan State University, Yerevan, Armenia
e-mail: amanasel@ysu.am

M.G. Barseghyan
e-mail: mbarsegh@ysu.am

V.M. Fomin (ed.), *Physics of Quantum Rings*, NanoScience and Technology,
https://doi.org/10.1007/978-3-319-95159-1_11

made QRs an attractive topic for experimental and theoretical studies with various quantum effects displayed in these quasi-one-dimensional systems [6–9]. In particular, recent work has indicated the great potentials of QRs as basis elements for a broad spectrum of applications, starting with terahertz detectors [10], efficient solar cells [11] and memory devices [12], through electrically tunable optical valves and single photon emitters [13, 14].

In the past, for investigations of nanoscale QRs, the materials of choice had been primarily the conventional semiconductors, for example, the GaAs or InAs heterostructures, where the high-mobility two-dimensional electron gas (2DEG) was quantum confined to create the quantum dots (the *artificial atoms*) [15] or quantum rings. However, in recent years many novel systems with unusual electronic properties have been developed, where the QR structure displayed a variety of intriguing physical phenomena that are the subjects of this chapter.

11.2 Planar Electrons at the ZnO Interface

In the past few years exciting developments have taken place with the creation of high mobility two-dimensional electron gas (2DEG) in heterostructures involving insulating complex oxides. Most notably, the fractional quantum Hall effect (FQHE) was observed [16, 17] in MgZnO/ZnO heterostructures grown by molecular-beam epitaxy, where the electron mobility exceeds 180,000 $\mathrm{cm}^2\ \mathrm{V}^{-1}\ \mathrm{s}^{-1}$. Further, technological advances in oxide electronics have demonstrated the opportunities to explore strongly correlated phenomena in quantum transport of dilute carriers. Unlike in traditional semiconductors, electrons in these systems are strongly correlated [18–21]. These should then exhibit effects ranging from strong electron correlations, magnetism, interface superconductivity, tunable metal-insulator transitions, among others, and of course, the exciting possibility of all-oxide electronic devices. Many surprising results were also found in the fractional quantum Hall states discovered in the MgZnO/ZnO heterojunctions. For example, the odd-denominator fractional states such as $\nu = 4/3$, $5/3$ and $8/3$ were observed with indications of the $\nu = 2/5$ state in the extreme quantum limit [16, 17]. Soon after, the even-denominator states, such as $\nu = 3/2$ and $7/2$, were also observed [22], but surprisingly, the most prominent even-denominator state of the GaAs systems, the $\nu = 5/2$ state, was found to be conspicuously absent in the ZnO system. The system of 2DEG in ZnO is unique as compared to that in GaAs (see Table 11.1). In the case of GaAs-based 2DEG, the Landau level (LL) gap is large compared to that for the Coulomb interaction ($e^2/\varepsilon l$, where ε is the dielectric constant and $l = \sqrt{\hbar/eB}$ is the magnetic length with a magnetic field induction B). However, in a ZnO heterosturcutre the LL gap is very small [22, 23]. The ratio κ between the Coulomb interaction and the LL gap is the relevant parameter in this context. In GaAs, $\kappa = 2.5/\sqrt{B}$, which would be very small in a strong magnetic field. In the ZnO heterointerface, where the dielectric constant is 8.5, that ratio is $\kappa = 25.1/\sqrt{B}$, i.e., about an order of magnitude larger than that of

Table 11.1 Some useful material parameters for GaAs, InAs and ZnO

	GaAs	InAs	ZnO
Crystal structure	Zincblende	Zincblende	Wurtzite
Lattice constant	5.65 Å	6.05 Å	3.24 Å
Energy band gap	1.51 eV	0.42 eV	3.37 eV
Electron effective mass	$0.067m_0$	$0.024m_0$	$0.24m_0$
Dielectric constant	13.18	14.6	8.5
Lande factor	–0.44	–14	4.3

GaAs. Therefore, considering the electron system in a single LL may not be entirely appropriate when dealing with this new system.

As mentioned above, in the experiment of Falson et al. [22] the FQHE was found to be missing at the filling factor 5/2 but survives at 7/2, which suggests that the electron-hole symmetry must be broken in the N = 1 LL. Hence, the Coulomb interaction in the two cases has to be different to make the two different spins distinguishable. In [23] the screened Coulomb interaction was introduced to study the collective modes of the FQHE states in the ZnO system using the exact diagonalization scheme. Interestingly, the authors were able to satisfactorily explain the unique experimental observations by Falson et al. [22], such as the absence of the 5/2 state but the presence of the 9/2 state and spin-reversed excitations of the 7/2 state. Interesting effects were also uncovered in a tilted magnetic field [22, 24]. Further studies indicated that the small Landau level gaps in ZnO is also expected to display novel topological phase transitions [25].

ZnO is also a perfect material for creation of different nanostructures. Preparation of various nanostructures such as nanorings, nanobelts, nanowires etc, using a solid-vapor phase thermal sublimation technique, have been reported [26]. Preparation of self-assembled ZnO quantum dots with tunable optical properties have been reported in [27]. It has been stressed there that the electron correlation effects are strong in these systems due to the increased electron effective mass and reduced dielectric constant of ZnO. Given the enormous potential of this newly developed source of 2DEG, it is therefore important that the electronic properties of quantum confined systems at the oxide interfaces are thoroughly understood. The electronic states of planar quantum dots at the ZnO interface containing a few interacting electrons in an externally applied magnetic field have been studied [28]. The electron-electron interaction effects are expected to be much stronger in this case than in traditional semiconductor quantum systems, such as in GaAs or InAs quantum dots. In order to highlight that strong Coulomb effects in ZnO quantum dots, the authors have compared the energy spectra and magnetization in this system to those of the InAs quantum dots. It has been shown that in the ZnO quantum dots the signatures of stronger Coulomb interaction manifest in an unique ground state that has very different properties than the corresponding ones in the InAs dot. Theoretical results for the magnetization also exhibits behaviors never before observed in a quantum dot for a

realistic set of parameters. A stronger temperature dependence of magnetization and other unexpected features, such as paramagnetic-like behavior at high temperatures for a ZnO quantum-dot helium have been demonstrated.

11.2.1 Properties of ZnO Quantum Rings

Let us consider here a two-dimensional quantum ring with inner radius R_1 and the outer radius R_2 having cylindrical symmetry, containing a few electrons, in a magnetic field applied in the growth direction. The Hamiltonian of this system is then

$$\mathscr{H} = \sum_{i}^{N_e} \mathscr{H}_{\rm SP}^{i} + \tfrac{1}{2} \sum_{i \neq j}^{N_e} V_{ij}, \tag{11.1}$$

where N_e is the electron number in the ring, $V_{ij} = e^2/\varepsilon|\mathbf{r}_i - \mathbf{r}_j|$ is the Coulomb interaction term, with the dielectric constant of the ring material ε, and $\mathscr{H}_{\rm SP}$ is the single-particle Hamiltonian in the presence of an external perpendicular magnetic field

$$\mathscr{H}_{\rm SP} = \frac{1}{2m}\left(\mathbf{p} - \frac{e}{c}\mathbf{A}\right)^2 + V_{\rm conf}(r) + \tfrac{1}{2} g \mu_B B \sigma_z. \tag{11.2}$$

In the above equation $\mathbf{A} = B/2(-y, x, 0)$ is the vector potential of the magnetic field, and m is the electron effective mass. We chose the confinement potential of the QR to have infinitely high borders: $V_{\rm conf}(r) = 0$, if $R_1 \leq r \leq R_2$ and infinity outside of the QR. This choice of the confinement potential is suitable for ZnO/MgZnO heterostructures because of the large values of the conduction band offset and the electron effective mass [29]. The last term of (11.2) is the Zeeman interaction.

The numerical studies are based on the exact diagonalization scheme [30]. As for the basis states, we consider the eigenfunctions of $\mathscr{H}_{\rm SP}$ for $B = 0$. The eigenfunctions of this Hamiltonian will then have the form [31, 32]

$$\phi_{nl}(r, \theta) = \frac{C}{\sqrt{2\pi}} e^{{\rm i}l\theta} \left(J_l(\gamma_{nl} r) - \frac{J_l(\gamma_{nl} R_1)}{Y_l(\gamma_{nl} R_1)} Y_l(\gamma_{nl} r) \right), \tag{11.3}$$

where $J_l(r)$ and $Y_l(r)$ are Bessel functions of the first and second kind respectively, $\gamma_{nl} = 2mE_{nl}/\hbar^2$, where E_{nl} are the eigenstates defined by the boundary conditions

$$J_l(\gamma_{nl} R_2) - \frac{J_l(\gamma_{nl} R_1)}{Y_l(\gamma_{nl} R_1)} Y_l(\gamma_{nl} R_2) = 0. \tag{11.4}$$

The constant C is determined from the normalization integral, and n and l are the radial and angular quantum numbers respectively. For evaluation of the energy spectrum in a many-electron (interacting) system, we have to digonalize the matrix of

the Hamiltonian (11.1) in a basis of the slater determinants constructed from the single-electron wave functions [6].

We have also studied the intraband optical transitions in the conduction band. According to the Fermi golden rule the intensity of absorption in the dipole approximation is proportional to the square of the matrix element [30, 33]

$$I = \langle f | \sum_{i=1}^{N} r_i e^{\pm i\theta_i} | i \rangle \tag{11.5}$$

when the transition is from the initial N-particle state $|i\rangle$ to the final state $|f\rangle$. In this work we always consider $|i\rangle$ to be the N-particle ground state. To evaluate (11.5) we need to calculate the dipole matrix elements between the one electron states $|n, l\rangle$ and $|n', l'\rangle$

$$M = \int_{R_1}^{R_2} \int_{0}^{2\pi} \phi_{nl}(r, \theta)(re^{\pm i\theta})\phi_{n'l'}(r, \theta) r \, dr \, d\theta. \tag{11.6}$$

After the angular integration we arrive at the optical transition selection rule for the total angular momentum $L_f = L_i \pm 1$.

The numerical studies were carried out for the ZnO quantum ring with parameters $m = 0.24m_0$, $g = 4.3$, $\varepsilon = 8.5$ [29]. For the purpose of comparison we also present similar studies for the GaAs quantum ring with parameters $m = 0.067m_0$, $g = -0.44$, $\varepsilon = 13.18$ respectively [30]. The two QRs were taken to be of same sizes with radii $R_1 = 10$ nm and $R_2 = 40$ nm.

The low-lying energy levels of the ZnO QR containing one and two electrons are shown in Fig. 11.1 as a function of the magnetic field B. For comparison, similar results are also presented for the GaAs QR in Fig. 11.1c, d. In all these figures different colors correspond to different values of the total angular momentum L of the electrons. In the QR containing only one electron in both systems, the ground state changes periodically with increasing magnetic field (Fig. 11.1a, c) thereby providing the direct signature of the Aharonov-Bohm effect in a QR. For the ZnO QR the energy eigenvalues are lower due to the larger value of the electron effective mass. Additionally, the states with different spin are highly split due to the larger value of the g-factor for ZnO. More importantly, for the non-interacting electrons the AB effect survives in both systems.

In the QRs having two interacting electrons, there are several substantial differences between the energy spectra of the ZnO and GaAs QRs. For instance, in the GaAs QR we see the usual and well observed AB oscillations due to level crossings between the singlet and triplet ground states, and for each crossing of the two-electron ground state the total angular momentum L changes by unity. On the other hand, for the ZnO QR containing two electrons (Fig. 11.1b), due to the combined effect of the strong Zeeman splitting and the strong Coulomb interaction, the singlet-triplet crossings no longer appear in the ground state. Interestingly, the periodic crossings can be noticed only in the excited states. For small values of the magnetic field the ground state is a singlet with $L = 0$ and the total electron spin $S = 0$. With an

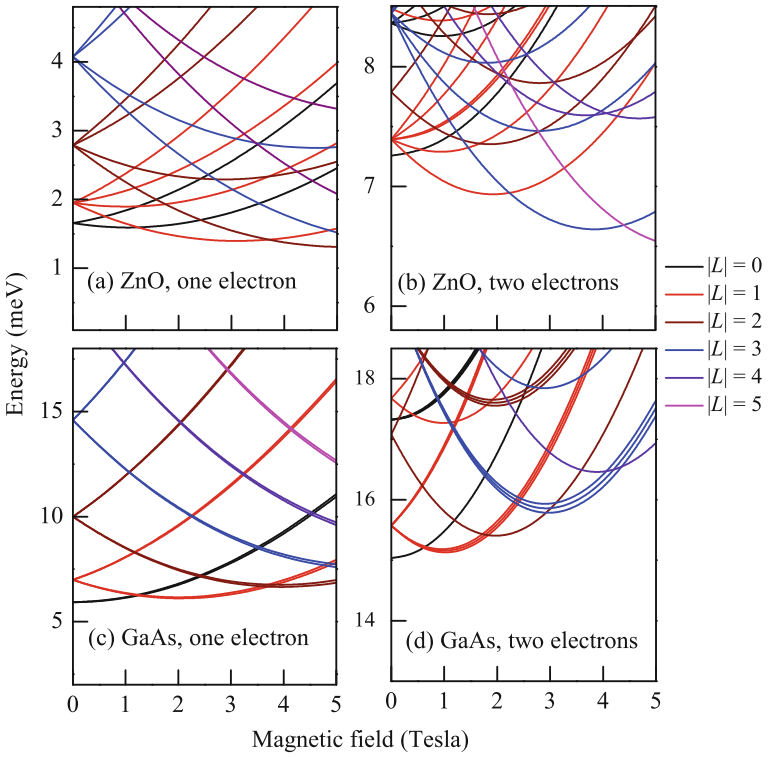

Fig. 11.1 The low-lying energy levels versus the magnetic field for **a** the ZnO QR with one electron, **b** the ZnO QR with two electrons, **c** the GaAs QR with one electron and **d** the GaAs QR containing two electrons. Different colors represent different values of the total angular momentum L

increase of the magnetic field the ground state changes to a triplet state with $L = -1$ and $S = -1$. With a further increase of the magnetic field all the observed crossings of the ground state correspond to triplet-triplet transitions between the states with odd number of total angular momentum ($|L| = 1, 3, 5 \ldots$). These interesting and unexpected results will result in distinct behaviors of optical transitions in the ZnO QR.

The dipole-allowed optical transition energies are shown in Fig. 11.2 as a function of the magnetic field for the ZnO [(a) and (c)] and the GaAs [(b) and (d)] QRs containing one and two electrons respectively. Different colors in Fig. 11.2 correspond to the value of the ground state angular momentum (see Fig. 11.1) of the optical transition and the sizes of the points are proportional to the intensity of the optical transitions. For the QRs containing only one electron for both materials we can see the expected features: periodic optical AB oscillations. Comparing Fig. 11.2a, b we notice that although the strong Zeeman effect changes the one-electron energy spectra of the ZnO QR, it does not change the periodicity of the optical AB oscillations. In the case of the QRs with two electrons, again we see considerable differences in features

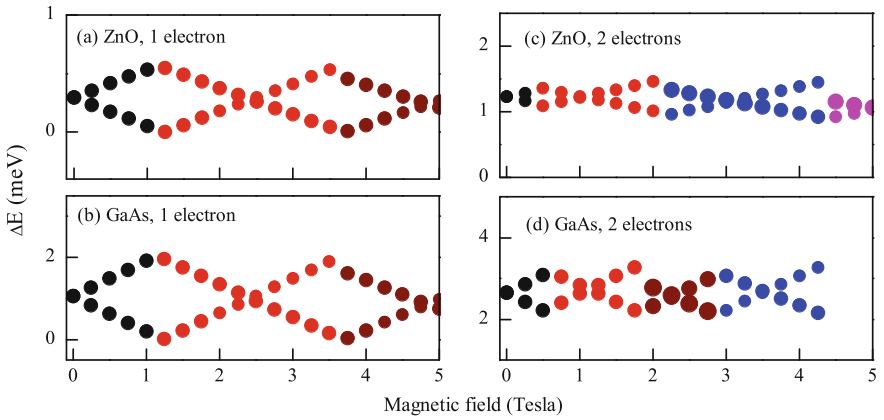

Fig. 11.2 Dipole-allowed optical transition energies versus the magnetic field, for **a** the ZnO QR with one electron, **b** the GaAs QR having one electron, **c** the ZnO QR containing two electrons and **d** the GaAs QR with two electrons. The size of the colored dots is proportional to the intensity of the calculated optical transitions

displayed by these two systems. In the case of the two-electron GaAs QR, we see the periodic optical AB oscillations with the period that is half the flux quantum, which is an well-known result [4, 8]. In contrast, for the two-electron ZnO QR we notice an aperiodic behavior of the optical AB oscillations. The first oscillation, which corresponds to the singlet-triplet transition from the state with $L = 0$ to the state with $L = -1$ has a smaller period compared to the other oscillations which correspond to transitions between the triplet states with odd angular momentum. The period of these triplet-triplet oscillations is almost equal to the period of the single-electron case. This unexpected effect is a result of the different properties of the energy spectra of the two-electron ZnO QR discussed above and can be explained by the combined effect of the strong Zeeman interaction and the strong electron-electron interaction in the ZnO.

The low-lying energy levels for the ZnO and GaAs QRs containing three electrons are shown as a function of the magnetic field B in Fig. 11.3a, b. For the three-electron GaAs QR we again notice the periodic ground-state transitions and during each transition the ground-state angular momentum changes by one. In contrast, for the three-electron ZnO QR only two ground-state transitions are visible in that range of the magnetic field. At low magnetic fields the ground state has the angular momentum $L = 0$. With an increase of the magnetic field at $B = 1.3$T the ground state changes to $L = -3$. The next ground-state transition occurs at $B = 6$T and the angular momentum changes to $L = -5$. Therefore, we can conclude that within the range of the magnetic field considered here the Aharonov-Bohm effect disappears. The corresponding optical transition energies for the three-electron ZnO QR are shown in Fig. 11.3c. That figure clearly illustrates the disappearence of the optical Aharonov-Bohm oscillations in a ZnO quantum ring.

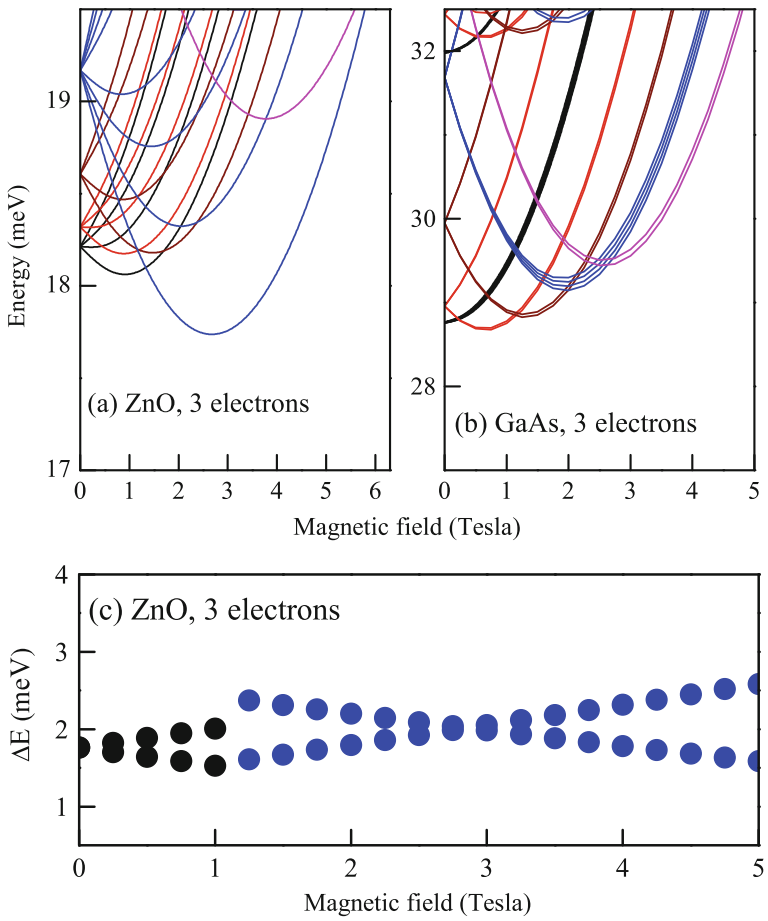

Fig. 11.3 Same as in Fig. 11.1 but for **a** the ZnO QR containing three electrons and **b** the GaAs QR with three electrons. **c** Dipole allowed optical transition energies versus the magnetic field for the ZnO QR containing three electrons

To summarize, the electronic states and optical transitions of a ZnO quantum ring containing a few interacting electrons in an applied magnetic field were studied via the exact diagonalization scheme. These results are also compared with similar quantities for a conventional GaAs ring. We found that the strong Zeeman interaction and the strong electron-electron Coulomb interaction, two major characteristics of the ZnO system, exert a profound influence on the electron states and as a consequence, the optical properties of the ring also displays unexpected behaviors. In particular, we find that the AB effect is strongly electron number dependent. Our study indicated that in the case of two interacting electrons in a ZnO ring, the AB oscillations become aperiodic. For three electrons (interacting) we found that the the AB oscillations actually *disappear*. These unusual properties of the ZnO QR are explained in terms

of the energy level crossings that are very different from those of the conventional semiconductor QRs, such as for the GaAs. The AB effect (and thereby the persistent current) in a ZnO quantum ring can therefore be controlled by varying the electron number, an interesting prospect for possible future applications of this novel system.

11.2.2 Properties of ZnO Dot-Ring Nanostructures

Recently we have witnessed an increasing demand for the realization of complex quantum confined systems, such as laterally coupled quantum dots, QRs and also quantum dot-ring (QDR) complexes [34–36]. The reason lies in both practical applications and fundamental studies of these structures, that include geometrical quantum phase [37], spin-spin interactions [38] and quantum-state couplings [39]. Due to the unique topology of the QDR structures and their potentials for applications, theoretical investigation of QDR's properties has received plenty of attention in recent years. A few electrons confined in a QDR in the presence of an external magnetic field indicates that the distribution of electrons between the dot and the ring is influenced by the relative strength of the dot-ring confinement and the magnetic field which induces transitions of electrons between the two regions of the system [40]. These transitions are also accompanied by changes in the periodicity of the AB oscillations. It has been recently reported [41–43] that many measurable properties of a QDR, such as spin relaxation or optical absorption, can be significantly changed by modifying the confinement potentials. This demonstrates the high controllability and flexibility of these systems. The transport properties of QDR nanostructures are also known to be intensely modified due to the unique geometry [44]. Theoretical studies of the dc current through a QDR in the Coulomb blockade regime have revealed that it can efficiently work as a single-electron transistor or a current rectifier. In recent theoretical works the electronic and optical properties of QDRs containing the hydrogenic donor impurity were investigated in external electric and magnetic fields [45–47].

In what follows, we consider a two dimensional quantum dot-ring structure with cylindrical symmetry, based on the 2DEG at the ZnO interface, containing few interacting electrons, in a magnetic field that is applied in the growth direction. The many-body and single-particle Hamiltonians of our system are similar to (11.1) and (11.2), but here the confinement potential of the QDR is chosen to consist of double parabolas [40, 47]

$$V_{\text{conf}}(r) = \min\left[\tfrac{1}{2}m\omega_{\text{d}}^2 r^2, \tfrac{1}{2}m\omega_{\text{r}}^2 (r-R)^2\right]. \tag{11.7}$$

Here ω_{d} and ω_{r} are the parameters that describe the strength of the confinement potential and also the sizes of the dot and the ring respectively. The radius

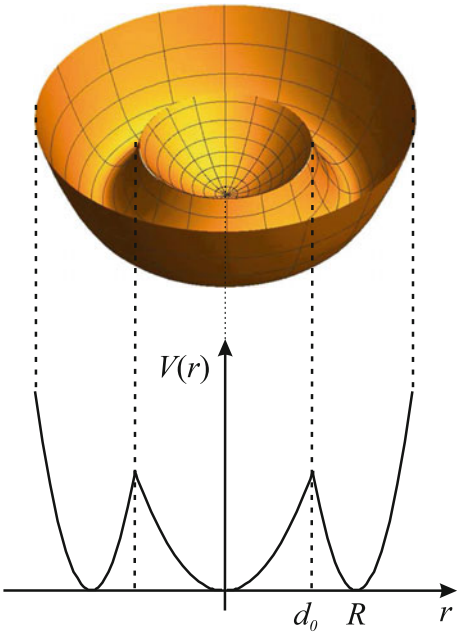

Fig. 11.4 The QDR confinement potential (schematic)

of the ring R is defined as the sum of oscillator lengths for the dot and ring related wells and the barrier thickness d between the dot and the ring according to $R = \sqrt{2\hbar/m\omega_d} + \sqrt{2\hbar/m\omega_r} + d$. The QDR confinement potential is presented schematically in Fig. 11.4.

Just as for other interacting systems described in this chapter, the eigenfunctions and the eigenenergies of the single-electron Hamiltonian (11.2) are obtained with the help of the exact diagonalization technique, with the basis of wave functions of the cylindrical QD with larger radius. We have used the exact diagonalization scheme also to evaluate the energy spectra and the wave functions of the few-electron QDR. In order to evaluate the energy spectrum of the many-electron system, we need to digonalize the matrix of the Hamiltonian (11.1) with confinement potential (11.7) in a basis of the Slater determinants constructed from the single-electron wave functions [32]. In our model we have used 132 single-electron basis states. As a result we have 8646 two-electron states and 374,660 three-electron basis states that are adequate for accurately determining the first few energy eigenvalues for a given value of the total angular momentum of electrons.

In order to determine the average electron numbers in the dot or in the ring we have also studied the electron densities for few-electron states in the QDR

$$\rho(\mathbf{r}) = \int d\mathbf{r}_2 d\mathbf{r}_3 \ldots |\Psi_i(\mathbf{r}, \mathbf{r}_2, \mathbf{r}_3, \ldots)|^2, \tag{11.8}$$

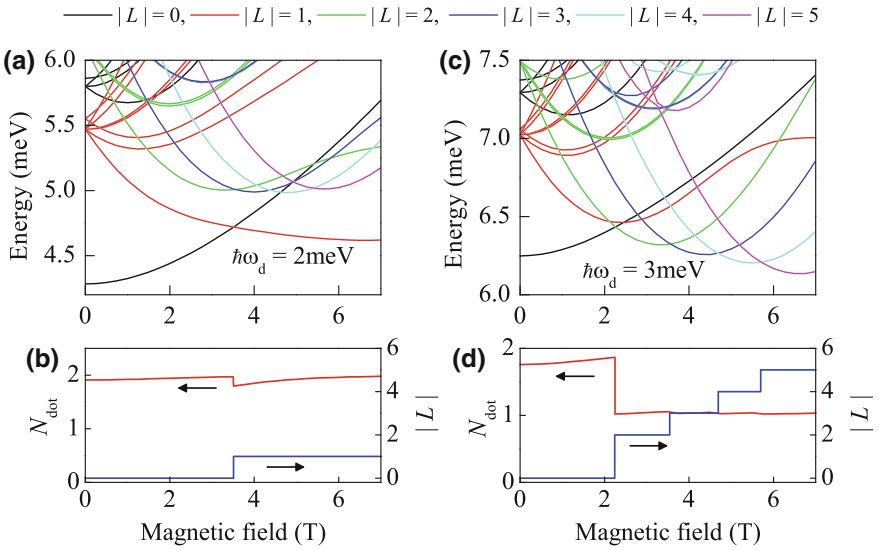

Fig. 11.5 Magnetic field dependence of the two-electron energy spectra, the corresponding average electron number in the dot (left scales of the lower row) and the ground state angular momenta (right scales of the lower row) for $\hbar\omega_d = 2$ meV (**a**, **b**) and for $\hbar\omega_d = 3$ meV (**c**, **d**). All results are given for $\hbar\omega_r = 8$ meV and $d = 10$ nm

where $\Psi_i(\mathbf{r}, \mathbf{r}_2, \mathbf{r}_3, \ldots)$ is the wave function of the few-electron state i. For the average electron number in the dot region of the QDR we have

$$N_{\text{dot}} = \int_0^{d_0} \int_0^{2\pi} \rho(\mathbf{r}) r \, dr \, d\varphi, \tag{11.9}$$

where $d_0 = \omega_r R/(\omega_d + \omega_r)$ is the radius of the border between the dot and the ring.

Our investigations were carried out for the ZnO QDR with parameters $m = 0.24m_0$, $g = 4.3$, $\varepsilon = 8.5$ [29]. In Fig. 11.5a, the magnetic field dependence of the first few energy levels are shown for a two-electron QDR with $\hbar\omega_d = 2$ meV, $\hbar\omega_r = 8$ meV, $d = 10$ nm for various values of the total angular momenta L. In Fig. 11.5b the corresponding ground state average electron number in the dot (left scale, red line) and the ground state angular momentum (right scale, blue line) are presented. It is clear from these figures that for all values of the magnetic field, both electrons are localized in the dot region and the ground state behaves like in a two-electron single quantum dot [28]. For weak values of the magnetic field the ground state is a singlet state with angular momentum $L = 0$ and total spin $S = 0$. With an increase of the magnetic field, at $B \approx 3.5$T, a singlet-triplet transition of the ground state is observed to the state $L = -1$, $S = -1$. Similar results are presented also in Fig. 11.5c, d but for $\hbar\omega_d = 3$ meV. Again for weak values of the magnetic field both electrons are located in the dot region, but starting from $B \approx 2.2$T one of the

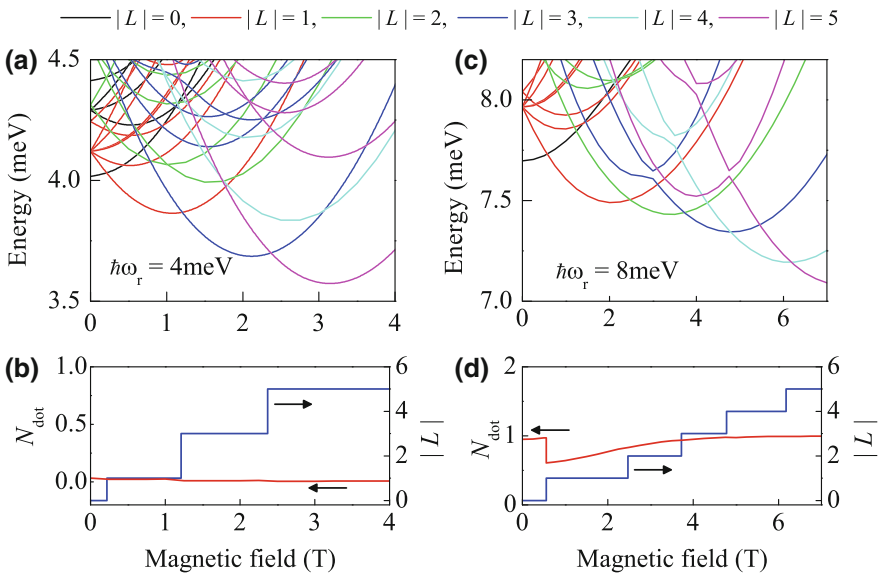

Fig. 11.6 Magnetic field dependence of two-electron energy spectra, the corresponding average electron number in the dot (left scale of lower row) and the ground state angular momenta (right scales of lower row) for $\hbar\omega_r = 4$ meV (**a**, **b**) and for $\hbar\omega_r = 8$ meV (**c**, **d**). All results are given for $\hbar\omega_d = 4$ meV and $d = 10$ nm

electrons moves to the ring region (Fig. 11.5d red line) and the ground state changes to the triplet state $L = -2$, $S = -1$. Starting from 2.2T the behavior of the energy spectra in Fig. 11.5c changes drastically and the regular periodic AB oscillations of the ground state can be observed with periodic change of the total angular momentum by $\Delta L = 1$. This is qualitatively similar to the case of one-electron ZnO QR, discussed above and in [32], but now all AB oscillations occur between the triplet states.

Figure 11.6 is similar to Fig. 11.5 but for a fixed value of $\hbar\omega_d = 4$ meV and for two values of the ring confinement parameter $\hbar\omega_r = 4$ meV (Fig. 11.6a, b) and $\hbar\omega_r = 8$ meV (Fig. 11.6c, d). For $\hbar\omega_r = 4$ meV both electrons are localized in the ring (Fig. 11.6b) and the energy spectra is similar to the one of the two-electron ZnO QR observed in the previous section. In this case we observe irregular AB oscillations which is typical for the ZnO QRs, as previously described. Due to the combined effect of the strong Zeeman splitting and the strong Coulomb interaction in ZnO, the singlet-triplet crossings disappear from the ground state. For small magnetic fields the ground state is a singlet with $L = 0$. As the magnetic field is increased, the ground state changes to a triplet with $L = -1$ and $S = -1$. With further increase of the magnetic field all the observed crossings of the ground state correspond to triplet-triplet transitions between the states with an odd number of total angular momentum ($|L| = 1, 3, 5 \ldots$). With an increase of $\hbar\omega_r$, one of the electrons moves to the dot region (Fig. 11.6d) while the other remains in the ring. In this case the magnetic field

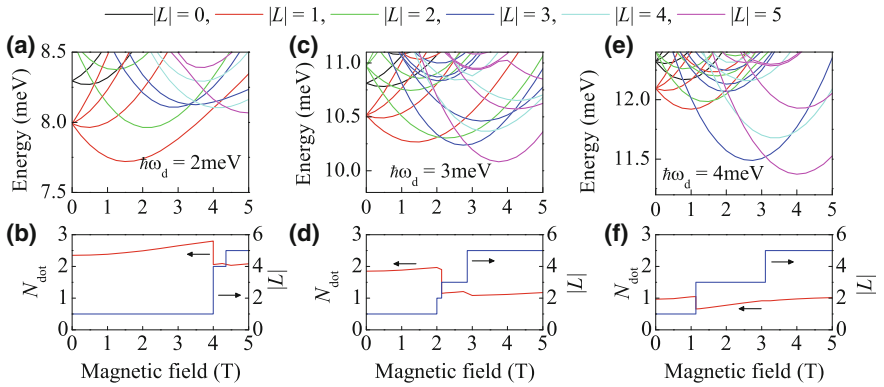

Fig. 11.7 Magnetic field dependence of the three-electron energy spectra, the corresponding average electron number in the dot (left scales of lower row) and ground state angular momenta (right scales of lower row) for $\hbar\omega_d = 2$ meV (**a**, **b**), for $\hbar\omega_d = 3$ meV (**c**, **d**) and for $\hbar\omega_d = 4$ meV (**e**, **f**). All results are for $\hbar\omega_r = 8$ meV and $d = 10$ nm

almost does not change the average electron number in the dot, and as a consequence, we observe almost regular AB oscillations similar to the ZnO QR containing a single electron (Fig. 11.6c).

The energy spectra and the average electron numbers in the dot region are shown in Fig. 11.7 against the magnetic field for a QDR containing three electrons, for a fixed value of $\hbar\omega_r = 8$ meV, and for various values of $\hbar\omega_d$. When $\hbar\omega_d = 2$ meV (Fig. 11.7a, b) and for weak magnetic fields all three electrons are mostly located in the dot region, the ground state is $L = -1$, $S = -1/2$ and the AB oscillations are absent. But at $B \approx 4$T one of the electrons moves to the ring region and the ground state changes to $L = -4$, $S = -3/2$. Starting from $B \approx 4$T the usual AB effect appears.

For $\hbar\omega_d = 3$ meV (Fig. 11.7c, d) and in the absence of the magnetic field, only two electrons are located in the dot and one in the ring region. With an increase of the magnetic field we observe a charge switching between the dot and the ring of the QDR. At $B \approx 2.1$T the electron number in the dot changes to 1 and the irregular AB effect is observed with odd angular momenta $|L| = 3, 5 \ldots$.

Finally, when $\hbar\omega_d = 4$ meV (Fig. 11.7e, f) for the entire range of the magnetic field, only one electron is located in the dot region and the other two resides in the ring. As a result, in Fig. 11.7e the irregular AB oscillations are observed for the ground state, similar to the case of two-electron ZnO QR, as discussed in the previous section.

To summarize: we have studied the electronic states and the Aharonov-Bohm effect in ZnO quantum dot-ring nanostructures containing a few electrons. We have shown that in contrast to the QDRs made out of conventional semiconductors, such as InAs or GaAs, QDRs in ZnO heterojunctions demonstrate several unique characteristics. In particular, the energy spectra of the ZnO QDR and the Aharnov-Bohm oscillations are strongly dependant on the electron number in the dot or in the ring.

Therefore, even a small change of the confinement potential, the dot-ring size or the magnetic field can drastically alter the energy spectra and the behavior of Aharonov-Bohm oscillations in the system. This interesting phenomenon can certainly lead to effective control with high accuracy of the electron charge and spin distribution inside the dot-ring structure. These unique properties will certainly have important implications for possible applications in spintronic devices and quantum information technologies.

11.3 Interaction of Single Quantum Rings with Intense Laser Fields: Continuous Evolution of Quantum States

Although the mostly circular or slightly oval shaped QRs have been fabricated by various experimental groups [48–51], anisotropic QRs are the ones most commonly obtained during the growth process [50, 52–54]. Theoretically, the effect of anisotropy on electronic, magnetic and optical properties of quantum rings have been investigated by various authors [55–62]. Those studies report the influence of different types of anistropies. For example, in [57, 58, 60, 61] the shape anisotropy of the QR was considered, while in [55, 56, 59] the anisotropy associated with defects was studied. Also in [62] the effective mass anisotropy was investigated. All these studies have indicated that the anisotropy can dramatically alter the AB oscillations in the QR. In particular, in [62] it was demonstrated that the unusual AB oscillations caused by the effective mass anisotropy in the QR can be converted to usual AB oscillations if the QR has an elliptical shape. Further, in [63] the unusual AB oscillation caused by the eccentricity effect was compensated by the lateral electric field. On the other hand, the unusual AB oscillation under the influence of lateral electric field in infinitely narrow QR was observed [64–67]. Clearly, to experimentally confirm these results, one is forced to grow QRs having different anisotropies and then compare their measurable optical and magnetic characteristics individually.

Rapid advances in laser technology have greatly contributed to the exploration of light-matter interaction in various branches of physics. In the past few years, the development of modern high-power, tunable laser sources, e.g. the free-electron lasers, has allowed the experimental study of the interaction of intense laser fields (ILFs) with charge carriers in semiconductors, mainly in the terahertz frequency range [68–70]. Interestingly, by illuminating nanostructures with ILFs some new physical phenomena were theoretically anticipated and observed. We can mention, for instance, terahertz resonant absorption [71], strong distortions in the optical absorption spectra [72], and Floquet-Bloch states in single-walled carbon nanotubes [73].

The THz technology has been garnering increasing attention from specialists in various fields, such as imaging, sensing, quality control, wireless communication, and basic science [74]. The development of this technology depends on realizing efficient and robust sources and detectors. For example, the development of terahertz

time-domain spectroscopy [75] more than two decades ago opened a new chapter in THz science, initiating great efforts to develop applications to exploit the unique opportunities that THz waves offer. With remarkable advances in THz technology, there has recently been a considerable surge in the research on intense THz sources and their applications. Nevertheless, there is also an immediate need to develop nonlinear THz spectroscopy techniques and intense terahertz sources that have the potential to reveal a new category of nonlinear phenomena and explore nonlinear effects in various materials. Intense THz pulses can induce an ultrafast electric- or magnetic-field switching operation at tens of femtoseconds to picosecond timescale, which is much faster than what can be achieved through conventional electronics. The study of such nonlinear phenomena has been possible thanks to the development of ultrafast nonlinear THz spectrometers [76]. Recently the effect of ILF on single electron states and intraband optical properties in isotropic $GaAs/Ga_{0.7}Al_{0.3}As$ single QR has been investigated [77]. It has been shown that the laser field destroys the cylindrical symmetry and laser-dressed effective confinement potential gets an elliptic shape (see Fig. 11.8).

The splitting and increment of energy levels induced by the ILF has been observed. The simultaneous influences of the ILF and lateral electric field on one-electron states in isotropic $GaAs/Ga_{0.7}Al_{0.3}As$ single QR have been investigated [78]. These authors have observed the splitting and increasing of energy levels induced by the ILF. Meanwhile, the energy splitting, decreasing and increasing of the energy levels induced by the lateral electric field have been reported. It was found that the incident light polarization direction can induce redshifts and blueshifts in the intraband absorption spectrum of the QR. On the other hand, the simultaneous influences of the ILF and lateral electric field can lead both to the blueshift and redshift of the intraband optical absorption spectrum.

We discuss below the effect of a terahertz ILF on isotropic and anisotropic QRs and demonstrate that in the case of isotropic QRs the ILF can create unusual AB oscillations that are characteristics of anisotropic rings. We have also shown that in the case of anisotropic QRs the ILF can be used as an anisotropy controlling tool with the help of which it will be possible to visualize both the isotropic and anisotropic properties on a single QR. As an example, we show below that the unusual AB

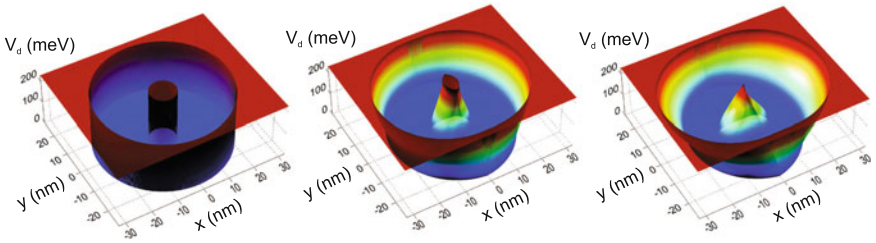

Fig. 11.8 The laser dressed confining potential of the QR for different values of laser field parameter [77] [Reproduced from (A. Radu et al., J. Appl. Phys. **116**, 093101 (2014)), with the permission of AIP Publishing]

oscillations obtained for the elliptic QR can be made usual with the help of the ILF. In this regard, the ILF can unify all the electronic properties of isotropic and anisotropic rings in a single system, thereby providing a simplified route to their investigations.

We begin with a two-dimensional anisotropic QR structure containing electrons that are under the action of laser radiation and an external magnetic field that is oriented along the growth direction. The laser field is represented by a monochromatic plane wave of frequency ω. The laser beam is non-resonant with the semiconductor structure, and linearly polarized along a radial direction of the structure (chosen along the x-axis). In the non-interacting case, the electron motion is described by the solution of the time-dependent Schrödinger equation

$$\left[\frac{1}{2m}\left(\widehat{\mathbf{p}}-\frac{e}{c}(\mathbf{A}(t)+\mathbf{A}_m)\right)^2+V(x,y)\right]\Phi(x,y,t)=\mathrm{i}\hbar\frac{\partial}{\partial t}\Phi(x,y,t)\,. \tag{11.10}$$

Here m is the electron effective mass, $\mathbf{p}$ is the lateral momentum of the electron, e is the absolute value of the electron charge, $\mathbf{A}(t)=\mathbf{e}_x A_0\cos(\omega t)$ is the laser field's vector potential, where $\mathbf{e}_x$ denotes the unit vector along the x-axis. In (11.10), $\mathbf{A}_m$ is the vector potential of the magnetic field that is taken to be $\mathbf{A}_m=(0,Bx,0)$. In this case the scalar product $(\mathbf{A}(t)\cdot\mathbf{A}_m)=0$.

As for the lateral confinement potential $V(x,y)$, we model it as finite, square-well type:

$$V(x,y)=\begin{cases}0, & \text{if } R_1\le\sqrt{x^2+(y/\sqrt{1-\varepsilon^2})^2}\le R_2,\\ V_0, & \text{otherwise,}\end{cases} \tag{11.11}$$

where R_1 and R_2 are the inner and outer radii of the QR respectively, the ε describes the anisotropy of the QR ($\varepsilon=0$ corresponds to the case of circular QR) [62]. The Kramers-Henneberger unitary translation transformation [79] can be performed on (11.10) to transfer the time dependence from the kinetic to the potential term in the Hamiltonian operator at the left hand side of the aforementioned equation. Using the dipole approximation and Kramers-Henneberger unitary transformation in the high-frequency regime [68, 80–84] the laser-dressed energies of the QR can be obtained from the following time-independent Schrödinger equation [85]:

$$\left[\frac{1}{2m}\left(\widehat{\mathbf{p}}-\frac{e}{c}\mathbf{A}_m\right)^2+V_d(x,y)\right]\Phi_d(x,y)=E_d\Phi_d(x,y)\,, \tag{11.12}$$

where $V_d(x,y)$ is the time-averaged laser-dressed potential that can be expressed by the following analytical expression [77, 78]

$$\begin{aligned}V_d(\mathbf{r}_\perp,\alpha_0)=&\tfrac{V_0}{\pi}\Big[\pi-\\ &\theta\left(\alpha_0-x-\Gamma_1\right)\arccos\left(\tfrac{\Gamma_1+x}{\alpha_0}\right)+\theta\left(\alpha_0-x-\Gamma_2\right)\arccos\left(\tfrac{\Gamma_2+x}{\alpha_0}\right)-\\ &\theta\left(\alpha_0+x-\Gamma_1\right)\arccos\left(\tfrac{\Gamma_1-x}{\alpha_0}\right)+\theta\left(\alpha_0+x-\Gamma_2\right)\arccos\left(\tfrac{\Gamma_2-x}{\alpha_0}\right)\Big],\end{aligned} \tag{11.13}$$

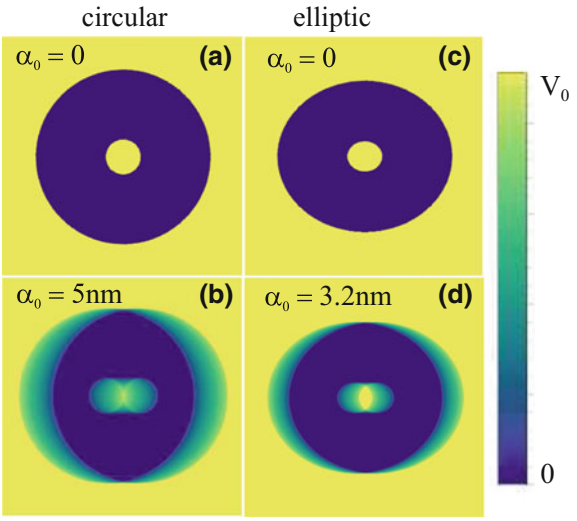

Fig. 11.9 The density plot of the dressed confinement potential for different values of the ILF parameter α_0 for both circular and elliptic QRs

where $\theta(u)$ is the Heaviside unit-step function and $\Gamma_i = Re(\sqrt{R_i^2 - (y/\sqrt{1-\varepsilon^2})^2})$. It is worth mentioning that in the case of a more realistic confinement potential other than the square-well type, the laser-dressed potential can not be presented by the analytical form and the obtained results do not change qualitatively. The parameter $\alpha_0 = (e/m\varepsilon_h^{1/4}\nu^2)\sqrt{I/(2c\pi^3)}$ describes the strength of the laser field, and comprises both the intensity I and frequency ν of the laser field that can be chosen for a broad range in units of kW/cm^2 and THz correspondingly [68]. Here ε_h is the high-frequency dielectric constant of the system. In Fig. 11.9 the schematic picture of dressed potential for different values of the ILF parameter α_0 is presented. The circular and elliptic cases of QRs are shown. The laser dressed energy eigenvalues E_d and eigenfunctions $\Phi_d(x, y)$ may be obtained by solving (11.12) with the help of the exact diagonalization technique. The eigenfunctions are presented as a linear expansion of the eigenfunctions of the two-dimensional rectangular infinitely high potential well [77, 78]. In our calculations we have used 361 basis states which is adequate for determining the first few energy eigenvalues with high accuracy.

We also consider here the intraband optical transitions in the conduction band. According to the Fermi golden rule for the x-polarization of the incident light the intensity of absorption in the dipole approximation is proportional to the square of the matrix element $M_{fi} = \langle f|x|i\rangle$, when the transition goes from the initial state $|i\rangle$ to the final state $|f\rangle$. In what follows we always consider $|i\rangle$ to be the ground state.

Our numerical studies have been carried out for GaAs QRs having parameters $V_0 = 228$ meV, $m = 0.067m_0$ (m_0 is the free electron mass), $\varepsilon_h = 10.5$, $R_1 = 5$ nm [29]. In Fig. 11.10, the low-lying energy levels of a circular QR with outer radius $R_2 = 25$ nm are shown as a function of the magnetic field B for various values of the laser field parameter α_0. In Fig. 11.10a the AB effect has been observed without the laser field, which corresponds to the case of a circular QR. The ILF applied

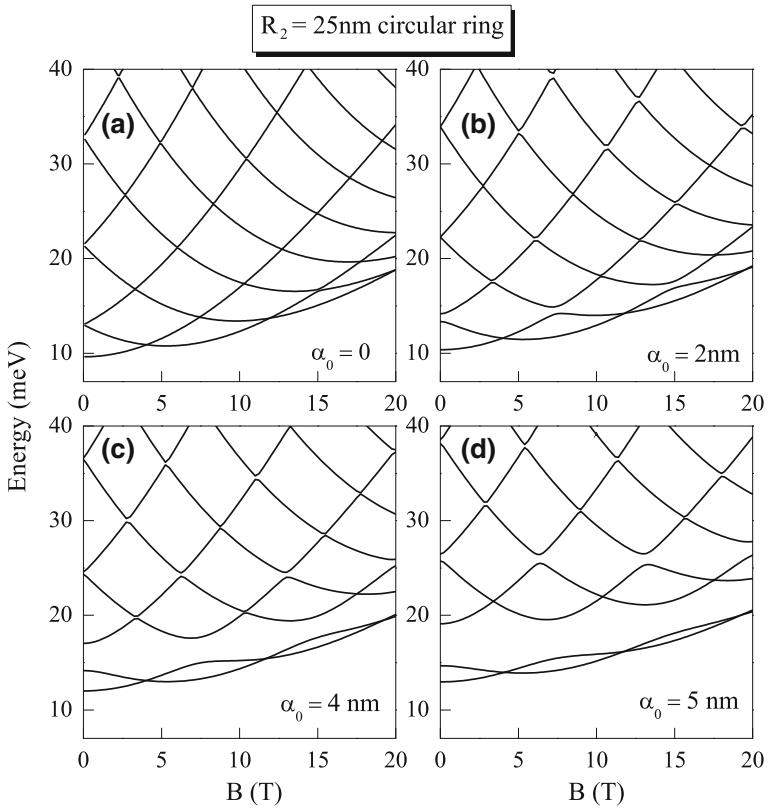

Fig. 11.10 The low-lying energy levels of a circular QR as a function of the magnetic field B for different values of the laser field parameter α_0. The results are for $R_2 = 25$ nm

on a QR creates an anisotropy in the confinement potential (Fig. 11.9b) as a result of which the effective length of the confinement along the x-direction decreases in the lower part of QR potential well. It is worth noting that with the increase of α_0, the anisotropy of the QR is strengthened and the degeneracy of the excited states at $B = 0$ disappears. With an increase of α_0 due to the reduced symmetry from C_∞ to C_2, one should expect an energy spectrum split into non-crossing pairs of states which in turn cross repeatedly as B increases (each pair of repeatedly crossing states containing one instance of each of two C_2 symmetries). A similar behavior of the energy levels, which can be called 'unusual' AB oscillations, was reported earlier in QRs by other authors that is caused by the effective mass anisotropy [60, 62] and structural distortions in QRs [58]. For $\alpha_0 = 2$ nm, only the ground and first excited states feel the deformation of the potential (see Fig. 11.10b). Whereas, for larger values of α_0 more excited states start to feel the deformation of the QR confinement potential and the two periodically crossing pairs can be visible (Fig. 11.10d).

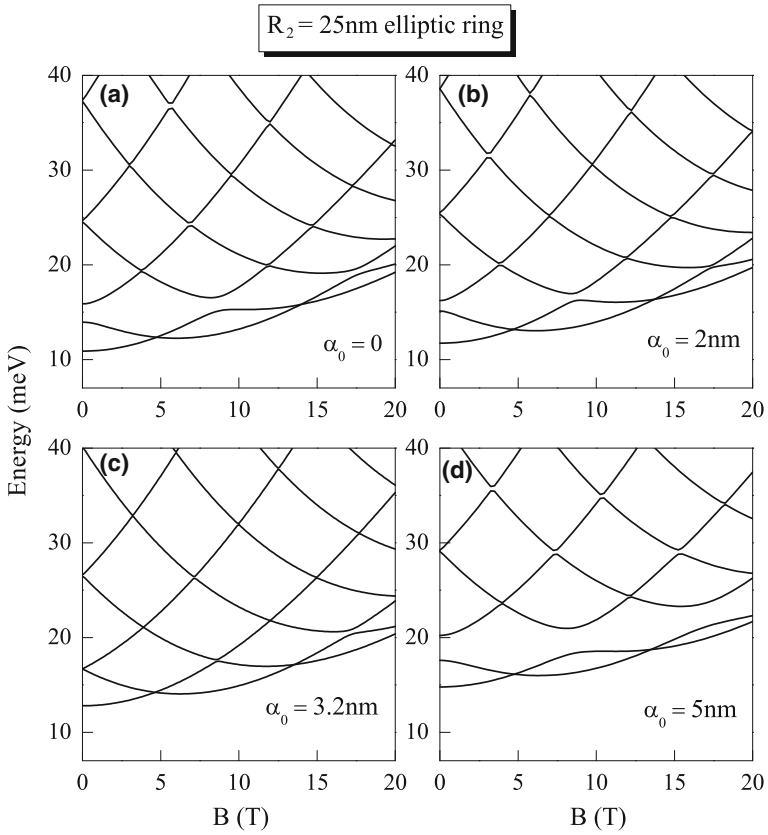

Fig. 11.11 The low-lying energy levels of an elliptic QR as a function of the magnetic field B for different values of α_0. The results are for $R_2 = 25$ nm [85]

Let us now consider the case of the anisotropic QR under the action of ILF. From expression (11.11) and Fig. 11.9c it is clear that if $\varepsilon \neq 0$ the undressed confinement potential is anisotropic, and the QR is compressed along the y direction. On the other hand the laser field brings an anisotropy of the confinement potential along the x direction due to which the bottom of the effective confinement potential can have almost circular form (see Fig. 11.9c, d). Therefore, we have two competing different effects, the first one is caused by the structural anisotropy of the system while the other is caused by the external ILF. In Fig. 11.11 the magnetic field dependence of the low-lying energy levels are presented, for an anisotropic QR ($\varepsilon = 0.5$) and for different values of α_0. Figure 11.11a displays the unusual AB oscillations without the ILF due to the structural anisotropy of the QR. With an increase of α_0 the effect of structural anisotropy on the energy levels weakens (Fig. 11.11b), and for $\alpha_0 = 3.2$ nm the usual AB oscillations are completely recovered (Fig. 11.11c). A further increase of the ILF parameter again creates an anisotropy in the x direction,

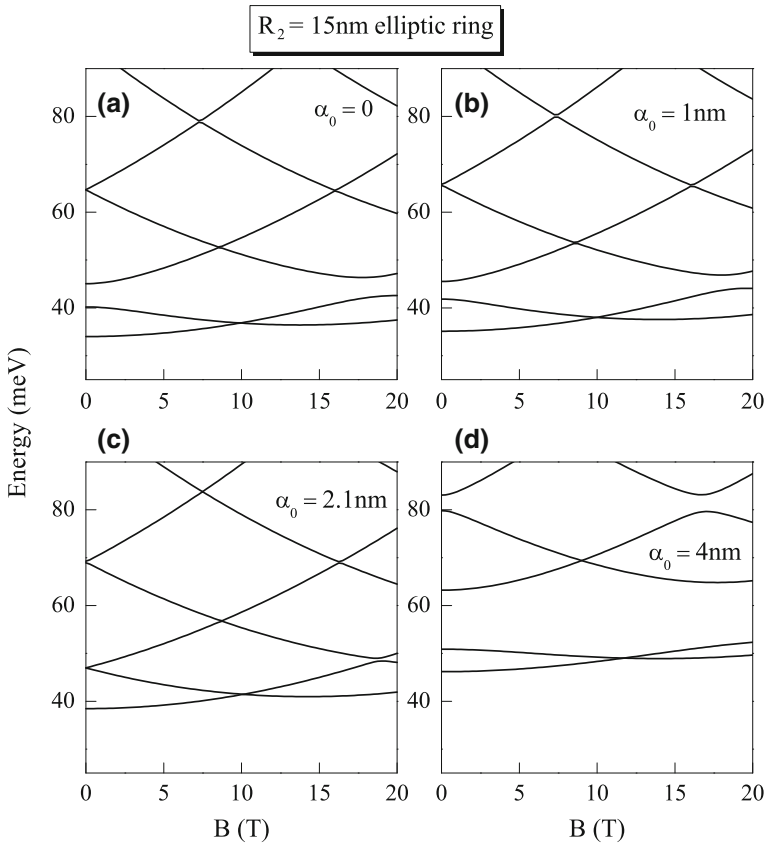

Fig. 11.12 The low-lying energy levels of an elliptic QR as a function of the magnetic field B for different values of α_0. The results are for $R_2 = 15$ nm [85]

and again the unusual AB oscillations can be observed in Fig. 11.11d. This behavior of the electronic states have never been reported earlier in a quantum ring. Similar effects also can be observed for smaller QRs, which is presented in Fig. 11.12. The influence of ILF on the confinement potential of the QR is stronger for smaller QRs, and therefore the usual AB oscillations are recovered for $\alpha_0 = 2.1$ nm (see Fig. 11.12c).

These interesting properties of the energy spectra are expected to influence the optical properties of the QRs. In Fig. 11.13 the dipole-allowed optical transition energies as a function of the magnetic field are presented for different values of α_0 for isotropic QR with outer radius $R_2 = 25$ nm. The size and the color of the circles in this figure are proportional to the intensity $|M_{fi}|^2$ of the calculated optical transitions. Without the laser field the signature of the usual AB optical oscillations is seen in Fig. 11.13a. The energies in Fig. 11.13a correspond to the transitions from the ground state to the first and second excited states. All other transitions are forbidden due to

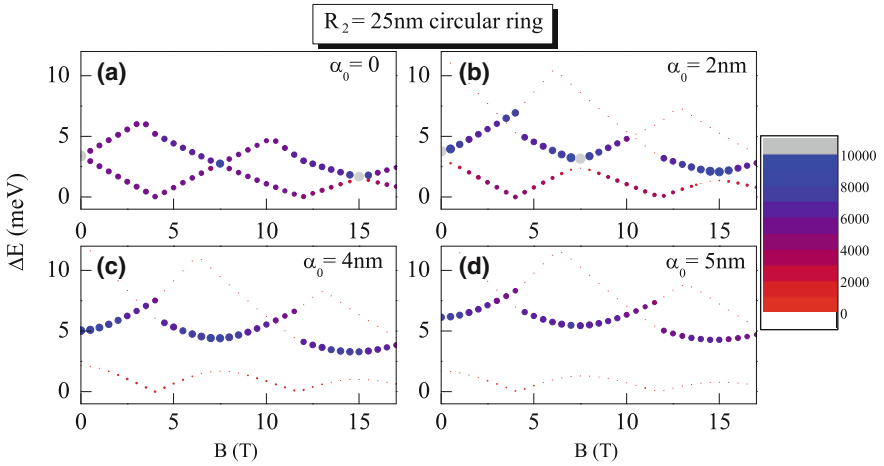

Fig. 11.13 Dipole allowed optical transition energies as a function of magnetic field B for different values of α_0. The results are for a $R_2 = 25$ nm circular QR. The size and the color of the circles is proportional to the intensity of the calculated optical transitions [85]

the cylindrical symmetry of the structure. With the increase of α_0 the unusual optical AB oscillations are again visible. Further, it should be noted that with the increase of α_0 the intensity of the $1 \rightarrow 2$ transition weakens and the intensity of the $1 \rightarrow 3$ transition strengthens. As an example, for $\alpha_0 = 5$ nm the $1 \rightarrow 2$ transition has almost disappeared. This fact can be explained by the anisotropy of the system created by the ILF in the x direction.

In Fig. 11.14 the same results as in Fig. 11.13 are presented for an anisotropic QR and for the value $\varepsilon = 0.5$. Without the laser field the optical AB oscillations again have unusual behavior (Fig. 11.14a), but now the intensity of the $1 \rightarrow 2$ transition is stronger than that of $1 \rightarrow 3$. This is because the structural anisotropy is created in the y direction. With an increase of α_0 the intensity of $1 \rightarrow 3$ increases and the intensity of $1 \rightarrow 2$ decreases. For the value of $\alpha_0 = 3.2$ nm the usual optical AB oscillations are completely recovered for an anisotropic QR (Fig. 11.14c). Therefore, we believe that these interesting effects can be confirmed experimentally.

In conclusion, we have investigated the strong influence of intense terahertz laser field on the electronic and optical properties of isotropic and anisotropic QRs in an applied magnetic field [85]. In isotropic QRs the laser field creates the unusual AB oscillations, which is usually expected in anisotropic rings. Therefore, with the laser field we can observe a *continuous evolution of AB oscillations* within the same ring. In the case of anisotropic QRs we have shown that with the ILF it is possible to completely 'control' the anisotropy of the QR and thus also the physical characteristics. We have demonstrated that the energy spectra and the AB oscillations can be made completely usual by the ILF for anisotropic QRs. It is also worth noting that the ILF can in principle restore isotropic properties of a QR from any type of anisotropy (structural, effective masses, defects, etc.) of the QRs. This important outcome has

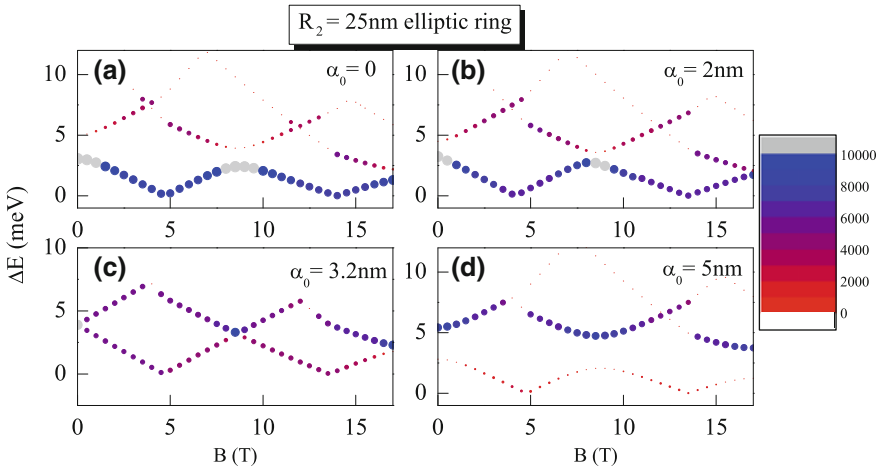

Fig. 11.14 Dipole-allowed optical transition energies as a function of the magnetic field B for different values of the laser field parameter α_0. The results are for $R_2 = 25$ nm elliptic QR. The size and the color of the circles in the figure are proportional to the intensity of the calculated optical transitions

the potential to open up new route to exploration of quantum rings. In fact, in addition to providing an unified picture of the electronic and optical properties of quantum rings, we believe that our studies will offer new possibilities to design, fabricate and improve new devices based on QRs, such as therahertz detectors, efficient solar cells, photon emitters, etc.

11.4 Properties of Graphene Quantum Rings

The term 'graphene' was originally attributed to a single layer of graphite consisting of a honeycomb lattice with two carbon atoms per unit cell [86]. It is a bipartite lattice made up of two interpenetrating triangular sublattices. Long before graphene and other related systems (bilayer graphene [87–91], graphane [92], phosphorene [93, 94], silicene [95, 96], germanene [97] just to name a few) became a sensational research topic all across the globe [98], a few pioneering theoretical studies already unfolded most of the unusual electronic properties of this unique two-dimensional electron system (2DES). In 1947, Wallace [99] reported that the nearest-neighbor tight-binding description of graphene results in a very unique band structure, where two of the six corners of the first Brillouin zone are inequivalent points in the reciprocal space (denoted as K and K′) [87–89, 100]. Within the effective mass approximation, that describes the low-energy properties, these points correspond to two

'valleys', In each valley the low-energy electron dynamics near the Fermi energy is described by the following Hamiltonian [101]

$$\mathscr{H}_{\xi} = \xi v_{\mathrm{F}} \begin{pmatrix} 0 & p_{-} \\ p_{+} & 0 \end{pmatrix}$$

where $p_{-} = p_x - \mathrm{i}p_y$, $p_{+} = p_x + \mathrm{i}p_y$, and $\mathbf{p}$ is the two-dimensional momentum of an electron. Here $v_{\mathrm{F}} \approx 10^6$ m/s is the Fermi velocity. The index ξ is 1 and -1 for valleys K and $K\prime$ respectively. Without the spin-orbit interaction [102], each level determined by the above Hamiltonian has a two-fold degeneracy. The single-electron state obtained from the above Hamiltonian has a linear dispersion relation given by

$$\varepsilon(p) = \pm v_{\mathrm{F}} p,$$

which is the dispersion relation of Dirac "relativistic" massless particle. In addition to the spin degeneracy, each energy level has a two-fold valley degeneracy. Helicity (chirality) is a good quantum number in graphene. In an external perpendicular magnetic field B, the relativistic-like energy dispersion brings in very specific form of the Landau levels of electrons in graphene, viz., a square root dependence of both B and n the LL index, and $\varepsilon = 0$ for $n = 0$ [87–89, 100, 103]. The resulting quantum Hall effect was observed experimentally and the Dirac nature of electron dynamics was thereby confirmed [104, 105].

However, all these wonderful phenomena remained strictly 'theoretical' until free-standing graphene flakes were obtained experimentally by Geim et al. [106]. Although the idea of a technological revolution to be ushered in by graphene can be safely relegated to the distant horizon, graphene has made possible a quantum leap in the exploration of several very interesting physical phenomena related to the 2DES, many studied by us. Most notably, the fractal butterflies [96, 107, 108], possible presence of the pfaffians [89, 100, 109], unique features of the fractional quantum Hall effect [110, 111], magnetism [92], the quantum dots [112], and quantum rings [113].

Theoretical studies of graphene QR was initiated by Recher et al. [114], who used the Dirac model to analyze the electronic properties of AB rings made out of graphene (Fig. 11.15). They demonstrated that the ring confinement and the external magnetic field have the combined effect to break the valley degeneracy in graphene. If confirmed, it will open up the intriguing possibility to control valley polarization for device applications. The interelectron interaction effects were however ignored in this work, thereby reducing the practicality of this idea. The important and interesting question of the interplay between valley polarization and the Coulomb interaction was first addressed by Abergel et al. [113]. They found that the interaction causes drastic changes in the nature of the ground state. The Coulomb interaction has a strong influence on the energy spectrum, the persistent current, and the optical-absorption spectrum of a graphene ring.

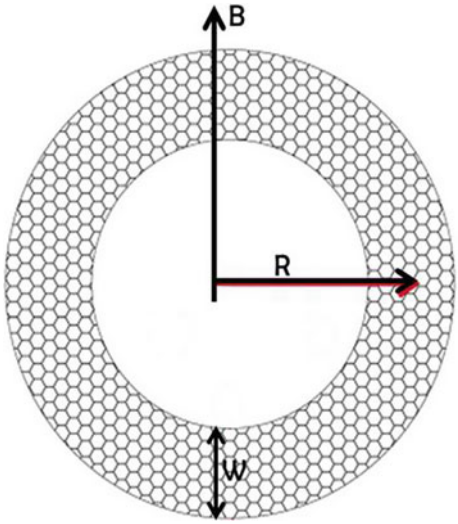

Fig. 11.15 The geometry of a quantum ring. The magnetic field is perpendicular to the graphene plane

In the continuum model, the valley-symmetric graphene Hamiltonian is written as [113, 114]

$$\mathscr{H} = \tau_0 \otimes \mathscr{H}_0 + \tau_z \otimes \sigma_z V(r)$$

where $V(r)$ is a mass term which describes the confinement of the electron, $\mathscr{H}_0 = v_{\mathrm{F}}\,(\mathbf{p}\cdot\boldsymbol{\sigma})$ is the graphene Hamiltonian in the bulk, $\sigma_{x,y,z,0}$ and $\tau_{x,y,z,0}$ are Pauli matrices in the sublattice and valley spaces respectively, $\mathbf{p} = -\mathrm{i}\hbar\boldsymbol{\nabla} + e\mathbf{A}$ and v_{F} is the Fermi velocity. The vector potential is taken as $\mathbf{A} = (\Phi/2\pi r)\mathbf{e}_\varphi$ where Φ is the total magnetic flux threading the ring. The index N stands for the pair of quantum numbers $[m, \tau]$, where m is the orbital angular momentum, and $\tau = +1(-1)$ in the K (K') valley. The single-electron wave function $\psi_N(\rho)$ for a ring of width W and radius R (see Fig. 11.15) written in terms of the dimensionless radial coordinate $\rho = R/W$ is given by

$$\psi_N(\rho) = e^{\mathrm{i}(m-\frac{1}{2})\varphi} b_N \begin{bmatrix} f_N(|\varepsilon_N|\rho) \\ \mathrm{isgn}(\varepsilon_N) e^{\mathrm{i}\varphi} g_N(|\varepsilon_N|\rho) \end{bmatrix}$$

$$f_N = \alpha_N H^{(1)}_{\tilde{m}-\frac{1}{2}}(|\varepsilon_N|\rho) + H^{(2)}_{\tilde{m}-\frac{1}{2}}(|\varepsilon_N|\rho),$$

$$g_N = \alpha_N H^{(1)}_{\tilde{m}+\frac{1}{2}}(|\varepsilon_N|\rho) + H^{(2)}_{\tilde{m}+\frac{1}{2}}(|\varepsilon_N|\rho),$$

$$\alpha_N = -\frac{H^{(2)}_{\tilde{m}-\frac{1}{2}}(|\varepsilon_N|\rho_-) + \tau\,\mathrm{sgn}(\varepsilon_N) H^{(2)}_{\tilde{m}+\frac{1}{2}}(|\varepsilon_N|\rho_-)}{H^{(1)}_{\tilde{m}-\frac{1}{2}}(|\varepsilon_N|\rho_-) + \tau\,\mathrm{sgn}(\varepsilon_N) H^{(1)}_{\tilde{m}+\frac{1}{2}}(|\varepsilon_N|\rho_-)}$$

with $\rho_{\pm} = \frac{R}{W} \pm \frac{1}{2}$, $\bar{m} = m + \frac{\Phi}{\Phi_0}$, b_N is the normalization factor and $\mathrm{sgn}(x) = 1$ for $x \geq 0$ and $\mathrm{sgn}(x) = -1$ for $x < 0$. The functions $H_\nu^{(1)}(x)$ and $H_\nu^{(2)}(x)$ are respectively Hankel functions of the first and second kind.

The ring confinement used to derive the above equations is defined by the mass term [written as the potential $V(r)$] in the Hamiltonian. We employ the infinite mass boundary conditions [113–115] so that $V(r) \to \infty$ outside the ring. This yields the boundary condition $\psi(\rho_{\pm}) = \tau(\mathbf{n} \cdot \boldsymbol{\sigma})\psi(\rho_{\pm})$. The coefficient α_N is found by applying this condition at the inside edge, an eigenvalue equation for ε_N is derived by subsequently imposing the boundary condition at the outside edge, and b_N is numerically evaluated for each state and value of the flux via the normalization condition for the wave function.

The Coulomb interaction does not change the valley state of the electron, and conserves the total angular momentum between the initial and final states. The exact diagonalization scheme was then applied to determine the energy and eigenstates of the interacting system. The persistent current j was then calculated by taking the derivative of the ground state energy E_0 of the few electron system with respect to the flux: $j(\Phi) = \frac{\partial}{\partial \Phi} E_0$.

Absorption of incident light by the graphene ring can be studied by adding a term to the Hamiltonian which describes the coupling of electrons to the field via the vector potential $\mathbf{A}_{\mathrm{EM}} = 2A_0\boldsymbol{\alpha}\cos(\mathbf{k} \cdot \mathbf{r} - \omega t)$. We assume that the radiation propagates as a plane wave with wave vector $\mathbf{k}$, frequency ω, and polarization described by the unit vector $\boldsymbol{\alpha}$. The Hamiltonian can then be written

$$\mathscr{H} = v_{\mathrm{F}}\boldsymbol{\sigma} \cdot \left(\mathbf{p} + e\mathbf{A}_{\mathrm{B}} + e\mathbf{A}_{\mathrm{EM}}\right) + \tau V(r)\sigma_z + C(\mathbf{r_1} - \mathbf{r_2}) \tag{11.14}$$

in the valley symmetric representation. Here, $C = \tau_0 \otimes \sigma_0\, V(\mathbf{r_1} - \mathbf{r_2})$ is the Coulomb interaction operator. The transition rate from state N to state N' is calculated from

$$w_{N'N} \propto \left|\left\langle N' \right| \sigma_x\alpha_x + \sigma_y\alpha_y \left| N \right\rangle\right|^2 = 4\pi^2 \left|I_{N'N}\right|^2, \tag{11.15}$$

with

$$I_{N'N} = \int_{\rho_-}^{\rho_+} \rho\, d\rho\, b_{N'}^* b_N \left(\delta_{\tau',K}\delta_{\tau,K} + \delta_{\tau',K'}\delta_{\tau,K'}\right) \times \\ \times \left[\delta_{m',m+1}(\alpha_x - i\alpha_y) f_{N'}^* g_N - \delta_{m',m-1}(\alpha_x + i\alpha_y) g_{N'}^* f_N\right] \tag{11.16}$$

in the dipole approximation. The integral (where the coordinate dependence of the spatial functions was dropped for brevity) must be evaluated numerically. The intensity of the absorption is proportional to this transition rate and the area of the dots in the lowest panels of Fig. 11.16a–c scale with this quantity. In all figures we show the absorption of unpolarized light [i.e. $\boldsymbol{\alpha} = (\mathbf{e}_x + \mathbf{e}_y)/\sqrt{2}$]. Equation (11.16) shows

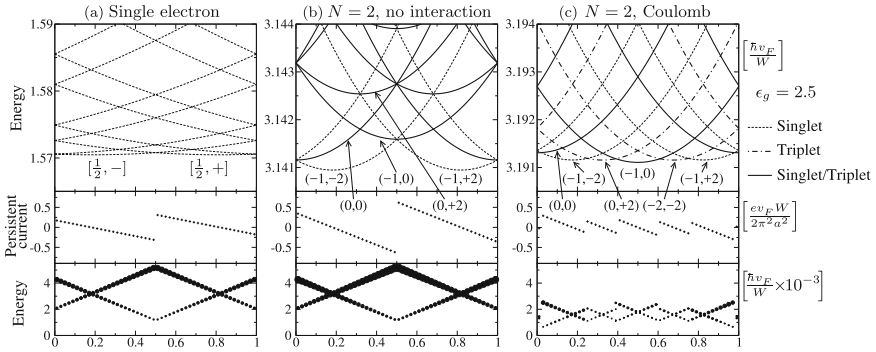

Fig. 11.16 Energy spectrum (top pane), persistent current (middle pane) and optical absorption of unpolarized light (lower pane) as a function of Φ/Φ_0 by **a** a single electron, **b** two non-interacting electrons, and **c** two electrons with the Coulomb interaction included. States in the two-electron plots are labelled by the pair of quantum numbers (M, T) where M is the total angular momentum, and T is the total valley index. The area of the points in the absorption plots represent the intensity of the peak in arbitrary units. In all three plots, $W = 10\,nm$ and $\frac{R}{W} = 10$, and $\varepsilon_g = 2.5$ [116]. Reproduced from [113]

that transitions which change the angular momentum quantum number by ± 1 are permitted, as long as the valley index remains unchanged. Where the initial state of a transition is degenerate, we take the average of the intensity of all possible pairs of initial and final states.

The energy spectrum, persistent current and optical absorption for a single electron in the graphene ring with $R/W = 10$ are shown in Fig. 11.16a. Lifting of the valley degeneracy previously described causes the step in the persistent current at $\phi = \Phi/\Phi_0 = 0.5$. For $0 < \phi < 0.5$ the ground state consists of one electron in the $m = -\frac{1}{2}$, $\tau = -1$ state whereas for $0.5 < \phi < 1$ the valley index is $\tau = +1$. For $\phi \gtrsim 0$, transitions to the lowest-lying states $m = +\frac{1}{2}$, $\tau = +1$ and $m = -\frac{1}{2}$, $\tau = -1$ are not allowed since the optical absorption cannot mix valleys.

For two non-interacting electrons, the ground state consists of a pair of electrons with anti-parallel spins occupying the same single-particle states as in the single-electron system (Fig. 11.16b). The persistent current reflects the similarity between the ground states of the single-particle and $N = 2$ non-interacting system, and since there are now two electrons, the persistent current is doubled. The excited states can have varying degrees of degeneracy: If the quantum number pairs $P = [m_P, \tau_P]$ and $Q = [m_Q, \tau_Q]$ of the two electrons are identical then there is only one permitted configuration of the electron spins, the singlet state. However, if $P \neq Q$ then there are four degenerate possibilities: the singlet and three triplet states.

In the presence of the Coulomb interaction (Fig. 11.16c), the picture changes drastically. In order to describe the two particle states, we introduce the notation $M = m_1 + m_2$ for the total angular momentum and $T = \tau_1 + \tau_2$ for the total valley quantum number. The exchange interaction will split the degenerate singlet-triplet states when both of the electrons are in the same valley i.e. for $T = \pm 2$. In this case,

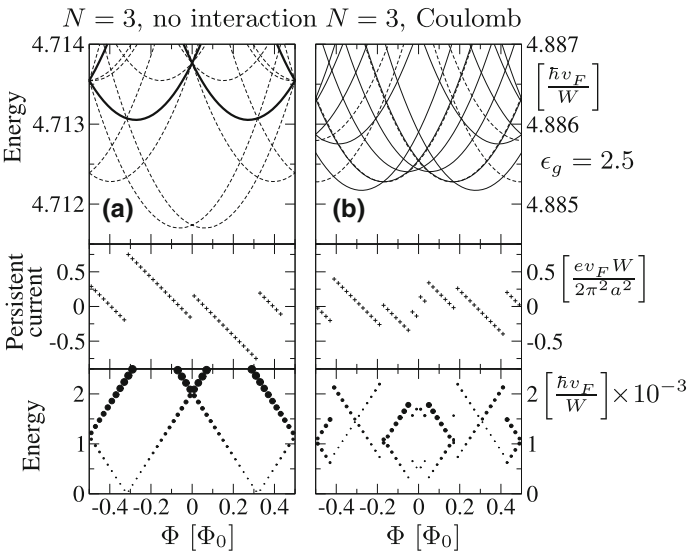

Fig. 11.17 **a** Non-interacting, and **b** interacting three electron energy spectrum, persistent current and optical absorption for $\frac{R}{W} = 10$. Dashed lines denote two-fold degeneracy, solid lines four-fold degeneracy and thick solid line eight-fold degeneracy of the state [113]

the energy of the singlet does not contain any contribution from the exchange and as a consequence, has a rather higher energy than the corresponding triplet. This is exemplified by the ($M = 0, T = 2$) state. The triplet part experiences the exchange and this reduces its energy sufficiently for it to form the ground state for $\phi \approx 0.3$ with $\varepsilon \simeq 3.191$. At the same flux the singlet state has $\varepsilon \simeq 3.205$ and therefore has energy too high to be shown in Fig. 11.16c. On the other hand, the singlet and triplet parts of the $(-1, 0)$ degenerate state are not split by the exchange interaction.

For three non-interacting electrons in the ring (Fig. 11.17), the ground state is composed of spin and valley unpolarized states (i.e. $T = \pm 1$). When the interaction is added, the contribution from exchange is largest for $T = \pm 3$ states so the low-energy spectrum becomes much more compact, just as in the $N = 2$ case. Qualitatively, the effect of the interaction is the same as previously, so that the changing nature of the ground state again demonstrates the complexity due to the absence of the valley degeneracy. However, because there are more possible combinations of states, the persistent current and absorption spectrum are correspondingly more complex in their structure. In particular it is not possible to have $T = 0$ so the exchange energy is always finite. However, its contribution is larger for $T = \pm 3$ states than for $T = \pm 1$ states. The interesting interplay of the interaction and the total valley quantum number allow for an intricate manifestation of the breaking of valley degeneracy in this geometry. The change of the interacting ground state between singlet, triplet and degenerate singlet-triplet natures are reflected in the fractional nature of the AB

oscillations in the persistent current, and in the steps and intensity changes in the absorption spectrum as the flux is varied.

A brief review of all the subsequent works on graphene QRs can be found in Schelter et al. [117]. Experimental realization of a graphene ring was first reported in 2008 [118]. Electron transport in that ring displayed clear AB oscillations in magnetoconductance.

11.5 Quantum Rings Proximity Coupled to Superconductors: Possible Signatures of Majorana Fermions

Another type of novel material where the QR can play an important role is a semiconductor heterostructure that is proximity coupled to a superconductor. Recently these types of hybrid semiconductor-superconductor structures became attractive due to the possibility to find Majorana fermions (MFs) [119] inside them.

In particle physics, the MFs are defined as particles which are their own antiparticles [120]. It is still unclear if there are elementary particles which are MFs, but they are more likely to exist in condensed matter systems as a zero energy quasiparticle excitation which is its own hole. The condensed matter version of the MFs became attractive mainly because of their special non-Abelian exchange statistics [121]. In other words, MF is half of a normal fermion, meaning that a fermionic state is obtained as a superposition of two MFs [122]. In principle, any fermion can be written as a combination of two MFs which corresponds to splitting the fermion into a real and an imaginary part, each of which is an MF. But usually this is a purely mathematical operation without any physical consequences because both MFs are spatially localized close to each other and cannot be addressed individually due to the significant overlap. Starting from here when we talk about the MFs we mean a fermionic state which can be presented as a superposition of two MFs that are spatially separated.

Being its own hole means that the MF must be a superposition of an electron and a hole state. Therefore, it is natural to search such excitations in supeconducting systems where the wave functions of Bogoliubov quasiparticles have both electron and hole components. A simple model where the MFs can be observed was first suggested by Kitaev [123]. He considered a one-dimensional tight-binding atomic chain with p-wave superconducting pairing and has shown that the MFs can be observed at the two ends of the chain.

Recently MFs have gained considerable attention due to several proposals for the existence of Majorana modes in semiconductor systems proximity coupled to a superconductor [124–127]. If a good interface is made between a semiconductor and a superconductor, electrons can tunel between these two systems. The effect is that the electrons in the semiconductor feel an effective proximity-induced superconducting pairing field. The strength of that field depends on the details of the semiconductor

and the superconductor, as well as the interface. One of the proposed methods for realization of MFs is the observation of the topological superconducting phase in a one-dimensional semiconductor wire with large Rashba spin orbit coupling [128], proximity coupled to an s-wave superconductor. By tuning the chemical potential of this system in the gap region created by the magnetic field, the system effectively becomes spinless and is expected to support the MFs at the edges of the wire similar to Kitaev's p-wave superconductor chain model [123].

In all these studies of the characteristics of topological superconductivity and MFs in semiconductor quantum wires, the role of the interaction between electrons have been ignored. The effects of screened and unscreened long-range Coulomb interaction on the topological superconductivity phase in a quasi-one-dimensional semiconductor wire, proximity-coupled to an s-wave superconductor was reported in [129]. It appears that inclusion of the Coulomb interaction results in an enlargement of the region of parameter values where topological superconductivity can be observed. This enlargement is proportional to the screening length of the Coulomb interaction. The authors have also found that the interaction decreases the superconducting bulk gap. Some screening of the Coulomb interaction was found to be essential for observing topological superconductivity in a quasi-one-dimensional semiconductor wire proximity-coupled to an s-wave superconductor.

We wish to demonstrated below that elongated elliptical QRs with large Rashba spin orbit coupling could reveal the signatures of MFs. Although almost circular QRs have been grown by various experimental groups, anisotropic QRs are the ones mostly obtained during the fabrication process. Elongated InAs/InP QRs were fabricated by several groups [53, 54]. Here we propose that an anisotropic InAs QR with few electrons, proximity coupled to an s-wave superconductor is an excellent candidate for detecting the signatures of the MFs.

We consider an elliptical QR with strong Rashba SO coupling, which is proximity coupled to a superconductor. In order to model the elliptical ring, we define the coordinate system in the form $x = ar\cos\theta$, $y = br\sin\theta$, where a and b are constants defining the ellipticity of the QR, and r is the dimensionless radius of the QR [130]. Clearly, for $a = b$ the QR is circular, while for $a \neq b$ it has elliptical boundaries with the eccentricity $\varepsilon = \sqrt{1 - b^2/a^2}$. The confinement potential of the QR was chosen to be $V_{\text{conf}}(r) = 0$, if $R_1 \leq r \leq R_2$ and infinity otherwise.

Without the superconducting pairing potential the Hamiltonian of our system is

$$\mathscr{H} = \sum_{i}^{N_e} \mathscr{H}_{\text{SP}}^{i} + \frac{1}{2}\sum_{i\neq j}^{N_e} V_{ij}, \tag{11.17}$$

where N_e is the number of electrons and

$$V_{ij} = \frac{e^2 e^{-\lambda\left|\mathbf{r}_i - \mathbf{r}_j\right|}}{\varepsilon|\mathbf{r}_i - \mathbf{r}_j|} \tag{11.18}$$

is the Yukawa type screened Coulomb potential with screening parameter λ [129], and ε is the dielectric constant of the QR. Finally, $\mathscr{H}_{\rm SP}$ is the single-particle Hamiltonian in the presence of an external magnetic field and the Rashba spin-orbit interaction (SOI).

$$\mathscr{H}_{\rm SP} = H_0 + H_{\rm SO} = \frac{1}{2m_e}\boldsymbol{\Pi}^2 - \mu + V_{\rm conf}(r) + \tfrac{1}{2}g\mu_{\rm B}B\sigma_z + H_{\rm SO}. \quad (11.19)$$

In (11.19), $\boldsymbol{\Pi} = \mathbf{p} + \frac{e}{c}\mathbf{A}$, the vector potential of the magnetic field $\mathbf{A} = B/2\,(-y, x, 0)$, and μ is the chemical potential. The last two terms of (11.19) are the Zeeman splitting and the Rashba SOI respectively:

$$H_{\rm SO} = \frac{\alpha}{\hbar}\left[\boldsymbol{\sigma} \times \boldsymbol{\Pi}\right]_z, \quad (11.20)$$

with α being the Rashba SOI parameter. In the case of a circular QR ($a = b$) we take the eigenfunctions of H_0 without the magnetic field ($B = 0$) as the basis states.

$$\phi_{nl}(r,\theta) = \frac{C}{\sqrt{2\pi}}e^{{\rm i}l\theta}\left(J_l(\gamma_{nl}r) - \frac{J_l(\gamma_{nl}R_1)}{Y_l(\gamma_{nl}R_1)}Y_l(\gamma_{nl}r)\right) = \frac{1}{\sqrt{2\pi}}e^{{\rm i}l\theta}\chi_{nl}(r), \quad (11.21)$$

where $J_l(r)$ and $Y_l(r)$ are Bessel functions of the first and second kind respectively, and $\gamma_{nl} = 2m_e a^2 E_{nl}/\hbar^2$, with the eigenstates E_{nl} defined from the boundary conditions. The normalization constant C is determined from the integral

$$\int_0^{2\pi} {\rm d}\theta \int_{R_1}^{R_2} {\rm d}r a^2 r \left|\phi_{nl}(r,\theta)\right|^2 = 1.$$

For an elliptical QR we choose the following orthonormal basis states

$$\Phi_{nl}(r,\theta) = \frac{1}{\sqrt{2\pi}}\sqrt{\frac{a}{b}}e^{{\rm i}l\theta}\chi_{nl}(r) = \sqrt{\frac{a}{b}}\psi_{nl}(r,\theta), \quad (11.22)$$

where the $\sqrt{a/b}$ term is included for the normalization of the basis states:

$$\int_0^{2\pi} {\rm d}\theta \int_{R_1}^{R_2} r{\rm d}r\, ab \left|\Phi_{nl}(r,\theta)\right|^2 = 1. \quad (11.23)$$

The many-body Hamiltonian (11.17) in the second-quantized form is written as

$$\mathscr{H} = \sum_{n'l'nl}\Bigg[\sum_s \langle n'l'|H_0|nl\rangle c^\dagger_{n'l's}c_{nls} + \frac{{\rm i}\alpha}{\hbar}\langle n'l'|\Pi_-|nl\rangle \times c^\dagger_{n'l'\uparrow}c_{nl\downarrow} - \frac{{\rm i}\alpha}{\hbar}\langle n'l'|\Pi_+|nl\rangle c^\dagger_{n'l'\downarrow}c_{nl\uparrow}\Bigg]$$

$$+\frac{1}{2}\sum_{n_1'l_1',n_2'l_2'}\sum_{nl_1,n_2l_2}\sum_{s_1s_2}\langle n_1'l_1',n_2'l_2'|V_{12}|n_1l_1,n_2l_2\rangle$$
$$\times c^{\dagger}_{n_1'l_1's_2}c^{\dagger}_{n_2'l_2's_1}c_{n_1l_1s_1}c_{n_2l_2s_2}, \tag{11.24}$$

where $c^{\dagger}_{nls}$ and c_{nls} are creation and annihilation operators and $\Pi_{\pm}=\Pi_x\pm \mathrm{i}\Pi_y$. The corresponding non-zero matrix elements were calculated in [61] and have the following form:

for $l'=l$,

$$\langle n'l|H_0|nl\rangle=\frac{E_{nl}}{2}\left(1+\frac{a^2}{b^2}\right)\delta_{n'n}+\frac{\hbar\omega_{\mathrm{B}}l}{4}\left(\frac{a}{b}+\frac{b}{a}\right)\delta_{n'n}$$
$$+\frac{e^2B^2}{16mc^2}\left(a^2+b^2\right)\Gamma^{(3)}_{n'l,nl}, \tag{11.25}$$

for $l'=l+2$,

$$\langle n'l'|H_0|nl\rangle=\frac{E_{nl}}{4}\left(1-\frac{a^2}{b^2}\right)\Gamma^{(1)}_{n'l',nl}-\frac{\hbar^2\gamma_{nl}(l+1)}{4m_e}\left(\frac{1}{a^2}-\frac{1}{b^2}\right)\Lambda^{(0)}_{n'l',nl}$$
$$+\frac{\hbar\omega_{\mathrm{B}}\gamma_{nl}}{8}\left(\frac{a}{b}-\frac{b}{a}\right)\Lambda^{(2)}_{n'l',nl}+\frac{e^2B^2}{32m_ec^2}\left(a^2-b^2\right)\Gamma^{(3)}_{n'l',nl}, \tag{11.26}$$

for $l'=l+1$,

$$\langle n'l'|\Pi_+|nl\rangle=\frac{\mathrm{i}\hbar\gamma_{nl}}{2}\left(\frac{1}{a}+\frac{1}{b}\right)\Lambda^{(1)}_{n'l',nl}+\frac{\mathrm{i}eB}{4c}(a+b)\,\Gamma^{(2)}_{n'l',nl}, \tag{11.27}$$
$$\langle n'l'|\Pi_-|nl\rangle=\frac{\mathrm{i}\hbar\gamma_{nl}}{2}\left(\frac{1}{a}-\frac{1}{b}\right)\Lambda^{(1)}_{n'l',nl}-\frac{\mathrm{i}eB}{4c}(a-b)\,\Gamma^{(2)}_{n'l',nl}, \tag{11.28}$$

for $l'=l-1$,

$$\langle n'l'|\Pi_+|nl\rangle=\mathrm{i}\hbar\left(\frac{\gamma_{nl}}{2}\Lambda^{(1)}_{n'l',nl}-l\Gamma^{(0)}_{n'l',nl}\right)\left(\frac{1}{a}-\frac{1}{b}\right)+\frac{\mathrm{i}eB}{4c}(a-b)\,\Gamma^{(2)}_{n'l',nl}, \tag{11.29}$$

$$\langle n'l'|\Pi_-|nl\rangle=\mathrm{i}\hbar\left(\frac{\gamma_{nl}}{2}\Lambda^{(1)}_{n'l',nl}-l\Gamma^{(0)}_{n'l',nl}\right)\left(\frac{1}{a}+\frac{1}{b}\right)-\frac{\mathrm{i}eB}{4c}(a+b)\,\Gamma^{(2)}_{n'l',nl}. \tag{11.30}$$

Here $\omega_{\mathrm{B}}=eB/m_ec$ is the cyclotron frequency and $\Gamma^{(m)}_{n'l',nl}$ and $\Lambda^{(m)}_{n'l',nl}$ are defined as

$$\Gamma^{(m)}_{n'l',nl}=\int_{R_1}^{R_2}\mathrm{d}r\;a^2r^m\chi_{n'l'}(r)\chi_{nl}(r), \tag{11.31}$$

$$\Lambda^{(m)}_{n'l',nl} = \int_{R_1}^{R_2} \mathrm{d}r\, a^2 r^m \chi_{n'l'}(r) K_{nl}(r), \tag{11.32}$$

with

$$K_{nl}(r) = C\left(J_{l+1}(\gamma_{nl} r) - J_l(\gamma_{nl} R_1) Y_{l+1}(\gamma_{nl} r)/Y_l(\gamma_{nl} R_1)\right).$$

In order to evaluate the Coulomb matrix elements, it will be convenient to use the Fourier transform of the Yukawa type screened Coulomb potential, which is $V(\mathbf{k}) = 2\pi e^2/\varepsilon\sqrt{\lambda^2 + k^2}$. The corresponding Coulomb matrix elements are

$$\begin{aligned}
&\langle n_1' l_1', n_2' l_2' | V_{12} | n_1 l_1, n_2 l_2 \rangle = \frac{e^2}{2\pi\varepsilon} (-1)^{l_1 - l_2'} \mathrm{i}^{(l_1 + l_2 - l_1' - l_2')} \\
&\times \int_0^\infty k\mathrm{d}k \int_0^{2\pi} \mathrm{d}\theta_k \frac{e^{\mathrm{i}(l_1 + l_2 - l_1' - l_2')}}{\sqrt{\lambda^2 a^2 b^2 + k^2 b^2 \cos^2\theta_k + k^2 a^2 \sin^2\theta_k}} \\
&\times \int_{R_1}^{R_2} r_1\, \mathrm{d}r_1 a^2 \chi_{n_1' l_1'}(r_1) \chi_{n_2 l_2}(r_1) J_{l_2 - l_1'}(k r_1) \\
&\times \int_{R_1}^{R_2} r_2\, \mathrm{d}r_2 a^2 \chi_{n_2' l_2'}(r_2) \chi_{n_1 l_1}(r_2) J_{l_1 - l_2'}(k r_2).
\end{aligned} \tag{11.33}$$

We can start the derivation of the induced superconducting potential for the QR using its general form presented with the help of the field operators [122]

$$\mathscr{H}_{\mathrm{SC}} = \int \mathrm{d}^2 r \Psi_\downarrow(\mathbf{r}) \Delta(\mathbf{r}) \Psi_\uparrow(\mathbf{r}) + \mathrm{h.c.} \tag{11.34}$$

For the s-wave superconductors $\Delta(\mathbf{r}) = \Delta e^{-\mathrm{i}n_\Phi \theta}$ and $n_\Phi = [2\Phi/\Phi_0]$ [131, 132]. In our model Δ is real and $\Phi = \pi a b R_1^2 B$, $\Phi_0 = hc/e$ ($[v]$ denotes the integer closest to v). After the transition from field operators to creation-annihilation operators defined for the basis (11.22): $\Psi_s(\mathbf{r}) = \sum_{nl} \Phi_{nl}(r, \theta) c_{nls}$, we get the following final form for the superconducting potential

$$\mathscr{H}_{\mathrm{SC}} = \Delta \sum_{n'nl} \Gamma^{(1)}_{n'(n_\Phi - l),nl} \left[c_{n'(n_\Phi - l)\downarrow} c_{nl\uparrow} + c^\dagger_{n'(n_\Phi - l)\uparrow} c^\dagger_{nl\downarrow} \right] \tag{11.35}$$

The eigenstates of the total Hamiltonian $\mathscr{H}_{\mathrm{PSC}} = \mathscr{H} + \mathscr{H}_{\mathrm{SC}}$ can be evaluated with the help of the exact diagonalization procedure in even and odd sectors [129]. For example, for the odd sector we can diagonalize $\mathscr{H}_{\mathrm{PSC}}$ using the basis set with non-constant odd number of electrons $1, 3, \ldots N_e$. Similarly we can diagonalize the Hamiltonian also for the even sector. As a result we determine the low-lying energy spectra and the wave functions for even and odd sectors with high accuracy.

Several different approaches for identification of the signatures of topological superconductivity and the existence of separated MFs in the QR are available. In semiconductors isolated MFs are zero-energy quasi-excitations without charge [126]. The fermion number parity is a good quantum number. Therefore, the addition of a non-local electron which consists of two well separated MFs will not change the total energy and the charge of the system. Even in the case of the system without boundaries where isolated MFs usually reside, the phase transition between the trivial and non-trivial (topological) superconducting states results in closing of the superconducting bulk gap. Therefore, the first parameter which can be used for identification of the phase transition between two superconducting phases and for the appearance of isolated MFs is the energy difference between the odd and even sectors [133]

$$\Delta E = \left| E_{\text{odd}} - E_{\text{even}} \right|. \tag{11.36}$$

This difference vanishes in the topological phase but remains finite for the ordinary superconducting state [133]. The next parameter is the charge difference between the even and odd sectors ΔN, which can be defined as the mean electron number difference between the two sectors. For the evaluation of this parameter at first we have to calculate the electron densities in each sector

$$\rho_{\text{even(odd)}}(\mathbf{r}) = \int d\mathbf{r}_2\, d\mathbf{r}_3 \ldots \left| \Psi_{\text{even(odd)}}\left(\mathbf{r}, \mathbf{r}_2, \ldots\right) \right|^2. \tag{11.37}$$

Here $\Psi_{\text{even(odd)}}\left(\mathbf{r}_1, \mathbf{r}_2, \ldots\right)$ is the wave function of the system in the even (odd) sector, which can be represented as a superposition of the basis states with different number of electrons up to maximum number N_e due to the cutoff in the exact-diagonalization procedure. The basis states with different number of electrons are orthogonal and the number of integrals in (11.37) will be equal to the number of electrons for each basis state component of $\Psi_{\text{even(odd)}}\left(\mathbf{r}_1, \mathbf{r}_2, \ldots\right)$.

It has been shown that for a semiconductor quantum wire in the topological superconducting phase, the ground state parity could be changed by the changes of the system parameters, such as the chemical potential or the magnetic field. For a wire of finite size this can be accompanied by a jump of the total electron number and the charge, because the jump is spread along the wire and has an oscillating behavior [134]. Therefore, at first we have to calculate the difference between the electron densities in odd and even sector $\Delta\rho(\mathbf{r}) = \rho_{\text{odd}}(\mathbf{r}) - \rho_{\text{even}}(\mathbf{r})$ and compare the results for the ring with similar ones for the quantum wire [134]. The charge difference between the odd and even sector ΔN is the cumulative difference between the particle densities, i.e., $\Delta N = \int d\mathbf{r}\Delta\rho(\mathbf{r})$. Finally, we have calculated also the MF probability distributions using the procedure outlined in [129, 133].

$$p^{(j)}(r,\theta) = \sum_s \left| \sum_{nl} d_{nls}^{(j)} \Phi_{nl}^*(r,\theta) \right|^2. \tag{11.38}$$

Here $d_{nls}^{(j)}$ are the coefficients of the linear expansion of the MFs operators γ_a in terms of the electron creation and annihilation operators $c_{nls}^{\dagger}$ and c_{nls}, and $j = 1, 2$ correspond to two Majorana states.

Numerical calculations are performed for the InAs QR with parameters listed in Table 11.1. We take the SO coupling strength to be $\alpha = 20\,\text{meV} \cdot \text{nm}$, the superconducting pairing potential strength to be $\Delta = 0.225$ meV and consider the cases when $n_\Phi = [2\Phi/\Phi_0]$ or $n_\Phi = 0$. The geometrical parameters of the ring are $R_1 = 3$, $R_2 = 8$, $a = 10\,\text{nm}$, and for b we use two values $b = 6$ nm and $b = 8$ nm, which correspond to the values of the eccentricities $\varepsilon = 0.8$ and $\varepsilon = 0.6$ respectively. At this point we disregard the electron-electron interaction which means that we take $\lambda = \infty$. The role of interaction will be discussed below.

In Fig. 11.18, the single-electron energy spectra are presented against the magnetic field in an elliptical QR with $b = 6$ nm (a) and $b = 8$ nm (b). Due to the reduced symmetry of the ring from circular to C_2 the first two low-lying energy levels (for each spin component) are highly separated from the other states. This separation (more than 1 meV) is clearly visible in Fig. 11.18. The AB oscillations are also visible in Fig. 11.18, both for the low-lying group of states as well as for the higher excited states. It should be noted that observation of the AB oscillations for the low-lying states means that there is a finite probability for electron transfer from one side of the major axis of the QR to the other. We will show below that this fact is essential for confining two MFs of the non-local electron at the two sides of the QR. In order to consider the topological superconducting phase in the QR, we have to tune the chemical potential in the energy range of the first quadruplet. During our calculations we can limit the maximum number of electrons by four due to the fact that $\Delta < 1$ meV. Therefore, for the odd sector the number of electrons will be one or three. For the even sector considering system size up to four electrons results in the Hilbert space size bigger than 700,000, which makes the calculations somewhat

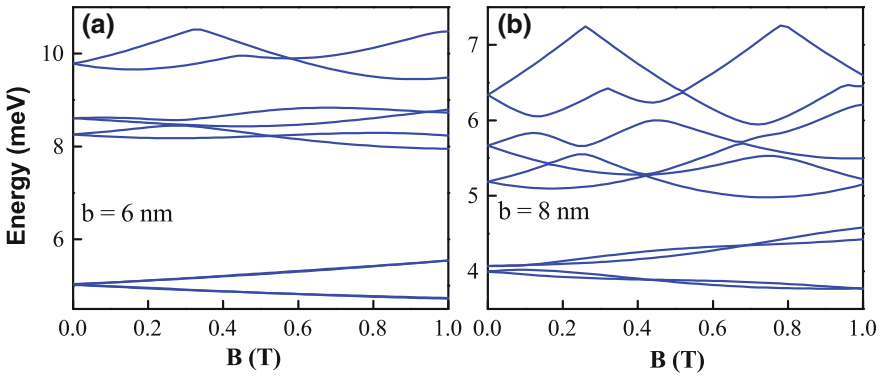

Fig. 11.18 The dependence of the low-lying energy states on magnetic field B for a single electron in an elliptical quantum ring for **a** $b = 6$ nm and **b** $b = 8$ nm. Chemical potential is chosen to be $\mu = 0$ [61]

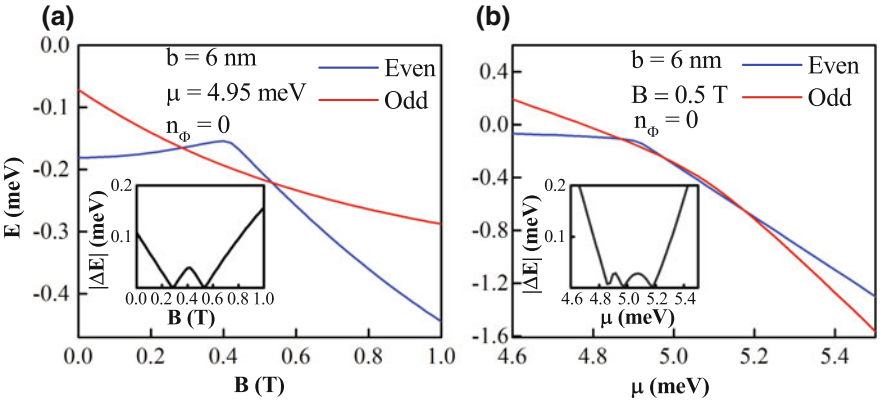

Fig. 11.19 The dependence of the energies of the ground states of odd and even sector on the magnetic field B (**a**) and the chemical potential μ (**b**). Insets show the absolute difference between the energies of the ground states. The ring parameter is $b = 6$ nm and $n_\Phi = 0$ [61]

cumbersome. In order to make the Hilbert space smaller we will take the number of electrons for the even sector to be zero or two. This approximation will be valid only if the separation between two doublets in the quadruplet is comparable to Δ, which is correct for $B > 0.3$ T.

In Fig. 11.19, the ground state energies for even and odd sectors are presented as a function of the magnetic field B (a) and the chemical potential μ (b), for the ring parameter $b = 6$ nm and the superconducting phase $n_\Phi = 0$. The absolute energy differences for the same ranges are presented as insets. It is clear from Fig. 11.19a that for the range of the magnetic field $B = 0.28 - 0.55$ T two ground states are close to each other (the energy difference is less than 0.05 meV). It is known that in a quantum wire proximity coupled to an s-wave superconductor, the topological phase appears above certain threshold values of the magnetic field ($V_Z > \sqrt{\mu^2 + \Delta^2}$, where V_Z is the Zeeman energy) and remains until the high values of the magnetic field for which s-wave pairing is suppressed due to the spin alignment. This is not the case for the QR, because the orbital effects and the AB oscillations start to push the states far from each other after a certain value of the magnetic field. That is why, for a QR we get only a range of about 0.3 T when the topological superconducting state can be observed. A similar picture is observed also in Fig. 11.19b for the dependence on the chemical potential. In this case the topological phase is visible from $\mu = 4.85$ meV to $\mu = 5.2$ meV. There are crossings between the two ground state energies inside this range and therefore the absolute energy difference shows an oscillatory behavior.

Similar results as in Fig. 11.19 but for the ring parameter $b = 8$ nm are shown in Fig. 11.20. As seen in Fig. 11.20a the magnetic field range where the two ground states come close to each other is slightly shifted to higher magnetic fields, namely $B = 0.34 - 0.66$ T, but the range remains almost the same. Similar picture is also visible in Fig. 11.20b. The chemical potential range of the topological phase is shifted

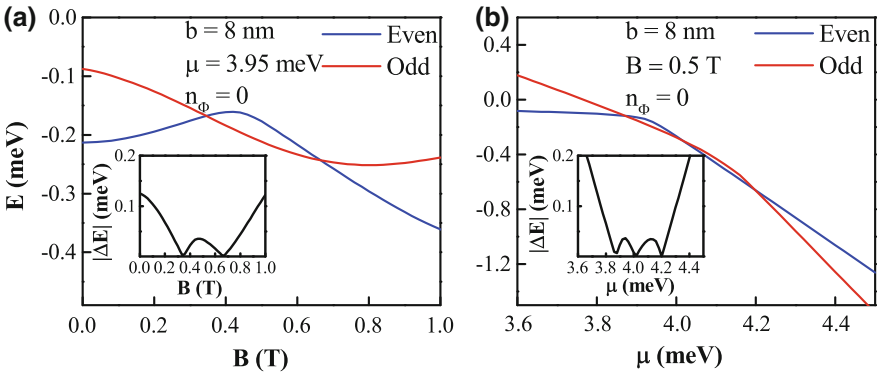

Fig. 11.20 Same as in Fig. 11.19 but for $b = 8$ nm [61]

by 1 meV to the smaller values, which is the consequence of the single-particle energy difference between $b = 6$ nm and $b = 8$ nm (Fig. 11.18). This confirms that the presence of the parameter ranges for which the ground state energies of odd and even sectors coming close to each other is not accidental, but rather a clear indication of the topological superconducting phase which is universal for the anisotropic QR. This will result in the observation of confined MFs inside the region of the topological phase, as will be shown below. Similar dependence as in Fig. 11.20, but for $n_\Phi = \left[2\Phi/\Phi_0\right]$ are shown in Fig. 11.21. As seen from the figure, in the case of $b = 8$ nm, the transition between $n_\Phi = 0$ and $n_\Phi = 1$ takes place in the region of topological superconducting phase. This has a detrimental effect on the robustness of topological superconducting phase or the extent of confinement of the MFs. For the magnetic field dependence the range of the topological superconducting phase is reduced as compared to the case of $n_\Phi = 0$ and is about 0.12 T. As for the chemical potential dependence, the range is almost the same as for $n_\Phi = 0$, but the absolute difference between the ground state energies is considerably higher and reaches up to 0.1 meV for $\mu = 4.1$ meV. This is a clear indication of the increase of the overlap between two MFs confined at the two sides of the major axis of the QR.

In order to present a clear indication of the confined MFs in a QR, the MF probability distribution is presented in Fig. 11.22 for the parameters $b = 8$ nm, $B = 0.5$ T and $\mu = 3.95$ meV. In Fig. 11.22a, b the contour plots of the probability distribution for MF(1) and MF(2) respectively are presented as defined by (11.38). Clearly, each MF is located at one side of the major axis of QR. Both MFs are mostly confined in the center of the QR along the r direction, but MF(1) is confined near $\theta = \pi$ and MF(2) is confined near $\theta = 0$. Similar distribution is observed also for $b = 6$ nm. The angular dependence of the MF distribution for MF(1) at $r = 5.5$ (which corresponds to the center of the QR) is presented in Fig. 11.22c. The MF distribution has a Gaussian form and the probability to find MF(1) on the other side of the major axis of the QR is considerably smaller. The main reason why a QR with sizes of a few hundred angstrom can localize the MFs, is the infinite central barrier of the

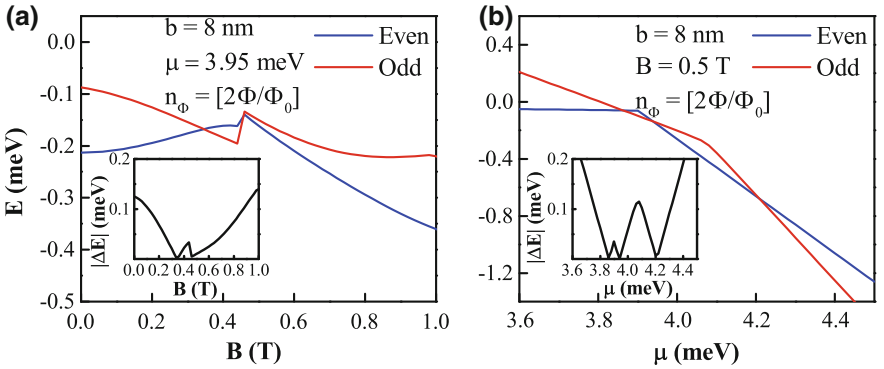

Fig. 11.21 Same as in Fig. 11.19 but for $b = 8$ nm and $n_{\Phi} = [2\Phi/\Phi_0]$ [61]

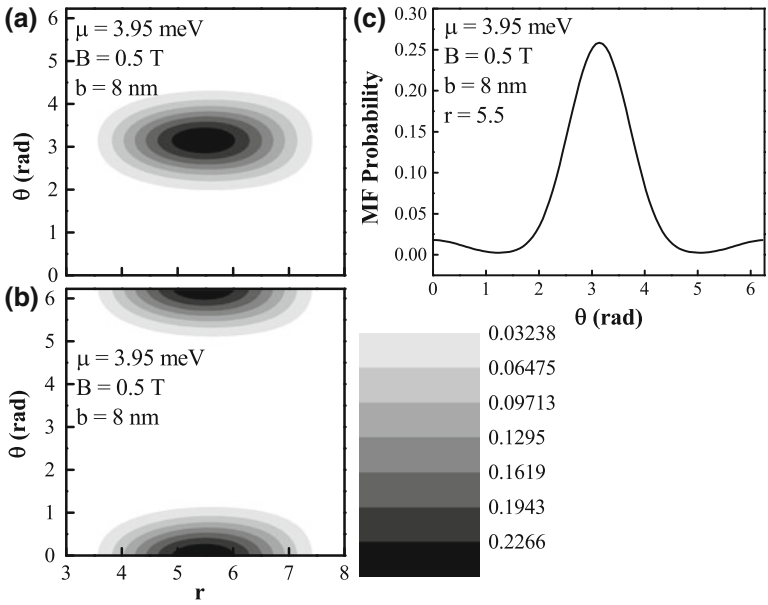

Fig. 11.22 The MF probability distribution inside the ring for $B = 0.5$ T, $\mu = 3.95$ meV and for ring parameter $b = 8$ nm. In **a** and **b** we show the contour plots of the MF probability distribution for the MF(1) and MF(2) as defined by (11.38). **c** The dependence of MF probability distribution on angle θ for MF(1) and $r = 5.5$. In all figures $n_{\Phi} = 0$ [61]

QR, which prevents a direct overlap of the MFs. The only way the MFs can overlap would be through two narrow strips that connect the two sides of the major axis of the elliptic QR. This property is only present in a QR and not in other low-dimensional systems, such as the quantum wires or quantum dots. The transfer amplitude between the two sides of the QR can be controlled by changing the value of the parameter b.

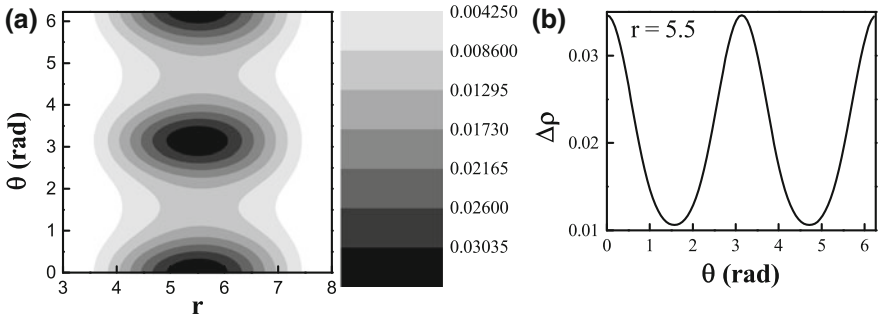

Fig. 11.23 **a** Contour plot of the difference between the single-particle densities of the many-body states in odd and even sector for $b = 8$ nm. The parameters are $B = 0.5$ T, $n_\Phi = 0$ and $\mu = 3.95$ meV **b** The dependence of the difference between the single-particle densities on the angle θ for $r = 5.5$ and for the same parameters as in (**a**) [61]

Further, confined MFs appear only at the major axis of the QR, which means that the direction at which the QR is elongated defines where the MFs will likely be confined. Therefore in a QR, both the position of the MFs and the extent by which they are confined can be controlled by external means. This is an important result for moving the Majoranas along the ring.

In Fig. 11.23a the contour plot of the difference between the electron densities of the many-body states in odd and even sectors is shown for a QR with parameters $b = 8$ nm, $B = 0.5$ T and $\mu = 3.95$ meV. The corresponding angular dependence for $r = 5.5$ is presented in Fig. 11.23b. We have also calculated the mean electron number difference between odd and even sectors for these parameter values and have found that $\Delta N = 0.32$. The mean electron number difference being less than one indicates once again that the MFs are confined at the two sides of the major axis of the QR. Figure 11.23 shows how this charge difference is distributed in the ring. In fact, Fig. 11.23 indicate that the charge is mostly confined in the central part of the ring in the r direction but is spread through the whole ring in the θ direction and has the oscillatory behavior with maxima at the two sides of the QR. This result is in good agreement with the similar result for a semiconductor wire [134], and can be used in the single-electron transistor measurement as an indication of the topological superconducting phase and confined MFs.

We have also performed similar investigations with the Coulomb interaction included. As was mentioned earlier [129], the screening is essential for the stability of the topological superconducting phase. Therefore, we have done the calculations using the screening parameter value $\lambda = 0.1\,\text{nm}^{-1}$. While a detailed investigation of the complete phase diagram is needed for understanding of the comprehensive effect of interaction on the obtained results, our calculations for some points of the diagram indicate that in most cases the interaction does not improve either the stability of the topological superconducting phase or confinement of the MFs in a QR. Therefore, superconducting materials with high level of screening for electrons in the semiconductor QR will perhaps be most suitable for detection of the Majorana fermions.

To summarize, we have studied the electronic states in a few-electron semiconductor QR with a strong SOI and proximity coupled to an *s*-wave superconductor. We have demonstrated that both the topological superconducting phase and confined MFs can be found in a QR system. In particular, we have demonstrated that for the ranges of the magnetic field and the chemical potential considered here, the difference between the ground state energies of even and odd electron number system is close to zero and has the oscillatory behavior. This effect is not specific to special ring parameters. From the MF probability distribution we have demonstrated that the MFs are located at the two sides of the major axis of the QR. Both the position and the extent of the MF confinement can be controlled externally by choosing the direction of elongation and the eccentricity of the elliptical barriers. Therefore, we believe that in many ways, few-electron QRs are perhaps more appropriate for locating the elusive MFs than in quantum wires or in quantum dots.

11.6 Conclusion

In recent years many novel systems with unusual electronic properties have been created, where the QR structure has displayed many intriguing physical phenomena that are the subject of this chapter. More significantly, we have considered the electronic states and optical transitions of a ZnO quantum ring and dot-ring systems containing few interacting electrons in an applied magnetic field. The strong Zeeman interaction and the strong electron-electron Coulomb interaction, two major characteristics of the ZnO system, exert a profound influence on the electron states and as a consequence, on the optical properties of the ring. In particular the AB effect in the ZnO QR is strongly electron number dependent. In the case of the ZnO QDR the energy spectra of the ZnO QDR and the Aharonov-Bohm oscillations are strongly dependant on the electron number in the dot or in the ring. Therefore even a small change of the confinement potential, sizes of the dot-ring or the magnetic field can drastically change the energy spectra and the behavior of the Aharonov-Bohm oscillations in such a system. Due to this interesting phenomena it is possible to effectively control with high accuracy the electron charge and spin distribution inside the dot-ring structure.

We have also studied the strong influence of intense terahertz laser field on the electronic and optical properties of isotropic and anisotropic QRs. We have shown that in isotropic QRs the laser field creates unusual AB oscillations that is usually expected in anisotropic rings. Therefore with the laser field we can observe a continuous evolution of AB oscillations within the same ring. In the case of anisotropic QRs we have shown that with the ILF it is possible to completely 'control' the anisotropy of the QR and thus also the physical characteristics. In particular we have shown here that the energy spectra and the AB oscillations have been made completely usual by the ILF for anisotropic QRs. Last but not the least, it is worth noting that the ILF can in principle restore isotropic properties of a QR from any type of anisotropy (structural, effective masses, defects, etc.) of the QRs.

Next we have reviewed the physical properties of graphene QR. We have discussed about the interplay of valley polarization and the Coulomb interaction on the energy spectrum, persistent current, and optical absorption of a graphene quantum ring. We show that the interaction has a dramatic effect on the nature of the ground state as a function of the magnetic flux and that the absence of exchange interaction between electrons in opposite valleys means that the singlet-triplet degeneracy is not lifted for certain few-electron states. The additional energy-level crossings (fractional flux periodicity) due to the interaction directly lead to extra steps in the persistent current and intricate structures in the absorption spectrum that should be experimentally observable. As the nanoscale graphene rings are already available for experimental studies, we expect future confirmation of the novel properties discussed here.

Another type of novel material where the QR can play an important role is a semiconductor heterostructure that is proximity coupled to a superconductor. Recently these types of hybrid semiconductor-superconductor structures have become attractive due to the possibility to find Majorana fermions inside them. We have studied the electronic states in a few-electron semiconductor quantum ring with a strong SOI and proximity coupled to an *s*-wave superconductor. We have shown that both the topological superconducting phase and confined Majorana fermions can possibly be found in this system. From the Majorana fermion probability distribution we have shown that the Majorana fermions are located at the two sides of the major axis of the anisotropic quantum ring. Both the position and the extent of the MF confinement can be controlled externally by choosing the direction of elongation and the eccentricity of the elliptical barriers.

Acknowledgements The work has been supported by the Canada Research Chairs Program of the Government of Canada and the Armenian State Committee of Science (Project no. 15T-1C331).

References

1. Y. Aharonov, D. Bohm, Phys. Rev. **115**, 485 (1959)
2. M. Büttiker, Y. Imry, R. Landauer, Phys. Lett. A **96**, 365 (1983)
3. A. Lorke et al., Phys. Rev. Lett. **84**, 2223 (2000)
4. U.F. Keyser, C. Fühner, S. Borck, R.J. Haug, M. Bichler, G. Abstreiter, W. Wegscheider, Phys. Rev. Lett. **90**, 196601 (2003)
5. A. Fuhrer, S. Lüscher, T. Ihn, T. Heinzel, K. Ensslin, W. Wegscheider, M. Bichler, Nature **413**, 822 (2001)
6. T. Chakraborty, Adv. Solid State Phys. **43**, 79 (2003)
7. S. Viefers, P. Koskinen, P. Singha Deo, M. Manninen, Physica E **21**, 1 (2004); P. Pietiläinen, T. Chakraborty, Solid State Commun. **87**, 809 (1993); T. Chakraborty, P. Pietiläinen. Phys. Rev. B **50**, 8460 (1994)
8. K. Niemelä, P. Pietiläinen, P. Hyvönen, T. Chakraborty, EPL **36**, 533 (1996)
9. H.-Y. Chen, P. Pietiläinen, T. Chakraborty, Phys. Rev. B **78**, 073407 (2008)
10. G. Huang, W. Guo, P. Bhattacharya, G. Ariyawansa, A.G.U. Perera, Appl. Phys. Lett. **94**, 101115 (2009)
11. J. Wu, Z.M. Wang, V.G. Dorogan, S. Li, Z. Zhou, H. Li, J. Lee, E.S. Kim, Y.I. Mazur, G.J. Salamo, Appl. Phys. Lett. **101**, 043904 (2012)

12. R.J. Young, E.P. Smakman, A.M. Sanchez, P. Hodgson, P.M. Koenraad, M. Hayne, Appl. Phys. Lett. **100**, 082104 (2012)
13. R.J. Warburton, C. Schäflein, D. Haft, F. Bickel, A. Lorke, K. Karrai, J.M. Garcia, W. Schoenfeld, P.M. Petroff, Nature **405**, 926 (2000)
14. M. Abbarchi, C. Mastrandrea, A. Vinattieri, S. Sanguinetti, T. Mano, T. Kuroda, N. Koguchi, K. Sakoda, M. Gurioli, Phys. Rev. B **79**, 085308 (2009)
15. T. Chakraborty, *Quantum Dots* (Elsevier, Amsterdam, 1999)
16. A. Tsukazaki, A. Ohtomo, T. Kita, Y. Ohno, H. Ohno, M. Kawasaki, Science **315**, 1388 (2007)
17. A. Tsukazaki, S. Akasaka, K. Nakahara, Y. Ohno, H. Ohno, D. Maryenko, A. Ohtomo, M. Kawasaki, Nat. Mater. **9**, 889 (2010)
18. J. Mannhart, D.H.A. Blank, H.Y. Hwang, A.J. Millis, J.-M. Triscone, MRS Bull. **33**, 1027 (2008)
19. J. Mannhart, D.G. Schlom, Science **327**, 1607 (2010)
20. H.Y. Hwang, Y. Iwasa, M. Kawasaki, B. Keimer, N. Nagaosa, Y. Tokura, Nat. Mater. **11**, 103 (2012)
21. Y. Kozuka, A. Tsukazaki, M. Kawasaki, Appl. Phys. Rev. **1**, 011303 (2014)
22. J. Falson, D. Maryenko, B. Friess, D. Zhang, Y. Kozuka, A. Tsukazaki, J.H. Smet, M. Kawasaki, Nat. Phys. **11**, 347 (2015)
23. W. Luo, T. Chakraborty, Phys. Rev. B **93**, 161103(R) (2016)
24. T. Chakraborty, P. Pietiläinen, Phys. Rev. B **39**, 7971 (1989); V. Halonen, P. Pietiläinen, T. Chakraborty. Phys. Rev. B **41**, 10202 (1990)
25. W. Luo, T. Chakraborty, Phys. Rev. B **96**, 081108(R) (2016)
26. Z.L. Wang, Mater. Today **7**, 26 (2004)
27. J.G. Lu, Z.Z. Ye, Y.Z. Zhang, Q.L. Liang, Sz Fujita, Z.L. Wang, Appl. Phys. Lett. **89**, 023122 (2006)
28. T. Chakraborty, A.Kh. Manaselyan, M.G. Barseghyan, J. Phys.: Condens. Matt. **29**, 215301 (2017)
29. S. Adachi, *Handbook on Physical Properties of Semiconductors*, vol. 3 (Kluwer Academic Publishers, New York, 2004)
30. T. Chakraborty, P. Pietiläinen, Phys. Rev. Lett. **95**, 136603 (2005); P. Pietiläinen, T. Chakraborty. Phys. Rev. B **73**, 155315 (2006)
31. A. Ghazaryan, A.Kh. Manaselyan, T. Chakraborty, Physica E **66**, 157 (2015)
32. T. Chakraborty, A.Kh. Manaselyan, M.G. Barseghyan, J. Phys.: Condens. Matt. **29**, 075605 (2017)
33. V. Halonen, P. Pietiläinen, T. Chakraborty, EPL **33**, 377 (1996)
34. L. Meier, A. Fuhrer, T. Ihn, K. Ensslin, W. Wegscheider, M. Bichler, Phys. Rev. B **69**, 241302(R) (2004)
35. S. Kiravittaya, A. Rastelli, O.G. Schmidt, Rep. Prog. Phys. **72**, 046502 (2009)
36. S. Somaschini, S. Bietti, N. Koguchi, S. Sanguinetti, Nanotechnology **22**, 185602 (2011)
37. R. Capozza, D. Giuliano, P. Lucignano, A. Tagliacozzo, Phys. Rev. Lett. **95**, 226803 (2005)
38. Y. Saiga, D. Hirashima, J. Usukura, Phys. Rev. B **75**, 045343 (2007)
39. L. Dias da Silva, J. Villas-Bôas, S. Ulloa, Phys. Rev. B **76**, 155306 (2007)
40. B. Szafran, F.M. Peeters, S. Bednarek, Phys. Rev. B **70**, 125310 (2004)
41. E. Zipper, M. Kurpas, M.M. Maśka, New J. Phys. **14**, 093029 (2012)
42. A. Biborski, A.P. Kądzielawa, A. Gorczyca-Goraj, E. Zipper, M.M. Maśka, J. Spałek, Sci. Rep. **6**, 29887 (2016)
43. M. Kurpas, B. Kędzierska, I. Janus-Zygmunt, M.M. Maśka, E. Zipper, Acta. Phys. Pol. A **126**, A-20 (2014)
44. M. Kurpas, B. Kędzierska, I. Janus-Zygmunt, A. Gorczyca-Goraj, E. Wach, E. Zipper, M.M. Maśka, J. Phys.: Condens. Matter **27**, 265801 (2015)
45. M.G. Barseghyan, Physica E **69**, 219 (2015)
46. M.G. Barseghyan, H.M. Baghramyan, D. Laroze, J. Bragard, A.A. Kirakosyan, Physica E **74**, 421 (2015)
47. M.G. Barseghyan, A.Kh Manaselyan, D. Laroze, A.A. Kirakosyan, Physica E **81**, 31 (2016)

48. V.M. Fomin (ed.), *Physics of Quantum Rings* (Springer, Berlin, 2014)
49. R. Blossey, A. Lorke, Phys. Rev. E **65**, 021603 (2002)
50. P. Offermans, P.M. Koenraad, J.H. Wolter, D. Granados, J.M. Garcia, V.M. Fomin, V.N. Gladilin, J.T. Devreese, Appl. Phys. Lett. **87**, 131902 (2005)
51. N.A.J.M. Kleemans, I.M.A. Bominaar-Silkens, V.M. Fomin, V.N. Gladilin, D. Granados, A.G. Taboada, J.M. García, P. Offermans, U. Zeitler, P.C.M. Christianen, J.C. Maan, J.T. Devreese, P.M. Koenraad, Phys. Rev. Lett. **99**, 146808 (2007)
52. J. Wu, Z.M. Wang, K. Holmes, E. Marega Jr., Z. Zhou, H. Li, Y.I. Mazur, G.J. Salamo, Appl. Phys. Lett. **100**, 203117 (2012)
53. T. Raz, D. Ritter, G. Bahir, Appl. Phys. Lett. **82**, 1706 (2003)
54. J. Sormunen, J. Riikonen, M. Mattila, J. Tiilikainen, M. Sopanen, H. Lipsanen, Nano. Lett. **5**, 1541 (2005)
55. L. Wendler, V.M. Fomin, Phys. Rev. B **50**, 4642 (1994)
56. L. Wendler, V.M. Fomin, Phys. Stat. Sol. (b) **191**, 409 (1995)
57. V.M. Fomin, V.N. Gladilin, S.N. Klimin, J.T. Devreese, N.A.J.M. Kleemans, P.M. Koenraad, Phys. Rev. B **76**, 235320 (2007)
58. J. Planeles, F. Rajadell, J.I. Climente, Nanotechnology **1**(8), 375402 (2007)
59. G.A. Farias, M.H. Degani, J.A.K. Freire, J. Costa e Silva, R. Ferreira, Phys. Rev. B **77**, 085316 (2008)
60. M.M. Milošević, M. Tadić, F.M. Peeters, Nanotechnology **19**, 455401 (2008)
61. A. Ghazaryan, A.Kh. Manaselyan, T. Chakraborty, Phys. Rev. B **93**, 245108 (2016)
62. G.O. de Sousa, D.R. da Costa, A. Chaves, G.A. Farais, F.M. Peeters, Phys. Rev. B **95**, 205414 (2017)
63. A. Bruno-Alfonso, A. Latgé, Phys. Rev. B **71**, 125312 (2005)
64. A.M. Alexeev, M.E. Portnoi, Phys. Rev. B **85**, 245419 (2012)
65. A.M. Alexeev, M.E. Portnoi, Phys. Status Solidi C **9**, 1309 (2012)
66. A.M. Alexeev, I.A. Shelykh, M.E. Portnoi, Phys. Rev. B **88**, 085429 (2013)
67. K.L. Koshelev, VYu. Kachorovskii, M. Titov, Phys. Rev. B **92**, 235426 (2015)
68. S.D. Ganichev, W. Prettl, *Intense Terahertz Excitation of Semiconductors* (Oxford University Press, Oxford, 2006)
69. A.G. Markelz, N.G. Asmar, B. Brar, E.G. Gwinn, Appl. Phys. Lett. **69**, 3975 (1996)
70. N. Mori, T. Takahashi, T. Kambayashi, H. Kubo, C. Hamaguchi, L. Eaves, C.T. Foxon, A. Patane, M. Henini, Phys. B **314**, 431 (2002)
71. N.G. Asmar, A.G. Markelz, E.G. Gwinn, J. Cerne, M.S. Sherwin, K.L. Chapman, P.E. Hopkins, A.C. Gossard, Phys. Rev. B **51**, 18041 (1995)
72. S. Hughes, D.S. Citrin, Phys. Rev. Lett. **84**, 4228 (2000)
73. H. Hsu, L.E. Reichl, Phys. Rev. B **74**, 115406 (2006)
74. Tonouchi, Nat. Photon. **1**, 97 (2007)
75. D.R. Grischkowsky, S.R. Keiding, M.P. van Exter, C. Fattinger, J. Opt. Soc. Am. B **7**, 2006 (1990)
76. T. Kampfrath, T. Tanaka, K.A. Nelson, Nat. Photon. **7**, 680 (2013)
77. A. Radu, A.A. Kirakosyan, D. Laroze, H.M. Baghramyan, M.G. Barseghyan, J. Appl. Phys. **116**, 093101 (2014)
78. A. Radu, A.A. Kirakosyan, D. Laroze, M.G. Barseghyan, Semicond. Sci. Technol. **30**, 045006 (2015)
79. W.C. Henneberger, Phys. Rev. Lett. **21**, 838 (1968)
80. M. Gavrila, J.Z. Kaminski, Phys. Rev. Lett. **52**, 613 (1984)
81. M. Pont, N.R. Walet, M. Gavrila, C.W. McCurdy, Phys. Rev. Lett. **61**, 939 (1988)
82. E.C. Valadares, Phys. Rev. B **41**, 1282(R) (1990)
83. M. Gavrila, J. Phys. B: At. Mol. Opt. Phys. **35**, R147 (2002)
84. M. Gavrila, *Atoms in Intense Laser Fields* (Academic, New York, 1992)
85. T. Chakraborty, A.Kh. Manaselyan, M.G. Barseghyan, D. Laroze, Phys. Rev. B **97**, 041304 (R) (2018)

86. H.P. Boehm, Angew. Chem. Int. Ed. **49**, 9332 (2010); H.P. Boehm, R. Setton, E. Stumpp, Carbon **24**, 241 (1986)
87. H. Aoki, M.S. Dresselhaus (eds.), *Physics of Graphene* (Springer, New York, 2014)
88. D.S.L. Abergel, V. Apalkov, J. Berashevich, K. Ziegler, T. Chakraborty, Adv. Phys. **59**, 261 (2010)
89. T. Chakraborty, V.M. Apalkov, Solid State Commun. **175–176**, 123 (2013)
90. E. McCann, Phys. Rev. B **74**, 161403 (2006)
91. X.F. Wang, T. Chakraborty, Phys. Rev. B **81**, 081402(R) (2010); D.S.L. Abergel, T. Chakraborty. Nanotechnology **22**, 015203 (2011)
92. J. Berashevich, T. Chakraborty, Nanotechnology **21**, 355201 (2010)
93. X. Ling, H. Wang, S. Huang, F. Xia, M.S. Dresselhaus, PNAS **112**, 4523 (2015)
94. A. Ghazaryan, T. Chakraborty, Phys. Rev. B **92**, 165409 (2015)
95. A. Kara, H. Enriquez, A.P. Seitsonen, C. Lew Yan Voon, S. Vizzini, B. Aufray, H. Oughaddou, Surf. Sci. Rep. **67**, 1 (2012)
96. V.M. Apalkov, T. Chakraborty, Phys. Rev. B **91**, 235447 (2015)
97. M.E. Davila, L. Xian, S. Cahangirov, A. Rubio, G. Le Lay, New J. Phys. **16**, 095002 (2014)
98. D.R. Dreyer, R.S. Ruoff, C.W. Bielawski, Angew. Chem. Int. Ed. **49**, 9336 (2010)
99. P.R. Wallace, Phys. Rev. **71**, 622 (1947)
100. T. Chakraborty, V. Apalkov, in [87] Ch. 8
101. T. Ando, Physica E **40**, 213 (2007)
102. X.F. Wang, T. Chakraborty, Phys. Rev. B **75**, 033408 (2007)
103. J.W. McClure, Phys. Rev. **104**, 666 (1956); R.R. Haering, P.R. Wallace. J. Phys. Chem. Solids **3**, 253 (1957)
104. K.S. Novoselov et al., Nature (London) **438**, 197 (2005)
105. Y. Zhang et al., Nature (London) **438**, 201 (2005)
106. A.K. Geim, K.S. Novoselov, Nat. mater. **6**, 183 (2007)
107. V.M. Apalkov, T. Chakraborty, Phys. Rev. Lett. **112**, 176401 (2014); A. Ghazaryan, T. Chakraborty, P. Pietiläinen. J. Phys.: Condens. Matter **27**, 185301 (2015)
108. C.R. Dean et al., Nature (London) **497**, 598 (2013); L. Wang et al., Science **350**, 1231 (2015)
109. V.M. Apalkov, T. Chakraborty, Phys. Rev. Lett. **107**, 186803 (2011); W. Luo, T. Chakraborty. Phys. Rev. B **96**, 081108(R) (2017)
110. T. Chakraborty, P. Pietiläinen, *The Quantum Hall Effects* (Springer, New York, 1995); *The Fractional Quantum Hall Effect* (Springer, New York, 1988)
111. V.M. Apalkov, T. Chakraborty, Phys. Rev. Lett. **97**, 126801 (2006); ibid.**105**, 036801 (2010)
112. H.Y. Chen, V. Apalkov, T. Chakraborty, Phys. Rev. Lett. **98**, 186803 (2007)
113. D.S.L. Abergel, V.M. Apalkov, T. Chakraborty, Phys. Rev. B **78**, 193405 (2008)
114. P. Recher, B. Trauzettel, A. Rycerz, YaM Blanter, C.W.J. Beenakker, A.F. Morpurgo, Phys. Rev. B **76**, 235404 (2007)
115. M.V. Berry, R.J. Mondragon, Proc. R. Soc. Lond. A **412**, 53 (1987); E. McCann, V.I. Fal'ko, J. Phys.: Consens. Matter **16**, 2371 (2004); J. Tworzydlo et al., Phys. Rev. Lett **96**, 246802 (2006); P.G. Silvestrov, K.B. Efetov, ibid. **98**, 016802 (2007)
116. T. Ando, J. Phys. Soc. Jpn. **75**, 074716 (2006)
117. J. Schelter, P. Recher, B. Trauzettel, Solid State Commun. **152**, 1411 (2012)
118. S. Russo, J.B. Oostinga, D. Wehenkel, H.B. Heersche, S.S. Sobhani, L.M.K. Vandersypen, A.F. Morpurgo, Phys. Rev. B **77**, 085413 (2008)
119. E. Majorana, Nuovo Cimento **14**, 171 (1937)
120. F. Wilczek, Nat. Phys. **5**, 614 (2009)
121. A. Stern, Nature **464**, 187 (2010)
122. M. Leijnse, K. Flensberg, Semicond. Sci. Tecnol. **27**, 124003 (2012)
123. A.Y. Kitaev, Phys. Usp. **44**, 131 (2001)
124. L. Fu, C.L. Kane, Phys. Rev. Lett. **100**, 096407 (2008)
125. Y. Oreg, G. Rafael, F. von Oppen, Phys. Rev. Lett. **105**, 177002 (2010)
126. J. Alicea, Rep. Prog. Phys. **75**, 076501 (2012)
127. C.W.J. Beenakker, Annu. Rev. Condens. Matter Phys. **4**, 113 (2013)

128. Y.A. Bychkov, E.I. Rashba, J. Phys. C **17**, 6039 (1984)
129. A. Ghazaryan, T. Chakraborty, Phys. Rev. B **92**, 115138 (2015)
130. D. Berman, O. Entin-Wohlman, M.Ya. Azbel, Phys. Rev. B **42**, 9299 (1990)
131. F. Pientka, A. Romito, M. Duckheim, Y. Oreg, F. Oppen, New J. Phys. **15**, 025001 (2013)
132. B. Scharf, I. Žutić, Phys. Rev. B **91**, 144505 (2015)
133. E.M. Stoudenmire, J. Alicea, O. Starykh, M.P.A. Fisher, Phys. Rev B **84**, 014503 (2011)
134. G. Ben-Shach, A. Haim, I. Appelbaum, Y. Oreg, A. Yacoby, B.I. Halperin, Phys. Rev. B **91**, 045403 (2015)

Chapter 12
Spin Interference Effects in Rashba Quantum Rings

Carmine Ortix

Abstract Quantum interference effects in rings provide suitable means to control spins at the mesoscopic scale. In this chapter we present the theory underlying spin-induced modulations of unpolarized currents in quantum rings subject to the Rashba spin-orbit interaction. We discuss explicitly the connection between the conductance modulations and the geometric phase acquired by the spin during transport, as well as pathways to directly control them.

12.1 Quantum Rings with Rashba Spin-Orbit Interaction: Effective One-Dimensional Hamiltonian

The effect of the Rashba spin-orbit interaction [1] on electrons moving in mesoscopic rings has been studied in several contexts, including magnetoconductance oscillations [2, 3] and persistence currents [4, 5]. Essentially all these theoretical studies have employed one-dimensional (1D) model Hamiltonians. Different Hamiltonians have been used by different authors in the past, and consequently some ambiguity with regard to the correct form of the 1D Hamiltonian exists in the literature. Aronov and Lyanda-Geller [2], for instance, studied the effect of the Rashba spin-orbit interaction on the Aharonov-Bohm conductance oscillations using a non-Hermitean operator. The procedure for obtaining the correct one-dimensional Hamiltonian in quantum rings in the presence of Rashba spin-orbit interaction has been first provided by Meijer et al. [6], who started out from the full two-dimensional (2D) Hamiltonian of a two-dimensional electron gas (2DEG) subject to a strong confining potential with circular symmetry forcing the electrons to be localized on the quantum ring in the radial direction. This procedure, which is the most rigorous, and physically sound one, corresponds precisely to the so-called "thin-wall" quantization procedure

C. Ortix (✉)
Institute for Theoretical Physics, Center for Extreme Matter and Emergent Phenomena, Utrecht University, Princetonplein 5, 3584 CC Utrecht, The Netherlands
e-mail: c.ortix@uu.nl

C. Ortix
Dipartimento di Fisica "E. R. Caianiello", Universitá di Salerno, 84084 Fisciano, Italy

V.M. Fomin (ed.), *Physics of Quantum Rings*, NanoScience and Technology,
https://doi.org/10.1007/978-3-319-95159-1_12

originally introduced by Jensen and Koppe [7], and da Costa (JKC) [8] to describe the quantum mechanics of non-relativistic particles constrained to generic "curved" n-dimensional manifolds but embedded in a $n+1$ Euclidean space.

In the absence of spin-orbit coupling, the JKC approach predicts the existence of a curvature-induced quantum geometric potential (QGP), which causes intriguing phenomena at the nanoscale [9–19]. In periodically minimal surfaces, for instance, the QGP leads to a topological band structure [10]. Similarly, in spirally rolled-up nanotubes the QGP has been shown to lead to winding-generated bound states [19]. These curvature effects have been predicted to become even more pervasive in strain-driven nanostructures where the nanoscale variation of strain induced by curvature leads to a strain-induced geometric potential that is of the same functional form as the QGP, but gigantically boosting it [20].

The JKC thin-wall approach has been recently shown to be well founded also in presence of externally applied electric and magnetic fields [21, 22] and subsequently employed to predict novel curvature-induced phenomena, such as the strongly anisotropic ballistic magnetoresistance of spirally rolled-up semiconducting nanotubes without magnetism and spin-orbit interaction [23]. Finally, the experimental realization of an optical analog of the curvature-induced QGP has provided empirical evidence for the validity of the JKC squeezing procedure [24]. As we will show below, the JKC procedure can be also applied without restrictions in the presence of spin-orbit coupling, thereby allowing to derive the correct Hermitean Hamiltonian of quantum rings with an arbitrary geometric shape.

To start with, we recall that in the usual effective-mass approximation, the movement of the charge carriers in presence of spin-orbit interaction can be described with an effective Schrödinger-Pauli equation acting on a two-dimensional spinor ψ:

$$\left(\frac{\mathbf{p}^2}{2m^\star} + \boldsymbol{\alpha}\cdot\boldsymbol{\sigma}\times\mathbf{p}\right)\psi = E\,\psi, \tag{12.1}$$

where $\mathbf{p} = -i\hbar\nabla$ is the canonical momentum operator and the $\boldsymbol{\sigma}$'s are the usual Pauli matrices generating the Clifford algebra of $\mathcal{R}^3$, which obey the anticommutation relations $\{\sigma_i, \sigma_j\} = 2\,\eta_{ij}$ with η_{ij} the standard spatial metric given by the identity matrix. In addition, we introduced the vector $\boldsymbol{\alpha}$ with magnitude corresponding to the spin-orbit interaction constant, and direction determined by the effective electric field from which the spin-orbit coupling originates. Finally $m^\star$ is the material dependent effective mass of the carriers. In the remainder, we will use Latin indices for spatial tensor components of the flat Euclidean three-dimensional space whereas Greek indices will be used for the corresponding tensor components in curved space. Adopting Einstein summation convention (12.1) can be generalized to a curved three-dimensional space as follows

$$\begin{aligned} E\psi = \Big[&-\frac{\hbar^2}{2m^\star}\left(G^{\mu\nu}\partial_\mu\partial_\nu - G^{\mu\nu}\,\Gamma^\lambda_{\mu\nu}\partial_\lambda\right) \\ &-i\,\hbar\,\mathcal{E}^{\mu\nu\lambda}\,\alpha_\mu\varsigma_\nu\partial_\lambda\Big]\psi, \end{aligned} \tag{12.2}$$

where $G^{\mu\nu}$ is the inverse of the metric tensor $G_{\mu\nu}$, $\mathcal{E}^{\mu\nu\lambda}$ is the contravariant Levi-Civita tensor – it can be written in terms of the usual Levi-Civita symbol as $\mathcal{E}^{\mu\nu\lambda} = \epsilon^{\mu\nu\lambda}/\sqrt{||G||}$ – and we introduced the affine connection

$$\Gamma^{\lambda}_{\mu\nu} = \frac{1}{2} G^{\lambda\xi} \left[\partial_{\nu} G_{\xi\mu} + \partial_{\mu} G_{\xi\nu} - \partial_{\xi} G_{\mu\nu} \right].$$

Finally, the ς's are the generators of the Clifford algebra in curved space $\left\{ \varsigma_{\mu}, \varsigma_{\nu} \right\} = 2\, G_{\mu\nu}$.

To proceed further, we need to define a coordinate system. We therefore start out by defining a planar curve $\mathcal{C}$ of parametric equations $\mathbf{r} = \mathbf{r}(s)$ with s indicating the corresponding arclength. The portion of the three-dimensional space in the immediate neighborhood of $\mathcal{C}$ can be then parametrized as $\mathbf{R}(s, q_2, q_3) = \mathbf{r}(s) + \hat{N}(s)\, q_2 + \hat{B}\, q_3$, where $\hat{N}$ is the unit vector normal to $\mathcal{C}$, but residing in the curve plane, while $\hat{B}$ is the binormal vector perpendicular to the quantum ring plane. The structure of the corresponding three-dimensional spatial metric tensor can be determined using that the two orthonormal vectors $\hat{T}(s) = \partial_s \mathbf{r}(s)$ and $\hat{N}(s)$ obey the Frenet-Serret type equations of motion as they propagate along s

$$\begin{pmatrix} \partial_s \hat{T}(s) \\ \partial_s \hat{N}(s) \end{pmatrix} = \begin{pmatrix} 0 & \kappa(s) \\ -\kappa(s) & 0 \end{pmatrix} \begin{pmatrix} \hat{T}(s) \\ \hat{N}(s) \end{pmatrix}, \tag{12.3}$$

where $\kappa(s)$ denotes the local curvature of the quantum ring. With this, the metric tensor corresponding to the three-dimensional portion of space explicitly assumes the diagonal form

$$G = \begin{pmatrix} \left[1 - \kappa(s) q_2\right]^2 & 0 & 0 \\ 0 & 1 & 0 \\ 0 & 0 & 1 \end{pmatrix},$$

whose determinant $||G|| = \left[1 - \kappa(s) q_2\right]^2$. The generators of the Clifford algebra for the metric tensor written above can be derived introducing the Cartan's dreibein formalism [25]. At each point, we define a set of one forms with components e^i_{μ} and a dual set of vector fields e^{μ}_i obeying the duality relations $e^i_{\mu} e^{\nu}_i = \delta^{\mu}_{\nu}$ and $e^i_{\mu} e^{\nu}_j = \delta^j_i$, and corresponding to the "square root" of the metric tensor $G_{\mu\nu} = e^i_{\mu} \delta_{ij} e^j_{\nu}$. The generators of the Clifford algebra can be then expressed as $\varsigma_{\mu} = e^i_{\mu} \sigma_i$. For the metric tensor written above, the dreibein field can be chosen as $e^i_s = \hat{T}^i(s)\, (1 - \kappa(s) q_2)$, $e^i_{q_2} = \hat{N}^i(s)$ and $e^i_{q_3} = \hat{B}^i(s)$. This immediately allows to identify the ς's as $\varsigma_s = \sigma_T\, (1 - \kappa(s) q_2)$, $\varsigma_{q_2} = \sigma_N$, and $\varsigma_{q_3} = \sigma_B$ written in terms of a local set of three Pauli matrices comoving with the Frenet-Serret frame $\sigma_{T,N,B} = \boldsymbol{\sigma} \cdot (\hat{T}, \hat{N}, \hat{B})$.

In the same spirit of JKC [7, 8], we now apply a thin-wall quantization procedure and take explicitly into account the effect of two strong confining potentials in the normal and binormal directions $V_{\lambda_N}(q_2)$, $V_{\lambda_B}(q_3)$ respectively, with $\lambda_{N,B}$ the two independent squeezing parameters. Furthermore, we introduce a rescaled spino-

rial wavefunction χ such that the line probability can be defined as $\int \chi^\dagger \chi \, dq_2 \, dq_3$. Conservation of the norm requires

$$\mathcal{N} = \int \sqrt{||G||} \, ds \, dq_2 \, dq_3 \, \psi^\dagger \psi = \int ds \, dq_2 \, dq_3 \, \chi^\dagger \chi ,$$

from which the rescaled spinor $\chi \equiv \psi \times ||G||^{1/4}$.

In the $\lambda_{N,B} \to \infty$ limit, the spinorial wavefunction will be localized in a narrow range close to $q_{2,3} = 0$. This allows us to expand all terms appearing in (12.2) in powers of $q_{2,3}$. At the zeroth order we then obtain the following Schrödinger-Pauli equation:

$$\begin{aligned} E \, \chi = \Bigg[& -\frac{\hbar^2}{2m^\star} \left(\eta^{\mu\nu} \partial_\mu \partial_\nu + \frac{\kappa(s)^2}{4} \right) - i\hbar \, \epsilon^{\mu\nu\lambda} \, \alpha_\mu \sigma_\nu \partial_\lambda \\ & - i\hbar \, \epsilon^{\mu\nu q_2} \, \alpha_\mu \sigma_\nu \frac{\kappa(s)}{2} + V_{\lambda_N}(q_2) + V_{\lambda_B}(q_3) \Bigg] \chi \end{aligned} \tag{12.4}$$

In the equation above, we have used that in the $q_{2,3} \to 0$ limit the only non-vanishing affine connection component $\Gamma^{q_2}_{ss} = \kappa(s)$, and employed the limiting relations for the derivatives of the original spinor in terms of the rescaled one

$$\begin{cases} \partial_{q_2} \psi = \partial_{q_2} \chi + \dfrac{\kappa(s)}{2} \chi \\ \\ \partial^2_{q_2} \psi = \partial^2_{q_2} \chi + \kappa(s) \partial_{q_2} \chi + \dfrac{3}{4} \kappa(s)^2 \chi . \end{cases}$$

The presence of the relativistic spin-orbit interaction in (12.4) prevents the separability of the quantum dynamics along the tangential direction of the planar curve from the normal quantum motion. However, the strong size quantization along the latter direction still allows us to employ an adiabatic approximation [20], encoded in the ansatz for the spinorial wavefunction $\chi(s, q_2, q_3) = \chi_T(s) \times \chi_N(q_2) \times \chi_B(q_3)$ where the normal and binormal wavefunctions solve the Schrödinger equation

$$-\frac{\hbar^2}{2m^\star} \partial^2_{q_2, q_3} \, \chi_{N,B} + V_{\lambda_{N,B}}(q_{2,3}) \, \chi_{N,B} = E_{N,B} \, \chi_{N,B} .$$

We can assume the two confining potential to take either the form of an harmonic trap $\propto q^2_{2,3}$ or an infinite potential well centered at $q_{2,3} \equiv 0$. Taken perturbatively, the first derivatives terms $\partial_{q_{2,3}}$ of (12.4) vanish and thus the effective one-dimensional Schrödinger-Pauli equation for the tangential wavefunction reads

$$E\,\chi_T = \left[-\frac{\hbar^2}{2m^\star}\left(\partial_s^2 + \frac{\kappa(s)^2}{4}\right) - i\hbar\alpha_N\sigma_B\partial_s \right. \\ \left. + i\hbar\alpha_B\left(\sigma_N\partial_s - \sigma_T\frac{\kappa(s)}{2}\right)\right]\chi_T, \tag{12.5}$$

where we explicitly considered a spin-orbit coupling originating either from an electric field orthogonal to the ring plane (α_N) or from an electric field pointing in the normal direction to the ring (α_B). Equation (12.5) represents the correct effective one-dimensional Schrödinger-Pauli equation for a single electron in presence of Rashba spin-orbit interaction, and generalizes the result obtained for a circular quantum ring [6, 26, 27]. The corresponding Schrödinger-Pauli operator is indeed Hermitian as can be shown by calculating its matrix elements in any complete basis, or simply noticing that it can be written, using anticommutators, in the compact form

$$E\chi_T = \left[\frac{\hat{p}_s^2}{2m^\star} - \frac{\hbar^2\kappa(s)^2}{8m^\star} + \frac{\alpha_N}{2}\left\{\hat{p}_s, \sigma_B\right\} \right. \\ \left. - \frac{\alpha_B}{2}\left\{\hat{p}_s, \sigma_N\right\}\right]\chi_T,$$

where the tangential momentum operator $\hat{p}_s = -i\hbar\partial_s$.

12.2 Conductance Modulations in Rashba Circular Quantum Rings

In this section, we discuss the quantum transport properties of a mesoscopic ballistic device in which a circular quantum ring with Rashba spin-orbit couplings is symmetrically coupled to two contact leads (c.f. Fig. 12.1a). The transport properties can be analyzed straightforwardly in the linear response regime, in which the system is subject to a constant, low-bias voltage. According to the Landauer formula, the zero-temperature conductance reads [26]

$$G = \frac{e^2}{h}\sum_{m,m'=1}^{N}\sum_{\sigma\sigma'} T_{m',m}^{\sigma',\sigma} \tag{12.6}$$

where $T_{m',m}^{\sigma',\sigma}$ denotes the quantum probability of transmission between incoming (m,σ) and outgoing (m',σ') states on the semi-infinite ballistic leads, with m, m' and σ, σ' the mode and spin quantum numbers, respectively. The total number of modes $M = 1$ in an effective one-dimensional description. Assuming perfect couplings between the leads and the ring, and thus neglecting backscattering effects, the quantum transmission probability are entirely determined by the eigenstates of the Hamiltonian (12.5) for the Rashba spin-orbit coupled quantum ring.

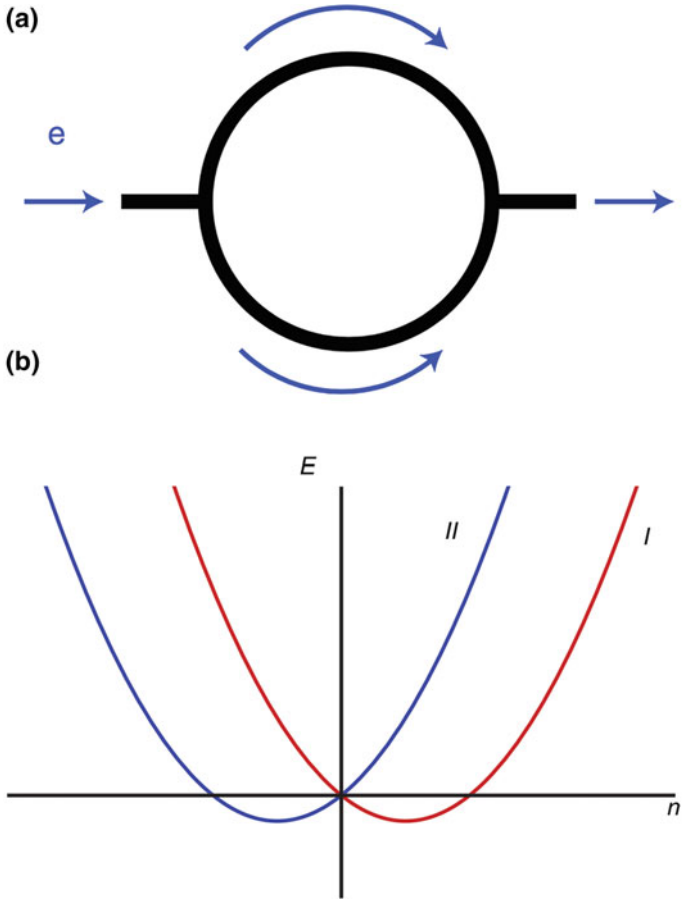

Fig. 12.1 **a** Sketch of the spin interferometer devices based on a mesoscopic ring with Rashba spin-orbit interaction (Adapted from [28]). **b** Energy levels in a quantum ring with Rashba spin-orbit interaction plotted as a function of the mode quantum number n. The two time-reversal channels I, II are indicated

We first analyze a circular quantum ring with a Rashba spin-orbit interaction due to a radial electric field [29, 30]. Adopting polar coordinates, the effective one-dimensional Hamiltonian (12.5) then takes the following form:

$$\mathcal{H} = -\frac{\hbar^2}{2m^\star R^2}\partial_\phi^2 + i\frac{\alpha\hbar}{R}\sigma_z\partial_\phi. \tag{12.7}$$

The corresponding one-dimensional spinorial eigenstates can be simply found as

$$\Psi_n^{\uparrow}(\phi) = \mathrm{e}^{in\phi}\begin{pmatrix}1\\0\end{pmatrix},$$

$$\Psi_n^{\downarrow}(\phi) = \mathrm{e}^{in\phi}\begin{pmatrix}0\\1\end{pmatrix},$$

with the associated eigenenergies reading

$$E_{\uparrow,\downarrow}(n) = \frac{\hbar^2}{2m^\star R^2}n^2 \mp \frac{\hbar\alpha}{R}n.$$

The energy splitting due to the Rashba spin-orbit interaction implies that incoming spins $|\sigma\rangle$ entering the ring at $\phi = 0$ with a Fermi energy E_F can propagate coherently along four different channels obtained by solving $E_{\uparrow,\downarrow}(n) \equiv E_F$. Specifically, two opposite spin states $|n_1;\uparrow\rangle$, $|n_2;\downarrow\rangle$ propagate along the upper branch of the ring, whereas their time-reversal partners $|-n_1;\downarrow\rangle, |-n_2;\uparrow\rangle$ propagate along the lower branch of the ring. The interference between the channels at $\phi = \pi$ then implies that injected spins leave the ring in a mixed spin state:

$$|\sigma_{out}\rangle = \sum_{s=\uparrow,\downarrow}\sum_{i=1,2}\langle n_i; s|\sigma\rangle \times \mathrm{e}^{in_i\pi}|n_i; s\rangle.$$

Choosing a complete basis of incoming and outgoing spin states, the spin-resolved transmission probabilities are obtained as $T^{\sigma'\sigma} = |\langle\sigma'|\sigma_{out}\rangle|^2$. By further summing over the spin indices σ' and σ, we thereby obtain the total conductance

$$G = \frac{e^2}{h}\left[1 + \cos\left(n_1 - n_2\right)\pi\right] \tag{12.8}$$

The relation between the two wave numbers n_1, n_2 can be simply found to be $n_1 - n_2 \equiv Q_R \equiv 2m^\star R\,\alpha/\hbar$. With this, it follows that the conductance exhibits uniform oscillations as a function of the spin-orbit interaction strength, which is the signature of the Aharonov-Casher effect [31] for spins traveling in an external electric field.

The radial electric field considered above, however, does not correspond to the normal situation in which the electric field is orthogonal to the plane in which the quantum ring resides. When considering this, the one-dimensional Hamiltonian (12.5) for a quantum ring with circular symmetry explicitly reads:

$$\mathcal{H} = -\frac{\hbar^2}{2m^\star R^2}\partial_\phi^2 + i\frac{\alpha\hbar}{R}\left[\sigma_N\partial_\phi + \frac{\sigma_T}{2}\right], \tag{12.9}$$

where we introduced the two local Pauli matrices

$$\begin{cases}\sigma_N = \;\cos\phi\,\sigma_x + \sin\phi\,\sigma_y\\ \sigma_T = -\sin\phi\,\sigma_x + \cos\phi\,\sigma_y\end{cases}. \tag{12.10}$$

The spinorial eigenstates of the Hamiltonian above can be found using a trial spinorial wavefunction of the form $\Psi = \mathrm{e}^{in\phi} \times \left[\chi_1\mathrm{e}^{-i\phi/2}, \chi_2\mathrm{e}^{i\phi/2}\right]^T$, where the amplitudes $\chi_{1,2}$ are determined by the effective Hamiltonian

$$\widetilde{\mathcal{H}} = \begin{pmatrix} \frac{\hbar^2}{2m^\star R^2}(n-\frac{1}{2})^2 & -\frac{\hbar\alpha}{R}n \\ -\frac{\hbar\alpha}{R}n & \frac{\hbar^2}{2m^\star R^2}(n+\frac{1}{2})^2 \end{pmatrix}. \tag{12.11}$$

Apart from a trivial rigid energy shift, the eigenenergies are simply obtained as

$$E_{I,II}(n) = \frac{\hbar^2}{2m^\star R^2}\left[n^2 \mp n\sqrt{1+Q_R^2}\right],$$

where the index I, II refers to the two time-reversed channels guaranteed by Kramers' theorem. The corresponding spinorial eigenstates can be found to be

$$\Psi_n^I(\phi) = \mathrm{e}^{in\phi}\begin{pmatrix} \cos\frac{\gamma}{2}\,\mathrm{e}^{-i\phi/2} \\ \sin\frac{\gamma}{2}\,\mathrm{e}^{i\phi/2} \end{pmatrix},$$

$$\Psi_n^{II}(\phi) = \mathrm{e}^{in\phi}\begin{pmatrix} \sin\frac{\gamma}{2}\,\mathrm{e}^{-i\phi/2} \\ -\cos\frac{\gamma}{2}\,\mathrm{e}^{i\phi/2} \end{pmatrix}.$$

Here the tilt angle γ is related to the dimensionless Rashba strength Q_R introduced above by $\tan\gamma = Q_R$. In the limit of strong Rashba spin-orbit interaction, i.e. $Q_R \to \infty$, the tilt angle $\gamma \to \pi/2$ in which case the eigenstates of the Hamiltonian correspond to the spin eigenstates of σ_N. This limit therefore corresponds to the "adiabatic" limit in which the spin carriers of the quantum ring orient along the effective momentum dependent Rashba magnetic field in the in-plane normal direction (c.f. Fig. 12.2a). For finite values of the dimensionless Rashba strength Q_R instead, the spin carriers acquire a finite out-of-plane component, which is a unique signature of the non-adiabatic spin transport along the ring (c.f. Fig. 12.2b). Such a non-adiabaticity in the spin motion is immediately reflected in the ballistic transport. Considering as before, incoming spins that propagate coherently along the four available channels of the quantum ring, i.e. $|n_1, I\rangle; |n_2, II\rangle; |-n_1, II\rangle; |-n_2, I\rangle$, we have that the mixed spin state leaving the ring at $\phi = \pi$ can be written as

$$|\sigma_{out}\rangle = \sum_{s=I,II}\sum_{i=1,2}\langle\Psi_{n_i}^s(\phi=0)|\sigma\rangle \times |\Psi_{n_i}^s(\phi=\pm\pi)\rangle.$$

where π $(-\pi)$ refers to the modes propagating along the upper branch and the lower branch of the quantum ring respectively. By summing the spin-resolved quantum transmission probabilities, we obtain that the total conductance takes the following form

$$G = \frac{e^2}{h}\left[1-\cos(n_1-n_2)\pi\right] \tag{12.12}$$

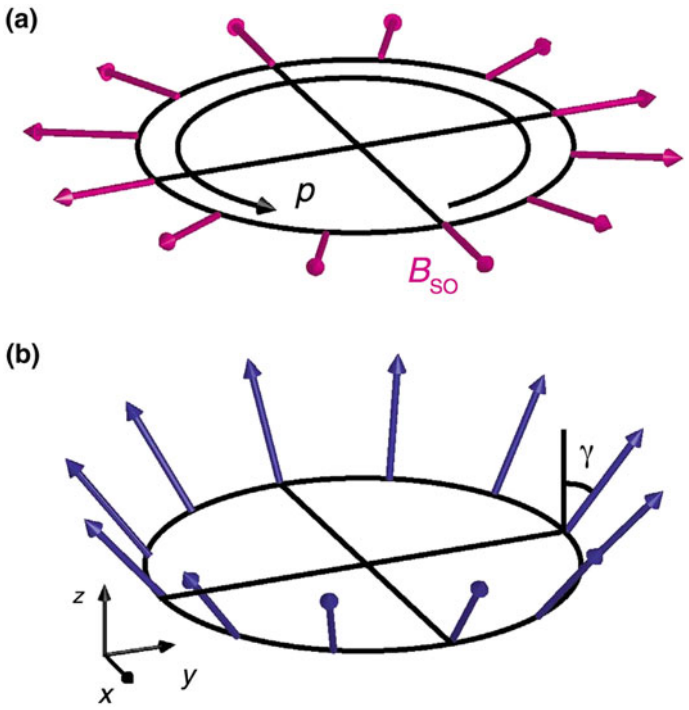

Fig. 12.2 **a** Quantum ring with Rashba spin-orbit coupling. The spin-orbit coupling induces an effective in-plane magnetic field B_{SO}, which is perpendicular to the electron momentum p. **b** In non-adiabatic transport, the electron spin do not align to B_{SO} but acquire an additional out-of-plane component (Adapted from [28])

From the eigenenergies written above, we have that $n_1 - n_2 = \sqrt{1 + Q_R^2}$ and thus the total conductance can be written as

$$G = \frac{e^2}{h}\left[1 + \cos\left(\pi\sqrt{1 + Q_R^2} - \pi\right)\right] \tag{12.13}$$

There are two features that differentiate the conductance oscillations in (12.13) as compared to the oscillations predicted for a quantum ring with a spin-orbit coupling originating from a radial electric field. First, contrary to the uniform oscillations found in (12.8), (12.13) implies the occurrence of quasiperiodic oscillations for small Rashba strength $Q_R < 1$. Second, in the large Rashba regime $Q_R \gg 1$, one observes a relative π phase shift between the two conductance modulations (c.f. Fig. 12.3).

As a spoiler for the next section, we here anticipate that this π phase shift is the principal consequence of the π Berry phase [32] acquired by the spins while precessing around the effective momentum dependent radial Rashba magnetic field

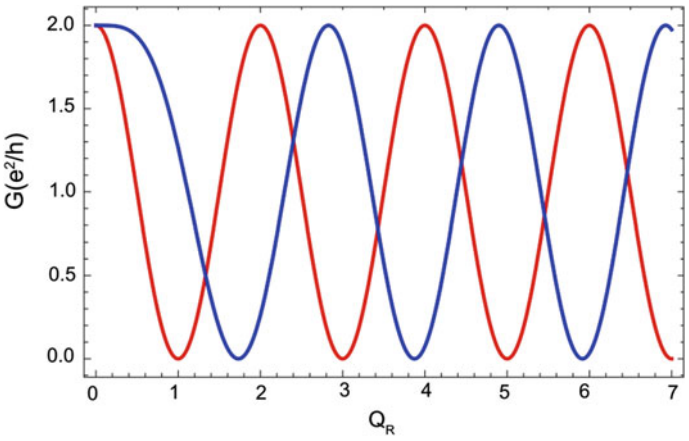

Fig. 12.3 Conductance modulation profiles of one-dimensional quantum rings as a function of the dimensionless Rashba strength Q_R. The blue line corresponds to a Rashba spin-orbit originating from an electric field orthogonal to the ring plane, whereas the red line is for a Rahsba spin-orbit due to a radial electric field. The latter also corresponds to the incomplete result of [33]. The conductance modulation profiles agree with a related model for one-dimensional rings based on a transfer matrix approach [34]

due to the out-of-plane electric field. Furthermore, the specific influence of quantum geometric phases in the conductance can be also seen by rewriting (12.13) as follows

$$G = \frac{e^2}{h}\left\{1 + \cos\left[\pi Q_R \sin\gamma - \pi\left(1 - \cos\gamma\right)\right]\right\}.$$

The phase in the equation above has then two important contributions: One is the dynamical phase $\pi Q_R \sin\gamma$ who also manifests itself for a radial electric field. The other is the Aharonov-Anandan [35] phase $\pi\left(1 - \cos\gamma\right)$ for non-adiabatic cyclic motion. It corresponds to the solid angle accumulated by the change of spinor orientation during transport, and reduces to the π spin Berry phase in the purely adiabatic limit $\gamma \to \pi/2$. This formulation of the conductance in terms of geometric and dynamical phases will be analyzed in detail in the next section (Sect. 12.3).

12.3 Conductance Modulations as a Probe of the Aharonov-Anandan Geometric Phase

In this section, we derive the relation between the conductance modulation and the Aharonov-Anandan geometric phase [35] for a quantum ring with generic shape. This will also allow us to show that real-space geometric deformations directly influence the geometric quantum phase and hence the spin transport properties.

We start out from the one-dimensional Hamiltonian in the presence of Rashba spin-orbit interaction (due to a perpendicular electric field) derived in Sect. 12.1:

$$\mathcal{H} = -\frac{\hbar^2}{2m^\star}\partial_s^2 + \frac{i\hbar\alpha}{2}\left[\sigma_N(s)\partial_s + \partial_s\sigma_N(s)\right], \tag{12.14}$$

where, for simplicity, we have disregarded the quantum geometric potential since it can be assumed to be a small perturbation as compared to the Rashba spin-orbit interaction. Let us discuss the spin textures that are generally realised in a quantum ring with Rashba spin-orbit interaction. To show this, we rewrite the Hamiltonian written above as

$$\mathcal{H} = H_l^2 - \frac{\alpha^2 m^\star}{2}\sigma_0$$

with σ_0 being the identity matrix and H_l reading:

$$H_l = \left(i\frac{\hbar}{\sqrt{2m^\star}}\partial_s + \frac{\alpha\sqrt{m^\star}}{\sqrt{2}}\sigma_N(s)\right).$$

Clearly, H_l and $\mathcal{H}$ have common eigenstates with an eigenvalue relation given by $E = E_l^2 - \alpha^2 m^\star/2$. Let us now introduce the spin orientation of a given spin eigenmode $|\Psi_E\rangle$ as the corresponding expectation value of the spin operators in the local Frenet-Serret reference frame (see Sect. 12.1), i.e. $\langle\boldsymbol{\sigma}\rangle = \{\langle\sigma_T\rangle, \langle\sigma_N\rangle, \langle\sigma_z\rangle\}$. It is possible to determine the equation for the spatial derivative of the local spin components using that the Schrödinger equation $H_l|\Psi_E\rangle = E_l|\Psi_E\rangle$ can be rewritten as

$$\begin{aligned} i\partial_s|\Psi_E\rangle &= \hat{G}(s)|\Psi_E\rangle \\ \langle\Psi_E|i\partial_s &= -\langle\Psi_E|\hat{G}(s) \end{aligned} \tag{12.15}$$

where we introduced the operator $\hat{G}(s)$

$$\hat{G}(s) = -\frac{\sigma_N(s)}{2\,l_\alpha} - \sigma_0\sqrt{\frac{2m^\star E}{\hbar^2} + \frac{{m^\star}^2\alpha^2}{\hbar^2}},$$

and l_α is the characteristic spin-orbit interaction length defined by $1/l_\alpha = 2m^\star\alpha/\hbar$. Equation (12.15) yield the general expression for the spatial derivative of the expectation value of the spin components

$$\partial_s\langle\boldsymbol{\sigma}\rangle = i\langle[G, \boldsymbol{\sigma}]\rangle + \langle\partial_s\boldsymbol{\sigma}\rangle \tag{12.16}$$

with $[A, B]$ indicating the commutator of A and B. Using the commutation relations for the local Pauli matrices we have

$$\begin{cases} \left[\hat{G}(s), \sigma_T(s)\right] = i\dfrac{\sigma z}{l_\alpha} \\ \left[\hat{G}(s), \sigma_N(s)\right] = 0 \\ \left[\hat{G}(s), \sigma_z\right] = -i\dfrac{\sigma_T}{l_\alpha} \end{cases} \tag{12.17}$$

To proceed further, we use that the spatial derivative of the local Pauli matrices obey the Frenet-Serret equations, $\partial_s \sigma_N(s) = -\kappa(s)\sigma_T(s)$ and $\partial_s \sigma_T(s) = \kappa(s)\sigma_N(s)$, with $\kappa(s)$ the local curvature. When combining these relations with (12.17), we therefore find the following equations for the spatial derivative of the spin expectation values:

$$\begin{cases} \partial_s \langle \sigma_N \rangle = -\kappa(s)\langle \sigma_T \rangle \\ \partial_s \langle \sigma_T \rangle = -\dfrac{\langle \sigma_z \rangle}{l_\alpha} + \kappa(s)\langle \sigma_N \rangle \\ \partial_s \langle \sigma_z \rangle = \dfrac{\langle \sigma_T \rangle}{l_\alpha} \end{cases} \tag{12.18}$$

The equations above represent a fundamental relation that links the geometric curvature of the quantum ring, the Rashba SO coupling, and the electron spin orientation in the local Frenet-Serret frame. It can be also written in the compact form

$$\partial_s \langle \boldsymbol{\sigma} \rangle = -\boldsymbol{h}_{\text{eff}} \times \langle \boldsymbol{\sigma} \rangle, \tag{12.19}$$

where we introduced the local field $\boldsymbol{h}_{\text{eff}} = \{0, l_\alpha^{-1}, \kappa(s)\}$ which lies in the normal-binormal plane, and depends on the local curvature and effective spin-orbit length introduced above. With this, it also follows that the spin direction lives in a Frenet-Serret-Bloch sphere [36] (see Fig. 12.4). Equation (12.19) generally implies that due to a non zero curvature, the electron spin acquires a finite out-of-plane binormal $\hat{z}$ component. In particular, for a circular quantum ring where the curvature is constant $\kappa(s) = -1/R$ we find, in agreement with the results presented in Sect. 12.2, a local spin orientation given by $\tan\theta = 2m^\star \alpha R/\hbar = Q_R$ (c.f. Fig. 12.4). More importantly, a non trivial component along the tangential direction appears provided the curvature is not constant. Although the derivative ∂_s of the spin vector locally vanishes if the spin is aligned to the effective spin-orbit field, variations of the local curvature yields a non-vanishing torque which results into a component of the spin vector parallel to the electron propagation direction. Such a torque effect due to the geometric shape of the quantum ring is manifested by considering the example of a quantum ring of total length L with an elliptical shape and a ratio a/b between the minor (a) and the major (b) axes of the ellipse. This is a paradigmatic case of a quantum ring with positive but non-uniform curvature that can be suitably enhanced (suppressed) at the positions nearby the poles of the major (minor) axes. There are two distinct spin texture regimes in this Rashba quantum ring. For very strong spin-orbit interactions or quasi-constant curvature, i.e. $a/b \simeq 1$, the electron spin is pinned nearby the quasi-

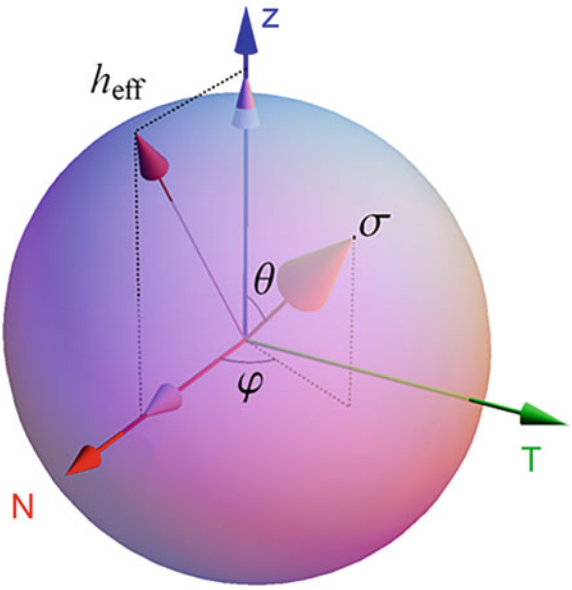

Fig. 12.4 The Frenet-Serret-Bloch sphere in the moving frame of the charge carriers in a generic quantum ring with the vectors associated to the electron spin orientation and the effective local field $\boldsymbol{h}_{eff}$ (Adapted from [36])

static effective field $\boldsymbol{h}_{\text{eff}}$ in the Frenet-Serret-Bloch sphere. In the regime of weaker spin-orbit interaction or sizable non-uniform curvature profile, instead, the electron spin is not able to follow the periodic motion of the effective spin-orbit field. As a result, a finite spin component along the tangential direction appears, and in the local frame the electron spin starts to wind both around the normal and the binormal directions. These features of the spin textures are shown in Fig. 12.5 where we report the spin textures of an elliptical quantum ring obtained by solving a tight-binding model Hamiltonian derived by discretizing (12.14) on an atomic chain [36]. For very weak spin-orbit coupling strength (c.f. Fig. 12.5a), the spin textures are almost aligned along the binormal direction $\hat{z}$. In an intermediate regime of Rashba spin-orbit strength instead, the torque exerted on the spin yields complex three-dimensional spin textures (c.f. Fig. 12.5b–f). In the very large spin-orbit interaction regime instead, the spin completely aligns along the normal direction signaling an almost adiabatic spin motion.

These variety of complex three-dimensional spin textures are not only interesting *per se*: they indeed strongly impact the spin transport properties. To show this, we will now find a link between the spin textures and the quantum phases for a cyclic evolution in a generic quantum ring. We therefore start by noticing that the real space evolution of the spin eigenmode is regulated by (12.15). Closely following Aharonov and Anandan [35], we use that for any one-dimensional quantum ring the spinorial wavefunction $|\Psi(s)\rangle$ must satisfy the condition

$$|\Psi(L)\rangle \equiv \mathrm{e}^{i\chi}|\Psi(0)\rangle.$$

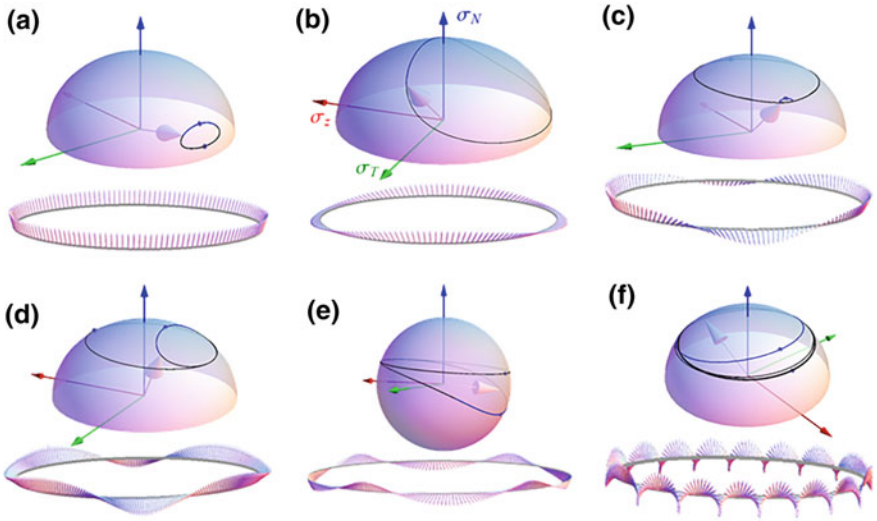

Fig. 12.5 Evolution of the electronic trajectories on the Bloch-Frenet-Serret sphere and spin textures in the lab frame for a quantum ring with elliptical shape with ratio between the minor and major axes $a/b = 0.4$ and different values of the spin-orbit coupling strength α. Panels (**a**–**f**) correspond to $m^\star \alpha L/\hbar = 1, 4, 8, 10, 12, 50$ (From [36])

We then define a new wavefunction $|\tilde{\Psi}(s)\rangle = e^{-i\beta(s)}|\Psi(s)\rangle$ in such a way that $\beta(L) - \beta(0) = \chi$. It immediately follows that $|\tilde{\Psi}(L)\rangle = |\tilde{\Psi}(0)\rangle$ and from (12.15) that

$$-\partial_s \beta(s) = \langle \Psi | \hat{G}(s) | \Psi \rangle - \langle \tilde{\Psi} | i\partial_s | \tilde{\Psi} \rangle \, .$$

Therefore, we can express the total phase χ accumulated by the charge carriers once they complete the spatial loop as the sum of a geometric Aharonov-Anandan (AA) phase and a dynamical phase as follows

$$g_{AA} = \int_0^L \langle \tilde{\Psi} | i\partial_s | \tilde{\Psi} \rangle ds \tag{12.20}$$

$$d = -\int_0^L \langle \Psi | \hat{G}(s) | \Psi \rangle ds \, . \tag{12.21}$$

The dynamical phase can be immediately linked to the expectation value of the local spin as

$$d = \frac{m^\star \alpha}{\hbar} \int_0^L \langle \sigma_N(s) \rangle ds + const. \tag{12.22}$$

In order to find the relation between the local spin expectation value and the geometric (AA) phase we first relate the local normal direction, as well as the tangential one, to the Euclidean coordinates via:

$$\begin{cases} \hat{N}(s) = \cos\phi(s)\hat{x} + \sin\phi(s)\hat{y} \\ \hat{T}(s) = -\sin\phi(s)\hat{x} + \cos\phi(s)\hat{y}, \end{cases}$$

where $\phi(s)$ is a real-valued function, which is related to the local curvature via the Frenet-Serret equations yielding

$$\phi(s) = -\int_0^s \kappa(s')ds'.$$

Next, we express the normalized spinorial eigenfunction in the following general form

$$|\Psi\rangle = \begin{pmatrix} \exp[-i\phi(s)/2]\ \exp[i\theta_{\Uparrow}(s)]A_{\Uparrow}(s) \\ \\ \exp[i\phi(s)/2]\ \exp[i\theta_{\Downarrow}(s)]A_{\Downarrow}(s) \end{pmatrix},$$

where $A_{\Uparrow,\Downarrow}(s)$ are real-valued functions. Such a general expression is convenient since we can express the expectation values of the local spin components in the following form

$$\begin{cases} \langle\sigma_T\rangle = 2A_{\Uparrow}(s)\,A_{\Downarrow}(s)\sin\left[\theta_{\Downarrow}(s) - \theta_{\Uparrow}(s)\right] \\ \langle\sigma_N\rangle = 2A_{\Uparrow}(s)\,A_{\Downarrow}(s)\cos\left[\theta_{\Downarrow}(s) - \theta_{\Uparrow}(s)\right] \\ \langle\sigma_z\rangle = A_{\Uparrow}(s)^2 - A_{\Downarrow}(s)^2 \end{cases} \tag{12.23}$$

Furthermore, we have that $\int_0^L \kappa(s')ds' = 2\pi N_\kappa$ with N_κ integer for a closed curve. The same holds true for the phase difference $\theta_{\Downarrow}(s) - \theta_{\Uparrow}(s)$, which acquires a phase shift $2\pi W$ with W the winding number of the normal and tangential local spin expectation values around the out-of-plane binormal direction, i.e. $W = \frac{1}{2\pi}\int_0^L q_{NT}(s)$ where we introduced

$$q_{NT}(s) = \frac{\langle\sigma_N\rangle\partial_s\langle\sigma_T\rangle - \langle\sigma_T\rangle\partial_s\langle\sigma_N\rangle}{\langle\sigma_T\rangle^2 + \langle\sigma_N\rangle^2}.$$

With this, it follows that

$$|\tilde{\Psi}\rangle = \begin{pmatrix} A_{\Uparrow}(s) \\ \exp[i\phi(s)]\ \exp[i(\theta_{\Downarrow}(s) - \theta_{\Uparrow}(s))]A_{\Downarrow}(s) \end{pmatrix},$$

and the AA phase can be simply expressed as

$$g_{AA} = \pi\left(N_\kappa + W - \frac{1}{2\pi}\int\langle\sigma_z\rangle[\kappa(s) + q_{NT}(s)]ds\right). \tag{12.24}$$

The knowledge of both the geometric AA phase (12.24) and the dynamical phase (12.22) also allows to express in a straightforward manner the conductance of a

generic ballistic one-dimensional ring. By using that the transmission along the arms of ring can be described using a spin rotation operator [36, 37], one finds the relation between the conductance and the quantum phases to be given by

$$G = \frac{e^2}{h}\left\{1 + \cos\left(g_{AA} + d\right)\right\}, \tag{12.25}$$

where the dynamical phase has to be computed disregarding the constant factor in (12.22).

For a circular quantum ring, the dynamical as well as the AA phases can be easily computed by noticing that $\langle \sigma_N \rangle = \sin\gamma$, and $\langle \sigma_z \rangle = \cos\gamma$. By also considering that $N_\kappa = -1$, we therefore find the result for the conductance modulation anticipated in Sect. 12.2, that is

$$G = \frac{e^2}{h}\left[1 + \cos\left[\pi Q_R \sin\gamma - \pi\left(1 - \cos\gamma\right)\right]\right].$$

Most importantly (12.22) and (12.24) directly yield a connection between the complex three-dimensional spin textures due to shape deformations and the spin transport properties. This is manifested in Fig. 12.6 where we show the influence of the geometric shape deformation on the spin interference patterns for the case of elliptical quantum rings [36]. One can observe distinct geometrically driven channels of electronic transport with a changeover from constructive to destructive interference as the ratio between the ellipse axis a/b increases. This results therefore yield a tight connection between the conductance and the character of the spin textures in a Rashba quantum ring.

12.4 Topological Transitions in Spin Interferometers

In the former section we have shown the connection between the spin textures realized in generic quantum rings and the spin geometric phase, with the latter that can be directly probed by changes in the conductance interference patterns. The spin textures of quantum rings can be also directly controlled using an externally applied magnetic field in the ring plane. The Zeeman coupling

$$\mathcal{H}_Z = g^\star \mu_B \sigma_y$$

indeed changes the solid angle accumulated by the spin eigenmode during transport in a quantum ring and consequently the non-adiabatic AA phase. This can be verified in the small B limit, in which case, by employing standard perturbation theory [28], the conductance modulations of a circular quantum ring can be written as

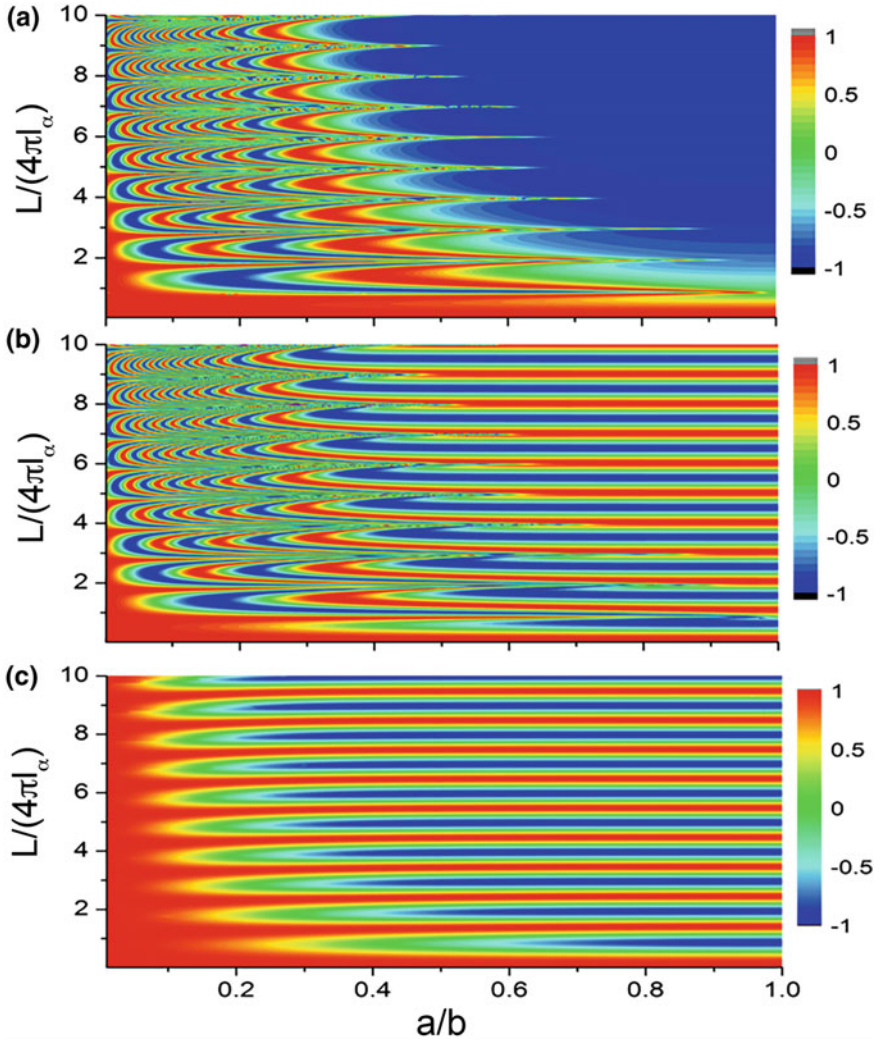

Fig. 12.6 Contour map of the cosine of the geometric phase (**a**), the spin component of the dynamical phase (**b**), and the total phase (**c**) contributing to the conductance for a quantum ring of total length L with elliptic shape as a function of the ellipse ration a/b and the dimensionless spin-orbit coupling strength $L/(4\pi l_\alpha)$ (From [36])

$$G = \frac{e^2}{h}\left\{1 + \cos\left[\pi\left(\sqrt{1+Q_R^2} - 1 + \phi(B)\right)\right]\right\},$$

where $\phi(B) \propto B^2$. This magnetic-field-induced shift in the interference pattern has been experimentally verified in arrays of InGaAs-based quantum rings [28]. Note that the magnetic field contribution to the conductance modulations only enters in

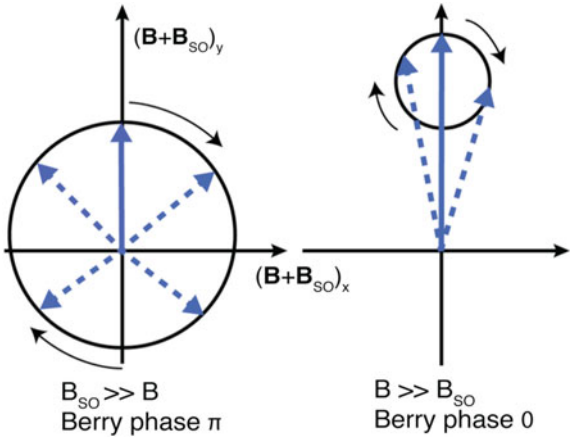

Fig. 12.7 The Berry phases in the adiabatic limit for a circular quantum ring with an additional planar magnetic field. For $B_{SO} \gg B$, the accumulated Berry phase correspond to π. The opposite limit gives instead a 0 Berry phase From [38] (Copyright 2015 American Physical Society)

the AA phase. This is because for a quantum ring with symmetrically coupled leads, electronic spins acquire the same Zeeman dynamical phase, and therefore the Zeeman effect only contributes the geometric part of the quantum phase.

An external magnetic field can, however, also directly modify the topology of the effective magnetic field felt by the carriers during transport, thereby paving the way for the development of topological spin engineering. An early proposal for the topological manipulation of electron spin, which has been put forward by Lyanda-Geller [39], involved the abrupt switching of Berry phases. Assuming an entirely adiabatic spin transport, it was predicted that a change in the winding number associated with the effective field felt by the charge carriers (c.f. Fig. 12.7) would manifest itself as a steplike characteristic in the quantum ring conductance. The intrinsic non-adiabatic nature of the spin transport discussed in the former section, however, requires a more sophisticated approach [38].

Saarikoski et al. have thereby analyzed the electronic transport characteristic of a spin interferometer with an externally applied planar magnetic field considering rings tangentially coupled to leads. In this geometric configuration, indeed, the dynamical Zeeman phases can yield both constructive and destructive interference. Henceforth, the conductance will be modulated by both a magnetic field dependent dynamical phase and the magnetic field dependent geometric phase. In Fig. 12.8 we report the behavior of the two quantum phases in the spin-orbit coupling, magnetic field parameter space. The interference pattern possesses radial wave fronts, which can be mainly ascribed to Zeeman oscillations. Most importantly, one observes distinct phase dislocations along the critical line where the effective magnetic field textures change topology, i.e. at $B_{SO} = B$ (c.f. Fig. 12.7). This result is surprising since the topology of the magnetic field textures is reflected in an abrupt change of the conductance modulations even though the spin dynamics is completely non-adiabatic as testified by the complex behaviors of the geometric and dynamic phase for $B_{SO} \simeq B$. Whether or not the existence of phase dislocation can be linked to an "effective" Berry phase with phase slips at the critical line is a matter of future investigations.

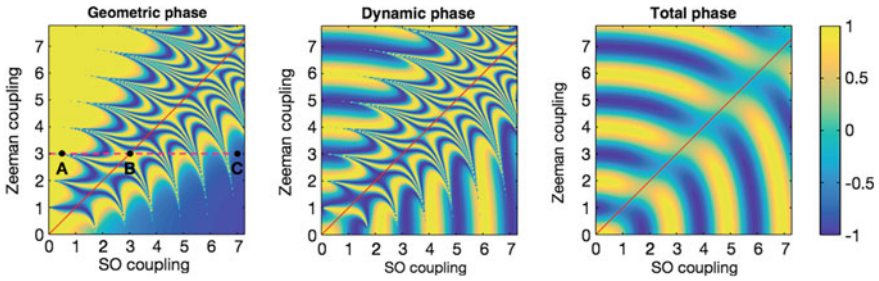

Fig. 12.8 Contour map of the cosine of the geometric phase (top panel), the dynamical phase (middle panel), and the total phase (bottom panel) as a function of the spin-orbit coupling and Zeeman splitting in a ballistic single-mode quantum ring tangentially coupled to leads From [38] (Copyright 2015 American Physical Society)

Acknowledgements I acknowledge the financial support from the Future and Emerging Technologies (FET) programme within the Seventh Framework Programme for Research of the European Commission under FET-Open grant number: 618083 (CNTQC), and from a VIDI grant (Project 680-47-543) financed by the Netherlands Organization for Scientific Research (NWO).

References

1. E.I. Rashba, Sov. Phys. Solid State **2**, 1109 (1960)
2. A.G. Aronov, Y.B. Lyanda-Geller, Phys. Rev. Lett. **70**, 343 (1993)
3. Y.-S. Yi, T.-Z. Qian, Z.-B. Su, Phys. Rev. B **55**, 10631 (1997)
4. S.-L. Zhu, Y.-C. Zhou, H.-Z. Li, Phys. Rev. B **52**, 7814 (1995)
5. T.-Z. Qian, Y.-S. Yi, Z.-B. Su, Phys. Rev. B **55**, 4065 (1997)
6. F.E. Meijer, A.F. Morpurgo, T.M. Klapwijk, Phys. Rev. B **66**, 033107 (2002)
7. H. Jensen, H. Koppe, Ann. Phys. **63**, 586 (1971)
8. R.C.T. da Costa, Phys. Rev. A **23**, 1982 (1981)
9. G. Cantele, D. Ninno, G. Iadonisi, Phys. Rev. B **61**, 13730 (2000)
10. H. Aoki, M. Koshino, D. Takeda, H. Morise, K. Kuroki, Phys. Rev. B **65**, 035102 (2001)
11. M. Encinosa, L. Mott, Phys. Rev. A **68**, 014102 (2003)
12. N. Fujita, O. Terasaki, Phys. Rev. B **72**, 085459 (2005)
13. M. Koshino, H. Aoki, Phys. Rev. B **71**, 073405 (2005)
14. J. Gravesen, M. Willatzen, Phys. Rev. A **72**, 032108 (2005)
15. A.V. Chaplik, R.H. Blick, New J. Phys. **6**, 33 (2004)
16. A. Marchi, S. Reggiani, M. Rudan, A. Bertoni, Phys. Rev. B **72**, 035403 (2005)
17. A.I. Vedernikov, A.V. Chaplik, JETP **90**, 397 (2000)
18. G. Cuoghi, G. Ferrari, A. Bertoni, Phys. Rev. B **79**, 073410 (2009)
19. C. Ortix, J. van den Brink, Phys. Rev. B **81**, 165419 (2010)
20. C. Ortix, S. Kiravittaya, O.G. Schmidt, J. van den Brink, Phys. Rev. B **84**, 045438 (2011)
21. G. Ferrari, G. Cuoghi, Phys. Rev. Lett. **100**, 230403 (2008)
22. C. Ortix, J. van den Brink, Phys. Rev. B **83**, 113406 (2011)
23. C.-H. Chang, J. van den Brink, C. Ortix, Phys. Rev. Lett. **113**, 227205 (2014)
24. A. Szameit, F. Dreisow, M. Heinrich, R. Keil, S. Nolte, A. Tünnermann, S. Longhi, Phys. Rev. Lett. **104**, 150403 (2010)
25. S. Carroll, *Spacetime and Geometry: An Introduction to General Relativity* (Addison Wesley, San Francisco, CA, 2004)

26. D. Frustaglia, K. Richter, Phys. Rev. B **69**, 235310 (2004)
27. P. Gentile, M. Cuoco, C. Ortix, SPIN **03**, 1340002 (2013)
28. F. Nagasawa, D. Frustaglia, H. Saarikoski, K. Richter, J. Nitta, Nat. Commun. **4**, 2526 (2013)
29. H. Mathur, A.D. Stone, Phys. Rev. Lett. **68**, 2964 (1992)
30. T. Choi, S.Y. Cho, C.-M. Ryu, C.K. Kim, Phys. Rev. B **56**, 4825 (1997)
31. Y. Aharonov, A. Casher, Phys. Rev. Lett. **53**, 319 (1984)
32. M.V. Berry, Proc. R. Soc. Lond. **392**, 45 (1984)
33. J. Nitta, F.E. Meijer, H. Takayanagi, Appl. Phys. Lett. **75**, 695 (1999)
34. B. Molnár, F.M. Peeters, P. Vasilopoulos, Phys. Rev. B **69**, 155335 (2004)
35. Y. Aharonov, J. Anandan, Phys. Rev. Lett. **58**, 1593 (1987)
36. Z.-J. Ying, P. Gentile, C. Ortix, M. Cuoco, Phys. Rev. B **94**, 081406 (2016)
37. D. Bercioux, D. Frustaglia, M. Governale, Phys. Rev. B **72**, 113310 (2005)
38. H. Saarikoski, J.E. Vázquez-Lozano, J.P. Baltanás, F. Nagasawa, J. Nitta, D. Frustaglia, Phys. Rev. B **91**, 241406 (2015)
39. Y. Lyanda-Geller, Phys. Rev. Lett. **71**, 657 (1993)

Chapter 13
Quantum Rings in Electromagnetic Fields

A.M. Alexeev and M.E. Portnoi

Abstract This chapter is devoted to optical properties of so-called Aharonov-Bohm quantum rings (quantum rings pierced by a magnetic flux resulting in Aharonov-Bohm oscillations of their electronic spectra) in external electromagnetic fields. It studies two problems. The first problem deals with a single-electron Aharonov-Bohm quantum ring pierced by a magnetic flux and subjected to an in-plane (lateral) electric field. We predict magneto-oscillations of the ring electric dipole moment. These oscillations are accompanied by periodic changes in the selection rules for inter-level optical transitions in the ring allowing control of polarization properties of the associated Terahertz radiation. The second problem treats a single-mode microcavity with an embedded Aharonov-Bohm quantum ring which is pierced by a magnetic flux and subjected to a lateral electric field. We show that external electric and magnetic fields provide additional means of control of the emission spectrum of the system. In particular, when the magnetic flux through the quantum ring is equal to a half-integer number of the magnetic flux quanta, a small change in the lateral electric field allows for tuning of the energy levels of the quantum ring into resonance with the microcavity mode, thus providing an efficient way to control the quantum ring-microcavity coupling strength. Emission spectra of the system are discussed for several combinations of the applied magnetic and electric fields.

A.M. Alexeev (✉) · M.E. Portnoi
School of Physics, University of Exeter, Stocker Road, Exeter EX4 4QL, UK
e-mail: a.alexeev@exeter.ac.uk

M.E. Portnoi
e-mail: m.e.portnoi@exeter.ac.uk

V.M. Fomin (ed.), *Physics of Quantum Rings*, NanoScience and Technology,
https://doi.org/10.1007/978-3-319-95159-1_13

13.1 Introduction and Overview. Quantum Mechanics in Semiconductor Aharonov-Bohm Quantum Rings and Quantum Electrodynamics in Microcavities

13.1.1 Introduction

In their celebrated paper [1] Aharonov and Bohm demonstrated that while in classical mechanics the fundamental equations of motion can always be expressed in terms of the field alone, in quantum mechanics a canonical formalism is essential and, as a result, potentials cannot be eliminated from the basic equations. Nanoscale-sized semiconductor rings, which are now commonly called Aharonov-Bohm quantum rings, are among other quantum systems used for experimental studies of the renowned discovery. Few-electron quantum rings with a radial size of 10–20 nm are now easily fabricated. The mean free path of particles confined in these nanostructures exceeds the ring length, which results in the self-interference effects experienced by particles. The influence of the field potentials upon this interference in the regions with vanishing field magnitudes is a direct evidence of the Aharonov-Bohm effect present in quantum rings.

This chapter is devoted to the optical properties of Aharonov-Bohm quantum rings in external electromagnetic fields. The research presented in Sect. 13.4 was motivated by a number of works which demonstrated the beneficial influence of an external electric field on some electronic and optical properties of an Aharonov-Bohm quantum ring. The list of these works and a brief description of their main results can be found in Sect. 13.1.2. In our work, we study an infinitely-narrow quantum ring subjected to a relatively weak static lateral electric field and pierced by a magnetic flux [2, 3]. We predict magneto-oscillations of the ring electric dipole moment and examine their electric field and temperature dependence. These oscillations are accompanied by periodic changes for the selection rules for inter-level optical transitions in the ring. Radiation associated with these transitions occurs at terahertz frequencies for quantum rings with the radial size of 10–20 nm. Most of the results obtained for the static in-plane electric field can be easily generalized to the case of the rotating field by a proper change of the coordinates system [4].

Exceptional opportunities to control the optical properties of quantum rings with external fields stimulated our further research, which is presented in Sect. 13.5. In this work, we study an Aharonov-Bohm quantum ring embedded into a single-mode terahertz microcavity [5].

Microcavity quantum electrodynamics is an area which keeps attracting a strong interest of both the condensed matter and quantum optics research communities. One of the reasons of this everlasting interest is the feasibility of utilizing novel effects originating from field-matter coupling for developing novel nanodevices such as terahertz polariton-lasers. In our studies, we calculate the emission spectrum of the coupled quantum ring-microcavity system and show how it can be tuned by variation of the magnetic field piercing the quantum ring and the lateral electric

field. Such control of the emission spectrum was never possible with quantum dots in microcavities. Advantages arising of using quantum rings instead of quantum dots as photon emitters in microcavities are discussed in Sects. 13.5.3 and in 13.6.

The rest of this chapter is organized as follows. In Sects. 13.1.2 and 13.2 we provide a cursory overview of quantum phenomena in quantum rings and optical microcavities. In Sect. 13.3 some theoretical basics needed for understanding of the later presented research are introduced. Sections 13.4 and 13.5 contain original work as described above. Conclusions and possible extension of this work are included in Sect. 13.6.

13.1.2 Quantum Mechanics in Nanoscale Aharonov-Bohm Quantum Rings

Progress in epitaxial techniques in recent decades has resulted in burgeoning developments in the physics of quantum dots (QDs), i.e., semiconductor-based 'artificial atoms'. More recently, a lot of attention has been turned towards non-simply-connected nanostructures, such as quantum rings (QRs), which have been obtained in various semiconductor systems [6–32]. Originally, QRs were fabricated accidently, when optimizing growth conditions for self-assembled InAs quantum dots on a GaAs substrate, the QD material was splashed out from the QD centre, forming a volcano-like structure [6–9]. Improved and perfected, it has now become a routine procedure for the fabrication of QRs with typical radii of 10–100 nm [11–14, 16, 18, 19, 21–30]. In the literature, QRs produced as described above are usually referred to as 'type-I quantum rings'.

Nanostructures with an alternative realization of the ring-shape confinement, the so-called 'type-II quantum dots', were suggested for exploring effects arising from the non-simply-connectedness of such objects. In these nano-sized structures one carrier is confined inside the QD and a carrier of an opposite charge is confined in the barrier [10]. As a result, the carrier in the barrier experiences a rotational movement with a radius of 10–20 nm around the QD [15, 20, 31–33].

Another possible way of QRs fabrication is based on using the evaporative templating method [17]. This fabrication procedure includes three stages: introduction of an aqueous solution which contains QDs and polystyrene microspheres onto the surface of a glass substrate, evaporation, and microsphere removal. During the evaporation stage, QDs surround the microspheres and merge, which finally results in the formation of a QR with the radial dimension of 80 nm–1 μm.

The fascination in QRs is caused by a wide variety of purely quantum mechanical effects, which are observed in ring-like nanostructures (for a review see [34–38]). The star amongst them is the Aharonov-Bohm effect, in which a charged particle [1, 39] is affected by a magnetic field away from the particle's trajectory, resulting in magnetic-flux-dependent oscillations of the ring-confined particle energy. The same research group which discovered type-I QRs was the first to observe the Aharonov-

Bohm type oscillations in these nanostructures [9]. This became the starting point for a series of experiments dedicated to the Aharonov-Bohm effect in both type-I QRs [9, 19] and type-II QDs [10, 18, 20, 40].

There is significant interest in the excitonic Aharonov-Bohm effect in QRs, which, in principle, should not exist as the exciton is a neutral particle and can not be influenced by the magnetic field. However, due to the finite size of the exciton, the excitonic Aharonov-Bohm effect is, in fact, possible. The excitonic Aharonov-Bohm effect was theoretically studied by a number of authors in both 1D QRs [41–46] and 2D QRs [33, 47–56]. It was shown that the Aharonov-Bohm type oscillations do exist in both 1D and 2D models, but vanish in QRs with the ring radial size larger than the exciton Bohr radius or with increased ring width. Recently, it was demonstrated that in the 2D exactly solvable model previously used in [57–59] the magneto-oscillations in the exciton ground state survive down to regimes with radius-width ratio less than unity [60].

To reveal the excitonic Aharonov-Bohm effect it was suggested to place the QR in an external electric field, which delocalizes the relative electron-hole motion around the entire ring [18, 61–63]. It was also shown that in the presence of an in-plane (lateral) electric field exceeding a particular threshold it is possible to switch the ground state of the QR exciton from being optically active (bright) to optically inactive (dark) [18, 62].

13.2 Quantum Electrodynamics in Microcavities: Light-Matter Coupling

The strong coupling regime requires a microcavity (MC) to sustain an isolated mode. Otherwise, the excited mode exponentially decays into the other MC modes. There are three main designs which achieve the goal of zero-dimensional radiation confinement, described below.

The first design, pillar MCs, are fabricated by etching a stack of conventional Bragg mirrors. The typical height of pillar MCs is about $10\,\mu$m. The lateral confinement in pillar MCs is provided by the reflecting interface between the MC walls and the surrounding media. The chances that the chosen pillar MC contains an emitter (usually, a QD) which is in the strong coupling regime with the MC mode are comparably small and one has to check all produced MCs one by one until a cavity with required characteristics is found.

Another possible realization of a single-mode MC is the photonic crystal cavity. The original idea of a photonic crystal was developed by Yablonovich [64] and John [65]. It is based on the same phenomena which leads to the appearance of bandgaps in semiconductors. A structure with periodic modulations of permittivity becomes forbidden for several ranges of wavelength due to the destructive interferences similar to those of Bragg physics. The first 3D photonic crystal was created by drilling holes in a slab at three different angles, resulting in a full bandgap in

the microwave range [66]. Several years later, a 2D photonic crystal with a bandgap in the optical spectrum was reported [67]. By introducing a defect in the photonic crystal periodic structure it is possible to create a MC (the so-called 'Noda cavity') - radiation becomes trapped within the defect region [68]. Originally, values of the Q-factor in photonic crystal MC were quite small (only around 400), but now using some cunning designs of the photonic crystals periodic structure, MC with Q-factors as large as 10^6 can be fabricated [69]. Some MC designs which promise Q-factors up to 10^9 were also suggested [70].

The last design, the microdisk MC, confines radiation in whispering gallery modes. For a review of microdisk cavities one can refer to [71].

One of phenomena which can be observed in semiconductor MCs in the Purcell effect [72] in which the time of spontaneous emission is affected by the environment of an emitter. The ratio of the times of spontaneous emission when the emitter is placed in two different environments (e.g., MC and vacuum) is usually referred as the Purcell factor. The first observation of the Purcell effect in semiconductor MCs was done with a QD embedded into a pillar MC [73]. In this experiment, the time of photon spontaneous emission was affected with a Purcell factor of 5. Several similar observations in different systems (e.g., [74, 75] in pillar MCs, [76] in microdisk MC, [77] in photonic crystal MC) followed this pioneering work. For instance, in the experiment of [77] when a QD was placed inside a photonic bandgap of a semiconductor the time of its spontaneous emission was extended to 2.52 ns comparing to the time of 0.65 ns when the same QD was placed in the bulk semiconductor. The time of spontaneous emission of another QD placed in the same photonic bandgap and brought into the resonance with the cavity was 0.21 ns.

There has been an impressive development towards a better quantum coupling with QDs in MC and improved external control. The latest achievements in fabrication techniques now allow one to position QDs inside MCs with spectacular accuracy. In [78] a photonic crystal MC with a single QD placed exactly at the maximum of the MC field intensity was demonstrated. In photonic crystal MCs one can spectrally match the MC mode emission with the QD emission by artful etching of the photonic crystal periodic structure. However, once the structure is fabricated, adjustment of any system parameters becomes a difficult task.

The strong coupling regime in QDs in semiconductor MCs was first attained in 2004 in two sequential papers, [79] in a photonic crystal MC and [80] in a pillar MC. The strong coupling in microdisc MC was reported a year later [81]. Since then, the strong coupling regime in semiconductor MCs was reported by several research groups, but the number of experiments that achieved this regime remains limited. In this cursory overview, we only provide the list of some of these works—please see [79–87]. Two of the listed experiments deserve a more detailed discussion.

In the first work, [84, 85], the authors developed an electronically controlled device which uses the quantum confined Stark effect [88], in which the external electric field shifts the QD exciton discrete states towards lower energies, to tune QDs in resonance with the mode of the photonic crystal MC. This experiment presents a

solution with on-chip control of the strong coupling. But still, due to the weakness of the phenomena, this way of controlling the QR-MC coupling strength remains somewhat limited. In the second work [82], the strong coupling regime was observed with a single QD in a photonic crystal MC. In this experiment the antibunching of the Rabi doublet peaks was proved, which is possibly the first real evidence of full field quantization in a coupled QD-MC system.

A system with a genuine strong coupling should noticeably change its behaviour when an additional quantum of excitation is added or removed. In an ideal picture, an emitter embedded in a MC (e.g., QD or QR) can be modelled as a two-level system coupled to the MC mode. Such a system possesses a Hamiltonian which eigenstates, hybrid light-matter states, form the so-called 'Jaynes-Cummings ladder'. The emission measured outside of the MC should mirror the structure of this 'ladder'.

Lastly, we would like to note that to the best of our knowledge there are no experimental works exploring the strong coupling phenomena in QRs embedded into MCs. We hope that our research presented in Sect. 13.5 will stimulate experiments in this area.

13.3 Theoretical Background. Quantum Description of Light-Matter Coupling and the Dipole Approximation for Optical Transitions

13.3.1 Introduction

This section contains a brief review of the background theory which is used in the rest of this chapter: quantization of the electromagnetic field, the two-level model for a single-photon emitter, the density matrix operator concept, the equations of motion for the density matrix operator, and the electric dipole approximation. We also refer the reader to various textbooks [89–96] covering these topics.

13.3.2 Light-Matter Coupling in Microcavities: Quantum Description

13.3.2.1 Quantization of the Electromagnetic Field

Field oscillators—harmonic oscillators

In the Coulomb gauge the vector potential of a sourceless classical electromagnetic field (CEF) satisfies the requirement

$$\mathrm{div}\mathbf{A}\,(\mathbf{r}, t) = 0, \tag{13.1}$$

and the homogeneous wave-equation

$$\frac{1}{c^2}\frac{\partial^2 \mathbf{A}\,(\mathbf{r},t)}{\partial t^2} - \nabla^2 \mathbf{A}\,(\mathbf{r},t) = 0, \tag{13.2}$$

where $\mathbf{r}$ is the position vector and t is the time variable. The field scalar potential can be chosen to be identically zero, so that the field is fully defined by the vector potential

$$\mathbf{E}\,(\mathbf{r},t) = -\frac{\partial}{\partial t}\mathbf{A}(\mathbf{r},t), \tag{13.3}$$

$$\mathbf{B}\,(\mathbf{r},t) = \nabla \times \mathbf{A}(\mathbf{r},t). \tag{13.4}$$

In what follows we consider a MC of a volume V without specifying its exact shape. The quantization procedure, which we introduce later, does not depend on the MC shape and is the same in MCs with various shapes (e.g., [97] in planar MCs, [98] in a spherical MCs, [99] in cylindrical MCs). The solution of (13.2) can be written in the following form with separated variables

$$\mathbf{A}\,(\mathbf{r},t) = \sqrt{1/\varepsilon_0}\sum_i Q_i\,(t)\,\mathbf{U}_i(\mathbf{r}), \tag{13.5}$$

where $Q_i\,(t)$ are the field amplitudes, $\mathbf{U}_i\,(\mathbf{r})$ is the set of field modes, and ε_0 is the vacuum dielectric permittivity. For the present moment, we assume that all field modes are linearly independent and thus can be orthonormalized. We discuss this assumption in more detail later.

Substitution of (13.5) into (13.3) and (13.4) results in the following expressions

$$\mathbf{E}\,(\mathbf{r},t) = -\sqrt{1/\varepsilon_0}\sum_i \dot{Q}_i\,(t)\,\mathbf{U}_i\,(\mathbf{r})\,, \tag{13.6}$$

$$\mathbf{B}\,(\mathbf{r},t) = \sqrt{1/\varepsilon_0}\sum_i Q_i\,(t)\,\nabla \times \mathbf{U}_i\,(\mathbf{r})\,. \tag{13.7}$$

Now let us return to the wave equation and substitute the chosen vector potential, given by (13.5), into (13.2) to obtain

$$\frac{1}{c^2}\left[\ddot{Q}_i\,(t) + \Omega_i^2 Q_i\,(t)\right]\mathbf{U}_i\,(\mathbf{r}) - Q_i\,(t)\left[\nabla^2 \mathbf{U}_i\,(\mathbf{r}) + \frac{\Omega_i^2}{c^2}\mathbf{U}_i\,(\mathbf{r})\right] = 0,$$

Here Ω_i are the frequencies of the field modes. Since each of these equations should be satisfied identically at any time moment and for any position in the space, the expressions in square brackets should vanish separately

$$\ddot{Q}_i\,(t) + \Omega_i^2 Q_i\,(t) = 0, \tag{13.8}$$

$$\nabla^2 \mathbf{U}_i(\mathbf{r}) + \frac{\Omega_i^2}{c^2}\mathbf{U}_i(\mathbf{r}) = 0. \tag{13.9}$$

One can see that the above equations define CEF time (13.8) and spatial (13.9) dynamics.

There are two boundary conditions imposed upon the electromagnetic field inside a MC. Namely, the tangential component of the electric field and the normal component of the magnetic field should vanish at the MC walls. Together with (13.1) they lead to the following set of restricting conditions

$$\mathbf{U}_i(\mathbf{r})\,|_{\text{tang}} = 0 \text{ on the MC walls,}$$

$$\text{curl}\mathbf{U}_i(\mathbf{r})\,|_{\text{norm}} = 0 \text{ on the MC walls,}$$

and

$$\text{div}\mathbf{U}_i(\mathbf{r}) = 0 \text{ in all MC volume.}$$

It can be shown that the first and the third conditions result in the electric field vanishing on the MC walls. That, in turn, gives $\mathbf{U}_i(\mathbf{r})\,|_{\text{walls}} = 0$.

Once the exact MC shape is given, using the above conditions, one can solve (13.9). The obtained solutions are unique for a given MC. Due to this fact, these solutions are usually called 'normal modes' of the MC. Normal modes fully characterize the geometry of a particular problem.

To be able to proceed with the field quantization we now need to define new functions, the so-called 'normal variables', a_i and a_i^*, which re-express the field amplitudes Q_i in the following way

$$Q_i = \sqrt{\frac{\hbar}{2\Omega_i}}(a_i + a_i^*),$$

$$\dot{Q}_i = -i\sqrt{\frac{\hbar\Omega_i}{2}}\left(a_i - a_i^*\right).$$

The expressions above can be inverted. Carrying out this simple operation one obtains the following result

$$a_i = \sqrt{\frac{1}{2\hbar\Omega_i}}(\Omega_i Q_i + i\dot{Q}_i),$$

$$a_i^* = \sqrt{\frac{1}{2\hbar\Omega_i}}\left(\Omega_i Q_i - i\dot{Q}_i\right).$$

Using the normal variables we can redefine the field vector potential (13.5) and the electric and magnetic fields (13.6)–(13.7) as

$$\mathbf{A}(\mathbf{r},t) = \sum_i \sqrt{\frac{\hbar}{2\varepsilon_0 \Omega_i}} \left(a_i + a_i^*\right) \mathbf{U}_i(\mathbf{r}),$$

$$\mathbf{E}(\mathbf{r},t) = i \sum_i \sqrt{\frac{\hbar\Omega_i}{2\varepsilon_0}} \left(a_i - a_i^*\right) \mathbf{U}_i(\mathbf{r}),$$

$$\mathbf{B}(\mathbf{r},t) = \sum_i \sqrt{\frac{\hbar}{2\varepsilon_0 \Omega_i}} \left(a_i + a_i^*\right) \mathrm{curl}\mathbf{U}_i(\mathbf{r}).$$

In classical electrodynamics the energy of the electromagnetic field is given by the integral

$$\mathscr{E}_{CEF} = \frac{\varepsilon_0}{2} \int_V \left[\mathbf{E}^2 + c^2\mathbf{B}^2\right] d\mathbf{r}.$$

Performing several transformations it is easy to rewrite this expression in terms of the field amplitudes and the normal variables

$$\mathscr{E}_{CEF} = \frac{1}{2} \sum_i \left[\dot{Q}_i^2 + \Omega_i^2 Q_i^2\right] = \sum_i \hbar\Omega_i a_i^* a_i. \tag{13.10}$$

Now we need to recall some basics of the quantum harmonic oscillator (QHO). The Hamiltonian of one-dimensional QHO with a unit mass reads as [95]

$$H_{QHO} = \hbar\omega(\hat{a}^\dagger \hat{a} + 1/2), \tag{13.11}$$

where ω is the oscillator frequency and $\hat{a}^\dagger$, $\hat{a}$ are the creation and annihilation operators. The eigenstates of the QHO can be denoted by $|n\rangle$ with $n = 0, 1, 2, \ldots$, so that

$$H_{QHO}|n\rangle = \hbar\omega(n + 1/2)|n\rangle.$$

These states form the so-called 'QHO ladder'. Each of these states can be constructed from the vacuum state $|0\rangle$, which possesses the property $\hat{a}|0\rangle = 0$, by application of the creation operator n-times:

$$|n\rangle = \frac{\left(\hat{a}^\dagger\right)^n |0\rangle}{\sqrt{n!}}.$$

One can notice that the QHO Hamiltonian given by (13.11) is of the same form as the (13.10), which defines energy of CEF expressed in terms of normal variables. The only difference is the term $\hbar\omega/2$ which appears due to the non-commutativity of the creation and annihilation operators. Later we show that this term should be omitted in order to normalize energy of the quantized electromagnetic field (QEF) with an infinite number of modes (e.g., QEF in vacuum).

This similarity allows us to proceed with the intuitively simple quantization of the electromagnetic field. The trick is to substitute the normal variables with the creation and annihilation operators, which satisfy the commutation relation $\left[\hat{a}_i, \hat{a}_j^\dagger\right] = \delta_{ij}$ with all other commutators vanishing. The above commutation relation reflects the linear independence of the field modes.

Performing this substitution we arrive at the following expressions for the field vector potential and the electric and magnetic fields

$$\hat{\mathbf{A}} = \sum_i \sqrt{\frac{\hbar}{2\varepsilon_0 \Omega_i}} \left(\hat{a}_i + \hat{a}_i^*\right) \mathbf{U}_i(\mathbf{r}),$$

$$\hat{\mathbf{E}} = i \sum_i \sqrt{\frac{\hbar \Omega_i}{2\varepsilon_0}} \left(\hat{a}_i - \hat{a}_i^*\right) \mathbf{U}_i(\mathbf{r}),$$

$$\hat{\mathbf{B}} = \sum_i \sqrt{\frac{\hbar}{2\varepsilon_0 \Omega_i}} \left(\hat{a}_i + \hat{a}_i^*\right) \nabla \times \mathbf{U}_i\left(\mathbf{r}\right).$$

From now on, the electromagnetic field is described with the quantum mechanical operators $\hat{\mathbf{A}}$, $\hat{\mathbf{E}}$, and $\hat{\mathbf{B}}$. Since the creation and annihilation operators entering the equations above do not commute, these operators do not commute as well. One can see that after quantization the time dynamics of the electromagnetic field is hidden in the creation and annihilation operators $\hat{a}_i$ and $\hat{a}_i^\dagger$. Recall that before the quantization procedure the time dependence was defined by the dynamical behaviour of the field amplitudes Q_i.

To finish with the electromagnetic field quantization we should define the Hilbert space of the field eigenstates. We employ once again the analogy with the quantum harmonic oscillator and define the vacuum state of any of the electromagnetic field modes by the requirement $\hat{a}_i |0\rangle = 0$. Due to the independence of field modes we can construct all other eigenstates as a tensor product

$$|n_1, n_2, \ldots, n_k, \ldots\rangle = |n_1\rangle \otimes |n_2\rangle \otimes \cdots \otimes |n_k\rangle \otimes \cdots = \bigotimes_i \frac{\left(\hat{a}_i^\dagger\right)^{n_i}}{\sqrt{n_i!}} |0\rangle,$$

where the index i numbers the field modes and n_i are the non-negative integers usually called 'mode occupation numbers'.

In some cases the number of the field modes in a MC can be infinite and the field energy should be renormalized by omitting the term which is responsible for the vacuum state energy in the field Hamiltonian [89–94]. In this case the Hamiltonian of the QEF reads

$$H_{QEF} = \sum_i \hbar \Omega_i \hat{a}_i^\dagger \hat{a}_i.$$

In our research presented in this chapter we will consider a MC which sustains just one mode of QEF. In this case the MC field Hamiltonian reads as

$$H_{MC} = \hbar\omega_{MC}\hat{a}^{\dagger}\hat{a}, \tag{13.12}$$

where ω_{MC} is the MC mode frequency and we have omitted creation and annihilation operators indices to simplify notation.

Quantization in a cubic box of volume V

As was discussed above, the set of field modes which is allowed for a particular problem is fully defined by the geometry of a given MC. In this section we study a MC with a cubic shape. This case is of significant importance as it allows one to introduce the plane wave representation for the QEF.

The most natural set of orthonormal functions in a cubic MC is the set of plane waves given by

$$\mathbf{f}_{\mathbf{k},\alpha} = \frac{\mathbf{e}_{\mathbf{k},\alpha}\exp(i\mathbf{kr})}{\sqrt{V}},$$

where $\mathbf{k}$ is the wave vector and index α represents the wave polarization. The wave vector $\mathbf{k}$ satisfies the dispersion relation $\omega_k = kc$ with $k = |\mathbf{k}|$. This is a consequence of the requirement for the plane wave functions to satisfy the Helmholtz equation. The polarization vectors $\mathbf{e}_{\mathbf{k},\alpha}$ are complex numbers normalized to unity.

The next step is to expand the field vector potential introduced in the previous section in terms of the cubic MC plane waves

$$\hat{\mathbf{A}} = \sum_{\mathbf{k},\alpha}\sqrt{\frac{\hbar}{2\varepsilon_0\Omega_k V}}\left[\mathbf{e}_{\mathbf{k},\alpha}\hat{a}_{\mathbf{k},\alpha}\exp(i\mathbf{kr}) + \mathbf{e}^{*}_{\mathbf{k},\alpha}\hat{a}^{\dagger}_{\mathbf{k},\alpha}\exp(-i\mathbf{kr})\right]. \tag{13.13}$$

In the Coulomb gauge, the field vector potential $\hat{\mathbf{A}}$ has only the transverse component. When applied to (13.13) this requirement gives

$$\mathbf{e}_{\mathbf{k},\alpha}\cdot\mathbf{k} = \mathbf{e}^{*}_{\mathbf{k},\alpha}\cdot\mathbf{k} = 0.$$

There are only two linearly independent vectors orthogonal to the wave vector $\mathbf{k}$. We refer to them with the index α, which, for a given $\mathbf{k}$, can now take only two values, $\alpha = 1, 2$. Real values of the polarization vector represent two linear polarizations of the electromagnetic field while complex values correspond to two different circular polarizations.

Finally, to finish with the plane wave representation, we reexpress the boundary conditions for the electric and magnetic fields inside a MC in terms of the plane wave functions $\mathbf{f}_{\mathbf{k},\alpha}$.

Using the boundary conditions imposed upon the field modes $\mathbf{U}_i$ in the previous section we obtain the following periodic boundary conditions for $\mathbf{f}_{\mathbf{k},\alpha}$

$$\mathbf{f}_{\mathbf{k},\alpha}\left(\mathbf{r}+\mathbf{l}_j L\right)=\mathbf{f}_{\mathbf{k},\alpha}(\mathbf{r}),$$

where L is the length of the MC sides and $\mathbf{l}_j$ is a set of unit vectors directed along the MC edges. From this condition it is easy to retrieve quantization rules for $\mathbf{k}$

$$\mathbf{k}=\frac{2\pi}{L}\left(N_x\mathbf{l}_x+N_y\mathbf{l}_y+N_z\mathbf{l}_z\right),$$

where N_x, N_y, N_z are integer numbers which allow an alternative way to number the MC plane waves. One should not confuse this numbering with the modes occupation numbers introduced earlier.

To conclude this section we provide expressions for the quantized electromagnetic field operators, the electromagnetic field Hamiltonian, and Hamiltonian eigenstates in the plane wave representation

$$\hat{\mathbf{E}}=i\sum_{\mathbf{k},\alpha}\sqrt{\frac{\hbar\Omega_k}{2\varepsilon_0 V}}\left[\mathbf{e}_{\mathbf{k},\alpha}\hat{a}_{\mathbf{k},\alpha}\exp\left(i\mathbf{kr}\right)-\mathbf{e}^*_{\mathbf{k},\alpha}\hat{a}^\dagger_{\mathbf{k},\alpha}\exp\left(-i\mathbf{kr}\right)\right], \tag{13.14}$$

$$\hat{\mathbf{B}}=i\sum_{\mathbf{k},\alpha}\sqrt{\frac{\hbar\Omega_k}{2\varepsilon_0 V}}\left[\left(\mathbf{k}\times\mathbf{e}_{\mathbf{k},\alpha}\right)\hat{a}_{\mathbf{k},\alpha}\exp\left(i\mathbf{kr}\right)-\left(\mathbf{k}\times\mathbf{e}^*_{\mathbf{k},\alpha}\right)\hat{a}^\dagger_{\mathbf{k},\alpha}\exp\left(-i\mathbf{kr}\right)\right], \tag{13.15}$$

$$H_{QEF}=\sum_{\mathbf{k},\alpha}\hbar\Omega_k\hat{a}^\dagger_{\mathbf{k},\alpha}\hat{a}_{\mathbf{k},\alpha}, \tag{13.16}$$

$$\left|\{n_{\mathbf{k},\alpha}\}\right\rangle=\left|\ldots,n_{\mathbf{k}_i,\alpha_i},\ldots\right\rangle=\bigotimes_{\mathbf{k},\alpha}\frac{\left(\hat{a}^\dagger_{\mathbf{k},\alpha}\right)^{n_{\mathbf{k},\alpha}}}{\sqrt{n_{\mathbf{k},\alpha}!}}\left|0\right\rangle. \tag{13.17}$$

From (13.14)–(13.16) it is clear that the electric and magnetic field are related by $\hat{\mathbf{B}}=\sum_{\mathbf{k},\alpha}\left(\mathbf{k}/\Omega_k\right)\times\hat{\mathbf{E}}_{\mathbf{k},\alpha}$.

13.3.2.2 Two-Level Photon Emitter

In Sect. 13.3.2.1 we introduced notation in which the QEF is described in the language of QEF modes occupation numbers. In this notation electric and magnetic fields are defined in terms of creation and annihilation operators. In this section we show how fermionic states of a single-photon emitter (SPE) can be described in the same language.

A single-photon emitter whose excitations obey fermionic statistics can populate only a finite number of eigenstates, with a maximum of one excitation per eigenstate. This restriction is known as the Pauli exclusion principle [95]. Considering such a

system in a general way we denote its eigenstates by $|i\rangle$ and the corresponding eigenenergies by ε_i. We assume that this set of eigenstates is orthonormal, $\langle i|j\rangle = \delta_{i,j}$, and complete, $\sum_i |i\rangle \langle i| = 1$. The eigenstate's index i may consist of several quantum numbers.

Instead of the creation and annihilation operators $a^\dagger$ and a, the system can be described with the projector operators

$$\sigma_{ij}^\dagger = |j\rangle\langle i|,$$

and

$$\sigma_{ij} = |i\rangle \langle j| .$$

These projector operators induce promotion from the state i to the state j and from the state j to the state i by creating an excitation in the system in the same way as operators $a^\dagger$ and a create and annihilate an excitation in a particular mode of the QEF. The main difference is that the projector operators can be applied only once as only one excitation is allowed for each of the emitter eigenstates. If $\varepsilon_i < \varepsilon_j$, the projector operator $\sigma_{ij}^\dagger$ acts as the rising operator while the projector operator σ_{ij} acts as the lowering operator, and if $\varepsilon_i > \varepsilon_j$, projector operators swap their roles.

Using this notation a single-photon emitter Hamiltonian can be defined in the following way

$$H_{SPE} = \sum_j \varepsilon_j |j\rangle \langle j| = \sum_j \varepsilon_j \sigma_{ij}^\dagger \sigma_{ij}. \tag{13.18}$$

In most practical cases there is only one mode of the QEF which interacts with the single-photon emitter in a MC. This mode is usually tuned to one of the resonances of the emitter and has a relatively narrow spectral bandwidth. If the other eigenstates are separated by energy gaps which are much larger than the energy associated with the MC mode, all eigenstates other than the two which are brought into the resonance can be safely disregarded.

From now on, we assume that the field causes transitions between only two particular eigenstates of the single-photon emitter. We denote these eigenstates by $|g\rangle$ (the ground state) and $|e\rangle$ (the excited state). The energy gap between these two eigenstates we denote by Δ. This approximation to a multi-level quantum emitter we call the 'two-level emitter' (2LE) approximation. It should be noted that such a basic model works exceptionally well for real systems and gives a good insight into the quantum phenomena occurring in realistic experimental systems (e.g., see [79–82, 100–102]).

The Hamiltonian given by (13.18) in the 'two-level emitter' approximation reads as

$$H_{2LE} = \Delta |e\rangle \langle e| = \Delta \sigma^\dagger \sigma, \tag{13.19}$$

where we chose the zero energy level to coincide with the energy of the ground state $|g\rangle$ and $\sigma^\dagger = \left(\sigma_x + i\sigma_y\right)/2$, $\sigma = \left(\sigma_x - i\sigma_y\right)/2$ with

$$\sigma_x = \begin{pmatrix} 0 & 1 \\ 1 & 0 \end{pmatrix}, \sigma_y = \begin{pmatrix} 0 & -i \\ i & 0 \end{pmatrix},$$

being the Pauli matrices acting in the space of the emitter ground $|g\rangle$ and excited $|e\rangle$ states.

13.3.2.3 Field-Emitter Coupling

Coupling of the QEF to SPE is the key phenomenon which enters all further considerations. Using the analogy with classical electrodynamics we take the interaction Hamiltonian in the dipole approximation as

$$H_{INT} = -\mathbf{d} \cdot \mathbf{E},$$

where $\mathbf{d}$ is the SPE dipole moment operator and $\mathbf{E}$ is the QEF electric field operator given by (13.14) and taken at the position of the SPE. The interaction Hamiltonian can be re-expressed in the following way

$$H_{INT} = -\sum_{\mathbf{k},\alpha} \hat{\mathbf{d}} \cdot \left(\mathbf{E}^+_{\mathbf{k},\alpha} + \mathbf{E}^-_{\mathbf{k},\alpha}\right), \tag{13.20}$$

where

$$\mathbf{E}^+_{\mathbf{k},\alpha} = i\sqrt{\frac{\hbar\Omega_k}{2\varepsilon_0 V}}\left[\mathbf{e}_{\mathbf{k},\alpha} a_{\mathbf{k},\alpha} \exp\left(i\mathbf{k}\mathbf{r}_{\mathbf{SPE}}\right)\right], \tag{13.21}$$

and

$$\mathbf{E}^-_{\mathbf{k},\alpha} = -i\sqrt{\frac{\hbar\Omega_k}{2\varepsilon_0 V}}\left[\mathbf{e}^*_{\mathbf{k},\alpha} a^\dagger_{\mathbf{k},\alpha} \exp\left(-i\mathbf{k}\mathbf{r}_{\mathbf{SPE}}\right)\right]. \tag{13.22}$$

Note that in (13.21)–(13.22) the field operators $\mathbf{E}^+_{\mathbf{k},\alpha}$ and $\mathbf{E}^-_{\mathbf{k},\alpha}$ are taken at the position of the SPE. We would like to stress once more that the time dynamics of the QEF is hidden in the creation and annihilation operators. The SPE electric dipole moment operator is given by

$$\mathbf{d} = \sum_{i,j} \mathbf{d}_{ij} |i\rangle \langle j|, \tag{13.23}$$

where $\mathbf{d}_{ij}$ is the dipole moment operator matrix element calculated between two different states of the SPE

$$\mathbf{d}_{ij} = \langle i| \mathbf{d} |j\rangle = e \int \psi_i^* (\mathbf{r})\, \mathbf{r} \psi_j (\mathbf{r})\, d\mathbf{r}.$$

In many cases the emitter eigenfunctions possess the property of parity and thus the diagonal matrix elements $\mathbf{d}_{ii} = 0$. Substituting (13.23) into (13.20) we obtain

$$H_{INT} = -\sum_{\mathbf{k},\alpha} \sum_{i,j} |i\rangle \langle j| \mathbf{d}_{ij} \cdot \left(\mathbf{E}^+_{\mathbf{k},\alpha} + \mathbf{E}^-_{\mathbf{k},\alpha} \right).$$

In order to show that the above Hamiltonian is Hermitian we open the brackets in the expression above, swap indices $i \leftrightarrow j$ in the second term under summations (since the second summation is over all possible combinations of (i, j) and the case $\mathbf{d}_{ii} = 0$ is allowed), and use the fact that $\mathbf{d}_{ji} = \mathbf{d}^*_{ij}$. This results in

$$H_{INT} = -\sum_{\mathbf{k},\alpha} \sum_{i,j} |i\rangle \langle j| \mathbf{d}_{ij} \cdot \mathbf{E}^+_{\mathbf{k},\alpha} + |j\rangle \langle i| \mathbf{d}^*_{ji} \cdot \mathbf{E}^-_{\mathbf{k},\alpha}. \tag{13.24}$$

From this equation it can be clearly seen that H_{INT} is indeed Hermitian. Let us now transform the interaction Hamiltonian into a form which will be more suitable for further calculations. For the case of 2LE from (13.24) we immediately get the following result

$$H_{INT} = \\ -\sum_{\mathbf{k},\alpha} \left(|e\rangle \langle g| \mathbf{d}_{eg} \cdot \mathbf{E}^+_{\mathbf{k},\alpha} + |g\rangle \langle e| \mathbf{d}^*_{ge} \cdot \mathbf{E}^-_{\mathbf{k},\alpha} + |e\rangle \langle g| \mathbf{d}^*_{eg} \cdot \mathbf{E}^-_{\mathbf{k},\alpha} + |g\rangle \langle e| \mathbf{d}_{ge} \cdot \mathbf{E}^+_{\mathbf{k},\alpha} \right). \tag{13.25}$$

In the expression above there are four terms under summation. We discuss each of them separately:

- The first term corresponds to the transition from the ground state $|g\rangle$ to the excited state $|e\rangle$. As expected, a photon is absorbed as a result of this transition (due to the presence of the anihilation operator in the expression for $\mathbf{E}^+_{\mathbf{k},\alpha}$).
- The second term corresponds to the transition from the excited state $|e\rangle$ to the ground state $|g\rangle$. As expected, a photon is emitted as a result of this transition (due to the presence of the creation operator in the expression for $\mathbf{E}^-_{\mathbf{k},\alpha}$).
- The third term corresponds to the transition from the ground state $|g\rangle$ to the excited state $|e\rangle$. We expect a photon to be absorbed. Contrary to this expectation, the photon is in fact created (due to the presence of the creation operator in the expression for $\mathbf{E}^-_{\mathbf{k},\alpha}$).
- The forth term corresponds to the transition from the excited state $|e\rangle$ to the ground state $|g\rangle$. We expect a photon to be emitted. Contrary to this expectation, the photon is in fact annihilated (due to the presence of the annihilation operator in the expression for $\mathbf{E}^+_{\mathbf{k},\alpha}$).

One can see that the third and forth terms are nonresonant, these terms do not satisfy the energy conservation law. This fact allows one to neglect these terms in the interaction Hamiltonian given by (13.24). Another argument which supports this approximation comes from time-dependent perturbation theory. It is well-known that non-resonant transitions have negligibly small probabilities. This approximation is called the 'rotating wave approximation' (the name originates from the form of the interaction Hamiltonian in the reference frame rotating with the frequency of the electromagnetic field) and is widely used in quantum electrodynamics problems [89–94]. It can be shown that the neglected terms lead to small corrections called Bloch-Siegert shifts [103].

Therefore, the final expression for quantized electromagnetic field - two-level emitter (QEF-2LE) interaction Hamiltonian reads as

$$H_{INT} = -\sum_{\mathbf{k},\alpha} \left(|e\rangle \langle g| \, \mathbf{d}_{eg} \cdot \mathbf{E}^{+}_{\mathbf{k},\alpha} + |g\rangle \langle e| \, \mathbf{d}^{*}_{ge} \cdot \mathbf{E}^{-}_{\mathbf{k},\alpha} \right), \tag{13.26}$$

where the electric field operators $\mathbf{E}^{+}_{\mathbf{k},\alpha}$ and $\mathbf{E}^{-}_{\mathbf{k},\alpha}$ are given by (13.21)–(13.22) from the previous section.

13.3.2.4 Density Matrix Operator

The most general way to describe a system, whether it is isolated from the external environment or interacts with it, is based on utilizing the density matrix operator. In what follows we first introduce the basic concept of the density matrix operator and then show how using the master equation approach it is possible to calculate a stationary density matrix of a system in the presence of incoherent pumping and dissipation processes.

Let us consider an ensemble of N identical emitters in quantum states denoted by i and with corresponding wave functions Ψ^i. An average value of an observable O can be calculated for each of these emitters using corresponding operator $\hat{O}$. The statistic average over the whole ensemble is given by

$$\overline{\langle O \rangle} = \frac{\sum_{i=1}^{N} \left\langle \Psi^i \right| \hat{O} \left| \Psi^i \right\rangle}{N}. \tag{13.27}$$

The equation above contains two types of averaging—the quantum mechanical averaging, which is given by the matrix element, and statistical averaging, which is given by the sum of the observable value over the ensemble elements divided by the number of elements.

As all emitters in the ensemble are identical, each of them possess the same set of eigenstates φ_n. Thus, the total emitter's states Ψ^i can be expanded in terms of the emitter's eigenstates φ_n as follows

$$\left|\Psi^i\right\rangle = \sum_n C_n^i \left|\varphi_n\right\rangle, \tag{13.28}$$

where $C_n^i = \left\langle \varphi_n | \psi^i \right\rangle$ and $\sum_n \left|C_n^i\right|^2 = 1$. Substituting (13.28) into (13.27) one obtains

$$\overline{\langle O \rangle} = \sum_{m,n} \left(\frac{\sum_{i=1}^N C_n^{i*} C_m^i}{N} \right) O_{nm} = \sum_{m,n} \rho_{nm} O_{nm}, \tag{13.29}$$

where we have introduced a new important entity, the density matrix ρ_{nm}, which is given by

$$\rho_{nm} = \sum_{i=1}^N C_n^{i*} C_m^i / N = \overline{C_n^{i*} C_m^i}. \tag{13.30}$$

The density matrix contains all statistical information about the considered ensemble of emitters. It is easy to show that the density matrix is normalized

$$\mathrm{Tr}\{\hat{\rho}\} = \sum_n \rho_{nn} = \sum_{i=1}^N \sum_n C_n^{i*} C_n^i / N = \sum_{i=1}^N 1/N = 1.$$

Using the matrix multiplication rule (13.29) can be written in a shorter and more convenient form

$$\overline{\langle O \rangle} = \sum_{m,n} \rho_{mn} O_{nm} = \sum_n \left(\hat{\rho} \hat{O} \right)_{nn} = \mathrm{Tr}\{\hat{\rho} \hat{O}\}. \tag{13.31}$$

For instance, for the identity operator $\hat{1}$ using (13.31) one straightforwardly obtains

$$\overline{\langle 1 \rangle} = \sum_{n,m} \rho_{mn} \left\langle \varphi_n \right| \hat{1} \left| \varphi_m \right\rangle = \sum_{n,m} \rho_{mn} \delta_{nm} = \mathrm{Tr}\{\hat{\rho}\} = 1.$$

The representation of the density matrix operator in terms of expansion coefficients C_n^i is only one of many possible expansions. One can see that the final expression for the average value of an observable O is given by the trace of the density matrix operator. The trace of an operator is independent of the basis chosen in the Hilbert space. That means that the density matrix operator can be defined in a more general way. However, it is convenient to try to define the density matrix operator in terms of system eigenstates, but independently of any basis in the Hilbert space. One of the possible definitions is as follows

$$\hat{\rho} = \frac{1}{N} \sum_{i=1}^N \left|\Psi^i\right\rangle \left\langle \Psi^i \right|.$$

There are no restrictions on the states Ψ^i, these states can even be non-orthogonal, although it is usually not convenient. It is easy to show that if the basis of the eigenstates φ_n is chosen as the set of system eigenstates, this definition is equivalent to (13.30).

In order to give a more clear insight into the nature of the density matrix operator and re-express it in an even more convenient form we introduce the so-called 'projector operators' (similar to those discussed in Sect. 13.3.2.2)

$$\hat{\pi}_\chi = |\chi\rangle \langle\chi| .$$

When acting on a state ψ these operators give a projection of the state ψ in the direction of the state χ. For the expectation value of the projector operator $\hat{\pi}_\chi$ in a state ψ one can easily obtain

$$\left\langle \hat{\pi}_\chi \right\rangle = \langle\psi| \hat{\pi}_\chi |\psi\rangle = \langle\psi|\chi\rangle \langle\chi|\psi\rangle = |\langle\chi|\psi\rangle|^2 . \tag{13.32}$$

Equation (13.32) gives the probability to find the system, which was originally prepared in the state $|\psi\rangle$, in the state $|\chi\rangle$.

Let us now return to the ensemble of emitters. Since the trace of an operator is independent of the basis in which this operator is defined, for convenience we will use the basis of the emitters eigenstates φ_n. In this case for the expectation value of the projector operator $\hat{\pi}_\chi$ one obtains

$$\overline{\left\langle \hat{\pi}_\chi \right\rangle} = \mathrm{Tr}\{\hat{\pi}_\chi \hat{\rho}\} = \sum_n \langle\varphi_n|\chi\rangle \left\langle \chi \left| \hat{\rho} \right| \varphi_n \right\rangle = \sum_n \left\langle \chi \left| \hat{\rho} \right| \varphi_n \right\rangle \langle\varphi_n|\chi\rangle = \left\langle \chi \left| \hat{\rho} \right| \chi \right\rangle . \tag{13.33}$$

One can see that the probability of finding the ensemble of emitters in the state $|\chi\rangle$ is given by a diagonal element of the density matrix operator.

Now it is possible to make some generalization of the density matrix operator. Instead of defining the density matrix operator as a sum over all emitters states Ψ^i one can to use the sum over all states accessible to the ensemble elements

$$\hat{\rho} = \sum_j \left|\psi^j\right\rangle P(j) \left\langle\psi^j\right| . \tag{13.34}$$

Here $P(j)$ are the statistical weights which satisfy the requirement $\sum_j P(j) = 1$. A few paragraphs later, we explain the physical meaning of these coefficients in more details.

Using (13.33) and (13.34) we obtain the probability of finding the system in one of the states ψ^j which were used for the density matrix operator basis

$$\langle\psi^\alpha| \hat{\rho} |\psi^\alpha\rangle = \sum_j \left\langle\psi^\alpha|\psi^j\right\rangle P(j) \left\langle\psi^j|\psi^\alpha\right\rangle = \sum_j P(j) \left|\left\langle\psi^\alpha|\psi^j\right\rangle\right|^2 . \tag{13.35}$$

If the set of states $\left|\psi^j\right\rangle$ is orthonormal, (13.35) can be simplified in the following way

$$\langle\psi^\alpha|\,\hat{\rho}\,|\psi^\alpha\rangle = \sum_j P\,(j)\,\delta_{\alpha j} = P\,(\alpha)\,. \tag{13.36}$$

From the (13.36) one can see that the statistical weight $P\,(\alpha)$, in fact, defines the population of the state $|\psi^\alpha\rangle$ (i.e., probability that the state is occupied).

If the set $\left|\psi^j\right\rangle$ is not orthonormal, it is clearly not possible to obtain any simple relation between probabilities $\langle\psi^\alpha|\,\hat{\rho}\,|\psi^\alpha\rangle$ and statistical weights $P\,(\alpha)$.

13.3.2.5 Equation of Motion for the Density Matrix

Coherent coupling: the von Neumann equation for the density matrix

In Sect. 13.3.2.4 it was demonstrated that an average value of an observable O in an ensemble of emitters can be calculated using the system density matrix operator $\hat{\rho}$.

In the Schrödinger picture, all operators are time-independent and thus the time dynamics of the average should be hidden in the time dependence of the density matrix operator

$$\overline{\langle O_{\rm S}\rangle}_t = {\rm Tr}\{\hat{\rho}\,(t)\,\hat{O}_{\rm S}\},$$

where the index 'S' refers to the Schrödinger representation. It is clear that in order to be able to predict time dynamics of the system, an equation of motion for the density matrix operator is needed. Such an equation can be derived from the fact that the physical contents should not depend on whether the Schrödinger or Heisenberg picture is chosen for describing the system.

The density matrix operator $\hat{\rho}$ is defined as a sum of projections on a given set of states. In the Heisenberg picture the states are time-independent, though operators are time-dependent. In this case one can expect the density matrix operator to be defined by the initial state of the system. Comparing expressions for the observable averages in the Schrödinger and Heisenberg quantum mechanics descriptions we obtain

$$\overline{\langle O_{\rm S}\rangle}_t = {\rm Tr}\{\hat{\rho}\,(t)\,\hat{O}_{\rm S}\} = \overline{\langle O_{\rm H}\,(t)\rangle} = {\rm Tr}\{\hat{\rho}\,(t_0)\,\hat{O}_{\rm H}\,(t)\}, \tag{13.37}$$

where the index "H" refers to the Heisenberg representation. The evolution of operators in the Heisenberg picture can be related to the operators representation in the Schrödinger picture in the following way

$$\hat{O}_{\rm H}\,(t) = U^\dagger\,(t, t_0)\,\hat{O}_{\rm S} U\,(t, t_0)\,. \tag{13.38}$$

In (13.38) $U\,(t, t_0)$ is the evolution operator given by

$$U\,(t, t_0) = \exp\left[-i\hat{H}\,(t, t_0)\,/\hbar\right],$$

where $\hat{H}$ is the system Hamiltonian. Substitution of (13.38) into (13.37) results in

$$\mathrm{Tr}\{\hat{\rho}\,(t)\,\hat{O}_{\mathrm{S}}\} = \mathrm{Tr}\{\hat{\rho}\,(t_0)\,U^{\dagger}\,(t,t_0)\,\hat{O}_{\mathrm{S}}U\,(t,t_0)\}.$$

Using the cycling property of the trace operation the equation above can be rewritten as

$$\mathrm{Tr}\{\hat{\rho}\,(t)\,\hat{O}_{\mathrm{S}}\} = \mathrm{Tr}\{U\,(t,t_0)\,\hat{\rho}\,(t_0)\,U^{\dagger}\,(t,t_0)\,\hat{O}_{\mathrm{S}}\}. \tag{13.39}$$

From (13.39) one can easily obtain the following expression for the density matrix operator time evolution

$$\hat{\rho}\,(t) = U\,(t,t_0)\,\hat{\rho}\,(t_0)\,U^{\dagger}\,(t,t_0)\,. \tag{13.40}$$

Differentiation of (13.40) results in

$$i\hbar\frac{\partial\hat{\rho}\,(t)}{\partial t} = \left[i\hbar\frac{\partial U\,(t,t_0)}{\partial t}\right]\hat{\rho}\,(t_0)\,U^{\dagger}\,(t,t_0) - U\,(t,t_0)\,\hat{\rho}\,(t_0)\left[-i\hbar\frac{\partial U^{\dagger}\,(t,t_0)}{\partial t}\right]. \tag{13.41}$$

We simplify (13.41) using the fact that the evolution operator $U\,(t,t_0)$ satisfies the Schrödinger equation and obtain

$$i\hbar\frac{\partial\hat{\rho}\,(t)}{\partial t} = \hat{H}U\,(t,t_0)\,\hat{\rho}\,(t_0)\,U^{\dagger}\,(t,t_0) - U\,(t,t_0)\,\hat{\rho}\,(t_0)\,\hat{H}U^{\dagger}\,(t,t_0) = \hat{H}\hat{\rho}\,(t) - \hat{\rho}\,(t)\,\hat{H}. \tag{13.42}$$

Here (13.40) was used for the last step of the simplification. This equation of motion for the density matrix operator (mixed state) is called the 'von Neumann equation' [104]. It is an equivalent of the Schrödinger equation for the state vector (a pure state). The von Neumann equation can be written in a more compact form

$$\frac{\partial\hat{\rho}\,(t)}{\partial t} = \frac{i}{\hbar}\left[\hat{\rho}\,(t)\,,\hat{H}\right]. \tag{13.43}$$

It should be stressed that the von Neumann equation corresponds to the Schrödinger quantum mechanics description, where all operators are time-independent. In the Heisenberg quantum mechanics description, the density operator does not depend on time and is defined by the initial conditions.

Incoherent processes: the Master Equation with the Linblad terms

A correct description of a system which interacts with the external environment should include decoherence processes such as dissipation (decay) of particles to an external reservoir and income (pump) of particles from an external reservoir. In the case of the coupled 2LE-MC system these particles are either the MC photons, which can be supplied into the system, for instance, by the optical pumping, but eventually

leak out, or the 2LE excitations, which can experience nonradioactive transitions from the excited to the ground state.

The leaking out photons not only cause decoherence in the system, but also provide an external observer with valuable information about the field-matter interaction inside the MC. This stresses once more the importance of considering the decoherence processes.

In order to account for the described processes the equation of motion for the density matrix operator should be upgraded from the von Neumann equation [104] to the master equation in the Lindblad form [105]

$$\frac{\partial \rho}{\partial t} = \frac{i}{\hbar}[\rho, H_{JC}] + \mathscr{L}_P^{MC}\rho + \mathscr{L}_\gamma^{MC}\rho + \mathscr{L}_\gamma^{2LE}\rho, \tag{13.44}$$

In (13.44) $H_{JC} = H_{MC} + H_{2LE} + H_{INT}$ is the full Hamiltonian of the coupled 2LE-MC system first introduced by *Jaynes and Cummings* [106] and now commonly called 'Jaynes-Cummings Hamiltonian' with H_{MC} given by (13.12), H_{2lE} given by (13.19), and H_{INT} given by (13.26). The operators $\mathscr{L}_P^{MC}$, $\mathscr{L}_\gamma^{MC}$, and $\mathscr{L}_\gamma^{2LE}$ are the so-called Lindblad terms. In the explicit form these three terms are given by

$$\mathscr{L}_P^{MC}\rho = \frac{P_{MC}}{2}(2a^\dagger \rho a - aa^\dagger \rho - \rho aa^\dagger + 2a\rho a^\dagger - a^\dagger a\rho - \rho a^\dagger a),$$

$$\mathscr{L}_\gamma^{MC}\rho = \frac{\gamma_{MC}}{2}(2a\rho a^\dagger - a^\dagger a\rho - \rho a^\dagger a),$$

and

$$\mathscr{L}_\gamma^{2LE}\rho = \frac{\gamma_{2LE}}{2}(2\sigma\rho\sigma^\dagger - \sigma^\dagger\sigma\rho - \rho\sigma^\dagger\sigma),$$

where P_{MC} is the intensity of the MC pumping, γ_{MC}, γ_{2LE} are the decaying rates of the MC and 2LE excitation, $a^\dagger$, a are MC creation and annihilation operators (the same that enter H_{MC}, see (13.12)), and $\sigma^\dagger$, σ are 2LE creation and annihilation operators (the same that enter H_{2LE}, see (13.19)).

In the scope of this chapter we are not interested in particular pumping and dissipation mechanisms which are present in various experimental systems. We only note that different pumping and dissipation process were studied by a number of authors, see, e.g., [107, 108]. For our further considerations only the fact that all such processes are well-described by the introduced master equation with Lindblad terms is important.

Mainly, there are two different derivations of the Lindblad terms in (13.44) which can be found in the literature. The first derivation is based on a microscopic study of the system coupling to an external reservoir, which is represented as a bath of oscillators [94, 109]. The second procedure utilizes the Monte-Carlo method and quantum jumps. This approach is preferred in [89, 90] as it is closer to the quantum information and measurement theories. In this case, the time evolution of the system is understood as a sequence of coherent periods of the Hamiltonian dynamics and

incoherent events taking place with some probability. In this picture the microscopic origin of the incoherent processes is not considered and they are just assumed to be present with a given probability.

All together, the Lindblad terms $\mathscr{L}_P^{MC}$, $\mathscr{L}_\gamma^{MC}$, and $\mathscr{L}_\gamma^{2LE}$ can be put in the form of a total superoperator $\mathscr{L}$

$$\frac{\partial \rho}{\partial t} = \frac{i}{\hbar}[\rho, H] + \mathscr{L}\rho.$$

Due to the balance between the pump and decay, after some time a steady state is established. We denote the density matrix which describes such steady state by ρ^{SS}. Throughout this chapter we consider only such values of the parameters P_{MC}, γ_{MC}, and γ_{2LE} which lead to establishing of some steady state with non-divergent populations. We do not discuss exact experimental conditions which result in a particular combination of these parameters and only note that all the considered values of P_{MC}, γ_{MC}, and γ_{2LE} correspond to attainable experimental systems.

13.3.3 Calculating Optical Transitions: Electric Dipole Approximation

Let us consider a system described by the full Hamiltonian $H(t) = H^0 + H'(t)$ where H^0 is the stationary (time-independent) Hamiltonian with eigenfunctions $|\psi_j\rangle$ satisfying

$$H^0 |\psi_j\rangle = \varepsilon_j |\psi_j\rangle,$$

with $\varepsilon_j = \hbar\omega_j$, and $H'(t)$ is the time-dependant perturbation given by

$$H'(t) = \tilde{H}' e^{-i\omega t},$$

where ω is the frequency of the exciting radiation. If perturbation is weak, it only causes transitions between the states $|\psi_j\rangle$. According to the first order time-dependant perturbation theory the rate of transitions between two different states $|\psi_i\rangle$ (initial state) and $|\psi_f\rangle$ (final state) is given by

$$T_{if} = \frac{1}{\hbar^2} \left|\langle \psi_f | H'(t) | \psi_i \rangle\right|^2 \frac{\sin^2\left[\frac{\tau}{2}\left(\omega_f - \omega_i - \omega\right)\right]}{\tau\left[\frac{1}{2}\left(\omega_f - \omega_i - \omega\right)\right]^2}.$$

Here τ is the time which corresponds to the broadening of the optical transitions and which can be defined as $\tau \geq 2\pi/\Delta\omega$ where $\Delta\omega$ is the linewith of the excitation radiation. If $\Delta\omega$ is small, τ becomes large and using

$$\delta(\xi) = \lim_{x\to 0} \frac{x}{\pi} \frac{\sin^2(\xi/x)}{\xi^2}$$

we obtain the rate of transitions between the system eigenstates $|\psi_i\rangle$ and $|\psi_f\rangle$ given by Fermi's golden rule

$$T_{if} = \frac{2\pi}{\hbar} \left|\langle\psi_f| H'(t) |\psi_i\rangle\right|^2 \delta(\varepsilon_f - \varepsilon_i - \hbar\omega). \tag{13.45}$$

The Hamiltonian operator of an electron interacting with electromagnetic field is given by

$$H = \frac{1}{2m}(\mathbf{p} + \frac{q}{c}\mathbf{A})^2 = H^0 + \frac{q}{2mc}(\mathbf{A}\cdot\mathbf{p} + \mathbf{p}\cdot\mathbf{A}) + \frac{1}{2m}\left(\frac{q}{c}\right)^2 \mathbf{A}\cdot\mathbf{A}, \tag{13.46}$$

where $H^0 = \mathbf{p}/2m$ is the Hamiltonian of the unperturbed system, m is the electron mass, $\mathbf{p}$ is the electron momentum operator, and $\mathbf{A}$ is the electromagnetic field vector potential.

The vector potential of a plane electromagnetic wave, hitting the sample at normal incidence, can be chosen as

$$\mathbf{A} = \mathbf{A_0}\cos(\mathbf{Qr} - \omega t),$$

where $\mathbf{Q}$ is the field wave vector and $\mathbf{r}$ is the position vector. The electric field of the perturbing radiation is calculated as the time derivative of the vector potential

$$\mathbf{E}(\mathbf{r}, t) = \frac{1}{c}\frac{\partial \mathbf{A}(\mathbf{r}, t)}{\partial t}.$$

In the Coulomb gauge the vector potential of a sourceless electromagnetic field in vacuum satisfied $\nabla\cdot\mathbf{A} = 0$ and therefore

$$[\mathbf{A}, \mathbf{p}] = i\hbar\nabla\cdot\mathbf{A} = 0.$$

The ratio of the third to the second term in (13.46) can be written in the following way

$$\frac{e}{c}\frac{A}{p} = \frac{eE}{\omega p} \approx \frac{e}{\omega p}\left(\frac{8\pi S}{c}\right)^{1/2} \tag{13.47}$$

where E is the magnitude of the electric field associated with the perturbing radiation and S is the Poynting vector, which gives energy flux density of the electromagnetic field (energy per time per unit area). Expression in (13.47) is much less than unity for the values of S up to $10^{12}\,\mathrm{W/m^2}$. For most material such field intensities are higher than the material damage threshold. Thus, the third term in (13.46) can be safely neglected

$$H = H^0 + \frac{q}{mc}(\mathbf{A}\cdot\mathbf{p}) + \frac{1}{2m}\left(\frac{q}{c}\right)^2 \mathbf{A}\cdot\mathbf{A} \approx H^0 + \frac{q}{mc}(\mathbf{A}\cdot\mathbf{p}).$$

The second term in this equation can be easily expressed as $H_+ e^{-i\omega t} + H_- e^{i\omega t}$ with $H_\pm$ given by

$$H_\pm = \frac{q}{2mc} e^{\pm i\mathbf{Qr}} \mathbf{A_0} \cdot \mathbf{p} = \frac{q}{2mc} |\mathbf{A}_0| \, e^{\pm i\mathbf{Qr}} \, (\mathbf{e} \cdot \mathbf{p}) \,,$$

where we have introduced the radiation polarization vector $\mathbf{e}$ and the vector $\mathbf{r}$ is taken at the position of the electron.

To simplify calculations we use the dipole approximation, which assumes that $\mathbf{Qr} \ll 1$ and thus $e^{\pm i\mathbf{Qr}} \approx 1$. Within this approximation $H_\pm$ becomes

$$H_\pm = \frac{q}{2mc} |A_0| \, (\mathbf{e} \cdot \mathbf{p}) \,. \tag{13.48}$$

Substituting (13.48) into (13.45) (the Fermi's golden rule) we get the final expression for the rate of optical transitions between the states $|\psi_i\rangle$ and $\left|\psi_f\right\rangle$ caused by the perturbing electromagnetic field

$$T_{if} = \frac{2\pi}{\hbar} \left(\frac{q}{2mc}\right)^2 |A_0|^2 \left|\left\langle \psi_f \right| \mathbf{e} \cdot \mathbf{p} \left| \psi_i \right\rangle\right|^2 \delta(\varepsilon_f - \varepsilon_i - \hbar\omega).$$

13.4 Quantum Rings in Classical Electromagnetic Fields. Electric Dipole Moment Oscillations and Terahertz Transitions in Aharonov-Bohm Quantum Rings

13.4.1 Introduction

Recently a lot of attention has been turned towards non-simply-connected nanostructures, quantum rings, which have been obtained in various semiconductor systems [9, 10, 17]. The fascination in quantum rings is partially caused by a wide variety of purely quantum mechanical effects, which are observed in ring-like nanostructures. The star amongst them is the Aharonov-Bohm effect [1, 39], in which a charged particle is influenced by a magnetic field away from the particle's trajectory, resulting in magnetic-flux-dependent oscillations of the ring-confined particle energy. The oscillations of the single-particle energy are strongly suppressed by distortion of the ring shape or by applying an in-plane (lateral) electric field, thus reducing the symmetry of the system [110, 111] (see Fig. 13.1). However, there are other physical quantities, which might have even more pronounced magneto-oscillations when the symmetry of the ring is reduced. For example, in the presence of a lateral electric field exceeding a particular threshold it is possible to switch the ground state of an exciton in an Aharonov-Bohm ring from being optically active (bright) to optically inactive (dark) [18, 62]. Another hitherto overlooked phenomenon is the flux-periodic change of an electric dipole moment of a quantum ring, which is the main subject of this work.

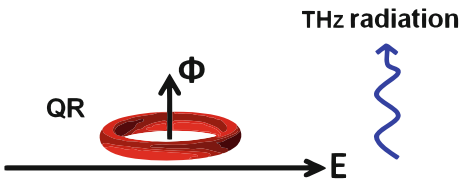

Fig. 13.1 An Aharonov-Bohm quantum ring pierced by a magnetic flux and subjected to a lateral electric field (from [3])

This section is organized as follows. In Sect. 13.4.2 we calculate the single-electron energy spectrum of an infinitely-narrow Aharonov-Bohm ring subjected to a lateral electric field. In Sect. 13.4.3 we consider magneto-oscillations of the ring's electric dipole moment and study their electric field and temperature dependence. Matrix elements of the dipole moment calculated between different states define selection rules for optical transitions. For experimentally attainable quantum rings these transitions occur at THz frequencies. In Sect. 13.4.4 we discuss optical selection rules for intraband optical transitions and show how the polarization properties of the associated THz radiation can be tuned by external electric and magnetic fields. Section 13.4.5 contains a brief discussion of the potential applications of the predicted phenomena.

13.4.2 Energy Spectrum of an Infinitely-Narrow Quantum Ring

13.4.2.1 Magneto-Oscillations of the Quantum Ring Eigenenergies

The Hamiltonian of an electron confined in an infinitely narrow QR pierced by magnetic flux Φ depends only on the polar coordinate φ

$$H_\Phi = -\frac{\hbar^2}{2M_eR^2}\frac{\partial^2}{\partial\varphi^2} - \frac{i\hbar e}{2\pi}\frac{\Phi}{M_eR^2}\frac{\partial}{\partial\varphi} + \frac{e^2\Phi^2}{8\pi^2M_eR^2}\,, \tag{13.49}$$

where M_e is the electron effective mass and R is the QR radius. The 2π-periodic eigenfunctions of the Hamiltonian defined by (13.49) are

$$\psi_m(\varphi) = \frac{e^{im\varphi}}{\sqrt{2\pi}}\,, \tag{13.50}$$

and the corresponding eigenvalues are given by

$$\varepsilon_m(f) = \frac{\hbar^2(m+f)^2}{2M_eR^2} = (m+f)^2\,\varepsilon_1(0)\,. \tag{13.51}$$

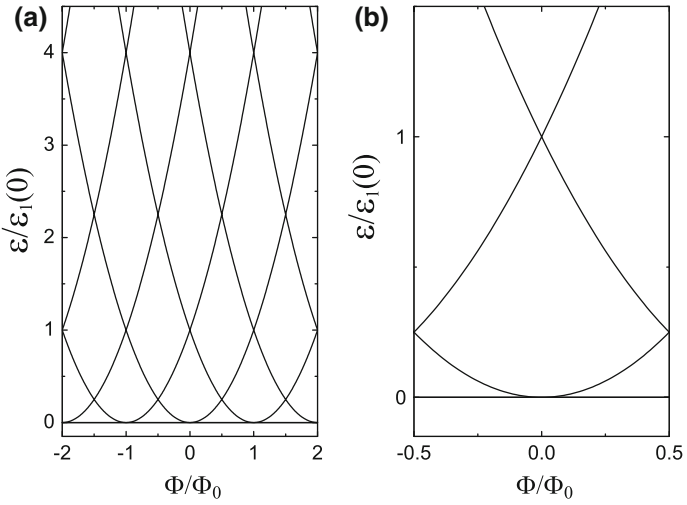

Fig. 13.2 **a** The energy spectrum of an infinitely narrow quantum ring pierced by a magnetic flux Φ. Each parabola corresponds to a particular value of the electron angular momentum m. The electron energies ε are plotted versus the number of flux quanta Φ/Φ_0. **b** Expanded view on a smaller energy scale (from [3])

Here $m = 0, \pm 1, \pm 2 \ldots$ is the angular momentum quantum number, and $f = \Phi/\Phi_0$ is the number of flux quanta piercing the QR ($\Phi_0 = h/e$). The electron energy spectrum defined by (13.51) is plotted in Fig. 13.2. It exhibits oscillations in magnetic flux with the period equal to Φ_0, known as Aharonov-Bohm oscillations [1, 9]. One can see intersections (degeneracy) of the energy levels with different angular momenta, when Φ is equal to an integer number of $\Phi_0/2$. Optical selection rules allow transitions between states with angular momentum quantum numbers different by unity ($\Delta m = \pm 1$). For typical nanoscale rings [9, 10] the energy scale of the inter-level separation, $\varepsilon_1(0) = \hbar^2/2M_eR^2$, is in the THz range. When Φ exceeds $\Phi_0/2$ the electron possesses a non-zero angular momentum in the ground state.

13.4.2.2 Energy Spectrum in the Presence of a Lateral Electric Field

Applying an in-plane electric field **E** removes the circular symmetry of the system. An additional term corresponding to the electric field appears in the Hamiltonian [2, 3], which acquires a form

$$H = H_\Phi + eER\cos\varphi. \tag{13.52}$$

Now the angle φ is counted from the direction of the electric field (geometry of the problem is shown in Fig. 13.3). The field mixes electron states with different angular momentum, which is not a good quantum number anymore. An eigenfunction of the

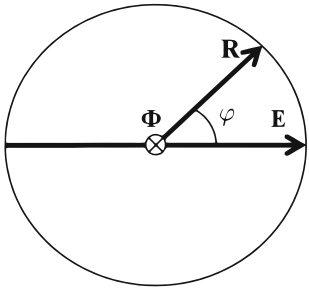

Fig. 13.3 Relative directions of the external electric field **E** and the electron position vector **R** (from [3])

Hamiltonian (13.52), which maintains the 2π-periodicity in φ, can be written as a linear combination of the wavefunctions (13.50)

$$\Psi_n(\varphi) = \sum_m c_m^n e^{im\varphi}. \tag{13.53}$$

Substituting the wavefunction (13.53) into the Schrödinger equation with the Hamiltonian (13.52), multiplying the resulting expression by $e^{-im\varphi}$ and integrating with respect to φ leads to an infinite system of linear equations for the coefficients c_m^n

$$\left[(m+f)^2 - \lambda_n\right] c_m^n + \beta\left(c_{m+1}^n + c_{m-1}^n\right) = 0\,, \tag{13.54}$$

where $\beta = eER/2\varepsilon_1(0)$ and $\lambda_n = \varepsilon_n/\varepsilon_1(0)$, with ε_n being the nth eigenvalue of the Hamiltonian (13.52). It is apparent from (13.54) that all the properties of the ring are periodic in magnetic flux. Therefore, it is sufficient to consider $0 \le f \le 1/2$, whereas the calculations for other values of f can be performed by shifting m in (13.54) by an integer number. Interestingly, exactly the same analysis is applicable to a nanohelix subjected to an electric field normal to its axis [112–114]. For a helix the role of magnetic flux is played by the electron momentum along the helical line.

It should be emphasized that we consider a single-electron problem and we are interested only in a few low-energy states. This treatment is relevant to nanoscale-sized semiconductor QRs or type-II QDs discussed in [9, 10, 17, 18, 36, 62] and neglects the many-body effects which are known to influence Aharonov-Bohm oscillations in mesoscopic rings [34, 35]. The energy levels ε_n as well as the coefficients c_m^n can be found by cutting off the sum in (13.53) at a particular value of $|m|$. The results of the numerical diagonalization of the matrix corresponding to the system of linear equations (13.54), with a cut-off value of $|m| = 11$, are plotted in Fig. 13.4. The same cut-off value was chosen in all numerical calculations presented in this section, since a further increase of the matrix size does not lead to any noticeable change in the results for the three lowest-energy states, which we are interested in.

In small electric fields, $eER \ll \hbar^2/2M_eR^2$, a significant change in the QR energy spectrum occurs only for the ground and two lowest excited states, when Φ is close

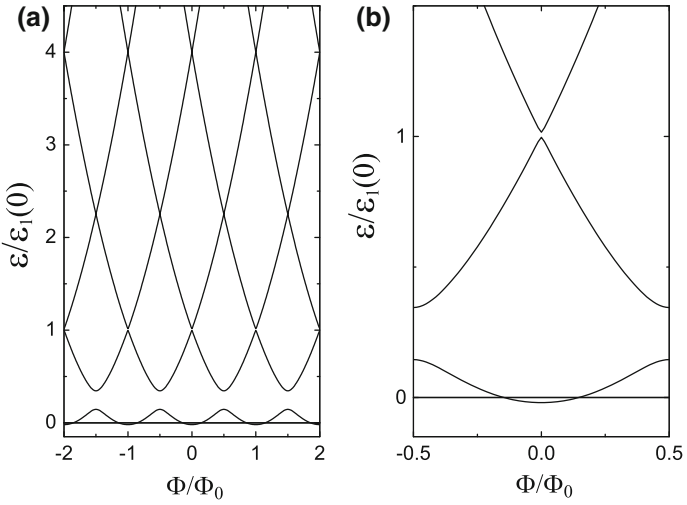

Fig. 13.4 **a** The energy spectrum of an infinitely narrow quantum rings of radius R pierced by a magnetic flux Φ and subjected to an in-plane electric field $E = 0.2\varepsilon_1(0)/eR$. The electron energies ε are plotted versus the number of flux quanta Φ/Φ_0. **b** Expanded view on a smaller energy scale (from [3])

to an integer number of $\Phi_0/2$ (the points of degeneracy in the absence of the electric field). The most prominent change is associated with the linear in electric field splitting between the ground and first excited states for half-integer f. The less pronounced quadratic in electric field splitting between the first and second excited states occurs for integer f. These splittings can be easily understood with the help of perturbation theory, as there is a non-zero matrix element of $eER\cos\varphi$ between the ground and the first excited state, whereas the two excited states are only repelled in the second order via the ground state. It is shown in Appendix 13.6.2, these essential features of the low-energy spectrum are fully captured by considering small-size matrices, which allow an analytical treatment: a two-by-two matrix for half-integer f and a three-by-three matrix for integer f.

As one can see from Fig. 13.4, energy oscillations in the ground state are strongly suppressed even for $eER = 0.2\hbar^2/2M_eR^2$. This suppression is a major source of difficulty in spectroscopic detection of Aharonov-Bohm oscillations. However, as we show in the next two sections, apart from the ground-state energy there are other physical quantities, such as a dipole moment of the QR and polarization properties of the inter-level transitions, which have highly-pronounced magneto-oscillations when the symmetry of the ring is reduced.

13.4.3 Magneto-Oscillations of the Quantum Ring Electric Dipole Moment

In this section we consider Aharonov-Bohm oscillations of the QR electric dipole moment. If an electron occupies the nth state of the neutral single-electron QR with a uniform positive background, or if a positive charge $+e$ is placed at the center of the QR (geometry of the problem is shown in Fig. 13.3), the projection of the dipole moment on the direction of the lateral electric field [2, 3] is given by

$$P_n = eR \int |\Psi_n|^2 \cos\varphi \, d\varphi. \tag{13.55}$$

Substituting the wavefunction (13.53) into (13.55) yields the following expression for P_n

$$P_n = \frac{eR}{2} \sum_m c_m^n \left(c_{m-1}^n + c_{m+1}^n \right), \tag{13.56}$$

where the coefficients c_m^n can be found from the system of linear equations (13.54). In the absence of an electric field, each of the electron states is characterized by a particular value of angular momentum. The electron charge density is spread uniformly over the ring and there is no net dipole moment. The same result is given by (13.56)—all the products $c_m^n c_{m\pm1}^n$ entering (13.56) vanish for any value of n resulting in the QR dipole moment being equal to zero. Let us now consider what happens to the ground state's dipole moment in the presence of a weak electric field, $eER \ll \hbar^2/2M_eR^2$. For $\Phi = 0$, the ground state is a practically pure $m = 0$ state with a tiny admixture of $m \neq 0$ wavefunctions. However, the situation changes drastically near the points of degeneracy when the magnetic flux through the QR is equal to any odd integer of $\Phi_0/2$. For a half-integer flux, even an infinitely small field modifies entirely the wavefunction of the ground state. As shown in Appendix 13.6.2, when $f = 1/2$ the ground state wavefunction angular dependence is well-described by $\sin(\varphi/2)$. Thus, the ground state electron density distribution becomes shifted to one side of the ring, in the opposite direction to the applied electric field. Such a shift is energetically favorable and results in the value of the dipole moment being close to eR. Simultaneously, the first excited state wavefunction angular dependence becomes well-described by $\cos(\varphi/2)$. For the excited state, the electron is localized near the opposite side of the ring resulting in a dipole moment of the same magnitude as for the ground state but with the opposite sign.

The electron density distributions in the ground and first excited states, when $\Phi = 0$ and $\Phi = \Phi_0/2$ and the degeneracy is lifted by a weak electric field, is shown in Fig. 13.5. With changing magnetic flux the ground state density oscillates with a period Φ_0 from an unpolarized to a strongly polarized distribution, resulting in the corresponding dipole moment oscillations. However, the oscillations of the total dipole moment of the QR should be partially compensated if the first excited state, which carries a dipole moment opposite to the ground state's dipole moment for a

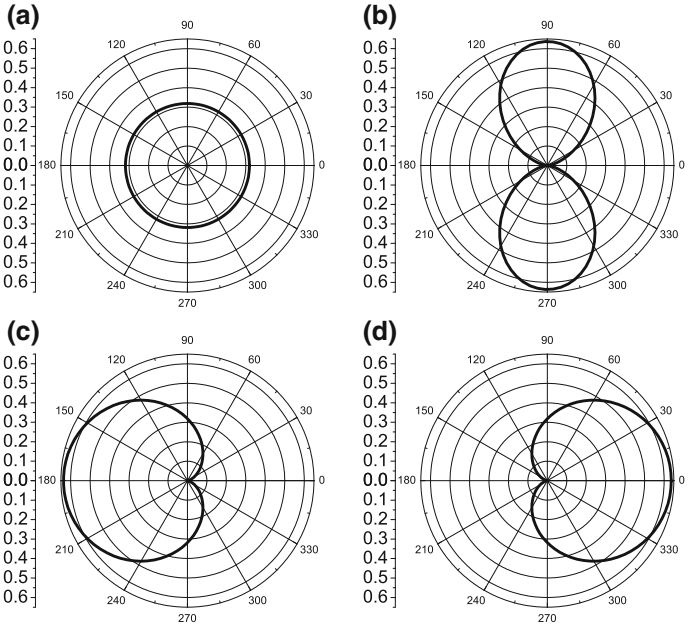

Fig. 13.5 A polar plot of the electron density distribution in a single-electron quantum ring pierced by the magnetic flux $\Phi = 0$ (top row) and $\Phi = \Phi_0/2$ (bottom row) and subjected to a weak in-plane electric field, $E \ll \varepsilon_1(0)/eR$: **a** and **c** for the electron ground state; **b** and **d** for the first excited state (from [3])

flux equal to an odd number of $\Phi_0/2$, is also occupied due to a finite temperature. The effect of temperature T can be taken into account by thermal averaging over all states

$$\langle P \rangle = \frac{\sum_n P_n \exp\left(-\varepsilon_n / k_{\mathrm{B}} T\right)}{\sum_n \exp\left(-\varepsilon_n / k_{\mathrm{B}} T\right)}. \tag{13.57}$$

The results of numerical calculations, using (13.57), for several temperature values are shown in Fig. 13.6. The dipole moment oscillations, which are well-pronounced for $k_{\mathrm{B}} T \ll eER$, become suppressed when the temperature increases.

In this work we consider the limit of weak electric field only. Higher fields, $eER > \hbar^2/2M_e R^2$, localize the ground state electron near one side of the ring even in the absence of a magnetic field and the change of magnetic flux through the QR can no longer influence the electron density distribution. For all values of Φ the ground state wavefunction consists of a mixture of functions with different angular momenta, ensuring that this state is always strongly polarized. The suppression of the dipole moment oscillations with increasing electric field can be seen in Fig. 13.7 where the upper curves, corresponding to higher electric fields and higher dipole moments, exhibit less pronounced oscillations. The energy oscillations for several lowest states are known to be completely suppressed in strong electric fields [111].

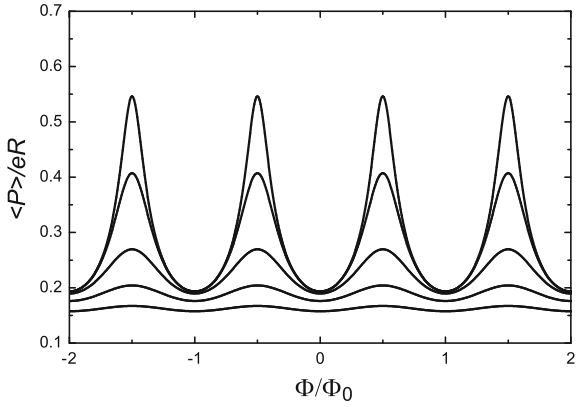

Fig. 13.6 Magneto-oscillations of the dipole moment of a ring at various temperatures for $E = 0.2\varepsilon_1(0)/eR$. Different curves correspond to different temperatures in the range from $T = 0.01\varepsilon_1(0)/k_{\mathbf{B}}$ to $T = 0.41\varepsilon_1(0)/k_{\mathbf{B}}$ with the increment $0.1\varepsilon_1(0)/k_{\mathbf{B}}$. The upper curve corresponds to $T = 0.01\varepsilon_1(0)/k_{\mathbf{B}}$ (from [3])

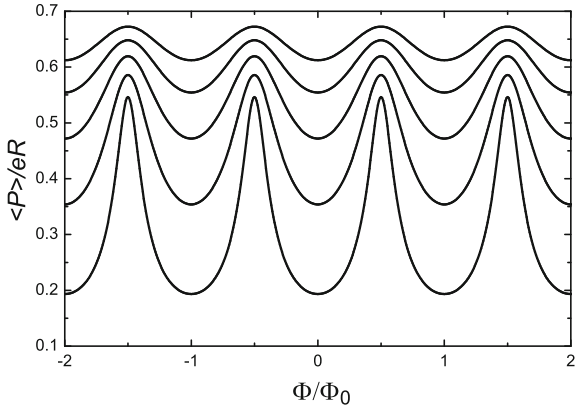

Fig. 13.7 Magneto-oscillations of the dipole moment of a ring at various magnitudes of the in-plane electric field for $T = 0.01\varepsilon_1(0)/k_{\mathrm{B}}$. Different curves correspond to different magnitudes of the electric field in the range from $E = 0.2\varepsilon_1(0)/eR$ to $E = 1.0\varepsilon_1(0)/eR$ with the increment $0.2\varepsilon_1(0)/eR$. The upper curve corresponds to $E = 1.0\varepsilon_1(0)/eR$ (from [3])

At this point it is instructive to discuss conditions needed for an experimental observation of electric dipole moment magneto-oscillations in QRs. A typical radius for experimentally attainable QRs [9, 10, 17] is $R \simeq 20\,\mathrm{nm}$. This gives the characteristic energy scale of the inter-level separation $\varepsilon_1(0) \simeq 2\,\mathrm{meV}$ (corresponding to 0.5THz) for an electron of effective mass $M_e = 0.05m_e$. For a ring with $R = 20\,\mathrm{nm}$, the magnitude of a magnetic field producing a flux $\Phi = \Phi_0$ is $B \simeq 3\,\mathrm{T}$. Therefore, a further decrease of the QR radius would require magnetic fields which are hard to achieve. A typical electric field needed for pronounced dipole moment oscillations is $E = 0.1\varepsilon_1(0)/eR \simeq 10^4\,\mathrm{V/m}$, which can be easily created. By far the most difficult condition to be satisfied is the requirement on the temperature regime, $T < eER/k_{\mathrm{B}}$. For the discussed electric field and ring radius this condition becomes $T < 2\,\mathrm{K}$. In principle such temperatures can be achieved in laboratory experiments and magneto-oscillations can be detected, for example, in capacitance measurements. However, for practical device applications, such as quantum-ring-based magnetometery, higher temperatures are desirable. In the next section we consider a process, which is less sensitive to the temperature-induced occupation of excited states.

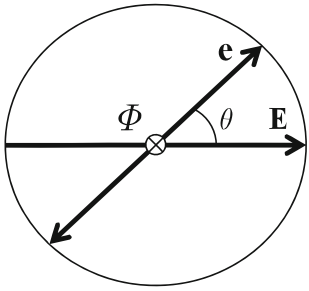

Fig. 13.8 Relative directions of the external electric field **E** and the projection **e** of the THz radiation polarization vector onto the quantum ring's plane (from [3])

13.4.4 Terahertz Transitions and Optical Anisotropy in Quantum Rings

In this section we study the influence of the in-plane electric field on polarization properties of radiative inter-level transitions in Aharonov-Bohm QRs. We restrict our consideration to linearly-polarized radiation and dipole optical transitions only.[1] The case of circular polarization is briefly discussed at the end of the section.

The transition rate T_{if} between the initial (i) and final (f) electron states is governed by the matrix element $P_{if} = \langle f|\mathbf{e}\hat{\mathbf{P}}|i\rangle$, where $\hat{\mathbf{P}}$ is the dipole moment operator and **e** is the projection of the radiation polarization vector onto the plane of the QR. For the model of an infinitely-narrow QR

$$P_{if}(\theta) = eR \int \Psi_f^* \Psi_i \cos(\theta - \varphi)\, d\varphi, \tag{13.58}$$

where θ is the angle between the vector **e** and the in-plane electric field **E**. The geometry of the problem is shown in Fig. 13.8.

Substituting the electron wavefunctions Ψ_i and Ψ_f, given by (13.53), into (13.58) yields

$$T_{if} \sim P_{if}^2(\theta) = P_{if}^{-2} + P_{if}^{+2} - 2P_{if}^- P_{if}^+ \cos 2\theta, \tag{13.59}$$

where

$$P_{if}^- = \frac{eR}{2}\left|\sum_m c_m^f c_{m-1}^i\right| \tag{13.60}$$

and

$$P_{if}^+ = \frac{eR}{2}\left|\sum_m c_m^f c_{m+1}^i\right|. \tag{13.61}$$

[1] For the theoretical background on the electric dipole approximation for optical transitions please see Sect. 13.3.3 of this chapter.

The double angle 2θ entering (13.59) ensures that the transition rate does not depend on the sign of **e**.

Let us consider transitions between the ground state and the first excited state of the Aharonov-Bohm QR in the limit of a weak in-plane electric field, $eER \ll \hbar^2/2M_eR^2$. Away from the points of degeneracy the ground and the first excited states are characterized by a particular value of m and either P_{if}^- or P_{if}^+ given by (13.60)–(13.61) vanishes. As a result, the angular dependence in (13.59) disappears and the transitions have no linear polarization. The picture changes drastically when Φ is equal to an integer number of $\Phi_0/2$. Then $P_{if}^- = P_{if}^+$ and therefore the rate of transitions induced by the radiation polarized parallel to the direction of the in-plane electric field ($\theta = 0$) is equal to zero, $T_{if} = T_\parallel = 0$. Simultaneously $T_\perp$, the rate of transitions induced by the light polarized perpendicular to the direction of the in-plane electric field ($\theta = \pi/2$), reaches its maximum possible value. This leads to the strong optical anisotropy of the system. The results of the calculations for the whole range of Φ are shown in Fig. 13.9. Very sharp peaks at Φ equal to an integer number of Φ_0 are the result of splitting between the first and second excited states, which were degenerate with energy $\varepsilon_1(0)$ in the absence of an external electric field (see Fig. 13.4). This splitting occurs in the second order in eER and the spectacular sharpness of the peaks is due to the very fast change in the electron first and second excited states wavefunctions when one moves away from the point of degeneracy (for details see Appendix 13.6.2). The optical transitions between the electron ground and second excited states are also linearly polarized, but with $\theta = 0$, so that the polarization of these transitions is normal to the polarization of transitions between the electron ground and first excited states. Because these two peaks are very closely separated for $\Phi = 0$, the polarization effects are strongly suppressed if the finite linewidth of the radiation is taken into account.

In the case of circularly polarized light, the degree of polarization oscillates as well. Inter-level transitions between the 'pure' states, characterized by the definite angular momentum values differing by one, are either right-hand or left-hand polarized. However, one can easily see that transitions involving the states, which are strongly

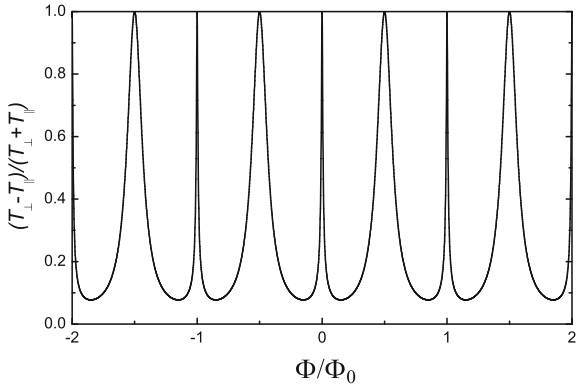

Fig. 13.9 Magneto-oscillations of the degree of polarization for the transitions between the ground state and the first excited state. Here $T_\parallel$ and $T_\perp$ correspond to the intensities of transitions polarized parallel (**e** ∥ **E**) and perpendicular (**e** ⊥ **E**) to the direction of the in-plane electric field, respectively (from [3])

'mixed' when the flux is an integer number of $\Phi_0/2$, have the same probabilities for both circular polarizations. Thus, the magnetic-field-induced optical chirality of QRs oscillates with the flux.

The total probabilities of the inter-level transitions indeed depend on the populations of the states involved. However, the discussed oscillations of the degree of polarization do not depend on temperature as the selection rules for the optical transitions are temperature-independent. This effect allows Aharonov-Bohm rings to be used as room-temperature polarization-sensitive detectors of THz radiation or optical magnetometers.

13.4.5 Results and Discussion

It is demonstrated that a lateral electric field, which is known to suppress Aharonov-Bohm oscillations in the ground state energy spectrum of a QR, results in strong oscillations of other physical characteristics of the system. Namely, the electric-field-induced dipole moment oscillates as a function of the magnetic flux piercing the QR, with pronounced maxima when the flux is equal to an odd number of one half of the flux quantum. This effect is caused by lifting the degeneracy of states with different angular momentum by arbitrary small electric fields. It should be emphasized that the discussed effect is not an artifice of the infinitely-narrow ring model used in the calculations, but it persists in finite-width rings in a uniform magnetic field. Indeed, the essential feature required for this effect is the degeneracy of the states with the angular momenta differing by one at certain magnetic field values, which is known to take place for finite-width rings as well [57–60, 115].

Future observation of the dipole moment magneto-oscillations would require careful tailoring of the QR parameters and experiment conditions. For example, the size of the QR should not exceed the electron mean free path but should be large enough so that, for experimentally attainable magnetic fields, the flux through the ring is near the flux quantum. The electric field should not be too large to avoid polarizing the QR strongly in the absence of a magnetic field, but it should be large enough to achieve a splitting between the ground and first excited states exceeding $k_B T$. Estimates presented in this section show that all these conditions can be met in existing QR systems. However, the temperature constraint constitutes the major obstacle for any potential applications outside the low-temperature laboratory.

The temperature restrictions are less essential for another predicted effect—giant magneto-oscillations of the polarization degree of radiation associated with inter-level transitions in Aharonov-Bohm QRs. Notably, these transitions for the QRs satisfying the remaining constraints should occur at THz frequencies. Creating reliable, portable and tunable sources of THz radiation is one of the most formidable problems of contemporary applied physics. The unique position of the THz range in between the frequencies covered by existing electronic or optical mass-produced devices results in an unprecedented variety of ideas aiming to bridge the so-called 'THz gap'. For example, the proposed methods of down-conversion of optical exci-

tation range from creating ultra-fast saturable absorbers [116] to utilizing magnetic-field-induced energy gap in metallic carbon nanotubes [117–120] to recent proposals of exciting THz transitions between exciton-polariton branches in semiconductor microcavities [121–123]. Arguably, the use of QRs for THz generation and detection has its merits, since their electronic properties can be easily tuned by external fields. The following scheme for using Aharonov-Bohm QRs as tuneable THz emitters can be proposed. Inversion of population in semiconductor QRs or type II QDs can be created by optical excitation across the semiconductor gap. Angular momentum and spin conservation rules do not forbid the creation of an electron in the first excited state as long as the total selection rules for the whole system, consisting of an electron-hole pair and a photon causing this transition, are satisfied. Terahertz radiation will be emitted when the electron undergoes a transition from the excited to the ground state of the QR. As was shown in the previous sections both the frequency and polarization properties of this transition can be controlled by external magnetic and electric fields.

Other potential applications of the discussed effects are in the burgeoning areas of quantum computing and cryptography. The discussed mixing of the two states, which are degenerate in the absence of electric field, is completely controlled by the angle between the in-plane field and a fixed axis. This brings the potential possibility for creating nanoring-based qubits, which do not require weak spin-orbit coupling between the electric field and electron spin. Arrays of the Aharonov-Bohm QRs can also be used for polarization sensitive single-photon detection, which is essential for quantum cryptography.

13.5 Quantum Rings in Quantized Electromagnetic Fields. Aharonov-Bohm Quantum Rings Embedded into High-Quality Terahertz Microcavities

13.5.1 Introduction

Progress in nanolithography and epitaxial techniques has resulted in burgeoning developments in the fabrication of micro-scale optical resonators, known as optical microcavities. If the quality factor of a cavity is sufficiently large, the formation of hybrid light-matter excitations occurs. Being first observed two decades ago [124], the strong coupling regime is now routinely achieved in different kinds of microcavities [125]. From the point of view of fundamental physics, this regime is interesting for investigation of various collective phenomena in condensed matter systems such as the high-temperature Bose-Einstein condensation (BEC) [126, 127] and superfluidity [128]. From the viewpoint of applications it opens a way towards to the realization of optoelectronic devices of the next generation [129]: room-temperature polariton lasers [130], polarization-controlled optical gates, [131], effective sources of THz radiation [121, 123, 132], and others.

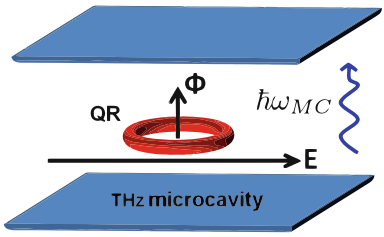

Fig. 13.10 An Aharonov-Bohm quantum ring embedded into a single-mode THz microcavity (from [5])

Several applications of the strong coupling regime were also proposed for quantum information processing [133–135]. In this case one should be able to tune the number of emitted photons in a controllable way. This is hard to achieve in planar microcavities, where the number of elementary excitations is macroscopically large, but is possible in microcavities containing single quantum dots, where the quantum dot exciton can be coupled to a confined electromagnetic mode provided by a micropillar (etched planar cavity) [80], a defect of the photonic crystal [79], or a whispering gallery mode [81, 136]. That is why the strongly coupled systems based on quantum dots have attracted particular attention recently. In the strong coupling regime the system possesses a rich multiplet structure, which maps transitions between quantized dressed states of the light-matter coupling Hamiltonian [79–82, 102, 137–140].

In this section we examine a single-mode THz microcavity [141–144] with an embedded Aharonov-Bohm quantum ring, which is pierced by a magnetic flux and subjected to a lateral electric field. We restrict our analysis to linearly polarized microcavity radiation only. The geometry of the system is shown in Fig. 13.10. The emission properties of such a system under continuous incoherent pumping are studied theoretically. We calculate the luminescence spectrum of the system using the master equation techniques for several combinations of the applied external electric and magnetic fields. We demonstrate that the resonance which is best for exploring quantum features of the system [138] can be achieved by means of tuning the magnitude of the lateral electric field. An additional degree of control can be achieved by changing the angle between the polarization plane of the optical pump and the lateral electric field. As we show, the quantum ring-microcavity coupling strength depends strongly on the above mentioned angle.

13.5.2 Quantum Rings in High-Quality Terahertz Microcavities

13.5.2.1 Aharonov-Bohm Quantum Rings as Two-Level Photon Emitters

In this section we briefly revise the energy spectrum and optical properties of a single-electron Aharonov-Bohm QR pierced by a magnetic flux Φ and subjected to

a lateral electric field **E**, which were studied in Sect. 13.4. We then show how the single-electron Aharonov-Bohm QR can be utilized as a two-level, single-photon emitter.

In the absence of the external electric field the eigenfunctions of an infinitely narrow Aharonov-Bohm QR of a radius R are given by

$$\psi_m(\varphi) = e^{im\varphi}/\sqrt{2\pi}, \tag{13.62}$$

where φ is the polar angle coordinate and $m = 0, \pm 1, \pm 2 \ldots$ is the angular momentum quantum number. The corresponding eigenvalues are defined by

$$\varepsilon_m(f) = \varepsilon_{QR}(m+f)^2,$$

where $\varepsilon_{QR} = \hbar^2/2M_eR^2$ is the energy scale of the interlevel separation in the QR, M_e is the electron effective mass and $f = \Phi/\Phi_0$ is the number of flux quanta piercing the QR ($\Phi_0 = h/e$). For experimentally attainable QRs, ε_{QR} corresponds to the THz frequency range.

When the lateral electric field is applied, the modified electron eigenfunctions can be expressed as a linear combination of the unperturbed wave functions (13.62):

$$\Psi_n(\varphi) = \sum_m c_m^n e^{im\varphi}. \tag{13.63}$$

Substituting the wave function (13.63) into the Schrödinger equation with the Hamiltonian containing a term which describes the presence of the lateral electric field, multiplying the resulting expression by $e^{-im\varphi}$, and integrating with respect to the angle φ results in an infinite system of linear equations for the coefficients c_m^n (for details see Sect. 13.4.2)

$$\left[(m+f)^2 - \lambda_n\right] c_m^n + \beta\left(c_{m+1}^n + c_{m-1}^n\right) = 0, \tag{13.64}$$

where $\beta = eER/2\varepsilon_{QR}$ is the normalized strength of the lateral electric field and λ_n is an energy eigenvalue normalized by ε_{QR}. It can be seen from the system of equations (13.64) that all the QR quantities are periodic in the magnetic flux Φ with the period equal to Φ_0. There is also an apparent symmetry with respect to the change of the sign of Φ. Therefore, in what follows we will consider only the case of $0 \le \Phi \le \Phi_0/2$.

It it shown in Appendix 13.6.2 that in the limit of a weak in-plane electric field, $eER \ll \varepsilon_{QR}$, all essential features of the first three states of the QR are fully captured by the following 3×3 system of linear equations:

$$\begin{pmatrix} (f+1)^2 & \beta & 0 \\ \beta & f^2 & \beta \\ 0 & \beta & (f-1)^2 \end{pmatrix} \begin{pmatrix} c_{+1}^n \\ c_0^n \\ c_{-1}^n \end{pmatrix} = \lambda_n \begin{pmatrix} c_{+1}^n \\ c_0^n \\ c_{-1}^n \end{pmatrix}. \tag{13.65}$$

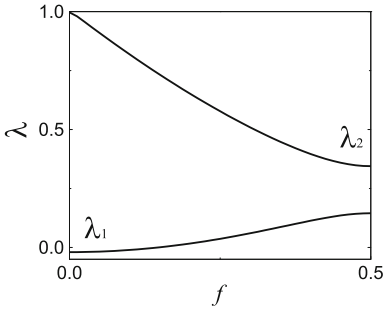

Fig. 13.11 The normalized energy spectrum for the electron ground and the first excited states in the quantum ring as a function of dimensionless parameter f for $\beta = 0.1$ (from [5])

In what follows we will be interested in the transitions between the ground and the first excited states in the QR only. However, in order to obtain accurate ground and first excited states eigenenergies and eigenfunctions all three listed states should be considered. The system of linear equations (13.65) can be reduced to a cubic equation for λ_n, which yields the following eigenvalues $\lambda_1 < \lambda_2 < \lambda_3$:

$$\lambda_1 = -2/3\sqrt{1 + 12f^2 + 6\beta^2}\cos(\alpha/3) + f^2 + 2/3, \tag{13.66}$$

$$\lambda_2 = -2/3\sqrt{1 + 12f^2 + 6\beta^2}\cos(\alpha/3 - 2\pi/3) + f^2 + 2/3, \tag{13.67}$$

$$\lambda_3 = -2/3\sqrt{1 + 12f^2 + 6\beta^2}\cos(\alpha/3 + 2\pi/3) + f^2 + 2/3, \tag{13.68}$$

where

$$\cos\alpha = \frac{1 - 36f^2 + 9\beta^2}{\left(1 + 12f^2 + 6\beta^2\right)^{3/2}}.$$

The set of corresponding eigenvectors (non-normalized) is given by substituting appropriate values of λ_n into

$$\begin{pmatrix} c_{+1}^n \\ c_0^n \\ c_{-1}^n \end{pmatrix} = \begin{pmatrix} \left[\lambda_n - (f-1)^2\right]\left(\lambda_n - f^2\right) - \beta^2 \\ \left[\lambda_n - (f-1)^2\right]\beta \\ \beta^2 \end{pmatrix}. \tag{13.69}$$

The energy spectrum for the electron ground and the first excited states defined by (13.66) and (13.67) respectively for $\beta = 0.1$ and $0 \le f \le 1/2$ is plotted in Fig. 13.11. Notably, the 3×3 system of equations (13.65) provides a very good accuracy for the ground and the first excited states when $\beta \lesssim 1$ (i.e. $eER \lesssim \varepsilon_{QR}$). A numerical check shows that the further increase in the system of linear equations, (13.64), does not provide any noticeable change in the results. A similar analysis is applicable to a nanohelix with an electric field applied normal to its axis. For a helix, the role of magnetic flux in the absence of a magnetic field is played by the electron momentum along the helical line [112–114, 145].

The QR can be represented as a two-level system with the energy gap between the ground state $|g\rangle$ ($n = 1$) and the excited state $|e\rangle$ ($n = 2$) denoted by Δ. From (13.66)–(13.67), it is clear that Δ depends on both the external electric field $\mathbf{E}$, applied in the QR plane, and the magnetic flux Φ, piercing the QR. In particular, when $\Phi = 0$ ($\Phi = \Phi_0/2$), one obtains $\Delta/\varepsilon_{QR} = 1 + 2\beta^2$ ($\Delta/\varepsilon_{QR} = 2\beta$).

Another quantity, which is needed for further calculations, is the product of the light polarization vector $\mathbf{e}$ and the matrix element $\mathbf{d} = \left\langle e \left| \hat{\mathbf{d}} \right| g \right\rangle = \left\langle g \left| \hat{\mathbf{d}} \right| e \right\rangle$ of the dipole moment calculated between the ground state $|g\rangle$ and the excited state $|e\rangle$. For linearly polarized light this product is given by the following integral:

$$\mathbf{d} \cdot \mathbf{e} = eR \int_0^{2\pi} \Psi_e \Psi_g \cos(\theta - \varphi)\, d\varphi, \tag{13.70}$$

where Ψ_g, Ψ_e are the ground and the first excited state wave functions defined by (13.63) and θ is the angle between $\mathbf{e}$ and $\mathbf{E}$.

Substituting eigenfunctions Ψ_g, Ψ_e given by (13.63) into (13.70) and performing the integration with respect to the angle φ we obtain

$$\mathbf{d} \cdot \mathbf{e} = \left(d_-^2 + d_+^2 - 2d_- d_+ \cos 2\theta\right)^{1/2}, \tag{13.71}$$

where

$$d_- = \frac{eR}{2} \left| c_0^e c_{-1}^g + c_{+1}^e c_0^g \right|, \tag{13.72}$$

and

$$d_+ = \frac{eR}{2} \left| c_{-1}^e c_0^g + c_0^e c_{+1}^g \right|. \tag{13.73}$$

Later in this work we use (13.71)–(13.73) with coefficients c^e, c^g obtained from (13.69) to calculate the QR-MC coupling strength. A detailed analysis of (13.69) and (13.72)–(13.73) shows that a noticeable θ-dependence in (13.71) occurs only when $f = 0$ or $f = 1/2$, as d_- vanishes otherwise.

13.5.2.2 The Jaynes-Cummings Hamiltonian and the Master Equation

The full Hamiltonian describing the system of a QR coupled to a single-mode THz MC is the Jaynes-Cummings [106][2]

$$H_{JC} = \Delta \sigma^\dagger \sigma + \hbar \omega_{MC} a^\dagger a + \mathscr{G}\left(\sigma^\dagger a + \sigma a^\dagger\right), \tag{13.74}$$

[2]For more details on MC-2LE interaction Hamiltonian, i.e. the Jaynes-Cummings Hamiltonian, please refer to Sects. 13.3.2.1–13.3.2.3 of this chapter.

where ω_{MC} is the MC eigenfrequency, $\mathscr{G}$ is the QR-MC coupling constant, $a^\dagger$ is the MC photon creation operator, a is the MC photon annihilation operator, $\sigma^\dagger = (\sigma_x + i\sigma_y)/2$ is the QR electron creation operator, $\sigma = (\sigma_x - i\sigma_y)/2$ is the QR electron annihilation operator, and σ_x, σ_y are the Pauli matrices acting in the space of $|g\rangle$ and $|e\rangle$ states. The frequency of the MC mode and the frequency of the transition between the QR states are assumed to be close enough to allow the use of the rotating wave approximation [146, 147]. If the MC mode is linearly polarized, $\mathscr{G}$ is given by

$$\mathscr{G} = -(\mathbf{d}\cdot\mathbf{e})\sqrt{\hbar\omega_{MC}/2\varepsilon_0 V}, \tag{13.75}$$

where $\mathbf{d}\cdot\mathbf{e}$ is given by (13.71), ε_0 is the vacuum dielectric permittivity, V is the quantization volume, which can be estimated as $V \approx (\lambda_{MC}/2)^3$, and $\lambda_{MC} = 2\pi c/\omega_{MC}$ is the MC characteristic wavelength. When the magnetic flux piercing the QR is equal to an integer number of half-flux quanta, $\mathscr{G}$ strongly depends on the angle θ between the projection of the radiation polarization vector onto the QR plane and the applied lateral electric field.

The eigenvalues of the Hamiltonian (13.74) are the same as in the case of a single-mode MC with embedded QD, whose excitations obey fermionic statistics [138, 146].

$$E_N^{\pm} = \hbar\omega_{MC}(N - 1/2) + \Delta/2 \pm \sqrt{(\hbar\omega_{MC} - \Delta)^2/4 + N\mathscr{G}^2}, \tag{13.76}$$

where N is the total number of electron-photon excitations in the system, i.e. the number of photons inside the MC if the electron is in the ground state. The corresponding eigenfunctions $\mathscr{X}_N^{\pm}$ can be expressed as a linear combination of the combined electron-photon states $|g, N\rangle = |g\rangle \otimes |N\rangle$ and $|e, N-1\rangle = |e\rangle \otimes |N-1\rangle$, which define both the QR state and the MC photon occupation number. Using this basis we solve a 2×2 system of linear equations which corresponds to the Hamiltonian (13.74) and obtain

$$\mathscr{X}_N^{\pm} = K_{g,N}^{\pm}|g, N\rangle + K_{e,N}^{\pm}|e, N-1\rangle, \tag{13.77}$$

where

$$K_{g,N}^{\pm} = \frac{\sqrt{N}\mathscr{G}}{\sqrt{\left(E_N^{\pm} - N\hbar\omega_{MC}\right)^2 + N\mathscr{G}^2}}, \tag{13.78}$$

and

$$K_{e,N}^{\pm} = \frac{E_N^{\pm} - N\hbar\omega_{MC}}{\sqrt{\left(E_N^{\pm} - N\hbar\omega_{MC}\right)^2 + N\hbar\mathscr{G}^2}}. \tag{13.79}$$

The main advantage of using a QR instead of a QD is the opportunity to control both the energy gap Δ between the first two states of the QR and the QR-MC coupling constant $\mathscr{G}$ by changing the external electric and magnetic fields. These fields can

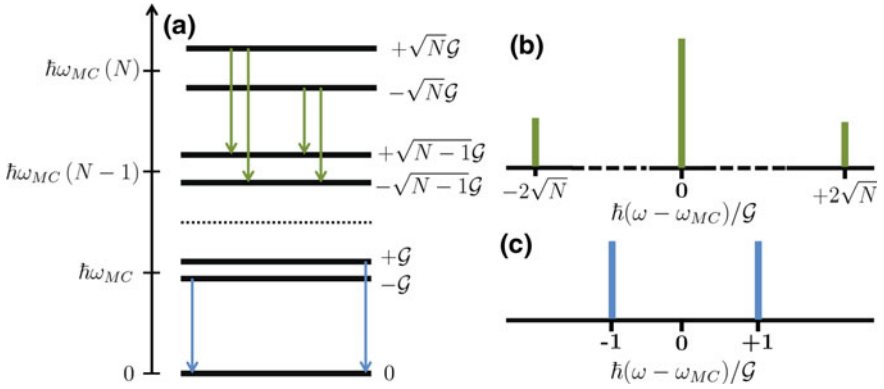

Fig. 13.12 Schematic diagram of the energy and emission spectra of the coupled QR-MC system in the resonant case $\Delta = \hbar\omega_{MC}$: **a** the "Jaynes-Cummings ladder"; **b** the Mollow triplet; **c** the Rabi doublet

be used to achieve the resonant condition $\Delta = \hbar\omega_{MC}$ and provide easy means of performing a transition from the strong to the weak coupling regime within the same system [138].

The eigenvalues $E_N^{\pm}$ defined by (13.76) form the so-called "Jaynes-Cummings ladder" and the emission spectrum of the system, which is observed outside of the MC, is defined by optical transitions between the states with total number of electron-photon excitations N different by unity (see Fig. 13.12). Inside a non-ideal MC, a photon has a limited lifetime and when the photon leaks out, one can measure its frequency. This provides a direct access to the quantized coupled electron-photon states of the system.

In order to describe any realistic experiment measuring the QR-MC emission spectrum one should introduce pump and decay in the system. We model the system dynamics under incoherent MC pumping and account for dissipation processes using the master equation approach for the full density matrix of the system ρ (see, e.g., [146, 147]).[3] The master equation reads

$$\frac{\partial\rho}{\partial t} = \frac{i}{\hbar}[\rho, H_{JC}] + \mathscr{L}_P^{MC}\rho + \mathscr{L}_\gamma^{MC}\rho + \mathscr{L}_\gamma^{QR}\rho, \tag{13.80}$$

where $\mathscr{L}_P^{MC}$, $\mathscr{L}_\gamma^{MC}$ are the Lindblad terms, which account for the MC pump and decay, and the Lindblad term $\mathscr{L}_\gamma^{QR}$ describes non-radiative transitions of the QR electron from the excited state $|e\rangle$ to the ground state $|g\rangle$. In the explicit form these three terms are given by

[3] For more details on the master equation approach for the full density matrix of a general MC-2LE system please see Sects. 13.3.2.4–13.3.2.5 of this chapter.

$$\mathscr{L}_P^{MC}\rho = \frac{P_{MC}}{2}(2a^\dagger\rho a - aa^\dagger\rho - \rho aa^\dagger + 2a\rho a^\dagger - a^\dagger a\rho - \rho a^\dagger a),$$

$$\mathscr{L}_\gamma^{MC}\rho = \frac{\gamma_{MC}}{2}(2a\rho a^\dagger - a^\dagger a\rho - \rho a^\dagger a),$$

$$\mathscr{L}_\gamma^{QR}\rho = \frac{\gamma_{QR}}{2}(2\sigma\rho\sigma^\dagger - \sigma^\dagger\sigma\rho - \rho\sigma^\dagger\sigma),$$

where P_{MC} is the intensity of the incoherent MC pumping and γ_{MC}, γ_{QR} are the lifetimes of the photonic and the QR excitations respectively. Due to the balance between the pump and the decay, after some time a steady state is established. We denote the corresponding density matrix as ρ^{SS}. The steady state density matrix can be found by solving numerically (13.80) with all the matrices truncated. When performing the truncation, all the states which can be excited as a result of the pumping should be accounted for.

13.5.2.3 Emission Spectrum of the System Under Incoherent Pumping

In the presence of the pump and the decay and after establishing an equilibrium, the system is in a mixed state, which is characterized by the full density matrix ρ^{SS}. If ρ^{SS} is written in the basis of eigenfunctions (13.77), the density matrix diagonal element ρ_{II}^{SS} gives the probability of the system to be in the Ith state. At low pumping, $P_{MC} \ll \mathscr{G}$, and in the case of a high-Q system, $\gamma_{MC}, \gamma_{QR} \ll \mathscr{G}$, which is the best regime to elucidate quantum coupling effects [138], the emission spectrum can be calculated using the so-called manifold method, which has been proved to provide qualitatively accurate results avoiding heavy numerical calculations (see, e.g., [138, 140, 148]). In this approximation the QR and MC emission spectra are given by

$$S_{QR}(\omega) \approx \frac{1}{\pi}\sum_{I,F}\frac{\left|M_{IF}^{QR}\right|^2\rho_{II}^{SS}\Gamma_{IF}}{(\hbar\Omega_{IF}-\hbar\omega)^2+\Gamma_{IF}^2}, \tag{13.81}$$

$$S_{MC}(\omega) \approx \frac{1}{\pi}\sum_{I,F}\frac{\left|M_{IF}^{MC}\right|^2\rho_{II}^{SS}\Gamma_{IF}}{(\hbar\Omega_{IF}-\hbar\omega)^2+\Gamma_{IF}^2}, \tag{13.82}$$

where $\left|M_{IF}^{QR}\right|^2 = |\langle\mathscr{X}_F, |\sigma|\mathscr{X}_I\rangle|^2$, $\left|M_{IF}^{MC}\right|^2 = |\langle\mathscr{X}_F|a|\mathscr{X}_I\rangle|^2$, $\hbar\Omega_{IF} = E^I - E^F$, $\mathscr{X}_i$ and $\mathscr{X}_f$ are the QR-MC initial and final states eigenfunctions defined by (13.77), E^i and E^f are the QR-MC initial and final states eigenenergies defined by (13.76), and Γ_{IF} is given by

$$\Gamma_{IF} = \frac{\gamma_{QR}}{2}\sum_J \left(\left|M_{JI}^{QR}\right|^2 + \left|M_{JF}^{QR}\right|^2\right) + \frac{\gamma_{MC}}{2}\sum_J \left(\left|M_{JI}^{MC}\right|^2 + \left|M_{JF}^{MC}\right|^2\right) + \frac{P_{MC}}{2}\sum_J \left(\left|M_{JI}^{MC}\right|^2 + \left|M_{JF}^{MC}\right|^2 + \left|M_{IJ}^{MC}\right|^2 + \left|M_{FJ}^{MC}\right|^2\right).$$

In (13.81)–(13.82) S_{QR} and S_{MC} correspond to photons of two different origins, which can be detected outside of the MC by an external observer: the direct emission of the QR and the leaking MC photons. In the first case a photon outside of the MC is created as a result of the QR electron transition from the excited state $|e\rangle$ to the ground state $|g\rangle$ and in the second case the photon is created due to annihilation of a MC photon. Substituting $\mathscr{X}_N^{\pm}$ from (13.77) into the expressions for $\left|M_{IF}\right|^2$ yields

$$\left|M_{IF}^{QR}\right|^2 = \left|K_{g,N_F}^{\pm} K_{e,N_I}^{\pm}\right|^2 \delta_{N_F,N_I-1},$$

$$\left|M_{IF}^{MC}\right|^2 = \left|\sqrt{N_I} K_{g,N_F}^{\pm} K_{g,N_I}^{\pm} + \sqrt{N_F} K_{e,N_F}^{\pm} K_{e,N_I}^{\pm}\right|^2 \delta_{N_F,N_I-1}.$$

It should be noted that only the transitions between the coupled electron-photon states with the total number of excitations differing by unity are allowed.

In the resonant case $\Delta = \omega_{MC}$, for transitions from the Nth state to the $(N-1)$th state we obtain

$$\left|M_{\pm\to\mp}^{QR}\right|^2 = 1/4, \tag{13.83}$$

$$\left|M_{\pm\to\pm}^{QR}\right|^2 = 1/4, \tag{13.84}$$

and

$$\left|M_{\pm\to\mp}^{MC}\right|^2 = \left|\sqrt{N} - \sqrt{N-1}\right|^2/4, \tag{13.85}$$

$$\left|M_{\pm\to\pm}^{MC}\right|^2 = \left|\sqrt{N} + \sqrt{N-1}\right|^2/4, \tag{13.86}$$

with corresponding eigenfrequencies given by

$$\Omega_{\pm\to\mp} = \omega_{MC} \pm \mathscr{G}\left(\sqrt{N} + \sqrt{N-1}\right)/\hbar, \tag{13.87}$$

$$\Omega_{\pm\to\pm} = \omega_{MC} \pm \mathscr{G}\left(\sqrt{N} - \sqrt{N-1}\right)/\hbar. \tag{13.88}$$

One can see that the observed emission spectrum consists of two symmetric inner peaks at frequencies (13.88) and two symmetric outer peaks at frequencies (13.87). Together, these peaks form the so-called "Jaynes-Cummings fork". From (13.83)–(13.86) it follows that when the total number of electron-photon excitations in the ini-

tial state $N = 1$, both S_{QR} and S_{MC} have a shape of the Rabi doublet (see Fig. 13.12c), and in the case of large excitation numbers, $N \gg 1$, S_{QR} is in the form of the Mollow triplet (see Fig. 13.12b) while S_{MC} collapses into a single lasing peak.

13.5.3 Results and Discussion

In this section we use the formalism which was developed in the previous sections to calculate emission spectra of the QR-MC system in the presence of a magnetic flux Φ piercing the QR and a lateral electric field $\mathbf{E}$. The QR-MC system has apparent advantages for exploring the quantum nature of light-matter coupling in nanostructured systems compared to the well-studied QD-based setup. Namely, the parameters of the system can be more easily tuned by external fields. Between all possible combinations of the applied magnetic and electric fields there are two cases of considerable interest: (a) $\Phi = 0$, $\mathbf{e} \perp \mathbf{E}$ and (b) $\Phi = \Phi_0/2$, $\mathbf{e} \perp \mathbf{E}$. In both cases, the energy gap between the QR states is tunable by the strength of the lateral electric field. From (13.66)–(13.67) we get $\Delta/\varepsilon_{QR} = 1 - 2\beta^2$ ($\Delta/\varepsilon_{QR} = 2\beta$) for $\Phi = 0$ ($\Phi = \Phi_0/2$). Thus, the energy gap Δ can be easily adjusted to coincide with the energy of the MC mode $\hbar\omega_{MC}$. From (13.71)–(13.73) and (13.75) one can see that when $\Phi = 0$ or $\Phi = \Phi_0/2$ the QR-MC coupling constant $\mathscr{G}$ strongly depends on the angle θ between the direction of the external electric field and the projection of the MC mode polarization vector onto the QR plane. If $\mathbf{e} \perp \mathbf{E}$, the coupling constant $\mathscr{G}$ reaches its maximum possible value, and if $\mathbf{e} \parallel \mathbf{E}$, the MC mode and the QR are completely uncoupled. By changing the direction of the lateral electric field one acquires additional means of control of the emission spectrum of the system.

The quantum structure of the Jaynes-Cummings states discussed in the previous section is known to be observed only in the low dissipation regime [138]. Therefore, it is natural to consider a QR embedded into a high-Q THz MC under a weak incoherent pumping. Similar to [138], we choose a MC with the decay rate $\gamma_{MC}/\mathscr{G} = 0.1$ and a QR with the decay rate $\gamma_{QR}/\mathscr{G} = 0.01$. The QR decay rate is chosen to be much smaller than the MC decay rate, as is the case in most experimental systems [80, 82]. In all the calculations we chose either $P_{MC}/\mathscr{G} = 0.005$ or $P_{MC}/\mathscr{G} = 0.095$. These conditions satisfy the applicability criteria of the manifold method for modelling the emission spectrum of the systems.

In order to estimate experimental conditions for the observation of the predicted emission spectra we use the following values of the other system parameters: a typical radius of experimentally attainable [9, 10, 17] QRs, $R = 20$nm and the electron effective mass $M = 0.05m_e$. This gives the energy scale of the QR interlevel separation $\varepsilon_{QR} \simeq 2$meV and the magnitude of the magnetic field, which produces a magnetic flux through the QR equal to a half of the flux quantum, $B \simeq 2$T. Unless specified otherwise, all the calculations are made in the presence of a weak lateral electric field $\mathbf{E} \perp \mathbf{e}$ with the magnitude $E = 0.1\varepsilon_{QR}/eR = 2 \times 10^4$V/m. The QR-MC coupling constant can now be estimated using (13.75). we obtain $\mathscr{G} = 8.3 \times 10^{-4}$ meV ($\mathscr{G} = 1.2 \times 10^{-3}$ meV) for $\Phi = 0$ ($\Phi = \Phi_0/2$) which results in the MC Q-factor

requirement $Q = \hbar\omega_{MC}/\gamma_{MC} \approx 16{,}000$ ($Q \approx 5000$). THz microcavities with the Q-factor of this order of magnitude have already been achieved [142].

We start with calculations of the emission spectrum of the system for $P_{MC}/\mathscr{G} = 0.005$ and $P_{MC}/\mathscr{G} = 0.095$ in the resonant case, $\hbar\omega_{MC} = \Delta$. The magnetic flux piercing the QR is either $\Phi = 0$ or $\Phi = \Phi_0/2$. Results of these calculations are shown in Fig. 13.13. Both the direct QR emission spectrum, S_{QR}, and the MC emission spectrum S_{MC} are plotted. When $P_{MC}/\mathscr{G} = 0.005$, there are two dominant peaks (the linear Rabi doublet) in S_{QR} and S_{MC} at the frequencies $\omega = \pm\mathscr{G}/\hbar$, which correspond to the transitions between the two $N = 1$ states and the ground $N = 0$ state. With increasing pumping, $P_{MC}/\mathscr{G} = 0.095$, the higher, $N > 1$, states are excited. The intensity of the Rabi doublet is decreased while the quadruplet peaks corresponding to the transitions between the $N = 2$ and $N = 1$ states emerge. Only the inner quadruplet peaks in S_{QR} and S_{MC} can be seen in the selected energy range. It should be mentioned that the outer peaks in the MC emission spectrum, S_{MC}, become suppressed with increasing N, as can be seen from the expression for the corresponding matrix elements, (13.85).

A different type of emission spectrum can be observed away from the resonance. This can be achieved for the same system by changing the magnitude of the lateral electric field. In Figs. 13.14 and 13.15 we plot S_{MC} and S_{QR} when $\Delta \neq \hbar\omega_{MC}$ for several values of E. Figure 13.14 corresponds to $\Phi = 0$, whereas Fig. 13.15 corresponds to $\Phi = \Phi_0/2$. Due to the fact that there are non-zero probabilities of finding the system in states with different N, the emission spectrum has a pronounced multiplet structure. The MC pumping rate is taken as $P_{MC}/\mathscr{G} = 0.095$. One can clearly see the avoided crossings in the plotted emission spectra, manifesting that the system is in the strong coupling regime. When $\Phi = \Phi_0/2$ and the detuning between Δ and $\hbar\omega_{MC}$ is of the order of $\mathscr{G}$, the direct QR emission spectrum has the most intensive peaks at the frequencies close to $\omega = \Delta/\hbar$. This indicates that the QR is almost uncoupled from the MC. The more pronounced changes in the emission spectra in Fig. 13.15 compared to Fig. 13.14 can be explained by different dependences of the energy gap Δ on the magnitude of the lateral electric field E: when $\Phi = \Phi_0/2$ the dependence is linear in E and when $\Phi = 0$ the dependence is quadratic in E.

For a nearly zero flux through the QR, a small change of the flux results in significant changes in S_{MC} and S_{QR}, as the presence of a weak magnetic field affects strongly both the QR gap Δ and the QR-MC coupling constant $\mathscr{G}$. The dependence of the QR gap Δ on the magnetic flux Φ piercing the QR can be seen from Fig. 13.11, while the QR-MC coupling constant $\mathscr{G}$ magnetic flux dependence can be easily calculated using (13.71)–(13.73) and (13.75). In Fig. 13.16 we plot S_{MC} and S_{QR} for several values of Φ near zero. The MC pumping rate is taken as $P_{MC}/\mathscr{G}_0 = 0.095$, where $\mathscr{G}_0$ denotes the value of the QR-MC coupling constant for $\Phi = 0$. The plotted emission spectra incorporate both the anticrossing behaviour due to detuning of the QR transition energy from the energy of the MC mode and the changes in the multiplet structure owing to varying the QR-MC coupling strength.

Finally, we calculate the emission spectrum of the QR-microcavity system altering the angle θ between the direction of the applied electric field and the projection of the microcavity mode polarization vector onto the QR plane. Again, the magnetic

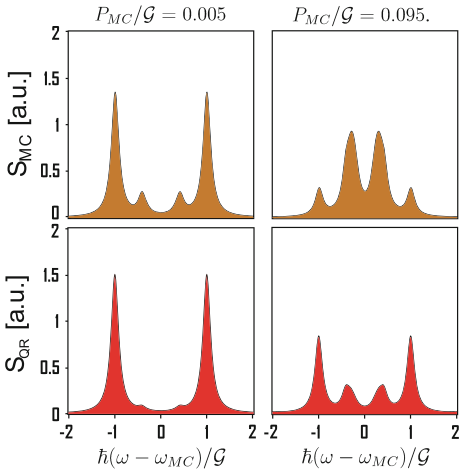

Fig. 13.13 Emission spectrum of the quantum ring-microcavity system in the presence of a lateral electric field $E = 2.00 \times 10^4$ V/m for $P_{MC}/\mathcal{G} = 0.005$ and $P_{MC}/\mathcal{G} = 0.095$. The microcavity mode is in resonance with the quantum ring transition. The upper row (brown) corresponds to the microcavity emission and the lower row (red) corresponds to the direct quantum ring emission. The magnetic flux piercing the quantum ring is either $\Phi = 0$ or $\Phi = \Phi_0/2$. The emission frequencies are normalized by the quantum ring-microcavity coupling constant $\mathcal{G}/\hbar$ and centred around ω_{MC} (from [5])

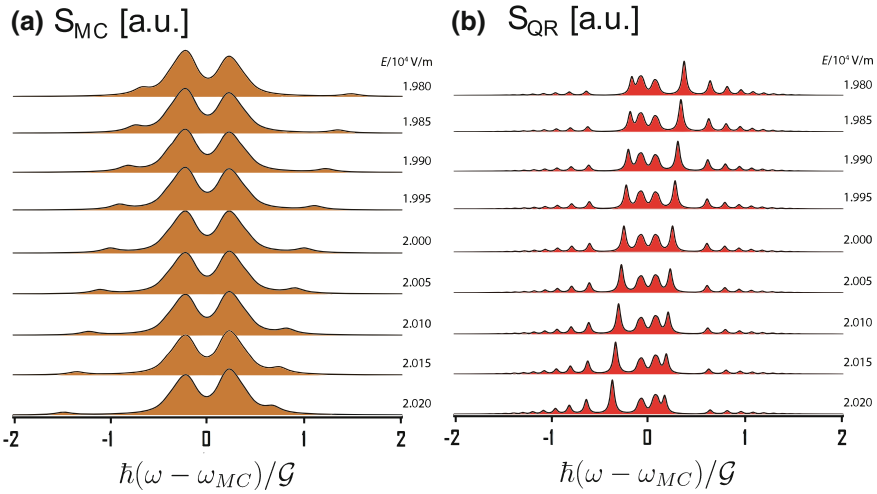

Fig. 13.14 Anticrossing in the emission spectrum of the quantum ring-microcavity system at various magnitudes of the external lateral electric field E from 1.98×10^4 V/m to 2.02×10^4 V/m with the increment 50 V/m: **a** microcavity emission spectrum (brown), **b** direct quantum ring emission spectrum (red). The magnetic flux piercing the quantum ring $\Phi = 0$. The resonance case $\Delta = \hbar\omega_{MC}$ corresponds to $E = 2.00 \times 10^4$ V/m. The microcavity pumping rate $P_{MC}/\mathcal{G} = 0.095$. The emission frequencies are normalized by the quantum ring-microcavity coupling constant $\mathcal{G}/\hbar$ and centred around ω_{MC} (from [5])

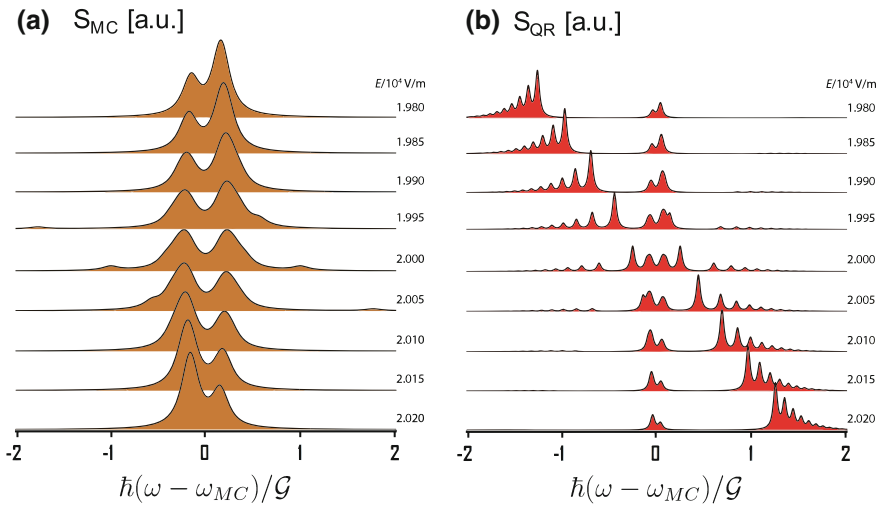

Fig. 13.15 Anticrossing in the emission spectrum of the quantum ring-microcavity system at various magnitudes of the external lateral electric field E from 1.98×10^4 V/m to 2.02×10^4 V/m with the increment 50 V/m: **a** microcavity emission spectrum (brown), **b** direct quantum ring emission spectrum (red). The magnetic flux piercing the quantum ring $\Phi = \Phi_0/2$. The resonance case $\Delta = \hbar\omega_{MC}$ corresponds to $E = 2.00 \times 10^4$V/m. The microcavity pumping rate $P_{MC}/\mathscr{G} = 0.095$. The emission frequencies are normalized by the quantum ring-microcavity coupling constant $\mathscr{G}/\hbar$ and centred around ω_{MC} (from [5])

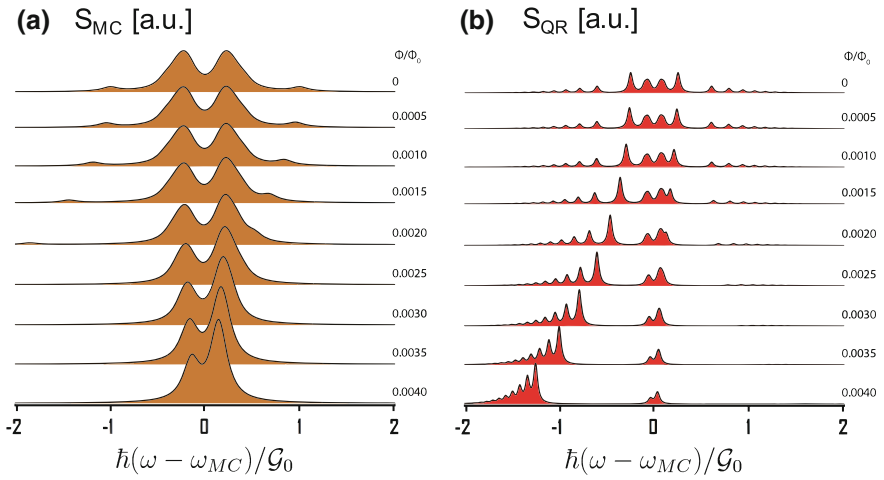

Fig. 13.16 Anticrossing in the emission spectrum of the quantum ring-microcavity system at various magnitudes of the magnetic flux Φ piercing the quantum ring from 0 to $0.004\Phi_0$ with the increment $5 \times 10^{-4}\Phi_0$ and in the presence of the lateral electric field $E = 2.00 \times 10^4$ V/m: **a** microcavity emission spectrum (brown), **b** direct quantum ring emission spectrum (red). The resonance case $\Delta = \hbar\omega_{MC}$ corresponds to $\Phi = 0$. The emission frequencies are normalized by the value of the quantum ring-microcavity coupling constant calculated for $\Phi = 0$ ($\mathscr{G}_0$) and centred around ω_{MC}. The microcavity pumping rate $P_{MC}/\mathscr{G}_0 = 0.095$ (from [5])

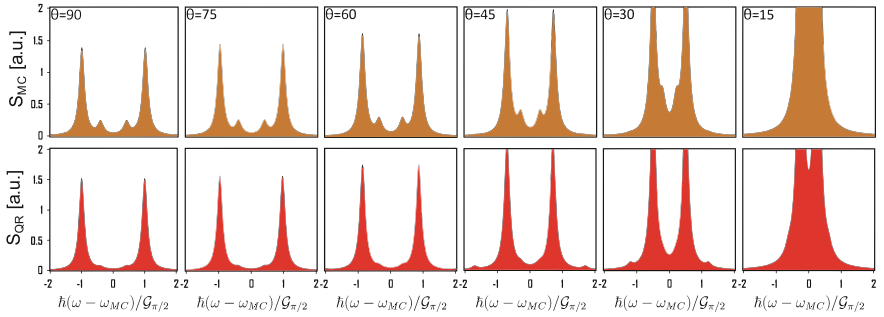

Fig. 13.17 Emission spectrum of the quantum ring-microcavity system when the lateral electric field $E = 2.00 \times 10^4$ V/m is rotated. The angle θ is counted between **E** and the projection of the microcavity mode polarization vector onto the quantum ring plane **e**. The upper row (brown) corresponds to the microcavity emission and the lower row (red) correspond to the direct quantum ring emission. The system is in resonance, $\Delta = \hbar\omega_{MC}$. The emission frequencies are normalized by the value of the quantum ring-microcavity coupling constant for $\theta = \pi/2$ ($\mathscr{G}_{\pi/2}$) and centred around ω_{MC}. The microcavity pumping rate $P_{MC}/\mathscr{G}_{\pi/2} = 0.095$ (from [5])

flux piercing the QR is either $\Phi = 0$ or $\Phi = \Phi_0/2$. The system is in the resonance, $\Delta = \hbar\omega_{MC}$. The microcavity pumping rate is taken as $P_{MC}/\mathscr{G}_{\pi/2} = 0.005$, where $\mathscr{G}_{\pi/2}$ denotes the value of the QR-microcavity coupling constant for $\theta = \pi/2$. The results are plotted in Fig. 13.17. One can see that as the angle θ is changed, the emission peaks shift towards the microcavity eigenfrequency ω_{MC}, which can be explained by reducing the coupling strength $\mathscr{G}$. This effect provides an additional way to control the frequency of the satellite peaks in the QR-microcavity emission spectrum and allows a purely spectroscopic measurement of the pump polarization.

In this work we dealt exclusively with the QR inter-subband transitions. However, a similar analysis should be possible for inter-band optical transitions, for which matrix elements and energies can also be tuned by the external fields more easily than in the widely studied QD systems.

In conclusion, we have analyzed the emission spectrum of an Aharonov-Bohm QR placed into a single-mode quantum MC. We have shown that the emission spectrum in the strong coupling regime has a multiplet structure and can be tuned by the variation of the magnetic field piercing the QR and by changing the strength and direction of the applied lateral electric field. Thus, it is demonstrated that a MC with an embedded QR is a promising system for use as a tunable optical modulator in the THz range. The QR-MC system, which allows manipulation of quantum states with external fields, might also prove to be useful for investigating dephasing mechanisms and for engineering and exploring enhanced light-matter interactions for novel quantum investigations.

13.6 Conclusions and Outlook. Bridging the THz Gap with Aharonov-Bohm Quantum Rings

13.6.1 Conclusions

In our work we studied the interaction of Aharonov-Bohm quantum rings with classical and quantized electromagnetic fields.

In Sect. 13.4 we examined an infinitely-narrow, single-particle quantum ring pierced by a magnetic flux and subjected to a static lateral electric field [2, 3]. This model is relevant to nanoscale-sized type-I quantum rings and type-II quantum dots, such as those studied in [6–32]. We show that the applied electric field, which is known to suppress magneto-oscillations in the ground state of a single-particle quantum ring [110, 111], results in strong oscillations of the ring electric dipole moment and selection rules for optical transitions between the ground and first excited states of the quantum ring. We attribute these phenomena to electric-field induced mixing of quantum ring states with different angular momenta, which occurs when magnetic flux through the quantum ring is equal to a half-integer of the magnetic flux quantum. It is shown that even a weak electric field causes this mixing. Most of the results obtained here for the static in-plane electric field can be easily generalized to the case of the rotating field by a proper change of the coordinates system [4].

It should be also emphasised that calculated effects are not an artifice of the infinitely-narrow ring model used in our calculations, but persist in finite-width rings in a uniform magnetic field. As we have shown, the only feature needed for the discussed phenomena is the degeneracy of the states with the angular momenta differing by one at certain magnetic field values, which is known to be present in quantum rings of finite width [57–60, 115].

In order to establish an understanding of the potential for observation of the predicted effects in real systems we provide estimates for experimental conditions essential for measuring these phenomena. While observation of the dipole moment magneto-oscillations would require a low-temperature laboratory, the oscillations of selection rules for optical transitions can be potentially observed at room temperatures. Indeed, when the ground and the first excited stated are equally occupied the dipole moment oscillations are completely suppressed while the intensity of the optical transitions is only four times lower comparing to the case when the ground state is fully occupied and the first excited state is empty.

For experimentally attainable quantum rings these transitions occur in the THz frequency range. It provides an opportunity of utilizing Aharonov-Bohm quantum rings as THz emitters and detectors. Despite significant progress made towards reliable and efficient THz sources, such as THz quantum cascade lasers [149–151], free electron THz lasers [152, 153], and recently proposed microcavity-polaritons THz lasers [122, 123, 130, 132], bridging of the so-called ‘THz gap’ remains a formidable task. The range of potential application of THz radiation is both vast and in high demand. The vibrational modes of many molecules, including molecules of explosive materials, occur at THz frequencies [154, 155], making THz spectroscopy

a powerful and non-invasive tool for molecular identification and characterization. An airport scanner, which detects molecules found in explosives is only one example of a highly-useful THz device. Other potential applications of the THz spectroscopy lie in the area of pharmaceutical research and biomedical diagnostics [156].

Arguably, the use of Aharonov-Bohm quantum rings for THz radiation and detection has its merits as polarization properties and frequencies of THz transitions in quantum rings are fully controlled by the applied external fields.

In Sect. 13.5 we examined a system of an Aharonov-Bohm quantum ring embedded into a single-mode THz microcavity [5]. It was shown that the discussed possibility to control optical properties of quantum rings with the external electric and magnetic fields suggests a new way of regulating the microcavity-emitter coupling strength. Such easy control was never possible with quantum dots embedded in microcavities where all main optical properties of the system are predefined at the growth stage. As a result, one can strongly influence emission spectra of the system by varying external fields.

We calculate the emission spectra of the system under continuous incoherent pumping when the quantum ring transitions are both in or out of the resonance with the microcavity mode and for various combinations of the applied electric and magnetic fields. We restrict our analysis to linearly polarized microcavity radiation only. It is shown that when the system is in resonance and the magnetic flux piercing the quantum ring is equal to a half-integer of the magnetic flux quantum, a precise control of the satellite peaks in the emission spectra is possible with (i) pumping intensity and (ii) the direction of the lateral electric field with respect to the microcavity radiation polarization vector. This effect can be used for creating the highly demanded THz electro-optical modulators. In a quantum ring-microcavity-based optical modulator, modulation of the intensity, frequencies and polarization of the THz radiation would be realized by periodic variation of the lateral electric field direction. Potentially, such a device can be indeed created as THz microcavities with high values of Q-factor based on both Bragg mirrors [157] and photonic crystals [142] have been already achieved.

The calculated non-resonant emission spectra can be of a great help during the procedure of modulator adjustment. As we discuss in Sect. 13.5, in order to establish a resonance in the quantum ring-microcavity system one would tune magnitudes of the applied electric and magnetic fields. Thus, the calculated non-resonant emission spectra can serve as a reference pattern.

To conclude, we believe Aharonov-Bohm quantum rings to be promising candidates for creating optical devices operating with radiation at THz frequencies and hope that our work will stimulate further experimental research in this area.

13.6.2 Outlook

A natural extension of the current work presented in Sect. 13.4 is to repeat our calculations using a more realistic (and consequently more complicated) 2D model of the

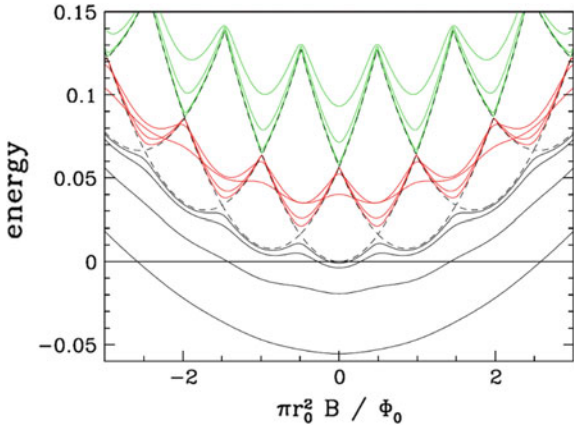

Fig. 13.18 A finite-width ring in a magnetic field for different values of in-plane electric field strength. The ring radius r_0=100 nm and its width is 20 nm

Aharonov-Bohm quantum ring. We chose the same model as was utilized in [57–60] as it allows an analytical treatment. Preliminary results of our calculations are shown in Fig. 13.18. One can see that, as it was stated, the main feature required for the predicted effects—degeneracy of the energy levels with angular momenta differing by unity at certain magnetic field values—is indeed present in this model.

The possible extension of the work presented in Sect. 13.5 is to use the quantum regression theorem [92–94, 146, 158] (together with the Wiener-Khintchine formula [92–94, 146, 159, 160]) to calculate the emission spectrum of the quantum ring-microcavity system. Such an approach can potentially reveal non-Lorentzian emission lineshapes.

Appendix. Analytical Solutions for Small Matrices.

In the limit of weak electric field, $\beta = eER/(\hbar^2/M_eR^2) \ll 1$, the electron ground, first and second excited states are well-described by the following three-by-three system, which is obtained from (13.54) for $|m| \leq 1$

$$\begin{pmatrix} (f+1)^2 & \beta & 0 \\ \beta & f^2 & \beta \\ 0 & \beta & (f-1)^2 \end{pmatrix} \begin{pmatrix} c^n_{+1} \\ c^n_0 \\ c^n_{-1} \end{pmatrix} = \lambda_n \begin{pmatrix} c^n_{+1} \\ c^n_0 \\ c^n_{-1} \end{pmatrix}. \tag{13.89}$$

Here $f = (\Phi - N\Phi_0)/\Phi_0$ with N integer, so that $0 \leq f \leq 1/2$. The eigenvalues λ_n of the system (13.89) are the roots of the cubic equation

$$\lambda_n^3 - \lambda_n^2\left(3f^2+2\right) + \lambda_n\left(3f^4+1-2\beta^2\right) - f^6 + 2f^4 - f^2 + 2f^2\beta^2 + 2\beta^2 = 0. \tag{13.90}$$

Solving (13.90) we find

$$\lambda_1 = -2/3\sqrt{1+12f^2+6\beta^2}\cos(\alpha/3)+f^2+2/3, \tag{13.91}$$

$$\lambda_2 = -2/3\sqrt{1+12f^2+6\beta^2}\cos(\alpha/3-2\pi/3)+f^2+2/3, \tag{13.92}$$

$$\lambda_3 = -2/3\sqrt{1+12f^2+6\beta^2}\cos(\alpha/3+2\pi/3)+f^2+2/3, \tag{13.93}$$

with

$$\cos\alpha = \frac{1-36f^2+9\beta^2}{\left(1+12f^2+6\beta^2\right)^{3/2}}.$$

Considering $\beta \ll 1$ (the limit of weak electric field) we expand (13.91–13.93) into Taylor series in f to obtain

$$\lambda_1 = f^2 - 2\beta^2\sum_{n=0}^{\infty}(2f)^{2n} + O(\beta^4), \tag{13.94}$$

$$\lambda_2 = 1+f^2+\beta^2\left[1-\sum_{n=0}^{\infty}\frac{(-1)^n(2n)!}{(1-2n)(n!)^2}\left(\frac{f}{\beta^2}\right)^{2n}\right]+O(\beta^4), \tag{13.95}$$

$$\lambda_3 = 1+f^2+\beta^2\left[1+\sum_{n=0}^{\infty}\frac{(-1)^n(2n)!}{(1-2n)(n!)^2}\left(\frac{f}{\beta^2}\right)^{2n}\right]+O(\beta^4). \tag{13.96}$$

It can be shown that (13.95, 13.96) coincide with the results of the perturbation theory in *eER* for quasi-degenerate states [96] if the coupling to the states with $|m| > 1$ is neglected.

The energy spectrum given by (13.91–13.93) is plotted in Fig. 13.19. It is nearly indistinguishable from the energy spectrum, which was obtained by numerical diagonalization of the 23×23 system in Sect. 13.4 for the same value of β. A small discrepancy between the plotted energy spectra is noticeable only for the first and second excited states. The energy spectrum obtained by numerical diagonalization of the 23×23 system is slightly shifted towards the smaller energies. This shift occurs because the considered 3×3 matrix does not take into account the coupling between the $m = \pm 1$ and $m = \pm 2$ states. For the infinite system and $f = 0$, perturbation theory up to the second order in β yields

$$\lambda_1 = -2\beta^2,\ \lambda_2 = 1-\beta^2/3,\ \lambda_3 = 1+5\beta^2/3, \tag{13.97}$$

whereas from (13.94–13.96) one gets

$$\lambda_1 = -2\beta^2,\ \lambda_2 = 1,\ \lambda_3 = 1+2\beta^2. \tag{13.98}$$

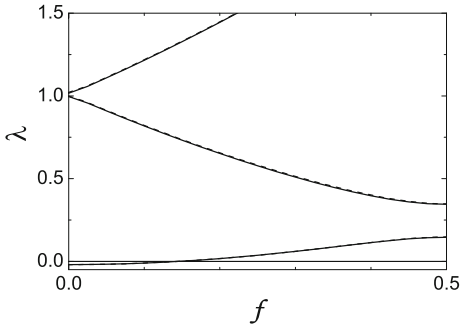

Fig. 13.19 The normalized energy spectrum as a function of dimensionless parameter f for $\beta = 0.1$. Dashed line—the result of analytical solution of the 3×3 system. Solid line—the result of numerical diagonalization of the 23×23 system. A horizontal line is shown to indicate $\lambda = 0$ value

The λ_2 and λ_3 values in (13.97) differ from the values in (13.98) by $-\beta^2/3$ which corresponds to the repulsion between the $m = \pm 1$ and $m = \pm 2$ states calculated using the second order perturbation theory.

When $f = 1/2$, and in the absence of a lateral electric field, the $m = 0$ and $m = -1$ states are degenerate with energy ε_1 (0) /4, i.e. $\lambda_1 = \lambda_2 = 1/4$, whereas the $m = +1$ state energy is nine times larger ($\lambda_3 = 9/4$). The contribution from this remote state can be neglected, and the electron ground and first excited states are well-described by the following two-by-two system, which contains c_{-1} and c_0 coefficients only,

$$\begin{pmatrix} f^2 & \beta \\ \beta & (f-1)^2 \end{pmatrix} \begin{pmatrix} c_0^n \\ c_{-1}^n \end{pmatrix} = \lambda_n \begin{pmatrix} c_0^n \\ c_{-1}^n \end{pmatrix}. \tag{13.99}$$

The eigenvalues λ_n of the system (13.99) are the roots of the quadratic equation

$$\lambda_n^2 - \lambda_n \left(2f^2 - 2f + 1\right) + f^4 - 2f^3 + f^2 - \beta^2 = 0. \tag{13.100}$$

Solving (13.100) we find

$$\lambda_{1,2} = f^2 - f + 1/2 \mp \sqrt{f^2 - f + \beta^2 + 1/4}, \tag{13.101}$$

yielding for $f = 1/2$ the eigenvalue difference $\lambda_2 - \lambda_1 = 2\beta$, corresponding to the energy splitting of *eER* as expected from the perturbation theory for degenerate states. The energy spectrum given by (13.101) is plotted in Fig. 13.20 together with two lowest eigenvalues of the 23×23 system demonstrating a spectacular accuracy of the approximate solution for $\beta = 0.1$.

Let us now return to the three-by-three matrix and examine how its eigenvectors are modified with changing f. Near the point $f = 0$ it is convenient to write the eigenvectors of the system (13.89) in the following form

$$\begin{pmatrix} c_{+1}^n \\ c_0^n \\ c_{-1}^n \end{pmatrix} = A_n \begin{pmatrix} \left[\lambda_n - (f-1)^2\right]\left(\lambda_n - f^2\right) - \beta^2 \\ \left[\lambda_n - (f-1)^2\right]\beta \\ \beta^2 \end{pmatrix}, \tag{13.102}$$

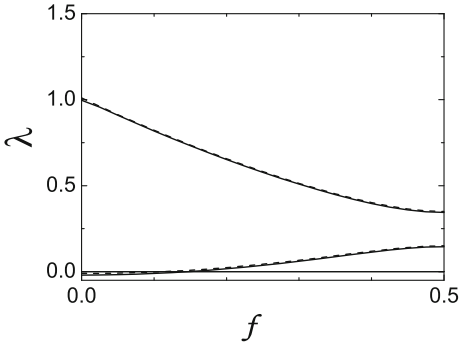

Fig. 13.20 The normalized energy spectrum as a function of dimensionless parameter f for $\beta = 0.1$. Dashed line - the result of analytical solution of the 2×2 system. Solid line - the result of numerical diagonalization of the 23×23 system. A horizontal line is shown to indicate $\lambda = 0$ value

where A_n denotes the normalization constant corresponding to the eigenvalue λ_n and (13.102) is valid only for $\beta \neq 0$. For $f = 0$ in the limit of weak electric field ($\beta \ll 1$) we obtain

$$\begin{pmatrix} c^1_{+1} \\ c^1_0 \\ c^1_{-1} \end{pmatrix} = \frac{\left(1 + 1\sqrt{1+8\beta^2} + 8\beta^2\right)^{-1/2}}{\sqrt{2}} \begin{pmatrix} -2\beta \\ 1 + \sqrt{1+8\beta^2} \\ -2\beta \end{pmatrix} \xrightarrow{\beta \to 0} \begin{pmatrix} 0 \\ 1 \\ 0 \end{pmatrix}, \tag{13.103}$$

$$\begin{pmatrix} c^2_{+1} \\ c^2_0 \\ c^2_{-1} \end{pmatrix} = \frac{1}{\sqrt{2}} \begin{pmatrix} -1 \\ 0 \\ 1 \end{pmatrix}, \tag{13.104}$$

$$\begin{pmatrix} c^3_{+1} \\ c^3_0 \\ c^3_{-1} \end{pmatrix} = \frac{\left(1 - 1\sqrt{1+8\beta^2} + 8\beta^2\right)^{-1/2}}{\sqrt{2}} \begin{pmatrix} 2\beta \\ \sqrt{1+8\beta^2} - 1 \\ 2\beta \end{pmatrix} \xrightarrow{\beta \to 0} \frac{1}{\sqrt{2}} \begin{pmatrix} 1 \\ 0 \\ 1 \end{pmatrix}. \tag{13.105}$$

From (13.103–13.105) one can see that for $f = 0$ and $\beta \ll 1$ the electron ground state is almost a pure $m = 0$ state, whereas the angular dependencies of the wavefunctions of the first and second excited states are well-described by $\sin\varphi$ and $\cos\varphi$ respectively.

The structure of eigenfunctions near $f = 1/2$ is best understood from (13.99), which yields

$$\begin{pmatrix} c^1_0 \\ c^1_{-1} \end{pmatrix} = A \begin{pmatrix} \beta \\ 1/2 - f - \sqrt{f^2 - f + \beta^2 + 1/4} \end{pmatrix}, \tag{13.106}$$

$$\begin{pmatrix} c^2_0 \\ c^2_{-1} \end{pmatrix} = A \begin{pmatrix} f - 1/2 + \sqrt{f^2 - f + \beta^2 + 1/4} \\ \beta \end{pmatrix}. \tag{13.107}$$

Here A is the normalization constant and $\beta \neq 0$. For $f = 1/2$ we get

$$\begin{pmatrix} c_0^1 \\ c_{-1}^1 \end{pmatrix} = \frac{1}{\sqrt{2}} \begin{pmatrix} 1 \\ -1 \end{pmatrix}, \quad \begin{pmatrix} c_0^2 \\ c_{-1}^2 \end{pmatrix} = \frac{1}{\sqrt{2}} \begin{pmatrix} 1 \\ 1 \end{pmatrix}. \tag{13.108}$$

From (13.108) one can see that for $f = 1/2$ the angular dependencies of the ground and first excited states wavefunctions are described by $\sin(\varphi/2)$ and $\cos(\varphi/2)$ respectively.

Figure 13.21 shows the magnetic flux dependencies of the coefficients $|c_0|^2$, $|c_{-1}|^2$, and $|c_{+1}|^2$ for the electron ground, first and second excited states. From these plots one can see that the electron ground state is almost a pure $m = 0$ state in a wide region $0 \leq f \lesssim 1/4$. An admixture of the $m = -1$ wavefunction increases smoothly as one approaches the point of degeneracy $f = 1/2$. Finally, when $f = 1/2$, the ground state wavefunction is expressed as a difference of the $m = -1$ and $m = 0$ wavefunctions. The first and the second excited states behave differently. In a small region near the point $f = 0$ the electron first and second excited states wavefunctions consist of a strong mixture of the $m = -1$ and $m = +1$ functions with a tiny admixture of the $m = 0$ function. In particular, when $f = 0$ the first and second excited states eigenfunctions with good accuracy can be expressed as the difference and the sum of the $m = -1$ and $m = +1$ functions respectively. Optical transitions between these states and the ground state are only allowed if the polarization of the associated

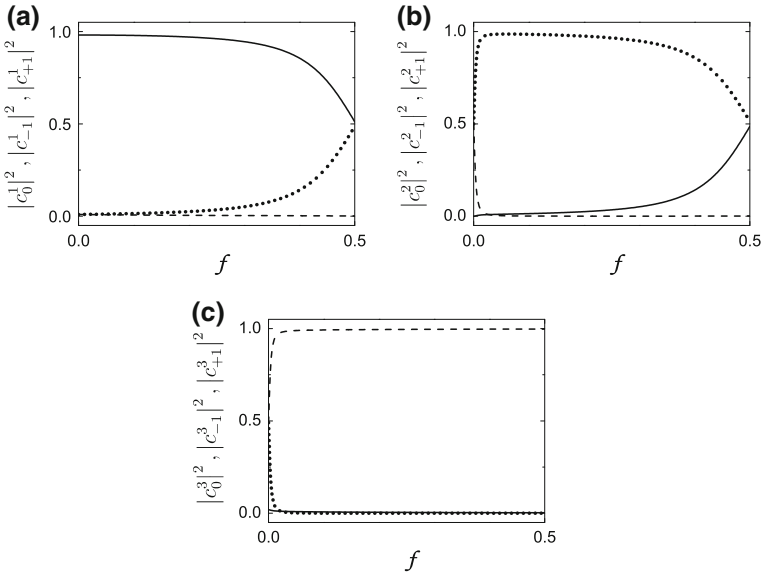

Fig. 13.21 Magnetic flux dependence of the wavefunction coefficients $|c_0|^2$ (solid line), $|c_{-1}|^2$ (dotted line), and $|c_{+1}|^2$ (dashed line): **a** for the ground state; **b** for the first excited state; **c** for the second excited state

optical excitations is either perpendicular (for the first excited state) or parallel (for the second excited state) to the direction of the applied in-plane electric field. Away from the $f = 0$ region, only the coefficient c_{-1} (in the case of the first excited state) or c_{+1} (in the case of the second excited state) remains in the (13.102), which now describes almost pure $m = +1$ and $m = -1$ states. When f exceeds $1/4$ the first excited state starts to contain a noticeable ad-mixture of $m = 0$ function, as discussed above, and for $f = 1/2$ the first excited state eigenfunction is expressed as a sum of the $m = -1$ and $m = 0$ wavefunctions in equal proportions, whereas the second excited state remains an almost pure $m = +1$ state.

The same trend in the evolution of wavefunctions of the three lowest energy states with changing the flux through the ring can be seen from perturbation theory. For $f = 0$, the degeneracy between the first and second excited states is removed in the second order in *eER* only. Nevertheless, as a result of the degeneracy, the introduction of any weak perturbation drastically modifies the wavefunctions corresponding to these states, turning them from the eigenstates of the angular momentum operator to the sine and cosine functions. With a slight increase of f, so that $f > \beta^2$, the first and the second excited states, which are not degenerate anymore for $f \neq 0$, become governed mainly by the diagonal terms of the Hamiltonian, which do not mix the $m = -1$ and $m = +1$ functions. When $f = 1/2$, the $m = -1$ and $m = 0$ states are degenerate in the absence of the electric field. This degeneracy is removed in the first order in *eER*. The off-diagonal matrix elements connecting $m = -1$ and $m = 0$ functions remain of the same order of magnitude as the difference between the diagonal terms of the Hamiltonian across a broad range of f values near $f = 1/2$. This results in strong mixing of the $m = -1$ and $m = 0$ components in the eigenfunctions of the ground and first excited states for $1/4 \lesssim f \leq 1/2$.

References

1. Y. Aharonov, D. Bohm, Significance of electromagnetic potentials in the quantum theory. Phys. Rev. **115**, 485 (1959)
2. A.M. Alexeev, M.E. Portnoi, Terahertz transitions in Aharonov-Bohm quantum rings in an external electric field. Phys. Stat. Sol. C **9**, 1309 (2012)
3. A.M. Alexeev, M.E. Portnoi, Electric dipole moment oscillations in Aharonov-Bohm quantum rings. Phys. Rev. B **85**, 245419 (2012)
4. K.L. Koshelev, V. Yu Kachorovskii, M. Titov, Resonant inverse faraday effect in nanorings. Phys. Rev. B **92**(23), 235426 (2015)
5. A.M. Alexeev, I.A. Shelykh, M.E. Portnoi, Aharonov-bohm quantum rings in high-q microcavities. Phys. Rev. B **88**(8), 085429 (2013)
6. J.N. García, G. Medeiros-Ribeiro, K. Schmidt, T. Ngo, J.L. Feng, A. Lorke, J. Kotthaus, P.M. Petroff, Intermixing and shape changes during the formation of InAs self-assembled quantum dots. Appl. Phys. Lett. **71**, 2014 (1997)
7. J.M. García, T. Mankad, P.O. Holtz, P.J. Wellman, P.M. Petroff. Electronic states tuning of InAs self-assembled quantum dots. Appl. Phys. Lett. **24**:3172 (1998)
8. A. Lorke, R.J. Luyken, M. Fricke, J.P. Kotthaus, G. Medeiros-Ribeiro, J.M. Garcia, P.M. Petroff, Electronic structure of nanometer-size quantum dots and quantum rings. Microelectron. Eng. **47**(1), 95 (1999)

9. A. Lorke, L.R. Johannes, A.O. Govorov, J.P. Kotthaus, J.M. Garcia, P.M. Petroff, Spectroscopy of nanoscopic semiconductor rings. Phys. Rev. Lett. **84**, 2223 (2000)
10. E. Ribeiro, A.O. Govorov, W. Carvalho, G. Medeiros-Ribeiro, Aharonov-Bohm signature for neutral polarized excitons in type-II quantum dot ensembles. Phys. Rev. Lett. **92**, 126402 (2004)
11. T. Mano, T. Kuroda, S. Sanguinetti, T. Ochiai, T. Tateno, J. Kim, T. Noda, M. Kawabe, K. Sakoda, G. Kido et al., Self-assembly of concentric quantum double rings. Nano Lett. **5**, 425 (2005)
12. T. Kuroda, T. Mano, T. Ochiai, S. Sanguinetti, K. Sakoda, G. Kido, N. Koguchi, Optical transitions in quantum ring complexes. Phys. Rev. B **72**, 205301 (2005)
13. P. Offermans, P.M. Koenraad, J.H. Wolter, D. Granados, J.M. Garcia, V.M. Fomin, V.N. Gladilin, J.T. Devreese, Atomic-scale structure of self-assembled In(Ga)As quantum rings in GaAs. Appl. Phys. Lett. **87**, 131902 (2005)
14. M. Hanke, Y.I. Mazur, E. Marega Jr., Z.Y. AbuWaar, G.J. Salamo, P. Schäfer, M. Schmidbauer, Shape transformation during overgrowth of InGaAs/GaAs (001) quantum rings. Appl. Phys. Lett. **91**, 043103 (2007)
15. I.G. Kuskovsky, W. MacDonald, A.O. Govorov, L. Mourokh, X. Wei, M.C. Tamargo, M. Tadic, F.M. Peeters, Optical Aharonov-Bohm effect in stacked type-II quantum dots. Phys. Rev. B **76**, 035342 (2007)
16. C. Somaschini, S. Bietti, N. Koguchi, S. Sanguinetti, Fabrication of multiple concentric nanoring structures. Nano Lett. **9**, 3419 (2009)
17. J. Chen, W.S. Liao, X. Chen, T. Yang, S.E. Wark, D.H. Son, J.D. Batteas, P.S. Cremer, Evaporation-induced assembly of quantum dots into nanorings. ACS Nano **3**, 173 (2009)
18. M.D. Teodoro, V.L. Campo, V. Lopez-Richard, E. Marega, G.E. Marques, Y. Galv ao Gobato, F. Iikawa, M.J.S.P. Brasil, Z.Y. AbuWaar, V.G. Dorogan, Yu.I. Mazur, M. Benamara, G.J. Salamo, Aharonov-Bohm interference in neutral excitons: effects of built-in electric fields. Phys. Rev. Lett. **104**, 086401 (2010)
19. F. Ding, N. Akopian, B. Li, U. Perinetti, A. Govorov, F.M. Peeters, C.C. Bufon, C. Deneke, Y.H. Chen, A. Rastelli et al., Gate controlled Aharonov-Bohm-type oscillations from single neutral excitons in quantum rings. Phys. Rev. B **82**, 075309 (2010)
20. B. Roy, H. Ji, S. Dhomkar, F.J. Cadieu, L. Peng, R. Moug, M.C. Tamargo, I.L Kuskovsky. Determination of excitonic size with sub-nanometer precision via excitonic Aharonov-Bohm effect in type-II quantum dots. Appl. Phys. Lett. **100**, 213114 (2012)
21. M. Elborg, T. Noda, T. Mano, T. Kuroda, Y. Yao, Y. Sakuma, K. Sakoda, Self-assembly of vertically aligned quantum ring-dot structure by multiple droplet epitaxy. J. Crystal Growth (2017)
22. Y.D. Sibirmovskii, I.S. Vasilevskii, A.N. Vinichenko, I.S. Eremin, N.I. Kargin, O.S. Kolentsova, M.N. Strikhanov, Features of diffusion processes during drop epitaxy of quantum rings. Bull. Lebedev Phys. Inst. **41**(9), 243–246 (2014)
23. Y.D. Sibirmovskii, I.S. Vasilevskii, A.N. Vinichenko, I.S. Eremin, D.M. Zhigunov, N.I. Kargin, O.S. Kolentsova, P.A. Martyuk, M.N. Strikhanov, Photoluminescence of gaas/algaas quantum ring arrays. Semiconductors **49**(5), 638–643 (2015)
24. Y.I. Mazur, V. Lopes-Oliveira, L.D. de Souza, V. Lopez-Richard, M.D. Teodoro, V.G. Dorogan, M. Benamara, J. Wu, G.G. Tarasov, E. Marega Jr. et al., Carrier transfer in vertically stacked quantum ring-quantum dot chains. J. Appl. Phys. **117**(15), 154307 (2015)
25. H.D. Kim, R. Okuyama, K. Kyhm, M. Eto, Robert A. Taylor, Aurelien L. Nicolet, Marek Potemski, Gilles Nogues, Le Si Dang, Ku-Chul Je et al., Observation of a biexciton wigner molecule by fractional optical aharonov-bohm oscillations in a single quantum ring. Nano Lett. **16**(1), 27–33 (2015)
26. H. Kim, W. Lee, S. Park, K. Kyhm, K. Je, R.A Taylor, G. Nogues, L.S. Dang, J.D. Song, Quasi-one-dimensional density of states in a single quantum ring. Sci. Rep. **7** (2017)
27. H.D. Kim, K. Kyhm, R.A. Taylor, A.A.L. Nicolet, M. Potemski, G. Nogues, K.C. Je, E.H. Lee, J.D. Song, Excited exciton and biexciton localised states in a single quantum ring. Appl. Phys. Lett. **103**(17), 173106 (2013)

28. V. Lopes-Oliveira, Y.I. Mazur, L. Dias, L.A. de Souza, Bernardes Maral, Wu Jiang, Marcio Daldin Teodoro, Angelo Malachias, Vitaliy G. Dorogan, Mourad Benamara, Georgiy G. Tarasov et al., Structural and magnetic confinement of holes in the spin-polarized emission of coupled quantum ring-quantum dot chains. Phys. Rev. B **90**(12), 125315 (2014)
29. A.M. Beltrán, E.A. Marquis, A.G. Taboada, J.M. Ripalda, J.M. García, S.I. Molina, Three dimensional atom probe imaging of gaassb quantum rings. Ultramicroscopy **111**(8), 1073–1076 (2011)
30. W.-H. Lin, K.-W. Wang, Y.-A. Liao, C.-W. Pao, Shih-Yen Lin, The formation mechanisms and optical characteristics of gasb quantum rings. J. Appl. Phys. **114**(5), 053509 (2013)
31. B. Roy, H. Ji, S. Dhomkar, M.C. Tamargo, I.L. Kuskovsky, Observation of oscillations in energy of aharonov-bohm excitons in type-ii znte/znse stacked submonolayer quantum dots. Phys. Status Solidi (c) **11**(7—-8), 1248–1251 (2014)
32. H. Ji, R. Wu, S. Dhomkar, V. Shuvayev, V. Deligiannakis, M.C. Tamargo, J. Ludwig, Z. Lu, D. Smirnov, A. Wang et al., Optical anisotropy in type-ii znte/znse submonolayer quantum dots. J. Appl. Phys. **119**(22), 224306 (2016)
33. M. Grochol, F. Grosse, R. Zimmermann, Optical exciton Aharonov-Bohm effect, persistent current, and magnetization in semiconductor nanorings of type I and II. Phys. Rev. B **74**, 115416 (2006)
34. A.G. Aronov, YuV Sharvin, Magnetic flux effects in disordered conductors. Rev. Mod. Phys. **59**, 755 (1987)
35. S. Viefers, P. Koskinen, P. Singha Deo, M. Manninen, Quantum rings for beginners: energy spectra and persistent currents. Phys. E (Amsterdam) **21**, 1 (2004)
36. T. Ihn, A. Fuhrer, L. Meier, M. Sigrist, K. Ensslin, Quantum physics in quantum rings. Europhys. News **36**, 78 (2005)
37. I. Filikhin, S.G. Matinyan, B. Vlahovic, Quantum mechanics of semiconductor quantum dots and rings. ArXiv preprint arXiv:1206.1354 (2012)
38. M. Manninen, S. Viefers, S.M. Reimann, Quantum rings for beginners ii: Bosons versus fermions. Phys. E: Low-Dimension. Syst. Nanostruct. **46**, 119–132 (2012)
39. W. Ehrenberg, R.E. Siday, The refractive index in electron optics and the principles of dynamics. Proc. Phys. Soc. Lond. Sect. B **62**, 8 (1949)
40. H. Roy, B. Ji, S. Dhomkar, F.J. Cadieu, L. Peng, R. Moug, M.C. Tamargo, I.L. Kuskovsky, Distinguish ability of stacks in ZnTe/ZnSe quantum dots via spectral analysis of Aharonov-Bohm oscillations. Eur. Phys. J. B **86**, 1 (2013)
41. A.V. Chaplik, Magnetoexcitons in quantum rings and in antidots. JETP **62**, 900 (1995)
42. A.V. Chaplik, A.O. Govorov, Multiply-charged magnetoexcitons in quantum-well systems. Phys. B: Condens. Matter **256**, 477 (1998)
43. R.A. Römer, M.E. Raikh, Aharonov-Bohm effect for an exciton. Phys. Rev. B **62**, 7045 (2000)
44. T.V. Shahbazyan, I.E. Perakis, M.E. Raikh, Spin correlations in nonlinear optical response: light-induced Kondo effect. Phys. Rev. Lett. **84**
45. K. Maschke, T. Meier, P. Thomas, S.W. Koch, Coherent dynamics of magnetoexcitons in semiconductor nanorings. Eur. Phys. J. B-Condens. Matter Complex Syst. **19**, 599 (2001)
46. T. Meier, P. Thomas, S.W. Koch, Linear and nonlinear optical properties of semiconductor nanorings with magnetic field and disorder-influence on excitons and biexcitons. Eur. Phys. J. B-Condens. Matter Complex Syst. **22**, 249 (2001)
47. H. Hu, D.-J. Li, J.-L. Zhu, J.-J. Xiong, Size effects on excitons in nano-rings. J. Phys. Condens. Matter **12**
48. H. Hu, J.-L. Zhu, D.-J. Li, J.-J. Xiong, Aharonov-Bohm effect of excitons in nanorings. Phys. Rev. B **63**, 195307 (2001)
49. J. Song, S.E. Ulloa, Magnetic field effects on quantum ring excitons. Phys. Rev. B **63**, 125302 (2001)
50. I. Galbraith, F.J. Braid, R.J. Warburton, Magneto-excitons in semiconductor quantum rings. Phys. Stat. Sol. A **190**, 781 (2002)
51. A.O. Govorov, A.V. Kalameitsev, R. Warburton, K. Karrai, S.E. Ulloa, Excitons in quantum-ring structures in a magnetic field: optical properties and persistent currents. Phys. E: Low-Dimension. Syst. Nanostruct. **13**, 297 (2002)

52. L.G.G.V. Dias da Silva, S.E. Ulloa, A.O. Govorov, Impurity effects on the Aharonov-Bohm optical signatures of neutral quantum-ring magnetoexcitons. Phys. Rev. B **70**, 155318 (2004)
53. F. Palmero, J. Dorignac, J.C. Eilbeck, R.A. Römer, Aharonov-Bohm effect for an exciton in a finite-width nanoring. Phys. Rev. B **72**, 075343 (2005)
54. T.V. Bandos, A. Cantarero, A. Garcia-Cristobal, Finite size effects on the optical transitions in quantum rings under a magnetic field. Eur. Phys. J. B-Condens. Matter Complex Syst. **53**, 99 (2006)
55. Z. Barticevic, M. Pacheco, J. Simonin, C.R. Proetto, Coulomb-interaction effects on the electronic structure of radially polarized excitons in nanorings. Phys. Rev. B **73**, 165311 (2006)
56. Z. Dai, J.-L. Zhu, Dimensional effects on exciton states in nanorings. J. Phys. Condens. Matter **19**, 346202 (2007)
57. E.N. Bogachek, U. Landman, Edge states, Aharonov-Bohm oscillations, and thermodynamic and spectral properties in a two-dimensional electron gas with an antidot. Phys. Rev. B **52**, 14067 (1995)
58. W.C. Tan, J.C. Inkson, Electron states in a two-dimensional ring-an exactly soluble model. Semicond. Sci. Technol. **11**, 1635 (1996)
59. V.M. Kovalev, A.V. Chaplik, Aharonov-Bohm effect for plasmons in a finite-width quantum ring. JETP Lett. **90**, 679 (2010)
60. C. González-Santander, F. Domínguez-Adame, R.A. Römer, Excitonic Aharonov-Bohm effect in a two-dimensional quantum ring. Phys. Rev. B **84**, 235103 (2011)
61. A.V. Maslov, D.S. Citrin, Enhancement of the Aharonov-Bohm effect of neutral excitons in semiconductor nanorings with an electric field. Phys. Rev. B **67**, 121304 (2003)
62. A.M. Fischer, V.L. Campo, M.E. Portnoi, R.A. Römer, Exciton storage in a nanoscale Aharonov-Bohm ring with electric field tuning. Phys. Rev. Lett. **102**, 096405 (2009)
63. B. Li, F.M. Peeters, Tunable optical Aharonov-Bohm effect in a semiconductor quantum ring. Phys. Rev. B **83**, 115448 (2011)
64. E. Yablonovitch, Inhibited spontaneous emission in solid-state physics and electronics. Phys. Rev. Lett. **58**, 20592 (1987)
65. S. John, Strong localization of photons in certain disordered dielectric superlattices. Phys. Rev. Lett. **58**, 2486 (1987)
66. E. Yablonovitch, T.J. Gmitter, K.M. Leung, Photonic band structure: the face-centered-cubic case employing nonspherical atoms. Phys. Rev. Lett. **67**
67. T.F. Krauss, R.M.D.L. Rue, S. Brand, Two-dimensional photonic-bandgap structures operating at near-infrared wavelengths. Nature **383**, 699 (1996)
68. S. Noda, A. Chutinan, M. Imada, Trapping and emission of photons by a single defect in a photonic bandgap structure. Nature **407**, 608 (2000)
69. Y. Takahashi, H. Hagino, Y. Tanaka, B.-S. Song, T. Asano, S. Noda, High-Q nanocavity with a 2-ns photon lifetime. Optics Express **15**, 17206 (2007)
70. Y. Tanaka, T. Asano, S. Noda, Design of photonic crystal nanocavity with Q-factor of $\sim 10^9$. J. Lightwave Technol. **26**, 1532 (2008)
71. A.I. Nosich, E.I. Smotrova, S.V. Boriskina, T.M. Benson, P. Sewell, Trends in microdisk laser research and linear optical modelling. Opt. Quantum Electron. **39**, 1253 (2007)
72. E.M. Purcell, Spontaneous emission probabilities at radio frequencies. Phys. Rev. **69**, 681 (1946)
73. J.-M. Gérard, B. Gayral, Strong Purcell effect for InAs quantum boxes in three-dimensional solid-state microcavities. J. Lightwave Technol. **17**, 2089 (1999)
74. G.S. Solomon, M. Pelton, Y. Yamamoto, Single-mode spontaneous emission from a single quantum dot in a three-dimensional microcavity. Phys. Rev. Lett. **86**, 3903 (2001)
75. A.J. Bennett, D.J.P. Ellis, A.J. Shields, P. Atkinson, I. Farrer, D.A. Ritchie, Observation of the Purcell effect in high-index-contrast micropillars. Appl. Phys. Lett. **90**, 191911 (2007)
76. A. Kiraz, P. Michler, C. Becher, B. Gayral, A. Imamoglu, L. Zhang, E. Hu, W.V. Schoenfeld, P.M. Petroff, Cavity-quantum electrodynamics using a single InAs quantum dot in a microdisk structure. Appl. Phys. Lett. **78**, 3932 (2001)

77. W.-H. Chang, W.-Y. Chen, H.-S. Chang, T.-P. Hsieh, J.-I. Chyi, T.-M. Hsu, Efficient single-photon sources based on low-density quantum dots in photonic-crystal nanocavities. Phys. Rev. Lett. **96**, 117401 (2006)
78. A. Badolato, K. Hennessy, M. Atatüre, J. Dreiser, E. Hu, P.M. Petroff, A. Imamoğlu, Deterministic coupling of single quantum dots to single nanocavity modes. Science **308**, 1158 (2005)
79. T. Yoshie, A. Scherer, J. Hendrickson, G. Khitrova, H.M. Gibbs, G. Rupper, C. Ell, O.B. Shchekin, D.G. Deppe, Vacuum Rabi splitting with a single quantum dot in a photonic crystal nanocavity. Nature (London) **432**, 200 (2004)
80. J.P. Reithmaier, G. Sek, A. Löffler, C. Hofmann, S. Kuhn, S. Reitzenstein, L.V. Keldysh, V.D. Kulakovskii, T.L. Reinecke, A. Forchel, Strong coupling in a single quantum dotsemiconductor microcavity system. Nature (London) **432**, 197 (2004)
81. E. Peter, P. Senellart, D. Martrou, A. Lemaitre, J. Hours, J.M. Gerard, J. Bloch, Exciton-photon strong-coupling regime for a single quantum dot embedded in a microcavity. Phys. Rev. Lett. **95**, 067401 (2005)
82. K. Hennessy, A. Badolato, M. Winger, D. Gerace, M. Atatüre, S. Gulde, S. Fält, E.L. Hu, A. Imamoğlu, Quantum nature of a strongly coupled single quantum dotcavity system. Nature (London) **445**, 896 (2007)
83. M. Nomura, Y. Ota, N. Kumagai, S. Iwamoto, Y. Arakawa, Large vacuum Rabi splitting in single self-assembled quantum dot-nanocavity system. Appl. Phys. Express **1** (2008)
84. A. Laucht, N. Hauke, J.M. Villas-Bôas, F. Hofbauer, G. Böhm, M. Kaniber, J.J. Finley, Dephasing of exciton polaritons in photoexcited InGaAs quantum dots in GaAs nanocavities. Phys. Rev. Lett. **103**, 87405 (2009)
85. A. Laucht, F. Hofbauer, N. Hauke, J. Angele, S. Stobbe, M. Kaniber, G. Böhm, P. Lodahl, M.C. Amann, J.J. Finley, Electrical control of spontaneous emission and strong coupling for a single quantum dot. New J. Phys. **11**
86. C. Kistner, K. Morgener, S. Reitzenstein, C. Schneider, S. Hofling, L. Worschech, A. Forchel, P. Yao, S. Hughes, Strong coupling in a quantum dot micropillar system under electrical current injection. Appl. Phys. Lett. **96**, 221102 (2010)
87. M. Lermer, N. Gregersen, F. Dunzer, S. Reitzenstein, S. Höfling, J. Mørk, L. Worschech, M. Kamp, A. Forchel, Bloch-wave engineering of quantum dot micropillars for cavity quantum electrodynamics experiments. Phys. Rev. Lett. **108**, 057402 (2012)
88. D.A.B. Miller, D.S. Chemla, T.C. Damen, A.C. Gossard, W. Wiegmann, T.H. Wood, C.A. Burrus, Band-edge electroabsorption in quantum well structures: the quantum-confined Stark effect. Phys. Rev. Lett. **53**, 2173 (1984)
89. C. Gerry, P. Knight, *Introductory Quantum Optics* (Cambridge University Press, 2005)
90. S. Haroche, J.M. Raimond, *Exploring the Quantum: Atoms, Cavities, and Photons* (Oxford Graduate Texts in Mathematics, OUP Oxford, 2006)
91. L. Mandel, E. Wolf, *Optical Coherence and Quantum Optics* (Cambridge University Press, 1995)
92. M.O. Scully, S. Zubairy, *Quantum Optics* (Cambridge University Press, 1997)
93. H.J. Carmichael. *Statistical Methods in Quantum Optics. Number v. 1 in Statistical Methods in Quantum Optics* (Springer, 1999)
94. H.J. Carmichael, *Statistical Methods in Quantum Optics 2: Non-Classical Fields* (Springer, Theoretical and Mathematical Physics, 2008)
95. L.D. Landau, E.M. Lifshitz, Quantum mechanics. Course of Theoretical. Physics **3**, 768 (1977)
96. A. Messiah, *Quantum Mechanics*, vol. 2 (North-Holland, Amsterdam, 1965)
97. H. Rigneault, S. Monneret, Field quantization and spontaneous emission in lossless dielectric multilayer structures. Quantum Semiclassical Opt.: J. Eur. Opt. Soc. Part B **9**, 1017 (1999)
98. G. Hétet, L. Slodička, A. Glätzle, M. Hennrich, R. Blatt, QED with a spherical mirror. Phys. Rev. A **82**, 063812 (2010)
99. M.A. Rippin, P.L. Knight, Modified spontaneous emission in cylindrical microcavities: waveguiding and distributed Bragg reflecting structures. J. Mod. Opt. **43**, 807 (1996)

100. L.C. Andreani, G. Panzarini, J.-M. Gérard, Strong-coupling regime for quantum boxes in pillar microcavities: theory. Phys. Rev. B **60**, 13276 (1999)
101. I. Schuster, A. Kubanek, A. Fuhrmanek, T. Puppe, P.W.H. Pinkse, K. Murr, G. Rempe, Nonlinear spectroscopy of photons bound to one atom. Nat. Phys. **4**, 382 (2008)
102. F.P. Laussy, E. del Valle, C. Tejedor, Strong coupling of quantum dots in microcavities. Phys. Rev. Lett. **101**, 083601 (2008)
103. F. Bloch, A. Siegert, Magnetic resonance for nonrotating fields. Phys. Rev. **57**, 522 (1940)
104. J. Von Neumann, Wahrscheinlichkeitstheoretischer Aufbau der Quantenmechanik. Göttinger Nachr. **1**(10), 245–272 (1927)
105. G. Lindblad, On the generators of quantum dynamical semigroups. Commun. Mathem. Phys. **48**
106. E.T. Jaynes, F.W. Cummings, Comparison of quantum and semiclassical radiation theories with application to the beam maser. Proc. IEEE **51**, 89 (1963)
107. T.R. Nielsen, P. Gartner, F. Jahnke, Many-body theory of carrier capture and relaxation in semiconductor quantum-dot lasers. Phys. Rev. B **69**, 235314 (2004)
108. N.S. Averkiev, M.M. Glazov, A.N. Poddubnyi, Collective modes of quantum dot ensembles in microcavities. JETP **108**, 836 (2009)
109. C.W. Gardiner, P. Zoller, *Quantum Noise: A Handbook of Markovian and Non-Markovian Quantum Stochastic Methods with Applications to Quantum Optics*, Vol. 56 (Springer, 2004)
110. Z. Barticevi, G. Fuster, M. Pacheco, Effect of an electric field on the Bohm-Aharonov oscillations in the electronic spectrum of a quantum ring. Phys. Rev. B **65**, 193307 (2002)
111. A. Bruno-Alfonso, A. Latgé, Aharonov-Bohm oscillations in a quantum ring: eccentricity and electric-field effects. Phys. Rev. B **71**, 125312 (2005)
112. O.V. Kibis, S.V. Malevannyy, L. Huggett, D.G.W. Parfitt, M.E. Portnoi, Superlattice properties of helical nanostructures in a transverse electric field. Electromagnetics **25**, 425 (2005)
113. O.V. Kibis, M.E. Portnoi, Semiconductor nanohelix in electric field: a superlattice of the new type. Tech. Phys. Lett. **33**, 878 (2007)
114. O.V. Kibis, M.E. Portnoi, Superlattice properties of semiconductor nanohelices in a transverse electric field. Phys. E (Amsterdam) **40** 1899 (2008)
115. M.E. Portnoi, O.V. Kibis, V.L. Campo Jr., M. Rosenau da Costa, L. Huggett, S.V. Malevannyy, Helical nanostructures and Aharonov-Bohm quantum rings in a transverse electric field in *Proceedings of 28th ICPS, AIP Conference Proceedings*, vol 893, 703 (2007)
116. E.A. Avrutin, M.E. Portnoi, Estimate of the lifetimes of nonequilibrium carriers in a semiconductor irradiated with heavy ions. Sov. Phys. Semicond. **22**, 968 (1988)
117. M.E. Portnoi, O.V. Kibis, M. Rosenau da Costa, Terahertz applications of carbon nanotubes. Superlatt. Microstruct. **43**, 399 (2008)
118. M.E. Portnoi, M. Rosenau da Costa, O.V. Kibis, I.A. Shelykh, Magnetically controlled terahertz absorption and emission in carbon nanotubes. Int. J. Mod. Phys. B **23**, 2846 (2009)
119. K.G. Batrakov, O.V. Kibis, P.P. Kuzhir, M. Rosenau da Costa, M.E. Portnoi, Terahertz processes in carbon nanotubes. J. Nanophoton. **4**, 041665 (2010)
120. R.R. Hartmann, I.A. Shelykh, M.E. Portnoi, Excitons in narrow-gap carbon nanotubes. Phys. Rev. B **84**, 035437 (2011)
121. K.V. Kavokin, M.A. Kaliteevski, R.A. Abram, A.V. Kavokin, S. Sharkova, I.A. Shelykh, Stimulated emission of terahertz radiation by exciton-polariton lasers. Appl. Phys. Lett. **97**, 201111 (2010)
122. E. del Valle, A. Kavokin, Terahertz lasing in a polariton system: quantum theory. Phys. Rev. B **83**, 193303 (2011)
123. I.G. Savenko, I.A. Shelykh, M.A. Kaliteevski, Nonlinear terahertz emission in semiconductor microcavities. Phys. Rev. Lett. **107**, 027401 (2011)
124. C. Weisbuch, M. Nishioka, A. Ishikawa, Y. Arakawa, Observation of the coupled exciton-photon mode splitting in a semiconductor quantum microcavity. Phys. Rev. Lett. **69**, 3314 (1992)
125. See, e.g., a special volume devoted to the physics of microcavities. Phys. Stat. Sol. B **242**(11) (2005)

126. J. Kasprzak, M. Richard, S. Kundermann, A. Baas, P. Jeambrun, J.M.J. Keeling, F.M. Marchetti, M.H. Szymanska, R. André, J.L. Staehli, V. Savona, P.B. Littlewood, B. Deveaud, Le Si Dang, Boseeinstein condensation of exciton polaritons. Nature (London) **443**, 409 (2006)
127. R. Balili, V. Hartwell, D. Snoke, L. Pfeiffer, K. West, Bose-einstein condensation of microcavity polaritons in a trap. Science **316**, 1007 (2007)
128. A. Amo, D. Sanvitto, F.P. Laussy, D. Ballarini, E. del Valle, A. Lemaître, M.D. Martin, J. Bloch, D.N. Krizhanovskii, M.S. Skolnick, C. Tejedor, L. Vina, Collective fluid dynamics of a polariton condensate in a semiconductor microcavity. Nature (London) **457**, 291 (2009)
129. T.C.H. Liew, I.A. Shelykh, G. Malpuech, Polaritonic devices. Phys. E **43**, 1543 (2011)
130. S. Christopoulos, G. Baldassarri, Höger von Högersthal, A.J.D. Grundy, P.G. Lagoudakis, A.V. Kavokin, J.J. Baumberg, G. Christmann, R. Butté, E. Feltin, J.-F. Carlin, and N. Grandjean. Room-temperature polariton lasing in semiconductor microcavities. Phys. Rev. Lett. **98**, 126405 (2007)
131. C. Leyder, T.C.H. Liew, A.V. Kavokin, I.A. Shelykh, M. Romanelli, JPh Karr, E. Giacobino, A. Bramati, Interference of coherent polariton beams in microcavities: polarization-controlled optical gates. Phys. Rev. Lett. **99**, 196402 (2007)
132. A.V. Kavokin, I.A. Shelykh, T. Taylor, M.M. Glazov, Vertical cavity surface emitting terahertz laser. Phys. Rev. Lett. **108**, 197401 (2012)
133. C. Ciuti, Branch-entangled polariton pairs in planar microcavities and photonic wires. Phys. Rev. B **69**, 245304 (2004)
134. S. Savasta, O. Di Stefano, V. Savona, W. Langbein, Quantum complementarity of microcavity polaritons. Phys. Rev. Lett. **94**, 246401 (2005)
135. R. Johne, N.A. Gippius, G. Pavlovic, D.D. Solnyshkov, I.A. Shelykh, G. Malpuech, Entangled photon pairs produced by a quantum dot strongly coupled to a microcavity. Phys. Rev. Lett. **100**, 240404 (2008)
136. M.A. Kaliteevski, S. Brand, R.A. Abram, A. Kavokin, Le Si Dang, Whispering gallery polaritons in cylindrical cavities. Phys. Rev. B **75**, 233309 (2007)
137. F.P. Laussy, E. del Valle, C. Tejedor, Luminescence spectra of quantum dots in microcavities. I. Bosons. Phys. Rev. B **79**, 235325 (2009)
138. E. del Valle, F.P. Laussy, C. Tejedor, Luminescence spectra of quantum dots in microcavities. II. Fermions. Phys. Rev. B **79**, 235326 (2009)
139. E. del Valle, F.P. Laussy, Mollow triplet under incoherent pumping. Phys. Rev. Lett. **105**, 233601 (2010)
140. I.G. Savenko, O.V. Kibis, I.A. Shelykh, Asymmetric quantum dot in a microcavity as a nonlinear optical element. Phys. Rev. A **85**, 053818 (2012)
141. P.A. George, C. Manolatou, F. Rana, A.L. Bingham, D.R. Grischkowsky, Integrated waveguide-coupled terahertz microcavity resonators. Appl. Phys. Lett. **91**, 191122 (2007)
142. C.M. Yee, M.S. Sherwin, High-Q terahertz microcavities in silicon photonic crystal slabs. Appl. Phys. Lett. **94**, 154104 (2009)
143. Y. Todorov, A.M. Andrews, I. Sagnes, R. Colombelli, P. Klang, G. Strasser, C. Sirtori, Strong light-matter coupling in subwavelength metal-dielectric microcavities at terahertz frequencies. Phys. Rev. Lett. **102**, 186402 (2009)
144. S. Sree Harsha, N. Laman, D. Grischkowsky, D. Grischkowsky, High-Q terahertz Bragg resonances within a metal parallel plate waveguide. Appl. Phys. Lett. **94**, 091118 (2009)
145. O.V. Kibis, D.G.W. Parfitt, M.E. Portnoi, Superlattice properties of carbon nanotubes in a transverse electric field. Phys. Rev. B **71**, 035411 (2005)
146. M.O. Scully, M.S. Zubairy, *Quantum Optics* (University Press, Cambridge, 2001)
147. C. Cohen-Tannoudji, J. Dupont-Roc, G. Grynberg, *Atom-Photon Interactions: Basic Processes and Applications* (Wiley, Chichester, 1998)
148. C.A. Vera, H. Vinck-Posada, A. González, Polariton lasing in a multilevel quantum dot strongly coupled to a single photon mode. Phys. Rev. B **80**, 125302 (2009)
149. B.S. Williams, Terahertz quantum-cascade lasers. Nat. Photon. **1**, 517 (2007)

150. M.A. Belkin, J.A. Fan, S. Hormoz, F. Capasso, S.P. Khanna, M. Lachab, A.G. Davies, E.H. Linfield et al., Terahertz quantum cascade lasers with copper metal-metal waveguides operating up to 178 K. Opt. Express **16**, 3242 (2008)
151. S. Kumar, Q. Hu, J.L. Reno, 186 K operation of terahertz quantum-cascade lasers based on a diagonal design. Appl. Phys. Lett. **94**
152. G.L. Carr, M.C. Martin, W.R. McKinney, K. Jordan, G.R. Neil, G.P. Williams, High-power terahertz radiation from relativistic electrons. Nature **420**
153. M. Tonouchi, Cutting-edge terahertz technology. Nat. Photon. **1**, 97 (2007)
154. D.L. Woolard, T.R. Globus, B.L. Gelmont, M. Bykhovskaia, A.C. Samuels, D. Cookmeyer, J.L. Hesler, T.W. Crowe, J.O. Jensen, J.L. Jensen et al., Submillimeter-wave phonon modes in DNA macromolecules. Phys. Rev. E **65**, 051903 (2002)
155. T.R. Globus, D.L. Woolard, T. Khromova, T.W. Crowe, M. Bykhovskaia, B.L. Gelmont, J. Hesler, A.C. Samuels, THz-spectroscopy of biological molecules. J. Biol. Phys. **29**, 89 (2003)
156. P.F. Taday, I.V. Bradley, D.D. Arnone, M. Pepper, Using terahertz pulse spectroscopy to study the crystalline structure of a drug: a case study of the polymorphs of ranitidine hydrochloride. J. Pharm. Sci. **92**, 831 (2003)
157. C. Jansen, F. Neubauer, J. Helbig, D.M. Mittleman, M. Koch, Flexible Bragg reflectors for the terahertz regime composed of polymeric compounds. in *Infrared and Millimeter Waves, 2007 and the 2007 15th International Conference on Terahertz Electronics. IRMMW-THz. Joint 32nd International Conference*. IEEE, p. 984 (2007)
158. M. Lax, Formal theory of quantum fluctuations from a driven state. Phys. Rev. **129**, 2342 (1963)
159. N. Wiener, Generalized harmonic analysis. Acta Mathem. **55**, 117 (1930)
160. A. Khintchine, Korrelationstheorie der stationären stochastischen prozesse. Math. Ann. **109**, 604 (1934)

Chapter 14
Intense Terahertz Radiation Effect on Electronic and Intraband Optical Properties of Semiconductor Quantum Rings

H.M. Baghramyan, M.G. Barseghyan, A.A. Kirakosyan and D. Laroze

Abstract The current chapter aims to theoretically demonstrate that intense Terahertz (THz) laser field can be a powerful method for the controlling of electro-optical properties of quantum rings (QRs). We explore the electronic and impurity states, charge localization and intraband optical phenomena in GaAs/GaAlAs QRs irradiated by the intense THz laser field. Single and concentric double QRs, as well as artificial molecules formed by the laterally aligned QRs are explored. It is demonstrated how the laser field modifies the energy spectrum and wave functions by the strong distortion of the original cylindrical geometry of quantum confinement. Moreover, our findings give an insight on the laser field-affected inter-ring coupling of concentric double QRs and dissociation of QR molecules. Additionally, the new way of control of quantum-confining Stark effect with intense THz laser field is introduced.

H.M. Baghramyan (✉) · D. Laroze
Instituto de Alta Investigación, CEDENNA, Universidad de Tarapacá,
Casilla 7D, Arica, Chile
e-mail: hbaghramyan@uta.cl

H.M. Baghramyan
Armenian State Pedagogical University after Khachatur Abovyan,
Tigran Mets ave. 17, Yerevan 0010, Armenia

M.G. Barseghyan · A.A. Kirakosyan
Department of Solid State Physics, Yerevan State University,
Alex Manoogian 1, 0025 Yerevan, Armenia
e-mail: mbarsegh@ysu.am

A.A. Kirakosyan
e-mail: kirakosyan@ysu.am

M.G. Barseghyan
National University of Architecture and Construction of Armenia,
Teryan 105, 0009 Yerevan, Armenia

D. Laroze
Yachay Tech University, School of Physical Sciences and Nanotechnology,
00119 Urcuquí, Ecuador
e-mail: dlarozen@uta.cl

V.M. Fomin (ed.), *Physics of Quantum Rings*, NanoScience and Technology,
https://doi.org/10.1007/978-3-319-95159-1_14

14.1 Introduction

The THz range is known to be from 0.3 to 10 THz, so it bridges the microwave and infrared regions of electromagnetic radiation. The THz technology can be applied in numerous areas such as information and communications [1], biology and medical sciences [2, 3], homeland security [4], nondestructive evaluation [5, 6], environmental monitoring [7]; astronomy [8], etc. In all these areas the semiconductor nanostructures have a significant role [9], among which a particular place has already been given to QRs. Indeed, if compared with widely studied quantum dots (QDs), the confinement in QRs is stronger owing to the altered and multiply connected shape, which can result in a single bound state and be suitable for THz intersublevel detectors with a strong response in the 1–3 THz range [10]. In addition, the tunneling effect in QRs is responsible for the intermediate-band in the coupled array of QRs [11], that was used as an additional path for the electron transitions to the continuum to enhance the photocurrents for solar cell applications [12, 13] and resonant tunneling devices as well [14]. Besides that, doubly-connected ring-like geometry is currently used to form materials with unique properties: in quantum dot-ring nanostructures [15, 16] wave function engineering [17, 18] demonstrated that THz optical absorption, spin relaxation times, and conducting properties are highly tunable by means of the confinement; the core-shell nano-ring structure of $\alpha - Fe_2O_3$@Carbon leads to much improved specific capacity, cycling stability and rate capability compared with that of bare nano-ring $\alpha - Fe_2O_3$ [19]; the electrical properties of a p-type semiconductor can be mimicked by a metamaterial solely made up of an n-type semiconductor ZnO rings [20]; etc.

Besides that, research on the electronics and optical response of intense THz radiation excited QRs is very interesting, if compared with the studies done under with solid-state lasers [13, 21]. High-power THz radiation of CO_2 or free electron lasers creates a variety of nonlinear effects that considerably differ from the relevant effects at visible and infrared ranges [22]. The point is that the semiclassical description of electron interaction with the radiation changes to completely quantized limit at THz frequencies. Certainly, it is manifested by the pioneering works like the dynamical Franz-Keldysh effect [23–25] or the photon drag effect in bulk [26, 27] and low-dimensional semiconductors [28, 29]. In this context, the recent observations also should be considered such as the photon drag effect in promising topological insulators [30], the photon-mediated tunneling in single-C_{60}-molecule transistors [31], the high-order-sideband generation in $In_{0.06}Ga_{0.94}As/Al_{0.3}Ga_{0.7}As$ quantum wells (QWs) caused by the electron-hole recollisions [32], or the saturation of the photoresponse to intense THz radiation in AlGaN/GaN high electron mobility transistors [33].

This chapter dwells upon the theoretical investigations of electronic states influenced by intense THz laser field and related intraband optical processes in quantum rings of various configurations adopting the high-frequency approximation of Floquet theory. In addition, the effects of laser field are discussed considering a homogeneous electric field and hydrogenic impurity effects.

14.2 Laser-Dressed States in High-Frequency Approximation

We consider two-dimensional GaAs/GaAlAs QRs, since the heights of the QRs can be 10 times smaller than the radial sizes [34]. Under the laser field with vector potential $\mathbf{A}_\perp(\mathbf{r}, t)$ the time-dependent Schrödinger equation of the system is given by

$$\left[\frac{1}{2m}\left(\widehat{\mathbf{p}}_\perp - \frac{e}{c}\mathbf{A}_\perp(\mathbf{r}, t)\right)^2 + V(\mathbf{r}_\perp)\right]\Phi(\mathbf{r}_\perp, t) = i\hbar\frac{\partial}{\partial t}\Phi(\mathbf{r}_\perp, t), \tag{14.1}$$

where $m = 0.067\, m_0$ is the effective mass in GaAs [40], m_0 is the free-electron mass, $\widehat{\mathbf{p}}_\perp$ is the momentum operator, e is the electron charge and $V(\mathbf{r}_\perp)$ is the confining potential. The dipole approximation is considered [35, 36], so the vector potential is independent on spacial parameters - $\mathbf{A}_\perp(\mathbf{r}, t) \approx \mathbf{A}(t) = A_0\cos(2\pi\nu t)\widehat{\mathbf{e}}_x$. Here $\widehat{\mathbf{e}}_x$ is the unit vector of polarization of linearly polarized laser field and $A_0 = cE_0/(2\pi\nu)$ is defined by the E_0 electric field strength and ν frequency. Laser field is taken nonresonant with the bandgap of GaAs following the $\nu < E_{\text{gap}}^{\text{GaAs}}/(2\pi\hbar) \approx 367\text{THz}$ condition [37].

Under dipole approximation the Kramers-Henneberger [38, 39] unitary transformation can be used:

$$\Psi(\mathbf{r}_\perp, t) = \exp\left[\left(\frac{i}{\hbar}\right)\boldsymbol{\alpha}\cdot\widehat{\mathbf{p}}_\perp\right] \times \exp\left[\frac{i}{\hbar}\frac{e^2}{2mc^2}\int^t \mathbf{A}^2(t')dt'\right]\Phi(\mathbf{r}_\perp, t), \tag{14.2}$$

where

$$\boldsymbol{\alpha}(t) = -\frac{e}{mc}\int^t \mathbf{A}(\tau)d\tau. \tag{14.3}$$

Now, after Kramers-Henneberger transformation, the confining potential depends on time and not the vector potential, that is equivalent to moving from the laboratory to accelerated frame of reference, that follows the quiver motion $\boldsymbol{\alpha}(t)$:

$$\left[\frac{\widehat{\mathbf{p}}_\perp^2}{2m} + V\left(\mathbf{r}_\perp + \boldsymbol{\alpha}(t)\right)\right]\Psi(\mathbf{r}_\perp, t) = i\hbar\frac{\partial}{\partial t}\Psi(\mathbf{r}_\perp, t). \tag{14.4}$$

From (14.3) we have $\alpha(t) = \alpha_0\sin(2\pi\nu t)$, $\alpha_0 = -\left(e/\left(m\epsilon_h^{1/4}\nu^2\right)\right)\sqrt{I/\left(2c\pi^3\right)}$ parameter that considers laser field effect, comprises both the intensity I and frequency ν of laser field. The latters can be chosen in a broad range in units of kW/cm^2 and THz correspondingly [22], and $\epsilon_h = 10.9$ is the high-frequency dielectric constant of GaAs [40].

Equation (14.4) is solved using the nonperturbative Floquet method [41], that is used for linear partial differential equations with periodic coefficients. Originally, Floquet method was applied for atoms affected by intense laser radiation [36], then for semiconductor low-dimensional structures [35, 42–45]. Following the Floquet

theory, the solution of (14.4) is sought by expanding $\Psi(\mathbf{r}_\perp, t)$ and confining potential $V(\mathbf{r}_\perp + \boldsymbol{\alpha}(t))$ to an infinite Fourier series:

$$\Psi(\mathbf{r}_\perp, t) = \exp(-i(E/\hbar)t) \sum_{n=-\infty}^{n=\infty} \exp(-2i\pi n\nu t)\, \phi_n(\mathbf{r}_\perp), \tag{14.5}$$

and

$$V(\mathbf{r}_\perp + \boldsymbol{\alpha}(t)) = \sum_{n=-\infty}^{n=\infty} \exp(-2i\pi n\nu t)\, V_n(\mathbf{r}_\perp, \alpha_0), \tag{14.6}$$

where

$$V_n(\mathbf{r}_\perp, \alpha_0) = \frac{1}{T}\int_0^T \exp(2i\pi n\nu\tau)\, V(\mathbf{r}_\perp + \boldsymbol{\alpha}(\tau))\, \mathrm{d}\tau, \tag{14.7}$$

with T being the laser field period. Substituting (14.5) and (14.6) expressions into (14.4), the following infinite system of time-independent coupled equations is obtained:

$$\left[\frac{\widehat{\mathbf{p}}_\perp^2}{2m} + V_0(\mathbf{r}_\perp, \alpha_0) - (E + 2\pi\nu n)\right]\phi_n(\mathbf{r}_\perp) = -\sum_{\substack{m=-\infty \\ m\neq n}}^{m=\infty} V_{n-m}(\mathbf{r}_\perp, \alpha_0)\phi_m(\mathbf{r}_\perp). \tag{14.8}$$

This system of equations is solved employing the iteration procedure, the detailed description of which is given in [36]. We study the stationary states, that appear if the Floquet method is applied in high-frequency approximation [35, 45, 46]. Namely, it is assumed that the laser field frequency ν is very high, so the electron *feels* only the time-averaged laser-dressed confining potential. High values of (ν, I) always can be manipulated, at the same time remaining in the range for the dipole approximation and nonresonant laser field requirements to be fulfilled [35]: for GaAs/GaAlAs the intensity can be taken up to the MW/cm^2 [47]. In high-frequency approximation only the zeroth-order solution of (14.8) contributes, leading to the following time-independent Schrödinger [36]:

$$\left[\frac{\widehat{\mathbf{p}}_\perp^2}{2m} + V_d(\mathbf{r}_\perp, \alpha_0)\right]\Psi_d(\mathbf{r}_\perp) = E_d\Psi_d(\mathbf{r}_\perp). \tag{14.9}$$

Here $\Psi_d(\mathbf{r}_\perp) = \phi_0(\mathbf{r}_\perp)$ and E_d define correspondingly the laser-dressed Floquet eigenstates and eigenvalues. Equation (14.9) can be interpreted as one-electron stationary problem in $V_d(\mathbf{r}_\perp, \alpha_0)$ dressed confining potential:

$$V_d(\mathbf{r}_\perp, \alpha_0) = \frac{1}{T}\int_0^T V(\mathbf{r}_\perp + \boldsymbol{\alpha}(\tau))\, \mathrm{d}\tau = \frac{1}{T}\int_0^T V(x + \alpha(\tau), y)\, \mathrm{d}\tau. \tag{14.10}$$

The developed above theoretical model is used in the subsequent sections as a basis for the study of laser-dressed electronic states and intraband optical properties in QRs with various geometry.

14.3 Intense Terahertz Radiation Effect on a Single Quantum Ring

The dressing effect of intense laser field strongly modifies the confined states in semiconductor nanostructures. In fact, laser field can change the density of states profile of QWs to a profile characteristic to quantum wires [42] and the density of states profile of quantum wires to a profile typical to QDs [44, 45] and a single QW can be reformed to double QW by the appropriate manipulation with laser field parameters [35]. Moreover, research on the intense laser field assisted transport phenomena in semiconductor nanostructures were performed [48–50]. In this connection, it was demonstrated that the dressing field immensely increases the conductivity of two-dimensional electron gas in GaAs QWs [49]. Also, the theory of spin-dependent transport developed in [50] demonstrates that the high-frequency laser field induces the renormalization of spin-orbit coupling constants that modify the conductivity of a Datta-and-Das spin transistor. Furthermore, the studies of laser fields with different polarizations, showed that a circular polarization can lead to a monotonic reducing of the isotropic conductivity of graphene, while a linear polarization augments the huge anisotropy of conductivity if laser field intensity is incremented [51].

This section begins the study of the laser-dressed states in QRs considering a single GaAs/GaAlAs QR [52, 53]. We demonstrate and give a detailed description of the effects induced by the laser field reformation of the confining potential, an analytical expression of which is obtained. Eventually, intraband transitions are explored considering the interplay of laser and homogeneous electric fields.

14.3.1 Laser-Dressed States

In Fig. 14.1 the schematic view of a single QR structure is presented. The inner and outer radii, as well as the direction of laser field polarization and propagation, are shown.

As a $V(\mathbf{r}_\perp)$ confining potential in (14.1) for a single QR a finite square-type well is taken:

$$V(x, y) = \begin{cases} 0, & \text{if } R_1 \leq \sqrt{x^2 + y^2} \leq R_2, \\ V_0, & \text{if } \sqrt{x^2 + y^2} < R_1, \text{ or } \sqrt{x^2 + y^2} > R_2. \end{cases} \tag{14.11}$$

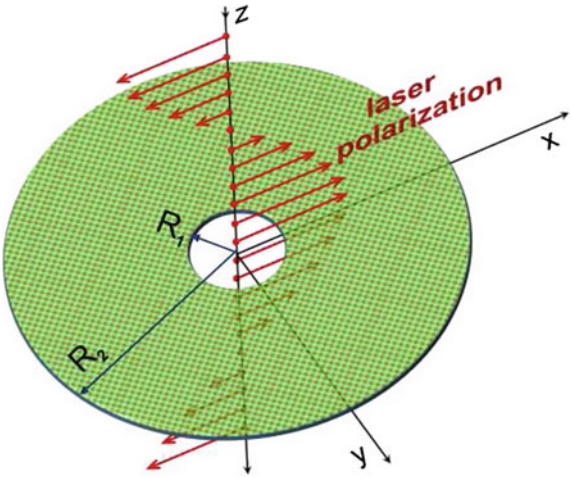

Fig. 14.1 The schematic view of a single QR heterostructure. R_1 and R_2 are the inner and outer radii, respectively. The directions of the laser beam propagation and its polarization are presented as well (reprinted from [52] with the permission of AIP Publishing)

For the particular potential function given by (14.11), laser-dressed potential in (14.10) may be analytically integrated into the closed form:

$$
\begin{aligned}
V_d(\mathbf{r}_\perp, \alpha_0) = \tfrac{V_0}{\pi}\mathrm{Re}\Bigg[\pi - \\
-\theta\left(\alpha_0 - x - \mathrm{Re}\left(\sqrt{R_1^2 - y^2}\right)\right)\arccos\left(\frac{\mathrm{Re}\left(\sqrt{R_1^2-y^2}\right)+x}{\alpha_0}\right) + \\
+\theta\left(\alpha_0 - x - \mathrm{Re}\left(\sqrt{R_2^2 - y^2}\right)\right)\arccos\left(\frac{\mathrm{Re}\left(\sqrt{R_2^2-y^2}\right)+x}{\alpha_0}\right) - \\
-\theta\left(\alpha_0 + x - \mathrm{Re}\left(\sqrt{R_1^2 - y^2}\right)\right)\arccos\left(\frac{\mathrm{Re}\left(\sqrt{R_1^2-y^2}\right)-x}{\alpha_0}\right) + \\
+\theta\left(\alpha_0 + x - \mathrm{Re}\left(\sqrt{R_2^2 - y^2}\right)\right)\arccos\left(\frac{\mathrm{Re}\left(\sqrt{R_2^2-y^2}\right)-x}{\alpha_0}\right)\Bigg],
\end{aligned}
\tag{14.12}
$$

where $\theta(u)$ is the Heaviside unit-step function.

In Sects. 14.3 and 14.4 the laser-dressed energy eigenvalues and eigenfunctions are calculated by solving (14.9) with a two-dimensional diagonalization technique [54–56]. The $\Psi_d(x, y)$ are linearly expanded in terms of the eigenfunctions of a rectangle with dimensions $L_x \times L_y$ and quantum numbers (n, m) [57].

The numerical calculations are carried out for $V_0 = 228\,\mathrm{meV}$. The Fig. 14.2 presents the wave functions of the first three laser-dressed states for various values of the parameter α_0. The upper panel of Fig. 14.2 demonstrates that the laser field destroys the cylindrical symmetry, resulting in the ground state wave function localized along the direction (y-axis) perpendicular to the laser field polarization. The further increase of the laser parameter α_0 strengthens the confinement of the effective potential and the probability density of the ground state increases along the y-axis. At the same time, the peaks of the wave function for $j = 2$ and $j = 3$ become

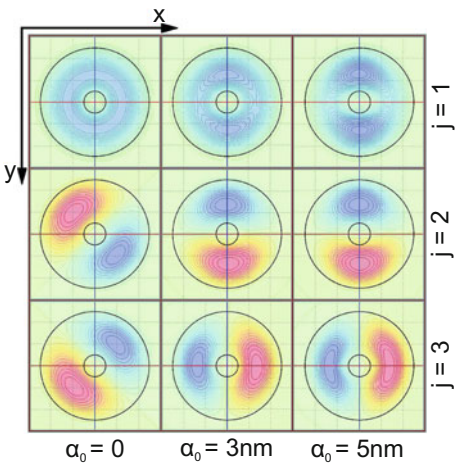

Fig. 14.2 The wave functions of the first three ($j = 1, 2, 3$) laser-dressed states for different values of the laser field parameter α_0. The results are presented for $R_1 = 5$ nm and $R_2 = 25$ nm (reprinted from [53] under a CC BY license)

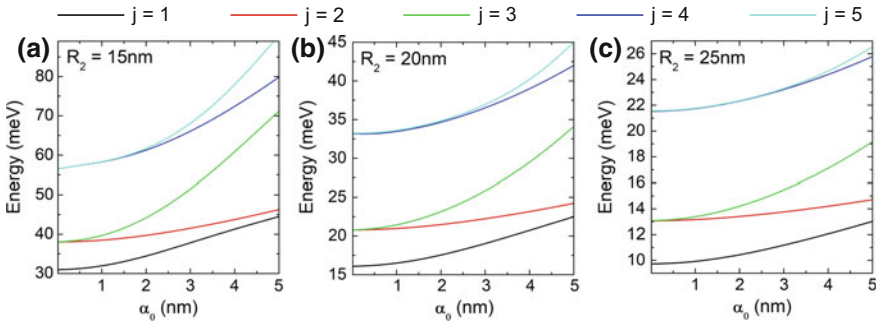

Fig. 14.3 The first five dressed energy levels of the electron as a function of the laser field parameter α_0. The results are presented for fixed inner radius $R_1 = 5$ nm. Several values of outer radius R_2 are considered (reprinted from [52] with permission of AIP Publishing)

exactly positioned along y- and x-axes, respectively. Thereby, the laser field totally destroys the axial symmetry and the cylindrical QR is transformed into a QR with an elliptic cross-section.

In Fig. 14.3a–c the dependencies of the first five laser-dressed low energy levels of the confined electron on the laser parameter α_0 are presented for different values of outer radius R_2. As it is clearly observed, the first two excited levels are twice degenerated in the absence of the laser field ($\alpha_0 = 0$). The laser field removes this degeneracy as a result of a broken axial symmetry. Comparing the curves in Fig. 14.3a–c, one can observe that the increment of the outer radius lowers the energy levels for all values of the laser field parameter, due to the weakening of the size quantization for

the electron. Note, that the influence of the laser field-induced deformation of the confining potential of the electronic states is stronger for smaller values of the outer radius R_2. For example, in a case with $R_2 = 15$ nm, an increase in α_0 from 0 to 5 nm produces an increase of the ground state energy of 13.56 meV, while for $R_2 = 25$ nm, the ground state energy changes only with 3.3meV. On the other hand, the splitting of the first and second excited energy levels for different values of the laser field parameter also can be clearly inferred from Fig. 14.3. This is a result of some delay of the broken symmetry influence on the electron for higher energy levels. For instance, if $R_2 = 25$ nm (Fig. 14.3c), the splitting of the first excited state starts approximately at $\alpha_0 = 0.5$ nm, while the second excited state splitting starts at $\alpha_0 = 3$ nm.

Now let us commence to study the impact of external static homogeneous electric field on laser-dressed states.

14.3.2 Electric Field Influence on Laser-Dressed States

The influence of electric field in (14.1) is considered by adding the potential term $-e\mathbf{F}\cdot\mathbf{r}_\perp$, where $\mathbf{F}$ is the strength of the homogeneous electric field. We remark that since the dependence of $-e\mathbf{F}\cdot\mathbf{r}_\perp$ on $\mathbf{r}_\perp$ is linear after the time-averaging integration (similar to the one for the confining potential in (14.10)) this potential remains unchanged. Considering this, the Schrödinger equation takes the following form:

$$\left[\frac{\widehat{\mathbf{p}}_\perp^2}{2m} + V_d(\mathbf{r}_\perp, \alpha_0) - e\mathbf{F}\cdot\mathbf{r}_\perp\right]\Psi_d(\mathbf{r}_\perp) = E_d\Psi_d(\mathbf{r}_\perp), \tag{14.13}$$

where $V_d(\mathbf{r}_\perp, \alpha_0)$ is defined by (14.10).

It should be recalled that for any finite barrier potential well influenced by the electric field there is no veritable electron bound state. Every energy level associated with a quantum state has a nonzero linewidth correlated with the mean time of tunneling out from the biased structure [58]. As the static electric field increases, the electron energies start to descend (quantum confined Stark effect), the tunneling time of a given state becomes smaller, and the energy linewidth of the level augments [59]. However, this could be a real theoretical problem only for highly excited states which become unsteady at high enough values of the electric field. The lower electronic states are quasi-bound since the associated tunneling time is much longer than any characteristic time involved in the intraband or interband transitions [58]. Later on, a simple criterion will be established in order to consider an excited state as a *quasi-bound* one.

Figure 14.4 presents the biased laser-dressed confinement potential of the QR. The direction of electric field is fixed along the x-axis. Let us further consider as the *interior* of the unbiased dressed potential well all points having the potential smaller than V_0. We will denote by R_x and R_y the *effective radii* (the effective radius is defined as the half of the maximum confinement length on some particular direction) of the potential well on the direction of the electric field and the transverse direction

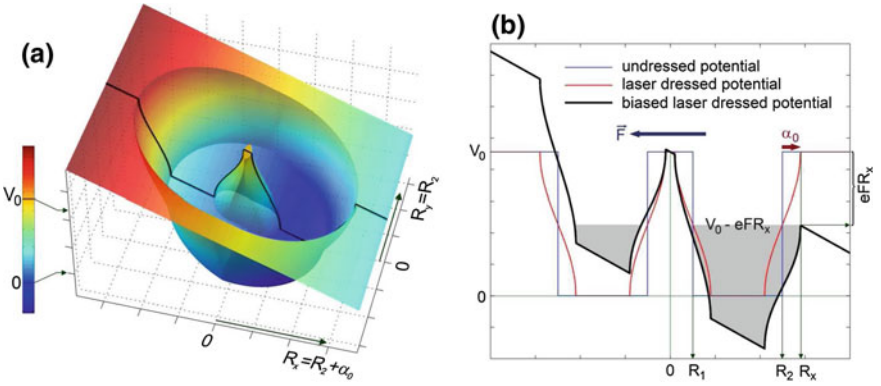

Fig. 14.4 **a** Confinement potential of the QR modified by simultaneous actions of the laser and electric fields. The effective radius R_x in the field direction depends on the laser field parameter. **b** Axial section of the confinement potential along the x-axis. The grey area symbolizes the *stability zone* of the electron bound states (reprinted from [53] under a CC BY license)

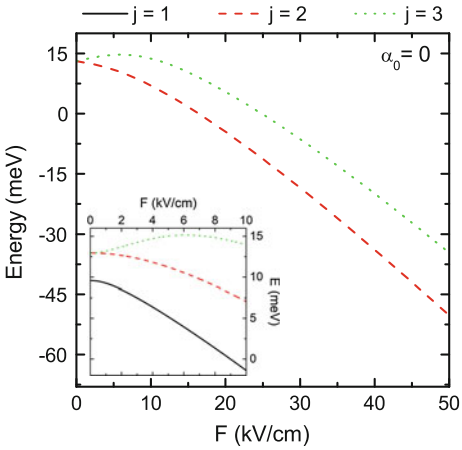

Fig. 14.5 The first three undressed ($\alpha_0 = 0$) energy levels of the electron as function of the electric field strength F. The results are presented for $R_1 = 5\,\text{nm}$ and $R_2 = 25\,\text{nm}$ (reprinted from [53] under a CC BY license)

y, respectively. Figure 14.4b shows the cross-section of the confinement potential along the $y = 0$ direction. One may observe that the right edge of the potential well at $R_x = R_2 + \alpha_0$ is the lowest point of the confinement zone. Our approximate criterion of energy level stability is based on the assumption that any electronic state j in the well which energy E_d^j is still far below the lowest point of confinement may be considered as *quasi-bound*: $E_d^j \ll V_0 - eF(R_2 + \alpha_0)$. As an example, for $R_2 = 25\,\text{nm}$, and $\alpha_0 = 5$ nm the lowest energy of confinement is 78 meV. Thus, only excited states with considerably smaller energies should be considered in the calculations.

In Fig. 14.5 the dependencies of the first three undressed energy levels of the confined electron on the electric field strength F are presented. Similar to the results

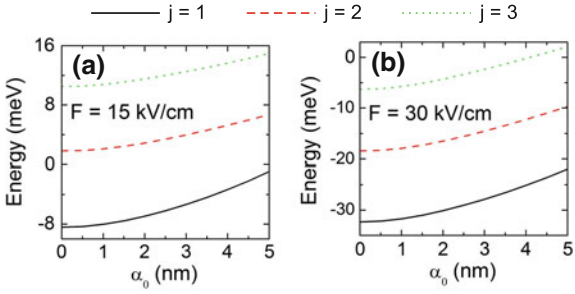

Fig. 14.6 The first three dressed energy levels of the electron as function of the laser field parameter α_0. The results are presented for $R_1 = 5$ nm and $R_2 = 25$ nm. Several values of the electric field strength F are considered (reprinted from [53] under a CC BY license)

in Fig. 14.3, the excited state is twice degenerated in the absence of both fields. The electric field (like the laser field in Fig. 14.3) removes this degeneracy as a result of broken axial symmetry. With the increase of the electric field strength, the ground state energy only decreases due to the lowering of the bottom of the confinement potential, which is the analog of the quantum confined Stark effect in QWs [60]. On the other hand, the second excited level increases a bit at the smaller values of F, that can be clearly seen in the inset figure of a smaller scale. Additionally, the inset shows that the derivative of ground state energy is zero at $F = 0$ [61]

In Fig. 14.6a, b the dependencies of first three dressed energy levels of the confined electron on the laser field parameter α_0 are presented for different values of electric field strength F. In all the investigated cases the laser field brings the increment of the dressed energies, similar to the scenario in Fig. 14.3. On the other hand, as expected in all the regions of the α_0 variation, the increment of the electric field strength moves the energy levels down. Besides that, the influence of the laser field on the ground state energy is stronger for bigger values of the electric field strength. The aforementioned effect finds its explanation with the help of the laser field-dressed wave functions in the absence (Fig. 14.2) and presence (Fig. 14.7) of the electric field. In the absence of laser field for $F = 0$ and $F = 30$ kV/cm cases the effect of electric field on the electron distribution in the structure is equivalent to an increase of the spatial confinement. At $F = 0$, the localization probability is uniformly distributed in the ring and the electron is *less confined*. At $F = 30$ kV/cm, the electron is strongly *pushed* against the right side of the QR and is *more confined*. Thus, the electron has an additional spatial confinement induced by the electric field. For example, in the case with $F = 0$, an increase in the laser field parameter from 0 to 5 nm produces an increase of the ground state energy of 3.3 meV, while in the case with $F = 15$ and $F = 30$ kV/cm the ground state energies changes are 9.3 and 10.4 meV, respectively.

On the other hand, the Fig. 14.7 shows that like the laser field, the presence of the electric field eliminates the degeneracy. For all the first three states, the peaks of the electronic wave functions are forced to be in the tilted part of the confinement potential (see Fig. 14.4). This is clearly visible in Fig. 14.7 where the localization probability is almost zero in the left part of the QR, for $j = 1, 2, 3$. The further increase

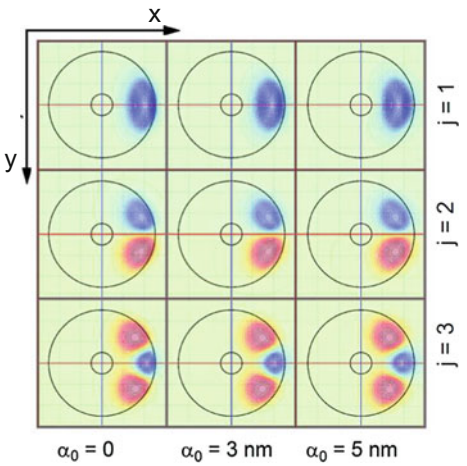

Fig. 14.7 The wave functions of the first three dressed states of the electron ($j = 1, 2, 3$) depending on the laser field parameter. The results are presented for $R_1 = 5$ nm, $R_2 = 25$ nm and $F = 30$ kV/cm (reprinted from [53] under a CC BY license)

of laser parameter has little effect on the wave function spatial configuration, but its effect is visible on the energies.

14.3.3 Intraband Absorption in a Single Quantum Ring

Before discussing the intraband absorption, it is important to overview the symmetry of the wave functions.

Figure 14.2 demonstrates that for $\alpha_0 = 0$ and $F = 0$ both the ground and the double-degenerated excited states have wave functions with defined parity with respect to any direction in the QR plane (ground state is even, excited state is odd). If $\alpha_0 \neq 0$ the cylindrical symmetry is reduced down to Cartesian symmetry with respect to x-polarization direction of the laser field and transverse y-axis: $\Psi_d^1(-x, y) = \Psi_d^1(x, y), \Psi_d^1(x, -y) = \Psi_d^1(x, y), \Psi_d^2(-x, y) = \Psi_d^2(x, y), \Psi_d^2(x, -y) = -\Psi_d^2(x, y), \Psi_d^3(-x, y) = -\Psi_d^3(x, y), \Psi_d^3(x, -y) = \Psi_d^3(x, y)$. Finally, Fig. 14.7 demonstrates that if $F > 0$ there is no symmetry with respect to $y-$axis, so there will be no defined parity of the wave functions in x variable; first and third states have even wave functions in y variable, while second state has an odd wave function in y: $\Psi_d^1(x, -y) = \Psi_d^1(x, y), \Psi_d^2(x, -y) = -\Psi_d^2(x, y), \Psi_d^3(x, -y) = \Psi_d^3(x, y)$.

The oscillator strength O_{if} depicted in Fig. 14.8 is an important physical quantity for the study of the optical properties of electronic dipole-allowed transitions. It is expressed as follows [62]:

$$O_{if} = \frac{2m}{\hbar} \Delta_{if} \left| M_{if} \right|^2, \tag{14.14}$$

where $\Delta_{if} = E_d^f - E_d^i$ is the energy difference between the final (f) and initial (i) states and M_{if} denotes the matrix element. The dependence of the oscillator

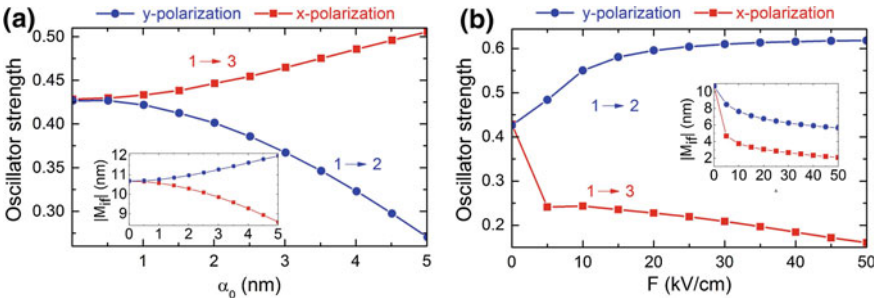

Fig. 14.8 Oscillator strength as a function of laser field parameter (with $F = 0$) and electric field strength (with $\alpha_0 = 0$), respectively. Figure insets show the absolute value of the matrix elements $|M_{if}|$ as functions of the α_0 and F. The results are presented for $R_1 = 5\,\text{nm}$ and $R_2 = 25\,\text{nm}$. Different light polarizations are considered (reprinted from [53] under a CC BY lincese) (Color figure online)

strength on the laser field parameter α_0 and electric field strength F are presented in Fig. 14.8a and b respectively. The incident light is linearly polarized and different directions of it are considered. The insets in Fig. 14.8a and b show the absolute value of matrix elements of the allowed transitions as a function of α_0 and F respectively. For nonzero values of α_0 and F different selection rules are obtained. In the case of x-polarization, transitions from the ground state $j = 1$ to the second excited state $j = 3$ are allowed (see the red lines in Fig. 14.8) and in the case of y-polarization the $1 \rightarrow 2$ transitions are allowed (see blue lines in Fig. 14.8).

The obtained selection rules can be explained in the following manner. If the initial (i) and final (f) states have different but defined parity with respect to an axis, the transition matrix element is nonzero for a light wave polarized on that axis: for $\alpha_0 = 0$ and $F = 0$ (i) is even and (f) is odd, independent on the polarization of the absorbed light; therefore, it is expected that the transition matrix element is nonzero and invariant to the light polarization, which is confirmed by the numerical calculations shown in Fig. 14.8a. For $\alpha_0 > 0$ and $F = 0$ the transition $1 \rightarrow 2$ is forbidden for x-polarization since Ψ_d^1 and Ψ_d^2 are even functions with respect to x variable, so that the associated matrix element is zero at all nonzero values of the laser parameter; similarly, the transition $1 \rightarrow 3$ will be forbidden for y- polarization of the light, since Ψ_d^1 and Ψ_d^3 are both even functions of variable y; these remarks are confirmed by the numerical calculation of the matrix elements in the inset of Fig. 14.8a; similarly, for $F \neq 0$ transitions $1 \rightarrow 2$ (in the case of x- polarization) and $1 \rightarrow 3$ (in the case of y- polarization) are forbidden by the parities of the wave functions, as illustrated in Fig. 14.7 and confirmed by the calculations in the inset of Fig. 14.8b.

The physics behind the behaviors of the matrix elements can be explained using the wave function distributions of corresponding states [63]: As seen from Fig. 14.7, with the increase of α_0, overlapping of $j = 1$ and $j = 2$ states decreases, while the overlapping of $j = 1$ and $j = 3$ states increases. Therefore, the matrix elements

$|M_{12}|$ and $|M_{13}|$ augment and diminish, respectively. The opposite behavior has the oscillator strength of mentioned transitions, which can be explained by the simultaneous variations of energy difference and squared matrix elements.

The absorption coefficient for the intraband transitions from the ground state to the excited states can be cast in the form [64, 65]:

$$\alpha(\Omega) = \zeta \cdot \hbar\Omega \sum_f N_{if} \left|M_{if}\right|^2 \frac{\Gamma}{\left(\hbar\Omega - \Delta_{if}\right)^2 + \Gamma^2}, \tag{14.15}$$

where $N_{if} = N_i - N_f$ is the occupation difference between the initial and final states and $N_{if} = 1$ because the final state is always vacant and the initial one is occupied by one electron. In current calculations the Lorentzian parameter Γ is taken as $\Gamma = 0.4$ meV, and ζ contains all the other factors [52, 53].

As mentioned before, the laser field results in the anisotropy in the confining potential, by destroying the cylindrical symmetry of it. Therefore, changes in the light polarization direction must also lead to changes in the intraband absorption spectrum. Figure 14.9a and b present the intraband optical absorption coefficient for several values of the laser field parameter α_0. In case that $\alpha_0 > \alpha_{0min}$, where α_{0min} is the minimal value of the laser field parameter when the cylindrical symmetry is destroyed, different selection rules are obtained. In the case of x- polarization, transitions between the ground state $j = 1$ to the second excited state $j = 3$ are allowed. If laser field has y- polarization, the $1 \rightarrow 2$ transitions are allowed. In the

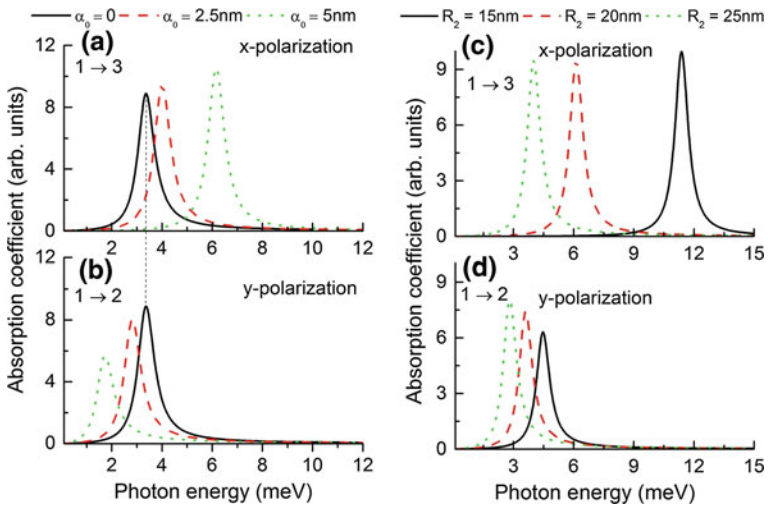

Fig. 14.9 The dependence of the intraband absorption coefficient (in arbitrary units) of $1 \rightarrow 2$ and $1 \rightarrow 3$ transitions on incident photon energy. The results in (**a**) and (**b**) are for fixed $R_1 = 5$ nm and $R_2 = 25$ nm and varying α_0, and in (**c**) and (**d**) for fixed $R_1 = 5$ nm and $\alpha_0 = 2.5$ nm and varying R_2. x- and y- polarizations of incident light are considered (reprinted from [52] with permission of AIP Publishing)

absence of laser field, confining potential has cylindrical symmetry and $\Delta l = \pm 1$ condition on l angular quantum number defines the permitted transitions for both polarizations. Accordingly, if $\alpha_0 = 0$ absorption coefficients of $1 \to 2$ and $1 \to 3$ transitions ideally overlap for x- and y- polarized light (see the black curves in Fig. 14.9a and b). The strengthening of the laser field yields a blueshift in the absorption spectrum by incrementing the energy distance of $j = 1$ and $j = 3$ levels and an increase of the absorption peak value when light is x-polarized (Fig. 14.9a). In contrary, with y-polarized light the increase of α_0 results in a redshift in the absorption spectrum (Fig. 14.9b) and a weakening of the peak value. In addition, for fixed $R_1 = 5$ nm and $\alpha_0 = 2.5$ nm the increment of the outer radius brings to the weakening of the size quantization and hence to the decrease of the energy distances between the ground and both excited state energy levels. Correspondingly, only a redshift in the absorption spectrum is observed in Fig. 14.9c and d. Besides that, the augmentation of R_2 reduces the peak value of $\alpha(\Omega)$ if the light is x-axis polarized and respectively increases it for y-polarization.

In Fig. 14.10 the dependence of the intraband absorption coefficient on the incident photon energy is presented considering several values of the laser field parameter (Fig. 14.10a–c) and electric field strength (Fig. 14.10d–f). The simultaneous influences of intense laser field and lateral electric field affect the intraband absorption spectrum in the following ways:

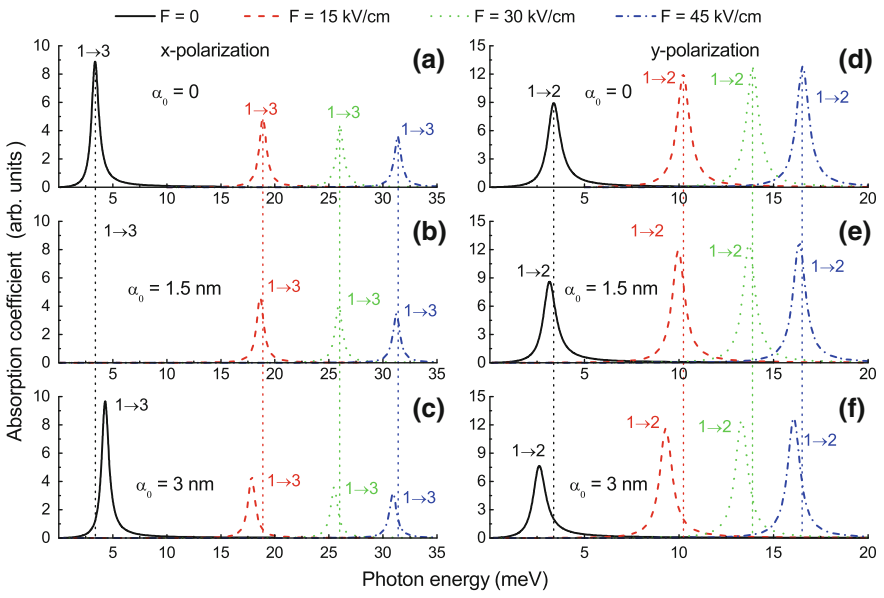

Fig. 14.10 The dependence of the intraband absorption coefficient on the incident photon energy in QR. The results are presented for $R_1 = 5$ nm and $R_2 = 25$ nm. x- and y- polarizations of light are considered for several values of laser field parameter α_0 and electric field strength F (reprinted from [52] permission of AIP Publishing and from [53] under CC BY)

1. For both directions of polarization the increment of the electric field results in a blueshift of the spectrum induced by the increment of the energy distances between the ground and excited energy levels. On the other hand, with x-polarized light a increase of the peak value is observed, and y-polarization results in the decrease of it. These observations are the consequence of the corresponding variations of the oscillator strength for x- and y-polarizations shown in Fig. 14.8b.
2. If the electric field is absent and the incident light is x-polarized, the augmentation of α_0 enlarges the energy distance between $j = 1$ and $j = 3$ levels and, correspondingly, the blueshift is observed. Alternatively, the strengthening of the laser field decreases the energy distance between the $j = 1$ and $j = 2$ states, thus, leading to the redshift. Finally, in the presence of electric field the increment of α_0 creates the redshifts in the spectrum. The variations of the peak values result from the appropriate behavior of the oscillator strengths demonstrated in Fig. 14.8a.

14.4 Laser-Dressed Impurity States in a Single Quantum Ring

The hydrogenic impurity problem is a helpful task to grasp the electronic and optical properties of semiconductor nanostructures. It is explained by the vast possibilities of purposeful manipulation of the impurity binding energy by means of external influences, which in turn can be used for the controlling means of functional optoelectronic devices based on such heterostructures [66]. The impurity states in semiconductor nanostructures under the action of intense laser field are studied theoretically using two major approaches based on the effective mass approximation. In the first approach, the variational method for both laser-dressed confining and Coulomb potentials is realized [67, 68]. In the second technique, the Schrödinger equation with the laser-dressed potential is solved numerically [69], while the problem with the Coulomb potential is treated by the variational method [70].

In this section, we address the effect of electron-impurity interaction on energy levels and far-infrared absorption in semiconductor QR under the action of intense laser and lateral electric fields [71–73].

14.4.1 Impurity States

Laser-dressed impurity states in high-frequency approximation in a single QR are considered via time-averaged Schrödinger (14.9) by adding the laser-dressed hydrogenic donor impurity potential $V_d(x, y, \alpha_0)$ in Ehlotzky [74] approximation:

$$V_c(\mathbf{r}_\perp) = -\frac{e^2}{2\varepsilon}\left[\frac{1}{\sqrt{\Delta_+^2 + y^2}} + \frac{1}{\sqrt{\Delta_-^2 + y^2}}\right], \tag{14.16}$$

where ε is the dielectric constant of the material, which, for simplicity, is taken the same inside and outside the QR and $\Delta_\pm^2 = (x - x_0 \pm \alpha_0)^2$, where x_0 is the impurity coordinate. The final time-averaged Schrödinger equation takes the following form:

$$\left[\frac{\widehat{\mathbf{p}}_\perp^2}{2m} + V_d(\mathbf{r}_\perp, \alpha_0) + V_c(\mathbf{r}_\perp)\right]\Psi_d^c(\mathbf{r}_\perp) = E_d\Psi_d^c(\mathbf{r}_\perp). \tag{14.17}$$

The localization probability density in QR is depicted in Fig. 14.11. Figure 14.11a demonstrates that the electron cloud of the ground state is no longer ring-shaped as it must be in the absence of the impurity (see Fig. 14.2), but tightly centered around the impurity. In addition, since for inner and outer border impurity positions the electron cloud is more spread out, the lowest ground state energy is expected to be obtained for $x_0 = (R_1 + R_2)/2$. The laser dressing visibly reduces the electron cloud compression by the impurity. Thus, the increment of all energies with the increasing of laser parameter is predictable. The first excited state is addressed in Fig. 14.11b. The p-type orbital is oriented along the x-axis and is much less aggregated around the impurity position, if compared with the results for the ground state. The latter effect is slightly reduced if the laser field is turned on. Besides that, the strongest effect of impurity on the electronic cloud is observed for $x_0 = (R_1 + R_2)/2$. p-type orbital in Fig. 14.11c presents the second excited state, which is now oriented along the y-axis. The impurity induces a strong dissymmetry of the electron cloud, which is only attenuated by the laser dressing effect.

Figure 14.12 shows the electron energies of the first five impurity states in a QR as functions of α_0. In this figure and in the further results of this section radii are fixed to $R_1 = 5$ nm and $R_2 = 25$ nm. Figure 14.12a considers an impurity located at the half distance between inner and outer energy barriers of the ring: $x_0 = (R_1 + R_2)/2$.

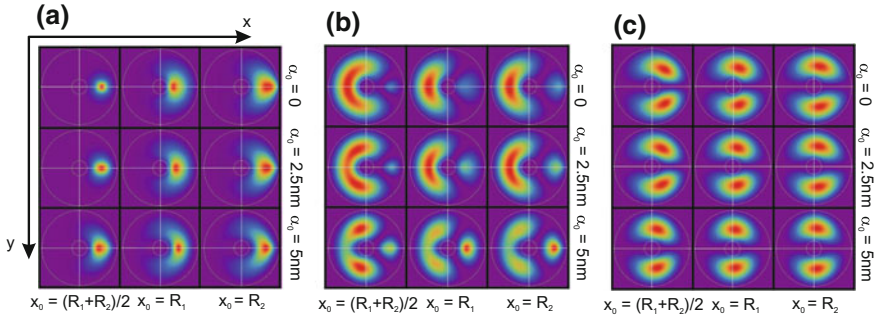

Fig. 14.11 Electron localization probability in QR for different impurity positions (reprinted from [71] Copyright 2017 with permission from Elsevier)

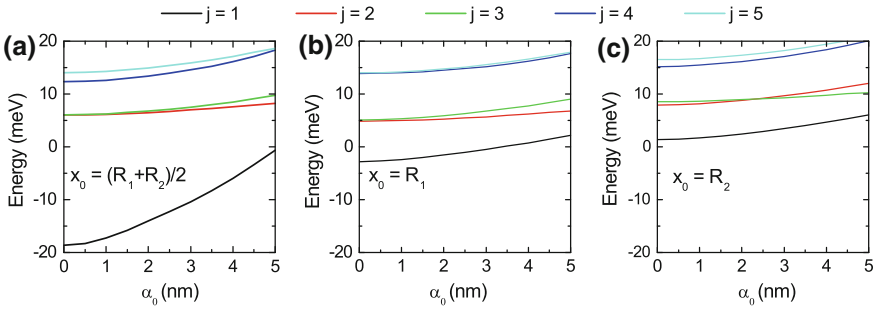

Fig. 14.12 The dependence of the electron energy levels on α_0 of the first five laser-dressed impurity states. The following impurity coordinates are considered: (**a**): $x_0 = (R_1 + R_2)/2$; (**b**): $x_0 = R_1$; (**c**): $x_0 = R_2$ (reprinted from [71] Copyright 2017 with permission from Elsevier)

It is worth to compare the current results with those in Fig. 14.3a. In the presence of electron−impurity interaction electronic states are more localized and sensitive to laser field and, thus, the energy levels are lower. Certainly, especially the energy of the ground state has noticeable deep values. In addition, ground state energy of impurity increases rapidly with laser parameter: from −18meV to −1meV if α_0 is varied from 0 to 5 nm, while for the same interval of α_0 Fig. 14.3a gives only 3.3meV of increment. The other four energy levels have an increase of 5 meV, at most. Considering the different speed of variation of the ground and excited energies, one may expect a strong dependence of the ground state-related intraband optical transitions on the laser field intensity. On the other hand, the panels (b) and (c) present the energies calculated for impurities located at the inner border of the QR $x_0 = R_1$ and the outer border $x_0 = R_2$, respectively. It can be noted, that the dependencies on the laser parameter are qualitatively similar. Nevertheless, the ground state energy remains more sensitive to laser field-affected deformation of the confining potential, because the electron probability is shifted from the QR center, as confirmed by Fig. 14.11. It is remarkable, that Fig. 14.12c demonstrates an accidental degeneracy, as the first and second excited levels cross at $\alpha_0 = 2.5$ nm.

14.4.2 Impurity-Related Intraband Transitions

Now we consider the intraband transition induced by the radiation, that is linearly polarized along the x- or y-axes. To begin with, in Fig. 14.13 the threshold energies of the $1 \rightarrow 2$ (blue line) and $1 \rightarrow 3$ (red line) transitions are explored affected by the variation of the parameter α_0. As it is pointed out in the discussion of Fig. 14.12, the energy of the ground state bends steeper than that of the excited states resulting in the decreasing variation on α_0 of threshold energies. On the other hand, in $x_0 = (R_1 + R_2)/2$ case, the excited levels are very close at the beginning of α_0 variation, but if α_0 reaches 2 nm value the levels become visibly separated. Resulting from this, the curves of threshold energies almost coincide only until $\alpha_0 = 2$ nm.

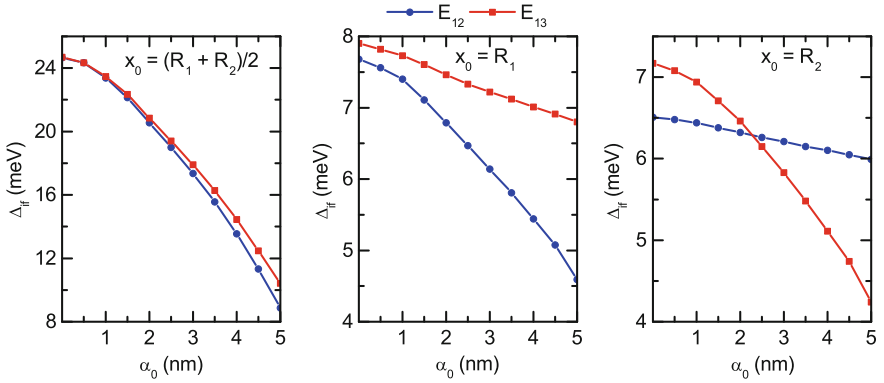

Fig. 14.13 The dependencies of the threshold energies between the ground and first two excited states on α_0 (reprinted from [73] Copyright 2017 with permission from Elsevier)

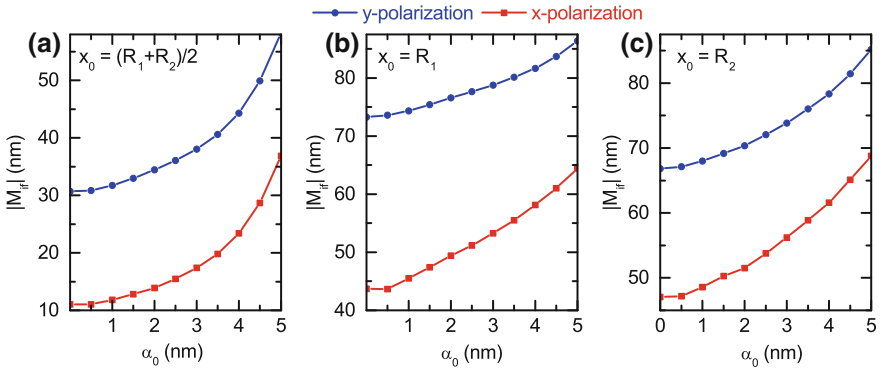

Fig. 14.14 The matrix elements as functions of α_0. x and y directions of polarizations are considered (reprinted from [73] Copyright 2017 with permission from Elsevier) (Color figure online)

For $x_0 = R_1$ laser field again affects the separation and if $x_0 = R_2$ leads to the crossing of threshold energies.

In Fig. 14.11 we saw that the presence of impurity and intense laser field creates a space of the electron cloud distribution thus, the polarization-dependent selection rules of intraband transitions are expected. Indeed the results for the dipole matrix elements in Fig. 14.14 demonstrate that, if the light is polarized along x-axis, the transition from the ground state $j = 1$ to the second excited state $j = 3$ is allowed (red lines in Fig. 14.14) and in the case of y-polarization, transition to the first $j = 3$ excited state is allowed (blue lines in Fig. 14.14). Therefore, the scenario is similar to the intraband transitions in undoped QRs considered in Sect. 14.3.3. Besides that, the dependence of matrix elements on α_0 monotonically increases, and the lowest values of them are obtained in $x_0 = (R_1 + R_2)/2$, dictated by the distributions of the wave functions of corresponding states.

The combined modifications of threshold energy and matrix element are vividly demonstrated by the absorption curves in Fig. 14.15. It is interesting to compare the current curves of the absorption with a QR without impurity given by Fig. 14.9a and

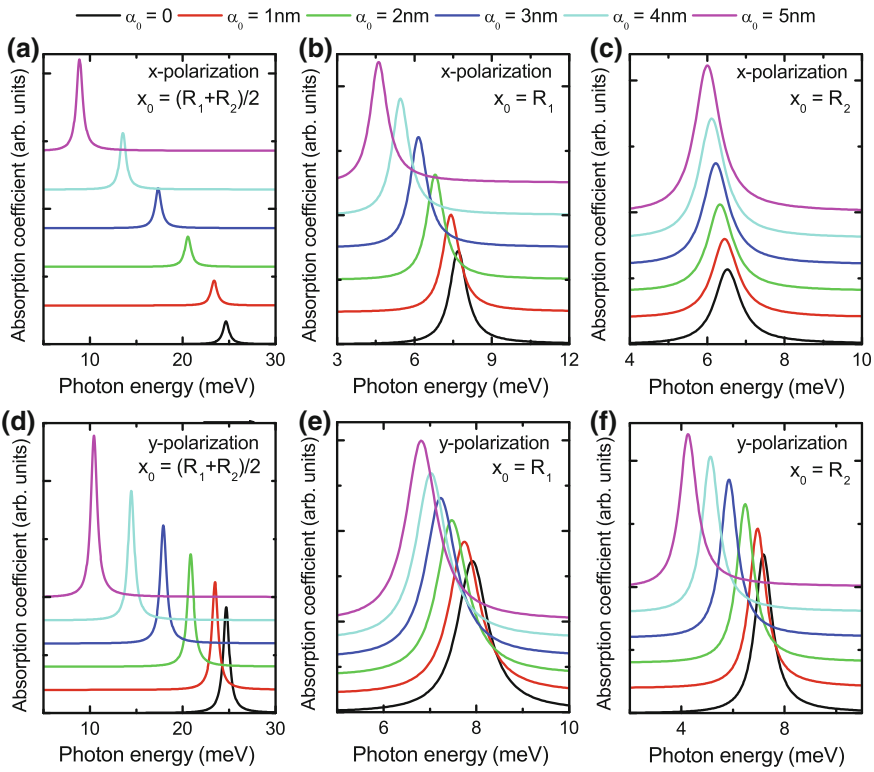

Fig. 14.15 The dependence of intraband absorption coefficient (in arbitrary units) on the incident photon energy for different values of α_0. x and y directions of polarizations are considered (reprinted from [73] Copyright 2017 with permission from Elsevier)

b: a doped QR manifest, interestingly, only the redshift of the absorption with the increment of α_0, and this redshift is now independent on the direction of the incident light polarization direction.

14.4.3 Electric Field Influence on Impurity States and Related Intraband Absorption

Finally, in this section, we explore the static x-axis-directed electric field influence on the laser-dressed impurity states and related intraband transitions. Considering the electric field contribution, time-averaged Schrödinger equation (14.17) takes the following form:

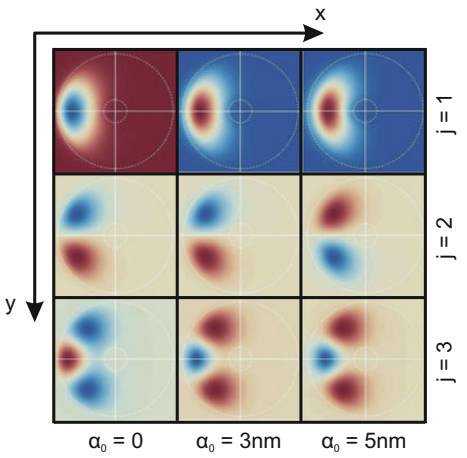

Fig. 14.16 The influence of laser and $F = 30\,\text{kV/cm}$ electric fields on the wave functions of the first three dressed states of the electron ($j = 1, 2, 3$) (reprinted from [72] Copyright 2017 with permission from Elsevier)

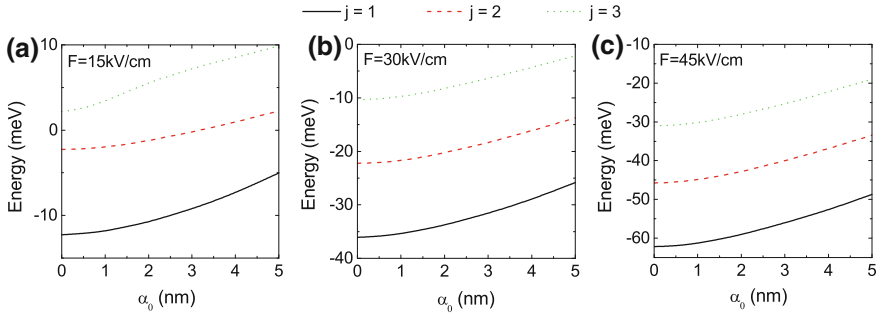

Fig. 14.17 The dependencies of the low-lying energy levels on α_0 for several values of the electric field strength (reprinted from [72] Copyright 2017 with permission from Elsevier)

$$\left[\frac{\widehat{\mathbf{p}}_\perp^2}{2m} + V_d(\mathbf{r}_\perp, \alpha_0) + V_c(\mathbf{x}, \mathbf{y}) - e\mathbf{F}\cdot\mathbf{r}_\perp\right]\Psi_d^c(\mathbf{r}_\perp) = E_d\Psi_d^c(\mathbf{r}_\perp). \tag{14.18}$$

The calculations are made for fixed radii $R_1 = 5\,\text{nm}$ and $R_2 = 25\,\text{nm}$ and impurity position $x_0 = (R_1 + R_2)/2$. Figure 14.16 presents the wave functions of the first three $j = 1, 2, 3$ laser-dressed impurity states. Now, (compare with Fig. 14.11) the presence of electric field forces the electron wave function to the left part of the QR, so there is almost zero localization around the impurity site. In addition, the impurity does not destroy the symmetry of the wave functions, which keep the same parity as in the undoped case presented in Fig. 14.7. The obtained wave functions share the light to understand the dependencies of the laser-dressed energy levels on α_0 explored by Fig. 14.17a–c. As obtained for the unbiased QR in Fig. 14.12, the dependence of

the ground state energy drastically differs from the excited ones. Now the shifting of the wave functions by the electric field diminishes the electron−impurity interaction. As a result, the laser field influence prevails, and the energy levels show quite similar behavior. As expected, the stronger is the electric field, the clearer is the observed phenomenon. Additionally, the energies are decreasing as the electric field takes greater values.

The symmetry of the wave functions again allows the $1 \rightarrow 3$ intraband transitions with the x-polarized light, and the $1 \rightarrow 2$ ones with y-polarization. In Fig. 14.18a matrix elements for both transitions are increasing with laser field being strengthened. On the contrary, the strengthening of the electric field leads to the augmenting elements for the $1 \rightarrow 2$ transitions, and decreasing ones in case of $1 \rightarrow 3$ transitions. In addition, the matrix elements become less sensitive to α_0 variation once the electric field is increased. The obtained numerical results have a physical explanation. For example, on the grounds that the laser field has a small impact on the wave functions of a QR biased by $F = 30$kV/cm electric field (see Fig. 14.16), the matrix element exhibit small alternation.

At the end of this section, we explore the absorption of a linearly polarized light. Unlike the results in Fig. 14.15a and d with $F = 0$, where only the redshift was observed, now Fig. 14.19 demonstrates that with $F = 15$kV/cm the increment of α_0 can also yield the blueshift. Truly, if the incident light is y-polarized the same redshift is obtained, but if x-polarized light is considered the spectrum gets both red- and blueshifts. Besides that, the comparison with the data in Fig. 14.10 shows that the presence of the impurity does not affect the spectrum shift direction: if α_0 is kept fixed the strengthening of F brings the blueshift of the spectrum.

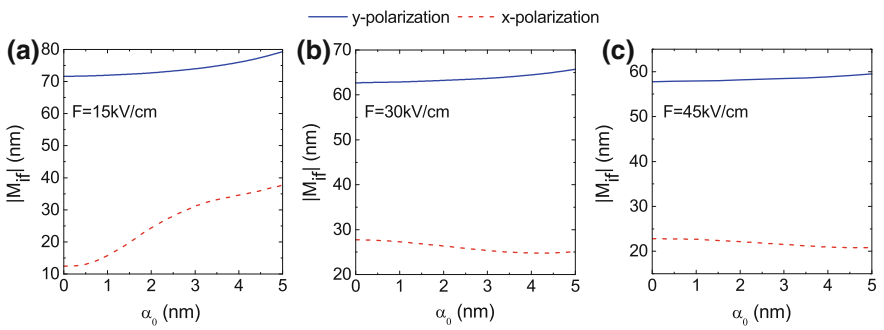

Fig. 14.18 The dependence of the absolute value of the matrix elements M_{if} on α_0. Different directions of the light polarization and different values of electric field strength F are considered (reprinted from [72] Copyright 2017 with permission from Elsevier)

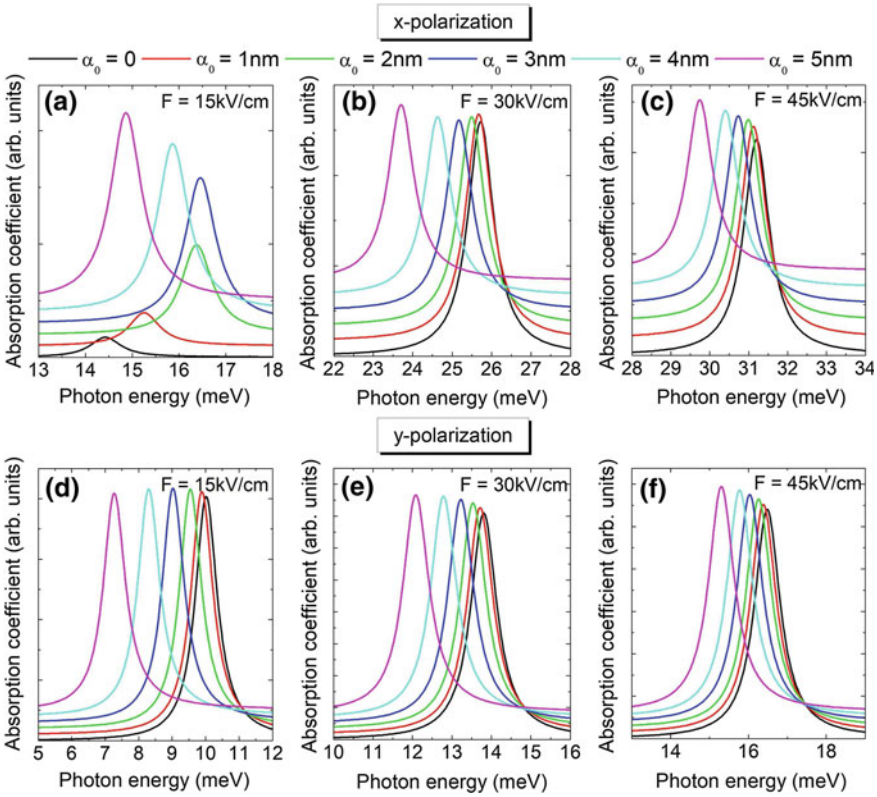

Fig. 14.19 The dependence of the intraband optical absorption coefficient on incident photon energy in a single nanoring. The results are presented for x-polarization of the incident light and laser field parameter α_0 is considered from 0 (bottom) to 5 nm (top) with a 1 nm step (reprinted from [72] Copyright 2017 with permission from Elsevier)

14.5 Quantum-Confined Stark Effect in the Laser-Dressed Concentric Quantum Rings

The effects on optical spectra when an external electric field is applied, known in atomic physics as the Stark effect, evolved very rapidly with the invention and development of semiconductor nanostructures. The effects of interaction of the confined carriers with the field give rise to a new phenomenon known as the quantum-confined Stark effect. First reported in QWs by Miller et al. [60, 75], the quantum-confined Stark effect is still the subject of a high interest [76, 77]. From the point of view of applications in optoelectronic and tunneling devices based on QRs, it is essential to investigate the effects of an electric field on the electronic and impurity states. For that reason in the past decade, a number of works were devoted to the theoretical investigation of the influence of electric fields on the electronic and optical properties

of QR nanostructures [78–82]. Very recently, the influence of lateral electric field on one-electron states and intraband absorption in two-dimensional concentric double quantum rings (CDQR) is investigated [83].

In this section, the rendering of different shapes of a single sample of a CDQR is demonstrated realizable with a THz laser field, that in turn, allows the manipulation of electronic and optical properties of a sample [84].

The CDQRs consists of GaAs QRs (well material) separated by GaAlAs (barrier material). Laser-dressed states of the biased CDQRs are defined by the (14.13) and in the expression (14.10) the confining potential in the absence of laser field is modeled according to:

$$V(\mathbf{r}_\perp) = \begin{cases} 0, & \text{if } r_\perp \in \left[R_1^{\text{in}}, R_2^{\text{in}}\right] \cup \left[R_1^{\text{out}}, R_2^{\text{out}}\right] \\ V_0, & \text{elsewhere,} \end{cases}, \tag{14.19}$$

where $V_0 = 257$ meV is the height of the potential, R_1^{in}, R_2^{in}, R_1^{out}, and R_2^{out} are correspondingly inner (subscript "1") and outer (subscript "2") radii of inner (superscript "in") and outer (superscript "out") rings. Figure 14.20 depicts the effective potential $V_{\text{d}}^{\text{F}}(\mathbf{r}_\perp)$ for $\alpha_0 = 3$ nm and electric field is absent in Fig. 14.20a and $F = 3$kV/cm in Fig. 14.20b. The impact of laser field contracts the lower part of the potential along the x-axis and enlarges the upper part. Thereby, we can expect that the electric field direction variation will strongly influence the dressed energies.

The finite element method is applied using COMSOL Multiphysics to calculate laser-dressed eigenvalues E_{d} and eigenvectors $\psi_{\text{d}}(\mathbf{r}_\perp)$ [85]. Triangular elements and Lagrangian shape functions are used for meshing [86]. In order to evade having eigenfunction values out of computational domain that is taken in a form of a square the side of it is taken as $L = 2.8R_2^{\text{out}}$. Figure 14.21a shows the mesh in the absence of laser and electric fields, while Fig. 14.21b depicts the finer mesh used for $\alpha_0 = 3$ nm and $F = 3$kV/cm. The values of radii are fixed to

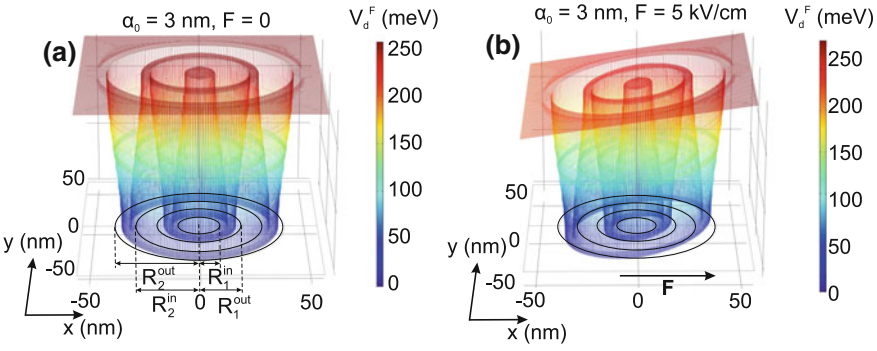

Fig. 14.20 The laser-dressed confining potential in the absence of electric field (**a**) and considering $F = 3$ kV/cm electric field applied along the x-axis (**b**). The parameter α_0 is fixed to 3nm (reproduced from [84] under a Creative Commons Attribution 4.0 International License)

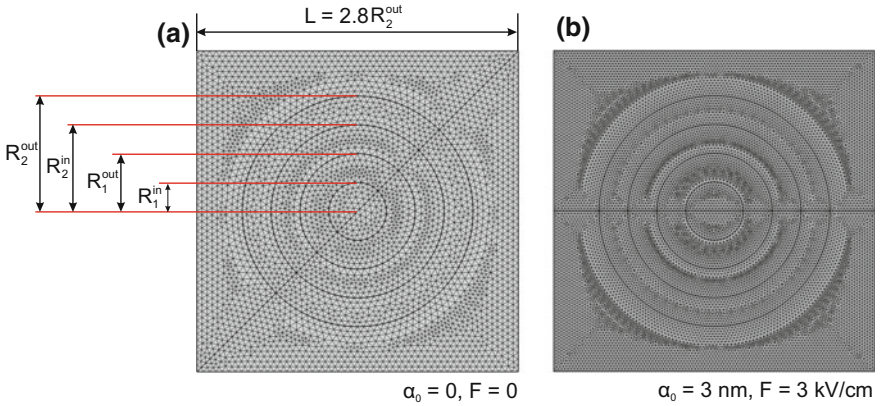

Fig. 14.21 Numerical mesh used in the calculations

$R_1^{\text{in}} = 10\,\text{nm}$, $R_2^{\text{in}} = 20\,\text{nm}$, $R_1^{\text{out}} = 30\,\text{nm}$, $R_2^{\text{out}} = 40\,\text{nm}$. In the absence of laser and electric fields, correct wave functions are obtained considering the following meshing style: the square is divided into two triangles via the diagonal, one of the triangles is meshed and then that mesh is copied into the other triangle. Using this method one can be confident that the eigenfunctions are symmetric or antisymmetric with respect to the diagonal of the square, that is decisive to obtain any physical characteristic of a CDQR system, for example, the intraband absorption coefficient. In the case of nonzero laser and electric fields, the mesh is created by copying the mesh from one of the rectangles in Fig. 14.21b to another one to follow the new symmetry enforced by fields. If the fields are not zero the fourth order Lagrangian shape functions are used and the domain is meshed with "*Extremely fine*" option of "*General physics*" calibration node. If the fields are absent, the third order Lagrangian shape functions and "*Extra fine*" option [85] are used.

Figure 14.22 presents the energy spectrum dependence on electric field direction, by varying the $\beta = \angle(\widehat{\mathbf{u}}, \widehat{\mathbf{e}}_x)$ angle, with $\widehat{\mathbf{u}}$ being the unit vector of electric field direction and $\widehat{\mathbf{e}}_x$ of laser field polarization direction (polarization direction is kept fixed). In case of an electric field parallel to laser field ($\beta = 0°$ case considered in Figs. 14.22a, d) a quadratic Stark effect [61] is obtained. Besides that, the energies decline caused by the tilting of effective confining potential shown in Fig. 14.20b. Moreover, electric field direction is symmetric for the confining potential that is influenced only by laser field (see frame (a) of Fig. 14.20). Because of that, the corresponding wave functions are either symmetric or antisymmetric with respect to the x-axis, and, in turn, energy levels present both crossing and anti-crossing points. If $\beta = 45°$ (see Fig. 14.22b, e), then $\widehat{\mathbf{u}}$ does not fit with the symmetry of $V_{\text{d}}(\mathbf{r}_\perp)$ potential. This signifies that wave functions are neither symmetric nor antisymmetric and the energies cannot cross and only anti-crossing is observed. If the electric field is applied perpendicular to laser field ($\beta = 90°$ case considered in Fig. 14.22c, f) then energies demonstrate linear behavior on F. This effect is more evident if the

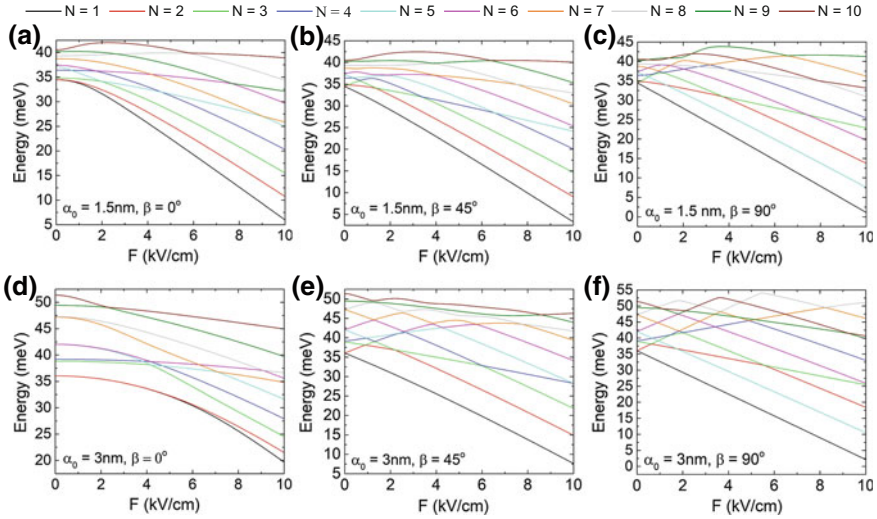

Fig. 14.22 Stark effect on laser-dressed energy levels. α_0 and β parameters are considered as follows: (**a**) $\alpha_0 = 1.5$ nm, $\beta = 0°$; (**b**) $\alpha_0 = 1.5$ nm, $\beta = 45°$; (**c**) $\alpha_0 = 1.5$ nm, $\beta = 90°$; (**d**) $\alpha_0 = 3$ nm, $\beta = 0°$; (**e**) $\alpha_0 = 3$ nm, $\beta = 45°$ and (**f**) $\alpha_0 = 3$ nm, $\beta = 90°$ (reproduced from [84] under a Creative Commons Attribution 4.0 International License)

laser field influence is greater with $\alpha_0 = 3$ nm parameter value. Alike effect has been recently discussed in [87], where the quadratic and linear Stark effects were attributed to the effective mass anisotropy. Our results show that these different Stark effects can be attributed to the anisotropy created by THz laser field.

But the electric field can also be a potential tool to control the optical properties of CDQR. The structure is irradiated by circularly polarized light that is propagating along the z-axis. In the presence of electric field all the transitions are allowed, because M_{if} matrix element cannot be zero. The oscillator strengths of the most intensive transitions are presented in Fig. 14.23. $1 \rightarrow 2$ transition has the biggest probability if $\beta = 0°$, but if β is nonzero the situation is different. If $\alpha_0 = 1.5$ nm and $\beta = 45°$ O_{12} is the biggest at $F = 0$ value (Fig. 14.23b), but in [0.25kV/cm, 1.25kV/cm] interval other transitions are more probable. Further increase of F makes O_{12} again the biggest as shown in Fig. 14.23b. If again $\beta = 45°$ value is taken but greater $\alpha_0 = 3$ nm is considered (Fig. 14.23e), then O_{13}, O_{14} and O_{15} are the biggest in [0, 2kV/cm] range, and, thus, the corresponding transitions are the most probable. Finally, the case of an electric field that is perpendicular ($\beta = 90°$) to $\widehat{\mathbf{e}}_x$ is addressed in Fig. 14.23c, f. Now $1 \rightarrow 5$ has the biggest probability, and only if the electric field is zero $1 \rightarrow 2$ transitions are the most intensive.

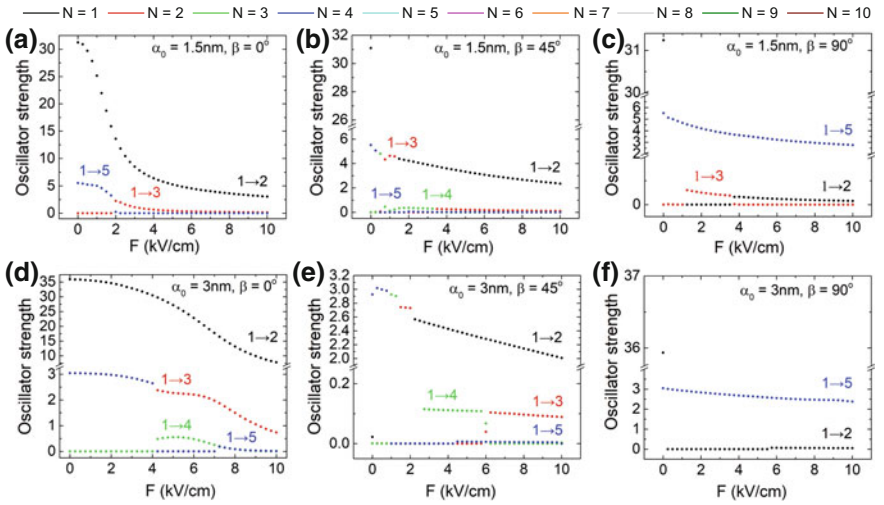

Fig. 14.23 The oscillator strengths of the most intensive intraband transitions. α_0 and β parameters are considered as follows: (**a**) $\alpha_0 = 1.5\,\text{nm}$, $\beta = 0°$; (**b**) $\alpha_0 = 1.5\,\text{nm}$, $\beta = 45°$; (**c**) $\alpha_0 = 1.5\,\text{nm}$, $\beta = 90°$; (**d**) $\alpha_0 = 3\,\text{nm}$, $\beta = 0°$; (**e**) $\alpha_0 = 3\,\text{nm}$, $\beta = 45°$ and (**f**) $\alpha_0 = 3\,\text{nm}$, $\beta = 90°$ (reproduced from [84] under a Creative Commons Attribution 4.0 International License)

14.6 Molecular Spectrum of Laterally Coupled Quantum Rings Under Intense Terahertz Radiation and Lateral Electric Field

For application purposes, a great interest is also given to the coupled arrays of QRs. Arrays of magnetic nanorings have potential for random access memory, recording, and other spintronic applications [88, 89]. In addition, scattering studies at microwaves showed that QR metamaterials can manifest negative refractive index [90, 91]. Also, the vertically aligned layers of QRs can strengthen the single-mode operation of laser diods [21]. Thereby, coupled semiconductor QRs can be considered as artificial molecules similar to the chain of molecules of benzene rings [92, 93]: in fact, in laterally coupled molecules of QRs of different radii the electron charge can be shifted between the rings by magnetic field [94]. Besides that, coupling in a two-dimensional array of QRs is a cause of decreased persistent currents and magnetic dipole moments [95] and Aharonov-Bohm oscillations were observed in QR molecules although the total magnetic flux was absent [96].

This section is devoted to the study of the influence intense THz laser field and electric field on molecular states and intraband optical properties of laterally coupled quantum rings [97].

14.6.1 Decoupling of a Quantum Ring Molecule and 2-Fold Degeneracy

An artificial molecule is modeled by two laterally aligned GaAs/GaAlAs QRs. The Hamiltonian of laser field dressed and electric field biased molecule is defined by (14.13). $V(\mathbf{r}_\perp)$ confining potential without laser field influence is taken 0 in $R_{in} < \sqrt{(x \pm d/2)^2 + y^2} < R_{out}$ («−»if $x > 0$ half plane and «+»if $x \leq 0$) and is 257meV elsewhere, with R_{in} being the inner and R_{out} the outer radii, and d is the distance between the centers of the rings. Radii are taken as follows: $R_{in} = 10$ nm and $R_{out} = 50$ nm [34]. In Fig. 14.24 V_d dressed confining potential is depicted considering different values of α_0 and $F = 0$ condition for electric field. The greater values of α_0 bring a bigger splitting of the bottom part of V_d, resulting from the decreasing sizes of QRs. The (14.13) is numerically solved in COMSOL Multiphysics [85].

The splitting of the confining potential leads to the decoupled QRs, or in other words, to the dissociated molecule. In Fig. 14.25a the dissociation effect is demonstrated by a phase diagram of α_0 and overlapping $w = 2R_{out} - d$ (as depicted in Fig. 14.24) parameter values for the ground state. The calculations showed that the

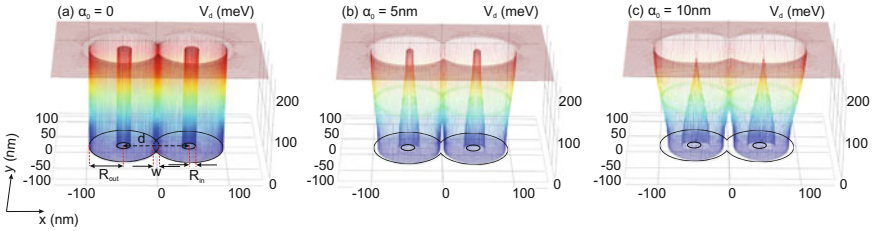

Fig. 14.24 Laser-dressed confining potential for varying α_0 and zero electric field (reproduced from [97] under a Creative Commons Attribution 4.0 International License)

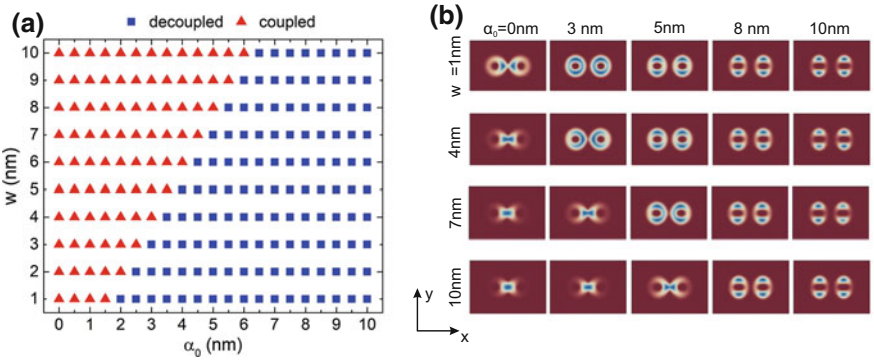

Fig. 14.25 **a** $w - \alpha_0$ phase diagram of the coupled-decoupled transition and **b** the ground state probability density for varying w and α_0 (reproduced from [97] under a Creative Commons Attribution 4.0 International License)

coupled states become decoupled states that are localized in QRs at points that form a line with a slope $k = 2$. The related probability densities are given in Fig. 14.25b. It is worth to point out, that the coupling can be done by laser field, even when w is fixed. In the remaining part of this section $w = 5$ nm value is used.

Figure 14.26 exhibits the dependence of the energy levels of the first ten dressed states on α_0 and the wave functions for $\alpha_0 = 0$ and $\alpha_0 = 5$ nm, and electric field is absent in frame (a) and is taken 1kV/cm in frame (b). It can be observed that the influence of laser field results in the rearranging of energy spectrum. Indeed, the augmented α_0 affects the energies of the ground and first excited states in a way, that they form a single 2-fold degenerated eigenvalue. This degeneracy is a result of the decoupling that forces the ground and first excited states to have probability densities that are very similar. Nevertheless, the parity values for the ground state are $P_x = 1$ and $P_y = 1$ (with respect to x- and y-axis) and for the excited state $P_x = -1$ and $P_y = 1$. Considering the form of wave functions the ground and first excited states can be treated as bonding and antibonding ones respectively. Another pairs of bonding and antibonding states are third and sixth, fourth and fifth, seventh and tenth, eighth and ninth. Besides that, the dependence of the first, third, and seventh energy levels on α_0 is different from that of the other levels. This phenomenon is induced by the laser field that by localizing the electron in the rings, strengthens the confinement. On the other hand, other states have energies that are nearly linear functions of α_0, because these states are localized in the rings even if the laser field is not turned on. In the presence of x-axis directed electric field considered in Fig. 14.26b the laser field induced degeneracy is no longer present, because under electric field influence the only possible parity is $P_y = \pm 1$. In addition, in biased structure all the levels undergo decreasing, with exception of 9th and 10th levels that increase.

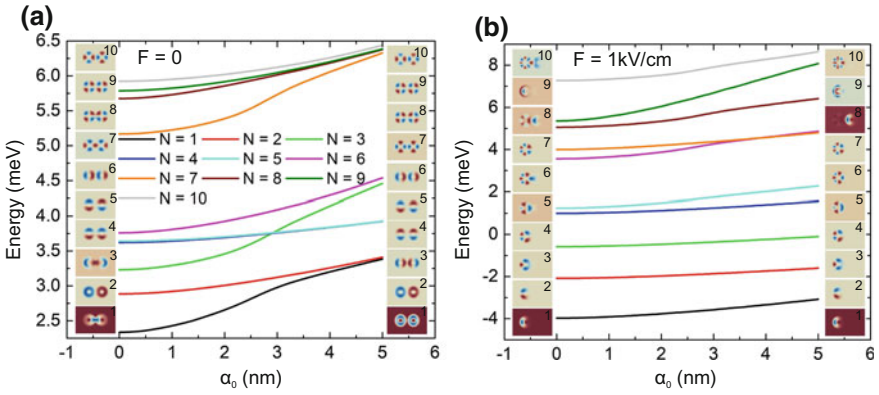

Fig. 14.26 The dependence of the first ten energy levels on α_0 and the electric field is absent in Fig. 14.26a and 1kV/cm in Fig. 14.26b. The wave functions in the left and right sides of the frames are for $\alpha_0 = 0$ and $\alpha_0 = 5$ nm respectively (reproduced from [97] under a Creative Commons Attribution 4.0 International License)

14.6.2 Intraband Absorption in a Quantum Ring Molecule

The qualitative estimation of the coupling of the dressed states can be inferred from the study of related additive absorption coefficient given by (14.15), where $\Gamma = 0.1$meV. The Δ_{if} dependence on α_0 is presented in Fig. 14.27a, c, in which the area of the circles is proportional to the respective square of the modulus of the matrix element - $\left|M_{if}\right|^2$. The transitions are considered only from the ground state to excited states and the light is circularly polarized and propagates along the z-axis. The corresponding absorption coefficient are depicted in Fig. 14.27b and d. If the electric field is absent then transitions are permitted only to the second, fourth, sixth, eighth and tenth states. The parities of these states are not the same as it can be understood from Fig. 14.26a: $P_x = -1$ and $P_y = 1$ for the second, sixth and tenth states, $P_x = 1$ and $P_y = -1$ for the fourth and eighth states. The $1 \rightarrow 2$ transition is

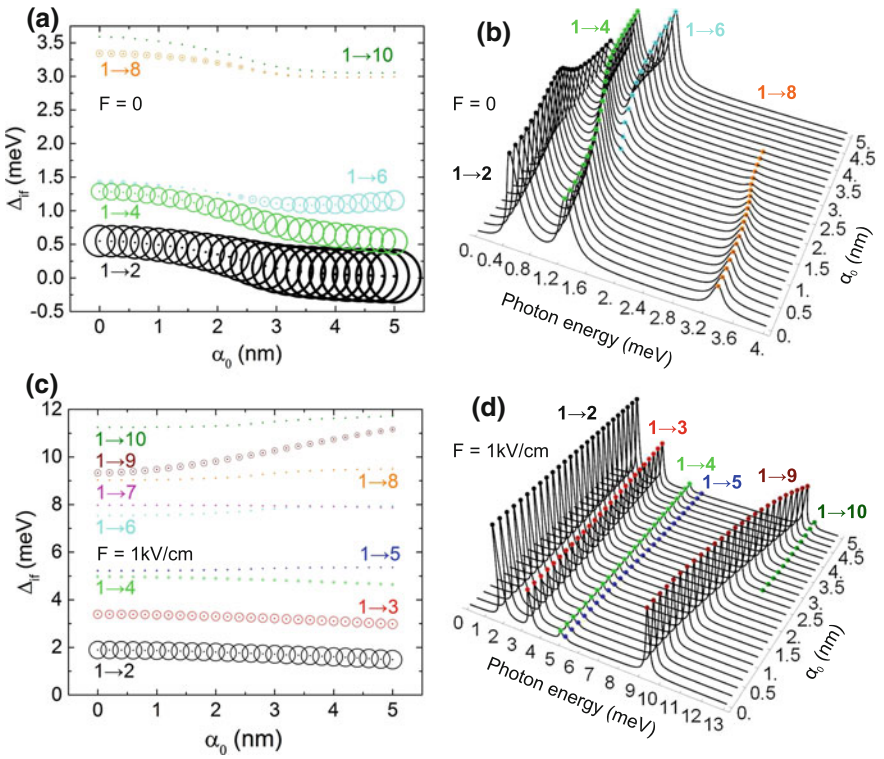

Fig. 14.27 The Δ_{if} energy difference dependence on α_0 (**a**) and (**c**): the area of the circles is proportional to the respective $\left|M_{if}\right|^2$, and the absorption coefficient (in arbitrary units) dependence on incident photon energy $\hbar\Omega$ for different values of α_0 (**b**) and (**d**). The electric field is absent in (**a**) and (**b**) and has 1kV/cm strength in (**c**) and (**d**) (reproduced from [97] under a Creative Commons Attribution 4.0 International License)

the most probable, but, the magnitude of absorption coefficient is not defined only by that probability. $1 \to 4$ transition is evidently less probable than $1 \to 2$, but $1 \to 4$ transition related absorption coefficient is bigger, caused by the multiplication with Ω in (14.15). Alike effect is observed for α_0 values that are near to 5 nm: $1 \to 4$ is more probable than $1 \to 6$ transition but results in a smaller absorption coefficient. Moreover, only $1 \to 6$ transition has the absorption spectrum that undergoes both redshift and blueshift; for other transitions the spectrum has only the redshift. The absorption related with $1 \to 10$ transition, even though allowed, is not observable, since is has very small probability. Electric field with strength 1 kV/cm removes the symmetry with respect to the y-axis, and permits all the transitions. Certainly, Fig. 14.27c demonstrates that the $1 \to 2$ transition is the most probable. At the same time, the absorption coefficient related to $1 \to 9$ transition exhibits values of the same order than absorption related to $1 \to 2$. Now, the absorption spectrum shown in Fig. 14.27d reveals redshift in transitions to the second, third, fourth states, and blueshift in $1 \to 5$, $1 \to 9$ and $1 \to 10$ transitions. Transitions to sixth, seventh, and eighth states have much less values for the absorption coefficient.

Figure 14.28 considers the situation when the angle β between laser and electric field is changing. Magnitudes of electric field strength and laser field parameter are fixed to $F = 0.5$ kV/cm and $\alpha_0 = 2.5$ nm correspondingly and the laser field polarization $\widehat{\mathbf{e}}_x$ is fixed. Figure 14.28 reveals that the energy levels exhibit oscillations, caused by the distributions of wave functions with β variation. In addition, energies are symmetric with respect to $\beta = 90°$ value, since the $V_d(\mathbf{r}_\perp, \alpha_0)$ potential is

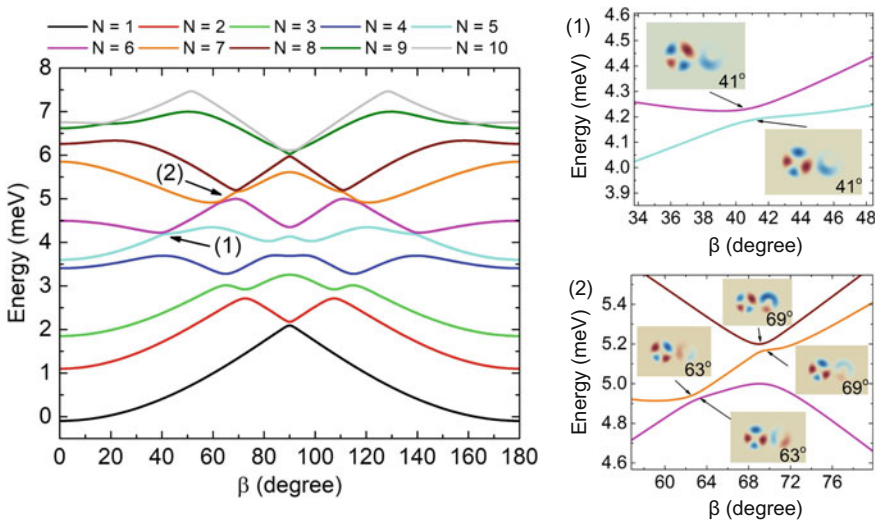

Fig. 14.28 The dependence of the first ten energy levels on the electric field direction at fixed $F = 0.5$kV/cm and $\alpha_0 = 2.5$ nm. Figures 14.28 (1) and 14.28 (2) demonstrate energy behavior around the anti-crossing-like points (reproduced from [97] under a Creative Commons Attribution 4.0 International License)

symmetric with respect to x- and y- axis. It is also worth to mention the appearance of *anti-crossing-like points*, caused by the angle variation. Mostly, an anti-crossing point is a point where the energy levels are very closely positioned, and the respective wave functions have the same symmetry [98]. Therefore, we consider that at anti-crossing-like points the energies again are very close and but the shapes of respective wave functions is similar. Figure 14.28 (1) and (2) present energy variation around three anti-crossing-like points. An interesting and unexpected observation is that the anti-crossing-like appear when the direction of electric field does not coincide with x- and y- axis. Alike investigation was done in [99] where the study of impurity states demonstrated anti-crossings while the nanocrystal radius was increased. The authors attributed this effect to the spatial motion of charge carriers that is influenced by the Coulomb potential of the impurity ion and the confining potential of the nanocrystal. In our case, the anti-crossing-like points appear when the electric field is rotating but the polarization and α_0 parameter of laser field are fixed.

The related energy difference Δ_{if} and absorption coefficients are depicted in Fig. 14.29a and b correspondingly. As expected from the symmetric behavior of energy levels in Fig. 14.28 Δ_{if} energies and absorption coefficients are symmetric as well. $F = 0.5$kV/cm electric field permits all the transitions similar to the situation in Fig. 14.27d. The absorption spectrum demonstrates redshift and blueshift in $[0°, 90°]$ and $[90°, 180°]$ intervals correspondingly, but the following exceptions should be considered (see Fig. 14.29a): blue(red)shift in $[0°, 60°]$ ($[120°, 180°]$) for $1 \rightarrow 2$, $[0°, 40°]$ ($[140°, 180°]$) for $1 \rightarrow 5$, $[45°, 60°]$ ($[120°, 135°]$) for $1 \rightarrow 6$, $[70°, 90°]$ ($[90°, 110°]$) for $1 \rightarrow 8$ and $[20°, 45°]$ ($[135°, 160°]$) for $1 \rightarrow 10$. Since Δ_{if} is oscillating and anti-crossing-like points appear, the absorption coefficient

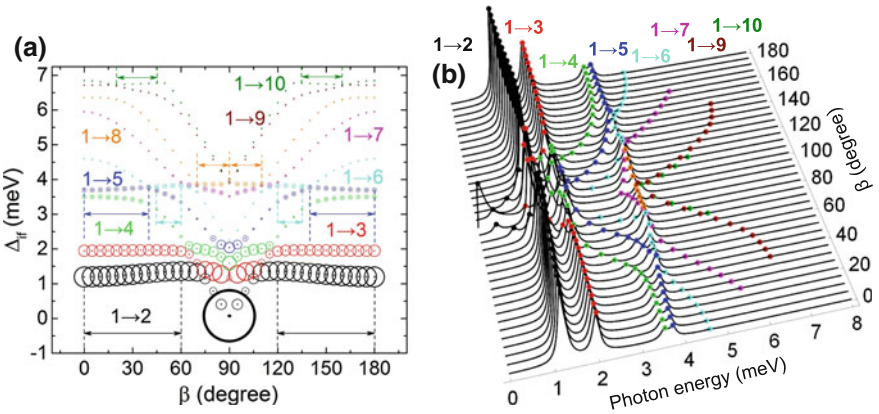

Fig. 14.29 Δ_{if} energy difference dependence on β angle (**a**) and absorption coefficient (**b**) (in arbitrary units) dependence on incident photon energy $\hbar\Omega$ for different directions of $F = 0.5$ kV/cm electric field defined by β and for $\alpha_0 = 2.5$ nm. The area of the circles in (**a**) is proportional to the respective $|M_{if}|^2$ (reproduced from [97] under a Creative Commons Attribution 4.0 International License)

peaks are dispersed in a much more complex way, if compared with Fig. 14.27a and b. However, the biggest values of absorption coefficient are observed in $1 \rightarrow 2$, $1 \rightarrow 3$, and $1 \rightarrow 4$ transitions.

14.7 Final Remarks

In conclusion, we studied the influence of intense THz laser field influence on electronic states and related intraband optical response of various configurations of GaAs/GaAlAs semiconductor QRs. Here we give a short synopsis of the main results. The external homogeneous electric field and hydrogenic-like donor impurity presence were also considered. The strengthening of laser field influence resulted in the increased confinement energies and strongly affected the impact of the electric field in all the configurations. The absorption of the linearly polarized light in single laser-dressed QR demonstrated dependence on the polarization direction in its spectrum. On the other hand, the addition of an impurity in a single QR resulted in the only in the redshift of the absorption spectrum, independent on the change of polarization direction from x-axis to y-axis. In CDQRs both linear and nonlinear quantum confined Stark effects were observed, caused by the distortion of confinement potential by a laser field. In addition, the dissociation of a molecule modeled by a laterally aligned couple of QRs was demonstrated only by the increment of laser intensity, thereby the internal intervention such as the changes of the sizes of the structure or material composition can be bypassed. Besides, the unexpected oscillations in the energy spectrum dependence on the electric field were presented in QR molecules.

Overall, the obtained results demonstrated a significant influence of intense radiation in QRs, manifested by the modified energy spectrum and optical response. We consider the findings useful to understand the laser-dressed states in semiconductor nanostructures with a ring-like geometry. Finally, we hope that our studies made another step to prove the potential of QRs in optoelectronic applications.

Acknowledgements H.M.B. acknowledges the financial support from CONICYT-FONDECYT Postdoctoral program fellowship under grant 3150109, M.G.B. acknowledges the financial support from Armenian State Committee of Science project no. 15T-1C331, A.A.K. acknowledges the financial support from Armenian State Committee of Science project no. 15T-1C363, D.L. acknowledges partial financial support from Centers of excellence with BASAL/CONICYT financing, Grant FB0807, CEDENNA, CONICYT-ANILLO ACT 1410.

References

1. T. Nagatsuma, G. Ducournau, C.C. Renaud, Nat. Photonics **10**, 371 (2016)
2. G.-S. Park, Y.H. Kim, H. Han, J.K. Han, J. Ahn, J.-H. Son, W.-Y. Park, Y.U. Jeong (eds.), *Convergence of Terahertz Sciences in Biomedical Systems* (Springer, Dordrecht, 2012)
3. A.Y. Pawar, D.D. Sonawane, K.B. Erande, D.V. Derle, Drug Invent. Today **5**, 157 (2013)
4. C. Corsi, F. Sizov (eds.), *THz and Security Applications* (Springer, Netherlands, 2014)

5. I. Amenabar, F. Lopez, A. Mendikute, J. Infrared Millim. Terahertz Waves **34**, 152 (2013)
6. J.P. Guillet, B. Recur, L. Frederique, B. Bousquet, L. Canioni, I. Manek-Hönninger, P. Desbarats, P. Mounaix, J. Infrared Millim. Terahertz Waves **35**, 382 (2014)
7. M.F. Pereira, O. Shulika, *Terahertz and Mid Infrared Radiation: Detection of Explosives and CBRN (Using Terahertz)* (Springer, Heidelberg, 2014), pp. 153–165
8. S.S. Dhillon et al., J. Phys. D: Appl. Phys. **50**, 043001 (2017)
9. A. Latyshev, A. Dvurechenskii, A. Aseev (eds.), *Advances in Semiconductor Nanostructures* (Elsevier, New York, 2016)
10. S. Bhowmick, G. Huang, W. Guo, C.S. Lee, P. Bhattacharya, G. Ariyawansa, A.G.U. Perera, Appl. Phys. Lett. **96**, 231103 (2010)
11. J. Wu, D. Shao, Zh. Li, M.O. Manasreh, V.P. Kunets, Zh.M. Wang, G.J. Salamo, Appl. Phys. Lett. **95**, 071908 (2009)
12. J. Wu, Zh.M. Wang, V.G. Dorogan, Sh. Li, Zh. Zhou, H. Li, J. Lee, E.S. Kim, Y.I. Mazur, G.J. Salamo, Appl. Phys. Lett. **101**, 043904 (2012)
13. Yu.I. Mazur, V. Lopes-Oliveira, L.D. de Souza, V. Lopez-Richard, M.D. Teodoro, V.G. Dorogan, M. Benamara, J. Wu, G.G. Tarasov, E. Marega Jr., Z.M. Wang, G.E. Marques, G.J. Salamo, J. Appl. Phys **117**, 154307 (2015)
14. V.O. Gordo, Y.G. Gobato, H.V.A. Galeti, M.J.S.P. Brasil, D. Taylor, M. Henini, J. Electron. Mater. **46**, 3851 (2017)
15. G. Linares-García, L. Meza-Montes, E. Stinaff, S.M. Alsolamy, M.E. Ware, Y.I. Mazur, Z.M. Wang, J. Lee, G.J. Salamo, Nanoscale Res. Lett. **11**, 309 (2016)
16. M. Elborg, T. Noda, T. Mano, T. Kuroda, Y. Yao, Y. Sakuma, K. Sakoda, J. Cryst. Growth **477**, 239 (2017)
17. E. Zipper, M. Kurpas, M.M. Maśka, New J. Phys. **14**, 093029 (2012)
18. A. Biborski, A.P. Kądzielawa, A. Gorczyca-Goraj, E. Zipper, M.M. Maśka, J. Spałek, Sci. Rep. **6**, 29887 (2016)
19. Yan-Hui Sun, Shan Liu, Feng-Chen Zhou, Jun-Min Nan, Appl. Surf. Sci. **390**, 175 (2016)
20. C. Kern, M. Kadic, M. Wegener, Phys. Rev. Lett. **118**, 016601 (2017)
21. W. Ouerghui, J. Martinez-Pastor, J. Gomis, M.A. Maaref, D. Granados, J.M. García, Eur. Phys. J. B **54**, 217 (2006)
22. S.D. Ganichev, W. Prettl (eds.), *Intense Terahertz Excitation of Semiconductors* (Oxford University Press, Oxford, 2006)
23. Y. Yakoby, Phys. Rev. **169**, 610 (1968)
24. A.H. Chin, J.M. Bakker, J. Kono, Phys. Rev. Lett. **85**, 3293 (2000)
25. A. Srivastava, R. Srivastava, J. Wang, J. Kono, Phys. Rev. Lett. **93**, 157401 (2004)
26. A.M. Danishevskiĭ, A.A. Kastal'skiĭ, S.M. Ryvkin, I.D. Yaroshetskiĭ, Zh. Eksp., Teor. Fiz. **58**, 544 (1970). [Sov. Phys. JETP **31**, 292 (1970)
27. A.F. Gibson, M.F. Kimmit, A.C. Walker, Appl. Phys. Lett. **17**, 75 (1970)
28. A.F. Kravchenko, A.M. Palkin, V.N. Sozinov, O.A. Shegaĭ, Pis'ma. Zh. Eksp. Teor. Fiz. **38**, 328 (1983). [JETP Lett. **38**, 393 (1983)]
29. A.D. Wieck, H. Sigg, K. Ploog, Phys. Rev. Lett. **64**, 463 (1990)
30. H. Plank, L.E. Golub, S. Bauer, V.V. Bel'kov, T. Herrmann, P. Olbrich, M. Eschbach, L. Plucinski, C.M. Schneider, J. Kampmeier, M. Lanius, G. Mussler, D. Grützmacher, S.D. Ganichev, Phys. Rev. B **93**, 125434 (2016)
31. K. Yoshida, K. Shibata, K. Hirakawa, Phys. Rev. Lett. **115**, 138302 (2015)
32. B. Zaks, R.B. Liu, M.S. Sherwin, Nature **483**, 580 (2012)
33. N. Dyakonova, P. Faltermeier, D.B. But, D. Coquillat, S.D. Ganichev, W. Knap, K. Szkudlarek, G. Cywinski, J. Appl. Phys. **120**, 164507 (2016)
34. T. Mano, T. Kuroda, S. Sanguinetti, T. Ochiai, T. Tateno, J. Kim, T. Noda, M. Kawabe, K. Sakoda, G. Kido, N. Koguchi, Nano Lett. **5**, 425 (2005)
35. F.M.S. Lima, M.A. Amato, O.A.C. Nunes, A.L.A. Fonseca, B.G. Enders, E.F. da Silva, J. Appl. Phys. **105**, 123111 (2009)
36. M. Gavrila, *Atoms in Intense Laser Fields, vol. 1, Advances in atomic, molecular, and optical physics* (Academic Press, Boston, 1992)

37. C. Bosio, J.L. Staehli, M. Guzzi, G. Burri, R.A. Logan, Phys. Rev. B **38**, 3263 (1988)
38. H. A. Kramers, *Collected Scientific Papers* (North-Holland, 1956)
39. W.C. Henneberger, Phys. Rev. Lett. **21**, 838 (1968)
40. O. Madelung, U. Rössler, M. Schulz (eds.), *Group IV Elements* (IV-IV and III-V Compounds. Part a - Lattice Properties, Landolt-Börnstein - Group III Condensed Matter (Springer, Berlin Heidelberg, 2001)
41. P.A. Kuchment, *Floquet Theory for Partial Differential Equations*, 1st edn. (Birkhäuser, Basel, 1993)
42. B.G. Enders, F.M.S. Lima, O.A.C. Nunes, A.L.A. Fonseca, D.A. Agrello, F. Qu, E.F. da Silva Jr., V.N. Freire, Phys. Rev. B **70**, 035307 (2004)
43. Q. Fanyao, A.L.A. Fonseca, O.A.C. Nunes, Phys. Stat. Sol. (b) **197**, 349 (1996)
44. F.M.S. Lima, O.A.C. Nunes, A.L.A. Fonseca, M.A. Amato, E.F. da Silva Jr., Semicond. Sci. Technol. **23**, 125038 (2008)
45. C.P. Lima, F.M.S. Lima, A.L.A. Fonseca, O.A.C. Nunes, New J. Phys. **13**, 073005 (2011)
46. M.G. Barseghyan, C.A. Duque, E.C. Niculescu, A. Radu, Superlattices Microstruct. **66**, 10 (2014)
47. S.D. Ganichev, S.N. Danilov, V.V. Bel'kov, E.L. Ivchenko, M. Bichler, W. Wegscheider, D. Weiss, W. Prettl, Phys. Rev. Lett. **88**, 057401 (2002)
48. G. Platero, R. Aguado, Phys. Rep. **395**, 1 (2004)
49. S. Morina, O.V. Kibis, A.A. Pervishko, I.A. Shelykh, Phys. Rev. B **91**, 155312 (2015)
50. A.S. Sheremet, O.V. Kibis, A.V. Kavokin, I.A. Shelykh, Phys. Rev. B **93**, 165307 (2016)
51. K. Kristinsson, O.V. Kibis, S. Morina, I.A. Shelykh, Sci. Rep. **6**, 20082 (2016)
52. A. Radu, A.A. Kirakosyan, D. Laroze, H.M. Baghramyan, M.G. Barseghyan, J. Appl. Phys. **116**, 093101 (2014)
53. A. Radu, A.A. Kirakosyan, D. Laroze, M.G. Barseghyan, Semicond. Sci. Technol. **30**, 045006 (2015)
54. T. Chakraborty, P. Pietiläinen, Phys. Rev. B **50**, 8460 (1994)
55. B. Szafran, F.M. Peeters, Phys. Rev. B **72**, 155316 (2005)
56. J. Simonin, C.R. Proetto, M. Pacheco, Z. Barticevic, Phys. Rev. B **89**, 075304 (2014)
57. S. Gangopadhyay, B.R. Nag, Phys. Stat. Sol. (b) **195**, 123 (1996)
58. E.C. Niculescu, A. Radu, Eur. Phys. J. B **80**, 73 (2011)
59. W.L. Bloss, J. Appl. Phys. **66**, 3639 (1989)
60. D.A.B. Miller, D.S. Chemla, T.C. Damen, A.C. Gossard, W. Wiegmann, T.H. Wood, C.A. Burrus, Phys. Rev. Lett. **53**, 2173 (1984)
61. G. Bastard, *Wave Mechanics Applied to Semiconductor Heterostructures* (Editions de Physique, Paris, 1990)
62. S. Liang, W. Xie, H.A. Sarkisyan, A.V. Meliksetyan, H. Shen, J. Phys.: Condens. Matter **23**, 415302 (2011)
63. R.C. Iotti, L.C. Andreani, Phys. Rev. B **56**, 3922 (1997)
64. M. Şahin, Phys. Rev. B **77**, 045317 (2008)
65. H. Haug, S. W. Koch, Quantum Theory of the Optical and Electronic Properties of Semiconductors (World Scientific, 5 edn. (2009)
66. A.D. Yoffe, Adv. Phys. **50**, 1 (2001)
67. Q. Fanyao, A.L.A. Fonseca, O.A.C. Nunes, Phys. Rev. B **54**, 16405 (1996)
68. Q. Fanyao, A.L.A. Fonseca, O.A.C. Nunes, J. Appl. Phys. **82**, 1236 (1997)
69. E. C. Niculescu, M. Cristea, A. Radu, Superlattices Microstruct. **69**, 65 (2014)
70. A. Radu, E.C. Niculescu, Phys. Lett. A **374**, 1755 (2010)
71. D. Laroze, M.G. Barseghyan, A. Radu, A.A. Kirakosyan, Physica B **501**, 1 (2016)
72. M.G. Barseghyan, Chem. Phys. **479**, 1 (2016)
73. M.G. Barseghyan, A.A. Kirakosyan, D. Laroze, Opt. Commun. **383**, 571 (2017)
74. F. Ehlotzky, Phys. Lett. A **126**, 524 (1988)
75. D.A.B. Miller, D.S. Chemla, T.C. Damen, A.C. Gossard, W. Wiegmann, T.H. Wood, C.A. Burrus, Phys. Rev. B **32**, 1043 (1985)

76. Y.-H. Kuo, Y.K. Lee, Y. Ge, Sh. Ren, J.E. Roth, T.I. Kamins, D.A.B. Miller, J.S. Harris, Nature **437**, 1334 (2005)
77. L.F. Zagonel, S. Mazzucco, M. Tencé, K. March, R. Bernard, B. Laslier, G. Jacopin, M. Tchernycheva, L. Rigutti, F.H. Julien, R. Songmuang, M. Kociak, Nano Lett. **11**, 568 (2011)
78. J.M. Llorens, C. Trallero-Giner, A. García-Cristóbal, A. Cantarero, Phys. Rev. B **64**, 035309 (2001)
79. B.S. Monozon, M.V. Ivanov, P. Schmelcher, Phys. Rev. B **70**, 205336 (2004)
80. L.A. Lavenère-Wanderley, A. Bruno-Alfonso, A. Latgé, J. Phys.: Condens. Matter **14**, 259 (2002)
81. Z. Barticevic, G. Fuster, M. Pacheco, Phys. Rev. B **65**, 193307 (2002)
82. A.Kh. Manaselyan, M.G. Barseghyan, A.A. Kirakosyan, D. Laroze, C.A. Duque, Phys. E **60**, 95 (2014)
83. H.M. Baghramyan, M.G. Barseghyan, D. Laroze, A.A. Kirakosyan, Phys. E **77**, 81 (2016)
84. H. M. Baghramyan, M. G. Barseghyan, A. A. Kirakosyan, J. H. Ojeda, J. Bragard, D. Laroze, Sci. Rep. **8**, 6145 (2018)
85. COMSOL Multiphysics, v. 5.2a. www.comsol.com. COMSOL AB, Stockholm, Sweden
86. E. Oñate, *Structural Analysis with the Finite Element Method. Linear Statics*, vol. 1 (Springer, Netherlands, Barcelona, 2009)
87. G.O. de Sousa, D.R. da Costa, A. Chaves, G.A. Farias, F.M. Peeters, Phys. Rev. B **95**, 205414 (2017)
88. Z.C. Wen, H.X. Wei, X.F. Han, Appl. Phys. Lett. **91**, 122511 (2007)
89. Y. Luo, Y. Du, V. Misra, Nanotechnology **19**, 265301 (2008)
90. R.A. Shelby, D.R. Smith, S. Schultz, Science **292**, 77 (2001)
91. S. Linden, Ch. Enkrich, M. Wegener, J. Zhou, Th. Koschny, C.M. Soukoulis, Science **306**, 1351 (2004)
92. J.H. Ojeda, R.R. Rey-González, D. Laroze, J. Appl. Phys. **114**, 213702 (2013)
93. J.H. Ojeda, C.A. Duque, D. Laroze, Org. Electron. **41**, 369 (2017)
94. T. Chwiej, B. Szafran, Phys. Rev. B **78**, 245306 (2008)
95. B. Szafran, Phys. Rev. B **77**, 205313 (2008)
96. J.I. Climente, J. Planelles, J. Phys.: Condens. Matter **20**, 035212 (2008)
97. H.M. Baghramyan, M.G. Barseghyan, D. Laroze, Sci. Rep. **7**, 10485 (2017)
98. L.D. Landau, L.M. Lifshitz, *Quantum Mechanics* (Pergamon Press, Oxford, 1977)
99. A.S. Baimuratov, I.D. Rukhlenko, V.K. Turkov, I.O. Ponomareva, M.Yu. Leonov, T.S. Perova, K. Berwick, A.V. Baranov, A.V. Fedorov, Sci. Rep. **4**, 6917 (2014)

Chapter 15
Electron-Phonon Interaction in Ring-Like Nanostructures

C. Trallero-Giner, Darío G. Santiago-Pérez, Leonor Chico and R. Pérez-Álvarez

Abstract General expressions of the electron-phonon Hamiltonians in ring-like nanostructures are settled. A unified macroscopic continuum approach for the treatment of acoustical and optical phonon modes in semiconductor core-shell nanowires is established. A basis for the space of solutions is derived, and by applying the appropriate boundary conditions, the dispersion relation curves, as well as the displacement fields and the electrostatic potential for non-polar and polar optical modes are reported. Employing the methods of quantum field theory, the electron- and hole-zone-center optical phonon deformation potential and optical long-range as well as electron-acoustical phonon Hamiltonians are deduced in a systematic way. The results are valid for the study of polar and non-polar semiconductor based core-shell nanowires and to analyze the role of intrinsic strain and the geometric factors on the electron-phonon coupling strengths. Special emphasis is placed on the importance of the cylindrical symmetry in the interaction Hamiltonians.

C. Trallero-Giner (✉)
Department of Theoretical Physics, University of Havana, 10400 Havana, Cuba
e-mail: trallerocarlos@gmail.com

D.G. Santiago-Pérez
Universidad de Sancti Spiritus José Martí Pérez, Ave. de los Mártires 360, 62100 Sancti Spiritus, Cuba
e-mail: dario.g.santiago@gmail.com

L. Chico
Materials Science Factory, Instituto de Ciencia de Materiales de Madrid (ICMM), Consejo Superior de Investigaciones Científicas (CSIC), C/ Sor Juana Inés de la Cruz 3, 28049 Madrid, Spain
e-mail: leonor.chico@icmm.csic.es

R. Pérez-Álvarez
Centro de Investigación en Ciencias, Instituto de Investigación en Ciencias Básicas y Aplicadas, Universidad Autónoma del Estado de Morelos, Av. Universidad 1001, 62209 Cuernavaca, Morelos, Mexico
e-mail: rpa@uaem.mx

V.M. Fomin (ed.), *Physics of Quantum Rings*, NanoScience and Technology,
https://doi.org/10.1007/978-3-319-95159-1_15

15.1 Introduction: Phonons in Ring-Like Geometries

The development of growth techniques has allowed for the fabrication of high quality semiconductor nanowires (NWs). These systems are of the utmost importance for the progress of the nanoscale devices. In particular, the core-shell architecture is of great interest [1]: a cylindrical core of a semiconductor material is surrounded by a shell of a different semiconductor. They constitute unique systems to explore novel low-dimensional phenomena with great basic interest [2–4]. Employing larger bandgap semiconductors provides NWs for direct applications as waveguide or cavity for optoelectronic devices. Different pairs of core-shell materials have been synthesized such as GaAs-GaAsP [5], InAs-GaAs [6], GaN-GaP [7], GaP-GaN [7], GaAs-GaP [8], AlN-GaN [9], GaAsP-GaP [10], GaAs-AlGaAs [11] CdSe/CdS [12], and Si-Ge [13]. A great variety of applications for these core-shell nanowires have appeared, for instance, nanowire lasers [5], nanowire nanosensors [14, 15], photovoltaic devices [16], and light emission diodes [17], to name a few. Furthermore, if the core and shell materials are grown with a lattice mismatch, the strain can be employed as an additional degree of freedom for band structure engineering. Also, with the cylindrical geometry it is possible to achieve much higher strains between the two materials without losing crystalline coherence [18], which can be of interest to modify the carrier mobility and effective masses in these nanostructures. Systems composed by Si, Ge and their solid solutions, are among the most studied and emerging as natural choices for integration with Si-based electronics. The variety of applications foreseen for these materials has boosted the interest of many researchers [19–28]. The separation of electron and hole carriers or the dramatic reduction of the thermal conductivity, are attained in Ge-Si core-shell NWs. The study of acoustic phonons in strained Si-Ge nanowires and its effect on the lifetimes of spin qubits has important consequences in the electronic and optical properties [29, 30]. Also, and based on widespread use of Si nanowires (NWs) linked to thermal conductivity [31], photodetectors [32], and solar cells [33–35], a notable effort has been addressed to study Si-Ge and Ge-Si core-shell semiconductor NWs [36–39]. A suppression of the thermal conductivity in the core-shell Si-Ge NWs has been reported in [40–42]. The reduction of the thermal conductivity and the characteristics of the carrier mobility are directly linked to the confinement effects on the phonon dispersion relation [42–46]. Thus, polar optical, non-polar optical and acoustical phonons and the knowledge of the electron-phonon Hamiltonian (EPH) play an important role on transport, on carrier scattering rates, on the flow of electric current, on the carrier mobility, on the thermal flux, on the spectroscopic characterization, on Raman selection rules of core-shell nanowires of compound semiconductors. To characterize the electron-phonon Hamiltonian, it is necessary the knowledge of phonon displacement vectors and their spatial symmetries. Hence, a straightforward explicit expression for the EPH, as well as the understanding of its physical relevance, represent a central issue for the investigation of these novel structures.

It is well-known (see [47]) that in III-V and II-VI semiconductor nanostructures, the Fröhlich-like long range electrostatic potential is the most relevant interaction. In non-polar materials, the electrostatic contribution due to the anion-cation atomic vibrations is absent and consequently, the dominant contribution to the EPH is the mechanical deformation potential [48]. Polar optical oscillations have been successfully studied for different nanostructures applying a long-wavelength approximation, based on different continuum approaches; see, for example, [49–51] and references therein. In particular, oscillations in cylindrical systems have been studied in [52–54], but only for solid nanowires made of a single material, and in some cases neglecting the dispersion along the nanowire axis. Several works have been devoted to obtain the acoustic phonon dispersion in wires and core-shell nanowires using both ab initio calculations [55, 56] and phenomenological continuum approaches (see [30, 57–59] and references therein). The phenomenological approach has also been used successfully in nanotube structures [60–62]. In addition, studies of electron-phonon interaction for the conduction band have been reported [63–65].

The chapter is organized as follows: Based on a phenomenological theory, Sect. 15.2 presents fundamental equations which describe the acoustical, non-polar and polar oscillation modes, obtaining, for each considered case, a basis of solutions for the phonon amplitudes with cylindrical symmetry, taking into account the possible angular and axial dependence the modes may have. We discuss the inclusion of strain which builds up at the core-shell interface, the matching boundary conditions and a special emphasis is made on the phonon spectrum calculations, on the role of the spatial confinement effect, and on the symmetry of the space of solutions. The macroscopic theoretical treatment of the phonon spatial eigensolutions provides a powerful tool to tackle the electron-phonon Hamiltonian in cylindrical core-shell NWs. Thus, in Sect. 15.3 the electron and hole acoustical-phonon interactions is derived, specifying the properties of symmetry of the conduction and valence bands on the scattering amplitude. Electron-optical-phonon interaction for the short-range deformation potential and Pekar-Fröhlich-type Hamiltonians are derived in detail in Sect. 15.4. Section 15.5 addresses possible implications and manifestations of electron-phonon Hamiltonians for ring-like geometries. Finally, in the Appendices the most relevant technical elements in the development of Sects. 15.2–15.4 are summarized.

15.2 Phonon Dispersion in Core-Shell Nanowires: Effects of Double-Connectedness

In Fig. 15.1 shows a schematic representation of the NWs under study. An infinite core-shell with cylindrical cross section, core radius a, shell radius b with shell thickness $\Delta = b - a$ is considered. The z-axis is chosen parallel to the growth direction and it is assumed that all parameters involved in the present model are piece-wise functions of r, that is, all parameters of the core and shell materials are isotropic.

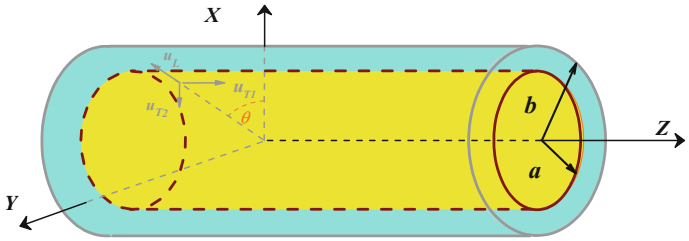

Fig. 15.1 Schematic representation of the core-shell nanowire under study. a and b are the core and shell radii, respectively. Longitudinal, u_L, and transverse, u_{T1}, and u_{T2} vibrational phonon amplitudes are indicated

15.2.1 Acoustical Phonons

In order to derive the dependence of the phonon displacement vector, $\mathbf{u}$, as well as the acoustical phonon dispersion relations, $\omega(k_z)$, on the cylindrical spatial geometry, the elastic continuum approach is followed, where the equation of motion for the displacement $\mathbf{u}$ takes the form [66]

$$\rho\omega^2\mathbf{u} - \nabla\cdot\sigma = \mathbf{0}. \tag{15.1}$$

Here ρ is the mass density, $\sigma = \mathbf{C}\cdot\varepsilon$ is the mechanical stress tensor with $\mathbf{C}$ the elastic stiffness tensor and ε the strain tensor. It will be useful to rewrite the tensor σ and the strain tensor in terms of the displacement vector $\mathbf{u} = (u_r, u_\theta, u_z)$ in cylindrical coordinates $\mathbf{r} = (r, \theta, z)$. Assuming cubic crystal symmetry, all the coordinate axes are fourfold symmetry axes and the tensors have three independent nonzero components. Thus, in cylindrical coordinates the relation between stress and strain tensors can be written as

$$\begin{pmatrix} \sigma_{rr} \\ \sigma_{\theta\theta} \\ \sigma_{zz} \\ \sigma_{r\theta} \\ \sigma_{rz} \\ \sigma_{\theta z} \end{pmatrix} = \begin{pmatrix} C_{11} & C_{12} & C_{12} & 0 & 0 & 0 \\ C_{12} & C_{11} & C_{12} & 0 & 0 & 0 \\ C_{12} & C_{12} & C_{11} & 0 & 0 & 0 \\ 0 & 0 & 0 & C_{44} & 0 & 0 \\ 0 & 0 & 0 & 0 & C_{44} & 0 \\ 0 & 0 & 0 & 0 & 0 & C_{44} \end{pmatrix} \begin{pmatrix} \varepsilon_{rr} \\ \varepsilon_{\theta\theta} \\ \varepsilon_{zz} \\ 2\varepsilon_{r\theta} \\ 2\varepsilon_{rz} \\ 2\varepsilon_{\theta z} \end{pmatrix}, \tag{15.2}$$

where the C_{ij} are the elastic stiffness coefficients. Considering isotropic bulk materials, the tensor $\mathbf{C}$ has three non-zero components [67] and it is given by two independent parameters $C_{11} = \rho v_L^2$, $C_{44} = \rho v_T^2$ and $C_{12} = \rho v_L^2 - 2\rho v_T^2$ with v_T and v_L the transverse and longitudinal sound velocities. In consequence, the acoustic phonon branches at Γ are degenerate. In Appendix 1, the relation between the componentes of the stress tensor ε as a function of the displacement vector components (u_r, u_θ, u_z)

is summarized. Thus, employing (15.71) it follows immediately that the stress tensor takes the form

$$\sigma = \rho(v_L^2 - 2v_T^2)(\nabla \cdot \mathbf{u})\mathbf{I} + 2\rho v_T^2(\nabla \mathbf{u}), \tag{15.3}$$

with $\mathbf{I}$ the identity matrix. According to (15.1) and (15.3) the equation of motion for the acoustic phonon can be cast as

$$\rho\omega^2\mathbf{u} = \nabla(\rho v_L^2 \nabla \cdot \mathbf{u}) - \nabla \times (\rho v_T^2 \nabla \times \mathbf{u}). \tag{15.4}$$

In the case of bulk semiconductors, (15.4) can be split into two independent equations. One for the longitudinal solution where $\nabla \times \mathbf{u}_L = \mathbf{0}$ but $\nabla \cdot \mathbf{u}_L \neq 0$, whereas the second equation for the description of the two transverse oscillations fulfills the conditions $\nabla \times \mathbf{u}_T \neq \mathbf{0}$ and $\nabla \cdot \mathbf{u}_T = 0$. Due to the presence of interfaces in a core-shell nanostructure with cylindrical geometry, neither the displacement vectors $\mathbf{u}_T$, nor $\mathbf{u}_L$ represent eigenmodes for the description of phonon modes.

The solution of (15.4) can be written as a linear combination of the basis vectors $\mathbf{u}_L$, $\mathbf{u}_{T1}$ and $\mathbf{u}_{T2}$ as given in Appendix 2, (15.86), i.e.

$$\mathbf{u} = A_L\mathbf{u}_L + A_{T1}\mathbf{u}_{T1} + A_{T2}\mathbf{u}_{T2}, \tag{15.5}$$

whose coefficients are determined by imposing the appropriate boundary conditions. Since the system is not homogeneous, the acoustic dispersion relations for the L and T branches are not independent and the normal modes become a hybrid combination of L, $T1$ and $T2$ phonon vibrational motions.

15.2.1.1 Core-Shell Ge-Si and Si-Ge Nanowires

In order to determine the eigenfrequencies it is necessary to impose appropriate boundary conditions. For a core-shell nanowire with free boundaries, the mechanical stress should vanish at the shell surface $r = b$, $\sigma \cdot \mathbf{e}_r|_{r=b} = \mathbf{0}$. Besides, it follows directly from (15.4) that the mechanical displacement vector and the normal component of the stress tensor should be continuous at the core-shell interface $r = a$ [49, 68], i.e., $\mathbf{u}|_{r=a_-} = \mathbf{u}|_{r=a_+}$ and $\sigma \cdot \mathbf{e}_r|_{r=a_-} = \sigma \cdot \mathbf{e}_r|_{r=a_+}$.

Strains at the interface play an important role on the phonon frequencies (see [69, 70]). For the acoustic phonons, the effects of lattice mismatch between Ge and Si are taken into account through the continuity of the normal component of the stress tensor.

As stated above, the phonon displacement vector $\mathbf{u}$ has all three components ($\mathbf{u}_{T1}$, $\mathbf{u}_{T2}$ and $\mathbf{u}_L$), since neither of the coefficients A_L, A_{T1} and A_{T2} are zero, therefore, it cannot be decoupled into independent motions and it is not possible to characterize the modes as pure torsional, dilatational, or flexural modes. Nevertheless, from the symmetry of general basis (15.86) as given in Appendix 2, the following results emerge:

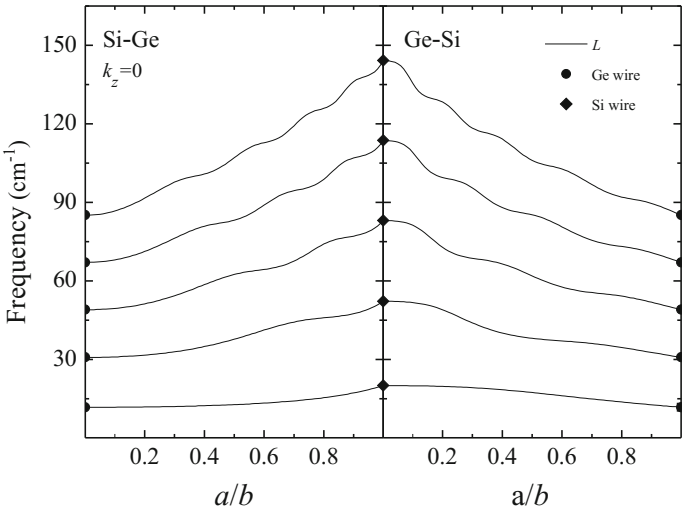

Fig. 15.2 Frequencies ω_L of the first five breathing modes as a function of the ratio a/b. In the calculation it is fixed the shell $b = 5$ nm. Si-Ge (left panel) and Ge-Si (right panel) NWs grown along the [110] crystallographic direction. The limits of Ge and Si nanowires are shown by circles and diamonds, respectively (after [70])

(i) *Phonons with* $k_z = 0$

For $n = 0$ and $k_z = 0$, there are three independent $L, T1$ and $T2$ uncoupled modes with amplitude u_r, u_z and u_θ, respectively. The longitudinal modes correspond to the radial breathing mode (RBM) and their eigenfrequencies are ruled by the secular equation (15.87) (see Appendix 2). Preliminary studies of RBM modes have been carried out in [71–74]. Here, the focus is on the relevance of these particular modes in Ge-Si and Si-Ge core-shell nanowires. The frequencies of the RBM modes are strongly dependent on the material composition, $\lambda_L = v_{L_c}/v_{L_s}$ and size ratio, $\gamma = b/a$.

Figure 15.2 shows the frequency dependence on the core-shell ratio a/b. The limit cases $a = 0$ and $a = b$ of Ge and Si homogeneous NWs are indicated by circles and diamonds, respectively. The data of Table 15.1 for Si and Ge bulk semiconductors are employed in the calculations. It is important to remark that the equation of motion (15.4) for $r < a$ or $a < r < b$ corresponds to an isotropic model. Along the [110] crystallographic direction the transversal phonon velocities are not degenerate, with two different sound velocities v_{T1} and v_{T2}. Here, the average velocity $v_T = (v_{T1} + v_{T2})/2$ is assumed.

The oscillations observed in Fig. 15.2 of ω_L as a function of the ratio a/b can be explained by the interference between shell and core structures. Thus, for small values of the ratio a/b, the influence of the shell on the core phonon amplitude becomes stronger, enhancing the number of oscillations. Moreover, the lower phonon frequencies are less affected, showing almost a flat dispersion on a/b, while the higher excited modes are more sensitive with pronounced oscillations.

Table 15.1 Bulk parameters for Ge and Si

	$v_L(10^5\ \mathrm{cm\ s^{-1}})$	$v_{T1}(10^5\ \mathrm{cm\ s^{-1}})$	$v_{T2}(10^5\ \mathrm{cm\ s^{-1}})$	$v_T(10^5\ \mathrm{cm\ s^{-1}})$	$\rho(\mathrm{g\ cm^{-3}})$
Ge[a]	5.39	3.84	2.76	3.30	5.32
Si[a]	9.36	5.84	4.67	5.25	2.33

[a]Reference [75]

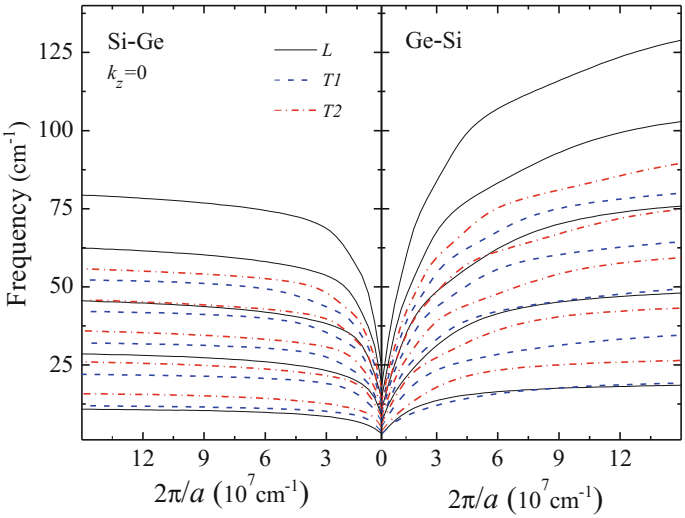

Fig. 15.3 The same as Fig. 15.2 for the uncoupled L, $T1$ and $T2$ phonon modes as a function of $2\pi/a$, for fixed shell thickness $\Delta = b - a = 5$ nm (after [70])

The confined eigenfrequencies, ω_{T2}, for the transversal $T2$ modes are obtained by solving (15.88) taking $k_z = 0$ in Appendix 2. Figure 15.3 displays the dependence on $2\pi/a$ of the uncoupled L, $T1$ and $T2$ phonon frequencies for fixed shell thickness $\Delta = b - a$. In the limit of $a \to \infty$ the pure Si and Ge NWs wires are recovered. As $a \to \infty$, it is found that the phonon frequency resembles the typical linear acoustic bulk phonon dispersion on the phonon wavevector. The effect of the spatial phonon confinement is to renormalize the sound velocity and, for large values of a, the frequency can be written as $\omega_{L,T}^{(j)} = (2\pi/a)v_{L,T}^{(j)}$ $(j = 1, 2, ...)$ with different slopes $v_{L,T}^{(j)}$ for each particular mode. Also, Fig. 15.3 emphasizes that the cylindrical symmetry breaks the $T1$ and $T2$ degeneracy, and two different sound velocities, $v_{T1}^{(j)}$ and $v_{T2}^{(j)}$, appear.

(ii) *Phonons dispersion with* $k_z \neq 0$

For $n = 0$ and $k_z \neq 0$, the longitudinal, L, and transverse, $T1$, motions, $L - T1$, are coupled, while the $T2$ vibrational mode remains uncoupled. Following the secular equation (15.88) deduced in Appendix 2, we display in Fig. 15.3 the pure confined transverse $T2$ phonon dispersion. The bulk phonon dispersions, $\omega_{\mathrm{Ge}}(k_z)$ and $\omega_{\mathrm{Si}}(k_z)$,

are represented by blue and red dashed lines, respectively. Figure 15.3 shows a strong modification of the Si and Ge bulk phonon group velocities which depend on the surrounding material. If the shell is composed of a softer or harder material than the core semiconductor, the resulting group velocity has lower or higher values. In Ge-Si core-shell NWs the Si shell compresses the Ge core lattice, while for Si-Ge NWs the Ge shell is compressed by the Si core [57]. In the case of Ge-Si, if the set of the values (ω, k_z) lies in the region $\omega_{\rm Ge}(k_z) < \omega < \omega_{\rm Si}(k_z)$, the parameter $x_c = a\sqrt{(\omega/v_{T_c})^2 - k_z^2}$ is real while $x_s = a\sqrt{(\omega/v_{T_s})^2 - k_z^2}$ becomes a complex number. Accordingly, in (15.88) the function $P_{nm}(x_s) \Rightarrow P_{nm}(|x_s|)$ and

$$P_{nm}(|x_s|) = I_n(|x_s|)K_m(\gamma\,|x_s|) - I_m(\gamma\,|x_s|)K_n(|x_s|), \tag{15.6}$$

where I_n [K_n] is the order-n Infield [MacDonald] cylindrical function. Thus, for small values of the phonon wave vector k_z from (15.88) and using the asymptotic behavior $J_1(x_c) \approx x_c/2$, $P_{12}(\gamma, |x_s|) \approx 1/(\gamma^2\,|x_s|)$, $P_{22}(\gamma, |x_s|) \approx \left(1-\gamma^4\right)/(4\gamma^2)$ and $J_2(x_c) \approx x_c^2/8$, it follows the analytical dispersion relation valid for Ge-Si (x_c real and x_s is a complex number)

$$\omega = v_{T_c}\sqrt{1 + \frac{\left(\lambda_T^2 - 1\right)\left(\gamma^4 - 1\right)\rho_r}{\left(\gamma^4 - 1\right)\rho_r + 1}}\,k_z = \overline{v_T}k_z. \tag{15.7}$$

A similar equation is achieved for the Si-Ge NWs, where x_c is a complex number and x_s is real. Equation (15.7) shows that for $k_z \Rightarrow 0$, the acoustical phonon modes present a renormalized sound velocity $\overline{v_T}$ that takes into account the parameters of the materials: the ratio of the shell and core radius, as well as the densities, ρ_r, and transverse velocities, λ_T [30]. Equation (15.7) suggests the way to modify the sound velocity as a function of the geometric factors ranging between the values of $v_T^{\rm Ge}$ and $v_T^{\rm Si}$. In the domain of (ω, k_z) where the phonon are confined (x_c and x_s are both real functions), (15.88) provides the dispersion relation for small values of k_z,

$$\omega_{T2}(k_z) = \omega_{T2}(0) + \frac{1}{2}\frac{v_{T_s}^2}{\omega_{T2}^2(0)}k_z^2, \tag{15.8}$$

with $\omega_{T2}(0)$ the confined phonon frequency of the core-shell NWs for $k_z = 0$. In Fig. 15.4 the solutions given by (15.7) and (15.8) are represented by open diamonds. By comparison with the numerical calculation of (15.88), it can be seen that explicit expressions (15.7) and (15.8) are good approximations for $k_z(\pi/b) \leq 1$.

Figure 15.5 is devoted to the phonon dispersion of the mixed $L-T1$ modes for $\gamma = 1.25$. The longitudinal, L, and transverse, $T1$, labels are taken from the character of the modes at $k_z = 0$. For the sake of comparison, the phonon dispersion for the homogeneous Si and Ge cylindrical wires are shown in Fig. 15.5. Here, the corresponding longitudinal and transverse modes are represented by red straight and red dashed-dotted lines, respectively. Solutions for core-shell NWs correspond to the hybridized longitudinal and transverse motions. Due to the strain effect at the inter-

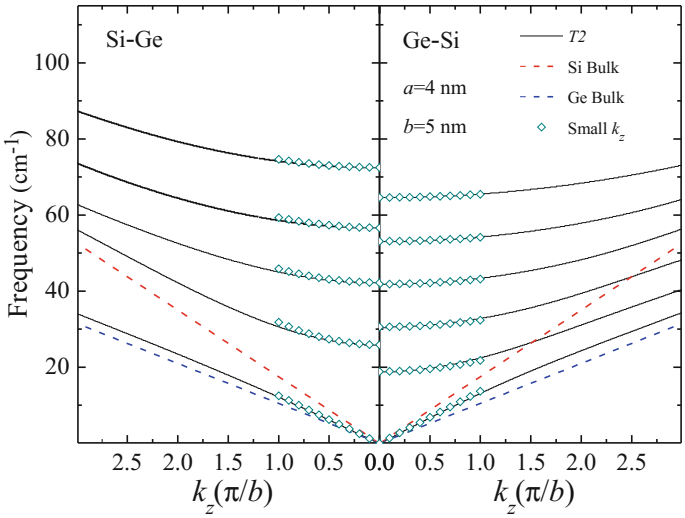

Fig. 15.4 Phonon dispersion for the uncoupled $T2$ modes as a function of the phonon wave vector $\mathbf{k_z}$ in units of π/a. Left panel Si-Ge; right panel Ge-Si NWs. Dashed lines represent the bulk dispersion relation for Si and Ge. Open diamonds are solutions of (15.7) and (15.8) (after [70])

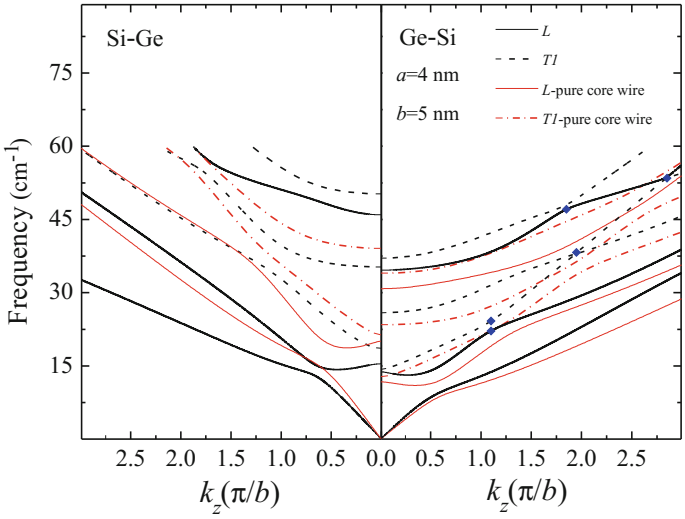

Fig. 15.5 The same as Fig. 15.4 for the mixed $L-T1$ modes. Phonon dispersion relations for homogeneous Si and Ge cylinder wires are represented by red straight (longitudinal modes) and dashed-dotted (transversal modes) lines. Full diamonds represent the anticrossings between two nearby modes as explained in the text (after [70])

face, the phonon frequencies of the Ge-Si NW lie above those of the Ge wire, while the opposite is obtained for the Si-Ge NW, where $\omega_{\rm Si}$ are well above the core-shell Si-Ge phonon frequencies. At $k_z \Rightarrow 0$, the lower mode presents a linear dependence of ω_{L-T1} on the wave number k_z, with an effective sound velocity v_{L-T1} that depends on the radii a and b. Assuming in (15.4) that L and T motions are decoupled, an assumption not valid even for $n = 0$, a compact analytical expression for the longitudinal frequency ω_L is obtained as a function of the wave number k_z [30].

On the same basis of (15.4), Fomin and Balandin [59] studied the phonon dispersions of hollow multishell QWs and the influence of the number of shells on the sound velocities, $\overline{v_T}$, for GaAs and InAs. In the case of two shells, the torsional mode, u_z, $u_r = 0$ and $u_\theta \neq 0$, is very similar to the results of Fig. (15.4). For the coupled or nontorsional mode, where the displacement components are u_z, $u_r \neq 0$ and $u_\theta = 0$, the dispersion relations of coupled modes are strongly dependent on the ratio between the sound speeds of the constituent materials and on the differences between both types of quantum wires.

The bendings appearing in Fig. 15.5 are a manifestation of the strongest coupling between L and $T1$ modes. The mixed character of the states avoids crossing points in the phonon dispersion relation, i.e., a repulsion between near modes with the same symmetry occurs. This effect is observed in all the dispersion relations, having an important consequence in the electron-phonon Hamiltonian $H_{\rm e-ph}$ (see discussion in Sect. 15.3 below). In Fig. 15.5 some anticrossings, associated with the mixing of L and $T1$ states, have been indicated by full diamonds. The proximity of the levels belonging to the same space of solutions or with the same symmetry is avoided by the repulsion between the phonon states. At the anticrossings, a strong mixing of the L and $T1$ states occurs and an exchange of the character of the constants A_L and A_{T1} is obtained as a function of k_z. Figure 15.6 shows the behavior of the coefficient A_L as a function of z-component of the phonon wavevector where the exchange of characters between longitudinal and transverse motions is clearly observed.

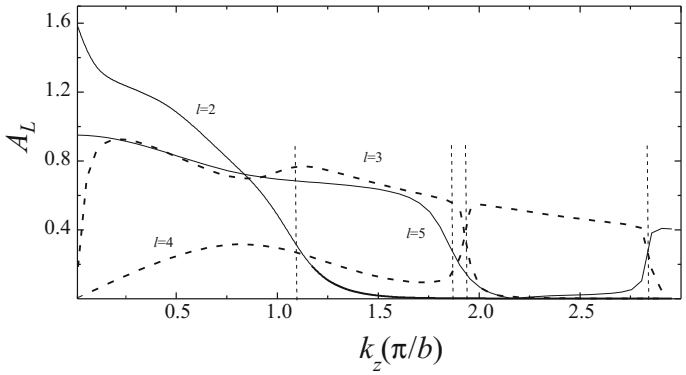

Fig. 15.6 Coefficient A_L in (15.5) as a function of k_z in units of π/b for the phonon modes $l = 2, 3, 4, 5$ of Ge-Si NWs as shown in Fig. 15.5. Dashed lines shows the values of k_z where the anticrossings between two nearby modes occur

The higher excited states for $k_z \sim 0$ do not present a strong mixing effect and the phonon dispersion relation can be described by a simple parabolic law, $\omega_{L(T1)}(k_z) = \omega_{L(T1)}(0) + \beta^2_{L(T)} k_z^2$. Here, $\beta_{L(T)}$ measures the curvature of the phonon dispersion and $\omega_{L-T1}(0)$ is the NW phonon frequency for $k_z = 0$. The same conclusion is achieved for the homogeneous Si and Ge cylindrical wires.

(iii) *Modes for* $n \neq 0$ *and* $k_z = 0$

Using the general curvilinear basis (15.86) as given in the Appendix 2, it is observed that the $T1$ transverse phonon modes, with amplitudes $u_r, u_\theta = 0$ and $u_z \neq 0$, are independent solutions of (15.4), while the other two modes, L and $T2$, with $u_r, u_\theta \neq 0$ and $u_z = 0$, are mixed states.

(iv) *Acoustical phonon with* $n \neq 0$ and $k_z \neq 0$

In this case the various subspaces in (15.86) are not independent and the longitudinal L and the transverse $T1$, $T2$ motions are coupled.

15.2.2 Non-polar Optical Phonons

Here it follows a systematic study of the long-wavelength optical phonons for non-polar media and cylindrical core-shell geometry. The consequence of the cylindrical spatial geometry on confined phonon frequencies, the mixing of phonon modes and their corresponding displacement vector are described by the relatively simple unified macroscopic continuum theory [76, 77]. Using the equation of motion derived in [68, 78] from the hydrodynamic phenomenological model for cubic polar semiconductors and considering that the polarization and electric field associated with the atom vibrations are zero, the equations of motion for the optical modes in an isotropic nonpolar media is given by

$$\omega^2 \mathbf{u} = \omega_0^2 \mathbf{u} - \nabla \cdot \sigma, \tag{15.9}$$

where ω_0 is the bulk optical phonon frequency at Γ point and the tensor components σ are given by

$$\sigma = -(\beta_L^2 - 2\beta_T^2)(\nabla \cdot \mathbf{u})\mathbf{I} - 2\beta_T^2(\nabla \mathbf{u}). \tag{15.10}$$

Equation (15.10) includes dispersion effects through the terms β_L and β_T describing the quadratic dispersions of the *LO*- and *TO*-bulk phonon branches of the optical modes in the long-wave limit, respectively. These are phenomenological parameters and can be obtained by fitting the bulk phonon dispersion relations. Hence, in the framework of this model the dynamical equations for the optical modes in an isotropic nonpolar media can be cast as

$$\omega^2 \mathbf{u} = \omega_0^2 \mathbf{u} + \beta_L^2 \nabla(\nabla \cdot \mathbf{u}) - \beta_T^2 \nabla \times (\nabla \times \mathbf{u}). \tag{15.11}$$

Equation (15.11) is based on the fact that because the bulk optical frequencies of core and shell materials are very different, it is a valid assumption that the states are completely confined in the core or in the shell regions. In addition, it is assumed a large separation between the optical branches of the shell and the host material. These approaches are fulfilled for several II-VI, III-V, Si and Ge semiconductors. Applying the Helmholtz's method of potentials of [79, 80], one can find that (15.86) with (15.85) is a general basis of solutions for the problem (15.11).

A direct evaluation of (15.11) requires one to obtain the general solution of the problem. This can be written as a linear combination of the basis vectors (15.86) given in Appendix 2, whose coefficients are determined by imposing the appropriate boundary conditions.

For Si and Ge, whose characteristic bulk optical phonon frequencies are 521 cm^{-1} and 301 cm^{-1}, respectively [81], and assuming a large separation between the optical branches of shell and the host material, the amplitude of the oscillations should be zero at the surfaces S ($r = a$ and $r = b$), i.e., $\mathbf{u}|_{r=a} = \mathbf{u}|_{r=b} = \mathbf{0}$.

15.2.2.1 Strain-Induced Shift of Bulk Modes

Core-shell NWs present strain fields as well as the strain-induced frequency shift as a function of core radius and shell thickness [19]. Assuming an isotropic medium, the shift in bulk frequencies is proportional to the volume change due to stress [82, 83]

$$\Delta\omega_i(k_z) = -\gamma_i\omega_i(k_z)\Delta V_c/V_c, \quad (i = LO \text{ and } TO), \tag{15.12}$$

where γ_i is the Grüneisen parameter, ω_i the bulk optical phonon frequencies, V_c the volume of unit cell, and ΔV_c the volume change due to the lattice mismatch. The ratio $\Delta V_c/V_c = Tr(\varepsilon)$ with $Tr(\varepsilon)$ being the trace of the stress tensor. The explicit forms of $Tr(\varepsilon)$ in cylindrical coordinates for the core and shell are displayed in Appendix 1 for the fully strained case. Nevertheless, in core-shell silicon and germanium NWs the strain depends on the crystallographic direction of the nanowire axis [20, 22] and the phonon frequency shift can be estimated by solving the phonon dynamic equations [84] along the desired crystallographic direction. Considering the Cartesian coordinates along the cubic axis of the crystal, it follows the secular equation [85]

$$\begin{pmatrix} p\varepsilon_{11} + q\widetilde{\varepsilon_{11}} - \Delta\omega^2 & 2t\varepsilon_{12} & 2t\varepsilon_{13} \\ 2t\varepsilon_{21} & p\varepsilon_{22} + q\widetilde{\varepsilon_{22}} - \Delta\omega^2 & 2t\varepsilon_{23} \\ 2t\varepsilon_{31} & 2t\varepsilon_{32} & p\varepsilon_{33} + q\widetilde{\varepsilon_{33}} - \Delta\omega^2 \end{pmatrix} \begin{pmatrix} U_1 \\ U_2 \\ U_3 \end{pmatrix} = 0. \tag{15.13}$$

Here, ε_{ij} $(i, j = 1, 2, 3)$ is the strain components, $\mathbf{U} = (U_1, U_2, U_3)$ is the unperturbed phonon displacement eigenvector in Cartesian coordinates, $\widetilde{\varepsilon_{ii}} = Tr\{\varepsilon\} - \varepsilon_{ii}$, $\Delta\omega^2 = \omega^2 - \omega_0^2$ is the strain-induced frequency shift, and p, q, t are the nonzero components of the phonon deformation potential tensor in cubic symmetry.

As the NW growth direction is that of the z-axis in cylindrical coordinates, it is immediate that for [001] case the unperturbed phonon eigenvector $\mathbf{U}_3$ is chosen as $\mathbf{U}_3 \rightarrow \mathbf{u}_{T1}$ and the strain tensor ε in cylindrical components is given by

$$\varepsilon = \begin{pmatrix} \varepsilon_{rr}\cos^2\theta + \varepsilon_{\theta\theta}\sin^2\theta & -(\varepsilon_{rr}-\varepsilon_{\theta\theta})\sin\theta\cos\theta & 0 \\ -(\varepsilon_{rr}-\varepsilon_{\theta\theta})\sin\theta\cos\theta & \varepsilon_{rr}\sin^2\theta + \varepsilon_{\theta\theta}\cos^2\theta & 0 \\ 0 & 0 & \varepsilon_{zz} \end{pmatrix}. \tag{15.14}$$

Thus, the secular equation (15.13) is reduced to

$$\begin{vmatrix} q\varepsilon_{zz} + \widetilde{\varepsilon(P,Q)} - \Delta\omega^2 & -t(\varepsilon_{rr}-\varepsilon_{\theta\theta})\sin 2\theta & 0 \\ -t(\varepsilon_{rr}-\varepsilon_{\theta\theta})\sin 2\theta & q\varepsilon_{zz} + \widetilde{\varepsilon(Q,P)} - \Delta\omega^2 & 0 \\ 0 & 0 & p\varepsilon_{zz} + q(\varepsilon_{rr}+\varepsilon_{\theta\theta}) - \Delta\omega^2 \end{vmatrix} = 0, \tag{15.15}$$

with $\widetilde{\varepsilon(P,Q)} = P\cos^2\theta + Q\sin^2\theta$, $P = p\varepsilon_{rr} + q\varepsilon_{\theta\theta}$ and $Q = q\varepsilon_{rr} + p\varepsilon_{\theta\theta}$. The explicit forms of ε_{rr}, $\varepsilon_{\theta\theta}$ and ε_{zz} for the core and shell in cylindrical coordinates are reported in Appendix 1 and [85] for the fully strained case. From (15.74–15.78) it can be seen that the strain tensor components at the core depend only on the ratio $\gamma = b/a$, while ε^s is a function of the coordinate r. The strain-induced frequency shift, $\Delta\omega^2$, solution of (15.13), is

$$\begin{aligned} \Delta\omega_L^2 &= (p+q)\varepsilon_{rr}^{\mathrm{c}} + q\varepsilon_{zz}^{\mathrm{c}}, \\ \Delta\omega_{T1}^2 &= 2q\varepsilon_{rr}^{\mathrm{c}} + p\varepsilon_{zz}^{\mathrm{c}}, \\ \Delta\omega_{T2}^2 &= (p+q)\varepsilon_{rr}^{\mathrm{c}} + q\varepsilon_{zz}^{\mathrm{c}}. \end{aligned} \tag{15.16}$$

Likewise, we can also make the correspondence $\mathbf{U}_2 \rightarrow \mathbf{u}_{T1}$ for the [011] direction. Following the same procedure, the frequency shifts for NWs growth along [011] direction are given by

$$\begin{aligned} \Delta\omega_L^2 &= \left(\frac{3}{4}p + \frac{5}{4}q + \frac{1}{2}t\right)\varepsilon_{rr}^{\mathrm{c}} + \left(\frac{1}{4}p + \frac{3}{4}q - \frac{1}{2}t\right)\varepsilon_{zz}^{\mathrm{c}}, \\ \Delta\omega_{T1}^2 &= \left(\frac{1}{2}p + \frac{3}{2}q - t\right)\varepsilon_{rr}^{\mathrm{c}} + \left(\frac{1}{2}p + \frac{1}{2}q + t\right)\varepsilon_{zz}^{\mathrm{c}}, \\ \Delta\omega_{T2}^2 &= \left(\frac{3}{4}p + \frac{5}{4}q + \frac{1}{2}t\right)\varepsilon_{rr}^{\mathrm{c}} + \left(\frac{1}{4}p + \frac{3}{4}q - \frac{1}{2}t\right)\varepsilon_{zz}^{\mathrm{c}}. \end{aligned} \tag{15.17}$$

Similarly, in the case of [111] growth direction and choosing $\mathbf{U}_1 \rightarrow \mathbf{u}_{T1}$, the shift for the three modes are

$$\Delta\omega_L^2 = \frac{1}{3}(p+2q)(2\varepsilon_{rr}^c + \varepsilon_{zz}^c) - \frac{2}{3}t(\varepsilon_{rr}^c - \varepsilon_{zz}^c),$$
$$\Delta\omega_{T1}^2 = \frac{1}{3}(p+2q)(2\varepsilon_{rr}^c + \varepsilon_{zz}^c) + \frac{4}{3}t(\varepsilon_{rr}^c - \varepsilon_{zz}^c),$$
$$\Delta\omega_{T2}^2 = \frac{1}{3}(p+2q)(2\varepsilon_{rr}^c + \varepsilon_{zz}^c) - \frac{2}{3}t(\varepsilon_{rr}^c - \varepsilon_{zz}^c). \quad (15.18)$$

Raman measurements in core-shell Si-Ge NWs [20] prove that strain is partially relaxed for core diameters larger than 11 nm. In order to avoid an overestimation of the strain effects, Singh et al. [20] introduced an axial relaxation parameter ρ_0 in the misfit factor, $\varepsilon_{\text{misfit}} = (a_s - a_c)/a_c$, with a_c (a_s) being the lattice constant of the core (shell) bulk semiconductor. Thus, the misfit strain is rewritten as $\varepsilon_{\text{misfit}} \to \varepsilon_{\text{misfit}}(1-\rho_0)$. This parameter varies between 0 and 1, so that when $\rho_0 = 0$, the system is fully strained. For the numerical evaluations a relaxation parameter $\rho_0 = 0.5$ is taken, avoiding the unrealistic overestimation of the strain. The results for fully strained NWs are very similar, save for the larger shift due to strain effects. Once the phonon bulk frequencies are corrected including strain through the replacement $\omega_0^2 \to \omega_0^2 + \Delta\omega_i^2$ ($i = L, T1, T2$) in the corresponding expressions for the phonon wavenumber $q_{L,T}$ as given by (15.85), it is possible to evaluate the phonon dispersion relations using (15.90).

15.2.2.2 Dispersion Relations for Ge-Si and Si-Ge Core-Shell Nanowires

This section is devoted to study the core modes in Ge-Si and Si-Ge systems and, in particular, to analyze the coupling of the phonon modes for different values of n and k_z, as well as the frequency shift due to confinement and interface stress as a function of the core and shell radii a, b, and the wavevector k_z. Table 15.2 shows the input parameters employed in the calculations. The values given in Table 15.2 are assumed to be size-independent, a hypothesis that should not be valid for very small radii. Dimensionless quadratic curvature parameters for the transversal (β_T^2) and longitudinal (β_L^2) bulk optical phonon bands, along the [011] crystallographic direction are 6.33×10^{-12}, 11.53×10^{-12} and 17.59×10^{-12}, 31.95×10^{-12} for Ge and Si respectively. These values have been fitted to the neutron dispersion data collected in [86–89]. As it is well-known, the transversal optical phonons are non-degenerate along the [011] crystallographic direction, showing different β_{T1} and β_{T2} curvatures. For Si and Ge bulk semiconductors these values are similar. Thus, in the framework of the isotropic approximation, we have chosen for β_T the average values of β_{T1} and β_{T2} fitted by neutron scattering for our calculations.

Table 15.2 Bulk parameters for Ge and Si with diamond structure. ω_0 is given in cm^{-1}, the Young's modulus E in 10^{12} dyn/cm^2 and the lattice constant a_0 in nm

	ω_0	p/ω_0^2	q/ω_0^2	t/ω_0^2	E	ν	a_0
Ge	301[a]	−1.47[b]	−1.93[b]	−1.11[b]	1.28[c]	0.21[c]	0.566[c]
Si	521[a]	−1.83[b]	−2.33[b]	−0.71[b]	1.59[b]	0.23[c]	0.543[c]

[a]Reference [81]
[b]Reference [84]
[c]Reference [75]

The general phonon dispersion relations for the core phonons are obtained by solving (15.90) in Appendix 2. From the basis function (15.86) and (15.90) the following symmetry properties are obtained:

(i) *Modes with* $n = 0$ *and* $k_z = 0$

The triple degeneracy of the optical modes is broken and all modes L, $T1$ and $T2$ are completely decoupled with three independent subsets of confined modes. The frequencies of core modes are found to be

$$\begin{aligned}
\omega_L^2 &= \omega_0^2 - \frac{\beta_L^2(\mu_1^{(m)})^2}{a^2} + \Delta\omega_L^2(\gamma), \\
\omega_{T1}^2 &= \omega_0^2 - \frac{\beta_T^2(\mu_0^{(m)})^2}{a^2} + \Delta\omega_{T1}^2(\gamma), \\
\omega_{T2}^2 &= \omega_0^2 - \frac{\beta_T^2(\mu_1^{(m)})^2}{a^2} + \Delta\omega_{T2}^2(\gamma),
\end{aligned} \tag{15.19}$$

where $\mu_i^{(m)}$ $(i = 0, 1)$ are the roots of $J_i(\mu_i^{(m)}) = 0$, with $m = 1, 2, \ldots$. The second term in the right hand side of (15.19) gives the effect of confinement, producing a downshift of the modes proportional to $1/a^2$. The third term is the effect of strain, $\Delta\omega_i^2$, $(i = L, T1, T2)$ which depends on the ratio γ and the crystallographic direction.

Figure 15.7 shows the core modes as a function of the core radius a in a core-shell system for fixed shell thickness. The left panel presents the Ge-Si case, and the right panel depicts results for the Si-Ge nanowire. Recall that the role of the shell is essential to obtain the shift of the core bulk frequency, as explained in Sect. 15.2.2.1 but, besides that, it does not play any role for the core modes, because of the boundary condition of complete confinement. There is an overall increase of the core mode frequencies in the left panel of Fig. 15.7, in which Ge is the core material (Ge bulk frequency $\omega_0 = 301\ \text{cm}^{-1}$), while the modes are downshifted (for Si $\omega_0 = 521\ \text{cm}^{-1}$) in the right panel of Fig. 15.7, where Si is the core medium. This is related to the difference of lattice constants of Si and Ge; as it can be seen in Table 15.2, the lattice constant of Si is smaller than that of Ge, thus the strain always produces a redshift in the Si part of the wire, and a blueshift in the Ge part, no matter whether they constitute the core or the shell. The highest frequency mode of the Ge-core case (left panel) shows an increase of frequency for diminishing a in a substantial radius

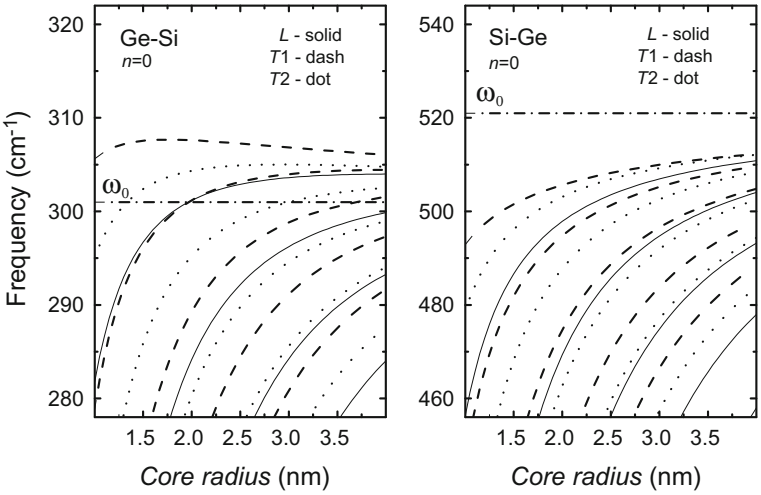

Fig. 15.7 Frequencies of the core modes with $n = 0$ and $k_z = 0$ as a function of the core radius in a core-shell system grown in the [011] direction. Left panel: Ge-Si NW. Right panel: Si-Ge NW, for fixed shell thickness $b - a = 1$ nm (after [90])

range, which indicates the importance of strain for this mode. Equations (15.19) and (15.74)–(15.78) allow us to conclude that for increasing values of a and fixed shell thickness, the frequencies tend to the bulk core value, while for γ fixed confinement effects disappear, leaving the strain as the main contribution. In a nanowire with fixed core radius, the frequency dependence is due to the strain, which varies with the shell radius via the ratio γ. As discussed above, the NWs with Ge core will always show an increasing blueshift of all modes with increasing strain, because of the smaller Si lattice constant. For the same reason, all modes of strained Si-core NWs are redshifted.

(ii) *Modes with* $n \neq 0$ *and* $k_z = 0$

In the case of modes without axial symmetry, i.e., $n \neq 0$, for $k_z = 0$ the L and $T2$ modes are coupled, while the $T1$ one remains uncoupled. The dispersion relation for the latter is given by

$$\omega_{T1}^2 = \omega_0^2 - \frac{\beta_T^2 (\mu_n^{(m)})^2}{a^2} + \Delta\omega_{T1}^2(\gamma), \tag{15.20}$$

where $J_n(\mu_n^{(m)}) = 0$ with $m = 1, 2, \ldots$. The coupled $L - T2$ modes are obtained from (15.91) (see Appendix 2).

Fig. 15.8 is devoted to the core modes with $n = 1$ and $k_z = 0$ as a function of the core radius for fixed shell thickness. The uncoupled $T1$ modes behave as for the $n = 0$ case, while the coupled $L - T2$ modes are closer in frequencies compared to

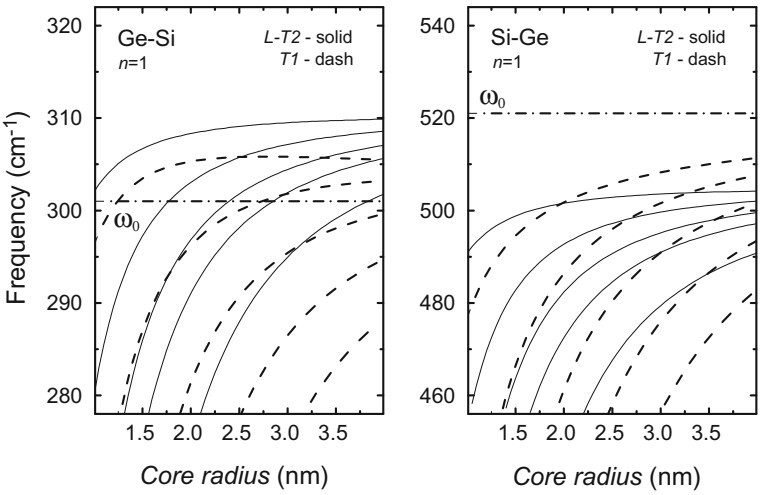

Fig. 15.8 The same as Fig. 15.7 for $n = 1$ (after [90])

the $n = 0$ case. This behavior holds for varying core radius if the same shell/core ratio is maintained.

(iii) Modes with $n = 0$ and $k_z \neq 0$

Here it is considered the dependence of the phonon frequencies with the wavevector $k_z \neq 0$. For the quantum number $n = 0$ the transverse $T2$ mode is uncoupled while L and $T1$ modes are coupled. The uncoupled transverse mode is given by $J_1(\mu_1^{(m)}) = 0$, which leads to the dispersion relation

$$\omega_{T2}^2 = \omega_0^2 - \frac{\beta_T^2 (\mu_1^{(m)})^2}{a^2} + \Delta\omega_{T2}^2(\gamma) - \beta_T^2 k_z^2. \tag{15.21}$$

Equation (15.21) is just like the bulk dispersion relation, except for the shifts due to the spatial confinement $\beta_T^2(\mu_1^{(m)})^2/a^2$ and the strain, $\Delta\omega_{T2}^2(\gamma)$. The coupled $L - T1$ modes are obtained from (15.94) in Appendix 2.

15.2.3 Polar Optical Phonons

Polar optical phonons are of great interest for the spectroscopic characterization of core-shell nanowires of compound semiconductors. Nowadays, several particular systems have been synthesized employing different pairs of core-shell materials, such as GaAs-GaAsP [5], InAs-GaAs [6], GaN-GaP [7], GaP-GaN [7], GaAs-GaP [8], AlN-GaN [9], GaAsP-GaP [10], GaAs-AlGaAs [11], and CdSe/CdS [12], among others. Polar phonon modes have been successfully studied for different

nanostructures applying a long-wavelength approximation and based on different continuum approaches; see, for example, [49–51, 91] and references therein. In particular, oscillations in cylindrical systems have been studied in [52–54], but only for solid nanowires made of a single material.

In the framework of the phenomenological continuum model [68, 92, 93] the phonon oscillations are described by the relative displacement vector field $\mathbf{u} = \mathbf{u}_+ - \mathbf{u}_-$ of the two ions involved and the electric potential φ related with the macroscopic electric field $\mathbf{E} = -\nabla\varphi$. The fundamental equations of motion which include the bulk phonon dispersion are given by [79]

$$\rho_m(\omega^2 - \omega_{TO}^2)\mathbf{u} = \rho_m\beta_L^2\nabla(\nabla\cdot\mathbf{u}) - \rho_m\beta_T^2\nabla\times\nabla\times\mathbf{u} + \alpha\nabla\varphi, \tag{15.22}$$

and

$$\nabla^2\varphi = \frac{4\pi\alpha}{\varepsilon_\infty}\nabla\cdot\mathbf{u}, \tag{15.23}$$

with the parameter α defined as

$$\alpha^2 = \frac{(\varepsilon_0 - \varepsilon_\infty)\rho_m\omega_{TO}^2}{4\pi}. \tag{15.24}$$

In these expressions, ω_{TO} is the transversal bulk frequency at Γ point, ρ_m is the reduced mass density, β_L (β_T) describes the quadratic dispersion of the LO (TO)-bulk phonon dispersion of the optical modes in the long-wave limit, and ε_0 (ε_∞) is the static (high frequency) dielectric constant. This phenomenological continuum model takes into account the coupled electro-mechanical character of the vibrations, the longitudinal bulk frequency ω_{LO} is given by the Lyddane-Sachs-Teller relation $\omega_{LO}^2 = (\varepsilon_0/\varepsilon_\infty)\omega_{TO}^2$ and all quantities are piecewise-dependent on the coordinates. The scalar potential is a solution of the Poisson equation (15.23) with a polarization charge $\rho_P = \nabla\cdot\mathbf{P}$ of the polarization field $\mathbf{P} = \alpha\mathbf{u} + (\varepsilon_\infty - 1)\mathbf{E}/4\pi$.

Equations (15.22) and (15.23) represent a system of four coupled partial differential equations which describe the polar optical phonons in each region of the nanowire embedded in a host characterized by its dielectric constant ε_D as depicted in Fig. 15.1.

15.2.3.1 Polar Optical Oscillation Modes in Core-Shell Nanowires

In order to obtain the solution of (15.22) and (15.23), boundary conditions for $\mathbf{u}$ and φ at each interface should be applied. The electric potential φ and the normal component of the displacement field $\mathbf{D} = 4\pi\alpha\mathbf{u} - \varepsilon_\infty\nabla\cdot\varphi$ should be continuous at the interfaces [49]. For the mechanical displacement vector $\mathbf{u}$ it is considered that the oscillations occurring in one of the materials do not penetrate significantly into the other. This is the case of the GaAs-GaP core-shell nanowire (in fact, a significant number of pairs of materials of current interest satisfies this requisite) and it can

be assumed complete mechanical confinement, $\mathbf{u}|_a = \mathbf{u}|_b = \mathbf{0}$. Thus, the matching boundary conditions are reduced to

$$\begin{aligned} \mathbf{u}|_S &= \mathbf{0}, \\ \varphi^-\big|_S &= \varphi^+\big|_S, \\ \varepsilon_\infty^- \frac{\partial \varphi^-}{\partial r}\bigg|_S &= \varepsilon_\infty^+ \frac{\partial \varphi^+}{\partial r}\bigg|_S. \end{aligned} \tag{15.25}$$

In (15.25) the symbol $-(+)$ represents that the associated quantity is evaluated at the inside (outside) of the corresponding interface S, namely, the cylindrical surfaces of radii a and b.

15.2.3.2 Interface Optical Phonons

The system of (15.22) and (15.23) leads to coupled modes at the interfaces. These modes shows a predominant electric character and are related to interface phonons (IP). It is possible to evaluate IP in a simple way employing the dielectric continuum approach (DCA). Considering that the electric field satisfies the quasi-static Maxwell equations, we have

$$\varepsilon_{c(s)}(\omega)\nabla^2\varphi = 0,$$

where the frequency-dependent dielectric function $\varepsilon_{c(s)}(\omega)$ for the core (shell) is given by the standard expression

$$\varepsilon_{c(s)}(\omega) = \varepsilon_\infty^{c(s)} \frac{\omega_{LO}^{c(s)2} - \omega^2}{\omega_{TO}^{c(s)2} - \omega^2}. \tag{15.26}$$

In the above equation $\omega_{LO}^{c(s)}$ and $\omega_{TO}^{c(s)}$ are the bulk longitudinal and transversal polar optical phonons frequencies at Γ point for the core (shell) semiconductor material. From (15.99) in Appendix 2 it follows that for each value of the index n there are three independent IP branches. One is linked to the cylindrical core embedded in a host material with an effective dielectric constant, and the other two correspond to the cylindrical shell structure sandwiched between the core and a host dielectric medium. These interface phonons depend on the geometrical parameter γ.

15.2.3.3 Strain Effects

Employing (15.12) strain effects can be included on the phonon frequencies of NWs, allowing to study its importance by comparing to the strain-free case. From (15.72) and (15.73) follow the limits

$$
\begin{aligned}
Tr(\varepsilon_c)_{\lim\gamma\to 1} &= 0,\\
Tr(\varepsilon_s)_{\lim\gamma\to 1} &= 2\varepsilon_{\text{misfit}}\frac{1-2P_{\nu_c}}{P_{\nu_c}-1},\\
Tr(\varepsilon_c)_{\lim\gamma\to\infty} &= \varepsilon_{\text{misfit}}\frac{(1-2P_{\nu_c})\left(3+P_{\nu_c}\right)}{1-2P_{\nu_c}+E_r},\\
Tr(\varepsilon_s)_{\lim\gamma\to\infty} &= 0.
\end{aligned}
\tag{15.27}
$$

In consequence, the strain field in the nanowire is modeled by replacing in (15.95) and (15.99) the unstrained bulk frequencies at Γ, ω_{TO} and ω_{LO}, by $\omega_T(\gamma)$, $\omega_L(\gamma)$:

$$\omega_T(\gamma) = \omega_{TO} + \Delta\omega_{TO}(\gamma), \tag{15.28}$$

$$\omega_L(\gamma) = \omega_{LO} + \Delta\omega_{LO}(\gamma). \tag{15.29}$$

15.2.3.4 Confined and Interface Modes in NWs

The method described in the Appendix 2 provides a basis of functions $\{\mathbf{F}_M(r,\theta,z)\}$ for the solutions of (15.22) and (15.23). The dispersion relations are then obtained applying the boundary conditions (15.25) to a general linear combination of the basis functions (15.97), that can be written as

$$
\mathbf{F} = \begin{cases} \displaystyle\sum_M A_M^{(c)}\mathbf{F}_M^{(1)}. & r \le a \\ \displaystyle\sum_M A_M^{(s)}\mathbf{F}_M^{(1)} + \sum_M B_M^{(s)}F_M^{(2)}, & a \le r \le b \\ \displaystyle\sum_M B_M^{(D)}\mathbf{F}_M^{(2)}. & r \ge b, \end{cases}
\tag{15.30}
$$

where $M = T1, T2, L, H$ and $i = 1, 2$ denotes that the corresponding Bessel and modified Bessel functions f_n, g_n appear in the basis functions $F_M^{(i)}$.

In what follows some analytical and numerical results for core and shell modes, without and with stress effects, are presented. The parameters chosen for GaAs/GaP are listed in Table 15.3. The uncoupled modes ($k_z = 0$, $n = 0$) have been analyzed in [94]. The modes with $k_z = 0$, $n > 0$ are discussed below; in a similar way it is possible to study the cases with $k_z \neq 0$ and $n = 0, 1$. In order to avoid a heavy notation, the indices c, s in the parabolicity parameters and in the bulk frequencies are dropped when there is no possible ambiguity.

(i) Core Modes

Assuming complete mechanical confinement, core modes are modeled by considering $\mathbf{u} \equiv \mathbf{0}$ for $a < r < b$ and $\mathbf{u} \neq \mathbf{0}$ for $r < a$. The application of the boundary conditions indicated in (15.25) yields one family of uncoupled $T1$ modes

Table 15.3 Bulk parameters for GaAs and GaP in zinc blende phase. Frequency is given in cm^{-1}, the Young's modulus E in 10^{12} dyn/cm^2, dispersion parameters $\beta \times 10^{-6}$ and the lattice constant a_0 in nm

Material	ϵ_0	ϵ_∞^a	ω_{TO}	ω_{LO}	β_T	β_L	γ_{TO}	γ_{LO}	E	ν	a_0
GaAs	12.80[b]	11.26	267[b]	285[b]	1.70[c]	1.76[c]	1.11[d]	0.97[d]	0.853[d]	0.312[d]	0.565[d]
GaP	11.11[b]	9.15	365.3[b]	402.5[b]	0.72[e]	1.60[e]	1.09[d]	0.95[d]	1.03[d]	0.306[d]	0.545[d]

[a]Using the Lyddane-Sachs-Teller relation
[b]Reference [95]
[c]Reference [49]
[d]Reference [75]
[e]Reference [96]

and one of coupled L-$T2$ modes. The eigenvalue equations for the uncoupled $T1$ modes are given by $J_n(\mu_n^{(m)}) = 0, m = 1, 2, \ldots$ which yield the dispersion relations $\omega^2 = \omega_{TO}^2 - (\mu_n^{(m)}\beta_T/a)^2$.

Figure 15.9 shows the frequency dependence of the confined modes on the core radius a for the GaAs-GaP core-shell nanowire. For the strain-free case (Fig. 15.9a), the mode frequency is independent of the shell radius b. The uncoupled transversal modes in the nanostructure are not mixed with the electrostatic potential and the complete confined matching boundary conditions $\mathbf{u}|_{r=a} = \mathbf{0}$ and $\mathbf{u}|_{r=b} = \mathbf{0}$, define the confined phonon frequencies. Thus, core (shell) frequencies depend solely on the radius a (b). This behavior changes when the effects of strain are taken into account, which yields the eigenfrequencies dependent on the shell radius b. There is an increase on the frequencies of the modes when considering strain effects, clearly shown in Fig. 15.9b.

The secular equation for the coupled L-$T2$ core modes is reported in the Appendix 2. The phonon frequencies for $n = 1$ as a function of core radius a, given by (15.101), are presented in Fig. 15.10. The interface (I) mode manifests in the abrupt change of slope in the frequencies, where the mixing between longitudinal and transversal modes occurs. The electrostatic potential of the surface oscillation is manifested when the interaction of the LO-confined phonon with the surface mode becomes strong for certain values of the core radius a. In this region the electric character of the modes is dominant. As $a \to \infty$, the bulk LO and TO phonon dispersion relations are recovered. The effect of strain is also an increase of the phonon frequencies (Fig. 15.10b). As the core radius increases, the parameter $\gamma \to 1$ and the phonon frequencies decrease, reaching the bulk limit $\omega_{T(L)}(\gamma = 1) = \omega_{TO(LO)}$; then, the spatial confinement and the influence of the strain on the core are negligible (see (15.72)).

(ii) Shell Modes

The matching boundary conditions (15.25) lead to one family of uncoupled $T1$ modes and one of coupled L-$T2$ modes. The secular equation for the uncoupled T1 shell modes is reported elsewhere [79], in this case the $T1$ frequency depends on both core and shell radius. Although the general expressions for L-$T2$ modes can be obtained [79], the explicit equations are not given, but the numerical solutions

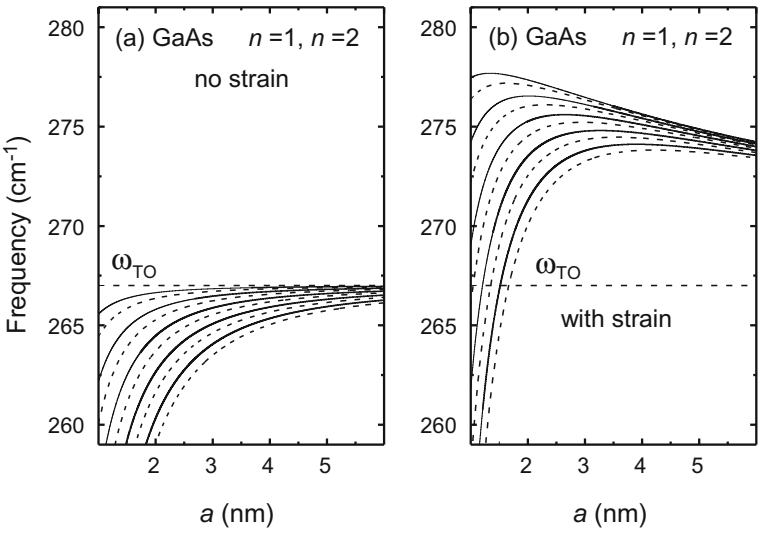

Fig. 15.9 GaAs optical uncoupled transversal phonon modes at $k_z = 0$ for $n = 1$ (full lines) and $n = 2$ (dashed lines) in a GaAs-GaP core-shell nanowire as a function of the core radius a. Panel **a** without strain; panel **b** including strain effects, in panel **b** $b - a = 3$ nm. The bulk GaAs *TO* phonon frequency is indicated by a red horizontal dashed line (after [79])

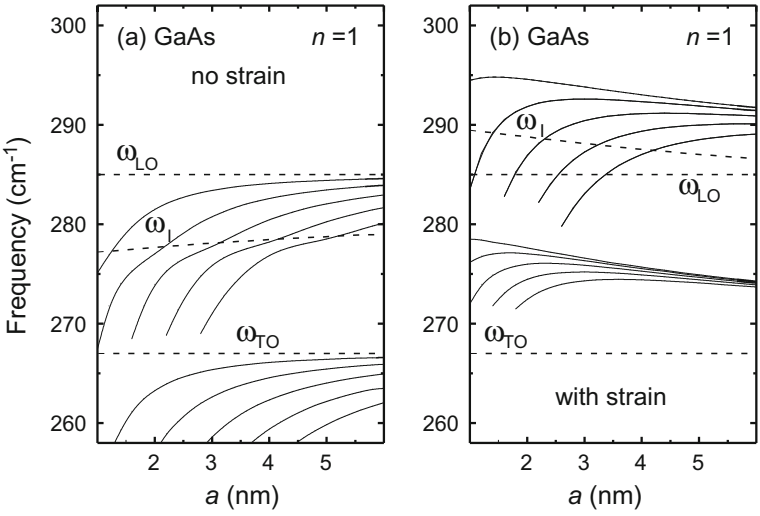

Fig. 15.10 GaAs optical coupled phonon modes at $k_z = 0$ for $n = 1$ in GaAs-GaP core-shell nanowire as a function of the core radius a. Panel **a** neglecting strain effects, panel **b** including strain. $b - a = 3$ nm and $\varepsilon_D = 2.56$. The bulk GaAs *LO* and *TO* and interface phonon, *I* (see (15.99)), frequencies are indicated by red dashed lines (after [79])

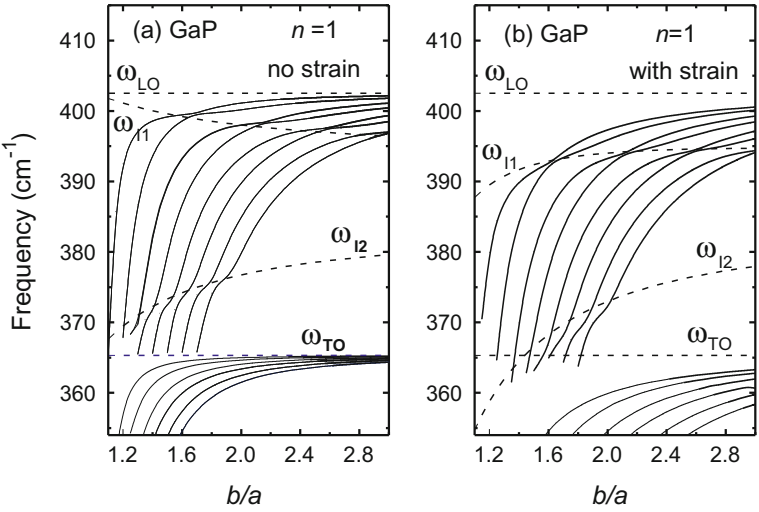

Fig. 15.11 GaP optical coupled phonon modes at $k_z = 0$ for $n = 1$ in GaAs-GaP core-shell nanowire as a function of the relation $\gamma = b/a$. Panel **a** neglecting strain, panel **b** considering strain effects. In the calculation $a = 3$ nm and $\varepsilon_D = 2.56$. The bulk *LO* and *TO* phonon frequencies are indicated by red dashed lines. The corresponding I-phonon frequencies, ω_{I1} and ω_{I2} obtained in the framework of the DCA are also represented by dashed lines (after [79])

corresponding to these dispersion relations for $n = 1$ and $k_z = 0$ as functions of γ are shown in Fig. 15.11. The two interface shell branches $I1$ and $I2$ (shown by dashed lines) are solutions of (15.100). For frequencies near the interface phonons ω_{I1} and ω_{I2}, there is a remarkable mixing between the longitudinal and transversal modes. This effect is more remarkable for phonon frequencies ω near ω_{I2}, where the anticrossing between two modes with different symmetry is stronger if compared with the upper interface branch $I1$. Figure 15.11 shows that the interface strain pushes down the phonon shell modes with respect to the bulk phonon frequencies. Recall that in the core the effect is the opposite (see Fig. 15.10). Noting the limit $\mathrm{tr}(\varepsilon_s) \to 0$ for $\gamma \gg 1$, it can be seen from Fig. 15.11 that the confined phonon frequencies approach the unstrained $\omega_{LO(TO)}$ bulk phonon frequencies.

15.3 Electron-Acoustical-Phonon Interaction

The Hamiltonian of the electrons interacting with the acoustic phonons can be expressed as [81]

$$H_{\mathrm{e-ph}} = \sum_{\alpha',\alpha} M_{\alpha',\alpha} \left[a_j^{\dagger}(k_z) + a_j(-k_z) \right] c_{\alpha'}^{\dagger} c_{\alpha}, \tag{15.31}$$

where $a_j^{\dagger}(fk_z)$ $(a_j(-k_z))$ denotes the phonon creation (annihilation) operator in the $j-$branch with wavevector $k_z(-k_z)$ and $c_{\alpha'}^{\dagger}$ (c_{α}), the corresponding operators for electrons in the electronic states α' (α). Here, $M_{\alpha',\alpha}$ takes into account the electronic scattering event between the states $\alpha \to \alpha'$ by the interaction with an acoustic phonon.

The electron-acoustic-phonon coupling in semiconductors can be determined using the short range deformation-potential (DP) model [97]. In a first approach, this interaction is treated in the same way as in the bulk DP approach. Nevertheless, it has been reported that the DP constants are anisotropic and that depend on the spatial confinement (see [34] and references therein). Furthermore, the DP mechanism can be treated as a perturbation of the band energies due to the lattice distortion; as a consequence, the electron-phonon coupling depends on the electronic band structure [97]. In the case of the Ge-Si and Si-Ge core-shell nanowires grown in the [110] direction is found a direct band gap at Γ point of the Brillouin zone [98–101]. Hence, the conduction band minimum shows a Γ_{1c} symmetry, while the maximum valence band has a Γ_{15v} one, respectively.

Due to translational and cylindrical symmetries, the matrix element $M_{\alpha',\alpha}$ can be cast as follows

$$M_{\alpha',\alpha} = S_{e-ph}\delta_{m',m+n}\delta_{k',k+k_z}, \tag{15.32}$$

where the angular momentum and momentum conservation are written explicitly. $S_{e-ph} = \langle m' | H_{e-ph} | m \rangle$ is the scattering amplitude due to the electronic transition between the electron or hole states $|m'\rangle \to |m\rangle$ assisted by an acoustical phonon (see Appendix 3). For the phonon eigenvectors $\{\mathbf{u}_{n,k_z}\}$ it is chosen the normalization condition

$$\int \rho(r)|\mathbf{u}_{n,k_z}(\mathbf{r})|^2 dV = \frac{\hbar}{2\omega_n(k_z)}, \tag{15.33}$$

with $\omega_n(k_z)$ the acoustic-phonon dispersion of the core-shell problem. Below is discussed a general formulation for the electron-acoustic deformation potential Hamiltonian, H_{e-ph} and an evaluation of the scattering amplitudes for the electrons and holes.

15.3.1 Electron-Longitudinal-Acoustical-Phonon Hamiltonian

The electron-phonon scattering amplitude probability can be cast as

$$M_{\alpha'_e,\alpha_e} = \langle \Psi_{\alpha'_e} | a(\Gamma_{1c}) \nabla \cdot \mathbf{u} | \Psi_{\alpha_e} \rangle, \tag{15.34}$$

where $a(\Gamma_{1c})$ is the volume deformation potential [97], $\mathbf{u}$ is the vector phonon amplitude and $|\Psi_{\alpha_e}\rangle$ is the electron wave function for the core-shell NWs. The transverse or torsional mode does not induce volume change, and only the longitudinal acoustic motion $\mathbf{u}_L(\mathbf{r})$ contributes to electron-phonon Hamiltonian H_{E-DP}. By assuming in (15.5) A_L as independent constant follows that

$$H_{E-DP} = a(\Gamma_{1c})\nabla\cdot\mathbf{u}_L = -\sqrt{\frac{\hbar\omega_n^3(k_z)}{4\pi a^2 L_0\rho_c v_{_L}^4}}\frac{a(\Gamma_{1c})}{\mathscr{N}_{n,k_z}}f_n(q_{_L}r)e^{i(n\theta+k_z z)}, \tag{15.35}$$

where $\mathscr{N}_{n,k_z} = \sqrt{\int_0^\gamma \rho(z)|\overline{\mathbf{u}_{n,k_z}(z)}|^2 z dz/(\rho_c A_{L_c}^2)}$ is the normalization constant for the dimensionless phonon amplitude $\overline{\mathbf{u}_{n,k_z}(z)}$. Taking into account (15.35), (15.104) and (15.105), the electron scattering amplitude can be written as

$$S_{E-DP} = \frac{1}{a^2}\left\langle F_{m_e'}\right| H_{OE}\frac{\omega_n}{v_{_L}\mathscr{N}_{n,k_z}}f_n\left|F_{m_e}\right\rangle, \tag{15.36}$$

where $H_{OE} = -a(\Gamma_{1c})\sqrt{\hbar\omega_{n=0}(k_z=0)/4\pi a^2 L_0\rho_c v_{_L}^2}$. From (15.36) it follows immediately that the phonon modes with $n=0$ assist the electron intrasubband transitions, $m_e' = m_e$, while for $n\neq 0$ intersubband transitions with $m_e'\neq m_e$ occur. In the case of an homogeneous wire, $\left\langle F_{m_e'}\right| f_n \left|F_{m_e}\right\rangle/a^2$ corresponds to the electron form factor or overlap integral between the normalized radial electronic states and the phonon function f_n of the quantum wire.

For a homogeneous wire and assuming the size-quantum-limit (strong spatial confinement) where electrons populate the lowest subband ($m_e' = m_e = 0$ and $n=0$) and intersubband transitions $|p_e'\rangle \to |p_e\rangle$ are discarded, the scattering amplitude, (15.36), at $k_z = 0$ reduces to

$$S_{E-DP}^H = H_{OE}\left(\frac{a^2q_{_L}^2}{4}\delta^4 - \delta^2 + 1\right)^{-\frac{1}{2}}\frac{\langle J_0(p_e a)|J_0(q_L a)|J_0(p_e a)\rangle}{a^2 J_1^2(p_e a)J_0(q_L a)}, \tag{15.37}$$

with $\delta = v_{_L}/v_{_T}$.

Figure 15.12 displays the reduced scattering amplitude S_{E-DP}/H_{OE} as a function of the ratio a/b for both core-shell NWs. In the calculation for the Si-Ge (Ge-Si) NWs we fixed the value of H_{OE} with the parameters of Si (Ge) semiconductor. For each structure, in the quantum limit approach the first three L modes of the structure with frequencies $\omega_{_L}^{(j)}$ ($j=1,2,3$)$\neq 0$ at $k_z = 0$ are considered. In the figure the form factor using (15.37) and $a = 5$ nm is represented by dashed lines. In NWs of Si-Ge and Ge-Si the electrons are confined in the core and shell, respectively. For the evaluation of (15.36) the results displayed in Appendix 3 are employed. In the upper panel of Fig. 15.12 (Si-Ge NWs) the influence of the shell of Ge on the S_{E-DP} is shown. If $a = b$ a quantum wire of Si is reached with S_{E-DP}/H_{OE} as described by (15.37). If $a/b \neq 1$ the Si-Ge core-shell NWs show that the amplitude of S_{E-DP}, for the $\omega_{_L}^{(1)}$

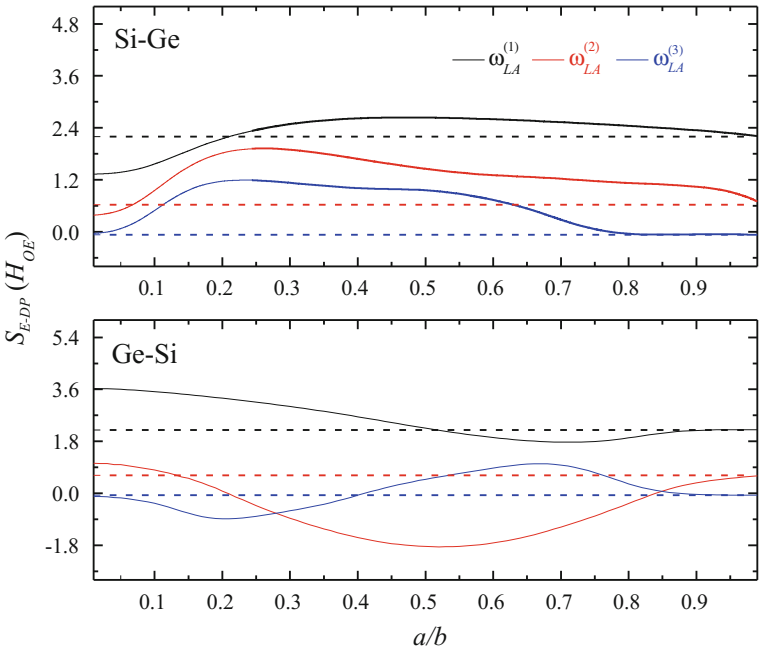

Fig. 15.12 Electron scattering amplitude for the excited frequencies $\omega_L^{(1)}$, $\omega_L^{(2)}$ and $\omega_L^{(3)}$ (see text) as a function of the ratio a/b. Dashed lines: homogeneous wires as given by (15.37). Upper panel Si-Ge, lower panel Ge-Si (after [70])

modes, firstly increases, reaching a maximum for $\gamma_{\max}^{(1)} = (a/b)_{\max}^{(1)} \approx 0.4$ and for $\gamma < \gamma_{\max}^{(1)}$ the quantity S_{E-DP}/H_{OE} reaches asymptotically the Si homogeneous wire value. In the case of $\omega_L^{(j)}$ $(j = 2, 3)$, the reduced scattering amplitude grows, reaching a maximum value near $(a/b)_{\max}^{(2)} \approx 0.23$. For $\gamma < \gamma_{\max}^{(2)}$, S_{E-DP}/H_{OE} decreases to the limit value of (15.37). In the lower panel of Fig. 15.12 (Ge-Si NWs) the wire of Ge is reached at $a = b$. From the figure it can be observed the strong influence of the shell on the S_{E-DP}^H for $a/b < 0.8$ and also the oscillations of S_{E-DP} around the S_{E-DP}^H values, a fact reflecting the oscillator behavior of the phonon modes with γ (see Fig. 15.2). A similar result for the electron scattering amplitude has been reported in [102] for Si nanowires.

15.3.2 Bir-Pikus Hamiltonian in Core-Shell Nanowires

For the scattering amplitude, M_{α_h',α_h}, of a hole in the valence band interacting with an acoustic phonon we have

$$M_{\alpha_h',\alpha_h} = \langle \Psi_{\alpha_h'} | H_{BP} | \Psi_{\alpha_h} \rangle, \tag{15.38}$$

where $|\Psi_{\alpha_h}\rangle$ is the hole wave function in the NW and H_{BP} is the Bir-Pikus Hamiltonian for the $J = 3/2$ valence bands states [48, 97]. Assuming the zinc-blende symmetry, the H_{BP} Hamiltonian in cylindrical coordinates and in the framework of the axial approximation, can be written as

$$H_{BP} = \left[a(\Gamma_{15v}) - \frac{1}{2}b(\Gamma_{15v})\left(J_z^2 - J^2/3\right)\right]\nabla\cdot\mathbf{u} + b(\Gamma_{15v})\left[\frac{1}{2}J_{\mp}^2\mathscr{X}^{\pm} + \sqrt{2}\{J_{\mp}, J_z\}\mathscr{Y}^{\pm} + \frac{3}{2}(J_z^2 - J^2/3)\varepsilon_{zz}\right], \tag{15.39}$$

with $a(\Gamma_{15v})$ and $b(\Gamma_{15v})$ the volume and shear deformation potentials for the highest energy Γ_{15v} valence band,[1] $\mathscr{X}^{\pm} = e^{\pm 2i\theta}(\varepsilon_{rr} - \varepsilon_{\theta\theta} \pm 2i\varepsilon_{r\theta})$, $\mathscr{Y}^{\pm} = e^{\pm i\theta}(\varepsilon_{rz} \pm i\varepsilon_{\theta z})$, $\{J_{\mp}, J_z\} = \frac{1}{2}(J_{\mp}J_z + J_zJ_{\mp})$, $J_{\pm} = (J_x \pm iJ_y)/\sqrt{2}$, being J_i the Cartesian angular-momentum operators for a particle with spin 3/2 and ε_{ij} the component of the stress tensor (see Appendix 1, (15.70)). Employing the solutions for the phonon amplitude (15.5), the matrix representation of the angular momentum $J = 3/2$ [103, 104] and the strain relations given in Appendix 1, the hole scattering amplitude for the Hamiltonian (15.39) can be cast as

$$S_{H-BP} = \left\langle \widehat{F}_{m_h'}^{(i)} \right| H_{BP} \left| \widehat{F}_{m_h}^{(i)} \right\rangle, \tag{15.40}$$

where $i = hh^+, lh^+, lh^-, hh^-$,

$$S_{H-BP} = \left\langle \begin{matrix} a_{1i}F_{m_h+n} \\ a_{2i}F_{m_h+n+1} \\ a_{3i}F_{m_h+n+2} \\ a_{4i}F_{m_h+n+3} \end{matrix} \right| \begin{pmatrix} \mathscr{T}_+ & \mathscr{Y}^- & \mathscr{X}^- & 0 \\ \mathscr{Y}^+ & \mathscr{T}_- & 0 & \mathscr{X}^- \\ \mathscr{X}^+ & 0 & \mathscr{T}_- & -\mathscr{Y}^- \\ 0 & \mathscr{X}^+ & -\mathscr{Y}^+ & \mathscr{T}_+ \end{pmatrix} \left| \begin{matrix} a_{1i}F_{m_h} \\ a_{2i}F_{m_h+1} \\ a_{3i}F_{m_h+2} \\ a_{4i}F_{m_h+3} \end{matrix} \right\rangle, \tag{15.41}$$

$$\begin{aligned}
\mathscr{T}_{\pm} &= -\left[A_L\left(\left[a(\Gamma_{15v}) \pm \frac{1}{2}b(\Gamma_{15v})\right]\frac{\omega^2}{v_L^2} \mp \frac{3}{2}k_z^2 b(\Gamma_{15v})\right)f_n(q_L r) \pm \frac{3}{2}A_{T1}b(\Gamma_{15v})k_z q_T f_n(q_T r)\right], \\
\mathscr{Y}^{\pm} &= \mp i\sqrt{3}b(\Gamma_{15v})\left[A_L k_z q_L f_{n\pm1}(q_L r) \mp \frac{1}{2}\left[A_{T1}\left(q_T^2 - k_z^2\right) + A_{T2}k_z q_T\right]f_{n\pm1}(q_T r)\right], \\
\mathscr{X}^{\pm} &= \frac{\sqrt{3}}{2}b(\Gamma_{15v})\left[A_L q_L^2 f_{n\pm2}(q_L r) + (A_{T1}k_z q_T - A_{T2}q_T^2)f_{n\pm2}(q_T r)\right].
\end{aligned} \tag{15.42}$$

From (15.40), (15.42) and the basis of solutions (15.86), the following conclusions are derived: (a) For the phonon states with $n = 0$, $k_z = 0$ the system presents three independent hole-phonon interaction Hamiltonians, accounting for the three uncoupled subspaces, $L, T1, T2$ with eigenfrequencies ω_L, ω_{T1} and ω_{T2}, respectively. Eval-

[1] It is established that the values of deformation potentials are modified by the orientation and the spatial confinement. In a first approach we are choosing the bulk values from [34].

uating (15.42) at $\omega = \omega_L$ and using the fact that $A_L \neq 0$ and $A_{T1}, A_{T2} = 0$, the Hamiltonian (15.40) couples the diagonal intraband hole sates $|i\rangle \Rightarrow |i\rangle$ and the weak coupling interband between $|v_{\pm 1/2}\rangle \Leftrightarrow |v_{\mp 3/2}\rangle$ Bloch states; if is chosen $\omega = \omega_{T1}$ where $A_L, A_{T2} = 0$ and $A_{T1} \neq 0$, the interband transitions $|v_{\pm 1/2}\rangle \Leftrightarrow |v_{\pm 3/2}\rangle$ are turned on; and for $\omega = \omega_{T2}$ with $A_L, A_{T1} = 0$ and $A_{T2} \neq 0$, results in the $|v_{\mp 1/2}\rangle \Leftrightarrow |v_{\pm 3/2}\rangle$, holes scattering. (b) Fixing $n = 0$, with $k_z \neq 0$, it is found two independent subspaces, $L - T1$ and $T2$. The first one couples the L and $T1$ motions, while the second corresponds to pure $T2$ transverse phonons. Similar expressions are obtained for homogeneous wires by choosing properly the function $F_{m_h}(r)$ and $f_n(r)$ inside the cylinder.

In the size-quantum-limit and not too large values of k_z, the Luttinger-Kohn (LK) Hamiltonian splits into two independent 2×2 matrices, coupling $(|v_{3/2}\rangle, |v_{-1/2}\rangle)$ or $(|v_{-3/2}\rangle, |v_{1/2}\rangle)$ Bloch states (see Appendix 3). For $k_z = 0$ and angular momentum quantum number $n = 0$, the scattering amplitude (15.41) splits into two independent terms, which correspond to the subspaces L and $T2$ of the hole-phonon interaction Hamiltonian.

Figure 15.13 is devoted to the hole scattering amplitude (15.41) in units of $H_{OH} = -a(\Gamma_{15v})\sqrt{\hbar\omega_{n=0}(k_z = 0)/4\pi a^2 L_0 \rho_c v_L^2}$ for the first three $T2$ transverse modes (upper panel) and three L longitudinal modes (lower panel) of the Ge-Si structure as functions of the ratio a/b. It is assumed in the calculation that the lower hole state is completely confined in the core (hard wall potential approximation). As

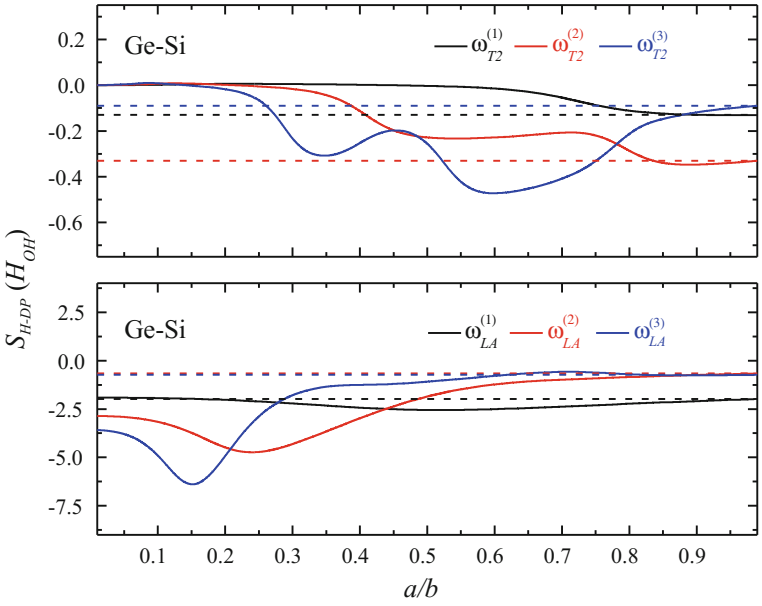

Fig. 15.13 Reduced valence band scattering amplitude S_{H-BP}/H_{OH} for Ge-Si NWs as a function of the ratio a/b. For $k_z = 0$ and $n = 0$, the two sets of of independent subspaces are displayed (see text): Upper panel transverse phonons with frequencies, $\omega_{T2}^{(j)}$; lower panel longitudinal modes and frequencies $\omega_L^{(j)}$ $(j = 1, 2, 3)$. Dashed lines: homogeneous Ge NW (after [70])

in Fig. 15.12, dashed lines represent the form factor for the Ge NW with a radius of 5 nm. Here, the influence of the shell is solely due to Ge-Si phonon spectrum. From the figure it is observed that S_{H-BP} for the longitudinal modes are one order of magnitude larger than the transverse ones, reflecting the coupling between the hole states. In the case of $T2$ we have a coupling between *hh* and *lh* states, while for the L we are in the presence of the diagonal components $hh \rightarrow hh$ and $lh \rightarrow lh$. Another feature is the strong oscillation of the S_{H-BP} for transverse modes with respect to the L phonons. The $T2$ vibrations couple the cylindrical function of second order, while for the L modes, S_{H-BP} is proportional to the Bessel function J_0. In addition, a useful result can be extracted from Fig. 15.13, that is, the minimum value of a/b where the hole-phonon Hamiltonian for core-shell NWs can be considered as a pure Ge wire. This result depends on the type of interaction; for L modes, $a/b \geq 0.6$ and for $T2$ modes $a/b \geq 0.8$.

15.4 Electron-Optical-Phonon Interaction

It is well known that in III-V and II-VI semiconductor nanostructures, the Pekar-Fröhlich long-range electrostatic potential is the most relevant interaction. Nevertheless, the mechanical deformation potential (DP) or short-range interaction is present. Moreover, in nonpolar materials the electrostatic contribution due to the anion-cation atomic vibrations is absent and the dominant contribution to the EPH is the electron-phonon DP interaction.

15.4.1 Short-Range Interaction

In the framework of the Born-Oppenheimer linear approximation, the electron-phonon deformation potential interaction can be written as [48]

$$H_{\mathrm{e-ph}} = \mathbf{u} \cdot \frac{\partial H}{\partial \mathbf{u}}, \tag{15.43}$$

where $\mathbf{D} = \partial H/\partial \mathbf{u}$ takes into account the perturbation of the electronic Hamiltonian by the optical phonon modes at the center of the Brillouin zone. The electron-deformation potential Hamiltonian is written as

$$u_{\hat{e}_x}(\mathbf{r}) D_{\hat{e}_x}(\mathbf{r}) + u_{\hat{e}_y}(\mathbf{r}) D_{\hat{e}_y}(\mathbf{r}) + u_{\hat{e}_z}(\mathbf{r}) D_{\hat{e}_z}(\mathbf{r}), \tag{15.44}$$

and the matrix elements of (15.44), in terms of the envelope function $F(\mathbf{r})$ and the Bloch functions $\mathscr{U}(\mathbf{r})$, are proportional to $\langle \mathscr{U}(\mathbf{r}) | \mathbf{D}(\mathbf{r}) | \mathscr{U}(\mathbf{r}) \rangle$, where it is assumed a rapid spatial variation of the Bloch functions in the unit cell in comparison with the envelope functions $F(\mathbf{r})$. Hence, the deformation potential $\mathbf{D}(\mathbf{r})$ can be characterized

by the matrix element between band-edge wavefunction $|\mathscr{U}\rangle$. At the Γ point of the Brillouin zone, the matrix elements between s-like conduction band states are zero and, in consequence, there is no deformation potential interaction between electrons in the conduction band and optical phonons. For the diamond structure, the degenerate valence bands present Γ_8 symmetry at the Γ point of the Brillouin zone. The inclusion of the spin-orbit interaction splits the valence band degeneracy into four-fold $J = 3/2$, $m_Z = \pm 3/2, \pm 1/2$ and two-fold $J = 1/2$, $m_Z = \pm 1/2$ degenerate states, with J the total angular momentum and m_Z the z-component. The four-fold multiplet $j = 3/2$ valence-band edge wavefunctions are given by Kittel [105]

$$
\begin{aligned}
|v_{-\frac{3}{2}}\rangle &= \frac{i}{\sqrt{2}}|(X - iY)\rangle|\downarrow\rangle, \\
|v_{-\frac{1}{2}}\rangle &= \frac{1}{\sqrt{6}}|(X - iY)\rangle|\uparrow\rangle + \sqrt{\frac{2}{3}}|Z\rangle|\downarrow\rangle, \\
|v_{\frac{1}{2}}\rangle &= \frac{i}{\sqrt{6}}|(X + iY)\rangle|\downarrow\rangle - i\sqrt{\frac{2}{3}}|Z\rangle|\uparrow\rangle, \\
|v_{\frac{3}{2}}\rangle &= \frac{1}{\sqrt{2}}|(X + iY)\rangle|\uparrow\rangle,
\end{aligned}
\tag{15.45}
$$

where $|\uparrow\rangle$ ($|\downarrow\rangle$) denotes the spin parallel (antiparallel) to the growth direction z and the function $|X\rangle$, $|Y\rangle$ and $|Z\rangle$ transform as atomic $p-$like functions. Under the symmetry operations of the representation Γ_8, the only non-zero elements of the deformation potential $\mathbf{D}$ are $\langle Y|D_x|Z\rangle$, $\langle Z|D_y|X\rangle$, $\langle Y|D_z|X\rangle$ and equivalents [97]. Thus, each component of $\mathbf{D}$ in matrix representation can be cast as

$$
D_{\hat{e}_x} = \frac{du_0}{a_0}\begin{pmatrix} 0 & -1 & 0 & 0 \\ -1 & 0 & 0 & 0 \\ 0 & 0 & 0 & 1 \\ 0 & 0 & 1 & 0 \end{pmatrix}, \tag{15.46}
$$

$$
D_{\hat{e}_y} = \frac{idu_0}{a_0}\begin{pmatrix} 0 & -1 & 0 & 0 \\ 1 & 0 & 0 & 0 \\ 0 & 0 & 0 & 1 \\ 0 & 0 & -1 & 0 \end{pmatrix}, \tag{15.47}
$$

$$
D_{\hat{e}_z} = \frac{idu_0}{a_0}\begin{pmatrix} 0 & 0 & -1 & 0 \\ 0 & 0 & 0 & -1 \\ 1 & 0 & 0 & 0 \\ 0 & 1 & 0 & 0 \end{pmatrix}, \tag{15.48}
$$

with d being the optical deformation potential constant as defined by Bir and Pikus, [48] $u_0 = (\hbar V_c / VM\omega_0)^{\frac{1}{2}}$ the unit of phonon displacement, M the atomic mass, a_0 the lattice constant, V the volume of the nanowire and ω_0 the optical bulk

phonon frequency at the Γ point. Under the unitary transformation

$$T = \begin{pmatrix} \cos\theta & \sin\theta & 0 \\ -\sin\theta & \cos\theta & 0 \\ 0 & 0 & 1 \end{pmatrix}, \tag{15.49}$$

the tensor components $\mathbf{D}$ in cylindrical coordinates can be expressed in terms of the components D_i $(i = \hat{e}_r, \hat{e}_\theta, \hat{e}_z)$ as:

$$\begin{aligned} D_{\hat{e}_r} &= \cos\theta D_{\hat{e}_x} + \sin\theta D_{\hat{e}_y}, \\ D_{\hat{e}_\theta} &= -\sin\theta D_{\hat{e}_x} + \cos\theta D_{\hat{e}_y}, \\ D_{\hat{e}_z} &= D_{\hat{e}_z}. \end{aligned} \tag{15.50}$$

Hence, for the $p-$like valence band, the $\mathbf{D} = \partial H/\partial \mathbf{u}$ components in cylindrical coordinates can be expressed, in matrix representation, as follows:

$$D_{\hat{e}_r} = \frac{du_0}{a_0} \begin{pmatrix} 0 & -e^{i\theta} & 0 & 0 \\ -e^{-i\theta} & 0 & 0 & 0 \\ 0 & 0 & 0 & e^{i\theta} \\ 0 & 0 & e^{-i\theta} & 0 \end{pmatrix}, \tag{15.51}$$

$$D_{\hat{e}_\theta} = \frac{idu_0}{a_0} \begin{pmatrix} 0 & -e^{i\theta} & 0 & 0 \\ e^{-i\theta} & 0 & 0 & 0 \\ 0 & 0 & 0 & e^{i\theta} \\ 0 & 0 & -e^{-i\theta} & 0 \end{pmatrix}, \tag{15.52}$$

and

$$D_{\hat{e}_z} = \frac{idu_0}{a_0} \begin{pmatrix} 0 & 0 & -1 & 0 \\ 0 & 0 & 0 & -1 \\ 1 & 0 & 0 & 0 \\ 0 & 1 & 0 & 0 \end{pmatrix}. \tag{15.53}$$

In (15.31), $M^{(j)}_{\alpha'_h,\alpha_h}$ represents the amplitude probability of scattering between the electronic states $\alpha_h \to \alpha'_h$ due to the interaction with an optical phonon with a vector displacement $\mathbf{u}^{(j)}$. This probability amplitude is reduced to

$$M^{(j)}_{\beta,\alpha} = \frac{1}{\sqrt{N_j}} \langle \beta | \mathbf{u}^{(j)} \cdot \mathbf{D} | \alpha \rangle, \tag{15.54}$$

where $N_j = \|\mathbf{u}^{(j)}\|$ is a displacement vector normalization constant for the optical phonon in the branch j. In the framework of the envelope function approximation for the 4×4 Luttinger Hamiltonian [106] in the axial approximation, and taking into account stress effects [48, 104, 107] due to lattice mismatch, the fourfold wavefunction of the Γ_8 valence band states can be expressed as (see also Appendix 3)

$$\langle \mathbf{r}|\alpha_h\rangle = \begin{pmatrix} F^{(1)}_{\nu_h}(r)|v_{\frac{3}{2}}\rangle \\ F^{(2)}_{\nu_h+1}(r)\mathrm{e}^{i\theta}|v_{\frac{1}{2}}\rangle \\ F^{(3)}_{\nu_h+2}(r)\mathrm{e}^{2i\theta}|v_{-\frac{1}{2}}\rangle \\ F^{(4)}_{\nu_h+3}(r)\mathrm{e}^{3i\theta}|v_{-\frac{3}{2}}\rangle \end{pmatrix} \mathrm{e}^{i(k_h z+\nu_h\theta)}. \tag{15.55}$$

Each component of the spinor (15.55) is characterized by the set of quantum numbers α_h, with ν_h the z-component of the angular momentum and k_h the z-component of the wavevector. Functions $F^{(i)}_{\nu_h}(r) = A^{(i)}_{\nu_h} J_{\nu_h}(r)$ $(i = 1, \ldots, 4)$ for $r < a$ and $F^{(i)}_{\nu_h}(r) = B^{(i)}_{\nu_h} J_{\nu_h}(r) + C^{(i)}_{\nu_h} N_{\nu_h}(r)$ for $a < r < b$, where $J_{\nu_h}(r)$, $N_{\nu_h}(r)$ are the Bessel and Neumann functions. The constants $A^{(i)}_{\nu_h}$, $B^{(i)}_{\nu_h}$, $C^{(i)}_{\nu_h}$ and energy $E_{\nu_h,l_h}(k_h)$ are determined by the matching boundary conditions at $r = a$ and $r = b$. In consequence, the scattering matrix elements (15.34) can be cast as

$$M^{(j)}_{\alpha'_h,\alpha_h} = \frac{1}{\sqrt{N_j}} \left\langle \begin{pmatrix} F^{(1)}_{\nu'_h}(r)|v_{\frac{3}{2}}\rangle \\ F^{(2)}_{\nu'_h+1}(r)\mathrm{e}^{i\theta}|v_{\frac{1}{2}}\rangle \\ F^{(3)}_{\nu'_h+2}(r)\mathrm{e}^{2i\theta}|v_{-\frac{1}{2}}\rangle \\ F^{(4)}_{\nu'_h+3}(r)\mathrm{e}^{3i\theta}|v_{-\frac{3}{2}}\rangle \end{pmatrix} \right| \mathbf{u}^{(j)} \cdot \mathbf{D}$$

$$\times\, \mathrm{e}^{i(\nu_h-\nu'_h)\theta} \left| \begin{pmatrix} F^{(1)}_{\nu_h}(r)|v_{\frac{3}{2}}\rangle \\ F^{(2)}_{\nu_h+1}(r)\mathrm{e}^{i\theta}|v_{\frac{1}{2}}\rangle \\ F^{(3)}_{\nu_h+2}(r)\mathrm{e}^{2i\theta}|v_{-\frac{1}{2}}\rangle \\ F^{(4)}_{\nu_h+3}(r)\mathrm{e}^{3i\theta}|v_{-\frac{3}{2}}\rangle \end{pmatrix} \right\rangle \delta_{k'_h,k_h\pm k_z}, \tag{15.56}$$

where the momentum conservation along the z-direction is written explicitly. The influence of the geometric factors, as well as the strain and bulk parameters on the matrix elements (15.56), are embedded in the phonon dispersion relations and the corresponding displacement vectors.

In order to derive a comprehensive expression for the electron-phonon DP matrix elements (15.56), it is required to discuss the phonon dispersion relations as functions of the radii a and b, wavevector k_z, and influence of the strain effects across the core-shell surface, as well as the spatial symmetry properties of the phonon displacement vector. The evaluation of (15.56) implicitly involves the results presented in Sect. 15.2.2. The symmetry properties, stemming from the peculiarities of the cylindrical geometry, have profound consequences on the electron-phonon Hamiltonian. Thus, for phonon modes with $n = 0$ and $k_z = 0$ the $H_{\mathrm{e-ph}}$ is decoupled into three independent Hamiltonians, $H^{L}_{\mathrm{e-ph}}$, $H^{T1}_{\mathrm{e-ph}}$ and $H^{T2}_{\mathrm{e-ph}}$, which characterize the three

orthogonal phonon displacements along the radial ($\hat{e}_r$), axial ($\hat{e}_z$) and azimuthal ($\hat{e}_\theta$) directions, respectively (see (15.19)). For the case of phonon states with $n \neq 0$ and $k_z = 0$ the $H_{\text{e-ph}}$ is decoupled into two independent blocks. One corresponds to $H^{T1}_{\text{e-ph}}$ and the other to a mixture of u_L and u_{T2} amplitudes, with phonon polarization vector on the $(\hat{e}_r,\hat{e}_\theta)$ plane, which leads to $H^{L-T2}_{\text{e-ph}}$. If $k_z \neq 0$, the axial symmetry is broken and for $n = 0$, the amplitudes u_L and u_{T1} are coupled, so we obtain the $H^{L-T1}_{\text{e-ph}}$ which describes the electronic interaction with phonons polarized on the $(\hat{e}_r,\hat{e}_z)$ plane. Besides, we have a $H^{T2}_{\text{e-ph}}$ term for the uncoupled $T2$ optical modes.

To explore the dependence of mode frequencies, phonon amplitudes and the spatial symmetry on the $H_{\text{e-ph}}$, it is important to evaluate the electron-deformation potential scattering rate as a function of the structural parameters of these core-shell structures. Near the Γ point of the Brillouin zone the conduction band does not play any role in the electron-optical phonon deformation potential Hamiltonian, and the hole states are the only contribution to $H_{\text{e-ph}}$. On the basis of the calculated frequencies and phonon amplitudes, explicit expressions for the DP matrix elements (15.34) can be carried forward. From (15.56), it becomes clear that the hole-phonon scattering rate depends on the phonon polarization. There are three main results for the hole-phonon scattering: phonon polarization along the (a) axial, (b) radial and (c) azimuthal directions.

(a) *Phonon modes polarized along the growth direction*

From the basis vectors shown in (15.86), the z component of the vector amplitude $\mathbf{u}^{(j)}$ is written as

$$u_z^{(\hat{e}_z)} = U_z e^{in\theta} = \left(J_n(\mu_{T1} r/a) J_n(\mu_L) \; -J_n(\mu_L r/a) J_n(\mu_{T1})\right) e^{in\theta}/\sqrt{N_z}\,. \quad (15.57)$$

Consequently, combining (15.53) and (15.55), the amplitude (15.56) is reduced to

$$M^{(\hat{e}_z)}_{\alpha'_h,\alpha_h} = \frac{idu_0}{a_0}\Big(\delta_{\nu'_h,\nu_h+n+2}\Big[-\langle F^{(1)}_{\nu'_h}|U_z|F^{(3)}_{\nu_h+2}\rangle - \langle F^{(2)}_{\nu'_h+1}|U_z|F^{(4)}_{\nu_h+3}\rangle\Big] + \delta_{\nu'_h,\nu_h+n-2}\Big[\langle F^{(3)}_{\nu'_h+2}|U_z|F^{(1)}_{\nu_h}\rangle + \langle F^{(4)}_{\nu'_h+3}|U_z|F^{(2)}_{\nu_h+1}\rangle\Big]\Big)\delta_{k'_h,k_h\pm k_z}\,. \quad (15.58)$$

This scattering rate is ruled by the combination of longitudinal L and transverse $T1$ amplitudes. In the particular case of $k_z = 0$, as it is required for example in infrared spectroscopy measurements, the hole transition is assisted by a pure transversal $T1$ optical phonon.

Figure 15.14 shows the contribution of the amplitude u_z to the $H^{(\hat{e}_z)}_{\text{e-ph}}$. The left panel is devoted to the three first modes ($m = 1, 2, 3$) with $n = 0$, 1 and $k_z = 0$. The right panel presents the elongation for $n = 0$ and $k_z \neq 0$ for Ge-Si and Si-Ge NWs.

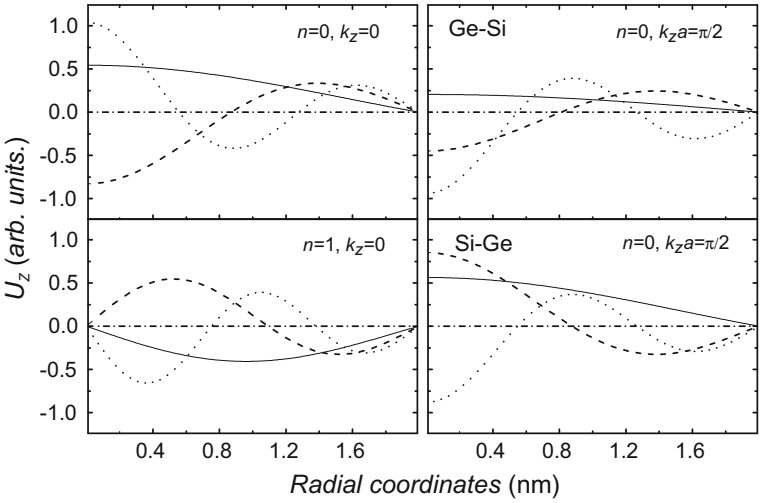

Fig. 15.14 Core phonon amplitude U_z for Ge-Si and Si-Ge core-shell NWs. Left panel: $n = 0$, 1 and $k_z = 0$; right panel: $n = 0$ and $\widetilde{k}_z^2 = \pi/2$. In the calculation $a = 2$ nm and $b = 4$ nm (after [90])

(b) *Polarization along the radial direction*

Employing (15.86) the vector component $u_r^{(\hat{e}_r)}$ is a mixture of the tree amplitudes, u_L, u_{T1} and u_{T2}, thus

$$u_r^{(\hat{e}_r)} = U_r e^{in\theta} = \left(A_{T2} J_n'(\mu_{T2} r/a) + A_{T1} J_n(\mu_{T1} r/a) \; + J_n'(\mu_L r/a)\right) e^{in\theta}/\sqrt{N_r}\,, \tag{15.59}$$

where the coefficients for the phonon elongation U_r in (15.59) are given by

$$A_{T1} = -\left(\frac{\widetilde{k}_z^2}{\mu_{T1}\mu_L}\frac{J_n(\mu_L)J_n'(\mu_{T2})}{J_n^2(\mu_{T1})} + \frac{J_n'(\mu_L)}{J_n(\mu_{T1})}\right)\,, \tag{15.60}$$

and

$$A_{T2} = \frac{\widetilde{k}_z^2}{\mu_{T1}\mu_L}\frac{J_n(\mu_L)}{J_n(\mu_{T1})}\,. \tag{15.61}$$

This allows us to reduce the matrix elements (15.56) to

$$M_{\beta,\alpha}^{(\hat{e}_r)} = \Big(\delta_{\nu',\nu+n+2}\Big[-\langle\nu'|U_r|\nu+1\rangle + \langle\nu'+2|U_r|\nu+3\rangle\Big] + \delta_{\nu',\nu+n-2}\Big[-\langle\nu'+1|U_z|\nu\rangle + \langle\nu'+3|U_r|\nu+2\rangle\Big]\Big)\delta_{k_e',k_e\pm k_z}\,. \tag{15.62}$$

For $k_z = 0$ the EPH $H_{\mathrm{e-ph}}^{(\hat{e}_r)}$ presents a mixture of the $L - T2$ modes. Only for $n = 0$ there is a pure longitudinal oscillation along the radial direction.

(c) *Polarization along the azimuthal direction*

From the basis (15.86) the amplitude $u_\theta^{(\hat{e}_\theta)}$ is written as

$$u_\theta^{(\hat{e}_\theta)} = U_\theta e^{in\theta} = \Big(B_{T1} J_n(\mu_{T1} r/a) - J_n{}'(\mu_{T2} r/a) + B_L J_n(\mu_L r/a)\Big) e^{in\theta}/\sqrt{N_r}, \tag{15.63}$$

where the coefficients B_{T1} and B_L are given by

$$B_{T1} = \frac{\widetilde{k}_z^2}{\widetilde{k}_z^2 + \mu_{T1}^2} \frac{J_n{}'(\mu_{T2})}{J_n(\mu_{T1})}\,, \tag{15.64}$$

$$B_L = \frac{\mu_{T1}^2}{\widetilde{k}_z^2 + \mu_{T1}^2} \frac{J_n{}'(\mu_{T2})}{J_n(\mu_L)}\,. \tag{15.65}$$

With the former expression, the scattering matrix element with a deformation potential $D_{(\hat{e}_\theta)}$ becomes

$$M_{\beta,\alpha}^{(\hat{e}_\theta)} = \Big(\delta_{\nu',\nu+n+2}\Big[- \langle \nu' | U_\theta | \nu + 1\rangle - \langle \nu' + 2 | U_\theta | \nu + 3\rangle\Big] + \delta_{\nu',\nu+n-2}\Big[\langle \nu' + 1 | U_\theta | \nu\rangle + \langle \nu' + 3 | U_\theta | \nu + 2\rangle\Big]\Big)\delta_{k_e', k_e \pm k_z}\,. \tag{15.66}$$

The dependence on r of the phonon elongations U_r and U_θ which appear in $H_{\mathrm{e-ph}}^{(\hat{e}_r)}$ and $H_{\mathrm{e-ph}}^{(\hat{e}_\theta)}$ are shown in Figs. 15.15 and 15.16 respectively. For both, Si-Ge and Ge-Si NWs we take $n = 0, 1$, $k_z a = 0, \pi/2$ and $m = 1, 2, 3$. The deformation potential scattering amplitudes (15.56) given by (15.58), (15.62) and (15.66) take into account the phonon symmetries of Ge-Si and Si-Ge NWs and the corresponding strain effects. All the information of the shell structure is carried out in the phonon symmetry and frequency calculations $\omega_{m,n} = \omega_{m,n}(a, \Delta\omega_i^2(\gamma))$.

15.4.2 Pekar-Fröhlich-Type Hamiltonian

One of the crucial results of the Sect. 15.2.3.1 is straightforward implementation of the Pekar-Fröhlich-like electron-phonon interaction Hamiltonian, $H_F = e\widehat{\varphi}$, for the

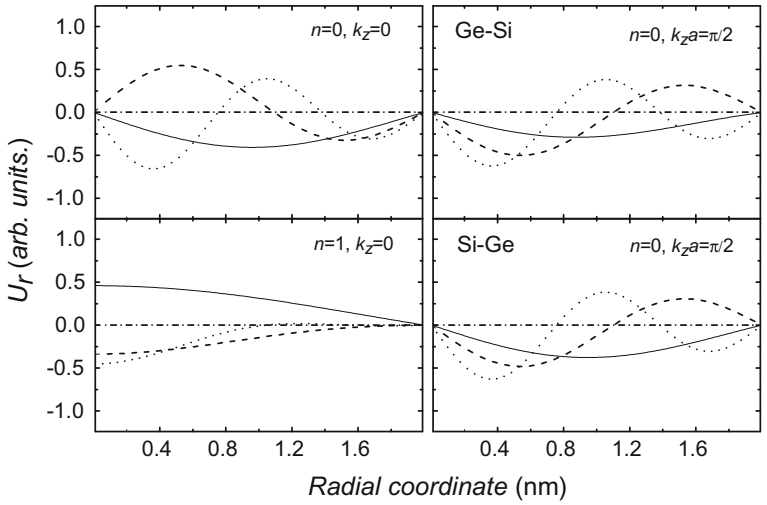

Fig. 15.15 Same as in Fig. 15.14 for core phonon amplitude U_r (after [90])

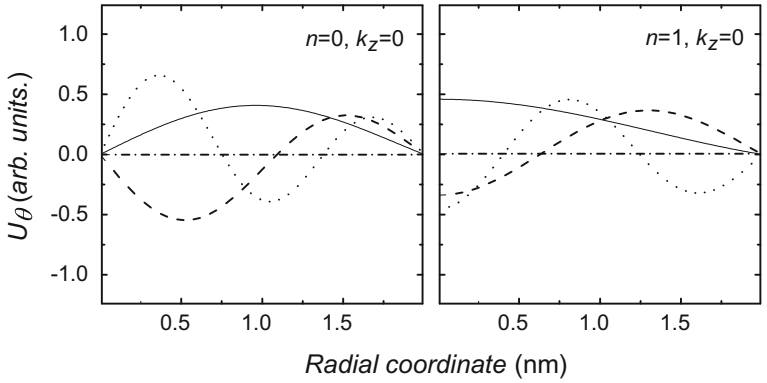

Fig. 15.16 Core phonon amplitude U_θ for Ge-Si and Si-Ge core-shell NWs and $k_z = 0$. Left panel $n = 0$; right panel $n = 1$. In the calculation $a = 2$ nm and $b = 4$ nm (after [90])

core-shell nanowires. Using the general basic expression for the basis vectors (15.97) and employing (15.30) with the appropriate boundary conditions (15.25), the eigenfrequencies ω_{n,m,k_z} and the eigensolutions $F_{n,m,k_z}(r)\exp i(n\theta + k_z z)$ are obtained, which fulfill the orthonormalization condition

$$\int_V \rho_M(r)\mathbf{u}_{n,m,k_z}(r)\mathbf{u}_{n',m,k_z}(r)rdr = \delta_{nn'} \ .$$

Thus, we can construct the general solution for the displacement vector $\mathbf{u}(r, \theta, z)$ and the electrostatic potential $\varphi(r, \theta, z)$ which in second quantization read

$$\widehat{\mathbf{u}} = \sum_{n,m,k_z} C_{n,m,k_z} \left[\mathbf{u}_{n,m,k_z}(r) \exp i(n\theta + k_z z)\widehat{a}_{n,m,k_z} + H.c.\right]$$

and

$$\widehat{\varphi} = \sum_{n,m,k_z} C_{n,m,k_z} \left[\varphi_{n,m,k_z}(r) \exp i(n\theta + k_z z)\widehat{a}_{n,m,k_z} + H.c.\right] .$$

where $\widehat{a}_{n,m,k_z}$ ($\widehat{a}^{+}_{n,m,k_z}$) is the phonon annihilation (creation) operator and the C_{n,m,k_z} coefficients are determined by the commutation rules

$$\left[\mathbf{u}(\mathbf{r}), \boldsymbol{\pi}(\mathbf{r}')\right] = i\hbar\delta(r - r').$$

with $\boldsymbol{\pi}(\mathbf{r})$ being the momentum conjugate. Thus, it is possible to show that [92]

$$C_{n,m,k_z} = \sqrt{\frac{\hbar}{2\omega_{n,m,k_z}}}$$

and the normalized Fröhlich interaction Hamiltonian can be cast as

$$H_F = \sum_{n,m,k_z} e\sqrt{\frac{\hbar}{2\omega_{n,m,k_z}}} \left[\varphi_{n,m,k_z}(r) \exp i(n\theta + k_z z)\widehat{a}_{n,m,k_z} + H.c.\right]. \tag{15.67}$$

The electron-phonon interaction (15.67) takes into account the spatial confinement effect, the electrostatic influence on the phonon modes due to the interfaces and the strain effect of the core-shell nanowires. This result is of particular relevance for the spectroscopic characterization of core-shell nanowires.

15.5 Possible Manifestation of the Electron-Phonon Interaction Specific for Ring-Like Geometries

The present results are relevant for the spectroscopic characterization of core-shell nanowires and they can be of interest for the experimental identification of these nanostructures. The infrared spectroscopy and Raman scattering spectra allow a determination of shift frequencies $\omega_L(\gamma) - \omega_{LO}$ and $\omega_T(\gamma) - \omega_{TO}$ with respect to the ω_{LO} and ω_{TO} bulk phonon frequencies for the core and shell of the quantum wire. This should provide a precise determination of the geometrical factors and/or

structural parameters of the stress tensor of the core-shell NWs. For instance, the Raman spectra at $T = 10$ K of a $GaAs_{0.68}P_{0.32}$/GaP NW [108] show the effect of the core-shell strain, where the *LO* and *TO* phonon lines of the GaP-shell are redshifted with respect to the frequencies of the bulk *LO* and *TO* values. The spatial confinement is negligible (for $GaAs_{0.68}P_{0.32}$ the core radius $a \sim 5$ nm) [94], and the reported shifts are mainly produced by the stress at the interfaces. According to (15.12) it follows immediately that

$$\frac{\Delta\omega_{LO}}{\Delta\omega_{TO}} = \frac{\gamma_{LO}}{\gamma_{TO}} \frac{\omega_{LO}}{\omega_{TO}}. \tag{15.68}$$

The above equation is independent of the geometric factor b/a. According to [108] $\Delta\omega_{LO} = 3.8$ cm^{-1} (bulk GaP-*LO* phonon 404 cm^{-1}) and $\Delta\omega_{TO}$ =3.5 cm^{-1} (bulk GaP-*TO* phonon 365.8 cm^{-1} from [109]) it follows that the value $\gamma_{LO}/\gamma_{TO} = 0.983$ at 10 K. Using the same procedure, along with the first-order Raman scattering data it is possible to determine the dependence of γ_{LO}/γ_{TO} on the geometry factors and on the temperature.

An important application of the electron-phonon interaction specific for ring-like geometries is the Raman selection rules. The first-order phonon resonant Raman tensor of a core-shell NWs is proportional to the scattering amplitude [97], $\mathscr{M}_{FI}$, between the initial ($|I\rangle$) and final ($|F\rangle$) states as given by

$$\mathscr{M}_{FI} \sim \sum_{\mu_1\mu_2} \frac{\langle F|\,\hat{e}_F.\mathbf{p}\,|\mu_2\rangle\,\langle\mu_2|\,H_{\text{e-ph}}\,|\mu_1\rangle\,\langle\mu_1|\,\hat{e}_I.\mathbf{p}\,|I\rangle}{\left(\hbar\omega_s - E_{\mu_2}\right)\left(\hbar\omega_l - E_{\mu_1}\right)}, \tag{15.69}$$

where ω_l (ω_s) is the incident frequency light (Stokes Raman shift) and polarization $\hat{e}_I$ ($\hat{e}_S$), $\mathbf{p}$ the single-particle momentum, $|\mu_i\rangle$ ($i = 1, 2$) are the intermediate electron-hole pair states being a proper combination of the cylindrical real Bessel functions as $r < a$ or $a < r < b$ with energy E_{μ_i}. By introducing the electron-hole wavefunctions and electron-phonon interaction given by (15.51)–(15.53) the Raman selection rules are obtained. In the dipole approximation, where the phonon wavevector $k_z \approx 0$, and considering the backscattering configuration from the quantum wire along the z-growth direction $\overline{Z}(\hat{e}_F, \hat{e}_I)Z$,[2] it is chosen the phonon propagating direction to be z with amplitude $U_z^{(\hat{e}_z)}$ and $H_{\text{e-ph}}^{T1}$ for the pure $T1$ transversal phonons. In this case, from (15.69) and taking into account the cylindrical symmetry of the electron-hole wavefunctions $|\mu_i\rangle$, it is possible to show that the DP interaction for the $T1$ confined phonon is Raman-forbidden in any parallel $\hat{e}_F||\hat{e}_I$ or perpendicular $\hat{e}_F \perp \hat{e}_I$ configurations. The $T1$ phonon mode with quantum number $n = 1$ is *infrared-active*. Now, in the scattering configuration $\overline{X}'(Y', Z)X'$, the phonon is a combination of L and $T2$ modes polarized along the radial direction and EPH $H_{\text{e-ph}}^{L-T2}$. In bulk semiconductors

[2] It is chosen X, Y, Z, X', and Y' the [100], [010], [001], [110], [1$\bar{1}$0] crystallographic directions with [001] the quantization axis.

this scattering configuration allows the transversal *TO* phonon, while in NWs a mixture of modes is obtained as consequence of the reduced symmetry. An important manifestation of the electron-phonon interaction in NWs is the fact that the magnitude of the deformation potential Hamiltonian (15.43) is proportional to $1/\sqrt{a}$ [90]. Hence, the Raman intensity and infrared spectroscopy increase as the core radius decreases, and in consequence the effects of the mechanical boundary conditions become important. Similar results have been reported and observed experimentally in spherical quantum dots [47]. For the case of Si-Ge based NWs, the shell has a role on the frequency shift of the core optical modes through the strain. The present formalism allows one to study the influence of the longitudinal and transversal mixture on H_{e-ph} as a function of the confinement and wave vector k_z. The electron and hole-acoustical phonon Hamiltonians in core-shell NWs are basic tools for exploration of carrier transport phenomena and Brillouin light scattering. Thus, searching at different light scattering configurations of the Brillouin processes, it is possible to study the dependence of the L and $T2$ phonon modes on the spatial confinement and the intrinsic stress at the interface.

A potential application and interesting research problem is linked to polaron effects in core-shell NWs. Typically, such structures are made from ionic semiconductors and in consequence the Pekar-Fröhlich Hamiltonian plays an important role in the determination of the electron dynamics. The electron or hole selfenergies, the associated effective masses and the binding energy must be considered in the NWs, taking into account the electron-phonon interaction, geometric factors and spatial symmetry providing quantitative estimation of polaronic correction. A possible study is the manifestation of electron-phonon interaction on the persistent current (PC) in cylindrical core-shell ring nanowires [110]. This opens an opportunity to look for the effects of the cylindrical geometry and the core shell materials on the PC in correlated NWs ring threaded by an Aharonov-Bohm flux. As it is stated in Sects. 15.3 and 15.4, the $H_{\mathrm{e-ph}}$ can be manipulated as a function of the core-shell NWs parameters and spatial geometry in order to handle the persistent current.

Acknowledgements Authors want to thank to Dr. Vladimir M. Fomin for a critical reading of the manuscript and helpful discussions. This work was partially supported by the Brazilian Agency CNPq and Spanish MINECO under Grant No. FIS2015-64654-P.

Appendix 1: Stress Tensor in Cylindrical Coordinates

The relation between Cartesian $\varepsilon_{ij} = \frac{1}{2}(\partial u_i/\partial x_j + \partial u_j/\partial x_i)$ $(x_1 = x, x_2 = y, x_3 = z)$ and cylindrical strain tensors is given by

$$\varepsilon_{xx} = \varepsilon_{rr} cos^2\theta + \varepsilon_{\theta\theta} sin^2\theta - \varepsilon_{r\theta} sin2\theta \ ;$$
$$\varepsilon_{yy} = \varepsilon_{rr} sin^2\theta + \varepsilon_{\theta\theta} cos^2\theta + \varepsilon_{r\theta} sin2\theta \ ;$$
$$\varepsilon_{xy} = \frac{1}{2}\left(\varepsilon_{rr} - \varepsilon_{\theta\theta}\right) sin2\theta + \frac{1}{2}\varepsilon_{r\theta} cos2\theta \ ;$$

$$\varepsilon_{yz} = \frac{1}{2}\left(\varepsilon_{rz} sin\theta - \varepsilon_{\theta z} cos\theta\right) \; ;$$
$$\varepsilon_{xz} = \frac{1}{2}\left(\varepsilon_{rz} cos\theta - \varepsilon_{\theta z} sin2\theta\right) \; ;$$
$$\varepsilon_{zz} = \varepsilon_{zz}. \tag{15.70}$$

Hence, the components of the strain tensor in terms of the vector phonon displacement $\mathbf{u} = (u_r, u_\theta, u_z)$ can be written as

$$\varepsilon_{rr} = \frac{\partial u_r}{\partial r} \; ; \; \varepsilon_{r\theta} = \frac{1}{2}\left(\frac{1}{r}\frac{\partial u_r}{\partial \theta} + \frac{\partial u_\theta}{\partial r} - \frac{u_\theta}{r}\right) \; ; \; \varepsilon_{\theta\theta} = \frac{1}{r}\left(\frac{\partial u_\theta}{\partial \theta} + u_r\right) \; ;$$
$$\varepsilon_{zz} = \frac{\partial u_z}{\partial z} \; ; \; \varepsilon_{\theta z} = \frac{1}{2}\left(\frac{\partial u_\theta}{\partial z} + \frac{1}{r}\frac{\partial u_z}{\partial \theta}\right) \; ; \quad \varepsilon_{rz} = \frac{1}{2}\left(\frac{\partial u_r}{\partial z} + \frac{\partial u_z}{\partial r}\right). \tag{15.71}$$

The trace of the stress tensor $Tr(\varepsilon)$, can be evaluated for the core and shell materials in cylindrical geometry [85], yielding

$$Tr(\varepsilon_c) = -2\varepsilon_{\text{misfit}}\left(\frac{(1+P_{\nu_c})(1-P_{\nu_c})(\gamma^2-1)}{(1-E_r)(1-2P_{\nu_c})-(1-2P_{\nu_c}+E_r)\gamma^2} + \frac{P_{\nu_c}(\gamma^2-1)}{(\gamma^2-1)+E_r}\right)$$
$$+ \varepsilon_{\text{misfit}}\left(\frac{(\gamma^2-1)}{(\gamma^2-1)+E_r}\right). \tag{15.72}$$

and

$$Tr(\varepsilon_s) = 2\varepsilon_{\text{misfit}}\left(\frac{(1+P_{\nu_s})(1-2P_{\nu_s})E_r}{(1-E_r)(1-2P_{\nu_s})-(1-2P_{\nu_s}+E_r)\gamma^2} + \frac{P_{\nu_s}E_r}{(\gamma^2-1)+E_r}\right)$$
$$- \varepsilon_{\text{misfit}}\frac{E_r}{(\gamma^2-1)+E_r}, \tag{15.73}$$

where $E_r = E_c/E_s$ is the ratio between the core and shell Young moduli, P_{ν_c}, P_{ν_s} are the Poisson ratios of the core and shell materials respectively, $\varepsilon_{\text{misfit}} = (a_s - a_c)/a_c$ is the lattice mismatch, and a_c (a_s) the core (shell) lattice constant.

The explicit forms of ε_{rr}, $\varepsilon_{\theta\theta}$ and ε_{zz} in cylindrical coordinates for the core are given by

$$\varepsilon^c_{rr} = -\varepsilon_{\text{misfit}}\left(\frac{(1+P_{\nu_c})(1-2P_{\nu_c})}{(1-E_r)(1-2P_{\nu_c})-(1-2P_{\nu_c}+E_r)\gamma^2} + \frac{P_{\nu_c}}{(\gamma^2-1)+E_r}\right), \tag{15.74}$$

$$\varepsilon^c_{\theta\theta} = \varepsilon^c_{rr} \qquad \varepsilon^c_{zz} = \varepsilon_{\text{misfit}}\left(\frac{(\gamma^2-1)}{(\gamma^2-1)+E_r}\right), \tag{15.75}$$

and for the shell

$$\varepsilon^s_{rr} = \varepsilon_{\text{misfit}} E_r \left[\frac{(1+P_{\nu_s})}{(1-E_r)(1-2P_{\nu_s}) - (1-2P_{\nu_s}+E_r)\gamma^2} \times \left(1 - 2P_{\nu_s} - \frac{b^2}{r^2}\right) + \frac{P_{\nu_s}}{(\gamma^2-1)+E_r} \right], \tag{15.76}$$

$$\varepsilon^s_{\theta\theta} = \varepsilon_{\text{misfit}} E_r \left[\frac{(1+P_{\nu_s})}{(1-E_r)(1-2P_{\nu_s}) - (1-2P_{\nu_s}+E_r)\gamma^2} \times \left(1 - 2P_{\nu_s} + \frac{b^2}{r^2}\right) + \frac{P_{\nu_s}}{(\gamma^2-1)+E_r} \right], \tag{15.77}$$

$$\varepsilon^s_{zz} = -\varepsilon_{\text{misfit}} \frac{(\gamma^2-1)}{(\gamma^2-1)+E_r}. \tag{15.78}$$

Appendix 2: Phonon Eigenfrequencies in Core-Shell Nanowires

Acoustic Phonons

In order to find a basis for the solutions of the equation of motion for the displacement vector $\mathbf{u}$ in cylindrical coordinates, it is useful to define the auxiliary potentials Γ and Λ (see [49, 80, 111])

$$\Gamma = \nabla \times \mathbf{u} \quad \text{and} \quad \Lambda = \nabla \cdot \mathbf{u}. \tag{15.79}$$

From (15.4) and (15.79) it follows the equations for the potentials:

$$\nabla^2 \Gamma + Q_T^2 \Gamma = \mathbf{0}, \tag{15.80}$$

$$\nabla^2 \Lambda + Q_L^2 \Lambda = 0, \tag{15.81}$$

where $Q_T^2 = \omega^2/v_T^2$, and $Q_L^2 = \omega^2/v_L^2$. Using (15.4) and the above definitions, it can be seen that $\mathbf{u}$ is given by

$$\mathbf{u} = -\frac{1}{Q_L^2}\nabla\Lambda + \frac{1}{Q_T^2}\nabla \times \Gamma. \tag{15.82}$$

Thus, solving the Helmholtz equations (15.80) and (15.81) for Γ and Λ it is obtained the general solution for the relative mechanical displacement $\mathbf{u}$.

The solution for the Helmholtz vectorial equation (15.80) in cylindrical coordinates is reported in [80, 112]. In the case of core-shell NWs with cylindrical symmetry the displacement vector (15.82) cannot be decoupled into two independent perpendicular directions of motion, pure longitudinal, $\mathbf{u}_L$, or transversal motion, $\mathbf{u}_T$. By definition, the auxiliar potential Γ satisfies the equation $\nabla \cdot \Gamma = 0$, denoting that only two components of the vector Γ in the cylindrical bases $(\mathbf{e}_r, \mathbf{e}_\theta, \mathbf{e}_z)$ are independent. These two vector components are the rotational of certain vector field, in consequence $\Gamma = \mathbf{M} + \mathbf{N}$ with

$$\mathbf{M} = \nabla \times (v_1 \mathbf{e}_z) \quad \text{and} \quad \mathbf{N} = \frac{1}{Q_T^2} \nabla \times \nabla \times (v_2 \mathbf{e}_z), \tag{15.83}$$

where v_i, $(i = 1, 2)$ are linearly independent solutions of the scalar Helmholtz equation in cylindrical coordinates. The solution of (15.3) has full axial symmetry; hence, the displacement vector can be searched as $\mathbf{u} = (u_r, u_\theta, u_z) \exp i(n\theta + k_z z)$ and the bounded solution of the scalar Helmholtz equation in cylindrical geometry is

$$v(\mathbf{r}) \sim f_n(qr) \exp i(n\theta + k_z z), \tag{15.84}$$

where $n = 0, \pm 1, \pm 2, \ldots$ labels the azimuthal motion, k_z is the z-component of the phonon wavevector, and q is given by

$$q^2 = \frac{\omega^2}{v^2} - k_z^2. \tag{15.85}$$

In (15.84), $f_n(qr)$ is taken as Bessel function J_n if $q^2 > 0$ or Infeld I_n if $q^2 < 0$ for $0 \le r \le a$ and a linear combination of J_n and Neumann N_n, or combination of $I_n(x)$ and MacDonald $K_n(x)$ [113] for $a \le r \le b$.

For calculating $\mathbf{u}$ it is necessary to obtain the vector $\mathbf{M}$ and $\nabla \times \mathbf{N}$. In consequence, and following the method of solution described in [80, 111], one can derive a general curvilinear coordinate basis to describe the oscillation modes in a cylindrical NWs, namely,

$$\mathbf{u}_{T1} = \begin{pmatrix} k_z a f_n'(q_T r) \\ i \frac{n k_z a}{q_T r} f_n(q_T r) \\ -i q_T a f_n(q_T r) \end{pmatrix} e^{i(n\theta + k_z z)},$$

$$\mathbf{u}_{T2} = \begin{pmatrix} \frac{na}{r} f_n(q_T r) \\ i q_T a f_n'(q_T r) \\ 0 \end{pmatrix} e^{i(n\theta + k_z z)},$$

$$\mathbf{u}_L = \begin{pmatrix} q_L a f_n'(q_L r) \\ \frac{ina}{r} f_n(q_L r) \\ i k_z a f_n(q_L r) \end{pmatrix} e^{i(n\theta + k_z z)}, \tag{15.86}$$

with the wavenumbers $q_{L,T}^2 = Q_{L,T}^2 - k_z^2$. The basis solutions in (15.86) satisfy the conditions $\nabla \times \mathbf{u}_L = \mathbf{0}$, $\nabla \cdot \mathbf{u}_L = 0$, $\nabla \cdot \mathbf{u}_{T1} = \nabla \cdot \mathbf{u}_{T2} = 0$, whereas $\nabla \times \mathbf{u}_{T1} \neq 0$, $\nabla \times \mathbf{u}_{T2} \neq 0$ underlying the transverse and longitudinal character of the vector fields $\mathbf{u}_{T1}$, $\mathbf{u}_{T2}$ and $\mathbf{u}_L$.

(i) Secular equations for $n = 0$, $k_z = 0$

Following the symmetry properties of the basis function (15.86) and applying the boundary conditions $\mathbf{u}|_{r=a_-} = \mathbf{u}|_{r=a_+}$, $\sigma \cdot \mathbf{e}_r|_{r=a_-} = \sigma \cdot \mathbf{e}_r|_{r=a_+}$ and $\sigma \cdot \mathbf{e}_r|_{r=b} = 0$, the radial breathing modes are obtained by solving the transcendental equation

$$F_s(\gamma\lambda_L x)[G_s(\lambda_L x)J_1(x) - \rho_r F_c(x)N_1(\lambda_L x)] - G_s(\gamma\lambda_L x)[F_s(\lambda_L x)J_1(x) - \rho_r F_c(x)J_1(\lambda_L x)] = 0, \tag{15.87}$$

where c (s) labels the core (shell) region, $x = \omega a/v_{L_c}$, $\lambda_L = v_{L_c}/v_{L_s}$, $\gamma = b/a$, $\rho_r = \rho_s/\rho_c$, $F_i(x) = v_{L_i}^2 x J_0(x) - 2v_{T_i}^2 J_1(x)$, and $G_i(x) = v_{L_i}^2 x N_0(x) - 2v_{T_i}^2 N_1(x)$ ($i = s, c$).

The homogeneous NW dispersion relation is recovered for shell ($a \to 0$) or core ($a \to b$) semiconductors from (15.87) solving the secular equation $F_i(z_i) = 0$ with $z_i = \omega r_0/v_{L_i}$ ($i = s, c$) and r_0 the radius of the wire.

In the case of confined transversal $T2$ modes the eigenfrequencies can be obtained from the general expression

$$x_s J_1(x_c)P_{22}(x_s) + \frac{\rho_r}{\lambda_T^2} x_c J_2(x_c)P_{12}(x_s) = 0, \tag{15.88}$$

with $x_c[x_s] = a\sqrt{(\omega/v_{T_c}[v_{T_s}])^2 - k_z^2}$, $\lambda_T = v_{T_s}/v_{T_c}$ and $P_{n,m}(x) = J_n(x)N_m(\gamma x) - J_m(\gamma x)N_n(x)$ Similar results are achieved for the $T1$ frequency mode.

Optical Phonons

Equation (15.86) is a general basis of solutions for the (15.11) but with $q_{L,T}$ rewritten as

$$q_{L,T}^2 = \frac{\omega_0^2 - \omega^2}{\beta_{L,T}^2} - k_z^2. \tag{15.89}$$

Similar to the case of acoustic phonons if $q_{L,T}^2 > 0$ ($q_{L,T}^2 < 0$) and $r < a$ the function $f_n = J_n$ (I_n) order-n Bessel (modified Bessel) function. For $a < r < b$, $f_n = AJ_n + BN_n$ ($f_n = AI_n + BK_n$) is a linear combination of Bessel and Neumann (Infield I_n and MacDonald K_n) cylindrical functions. The basis (15.86) with (15.85) continue to comply with the conditions that the longitudinal solution $\nabla \times \mathbf{u}_L = \mathbf{0}$, whereas the transverse solutions satisfy $\nabla \cdot \mathbf{u}_{T1} = \nabla \cdot \mathbf{u}_{T2} = 0$, as it should be.

Taking a linear combination of the basis functions (15.86) and applying the boundary condition $\mathbf{u}|_{r=a} = \mathbf{0}$, the general dispersion relations for core phonons are obtained by solving the transcendental equation

$$J_n(\mu_{T1})\left[J_n'(\mu_L)J_n'(\mu_{T2}) - \frac{n^2}{\mu_L\mu_{T2}}J_n(\mu_L)J_n(\mu_{T2})\right] = \frac{\widetilde{k}_z^2}{\mu_L\mu_{T1}}J_n(\mu_L)\left[J_n'(\mu_{T1})J_n'(\mu_{T2}) - \frac{n^2}{\mu_{T1}\mu_{T2}}J_n(\mu_{T1})J_n(\mu_{T2})\right], \quad (15.90)$$

where $\widetilde{k}_z = k_z a$ and $\mu_i^2 = q_i^2 a^2 + \Delta\omega_i^2(\gamma)a^2/\beta_i^2$, $(i = L, T1, T2)$.

In the case of $n \neq 0$ and $k_z = 0$ from (15.90), the dispersion relations for the coupled $L - T2$ modes fulfill the transcendental equation

$$J_n'(\mu_L)J_n'(\mu_{T2}) - \frac{n^2}{\mu_L\mu_{T2}}J_n(\mu_L)J_n(\mu_{T2}) = 0, \quad (15.91)$$

with

$$\mu_L^2 = (\omega_0^2 + \Delta\omega_L^2(\gamma) - \omega^2)\left(\frac{a}{\beta_L}\right)^2, \quad (15.92)$$

$$\mu_{T2}^2 = (\omega_0^2 + \Delta\omega_{T2}^2(\gamma) - \omega^2)\left(\frac{a}{\beta_T}\right)^2. \quad (15.93)$$

If it is considered the dependence of the mode frequencies with wave vector $k_z \neq 0$ and $n = 0$, the coupled $L - T1$ phonons are described by

$$J_0'(\mu_L)J_0(\mu_{T1}) - \frac{\widetilde{k}_z^2}{\mu_L\mu_{T1}}J_0(\mu_L)J_0'(\mu_{T1}) = 0, \quad (15.94)$$

with $\mu_L^2 = (\omega_0^2 + \Delta\omega_L^2(\gamma) - \omega^2)\,(a/\beta_L)^2 - k_z^2 a^2$ and $\mu_{T1}^2 = (\omega_0^2 + \Delta\omega_{T1}^2(\gamma) - \omega^2) \times (a/\beta_T)^2 - k_z^2 a^2$.

Polar Optical Phonons

In the present case the equation of motions for polar optical phonons are described by four coupled partial differential equations, (15.22) and (15.23). As in the acoustic and non-polar optical phonons, it is defined the auxiliar potential Γ and Λ as given by (15.79) with

$$Q_T^2 = \frac{\omega_{TO}^2 - \omega^2}{\beta_T^2}, \quad (15.95)$$

$$Q_L^2 = \frac{\omega_{LO}^2 - \omega^2}{\beta_L^2}.$$

It can be seen that the solution of (15.23) can be written as

$$\varphi = \varphi_H - \frac{4\pi\alpha}{\varepsilon_\infty Q_L^2}\Lambda\,,$$

where φ_H is the solution of the Laplace equation $\nabla^2\varphi_H = 0$. For the displacement vector $\mathbf{u}$ follows the expression

$$\mathbf{u} = -\nabla\left[\frac{\alpha}{\rho_m\beta_T^2 Q_T^2}\varphi_H + \frac{\Lambda}{Q_L^2}\right] + \frac{1}{Q_T^2}\nabla\times\Gamma. \tag{15.96}$$

Once the functions Λ, Γ and φ_H have been obtained, it is easy to prove that the basis functions for the space of solutions of (15.22) and (15.23) are given by

$$\begin{aligned}
\mathbf{F}_{T1} &= \begin{pmatrix}\mathbf{u}_{T1}\\ \varphi_{T1}\end{pmatrix} = \begin{pmatrix} \frac{ik_z}{q_T}f_n'(q_T r)\\ -\frac{nk_z}{q_T}\frac{1}{q_T r}f_n(q_T r)\\ f_n(q_T r)\\ 0\end{pmatrix} e^{i(n\theta+k_z z)},\\
\mathbf{F}_{T2} &= \begin{pmatrix}\mathbf{u}_{T2}\\ \varphi_{T2}\end{pmatrix} = \begin{pmatrix} \frac{in}{q_T r}f_n(q_T r)\\ -f_n'(q_T r)\\ 0\\ 0\end{pmatrix} e^{i(n\theta+k_z z)},\\
\mathbf{F}_{L} &= \begin{pmatrix}\mathbf{u}_{L}\\ \varphi_{L}\end{pmatrix} = \begin{pmatrix} f_n'(q_L r)\\ \frac{in}{q_L r}f_n(q_L r)\\ \frac{ik_z}{q_L}f_n(q_L r)\\ \frac{4\pi\alpha}{\varepsilon_\infty}\frac{1}{q_L}f_n(q_L r)\end{pmatrix} e^{i(n\theta+k_z z)},\\
\mathbf{F}_{H} &= \begin{pmatrix}\mathbf{u}_{H}\\ \varphi_{H}\end{pmatrix} = \begin{pmatrix} g_n'(k_z r)\\ \frac{in}{k_z r}g_n(k_z r)\\ g_n(k_z r)\\ -\frac{\rho_m\beta_T^2 q_T^2}{\alpha}\frac{1}{k_z}g_n(k_z r)\end{pmatrix} e^{i(n\theta+k_z z)}.
\end{aligned} \tag{15.97}$$

Here, tetra-vector components are understood in the form $\mathbf{F} = (u_r, u_\theta, u_z, \varphi)$ with the wavenumbers

$$q_{L,T}^2 = Q_{L,T}^2 - k_z^2. \tag{15.98}$$

If $q_{L,T}^2 > 0$ ($q_{L,T}^2 < 0$) the function f_n is an order-n Bessel (modified Bessel) function of the first or second kind, i.e., Bessel J_n or Neumann N_n (Infeld I_n or MacDonald K_n). On the other hand, g_n is an order-n modified Bessel function of the first or second kind, i.e., Infeld I_n or MacDonald K_n. It is straightforward to check that $\nabla\times\mathbf{u}_L = \nabla\times\mathbf{u}_H = \mathbf{0}$ and $\nabla\cdot\mathbf{u}_{T1} = \nabla\cdot\mathbf{u}_{T2} = \nabla\cdot\mathbf{u}_H = 0$.

Dielectric continuum approach

The IP satisfy the Laplace equation $\nabla^2\varphi = 0$ and $\varepsilon_{c(s)}(\omega) \neq 0$. Employing the standard electrostatic boundary condition at the interfaces it is obtained the secular equation

$$\begin{aligned}(\varepsilon_c(\omega) - \varepsilon_s(\omega))(\varepsilon_D - \varepsilon_s(\omega))I_n(k_z a)I_n'(k_z a)K_n(\gamma k_z a)K_n'(\gamma k_z a) - \\ (\varepsilon_c(\omega)K_n(k_z a)I_n'(k_z a) - \varepsilon_s(\omega)I_n(k_z a)K_n'(k_z a)) \times \\ (\varepsilon_d I_n(\gamma k_z a)K_n'(\gamma k_z a) - \varepsilon_s(\omega)K_n(\gamma k_z a)I_n'(\gamma k_z a)) = \quad 0 \end{aligned} \tag{15.99}$$

Equation (15.99) gives the dispersion relations of IP as functions of k_z and the parameter γ for different values of $n = 0, 1, 2, \ldots$. In the case of $k_z = 0$ (15.99) is reduced to

$$(\varepsilon_c(\omega) - \varepsilon_s(\omega))(\varepsilon_D - \varepsilon_s(\omega)) - (\varepsilon_c(\omega) + \varepsilon_s(\omega))(\varepsilon_D + \varepsilon_s(\omega))\gamma^{2n} = 0. \tag{15.100}$$

Coupled modes

It is possible to show that the secular equation for core L-$T2$ modes with $n > 0$ and $k_z = 0$ is given by

$$\left[J_n'(\mu_{Tc}) - \frac{n}{\mu_{Tc}}J_n(\mu_{Tc})\right]\left[J_n'(\mu_{Lc}) - C_1\frac{n}{\mu_{Lc}}J_n(\mu_{Lc})\right] - C_2\left[1 - \frac{\omega^2}{\omega_{TO}^2}\right] \tag{15.101}$$

$$\times\left[J_n'(\mu_{Tc})J_n'(\mu_{Lc}) - \frac{n^2}{\mu_{Tc}\mu_{Lc}}J_n(\mu_{Tc})J_n(\mu_{Lc})\right] = 0\,, \tag{15.102}$$

where

$$\begin{aligned} C_1 &= \frac{\varepsilon_\infty^s[(\varepsilon_D - \varepsilon_\infty^s) + \gamma^{2n}(\varepsilon_D + \varepsilon_\infty^s)]}{\varepsilon_\infty^c[(\varepsilon_D - \varepsilon_\infty^s) - \gamma^{2n}(\varepsilon_D + \varepsilon_\infty^s)]}\,, \\ C_2 &= \frac{[(\varepsilon_\infty^s - \varepsilon_\infty^c)(\varepsilon_D - \varepsilon_\infty^s) + \gamma^{2n}(\varepsilon_\infty^c + \varepsilon_\infty^s)(\varepsilon_D + \varepsilon_\infty^s)]}{(\varepsilon_0^c - \varepsilon_\infty^c)[(\varepsilon_D - \varepsilon_\infty^s) - \gamma^{2n}(\varepsilon_D + \varepsilon_\infty^s)]}\,, \end{aligned} \tag{15.103}$$

and $\mu_{Tc} = q_T a$, $\mu_{Lc} = q_L a$.

Appendix 3: Electronic States in Core-Shell Nanowires

Conduction band

In the framework of the Envelope Function Approximation, the electron wave function $|\Psi_{\alpha_e}\rangle$ in cylindrical symmetry can be written as

$$\langle \mathbf{r}|\Psi_{\alpha_e}\rangle = \frac{1}{\sqrt{2V_c}}F_m(r)e^{i(m_e\theta + k_e z)}, \tag{15.104}$$

where $V_c = \pi a^2 L_0$ is the core volume, $m_e\hbar$ ($m_e = 0, 1, 2\ldots$) and k_e are the z-component of the angular momentum and electron wave number, respectively, and $F_{m_e}(r)$ the radial wave function. Considering bound states, two cases have to be considered: [36, 114]
(a) Si-Ge NW, where the states are confined in the core. Hence, it is possible to show that

$$F_m(r) = \begin{cases} A_m^{(1)} J_m(p_c r)\ ; & 0 \le r \le a \\ A_m^{(2)} \mathscr{Q}_{m,m}^{-}(|p_s|\, r)\ ; & a \le r \le b \end{cases}, \tag{15.105}$$

with

$$\mathscr{Q}_{m,n}^{\pm}(x) = I_m(x)K_n(\gamma x) \pm I_n(\gamma x)K_m(x),$$

$$A_m^{(1)} = \frac{1}{2}\frac{\sqrt{\mathscr{Q}_{m+1,m}^{+}(|\tilde{p}_s|)\mathscr{Q}_{m-1,m}^{+}(|\tilde{p}_s|)}}{\sqrt{J_{m+1}(\tilde{p}_c)J_{m-1}(\tilde{p}_c)}}\frac{\tilde{p}_s}{\tilde{p}_c}\mathscr{W}_m(|\tilde{p}_s|), \tag{15.106}$$

$$A_m^{(2)} = \frac{1}{2}\mathscr{W}_m(|\tilde{p}_s|), \tag{15.107}$$

and

$$\mathscr{W}_m(\tilde{p}_s) = \Big[\mathscr{Q}_{m+1,m}^{-}(|\tilde{p}_s|)\mathscr{Q}_{m-1,m}^{-}(|\tilde{p}_s|) - \gamma^2\mathscr{Q}_{m+1,m}^{-}(\gamma|\tilde{p}_s|)\mathscr{Q}_{m-1,m}^{-}(\gamma|\tilde{p}_s|) + \mathscr{Q}_{m+1,m}^{+}(|\tilde{p}_s|)\mathscr{Q}_{m-1,m}^{+}(|\tilde{p}_s|)\frac{|\tilde{p}_s|^2}{\tilde{p}_c^2}\Big]^{-\frac{1}{2}}. \tag{15.108}$$

(b) In the case of Ge-Si core/shell, the electronic states are localized in the shell and the above equations are reduced to

$$F_m(r) = \begin{cases} A_m^{(1)} I_m(|p_c|\, r)\ ; & 0 \le r \le a \\ A_m^{(2)} P_{m,m}(p_s r)\ ; & a \le r \le b \end{cases}, \tag{15.109}$$

where $P_{m,m}$ is defined in (15.6) and the coefficients $A_m^{(i)}$ ($i = 1, 2$) are equal to

$$A_m^{(1)} = \frac{1}{2}\frac{1}{\sqrt{I_{m+1}(|\tilde{p}_c|)I_{m-1}(|\tilde{p}_c|)}}\mathscr{R}_m(\tilde{p}_s), \tag{15.110}$$

$$A_m^{(2)} = \frac{1}{2}\frac{1}{\sqrt{P_{m+1,m}(\tilde{p}_s)P_{m-1,m}(\tilde{p}_s)}}\frac{|\tilde{p}_c|}{\tilde{p}_s}\mathscr{R}_m(\tilde{p}_s), \tag{15.111}$$

and

$$\mathscr{R}_m(\tilde{p}_s) = \left[1 - \frac{|\tilde{p}_c|^2}{\tilde{p}_s^2} \times \left(1 - \frac{4}{\pi^2 \tilde{p}_s^2} \frac{1}{P_{m+1,m}(\tilde{p}_s) P_{m-1,m}(\tilde{p}_s)}\right)\right]^{-\frac{1}{2}}.$$

As it is stated above $c(s)$ labels the core (shell) semiconductor and $p_c(p_s)$ is related to the electron energy by the equation

$$\overline{E}_e = \Delta E_g^{(c,s)} + \frac{\hbar^2 p_{c,s}^2}{2m_t^{(c,s)}} + \frac{\hbar^2 k_e^2}{2m_l^{(c,s)}}, \tag{15.112}$$

with $\tilde{p}_c(\tilde{p}_s) = p_c a(p_s a)$ and m_l (m_t) the longitudinal (transverse) conduction electron mass at Γ point of the Brillouin zone. In (15.112) $\overline{E}_e = E_g^{(c,s)} - E_{strained}$ takes into account the gap energy correction due to the intrinsic strain at the interface [115, 116] and $\Delta E_g^{(c,s)}$ is the band offset between the core and shell measured from the bottom of the band. For NWs grown along the [110] direction, the band gap $\Delta E_g^{(c,s)} \simeq 300$ meV [114]. In the calculations is assumed $\Delta E_g^{(c,s)}$ independent of γ.

There is a third option, here not considered, where both, p_c and p_s are real, and the radial wave function $F_m(r)$ presents an oscillatory behavior in both the core and shell part, which correspond to higher excited states of the core/shell NWs.

Valence band

For a description of the hole states in the valence band is considered the LK Hamiltonian model neglecting the coupling from the split-off band. This Hamiltonian provides a good description for heavy-hole and light-hole states and the coupling between them due to the Γ_{15v} degeneracy of valence bands at Γ point. Along the [110] direction and assuming the axial approximation, $\gamma_2 \simeq \gamma_3$, the 4×4 Hamiltonian can be written as [103, 106, 117]

$$H_{LK} = \frac{\hbar^2}{m_0} \begin{pmatrix} D_{hh} & A_- & B_- & 0 \\ A_-^* & D_{lh} & 0 & B_- \\ B_-^* & 0 & D_{lh} & A_+^* \\ 0 & B_-^* & A_+ & D_{hh} \end{pmatrix}, \tag{15.113}$$

where

$$\begin{aligned} D_{hh} &= -\frac{(\gamma_1 + \gamma_s)}{2}\{\hat{k}_+, \hat{k}_-\} - \frac{(\gamma_1 - 2\gamma_s)}{2}\hat{k}_h^2, \\ D_{lh} &= -\frac{(\gamma_1 - \gamma_s)}{2}\{\hat{k}_+, \hat{k}_-\} - \frac{(\gamma_1 + 2\gamma_s)}{2}\hat{k}_h^2, \\ A_\pm &= \mp\sqrt{3}\hat{\gamma}\hat{k}_\pm\hat{k}_h \; ; B_\pm = -\frac{\sqrt{3}}{2}\gamma_t \hat{k}_\pm^2, \end{aligned} \tag{15.114}$$

$\hat{\gamma} = (\gamma_2 + \gamma_3)/2$, $\gamma_s = (\gamma_2 + 3\gamma_3)/4$, $\gamma_t = (3\gamma_2 + 5\gamma_3)/8$, γ_1, γ_2 and γ_3 are the Luttinger parameters. The total Hamiltonian for the valence band can be cast

as $H = H_{LK} + V(r)$ with $V(r)$ the NWs confinement potential. The wave function $\langle \mathbf{r}|\Psi_\alpha\rangle$, as given by (15.104), represents a basis for the effective 4×4 LK-Hamiltonian. Since the Bloch states, $|v_{3/2}\rangle$, $|v_{1/2}\rangle$, $|v_{-1/2}\rangle$ and $|v_{-3/2}\rangle$ are mixed by the effects of the cylindrical symmetry and the non-zero matrix elements $A_\pm$ and $B_\pm$ in (15.114), the general solution of the wave function $\langle \mathbf{r}|\Psi_{\alpha_h}\rangle$ can be obtained with a special sequence of the angular quantum number m for each hole state. Thus, by exploring the symmetry of the Hamiltonian (15.113), the exact wave function for the hole state $\langle \mathbf{r}|\Psi_{\alpha_h}\rangle$ is

$$\langle \mathbf{r}|\Psi^{(i)}_{\alpha_h}\rangle = \widehat{F}^{(i)}_m(r)e^{i(m\theta+k_hz)} = \begin{pmatrix} a_{1i}F_m(p_{hh}r)|v_{\frac{3}{2}}\rangle \\ a_{2i}F_{m+1}(p_{hl}r)e^{i\theta}|v_{\frac{1}{2}}\rangle \\ a_{3i}F_{m+2}(p_{hl}r)e^{2i\theta}|v_{-\frac{1}{2}}\rangle \\ a_{4i}F_{m+3}(p_{hh}r)e^{3i\theta}|v_{-\frac{3}{2}}\rangle \end{pmatrix} e^{i(m\theta+k_hz)}, \quad (15.115)$$

where $p_{hh(lh)}$ is related to the heavy (light) hole energy by the expression

$$\overline{E}_{hh(lh)} = -\Delta E_g^{(c,s)} - \frac{1}{2m_{hh(lh)}}(p^2_{hh(lh)} + \hbar^2k_h^2), \quad (15.116)$$

and $m_{hh(lh)} = 1/(\gamma_1 - (+)2\gamma_s)$. As in the case of the conduction band in $E_{hh(lh)}$ we consider the band gap correction. The vector coefficients $\mathbf{a}_i$ $|i\rangle$ ($i = hh^+, lh^+, lh^-, hh^-$) in (15.115) are [118]

$$\begin{aligned}
\mathbf{a}^\dagger_{hh^+} &= a_{hh^+}\left(-\frac{1}{\sqrt{3}}\left(1+\frac{4k_h^2}{p_{hh}^2}\right), -\frac{2k_h}{p_{hh}}, 1, 0\right), \\
\mathbf{a}^\dagger_{lh^+} &= a_{lh^+}\left(-\sqrt{3}, -\frac{2k_h}{p_{lh}}, 1, 0\right), \\
\mathbf{a}^\dagger_{lh^-} &= a_{lh^-}\left(-\frac{2k_h}{p_{lh}}, \frac{1}{\sqrt{3}}\left(1+\frac{4k_h^2}{p_{lh}^2}\right), 0, 1\right), \\
\mathbf{a}^\dagger_{hh^-} &= a_{hh^-}\left(-\frac{2k_h}{p_{hh}}, -\sqrt{3}, 0, 1\right),
\end{aligned}$$

where the weight coefficients a_{hh^+}, a_{lh^+}, a_{lh^-}, a_{hh^-} give a measure of the mixtures of Bloch states $|i\rangle = |v_{3/2}\rangle$, $|v_{1/2}\rangle$, $|v_{-1/2}\rangle$ and $|v_{-3/2}\rangle$. Imposing continuity of the wave function $\langle \mathbf{r}|\Psi^{(i)}_{\alpha_h}\rangle$ and its derivative at the core/shell interface $r = a$ and choosing the boundary condition $\langle \mathbf{r}|\Psi^{(i)}_{\alpha_h}\rangle\,|_{r=b} = 0$, it follows immediately the normalized eigensolutions and eigenenergies for the hole states.

In the case of Ge-Si core/shell NWs, the hole are mostly confined in the core and the valence band offset is of the order 0.5 eV [36, 114]. Thus, in the limit of strong spatial confinement we can assume a hard wall potential and the holes are completely confined in the core. In the evaluation of the hole energy and wave function are employed for Si[Ge] the values: $\gamma_1 = 4.22[13.4]$, $\gamma_2 = 0.39[4.24]$, $\gamma_3 = 1.44[5.69]$, $a(\Gamma_{15v}) = -5.0[-5.2]$ eV and $b(\Gamma_{15v}) = -2.3[-2.4]$ eV [75].

References

1. P. Yang, R. Yan, M. Fardy, Nano Lett. **10**, 1529 (2010)
2. W. Lu, C.M. Lieber, J. Phys. D **39**, R387 (2006)
3. O. Hayden, R. Agarwal, W. Lu, Nano Today **3**, 12 (2008)
4. N.P. Dasgupta, J. Sun, C. Liu, S. Brittman, S.C. Andrews, J. Lim, H. Gao, R. Yan, P. Yang, Adv. Mater. **26**, 2137 (2014)
5. B. Hua, J. Motohisa, Y. Kobayashi, S. Hara, T. Fukui, Nano Lett. **9**, 112 (2009)
6. Y.M. Niquet, Nano Lett. **7**, 1105 (2007)
7. H.M. Lin, Y.L. Chen, J. Yang, Y.C. Liu, K.M. Yin, J.J. Kai, F.R. Chen, L.C. Chen, Y.F. Chen, C.C. Chen, Nano Lett. **3**, 537 (2003)
8. M. Montazeri, M. Fickenscher, L.M. Smith, H.E. Jackson, J. Yarrison-Rice, J.H. Kang, Q. Gao, H.H. Tan, C. Jagadish, Y. Guo, J. Zou, M.-E. Pistol, C.E. Pryor, Nano Lett. **10**, 880 (2010)
9. L. Zhang, J.J. Shi, Semicond. Sci. Technol. **20**, 592 (2005)
10. P.K. Mohseni, A.D. Rodrigues, J.C. Galzerani, Y.A. Pusep, R.R. LaPierre, J. Appl. Phys. **106**, 124306 (2009)
11. M.F. Bailon-Somintac, J.J. Ibaez, R.B. Jaculbia, R.A. Loberternos, M.J. Defensor, A.A. Salvador, A.S. Somintac, J. Cryst. Growth **314**, 268 (2011)
12. A. Giugni, G. Das, A. Alabastri, R.P. Zaccaria, M. Zanella, I. Franchini, E. Di Fabrizio, R. Krahne, Phys. Rev. B **85**, 115413 (2012)
13. L.J. Lauhon, M.S. Gudiksen, D. Wang, C.M. Lieber, Nature (London) **420**, 57 (2002)
14. Y. Cui, Q. Wei, H. Park, C.M. Lieber, Science **293**, 1289 (2001)
15. G. Zheng, F. Patolsky, Y. Cui, W. Wang, C. Lieber, Nat. Biotechnol. **23**, 1294 (2005)
16. Y. Dong, B. Tian, T.J. Kempa, C.M. Lieber, Nano Lett. **9**, 2183 (2009)
17. E.D. Minot, F. Kelkensberg, M. van Kouwen, J.A. van Dam, L.P. Kouwenhoven, V. Zwiller, M.T. Borgstrm, O. Wunnicke, M.A. Verheijen, E.P.A.M. Bakkers, Nano Lett. **7**, 367 (2007)
18. T.E. Trammell, X. Zhang, Y. Li, L.Q. Chen, E.C. Dickey, J. Cryst. Growth **310**, 3084 (2008)
19. D.C. Dillen, K.M. Varahramyan, C.M. Corbet, E. Tutuc, Phys. Rev. B **86**, 045311 (2012)
20. R. Singh, C.D. Poweleit, E. Dailey, J. Drucker, J. Menéndez, Semicond. Sci. Technol. **27**, 085008 (2012)
21. H. Kallel, A. Arbouet, G. BenAssayag, A. Chehaidar, A. Potie, B. Salem, T. Baron, V. Paillard, Phys. Rev. B **86**, 085318 (2012)
22. R. Singh, E.J. Dailey, J. Drucker, J. Menéndez, J. Appl. Phys. **110**, 124305 (2011)
23. D. Martínez-Gutiérrez, V. Velasco, Physica E **54**, 86 (2013)
24. M. Hu, X. Zhang, K.P. Giapis, D. Poulikakos, Phys. Rev. B **84**, 085442 (2011)
25. X. Liu, J. Hu, B. Pan, Physica E **40**, 3042 (2008)
26. R. Peköz, J.Y. Raty, Phys. Rev. B **80**, 155432 (2009)
27. R.N. Musin, X.Q. Wang, Phys. Rev. B **71**, 155318 (2005)
28. M.K.Y. Chan, J. Reed, D. Donadio, T. Mueller, Y.S. Meng, G. Galli, G. Ceder, Phys. Rev. B **81**, 174303 (2010)
29. F. Maier, D. Loss, Phys. Rev. B **85**, 195323 (2012)
30. C. Kloeffel, M. Trif, D. Loss, Phys. Rev. B **90**, 115419 (2014)
31. A. Khitun, A. Balandin, K. Wang, Superlattices Microstruct. **26**, 181 (1999)
32. P. Servati, A. Colli, S. Hofmann, Y. Fu, P. Beecher, Z. Durrani, A. Ferrari, A. Flewitt, J. Robertson, W. Milne, Physica E **38**, 64 (2007)
33. B. Tian, X. Zheng, T.J. Kempa, Y. Fang, N. Yu, G. Yu, J. Huang, C.M. Lieber, Nature (London) **449**, 885 (2007)
34. F. Murphy-Armando, G. Fagas, J.C. Greer, Nano Lett. **10**, 869 (2010)
35. A.I. Hochbaum, R. Fan, R. He, P. Yang, Nano Lett. **5**, 457 (2005)
36. X. Peng, P. Logan, Appl. Phys. Lett. **96**, 143119 (2010)
37. M.C. Wingert, Z.C.Y. Chen, E. Dechaumphai, J. Moon, J.-H. Kim, J. Xiang, R. Chen, Nano Lett. **11**, 5507 (2011)

38. M. Hu, K.P. Giapis, J.V. Goicochea, X. Zhang, D. Poulikakos, Nano Lett. **11**, 618 (2011)
39. M. Amato, M. Palummo, R. Rurali, S. Ossicini, Chem. Rev. **114**, 1371 (2014)
40. D.L. Nika, E.P. Pokatilov, A.A. Balandin, V.M. Fomin, A. Rastelli, O.G. Schmidt, Phys. Rev. B **84**, 165415 (2011)
41. D.L. Nika, A.I. Cocemasov, C.I. Isacova, A.A. Balandin, V.M. Fomin, O.G. Schmidt, Phys. Rev. B **85**, 205439 (2012)
42. D.L. Nika, A.I. Cocemasov, D.V. Crismari, A.A. Balandin, Appl. Phys. Lett. **102**, 213109 (2013)
43. R. Yang, G. Chen, M.S. Dresselhaus, Nano Lett. **5**, 1111 (2005)
44. J. Chen, G. Zhang, B. Li, Nano Lett. **12**, 2826 (2012)
45. N. Neophytou, H. Kosina, Nano Lett. **10**, 4913 (2010)
46. I.M. Tienda-Luna, F.G. Ruiz, A. Godoy, L. Donetti, C. Martinez-Blanque, F. Gmiz, Appl. Phys. Lett. **103**, 163107 (2013)
47. A.G. Rolo, M.I. Vasilevskiy, M. Hamma, C. Trallero-Giner, Phys. Rev. B **78**, 081304 (2008)
48. G. Bir, G. Pikus, *Symmetry and Strain-Induced Effects in Semiconductors*, A Halsted Press book (Wiley, New York, 1974)
49. C. Trallero-Giner, R. Pérez-Álvarez, F. García-Moliner, *Long Wave Polar Modes in Semiconductor Heterostructures* (Pergamon Elsevier Science, London, 1998)
50. M.A. Stroscio, M. Dutta, *Phonons in Nanostructures* (Cambridge University Press, Cambridge, 2001)
51. B.K. Ridley, *Electrons and Phonons in Semiconductor Multilayers* (Cambridge University Press, Cambridge, 1997)
52. M.A. Stroscio, K.W. Kim, M.A. Littlejohn, H. Huang, Phys. Rev. B **42**, 1488 (1990)
53. R. Enderlein, Phys. Rev. B **47**, 2162 (1993)
54. F. Comas, A. Cantarero, C. Trallero-Giner, M. Moshinsky, J. Phys. Condens. Matter **7**, 1789 (1995)
55. H. Peelaers, B. Partoens, F.M. Peeters, Acta Phys. Pol. A **122**, 294 (2012)
56. H. Peelaers, B. Partoens, F.M. Peeters, Phys. Rev. B **82**, 113411 (2010)
57. E. Pokatilov, D. Nika, A. Balandin, Superlattices Microstruct. **38**, 168 (2005)
58. G.Y. Huang, Y.L. Kang, J. Appl. Phys. **110**, 023526 (2011)
59. V.M. Fomin, A.A. Balandin, Appl. Sci. **5**, 728 (2015)
60. L. Chico, R. Pérez-Álvarez, Phys. Rev. B **69**, 035419 (2004)
61. L. Chico, R. Pérez-Álvarez, C. Cabrillo, Phys. Rev. B **73**, 075425 (2006)
62. R. Pérez-Álvarez, D.G. Santiago-Pérez, L. Chico, Physica E **74**, 129 (2015)
63. J. Hattori, S. Uno, N. Mori, K. Nakazato, Math. Comput. Model. **51**, 880 (2010)
64. A.K. Buin, A. Verma, M.P. Anantram, J. Appl. Phys. **104**, 053716 (2008)
65. S. Yu, K.W. Kim, M.A. Stroscio, G.J. Iafrate, Phys. Rev. B **51**, 4695 (1995)
66. M. Born, K. Huang, *Dynamical Theory of Crystal Lattices* (Clarendon Press, Oxford, 1988)
67. L. Landau, M. Lifshitz, *Course of Theoretical Physics, Theory of Elasticity*, vol. 7 (Pergamon, Oxford, 1970)
68. C. Trallero-Giner, F. Comas, Philos. Mag. B **70**, 583 (1994)
69. R. Singh, E.J. Dailey, J. Drucker, J. Menndez, J. Appl. Phys. **110**, 124305 (2011)
70. D.G. Santiago-Pérez, C. Trallero-Giner, G.E. Marques, Phys. Rev. B **95**, 155317 (2017)
71. J. Maultzsch, H. Telg, S. Reich, C. Thomsen, Phys. Rev. B **72**, 205438 (2005)
72. J. Krti, V. Zlyomi, M. Kertesz, S. Guangyu, New J. Phys. **5**, 125 (2003)
73. E. Bourgeois, M.V. Fernández-Serra, X. Blase, Phys. Rev. B **81**, 193410 (2010)
74. A. Trejo, R. Vazquez-Medina, G. Duchen, M. Cruz-Irisson, Physica E **51**, 10 (2013)
75. S. Adachi, *Properties of Group-IV, III-V and II-VI Semiconductors* (Wiley, Chichester, 2005)
76. F. Comas, C. Trallero-Giner, A. Cantarero, Phys. Rev. B **47**, 7602 (1993)
77. F. Comas, A. Cantarero, C. Trallero-Giner, M. Moshinsky, J. Phys.: Condens. Matter **7**, 1789 (1995)
78. C. Trallero-Giner, F. Comas, Phys. Rev. B **37**, 4583 (1988)
79. D.G. Santiago-Pérez, C. Trallero-Giner, R. Pérez-Álvarez, L. Chico, Physica E **56**, 151 (2014)
80. P.M. Morse, H. Feshbach, *Methods of Theoretical Physics* (McGraw-Hill, New York, 1953)

81. O. Madelung, *Physics of Group IV Elements and III-V Compounds*, vol. 17a (Springer, Berlin, 1982)
82. J.E. Spanier, R.D. Robinson, F. Zhang, S.W. Chan, I.P. Herman, Phys. Rev. B **64**, 245407 (2001)
83. Z.D. Dohcevic-Mitrovica, M.J. Scepanovica, M.U. Grujic-Brojcina, Z.V. Popovica, S.B. Boskovicb, B.M. Matovicb, M.V. Zinkevichc, F. Aldinger, Solid State Commun. **137**, 387 (2006)
84. E. Anastassakis, M. Cardona, in *High Pressure in Semiconductor Physics II*, ed. by T. Suski, W. Paul (Academic, New York, 1998)
85. J. Menéndez, R. Singh, J. Drucker, Ann. Phys. (Berlin) **523**, 145 (2011)
86. G. Nilsson, G. Nelin, Phys. Rev. B **3**, 364 (1971)
87. G. Nilsson, G. Nelin, Phys. Rev. B **6**, 3777 (1972)
88. J. Kulda, D. Strauch, P. Pavone, Y. Ishii, Phys. Rev. B **50**, 13347 (1994)
89. K. Hummer, J. Harl, G. Kresse, Phys. Rev. B **80**, 115205 (2009)
90. D.G. Santiago-Pérez, C. Trallero-Giner, R. Pérez-Álvarez, L. Chico, G.E. Marques, Phys. Rev. B **91**, 075312 (2015)
91. V.M. Fomin (ed.), *Physics of Quantum Rings* (Springer, Berlin, 2014)
92. C. Trallero-Giner, F. García-Moliner, V.R. Velasco, M. Cardona, Phys. Rev. B **45**, 11944 (1992)
93. C. Trallero-Giner, Phys. Scr. **55**, 50 (1994)
94. D.G. Santiago-Pérez, C. Trallero-Giner, R. Pérez-Álvarez, L. Chico, R. Baquero, G.E. Marques, J. Appl. Phys. **112**, 084322 (2012)
95. W. Martienssen, H. Warlimont (eds.), *Springer Handbook of Condensed Matter and Materials Data* (Springer, Berlin, 2005)
96. P.H. Borcherds, K. Kunc, G.F. Alfrey, R.L. Hall, J. Phys. C: Solid State Phys. **12**, 4699 (1979)
97. M. Cardona, *Light Scattering in Solids II* (Springer, Berlin, 1982)
98. X. Peng, F. Tang, P. Logan, J. Phys.: Condens. Matter **23**, 115502 (2011)
99. S.P. Beckman, J. Han, J.R. Chelikowsky, Phys. Rev. B **74**, 165314 (2006)
100. J.T. Arantes, A. Fazzio, Nanotechnology **18**, 295706 (2007)
101. D. Medaboina, V. Gade, S.K.R. Patil, S.V. Khare, Phys. Rev. B **76**, 205327 (2007)
102. E.B. Ramayya, D. Vasileska, S.M. Goodnick, I. Knezevic, J. Appl. Phys. **104**, 063711 (2008)
103. J.M. Luttinger, Phys. Rev. **102**, 1030 (1956)
104. C. Kloeffel, M. Trif, D. Loss, Phys. Rev. B **84**, 195314 (2011)
105. C. Kittel, *Quantum Theory of Solids* (Wiley, New York, 1987)
106. J.M. Luttinger, W. Kohn, Phys. Rev. **97**, 869 (1955)
107. S.S. Li, J.B. Xia, Z.L. Yuan, Z.Y. Xu, W. Ge, X.R. Wang, Y. Wang, J. Wang, L.L. Chang, Phys. Rev. B **54**, 11575 (1996)
108. P.K. Mohseni, A.D. Rodrigues, J.C. Galzerani, Y.A. Pusep, R.R. LaPierre, J. Appl. Phys. **106**, 124306 (2009)
109. *Semiconductors: Intrinsic Properties of Group IV Elements and IIIV, IIVI and IVII Compounds, Semimagnetic Semiconductors*, vol. 22, ed. by O. Madelung, Landolt-Bornstein (Springer, Berlin, 1986)
110. P.J. Monisha1, I.V. Sankar, Sh. Sil, A. Chatterjee, Sci. Rep. **6**, 20056 (2016)
111. E. Roca, C. Trallero-Giner, M. Cardona, Phys. Rev. B **49**, 13704 (1994)
112. R. Ruppin, R. Engleman, Rep. Prog. Phys. **33**, 149 (1970)
113. M. Abramowitz, I. Stegun, *Handbook of Mathematical Functions* (U.S. Goverment Printing Office, Washinton, DC, 1964)
114. L. Yang, R.N. Musin, X.-Q. Wang, M.Y. Chou, Phys. Rev. B **77**, 195325 (2008)
115. C. Herring, E. Vogt, Phys. Rev. **101**, 944 (1956)
116. Y. Sun, S.E. Thompson, T. Nishida, J. Appl. Phys. **101**, 104503 (2007)
117. U. Rössler, Solid State Commun. **49**, 943 (1984)
118. P.C. Sercel, K.J. Vahala, Phys. Rev. B **42**, 3690 (1990)

Chapter 16
Differential Geometry Applied to Rings and Möbius Nanostructures

Benny Lassen, Morten Willatzen and Jens Gravesen

Abstract Nanostructure shape effects have become a topic of increasing interest due to advancements in fabrication technology. In order to pursue novel physics and better devices by tailoring the shape and size of nanostructures, effective analytical and computational tools are indispensable. In this chapter, we present analytical and computational differential geometry methods to examine particle quantum eigenstates and eigenenergies in curved and strained nanostructures. Example studies are carried out for a set of ring structures with different radii and it is shown that eigenstate and eigenenergy changes due to curvature are most significant for the groundstate eventually leading to qualitative and quantitative changes in physical properties. In particular, the groundstate in-plane symmetry characteristics are broken by curvature effects, however, curvature contributions can be discarded at bending radii above 50 nm. A more complicated topological structure, the Möbius nanostructure, is analyzed and geometry effects for eigenstate properties are discussed including dependencies on the Möbius nanostructure width, length, thickness, and strain. In the final part of the chapter, we derive the phonon equations-of-motion of thin shells applied to 2D graphene using a differential geometry formulation.

B. Lassen
Mads Clausen Institute, University of Southern Denmark, Alsion 2,
6400 Sønderborg, Denmark
e-mail: benny@mci.sdu.dk

M. Willatzen
Department of Photonics Engineering, Technical University of Denmark,
Ørsteds Plads, 2800 Kongens Lyngby, Denmark

M. Willatzen (✉)
Beijing Institute of Nanoenergy and Nanosciences,
Chinese Academy of Sciences, Beijing, China
e-mail: morwi@fotonik.dtu.dk; mortenwillatzen@binn.cas.cn

J. Gravesen
Department of Applied Mathematics and Computer Science,
Technical University of Denmark, Ørsteds Plads, 2800 Kongens Lyngby, Denmark
e-mail: jgra@dtu.dk

V.M. Fomin (ed.), *Physics of Quantum Rings*, NanoScience and Technology,
https://doi.org/10.1007/978-3-319-95159-1_16

16.1 Introduction

With the possibility to shape objects in the nano range using novel fabrication technologies it becomes increasingly important to assess experimentally and theoretically the combined influence of shape and size on physical properties of nanostructures. Experimental studies revealing these geometry properties include electronic, magnetic, and optical properties of electrons and holes confined to curved surfaces such as graphene strips and semiconductor nanorings. An exotic nanostructure which has been examined experimentally is the Möbius nanostructure produced by spooling a single crystalline $NbSe_3$ ribbon on a selenium droplet whereby surface tension leads to a twist in the ribbon [1]. Topological insulators having unusual properties and potential interesting applications have been studied experimentally [2, 3] and theoretically for a Möbius graphene strip [4].

Since the first Möbius nanostructure fabrications, several investigations have been carried out on Möbius structures both for classical and nanostructure dimensions [4–13]. Gravesen and Willatzen computed electronic eigenstates and the shape of Möbius nanostructures using differential geometry arguments taking into account bending effects [5, 17]. Heijden and Starostin solved a classical problem in geometry by employing an invariant variational bi-complex formalism to derive the first equilibrium equations for a wide developable strip undergoing large deformations [6, 7]. Ballon et al. showed that classical Möbius ring resonators exhibit fermion-boson rotational symmetry [8]. Yoneya et al. determined theoretically the structure of domain walls in ferromagnetic states on Möbius strips [9]. Guo studied electronic properties of a Möbius graphene strip with a zigzag edge [4]. Optical activity for a Möbius nanostructure was examined by Rockstuhl et al. [10]. Zhao et al. analyzed topological properties of quantum states for a spinless particle hopping in a Möbius ladder [11]. Li and Ram-Mohan [12] theoretically discussed several quantum-mechanical properties of Möbius nanostructures including level splittings, symmetry (in particular the absence of rotational symmetry for eigenstates), the influence of magnetic field and optical transitions. In a recent study, Fomin et al. examined electron localization in inhomogeneous Möbius rings [13].

In order to assess and optimize the influence of geometry on physical properties of nanostructures, it is important to develop effective analytical and computational techniques. This chapter presents analytical techniques to compute quantum-mechanical particle eigenstates confined to complicated geometries. We start out by deriving the governing equations of a conduction electron confined to a curved semiconductor nanoring. It is shown that if the nanoring is characterized by a large aspect ratio, i.e., nanorings where the length is much larger than the cross-sectional dimensions, then the three-dimensional Schrödinger equation can be separated in three ordinary differential equations. Two of these can be solved analytically and lead to sinusoidal solutions, while the wave-function part that depends on the last coordinate parametrizing the length contains curvature contributions. Open and closed nanoring boundary conditions are considered and the influence of boundary conditions on eigenstate symmetries and energies is discussed. The general effect of a curved

geometry is to decrease electronic energies compared to the corresponding straight nanowire of the same volume. The discussion is continued to include contributions from strain through the deformation potential. For typical semiconductors this effect is huge if strain is present and by far the major effect compared to the direct geometry and curvature influence on the Laplacian. In the second part of the chapter, an exotic example of a complicated nanostructure geometry is analyzed: the Möbius structure. By inclusion of the bending energy in determining the shape of a Möbius nanostructure, the median or centerline parametrization is derived and described in terms of the generalized coordinate u^1 and the width and thickness of the Möbius nanostructure are parametrized by coordinates u^2 and u^3. It is shown that for thin Möbius nanostructures, the electronic eigenstates can be written as a semi-separable problem. The thickness-coordinate part of the wavefunction separates out while the median- and width-coordinate parts couple in a non-separable manner. Results are compared with exact finite element calculations for a general Möbius nanostructure. It is verified that the differential geometry formulation presented is accurate whenever the thickness is much smaller than the median length and the width in agreement with the assumptions.

In the Second Edition of the chapter, we added a differential-geometric formulation of dynamic elastic equations to solve the phonon problem of thin shells. This study is gaining interest due to the plethora of 2D materials and functionalized 2D structures that can be grown in laboratories today and the richness of new physics they display. 2D materials are indeed thin shells as their thicknesses range from one to a few atomic layers. Graphene [14] is an important example of 2D structures that have promising application possibilities for mechanics [15] and electronics [16], however, not much is known about carrier mobilities and the scattering mechanisms that force a limit to their values. A main reason for our present study of 2D materials is the possibility to form complex geometrical and topological structures from them and to examine the physics and applications that emerge from changing the 2D geometry and topology. A detailed understanding of phonon dynamics is essential to determine carrier mobilities and scattering mechanisms in 2D materials. As a case study, we derive the acoustic phonon equations for a thin shell using a differential-geometric formulation of the elastic energy and compute the phonon dispersion curves for a cylinder-shaped and flat 2D graphene sheet.

16.1.1 Arc-Length Parametrization

It is convenient for the analysis of complex-shaped nanowires or nanorings to introduce a set of orthogonal vectors where one is the local tangent vector of the nanowire axis and the two others supplement to span the local cross section of the nanowire [18]. The nanowire axis $\mathbf{r}(s)$ is assumed to be parametrized by arc length s, but this is not really a restriction since any curve can be parametrized by arc length. The tangent vector $\mathbf{t}(s) = \mathbf{r}'(s) = \mathrm{d}\mathbf{r}/\mathrm{d}s$ is a unit vector field along the curve and the two vectors spanning the local cross section of the nanowire are designated $\mathbf{p}(s)$ and $\mathbf{q}(s)$ such

that $\mathbf{t}(s), \mathbf{p}(s), \mathbf{q}(s)$ constitute an orthonormal frame at each point $\mathbf{r}(s)$ along the axis. Differentiation of the identities,

$$\begin{aligned} &\mathbf{t}\cdot\mathbf{t}=1,\ \ \mathbf{p}\cdot\mathbf{p}=1,\ \ \mathbf{q}\cdot\mathbf{q}=1\,,\\ &\mathbf{t}\cdot\mathbf{p}=0,\ \ \mathbf{t}\cdot\mathbf{q}=0,\ \ \mathbf{p}\cdot\mathbf{q}=0\,, \end{aligned} \tag{16.1}$$

yields

$$\begin{aligned} &2\frac{\mathrm{d}\mathbf{t}}{\mathrm{d}s}\cdot\mathbf{t}=0,\ \ 2\frac{\mathrm{d}\mathbf{p}}{\mathrm{d}s}\cdot\mathbf{p}=0,\ \ 2\frac{\mathrm{d}\mathbf{q}}{\mathrm{d}s}\cdot\mathbf{q}=0\,,\\ &\frac{\mathrm{d}\mathbf{t}}{\mathrm{d}s}\cdot\mathbf{p}+\mathbf{t}\cdot\frac{\mathrm{d}\mathbf{p}}{\mathrm{d}s}=0,\ \ \frac{\mathrm{d}\mathbf{t}}{\mathrm{d}s}\cdot\mathbf{q}+\mathbf{t}\cdot\frac{\mathrm{d}\mathbf{q}}{\mathrm{d}s}=0,\ \ \frac{\mathrm{d}\mathbf{p}}{\mathrm{d}s}\cdot\mathbf{q}+\mathbf{p}\cdot\frac{\mathrm{d}\mathbf{q}}{\mathrm{d}s}=0\,. \end{aligned} \tag{16.2}$$

If we now let

$$a(s)=\frac{\mathrm{d}\mathbf{t}}{\mathrm{d}s}\cdot\mathbf{p},\ \ b(s)=\frac{\mathrm{d}\mathbf{t}}{\mathrm{d}s}\cdot\mathbf{q},\ \ c(s)=\frac{\mathrm{d}\mathbf{p}}{\mathrm{d}s}\cdot\mathbf{q}\,, \tag{16.3}$$

then we obtain the following equation

$$\frac{\mathrm{d}}{\mathrm{d}s}\begin{bmatrix}\mathbf{t}\\ \mathbf{p}\\ \mathbf{q}\end{bmatrix}=\begin{bmatrix}0 & a & b\\ -a & 0 & c\\ -b & -c & 0\end{bmatrix}\begin{bmatrix}\mathbf{t}\\ \mathbf{p}\\ \mathbf{q}\end{bmatrix}\,. \tag{16.4}$$

Observe that the curvature κ of the axis is:

$$\kappa(s)=\left|\mathbf{r}''(s)\right|=\left|\mathbf{t}'(s)\right|=\sqrt{a^2+b^2}\,. \tag{16.5}$$

The above does not uniquely determine $\mathbf{p}, \mathbf{q}$. A typical choice of vector fields $\mathbf{p}, \mathbf{q}$ is to let $\mathbf{p}$ be the principal normal $\mathbf{n}=\mathbf{t}'/\kappa$ and $\mathbf{q}$ is the binormal $\mathbf{b}=\mathbf{t}\times\mathbf{n}$. In this case, (16.4) leads to the Frenet-Serret equations, where $a=\kappa$, $b=0$, and $c=\tau$ is the torsion of the axis. If further the nanowire axis lies in a plane, the torsion vanishes: $\tau=0$. It should be noted that the frame chosen here does not always exist in principle; this happens if the curvature vanishes locally. The problem can be circumvented by choosing the minimal rotation frame. In the latter frame $c=0$ even if the torsion is non-zero.

16.1.2 Planar Nanowire Axis Curves

In the following, the analysis is restricted to nanowire structures where the nanowire axis lies in a plane, and we choose $b=0$ and $c=0$ which allows for some simplifications in the model setup (Fig. 16.1).

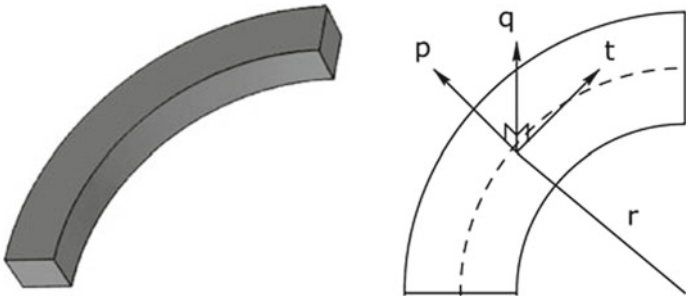

Fig. 16.1 Schematic picture of a curved nanowire structure (left plot) and a figure showing the chosen curvilinear coordinates (right plot)

We can now parametrize a curved tube of rectangular cross section, i.e., a tubular neighbourhood in $\mathbb{R}^3$ of the curve $\mathbf{r}(s)$, according to:

$$\mathbf{x}(u^1, u^2, u^3) = \mathbf{r}(u^1) + u^2\mathbf{p}(u^1) + u^3\mathbf{q}(u^1)\,, \tag{16.6}$$

where $-\varepsilon_2 \leq u_2 \leq \varepsilon_2$ and $-\varepsilon_3 \leq u_3 \leq \varepsilon_3$ for two constants ε_2 and ε_3. Albeit the formulation is for rectangular-shaped nanowire cross sections it is easy, afterwards, to adjust the theory to curved nanowires with, e.g., a circular cross section.

Using (16.4), simple manipulations give

$$\frac{\partial \mathbf{x}}{\partial u^1} = (1 - u^2 a(u^1))\mathbf{t}(u^1)\,, \tag{16.7}$$

$$\frac{\partial \mathbf{x}}{\partial u^2} = \mathbf{p}(u^1)\,, \tag{16.8}$$

$$\frac{\partial \mathbf{x}}{\partial u^3} = \mathbf{q}(u^1)\,. \tag{16.9}$$

The metric tensor $G_{ij} = \frac{\partial \mathbf{x}_i}{\partial u^i} \cdot \frac{\partial \mathbf{x}_j}{\partial u^j}$ of $\mathbb{R}^3$ becomes

$$[G_{ij}] = \begin{bmatrix} (1 - u^2 a(u^1))^2 & 0 & 0 \\ 0 & 1 & 0 \\ 0 & 0 & 1 \end{bmatrix}. \tag{16.10}$$

The determinant is

$$G = (1 - u^2 a(u^1))^2\,, \tag{16.11}$$

and the inverse $\left[G_{ij}\right]^{-1} = \left[G^{ij}\right]$ reads

$$[G^{ij}] = \begin{bmatrix} \frac{1}{(1-u^2 a(u^1))^2} & 0 & 0 \\ 0 & 1 & 0 \\ 0 & 0 & 1 \end{bmatrix}. \tag{16.12}$$

If we expand the determinant and the inverse in u^2 and u^3 then we obtain to zeroth order

$$G \approx 1\,, \qquad \partial_1 G \approx 0\,, \tag{16.13}$$

$$\partial_2 G \approx -2a(u^1)\,, \qquad \partial_3 G \approx 0\,, \tag{16.14}$$

$$[G^{ij}] \approx \begin{bmatrix} 1 & 0 & 0 \\ 0 & 1 & 0 \\ 0 & 0 & 1 \end{bmatrix}\,, \qquad \partial_1[G^{ij}] \approx \begin{bmatrix} 0 & 0 & 0 \\ 0 & 0 & 0 \\ 0 & 0 & 0 \end{bmatrix}\,, \tag{16.15}$$

$$\partial_2[G^{ij}] \approx \begin{bmatrix} 2a(u^1) & 0 & 0 \\ 0 & 0 & 0 \\ 0 & 0 & 0 \end{bmatrix}\,, \qquad \partial_3[G^{ij}] \approx \begin{bmatrix} 0 & 0 & 0 \\ 0 & 0 & 0 \\ 0 & 0 & 0 \end{bmatrix}\,. \tag{16.16}$$

The Laplace operator $\triangle_{\mathbb{R}^3} = \frac{\partial^2}{\partial x^2} + \frac{\partial^2}{\partial y^2} + \frac{\partial^2}{\partial z^2}$ in $\mathbb{R}^3$ is in the curvilinear coordinates u^1, u^2, u^3 given by [19]

$$\triangle_{\mathbb{R}^3} = G^{ij}\partial_i\partial_j + \left(\frac{G^{ij}}{2}\frac{\partial_j G}{G} + \partial_j G^{ij}\right)\partial_i\,, \tag{16.17}$$

where $\partial_i = \frac{\partial}{\partial u^i}$ and reads to zeroth order in u^2 and u^3:

$$\triangle_{\mathbb{R}^3} = G^{ij}\partial_i\partial_j + \left(G^{ij}\frac{\partial_j G}{2G} + \partial_j G^{ij}\right)\partial_i \approx \partial_1^2 + \partial_2^2 + \partial_3^2 - a(u^1)\partial_2\,. \tag{16.18}$$

Next, introducing

$$F = \sqrt{G} = 1 - u^2 a(u^1)\,, \tag{16.19}$$

and letting $\chi = \sqrt{F}\psi$ allow us to write, again to zeroth order in u^2 and u^3,

$$\triangle_{\mathbb{R}^3}\psi = \triangle_{\mathbb{R}^3}\left(\frac{\chi}{\sqrt{F}}\right) \approx \partial_1^2\chi + \partial_2^2\chi + \partial_3^2\chi + \frac{\kappa^2}{4}\chi\,. \tag{16.20}$$

Hence, the benefit in recasting the Laplacian operator problem in terms of χ instead of ψ is that the right-hand-side of (16.20) is separable in the three coordinates u^1, u^2, u^3 while the right-hand-side of (16.18) is not. When we address the electron one-band heterostructure problem, separability of the scaled wavefunction χ is maintained and considerable computational simplicity is gained.

16.1.3 General Nanowire Axis Parametrization

For most curves, it is difficult to find an explicit arc-length parametrization $\mathbf{r}(s)$. Hence, we need to look for a general parametrization $\mathbf{r}(t)$ with $t = t(s)$ and $\left|\mathbf{r}'(t)\right| \neq 1$ as follows:

$$\frac{\mathrm{d}}{\mathrm{d}s} = \frac{\mathrm{d}t}{\mathrm{d}s}\frac{\mathrm{d}}{\mathrm{d}t} = \left(\frac{\mathrm{d}s}{\mathrm{d}t}\right)^{-1}\frac{\mathrm{d}}{\mathrm{d}t}\,, \tag{16.21}$$

$$\frac{\mathrm{d}\chi_1}{\mathrm{d}s} = \left(\frac{\mathrm{d}s}{\mathrm{d}t}\right)^{-1}\frac{\mathrm{d}\chi_1}{\mathrm{d}t}\,,$$

$$\frac{\mathrm{d}^2\chi_1}{\mathrm{d}s^2} = \left(\frac{\mathrm{d}s}{\mathrm{d}t}\right)^{-1}\frac{\mathrm{d}}{\mathrm{d}t}\left(\left(\frac{\mathrm{d}s}{\mathrm{d}t}\right)^{-1}\frac{\mathrm{d}\chi_1}{\mathrm{d}t}\right) \tag{16.22}$$

$$= \left(\frac{\mathrm{d}s}{\mathrm{d}t}\right)^{-2}\frac{\mathrm{d}^2\chi_1}{\mathrm{d}t^2} - \left(\frac{\mathrm{d}s}{\mathrm{d}t}\right)^{-3}\frac{\mathrm{d}^2s}{\mathrm{d}t^2}\frac{\mathrm{d}\chi_1}{\mathrm{d}t}\,. \tag{16.23}$$

Now

$$\frac{\mathrm{d}s}{\mathrm{d}t} = |\mathbf{r}'(t)| = \sqrt{\mathbf{r}'\cdot\mathbf{r}'}\,, \tag{16.24}$$

$$\frac{\mathrm{d}^2s}{\mathrm{d}t^2} = \frac{\mathbf{r}'\cdot\mathbf{r}''}{\sqrt{\mathbf{r}'\cdot\mathbf{r}'}}\,, \tag{16.25}$$

$$\kappa^2 = \frac{|\mathbf{r}'\times\mathbf{r}''|^2}{|\mathbf{r}'|^6} = \frac{(\mathbf{r}'\times\mathbf{r}'')\cdot(\mathbf{r}'\times\mathbf{r}'')}{(\mathbf{r}'\cdot\mathbf{r}')^3} = \frac{|\mathbf{r}'|^2|\mathbf{r}''|^2 - (\mathbf{r}'\cdot\mathbf{r}')^2}{(\mathbf{r}'\cdot\mathbf{r}'')^3}\,. \tag{16.26}$$

16.2 Application to the Schrödinger Equation

Let s be nanowire axis arc length. With the above expression for the Laplacian, the Schrödinger equation for an electron with effective mass m and energy E reads in terms of χ and coordinates u^i (applies to zeroth order in s and u_2)

$$\frac{-\hbar^2}{2m}\left(\partial_s^2\chi + \partial_2^2\chi + \partial_3^2\chi + \frac{\kappa^2}{4}\chi\right) + V(u_1,u_2,u_3)\chi = E\chi\,, \tag{16.27}$$

where $\partial_s \equiv \frac{\partial}{\partial s}$, and the potential V satisfies

$$V(s,u_2,u_3) = 0\,, \tag{16.28}$$

if (s,u_2,u_3) is a point within the nanowire structure, i.e., the domain: $-\varepsilon_2 \leq u_2 \leq \varepsilon_2$ and $-\varepsilon_3 \leq u_3 \leq \varepsilon_3$. Similarly, the potential V is infinite outside the nanowire struc-

ture to mimic the infinite-barrier case. It must be emphasized that the infiniteness of the potential outside the nanowire is crucial for the following simple quasi-analytical method to work. In the general boundary condition case (including the finite barrier problem), and as long as eigenfunctions vanish sufficiently fast outside the nanowire so that singularities in the coordinate transformation do not occur within the domain of interest, the present coordinate transformation can be used. In this case, however, solutions must be found numerically in the transformed coordinates but the transformation is still valuable since the geometry of the problem is a simple geometry in transformed coordinates and easy to implement numerically.

As the curvature κ is a function of s only it follows that a separable solution $\chi = \chi_1(s)\chi_2(u_2)\chi_3(u_3)$ can be sought. For a general parametrization $t = t(s)$, using the expressions in (16.21)–(16.26) allows us to recast (16.27) as three ordinary differential equations:

$$\chi_1'' - \frac{\mathbf{r}' \cdot \mathbf{r}''}{\mathbf{r}' \cdot \mathbf{r}'}\chi_1' + \left(\frac{(\mathbf{r}' \cdot \mathbf{r}')(\mathbf{r}'' \cdot \mathbf{r}'') - (\mathbf{r}' \cdot \mathbf{r}'')^2}{4(\mathbf{r}' \cdot \mathbf{r}')^2} - (\lambda + \mu)(\mathbf{r}' \cdot \mathbf{r}') \right) \chi_1 = 0\,, \tag{16.29}$$

$$\partial_2^2 \chi_2 + \nu^2 \chi_2 = 0\,, \tag{16.30}$$

$$\partial_3^2 \chi_3 + \left(\mu - \nu^2\right) \chi_3 = 0\,, \tag{16.31}$$

with $\lambda = -\frac{2mE}{\hbar^2}$ and μ and ν separation constants; and a prime ($'$) denotes differentiation with respect to t.

16.2.1 Analytical Solution for χ_2, χ_3

The equations in χ_2 and χ_3 can be solved analytically. The general solution to (16.30) in χ_2 is

$$\chi_2(u^2) = \sin\left(\nu u^2 + \phi_2\right)\,, \tag{16.32}$$

where ν and ϕ_2 are constants determined by the hard-wall boundary conditions imposed, i.e.,

$$\begin{aligned} \chi_2(-\varepsilon^2) &= \sin\left(-\nu\varepsilon^2 + \phi_2\right) = 0\,, \\ \chi_2(\varepsilon^2) &= \sin\left(\nu\varepsilon^2 + \phi_2\right) = 0\,. \end{aligned} \tag{16.33}$$

Thus:

$$\nu = \frac{m'\pi}{2\varepsilon^2}\,, \tag{16.34}$$

where m' is an integer different from zero. The other constant, the phase ϕ_2, must be chosen such that

$$\phi_2 = -\nu\varepsilon^2 \,, \tag{16.35}$$

and the boundary conditions in (16.33) are fulfilled. If m' is even (and different from zero), χ_2 becomes

$$\chi_2(u^2) = \sin\left(\frac{m'\pi}{2\varepsilon^2}u^2\right) \,, \tag{16.36}$$

while for m' odd:

$$\chi_2(u^2) = \cos\left(\frac{m'\pi}{2\varepsilon^2}u^2\right) \,. \tag{16.37}$$

In exactly the same way, (16.31) allows the separation constant μ to be determined:

$$\mu - \nu^2 = \left(\frac{n'\pi}{2\varepsilon^3}\right)^2 \,, \tag{16.38}$$

where n' is an integer different from zero. If n' is even and different from zero, the eigenfunction χ_3 is

$$\chi_3(u^3) = \sin\left(\frac{n'\pi}{2\varepsilon^3}u^3\right) \,, \tag{16.39}$$

while for n' odd:

$$\chi_3(u^3) = \cos\left(\frac{n'\pi}{2\varepsilon^3}u^3\right) \,. \tag{16.40}$$

Combining (16.34) and (16.38) yields for μ the result

$$\mu = \left(\frac{m'\pi}{2\varepsilon^2}\right)^2 + \left(\frac{n'\pi}{2\varepsilon^3}\right)^2 \,, \tag{16.41}$$

with $m' = \pm 1, \pm 2, \pm 3$ and $n' = \pm 1, \pm 2, \pm 3$. The possible values of the particle energy E are finally found from the χ_1 eigenvalue equation (16.29) by imposing appropriate boundary conditions given the value of μ.

16.2.2 Case Study: Circular Nanoring

The circular nanoring can be treated analytically. An arc-length parametrization of a circular nanoring is

$$\mathbf{r}(u^1) = \left(R\cos\left(\frac{u^1}{R}\right), R\sin\left(\frac{u^1}{R}\right), 0\right) \,, \tag{16.42}$$

where

$$|\mathbf{r}'(u^1)| = 1\,,\ |\mathbf{r}''(u^1)| = \frac{1}{R^2}\,, \tag{16.43}$$

and R is the circular ring radius-of-curvature. Since $|\mathbf{r}'(u^1)| = 1$, the parametrization is an arc-length parametrization and (16.29) reads

$$\chi_1'' - \left(\lambda + \mu - \frac{1}{4R^2}\right)\chi_1 = 0 \tag{16.44}$$

with the general solution

$$\chi_1 = \sin\left(\sqrt{-\lambda - \mu + \frac{1}{4R^2}}u^1 + \phi_1\right)\,, \tag{16.45}$$

where ϕ_1 is an arbitrary phase. Further, imposing the boundary conditions:

$$\chi_1(u^1 = 0) = \chi_1(u^1 = L) = 0\,, \tag{16.46}$$

corresponding to an *open* circular-shaped nanowire structure, gives

$$\chi_1(u^1) = \sin\left(\frac{l\pi}{L}u^1\right), l = \pm 1, \pm 2, \pm 3, \ldots\,, \tag{16.47}$$

and the associated energy eigenvalue is

$$E = -\frac{\hbar^2\lambda}{2m} = \frac{\hbar^2}{2m}\left[\left(\frac{l\pi}{L}\right)^2 + \left(\frac{m'\pi}{2\varepsilon^2}\right)^2 + \left(\frac{n'\pi}{2\varepsilon^3}\right)^2 - \frac{1}{4R^2}\right]. \tag{16.48}$$

A *closed* circular-shaped nanowire structure is subject to less strict boundary conditions

$$\chi_1(u^1) = \chi_1(u^1 + 2\pi R)\,, \tag{16.49}$$

corresponding to

$$\sqrt{\frac{1}{4R^2} - \mu - \lambda}2\pi R = 2l\pi\,, \qquad l = 0, \pm 1, \pm 2, \pm 3, \ldots\,, \tag{16.50}$$

and the following eigenstate solutions (with $L = 2\pi R$):

$$\chi_1(u^1) = \sin\left(\frac{2l\pi}{L}u^1 + \phi_1\right), l = 0, \pm 1, \pm 2, \pm 3, \ldots\,. \tag{16.51}$$

The associated energy spectrum is

$$E = -\frac{\hbar^2\lambda}{2m} = \frac{\hbar^2}{2m}\left[\left(\frac{2l\pi}{L}\right)^2 + \left(\frac{m'\pi}{2\varepsilon^2}\right)^2 + \left(\frac{n'\pi}{2\varepsilon^3}\right)^2 - \frac{1}{4R^2}\right]. \tag{16.52}$$

In particular, note that $l = 0$ is possible since the phase ϕ_1 is arbitrary for the closed circular nanowire axis. This result is the same as found in the case of a cylinder surface of revolution [19] keeping in mind that L in [19] equals the present $2\varepsilon^2$. It was demonstrated in [19] that the energy expression (16.52) is an excellent approximation if the cylinder thickness is less than 10% of the radius R.

16.2.3 Case Study: Elliptic Nanoring

Consider an elliptical-shaped nanoring structure with an axis parametrization:

$$\mathbf{r}(u^1) = \left(R_1 \cos\left(2\pi\frac{u^1}{L}\right), R_2 \sin\left(2\pi\frac{u^1}{L}\right), 0\right), \tag{16.53}$$

where R_1 and R_2 define the elliptic semi-major and semi-minor axes, and the nanoring corresponds to the range: $0 \leq u^1 \leq L$.

From (16.53), the following relations are obtained:

$$\mathbf{r}'(u^1) = \left(-2\pi\frac{R_1}{L}\sin\left(2\pi\frac{u^1}{L}\right), 2\pi\frac{R_2}{L}\cos\left(2\pi\frac{u^1}{L}\right), 0\right), \tag{16.54}$$

$$\mathbf{r}''(u^1) = \left(-(2\pi)^2\frac{R_1}{L^2}\cos\left(2\pi\frac{u^1}{L}\right), -(2\pi)^2\frac{R_2}{L^2}\sin\left(2\pi\frac{u^1}{L}\right), 0\right) \tag{16.55}$$

and

$$\mathbf{r}' \cdot \mathbf{r}' = (2\pi)^2\frac{R_1^2}{L^2}\sin^2\left(2\pi\frac{u^1}{L}\right) + (2\pi)^2\frac{R_2^2}{L^2}\cos^2\left(2\pi\frac{u^1}{L}\right), \tag{16.56}$$

$$\mathbf{r}'' \cdot \mathbf{r}'' = (2\pi)^4\frac{R_1^2}{L^4}\cos^2\left(2\pi\frac{u^1}{L}\right) + (2\pi)^4\frac{R_2^2}{L^4}\sin^2\left(2\pi\frac{u^1}{L}\right), \tag{16.57}$$

$$\mathbf{r}' \cdot \mathbf{r}'' = (2\pi)^3\frac{R_1^2 - R_2^2}{L^3}\sin\left(2\pi\frac{u^1}{L}\right)\cos\left(2\pi\frac{u^1}{L}\right). \tag{16.58}$$

Using the latter expressions in (16.29) and solving for χ_1 with appropriate boundary conditions, we show in Table 16.1 the first three eigenvalues (relative to $\frac{\hbar^2}{2m}\mu$) for a nanowire with $R_1 = 5\,\text{nm}$, $R_2 = 8\,\text{nm}$, and $L = 2\pi \cdot 10\,\text{nm}$. In our case, we assumed the elliptic nanoring to be cut open such that $\chi_1(u^1 = L) = \chi_1(u^1 = 0) = 0$.

The three associated eigenstates for χ_1 can be seen in Fig. 16.2.

Table 16.1 The first three energy levels for an elliptical nanoring. Here m is the InAs electron effective mass equal to $0.022m_0$ [28] where m_0 is the free electron mass

energy	$E(1) - \frac{\hbar^2}{2m}\mu$ (meV)	$E(2) - \frac{\hbar^2}{2m}\mu$ (meV)	$E(3) - \frac{\hbar^2}{2m}\mu$ (meV)
	−3	23	78

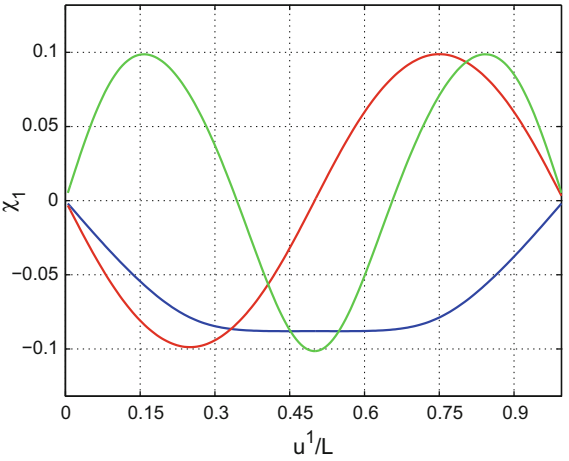

Fig. 16.2 The first three eigenstates for χ_1 for an elliptical nanoring. The blue, red, and green curves are the groundstate, the first-excited state, and the second-excited state, respectively

16.3 Strain in Nanorings

In what follows, we consider large aspect-ratio nanowires, i.e., nanowires where the cross-sectional dimensions are much smaller than the nanowire length. The nanoring axis coordinate is u^1 and the cross-sectional coordinates are u^2 and u^3, see Fig. 16.1.

16.3.1 Stress Tensor for a Bent Nanowire

It is assumed that the nanowire is free-standing, i.e., the nanoring structure obeys the boundary stress relations:

$$\sigma_{ik} n_k = 0\,, \tag{16.59}$$

where σ_{ik} is the stress tensor, n_k is the boundary normal vector components, and summation from 1 to 3 is implied for repeated indices. The indices i and k take on values 1, 2, 3 corresponding to the u^1, u^2, u^3 coordinate directions, respectively. The normal vector $\mathbf{n}$ always lies in the u^2-u^3 plane, i.e., $n_1 = 0$. Further, locations exist on the cross-sectional boundary where $n_2 = 1$ and $n_3 = 0$ such that (16.59) with $i = 1$ gives $\sigma_{12} = 0$. Similarly, locations exist at the cross-sectional boundary where $n_2 = 0$ and $n_3 = 1$ hence with $i = 1$ we get $\sigma_{13} = 0$. Using similar arguments for $i = 2$ and $i = 3$ we conclude that only σ_{11} can be nonzero at the cross-sectional boundary.

Since the cross-sectional dimensions are small, it is reasonable to assume that the stress tensor components are constant over the cross section and we immediately conclude that σ_{11} is the only non-zero stress component *everywhere* in the nanowire.

16.3.2 Strain Tensor Results in the Zincblende Case

Using the stress-strain relations for cubic materials:

$$\sigma_{11} = c_{11}\varepsilon_{11} + c_{12}\varepsilon_{22} + c_{12}\varepsilon_{33}\,, \tag{16.60}$$
$$\sigma_{22} = c_{12}\varepsilon_{11} + c_{11}\varepsilon_{22} + c_{12}\varepsilon_{33} = 0\,, \tag{16.61}$$
$$\sigma_{33} = c_{12}\varepsilon_{11} + c_{12}\varepsilon_{22} + c_{11}\varepsilon_{33} = 0\,, \tag{16.62}$$
$$\sigma_{23} = c_{44}\varepsilon_{23} = 0\,, \tag{16.63}$$
$$\sigma_{13} = c_{44}\varepsilon_{13} = 0\,, \tag{16.64}$$
$$\sigma_{12} = c_{44}\varepsilon_{12} = 0\,, \tag{16.65}$$

where ε_{ij} is the strain tensor and c_{ij} is the stiffness tensor, it is found that

$$\varepsilon_{22} = \varepsilon_{33} = -\frac{c_{12}}{c_{11} + c_{12}}\varepsilon_{11}\,, \tag{16.66}$$

and all other strain components are zero.

16.3.3 Nonlinear Expression for the Strain Component ε_{11}

With the above relations between strain components, it is possible to find all strain components once we know, say, ε_{11}. The general expression for the strain tensor to second order is [20]

$$\varepsilon_{ik} = \frac{1}{2}\left(\frac{\partial d_i}{\partial x_k} + \frac{\partial d_k}{\partial x_i} + \frac{\partial d_l}{\partial x_i}\frac{\partial d_l}{\partial x_k}\right)\,, \tag{16.67}$$

where d_i is the i'th component of the displacement. In the following, we shall restrict our analysis to nanowires bent uniformly, i.e., nanowires with a constant radius of curvature: R along the nanowire length. In this case, if the bending is assumed to be in the u^1-u^2 plane, then we have:

$$\varepsilon_{11} = \frac{1}{2}\left(\frac{\partial d_1}{\partial u^1} + \frac{\partial d_1}{\partial u^1} + \frac{\partial d_1}{\partial u^1}\frac{\partial d_1}{\partial u^1}\right)\,. \tag{16.68}$$

In the presence of bending forces only, a simple geometry analysis to first order in the deformation d_1 shows that:

$$\frac{\partial d_1}{\partial u^1} = \frac{u^2}{R} \tag{16.69}$$

and

$$\varepsilon_{11} = \frac{u^2}{R} + \frac{1}{2}\left(\frac{u^2}{R}\right)^2 . \tag{16.70}$$

Note that all other terms (shear second-order components) vanish due to the stress-strain relations given by (16.63)–(16.65) and thus do not contribute to (16.67). It may seem strange to keep the second-order term in the strain expression for ε_{11} since strain values are typically small, i.e., much less than 1. The reason is that the first-order strain term ($\frac{u^2}{R}$), being proportional to the coordinate u^2, corresponds to a parity changing operator. Hence, energy contributions to first order in $\frac{u^2}{R}$ vanish in first-order non-degenerate perturbation theory and the most significant non-zero contribution from strain to electronic eigenstates is of the second order in $\frac{u^2}{R}$. The origin of the second-order terms stems from either second-order perturbation theory in the $\frac{u^2}{R}$ strain term or first-order perturbation theory in the $\frac{1}{2}\left(\frac{u^2}{R}\right)^2$ strain term. In other words, we must take care in keeping all strain terms to second order when analyzing influence of strain on electronic eigenstates.

With the determination of ε_{11}, the other non-zero diagonal strain components follow from (16.66).

16.3.4 The Strain Hamiltonian Contribution for Conduction Electrons

Having determined the strain tensor, the ingredients needed for the zincblende conduction-band effective-mass problem are assembled. The one-band heterostructure effective-mass equation in the presence of strain reads [23]:

$$-\frac{\hbar^2}{2}\nabla\cdot\left(\frac{1}{m_{\text{eff}}(\mathbf{r})}\nabla\right)\psi(\mathbf{r}) + \left[V_{BE}(\mathbf{r}) + D_e\left(\varepsilon_{11}+\varepsilon_{22}+\varepsilon_{33}\right)\right]\psi(\mathbf{r}) = E\psi(\mathbf{r}) , \tag{16.71}$$

where $\hbar$, m_{eff}, V_{BE}, D_e, E, ψ, $\mathbf{r}$ are Planck's constant divided by 2π, the position-dependent electron effective mass, the position-dependent heterostructure band-edge potential for electrons, the electron hydrostatic deformation potential, the electron energy, electron eigenstate, and position vector, respectively. The above differential equation in the wavefunction ψ can be formulated as a perturbative problem:

$$H\psi = (H_0 + H_1)\,\psi = E\psi\,, \tag{16.72}$$

$$H_0\psi^0 = E^0\psi^0\,, \tag{16.73}$$

$$H_0 = -\frac{\hbar^2}{2}\nabla\cdot\left(\frac{1}{m_{\text{eff}}(\mathbf{r})}\nabla\right) + V_{BE}(\mathbf{r})\,, \tag{16.74}$$

$$H_1 = D_e\left(\varepsilon_{11} + \varepsilon_{22} + \varepsilon_{33}\right)\,, \tag{16.75}$$

where H_0, H_1, E^0, and ψ^0 are the unperturbed Hamiltonian (i.e., in the absence of strain), the strain perturbation, the unperturbed electron energy, and the unperturbed electron energy, respectively. The above splitting of the Hamiltonian into an unperturbed part and a strain Hamiltonian perturbation is only meaningful if the strain energy contribution is substantially smaller than energy differences between any two unperturbed eigenstates. If not so, a Löwdin degenerate perturbation method [22] should be employed.

Let us next rewrite the strain Hamiltonian as:

$$H_1 = H_1^A + H_1^B\,, \tag{16.76}$$

$$H_1^A = D_e\left(1 - 2\frac{c_{12}}{c_{11}+c_{12}}\right)\frac{u^2}{R}\,, \tag{16.77}$$

$$H_1^B = \frac{1}{2}D_e\left(1 - 2\frac{c_{12}}{c_{11}+c_{12}}\right)\left(\frac{u^2}{R}\right)^2\,. \tag{16.78}$$

Evidently, the Hamiltonian part H_1^A contributes to the second order in the perturbation only while H_1^B contributes to the first order.

16.3.5 Computation of Eigenstates for Circular-Bent Nanowires Using Differential Geometry

In this section, curvilinear coordinates are used to determine, in a simple way, eigenstates and eigenvalues in the case of a bent nanowire subject to homogeneous strain. Since electrons are completely confined to the nanowire structure and the heterostructure potential is an infinite-barrier potential, the eigenstate problem is a Dirichlet problem, and the effective-mass equation for a nanoring can be recast in terms of the transformed wavefunction χ [refer to (16.20)]:

$$\frac{-\hbar^2}{2m_{\text{eff}}}\left(\partial_1^2 + \partial_2^2 + \partial_3^2 + \frac{\kappa^2}{4} + D_e\left(\varepsilon_{11} + \varepsilon_{22} + \varepsilon_{33}\right)\right)\chi = E\chi\,. \tag{16.79}$$

As the curvature $\kappa = \frac{1}{R}$ is a constant for homogeneous bending of a nanoring with a radius of curvature R, it is apparent that a separable solution $\chi = \chi_1(u^1)\chi_2(u^2)\chi_3(u^3)$ can be sought. This follows by noticing that also the strain perturbation [(16.76)–

(16.78)] is a function of u^2 solely. In the general case of inhomogeneous deformations, the strain perturbation will, however, depend on u^2, u^3 and a separable solution cannot be found.

Thus, for the nanoring problem with homogeneous bending strains, insertion of $\chi = \chi_1(u^1)\chi_2(u^2)\chi_3(u^3)$ into (16.79) gives

$$\partial_1^2\chi_1 + \left(\frac{1}{4R^2} - \lambda - \mu\right)\chi_1 = 0\,, \tag{16.80}$$

$$\partial_2^2\chi_2 - \left[\frac{2m_{\text{eff}}}{\hbar^2}D_e\left(1 - 2\frac{c_{12}}{c_{11}+c_{12}}\right)\left(\frac{u^2}{R} + \frac{1}{2}\left(\frac{u^2}{R}\right)^2\right) - c^2\right]\chi_2 = 0\,, \tag{16.81}$$

$$\partial_3^2\chi_3 + \left(\mu - c^2\right)\chi_3 = 0\,, \tag{16.82}$$

with $\lambda = -\frac{2mE}{\hbar^2}$.

In the next section we describe an approach to find exact quasi-analytical solutions to this problem. Following that section we will return to the perturbative approach.

16.4 Results and Discussions

As an example, we consider InAs zincblende nanowires with a rectangular cross section of side lengths: $2\varepsilon_2 = 2\varepsilon_3$ and assume the nanowire centerline length L to be much larger than the cross-sectional dimensions. The zincblende InAs stiffness components are (in units of Pa): $c_{11} = 8.33 \times 10^{10}$, $c_{12} = 4.53 \times 10^{10}$, $c_{44} = 3.96 \times 10^{10}$. For InAs [28] the effective mass is $m_{eff} = 0.022m_0$ where m_0 is the free electron mass and the conduction-band hydrostatic deformation potential $D_e = -5.1$ eV.

16.4.1 Eigenstate and Eigenenergy Changes Due to Circular Bending

In Fig. 16.3, eigenenergy changes due to strain and geometry-bending effects are plotted for a nanowire with cross-sectional side length $\varepsilon_2 = 2$ nm based on (16.80)–(16.82). The first three eigenenergy changes ΔE_β ($\beta = 1, 2, 3$) are shown in the figure as given by the relation:

$$\Delta E_\beta = -\frac{\hbar^2}{2m_{\text{eff}}}\left[\frac{1}{4R^2} + \left(\frac{\beta\pi}{2\varepsilon_2}\right)^2 - c_\beta^2\right], \tag{16.83}$$

where c_β are the corresponding first three eigenvalues c of (16.81). Note that the first term in the parenthesis of (16.83) is the geometry bending shift present *even* in

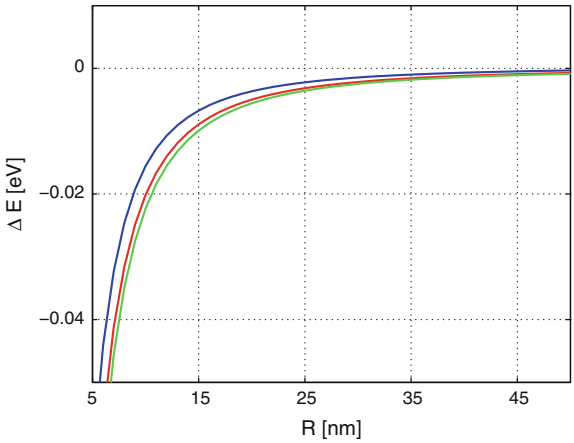

Fig. 16.3 Eigenenergy changes due to strain and geometry-bending as a function of the bending radius. The first three eigenenergy shifts are shown for a InAs zincblende nanowire with $\varepsilon_2 = 2$ nm (refer to the text for details and other parameters used in the calculations). The blue, red, and green curves correspond to the first, second, and third eigenstates, respectively. Both linear and squared contributions in u^2 are included in the strain coefficients

the absence of strain while the difference between the other two terms is the strain contribution stemming from the nanowire bending.

Evidently, the effect of strain and curvature is rather small for all three states in the range 5 nm $\leq R \leq$ 50 nm. The eigenenergy changes at $R = 15$ nm are approximately -7, -9, and -10 meV for the first, second, and third eigenstates, respectively. Clearly, the dependence on the bending radius is becoming increasingly pronounced as R decreases. This is in qualitative agreement with results obtained using perturbation theory based on the perturbation Hamiltonian H_1 in (16.76). The pure geometry bending effect, i.e., the term $-\frac{\hbar^2}{2m_{eff}}\frac{1}{4R^2}$ is small only accounting for -2 meV when $R = 15$ nm. Evidently, this term leads to significant contributions in case of large bending only. Quantitative agreement between perturbation theory results and the more accurate Frobenius method result is also found but we find no reason to show that here.

Figure 16.4 depicts the first three eigenfunctions χ_2 [see (16.81)] in the case where $\varepsilon_2 = 2$ nm. Clearly, the number of nodes along the u^2 direction is equal to the solution number minus one. As expected, parity is broken due to bending and bending-induced eigenstate asymmetry is visible as the bending radius is decreased to 5 nm. Note also that the state asymmetry is due to strain and not the pure geometry-bending effect since the geometry effect changes the potential by a constant only $(-\frac{1}{4R^2})$. The computed state changes are likely to affect optoelectronic properties only for nanorings with a large bending radius, however, at a bending radius above 50 nm, the asymmetry effect apparently becomes insignificant. A similar calculation for GaAs nanorings shows that significant asymmetries in eigenstates occur at bending radii up to 30 nm.

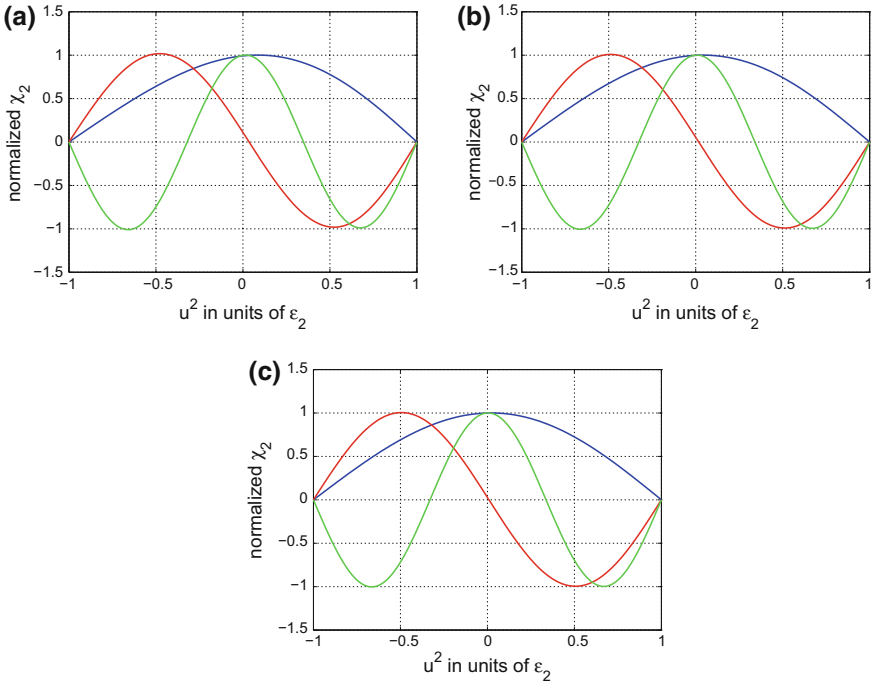

Fig. 16.4 First three χ_2 eigenfunctions as a function of the bending radius for a InAs zincblende nanowire with $\varepsilon_2 = 2$ nm (refer to the text for details and other parameters used in the calculations). The panels **a** and **b** are for a curvature radius equal to 5 and 10 nm, respectively. The blue, red, and green curves correspond to the first, second, and third eigenstates, respectively. A close inspection of the figures reveals the effect of the curvature in breaking eigenstate parity. This is most clearly seen in panel a for the first eigenstate tilted slightly to the right (blue curve)

16.5 How Are the Möbius Strips Constructed?

We consider Möbius strips that are constructed from a planar rectangle by pure bending. Mathematically such a Möbius strip forms a developable surface. It is in particular a ruled surface, i.e., it is of the form $\mathbf{x}(u, v) = \mathbf{r}(u) + v\mathbf{v}(u)$ where $\mathbf{r}$ is some curve on the surface crossing all the rulings. If we let $\mathbf{r}$ be the image of the line down the middle of the rectangle, the *median curve*, then it is a geodesic. Thus the principal normal $\mathbf{n}$ of $\mathbf{r}$ is orthogonal to the tangent plane. We have in particular that $\mathbf{v}$ it is orthogonal to $\mathbf{n}$. As the Frenet-Serret frame $\mathbf{t}$, $\mathbf{n}$, $\mathbf{b}$ is an orthonormal basis we can conclude that $\mathbf{v} = \alpha\mathbf{t} + \beta\mathbf{b}$. A ruled surface is developable if and only if $\det(\mathbf{t}, \mathbf{v}, \dot{\mathbf{v}})$ vanishes. As $\dot{\mathbf{v}} = \dot{\alpha}\mathbf{v} + \alpha\kappa\mathbf{n} + \dot{\beta}\mathbf{v} - \beta\tau\mathbf{n}$, where κ and τ is the curvature and torsion of $\mathbf{r}$ respectively, we see that we have a developable surface if and only if $\alpha\kappa = \beta\tau$. That is, we can parametrize the Möbius strip as

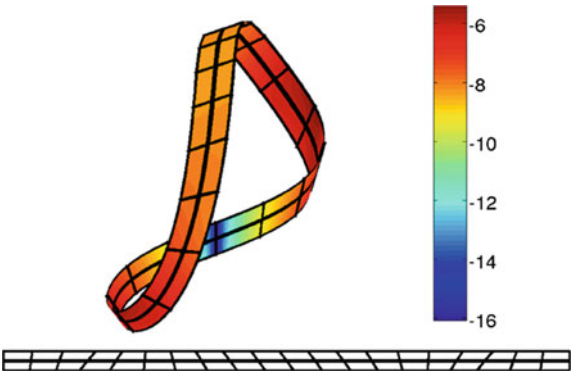

Fig. 16.5 A Möbius strip with length 200 nm and half width $w = 3.333$ nm, coloured according to $\log(M^2)$. The median curve and some of the rulings are shown on both the Möbius strip and the original planar rectangle

$$\mathbf{x}(u, v) = \mathbf{r}(u) + v\left(\mathbf{b}(u) + \frac{\tau(u)}{\kappa(u)}\mathbf{t}(u)\right), \quad v \in [-w, w], \tag{16.84}$$

where $\mathbf{r}$ is a parametrization of the median curve and w is half the width of the Möbius strip, see Fig. 16.5 and [5]. Note that the Möbius strip is completely determined by the median curve $\mathbf{r}$. The shape of the Möbius strip is determined by the bending energy which in absence of exterior forces has to be minimized. Locally the strip bends around the rulings and the energy is proportional to the square of the curvature of a section orthogonal to the ruling. One of the principal curvature is zero, $\kappa_1 = 0$, and the corresponding principal direction is in the direction of the rulings. As the principal directions are orthogonal the other principal curvature, κ_2, is exactly the curvature of a section orthogonal to the rulings. So the energy density is proportional to $\kappa_2^2 = (\kappa_1 + \kappa_2)^2 = 4M^2$, where M denotes the mean curvature. We conclude that the energy density is proportional to the square of the mean curvature. To simplify notation, we let

$$\Psi = \frac{\tau}{\kappa}, \qquad \text{and} \qquad \psi = \frac{\mathrm{d}\Psi}{\mathrm{d}s}, \tag{16.85}$$

where s denotes arc-length on the median curve. If we assume that the median curve is parametrized by arc-length, then the first and second fundamental forms of the Möbius strip are given by

$$[g_{ij}] = \begin{bmatrix} (1 + v\psi)^2 & \Psi(1 + v\psi) \\ \Psi(1 + v\psi) & 1 + \Psi^2 \end{bmatrix} \quad \text{and} \quad [b_{ij}] = \begin{bmatrix} -\kappa(1 + v\psi) & 0 \\ 0 & 0 \end{bmatrix}, \tag{16.86}$$

respectively. The mean curvature is then

$$M = \frac{\kappa}{2}\frac{1 + \Psi^2}{1 + v\psi}. \tag{16.87}$$

So the bending energy is proportional to

$$E = \frac{1}{2}\int M^2 \,\mathrm{d}A = \frac{1}{8}\int_0^L \int_{-w}^{w} \frac{\kappa^2(1+\Psi^2)^2}{1+v\psi}\,\mathrm{d}v\,\mathrm{d}s$$
$$= \frac{1}{8}\int_0^L \frac{\kappa^2(1+\Psi^2)^2}{\psi}\log\left(\frac{1+w\psi}{1-w\psi}\right)\mathrm{d}s\,, \quad (16.88)$$

where L is the length of median curve and w still is half the width of the Möbius strip. Finding the exact shape of a Möbius strip is a hard problem with a history going back to [21] where (16.88) was first written down, see [6, 7] and references therein. We do not try to minimize the energy in the space of all curves. Instead, we look at the same three parameter family of curves as in [5]. This family of curves is part of a six-parameter family of median curves of Möbius strips in [24]. The latter family was, in turn, an extension of a single Möbius strip in [25]. Some experiments revealed that the extra three parameters could be set to zero without affecting the final shape of the Möbius strip much. The family of median curves is given as

$$\mathbf{r}(u^1) = \begin{bmatrix} c_1 \sin(u^1) \\ c_2\left(\sin(u^1) - \frac{1}{2}\sin(2u^1)\right) \\ c_3\left(\frac{5}{3} - \frac{5}{2}\cos(u^1) + \cos(2u^1) - \frac{1}{6}\cos(3u^1)\right) \end{bmatrix}. \quad (16.89)$$

We do not have an arc-length parametrization so we need to change (16.85) to

$$\psi = \frac{\mathrm{d}\Psi}{\mathrm{d}s} = \frac{\mathrm{d}\Psi}{\mathrm{d}u}\frac{\mathrm{d}u}{\mathrm{d}s} = \frac{\dot{\psi}}{\|\dot{\mathbf{r}}\|}\,, \quad (16.90)$$

where $\cdot$ denotes differentiation with respect to u. We want to minimize the energy, but we also want to get a specific length and to obtain a Möbius strip without singularities. We end up with the following constrained optimization problem:

$$\underset{c_1,c_2,c_3}{\text{minimize}} \quad \int_0^{2\pi} \frac{\kappa^2(1+\Psi^2)^2}{\psi}\log\left(\frac{1+h\psi}{1-h\psi}\right)\|\dot{\mathbf{r}}\|\,\mathrm{d}u\,, \quad (16.91a)$$

such that

$$\int_0^{2\pi} \|\dot{\mathbf{r}}\|\,\mathrm{d}u = 200\,\mathrm{nm}\,, \quad (16.91b)$$
$$h\psi(u) < 1\,, \qquad u \in [0, 2\pi]\,, \quad (16.91c)$$
$$h\psi(u) > -1\,, \qquad u \in [0, 2\pi]\,. \quad (16.91d)$$

We use the MATLAB function fmincon from the optimization toolbox [26] to solve this problem. All functions are evaluated in 1000 evenly spaced points and the conditions (16.91c) and (16.91d) are only checked in these points. Similarly, the integrals are replaced by a finite sum over these 1000 points. The optimization method is gra-

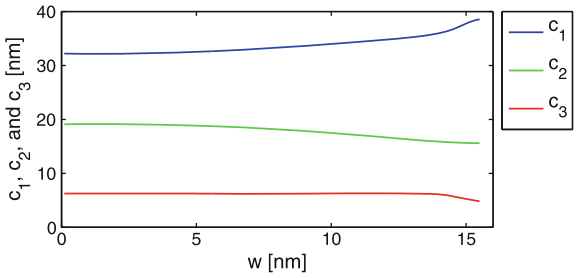

Fig. 16.6 The coefficients c_1, c_2, and c_3 as a function of half width w, with $L = 200$ nm

dient driven, so it is necessary to calculate the gradient of both the objective function (16.91a) and the constraints (16.91b)–(16.91d). This is a lengthy but straightforward calculation, which we omit here.

As a result we find the coefficients c_i shown in Fig. 16.6 for a varying set of w values. Values for different lengths of the Möbius strip are obtained by the scaling relations $\tilde{L} = KL$, $\tilde{c}_i = Kc_i$, and $\tilde{w} = Kw$, for a given scaling constant K.

16.6 Curvature Induced Potential

Consider next the one-band envelope-function equation for a conduction electron confined to a semiconductor surface Σ [27]:

$$-\frac{\hbar^2}{2m_e}\left(\Delta_0 + \partial_3^2\right)\chi(u^1,u^2) + \left[V_S(u^1,u^2,u^3) + V(u^1,u^2,u^3)\right]\chi(u^1,u^2) = E\chi(u^1,u^2)\,, \tag{16.92}$$

where m_e is the effective mass, χ is the envelope eigenfunction, and E its energy. The surface Σ is defined as the center surface corresponding to the third coordinate u^3 being zero, V_S is the deformation potential term proportional to the sum of the diagonal strain components in Cartesian coordinates, and the potential barrier term V due to material inhomogeneity is assumed to be of the infinite-barrier type, i.e.,

$$V(u^1,u^2,u^3) = \begin{cases} 0\,, & \text{if } u^3 = 0\,, \\ \infty\,, & \text{else}\,. \end{cases} \tag{16.93}$$

The details of the strain potential V_S in curvilinear coordinates u^1, u^3, u^3 are given in Sect. 16.7. The operator Δ_0 in (16.92) is [19]:

$$\Delta_0 = \Delta_\Sigma + M^2 - K\,, \tag{16.94}$$

where Δ_Σ is the Laplace-Beltrami operator on Σ, and M and K are the mean and Gaussian curvatures, respectively. In our case, M is non-zero but K is zero.

The effect of M^2 on energies is to shift eigenenergies downwards. Note that since M^2 is much smaller than Δ_Σ), it follows from first-order perturbation theory that

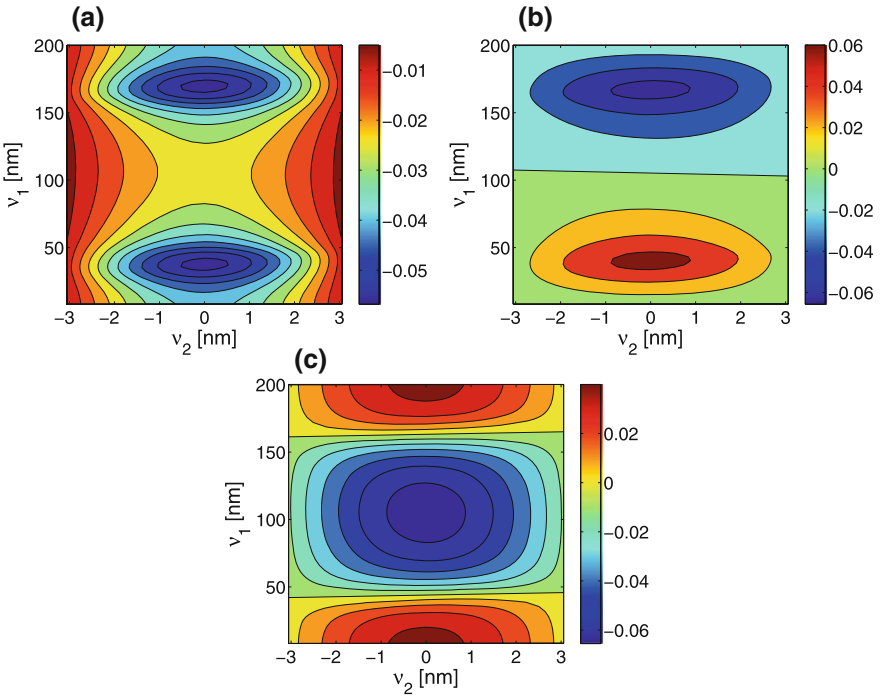

Fig. 16.7 The panels **a**, **b**, and **c** are the groundstate, the first-excited state, and the third-excited state, respectively for the Möbius strip with dimensions $w = 3.333$ nm and $L = 200$ nm. Parameters used in the calculation are given in the main text. See (16.104) for the definition of ν_1 and ν_2

Möbius structure eigenstates more or less retain the same symmetries (even or odd in the u^1 and u^2 coordinates) as the corresponding eigenstates for the flat cylinder problem even though M^2 is not an even or odd function in u^1 and u^2. This argument is only strictly valid if states are non-degenerate in the absence of the bending term, and if the energy separation between non-degenerate states is larger than the bending energy contribution.

In Fig. 16.7, we plot the first three eigenstates are found by solving (16.79) in the absence of strain effects ($V_S = 0$) using the finite-difference method. The structure considered corresponds to the parameters: $L = 200$ nm, $w = 3.333$ nm.

16.7 Möbius Strip of Finite Thickness

Next, we solve for the eigenstates and associated energies of an electron bound to a Möbius strip of finite thickness. Since it is computationally cumbersome and, for thin Möbius structure, unnecessarily expensive to solve the one-band problem in

Cartesian coordinates, it is convenient to formulate the problem in the (u^1, u^2, u^3) coordinate system, thereby reducing the complexity of the geometry to a simple box at the price of having to solve a more complicated differential equation. In Cartesian coordinates the one-band model is given by

$$-\frac{\hbar^2}{2m_{\text{eff}}}\Delta\chi + [V_S + V]\,\chi = E\chi\,. \tag{16.95}$$

The parametrization for a Möbius strip with finite thickness is given by

$$\mathbf{x}(u^1, u^2, u^3) = \mathbf{r}(u^1) + u^2\left(\mathbf{b}(u^1) + \frac{\tau(u^1)}{\kappa(u^1)}\mathbf{t}(u^1)\right) - u^3\mathbf{n}(u^1)\,, \tag{16.96}$$

so that

$$\frac{\partial\mathbf{x}}{\partial u^1} = |\mathbf{r}'(u^1)|\left((1 + u^2\psi + u^3\kappa)\mathbf{t} - u^3\tau\mathbf{b}\right), \quad \frac{\partial\mathbf{x}}{\partial u^2} = \mathbf{b} + \Psi\mathbf{t}, \quad \frac{\partial\mathbf{x}}{\partial u^3} = -\mathbf{n}\,, \tag{16.97}$$

where Frenet's relations have been used. The metric tensor is now found to be

$$\mathbf{G} = \begin{bmatrix} |\mathbf{r}'|^2\left((1 + u^2\psi + u^3\kappa)^2 + (u^3\tau)^2\right) & |\mathbf{r}'|\Psi\,(1+\psi) & 0 \\ |\mathbf{r}'|\Psi\,(1+\psi) & 1 + \Psi^2 & 0 \\ 0 & 0 & 1 \end{bmatrix}. \tag{16.98}$$

Further on,

$$G = |\mathbf{r}'|^2\left[\left(1 + u^2\psi + u^3\kappa\right)^2 + 2(u^3\tau)^2 + 2u^3\kappa\Psi^2\,(1+\psi) + \left(\frac{u^3\tau^2}{\kappa}\right)^2\right], \tag{16.99}$$

and

$$\mathbf{G}^{-1} = \frac{1}{G}\begin{bmatrix} 1 + \Psi^2 & -|\mathbf{r}'|\Psi\,(1+\psi) & 0 \\ -|\mathbf{r}'|\Psi\,(1+\psi) & |\mathbf{r}'|^2\left((1 + u^2\psi + u^3\kappa)^2 + (u^3\tau)^2\right) & 0 \\ 0 & 0 & G \end{bmatrix}. \tag{16.100}$$

It is clear from the expression of the metric tensor, that the problem is not separable in any of the three coordinates u^1, u^2, u^3. However, it is possible, for small thicknesses, to carry out a perturbative analysis in terms of the effective-mass equation that couples the Möbius thickness coordinate u^3 to the other two coordinates u^1, u^2. Then, the unperturbed three-dimensional problem is separable in one coordinate and decouples into a two-dimensional problem in u^1, u^2 and a one-dimensional problem in u^3.

As the electron is completely confined to the Möbius strip, Dirichlet conditions $\chi = 0$ are invoked at the boundary:

$$\chi(u^1, u^2 = \pm w, u^3) = \chi(u^1, u^2, u^3 = \pm h) = 0\,, \tag{16.101}$$

and since the Möbius strip is rotated by 180° during one revolution along the median line defined by $u^2 = u^3 = 0$, anti-periodic boundary conditions are imposed at the u^1 end surfaces:

$$\chi(u^1 = 0, u^2, u^3) = \chi(u^1 = 2\pi, -u^2, -u^3)\,. \tag{16.102}$$

16.7.1 Inclusion of Strain

As before, this effect is included in its simplest form by a hydrostatic deformation potential of the form [29]

$$V_S = a_c \mathrm{Tr}(\varepsilon)\,, \tag{16.103}$$

where a_c is the deformation potential, ε is the strain tensor, and Tr denotes the trace. Since the (u^1, u^2, u^3) coordinate system has been chosen solely based on the convenience of the domain, it is less convenient to use the (u^1, u^2, u^3) coordinate system as a reference configuration in the calculation of the strain. A more useful coordinate system, (v_1, v_2, v_3), is parametrized as follows:

$$v_1 = \int_0^{u^1} |\mathbf{r}'(s)| ds + u^2 \Psi, \quad v_2 = u^2, \text{ and } v_3 = u^3\,. \tag{16.104}$$

In this coordinate system, the Möbius strip is given by the natural domain $[0, L] \times [-w, w] \times [-h, h]$ where L is the length of median curve. This choice of reference configuration is made since the flat nanostrip is neither stretched nor compressed when deformed into the Möbius strip by the deformation $\mathbf{R}(v_1, v_2, v_3) = \mathbf{x}(u^1(v_1, v_2), v_2, v_3)$. Given the deformation $\mathbf{R}$, the strain tensor becomes

$$\varepsilon_{ij} = \frac{1}{2}\left(\delta_{ij} - \frac{\partial \mathbf{R}}{\partial v_i} \cdot \frac{\partial \mathbf{R}}{\partial v_j}\right) = \frac{1}{2}\left(\delta_{ij} - \sum_{k,l=1}^{3} \frac{\partial u_k}{\partial v_i} \frac{\partial \mathbf{x}}{\partial u_k} \cdot \frac{\partial u_l}{\partial v_j} \frac{\partial \mathbf{x}}{\partial u_l}\right)\,. \tag{16.105}$$

16.8 Results

In this section the energies and eigenstates are studied as a function of the width, thickness, and length of the Möbius strip with emphasis on the effect of inclusion of strain in the calculations. The Möbius strip considered here is made of InAs, but similar results would be obtained with other choices of material.

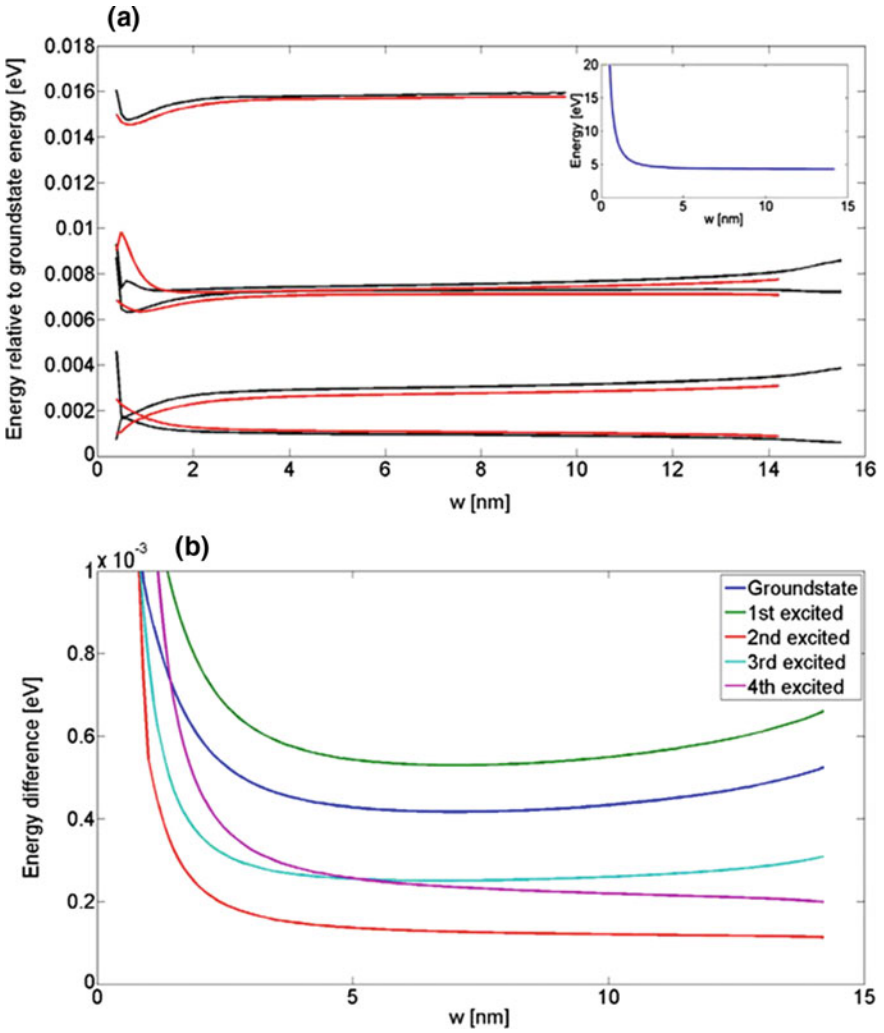

Fig. 16.8 Panel **a** shows the energy difference relative to the ground state energy both for the case including strain (dashed blue lines) and the case disregarding strain (solid black lines). Panel **b** shows the difference in energy between a model with strain and a model without strain. In both panels the length and thickness of the Möbius strip are 200 and 2 nm, respectively

In the inset of Fig. 16.8a the groundstate energy as a function of width is shown for a 200 nm long and 2 nm thick Möbius strip. As expected, the energies decrease as the width is increased, due to electron confinement effects.

In Fig. 16.8a the energy differences relative to the groundstate energy are also shown. The eigenstates are very close in energy. This is due to the relatively large length of the Möbius strip. This fact is most readily illustrated by plotting the energies as a function of length of the Möbius strip, see Fig. 16.9. In this figure it is clearly

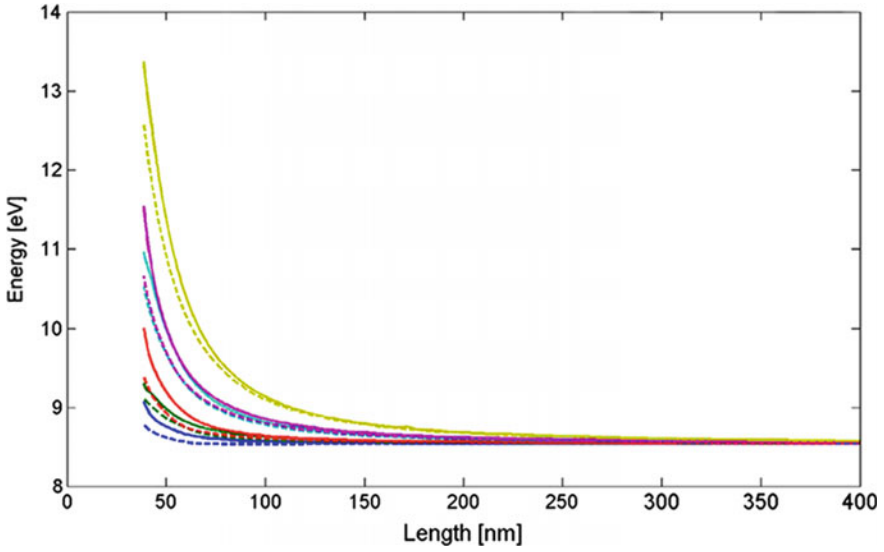

Fig. 16.9 The first 6 eigenenergies for a model with strain (solid lines) and a model without strain (dashed lines) as a function of the length of the Möbius strip. In the plots the width and thickness of the Möbius strip are 6 and 2 nm, respectively

seen that the level spacing increases as the length of the Möbious strip is decreased. In Fig. 16.8b the energy difference is shown between a model with strain relative to a model without strain. Strain only has a minor influence on the electron energies. This is in agreement with results from paper [17].

In Fig. 16.8b it is furthermore observed that the first and second excited states cross at the width of 2 nm. This can also be seen in the symmetries of the wave-functions shown in Fig. 16.10, where in the left column the first excited state is shown for different widths and in the right column the second excited state is shown. In all plots the wave-function are given as a function of v^1 and v^2 at $v^3 = 0$.

In Fig. 16.11, the influence of the thickness on the electron energies is studied. The energy decreases as the thickness is increased due to a decrease in the confinement of the electron. More interestingly, it is seen that the impact of strain on the eigenenergies increases as the thickness is increased. The reason is that the strain due to bending in the structure increases nearly linearly as a function of the thickness. This is seen in Fig. 16.12, where the hydrostatic strain is shown as a function of v^1 and v^3 at $v^2 = 0$. This can also been seen from the approximate result based on the Euler beam theory, where bending strain is given by ku^3 to the first order in the curvature [similarly to (16.70)].

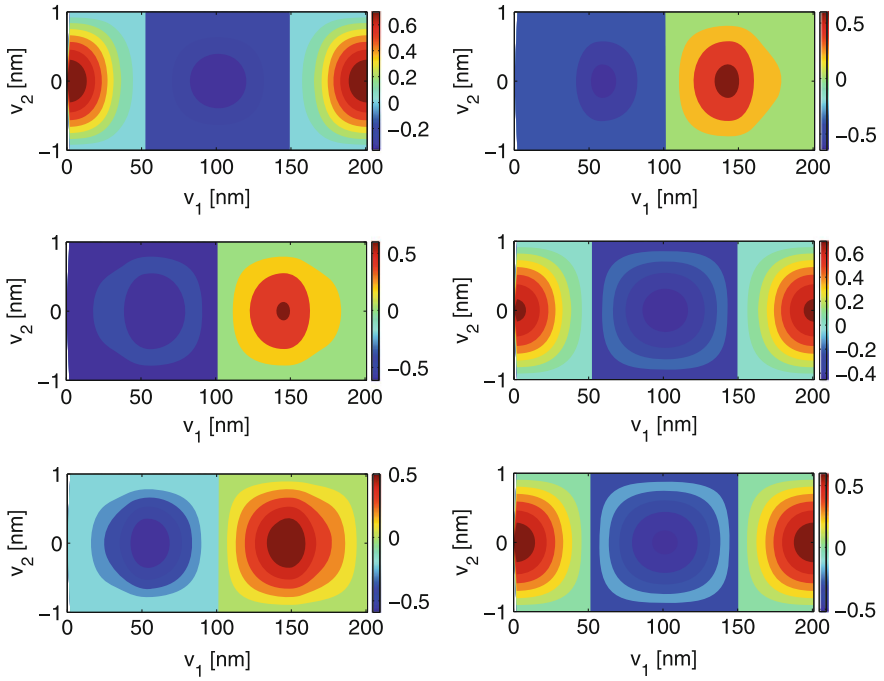

Fig. 16.10 The left and right column shows the first and second excited state, respectively. The upper row wave functions have a width of 1.6 nm, the middle row wave functions have a width of 2 nm, and the lower row wave functions have a width of 2.4 nm. In all plots the length and thickness of the Möbius strip is 200 and 2 nm, respectively, and all plots are given as functions of v^1 and v^2 with $v^3 = 0$

16.9 Phonon Dynamics in Ring Structures

We shall next determine the governing equations of the acoustic phonon modes of ring structures where one dimension, the thickness, is very small. This assumption (shell problem) is excellently fulfilled for 2D materials such as graphene. In the following, consider a parametrization $(\xi, \eta) \mapsto \mathbf{x}(\xi, \eta)$ of the *middle surface* of a shell structure. If $\mathbf{N}$ is the unit normal, then the parametrization by tubular coordinates is

$$\mathbf{X}(\xi, \eta, \zeta) = \mathbf{x}(\xi, \eta) + \zeta\, \mathbf{N}(\xi, \eta)\,. \tag{16.106}$$

For $\alpha, \beta \in \{1, 2\}$ the metric coefficients are

$$\begin{aligned} G_{\alpha,\beta} &= \mathbf{X}_\alpha \cdot \mathbf{X}_\beta = \mathbf{x}_\alpha \cdot \mathbf{x}_\beta + \zeta(\mathbf{x}_\alpha \cdot \mathbf{N}_\beta + \mathbf{N}_\alpha \cdot \mathbf{x}_\beta) + \zeta^2 \mathbf{N}_\alpha \cdot \mathbf{N}_\beta \\ &= g_{\alpha,\beta} - 2\zeta\, b_{\alpha,\beta} + \zeta^2 c_{\alpha,\beta} = g_{\alpha,\beta} - 2\zeta\, b_{\alpha,\beta} + \zeta^2(2H b_{\alpha,\beta} - K g_{\alpha,\beta})\,, \end{aligned} \tag{16.107}$$

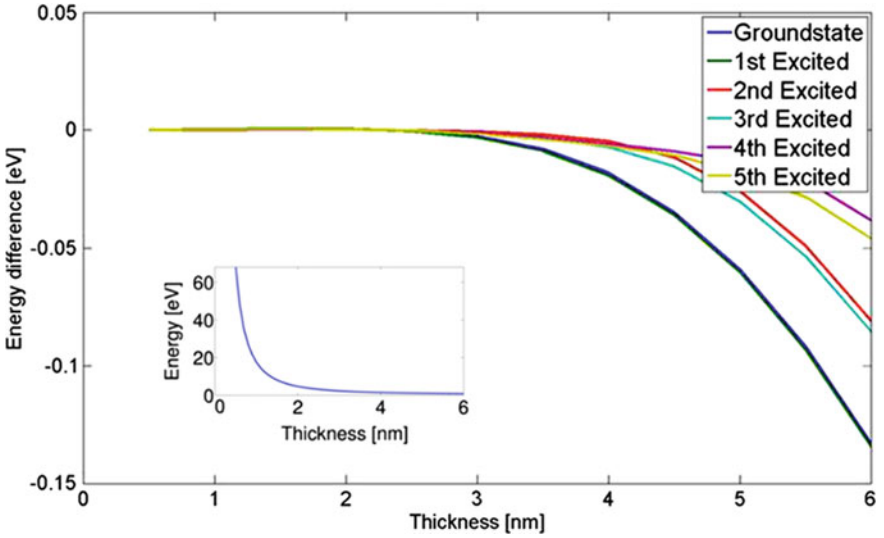

Fig. 16.11 Difference in energies between a model with strain and a model without strain as a function of the thickness of the Möbius strip. The inset shows the groundstate energy as a function of thickness using a model with strain. In the plots the length and thickness of the Möbius strip are 200 and 2 nm, respectively

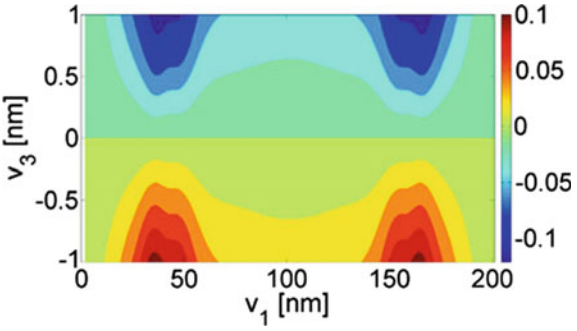

Fig. 16.12 The hydrostatic strain distribution as a function of v^1 and v^3 at $v^2 = 0$ for the Möbius strip with length of 200 nm, width of 2 nm, and thickness of 2 nm

where $g_{\alpha,\beta}$, $b_{\alpha,\beta}$, and $c_{\alpha,\beta}$ are the components of the first, second, and third fundamental form, respectively and H and K are the mean and Gaussian curvature. The full 3D metric tensor is

$$G = \begin{pmatrix} g_{11} - 2\zeta b_{11} + \zeta^2 c_{11} & g_{12} - 2\zeta b_{12} + \zeta^2 c_{12} & 0 \\ g_{21} - 2\zeta b_{11} + \zeta^2 c_{21} & g_{22} - 2\zeta b_{22} + \zeta^2 c_{12} & 0 \\ 0 & 0 & 1 \end{pmatrix} = \begin{pmatrix} (1 - \zeta^2 K) g_{\alpha\beta} - 2(\zeta - \zeta^2 H^2) b_{\alpha\beta} & 0 \\ 0 & 1 \end{pmatrix}. \tag{16.108}$$

Using shell theory [30] the three dimensional strain is described by a two dimensional strain tensor $E_{\alpha,\beta} = \frac{1}{2}(g^*_{\alpha\beta} - g_{\alpha\beta})$ and a bending tensor $K_{\alpha,\beta} = b^*_{\alpha\beta} - b_{\alpha\beta}$, where * denotes the deformed shell. That is, the 3D strain is given by

$$(\varepsilon_{ij}) = \begin{pmatrix} (1-\zeta^2 K)E_{\alpha\beta} - (\zeta - \zeta^2 H)K_{\alpha\beta} & 0 \\ 0 & 0 \end{pmatrix}, \quad i, j \in \{1, 2, 3\}. \tag{16.109}$$

Observe, that it is assumed that there is no strain in the normal direction.

Consider next the application to shells where the Gaussian curvature vanishes. Important examples include the round cylinder and the Möbius structure. If we ignore terms of order h/R and h^2/L^2, where h is the thickness of the shell, R is the minimal principal curvature, and L is a characteristic wave-length of the deformation pattern, then we obtain a simple form of the energy for a graphene single-layer sheet of symmetry $D_{6h} \equiv 6/mmm$ [30, (7.8)]:

$$\begin{aligned} W = {} & \frac{h}{2}\left((c_{11} - c_{12})E^\beta_\alpha E^\alpha_\beta + c_{12}E^\alpha_\alpha E^\beta_\beta\right) \\ & + \frac{h^3}{24}\left((c_{11} - c_{12})K^\beta_\alpha K^\alpha_\beta + c_{12}K^\alpha_\alpha K^\beta_\beta\right). \end{aligned} \tag{16.110}$$

As we consider deformations of a shell in pure bending, we can introduce the basis $(\mathbf{e}_1, \mathbf{e}_2, \mathbf{e}_3) = (\mathbf{x}_1, \mathbf{x}_2, \mathbf{N})$, where $\mathbf{N} = \mathbf{x}_1 \times \mathbf{x}_2$. As $\mathbf{x}_\alpha \cdot \mathbf{x}_\beta = \delta_{\alpha\beta}$ we have

$$\mathbf{x}_{\alpha\beta} \cdot \mathbf{x}_\gamma = 0, \qquad \mathbf{x}_{\alpha\beta} = b_{\alpha\beta}\mathbf{N}, \qquad \mathbf{N}_\gamma = -b_{1\gamma}\mathbf{e}_1 - b_{2\gamma}\mathbf{e}_2. \tag{16.111}$$

We can write a deformation of the shell as

$$\mathbf{y} = \mathbf{x} + u^i\mathbf{e}_i = \mathbf{x} + u\mathbf{e}_1 + v\mathbf{e}_2 + w\mathbf{N}, \tag{16.112}$$

where $(u^1, u^2, u^3) = (u, v, w)$. To first order in u^i we have

$$\mathbf{y}_\alpha = \mathbf{x}_\alpha + u^\gamma_\alpha\mathbf{e}_\gamma + u^\gamma\mathbf{x}_{\alpha\gamma} + w_\alpha\mathbf{N} + w\mathbf{N}_\alpha, \tag{16.113}$$

$$g^*_{\alpha\beta} = g_{\alpha\beta} + u^\alpha_\beta + u^\beta_\alpha - 2wb_{\alpha\beta}, \tag{16.114}$$

$$\begin{aligned} \mathbf{y}_1 \times \mathbf{y}_2 &= (1 + u_1 + v_2 - wb_{11} - wb_{22})\mathbf{N} - (u^\gamma b_{1\gamma} + w_2)\mathbf{e}_1 - (u^\gamma b_{2\gamma} + w_1)\mathbf{e}_2, \\ |\mathbf{y}_1 \times \mathbf{y}_2|^{-1} &= 1 - u_1 - v_2 + wb_{11} + wb_{22}, \\ \mathbf{N}^* &= \mathbf{N} - (u^\gamma b_{1\gamma} + w_2)\mathbf{e}_1 - (u^\gamma b_{2\gamma} + w_1)\mathbf{e}_2, \\ \mathbf{y}_{\alpha\beta} &= (b_{\alpha\beta} + u^\gamma_\alpha b_{\beta\gamma} + u^\gamma_\beta b_{\alpha\gamma} + u^\gamma b_{\alpha\beta;\gamma} + w_{\alpha\beta} - wb_{1\alpha}b_{1\beta} - wb_{2\alpha}b_{2\beta})\mathbf{N} \\ &\quad + (u_{\alpha\beta} - u^\gamma b_{\alpha\beta}b_{1\gamma} - w_\alpha b_{1\beta} - w_\beta b_{1\alpha} - w(b_{1\alpha;\beta})\mathbf{e}_1 \\ &\quad + (u_{\alpha\beta} - u^\gamma b_{\alpha\beta}b_{2\gamma} - w_\alpha b_{2\beta} - w_\beta b_{2\alpha} - w(b_{2\alpha;\beta})\mathbf{e}_2, \end{aligned} \tag{16.115}$$

$$b^*_{\alpha\beta} = b_{\alpha\beta} + u^\gamma_\alpha b_{\beta\gamma} + u^\gamma_\beta b_{\alpha\gamma} + u^\gamma b_{\alpha\beta;\gamma} + w_{\alpha\beta} - wb_{1\alpha}b_{1\beta} - wb_{2\alpha}b_{2\beta}. \tag{16.116}$$

We see that

$$(E_{\alpha\beta}) = \begin{pmatrix} u_1 & \frac{u_2+v_1}{2} \\ \frac{u_2+v_1}{2} & v_2 \end{pmatrix} - w \begin{pmatrix} b_{11} & b_{12} \\ b_{21} & b_{22} \end{pmatrix}, \tag{16.117}$$

$$K_{\alpha\beta} = u^\gamma_\alpha b_{\beta\gamma} + u^\gamma_\beta b_{\alpha\gamma} + u^\gamma b_{\alpha\beta;\gamma} + w_{\alpha\beta} - w b_{1\alpha} b_{1\beta} - w b_{2\alpha} b_{2\beta}\,. \tag{16.118}$$

As

$$K^\beta_\alpha K^\alpha_\beta = K^2_{11} + 2K^2_{12} + K^2_{22}\,, \qquad K^\alpha_\alpha K^\beta_\beta = K^2_{11} + 2K_{11}K_{22} + K^2_{22}\,,$$

and similar for $E_{\alpha\beta}$, (16.117) reads

$$\begin{aligned} W = {} & \frac{h}{2}\left(c_{11}\left(E^2_{11} + 2E^2_{12} + E^2_{22}\right) + 2c_{12}\left(E_{11}E_{22} - E^2_{12}\right)\right) \\ & + \frac{h^3}{24}\left(c_{11}\left(K^2_{11} + 2K^2_{12} + K^2_{22}\right) + 2c_{12}\left(K_{11}K_{22} - K^2_{12}\right)\right). \end{aligned} \tag{16.119}$$

16.10 The Round Cylinder Shell

Consider now a round cylinder with radius R. We then have

$$\mathbf{x}(u,v) = \left(R\,\cos\frac{u}{R}, R\,\sin\frac{u}{R}, v\right), \quad \mathbf{N}(u,v) = \left(\cos\frac{u}{R}, \sin\frac{u}{R}, 0\right), \tag{16.120}$$

$$g_{\alpha\beta} = \begin{pmatrix} 1 & 0 \\ 0 & 1 \end{pmatrix}, \qquad b_{\alpha\beta} = -\frac{1}{R}\begin{pmatrix} 1 & 0 \\ 0 & 0 \end{pmatrix}, \tag{16.121}$$

$$E_{\alpha\beta} = \begin{pmatrix} u_1 + \frac{w}{R} & \frac{u_2+v_1}{2} \\ \frac{u_2+v_1}{2} & v_2 \end{pmatrix}, \qquad K_{\alpha\beta} = \begin{pmatrix} 2\frac{u_1}{R} + w_{11} - \frac{w}{R^2} & \frac{u_2}{R} + w_{12} \\ \frac{u_2}{R} + w_{12} & w_{22} \end{pmatrix}. \tag{16.122}$$

So the energy density is

$$\begin{aligned} W = {} & \frac{h}{2}\left(c_{11}\left(\left(u_1 + \frac{w}{R}\right)^2 + 2\frac{(u_2+v_1)^2}{4} + v_2^2\right)\right. \\ & \left. + 2c_{12}\left(\left(u_1 + \frac{w}{R}\right)v_2 - \frac{(u_2+v_1)^2}{4}\right)\right) \\ & + \frac{h^3}{24}\left(c_{11}\left(\left(2\frac{u_1}{R} + w_{11} - \frac{w}{R^2}\right)^2 + 2\left(\frac{u_2}{R} + w_{12}\right)^2 + w_{22}^2\right)\right. \\ & \left. + 2c_{12}\left(\left(2\frac{u_1}{R} + w_{11} - \frac{w}{R^2}\right)w_{22} - \left(\frac{u_2}{R} + w_{12}\right)^2\right)\right). \end{aligned} \tag{16.123}$$

The total elastic energy is

$$\mathscr{E} = \int_0^L \int_{-d}^{d} W \,\mathrm{d}\eta \,\mathrm{d}\xi \,. \tag{16.124}$$

The elastic energy variation is

$$\begin{aligned}
\delta\mathscr{E} = \int_0^L \int_{-d}^{d} h\Bigg(& c_{11}\left(\left(u_1+\frac{w}{R}\right)\left(\delta u_1+\frac{\delta w}{R}\right)+\frac{(u_2+v_1)(\delta u_2+\delta v_1)}{2}+v_2\delta v_2\right)\\
& +2c_{12}\left(v_2\left(\delta u_1+\frac{\delta w}{R}\right)+\left(u_1+\frac{w}{R}\right)\delta v_2-\frac{(u_2+v_1)(\delta u_2+\delta v_1)}{4}\right)\Bigg)\\
& +\frac{h^3}{12}\Bigg(c_{11}\left(\left(2\frac{u_1}{R}+w_{11}-\frac{w}{R^2}\right)\left(2\frac{\delta u_1}{R}+\delta w_{11}-\frac{\delta w}{R^2}\right)\right.\\
& \left.+2\left(\frac{u_2}{R}+w_{12}\right)\left(\frac{\delta u_2}{R}+\delta w_{12}\right)+w_{22}\delta w_{22}\right)\\
& +2c_{12}\Bigg(w_{22}\left(2\frac{\delta u_1}{R}+\delta w_{11}-\frac{\delta w}{R^2}\right)+\left(2\frac{u_1}{R}+w_{11}-\frac{w}{R^2}\right)\delta w_{22}\\
& -\left(\frac{u_2}{R}+w_{12}\right)\left(\frac{\delta u_2}{R}+\delta w_{12}\right)\Bigg)\Bigg)\mathrm{d}\eta\,\mathrm{d}\xi.
\end{aligned}$$

Upon performing partial integrations in η and ξ and collecting terms, we obtain

$$\begin{aligned}
= & \int_0^L \Bigg[h\left((c_{11}-c_{12})\frac{u_2+v_1}{2}\delta u+\left(c_{11}v_2+2c_{12}\left(u_1+\frac{w}{R}\right)\right)\delta v\right)\\
& +\frac{h^3}{12}\Bigg(\frac{2}{R}(c_{11}-c_{12})\left(\frac{u_2}{R}+w_{12}\right)\delta u\\
& -2\left(c_{11}\left(\frac{u_{12}}{R}+w_{112}+\frac{w_{222}}{2}\right)+c_{12}\left(\frac{u_{12}}{R}-\frac{w_2}{R^2}\right)\right)\delta w\\
& +\left(c_{11}w_{22}+2c_{12}\left(2\frac{u_1}{R}+w_{11}-\frac{w}{R^2}\right)\right)\delta w_2\Bigg)\Bigg]_{-d}^{d}\mathrm{d}\xi\\
& +\int_0^L\int_{-d}^{d} h\Bigg(c_{11}\left(-\left(\frac{2u_{11}+u_{22}+v_{12}}{2}+\frac{w_1}{R}\right)\delta u-\frac{u_{12}+v_{11}+2v_{22}}{2}\delta v\right.\\
& \left.+\left(\frac{u_1}{R}+\frac{w}{R^2}\right)\delta w\right)\\
& +2c_{12}\left(\frac{u_{22}-3v_{12}}{4}\delta u-\left(\frac{3u_{12}}{4}-\frac{v_{11}}{4}+\frac{w_2}{R}\right)\delta v+\frac{v_2}{R}\delta w\right)\Bigg)\\
& +\frac{h^3}{12}\Bigg(c_{11}\left(-\frac{2}{R}\left(\frac{2u_{11}-u_{22}}{R}-\frac{w_1}{R^2}+w_{111}-w_{122}\right)\delta u\right.
\end{aligned}$$

$$+\left(-2\frac{u_1}{R^3}+2\frac{u_{122}}{R}+\frac{w}{R^4}-\frac{w_{11}}{R^2}+2\frac{u_{111}}{R}-\frac{w_{11}}{R^2}+w_{1111}+2w_{1122}+w_{2222}\right)\delta w\Big)$$
$$+2c_{12}\left(+\left(\frac{u_{22}}{R^2}+3\frac{w_{122}}{R}\right)\delta u-3\left(\frac{u_{122}}{R}+w_{1122}\right)\delta w\right)\Big)\mathrm{d}\eta\,\mathrm{d}\xi\,.$$

We can read off the equations of motions from the domain integral by equating the coefficients to $\delta u, \delta v, \delta w$ to $h\rho$ times the second t-derivative of u, v, and w, respectively:

$$\rho\frac{\partial^2 u}{\partial t^2}=c_{11}\left(\frac{2u_{11}+u_{22}+v_{12}}{2}+\frac{w_1}{R}\right)-c_{12}\frac{u_{22}-3v_{12}}{2}$$
$$+\frac{h^2}{6}c_{11}\left(\frac{2u_{11}-u_{22}}{R^2}-\frac{w_1}{R^3}+\frac{w_{111}-w_{122}}{R}\right)$$
$$-\frac{h^2}{6}c_{12}\left(\frac{u_{22}}{R^2}+3\frac{w_{122}}{R}\right), \tag{16.125}$$
$$\rho\frac{\partial^2 v}{\partial t^2}=c_{11}\frac{u_{12}+v_{11}+2v_{22}}{2}+c_{12}\left(\frac{3u_{12}-v_{11}}{2}+\frac{2w_2}{R}\right), \tag{16.126}$$
$$\rho\frac{\partial^2 w}{\partial t^2}=-c_{11}\left(\frac{u_1}{R}+\frac{w}{R^2}\right)-2c_{12}\frac{v_2}{R}-\frac{h^2}{12}c_{11}\Big(-2\frac{u_1}{R^3}+2\frac{u_{122}}{R}$$
$$+\frac{w}{R^4}-\frac{w_{11}}{R^2}+2\frac{u_{111}}{R}-\frac{w_{11}}{R^2}+w_{1111}+2w_{1122}+w_{2222}\Big)$$
$$+\frac{h^2}{2}c_{12}\left(\frac{u_{122}}{R}+w_{1122}\right), \tag{16.127}$$

and, similarly, the boundary conditions are obtained from the boundary integral by setting all coefficients to δu, δv, δw, and δw_2 to zero:

$$\left(3+\frac{h^2}{R^2}\right)u_2+3v_1+\frac{h^2}{R}w_{12}=0, \tag{16.128}$$
$$2c_{12}u_1+c_{11}v_2+\frac{2c_{12}}{R}w=0, \tag{16.129}$$
$$\frac{c_{11}+c_{12}}{R}u_{12}-\frac{c_{12}}{R}w_2+c_{11}w_{112}+\frac{c_{12}}{2}w_{222}=0, \tag{16.130}$$
$$\frac{4c_{12}}{R}u_1-\frac{2c_{12}}{R^2}w+2c_{12}w_{11}+c_{11}w_{22}=0. \tag{16.131}$$

16.11 Calculation of Acoustic Phonon Frequencies for a Cylinder-Shaped Graphene Sheet

Upon assuming general solutions

$$u=U_0\exp\left(i\omega t-ik\xi\right), \tag{16.132}$$

$$v = V_0 \exp\left(i\omega t - ik\xi\right), \tag{16.133}$$

$$w = W_0 \exp\left(i\omega t - ik\xi\right), \tag{16.134}$$

insertion into (16.125)–(16.127) leads to a 3×3 matrix equation in U_0, V_0, W_0. By solving the secular equation we find the dispersion curves of the acoustic phonon modes along the ξ direction. The following physical parameters of single-layer graphene are used [31]: $c_{11}h = 345$ Pa m, $c_{12}h = 73$ Pa m, $h = 3.4 \times 10^{-10}$ m, and $h\rho = 7.61 \times 10^{-7}$ kg/m^2. Three solutions exist for positive eigenfrequencies ω for each k value. In Fig. 16.13, solid lines are for a cylinder radius-of-curvature equal to 1 m (upper plots) and 1×10^{-6} m (lower plots), respectively. In both plots, we show for comparison the case of a flat graphene sheet (dashed lines). Evidently, for the

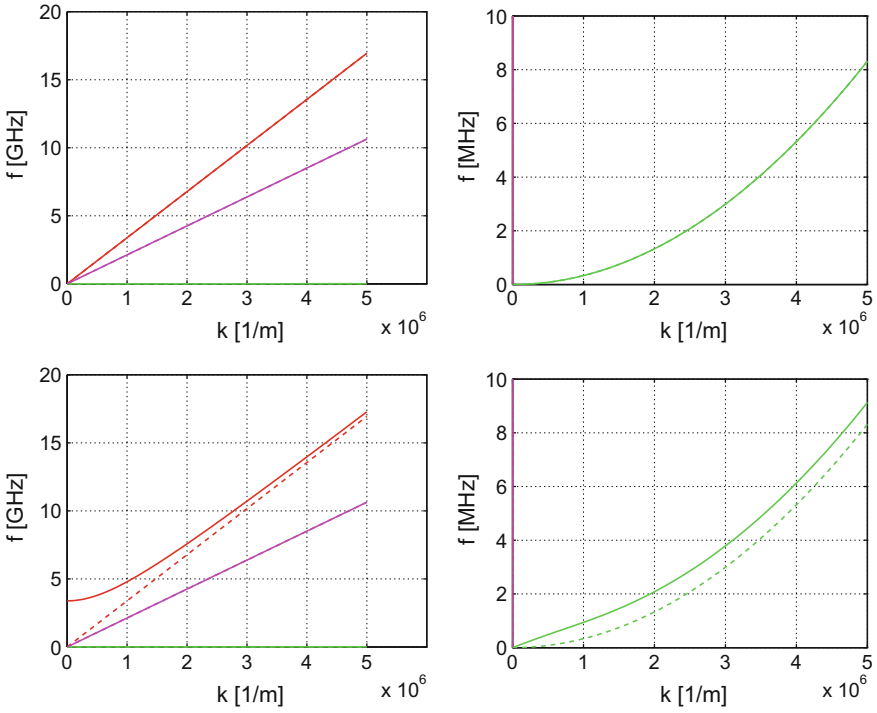

Fig. 16.13 The three acoustic phonon frequencies $f = \omega/(2\pi)$ as a function of the wavenumber component k along the cylinder ξ coordinate for a cylinder-shaped graphene sheet. The upper plots are for a cylinder radius-of-curvature R equal to 1 m while the lower plots correspond to $R = 1 \times 10^{-6}$ m. The right plots are zoomed in versions of the left plots to show the nonlinear dependence on k for the lowest mode. We point to that the case $R = \infty$ is equivalent to the flat graphene-sheet case. Three eigenfrequencies are found and plotted as solid lines while the dashed lines are for a flat graphene sheet. Parameters used are $c_{11}h = 345$ Pa m, $c_{12}h = 73$ Pa m, $h = 3.4 \times 10^{-10}$ m, and $h\rho = 7.61 \times 10^{-7}$ kg/m^2

upper plot case the radius-of-curvature R is so high compared to the graphene sheet thickness h that the eigenfrequencies are almost the same as for the flat graphene sheet case. We also note that, for the flat graphene-sheet case, there is one mode displaying a parabolic dispersion ($E \propto k^2$) due to the w_{1111} term in the equation-of-motion for w. The other two modes are linear ($E \propto k$) if the graphene sheet is flat. These characteristics are in perfect agreement with experimental and DFT results for phonon modes of graphene [31]. Finally, we clearly see a mode with a non-zero phonon frequency at $k = 0$ when $R = 1 \times 10^{-6}$ m. This mode corresponds to vibrations along the w direction and it follows directly from (16.127) that the associated eigenfrequency is given by

$$\omega(k = 0) = \sqrt{\frac{c_{11}}{\rho}} \sqrt{1 + \frac{1}{12} \frac{h^2}{R^2}} \frac{1}{R}. \tag{16.135}$$

16.12 Conclusion

Analytical and simple computational differential geometry methods applicable to curved nanostructures are presented and applied to geometries which cannot be solved analytically nor computationally effective using standard coordinate systems. Test cases of experimental interest are computed for electronic eigenstates of circular and elliptic nanorings as well as Möbius nanostructures, and it is shown that for bending radii of a few nanometers, significant changes in eigenstate symmetry properties and eigenenergy values exist due to curvature and strain effects affecting physical properties. At bending radii above approximately 50 nm, curvature effects are, however, negligible. A detailed study of a complicated geometry structures, the Möbius nanostructure, is discussed next. Consequences of curvature, strain, and Möbius nanostructure length, width, and thickness are assessed for electron eigenstates. In the Second Edition of the chapter, a derivation of the elastic energy for a thin shell using a differential-geometric formulation is added and we use it to determine the dynamic elastic equations for a cylinder-shaped nanostructure shell. We then compute, for 2D single-layer graphene, phonon dispersion curves and discuss differences between the flat- and cylinder-shaped graphene single-atomic layer cases. The method can be extended to the study of phonon dynamics of a Möbius-shaped graphene 2D layer following a similar procedure.

References

1. S. Tanda, T. Tsuneta, Y. Okajima, K. Inagaki, K. Yamaya, N. Hatekenaka, Nature (London) **417**, 397 (2002)
2. M. König, S. Wiedmann, C. Brüne, A. Roth, H. Buhmann, L.W. Molenkamp, X.L. Qi, S.C. Zhang, Science **318**, 766 (2008)

3. Y. Ran, Y. Zhang, A. Vishwanath, Nat. Phys. **5**, 298 (2009)
4. Z.L. Guo, Z.R. Gong, H. Dong, C.P. Sun, Phys. Rev. B **80**, 195310 (2009)
5. J. Gravesen, M. Willatzen, Phys. Rev. A **72**, 032108 (2005)
6. E.L. Starostin, G.H.M. van der Heijden, Nat. Mater. **6**, 563 (2007)
7. E.L. Starostin, G.H.M. van der Heijden, Phys. Rev. B **79**, 066602 (2009)
8. D.J. Ballon, H.U. Voss, Phys. Rev. Lett. **101**, 247701 (2008)
9. M. Yoneya, K. Kuboki, M. Hayashi, Phys. Rev. B **78**, 064419 (2008)
10. C. Rockstuhl, C. Menzel, T. Paul, F. Lederer, Phys. Rev. B **79**, 035321 (2009)
11. N. Zhao, H. Dong, S. Yang, C.P. Sun, Phys. Rev. B **79**, 125440 (2009)
12. Z. Li, L.R. Ram-Mohan, Phys. Rev. B **85**, 195438 (2012)
13. V.M. Fomin, S. Kiravittaya, O.G. Schmidt, Phys. Rev. B **86**, 195421 (2012)
14. K.S. Novoselov, A.K. Geim, S.V. Morozov, D. Jiang, Y. Zhang, S.V. Dubonos, I.V. Gregorieva, A.A. Firsov, Science **306**, 666 (2004)
15. C. Lee, X.D. Wei, J.W. Kysar, J. Hone, Science **382**, 385 (2008)
16. A.K. Geim, K.S. Novoselov, Nat. Mater. **6**, 183 (2007)
17. B. Lassen, M. Willatzen, J. Gravesen, J. Nanoelectron. Optoelectron. **6**, 68 (2011)
18. J. Gravesen, M. Willatzen, Phys. B **371**, 112–119 (2006)
19. J. Gravesen, M. Willatzen, L.C. Lew Yan Voon, J. Math. Phys. **46**, 012107 (2005)
20. L.D. Landau, E.M. Lifshitz, *Theory of Elasticity* Volume 7 of Course of Theoretical Physics, 3rd edn. (Butterworth Heinemann, Oxford, 1999)
21. M. Sadowski, *Verh. 3. Kongr. Techn. Mechanik* **II**, 444–451 (1930)
22. E.O. Kane, J. Phys. Chem. Solids **1**, 249 (1957)
23. P.Y. Yu, M. Cardona, *Fundamentals of Semiconductors*, 4th edn. (Springer, Berlin, 2010)
24. T. Randrup, P. Røgen, Arch. Math. **66**, 511 (1996)
25. G. Schwarz, Pac. J. Math. **143**, 195 (1990)
26. MATLAB version 7.8.0. (The MathWorks Inc., Natick, Massachusetts, 2009)
27. L.C. Lew Yan Voon, M. Willatzen, *The $k \cdot p$ Method* (Springer Series in Solid State Physics, Berlin, 2009)
28. I. Vurgaftman, J.R. Meyer, L.R. Ram-Mohan, J. Appl. Phys. **89**, 5815 (2001)
29. D. Barettin, S. Madsen, B. Lassen, M. Willatzen, Commun. Comput. Phys. **11**, 797 (2012)
30. F.I. Niordson, *Shell Theory* (North-Holland, Amsterdam, 1985)
31. M. Willatzen, L.C. Lew Yan Voon, A.N. Gandi, U. Schwingenschlögl, Beilstein J. Nanotechnol. **8**, 1345 (2017)

Chapter 17
Band Mixing Effects in InAs/GaAs Quantum Rings and in MoS_2 Quantum Dots Ring-Like Behaving

Carlos Segarra, Josep Planelles and Juan I. Climente

Abstract The physics of semiconductor quantum rings near the band edge is often well described considering decoupled bands. There are however instances where band coupling leads to relevant changes in the electronic structure and derived properties. In this chapter we analyze two such cases. First, we focus on the heavy hole-light hole band mixing in self-assembled InAs/GaAs quantum rings, which is important for current endeavour to develop quantum information science using the spin of holes. In InAs/GaAs quantum dots, the hole ground state is known to be mainly formed by the heavy hole subband. However, there is a finite spin-orbit coupling with the light-hole subband which is critical in determining the hole spin properties. Based on k·p theory, in this chapter we study the influence of hole subband mixing in quantum rings. It is shown that the inner cavity of the ring enhances the light hole component of the ground state. As the quasi-1D limit is approached, the light-hole character becomes comparable to that of the heavy hole. Strain reduces the coupling, but it is still larger than in quantum dots. Second, we study the electronic structure of monolayer MoS_2 quantum dots subject to a magnetic field. Here, the coupling between conduction and valence band gives rise to mid-gap topological states which localize near the dot edge. These edge states are analogous to those of 1D quantum rings. We show they present a large, Zeeman-like, linear splitting with the magnetic field, anticross with the delocalized Fock-Darwin-like states of the dot, give rise to Aharonov-Bohm-like oscillations of the conduction (valence) band low-lying states in the K (K′) valley, and modify the strong-field Landau levels limit form of the energy spectrum.

C. Segarra · J. Planelles (✉) · J.I. Climente
Departament de Química Física i Analítica, Universitat Jaume I, 12080 Castelló, Spain
e-mail: planelle@uji.es

C. Segarra
e-mail: csegarra@uji.es

J.I. Climente
e-mail: climente@uji.es

V.M. Fomin (ed.), *Physics of Quantum Rings*, NanoScience and Technology,
https://doi.org/10.1007/978-3-319-95159-1_17

17.1 Hole Mixing in Quantum Dots

An electron excited across the band gap of a semiconductor leaves behind a hole in the otherwise full valence states. This hole behaves like a charged particle, similar to an electron albeit with a few remarkable differences. In zinc-blende semiconductors, these generally include heavier (and significantly anisotropic) effective masses, stronger spin-orbit interaction (SOI) and multi-band coupling. The reason is that the conduction and valence bands (CB and VB) are constructed from different atomic orbitals. While the CB is mainly formed from the *s* orbitals of the crystal atoms, the VB is formed by *p* orbitals [1]. As a result, the band structure near the the center of the Brillouin zone looks like Fig. 17.1a. The CB is a single band well isolated from the VB and higher excited bands. It is doubly degenerate if we consider the spin degree of freedom. Instead, the VB has a more complex structure. Owing to the spin-orbit interaction, the total microscopic angular momentum of VB states is $\mathbf{J} = 3/2$. The symmetry properties at the zone center (momentum $k = 0$) are like those of *p* atomic states. Thus, we have a four fold degenerate state ($J = 3/2$, $J_z = +3/2, +1/2 - 1/2, -3/2$) which is separated by an energy distance Δ, the spin-orbit splitting, from a two fold degenerate state ($J = 1/2$, $J_z = +1/2, -1/2$). The $J = 1/2$ state is referred to as the split-off band (SO). The $J = 3/2$ state splits in the presence of a force (i.e. $k \neq 0$) into two subbands, one with $J_z = \pm 3/2$ and another with $J_z = \pm 1/2$. These are referred to as the heavy hole (HH) and light hole (LH) subbands [1].

In bulk semiconductors and quantum wells, hole states are severely affected by the HH-LH mixing, which leads to rather peculiar physics [2, 3]. In quantum dots (QDs), however, low-energy holes can be often described simply as HHs, with HH-LH mixing being but a weak perturbation [4]. The reason is that LHs are generally lighter than HHs (notice in Fig. 17.1a that $\frac{1}{m^*_{HH}} = \left|\frac{\delta^2 \varepsilon_{HH}}{\delta k^2}\right| < \frac{1}{m^*_{LH}} = \left|\frac{\delta^2 \varepsilon_{LH}}{\delta k^2}\right|$). LHs are then more sensitive to the three-dimensional confinement of QDs and show up at higher energies.

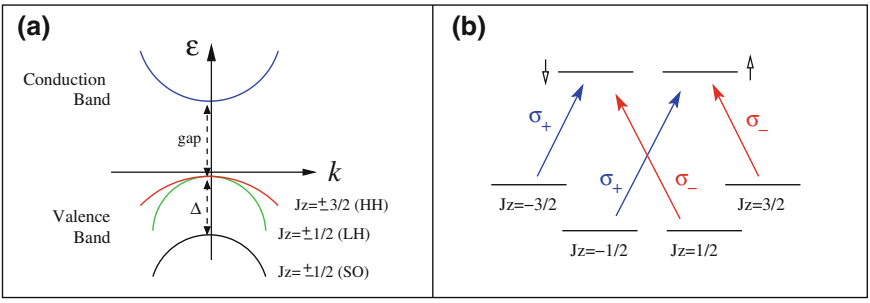

Fig. 17.1 **a** Band structure of the zone center in a zinc-blende semiconductor. **b** Optical transitions between VB states and CB states. $\sigma_\pm$ stand for left and right circularly polarized light

The high purity of the hole ground state in QDs has recently sparked great interest in using its spin for quantum information and spintronic applications [5–10]. Indeed, its spin lifetimes are comparable to those of electrons [11] and, owing to the p-like nature of the Bloch function, they suffer much less decoherence than electrons from the hyperfine interaction with lattice nuclei [12–16]. Even if weak, HH-LH mixing in these systems needs to be understood as it sets a limit for the fidelity and execution time of control operations [17, 18]. It is also important for optical initialization and read-out relying on optical orientation [2]. The underlying idea of these processes is summarized in Fig. 17.1b. The absorption/emission of circularly polarized photons enables selective transitions between HH states ($J_z = \pm 3/2$) and electron states with well-defined spin projection ($\sigma_z = \uparrow, \downarrow$). Photons with the same polarizations but higher energies enable transitions between LH states ($J_z = \pm 1/2$) and electron states with opposite spin projections. Thus, if HH and LH states are significantly coupled the photons give rise to final states with both spin projections and are not spin selective any more. Last, we note that HH-LH mixing is also important to determine other properties of holes in QDs, including the magnetic field dispersion [19, 20] and the tunneling rates in coupled quantum dots [21–27].

Semiconductor quantum rings (QRs) have emerged in the last decade as an alternative to QDs for optoelectronic devices such as lasers and photovoltaics [28–30]. Much of the basic research on these structures has focused on the magnetic response ensuing from their doubly-connected topology, which provides a suitable playground to probe the Aharonov-Bohm effect [31] (see also Chaps. 9, 10 and 12). As a matter of fact, Aharonov-Bohm oscillations of energy and emission intensity have been reported in different experiments [32–35]. These results are well understood from theoretical studies analyzing the influence of the confinement and external fields on the response of electrons, holes and excitons (see e.g. [36–41]). In principle, one can also expect QRs to be suited for quantum information systems, with additional potentialities as compared to QDs owing to the richer magnetic response [42, 43]. Understanding the properties of holes confined in these structures is a necessary step for further development in this direction. Because the strength of the HH-LH mixing is strongly dependent on the details of the quantum confinement, [44, 45] the inner cavity of QRs is expected to influence the hole admixture [46].

In this chapter, we analyze the hole ground state properties in InAs/GaAs QRs. Based on a 6-band Burt-Foreman k·p Hamiltonian, we study the effect of quantum confinement on the hole composition. It is shown that the inner cavity of the QR greatly enhances the HH-LH mixing, leading to much higher LH character than in QDs. We also explore the individual role of additional factors such as the elastic strain or ring eccentricity. The accuracy of usual approximations such as position-independent effective masses [47, 48] and the axial approximation of the VB Hamiltonian [49] are assessed. The chapter is organized as follows. In Sect. 17.1.1 we give details about the theoretical model used to calculate hole states confined in QRs. In Sect. 17.1.2 we discuss how the different factors influence the HH-LH admixture of the hole. Finally, in Sect. 17.1.3 we compare the spatial localization of the HH and LH components in QRs subject to strain or structural deformations.

17.1.1 Theory

An accurate description of holes in InAs/GaAs QRs can be obtained using 6-band k·p Hamiltonians including HH, LH and SO subbands. This requires spanning the Hamiltonian on the basis of periodic Bloch functions $|J, J_z\rangle$:

$$
\begin{aligned}
|\frac{3}{2}, +\frac{3}{2}\rangle &= \frac{1}{\sqrt{2}}\,|(X+iY)\uparrow\rangle = |HH_+\rangle,\\
|\frac{3}{2}, +\frac{1}{2}\rangle &= \frac{1}{\sqrt{6}}\,|(X+iY)\downarrow\rangle - \sqrt{\frac{2}{3}}\,|Z\uparrow\rangle = |LH_+\rangle,\\
|\frac{3}{2}, -\frac{1}{2}\rangle &= -\frac{1}{\sqrt{6}}\,|(X-iY)\uparrow\rangle - \sqrt{\frac{2}{3}}\,|Z\downarrow\rangle = |LH_-\rangle,\\
|\frac{3}{2}, -\frac{3}{2}\rangle &= \frac{1}{\sqrt{2}}\,|(X-iY)\downarrow\rangle = |HH_-\rangle,\\
|\frac{1}{2}, +\frac{1}{2}\rangle &= \frac{1}{\sqrt{3}}\,|(X+iY)\downarrow\rangle + \sqrt{\frac{1}{3}}\,|Z\uparrow\rangle = |SO_+\rangle,\\
|\frac{1}{2}, -\frac{1}{2}\rangle &= -\frac{1}{\sqrt{3}}\,|(X-iY)\uparrow\rangle + \sqrt{\frac{1}{3}}\,|Z\downarrow\rangle = |SO_-\rangle.
\end{aligned}
$$

The $|3/2, \pm 3/2\rangle$ components correspond to HH, the $|3/2, \pm 1/2\rangle$ to LH and the $|1/2, \pm 1/2\rangle$ to SO. One can see from the explicit $|J, J_z\rangle$ functions above that HH components have pure spin, while LH and SO components contain spin admixture. It then follows that HH-LH mixing has straightforward implications in the spin purity of holes.

Since the Luttinger parameters of InAs and GaAs are quite different, it is convenient to employ position-dependent effective mass parameters. Then, instead of the classical Luttinger Hamiltonian [50] one must use the Burt-Foreman one [47, 48]. The full Hamiltonian reads:

$$\mathscr{H}_6 = \mathscr{H}_{\mathrm{bf}} + V(x, y, z)\,\mathscr{I} + \mathscr{H}_{\mathrm{s}}, \tag{17.1}$$

where $\mathscr{H}_{\mathrm{bf}}$ is the Burt-Foreman Hamiltonian, $V(x, y, z)$ the confining potential, $\mathscr{I}$ the identity matrix and $\mathscr{H}_{\mathrm{s}}$ the strain Hamiltonian. A detailed description of $\mathscr{H}_{\mathrm{bf}}$ can be found in [51], where the due expression in cartesian coordinates is given. Because QRs are approximately circular, it is however convenient to use cylindrical coordinates instead. The Burt-Foreman Hamiltonian in atomic units and cylindrical coordinates reads:

$$\mathscr{H}_{\mathrm{bf}} = \frac{1}{2}\,\mathscr{M}, \tag{17.2}$$

where $\mathscr{M}$ is a rank-6 matrix with the following elements:

$$\begin{aligned}
\mathscr{M}[1,1] &= \frac{\partial}{\partial\rho}(\gamma_1+\gamma_2)\frac{\partial}{\partial\rho} + \frac{(\gamma_1+\gamma_2)}{\rho}\frac{\partial}{\partial\rho} \\
&\quad + \frac{\partial}{\partial z}(\gamma_1-2\gamma_2)\frac{\partial}{\partial z} - \frac{(F_z-\frac{3}{2})^2}{\rho^2}(\gamma_1+\gamma_2) \\
&\quad + \frac{(F_z-\frac{3}{2})}{2\rho}\left[\frac{\partial}{\partial\rho}(C_1+C_2) - (C_1+C_2)\frac{\partial}{\partial\rho}\right], \\
\mathscr{M}[1,2] &= \frac{1}{\sqrt{3}}\{\frac{\partial}{\partial\rho}C_1\frac{\partial}{\partial z} - \frac{\partial}{\partial z}C_2\frac{\partial}{\partial\rho} + \frac{(F_z-\frac{1}{2})}{\rho}\left[C_1\frac{\partial}{\partial z} - \frac{\partial}{\partial z}C_2\right]\}, \\
\mathscr{M}[1,3] &= -\sqrt{3}\{\frac{\partial}{\partial\rho}\tilde{\gamma}\frac{\partial}{\partial\rho} + \frac{(F_z+\frac{1}{2})}{\rho}\frac{\partial}{\partial\rho}\tilde{\gamma} + \frac{(F_z-\frac{1}{2})}{\rho}\tilde{\gamma}\frac{\partial}{\partial\rho} \\
&\quad + \frac{(F_z-\frac{3}{2})(F_z+\frac{1}{2})}{\rho^2}\tilde{\gamma}\}, \\
\mathscr{M}[1,4] &= 0, \\
\mathscr{M}[1,5] &= -\frac{1}{\sqrt{6}}\{\frac{\partial}{\partial\rho}C_1\frac{\partial}{\partial z} - \frac{\partial}{\partial z}C_2\frac{\partial}{\partial\rho} + \frac{(F_z-\frac{1}{2})}{\rho}\left[C_1\frac{\partial}{\partial z} - \frac{\partial}{\partial z}C_2\right]\}, \\
\mathscr{M}[1,6] &= -\sqrt{6}\{\frac{\partial}{\partial\rho}\tilde{\gamma}\frac{\partial}{\partial\rho} + \frac{(F_z+\frac{1}{2})}{\rho}\frac{\partial}{\partial\rho}\tilde{\gamma} + \frac{(F_z-\frac{1}{2})}{\rho}\tilde{\gamma}\frac{\partial}{\partial\rho} \\
&\quad + \frac{(F_z-\frac{3}{2})(F_z+\frac{1}{2})}{\rho^2}\tilde{\gamma}\}, \\
\mathscr{M}[2,1] &= \frac{1}{\sqrt{3}}\{\frac{\partial}{\partial z}C_1\frac{\partial}{\partial\rho} - \frac{\partial}{\partial\rho}C_2\frac{\partial}{\partial z} + \frac{(F_z-\frac{3}{2})}{\rho}\left[C_2\frac{\partial}{\partial z} - \frac{\partial}{\partial z}C_1\right]\}, \\
\mathscr{M}[2,2] &= \frac{\partial}{\partial\rho}(\gamma_1-\gamma_2)\frac{\partial}{\partial\rho} + \frac{(\gamma_1-\gamma_2)}{\rho}\frac{\partial}{\partial\rho} \\
&\quad + \frac{\partial}{\partial z}(\gamma_1+2\gamma_2)\frac{\partial}{\partial z} - \frac{(F_z-\frac{1}{2})^2}{\rho^2}(\gamma_1-\gamma_2) \\
&\quad + \frac{(F_z-\frac{1}{2})}{6\rho}\left[\frac{\partial}{\partial\rho}(C_1+C_2) - (C_1+C_2)\frac{\partial}{\partial\rho}\right], \\
\mathscr{M}[2,3] &= \frac{1}{3}\{\frac{\partial}{\partial\rho}(C_1+C_2)\frac{\partial}{\partial z} - \frac{\partial}{\partial z}(C_1+C_2)\frac{\partial}{\partial\rho} \\
&\quad + \frac{(F_z+\frac{1}{2})}{\rho}\left[(C_1+C_2)\frac{\partial}{\partial z} - \frac{\partial}{\partial z}(C_1+C_2)\right]\},
\end{aligned}$$

$$\mathscr{M}[2,4] = \sqrt{3}\{\frac{\partial}{\partial\rho}\tilde{\gamma}\frac{\partial}{\partial\rho} + \frac{(F_z+\frac{3}{2})}{\rho}\frac{\partial}{\partial\rho}\tilde{\gamma} + \frac{(F_z+\frac{1}{2})}{\rho}\tilde{\gamma}\frac{\partial}{\partial\rho} + \frac{(F_z+\frac{3}{2})(F_z-\frac{1}{2})}{\rho^2}\tilde{\gamma}\},$$

$$\mathscr{M}[2,5] = \sqrt{2}\{\frac{\partial}{\partial\rho}\gamma_2\frac{\partial}{\partial\rho} - 2\frac{\partial}{\partial z}\gamma_2\frac{\partial}{\partial z} + \frac{\gamma_2}{\rho}\frac{\partial}{\partial\rho} - \frac{(F_z-\frac{1}{2})^2}{\rho^2}\gamma_2 + \frac{(F_z-\frac{1}{2})}{6\rho}\left[\frac{\partial}{\partial\rho}(C_1+C_2) - (C_1+C_2)\frac{\partial}{\partial\rho}\right]\},$$

$$\mathscr{M}[2,6] = -\frac{1}{3\sqrt{2}}\{\frac{\partial}{\partial\rho}(C_1-2C_2)\frac{\partial}{\partial z} + \frac{\partial}{\partial z}(2C_1-C_2)\frac{\partial}{\partial\rho} + \frac{(F_z+\frac{1}{2})}{\rho}\left[(C_1-2C_2)\frac{\partial}{\partial z} + \frac{\partial}{\partial z}(2C_1-C_2)\right]\},$$

$$\mathscr{M}[3,1] = -\sqrt{3}\{\frac{\partial}{\partial\rho}\tilde{\gamma}\frac{\partial}{\partial\rho} - \frac{(F_z-\frac{3}{2})}{\rho}\frac{\partial}{\partial\rho}\tilde{\gamma} - \frac{(F_z-\frac{1}{2})}{\rho}\tilde{\gamma}\frac{\partial}{\partial\rho} + \frac{(F_z-\frac{3}{2})(F_z+\frac{1}{2})}{\rho^2}\tilde{\gamma}\},$$

$$\mathscr{M}[3,2] = \frac{1}{3}\{\frac{\partial}{\partial z}(C_1+C_2)\frac{\partial}{\partial\rho} - \frac{\partial}{\partial\rho}(C_1+C_2)\frac{\partial}{\partial z} + \frac{(F_z-\frac{1}{2})}{\rho}\left[(C_1+C_2)\frac{\partial}{\partial z} - \frac{\partial}{\partial z}(C_1+C_2)\right]\},$$

$$\mathscr{M}[3,3] = \frac{\partial}{\partial\rho}(\gamma_1-\gamma_2)\frac{\partial}{\partial\rho} + \frac{(\gamma_1-\gamma_2)}{\rho}\frac{\partial}{\partial\rho} + \frac{\partial}{\partial z}(\gamma_1+2\gamma_2)\frac{\partial}{\partial z} - \frac{(F_z+\frac{1}{2})^2}{\rho^2}(\gamma_1-\gamma_2) - \frac{(F_z+\frac{1}{2})}{6\rho}\left[\frac{\partial}{\partial\rho}(C_1+C_2) - (C_1+C_2)\frac{\partial}{\partial\rho}\right],$$

$$\mathscr{M}[3,4] = \frac{1}{\sqrt{3}}\{\frac{\partial}{\partial z}C_1\frac{\partial}{\partial\rho} - \frac{\partial}{\partial\rho}C_2\frac{\partial}{\partial z} - \frac{(F_z+\frac{3}{2})}{\rho}\left[C_2\frac{\partial}{\partial z} - \frac{\partial}{\partial z}C_1\right]\},$$

$$\mathscr{M}[3,5] = \frac{1}{3\sqrt{2}}\{\frac{\partial}{\partial\rho}(C_1-2C_2)\frac{\partial}{\partial z} + \frac{\partial}{\partial z}(2C_1-C_2)\frac{\partial}{\partial\rho} - \frac{(F_z-\frac{1}{2})}{\rho}\left[(C_1-2C_2)\frac{\partial}{\partial z} + \frac{\partial}{\partial z}(2C_1-C_2)\right]\},$$

$$\mathscr{M}[3,6] = \sqrt{2}\{\frac{\partial}{\partial\rho}\gamma_2\frac{\partial}{\partial\rho} - 2\frac{\partial}{\partial z}\gamma_2\frac{\partial}{\partial z} + \frac{\gamma_2}{\rho}\frac{\partial}{\partial\rho} - \frac{(F_z+\frac{1}{2})^2}{\rho^2}\gamma_2 - \frac{(F_z+\frac{1}{2})}{6\rho}\left[\frac{\partial}{\partial\rho}(C_1+C_2) - (C_1+C_2)\frac{\partial}{\partial\rho}\right]\},$$

$$\mathscr{M}[4,1]=0,$$

$$\mathscr{M}[4,2]=\sqrt{3}\{\frac{\partial}{\partial\rho}\tilde{\gamma}\frac{\partial}{\partial\rho}-\frac{(F_z-\frac{1}{2})}{\rho}\frac{\partial}{\partial\rho}\tilde{\gamma}-\frac{(F_z+\frac{1}{2})}{\rho}\tilde{\gamma}\frac{\partial}{\partial\rho}+\frac{(F_z+\frac{3}{2})(F_z-\frac{1}{2})}{\rho^2}\tilde{\gamma}\},$$

$$\mathscr{M}[4,3]=\frac{1}{\sqrt{3}}\{\frac{\partial}{\partial\rho}C_1\frac{\partial}{\partial z}-\frac{\partial}{\partial z}C_2\frac{\partial}{\partial\rho}-\frac{(F_z+\frac{1}{2})}{\rho}\left[C_1\frac{\partial}{\partial z}-\frac{\partial}{\partial z}C_2\right]\},$$

$$\begin{aligned}\mathscr{M}[4,4]=&\frac{\partial}{\partial\rho}(\gamma_1+\gamma_2)\frac{\partial}{\partial\rho}+\frac{(\gamma_1+\gamma_2)}{\rho}\frac{\partial}{\partial\rho}+\frac{\partial}{\partial z}(\gamma_1-2\gamma_2)\frac{\partial}{\partial z}\\&-\frac{(F_z+\frac{3}{2})^2}{\rho^2}(\gamma_1+\gamma_2)-\frac{(F_z+\frac{3}{2})}{2\rho}\left[\frac{\partial}{\partial\rho}(C_1+C_2)-(C_1+C_2)\frac{\partial}{\partial\rho}\right],\end{aligned}$$

$$\mathscr{M}[4,5]=\sqrt{6}\{\frac{\partial}{\partial\rho}\tilde{\gamma}\frac{\partial}{\partial\rho}-\frac{(F_z-\frac{1}{2})}{\rho}\frac{\partial}{\partial\rho}\tilde{\gamma}-\frac{(F_z+\frac{1}{2})}{\rho}\tilde{\gamma}\frac{\partial}{\partial\rho}+\frac{(F_z+\frac{3}{2})(F_z-\frac{1}{2})}{\rho^2}\tilde{\gamma}\},$$

$$\mathscr{M}[4,6]=-\frac{1}{\sqrt{6}}\{\frac{\partial}{\partial\rho}C_1\frac{\partial}{\partial z}-\frac{\partial}{\partial z}C_2\frac{\partial}{\partial\rho}-\frac{(F_z+\frac{1}{2})}{\rho}\left[C_1\frac{\partial}{\partial z}-\frac{\partial}{\partial z}C_2\right]\},$$

$$\mathscr{M}[5,1]=-\frac{1}{\sqrt{6}}\{\frac{\partial}{\partial z}C_1\frac{\partial}{\partial\rho}-\frac{\partial}{\partial\rho}C_2\frac{\partial}{\partial z}+\frac{(F_z-\frac{3}{2})}{\rho}\left[C_2\frac{\partial}{\partial z}-\frac{\partial}{\partial z}C_1\right]\},$$

$$\begin{aligned}\mathscr{M}[5,2]=&\sqrt{2}\{\frac{\partial}{\partial\rho}\gamma_2\frac{\partial}{\partial\rho}-2\frac{\partial}{\partial z}\gamma_2\frac{\partial}{\partial z}+\frac{\gamma_2}{\rho}\frac{\partial}{\partial\rho}-\frac{(F_z-\frac{1}{2})^2}{\rho^2}\gamma_2\\&+\frac{(F_z-\frac{1}{2})}{6\rho}\left[\frac{\partial}{\partial\rho}(C_1+C_2)-(C_1+C_2)\frac{\partial}{\partial\rho}\right]\},\end{aligned}$$

$$\begin{aligned}\mathscr{M}[5,3]=&\frac{1}{3\sqrt{2}}\{\frac{\partial}{\partial\rho}(2C_1-C_2)\frac{\partial}{\partial z}+\frac{\partial}{\partial z}(C_1-2C_2)\frac{\partial}{\partial\rho}\\&+\frac{(F_z+\frac{1}{2})}{\rho}\left[(2C_1-C_2)\frac{\partial}{\partial z}+\frac{\partial}{\partial z}(C_1-2C_2)\right]\},\end{aligned}$$

$$\mathscr{M}[5,4]=\sqrt{6}\{\frac{\partial}{\partial\rho}\tilde{\gamma}\frac{\partial}{\partial\rho}+\frac{(F_z+\frac{3}{2})}{\rho}\frac{\partial}{\partial\rho}\tilde{\gamma}+\frac{(F_z+\frac{1}{2})}{\rho}\tilde{\gamma}\frac{\partial}{\partial\rho}+\frac{(F_z+\frac{3}{2})(F_z-\frac{1}{2})}{\rho^2}\tilde{\gamma}\},$$

$$\begin{aligned}\mathscr{M}[5,5]=&\frac{\partial}{\partial\rho}\gamma_1\frac{\partial}{\partial\rho}+\frac{\partial}{\partial z}\gamma_1\frac{\partial}{\partial z}+\frac{\gamma_1}{\rho}\frac{\partial}{\partial\rho}-\frac{(F_z-\frac{1}{2})^2}{\rho^2}\gamma_1\\&+\frac{(F_z-\frac{1}{2})}{3\rho}\left[\frac{\partial}{\partial\rho}(C_1+C_2)-(C_1+C_2)\frac{\partial}{\partial\rho}\right]-2\Delta(\rho,z),\end{aligned}$$

$$\begin{aligned}\mathscr{M}[5,6]=&-\frac{1}{3}\{\frac{\partial}{\partial\rho}(C_1+C_2)\frac{\partial}{\partial z}-\frac{\partial}{\partial z}(C_1+C_2)\frac{\partial}{\partial\rho}\\&+\frac{(F_z+\frac{1}{2})}{\rho}\left[(C_1+C_2)\frac{\partial}{\partial z}-\frac{\partial}{\partial z}(C_1+C_2)\right]\},\end{aligned}$$

$$
\begin{aligned}
\mathscr{M}[6,1] &= -\sqrt{6}\{\frac{\partial}{\partial\rho}\tilde{\gamma}\frac{\partial}{\partial\rho} - \frac{(F_z-\frac{3}{2})}{\rho}\frac{\partial}{\partial\rho}\tilde{\gamma} - \frac{(F_z-\frac{1}{2})}{\rho}\tilde{\gamma}\frac{\partial}{\partial\rho} \\
&\quad + \frac{(F_z-\frac{3}{2})(F_z+\frac{1}{2})}{\rho^2}\tilde{\gamma}\}, \\
\mathscr{M}[6,2] &= -\frac{1}{3\sqrt{2}}\{\frac{\partial}{\partial\rho}(2C_1-C_2)\frac{\partial}{\partial z} + \frac{\partial}{\partial z}(C_1-2C_2)\frac{\partial}{\partial\rho} \\
&\quad - \frac{(F_z-\frac{1}{2})}{\rho}\left[(2C_1-C_2)\frac{\partial}{\partial z} + \frac{\partial}{\partial z}(C_1-2C_2)\right]\}, \\
\mathscr{M}[6,3] &= \sqrt{2}\{\frac{\partial}{\partial\rho}\gamma_2\frac{\partial}{\partial\rho} - 2\frac{\partial}{\partial z}\gamma_2\frac{\partial}{\partial z} + \frac{\gamma_2}{\rho}\frac{\partial}{\partial\rho} - \frac{(F_z+\frac{1}{2})^2}{\rho^2}\gamma_2 \\
&\quad - \frac{(F_z+\frac{1}{2})}{6\rho}\left[\frac{\partial}{\partial\rho}(C_1+C_2) - (C_1+C_2)\frac{\partial}{\partial\rho}\right]\}, \\
\mathscr{M}[6,4] &= -\frac{1}{\sqrt{6}}\{\frac{\partial}{\partial z}C_1\frac{\partial}{\partial\rho} - \frac{\partial}{\partial\rho}C_2\frac{\partial}{\partial z} - \frac{(F_z+\frac{3}{2})}{\rho}\left[C_2\frac{\partial}{\partial z} - \frac{\partial}{\partial z}C_1\right]\}, \\
\mathscr{M}[6,5] &= -\frac{1}{3}\{\frac{\partial}{\partial z}(C_1+C_2)\frac{\partial}{\partial\rho} - \frac{\partial}{\partial\rho}(C_1+C_2)\frac{\partial}{\partial z} \\
&\quad + \frac{(F_z-\frac{1}{2})}{\rho}\left[(C_1+C_2)\frac{\partial}{\partial z} - \frac{\partial}{\partial z}(C_1+C_2)\right]\}, \\
\mathscr{M}[6,6] &= \frac{\partial}{\partial\rho}\gamma_1\frac{\partial}{\partial\rho} + \frac{\partial}{\partial z}\gamma_1\frac{\partial}{\partial z} + \frac{\gamma_1}{\rho}\frac{\partial}{\partial\rho} - \frac{(F_z+\frac{1}{2})^2}{\rho^2}\gamma_1 \\
&\quad - \frac{(F_z+\frac{1}{2})}{3\rho}\left[\frac{\partial}{\partial\rho}(C_1+C_2) - (C_1+C_2)\frac{\partial}{\partial\rho}\right] - 2\Delta(\rho,z).
\end{aligned}
$$

Here γ_i are the position-dependent Luttinger parameters, $\tilde{\gamma} = (\gamma_2+\gamma_3)/2$ (axial approximation [49]), $C_1 = 1+\gamma_1-2\gamma_2-6\gamma_3$ and $C_2 = 1+\gamma_1-2\gamma_2$, $\Delta(\rho,z)$ is the spin-orbit splitting and $F_z = m + J_z$ is the total angular momentum z-projection, which is the sum of the envelope angular momentum m and the Bloch angular momentum J_z.

The strain terms are given by:

$$
\mathscr{H}_{\mathrm{S}} = \begin{pmatrix}
p+q & -s & r & 0 & \frac{s}{\sqrt{2}} & \sqrt{2}\,r \\
-s^* & p-q & 0 & -r & \sqrt{2}\,q & \sqrt{\frac{3}{2}}\,s \\
r^* & 0 & p-q & -s & -\sqrt{\frac{3}{2}}\,s^* & \sqrt{2}\,q \\
0 & -r^* & -s^* & p+q & -\sqrt{2}\,r^* & \frac{s^*}{\sqrt{2}} \\
\frac{s^*}{\sqrt{2}} & \sqrt{2}\,q & -\sqrt{\frac{3}{2}}\,s & -\sqrt{2}\,r & p & 0 \\
\sqrt{2}\,r^* & \sqrt{\frac{3}{2}}\,s^* & \sqrt{2}\,q & \frac{s}{\sqrt{2}} & 0 & p
\end{pmatrix}. \tag{17.3}
$$

where

$$p = a\,Tr(\varepsilon), \tag{17.4}$$

$$q = b\left(\frac{\varepsilon_{xx}}{2} + \frac{\varepsilon_{yy}}{2} - \varepsilon_{zz}\right), \tag{17.5}$$

$$s = d\left(\varepsilon_{xz} - i\,\varepsilon_{yz}\right), \tag{17.6}$$

$$r = -\frac{\sqrt{3}}{2}\,b\left(\varepsilon_{xx} - \varepsilon_{yy}\right) + i\,d\,\varepsilon_{xy}. \tag{17.7}$$

Here ε is the strain tensor, which is calculated by minimizing the elastic energy, [52] and a, b d are the VB deformation potentials.

The eigenstates of Hamiltonian (17.1) are six-component spinorial vectors, with each component composed of an envelope and a Bloch part. For the axially symmetric structures, the spinors can be classified by F_z and the main quantum number k.

$$|F_z, k\rangle = \begin{pmatrix} f^{(1)}_{F_z-3/2}(\rho,z)\ |HH_+\rangle \\ f^{(2)}_{F_z-1/2}(\rho,z)\ |LH_+\rangle \\ f^{(3)}_{F_z+1/2}(\rho,z)\ |LH_-\rangle \\ f^{(4)}_{F_z+3/2}(\rho,z)\ |HH_-\rangle \\ f^{(5)}_{F_z-1/2}(\rho,z)\ |SO_+\rangle \\ f^{(6)}_{F_z+1/2}(\rho,z)\ |SO_-\rangle \end{pmatrix} \tag{17.8}$$

where $f^{(i)}_m(\rho,z)$ is the envelope function of the i-th component. In QRs with strong vertical confinement the ground state is formed by $|F_z = +3/2, k = 0\rangle$ or $|F_z = -3/2, k = 0\rangle$. These two states are Kramers-degenerate in the absence of magnetic fields. For our discussion it is convenient to display one of these states, e.g. $|F_z = +3/2, k\rangle$ (an analogous discussion would follow for $|F_z = -3/2, k\rangle$):

$$|3/2, 0\rangle = \begin{pmatrix} f^{(1)}_0(\rho,z)\ |HH_+\rangle \\ f^{(2)}_1(\rho,z)\ |LH_+\rangle \\ f^{(3)}_2(\rho,z)\ |LH_-\rangle \\ f^{(4)}_3(\rho,z)\ |HH_-\rangle \\ f^{(5)}_1(\rho,z)\ |SO_+\rangle \\ f^{(6)}_2(\rho,z)\ |SO_-\rangle \end{pmatrix}. \tag{17.9}$$

Owing to the low angular momentum, the HH ($f^{(1)}_0$) component is dominant, as expected from a single-band approach.

For numerical simulations, we shall consider self-assembled InAs QDs with lens shape (spherical casket) embedded in a GaAs matrix. The height at the apex is $H = 3$ nm and the radius is $R = 10$ nm. The QR is formed by introducing a repulsive core in the center with radius R_{in} (see Fig. 17.2a). This is an idealization of the realistic volcano shape of InAs/GaAs QRs [53] (see also Chap. 4), which captures the fact that

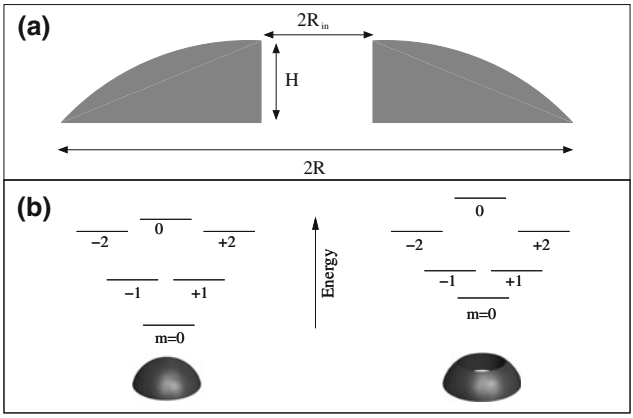

Fig. 17.2 **a** Schematic representation of the QR cross-section. **b** Energy levels of a QD (left) and a QR (right). Note that the ring cavity unstabilizes states with small angular momentum $|m|$

the potential governing the electron motion in the plane is asymmetric in the radial direction, with a profound minimum under the ring apex and a smooth (abrupt) increase on the outer (inner) side, see Fig. 17.1b in [38]. Material parameters of InAs and GaAs (Luttinger parameters, Δ, lattice constants) are taken from [54]. The deformation potentials are taken from [55] and the VB offset is set to $V_c = 0.265$ eV [56]. Hamiltonian (17.1) is solved numerically using COMSOL Multiphysics.

17.1.2 Hole Mixing

In this section we investigate the composition of the hole ground state as a function of the QR geometry. The composition is given in terms of the weight of each component within the spinor (17.8). For example, the weight of the $|HH_+\rangle$ component is:

$$c_{HH_+} = \frac{\langle f^{(1)}|f^{(1)}\rangle}{\sum_i \langle f^{(i)}|f^{(i)}\rangle}. \tag{17.10}$$

We start by considering the effect of quantum confinement alone. Constant (InAs) mass parameter is taken and strain effects are disregarded. Figure 17.3 shows the weight of the different spinor components as a function of R_{in}. Panel (a) shows the total HH, LH and SO weights, and panel (b) shows the J_z resolved components. While the SO components remain negligible in all the range under study, one can see that the LH character of the ground state rapidly increases as we depart from the QD limit ($R_{in} = 0$ nm), mainly due to an increase of the $|LH_-\rangle$ component. For $R_{in} = 5$ nm, the LH character is as large as ∼20%, over three times larger than in QDs [46]. The LH character will be even stronger in narrower QRs. The increase

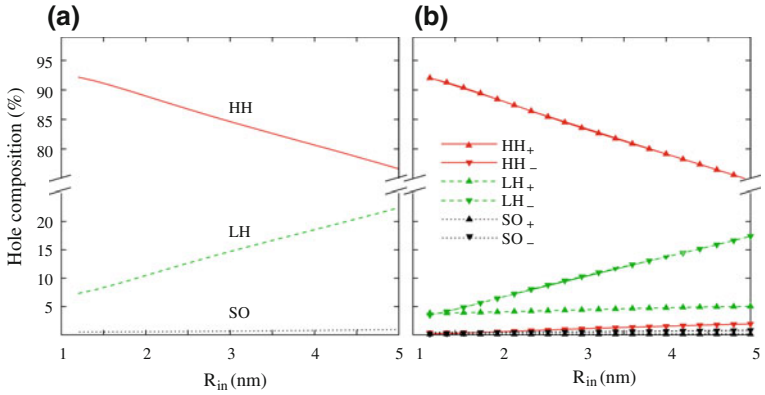

Fig. 17.3 Composition of the hole ground state in a QR with increasing inner radius R_{in}. **a** Comparison of HH, LH and SO character. Solid line: $c_{HH_+} + c_{HH_-}$, dashed line: $c_{LH_+} + c_{LH_-}$, dotted line: $c_{SO_+} + c_{SO_-}$. **b** J_z resolved components. Strain is disregarded and constant (InAs) effective mass is used

of the LH character in QRs can be explained from two factors: (i) the distinct QR energy structure and (ii) the enhanced lateral confinement.

Factor (i) can be understood by comparing the energy level diagrams of lens-shaped QDs and QRs, which is sketched in Fig. 17.2b – a single-band model has been used for simplicity–. The ground state of the QD has angular momentum $m = 0$, and the excited states follow the energy diagram shown on the figure. The $m = 0$ state has maximum charge density in the center of the QD, while states with increasing $|m|$ are gradually offcentered by centrifugal terms. Switching from a QD to a QR means including a repulsive core in the center. Because of the charge density distribution, the effect of the core is stronger on states with small $|m|$. Thus, in QRs the $m = 0$ states approach the $|m| = 1$ and $|m| = 2$ ones. Since the HH-LH coupling terms mix states with different angular momenta, it follows that the repulsive core of QRs favors HH-LH coupling. Mixing of $|m| = 0$ with $|m| = 2$ is more important than with $|m| = 1$ (compare $|LH_-\rangle$ with $|LH_+\rangle$ in Fig. 17.3b) because both components have the same chirality [24, 46]. Factor (ii) is related to the anistropy of hole masses. In InAs structures grown along the [001] direction, $m_{LH}^{\perp} > m_{HH}^{\perp}$. Thus, with increasing lateral confinement the kinetic energy of HH approaches that of LH and the HH-LH mixing becomes stronger. If the formation of QRs does not involve enhanced lateral confinement (e.g. the material of the cavity is pushed towards the ring edges [57]), the LH character still increases due to factor (i), but to a lesser extent than shown here [46].

We next analyze how the previous result is modified by the inclusion of other factors present in realistic self-assembled QRs. First, we consider the fact that the effective mass is different inside and outside the QR. Using the Burt-Foreman Hamiltonian with position-dependent effective masses, one obtains the ground state LH character shown in Fig. 17.4 (short-dashed lines). It can be seen that the LH admix-

ture is essentially the same as that reported above. This is because most of the wave function is localized inside the InAs ring, with only weak leakage into the GaAs matrix. Interestingly, the influence of the position-dependent effective mass is weak even in the case of small R_{in}, where the hole tunnels across the inner GaAs core (see Sect. 17.1.3).

Second, we consider the influence of artificially imposing axial symmetry in the VB Hamiltonian. The 6-band Luttinger Hamiltonian (Burt-Foreman Hamiltonian with constant mass) in cartesian coordinates reads:

$$\mathscr{H}_{\mathrm{LK}} = \begin{pmatrix} P+Q & -S & R & 0 & \frac{S}{\sqrt{2}} & \sqrt{2}R \\ -S^* & P-Q & 0 & -R & \sqrt{2}Q & \sqrt{\frac{3}{2}}S \\ R^* & 0 & P-Q & -S & -\sqrt{\frac{3}{2}}S^* & \sqrt{2}Q \\ 0 & -R^* & -S^* & P+Q & -\sqrt{2}R^* & \frac{S^*}{\sqrt{2}} \\ \frac{S^*}{\sqrt{2}} & \sqrt{2}Q & -\sqrt{\frac{3}{2}}S & -\sqrt{2}R & P & 0 \\ \sqrt{2}R^* & \sqrt{\frac{3}{2}}S^* & \sqrt{2}Q & \frac{S}{\sqrt{2}} & 0 & P \end{pmatrix}. \tag{17.11}$$

where

$$P = \frac{\gamma_1}{2}\, p^2, \tag{17.12}$$

$$Q = \frac{\gamma_2}{2}\, (p_x^2 + p_y^2 - 2\, p_z^2), \tag{17.13}$$

$$S = \sqrt{3}\, \gamma_3\, p_z\, p_-, \tag{17.14}$$

$$R = -\frac{\sqrt{3}}{2}\, \gamma_2\, (p_x^2 - p_y^2) + i\, \sqrt{3}\, \gamma_3\, p_x\, p_y, \tag{17.15}$$

and p_j is the j-projection of the momentum and $p_\pm = (p_x \pm i p_y)$. As can be seen, in (17.11) the term R lacks axial symmetry. To simplify the study of axially symmetric nanostructures, Sercel and Vahala proposed replacing it by: [51]

$$R = -\frac{\sqrt{3}}{2}\, \gamma\, p_-^2, \tag{17.16}$$

where $\gamma = (\gamma_2 + \gamma_3)/2$. This is known as the "axial approximation", for it enables analytical integration of the angular coordinate. Because self-assembled QDs and QRs are roughly axially symmetric, this approximation is employed in most multiband descriptions of the VB structure (including Hamiltonian $\mathscr{H}_{\mathrm{bf}}$). However, in the current context where high purity hole states is desirable for applications, it is worth assessing to which extent the approximation provides accurate estimates of the hole mixing. The long-dashed line in Fig. 17.4 shows the ground state LH character without the axial approximation. The weight of the LH component is found to increase by 1−2%, although the qualitative trend as a function of inner radii remains the same.

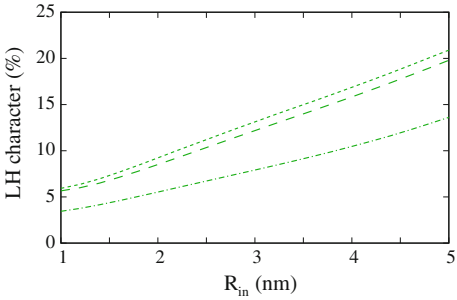

Fig. 17.4 Weight of the LH components in the hole ground state in a QR with increasing inner radius R_{in}. Position-dependent effective mass is used. Short-dashed lines: unstrained rings with axial approximation. Long-dashed lines: unstrained rings without axial approximation. Dashed-dotted lines: strained rings without axial approximation

Next, we consider the effect of strain forces, which are known to have a deep impact on the electronic structure of VB holes in InAs/GaAs QDs [55, 58, 59] and QRs [60] (see also Chap. 13). The results, dashed-dotted lines in Fig. 17.4, show a moderate decrease of the LH character of the QRs as compared to the unstrained case. Still, the same trend as observed before holds. Namely, the inner cavity of the ring systematically enhances the LH character.

The fact that strain-free simulations provide a reasonable reference is somewhat surprising, as biaxial strain is known to split HH and LH states energetically [58, 59]. One may then expect strained QRs to display much smaller LH character [46]. For further insight into this issue, in Fig. 17.5 the role of strain is analyzed in more detail. The LH character of the ground state is compared for different degrees of approximation to $\mathscr{H}_{\mathrm{S}}$: diagonal strain (dotted lines), biaxial strain [61] (dashed lines) and full strain (solid lines). One can see that diagonal strain predicts a strong decrease of the LH character as compared to the unstrained case of Fig. 17.4. This is because the $p+q$ and $p-q$ terms in (17.3) split HH and LH energetically, thus weakening the HH-LH mixing. By contrast, the biaxial approximation [(17.3) but setting the shear terms to zero, $d=0$] shows larger LH character, close to the full-strain value. This indicates that the weakening of the HH-LH mixing due to the diagonal terms is largely compensated by the strong off-diagonal terms of the Hamiltonian. As a result, the fully strained system has LH component of the same order as the strain-free system.

Next, we take into account that self-assembled InAs/GaAs QRs often deviate from the exact circular geometry assumed so far. This is because the anisotropic redistribution of the QD material during the capping and annealing processes results in elongated ring-shaped islands [53]. These deviations are known to affect the magnetic response of the QRs [34] and are required for quantitative interpretation of experimental observations [38, 62]. In Fig. 17.6 we study the hole mixing in QRs subject to an increasing degree of ellipticity. We start from circular QDs and let the eccentricity ε increase while keeping the basis area constant. The semi-major (semi-minor) axis R_a (R_b) of the elliptical QR is then:

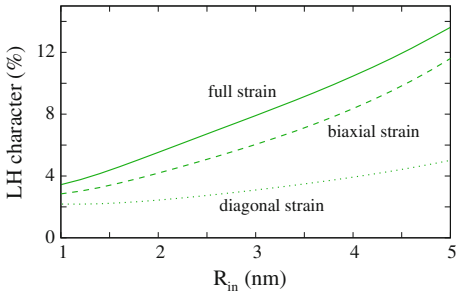

Fig. 17.5 Weight of the light hole components in the hole ground state of a QR with increasing inner radius R_{in}. Three approximations for strain are compared: diagonal strain (dotted line), biaxial strain (dashed line) and full strain (solid lines)

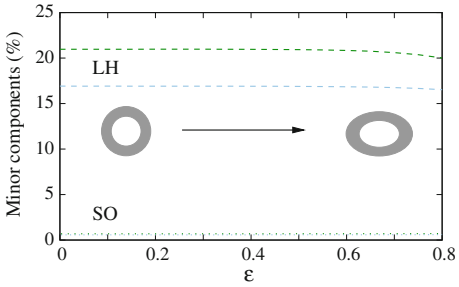

Fig. 17.6 Effect of the eccentricity on the composition of the hole ground state (minor components shown only). The QR has $R = 10$ nm. Light and dark lines correspond to $R_{in} = 4$ nm and $R_{in} = 5$ nm, respectively

$$R_a = R/(1-\varepsilon^2)^{1/4}, \tag{17.17}$$

$$R_b = R^2/R_a. \tag{17.18}$$

The hole states are calculated using the strain-free Hamiltonian in cartesian coordinates for a QR with $R_{in} = 4$ nm. The result is shown in Fig. 17.6 (light lines). As can be seen, the weight of both LH and SO components is barely affected by the eccentricity. This is inspite of the fact that for $R_{in} = 4$ nm and $\varepsilon = 0.8$, the ring width, $W = R - R_{in}$, changes from 6 nm all over the ring to 8.9 nm and 4 nm along the major and minor axis, respectively. The same behavior is observed for different inner radii (see e.g. $R_{in} = 5$ nm, dark lines in the figure).

17.1.3 Hole Localization

It has been suggested that strain plays an important role to determine the localization of electrons and holes in QRs, eventually leading to spatially separated (type-II-like) carriers [60]. In this section we investigate how strain influences the localization of the different hole components. In Fig. 17.7 we plot the potential energy originating in the diagonal strain terms for a QR with a small inner cavity ($R_{in} = 1$ nm, left panels) and a large inner cavity ($R_{in} = 5$ nm, right panels). The upper panel corresponds to HH potential and the lower one to LH potential. Dark (light) colors stand for strain-

induced potential well (barrier). As expected, Fig. 17.7 shows that strain stabilizes (unstabilizes) the HH (LH). It is worth noting that the small R_{in} geometry is is just a small departure from the lens-shaped QD. Yet, the inner cavity brings about significant differences. For HH, the strain in the cavity yields a potential minimum, which is more attractive than the InAs region itself. For LH, it is just the opposite. The inner cavity is strongly repulsive and strain favors localization around it, including the GaAs regions above and below the ring [46].

The actual hole localization, considering both strain and confinement potentials, is illustrated in Fig. 17.8 for the $m = 0$ (HH) and $m = 2$ (LH) components of the ground state. For large inner cavities ($R_{in} = 5$ nm, right panels), both HH and LH share localization inside the QR. By contrast, for small cavities ($R_{in} = 1$ nm, left panels) the HH shows a sizable density inside the cavity, while the LH stays away from it. Because the LH component has a node, half of it localizes around the core and the other half on the distant side, with significant leaking above the QR. This behavior is similar to that of holes in vertically coupled QDs with thin interdot barriers, [55, 63] except that here the localization in the GaAs region takes place for HH instead of LH. A more dramatic localization of HH in the inner cavity has been predicted by considering diagonal strain terms only [46]. This indicates that shear strain reduces this phenomenon through the enhancement of HH-LH coupling.

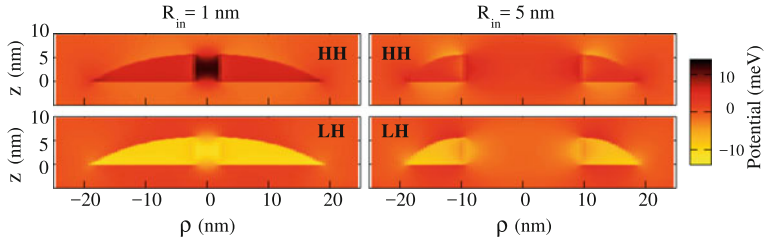

Fig. 17.7 Potential induced by strain on HH (top panels) and LH (bottom panels) confined in a QR. Left and right panels are for $R_{in} = 1$ nm and $R_{in} = 5$ nm, respectively. Note that positive potential is attractive for holes

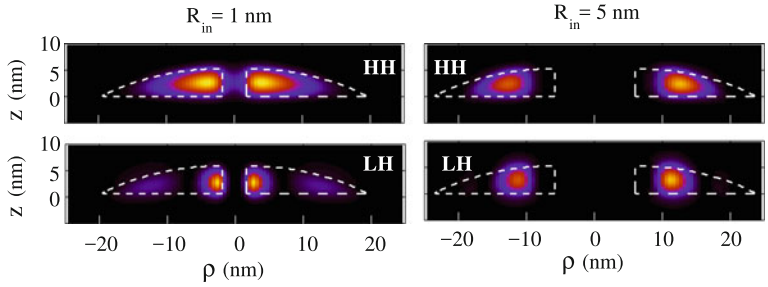

Fig. 17.8 Wave function of the HH (top panels) and LH (bottom panels) confined in a strained QR. Dashed lines show the edges of the QR structure. Left and right panels are for $R_{in} = 1$ nm and $R_{in} = 5$ nm, respectively. Dashed lines show the edges of the QR structure

In typical self-assembled InAs/GaAs QRs $R_{in} \gg 1$ nm [53]. In such a case, the strain in the core is weaker and cannot compete with the repulsive confinement potential (i.e., we are in the case illustrated by the right panels in Figs. 17.7 and 17.8). Yet, the results of this section suggest that using strained materials with small band-offset a spatial decoupling of HH and LH may be engineered.

17.1.4 Conclusions

Motivated by current interest in using confined hole spins for quantum information and spintronic devices, we have investigated the hole mixing in InAs/GaAs QRs. We have shown that the hole ground state has a fairly pure HH character in the QD limit, but it rapidly gains LH character as the inner cavity grows and the quasi-1D (wire-like) limit is approached. Because LH components have mixed spin projections, this suggests that narrow QRs are less suited than QDs for applications reyling on hole spin. On the other hand, the large LH component may be of interest for applications requiring enhanced tunneling rates [23, 24], enhanced spin-orbit mediated control [27, 64] and optoelectronic devices emitting z-polarized light [45]. Experiments probing the polarization of emitted light, like the ones in [65], would confirm the different strength of LH coupling in QRs and QDs.

Deviations of the QR from perfect axial symmetry due to eccentricity or the asymmetric nature of the zinc-blende Luttinger-Kohn Hamiltonian (beyond the axial approximation [49]) have been found to have a minor influence on the HH-LH admixture. The same holds for position-dependent effective mass. This validates the use of simplified models for qualitative estimates.

The role of strain has been investigated in detail. As in QDs, it reduces the LH character of the ground state by introducing a potential which splits HH and LH states energetically [58, 59]. However, this is partially compensated by the enhancement of the off-diagonal terms coupling HH and LH through biaxial and shear strain. As a result, the actual degree of HH-LH mixing is of the same order as that expected in strain-free systems. Besides, the qualitative trends set by quantum confinement are not altered. Last, we have also shown that strain can be used to engineer the wavefunction localization in QRs with narrow inner cavities, where the strong strain potential may compete against the band-offset potential.

17.2 Magnetic Response of Edge States in MoS_2 Quantum Dots

Two-dimensional transition metal dichalcogenides (TMDs) have arised as an alternative to graphene for electronic and opto-electronic applications where a finite gap is required [66]. Recently, single photon emitter TMDs have been observed, whose quantum dot like behavior is typically associated with lattice defects [67–73]. TMD quantum dots with controlled quantum confinement are now being pursued with

different techniques, including patterning of TMD monolayers [74], chemical synthesis [75, 76] and defect engineering [77, 78]. In this context, theoretical studies have arised investigating the electronic structure of TMD quantum dots. Particular interest has been placed in the response to external magnetic fields. Kormanyos and co-workers have analyzed the CB under perpendicular magnetic fields for hard wall circular MoS_2 and WS_2 dots [79]. The resulting spectrum is reminiscent of the Fock-Darwin spectrum in harmonically confined dots, but with sizable out-of-plane g factors due to spin-orbit interaction. Brooks and Burkard showed that the magnetic field can be used to force spin degeneracies in spite of the spin-orbit splitting, which is of interest for development of spin qubits [80]. Dias and co-workers investigated the energy levels of CB and VB in K and K' valleys of MoS_2, as well as the associated magneto-absorption spectrum [81, 82].

The above studies, however, have not considered the possible presence of edge states, which show up in the gap of finite MoS_2 systems under different conditions [83–89]. The origin of such states lies in the marginal topological properties of the single-valley MoS_2 Hamiltonian.[1] In k·p formalism [90], these properties manifest when one expands the Hamiltonian up to second order in k and explicitly considers the CB-VB coupling [89]. In this chapter, we analyze the response of mid-gap monolayer MoS_2 quantum dot states to perpendicular magnetic fields. To this end, we use a two-band k·p Hamiltonian:

$$H = \begin{pmatrix} E_v + \alpha\, p^2 - V(\mathbf{r}) & \tau\gamma p_- \\ \tau\gamma p_+ & E_c + \beta\, p^2 + V(\mathbf{r}) \end{pmatrix}. \tag{17.19}$$

where $p_\pm = p_x \pm i\tau p_y$ and $\mathbf{p} = \mathbf{k} + \mathbf{A}$, with $\mathbf{k}$ the momentum relative to the K/K' points and $\mathbf{A} = B/2\,(-y, x, 0)$ the vector potential. B is the magnetic field, $E_c = \Delta/2$ and $E_v = -\Delta/2$ the CB and VB edge energies, respectively, Δ is the band gap. The constants α, β and γ are material parameters, while τ identifies the valley K ($\tau = 1$) or K' ($\tau = -1$). $V(\mathbf{r})$ represents a possibly externally applied potential as e.g. electrostatic gating. If no external potential is present, then $V(\mathbf{r}) = 0$. We impose hard-wall potential at the QD border, the associated boundary conditions result in no intervalley coupling. Notice also that for clarity we ignore spin and spin-orbit terms, which in MoS_2 give rise to small energy splittings of levels at zero and finite magnetic fields [81]. We also disregard minor corrections like trigonal warping, [90] or the role of defects which can be relevant in some MoS_2 nanostructures [91]. Hamiltonian (17.19) is solved numerically.

To illustrate the effect of the magnetic field on the electronic structure, we first consider the highly symmetric case of circular quantum dots with equivalent masses

[1] In graphene systems one can associate an index to each of the inequivalent valleys. Then, the Chern number can be calculated as the sum of these indexes. It is found that while the individual Chern number per inequivalent valley does not vanish, the sum is zero, so that the system is topologically trivial. However, the non-vanishing valley index allows the system to sustain edge states. Such behavior is related to graphene's marginal topological character. In a similar sense, MoS_2 is marginal as well. The marginality implies that a small perturbation in the Hamiltonian (e.g. mass term) can have a big effect on the presence or absence of the gapless modes.

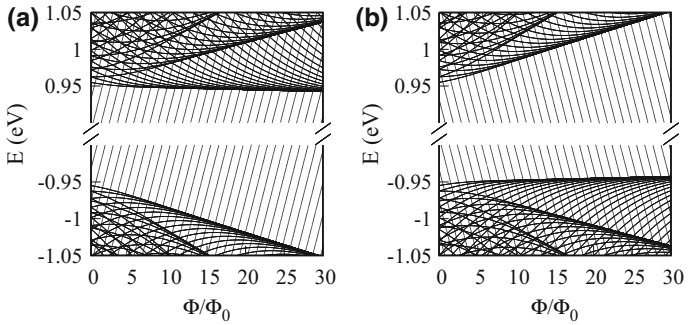

Fig. 17.9 Energy levels of circular dots as a function of a perpendicular magnetic flux, for $\alpha = -\beta = 1$ eV Å^2. **a** K valley. **b** K' valley

in CB and VB, $\alpha = 1$ eV Å^2 and $\beta = -1$ eV Å^2, along with other MoS_2 parameters ($\gamma = 3.82$ eV Å, $\Delta = 1.9$ eV) and radius $R = 9$ nm. Figure 17.9a, b show the energy levels in the K and K' valley, respectively, as a function of the magnetic flux $\Phi = BS/\Phi_0$, with S the dot surface and $\Phi_0 = 2\pi$ the unit quantum flux (in atomic units). As can be seen, CB ($E > 0.95$ eV) and VB ($E < -0.95$ eV) display a Fock-Darwin like spectra, where spatially confined states converge into Landau levels (LLs) with increasing flux. Notice the LLs of 2D TMDs include energy-locked levels which are independent of Φ, as can be seen in the lowest level of the CB of K, in Fig. 17.9a. Besides, CB of K (K') valley and VB of K' (K) valley are mirror images. Up to this point, all features are consistent with the picture described by Dias et al. [81, 82].

However, superimposed to the Fock-Darwin like spectrum, there are a series of iso-spaced states which show a identical linear dispersion with the field, covering the entire spectrum: CB, VB and gap region alike. These are the edge states of the dot, arising from the marginal topological character of Hamiltonian (17.19) [89].

The slope of edge states against Φ is positive for K and negative for K' valleys, evidencing a large Zeeman level splitting. The sign and magnitude can be understood by simplifying Hamiltonian (17.19) for a circular structure and fixing the radius to R, as expected for pure edge states. The resulting Hamiltonian, neglecting magnetic field for the moment, is:

$$H_R = \begin{pmatrix} \varepsilon_v + \frac{\alpha}{R^2}\widehat{L}_z^2 & -i\,\frac{\tau\gamma}{R}\,e^{-i\theta}\,\hat{L}_z \\ i\,\frac{\tau\gamma}{R}\,e^{i\theta}\hat{L}_z & \varepsilon_c + \frac{\beta}{R^2}\,\hat{L}_z^2 \end{pmatrix}. \tag{17.20}$$

with $\widehat{L}_z$ the azimuthal angular momentum operator. The eigenvectors are spinors $\Psi = \left(a\,e^{iM\theta}, b\,e^{i(M+1)\theta}\right)$, with $a^2 = \frac{|\beta|}{|\alpha|+|\beta|}$, $b^2 = \frac{|\alpha|}{|\alpha|+|\beta|}$, [89] and M is the $\hat{L}_z$ quantum number. The mean value of the energy, $E = \langle\Psi|H_R|\Psi\rangle$, is

$$E = (|a|^2\varepsilon_v + |b|^2\varepsilon_c) + \frac{i\,\tau\gamma}{R}(M\,(ab^* - a^*b) - a^*b) + \frac{|a|^2\alpha}{R^2}M^2 + \frac{|b|^2\beta}{R^2}(M+1)^2. \tag{17.21}$$

Since E must be real, so must be $i\,a^*b$ and $i\,(ab^* - a^*b)$. Therefore, one of the two complex constants must be a real number and the other one an imaginary number. Let us assume a is real and b a pure imaginary number. Then:

$$E = (|a|^2\varepsilon_v + |b|^2\varepsilon_c) + \frac{M^2}{R^2}(\alpha|a|^2 + \beta|b|^2) + (2M+1)\frac{\beta|b|^2}{R^2} + \frac{\tau\gamma}{R}(2a|b|M + a|b|)\,. \tag{17.22}$$

Furthermore, since $\alpha > 0, \beta < 0, a^2 = \frac{|\beta|}{|\alpha|+|\beta|}$ and $b^2 = \frac{|\alpha|}{|\alpha|+|\beta|}$, we have that $(\alpha|a|^2 + \beta|b|^2) = 0$. Thus,

$$E = (\frac{|\beta|}{|\alpha|+|\beta|}\varepsilon_v + \frac{|\alpha|}{|\alpha|+|\beta|}\varepsilon_c) + \frac{\beta\alpha}{|\alpha|+|\beta|}\frac{1}{R^2} + \frac{2\beta\alpha}{|\alpha|+|\beta|}\frac{M}{R^2} + \frac{2\tau\gamma\sqrt{\alpha|\beta|}}{(|\alpha|+|\beta|)R}M - \frac{\tau\gamma\sqrt{\alpha|\beta|}}{(|\alpha|+|\beta|)R}. \tag{17.23}$$

The presence of a magnetic flux Φ can be incorporated by the formal replacement $M \to M + \Phi$, so that the flux-dependent energy E_Φ results in a linear dependence on the magnetic flux:

$$E_\Phi = E + \left(\frac{2\beta\alpha}{|\alpha|+|\beta|}\frac{1}{R^2} + \frac{2\tau\gamma\sqrt{\alpha|\beta|}}{(|\alpha|+|\beta|)}\frac{1}{R}\right)\Phi \tag{17.24}$$

For the particular case of $|\alpha| = |\beta|$, i.e., $a^2 = b^2 = 1/2$, the slope of the flux becomes $(\frac{\sqrt{|\beta|\alpha}}{R^2} + \frac{\tau\gamma}{R})$, which is in quantitative agreement with the slope of the edge states numerically calculated and shown in Fig. 17.9. We note the second term in the slope, arising from the off-diagonal band coupling in Hamiltonian (17.19), is the dominant term, which explains the opposite slope in K ($\tau = 1$) and K' ($\tau = -1$) valleys.

Considering the pervasive presence of edge states in the magneto-spectrum of Fig. 17.9, one suspects they could have important implications for actual magneto-absorption and spin properties of TMD dots. Since early theoretical studies overlooked such states, [80–82] next we explore their robustness when using actual MoS_2 mass parameters, $\alpha = 1.72$ eV Å^2 and $\beta = -0.13$ eV Å^2 [92]. The results are shown in Fig. 17.10. As can be seen, the spectra are similar to those of Fig. 17.9, except for the CB of the K point –see top of Fig. 17.10a–, where drastic changes appear. Here, a gap opens up between the lowest (Φ-independent) LL and higher states, and Aharonov-Bohm like oscillations take place in the many-fold of states under each excited LL.

The interpretation of these effects is as follows. For $|\alpha| = |\beta|$ the Fermi level was in the center of the gap, $E \approx 0$ (notice the summands in the first parenthesis of (17.23) cancel out), and so were the edge states with small M angular momentum. Instead, for $|\alpha| \gg |\beta|$, the Fermi level shifts towards the vicinity of the CB. In the K valley, where such states have positive slope, this enables anticrossings between edge states and corresponding CB states with the same M. No anticrossings are observed in the K' valley because the low-M edge states, being close to the CB at zero field, require stronger Φ than we show in Fig. 17.10 to reach their VB counterparts.

Similar results are obtained if circular confinement is replaced by other shapes. Figure 17.11a, b show the magneto-spectrum of hexagonal and triangular MoS_2 quantum dots, respectively. Edge states again anticross with CB states, opening gaps and forming Aharonov-Bohm like oscillations. The main difference as compared to circular dots is that the oscillating many-folds are now formed by sets of six (Fig. 17.11a) and three (Fig. 17.11b) energy levels. This is due to the reduced symmetry of hexagons (C_6) and triangles (C_3) as compared to the circle.

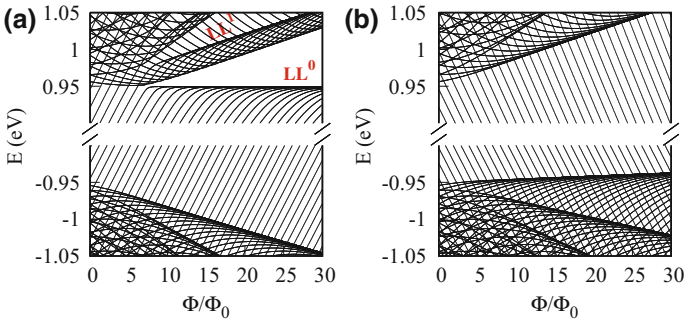

Fig. 17.10 Energy levels of a MoS_2 circular dot as a function of a perpendicular magnetic flux. $\alpha = 1.72$ eV Å^2 and $\beta = -0.13$ eV Å^2. **a** K valley. **b** K' valley. The lowest (LL^0) and first excited (LL^1) Landau levels of the CB are labeled

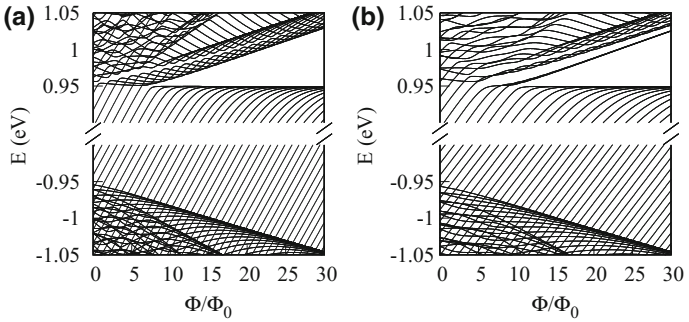

Fig. 17.11 Same as Fig. 17.10a, but for hexagonal (**a**) and triangular (**b**) dots

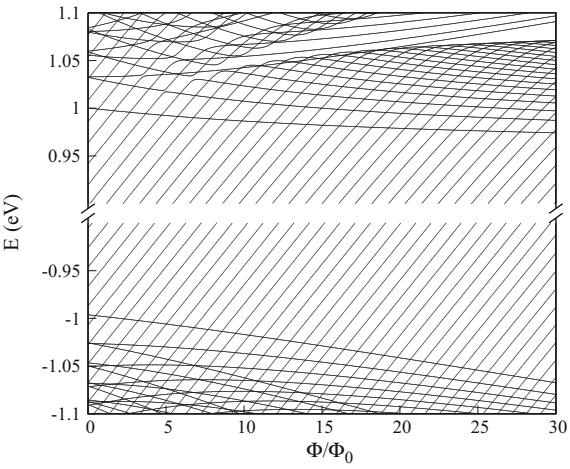

Fig. 17.12 Same as Fig. 17.10a, but including a harmonic confinement potential, $V(r) = 1/2\, m_j\, \omega_j^2\, r^2$ ($j = e, h$). $m_e = 1/\beta$, $m_h = 1/\alpha$, $\omega_e = 30$ meV and $\omega_h = \omega_e \sqrt{m_e/m_h}$

The quantum ring-like behavior of MoS_2 quantum dots arising from edge states can be tailored by means of external fields. As an example, in Fig. 17.12 we represent the K valley of a circular dot like that in Fig. 17.10a, but adding a harmonic confinement potential, which could be associated e.g. to electrostatic gating, $V(r) = 1/2\, k\, r^2$, with $k = m_j\, \omega_j^2$ ($j = CB, VB$ for electrons and holes). Edge states turn out to be robust against such potential, which is quite strong near the boundaries, see Fig. 17.12, but they are energetically unstabilized. In particular, low M edge states are blueshifted away from the middle of the gap, towards the proximity of the CB. This change shifts anticrossings with CB states to weaker Φ values as compared to the system with $V(r) = 0$, Fig. 17.10a. Consequently, anticrossings take place in excited CB states.

In conclusion, edge states in monolayer TMDs quantum dots exhibit a linear, Zeeman-like, response against perpendicular magnetic fields. When anticrossing with delocalized states of the dot, they can give rise to Aharonov-Bohm like oscillations. For MoS_2 quantum dots, these features are expected to show up in the CB of the K valley (and, for stronger fields, in the VB of the K' valley). The addition of external potentials, modifying the edge states energy with respect to that of delocalized states, can be used to tune the magnetic fields at which these quantum ring like features takes place.

Acknowledgements Support from MINECO project CTQ2017-83781-P and UJI project B2017-59 is acknowledged.

References

1. P.Y. Yu, M. Cardona, *Fundamentals of Semiconductors* (Springer, Berlin, 1999)
2. M. Dyakonov (ed.), *Spin Physics in Semiconductors* (Springer, Berlin, 2010)

3. R. Winkler, *Spin-Orbit Coupling Effects in Two-Dimensional Electron and Hole Systems* (Springer, Berlin, 2003)
4. L. Jacak, P. Hawrylak, A. Wójs, *Quantum Dots* (Springer, Berlin, 1998)
5. D. Brunner, B.D. Gerardot, P.A. Dalgarno, G. Wüst, K. Karrai, N.G. Stoltz, P.M. Petroff, R.J. Warburton, Science **325**, 70 (2009)
6. A. Greilich, S.G. Carter, D. Kim, A.S. Bracker, D. Gammon, Nat. Photonics **5**, 702 (2011)
7. T.M. Godden, J.H. Quilter, A.J. Ramsay, Y. Wu, P. Brereton, S.J. Boyle, I.J. Luxmoore, J. Puebla-Nunez, A.M. Fox, M.S. Skolnick, Phys. Rev. Lett. **108**, 017402 (2012)
8. K. De Greve, P.L. McMahon, D. Press, T.D. Ladd, D. Bisping, C. Schneider, M. Kamp, L. Worschech, S. Höfling, A. Forchel, Y. Yamamoto, Nat. Phys. **7**, 827 (2011)
9. K. Müller, A. Bechtold, C. Ruppert, C. Hautmann, J.S. Wildmann, T. Kaldewey, M. Bichler, H.J. Krenner, G. Abstreiter, M. Betz, J.J. Finley, Phys. Rev. B **85**, 241306(R) (2012)
10. E.A. Stinaff, M. Scheibner, A.S. Bracker, I.V. Ponomarev, V.L. Korenev, M.E. Ware, M.F. Doty, T.L. Reinecke, D. Gammon, Science **311**, 636 (2006)
11. D. Heiss, S. Schaeck, H. Huebl, M. Bichler, G. Abstreiter, J.J. Finley, D.V. Bulaev, D. Loss, Phys. Rev. B **76**, 241306(R) (2007)
12. B.D. Gerardot, D. Brunner, P.A. Dalgarno, P. Öhberg, S. Seidl, M. Kroner, K. Karrai, N.G. Stoltz, P.M. Petroff, R.J. Warburton, Nature **451**, 441 (2008)
13. J. Fischer, W.A. Coish, D.V. Bulaev, D. Loss, Phys. Rev. B **78**, 155329 (2008)
14. B. Eble, C. Testelin, P. Desfonds, F. Bernardot, A. Balocchi, T. Amand, A. Miard, A. Lemaitre, X. Marie, M. Chamarro, Phys. Rev. Lett. **102**, 146601 (2009)
15. P. Fallahi, S.T. Yilmaz, A. Imamoglu, Phys. Rev. Lett. **105**, 257402 (2010)
16. E.A. Chekhovich, A.B. Krysa, M.S. Skolnick, A.I. Tartakovskii, Phys. Rev. Lett. **106**, 027402 (2011)
17. C.-Y. Lu, Y. Zhao, A.N. Vamivakas, C. Matthiesen, S. Fält, A. Badolato, M. Atatüre, Phys. Rev. B **81**, 035332 (2010)
18. M.F. Doty, J.I. Climente, A. Greilich, M. Yakes, A.S. Bracker, D. Gammon, Phys. Rev. B **81**, 035308 (2010)
19. J.H. Blokland, F.J.P. Wijnen, P.C.M. Christiansen, U. Zeitler, J.C. Maan, Phys. Rev. B **75**, 23305 (2007)
20. J.I. Climente, J. Planelles, M. Pi, F. Malet, Phys. Rev. B **72**, 233305 (2005)
21. W. Jaskólski, M. Zielinski, G.W. Bryant, Phys. Rev. B **74**, 195339 (2006)
22. G. Bester, A. Zunger, Phys. Rev. B **72**, 165334 (2005)
23. M.F. Doty, J.I. Climente, M. Korkusinski, M. Scheibner, A.S. Bracker, P. Hawrylak, D. Gammon, Phys. Rev. Lett. **102**, 047401 (2009)
24. J.I. Climente, M. Korkusinski, G. Goldoni, P. Hawrylak, Phys. Rev. B **78**, 115323 (2008)
25. T. Chwiej, B. Szafran, Phys. Rev. B **81**, 075302 (2010)
26. A.I. Yakimov, A.A. Bloshkin, A.V. Dvurechenskii, Semicond. Sci. Technol. **24**, 095002 (2009)
27. G. Katsaros, V.N. Golovach, P. Spathis, N. Ares, M. Stoffel, F. Fournel, O.G. Schmidt, L.I. Glazman, S. De Franceschi, Phys. Rev. Lett. **107**, 246601 (2011)
28. F. Suarez, D. Granados, Dotor M. Luisa, J.M. Garcia, Nanotechnology **15**, S126 (2004)
29. J. Wu, Z.M. Wang, V.G. Dorogan, S. Li, Z. Zhou, H. Li, J. Lee, E.S. Kim, Y.I. Mazur, G.J. Salamo, Appl. Phys. Lett. **101**, 043904 (2012)
30. O. Tangmettajittakul, P. Boonpeng, P. Changmoung, S. Thainoi, S. Rattanathammaphan, S. Panyakeow, in *Photovoltaics Specialists Conference 37th IEEE*, vol. 002665 (2011)
31. Y. Aharonov, D. Bohm, Phys. Rev. **115**, 485 (1959)
32. A. Lorke, J. Luyken, A.O. Govorov, J.P. Kotthaus, Phys. Rev. Lett. **84**, 2223 (2000)
33. M. Bayer, M. Korkusinski, P. Hawrylak, T. Gutbrod, M. Michel, A. Forchel, Phys. Rev. Lett. **90**, 186801 (2003)
34. N.A.J.M. Kleemans, I.M.A. Bominaar-Silkens, V.M. Fomin, V.N. Gladilin, D. Granados, A.G. Taboada, J.M. Garcia, P. Offermans, U. Zeitler, Christianen, Maan J. C., Devreese J. T., Koenraad P. M. Phys. Rev. Lett. **99**, 146808 (2007)

35. Ding F., Li B., Akopian N., Perinetti U., Chen Y. H., Peeters F. M., Rastelli A., Zwiller V., and Schmidt O. G., J. Nanoelectron. and Optoelectron. **6**, 51 (2011); Ding F., Akopian N., Li B., Perinetti U., Govorov A., Peeters F. M., Bof Bufon C. C., Deneke C., Chen Y. H., Rastelli A., Schmidt O. G., and Zwiller V., Phys. Rev. B **82**, 075309 (2010)
36. J.I. Climente, J. Planelles, W. Jaskolski, Phys. Rev. B **68**, 075307 (2003)
37. L.G.G.V. Dias da Silva, S.E. Ulloa, A.O. Govorov, Phys. Rev. B **70**, 155318 (2004)
38. V.M. Fomin, V.N. Gladilin, S.N. Klimin, J.T. Devreese, Phys. Rev. B **76**, 235320 (2007)
39. N. Cukaric, M. Tadic, F.M. Peeters, Superlattice Microst. **48**, 491 (2010)
40. A.O. Govorov, S.E. Ulloa, K. Karrai, R.J. Warburton, Phys. Rev. B **66**, 081309(R) (2002)
41. B. Li, F.M. Peeters, Phys. Rev. B **83**, 115448 (2011)
42. E. Waltersson, E. Lindroth, I. Pilskog, J.P. Hansen, Phys. Rev. B **79**, 115318 (2009)
43. M. Szopa, E. Zipper, J. Phys.: Conf. Series **213**, 012006 (2006)
44. C. Segarra, J.I. Climente, J. Planelles, J. Phys.: Condens. Matter **24**, 115801 (2012)
45. J. Planelles, F. Rajadell, J.I. Climente, J. Phys. Chem. C **114**, 8337 (2010)
46. J.I. Climente, J. Planelles, J. Nanoelectron. Optoelectron. **6**, 81 (2011)
47. Burt M. G., J. Phys.: Condens. Matter **4**, 6651 (1992); ibid. **11**, R53 (1999)
48. B.A. Foreman, Phys. Rev. B **48**, 4964 (1993)
49. P.C. Sercel, K.J. Vahala, Phys. Rev. B **42**, 3690 (1990)
50. J.M. Luttinger, W. Kohn, Phys. Rev. **97**, 869 (1955); J.M. Luttinger, *ibid.***102**, 1030 (1956)
51. L. Voon, M. Willatzen, *The k·p Method: Electronic Properties of Semiconductors* (Springer, Berlin, 2009)
52. F. Rajadell, M. Royo, J. Planelles, J. Appl. Phys. **111**, 014303 (2012)
53. P. Offermans, P.M. Koenraad, J.H. Wolter, D. Granados, J.M. Garcia, Appl. Phys. Lett. **87**, 131902 (2005)
54. I. Vurgaftman, J.R. Meyer, L.R. Ram-Mohan, J. Appl. Phys. **89**, 5815 (2001)
55. M. Tadic, F.M. Peeters, K.L. Janssens, M. Korkusiński, P. Hawrylak, J. Appl. Phys. **92**, 5819 (2002)
56. J.A. Barker, R.J. Warburton, E.P. O'Reilly, Phys. Rev. B **69**, 035327 (2004)
57. R. Blossey, A. Lorke, Phys. Rev. E **65**, 021603 (2002)
58. C. Pryor, Phys. Rev. B **57**, 7190 (1998)
59. W. Sheng, J.P. Leburton, Phys. Stat. Sol. **237**, 394 (2003)
60. M. Tadic, N. Cukaric, V. Asoski, F.M. Peeters, Phys. Rev. B **84**, 125307 (2011)
61. C.Y.P. Chao, S.L. Chuang, Phys. Rev. B **46**, 4110 (1992)
62. N.A.J.M. Kleemans, J.H. Blokland, A.G. Taboada, H.C.M. van Genuchten, M. Bozkurt, V.M. Fomin, V.N. Gladilin, D. Granados, M.J.C. Christianen, J.T. Devreese, P.M. Koenraad, Phys. Rev. B **80**, 155318 (2009)
63. C. Pryor, Phys. Rev. Lett. **80**, 3579 (1998)
64. S.E. Economou, J.I. Climente, A. Badolato, A.S. Bracker, D. Gammon, M.F. Doty, Phys. Rev. B **86**, 085319 (2012)
65. T. Flissikowski, I.A. Akimov, A. Hundt, F. Henneberger, Phys. Rev. B **68**, 0161309(R) (2003)
66. M. Koperski, M.R. Molas, A. Arora, K. Nogajewski, A.O. Slobodeniuk, C. Faugeras, M. Potemski, Nanophotonics **6**, 1289 (2017)
67. M. Koperski, K. Nogajewski, A. Arora, V. Cherkez, P. Mallet, J.Y. Veuillen, J. Marcus, P. Kossacki, M. Potemski, Nat. Nanotechnol. **10**, 503 (2015)
68. A. Srivastava, M. Slider, A.V. Allain, D.S. Lembke, A. Kis, A. Imamoglu, Nat. Nanotechnol. **10**, 491 (2015)
69. Y.M. He, G. Clark, J.R. Schaibley, Y. He, M.C. Chen, Y.J. Wei, X. Ding, Q. Zhang, W. Yao, X. Xu, Nat. Nanotechnol. **10**, 497 (2015)
70. C. Chakraborty, L. Kinnischtzke, K.M. Goodfellow, R. Beams, A.N. Vamivakas, Nat. Nanotechnol. **10**, 507 (2015)
71. P. Tonndorf, R. Schmidt, R. Schneider, J. Kern, M. Buscema, G.A. Steele, A. Castellanos-Gomez, H.S.J. van der Zant, S.M. de Vasconcellos, R. Bratschitsch, Optical **2**, 347 (2015)
72. S. Kumar, A. Kaczmarczyk, B.D. Gerardot, Nano Lett. **15**, 7567 (2015)

73. A. Branny, G. Wang, S. Kumar, C. Robert, B. Lassagne, X. Marie, B.D. Gerardot, B. Urbaszek, Appl. Phys. Lett. **108**, 142101 (2016)
74. G. Wei, D.A. Czaplewski, E.J. Lenferink, T.K. Stanev, I.W. Jung, N.P. Stern, Sci. Rep. **7**, 3324 (2017)
75. L. Lin, Y. Xu, S. Zhang, I.M. Ross, A.C. Ong, D.A. Allwood, ACS Nano **7**, 8214 (2013)
76. T.T. Tran, K. Bray, M.J. Ford, M. Toth, I. Aharonovich, Nat. Natotechnol. **11**, 37 (2016)
77. S. Tongay, J. Suh, C. Ataca, W. Fan, A. Luce, J.S. Kang, J. Liu, C. Ko, R. Raghunathanan, J. Zhou, F. Ogletree, J. Li, J.C. Grossman, J. Wu, Sci. Rep. **3**, 2657 (2013)
78. W. Zhou, X. Zou, S. Najmaei, Z. Liu, Y. Shi, J. Kong, J. Lou, P.M. Ajayan, B.I. Yakobson, J.C. Idrobo, Nano Lett. **13**, 2615 (2013)
79. A. Kormanyós, V. Zóyomi, N.D. Drummond, G. Burkard, Phys. Rev. X **4**, 011034 (2014)
80. M. Brooks, G. Burkard, Phys. Rev. B **95**, 245411 (2017)
81. A.C. Dias, J. Fu, L. Villegas-Lelovsky, F. Qu, J. Phys.: Condens. Matter **28**, 375803 (2016)
82. F. Qu, A.C. Dias, J. Fu, L. Villegas-Lelovsky, D.L. Azevedo, Sci. Rep. **7**, 41044 (2017)
83. M.V. Bollinger, J.V. Lauritsen, K.W. Jacobsen, J.K. Norskov, S. Helveg, F. Besenbacher, Phys. Rev. Lett. **87**, 196803 (2001)
84. H. Pan, Y.W. Zhang, J. Mater. Chem. **22**, 7280 (2012)
85. E. Erdogan, I.H. Popov, A.N. Enyashin, G. Seifert, Eur. Phys. J. B **85**, 33 (2012)
86. S. Pavlovic, F.M. Peeters, Phys. Rev. B **91**, 155410 (2015)
87. D. Davelou, G. Kopidakis, G. Kioseoglou, I.N. Remediakis, Solid State Commun. **192**, 42 (2014)
88. C.G. Peterfalvi, A. Kormanyos, G. Burkard, Phys. Rev. B **92**, 245443 (2015)
89. C. Segarra, J. Planelles, S.E. Ulloa, Phys. Rev. B **93**, 085312 (2016)
90. A. Kormanyos, G. Burkard, M. Gmitra, J. Fabian, V. Z'olyomi, N.D. Drummond and V. Fal'ko, 2D Mater. **2**, 022001 (2015)
91. E. Ridolfi, L.R.F. Lima, E.R. Mucciolo, C.H. Lewenkopf, Phys. Rev. B **95**, 035430 (2017)
92. A. Kormanyos, V. Z'olyomi, N.D. Drummond, P. Rakyta, G. Burkard, V.I. Fal'ko, Phys. Rev. B **88**, 045416 (2013)

Chapter 18
Circular n-p Junctions in Graphene Nanoribbons

Alina Mreńca-Kolasińska and Bartłomiej Szafran

Abstract A characteristic feature of graphene as the Dirac conductor is that one can introduce doping by external voltages, so that the n-p junction can be defined and controlled by gating. The electrostatic n-p junctions in graphene act as waveguides that confine currents. The fact can be classically understood by the opposite orientation of the Lorentz force at both sides of the n-p junction, so that the carriers in both the conduction and valence band are shifted towards the junction by the external magnetic field. We describe our proposal for an Aharonov-Bohm interferometer at the n-p junction induced by the potential of the tip of an atomic force microscope. The conductance of the system exhibits Aharonov-Bohm oscillations provided that the persistent currents localized at the junction are coupled to the quantum Hall edge currents. The coupling is controlled by the Fermi energy and the tip potential. We discuss the Lorentz force effects in the system as compared to etched quantum rings in graphene and III-V semiconductors.

18.1 Introduction

Graphene [1] is an excellent material for studies of coherent electron transport with the mean free path [2, 3] of the order of several μm. The absence of the energy gap at the Dirac points of the dispersion relation allows for doping the material with external potentials [1]. The gating of the structure induces n- and p-type conductivity areas with potentials of the electrodes, which excludes the need for chemical doping [1]. For that reason an electrostatic control of the position of the chemical potential with respect to the Dirac point allows for a precise definition of n-p junctions within the sample. The bipolar graphene n-p junctions have been the focus of investigation early upon fabrication of the monolayer material with the Klein tunneling [4] as the most prominent example. Moreover, the n-p-n junctions were used for formation of

A. Mreńca-Kolasińska · B. Szafran (✉)
AGH University of Science and Technology, Kraków, Poland
e-mail: bszafran@agh.edu.pl

A. Mreńca-Kolasińska
e-mail: alina.mrenca-kolasinska@fis.agh.edu.pl

V.M. Fomin (ed.), *Physics of Quantum Rings*, NanoScience and Technology,
https://doi.org/10.1007/978-3-319-95159-1_18

the Fabry-Pérot interferometers [5–7]. The n-p junctions [8–10] are considered for studies of solid-state electron optics [11–16].

In the quantum Hall conditions [9, 17–19] the n-p junctions form waveguides [20] that confine electrical currents. Both the quantum Hall current transport near the edges of the sample and the current confinement along the n-p junction can be understood as due to the classical Lorentz force acting on the moving carrier in the external magnetic field. The classical counterpart of the current confinement at the n-p junction are the snake orbits [14, 21–33] along the junction which appear due to inversion [34] of the Lorentz force orientation with the carriers passing across the junction from the conductance to the valence band.

Mesoscopic n-p junctions in the quantum Hall conditions exhibit fractional quantization of the Hall conductance [9, 17, 19] which is explained by a non-coherent equilibration of the current flow along all the accessible edge and junction currents [9, 17, 19]. In this chapter we describe a proposal [35, 36] to induce a small nanosize circular n-p junction (see Fig. 18.1) of circumference much shorter than the coherence length within a narrow graphene strip (graphene nanoribbon [37]). The junction is formed by external electrostatic potential of a scanning probe (Fig. 18.2b) that is repulsive for electrons when the rest of the nanoribbon corresponds to the n-type conductivity region. Far from the junction the Fermi energy is set within the conduction band and the probe potential raises locally the Dirac point above the Fermi energy forming a circular region of p-type conductivity. The circular n-p junction in the quantum Hall conditions traps a persistent current and the coupling of the junction current to the edges of the ribbon [35, 36] produces an Aharonov-Bohm interferometer (see Fig. 18.2). We discuss the transport properties of the induced quantum ring (Fig. 18.2b) with respect to the etched graphene quantum rings (Fig. 18.2a) that were extensively studied by both experiment [38–43] and theory [44–54]. We pay a particular attention to the effects of the magnetic deflection. All the results to be discussed below are obtained for the out-of-plane orientation of the external magnetic field perpendicular to the plane of confinement (see Fig. 18.3). In classical terms the electrons of the conduction band are shifted to the left of the velocity vector. For the valence band the deflection has an opposite direction.

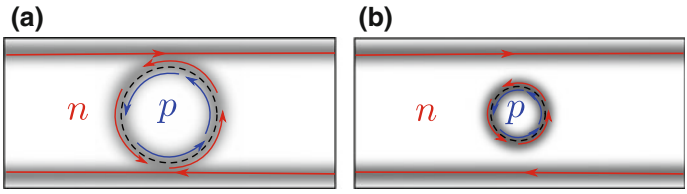

Fig. 18.1 Schematic drawing of the currents in the system in the quantum Hall regime for a circular p-type region induced by an external electrostatic potential within the n-type conductivity nanoribbon. The junction is marked with the dashed line. **a** Low E_F and edge current coupled to the n-p junction. **b** For high E_F the radius of the n-p junction decreases, and the junction is too far from the edge for the edge current to couple to the n-p junction. Reproduced from [35]

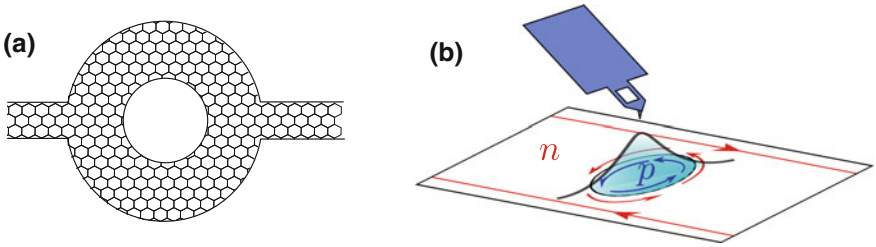

Fig. 18.2 AB interferometers: a ring etched out of graphene (**a**) and a circular n-p junction induced within a graphene nanoribbon (**b**). The potential in (**b**) is due to a charged tip of an atomic force microscope and the arrows indicate the orientation of the currents within the bipolar conductivity regions. Reproduced from [36]

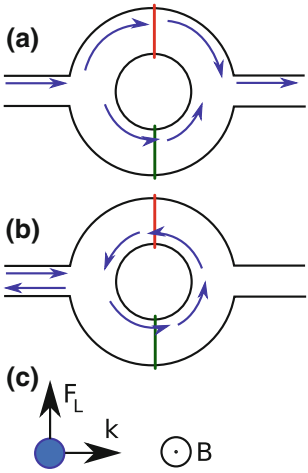

Fig. 18.3 Schematics of the electron flow at the maxima (**a**) and minima (**b**) of G in Fig. 18.12 and (**c**) the orientation of the Lorentz force for the electron moving right in the out-of-plane magnetic field. After [36]

A charged tip of the atomic force microscope (Fig. 18.2b) that is employed for formation of the circular n-p junction is used in the scanning probe microscopy (SGM) technique [55–61]. The SGM exploits a local modification of the potential landscape to study the reaction of the electric properties of the sample to the charged probe with a spatial resolution. The SGM technique was used for observation of the magnetic deflection effects for the electron trajectories in graphene, i.e. the cyclotron and skipping orbits [60, 61] as well as the magnetic focusing [16, 28, 62–65]. The effects of the magnetic deflection of the trajectories for induced and etched quantum rings are discussed below.

18.2 Modeling the Electron Transport in Nanoribbons with External Probe Potential

For description of the coherent single-electron transport in graphene we use an atomistic tight binding approach with the p_z orbitals forming the π bonding between the carbon atoms. The Hamiltonian that is used can be put in form

$$H = \sum_{\langle i,j \rangle} \left(t_{ij} c_i^\dagger c_j + h.c. \right) + \sum_i V(\mathbf{r}_i) c_i^\dagger c_i, \tag{18.1}$$

where $\langle i, j \rangle$ stands for a pair of nearest neighbors carbon atoms, and $V(\mathbf{r}_i)$ for the tip potential at the i-th ion. We consider a two-terminal transport (see Fig. 18.2) devices in which the current is fed and extracted by nanoribbons.

The original potential of the charged graphene probe is of the Coulomb form. The electron gas is deformed in response to the potential and the deformation results in screening of the long range part of the tip potential. The effective potential as determined by the Schrödinger-Poisson modeling [66, 67] is close to a Lorentzian form

$$V(\mathbf{r}) = \frac{V_t}{1 + (|\mathbf{r} - \mathbf{r}_t|/d)^2}, \tag{18.2}$$

where $\mathbf{r}_t = (x_t, y_t, 0)$ is the projection of tip position on the plane of the electron gas, d stands for the width of the effective tip potential, and V_t is the maximal value of the tip potential. The width of the tip potential d turns out [66] of the order of the distance between the tip and the electron gas and only weakly depends on the Fermi energy or electron density and the charged accumulated at the tip [66], which only influence the height of the potential V_t.

The hopping elements in the Hamiltonian (18.1) include the Peierl's phase, $t_{ij} = t \exp(\frac{2\pi i}{\phi_0} \int_{\mathbf{r}_i}^{\mathbf{r}_j} \mathbf{A} \cdot \mathbf{dl})$, where t is the hopping parameter. In the studies we are interested in the external magnetic field that is applied perpendicular to the plane of confinement $\mathbf{B} = (0, 0, B_0)$, and we describe it using the Landau gauge, $\mathbf{A} = (-yB_0, 0, 0)$.

The atomistic Hamiltonian that we use here produces large algebraic problems of the order of the number of atoms present within the computational box. In the low-energy transport conditions that we are interested in the size and the numerical cost of the problem can be reduced by the scaling trick introduced by [68]. The ribbons that we model below are scaled up with the condition for the lattice constant $a = a_0 s_f$ and $t = t^0/s_f$, where $t^0 = -2.7$ eV is the unscaled hopping parameter, $a_0 = 2.46$ Å is the graphene lattice constant. We apply a scaling factor up to $s_f = 4$.

We follow the Landauer approach and evaluate the conductance from solution of the scattering problem. We first determine the eigenstates of the input and output leads (graphene nanoribbons). We look for the electron eigenstates in the nanoribbon in the Bloch form,

$$\psi_{u,v}^{k_m} = \chi_v^{k_m} e^{ik_m u \Delta x}, \tag{18.3}$$

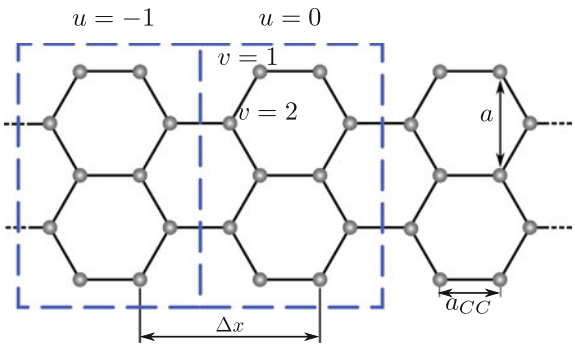

Fig. 18.4 Schematic drawing of a nanoribbon that is used as the input and output channel. An armchair ribbon is selected for presentation. In the Bloch waves (18.3) that serve as the eigenstates of the channels u numbers the elementary cells, v the ions within the cell, $a_{CC} = 0.142$ nm is the nearest neighbor distance, $a = 0.246$ nm is the lattice constant, and Δx is the period of the considered nanoribbon. After [69]

where k_m is the wave vector for the m-th subband, $\chi_{u,v}^{k_m}$ is a periodic function with the periodicity of the crystal structure of the ribbon at the vth site in the uth elementary cell within the ribbon which has the length of Δx (see Fig. 18.4). In presence of the scatterer within the computational box the resulting wave functions in the input lead are superpositions of the incident wave function $\psi_{in}^{k_{in}^+}$, and the backscattered ones,

$$\Psi_{in}^{u,v} = \sum_l c_{in}^l \psi_{u,v}^{k_{in}^+} + \sum_l d_{in}^l \psi_{u,v}^{k_l^-}, \tag{18.4}$$

where the summation runs over the subbands l that are responsible for the backscattered current with the current flux oriented from the scatterer back to the input lead. In order to evaluate the scattering for the incoming mode with wave vector k_{in}^+ we set $c_{in}^l = \delta_{l,in}$. At the output lead a general transferred wave function has the form

$$\Psi_{out}^{u,v} = \sum_l c_{out}^l \psi_{u,v}^{k_l^+}, \tag{18.5}$$

where, this time, the summation runs only over the subbands carrying the current to the right. The backscattered d_{in} and transferred amplitudes c_{out} are determined with the wave function matching method (WFM) [70, 71] which glues the wave function in the scattering region with the asymptotic Hamiltonian eigenstates. For evaluation of conductance within the Landauer approach we consider each mode of the input lead as the source of the electron current. After solution of the quantum scattering problem we obtain the transfer probability from the mode n input lead to modes m in the output lead t^{mn}. The total transmission probability is obtained by a summation

$$T^m = \sum_n |t^{mn}|^2. \tag{18.6}$$

The linear conductance [72] at the Fermi level for 0 K is evaluated as $G = G_0 T_{tot}$, with $T_{tot} = \sum_m T^m$ and $G_0 = 2e^2/h$. Note, that we neglect the spin Zeeman effect in the Hamiltonian.

For evaluation of the transfer probability [72] and for the purpose of the discussion of the electron motion within the rings we evaluate the the current that flows along the π bonds between the atoms m and n [73]

$$J_{mn} = \frac{i}{\hbar}\left[t_{mn}\Psi_m^*\Psi_n - t_{nm}\Psi_n^*\Psi_m\right], \tag{18.7}$$

where Ψ_n is the wave function at the nth atom.

18.3 Control of the Aharonov-Bohm Oscillations

A clear signal of the AB oscillations induced by the tip potential in the nanoribbon was found in the single-subband limit of a low Fermi energy. In Figs. 18.5 and 18.6 we consider the system defined within an armchair graphene nanoribbon. At $B = 0$ the armchair nanoribbon [37, 74] can be either metallic or semiconducting depending on its width. In the quantum Hall regime the currents flow near the edges of the sample and the Fermi level eigenstates are localized at a single edge of the ribbon. However, the conductance still depends on the width of the nanoribbons. The dependence can be expressed by the angle between the valley isospins of both edges [10]. For ribbons with N atoms across, the conductance tends to $2G_0$ (transparent junction) when $N + 1$ is a multiple of 3, and to $\frac{G_0}{2}$ for other N [10]. At $B = 0$ these ribbons happen to be metallic and semiconducting, respectively [74].

Conductance as a function of the external magnetic field is displayed in Figs. 18.5a and 18.6a for the tip above the center of the ribbon at $E_F = 30$ meV (Fig. 18.5a) and $E_F = 60$ meV (Fig. 18.6a). For low magnetic field the metallic ribbons (blue lines in Figs. 18.5a and 18.6a) are transparent for the electron flow. The Aharonov-Bohm oscillations appear earlier for the semiconducting ribbons (orange lines in Figs. 18.5a and 18.6a). However, conductance oscillation becomes periodic only above 10 T. Formation of a periodic oscillation pattern that is observed in Figs. 18.5a and 18.6a at higher B results from the current confinement at the n-p junction that only appears in the quantum Hall regime.

The n-p junction currents in the quantum Hall regime are stabilized by the Lorentz force, which also has consequences on the details of the AB oscillations. Figures 18.6c and 18.5c, e indicate that for increasing Fermi energy, the radius of the junction is reduced (see also Fig. 18.1) and the coupling of the edge current to the junction is weakened. Similar is the effect of the increased magnetic field, which reduces the penetration of the edge currents to the interior of the ribbon. The states localized at

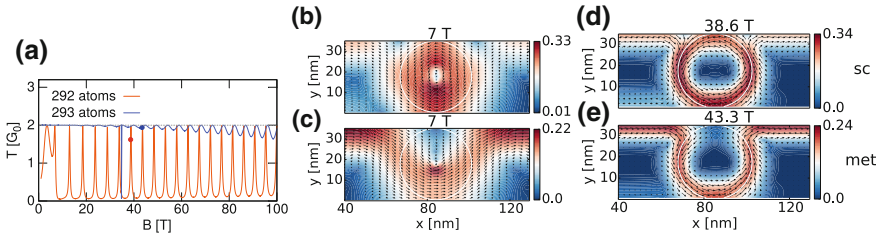

Fig. 18.5 **a** Summed electron transfer probability for armchair nanoribbons in the lowest subband transport conditions for $E_F = 30$ meV. Armchair nanoribbons are metallic when the number N of atoms across the ribbon satisfies the condition that $N + 1$ is a multiple of 3, and semiconducting for other N. We consider semiconducting nanoribbon with 292 atoms across the channel (35.79 nm) – orange lines, and metallic one with 293 atoms across the channel (35.92 nm) – blue lines. The tip is located above the axis of the channel. The applied tip potential is $V_t = 400$ meV, and $d = 4.92$ nm. In **b**–**e** maps of the square root of the current amplitude [current amplitude calculated using (18.7)] are plotted with orientation of the vector current distribution. The electron of the conduction band is incident from the left, and the Lorentz force acts to the left (right) of the carrier momentum for the conduction (valence) band. Plots **b**, **d** were calculated for the semiconducting, and (**c**, **e**) for the metallic ribbon. The external magnetic field is 7 T in **b**, **c** for B below formation of a periodic AB oscillation. Plot **d** was made for the semiconducting ribbon – see the orange dot in (**a**). Plot **e** corresponds to the metallic ribbon and was taken for the magnetic field marked by the blue dot in (**a**). After [35]

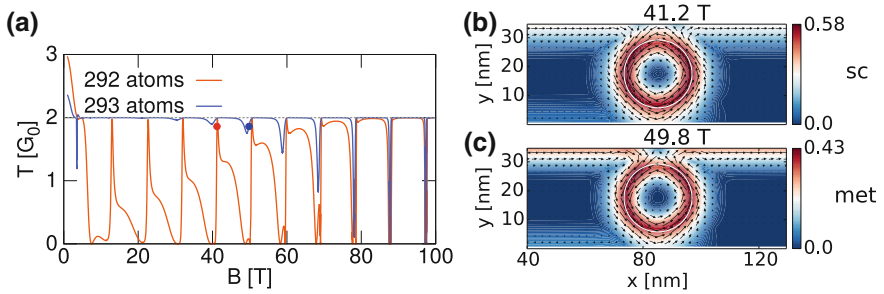

Fig. 18.6 **a** Same as Fig. 18.5a for $E_F = 60$ meV. **b**, **c** square root of the current amplitude [current amplitude calculated using (18.7)] plotted with orientation of the vector current distribution. The current plot **b** was made for the semiconducting ribbon – see the orange dot in (**a**). The plot **c** corresponds to the metallic ribbon and was taken for the magnetic field marked by the blue dot in (**a**). After [35]

the n-p junction, when separated from the edge, form long living resonances, which is at the origin of the abrupt form of the conductance oscillations at high B magnetic field. Outside these resonances (cf. the dips at Fig. 18.6a), the tip has no impact on the electron transfer probability (Fig. 18.6a).

The results for conductance oscillations are summarized for both the semiconducting and metallic ribbons by Fig. 18.7 which shows the conductance as a function of the Fermi energy and magnetic field (Fig. 18.7a, b), the Fourier transform of conductance (Fig. 18.7c, d). The conductance oscillation is present only for $\nu = 2$. The

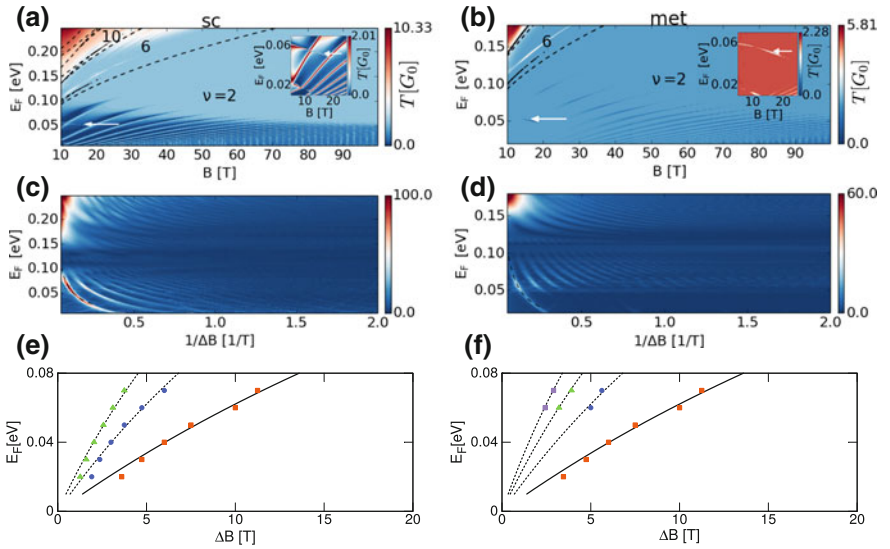

Fig. 18.7 Summed transfer probability for semiconducting (**a**) and metallic armchair ribbons (**b**) for parameters as in Fig. 18.5. Dashed black lines in (**a**) and (**b**) indicate transport threshold for subsequent subbands of the lateral quantization. The insets show the transfer probability for magnetic field below 25 T. The arrows in (**a**) and (**b**) indicate a feature due to a resonant state localized beneath the tip – entirely within the p-conductivity region. The power spectra (Fourier transform) of the $T(B)$ dependence are displayed in (**c**) and (**d**). Dashed black line in (**c**) and (**d**) indicate the Aharonov-Bohm period as calculated analytically from the radius of the n-p junction given by the condition $E_F = V(x, y)$. The numbers in (**a**, **b**) denote the Landau level filling factor ν. In (**e**, **f**) the AB period and its $1/2, 1/3, \ldots$ fractions calculated for the condition $E_F = V(x, y)$ are shown. The points represent values calculated from several values of the frequencies, at which peaks occur, extracted from the Fig. (**c**, **d**). After [35]

oscillation period distinctly depends on the Fermi energy (cf. Fig. 18.7a, b). The Fourier transform of conductance in Fig. 18.7c, d can be used for readout of the AB oscillation period. The period is determined by the radius of the n-p junction induced by the tip that corresponds to $E_F = V(x, y)$ line. The condition determines the radius of the circular junction $R = d\sqrt{V_t/E_F - 1}$, or $R = 17.3$ nm for $E_F = 30$ meV and $R = 11.7$ nm for $E_F = 60$ meV. The AB oscillation period for a ring of radius R can be estimated by $\Delta B = \frac{h}{eA}$, where A is the area encircled by the n-p junction current $A = \pi R^2$. One obtains $\Delta B = 4.4$ T for $E_F = 30$ meV and $\Delta B = 9.6$ T for $E_F = 60$ meV. These estimates are in a good agreement with the periods obtained by the Landauer calculations. The dashed lines in Fig. 18.7c, d indicate the period corresponding to the flux quantum. The Fourier spectrum contains also higher harmonics. The quantitative comparison of the fundamental period and higher harmonics is given in Fig. 18.7e, f.

Figure 18.7c, d shows that for the metallic ribbon (Fig. 18.7d) at low Fermi energy only the fundamental AB period can be observed, and the higher harmonics are much

better resolved for the semiconducting ribbon (Fig. 18.7c). Explanation of the effect can be found by analysis of the current circulation. In Figs. 18.5 and 18.6 one can notice that the edge current in the metallic ribbon passes smoothly to the circular n-p junction (Figs. 18.5c, e) and follows the junction to the other edge of the ribbon, with only a weak backscattered current at the upper edge of the ribbon. On the other hand in the semiconducting ribbons (Fig. 18.5b, d) the contact of the n-p junction and the edge of the ribbon splits the current influx and sends only a part of the current along the n-p junction. In that sense the edge-junction contact in semiconducting ribbon acts as a beam splitter [75]. Similarly, the junction-edge contact near the lower edge of the ribbon sends a part of the current back to the input lead. Finally, the upper contact to the right of the tip ejects a part of the current to the output lead, and keeps another part circulating around the junction. Due to the splitting of the current at the edge-junction contacts one observes a distinct current loop going all around the ring-like junction (the upper edge-junction contact in Figs. 18.5d and 18.6b). The visibility of the conductance oscillations for the semiconducting ribbon is much higher than those for the metallic ribbon (Figs. 18.5a and 18.6a).

The higher harmonics in the conductance dependence on the magnetic field are related to formation of resonances with multiple loops around the n-p junction performed by the electron [76, 77]. At lower Fermi energy, when the junction-edge coupling is strong the transfer probability is determined by the interference between the current that circulates around the junction and the residual one which goes straight at the upper edge (Fig. 18.5e). This interference corresponds to the one-pass electron passage as discussed in the original paper of Aharonov and Bohm [78]. For higher E_F, with reduced n-p junction radii and weaker coupling to the edge the current circulates around the n-p junction (Fig. 18.6c). The phase accumulated by the electron from the vector potential is proportional to the number of turns, and higher harmonics appear in the power spectrum (Fig. 18.7d). For the semiconducting ribbon, the higher harmonics are present also at low energy (Fig. 18.7b) due to the beam-splitting role of the junction/edge contacts (Fig. 18.5d).

In experiment one can manipulate the Fermi energy (by a back gate voltage [79]) or the potential applied to the tip. Thus, both the oscillation period and the coupling of the junction currents to the edge that determines the visibility of the oscillations should be subject to an intentional control.

18.4 Relation to Singly Connected Quantum Rings in III-V Semiconductors

The current distribution presented in Figs. 18.5b–e and 18.6b–c with the edge current coupled to the loop formed at the n-p junction is similar to the III-V semiconductor system of a channel with side attached singly-connected quantum ring – see Fig. 18.8. Quantum rings singly-connected to a conducting channel modify its coherent transport properties although they lie outside the classical current path [80], which is

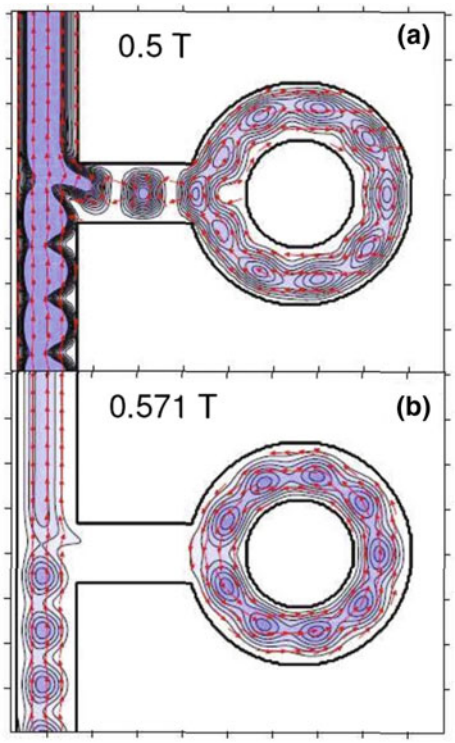

Fig. 18.8 Schematic plot of the 64 nm wide GaAs channel singly connected to a ring with inner and outer radii of 60 and 124 nm, respectively. The contours show the charge density for two peaks of backscattering probability of Fig. 18.10 obtained for $E = 2.65$ meV at $B = 0.5$ T (**a**) and at $B = 0.751$ T (**b**). The arrows show the probability current distribution. After [97]

a signature of the quantum interference effects for conductance. The side-attached structures usually support localized states in the energy continuum that may enter into a Fano [81] interference with the current-carrying delocalized states of the channel. The Fano resonances for III-V quantum dots and rings connected to a semiconducting channel by one or two contacts have been extensively discussed in the context of phase coherence probes [82], fabrication of spin valves [83, 84], Aharonov-Bohm interferometers [85], Kondo effect [86–89] or single-electron transistors [90].

Energy position of the localized states in the ring of Fig. 18.8 can be determined by the stabilization method [91]. For the purpose of the method one replaces an infinite channel by its segment of a finite length. Then one solves the Hamiltonian eigenequation with Dirichlet boundary conditions with wave functions vanishing at the edges of the system. The energy spectrum is calculated as a function of the length of the segment of the channel L. Next, the spectral positions of the ring-localized states are determined by counting the states of the energy close to E,

$$N(E) = \int dL \sum_l \delta(|E - E_l(E)|; dE), \tag{18.8}$$

where l runs over the Hamiltonian eigenvalues for the finite system, and $\delta(|E - E_l(L)|; dE)$ is equal to 1 for $|E - E_l(L)| < dE$ and 0 otherwise. The idea behind this method is that the states localized at the scattering center (here – the side-attached ring) only weakly depend on the length of the finite chanel segment. They do enter into avoided crossings with the channel eigenstates. The summation in (18.8) is supposed to extract the precise position of the resonance on the energy scale. The width of the avoided crossings then – that is determined by the coupling of the localized state to the channel – is translated in to the width of the peak corresponding to a specific resonance, that in turn can be associated with the lifetime of the localized resonance [91]. In Fig. 18.9b we plotted $N(E)$ calculated for the side-attached ring with the energy window $dE = 5\,\mu$eV.

Figure 18.9 shows the resonance counter $N(E)$ as a function of B (Fig. 18.9a) compared to the energy spectrum of a closed [92, 93] quantum ring (Fig. 18.9b) with the contact to the channel removed. In Fig. 18.9a two lowest-energy lines correspond to states bound at the T junctions of the bar linking the channel to the ring. The dashed green line shows the channel continuity threshold. Above the threshold we observe quasi localized levels corresponding to states localized in the ring. The positions of resonances oscillate with the magnetic field with a period of 0.165 T that corresponds to the Aharonov-Bohm effect for a ring of an effective radius of 92 nm. The resonances enter into avoided crossings that result from angular momentum mixing of closed-

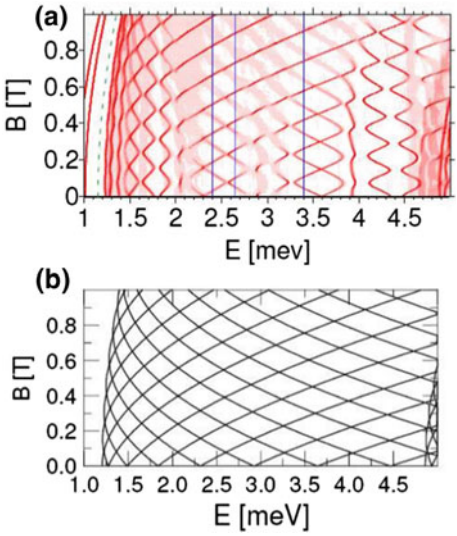

Fig. 18.9 **a** Positions of localized states in the energy continuum as calculated by formula (18.8) for the GaAs ring of Fig. 18.8. The darker the shade of red the larger value of $N(E)$. The thin vertical lines indicate energies of 2.4, 2.65 and 3.4 meV that are considered in detail below. The green dashed line indicates the continuum threshold (ground-state energy of the electron within the channel for $k = 0$). **b** Energy spectrum of the closed circular quantum ring that is not connected to the channel. After [97]

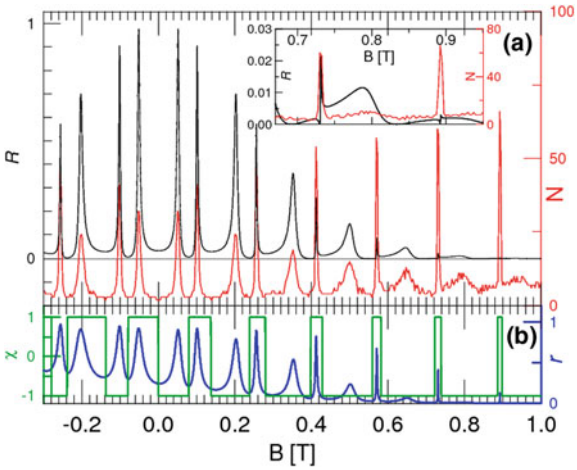

Fig. 18.10 **a** Black line shows the electron backscattering probability for energy $E = 2.65$ meV and the red one – the value of the resonance detection counter $N(E)$ (18.8). The inset shows a zoom of high B part of the figure. **b** The value of χ plotted in green indicates the direction of the current circulation inside the ring: $\chi = 1(-1)$ corresponds to counterclockwise (clockwise) direction. The blue line shows the fraction of the probability density r that is contained within the ring of the computational box of Fig. 18.8. After [97]

ring states by the attachment of the bar that breaks the rotational symmetry. Levels repulsion generated by the symmetry breaking was reported also in [94, 95]. Above 4.6 meV the states of the second channel subband appear in Fig. 18.9a. The wave functions of the second subband change sign across the channel.

The red lines in Fig. 18.10a show the resonance counter $N(E)$ of 18.8 for $E_F = 2.65$ meV. The backscattering probability R plotted with the black line in Fig. 18.10a exhibits peaks that perfectly coincide on the magnetic field scale with the energy positions of the ring-localized states. Thus, we can see that backscattering occurs as a result of an interference of the channel mode with a localized state within the ring. Outside the degeneracy of the two levels the side-attached structure is transparent for the current flow. The asymmetry of R is a characteristic signature of the Fano resonances [81]. Additionally, in Fig. 18.10b we plotted the fraction r of the probability density stored by the computational box of Fig. 18.8 contained within the ring. The electron wave function penetrates the ring for magnetic fields for which a localized state is present at a given energy. Although R is an even function of B, r is not $[r(B) \neq r(-B)]$. For $B > 0$ the Lorentz force deflects the electron trajectories to the left of its momentum vector, hence the penetration of the wave function to the ring is hampered for positive and enhanced for negative magnetic field. The maxima of the backscattering probability R get reduced for high B. The Lorentz force for $B > 0$ pushes the electron to the left edge of the vertical channel and weakens the coupling to the ring. At high B the presence of the ring still produces the Fano peaks but on a tiny scale (see the inset to Fig. 18.10a). In this sense the Lorentz force for $B > 0$ assists in the electron transport across the contact. Note, that due to the Onsager

microreversibility relation [96] one finds $R(B) = R(-B)$ although for negative B the electron penetration to the ring is enhanced.

$N(E)$ plot in Fig. 18.10a that is a cross section of Fig. 18.9a taken along the constant energy line $E_F = 2.65$ meV crosses the resonances of Fig. 18.9a that grow or decrease in energy as the magnetic field grows. The energy variation of the resonance is related to the orientation of the magnetic dipole moment generated by currents $\mu = -\frac{dE}{dB}$. For a closed 1D quantum ring one has $\mu = -\frac{1}{2}e\mathbf{r} \times \mathbf{j}$, where $\mathbf{j}$ is the probability density current. The resonances that grow (decrease) in the energy correspond to states with current circulation counterclockwise (clockwise) around the ring that produces μ that is antiparallel (parallel) to the $\mathbf{B}$ vector. The orientation of the current is denoted by $\chi = \pm 1$ (green line in Fig. 18.10b), where the plus sign stands for the counterclockwise circulation. For $B > 0$ the resonances that increase (decrease) in width correspond to clockwise (counterclockwise) current circulation. At high $B > 0$ the current circulation in the scattering eigenstates is counterclockwise with the exception of the magnetic fields near the sharp Fano resonances (Fig. 18.10).

The plots selected for Fig. 18.8 display the current distribution and the scattering density for two T peaks of Fig. 18.10a, a wide one (Fig. 18.8a) and a narrow one (Fig. 18.8b). The charge density is pushed to the left with respect to the electron momentum – to the external edge of the ring for the wide peak (Fig. 18.8a) and to the internal one for the narrow peak (Fig. 18.8b), in consistence with the orientation of the current circulation within the ring. The electron of the ring-localized state is either ejected into the horizontal bar to the channel or kept within the ring by the Lorentz force. Thus the magnetic deflection effects for $\mu < 0$ ($\mu > 0$) increase (decrease) both the localized state lifetime and the energy of the resonance. The lifetime on its turn is translated to the width of the resonance in the transfer probability.

Although the GaAs etched ring (Fig. 18.8) supports the resonances with both orientations of the persistent current, the results that we presented in the precedent section (Figs. 18.5b, e, 18.6b, c and 18.7a, b) for the quantum ring induced by the n-p junction in the graphene ribbon indicated the presence of AB periodic series of resonances that grow in the energy as the magnetic field is increased, i.e. the ones with $\mu < 0$ and counterclockwise current circulation. The other orientation of the current is simply not supported by the n-p junction and is missing in the conductance spectra of the system.

In Fig. 18.7a, b there is a single line that falls with B that is marked by an arrow in Figs. 18.7a, b. The resonance behind this line is localized beneath the tip, entirely in the p-conductivity region. The resonance that circulates clockwise is separated by the Lorentz force from the junction as the magnetic field grows.

18.5 The Lorentz Force Effects for Two-Terminal Graphene Rings

The series of the resonances including both the states with clockwise and counterclockwise current circulation, similar to the ones discussed in the precedent section

for GaAs structure, are present for quantum rings that are etched in graphene [38–54] (see Fig. 18.2a).

A narrow etched ring (the internal radius $R_1 = 41.05$ nm, and the external one $R_2 = 48.95$ nm – see the inset to Fig. 18.11a) presents a simple periodic behavior in the external magnetic field. The leads applied here are semiconducting armchair nanoribbons of width $W = 17.23$ nm. Both the linear conductance (Fig. 18.11a) as well as the resonance counter (Fig. 18.11b) contain a number of lines that change only weakly in the energy with B. These lines correspond to states that are localized near the edges of the ring whenever short zigzag segments appear. The weak dependence on B results from strong localization of these states. For larger magnetic field the resonance state diagram (Fig. 18.11b) contains a series of lines in the energy as B is increased. These lines are also visible – although weaker in the conductance plot (Fig. 18.11a).

In order to study the current circulation at the resonances a cross section of Fig. 18.11a for conductance was plotted in blue in Fig. 18.12 for $E = 0.0586$ eV

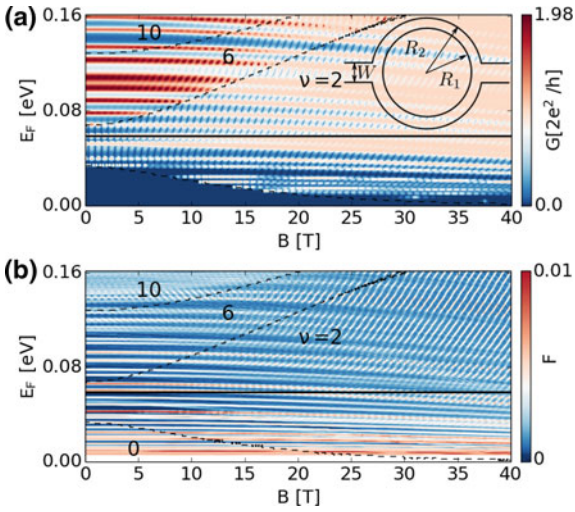

Fig. 18.11 **a** Conductance of a narrow quantum ring ($R_1 = 41.05$ nm, $R_2 = 48.95$ nm) connected to a semiconducting armchair ribbon of width $W = 17.23$ nm. **b** Counter of the localized states as determined by the stabilization method. Dashed lines separate the regions of varied filling factor ν in the ribbon. The solid vertical lines indicate the Fermi energies studied in detail. After [36]

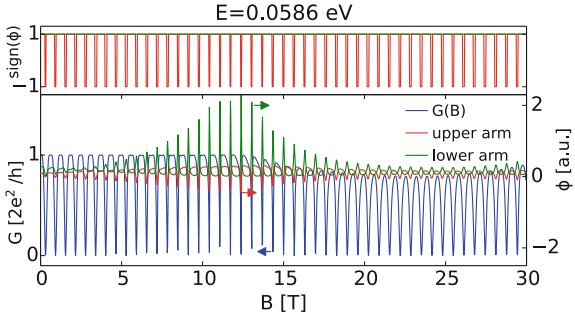

Fig. 18.12 Conductance (blue line) – cross section of Fig. 18.11a for $E = 0.0586$ eV, the current flux through the upper and lower arms of the ring (see Fig. 18.3) and the sign of the flux (upper panel). After [36]

(the horizontal black line in Fig. 18.11a, b). In Fig. 18.12 we also plotted the current fluxes that pass through the upper and lower arms of the ring, for the current injected to the ring from the left (Fig. 18.3a). We can see that the conductance oscillations of Fig. 18.12 are strictly correlated with the oscillations of the current fluxes with B. At the conductance maxima the current flows to the right at both the upper and lower arms of the ring (Fig. 18.3a). On the other hand for the dips of conductance a reversal of the current in the upper arm is found. Therefore, for the conductance dips the current forms then a counterclockwise loop around the ring (Fig. 18.3b). As we know from the precedent section this current circulation generates magnetic dipole $\mu < 0$ which is antiparallel to the external magnetic field [97] which leads to the growth of the resonance energy with B. The growth can indeed be spotted in Fig. 18.11a. In Fig. 18.13a the transfer probability – still for $E = 0.0586$ eV is confronted with the localized resonances counter that was denoted in the original paper [36] by F, but is identical with $N(E)$ given by (18.8). We can see that the peaks of the counter coincide with the dips of conductance. Hence, the backscattering of the incident current occurs at the Fermi energy that allows for an interference of the incoming electron with the ring localized quasi-bound states to appear. For the anticlockwise current circulation the Lorentz force keeps the current confined within the ring (Fig. 18.3c) hence the sharp resonances in the stabilization diagram (Fig. 18.11b). On the other hand, the localized states that correspond to the positive magnetic moment $\mu > 0$ are destabilized by the Lorentz force, so they leave weaker signal on the stability diagram of Fig. 18.11b – visible at the high energy part of the figure in the upper right corner of the plot. The reason why a high Fermi energy is needed to spot these lines is that in graphene the cyclotron radius for the Fermi energy E_F [61] is $R_c = \frac{E_F}{V_F eB}$, where the Fermi velocity V_F is the graphene material constant. For higher Fermi energy R_c exceeds the size of the ring-ribbon junction. In these conditions the effects of the magnetic deflection of the electron trajectories that tends to eject the resonance states out of the ring is weaker, the resonance has longer lifetime and appears in Fig. 18.11b.

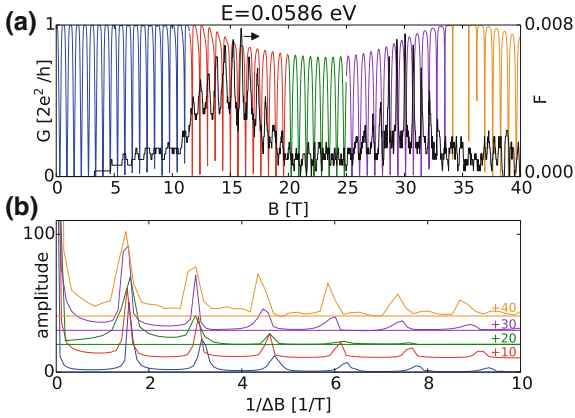

Fig. 18.13 **a** Conductance (line of varied colors) – same as in Fig. 18.12, and the resonance counter for $E = 0.0586$ eV. **b** Fourier transform calculated for intervals of the magnetic field which are marked in the corresponding colors. Each plot in (**b**) is normalized so that the first peak has the same amplitude as in the blue curve. After [36]

The Fourier transforms of conductance of the quantum rings are of an elementary interest for the electron transfer dynamics across the system. The presence of the high harmonics is considered [41, 98] a signature of phase coherence length being much larger than the circumference of the ring. The electrons paths encircling the ring n times [99, 100] produce a component of the conductance oscillation of the period of ϕ_0/n. Moreover, for strongly disordered conductors the Al'tshuler-Aronov-Spivak [76] periodicity of $\phi_0/2$ dominates over the Aharonov-Bohm ϕ_0 period. High harmonics of conductance for graphene quantum rings at high magnetic fields were observed in [41] and attributed to reduction of scattering involving electron spin flips at high B. The spin-flip induce decoherence and limits number of the electron turns around the ring before it dephases. In [36] we demonstrated that enhancement of the high harmonics at a stronger magnetic field can also be obtained in the absence of any dephasing effects, due to the magnetic forces.

The Fourier transform of $G(B)$ calculated in finite ranges of B are given in Fig. 18.13b with different colors as marked in Fig. 18.13a. The Fourier transforms are normalized to produce the first peak of the same amplitude. In Fig. 18.13b we find that: (i) the oscillation period increases with B and (ii) the higher harmonics are enhanced at high B. These features can be explained as due to the Lorentz force. Feature (i) results from a reduced effective radius of the ring that is due to the Lorentz force that pushes the scattering density to the internal core of the ring (cf. Fig. 18.3b). Reduction of the area A encircled by electrons reduces the AB period according to formula $\Delta B = \frac{h}{eA} = \frac{2\hbar}{eR^2}$. The other feature (ii) is a result of the stabilization of the anticlockwise loop of the current within the ring by the Lorentz force (see Fig. 18.3b) and the discussion in the precedent section) that increases the number of turns of the electron circulation around the ring.

Figures 18.11, 18.12 and 18.13 were obtained for the lowest subband transport $\nu = 2$. For higher ν the AB oscillations become pronounced for $B > 10$ T (Fig. 18.11a), only when the corresponding resonant lines can be resolved in Fig. 18.11b in this energy range. Fig. 18.14 shows the Fourier transform of the signal for the range of (0, 10)T (Fig. 18.14a) and (10, 30)T (Fig. 18.14b). We conclude that the magnetic field enhances the higher harmonics also for larger filling factors.

The magnetic deflection in order to be effective requires that the cyclotron radius is comparable or smaller to the channels and the junctions. Thus the effects of the Lorentz force get stronger for increased channel widths: In Fig. 18.15 the results for the ring radii to $R_1 = 23.4$ nm and $R_2 = 48.95$ nm are shown for conductance and the resonance counter. For $B \in (0, 10)$T one observes both the lines which grow and decrease in the energy with B – due to the resonant states of both current orientations as discussed above for the side attached GaAs ring (Figs. 18.8, 18.9 and 18.10). However, above 10 T the conductance plot (Fig. 18.15a) resolves only the states which go down in the energy (clockwise currents, magnetic moment antiparallel to the external field) with an increase of B. In contrast – the stability diagram (Fig. 18.15b) obtained for the resonance counter in the stabilization method retains only the states that increase in the energy with growing B. This apparent contradiction can be explained by analysis of the results in a closer resolution. Figure 18.17 shows the cross section of Fig. 18.15. We can see that the double peak structure which is present at low magnetic

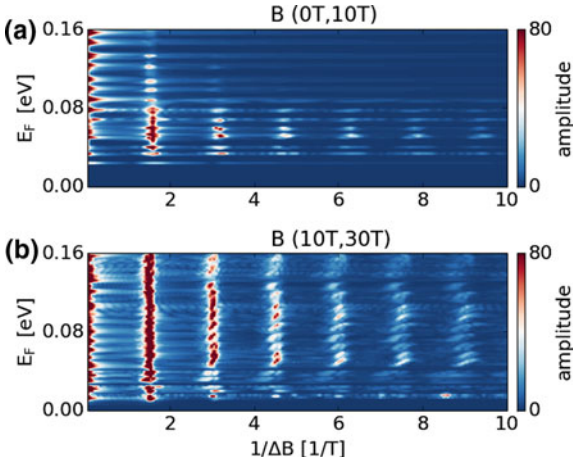

Fig. 18.14 Fourier transform of Fig. 18.11a for $B \in (0, 10\text{T})$ (**a**), and for $B \in (10\text{T}, 30\text{T})$ (**b**). After [36]

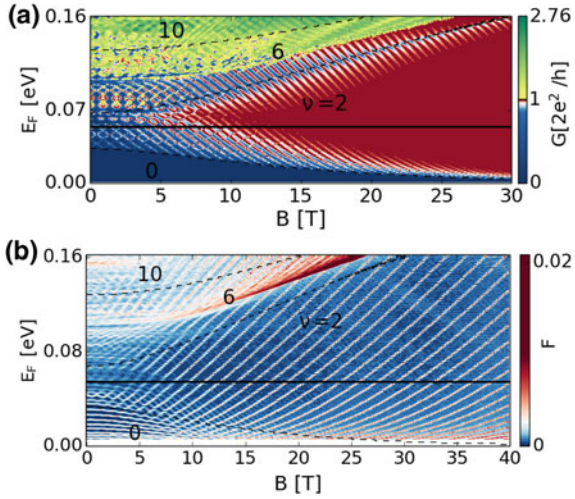

Fig. 18.15 Same as Fig. 18.11 only for a wider ring to $R_1 = 23.4$ nm and $R_2 = 48.95$ nm. After [36]

field starts to evolve at higher B with one of the peaks of the series getting wider and the other narrower. We find that the peaks that get wider correspond to the magnetic dipole moment generated by the clockwise current circulation (Fig. 18.16a) parallel to the external magnetic field, while the narrow dips appear with an anticlockwise current (Fig. 18.16b) and antiparallel magnetic moment orientation. The shifts of the peaks (Fig. 18.15a) and dips (Fig. 18.15b) in energy are consistent with the interaction of the magnetic moment with the external field given by the projection of the moment on the external field vector $\Delta E = \vec{\mu} \cdot \vec{B}$. At high external field the dips of conductance become too thin to be resolved on the 2D conductance plot (Fig. 18.17) and the peaks of $T = 1$ for $\mu > 0$ extend to cover most of the B scale at high field.

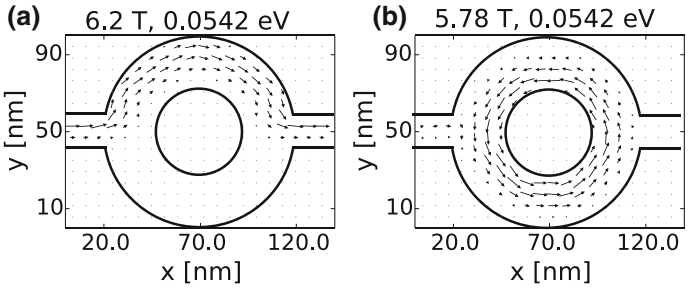

Fig. 18.16 The current distribution for the results of Fig. 18.17 for **a** $B = 6.2$ T (a peak of conductance) and **b** for $B = 5.78$ T (a dip of conductance). After [36]

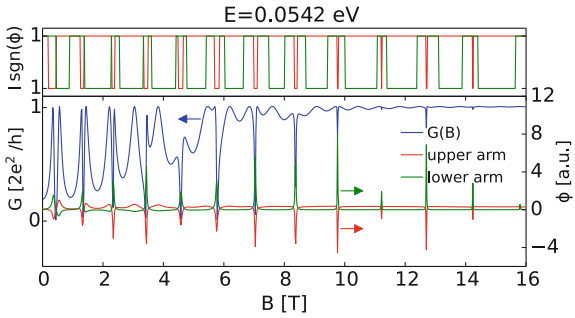

Fig. 18.17 Same as Fig. 18.12 only for a wider ring to $R_1 = 23.4$ nm and $R_2 = 48.95$ nm. The conductance plotted in blue is a cross section of Fig. 18.15 for $E = 0.0542$ eV. After [36]

The resonance/antiresonance width is related to the lifetime of the quasibound states that participate in the Fano interference. The lifetime of the antiresonances with $\mu < 0$ (with circulation as in Fig. 18.16b) becomes very large. The quasibound state rotates within the inner core of the ring and becomes decoupled from the incident current – and disappears from the conductance plot of Fig. 18.15a. The lifetime of the states with the opposite current circulation (Fig. 18.16a), on the other hand, becomes very small since their coupling to the lead currents is increased which removes their presence from the stability plot of Fig. 18.15b.

The change of the clockwise and anticlockwise current paths within the ring has also consequences on the Aharonov-Bohm periodicity since the flux of the external magnetic field threading the current loop becomes unequal for the two current orientations. In Fig. 18.15a, b one notices that below 10 T both the lines that grow and decrease with B appear at the same energy with the same period in B. However, at higher magnetic field the resonances that decrease with B (Fig. 18.15a) appear with a distinctly shorter period than the ones that grow in the energy (Fig. 18.15b). Similarly, opposite shifts for the two current circulations can be resolved in Fig. 18.16.

Figure 18.17 shows that the ring becomes transparent to electrons at high magnetic field. The absence of backscattering is a well known feature of the quantum Hall regime. In our case the current takes a single arm of the ring which attenuates the Aharonov-Bohm oscillations. The effect of the Lorentz force in the attenuation of the Aharonov-Bohm oscillation was predicted in [101]. For the three-terminal device the

effect was theoretically shown to be accompanied by an imbalance of the electron transfer to the two output leads [102]. An experimental verification of this finding was given in [103], with the elastic scattering phenomena described in [104].

18.6 Summary and Conclusions

We have discussed a proposal for formation of an Aharonov-Bohm interferometer by an electrostatic induction of a circular closed n-p junction within the graphene nanoribbon in the quantum Hall conditions. The proposal employs a floating gate of e.g. the tip of an atomic force microscope, that can give rise to a point like perturbation to the potential landscape seen by the carriers, the susceptibility of graphene to electrostatic doping, and the confinement of the currents at the n-p junction in graphene. The states with persistent current around the junction enter into Fano resonance with the edge currents that determine the conductance in the quantum Hall effect regime. The Fano interference has Aharonov-Bohm periodicity and the width of the resonances is determined by the lifetime of the quasibound states, which can be controlled by both the external magnetic field and the gate voltage. The gate voltage also determines the radius of the junction and hence the Aharonov-Bohm period on the magnetic field scale.

We have discussed the magnetic deflection effects which stabilize the junction currents in the context of the quantum rings etched in III-V semiconductor and in graphene. The most striking difference is that the Aharonov-Bohm interferometer formed by the n-p junction supports the quasibound resonances that produce only the magnetic dipole moment that is antiparallel to the external magnetic field, while for the etched rings both series of resonances are present. We indicated that the magnetic forces contribute to stabilization of the resonances with the magnetic dipole moment antiparallel to the external magnetic field which is responsible for appearance of the high Fourier harmonics in the quantum Hall regime. On the other hand, the resonances with the magnetic dipole moment antiparallel to the external magnetic field tend to lift the Aharonov-Bohm effect by injection of the current into a single arm of the etched quantum ring.

Acknowledgements This work was supported by the National Science Centre (NCN) according to decision DEC-2015/17/B/ST3/01161, by PL-Grid infrastructure and by Ministry of Science and Higher Education within the AGH University of Science and Technology statutory activity task no. 11.11.220.01.

References

1. A.H. Castro Neto, F. Guinea, N.M.R. Peres, K.S. Novoselov, A.K. Geim, Rev. Mod. Phys. **81**, 109 (2009)

2. K. Bolotin, K. Sikes, Z. Jiang, M. Klima, G. Fudenberg, J. Hone, P. Kim, H. Stormer, Solid. State. Commun. **146**, 351 (2008)
3. L. Banszerus, M. Schmitz, S. Engels, M. Goldsche, K. Watanabe, T. Taniguchi, B. Beschoten, C. Stampfer, Nano Lett. **16**, 1387 (2016)
4. M.I. Katsnelson, K.S. Novoselov, A.K. Geim, Nat. Phys. **2**, 620 (2006)
5. A.V. Shytov, M.S. Rudner, L.S. Levitov, Phys. Rev. Lett. **101**, 156804 (2008)
6. A.F. Young, P. Kim, Nat. Phys. **5**, 222 (2009)
7. A.L. Grushina, D.-K. Ki, A.F. Morpurgo, Appl. Phys. Lett. **102**, 223102 (2013)
8. T.K. Ghosh, A. De Martino, W. Häusler, L. Dell'Anna, R. Egger, Phys. Rev. B **77**, 081404 (R) (2008)
9. D.A. Abanin, L.S. Levitov, Science **317**, 641 (2007)
10. J. Tworzydło, I. Snyman, A.R. Akhmerov, C.W.J. Beenakker, Phys. Rev. B **76**, 035411 (2007)
11. V.V. Cheianov, V. Falḱo, B.L. Altshuler, Science **315**, 1252 (2007)
12. S. Chen, Z. Han, M. Elahi, K.M. Habib, L. Wang, B.W.Y. Gao, T. Taniguchi, K. Watanabe, J. Hone, A. Ghosh, C. Dean, Science **353**, 6307 (2016)
13. P. Rickhaus, R. Maurand, M.-H. Liu, M. Weiss, K. Richter, C. Schönenberger, Nat. Commun. **4**, 2342 (2013)
14. T. Taychatanapat, J.Y. Tan, Y. Yeo, K. Watanabe, T. Taniguchi, B. Özyilmaz, Nat. Commun. **6**, 6093 (2015)
15. G.-H. Lee, G.-H. Park, H.-J. Lee, Nat. Phys. **11**, 925 (2015)
16. M.-H. Liu, C. Gorini, K. Richter, Phys. Rev. Lett. **118**, 066801 (2017)
17. J.R. Williams, L. DiCarlo, C.M. Marcus, Science **317**, 638 (2007)
18. B. Huard, J.A. Sulpizio, N. Stander, K. Todd, B. Yang, D. Goldhaber-Gordon, Nat. Phys. **98**, 236803 (2007)
19. B. Özyilmaz, P. Jarillo-Herrero, D. Efetov, D.A. Abanin, L.S. Levitov, P. Kim, Phys. Rev. Lett. **99**, 166804 (2007)
20. J.R. Williams, T. Low, M.S. Lundstrom, C.M. Marcus, Nat. Nano. **6**, 222 (2011)
21. M. Barbier, G. Papp, F.M. Peeters, Appl. Phys. Lett. **100**, 16 (2012)
22. N. Davies, A.A. Patel, A. Cortijo, V. Cheianov, F. Guinea, V.I. Fal'ko, Phys. Rev. B **85**, 155433 (2012)
23. J.R. Williams, C.M. Marcus, Phys. Rev. Lett. **107**, 046602 (2011)
24. P. Carmier, C. Lewenkopf, D. Ullmo, Phys. Rev. B **84**, 195428 (2011)
25. J.-C. Chen, X.C. Xie, Q.-F. Sun, Phys. Rev. B **86**, 035429 (2012)
26. A. Cresti, G. Grosso, G.P. Parravicini, Phys. Rev. B **77**, 233402 (2008)
27. S.P. Milovanović, M. Ramezani Masir, F.M. Peeters, J. Appl. Phys. **115**, 043719 (2014)
28. S.P. Milovanović, M. Ramezani Masir, F.M. Peeters, Appl. Phys. Lett. **105**, 123507 (2014)
29. P. Rickhaus, P. Makk, M.-H. Liu, E. Tóvári, M. Weiss, R. Maurand, K. Richter, C. Schönenberger, Nat. Commun. **6**, 6470 (2015)
30. Y. Liu, R.P. Tiwari, M. Brada, C. Bruder, F.V. Kusmartsev, E.J. Mele, Phys. Rev. B **92**, 235438 (2015)
31. M. Zarenia, J.M. Pereira, F.M. Peeters, G.A. Farias, Phys. Rev. B **87**, 035426 (2013)
32. L. Oroszlány, P. Rakyta, A. Kormányos, C.J. Lambert, J. Cserti, Phys. Rev. B **77**, 081403 (2008)
33. K. Kolasiński, A. Mreńca-Kolasińska, B. Szafran, Phys. Rev. B **95**, 045304 (2017)
34. J.E. Müller, Phys. Rev. Lett. **68**, 385 (1992)
35. A. Mreńca-Kolasińska, S. Heun, B. Szafran, Phys. Rev. B **93**, 125411 (2016)
36. A. Mreńca-Kolasińska, B. Szafran, Phys. Rev. B **94**, 195315 (2016)
37. K. Wakabayashi, Y. Takane, M. Yamamoto, M. Sigrist, Carbon **47**, 124 (2009)
38. D. Cabosart, S. Faniel, F. Martins, B. Brun, A. Felten, V. Bayot, B. Hackens, Phys. Rev. B **90**, 205433 (2014)
39. S. Russo, J.B. Oostinga, D. Wehenkel, H.B. Heersche, S.S. Sobhani, L.M.K. Vandersypen, A.F. Morpurgo, Phys. Rev. B **77**, 085413 (2008)
40. D. Smirnov, H. Schmidt, R.J. Haug, Appl. Phys. Lett. **100**, 203114 (2012)
41. D. Smirnov, J.C. Rode, R.J. Haug, Appl. Phys. Lett. **105**, 082112 (2014)

42. M. Huefner, F. Molitor, A. Jacobsen, A. Pioda, C. Stampfer, K. Ensslin, T. Ihn, New J. Phys. **12**, 043054 (2010)
43. A. Rahman, J.W. Guikema, S.H. Lee, N. Marković, Phys. Rev. B **87**, 081401(R) (2013)
44. P. Recher, B. Trauzettel, A. Rycerz, Y.M. Blanter, C.W.J. Beenakker, A.F. Morpurgo, Phys. Rev. B **76**, 235404 (2007)
45. R. Jackiw, A.I. Milstein, S.-Y. Pi, I.S. Terekhov, Phys. Rev. B **80**, 033413 (2009)
46. J. Schelter, D. Bohr, B. Trauzettel, Phys. Rev. B **81**, 195441 (2010)
47. D. Faria, A. Latgé, S.E. Ulloa, N. Sandler, Phys. Rev. B **87**, 241403 (2013)
48. J. Wurm, M. Wimmer, H.U. Baranger, K. Richter, Semicond. Sci. Technol. **25**, 034003 (2010)
49. Z. Wu, Z.Z. Zhang, K. Chang, F.M. Peeters, Nanotechnology **21**, 185201 (2010)
50. D.S.L. Abergel, V.M. Apalkov, T. Chakraborty, Phys. Rev. B **78**, 193405 (2008)
51. D.R. da Costa, A. Chaves, M. Zarenia, J.M. Pereira, G.A. Farias, F.M. Peeters, Phys. Rev. B **89**, 075418 (2014)
52. P. Hewageegana, V. Apalkov, Phys. Rev. B **77**, 245426 (2008)
53. C.A. Downing, D.A. Stone, M.E. Portnoi, Phys. Rev. B **84**, 155437 (2011)
54. P. Rakyta, E. Tóvári, M. Csontos, S. Csonka, A. Csordás, J. Cserti, Phys. Rev. B **90**, 125428 (2014)
55. M.A. Topinka, B.J. LeRoy, S.E.J. Shaw, E.J. Heller, R.M. Westervelt, K.D. Maranowski, A.C. Gossard, Science **289**, 2323 (2000)
56. M.A. Topinka, B.J. LeRoy, R.M. Westervelt, S.E.J. Shaw, R. Fleischmann, E.J. Heller, K.D. Maranowski, A.C. Gossard, Nature **410**, 183 (2001)
57. A.A. Kozikov, R. Steinacher, C. Rössler, T. Ihn, K. Ensslin, C. Reichl, W. Wegscheider, Nano Lett. **15**, 7994 (2015)
58. M.P. Jura, M.A. Topinka, M. Grobis, L.N. Pfeiffer, K.W. West, D. Goldhaber-Gordon, Phys. Rev. B **80**, 041303 (2009)
59. H. Sellier, B. Hackens, M.G. Pala, F. Martins, S. Baltazar, X. Wallart, L. Desplanque, V. Bayot, S. Huant, Semicond. Sci. Technol. **26**, 064008 (2011)
60. S. Morikawa, Z. Dou, S.-W. Wang, C.G. Smith, K. Watanabe, T. Taniguchi, S. Masubuchi, T. Machida, M.R. Connolly, Appl. Phys. Lett. **24**, 243102 (2015)
61. S. Bhandari, G.-H. Lee, A. Klales, K. Watanabe, T. Taniguchi, E. Heller, P. Kim, R.M. Westervelt, Nano Lett. **16**, 1690 (2016)
62. V.E. Calado, S.-E. Zhu, S. Goswami, Q. Xu, K. Watanabe, T. Taniguchi, G.C.A.M. Janssen, L.M.K. Vandersypen, Appl. Phys. Lett. **104**, 023103 (2014)
63. P. Rakyta, A. Kormányos, J. Cserti, P. Koskinen, Phys. Rev. B **81**, 115411 (2010)
64. T. Stegmann, A. Lorke, Ann. Phys. (Berlin) **527**, 723 (2015)
65. T. Taychatanapat, K. Watanabe, T. Taniguchi, P. Jarillo-Herrero, Nat. Phys. **9**, 225 (2013)
66. B. Szafran, Phys. Rev. B **84**, 075336 (2011)
67. K. Kolasiński, B. Szafran, Phys. Rev. B **88**, 165306 (2013)
68. M.-H. Liu, P. Rickhaus, P. Makk, E. Tóvári, R. Maurand, F. Tkatschenko, M. Weiss, C. Schönenberger, K. Richter, Phys. Rev. Lett. **114**, 036601 (2015)
69. A. Mreńca, K. Kolasiński, B. Szafran, Semicond. Sci. Technol. **30**, 085003 (2015)
70. K. Kolasiński, B. Szafran, B. Brun, H. Sellier, Phys. Rev. B **94**, 075301 (2016)
71. M. Zwierzycki, P.A. Khomyakov, A.A. Starikov, K. Xia, M. Talanana, P.X. Xu, V.M. Karpan, I. Marushchenko, I. Turek, G.E.W. Bauer, G. Brocks, P.J. Kelly, Phys. Stat. Sol. (b) **245**, 623 (2008)
72. S. Datta, *Electronic Transport in Mesoscopic Systems* (Cambridge University Press, Cambridge, 1997)
73. K. Wakabayashi, Phys. Rev. B **64**, 125428 (2001)
74. L. Brey, H.A. Fertig, Phys. Rev. B **73**, 235411 (2006)
75. S. Sutar, E.S. Comfort, J. Liu, T. Taniguchi, K. Watanabe, J.U. Lee, Nano Lett. **12**, 4460 (2012)
76. B.L. Altshuler, A.G. Aronov, B.Z. Spivak, DYu. Sharvin, YuV Sharvin, JETP Lett. **35**, 588 (1982)
77. C. Benjamin, A.M. Jayannavar, Phys. Rev. B **65**, 153309 (2002)

78. Y. Aharonov, D. Bohm, Phys. Rev. **115**, 485 (1959)
79. X. Liu, J.B. Oostinga, A.F. Morpurgo, L.K. Vandersypen, Phys. Rev. B **80**, 121407 (2009)
80. R.A. Webb, S. Washburn, Phys. Today **41**, 46 (1988)
81. U. Fano, Phys. Rev. **124**, 1866 (1961)
82. A.A. Clerk, X. Waital, P.W. Brouwer, Phys. Rev. Lett. **86**, 4636 (2001)
83. M.E. Torio, K. Hallberg, S. Flach, A.E. Miroshnichenko, M. Titov, Eur. Phys. J. B **37**, 399 (2004)
84. M. Lee, C. Bruder, Phys. Rev. B **73**, 085315 (2006)
85. K. Kobayashi, H. Aikawa, S. Katsumoto, Y. Ire, Phys. Rev. Lett. **88**, 256806 (2002)
86. M.E. Torio, K. Hallberg, A.H. Ceccatto, C.R. Proetto, Phys. Rev. B **65**, 085302 (2002)
87. T.F. Fang, W. Zuo, J.Y. Chen, Phys. Rev. B **77**, 125136 (2008)
88. B.P. Bułka, P. Stefański, Phys. Rev. Lett. **86**, 5128 (2001)
89. K. Kang, S.Y. Cho, J.J. Kim, S.C. Shin, Phys. Rev. B **63**, 113304 (2001)
90. J. Göres, D. Goldhaber-Gordon, S. Heemeyer, M.A. Kastner, H. Shtrikman, D. Mahalu, U. Meirav, Phys. Rev. B **62**, 2188 (2000)
91. V.A. Mandelshtam, T.R. Ravuri, H.S. Taylor, Phys. Rev. Lett. **70**, 1932 (1993)
92. L. Wendler, V.M. Fomin, A.A. Krokhin, Phys. Rev. B **50**, 4642 (1994)
93. L. Wendler, V.M. Fomin, A.V. Chaplik, A.O. Govorov, Phys. Rev. B **54**, 4794 (1996)
94. H. Xu, L. Huang, Y.-C. Lai, C. Grebogi, Sci. Rep. **5**, 8963 (2015)
95. G.O. de Sousa, D.R. da Costa, A. Chaves, G.A. Farias, F.M. Peeters, Phys. Rev. B **95**, 205414 (2017)
96. M. Büttiker, Phys. Rev. Lett. **57**, 1761 (1986)
97. B. Szafran, M. Poniedzialek, Phys. Rev. B **80**, 155334 (2009)
98. Z.D. Kvon, D.A. Kozlov, E.B. Olshanetsky, A.E. Plotnikov, A.V. Latyshev, J.C. Portal, Sol. Stat. Comm. **147**, 230 (2008)
99. T.-M. Chen, M. Pepper, I. Farrer, D.A. Ritchie, G.A.C. Jones, Appl. Phys. Lett. **103**, eid 093503 (2013)
100. S. Morikawa, Z. Dou, S.-W. Wang, C.G. Smith, K. Watanabe, T. Taniguchi, S. Masubuchi, T. Machida, M.R. Connolly, Appl. Phys. Lett. **107**, 243102 (2015)
101. B. Szafran, F.M. Peeters, Phys. Rev. B **72**, 165301 (2005)
102. B. Szafran, F.M. Peeters, Euro. Lett. **70**, 810 (2005)
103. E. Strambini, V. Piazza, G. Biasiol, L. Sorba, F. Beltram, Phys. Rev. B **79**, 195443 (2009)
104. B. Szafran, M.R. Poniedzialek, Phys. Rev. B **82**, 075320 (2010)

Index

V.M. Fomin (ed.), *Physics of Quantum Rings*, NanoScience and Technology,
https://doi.org/10.1007/978-3-319-95159-1